

NO-A152 547

VIBRATION DAMPING WORKSHOP PROCEEDINGS HELD AT LONG
BEACH CALIFORNIA ON 2.. (U) AIR FORCE WRIGHT
AERONAUTICAL LABS WRIGHT-PATTERSON AFB OH L ROGERS

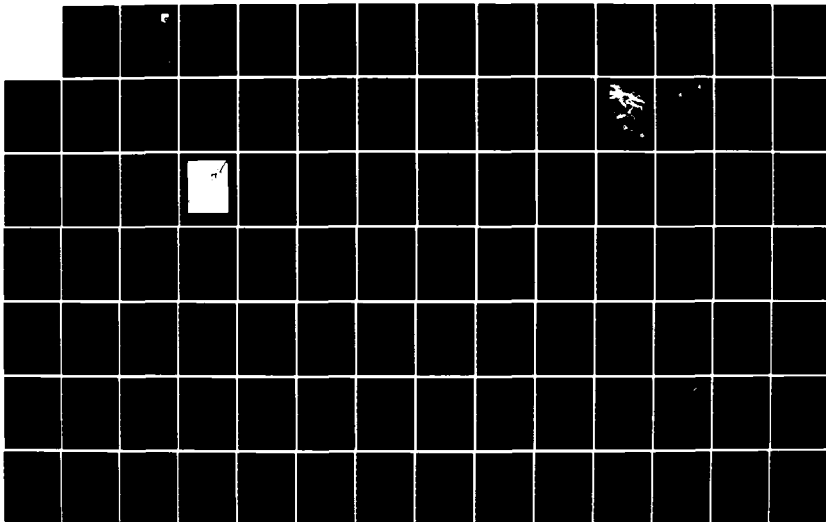
1/11

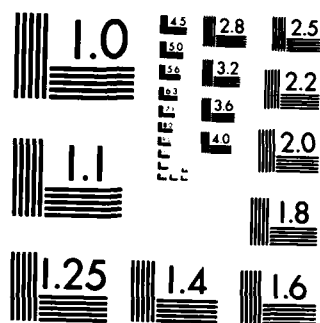
UNCLASSIFIED

11 NOV 84 AFMAL-TR-84-3064

F/G 20/11

NL





MICROCOPY RESOLUTION TEST CHART
NATIONAL BUREAU OF STANDARDS-1963-A

AD-A152 547

AFWAL-TR-84-3064

10



VIBRATION DAMPING 1984 WORKSHOP PROCEEDINGS

Dr. Lynn Rogers, Editor

November 1984

DTIC FILE COPY

Approved for public release; distribution unlimited.

FLIGHT DYNAMICS LABORATORY
AIR FORCE WRIGHT AERONAUTICAL LABORATORIES
AIR FORCE SYSTEMS COMMAND
WRIGHT-PATTERSON AIR FORCE BASE, OHIO 45433

DTIC
ELECTE
APR 16 1985
S D

85 3 26 060

UNCLASSIFIED

SECURITY CLASSIFICATION OF THIS PAGE

REPORT DOCUMENTATION PAGE				
1a. REPORT SECURITY CLASSIFICATION UNCLASSIFIED		1b. RESTRICTIVE MARKINGS		
2a. SECURITY CLASSIFICATION AUTHORITY		3. DISTRIBUTION/AVAILABILITY OF REPORT Approved for public release; distribution unlimited.		
2b. DECLASSIFICATION/DOWNGRADING SCHEDULE				
4. PERFORMING ORGANIZATION REPORT NUMBER(S) AFWAL-TR-84-3064		5. MONITORING ORGANIZATION REPORT NUMBER(S)		
6a. NAME OF PERFORMING ORGANIZATION Advanced Metallic Structures Adv. Development Prog. Office		6b. OFFICE SYMBOL (If applicable) AFWAL/FIBAA		7a. NAME OF MONITORING ORGANIZATION
6c. ADDRESS (City, State and ZIP Code) Wright-Patterson Air Force Base, OH 45433		7b. ADDRESS (City, State and ZIP Code)		
8a. NAME OF FUNDING/SPONSORING ORGANIZATION		8b. OFFICE SYMBOL (If applicable)		9. PROCUREMENT INSTRUMENT IDENTIFICATION NUMBER
8c. ADDRESS (City, State and ZIP Code)		10. SOURCE OF FUNDING NOS.		
		PROGRAM ELEMENT NO.	PROJECT NO.	TASK NO.
		63211F	486U	11
11. TITLE (Include Security Classification) (UNCLASSIFIED) Vibration Damping 1984 Workshop Proceedings		WORK UNIT NO. 02		
12. PERSONAL AUTHOR(S) Dr. Lynn Rogers				
13a. TYPE OF REPORT Summary		13b. TIME COVERED FROM Feb 78 TO Feb 84		14. DATE OF REPORT (Yr., Mo., Day) 1984 November
15. PAGE COUNT 1,002				
16. SUPPLEMENTARY NOTATION				
17. COSATI CODES			18. SUBJECT TERMS (Continue on reverse if necessary and identify by block number)	
FIELD	GROUP	SUB. GR.	Vibration damping, controls/structure interaction.	
19. ABSTRACT (Continue on reverse if necessary and identify by block number)				
Individual papers of the Vibration Damping Workshop held 27-29 February 1984 in Long Beach, California, are presented. The subjects included: mechanical properties of polymers; experimental methods; damping in metal matrix composites; friction damping; design of damping structure; modal damping values; and applications of damping, etc.				
20. DISTRIBUTION/AVAILABILITY OF ABSTRACT UNCLASSIFIED/UNLIMITED <input checked="" type="checkbox"/> SAME AS RPT. <input type="checkbox"/> DTIC USERS <input type="checkbox"/>			21. ABSTRACT SECURITY CLASSIFICATION UNCLASSIFIED	
22a. NAME OF RESPONSIBLE INDIVIDUAL Dr. Lynn Rogers			22b. TELEPHONE NUMBER (Include Area Code) (513) 255-5664	22c. OFFICE SYMBOL AFWAL/FIBAA

DD FORM 1473 83 APR

EDITION OF 1 JAN 73 IS OBSOLETE.

UNCLASSIFIED

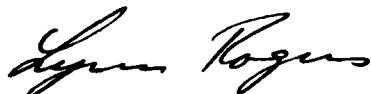
SECURITY CLASSIFICATION OF THIS PAGE

NOTICE

When Government drawings, specifications, or other data are used for any purpose other than in connection with a definitely related Government procurement operation, the United States Government thereby incurs no responsibility nor any obligation whatsoever; and the fact that the government may have formulated, furnished, or in any way supplied the said drawings, specifications, or other data, is not to be regarded by implication or otherwise as in any manner licensing the holder or any other person or corporation, or conveying any rights or permission to manufacture use, or sell any patented invention that may in any way be related thereto.

This report has been reviewed by the Office of Public Affairs (ASD/PA) and is releasable to the National Technical Information Service (NTIS). At NTIS, it will be available to the general public, including foreign nations.

This technical report has been reviewed and is approved for publication.



LYNN ROGERS, Ph.D.
Project Engineer



FRANK D. BOENSCH, Program Manager
Advanced Metallic Structures ADPO
Structures & Dynamics ADP Branch

FOR THE COMMANDER



ROGER J. HEGSTROM, COL, USAF
Chief, Structures & Dynamics Division

"If your address has changed, if you wish to be removed from our mailing list, or if the addressee is no longer employed by your organization please notify AFWAL/FIBAA, W-PAFB, OH 45433 to help us maintain a current mailing list".

Copies of this report should not be returned unless return is required by security considerations, contractual obligations, or notice on a specific document.

FOREWORD

This publication includes the individual papers of the Vibration Damping Workshop held 27-29 February 1984 in Long Beach, California. The Workshop was sponsored by the Flight Dynamics Laboratory, Air Force Wright Aeronautical Laboratories, Structures and Dynamics Division, Advanced Metallic Structures, Advanced Development Program Office (AFWAL/FIBAA).

It is desired to transfer vibration damping technology in a timely manner within the aerospace community thereby stimulating research, development, and applications.

Accession For	
NTIS GRA&I	<input checked="" type="checkbox"/>
DTIC TAB	<input type="checkbox"/>
Unannounced	<input type="checkbox"/>
Justification	
By _____	
Distribution/	
Availability Codes	
Dist	Avail and/or Special
A-1	



TABLE OF CONTENTS

	<u>SECTION</u>
SOME MUSINGS ON HOW TO MAKE DAMPING A CREATIVE FORCE IN DESIGN Professor James W. Mar	A-1
FRACTIONAL CALCULUS TO REPRESENT COMPLEX MODULUS Dr. Lynn Rogers	B-1
COMPARISON OF DAMPING MATERIAL PROPERTIES MEASURED BY A NUMBER OF ORGANIZATIONS M. L. Parin	C-1
INFLUENCE OF THE GEOMETRIC STIFFNESS ON THE DETERMINATION OF THE DYNAMIC CHARACTERISTICS OF VISCOELASTIC MATERIAL PROPERTIES M. Lalanne, P. Berthier, J. Der Hagopian, I. A. R. El Halawani, and B. Duperray	D-1
COMPLEX MODULUS BEHAVIOR OF A VISCOELASTIC ADHESIVE MEASURED AT HARMONIC STRAIN AMPLITUDES OF 10^{-10} T. J. Lagnese and D. I. G. Jones	E-1
EXPERIMENTAL MEASUREMENT OF MATERIAL DAMPING FOR SPACE STRUCTURES Edward F. Crawley and Raymond L. Sheen	F-1
COULOMB FRICTION APPLICATIONS Professor H. A. Scarton	G-1
DAMPING APPLICATIONS IN TURBINE ENGINES R. L. Jay and D. W. Burns	H-1
CHARACTERISTICS OF DRY FRICTION DAMPING A. V. Srinivasan, B. N. Cassenti, and D. G. Cutts	I-1
PRACTICAL ASPECTS OF DRY FRICTION DAMPING IN TURBINES T. J. Oldakowski	J-1
DAMPING PROPERTIES OF STEAM TURBINE BLADES Neville F. Rieger	K-1
CONCEPTS AND EFFECTS OF DAMPING IN ISOLATORS James Kerley	L-1
RESEARCH ON FRICTION DAMPING IN JET ENGINES AT CARNEGIE-MELLON UNIVERSITY J. H. Griffin and J. Bielak	M-1

TABLE OF CONTENTS (CONTINUED)

	<u>SECTION</u>
FRICITION DAMPING STUDIES AT IMPERIAL COLLEGE C. F. Beards	N-1
A DERIVATION OF EQUIVALENT LINEAR VISCOUS AND ELASTIC CONSTANTS FOR VISCOELASTIC MATERIALS S. R. Dahl and R. B. Rice	O-1
COMPOSITE MATERIAL DAMPING USING IMPULSE TECHNIQUE C. T. Sun, B. T. Lee, and S. K. Chaturvedi	P-1
IMPROVED EXTENSIONAL MODULUS MEASUREMENTS FOR POLYMERS AND METAL MATRIX COMPOSITES Walter Madigosky	Q-1
MATERIAL DAMPING OF CARBON/EPOXY COMPOSITES BY MEANS OF FREE-FREE BEAM RESONANCE TESTS Daniel W. Haines	R-1
IMPROVEMENT OF DAMPING IN FIBER REINFORCED POLYMER COMPOSITES R. F. Gibson, S. A. Suarez, and L. R. Deobald	S-1
DYNAMIC MECHANICAL PROPERTIES OF GRAPHITE/ALUMINUM WIRES AT AUDIO-FREQUENCIES Gilbert F. Lee and Clifford W. Anderson	T-1
DAMPING BEHAVIOR OF METAL MATRIX COMPOSITES M. S. Misra and P. D. LaGreca	U-1
DAMPING IN METAL MATRIX COMPOSITES G. L. Steckel	V-1
DAMPING IN METAL-MATRIX COMPOSITES: MEASUREMENT AND MODELING H. M. Ledbetter and S. K. Datta	W-1
DAMPING MEASUREMENT BY DYNAMIC STIFFNESS METHODS David I. G. Jones and Agnes Muszyńska	X-1
A COMPARISON OF MEASURED SPACECRAFT MODAL DAMPING VALUES B. K. Wada and J. C. Chen	Y-1
STRUCTURAL DAMPING OF SHUTTLE ORBITER AND ASCENT VEHICLES D. L. Jensen	Z-1
MEASURED DAMPING OF SHUTTLE ACOUSTIC TEST STRUCTURES C. E. Wallace, Mark Mielke, and Jack Joanides	AA-1
AVERAGE LOSS FACTORS FOR USE IN STATISTICAL ENERGY ANALYSIS K. T. Brown and B. L. Clarkson	BB-1

TABLE OF CONTENTS (CONTINUED)

STRUCTURAL DAMPING POTENTIAL OF WAVEGUIDE ABSORBERS Eric E. Ungar and Leonard G. Kurzweil	<u>SECTION</u> CC-1
NEW PROPOSED DYNAMIC VIBRATION ABSORBERS FOR EXCITED STRUCTURES Helmut F. Bauer	DD-1
EXTENSIONS OF THE RITZ-GALERKIN METHOD FOR THE FORCED, DAMPED VIBRATIONS OF STRUCTURAL ELEMENTS A. W. Leissa and T. H. Young	EE-1
FINITE ELEMENT DESIGN OF VISCOELASTICALLY DAMPED STRUCTURES-- METHODS C. D. Johnson and D. A. Kienholz	FF-1
FINITE ELEMENT DESIGN OF VISCOELASTICALLY DAMPED STRUCTURES-- APPLICATIONS D. A. Kienholz, C. D. Johnson, E. M. Austin, and M. E. Schneider	GG-1
FINITE ELEMENT DESIGN OF VISCOELASTICALLY DAMPED STRUCTURES Conor D. Johnson, David A. Kienholz, Eric M. Austin, and Michael E. Schneider	HH-1
ON VIBRATION DAMPING ANALYSIS USING THE FINITE ELEMENT METHOD R. A. Brockman	II-1
RESULTS OF FINITE ELEMENT ANALYSIS OF DAMPED STRUCTURES Matthew F. Kluesener	JJ-1
SEGMENTING AND MECHANICAL ATTACHMENT OF CONSTRAINED VISCOELASTIC LAYER DAMPING TREATMENTS FOR FLEXURAL AND EXTENSIONAL WAVES Edward M. Kerwin, Jr. and P. W. Smith, Jr.	KK-1
VIBRATION ISOLATION OF AN ELEVATOR SYSTEM H. -S. Tzou and A. J. Schiff	LL-1
DESIGN EVALUATION AND FIELD QUALIFICATION OF A DAMPING SYSTEM FOR AN AUXILIARY POWER UNIT Michael L. Drake	MM-1
DAMPING APPLICATIONS IN MASS PRODUCTION A. D. Nashif	NN-1
LAMINATED DAMPED FUSELAGE STRUCTURES Richard A. Ely	OO-1

TABLE OF CONTENTS (CONTINUED)

	<u>SECTION</u>
BEAM DAMPERS FOR SKIN VIBRATION AND NOISE REDUCTION IN THE 747 R. N. Miles	PP-1
INTEGRATED DAMPED FUSELAGE STRUCTURE L. M. Butzel	QQ-1
USE OF SKIN DAMPING TREATMENTS TO CONTROL AIRFRAME DYNAMIC RESPONSE FOR INTERIOR NOISE CONTROL C. I. Holmer	RR-1
DAMPING APPLICATION TO SPACECRAFT T. S. Nishimoto	SS-1
APPLICATION OF DAMPING TO IMPROVE RELIABILITY OF IUS-TYPE SATELLITE EQUIPMENT - RELSAT PROGRAM Dr. Roy Ikegami, Mr. Clark J. Beck, and Mr. William J. Walker	TT-1
DAMPING IN SUPPORT STRUCTURES FOR SATELLITE EQUIPMENT RELIABILITY - RELSAT J. A. Staley and C. V. Stahle	UU-1
A DESIGN GUIDE FOR DAMPING OF AEROSPACE STRUCTURES J. Soovere, M. L. Drake, and V. R. Miller	VV-1
DAMPED OPTICS FOR PULSED LASER APPLICATIONS R. G. Jaeger and M. J. Laughlin	WW-1
DISTRIBUTED PIEZOELECTRIC-POLYMER ACTIVE VIBRATION CONTROL OF A CANTILEVER BEAM Thomas Bailey and Dr. James E. Hubbard, Jr.,	XX-1
AN EXPERIMENTAL STUDY OF PASSIVE DAMPING AND ACTIVE CONTROL OF LARGE SPACE STRUCTURES Dr. S. S. Simonian, C. S. Major, and Dr. R. Gluck	YY-1
SIZING OF DISCRETE VISCOUS DAMPERS ON A FLEXIBLE BODY IN THE PRESENCE OF A FIXED CONTROLLER George R. Rapacki and Dr. Robert B. Rice	ZZ-1
CRITICAL DAMPING IN COMPLEX STRUCTURES AND CONTROL SYSTEMS D. J. Inman	AAA-1
AN APPROACH TO THE SIZING OF DISCRETE VISCOUS STRUCTURAL DAMPERS USING AN EXTENSION OF THE FINITE ELEMENT APPROACH AND MODAL STRAIN ENERGY Dr. Robert B. Rice and Eric C. Dalton	BBB-1

TABLE OF CONTENTS (CONCLUDED)

	<u>SECTION</u>
FLEXIBLE STRUCTURE CONTROL IN THE FREQUENCY DOMAIN R. Harding and Dr. A. Das	CCC-1
PASSIVELY DAMPED JOINTS FOR ADVANCED SPACE STRUCTURES Richard W. Trudell, Lawrence Rehfield, Ambur Reddy, Jacky Purcz, and James Peebles	DDD-1
PASSIVE AND ACTIVE CONTROL OF SPACE STRUCTURES (PACOSS) Charles W. White	EEE-1
EFFECTS OF DISSIPATION OF ENERGY (DAMPING) IN PARAMETRIC RESONANCE RESPONSES R. M. Evan-Iwanowski	FFF-1

APPENDICES

1	FINAL PROGRAM AGENDA	1-1
2	LIST OF PAID REGISTRANTS	2-1

SOME MUSINGS ON HOW TO MAKE DAMPING A CREATIVE FORCE IN DESIGN

Keynote Speaker

Former Chief Scientist
U. S. Air Force

Professor James W. Mar
Massachusetts Institute of Technology
Department of Aeronautics and Astronautics
Cambridge, Massachusetts 02138

SOME MUSINGS ON HOW TO MAKE DAMPING A CREATIVE FORCE IN DESIGN

Professor James W. Mar
Massachusetts Institute of Technology
Department of Aeronautics and Astronautics
Cambridge, MA 02138

ABSTRACT

Some suggestions are advanced toward making damping a complete technology so that damping can become a creative force in structural design. Examples cited include the invention of mechanisms to enhance and control damping, the testing of structural joints in simulated zero-g, the measurement of material damping without aerodynamic forces and the testing of structures in the zero-g and high vacuum of space.

Lynn Rogers had suggested that the title "Who Needs Damping" as the subject for this opening talk. The answer is that everyone does but engineers who build structures to be used in the environment of Space need it even more. Having said that I could sit down and there would be more time for the substantive material of this workshop; that is probably the motivation for Lynn's suggestion. But I changed the title.

Calling this a "workshop" is rather foreboding. A "workshop" is defined by various acts of the British Parliament to be a place where only manual labor is used. One doesn't come to Southern California to perform manual labor. Consider the fact that my oil burner used 10 gallons of oil per day in January and you can understand why an invitation to speak here in Long Beach required only a few milli-seconds of debate. I would suggest that the next such gathering be called a symposium rather than a workshop. The American College Dictionary on page 1228 defines a 'symposium' as a convivial meeting for discussion usually following a dinner for drinking, conversation and intellectual entertainment.

My first encounter with structural damping occurred in doing flutter analyses wherein I filled out a big table of numbers and then drew a curve of 'g', the structural damping versus airplane airspeed (see fig. 1). The point where this curve crossed the $g=0$ line was defined as flutter. I remember being told by my boss to replot the curve because the crossing occurred at an airspeed below the specification value but no amount of fudging using a thick line or parallax could get the crossing at a higher speed. The use of 'g' in flutter analyses has always been a mystery to me. I accepted it because people are viewed as harbingers of bad news. The usual solution to a flutter problem is to add stiffness, change the mass distribution, add mass balance or all of the above. None of these kinds of solutions improve the performance of the airplane but instead something undesirable, i.e., flutter, is prevented

from occurring. Changing the value of 'g' is not amongst the bag of tools available to the flutter engineer. In fact, the use of 'g' in flutter analyses is a mathematical device to get an answer as opposed to being a realistic representation of the physics of the phenomena.

The terminology to describe damping is varied and foments misunderstanding. There are factors of pi and 2 which float in and out of calculations, thus making it difficult for all except the damping specialist to understand the engineering significance of quantitative numbers. In Table 1 are shown most of the common descriptions. There is eta and g which are variously referred to as the damping factor or loss factor. But g is more commonly used for the acceleration of gravity. Q is the quality factor which is the inverse of the damping factor, ψ is the specific damping capacity, ζ is the fraction of critical damping, δ is the log decrement of an experimentally determined time history of vibration amplitudes and then there is the complex modulus which properly describes the behavior of a viscoelastic material. These various parameters are used, sometimes indiscriminately, to describe the same physical processes. If the same physical process is being described then these various parameters are related to one another as shown in equation 1.

$$n = \frac{\psi}{2\pi} = g = \frac{1}{Q} = 2\zeta = \frac{E''}{E'} \frac{\delta}{\pi} \quad (1)$$

Do we really need all of these? I believe that this an appropriate time to eliminate some of these terms. Perhaps Dr. Rogers can spearhead an effort to write an Air Force specification and/or standard which will bring a common terminology to the field and thus tear down the 'Tower of Babel' which presently exists.

In order to make damping a creative force in design, the community of damping specialists has to pull together the various facets of damping into a coherent technology. For example, the design of compression critical design structures brings together weight analysis, structural stability, plasticity, manufacturing, materials and detail design. The designer has the methodology at hand so that he can compare sheet-stiffener concepts with sandwich construction and he can make tradeoffs between materials and structural loadings. Additionally, and of great importance, structural weight, the figure of merit, can be exhibited against the structural loading index in a dimensional fashion so that the chief engineer has a gut feeling for the efficacy of the results. The same is required for damping technology if it is to be a positive and creative force in design. This suggests that damping technology must be advanced to the stage where it must be possible to create damping, to control the magnitude and kind of damping, and to exhibit tradeoffs in a manner that allows the chief engineer to make choices based upon quantitative parameters.

I would like to share some musing on what kinds of steps need to be taken to make damping a creative force in design. A reading of the papers of this workshop will suggest other "things".

In order to make a positive contribution to design as opposed to being asked to verify that a design is adequate, it is necessary to create designs wherein the amount of damping can apriori be specified. Let me illustrate this notion by means of research carried out by Sarver (reference 1). He created a design for truss members such that coulomb friction is induced when the truss members are loaded.

This is schematically represented in this figure 2. Visualize a truss whose load carrying members are cylindrical tubes. Inside of these load carrying members are placed cylindrical damping tubes which are pressed tightly against the outer load carrying member. Conceptually the damping is the result of the relative motion between the two members which occurs as the load carrying member experiences tension and compression loadings. This is shown in the figure 3. There will be a threshold value of the load on the load carrying member below which there is no slippage and the load-deflection diagram is linear-elastic as shown in figure 3. If the loading has sufficient magnitude to cause slippage then the load-deflection diagram shows the familiar hysteresis loop. Sarver has conducted experiments to determine the amount, quality and the governing parameters. Additionally, he created a model which can be used for tradeoff studies. Two of the parameters are defined as follows:

$$\beta = \frac{\text{stiffness of damping member}}{\text{stiffness of load member}}$$

$$e = \frac{\text{specific modulus of damping member}}{\text{specific modulus of load member}}$$

β is the ratio of the stiffness of the damping member and the load member while e is the ratio of the specific moduli of the damping and load members, respectively. Intuitively, it should be obvious that the amount of damping as well as the threshold at which slippage occurs should be dependent on parameters of this type.

With this model, the damping factor g can be calculated as a function of β , the relative ratio of stiffnesses, and a normalized load which is the ratio of the peak load to the load which causes slippage over the entire length of the damping member. The other parameters which can be controlled by the designer are the friction between the load and damping members and the segmented lengths of the damping members.

The use of this method of creating damping permits structural design studies of systems without and with damping. As an example of what should be possible, consider a simple one-dimensional system which is modeled as a payload carried by a structure with some inherent damping modeled as a dashpot (see fig. 4). This system is under sinusoidal loading at its undamped natural frequency. This is the reference system.

The alternative to meeting the requirement by stiffness alone is to add friction damping. This is shown schematically in figure 5 where the payload mass is shown sitting on the structural mass and a damping mass is shown attached to the structural mass. The friction damping is modeled as a dashpot. This system is designed so as to minimize the total mass.

Quite dramatic decreases in total mass can be achieved as shown in this figure 6. The ordinate scale is the ratio of the structural masses of the two systems; in the damped system the mass ($M_T - M_p$) consists of (a) the structure to carry the load and (b) the structure to provide the damping. In the reference system the total mass, ($M_{T0} - M_p$), is the mass M_{K0} of the structure to carry the payload.

Such design studies can also compare active control systems with passively damped systems. This is shown conceptually in the figure 7 where the two coordinate axes are as in the previous figure. The curve labeled 'friction damping' is determined as before. The total mass associated with the curve marked 'active control' must include the mass of the control jets as well as that of the fuel to power the jets.

Structural technology even for an airplane is not at the stage where design can be accomplished solely with analysis and a computer. If that stage ever arrives then the design of airplanes will no longer be interesting. In space the zero-g and high vacuum presents to the structural designer new and interesting challenges. One is the simulation of zero-g. Very few of us have experienced zero-g. Table 2 lists some of the ways in which zero-g for structural testing can be simulated/attained. The launch method (ref. 2) consists of launching specimens into 'free fall'. A trajectory with an altitude of 6 feet results in a duration of zero-g of about one second. The classic free fall method is to drop specimens inside of a drop tower which is evacuated to a vacuum. There is such a facility at the Lewis Research Center with a height of about 300 feet which results in a zero-g duration of about 4 seconds. The stopping of the specimen back to one-g requires the dissipation of kinetic energy in a controlled fashion if reusability of the specimen and the instruments are desired. Another method of attaining zero-g is to be inside of an airplane which is flying parabolic maneuvers. A small airplane such as a Beech or Cessna can be in zero-g for about 3 seconds. This is one way to get a gut feeling for zero-g. You can appreciate that this is lots of fun for the experimenter who does not get airsick. NASA has a KC-135 based at Johnson Space Flight Center which is used for these purposes. A few years ago two MIT Aeronautics and Astronautics students, Mary Bowden and Dave Akin (ref. 4), performed experiments during some 90 zero-g maneuvers in the KC-135. A typical flight mission will attain zero-g about 30 times. The duration of zero-g in the KC-135 varies from 20 to 30 seconds. The activities taking place inside of the KC-135 (see figures 8 and 9) during those tests had as an objective the correlation of zero-g simulation using neutral buoyancy with the real thing (ref. 5). Of course, the ultimate laboratory for zero-g is in low earth orbit. The STS Orbiter spacecraft has a mid-deck in which experiments can be performed. But the real excitement will come when a structural experiment can be performed in a free flying mode. The possibility of being the payload specialist in such an experiment motivates many of students and the prospect even excites aged professors.

One of the interesting experiments which is best performed in a zero-g environment is the characterization of the structural joints of large space structures. In zero-g the joint is unloaded and its response to loads may include a dead band during which the joint may be moving with little or no resistance. There may be inherent or purposefully induced friction in the joint and at end of the zone of dead band, there may be an elastic impact. At very low frequencies, the advantageous method of analyzing the dynamic behavior of a joint which has friction, dead bands and other non-linear kinds of behavior is by flexural waves rather than by mode superposition.

The characterization of a joint presents many interesting experimental and analytical challenges. Professor Crawley and his students have been doing experiments for a few years (ref. 6). There is shown in figure 10 a schematic representation of two structural members connected by a joint. The finite element modeling of the two members must be joined to a compatible model of the joint. In order to experimentally determine the characteristics of a joint, Crawley and his students have devised a methodology which they have named 'force-state' mapping (see ref. 7). With modern sensors and sophisticated data acquisition equipment it is possible to simultaneously in time measure sufficient parameters to determine the salient characteristics of a joint.

These characteristics are exhibited in a three dimensional plot whose orthogonal axes are force minus mass times acceleration, displacement and velocity. Representations of joints with ideal behavior are shown in figures 10, 11, and 12. Figure 10 depicts an ideal linear spring while figure 11 shows the force map for an ideal viscous damper. Figure 12 shows the force map for an ideal sliding friction force. A real joint will exhibit a force map with combinations of all of these plus other kinds of behavior. With modern digital techniques the experimental data can be analyzed to yield a model which, because it is compatible with an analytical model such as one created by finite elements, can be inserted into the structural model. In order to obtain data free from gravity and atmospheric effects, Crawley and his students have designed a zero-g space simulation chamber with dimensions as shown in figure 13. It will be evacuated to a high vacuum of 10^{-8} torr and the vertical height permits the attainment of about one and three-quarters seconds of zero-g by launching specimens from the bottom. The size will accommodate the testing of reasonably sized specimens thus permitting the study of scale effects to permit extrapolation to large space structures.

The high vacuum will eliminate the damping due to the paddling action of the air. At low amplitudes of vibration, the damping factor from log decrement measurements as a function of the amount of atmosphere is shown in figure 13 (ref. 8). The damping due to air is equal to that due to the material. At larger amplitudes, the air damping is even more as shown in figure 14 (ref. 9). Thus the accurate characterization of damping requires a reasonably high vacuum.

The penultimate if not the ultimate experiment would be to build a structure in space and then to perform structural experiments in the zero-g

and high vacuum environment of space. There are a number of such experiments in the planning stages. One such is called "SADE" which is a Marshall Space Flight Center project as depicted in figure 15. Imagine the fun we could have with such a structure in low earth orbit! The SADE structure consists of deployed space frames joined together by members which are put into place by space engineers in EVA (extra-vehicular activity).

This workshop will suggest many other ideas which can contribute to the technology of damping. Research avenues will also become evident.

My present short list of research needs are centered on joints and mechanisms. Joints are used in deployable structures as well as in structures which must be assembled in space. These will have different kinds of characteristics. There is also a need for the invention of mechanisms to enhance damping and to control damping. These may be incorporated into joints. Thus damping technology requires invention and creativity as well as analytical capabilities. These are some necessary steps which need to be taken in order to make damping a positive and creative factor in the design of structures.

(1) Crawley, E.F., Sarver, G.L. and Mohr, D.G., "Experimental Measurement of Passive Material and Structural Damping For Flexible Space Structures," Acta Astronautica, Vol. 10, No. 5-6, pp. 381-393, 1983.

(2) Crawley, E.F. and Mohr, D.G., "Experimental Measurement of Material Damping in Free Fall with Tuneable Excitation," Presented at AIAA/ASME/ASCE/AHS Structures, Structural Dynamics and Materials Conference, Paper No. 83-0858-CP, Tahoe, NV, May 1983, will be published in AIAA Journal.

(3) Ronney, Paul, "Effect of Gravity on Laminar Premixed Gas Combustion," M.I.T. Ph.D. Thesis, March 1983.

(4) Bowden, M.L., "Dynamics of Manual Assembly of Large Space Structures in Weightlessness," M.I.T. M.S. Thesis, SSL#9-81, January 1981.

(5) Akin, D.L. and Bowden, M.L., "EVA Capabilities for the Assembly of Large Space Structures," IAF #82-393 (Pari), SSL# 32-82, September 1982.

(6) Crawley, E.F. and Sheen, R.L., "Experimental Measurement of Material Damping for Space Structures in Simulated Zero-G," M.I.T. Space System Laboratory #1-84, December 1983.

(7) Aubert, A.C., Crawley, E.F. and O'Donnell, K.J., "Measurement of the Dynamic Properties of Joints in Flexible Space Structures," M.I.T. Space System Laboratory #35-83, September 1983.

(8) Boyce, D.A., "Material Damping of Graphite/Epoxy Double Cantilever Beams," M.S. Degree, M.I.T., September 1979.

(9) Baker, W.E., Woolam, W.E. and Young, D. "Air and Internal Damping of Thin Cantilever Beams," Int. J. Mech. Sci., 1967, Vol. 9, pp. 743-66.

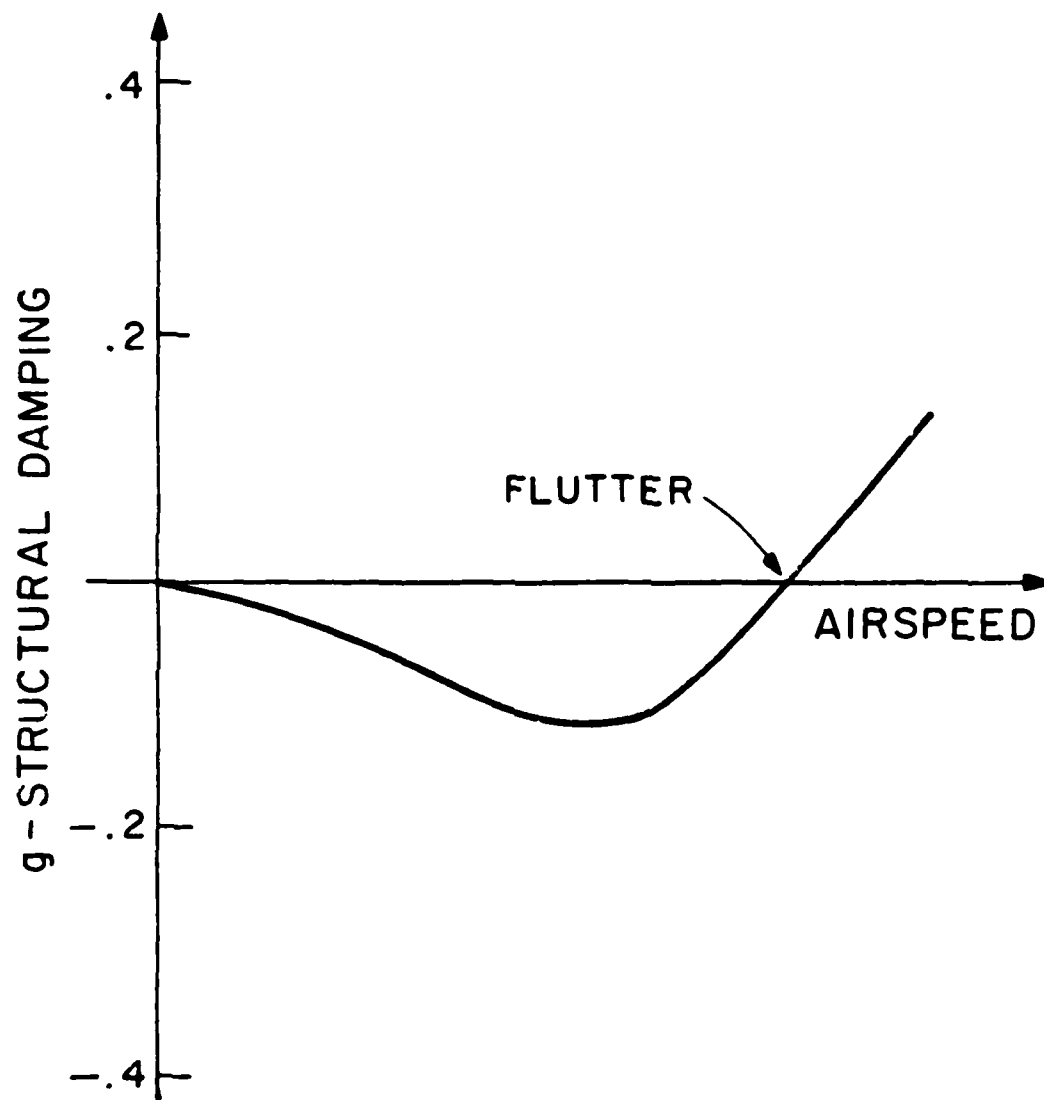


FIGURE 1
DAMPING VS. AIRSPEED

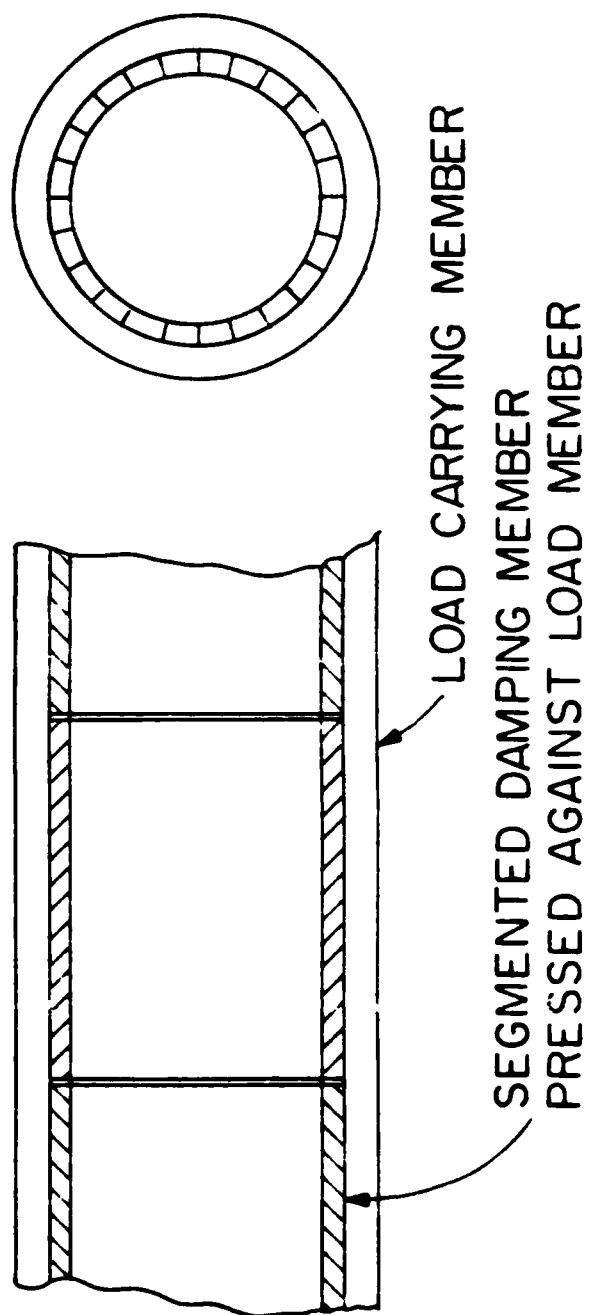


FIGURE 2
CONCEPT FOR CREATING FRICTION DAMPING

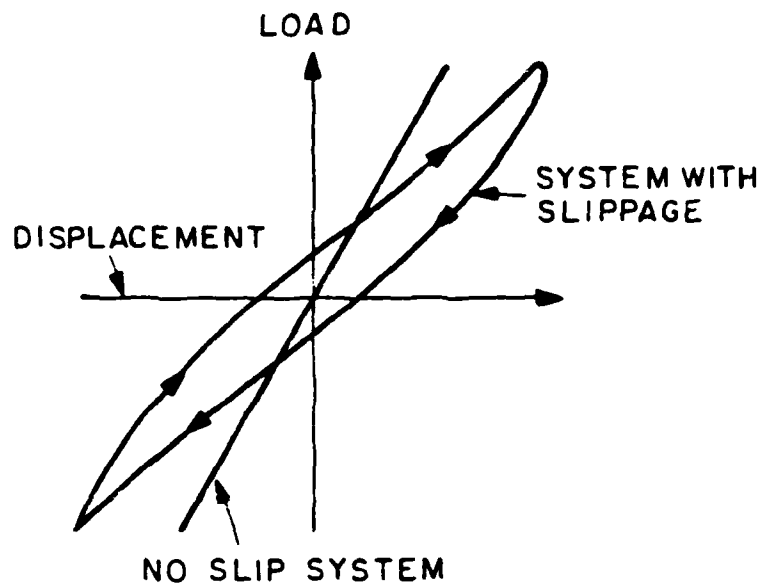


FIGURE 3
TYPICAL LOAD DEFLECTION DIAGRAMS

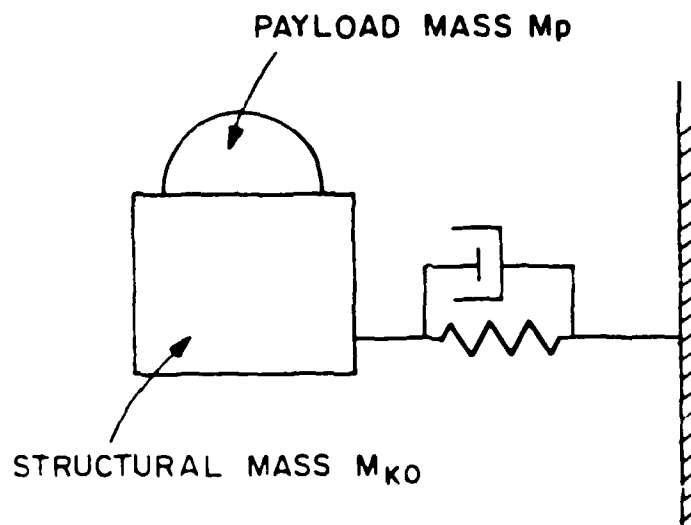


FIGURE 4
REFERENCE SYSTEM

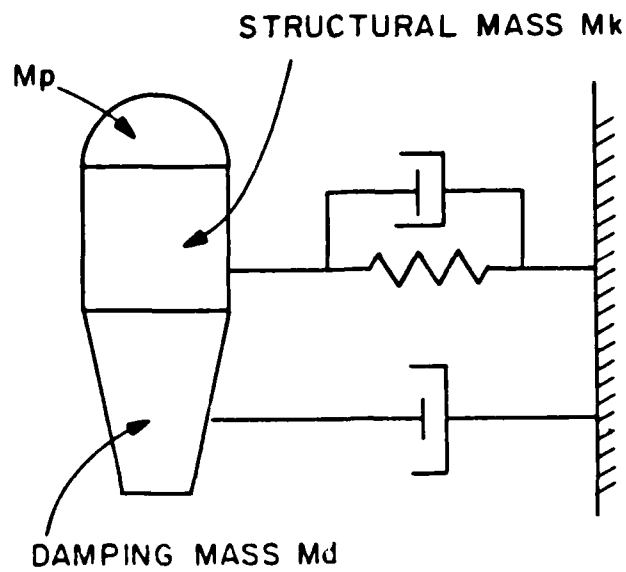


FIGURE 5
SYSTEM WITH DAMPING

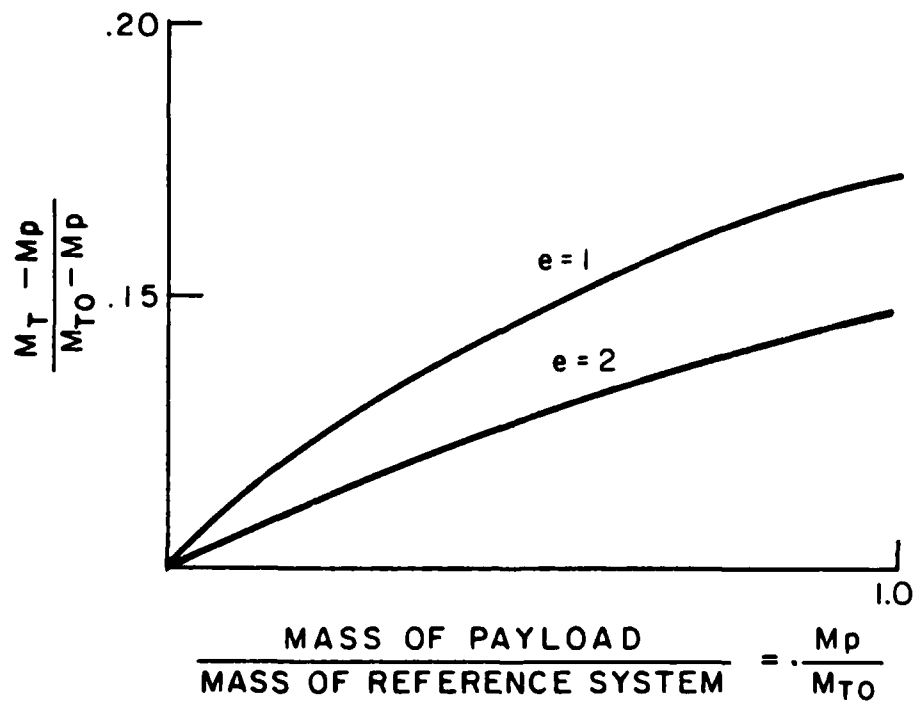


FIGURE 6
COMPARISON OF MASS OF FRICTION DAMPED SYSTEM TO REFERENCE SYSTEM

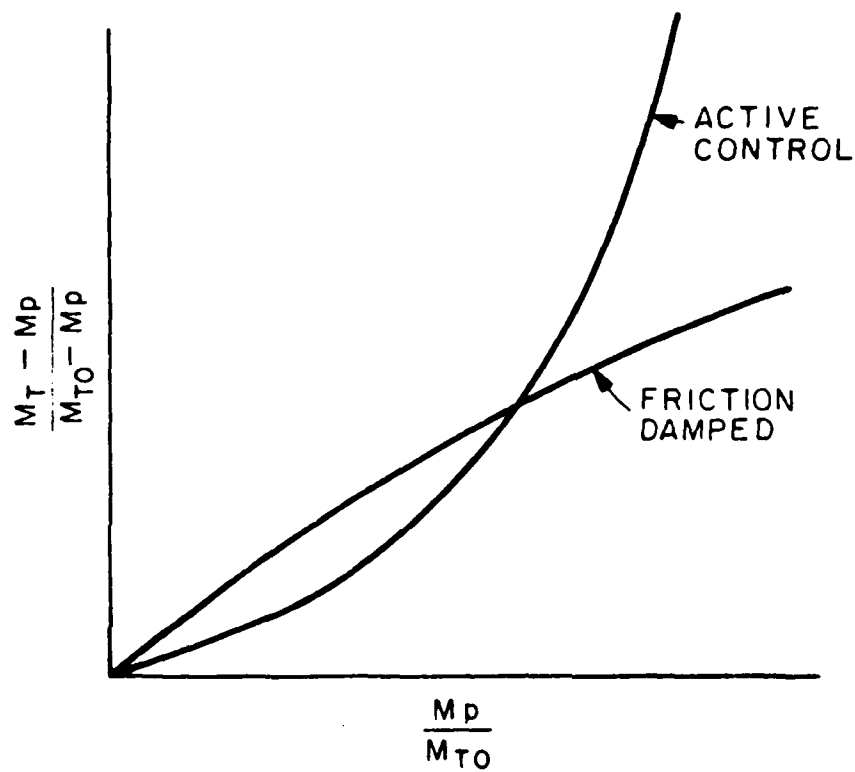


FIGURE 7
COMPARISON OF MASS OF ACTIVE CONTROL SYSTEM TO FRICTION DAMPED SYSTEM



FIGURE 8.



FIGURE 9

IDEAL SPRING

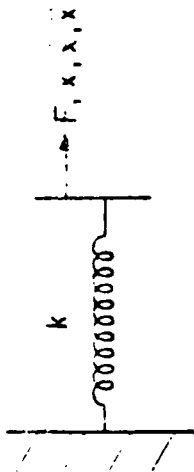
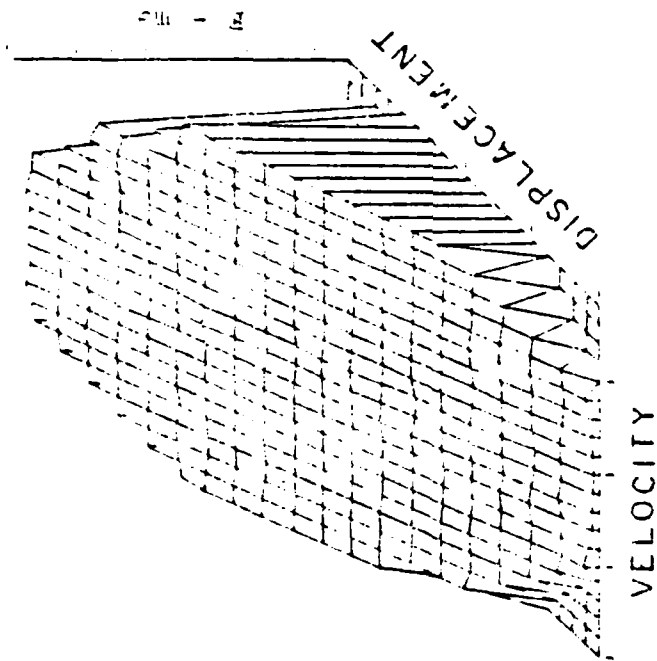


FIGURE 10
IDEAL LINEAR SPRING FORCE MAP

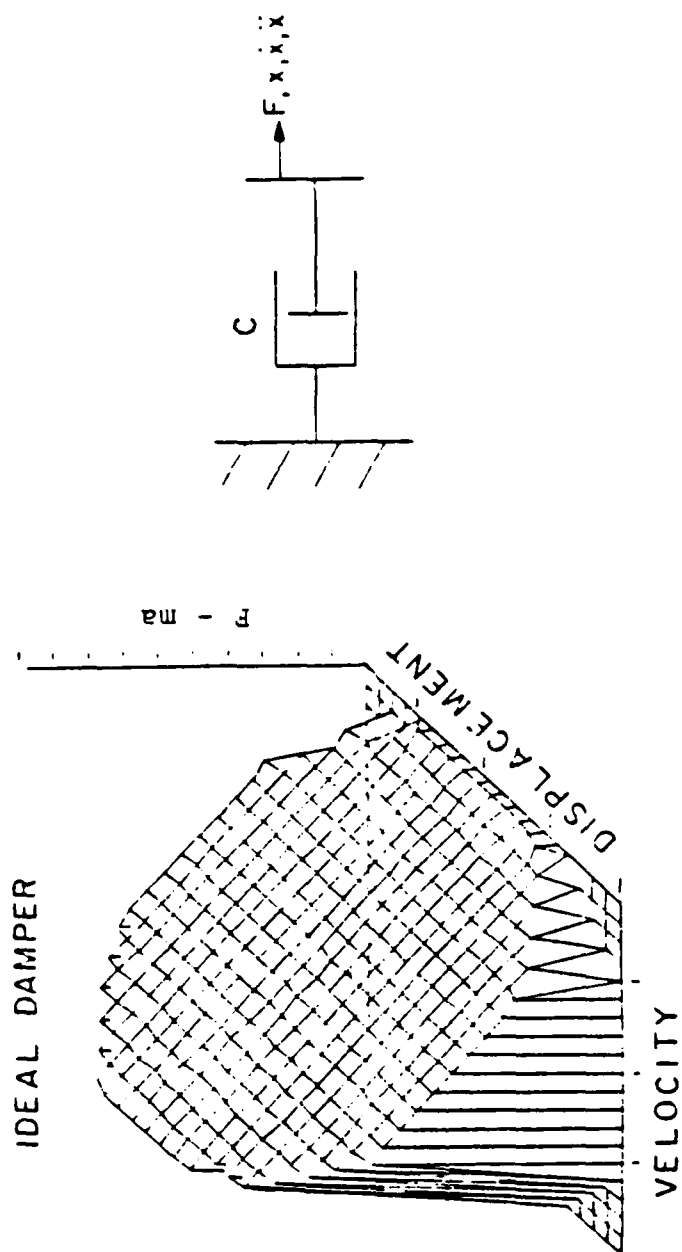


FIGURE 11
IDEAL LINEAR VISCOUS DAMPER FORCE MAP

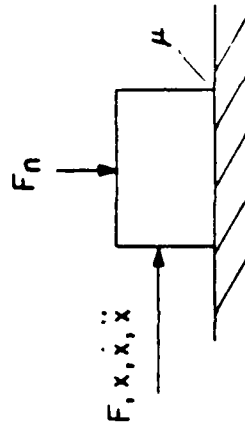
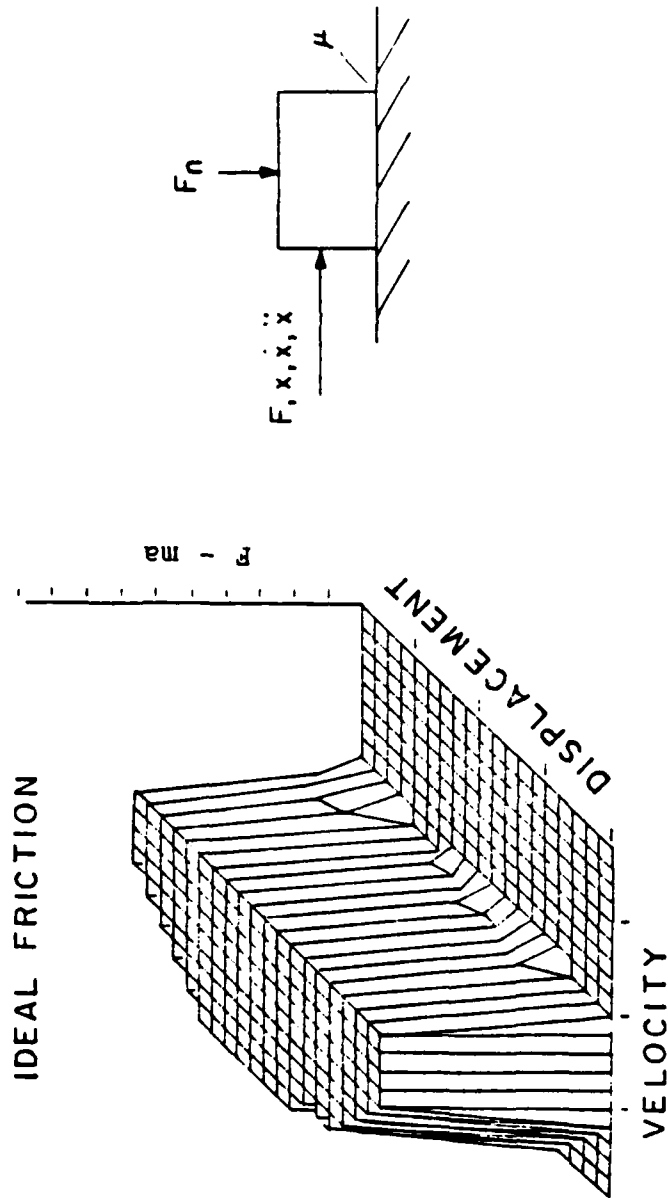


FIGURE 12
IDEAL SLIDING FRICTION FORCE MAP

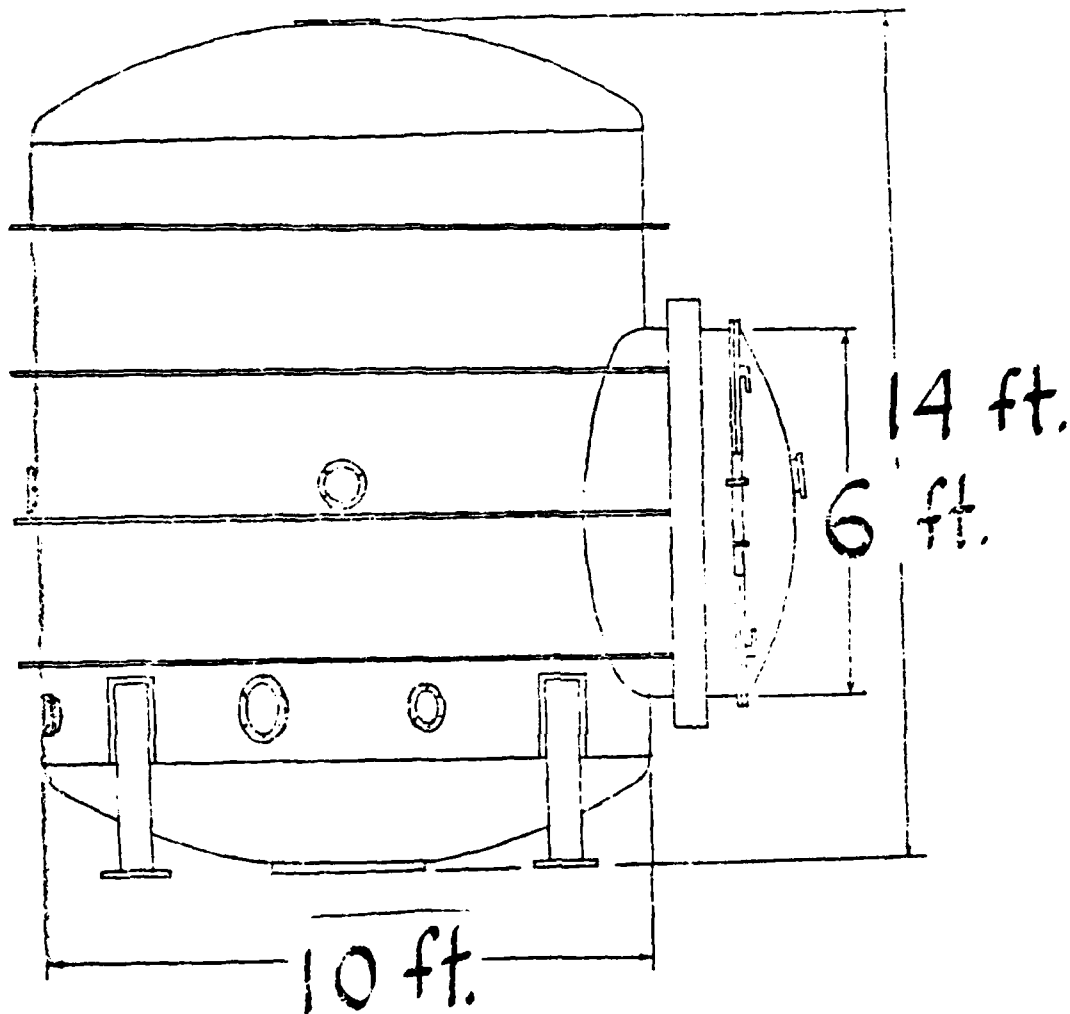


FIGURE 13
ZERO-G SPACE SIMULATION CHAMBER

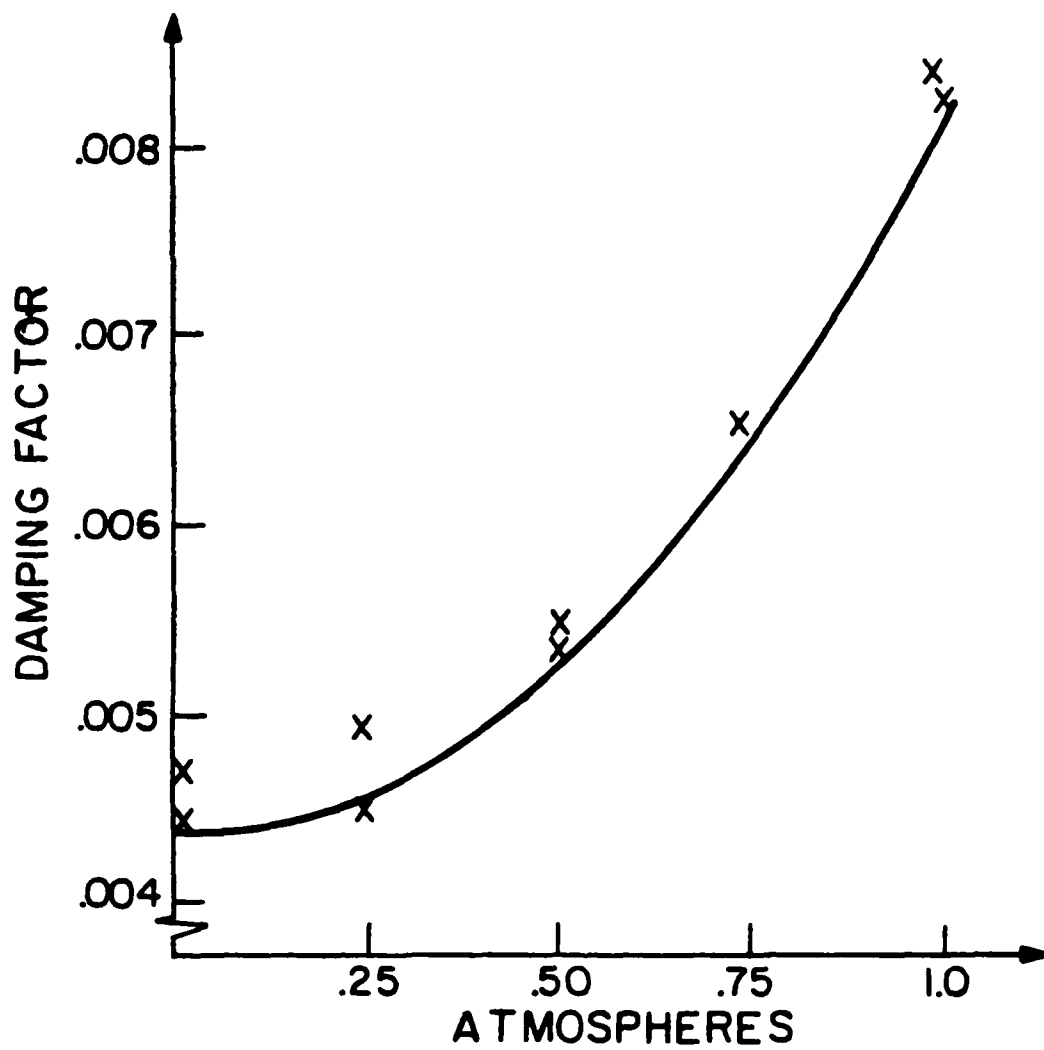


FIGURE 14

SADE

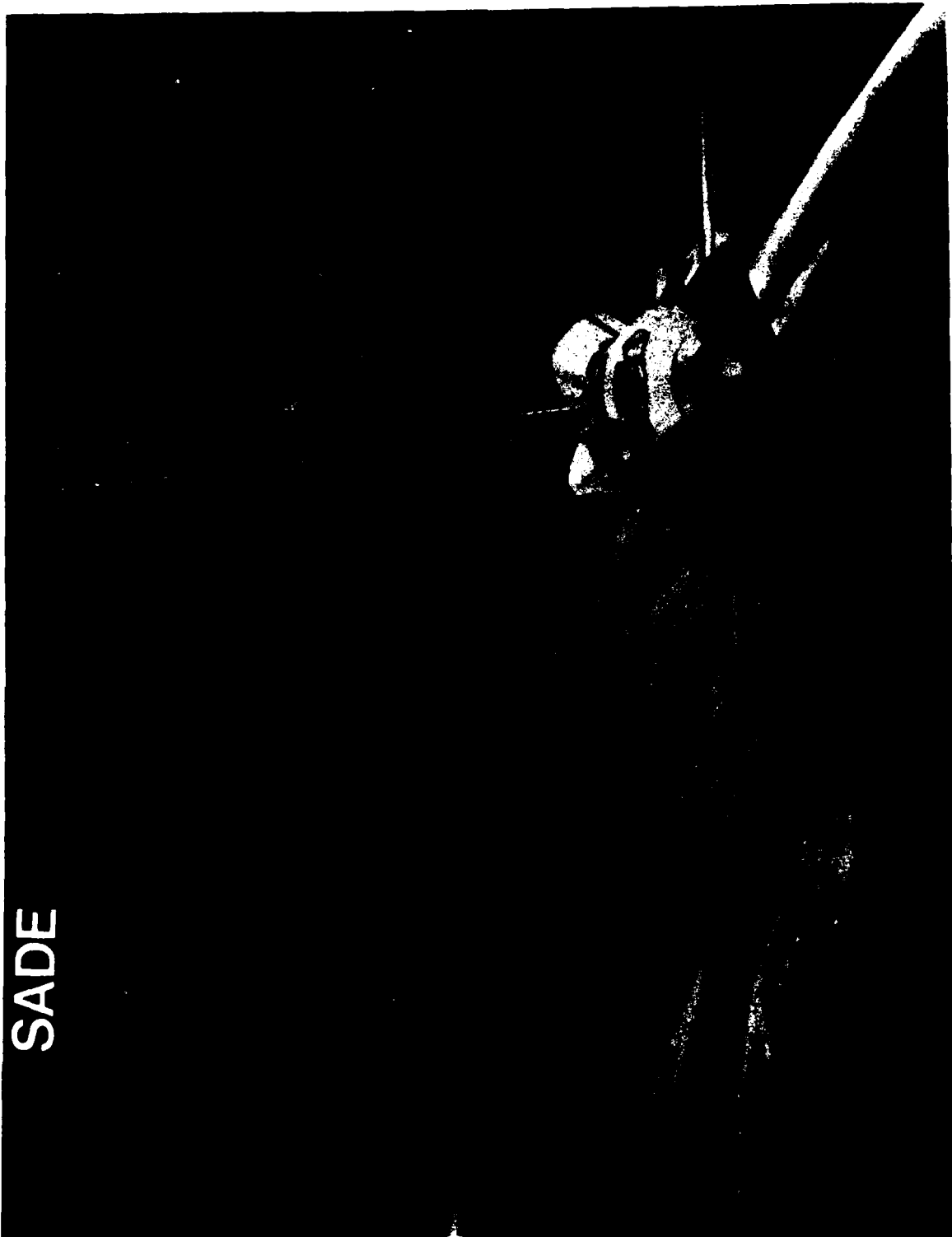


FIGURE 15

TABLE 1
THE BABEL OF DAMPING

Damping factor, loss factor	n, g
Specific damping capacity	ψ
Quality factor	Q
Fraction of critical damping	ζ
Log decrement	δ
Complex modulus	$E^* = E + iE''$

TABLE 2
METHODS TO SIMULATE ZERO-G

LAUNCH
DROP TOWERS
PARABOLIC MANEUVERS IN A/C
 KC-135
LOW EARTH ORBIT
 INSIDE STS ORBITER
 FREE FLYING

EXPERIMENTAL MEASUREMENT OF PASSIVE MATERIAL AND STRUCTURAL DAMPING FOR FLEXIBLE SPACE STRUCTURES

EDWARD F. CRAWLEY,[†] GEORGE L. SARVER[‡] and DAVID G. MOHR[§]

Space Systems Laboratory, Department of Aeronautics and Astronautics, Massachusetts Institute of Technology,
Cambridge, MA 02139 U.S.A.

(Received 6 January 1983)

Abstract—The results of an experimental effort to both characterize material damping and enhance structural damping are presented. In order to determine material damping in metallic and fibrous composite materials, a unique facility has been constructed in which transient decay measurements were made in free fall in a vacuum. Specimens were simultaneously excited and lofted with a tuned spring-cocked launcher. Damping data on the free-free mode was obtained by bonding strain gauges to the specimen and connecting them by fine wires to a terminal also in free fall. Graphite/epoxy laminates tested were unidirectional 0°, and $\pm 45^\circ$ symmetric, under environmental conditions of room temperature and near zero moisture content. Aluminum damping data agrees exactly with previous studies, as to stress and frequency dependence. The material damping in graphite/epoxy was found to be largely independent of frequency and stress level. In order to increase the passive damping level, it is possible to deliberately introduce dry frictional damping into a flexible structure. Experimental measurements of dry friction damping were carried out to investigate the effects of wear, and to correlate with an analytic model of the relative micro-slipping of two surfaces under differential strain and in frictional contact. The friction damping system investigated was a thin-walled aluminum outer tube with a split aluminum or steel inner tube. Dry Coulomb damping occurred at the interface of the inner and outer tube. The outer tube was cycled in compression-compression loading. The friction damping showed considerable correlation with the theoretical model. In order to investigate the effects of wear, the damping systems were cycled one million times. While wear was noticeable, the friction damping was not appreciably affected by the wear after the first few hundred cycles.

1. INTRODUCTION

Among the design objectives for large space structures are the maintenance of tight dimensional tolerance and the reduction of settling time after disturbance input. Two options are under consideration for the design of flexible structures to meet these objectives. In the active control option, active elements would be used to maintain dimensional control of the structure and to alter its dynamic response. In the passive control option, the inherent structural rigidity and dissipation characteristics would be used to meet mission objectives.

In either option a detailed understanding of the material and structural damping characteristics is important. In the passive control option, the material and structural damping provide the only means for dissipating vibrational energy. In an actively controlled structure, the structural damping must insure stability of the uncontrolled modes. Further, a detailed characterization of the origin of the structural damping is necessary for successful system identification, optimal estimator based control, and failure detection. Thus, in either an actively or passively controlled structure it is necessary to include material and structural damping in the design, to understand the dissipation mechanisms involved and be able to experimentally measure and analytically model those mechanisms.

The passive damping of a multi-element structure can be traced to at least three sources. First, there is the damping inherent in the structural material, which would

be present in any structural configuration, and can be thought of as a base level which all other active and passive schemes supplement. In any built-up assembly there are complex energy loss mechanisms at the joints and fittings. These have their origins in the macromechanical sliding and impacting of free surfaces. The third source of passive dissipation is by the deliberate additions of damper elements, such as frictional Coulomb dampers.

The fundamental mechanisms of all three of these passive damping schemes, material damping, joint "damping" and structural frictional damping are under active investigation at the M.I.T. Space Systems Laboratory. In this paper, the results of an experimental investigation of the damping of metallic and fibrous composite materials, and the analytical modeling and experimental verification of frictional damping schemes will be summarized. To demonstrate how material and frictional damping can be combined, a simple structural optimization is performed, indicating the potential for significant savings in mass by the addition of frictional dampers.

2. MATERIAL DAMPING INVESTIGATION

Among the several sources of passive damping in a flexible space structure, the most fundamental is the inherent material damping. Since material damping levels are quite low they are often obscured in terrestrial applications by aerodynamic and joint or support damping. But in unrestrained structures in the zero gravity and vacuum of space, material damping becomes relatively more important. Surprisingly little information is available on material damping levels, especially for advanced

[†]Boeing Assistant Professor of Aeronautics and Astronautics.

[‡]Research Assistant.

[§]Research Assistant.

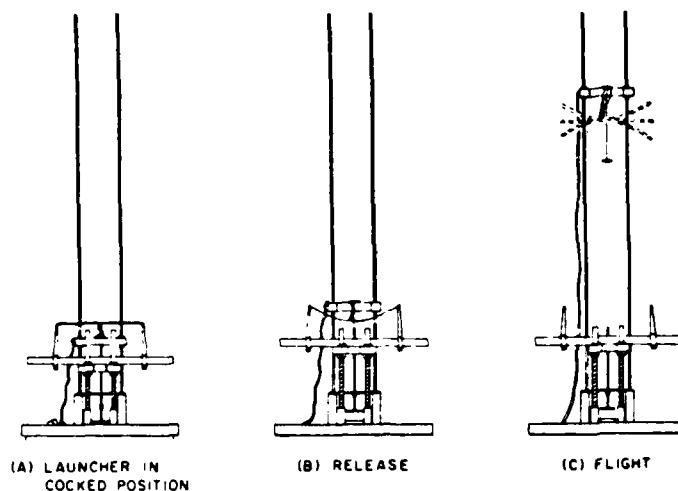


Fig. 1. Launch and excitation mechanism.

alloys and fibrous composite materials. Since most previous investigations have been motivated by fatigue considerations, available data tends to be for high strain levels and frequencies; whereas for space applications, data for lower strain levels and frequencies is needed.

2.1 Measurement facility

The requirements for the design of a facility to measure material damping levels for space applications are therefore clear. The experiment must be conducted in vacuum, at adjustable strain levels, low frequencies, and for an unrestrained free-free specimen. This latter requirement eliminates uncertainties associated with boundary conditions and energy dissipation at the support points. These objectives were met by designing a unique facility to test material damping by means of measuring the transient decay of a specimen while in free fall in a vacuum.

The central feature of the facility is a spring-loaded launcher located within a vacuum chamber, shown in Fig. 1. Specimens were simultaneously excited and lofted into free fall with this tuned spring-cocked launcher. The procedure was begun by cocking the launcher a predetermined distance and temporarily holding it in that position with an electromagnet (Fig. 1). An instrumented

specimen was then placed on two knife edge supports, the chamber sealed and evacuated to 1 torr. Upon release by the electromagnet, the launcher sprung upward, accelerating the specimen and causing a deflection, as shown in Fig. 1(B). After a predetermined stroke, the launcher was sharply decelerated and the specimen lofted into free flight in a free-free mode. The flight time up and down in the 2 m chamber was approximately one second. There were two adjustments on the launcher: the pre-compression and stroke. These were used to set the rigid body velocity at launch to that necessary to loft the specimen 2 m upward, and to set the initial strain level[1].

Data was obtained via strain gauges bonded to the specimen and connected via short, fine wires to a terminal block. To minimize the interference from these wires, the terminal block was simultaneously lofted on an identical trajectory, just 0.2 m to the side of the specimen. Damping ratios were found by performing a least-squares fit of an exponentially decaying sinusoid to the digitized data. Physical parameters for the aluminum and graphite/epoxy specimens are given in Tables 1 and 2 respectively.

Table 1.

ALUMINUM SPECIMENS mass/unit length = 1.088 grams/cm				
Specimen	Length (cm)	Width (cm)	Thickness (cm)	First Free-Free Frequency (Hz)
1*	45.72	2.54	0.155	19.67
2	45.72	2.54	0.155	39.60
3	35.56	2.54	0.155	65.47
4	25.40	2.54	0.155	128.41
5	15.24	2.54	0.155	357.50

*Specimen 1 is Specimen 2 with two 56.6 gram tip masses.

Table 2.

GRAPHITE/EPOXY SPECIMENS mass/unit length: $[G]_B = 0.416$ grams/cm $[445]_{2B} = 0.421$ grams/cm				
Specimen	Length (cm)	Width (cm)	Thickness (cm)	First Free-Free Frequency (Hz)
$[0]_B -1$	45.72	2.59	0.102	42.07
$[0]_B -2$	35.33	2.59	0.102	70.49
$[0]_B -3$	25.17	2.59	0.102	140.56
$[0]_B -4$	14.96	2.59	0.102	391.20
$[445]_{2B} -1$	45.72	2.51	0.104	17.95
$[445]_{2B} -2$	35.86	2.51	0.104	29.62
$[445]_{2B} -3$	25.40	2.51	0.104	54.16
$[445]_{2B} -4$	15.16	2.51	0.104	171.04

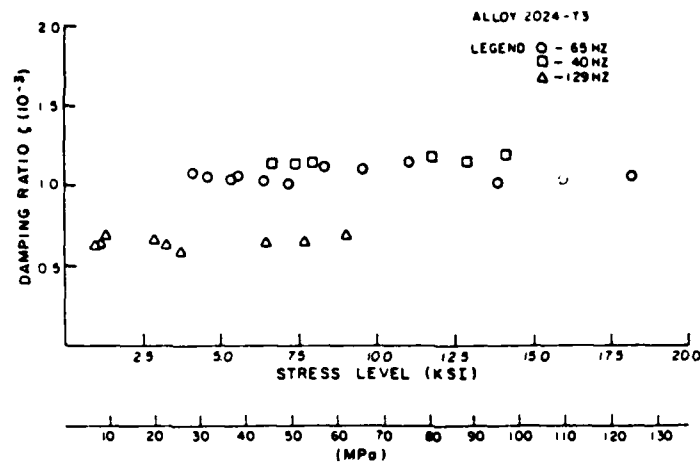


Fig. 2. Material damping ratio vs stress level in aluminum.

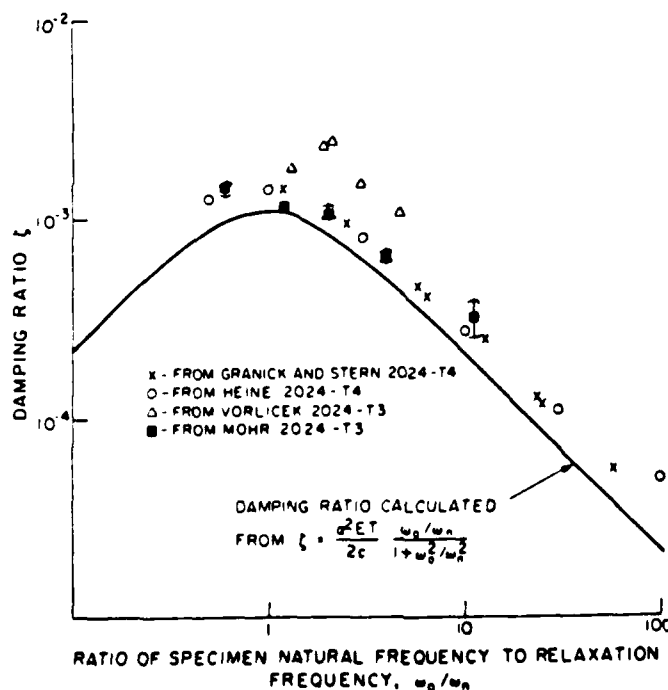
2.2 Material damping results

The aluminum specimens were tested at room temperature in stress levels from 3.5 to 130 MPa (0.5–18.7 ksi). Damping factors for the three intermediate frequencies tested were plotted against measured stress levels, as shown in Fig. 2. The damping ratio shows no significant dependence on stress level. This is in good agreement with previous studies [2, 3].

The plot of damping ratio vs frequency in Fig. 3 shows

an interesting trend. Above the maximum the results show excellent agreement with theory and previous experiments. However, unlike the theoretical curve and the results in [3], the damping ratio from the current data does not show a decline for frequencies below the relaxation frequency ω_n , given as

$$\omega_n = \frac{\pi^2 k}{h^2 c}, \quad (i)$$

Fig. 3. Material damping ratio vs ω_0/ω_n in aluminum.

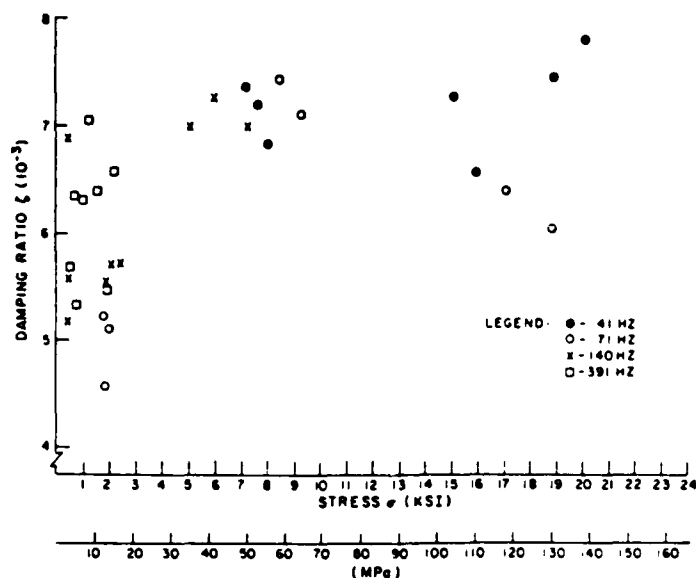


Fig. 4. Material damping ratio vs stress level in $G/E [0]_s$.

which is derived from the micromechanical heating model of Zener[4]. Since the data point on the low side of ω_n represents only a few tests, further work is necessary before any definite conclusions can be made. This low frequency range is important, as space structures would certainly operate at frequencies below the relaxation frequency, where the Zener model shows damping to decrease sharply.

The $[0]_s$ unidirectional specimens of Hercules AS1-3501/6 graphite/epoxy laminates were tested at stress levels ranging from 2.8 to 140 MPa (0.4–20.1 ksi), and environmental conditions of room temperature and near zero moisture content. The results show an appreciable amount of scatter. Damping factors versus stress level

are plotted in Fig. 4. Although the plot of ζ vs stress is not conclusive, one might suggest a trend of increased damping with higher stress levels. Although the stress-strain relationship in composites is very linear, several studies have pointed out a general inverse relationship between stiffness and damping[5, 6]. In Fig. 5, the damping ratio is plotted against frequency. The average damping values were several times higher than values obtained in previous studies[7, 8].

It should be pointed out that the $[0]_s$ specimens had a significant initial curvature ($e/L \sim 0.03$), possibly due to variations in fiber volume through the thickness. All tests were conducted with the beam curvature upward when the specimen rested on the launch mechanism, but two

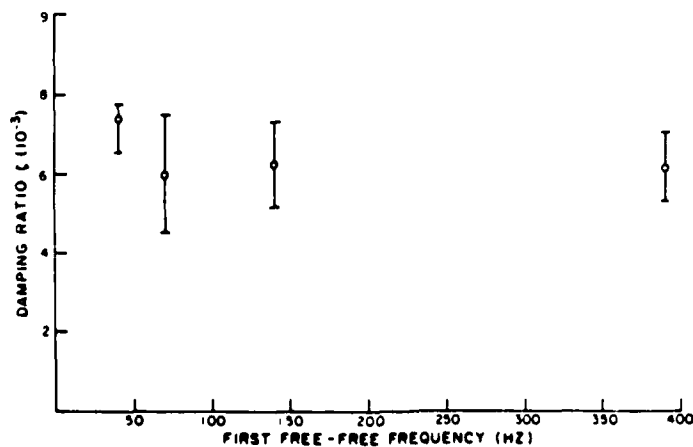
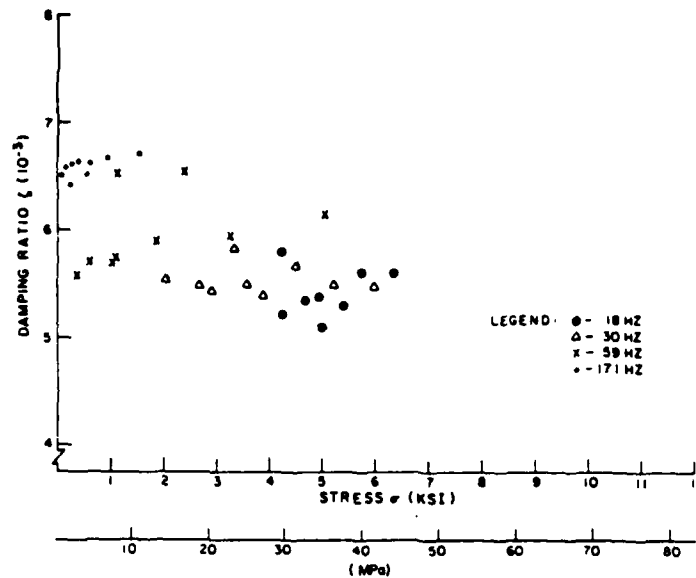


Fig. 5. Material damping ratio vs first free-free frequency in $G/E [0]_s$.

Fig. 6. Material damping ratio vs stress level in $G/E [\pm 45]_{2x}$.

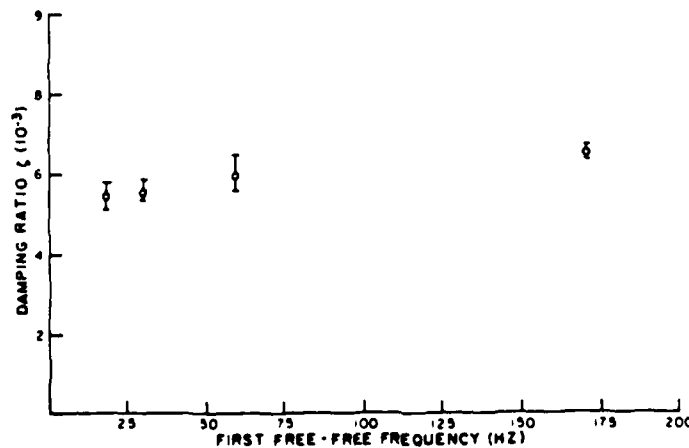
tests were performed with the curvature downward for comparison. The damping ratios obtained were found to be almost four times the values obtained with the curvature upward. The effects of curvature and its apparent influence are unclear, but decreased response has been predicted for curved viscoelastic beams [9], possibly also affecting the damping.

The $[\pm 45]_{2x}$ laminates were tested at stress levels from 1.4 to 44. MPa (0.2–6.35 ksi). A plot of damping ratio versus stress level shows much less scatter than the $[0]_8$ tests. Figure 6 shows damping to be perhaps only slightly dependent on stress level, agreeing with previous work [7]. In Fig. 7, a slight frequency dependence can be seen. The average damping values agree very closely with one previous study [8].

3. FRICTIONAL STRUCTURAL DAMPING

Since the material damping of most common structural materials is low, many schemes have been suggested for increasing the passive structural damping. Among these, dry Coulomb friction damping has been previously proposed, but consideration of wear and corrosion have prevented its practical application. The best environment for friction damping is one in which the cycle frequency is low, to minimize wear, and the environment is controlled, to keep the corrosion to a minimum. Large space structures which will have low vibratory frequencies provide such an environment.

The space structure assumed for the analysis of dry friction damping is a truss structure made of tubular members [10]. The friction damping mechanism consists

Fig. 7. Material damping ratio vs first free-free frequency in $G/E [\pm 45]_{2x}$.

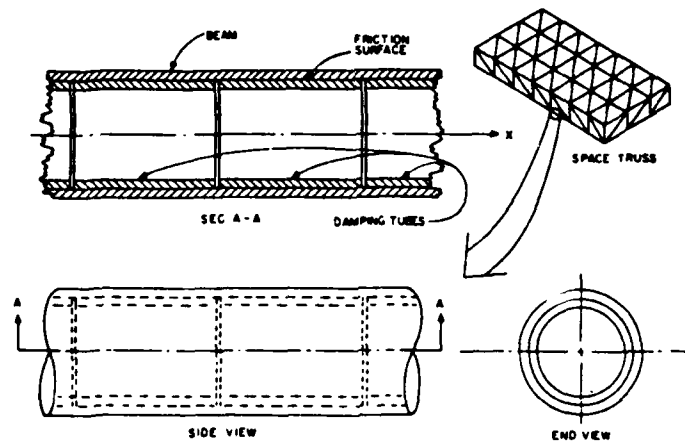


Fig. 8. Friction damped truss member.

of segmented damping tubes placed end to end inside the tubular load carrying members, as shown in Fig. 8. These concentric members are pressed against each other such that the entire load carrying member is in contact with a damping tube. When the truss structure is loaded, the resultant deflection causes sliding between the load carrying members and the damping tubes. The sliding causes friction heating which dissipates kinetic energy, thus damping the vibrations of the structure.

3.1 Microslip analytic model

The damping factor of this friction damping mechanism will now be derived in three steps. First, a micro-slip Coulomb friction model will be used to derive the stress distribution between the load carrying and damping tubes during a single loading cycle[11]. Secondly, the stress distribution will be used to calculate the cyclic displacement history at the ends of the load carrying element, and the resulting load-deflection hys-

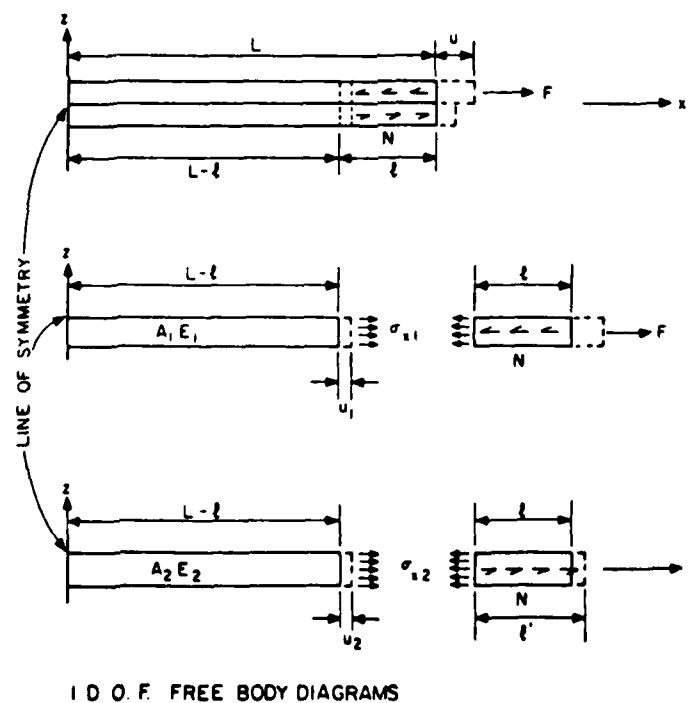


Fig. 9. One dimensional model of the damping system, showing geometry (top) and free body diagrams of the load bearing member (middle) and damping member (lower).

teresis curve will be integrated over one cycle to give an energy loss per cycle ΔE . Lastly, with a knowledge of the total strain energy, the damping factor g will be calculated:

$$g = \frac{\Delta E}{2\pi E} \approx 2\zeta. \quad (2)$$

As outlined, the first step is to derive the stress distribution. To simplify the analysis, the circumferential strain will be ignored, reducing the problem to a two-dimensional one of a thin load carrying member and a damping member in frictional contact (Fig. 9). As a small extensional load F is applied to a segment of load carrying tube $2L$ long, the strain in the load carrying and damping tubes are equal except in a small zone near the stress free ends of the damping tube, where the strain lags that of the loaded tube and the shear is transferred over a concentrated area several thicknesses in length. As the extensional force F is increased, the concentrated shear stress locally reaches the frictional slipping stress per length N , and the surfaces begin to slip. As the extensional force increases further, the length of slip grows from both ends of the damping tube symmetrically until the slip lengths equal L . An equivalent free body diagram of half of the segments is shown in Fig. 9. Assuming the tube walls are thin, the analysis can be reduced to a one dimensional model, with negligible shear strain and uniform extensional stress σ_x through the thickness of the walls. Further, it is assumed that the frictional stress is constant over the slip length, and zero over the non-slipped portion.

By equating the longitudinal strain in the unslipped segments, and balancing forces on the slipped segments,

the load F can be expressed in terms of the frictional slip force per length N , the slip length l , and the stiffnesses of the load carrying tube and damping tube

$$F = NE_1A_1 \left(\frac{l}{E_1A_1} + \frac{l}{E_2A_2} \right). \quad (3)$$

It is useful to normalize the load F by the load F' which sets $l = L$, that is the load which causes the length of the slip surface to exactly equal the length of damping tube. Setting $\beta = (A_2E_2)/(A_1E_1)$, the normalized load is just

$$n = \frac{F}{F'} = \frac{l}{L} = \frac{F\beta}{NL(1+\beta)}. \quad (4)$$

The stress distribution from $x = 0$ to $x = L$ can now be calculated for a load cycling between F_0 and $-F_0$. These stress distributions form two cases, $n \leq 1$ and $n \geq 1$. The case of $n \leq 1$ indicates that the maximum load F_0 is such that the entire surface does not slip during the loading cycle.

The second step in calculating the damping factor is to use the stress distribution in the load carrying member to calculate the end deflection, and then integrate over the loading cycle to obtain the energy loss per cycle (Fig. 10). The result of this integration gives the energy loss relationships,

$$\Delta E = \frac{2F_0^3\beta^2}{3E_1A_1N(1+\beta)^2}, \quad n \leq 1,$$

$$\Delta E = \left(\frac{NL^2}{E_1A_1} \right) \left[2F_0 - \frac{4}{3} \frac{NL(1+\beta)}{\beta} \right], \quad n \geq 1. \quad (5)$$

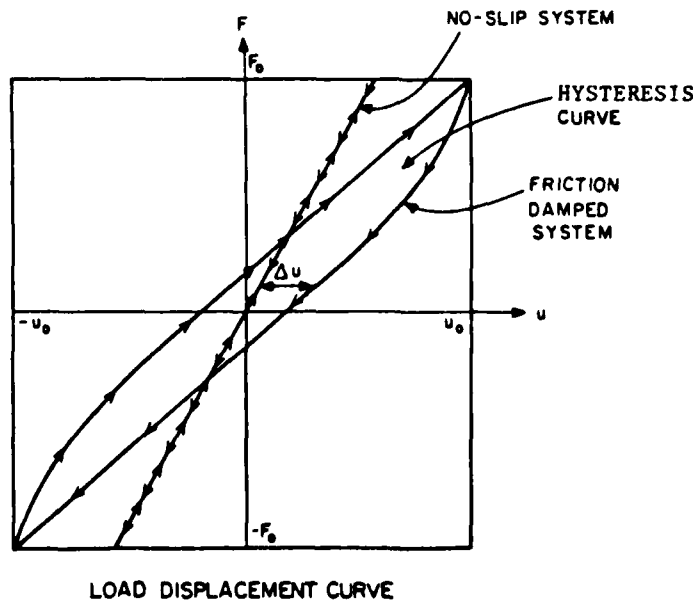


Fig. 10.

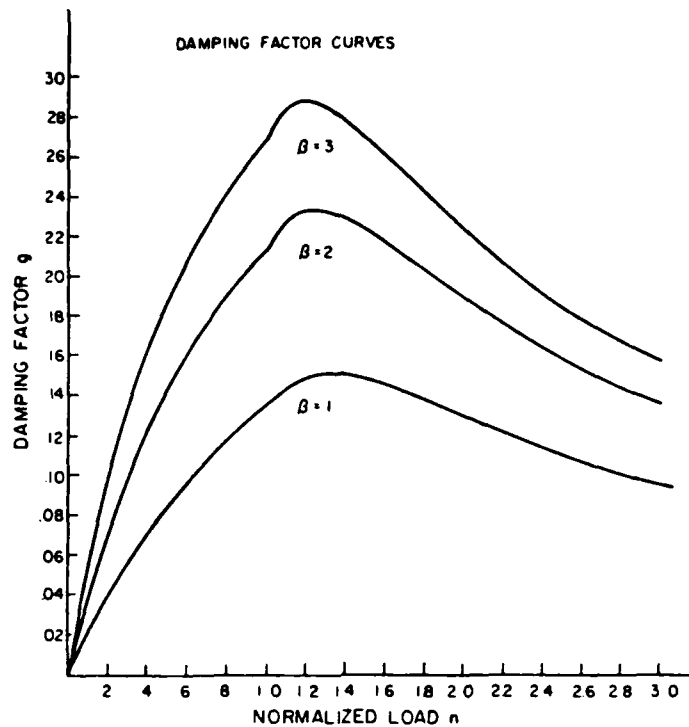


Fig. 11. Frictional damping factor vs normalized load.

Finally, to formulate an approximation of the damping factor represented by a friction damping system, the total energy of the system is required. Integrating over the entire system the strain energy at the time of maximum loading results

$$E = \frac{F_0^2(L-l)}{2(E_1A_1 + E_2A_2)} + \frac{3F_0l(F_0 - Nl) + N^2l^3}{6E_1A_1} + \frac{5N^2l^3}{12E_2A_2}, n \leq 1,$$

$$E = \frac{3F_0L(F_0 - NL) + N^2L^3}{6E_1A_1} + \frac{5N^2L^3}{12E_2A_2}, n \geq 1. \quad (6)$$

Inputting eqns (5) and (6) into eqn (2) the resulting damping factors are

$$g = \frac{2\beta(1+\beta)}{3\pi \left[\left(\frac{1+\beta}{n} \right) + \frac{5\beta}{6} + \frac{\beta^2}{3} \right]}, n \leq 1,$$

$$g = \frac{2(n-2/3)\beta(1+\beta)}{\pi \left[n^2(1+\beta)^2 + \frac{5\beta}{6} + \frac{\beta^2}{3} - n\beta(1+\beta) \right]}, n \geq 1. \quad (7)$$

The damping factor versus the normalized peak load n is plotted in Fig. 11. The cyclic damping factor is a nonlinear function of both the normalized force n and the ratio of stiffness β . By examining eqn (4), it can be seen that the designer has control over both ratios. The

ratio β can be increased by increasing the relative stiffness of the damping tube, and the normalized force can be adjusted by changing either the slip stress N or the length of the segment L . Thus the designer has almost complete freedom to set a structural damping factor using this distributed dry friction damping system. It should be noted that for β arbitrarily large, a limit of g equal to $2/\pi$ is reached.

3.2 Frictional damping experimental results

To validate the one dimensional friction damping model, a series of experiments were performed. The experiments were designed to allow independent variation of the governing nondimensional parameters of the model. A further objective was to experimentally measure the coefficients of friction in typical damper geometries and to investigate the effects of wear.

The experimental apparatus is shown in Fig. 12. The main components are the outer load carrying tube, an inner damping tube and a central rubber bladder. The outer 178 mm long, load carrying tube was 6061-T6 aluminum, with an outer diameter of 41 mm and a 1.5 mm wall thickness. A variety of different wall thickness tubes of steel and aluminum were used for the inner damping tube, which was split lengthwise and free at each end. These splits allowed unrestrained radial expansion of the damping tube. The combination of the split tube and rubber bladder connected to an air reservoir of variable pressure provided for control of the contact pressure between the damping and load bearing tubes.

Friction damping occurred when the compressive load

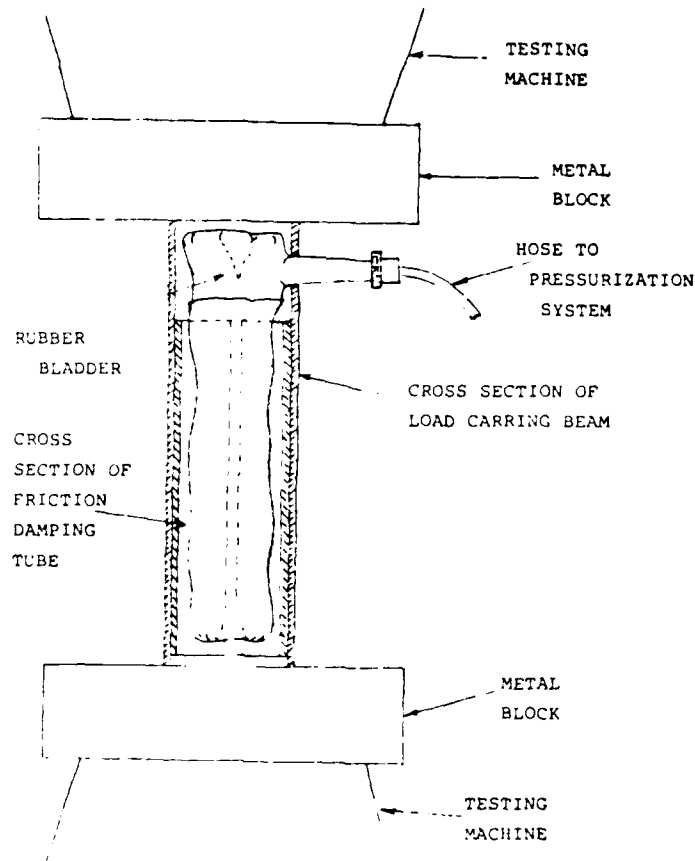


Fig. 12. Experimental specimen in testing machine.

was cyclicly applied at the ends of the load carrying tube by an MTS hydraulic testing machine. To prepare for a run, the specimen was placed in the testing machine and a mean compressive load applied. By exhausting the pressure in the bladder, the damping tube was put in a stress free state, relieving any residual stress due to friction. A run was then started by pressurizing the bladder. The load was cycled in compression-compression with amplitude F_n about the mean compressive load F_m , causing sliding friction at the interface. The minimum compressive load was chosen to prevent the inner bladder from pushing the end plates away from the load carrying tube. The experimental data was plotted on an x-y plot of applied load versus load cell displacement. This resulted in direct measurement of the load displacement hysteresis curves required to calculate the energy dissipation. The size and shape of these curves could be changed by varying the normalized load n and stiffness ratio β . Experimentally, control over these two governing nondimensional parameters was achieved by varying the peak loading on the load carrying tube the internal pressure, and the thickness and material of the damping tube.

Working from the load-displacement hysteresis curves, measurements of the hysteresis curve's internal area were made, giving the frictional energy loss per cycle ΔE (Fig. 10). Based on the analytic model developed above, the full cycle energy loss reduces to functions of the peak load amplitude F_n , and the constants C and D .

$$\frac{\Delta E}{p^2 C} = \frac{F^3 D^3}{3 p^3}, n \leq 1,$$

$$\frac{\Delta E}{p^2 C} = \left(\frac{FD}{p} - \frac{2}{3} \right), n \geq 1, \quad (8)$$

where C , and D are given by

$$D = \frac{\beta}{L \mu \pi R (1 + \beta)},$$

$$C = \frac{2 L^3 \mu^2 \pi^2 R^2 (1 + \beta)}{E_1 A_1 \beta}, \quad (9)$$

and are seen to depend on the specimen geometry, the

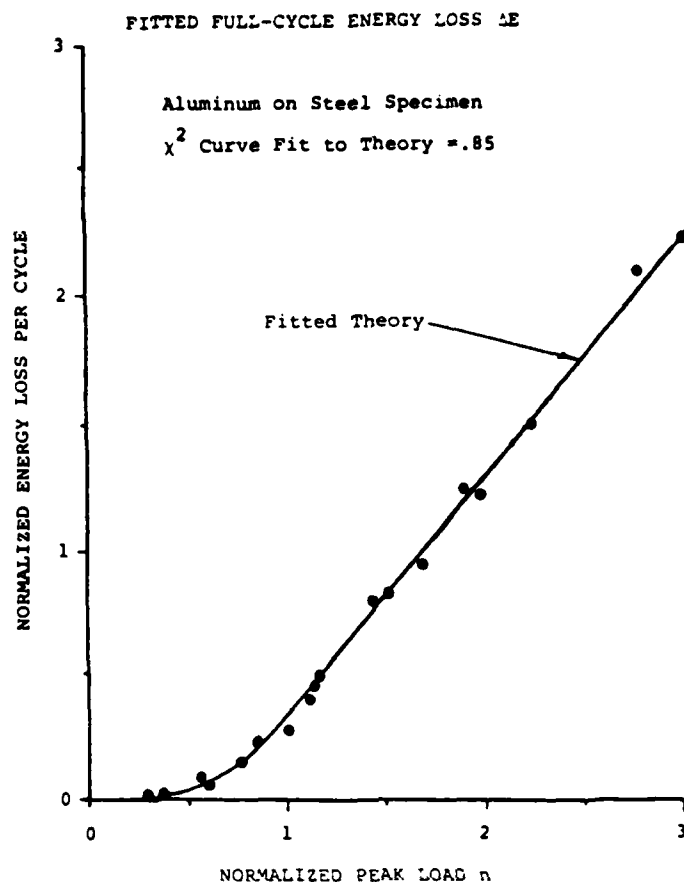


Fig. 13.

stiffness ratio, and the slip stress N ,

$$N = 2\pi R\mu p, \quad (10)$$

which is a function of the internal pressure p , coefficients of friction μ , and the radius of the tube R .

In order to correlate the experimental results and analytic model a least squares fit was made to the energy loss and residual displacement data. Since the coefficient of friction can be altered by contamination, surface preparation and wear, the constants D and C were taken as free parameters in the least squares fits. The resultant curve fits show close agreement between theory and experiment, as can be seen in Fig. 13. The estimated experimental error is not shown for clarity, but the chi square parameter is based on the estimated experimental uncertainty. Using the resultant constants D and C , the coefficients of friction μ , and the stiffness ratio β can be calculated. An example of this data is shown in Table 3. Close agreement was found between these values and the accepted values for aluminum on steel [12]. The aluminum on aluminum samples showed a much lower coefficient of friction than would be expected. Further analysis was performed to account for warping and wedging of the inner damping tube in the outer load

carrying tube. This analysis showed the warping was equivalent to a small residual internal pressure.

When the specimens were cycled repeatedly, wear effects occurred very rapidly and were noticeable in the hysteresis curves. The samples were cycled one million

Table 3.

FITTED PARAMETERS					
ALUMINUM ON STEEL					
ENERGY LOSS CURVE FIT					
TEST	χ^2	P_0 (KPa)	$D \times 10^{-4}$ (mm) ⁻²	C (m ³ /GPa)	μ_g
1	1.22	22	1.47	.76	.48
2	.79	63	1.60	.63	.48
3	2.17	84	1.95	.51	.46
4	.85	64	1.52	.67	.50
5	1.22	280	2.19	.51	.44
6	1.79	69	1.47	.71	.60
7	3.43	74	1.60	.63	.46
8	1.75	57	1.04	1.04	.51
average $\mu_g = .49$					
Theory $D = 1.67 \times 10^{-4}$ (mm) ⁻²					
$C = .63$ (m ³ /GPa)					
$\mu = .48$					

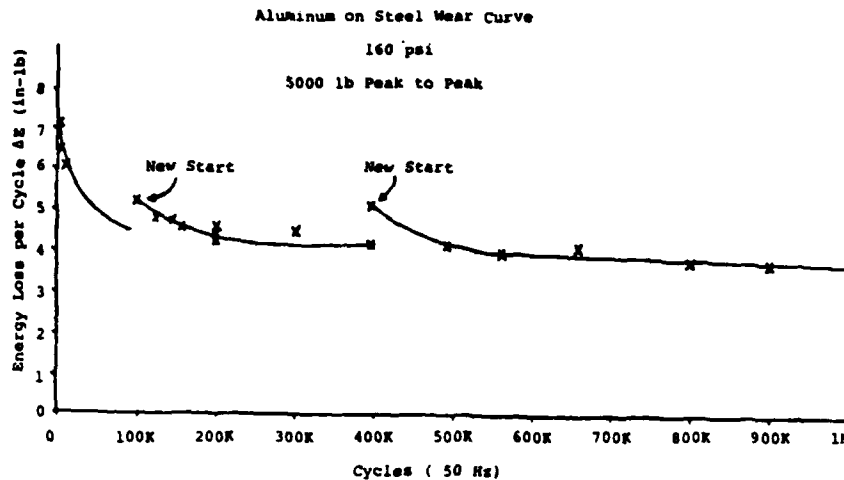


Fig. 14. Energy loss vs cycles showing the effect of wear.

times at a constant peak load, plotting the hysteresis curves at intervals of 100,000 cycles. The wear curves show a rapid drop in frictional energy loss per cycle, which reached an asymptotic value at about 60% of the initial value, as shown in Fig. 14. It is theorized that this is the result of particle and groove formation on the wear surfaces. It is expected that wear effects would be minimized with better wearing materials.

4. DAMPING OPTIMIZATION EXAMPLE

Having discussed both material and frictional damping, it might be illustrative to examine how the two can be combined to optimally utilize passive damping in a system, while minimizing its mass. Consider the following line of thought:

Assume the design criteria is to keep the deflection of the structure within certain dimensional tolerances under conditions of dynamic loading. Starting with a system with only material damping, removal of some load bearing structure will reduce the structural

stiffness and increase the deflection under dynamic load. But if the structural material is replaced by damping material, the dynamic amplification near resonance is reduced, reducing the deflection, and compensating for the loss of structural material. If addition of damping material can decrease the dynamic amplification factor "faster" than removal of structural material reduces the stiffness, an optimal system mass will be lower than the baseline system without the frictional dampers.

To quantify this reasoning, a simple one degree of freedom spring-mass system shown in Fig. 15 was optimized subject to several simplifying assumptions.

Both the material and frictional damping is assumed to be approximately viscous. The frictional damping ($g/2$) adds linearly to the inherent material damping ζ_0

$$\zeta = \zeta_0 + \zeta_D = \zeta_0 + g/2. \quad (11)$$

The baseline material damping was taken as $\zeta_0 = 0.005$,

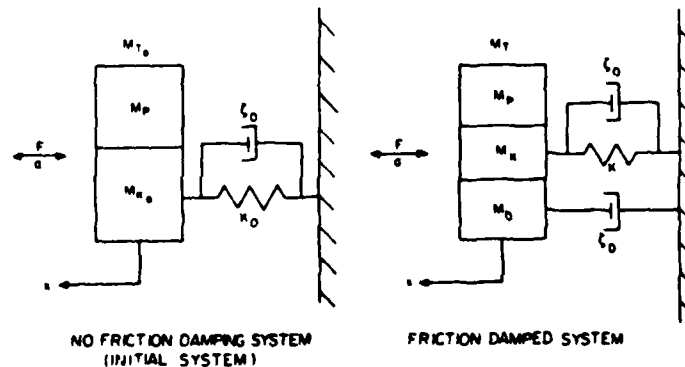


Fig. 15. Baseline and modified systems for structural optimization.

typical of graphite/epoxy and also of built-up metal structures. The lumped mass consists of a payload or non-structural mass M_p , and a structural mass. The structural mass is divided into load bearing mass M_K and damping mass M_D , coinciding with the load carrying element and the damping element of the friction damping system. The spring constant is assumed proportional to the mass of the load bearing element. Both inertial (i.e. proportional to total mass) and external (i.e., independent of total mass) forces were considered. Two frequency spectra of loading were considered, one in which the excitation is at resonance of the system, which is a worst case for dynamic overstress, and one in which the excitation spectrum is "white", that is, contains all frequencies in equal amplitude.

To non-dimensionalize the analysis, two dynamic systems are compared. The first system has only material damping. The second system has both friction and material damping. The structural design criteria for the friction damped system is that it have the same payload mass and the same maximum displacement under identical loading conditions as the initial system. This is taken as a constraint in the optimization. The optimization criterion is to minimize the mass of the friction damped system.

At this point it is convenient to define two new ratios:

$$\lambda_0 = M_p / M_{T0}$$

$$SR = \frac{M_T - M_p}{M_{T0} - M_p} \quad (12)$$

The ratio of the payload mass to the total mass of the initial system is defined at λ_0 . The quantity actually minimized is SR, the ratio of the structural plus damping mass of the friction damped system to the structural mass of the initial system.

For a given value of λ_0 , and e (the specific modulus ratio of the damping and load carrying beam) and ζ_0 , a minimum SR is found by varying the β and n . Curves showing SR versus λ_0 are shown in Fig. 16. One result of the optimization is that the optimum β and n are independent of λ_0 and the loading condition. It can be seen that the mass fraction SR is dependent on λ_0 under inertial excitation, but under force loading SR is independent of λ_0 and coincides with the optimum SR for $\lambda = 1$ and inertial excitation. Note that there is a better than 70% reduction in the structural mass of the system using friction damping, even in the case of a "white" disturbance.

It is evident from Fig. 16 that the greatest weight savings due to friction damping are for the systems with a relatively small payload, or non-structural mass. Of course, this analysis is far over-simplified, neglecting effects such as buckling of the tubes, but it does indicate the potential for significant mass savings by addition of frictional damping.

5. CONCLUSIONS

Material damping. From the aluminum studies and especially from Fig. 3 one can conclude that the free-fall

method is a valid, accurate experimental technique for measuring small damping ratios.

Material damping in 2024-T3 aluminum is independent of stress level and follows the theoretical values of Zener[4] closely for frequencies above the relaxation frequency. For frequencies below the relaxation frequency, the free-free damping behavior may deviate from theoretical Zener model.

Due to large scatter, no definite conclusions can be drawn from the graphite-epoxy [0]₄ data. The curvature orientation of the specimen at launch did seem significantly to affect the damping behavior.

Material damping in graphite/epoxy [± 45] was found to be only slightly dependent on stress level and frequency, increasing slightly with increasing stress level of frequency. Damping ratios ranged from 0.5% to 0.66% of critical damping in a frequency range of 18-171 Hz and a stress level range of 1.4-44. M Pa (0.2-6.35 KSY).

Structural friction damping. Friction damping, based on a thin beam, microslip model, has been found to produce significant increases in passive damping. This derived model has good correlation with experiment. Wear does reduce the effectiveness of friction damping but, even with poor wear materials, the energy loss per cycle levels out to approx. 60% of the initial value. It is expected that the use of better wear materials will give significantly better wear characteristics. In a one D.O.F.

OPTIMIZED PARAMETERS WITH "WHITE NOISE"

$e = 1$	$\zeta_0 = .005$	$\beta = .80$	$n = 1.31$
$e = 2$	$\zeta_0 = .005$	$\beta = 1.33$	$n = 1.28$

OPTIMIZED PARAMETERS AT RESONANCE

$e = 1$	$\zeta_0 = .005$	$\beta = 1.41$	$n = 1.28$
$e = 2$	$\zeta_0 = .005$	$\beta = 2.10$	$n = 1.24$

INERTIAL DISTURBANCE

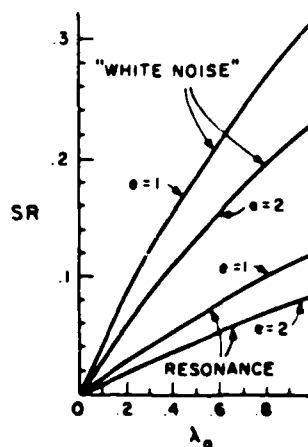


Fig. 16. Initial payload mass fraction, λ_0 vs structural mass ratio, SR.

optimization, better than 70% savings in structural mass was achieved using friction damping over an equivalent materially damped structure.

Acknowledgements—The authors wish to acknowledge the support of the National Aeronautics and Space Administration for their support under NASA grant NAGW-21, with Mr. Samuel Venneri as technical monitor, and the support of the Aerospace Corporation, with Mr. James Moore and Dr. Rudolph Meyer as monitors.

The authors wish to further acknowledge Prof. James W. Mar for his advice and support of this and many other projects in the M.I.T. Space Systems Lab.

REFERENCES

1. D. G. Mohr, Experimental measurements of material damping of aluminum and graphite epoxy in free-fall with tuneable excitation. M.I.T. Space Systems Laboratory #11-82 (June 1982).
2. N. Granick and J. D. Stern, Material damping of aluminum by a resonant-dwell technique. NASA TN D-2893 (Aug. 1965).
3. J. C. Heine, The stress and frequency dependence of material damping in some engineering alloys. Ph.D. Thesis, M.I.T., Cambridge Mass. (June 1966).
4. C. M. Zener, *Elasticity and Anelasticity of Metals*. University of Chicago Press, Chicago (1948).
5. R. D. Adams, M. A. O. Fox, R. J. L. Flood, R. J. Friend and R. L. Hewitt, The dynamic properties of unidirectional carbon and glass fiber reinforced plastics in torsion and flexure. *J. Composite Mater* 3, 594-603 (1969).
6. H. Georgi, Dynamic damping investigations on composites. AGARD Conf. Structures and Material Panel Specialists Meeting on Damping Effects in Aerospace Structures, Williamsburg, Virginia, April 1961.
7. D. A. Boyce, Material damping of graphite/epoxy double cantilever beams. S. M. Thesis, M.I.T., Cambridge, Mass. (Sept. 1979).
8. P. L. Vorlicek, Material damping of aluminium and graphite/epoxy in a simulated zero-gravity environment. M.I.T. Space Systems Laboratory #13-81 (Jan. 1981).
9. J. N. Rossettos and E. Perl, On the damped vibratory response of curved viscoelastic beams. *J. Sound Vibr.* 58 535-544 (1978).
10. G. L. Sarver, A novel method of friction damping for large space structures. M.I.T. Space Systems Laboratory #10-82 (May 1982).
11. T. H. H. Pian and F. C. Jr. Hallowell, Structural damping in a simple built-up beam. *Proc. 1st U.S. Nat. Cong. of Applied Mechanics*, pp. 97-102 (1952).
12. Baumeister, Avallone and Baumeister, *Standard Handbook for Mechanical Engineers*, pp. 3-26 McGraw-Hill, New York (1978).

FRACTIONAL CALCULUS TO REPRESENT
COMPLEX MODULUS

Dr. Lynn Rogers
AFWAL/FIBA
Air Force Wright Aeronautical Laboratories
Wright-Patterson Air Force Base, Ohio 45433

FRACTIONAL CALCULUS TO REPRESENT COMPLEX MODULUS

Dr. Lynn Rogers
AFWAL/FIBA
Air Force Wright Aeronautical Laboratories
Wright-Patterson Air Force Base, Ohio 45433

The following equations are extracted from References 1 and 2 and summarize recent developments in use of operators and fractional derivatives. References 1 and 2 unify and extend capability in viscoelasticity and give several citations to literature too numerous to repeat here.

The operator form of the constitutive equation is:

$$P(p_R)\tau(t_R) = Q(p_R)\gamma(t_R) \quad (1)$$

from which the complex modulus is given as:

$$G^*(j\omega_R) = Q(j\omega_R)/P(j\omega_R) \quad (2)$$

In this development t_R is reduced time, p_R is the reduced operator and ω_R is the familiar reduced frequency. Traditional Bode diagram techniques lead to representation of P and Q as factored polynomials.

$$Q(j\omega_R) = G_e \prod_l (1 + j\omega_R/\omega_{zl}) \quad (3a)$$

$$P(j\omega_R) = \prod_k (1 + j\omega_R/\omega_{pk}). \quad (3b)$$

Application of partial fractions and the Heaviside expansion formula lead to representation of the complex modulus as

$$G^*(j\omega_R) = G_e + \sum_k G_k/[1 + (j\omega_R/\omega_{pk})^{-1}] \quad (4)$$

Use of standard techniques leads to a representation of the relaxation modulus as

$$G_{rlx}(t_R) = G_e + \sum_k G_k e^{-\omega_{pk} t_R} \quad (5)$$

Extension of Bode diagrams to use of fractional order factors enables synthesis of another representation of the complex modulus.

$$Q(j\omega_R) = G_e \prod_k [1 + (j\omega_R/\omega_{nk})^{\alpha_k}] \quad (6a)$$

$$P(j\omega_R) = \prod_l [1 + (j\omega_R/\omega_{dl})^{\beta_l}]. \quad (6b)$$

Adaptation of the integer order Maxwell Model to the fractional case gives a related but much preferred (because it is causal and stable) representation.

$$G^*(j\omega_R) = G_R + \sum_k G_k / [1 + (j\omega_R/\omega_{d_k})^{-\beta_k}] \quad (7)$$

Extension to the series case of the fractional Maxwell model leads to

$$G^*(j\omega_R) = G_e + \sum_i G_i / [1 + a_i (j\omega_R/\omega_i)^{-\alpha_i} + (j\omega_R/\omega_i)^{-\beta_i}] \quad (8)$$

which may be required in order to represent certain sets of data. Similar representations exist for compliance.

The complex modulus as represented by Equation (7) or (8) is currently the preferred basis of characterization of all of the mechanical properties of a viscoelastic material. Properties other than complex modulus are expressed through interconversion based on the integer order factored polynomial [Equations (3a) and (3b)] approximation to Equation (7) [or (8)].

REFERENCES

1. Lynn Rogers, "Operators and Fractional Derivatives for Viscoelastic Constitutive Equations," J. of Rheology, 27(4), 351-372 (1983).
2. L. Rogers, "A New Algorithm for Interconversion of the Mechanical Properties of Viscoelastic Materials, AIAA Paper No. 84-1038CP, Presented at AIAA Dynamic Specialists Conference, Palm Springs, California, May 17-18, 1984.

(These two references are included in the present volume for convenience.)

Operators and Fractional Derivatives for Viscoelastic Constitutive Equations

LYNN ROGERS, *Flight Dynamics Laboratory, AFWAL/FIBA, Wright-Patterson AFB, Ohio 45433*

Synopsis

The operator form of the constitutive equation containing fractional derivatives leads to an expression for the complex modulus which is a ratio of polynomials of fractional order in reduced frequency. A ratio of factored polynomials is developed by use of Bode diagrams; another related form arises from the generalized fractional Maxwell model. Bode diagrams are used to determine parameter values. Interconversion to other mechanical properties is outlined. The results potentially form the basis of a new theory.

INTRODUCTION

Damping technology wherein viscoelastic materials are used for vibration and noise suppression is emerging rapidly and is growing in importance. Future aerospace applications will have payoff in terms of system viability, performance, cost, weight, reliability, and operational readiness. Historically, it has sufficed to work with the complex modulus covering the in-service ranges of temperature and frequency for the particular application. Accuracy and efficiency have been required in the experimental complex modulus data generation, validation, storage, retrieval, transmittal, and utilization. In practice, empirical equations have been fitted to the storage modulus and to the loss factor independently.^{1,2} While this has served well for this particular purpose, the storage and loss moduli are interrelated (ref. 3, p. 69). Therefore, this approach is based on a conceptual error.

Future applications of damping technology will be extended to require static (sustained or zero frequency) loads, shock mitigation, and interaction with active control systems. These applications cover an extremely broad range of frequency and types of loading including

impulsive, random, sinusoidal, and decaying. Thus, an accurate and mathematically convenient relationship between the forces and displacements of viscoelastic components for completely arbitrary time histories is required. Furthermore, in the near future, sophisticated analyses will indicate desired mechanical properties of new or modified polymers for an optimum design. A way will be required to communicate these desired properties for polymer dynamics and synthesis studies.

Conventional treatment of mechanical properties by viscoelasticians is based on an elegant body of formal mathematics that holds true for general time-invariant, stable linear systems. Such a system is a portion of viscoelastic material sufficiently small that stress and strain may be treated as uniform throughout and as functions of time only. When the strain is considered to be the input, the output is the stress. The constitutive relationship is the convolution integral using the relaxation modulus. Other integrals implicitly define the relaxation and the retardation spectra. In practice an empirical equation is used to describe one of these spectra. Ingenious numerical approximations to the integrals then give any resulting mechanical properties desired. Iterations are performed until the property resulting from the spectrum and the experimentally measured property agree. This approach is extremely inefficient for the advanced damping technology studies mentioned above.

This article starts with the operator form of the constitutive equation relating stress and strain for arbitrary conditions. It is established that the use of fractional derivatives in the operators results in accurate and efficient representation of the complex modulus. Bode diagrams are used to obtain factored polynomial operators of fractional degree. A generalized fractional Maxwell model is developed and offered as a feasible explanation of the relationship between fractional calculus and molecular dynamics. Interconversion based on the complex modulus defined by fractional operators is discussed.

GENERAL RELATIONSHIPS

Consider the operator form of the constitutive equation relating shear stress and strain for the linear isothermal isotropic case^{4,5}:

$$P_r(p_R)\tau(t) = P_r(p_R)\gamma(t) \quad (1)$$

This constitutive relationship makes use of a reduced time differential defined as

$$dt_R = dt/\alpha_T(T) \quad (2)$$

such that the reduced operator is given by

$$p_R = d/dt_R = \alpha_T d/dt = \alpha_T p, \quad (3)$$

where $\alpha_T(T)$ is the familiar temperature shift function. Inclusion of the α_T in this fashion is believed to be original to the present author.⁶ The Laplace transform (LT) of Eq. (1) is

$$P_r(s_R)\bar{\tau}(s_R) = P_r(s_R)\bar{\gamma}(s_R) \quad (4)$$

and the Fourier transform (FT) gives a relationship involving complex quantities valid for sinusoidal conditions:

$$P_r(j\omega_R)\tau^*(j\omega_R) = P_r(j\omega_R)\gamma^*(j\omega_R). \quad (5)$$

In general, the shear modulus transfer function is⁴

$$G(s_R) = \bar{\tau}(s_R)/\bar{\gamma}(s_R) = P_r(s_R)/P_r(s_R), \quad (6)$$

and the complex shear modulus is

$$G^*(j\omega_R) = \tau^*(j\omega_R)/\gamma^*(j\omega_R) = P_r(j\omega_R)/P_r(j\omega_R). \quad (7)$$

(The notation G^* is inconsistent but will be used because of convention.) Note that it is convenient to change domains by simple algebraic substitution:

$$p_R = \alpha_T p \leftrightarrow s_R = \alpha_T s \leftrightarrow j\omega_R = j\alpha_T \omega. \quad (8)$$

The reduced radian frequency ω_R is a product of the temperature shift function and the actual frequency. This concept implies thermorheologically simple behavior.

The LT of the relaxation modulus is given by⁴

$$\bar{G}_{111}(s) = G(s)/s = P_r(s)/sP_r(s), \quad (9)$$

and that of the creep compliance by

$$J_{\text{creep}}(s) = 1/sG(s) = P_r(s)/sP_r(s). \quad (10)$$

FRACTIONAL ORDER OPERATORS

Consider the integer order operators

$$P_r(p_R) = 1 + \sum_{k=1}^N C_k p_R^k \quad (11a)$$

and

$$R = \omega_R/\omega_{RO}. \quad (17)$$

This is recognized as a form of the equation developed by Cole and

The resulting complex modulus is⁴

$$G^*(j\omega_R) = \left[G_e + \sum_{l=1}^N d_l (j\omega_R)^l \right] / \left[1 + \sum_{k=1}^N C_k (j\omega_R)^k \right]. \quad (12)$$

Observe that the operators are interdependent to some extent: (i) together, they are arbitrary to one constant, a fact that has been used to define one of the constants as the equilibrium modulus; (ii) their degree must be equal for proper behavior of the modulus at very high values of frequency.

There has been a substantial, persistent interest in the use of fractional calculus to represent viscoelastic behavior.⁶⁻¹³ Consider the fractional order polynomial operators

$$P_r(p_R) = 1 + \sum_{k=1}^{N_e} a_k p_R^k \quad (13a)$$

and

$$P_r(p_R) = G_e + \sum_{l=1}^{N_b} b_l p_R^l. \quad (13b)$$

The simplest operators of current interest are

$$P_r(p_R) = 1 + a_1 p_R^k \quad (14a)$$

and

$$P_r(p_R) = G_e + b_1 p_R^k. \quad (14b)$$

It is convenient to change notation to

$$P_r(p_R) = 1 + (p_R/\omega_{RO})^\beta \quad (15a)$$

and

$$P_r(p_R) = G_e + G_e (p_R/\omega_{RO})^\beta. \quad (15b)$$

The corresponding complex modulus is

$$G^*(j\omega_R) = [G_e + G_e (jR)^\beta] / [1 + (jR)^\beta], \quad (16)$$

where the normalized reduced frequency is

Cole¹⁴ on an empirical basis. This equation was developed to represent the dielectric relaxation but has been used extensively in viscoelasticity, including both creep and relaxation. The equation was developed independently by Bagley⁷ and the present author introduced the current notation.⁶

The storage (real) modulus G_R , the loss (imaginary) modulus G_I , and the material loss factor D_G for typical parameter values are presented in Figure 1. Equation (16) requires far fewer terms than Eq. (12) to represent complex modulus data accurately.

The relaxation spectrum, stress relaxation, and creep compliance for the simplest case, Eq. (16), will be presented. This begins to build an argument for the appropriateness of the general case, Eq. (13). The relaxation spectrum associated with the Cole-Cole expression is well known:

$$H(\tau) = \frac{(2/\pi)(G_g - G_e) \sin(\beta\pi/2)}{(\tau/\tau_0)^\beta + 2 \cos(\beta\pi/2) + (\tau/\tau_0)^{-\beta}} \quad (18)$$

and compares favorably with the extensively used modified power law.⁴

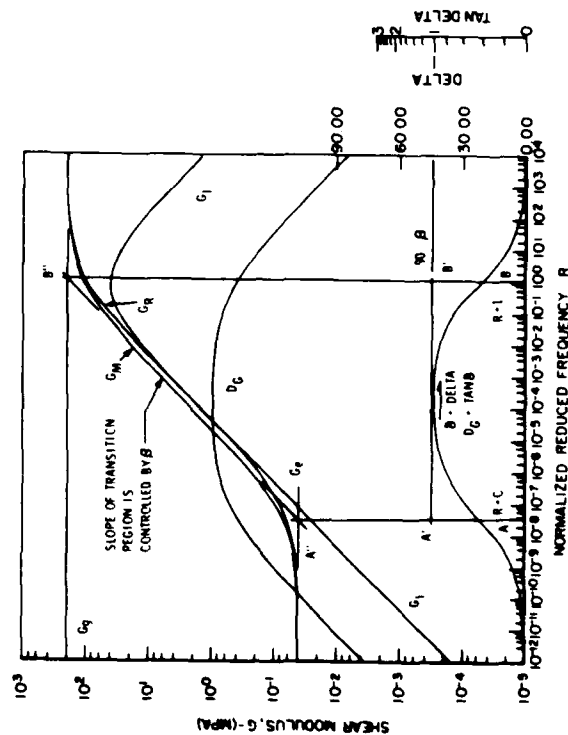


Fig. 1. Complex shear modulus quantities.

Substituting Eqs. (8) and (16) into Eq. (9) gives the LT of the stress relaxation:

$$\bar{G}_{rlx}(s_{rlx}) = G_e/s_{rlx} + (G_g - G_e)/s_{rlx}(1 + s_{rlx}^{-\beta}) \quad (19)$$

and Eq. (10) results in that for the creep compliance

$$J_{crp}(s_{crp}) = J_e/s_{crp} + (J_g - J_e)/s_{crp}(1 + s_{crp}^{-\beta}), \quad (20)$$

where

$$s_{rlx} = s_R/\omega_{RO}; \quad s_{crp} = J_e s_R^\beta/J_g; \quad J_e = 1/G_e; \quad J_g = 1/G_g \quad (21)$$

For either relaxation or creep, it is necessary to perform the inverse LT of

$$\bar{r}(s_x) = 1/s_x(1 + s_x^{-\beta}). \quad (22)$$

For constant temperature and $\beta = 1/2$, the inverse LT may be written explicitly as the product of an exponential and a complementary error function:

$$\begin{aligned} r(t_x) &= e^{t_x} \operatorname{erfc} t_x^{1/2} \\ &\simeq (\pi t_x)^{-1/2}, \quad t_x \text{ large.} \end{aligned} \quad (23)$$

It follows that the relaxation shear modulus is

$$G_{rlx}(t_{rlx}) = G_e + (G_g - G_e)r(t_{rlx}), \quad (24)$$

and the creep compliance is

$$J_{crp}(t_{crp}) = J_e + (J_g - J_e)r(t_{crp}), \quad (25)$$

where

$$t_{rlx} = \omega_{RO} t_R; \quad t_{crp} = (J_g/J_e)^2 \omega_{RO} t_R. \quad (26)$$

These quantities are presented in Figure 2.

BODE DIAGRAM FUNDAMENTALS

The following briefly summarizes the Bode diagram development in elementary texts covering feedback control system analysis.¹⁵ The logarithm of a complex number

$$z = |z|e^{j\phi} \quad (27)$$

is itself a complex number:

$$\log z = \log|z| + (0.434 \dots)j\phi. \quad (28)$$

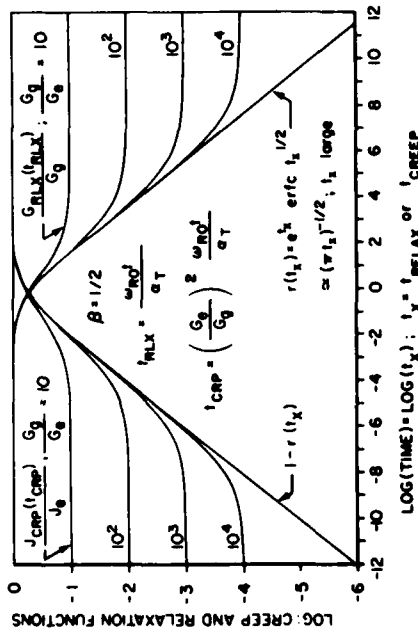


Fig. 2. Relaxation and creep quantities.

When dealing with the magnitude and the phase separately, the factor multiplying the phase may be cancelled out and omitted. The manner in which multiplication and division of complex numbers become addition and subtraction in the logarithmic domain may be illustrated:

$$G = N_1 N_2 / D_1 D_2, \quad (28a)$$

$$\log G = \log N_1 + \log N_2 - \log D_1 - \log D_2. \quad (28b)$$

Separating Eq. (28b) into real and imaginary components leads to

$$\log |G| = \log |N_1| + \log |N_2| - \log |D_1| - \log |D_2| \quad (28c)$$

and

$$\phi_G = \phi_{N_1} + \phi_{N_2} - \phi_{D_1} - \phi_{D_2}. \quad (28d)$$

In feedback control systems, the complex frequency response function is typically written as a ratio of factored polynomials:

$$H(j\omega) = \frac{K(1 + j\omega T_1)(1 + j\omega T_2) \dots}{(j\omega)^n [1 + j\omega 2b_1/\omega_i + (j\omega/\omega_i)^2] \dots} \quad (29)$$

There are three basic types of factors in addition to the constant. The factors are each functions of $j\omega$ rather than constants as in Eq. (28). The low-frequency and the high-frequency asymptotes of the magnitude for all of the types of factors are straight lines on log-log scales; similarly for the phase on linear-log scales. Semilog graph paper may

be used for both magnitude and phase provided the magnitude is expressed in decibel (db) units (not used here).

The asymptotes of individual factors play the dominant role in the Bode diagram technique.

The complex modulus, Eq. (7), is a frequency response function. Because of its particular characteristics, only one type of factor is needed to write an expression in terms of a ratio of factored polynomials of integer order⁶:

$$G^*(j\omega_R) = G_e \prod_{k=1}^N (1 + j\omega_R/\omega_{zk}) / \prod_{l=1}^N (1 + j\omega_R/\omega_{pl}) \quad (30)$$

from which

$$P_r(j\omega_R) = \prod_{l=1}^N (1 + j\omega_R/\omega_{pl}) \quad (31a)$$

and

$$P_\gamma(j\omega_R) = G_e \prod_{k=1}^N (1 + j\omega_R/\omega_{zk}). \quad (31b)$$

Equations (31) and (11) are different forms of the same expressions. From linear systems theory, if they are valid for the infinite frequency range, they are valid for arbitrary conditions in Eq. (1).

FRACTIONAL POWERS IN BODE DIAGRAMS

The previous material suggests a consideration of expressions for the fractional polynomials in the form of products of factors of fractional degree,

$$P_r(j\omega_R) = \prod_{l=1}^{N_d} [1 + (j\omega_R/\omega_{dl})^{\beta_l}] \quad (32a)$$

and

$$P_\gamma(j\omega_R) = G_e \prod_{k=1}^{N_n} [1 + (j\omega_R/\omega_{nk})^{\alpha_k}]. \quad (32b)$$

Retaining only one factor in each leads to

$$G^*(j\omega_R) = G_e [1 + (jR/c)^{\beta_l}] / [1 + (jR)^{\beta_l}], \quad (33)$$

where

$$R = \omega_R/\omega_{dl}; \quad c = \omega_{n1}/\omega_{dl}, \quad (34)$$

which is seen to be identical to Eq. (16) provided

$$\omega_{d1} = \omega_{RO}; \quad c = (G_e/G_g)^{1/\beta}; \quad \alpha_1 = \beta_1 = \beta. \quad (35)$$

Bode diagram techniques will now be extended to factors containing fractional powers. The first factor to be considered is

$$z = (jR)^\beta. \quad (36)$$

Recall from complex numbers that

$$j = (-1)^{1/2} = e^{j\pi/2} = \cos(\pi/2) + j \sin(\pi/2). \quad (37)$$

When Eq. (37) is raised to a power, it follows that

$$j^\beta = e^{j\beta\pi/2} = \cos(\beta\pi/2) + j \sin(\beta\pi/2). \quad (38)$$

Substituting Eq. (38) into Eq. (36) the magnitude is

$$|z| = R^\beta, \quad (39a)$$

which is a straight line of slope β on a log-log scale. The phase of Eq. (36) is a constant,

$$\phi_z = \arctan(\beta\pi/2). \quad (39b)$$

The other factor to be covered is

$$w = 1 + (jR)^\beta. \quad (40a)$$

Its magnitude is

$$|w| = [1 + 2R^\beta \cos(\beta\pi/2) + R^{2\beta}]^{1/2}, \quad (40b)$$

and its phase is

$$\phi_w = \arctan\{|R^\beta \sin(\beta\pi/2)|/[1 + R^\beta \cos(\beta\pi/2)]\}. \quad (40c)$$

These are plotted in Figure 3 for $\beta = 1/2$ and $\beta = 1$. When $\beta = 1/2$, the phase asymptote is A-B-C_{1/2}-D_{1/2} and the magnitude asymptote is E-F-G_{1/2}. When $\beta = 1$, the factor is a standard one in the usual Bode diagram development with asymptotes A-B-C₁-D₁ and E-F₁-G₁. The frequency where the low- and high-frequency magnitude asymptotes intersect (at $R = 1$) is called the "corner" or "break" frequency. A wide range of values for β is permissible.

When the factor Eq. (40a) appears in the denominator

$$w = 1/[1 + (jR)^\beta] \quad (41)$$

its magnitude and phase are mirror images reflected about one and zero, respectively.

Extending Bode diagram techniques to accommodate fractional

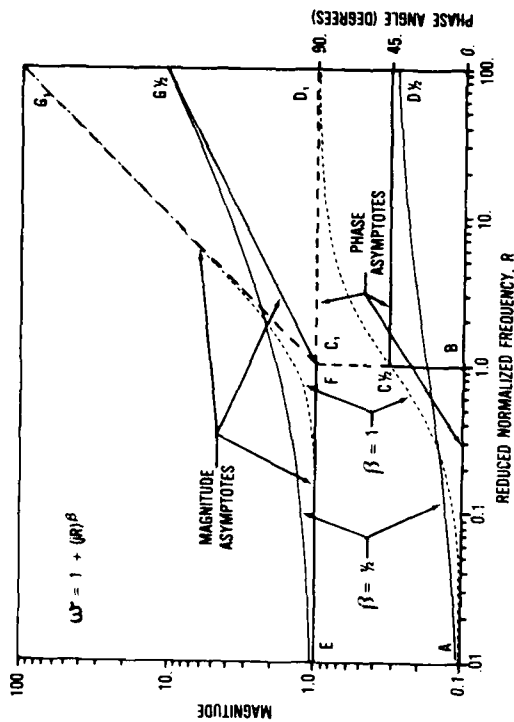


Fig. 3. Bode diagram of a polynomial factor.

powers is believed to be original to this article. The use of reduced frequency instead of the actual radian frequency used in standard texts presents no conceptual, mathematical, or graphical change.

It is seen that factors containing fractional powers of $j\omega_R$ behave much the same as ones with integer powers. The crucial difference is that instead of only phase asymptotes of $\pm k 90^\circ$ (k an integer) with their associated values of magnitude slope being possible, a continuum of values is now possible.

To illustrate the Bode diagram technique consider the expression (33) [equivalent to Eq. (16)] for the complex modulus quantities plotted in Figure 1. In addition to the G_R , G_I , D_I , D_C quantities previously mentioned, the magnitude G_M on a log scale and the phase δ on a linear scale are plotted. At very low values of reduced frequency,

$$R \ll c, \quad (42a)$$

the constant G_e determines behavior because both of the other two factors are each very near unity. When

$$R = c \quad (42b)$$

a break frequency occurs (point A") and the product of G_e and the

numerator determines behavior. The combined magnitude asymptote breaks up at point A" while the phase asymptote moves from point A to A'. When

$$R = 1 \quad (42c)$$

the denominator has also become important.

To further illustrate the Bode diagram technique, consider the expressions

$$P_z(j\omega_R) = 1 + z_3, \quad (43a)$$

$$P_\gamma(j\omega_R) = G_0 z_1(1 + z_2), \quad (43b)$$

$$G^*(j\omega_R) = G_0 z_1(1 + z_2)/(1 + z_3), \quad (44a)$$

$$z_k = (j\tau_k)^{\beta_k}; \quad \tau_k = \omega_R/\omega_k, \quad (44b)$$

$$\omega_1 = \omega_2 = c\omega_{RU}; \quad \omega_3 = \omega_{RO}, \quad (44c)$$

$$\beta_1 = \beta_R; \quad \beta_2 = \beta_T - \beta_R; \quad \beta_3 = \beta_T - \beta_G. \quad (44d)$$

Subscripts in this and succeeding developments are explained as follows: F = flow, R = rubbery, T = transition, P = plateau, and G = glassy.

In Figure 4 the magnitude asymptotes (labeled $|k|$) and the phase asymptote (labeled $\angle k$) of each factor and of their product (asymptote sum) are given.

SYNTHESIS OF OPERATORS

In the above development, the differential equation is the starting point. Here, however, the objective is the reverse operation—to synthesize the operators from complex modulus data. The technique of Bode plots is an essential tool. The procedure is to select factors for the numerator and denominator such that their asymptotes for magnitude and phase simultaneously approximate the corresponding experimental curves. The process begins at the lowest frequency of interest and progresses to higher frequencies.

Equation (44), used in the previous section, was actually synthesized. It represents a material that has a single transition and that may have either a lossy rubbery region or a glassy region or both. Consequently, Eq. (44) is significantly more general than Eq. (16). The corresponding differential equation (1) may be obtained by taking the numerator, Eq. (43b), as the operator on shear strain and the denominator, Eq. (43a), as the stress operator.

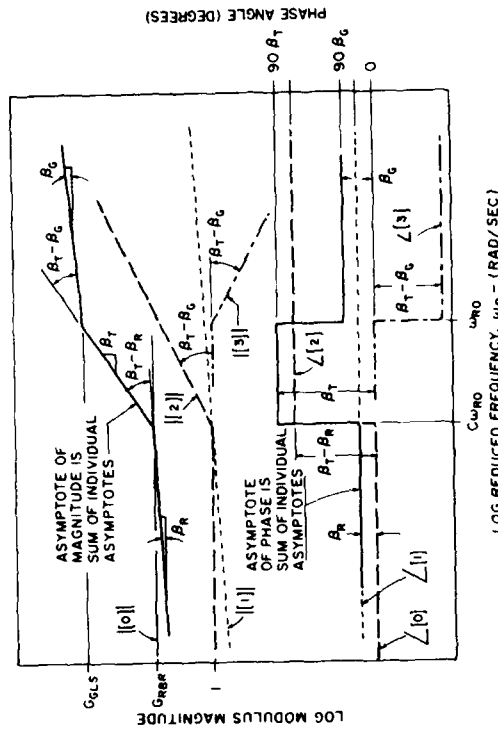


Fig. 4. Synthesis of complex modulus frequency response functions.

Equation (44a) correctly represents materials under sinusoidal or band-limited random conditions; however, there are three potential difficulties in directly using an expression of this form for creep, relaxation, constant strain rate, or related studies. First, if β_G is not zero, Eq. (44a) will indicate an infinite modulus at infinite frequency. Second, a negative phase angle (physically impossible) may be indicated at very low values of frequency, depending on the relative values of β_G and β_R .¹⁶ Third, the modulus is indicated to be zero at zero frequency when β_R is not zero. The expression for a single transition material,

$$G^* = G_e(1 + z_1)(1 + z_2)/(1 + z_3)(1 + z_4), \quad (45a)$$

where

$$\beta_1 = \beta_R; \quad \beta_2 = \beta_T - \beta_R; \quad \beta_3 = \beta_T - \beta_G; \quad \beta_4 = \beta_G; \quad (45b)$$

$$r_1 < r_2; \quad r_2 \approx r_3/c; \quad r_4 < r_3,$$

is adapted from Eq. (44a) and will have a finite modulus at infinite frequency and a nonzero modulus at zero frequency; also, it would seem that this expression would not have the negative phase angle, but this has not been verified analytically. The operators corresponding to Eq. (45a) may be written by inspection.

$$P_r(j\omega_R) = (1 + z_3)(1 + z_4) \quad (46a)$$

and

$$P_r(j\omega_R) = G_e(1 + z_1)(1 + z_2). \quad (46b)$$

An equation with flow, lossy rubbery plateau, transition, and lossy glassy regions is

$$G^* = G_{A21}(1 + z_3)/(1 + z_2)(1 + z_4), \quad (47a)$$

where

$$\beta_1 = \beta_F; \quad \beta_2 = \beta_F - \beta_R; \quad \beta_3 = \beta_T - \beta_R; \quad \beta_4 = \beta_T - \beta_G; \quad r_1 = r_2 = \omega_R/\omega_1; \quad r_3 = \omega_R/c\omega_2; \quad r_4 = \omega_R/\omega_2. \quad (47b)$$

An equation for a lossy rubbery, a transition -1, a lossy plateau, a transition -2, and a lossy glassy region is

$$G^* = G_{B21}(1 + z_2)(1 + z_4)/(1 + z_3)(1 + z_5), \quad (48a)$$

where

$$\beta_1 = \beta_R; \quad \beta_2 = \beta_{T1} - \beta_R; \quad \beta_3 = \beta_{T1} - \beta_F; \quad \beta_4 = \beta_{T2} - \beta_F; \quad \beta_5 = \beta_{T2} - \beta_G; \quad r_1 = r_2 = \omega_R/c\omega_1; \quad r_3 = \omega_R/\omega_1; \quad r_4 = \omega_R/c\omega_2; \quad r_5 = \omega_R/\omega_2. \quad (48b)$$

Equations (47a) and (48a) correctly represent properties under sinusoidal or band-limited conditions as does Eq. (44a). They have the same potential problems for other applications, but expressions which circumvent these difficulties could be developed.

For the present, expressions are based on fitting the form of the complex modulus curves while complex modulus data is used directly to determine parameter values. In the future, with interconversion procedures better mechanized, it will be possible to determine parameter values from other types of experimental data, e.g., stress relaxation.

GENERALIZED FRACTIONAL MAXWELL MODELS

The integer order differential equation defined by Eqs. (11a) and (11b) may be associated with a network of springs and dashpots; a common arrangement is the generalized Maxwell model, also called the Weichert model.⁴ The system of an equilibrium spring in parallel with N_k Maxwell series elements may be represented by

$$F(s)/\bar{\epsilon}(s) = k(s) = k_e + \sum_{i=1}^{N_k} k_i C_i s / (k_i + C_i s). \quad (49)$$

In Eq. (49), the k_i 's and C_i 's are the spring and dashpot coefficients and s is the Laplace variable. With a change in notation, Eq. (49) may be written as

$$k(s) = k_e + \sum_{i=1}^{N_k} k_i (s/\omega_{pi}) / (1 + s/\omega_{pi}). \quad (50)$$

The analogous complex modulus is

$$G^*(j\omega_R) = G_e + \sum_{k=1}^{N_k} G_k (j\omega_R/\omega_{pk}) / (1 + j\omega_R/\omega_{pk}), \quad (51)$$

which may be placed in the ratio of polynomial form such as Eqs. (11). The denominator is given by Eq. (31a), and the numerator is

$$P_r(j\omega_R) = G_e \left\{ P_r(j\omega_R) + \sum_{k=1}^{N_k} G_k (j\omega_R/\omega_{pk}) \prod_{i=1}^{N_k} (1 + j\omega_R/\omega_{pi}) \right\}. \quad (52)$$

In the Eq. (49) representation of the generalized Maxwell model, the ratio of the LT of the force across the dashpot to that of the relative displacement is

$$\bar{F}_i(s)/\bar{y}_i(s) = c_i s. \quad (53)$$

Extending the work of Cole and Cole,¹⁴ each dashpot is replaced by a fractional type of element,

$$\bar{F}_i(s_R)/\bar{y}_i(s_R) = a_i s_i^{\beta_i} = k_i (s_R/\omega_{dk})^{\beta_i}, \quad (54)$$

which both stores and dissipates energy. The complex modulus analogous to Eq. (51) for this generalized fractional Maxwell model is

$$G^*(j\omega_R) = G_e + \sum_{k=1}^{N_d} G_k (j\omega_R/\omega_{dk})^{\beta_k} / [1 + (j\omega_R/\omega_{dk})^{\beta_k}]. \quad (55)$$

This equation may be written in the form of ratios of polynomials of fractional degree, Eq. (13), and the denominator is again in factored form and is given by Eq. (32a). The numerator polynomial is

$$P_r(j\omega_R) = G_e \left\{ P_r(j\omega_R) + \sum_{k=1}^{N_d} G_k (j\omega_R/\omega_{dk})^{\beta_k} \prod_{i=1}^{N_d} [1 + (j\omega_R/\omega_{di})^{\beta_i}] \right\}. \quad (56)$$

In general, this numerator cannot be factored. However, the Bode plot technique still provides an essential tool in determining parameter values. The break frequencies where the magnitude slope decreases indicate the ω_k s. The slopes of the magnitude asymptotes (and the phase angle) indicate the β_k s. The G_k s are determined by arithmetic rather than logarithmic subtraction.

When only one element in Eq. (55) is considered, the complex modulus is

$$G^*(j\omega_R) = G_e + G_1(j\omega_R/\omega_{d1})^{\beta_1}/[1 + (j\omega_R/\omega_{d1})^{\beta_1}] \quad (57)$$

and could be placed in the form of Eq. (16) [or Eq. (33)]. In the transition region centered on

$$\omega_R \simeq (\omega_{n1}\omega_{d1})^{1/2} \quad (58)$$

it may be shown that

$$G^* \simeq G_1(j\omega_R/\omega_{d1})^{\beta_1}. \quad (59)$$

Bagley and Torvik⁸ have offered a physical explanation relating Eq. (59) and the fractional calculus to basic molecular dynamics theory. The origin of this term was the fractional dashpot. Each term in the summation Eq. (55) represents the share of the load (stress) carried by a component of the viscoelastic material and its particular transition. This feasible physical explanation may provide guidance in the future for polymer synthesis to achieve desired mechanical properties.

Recent work by Salvia¹⁷ has included two fractional dashpots in series in each Maxwell-type element to obtain

$$G^*(j\omega_R) = G_e + \sum_{i=1}^N G_i/[1 + a_i(j\omega_R/\omega_i)^{-\alpha_i} + (j\omega_R/\omega_i)^{-\beta_i}]. \quad (60a)$$

Early work indicates that improved data fits are achieved for

$$\alpha_i \simeq \beta_i/2; \quad a_i \simeq 0.5. \quad (60b)$$

It would seem that Eqs. (55) and (60a) would present none of the potential problems that Eq. (44a) does. The individual physical models only dissipate energy and the resulting combined mathematical model would reflect the same properties. Thus, causality and the relationships between the real and imaginary components are inherently satisfied.

A generalized fractional Kelvin model (GFKM) based on complex

compliance could be developed. The fact that Eq. (56) is not factorable implies that the generalized fractional Maxwell model given by Eq. (55) has no exactly corresponding GFKM. Future developments in analysis of series/parallel load paths may guide work in this area.

INTERCONVERSION

This article proposes taking the complex shear modulus expressed in the form of Eq. (55) [or perhaps Eq. (60a)] as the basic mechanical property to characterize a polymer. The operators for use in Eq. (1) are found easily; however, the mathematics of fractional calculus and resulting functions is not sufficiently mature to permit interconversion to other mechanical properties directly. A new algorithm has been developed to obtain parameter values for Eq. (30) to represent any specified complex modulus accurately.¹⁸ The relaxation modulus is then given by⁶

$$G_{1R}(t_R) = G_e + \sum_{k=1}^N G_k e^{-\omega_{pk} t_R}, \quad (61a)$$

where

$$G_k = -G_e \prod_{l=1}^N (1 - \omega_{pk}/\omega_{zl}) / \prod_{\substack{l=1 \\ l \neq k}}^N (1 - \omega_{pk}/\omega_{pl}). \quad (61b)$$

Incidentally, the G_k s in Eq. (61a) are the same ones as in Eq. (51). Similarly, the creep compliance is given by

$$J_{crp}(t_R) = J_g + \sum_{k=1}^N J_k (1 - e^{-\omega_{zk} t_R}), \quad (62a)$$

where

$$J_k = J_g \prod_{l=1}^N (1 - \omega_{zk}/\omega_{pl}) / \prod_{\substack{l=1 \\ l \neq k}}^N (1 - \omega_{zk}/\omega_{zl}). \quad (62b)$$

With the complex modulus basis Eq. (55) and expressed by Eq. (30) and both the relaxation modulus Eq. (61a) and the creep compliance Eq. (62a) expressed analytically, any other mechanical property may be obtained easily. Response to any specified input may also be obtained easily.

It seems that these equations could be used in iterative fashion to define a complex modulus with either relaxation or creep experi-

mental data similar to the way relaxation and retardation spectra are currently used.

TEMPERATURE NOMOGRAM

The temperature nomogram developed by Jones¹⁹ is a major advance in the graphical presentation of complex modulus data. The reading of storage (real) modulus, loss (imaginary) modulus, and loss factor as functions of temperature and frequency from graphical presentations is greatly facilitated by its use. In Figures 6 and 7 a vertical scale for actual frequency is included, as are a number of diagonal lines. Each diagonal line represents a particular temperature according to Eq. (8). The reduced frequency equation, Eq. (8), relates the temperature, reduced frequency, and frequency. A reduced frequency value (vertical line) is defined by the intersection of a frequency value (horizontal line) and a temperature value (diagonal line). The diagonal temperature lines may be used to indicate the bounds of experimental temperatures and so avoid inadvertent extrapolation of properties as a function of temperature. The concept is also applicable to reduced time for creep and relaxation plots.

SELECTED MATERIALS DATA

Figures 5, 6, and 7 present selected sets of complex modulus data. The data in Figure 5 were all taken at 21°C over approximately eight decades of experimental frequency for a secondary transition of poly(methyl methacrylate) (PMMA).²⁰ The fit of the very simple model, Eq. (16), to the data is outstanding.

Figure 6 presents a set of data for 3-M ISD-112, a viscoelastic material familiar to damping engineers. This set of data comes from a sandwich beam under random loading and was reduced using sixth-order theory.²¹ The scatter in this set of data is somewhat less than typical. The decrease of the loss factor with decreasing reduced frequency is seen here for the first time with this type of data. The fit of the model is quite good and is acceptable to applications engineers.

Figure 7 presents a set of complex Young's modulus for a polyurethane.²² The test method uses a sinusoidal extensional resonance of a solid rod covering wide temperature and frequency ranges. The scatter in the data is remarkably low but does suggest the possibility

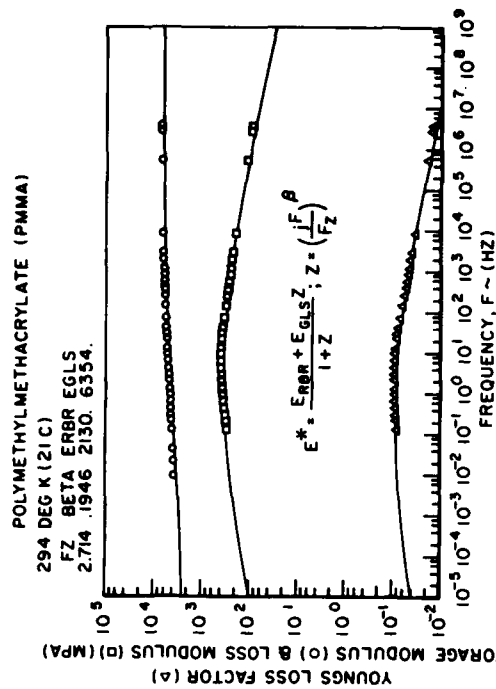


Fig. 5. Experimental complex modulus at constant temperature.

of systematic errors dependent on the mode. Here Eq. (44a) is used for the model. The use of this slightly more complicated model is dictated by the lossy glassy region, which is revealed by the high loss

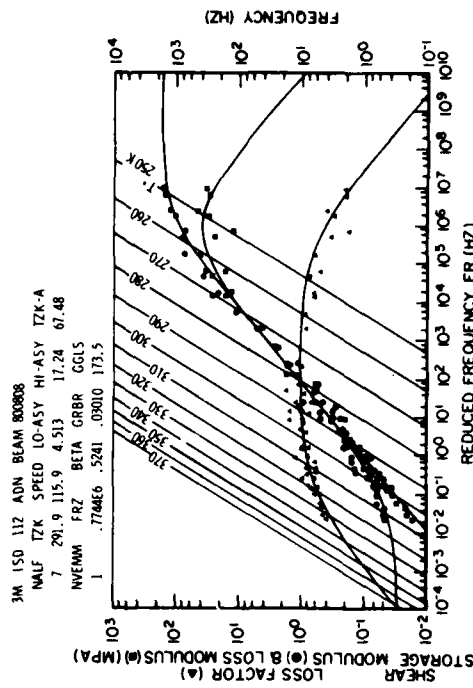


Fig. 6. Experimental complex modulus of a damping material.

The GFMM is proposed as the basic representation of the mechanical properties of a polymer. One reason is that physical explanation relates the fractional calculus to molecular dynamics; this may evolve into guidance in the development of polymers having desired mechanical properties. Another reason is the mathematical implications. Since each element in the GFMM only stores and/or dissipates energy, the complete model cannot create energy under any conditions. This means that the model is "causal" and satisfies all the established mathematical relationships for stable, time-invariant, linear systems. Therefore, all other mechanical properties are well behaved. By contrast, the RFPFD is known to have negative phase angles for certain parameter values, and therefore, is noncausal.

A generalized fractional Kelvin model (GFKM) could be developed which would have a single load path with arrangements in series rather than parallel load paths. The parallel paths and their associated transitions are easier to visualize. No doubt the actual mechanics combines the series and parallel. Perhaps fully interchangeable GFKM and GFMM will be developed. Another possibility is the development of an "exponential spectrum" to be associated with the relaxation and retardation spectra.

The RFPFD, whether from the RFPFD or the GFMM which represents the complex modulus, also give the operators for the constitutive equation (1). This equation is valid for arbitrary conditions. Little use can be made of these at present and interconversion and response to general inputs must be based on the approximation by large integer order systems outlined here.

Although the presentation is in the context of complex shear modulus, it is fully applicable to all other complex moduli including Young's, bulk, wave propagation, etc., and the corresponding complex compliances.

The operator form of the constitutive equation is used. The operators are defined by complex modulus data. Once the operators are defined, the constitutive equation represents material behavior in all modes of response (although explicit expressions may be unobtainable). The resulting expression for complex modulus contains very few terms when fractional powers are used. The fractional powers arise from fractional derivatives and vice versa. A physical explanation relates the fractional calculus to molecular dynamics. Collectively, these interrelated, consistent, and mutually supportive facts form the basis of a better understanding of behavior and, po-

OPERATORS FOR CONSTITUTIVE EQUATIONS

369

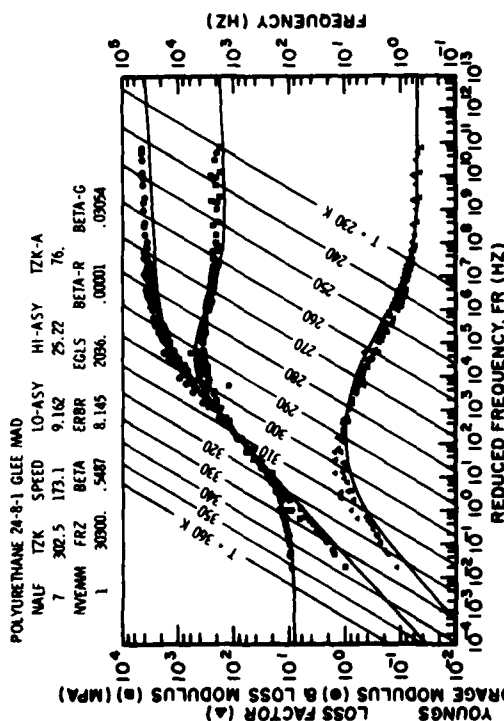


Fig. 7. Experimental complex modulus with lossy glassy region.

factor, the slope of the loss modulus, and the slope of the storage modulus. The rubbery region is not sufficiently defined to indicate whether or not it is lossy. The set of parameter values in the model has been selected as a compromise to fit the data over the entire frequency range; fit in any narrow region of specific interest could be improved, but at the expense of degrading the fit in other regions. The fit is considered adequate to support the model. Further investigations would be required to determine the need for an improved temperature shift function, a more complicated model, or the elimination of experimental or data reduction errors.

DISCUSSION

This article established that ratios of polynomials of fractional degree (RFPFD) represent the complex shear modulus accurately and efficiently. Two candidate forms were presented, namely ratios of factored polynomials of fractional degree (RFPFD) and the form arising from the generalized fractional Maxwell model (GFMM). Bode diagram techniques were summarized and gave rise to the form of the RFPFD; they also guide the determination of the parameter values in both forms.

tentially, a new theory. It is not "empirical" in the usual sense of the term.

Of many individuals and organizations contributing to this article, the contributions of Maj. Ron Bagley, Ph.D., AF Academy, Dr. D. I. G. Jones and Dr. J. P. Henderson, Materials Lab at Wright-Patterson AFB, both A. D. Nashif (President) and M. Parin of Anatrol Corp., and M. Drake of University of Dayton Research Institute are especially noteworthy. Reproduction for any purpose of the U.S. Government is permissible.

References

1. L. Rogers and A. D. Nashif, "Computerized Processing and Empirical Representation of Viscoelastic Material Property Data and Preliminary Constrained Layer Damping Treatment Design," *The Shock and Vibration Bulletin*, No. 48, September 1978, Part 2, pp. 23-37.
2. C. King, "Computerized Processing and Graphic Representation of Viscoelastic Material Property Data," AFML-TR-79-4099, Wright-Patterson AFB, 1979. (Available from Defense Technical Information Center as AD A079914.)
3. J. D. Ferry, *Viscoelastic Properties of Polymers*, Wiley, New York, 1980, 3rd ed.
4. M. L. Williams, *AIAA J.*, 2(5), 785-808 (1964).
5. R. M. Christensen, *Theory of Viscoelasticity, An Introduction*, Academic, New York, 1971.
6. L. Rogers, "On Modeling Viscoelastic Behavior," *The Shock and Vibration Bulletin* No. 51, May 1981, Part 1, pp. 55-69.
7. R. L. Bagley, "Applications of Generalized Derivatives to Viscoelasticity," AF Materials Lab TR-79-4103, November 1979. (Available from Defense Technical Information Center as ADA 081131.)
8. R. L. Bagley and P. J. Torvik, *J. Rheol.*, 27, 201 (1983).
9. M. Caputo, *J. Acoust. Soc. Am.*, 60(3), 634-639 (1976).
10. M. Caputo, *Ann. Geofis.*, XIX(4), 383-393 (1966).
11. R. D. Calleja and G. M. Guzman, *Am. R. Soc. Esp. Fis. Quim. Ser. A*, 71(4), 277-279 (1975).
12. W. Smit and H. de Vries, *Rheol. Acta*, 9(4), 525-534 (1970).
13. G. L. Slonimsky, *J. Polym. Sci. C*, 16, 1667-1672 (1967).
14. K. S. Cole and R. H. Cole, *J. Chem. Phys.*, 9, 341-351 (1941).
15. J. J. D'Azzo and C. H. Houpis, *Feedback Control System Analysis and Synthesis*, 2nd ed., McGraw-Hill, New York, 1966, pp. 175-194.
16. R. L. Bagley, private communication.
17. M. Salvia, "Propriétés Dynamiques des Propriétés Solides Composites," Thèse Doc. Ing., Université Claude Bernard Lyon I, France, 1981.
18. L. Rogers, "A New Algorithm for Approximate Inverse Laplace Transformation of Complex Modulus Functions," unpublished.
19. D. I. G. Jones, "A Reduced-Temperature Nomogram for Characterization of Damping Material Behavior," *The Shock and Vibration Bulletin* No. 48, September 1978, Part 2, pp. 13-22.

20. B. E. Read and J. C. Duncan, "Measurement of Dynamic Properties of Polymeric Glasses for Different Modes of Deformation," *Polym. Test.*, 2, 135-150 (1981).
21. L. Rogers and R. W. Gordon, "Damping Material Properties from Sandwich Beam Data Using Sixth Order Theory," presented at the 52nd Shock and Vibration Symposium, New Orleans, LA, October 27-29, 1981 (unpublished).
22. G. F. Lee and W. M. Madigosky, *J. Acoust. Soc. Am.*, 73(4), 1374 (1983).

Received April 14, 1982

Revised February 15, 1983

Accepted March 1, 1983

PRESENTED AT THE AIAA DYNAMICS SPECIALISTS CONFERENCE
Palm Springs, California, May 17-18, 1984
Paper No. 84-1038-CP

A NEW ALGORITHM FOR INTERCONVERSION OF THE MECHANICAL PROPERTIES
OF VISCOELASTIC MATERIALS

Dr. Lynn Rogers*
Flight Dynamics Laboratory of the
AF Wright Aeronautical Laboratories
Wright-Patterson AFB, Ohio

Abstract

The new algorithm presented consists of the use of a ratio of factored polynomials in the reduced frequency to approximate the complex modulus and an artful procedure to evaluate the parameters. A corresponding Prony series is easily obtained to represent the relaxation modulus; the creep compliance and discrete relaxation and retardation spectra are likewise easily obtained. Series representations with 50 terms are routinely used; they are very convenient and well-behaved.

Introduction

Conventional treatment of mechanical properties by viscoelasticians is based on an elegant body of formal mathematics which holds true for general time-invariant, stable linear systems having an input and a resulting output. A portion of viscoelastic material sufficiently small that stress, strain and temperature may be treated as uniform throughout and as functions of time only is such a system. Many times an empirical equation is used to describe either the retardation or the relaxation spectrum. Elaborate and ingenious numerical approximations then give any of the mechanical properties desired.

By contrast, the present effort starts with an approximation to the complex modulus with an expression in the form of a ratio of factored polynomials. This expression directly leads to representations for other mechanical properties. Convenience and well-behaved functions are guaranteed. Accuracy is achieved by using as many terms as desired. Historical methods of determining parameter values in series representations require considerable experience and often are limited to a few terms. There does not appear to be a practical limitation on the number of terms as an N of 50 has been used routinely. Moreover, the evaluation of parameters is done by computer in a completely automated fashion.

Selected Relationships

The standard viscoelastic model of the constitutive relation for the linear isothermal isotropic case^{1,2} in operator form is

$$P(p_R)\tau(t_R) = Q(p_R)\gamma(t_R) \quad (1)$$

where the operators may be integer order

$$P(p_R) = 1 + \sum_{k=1}^N a_k p_R^k \quad (2a)$$

$$Q(p_R) = G_e + \sum_{l=1}^N b_l p_R^l \quad (2b)$$

This constitutive relation makes use of a reduced time differential defined as

$$dt_R = dt/a_T(T) \quad (3)$$

where the a_T is the well known temperature shift function such that the reduced operator is

$$p_R = d/dt_R \quad (4)$$

The inclusion of a_T in this way is believed to be original to the present author.³ By taking the Laplace transform and substituting $j\omega_R$ for s_R , the complex shear modulus may be written¹

$$G^*(j\omega_R) = \frac{G_e + \sum_{l=1}^N b_l (j\omega_R)^l}{1 + \sum_{k=1}^N a_k (j\omega_R)^k} \quad (5)$$

where the reduced radian frequency is

$$\omega_R = \omega a_T \quad (6)$$

This may be written as a ratio of factored polynomials in $j\omega_R$ ³

$$G^*(j\omega_R) = \frac{G_e \prod_{l=1}^N (1 + j\omega_R/\omega_{z_l})}{\prod_{k=1}^N (1 + j\omega_R/\omega_{p_k})} \quad (7)$$

This form of the complex modulus is the one desired as the basis for the present effort. The preceding development was for the purpose of outlining its origin.

Shapery¹ has had success in representing the relaxation modulus as a Prony series

$$G_{RELAX}(t_R) = G_e + \sum_{k=1}^N G_k e^{-\omega_{p_k} t_R} \quad (8)$$

The complex shear modulus associated with (8) is given^{1,3}

$$G^*(j\omega_R) = G_e + \sum_{k=1}^N \frac{G_k j\omega_R/\omega_{p_k}}{1 + j\omega_R/\omega_{p_k}} \quad (9)$$

The ω_{p_k} 's are identical in (9) and (7). The G_k 's may be found using the method of partial fractions and the Heaviside expansion formula³

*Aerospace Engineer, Structure and Dynamics
Division, Associate Fellow AIAA

$$G_k = -G_e \frac{\prod_{l=1}^N (1 - \omega_{p_l}/\omega_{z_l})}{\prod_{l=1}^N (1 - \omega_{p_l}/\omega_{p_l})} \quad (10)$$

Similarly, Knaus,¹ following Shapery, had success in representing the creep compliance

$$J_{\text{CREEP}}(t_R) = J_g + \sum_{k=1}^N J_k (1 - e^{-\omega_{z_k} t_R}) \quad (11)$$

and the associated complex compliance may be obtained³

$$J^*(j\omega_R) = J_e - \sum_{k=1}^N \frac{J_k j\omega_R/\omega_{z_k}}{(1 + j\omega_R/\omega_{z_k})} \quad (12)$$

The ω_{z_k} 's are identical in (12) and (7), and the coefficients may be found³

$$J_k = \frac{J_e \prod_{l=1}^N (1 - \omega_{z_l}/\omega_{p_l})}{\prod_{l=1}^N (1 - \omega_{z_k}/\omega_{z_l})} \quad (13)$$

Other necessary relationships are

$$G_g = b_N/a_N = G_e \prod_{k=1}^N \omega_{p_k}/\omega_{z_k} = G_e + \sum_{k=1}^N G_k = 1/J_g \quad (14)$$

and

$$J_e = 1/G_e = J_g + \sum_{k=1}^N J_k \quad (15)$$

Bode Diagrams

The technique of Bode diagrams is a highly developed tool in feedback control systems.⁴ It has been adapted and extended^{3,5} to certain complications in viscoelasticity. One attraction of the Bode diagram technique is that multiplication and division of complex numbers (or functions or factors) become addition and subtraction, and the magnitude and phase may be treated somewhat separately. Another attraction is that asymptotes of individual factors and their composite provide a basis for visualizing and analyzing frequency response functions and expressions for the complex modulus.

The composite magnitude asymptote of (7) is illustrated in Fig. 1. Here the composite magnitude asymptote starts at the lowest frequencies of interest with a value of G_e and a slope of zero. Progressing to higher values of reduced frequency, at each ω_{z_l} it "breaks up" to a slope of 1, and at each ω_{p_l} , it "breaks down" to a slope of zero. The composite asymptote is seen to approximate the specified magnitude in staircase fashion where the tread has a slope of zero and the riser has a slope of unity (not infinity).

It is characteristic of complex modulus data that it is monotonic and its slope is less than one, often approximately 1/2 in the transition

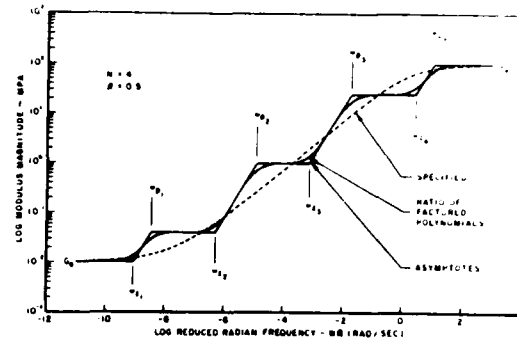


Fig. 1 Approximation for Magnitude of Complex Modulus.

region where it is a maximum. Under these conditions it follows that

$$\omega_{z_i} < \omega_{p_i} < \omega_{z_{i+1}} \quad (16)$$

A New Algorithm

Consider the sign of G_k given by (10) under the condition of (16). Note that each ω_{p_i} and each ω_{z_i} having a value less than that of ω_{p_k} gives rise to a negative term in (10). With reference to Fig. 1, it happens that for any k , the total number of ω_{p_i} 's and ω_{z_i} 's which is less than ω_{p_k} is an odd number. Because there is a negative sign in front of (10), every G_k will be positive. Similarly, every J_k from (13) will be positive. Previous methods in evaluating the parameters in (9) to approximate a given complex modulus require considerable art in avoiding negative values of G_k which give rise to spurious results in the relaxation modulus as represented by (8).

It is obvious that with a sufficiently large number, N , of stairsteps and with the parameter values properly chosen, the magnitude of the complex modulus is closely approximated to any required accuracy. It is asserted here without proof that it is a property of linear, constant coefficient systems that when the magnitude of its frequency response (here a complex modulus) is accurately represented over the infinite frequency range, the system is completely and uniquely determined. This includes system responses such as relaxation modulus and creep compliance. This is a generalization of the Kronig-Kramers relations.⁶

The present problem is reduced then to the method of choosing values for the $2N+1$ parameters in (7). It is assumed that the complex modulus is specified or defined (preferably analytically) over the range of reduced radian frequency from ω_{RMIN} to ω_{RMAX} . Note that it is a property of the complex modulus that its magnitude is monotonic and that the slope of the magnitude is less than one on a log-log scale.

The range is divided into N equally spaced intervals on the log scale and N specific values determined at the midpoints

$$\omega_i = \omega_{\text{RMIN}}(\omega_{\text{RMAX}}/\omega_{\text{RMIN}})^{(2i-1)/2N} \quad (17)$$

and the magnitude determined at those values of reduced radian frequency

$$G_{M_i} = G_{MAG}(\omega_i) \quad (18a)$$

and also at the end points

$$G_{MMIN} = G_{MAG}(\omega_{RMIN}) \quad (18b)$$

$$G_{MMAX} = G_{MAG}(\omega_{RMAX}) \quad (18c)$$

The $2N+1$ parameters will be determined such that the magnitude of (7) will yield the values (18) at the $N+2$ points. This will be done in two phases; first, a set of initial estimates and, secondly, an iterative refinement.

With reference to Fig. 2, the initial estimates are given by

$$\omega_{z_i} = \omega_i (G_{M_{i-1}}/G_{M_i})^{1/2} \quad (19a)$$

$$\omega_{p_i} = \omega_i (G_{M_{i+1}}/G_{M_i})^{1/2} \quad (19b)$$

except

$$\omega_{z_1} = \omega_1 G_{MMIN}/G_{M_1} \quad (19c)$$

$$\omega_{p_N} = \omega_N G_{MMAX}/G_{M_N} \quad (19d)$$

and by

$$G_e = G_{MMIN} \quad (19e)$$

These initial values specify a set of stairsteps as in Fig. 1.

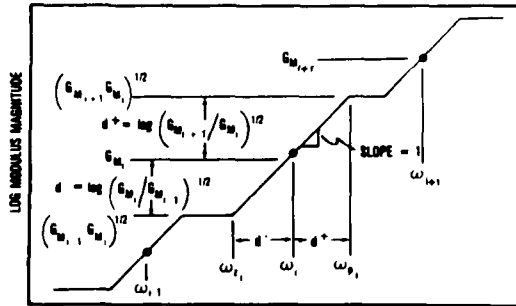


Fig. 2 Magnitude Asymptote Nomenclature.

The iterative improvement is begun by evaluating (7), the ratio of factored polynomials using the current parameter values at ω_{RMIN}

$$G_{MMIN_{RFP}} = G_{M_{RFP}}(\omega_{RMIN}) \quad (20a)$$

and adjusting the equilibrium modulus

$$A = G_{MMIN}/G_{MMIN_{RFP}} \quad (20b)$$

$$G_{e_{NEW}} = AG_{e_{OLD}} \quad (20c)$$

such that (7) yields G_{MMIN} when evaluated at ω_{RMIN} . The adjustment represented by (20a-c) is a vertical

translation of the entire curve or the entire set of stairsteps by the amount A .

Next the glassy asymptote is adjusted

$$A = G_{MMAX}/G_{M_{RFP}}(\omega_{RMAX}) \quad (21a)$$

$$\omega_{z_{NEW_i}} = \omega_{z_{OLD_i}}/A^{1/2N} \quad (21b)$$

$$\omega_{p_{NEW_i}} = \omega_{p_{OLD_i}}/A^{1/2N} \quad (21c)$$

based on (14) and allocating the deviation equally. This adjustment rotates the entire curve about G_{MMIN} at ω_{RMIN} such that (7) yields G_{MMAX} at ω_{RMAX} . This may be visualized as keeping the bottom of the set of stairsteps fixed and then rotating the top to a new level. The height of each riser is adjusted an equal amount.

Then the adjustment is made at each of the discrete points (17)

$$A_i = G_{M_{RFP_i}}/G_{M_i} \quad (22a)$$

$$\omega_{p_{NEW_i}} = A_i \omega_{p_{OLD_i}} \quad (22b)$$

$$\omega_{z_{NEW_i}} = A_i \omega_{z_{OLD_i}} \quad (22c)$$

This adjustment slides both ω_{p_i} and ω_{z_i} (which together define an individual riser) either right or left by the same appropriate amount. The curve is either raised or lowered, and the effect is confined to the vicinity of ω_i . The result is to cause (7) to yield G_{M_i} at each ω_i . The iteration is a repeated application of (20-22) in sequence. Convergence is achieved when all of the A 's are sufficiently close to unity.

This algorithm is basically an artful way of collocating the magnitude of the given complex modulus at $N+2$ points by evaluating $2N+1$ parameters. The set of values obviously is not unique. Some type of regression analysis would improve the overall curve representation accuracy for a specified N . The point is, however, that N may be made quite large, and the positive G_k 's are still guaranteed. Thus, step size may be made satisfactorily small in the desired regions. This results in steps smaller than necessary in other regions. The analyst must choose between this "inefficiency" in computer core and time vs. the spurious effects of negative G_k 's.

Numerical Results

The fractional derivative representation^{3,5,7} is used as the specified complex modulus

$$G^*(j\omega_R) \equiv [G_e + G_g(j\omega_R/\omega_{R0})^\beta]/[1 + (j\omega_R/\omega_{R0})^\beta] \quad (23)$$

For $\beta = 1/2$ this has been inverted in closed form⁵ to give

$$G_{RELAX}(t_{RLX}) = G_e + (G_g - G_e)r(t_{RLX}) \quad (24)$$

$$J_{CREEP}(t_{CRP}) = J_e + (J_g - J_e)r(t_{CRP}) \quad (25)$$

where

$$r(t_x) = e^{-t_x} \operatorname{erfc} t_x^{1/2} \quad (26)$$

$$t_{RLX} = \omega_{RO} t_R \quad (27)$$

$$t_{CRP} = (G_e/G_g)^2 \omega_{RO} t_R \quad (28)$$

The complex modulus as specified by (23) and as approximated by (7) is compared in Figs. 3a and 3b for $N = 8$ and 20, respectively. Figs. 4a and 4b compare the corresponding relaxation modulus (24) and (8) for the same values of N ; results for the creep compliance are similar. Using $N = 50$, Fig. 5a shows the series representation (7) for three values of the parameter beta, while Figs. 5b and 5c present the corresponding relaxation modulus and creep compliance.

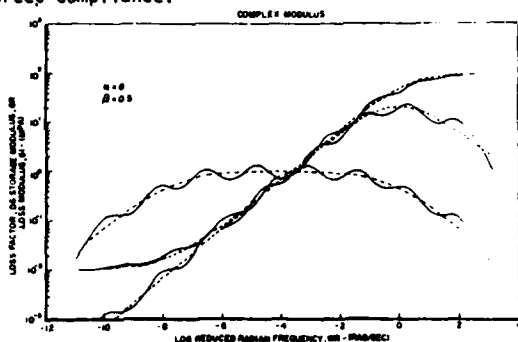


Fig. 3a Specified and Approximate Complex Modulus.

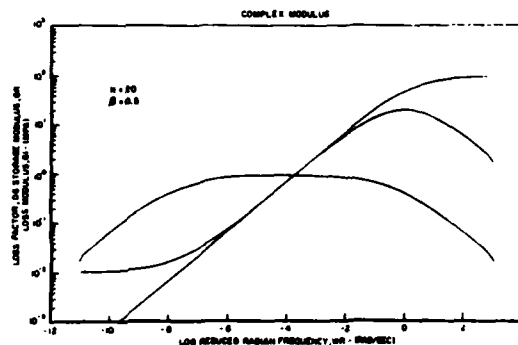


Fig. 3b Specified and Approximate Complex Modulus.

Discrete Relaxation and Retardation Spectra

It may happen that the discrete relaxation spectrum associated with the specified modulus is desired. It is defined implicitly in the present notation as:

$$G_i = H(\tau_{p_i}) \Delta_i \tau_{p_i} / \tau_{p_i}; \quad \tau_{p_i} = 1/\omega_{p_i} \quad (29)$$

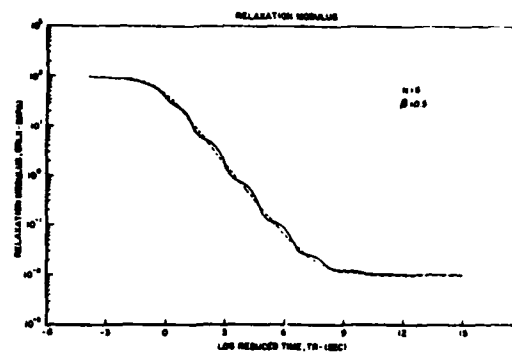


Fig. 4a Exact and Approximate Relaxation Modulus.

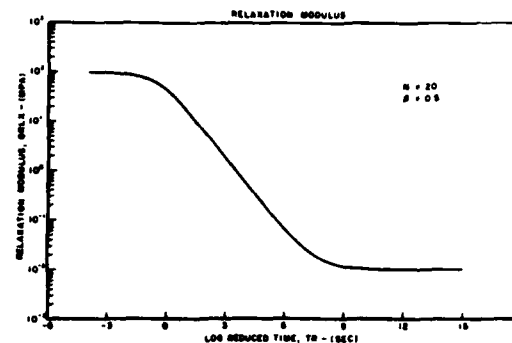


Fig. 4b Exact and Approximate Relaxation Modulus.

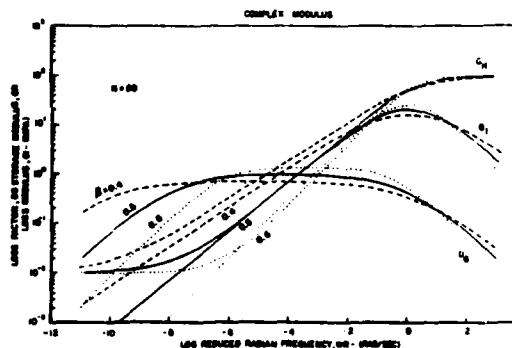


Fig. 5a Approximate Complex Modulus.

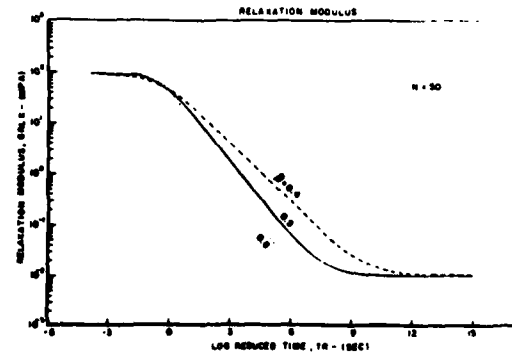


Fig. 5b Approximate Relaxation Modulus.

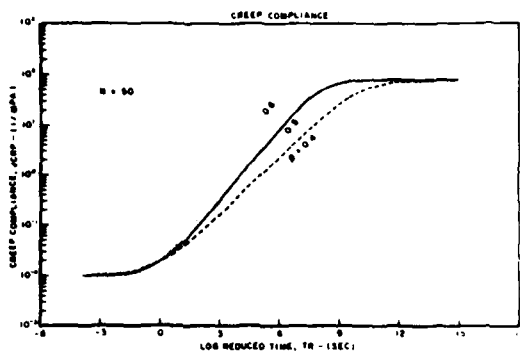


Fig. 5c Approximate Creep Compliance.

where the increment is taken as

$$\Delta \tau_p = (\tau_{p_{i+1}} - \tau_{p_i})/2 - (\tau_{p_i} - \tau_{p_{i-1}})/2 \quad (30)$$

Individual values are given by

$$H_i = H(\tau_{p_i}) = G_i / (.5(\tau_{p_{i+1}} + \tau_{p_{i-1}}) / \tau_{p_i} - 1); \quad (31)$$

$$i = 2, 3, \dots, N-1$$

Similarly the retardation is¹

$$L_i = L(\tau_{z_i}) = J_i / (.5(\tau_{z_{i+1}} + \tau_{z_{i-1}}) / \tau_{z_i} - 1); \quad (32)$$

$$\tau_{z_i} = 1/\omega_{z_i}; \quad i = 2, 3, \dots, N-1$$

Fig. 6 presents examples of spectra corresponding to the beta equals 0.5 case of Fig. 5a.

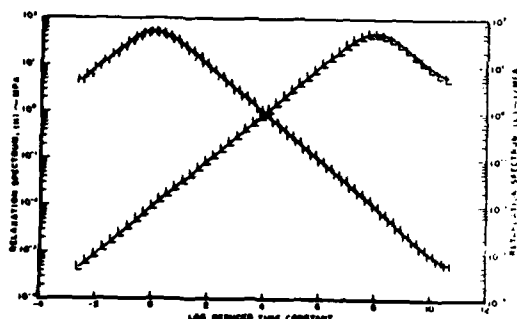


Fig. 6 Relaxation and Retardation Spectra.

Impulse Response

Consider a specimen subjected to a positive step shear strain input at time $t=0$, as in the stress relaxation case, but then followed by a negative step function at time $t = \Delta t$. The magnitude of the step is such that the area under the strain-time curve (i.e., the strain "impulse") is unity. The time increment Δt is then allowed to become a differential. In systems analysis, the resulting response quantity is called the impulsive admittance,⁸ and by analogy is here called the "impulsive modulus". It is found here by taking the derivative of (8)

$$G_{IM}(t_R) = - \sum_{k=1}^N G_k \omega_{p_k} e^{-\omega_{p_k} t_R} \quad (33)$$

When the specimen is subjected to a stress impulse, the "impulsive compliance" is found from (11)

$$J_{IM}(t_R) = \sum_{k=1}^N J_k \omega_{z_k} e^{-\omega_{z_k} t_R} \quad (34)$$

When the input function is a force, then the area is actually a mechanical impulse. The impulsive modulus and impulsive compliance would be useful in studies of response to impulsive types of loading, e.g., pyrotechnic shock. They are plotted in Fig. 7.

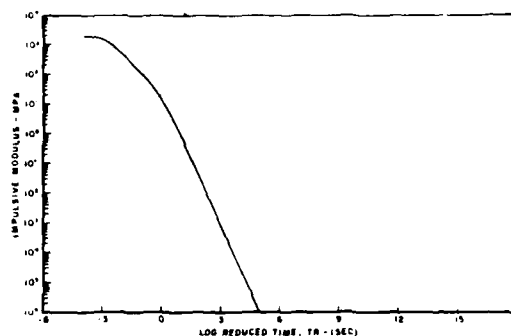


Fig. 7a Impulsive Modulus vs. Reduced Time.

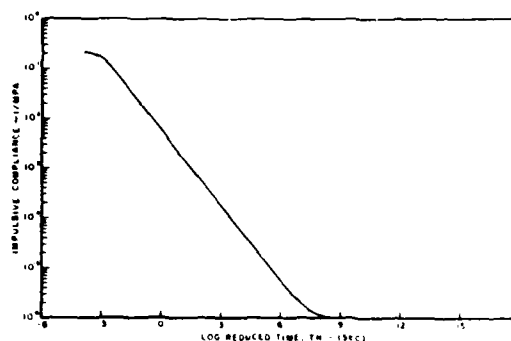


Fig. 7b Impulsive Compliance vs. Reduced Time.

Discussion

The new algorithm presented here is extremely convenient to use and is guaranteed to be numerically well-behaved. These characteristics depend entirely on the use of the ratio of factored polynomials form (7) of the complex modulus while subject to the constraint on the parameter values (16). In fact, the computational procedure and plotting is completely done by computer.

The current implementation assumes that it is the complex modulus which is available and which is used to obtain all other mechanical properties. There should be no difficulty in using some mechanical property other than complex modulus to obtain all others. This still involves using (7) and (16) for the complex modulus. If, for example, the

relaxation modulus was defined, the procedure would be as follows. First, obtain an estimate of the complex modulus using some approximate method. The magnitude of the modulus is then fit using the present algorithm. Equation (10) is used to evaluate the G_k 's. Equation (8) then gives a representation of the relaxation modulus. This representation is then compared to the original defined quantity. Some merit function must be developed to indicate goodness of fit. The value of the parameters in (7) are then adjusted in some iterative procedure to optimize the merit function, all the while observing the conditions given by (16).

It would be possible to develop an algorithm similar to the one above but based on a ratio of factored polynomials of the fraction degree, $1/2$

$$G^*(j\omega_R) = \frac{G_e \prod_{l=1}^N [1 + (j\omega_R/z_l)^{1/2}]}{\prod_{k=1}^N [1 + (j\omega_R/p_k)^{1/2}]} \quad (35)$$

The required number of terms would be considerably fewer. Expressions could be developed for the mechanical properties of interest except for the relaxation and retardation spectra. This additional development is not warranted at this time.

References

1. M. L. Williams, "Structural Analysis of Viscoelastic Materials," *AIAA Journal*, 2(5), 785-808 (1964).
2. R. M. Christensen, Theory of Viscoelasticity, An Introduction, New York: Academic Press, 1971.
3. L. Rogers, "On Modeling Viscoelastic Behavior," *The Shock and Vibration Bulletin* No. 51, Part 1, 1981, pp 55-69.
4. J. J. D'Azzo and C. H. Houpis, Feedback Control System Analysis and Synthesis, 2nd ed., McGraw-Hill, New York, 1966, pp 175-194.
5. L. Rogers, "Operators and Fractional Derivatives for Viscoelastic Constitutive Equations," *J. of Rheology*, 27(4), 351-372 (1983).
6. J. D. Ferry, Viscoelastic Properties of Polymers, Wiley, 3rd ed., 1980.
7. R. L. Bagley, "Applications of Generalized Derivatives to Viscoelasticity," Air Force Materials Laboratory TR-79-4103, November 1979 (Available from Defense Technical Information Center as AD A 081131).
8. B. Etkin, Dynamics of Flight-Stability and Control, Wiley, 1959, p 250.

COMPARISON OF DAMPING MATERIAL PROPERTIES
MEASURED BY A NUMBER OF ORGANIZATIONS

M. L. Parin
Anatrol Corporation
Cincinnati, Ohio

Paper presented; not available for publication.

INFLUENCE OF THE GEOMETRIC STIFFNESS ON THE DETERMINATION OF THE DYNAMIC
CHARACTERISTICS OF VISCOELASTIC MATERIAL PROPERTIES

M. Lalanne, P. Berthier, J. Der Hagopian, and I. A. R. El Halawani
Institute National Des Sciences Appliquees
Lyon, France

and

B. Duperray
Metravib
Ecully, France

Paper was not presented; not available for publication.

COMPLEX MODULUS BEHAVIOR OF A VISCOELASTIC ADHESIVE
MEASURED AT HARMONIC STRAIN AMPLITUDES OF 10^{-10}

T. J. Lagnese
Universal Energy Systems, Inc.
Dayton, Ohio

and

D. I. G. Jones
Materials Laboratory (AFWAL/MLLN)
Wright-Patterson Air Force Base, Ohio

COMPLEX MODULUS BEHAVIOR OF A VISCOELASTIC ADHESIVE
MEASURED AT HARMONIC STRAIN AMPLITUDES OF 10^{-10}

by

T. J. Lagnese
Universal Energy Systems, Inc.
Dayton, Ohio

&

D.I.G. Jones
Materials Laboratory (AFWAL/MLLN)
Wright-Patterson AFB, Ohio

ABSTRACT

The complex modulus behavior of a viscoelastic material, measured by a dynamic stiffness method, was determined at several low excitation levels, and several temperatures, to illustrate the effect of strain amplitude. The material was found to be linear to strain levels as low as 10^{-10} m/m.

1. INTRODUCTION

One of the more recently considered applications of damping polymers is as a method for reducing structural vibrations in large spacecraft structures. The dynamic environment of spacecraft structures is typically of very low cyclic strain amplitudes caused by slow cycling thermal changes and frequent small adjustments in spacecraft orientation. The polymer would be used in conjunction with active damping systems to control structural vibrations in an environment where the strain amplitudes are very low and the question of the linearity of the polymer material response may be raised.

It is difficult to measure the complex modulus properties of polymeric damping materials at extremely low strain amplitudes. One way of achieving the needed, low strain amplitudes is to apply extremely low force levels to a specimen and to measure the response with small transducers to minimize mass loading effects. This leads to difficulties in measuring the resulting response amplitudes since current, smaller sized, force and displacement or acceleration measurement transducers are limited at extremely low levels by sensitivity and system electronic noise. Another way is to combine the advantageous selection of specimen geometry and size with the use of the larger, more sensitive, force and acceleration measurement transducers available. In practice, this means that one must use a relatively large specimen along with a magnetic transducer for excitation and a seismic accelerometer for measurement of specimen response. This paper will describe some experiments to measure the complex modulus properties of a polymeric adhesive at very low strain amplitudes of the order of 10^{-10} , by means of a two degree of freedom impedance test.

2. APPROACH

2.1 Rationale for Choice of Test Method

The aim of the investigation was to measure the complex modulus of a specimen of viscoelastic material at very low strain levels. The question of whether to use a discrete specimen or a vibrating sandwich beam was resolved in favor of the discrete specimen because the strain distribution throughout the viscoelastic element of a sandwich beam is not spatially uniform, so that any non-linear effects which were being sought could well be obscured. The next question was whether to use a one or two degree of freedom system as illustrated in Figure 1.

2.1.1 One degree of freedom system

The one degree of freedom system is simply a mass-spring system excited by a force $F(t) = F e^{i\omega t}$. The equation of motion is:

$$m \ddot{w} + K(1 + i\eta)w = F e^{i\omega t} \quad (1)$$

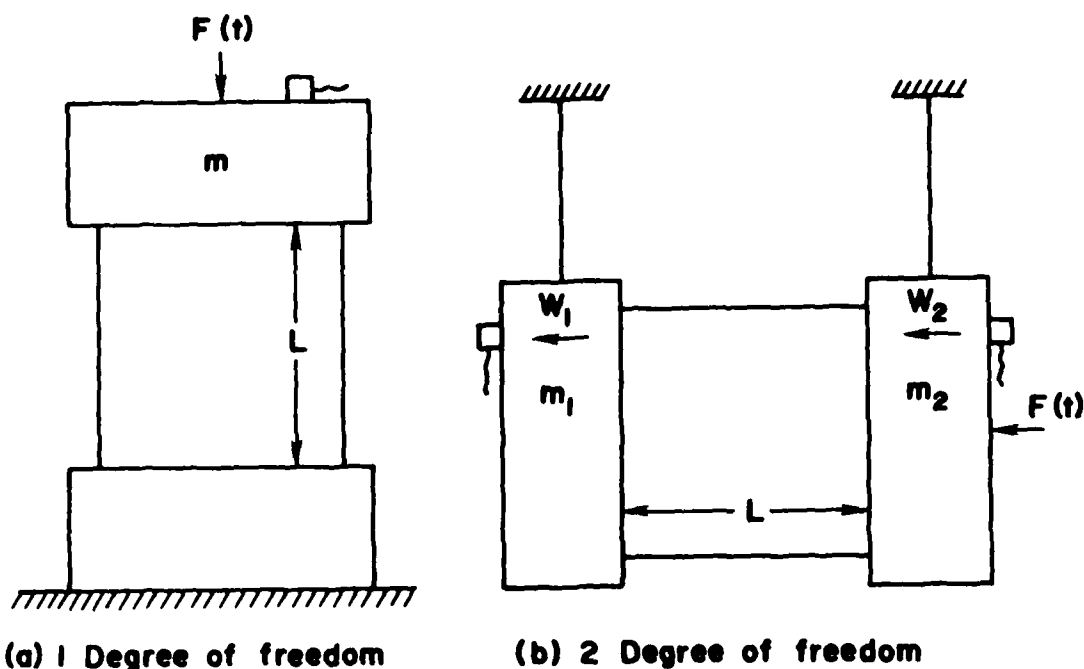


Figure 1. One and two degree of freedom system configurations for impedance test.

For steady state harmonic motion $w(t) = W e^{i\omega t}$:

$$\therefore W = F / [K(1 + i\eta) - m\omega^2] \quad (2)$$

At resonance, $k = m\omega^2$ and so:

$$W_{max} = \frac{F}{K\eta} = \frac{FL}{EA\eta} \quad (3)$$

where L is the specimen length and A the cross-sectional area. The peak strain is:

$$\xi_{max} = \frac{W_{max}}{L} = \frac{F}{EA\eta} \quad (4)$$

For values of F of the order of 0.001 Newtons, which was the lowest controlled force achievable by the typical available magnetic transducer [1], and a desired lowest value of ξ_{max} of the order of 10^{-10} , this gives: for $\eta=1$:

$$0.001/EA=10^{10}$$

$$\therefore EA=10^{-3}/10^{-10}=10^7 \text{ N}$$

For a typical value of $E = 10^7 \text{ N/m}^2$, this would require $A = 1.0 \text{ m}^2$, which is very large.

2.1.2 Two degree of freedom system

The equation of motion of the two degree of freedom system is:

$$\begin{bmatrix} K(1+i\eta)-m_1\omega^2 & -K(1+i\eta) \\ -K(1+i\eta) & K(1+i\eta)-m_2\omega^2 \end{bmatrix} \begin{Bmatrix} W_1 \\ W_2 \end{Bmatrix} = \begin{Bmatrix} F_1 \\ F_2 \end{Bmatrix} \quad (5)$$

For this system, if $F_1 = F$ and $F_2 = 0$: and $m_1 = m_2 = m$:

$$W_1/F = [K(1+i\eta)-m\omega^2] / m\omega^2 [m\omega^2 - 2K(1+i\eta)] \quad (6)$$

$$W_2/F = K(1+i\eta) / m\omega^2 [m\omega^2 - 2K(1+i\eta)] \quad (7)$$

The relative displacement of the two masses is:

$$\Delta W/F = (W_1 - W_2)/F = -1 / [m\omega^2 - 2K(1+i\eta)] \quad (8)$$

Resonance now occurs at $m\omega^2 = 2k$ and the peak relative strain, at resonance, is:

$$\xi_{\max} = \Delta W_{\max} / L = F / 2EA\eta \quad (9)$$

This is half the peak strain seen in the one degree of freedom system. Furthermore, the single degree of freedom system suffers from the static loading of the specimen by the weight of the mass m , while the masses are independently supported in the two degree of freedom system. For these reasons, the two degree of freedom system was selected.

3. RESULTS

3.1 Tests on the two degree of freedom system at 67°F

Figure 1b illustrates the two degree of freedom system which was used to evaluate the dynamic behavior of a very high damping viscoelastic material acting as the link $k(1+i\eta)$ between two masses m_1 and m_2 .

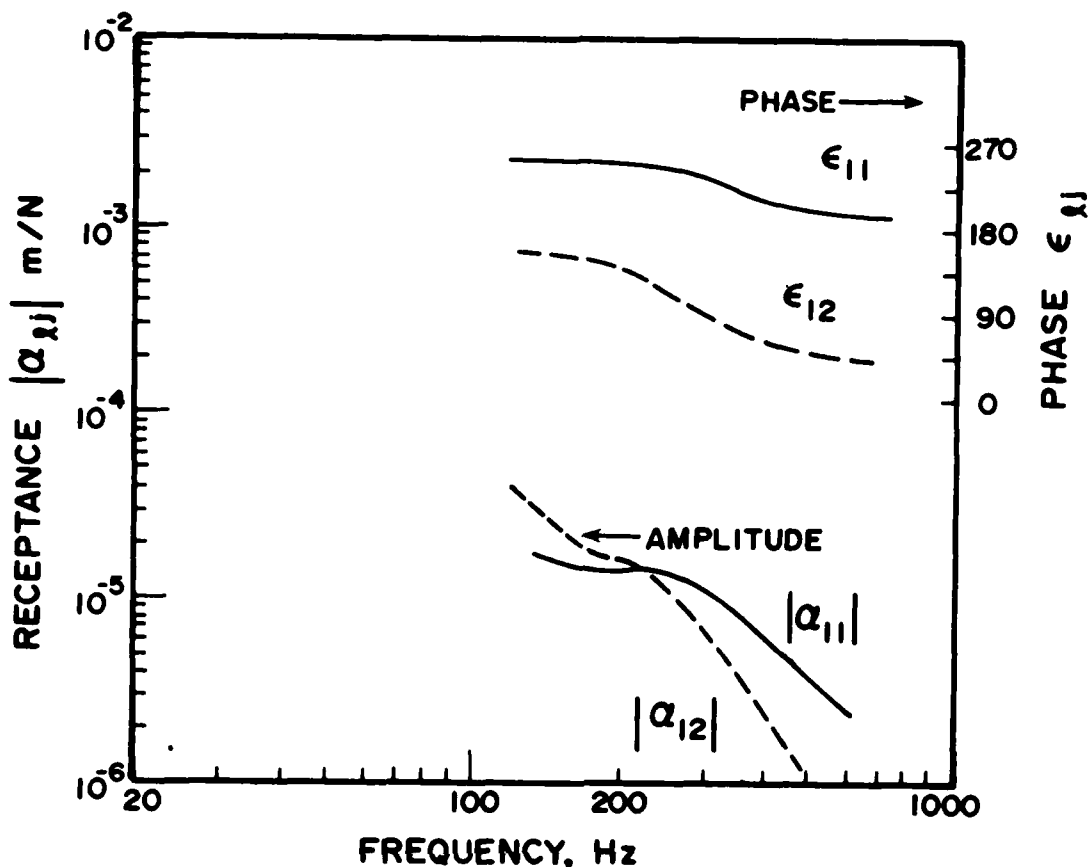


Figure 2. Point and transfer receptances and phase information of viscoelastic specimen at 72°F.

The masses m_1 and m_2 were actually equal in the particular tests conducted. The response of the system was measured by accelerometers placed on masses m_1 and m_2 as indicated, and the mass m_2 was excited by a small hammer, through a force gage, as is frequently used in present day modal testing. The transient force and acceleration signals were processed, by the FFT (Fast Fourier Transform), into linear frequency domain response obtained in terms of receptances $\alpha_{11} = W_1/F_1$ and $\alpha_{12} = W_2/F_1$. The receptances were, of course, complex quantities, described in terms of amplitudes $|\alpha_{11}(\omega)|$ and $|\alpha_{12}(\omega)|$ and phase angles $\epsilon_{11}(\omega)$ and $\epsilon_{12}(\omega)$, relative to the phase of the driving force transform $F_1(\omega)$. The receptance $\alpha_{22} = W_2/F_2$ was not measured, but symmetry of the system ensured that $\alpha_{22} = \alpha_{11}$. Some specific values of $|\alpha_{11}(\omega)|$, $|\alpha_{12}(\omega)|$, $\epsilon_{11}(\omega)$ and $\epsilon_{12}(\omega)$ are summarized in Table 1 and in Figure 2. These plots give little clue as to the variation of k and η with frequency. Note, however, that the measured receptances make up the matrix relationship:

TABLE 1

Measured Data for Two Degree of Freedom System
with High Damping ($m_1 = 5.355 \text{ Kg}$)

Freq (Hz)	α_{11} Lb/in($\times 10^{-6}$)	ϵ_{11} deg	α_{12} Lb/in($\times 10^{-6}$)	ϵ_{12} deg
20	732.0	152	1460	161
40	268.0	181	284	162
60	84.2	186	106	163
100	41.4	196	55.8	170
124	21.6	207	36.6	168
152	17.1	233	25.6	155
176	15.0	236	18.8	148
200	15.3	237	17.7	137
252	14.2	227	11.2	109
300	11.8	218	6.72	82
352	8.88	203	4.06	69
400	6.64	197	2.38	64
452	4.90	194	1.42	46
500	3.96	192	1.04	45
528	3.56	192	0.81	47

$$\begin{bmatrix} \alpha_{11} & \alpha_{12} \\ \alpha_{21} & \alpha_{22} \end{bmatrix} \begin{Bmatrix} F_1 \\ F_2 \end{Bmatrix} = \begin{Bmatrix} W_1 \\ W_2 \end{Bmatrix} \quad (10)$$

We can invert this matrix to obtain the dynamic stiffness matrix. One way of determining the mechanical properties for this simple system is to examine the required dynamic stiffness form of the equations:

$$\begin{bmatrix} \kappa_{11} & \kappa_{12} \\ \kappa_{21} & \kappa_{22} \end{bmatrix} \begin{Bmatrix} W_1 \\ W_2 \end{Bmatrix} = \begin{Bmatrix} F_1 \\ F_2 \end{Bmatrix} \quad (11)$$

We first let $F_1 = F_1$, $F_2 = 0$ to obtain two equations relating κ_{11} , κ_{12} , α_{11} , α_{12} and $\alpha_{11} = W_1/F_1$ and $\alpha_{12} = W_2/F_1$.

Then we let $F_1 = 0$, $F_2 = F_2$ and obtain two more equations relating

κ_{11} , κ_{12} and α_{22} and $\alpha_{12} = W_1/F_2$ and $\alpha_{22} = W_2/F_2$.

Taking this first and third, and the second and fourth of the equations, respectively, we get:

$$\left[\begin{array}{cc|cc} a_{11} & a_{21} & & 0 \\ a_{12} & a_{22} & & \\ \hline & & a_{11} & a_{21} \\ & 0 & a_{12} & a_{22} \end{array} \right] \begin{pmatrix} \kappa_{11} \\ \kappa_{12} \\ \kappa_{21} \\ \kappa_{22} \end{pmatrix} = \begin{pmatrix} 1 \\ 0 \\ 0 \\ 1 \end{pmatrix} \quad (12)$$

The solutions of these equations are:

$$\begin{aligned} \kappa_{11} &= a_{22} / [a_{11} a_{22} - a_{12} a_{21}] \\ \kappa_{12} &= \kappa_{21} = -a_{21} / [a_{11} a_{22} - a_{12} a_{21}] \\ \kappa_{22} &= a_{11} / [a_{11} a_{22} - a_{12} a_{21}] \end{aligned} \quad (13)$$

Since $a_{11} = a_{22}$ by symmetry and $a_{12} = a_{21}$ by reciprocity, and:

$$\begin{aligned} a_{11} &= |a_{11}| (\cos \epsilon_{11} + i \sin \epsilon_{11}) \\ a_{12} &= |a_{12}| (\cos \epsilon_{12} + i \sin \epsilon_{12}) \end{aligned} \quad (14)$$

We may write, after some simplification;

$$\begin{aligned} \kappa_{11} &= \left(\frac{AC + BD}{A^2 + B^2} \right) + i \left(\frac{AD + BC}{A^2 + B^2} \right) \\ \kappa_{12} &= \frac{AE + BF}{A^2 + B^2} + i \frac{(AF - BE)}{A^2 + B^2} \end{aligned} \quad (15)$$

Where:

$$\begin{aligned} A &= |a_{11}|^2 \cos 2\epsilon_{11} - |a_{12}|^2 \cos 2\epsilon_{12} \\ B &= |a_{11}|^2 \sin 2\epsilon_{11} - |a_{12}|^2 \sin 2\epsilon_{12} \\ C &= |a_{11}| \cos \epsilon_{11} \\ D &= |a_{11}| \sin \epsilon_{11} \\ E &= |a_{12}| \cos \epsilon_{12} \\ F &= |a_{12}| \sin \epsilon_{12} \end{aligned} \quad (16)$$

Finally, by comparing, for this particular problem, the dynamic stiffness matrix with the mass-stiffness of equation (5), we see that:

$$\begin{bmatrix} K(1+i\eta) - m\omega^2 & -K(1+i\eta) \\ -K(1+i\eta) & K(1+i\eta) - m\omega^2 \end{bmatrix} \begin{Bmatrix} W_1 \\ W_2 \end{Bmatrix} = \begin{Bmatrix} F_1 \\ 0 \end{Bmatrix} \quad (17)$$

must compare with:

$$\begin{bmatrix} \kappa_{11} & \kappa_{12} \\ \kappa_{21} & \kappa_{22} \end{bmatrix} \begin{Bmatrix} W_1 \\ W_2 \end{Bmatrix} = \begin{Bmatrix} F_1 \\ 0 \end{Bmatrix} \quad (18)$$

From which we at once see, from κ_{12} , that:

$$K(1+i\eta) = -\kappa_{12} \quad (19)$$

$$\therefore -\kappa_{12D} = K = (AE + BF) / (A^2 + B^2) \quad (20)$$

$$\eta = -\kappa_{12Q} / K = (AF - BE) / (AE + BF)$$

and, furthermore, from κ_{11} :

$$K(1+i\eta) - m\omega^2 = \kappa_{11} \quad (21)$$

$$\therefore K - m\omega^2 = \kappa_{11D} = (AC + BD) / (A^2 + B^2) \quad (22)$$

$$\eta = \kappa_{11Q} / K = (AD - BC) / K(A^2 + B^2)$$

From equation (19), we have a direct estimate of k for each frequency, using the data of Table 1. From equation (20) we have a direct estimate of η . From equation (21), we can estimate m_1 from the slope of the graph of κ_{11D} versus ω^2 at high frequency. Hence, by mathematically "cancelling" the $m\omega^2$ term from the lefthand side of equation (21), we have another independent estimate of k . Then, from equation (22), we have another estimate of η . Figures 3 and 4 illustrate the calculated variation of k and η , obtained from the data of Table 1 by means of equations (19) through (22). The results show that k and η may readily be calculated from the measured data using the dynamic stiffness approach. Note that the assumption $\alpha_{11} = \alpha_{22}$ was used to complete the $[\alpha]$ matrix, and if m_1 had not been equal to m_2 , it would have been absolutely necessary to measure α_{22} directly. Table 2 summarizes the calculated results.

Superimposed on Figure 4 are the bounds of observed variation of the stiffness k and loss factor η , based on available data for the

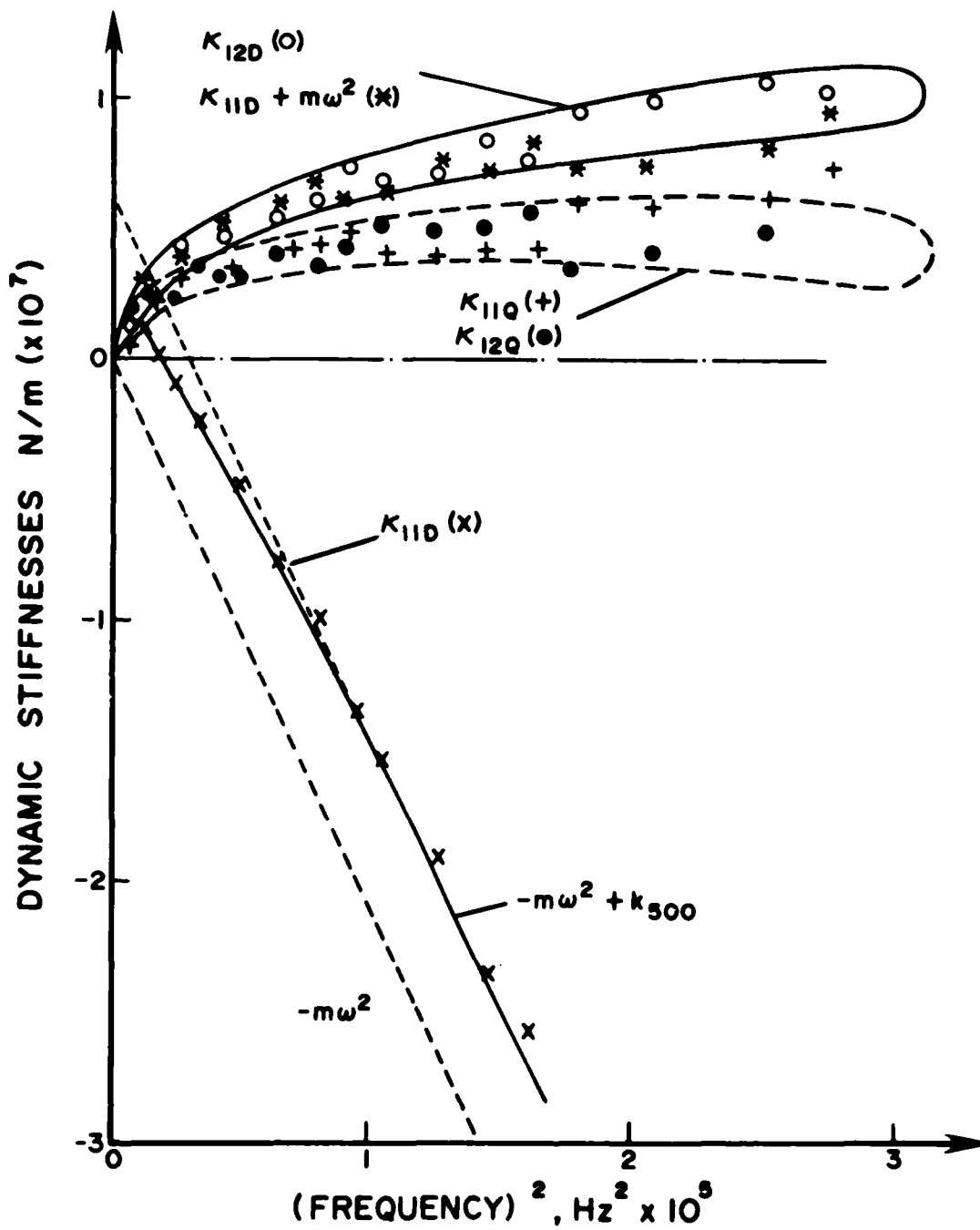


Figure 3. Calculated variation of stiffness obtained from experimental data.

TABLE 2

Calculated Stiffness and Loss Factor

Freq (Hz)	k, N/M($\times 10^6$) Eq 19	k, N/M($\times 10^6$) Eq 20	η Eq 21	η Eq 22
100	2.90	3.16	0.941	0.874
124	4.11	4.18	0.629	0.650
152	4.083	3.762	0.633	0.805
176	4.75	4.16	0.663	0.932
200	4.75	4.97	0.686	0.716
252	5.47	5.73	0.725	0.657
300	7.432	5.57	0.448	0.871
352	7.22	7.34	0.693	0.512
400	7.42	8.20	0.760	0.538
452	9.93	6.61	0.414	0.928
500	10.86	7.80	0.460	0.842
528	10.27	9.42	0.484	0.848

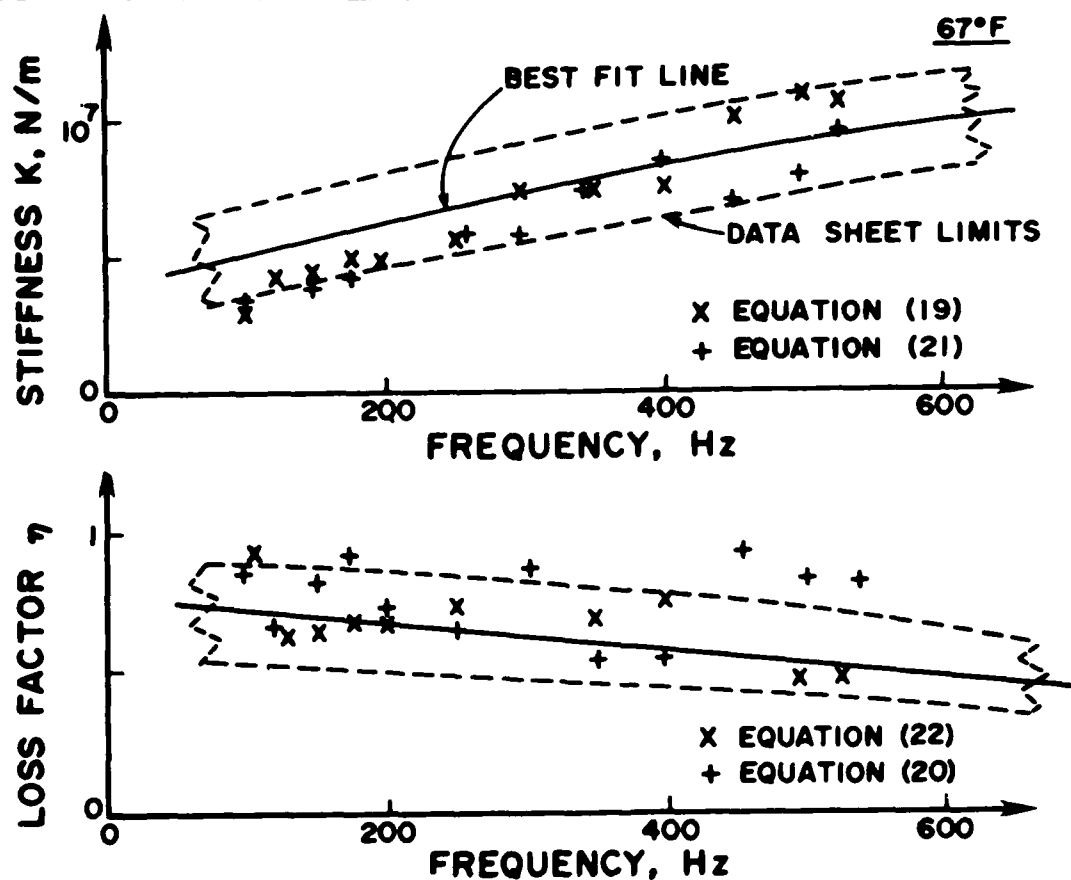


Figure 4. Calculated value of k and η vs. frequency (x k , eq. 19; + k , eq. 29; + η , eq. 20; x η , eq. 22).

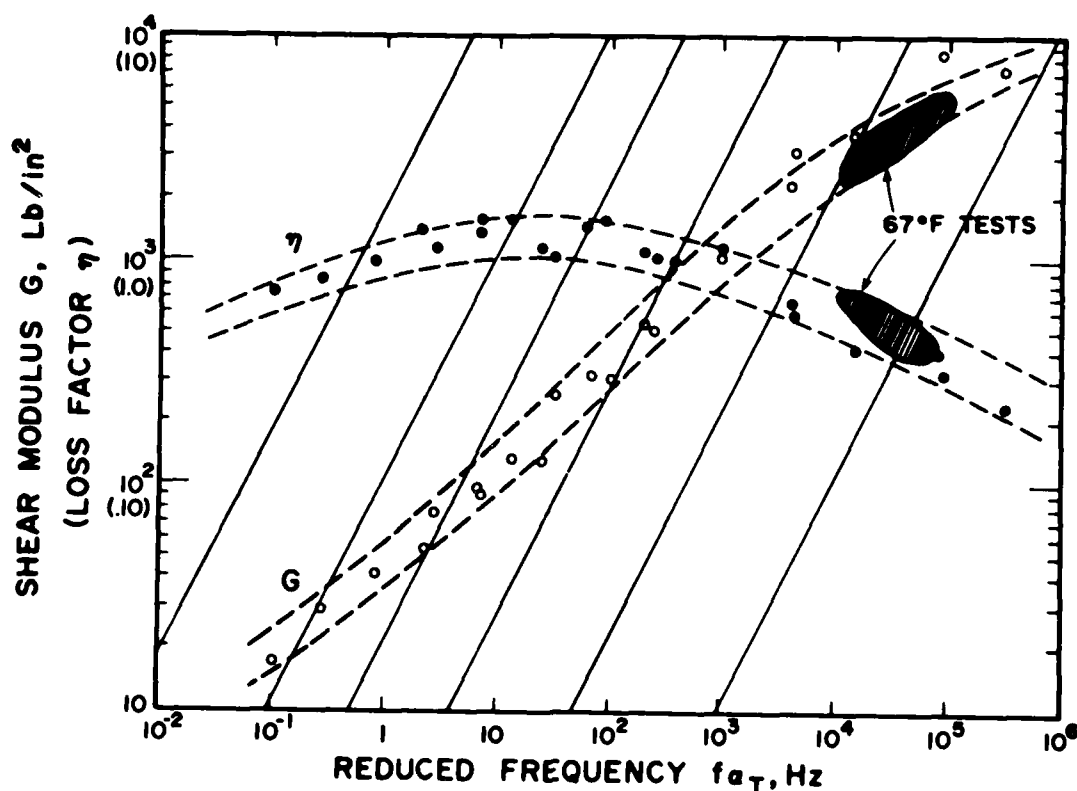


Figure 5. Complex modulus properties of viscoelastic adhesive.

properties of the viscoelastic material, summarized in nomogram form in Figure 5 [5]. It is seen that the values of G ($=E/3$) and η , measured in this way, are well within the scatter band of data from other sources.

3.2 Tests on two degree of freedom system using sine-sweep excitation at several temperatures.

Further tests were completed at several temperatures with sine sweep excitation. The excitation was provided by a magnetic transducer which drove the block through a small calibrated force gage. The load applied to the block varied typically from .00079 Newtons to .079 Newtons, a range of two orders of magnitude. The test system was suspended in an environmental chamber with the force gage/magnetic transducer arrangement driving the block on one side and the response measured on both sides by a very sensitive seismic accelerometer. Typical acceleration responses of the specimen are shown in Figures 6 to 8 at temperatures of 50°F, 67°F and 105°F. The predicted accelerations are also plotted against frequency in Figures 6 to 8, being the result of calculations based on the complex modulus data presented in Figure 5 with equations 6 and 7. The agreement between the experimental and the analytical results is quite good.

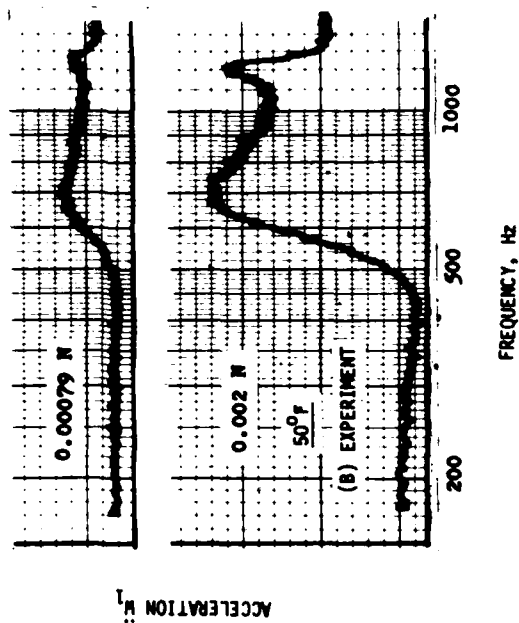
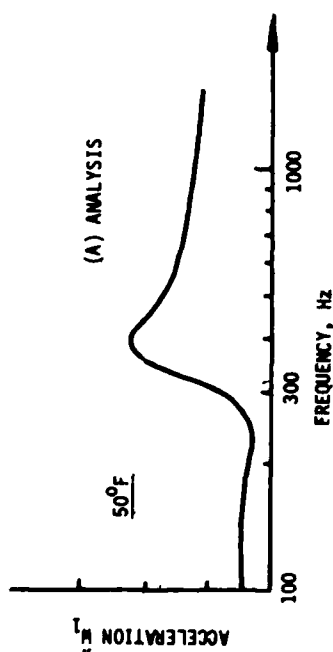


Figure 6a. Comparison of analytical and experimental driving point acceleration response at 50°F.

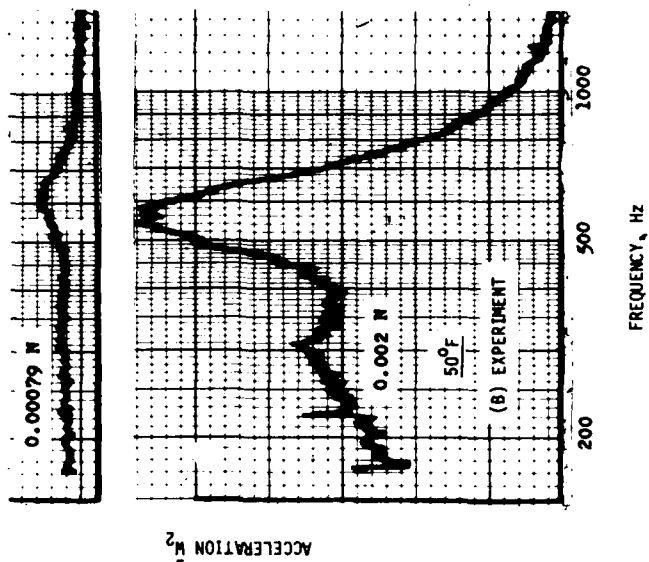
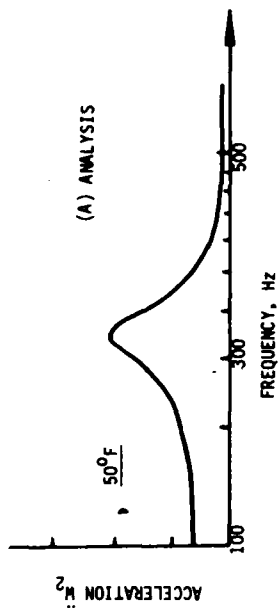


Figure 6b. Analytical and experimental transfer acceleration response at 50°F.

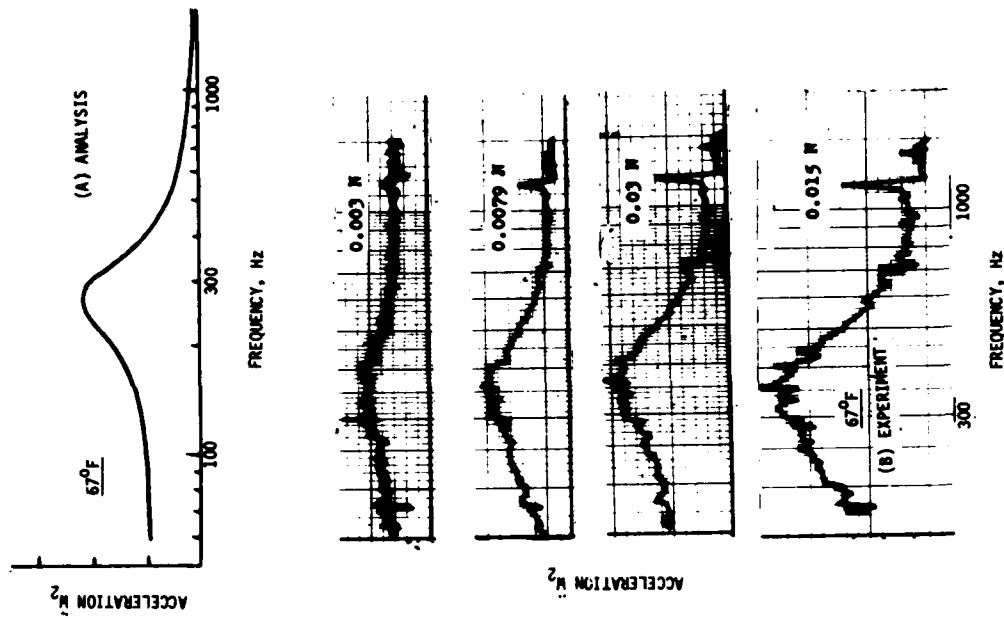


Figure 7a. Analytical and experimental driving point acceleration response at 67°F.

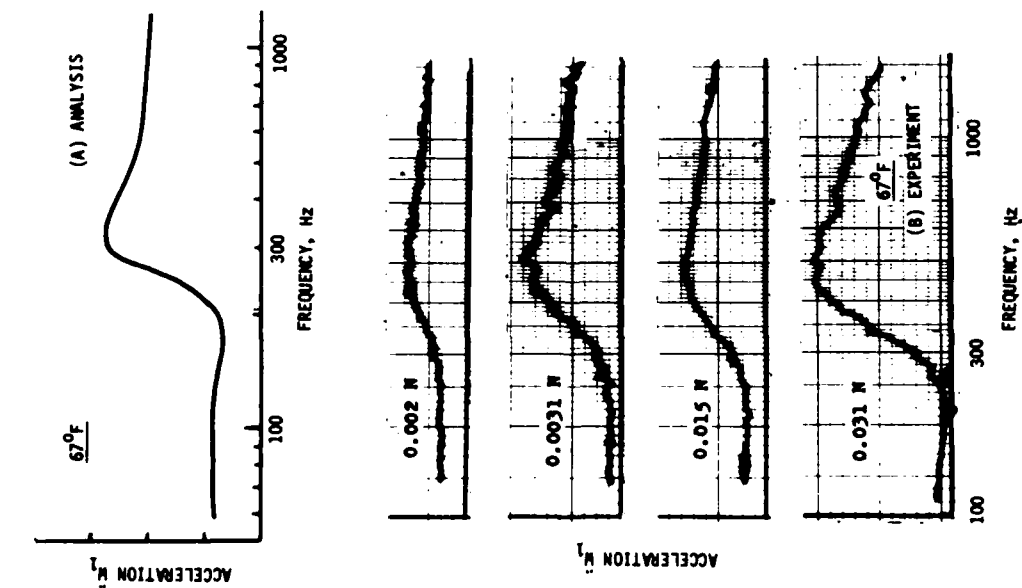


Figure 7b. Analytical and experimental transfer acceleration response at 67°F.

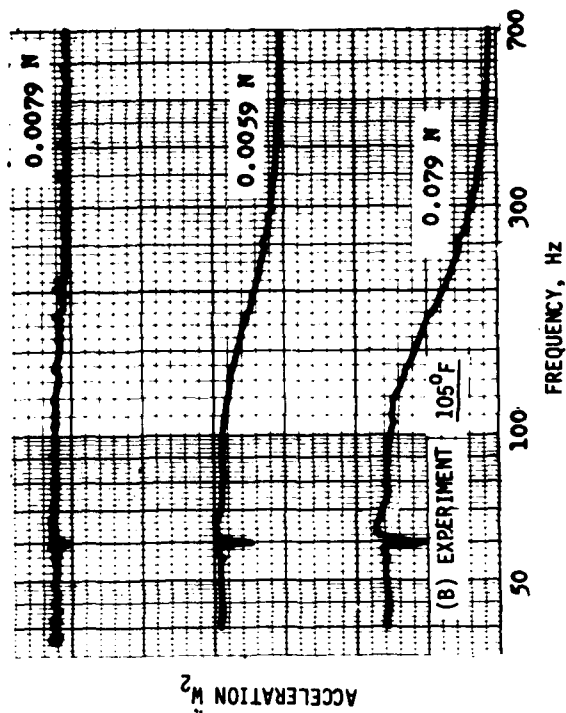
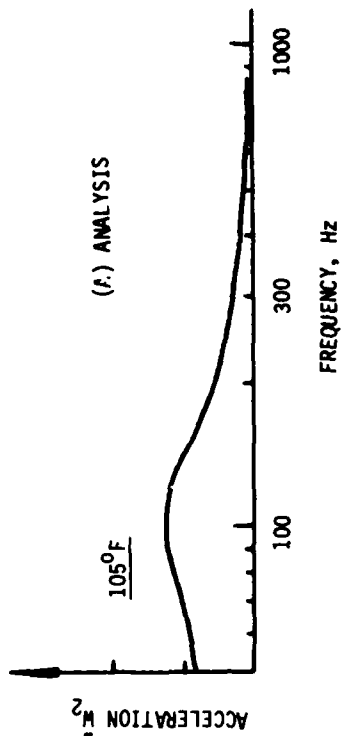


Figure 8b. Analytical and experimental transfer acceleration response at 105°F.

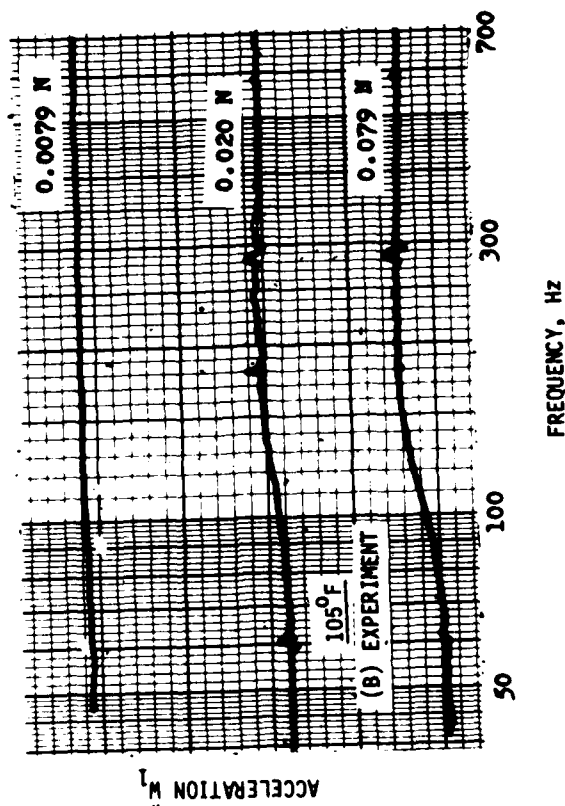
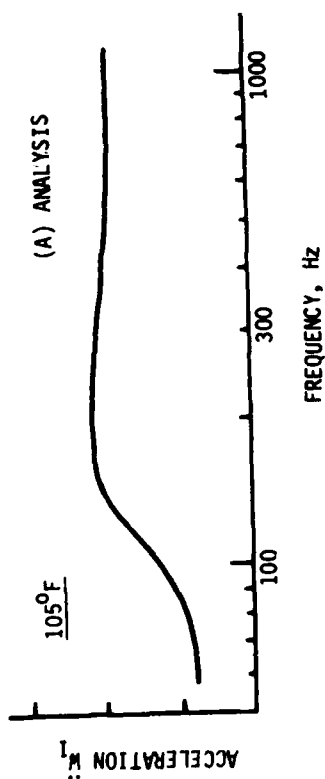


Figure 8a. Analytical and experimental driving point acceleration response at 105°F.

The experimental data does indicate that the acceleration response is not significantly dependent on the input excitation at the low force levels tested. The appearance of the acceleration plots at several input force levels shows no qualitative change. It was concluded that the properties of the viscoelastic element were independent of strain level within the range of measured values.

4. SUMMARY AND CONCLUSIONS

The two degree of freedom test system used for measuring the complex modulus properties of the viscoelastic adhesive avoids some of the difficulties encountered in other test methods. For example, the same configuration used in a one degree of freedom form could not readily avoid the load of the gravitational weight of the mass m , which would cause creep and deformation of the specimen over an extended period of time. Furthermore, the frequency range over which reliable data could be obtained seems to be of the order of a decade, and this could be extended to other ranges by changing the masses. The main disadvantage in this particular series of tests was the extreme size of the viscoelastic element, which was dictated by the need to make the measurements at very low strain amplitudes, rather than by the method itself. Far smaller specimens could be made if this requirement was not imposed. The test results, while not as complete as would be desired, do indicate that the complex modulus of the viscoelastic adhesive does not depend on strain amplitude at cyclic levels as low as $10E-10$ m/m.

ACKNOWLEDGMENTS

Particular thanks are extended to the 3M Company, Minneapolis, Minnesota, for providing the viscoelastic sample for these tests. This project was carried out at the Materials Laboratory, AFWAL/MLLN, Wright-Patterson AFB, Ohio under Project No. 2307P102, from 1979 to 1980.

1. Electro Corporation, 3030 HTB High Temperature Magnetic Sensor.
2. W. G. Flannelly, A. Berman and R. M. Barnsby, "Theory of Structural Dynamic Testing Using Impedance Techniques," Kaman Aerospace Corporation Report No. R-823 (2 vols.), 1970.
3. Adhesive ISD-110, Manufactured by 3M Company, St. Paul, MN.
4. M. L. Drake and G. E. Terborg, "Polymeric Material Testing Procedures to Determine Damping Properties and the Results of Selected Commercial Materials," AFWAL-TR-80-4093, Air Force Wright Aero. Labs, 1980.
5. D. I. G. Jones, "An Attractive Method for Displaying Material Damping Data," J. Aircraft, 18(8), pp. 644-649, 1981.

6. D. I. G. Jones and A. Muszyńska, "On the Modal Identification of Multiple Degree of Freedom Systems from Experimental Data," Shock and Vibration Bulletin 53, pp. 91-110 , 1983.

NOMENCLATURE

A	Cross-sectional area of specimen
E	Young's modulus
G	Shear modulus
i	$\sqrt{-1}$
j,l	Points on structure
k	Stiffness of viscoelastic link
m_n	Discrete element mass ($n=1,2$)
F_l, F_j	Exciting forces at points l,j
L	Length of specimen
t	Time
w_l, w_j	Response at points l,j
α	Receptance of 1 DOF system
α_{lj}	Transfer receptance (w_l/F_j)
α_{ll}	Point receptance (w_l/F_l)
ϵ	Phase between excitation and response
η	Loss factor
K_{lj}	Dynamic stiffness
K_{ljD}	Direct dynamic stiffness
K_{ljQ}	Quadrature dynamic stiffness
ω	Frequency
ω_n	n-th resonant frequency
ϵ	Strain amplitude

EXPERIMENTAL MEASUREMENT OF MATERIAL DAMPING
FOR SPACE STRUCTURES

Edward F. Crawley
Boeing Assistant Professor
Aeronautics and Astronautics
Massachusetts Institute of Technology
Cambridge, Massachusetts

and

Raymond L. Sheen
Captain, U. S. A. F.
Norton Air Force Base, California

Experimental Measurement of Material Damping for Space Structures

Edward F. Crawley
Boeing Assistant Professor
Aeronautics and Astronautics
Massachusetts Institute of Technology
Cambridge, Massachusetts

Raymond L. Sheen
Captain, U.S.A.F.

Abstract

An experimental procedure for the measurement of material damping is described. In this procedure, the free decay of free-free beams, when lofted into free fall in a vacuum, is recorded and analyzed. Tests were performed on aluminum, graphite/epoxy, and graphite/magnesium metal matrix materials. In tests on 2024-T3 aluminum, specimens whose fundamental free-free frequency was above the relaxation frequency of the Zener model gave results in close agreement with this model. However, specimens with a fundamental free-free frequency below the relaxation frequency showed a higher level of damping and of stress dependence than predicted. Tests were also performed on AS1/3501-6 graphite/epoxy laminates. For $[0]_8$ laminates, a material damping ratio of 0.00055 was found for frequencies varying from 45 Hz to 237 Hz. The damping was neither stress nor frequency dependent. For $[90]_8$ laminates, the damping ratio ranged from 0.0055 to 0.0066 as frequency ranged from 42 Hz to 143 Hz. Damping ratios for $[90]_8$ specimens were independent of stress. Stress and frequency dependence of damping in $[\pm 45]_2$ laminates, as measured in an earlier study, are similar to those of $[90]_8$. Experimentally measured damping ratios for metal matrix specimens with unidirectional graphite fibers, magnesium matrix, and either titanium or magnesium foil, ranged from .00039 to .00099, depending upon the matrix material, frequency, and possibly the stress range involved.

Introduction

In spacecraft structures, only material and structural damping are available for the passive dissipation of vibrational energy. The more common terrestrial mechanisms of acoustic dissipation, transmission to the supporting structure, and loss at the support interface are absent in the "zero gravity" free fall of space. But the presence of some passive dissipation is vital to the performance of all spacecraft, even those with actively controlled structures. Thus, renewed interest is focused on the characterization and enhancement of passive material damping.

There have been a wide variety of techniques and geometries which have been used to measure material damping. Among these are the free decay, resonant dwell and bandwidth techniques, combined with cantilever, double cantilever and wire supported "free-free" geometries [1]. However, the purest measurement of material damping can be made when a free-free specimen is completely unconstrained in free-fall, and in vacuum. An apparatus that provides the capability to measure material damping under these conditions has been developed at MIT, has already been used in previous studies [2,3], and is documented in references [4,5].

This unique facility was used to gather damping information on those materials which are being considered for application to large flexible space structures: aluminum, graphite/epoxy, and graphite/metal matrix. There has already been a great deal of study of damping in aluminum. Granick and Stern, who tested double cantilever specimens in both air and vacuum, did not find material damping to be stress dependent in their vacuum results for stress levels well below the proportional limit [6]. Their data showed damping values slightly higher than those given by the theoretical Zener model [7], as did previous tests in the MIT facility [5]. However, neither investigation tested specimens with natural frequencies below the Zener relaxation frequency. This study will examine aluminum specimens with frequencies in this frequency range, where little previous data is available.

Work done on damping in composite materials by other researchers is less comprehensive, and more difficult to correlate, due to the known or suspected dependence of material damping on laminate stacking and geometry [8,9], laminate fiber volume [10], and environmental effects on the matrix material [11]. Previous research at MIT has focused on characterizing the AS1/3501-6 graphite/epoxy system under conditions of low room temperature and moisture content. Results have been reported for angle ply laminates of the form $[\pm 45]_{2s}$ [3,4]. This study will concentrate on unidirectional laminates $[0]_8$ and $[90]_8$. To date only preliminary data on damping in metal matrix materials is available in the literature [12]. Measurements were made on three graphite fiber/magnesium matrix specimens.

Experimental Design

An experimental apparatus has been developed in the Space Systems Laboratory at the Massachusetts Institute of Technology to quantify the damping of material specimens. The apparatus, called the Tuneable Excitation Launch Mechanism (TELM), lofts the specimen into free-fall, eliminating interference caused by support and excitation interactions. The apparatus is contained within a seven foot tall circular vacuum chamber. The vacuum eliminates any aerodynamic drag and damping effects.

The test sequence is as follows. Prior to launch, the specimen is placed on the spring loaded launcher. The specimen is supported near its ends by two vertical stands which are, in turn, attached to the horizontal launcher bar. To begin the test, the launcher is drawn downward into the cocked position by a motor-driven worm-screw mechanism, which compresses a set of four springs (Fig. 1a). After the chamber has been evacuated to 1 Torr, the electromagnet, which holds the launcher in the cocked position, is released. The launcher translates upward, guided by linear bearings, until it strikes a hard mechanical stop. The acceleration during the upward motion causes the specimen to deflect. The sudden deceleration lofts the specimen vertically upwards in the chamber (Fig. 1b). The launcher system allows the mechanical setting of: the degree, or length, of precompression of the launcher springs; and the stroke, or length of travel, of the launcher prior to striking the mechanical stop. Conversely, there are two constraints placed on the launch process: that the specimen leave the launcher with the correct rigid body velocity to loft it approximately 6 feet vertically; and that the initial strain level of the specimen be adjustable. The initial elastic strain and rigid body velocity are coupled to the precompression and stroke through the dynamics of the launcher, an analysis of which is detailed in Ref. [3,4]. Within limits, the elastic strain can be varied, while the rigid body velocity at launch is held fixed at the prescribed value.

The time history of the free response of the specimen was measured by a pair of BLH FDE-25-35-ES dynamic strain gauges, mounted on the specimen's upper and lower surface at the midpoint. The strain gauges were connected via three 18 in. long, 39 gauge, enamel-coated signal wires, to a small terminal block which ran on a cable and pulley system (Fig. 1c). The lower pulley was driven by a high torque pancake motor, which was controlled by a microprocessor. The microprocessor would send to the motor a commanded position time history, such that the position of the terminal block on the cable would match the specimen's vertical position in free flight. In this way the specimen was connected to the minimum length of very fine signal wire, which was kept slack during the test, thus causing the least possible mechanical interference with the measurement.

In an effort to further reduce the effect of the strain gauge signal wires on the damping characteristics, a series of tests were run with the signal wires mounted near the center of the specimen next to the strain

gauge and, alternatively, with the signal wires mounted at the location of the node of the first free-free mode shape. No significant difference was observed in the damping measurements with the gauge wire mounted at the free-free node.

All specimens tested were small beams, approximately 1.0 in. in width. They varied in length from 5.3 in. to 20 in., and in thickness from .023 in. to .062 in. The specimens were made of aluminum, graphite/epoxy, and graphite/metal matrix composites. There were ten 2024-T3 aluminum specimens tested, the dimensions of which are listed in Table 1. The attachment location of the signal wires is also noted for each specimen. The specimens' geometries were chosen to yield different ratios of first modal frequency to Zener relaxation frequency. The surfaces of the aluminum specimens were sanded and cleaned prior to testing to relieve any residual machining stresses. A total of 14 graphite/epoxy specimens were tested (Table 2), including four $[\pm 45]_2$ ply laminates whose results previously had been reported [4]. The specimens were fabricated from Hercules AS1/3501-6 pre-preg tape, using a standard TELAC curing cycle [5]. Specimens $[0]_8$ -1 through $[0]_8$ -4 were cut from the same laminate sheet, in order to determine the variability in damping of specimens cut from different sections of a larger laminate. Specimens $[0]_8$ -5 through $[0]_8$ -7 were fabricated by successively cutting $[0]_8$ -4 to shorter lengths. Likewise, specimens $[90]_8$ -2 and -3 were made by cutting $[90]_8$ -1 and $[\pm 45]_2$ -2, -3, and -4, were made by cutting $[\pm 45]_2$ -1. By using the same specimen at different frequencies, the scatter introduced by nonuniform laminate properties was minimized. The lengths for the $[90]_8$ specimens were chosen essentially to obtain the same frequencies as those tested in the $[0]_8$ specimens. The specimens were tested within three weeks of initial fabrication and were stored in a zero-humidity chamber following fabrication and between tests, in order to minimize moisture effects. Three metal matrix composite specimens were tested. The dimensions of these specimens are listed in Table 3. All specimens were fabricated from graphite fiber and magnesium matrix. One was a single ply with a magnesium foil, and two were two ply with titanium foils.

The strain gauge time history was recorded during the test and processed digitally for identification of specimen frequency and damping. Data was recorded at a minimum rate of twenty points per vibrational cycle. Prior to identification some of the data was digitally filtered using a nearly equal ripple low pass digital filter, with the cut-off frequency set at the frequency logarithmically one-half way between that of the first and second symmetric free-free modes. The filtered data was analyzed when there was no stress dependence. The unfiltered data was analyzed when there was a stress dependence, as noted in Tables 1-3. Frequency and damping parameters were identified by fitting an exponentially decaying sinusoid to the data with a least squares algorithm [13]. When the damping exhibited stress dependence, the data was windowed and the measured damping for the window assigned to the average alternating stress amplitude for the window.

Experimental Results and Analysis

Aluminum

In order to provide a data base with which to validate the experimental procedure, a series of tests were conducted to measure the material damping in 2024-T3 aluminum beams in bending. A large experimental data base already exists for this material [6], and the damping properties are known to correlate well with the damping model of Zener [7], which stipulates that the damping ratio is related to the thermodynamic and oscillatory properties as

$$\zeta = \frac{\alpha^2 ET}{2C} \left[\frac{\omega\tau}{1 + (\omega\tau)^2} \right] \quad (1)$$

where α is the coefficient of thermal expansion, E is the Young's modulus, T the absolute temperature, C the specific heat per volume, and ω the vibration frequency. The relaxation time τ is given by

$$\tau = \frac{C h^2}{k \pi^2} \quad (2)$$

where h is the specimen thickness and k is the thermal conductivity. The inverse of τ is the relaxation frequency, ω_R , at which damping is expected to peak. The theory predicts damping independent of frequency when the stress is lower than the yield stress.

Initially, tests were performed on a number of specimens whose vibratory frequency was at or above the relaxation frequency, (specimens A1-1 through -4 and A1-9 and -10). The material damping measured in these specimens was found to be a strong function of frequency and a weak function of stress below 20 KSI. These are in agreement with results of previous experimental measurements [3,6], and lie just above the Zener curve, as shown in Fig. 2. The material constants used in calculating the Zener curve are taken from Ref. [14]. The standard deviation bars of Fig. 2 indicate the extremely low levels of damping which were reliably measured, on the order of 0.03 percent of critical. Estimates of the measurement precision and accuracy are discussed in Ref.[3,4].

For aluminum specimens whose vibratory frequency was below the Zener relaxation frequency, quite a different behavior was found. The total ranges of damping measured for these specimens (A1-5 through -8) is shown in Fig. 2. The upper limit on these ranges should not be considered as a maximum value of damping, but rather as the value obtained for the maximum value of stress at which the specimens were tested. The damping in these specimens was found to be highly stress dependent at stress levels as low as 8-10 KSI, as indicated on Fig. 3. The values on Fig. 3 represent an average value of damping ratio over a range of .5 KSI for the specimen referenced. These stress (or strain) values refer to the alternating stress (or strain) amplitude measured on the surface at the midpoint. Note that

the lowest values of damping measured for these specimens also does not correlate well with the Zener model. No other experimental measurements of damping in this aluminum alloy below the relaxation frequency were found in the literature, and the reason for this departure from Zener behavior is not apparent at this time.

Graphite/Epoxy Composites

To develop a data base for validation of theoretical models for graphite/epoxy composite damping, experimental data must be collected on a variety of ply lay ups, frequencies and stress levels. To somewhat simplify the problem by removing the effect of the shear coupling terms, only symmetric lay ups are commonly tested [3,10,11]. In a previous investigation using the current technique, $[\pm 45]_2$ specimens of Hercules AS1/3501-6 were tested. In order to enlarge the data base, tests were conducted on $[0]_8$ and $[90]_8$ specimens.

When analyzing the damping in graphite/epoxy, there are a series of questions to be addressed. The first is the question of the uniformity of the damping in nominally identical specimens cut from different laminates. The second deals with the dependence of damping on stress, frequency, and fiber orientation. Both of these questions will be addressed experimentally and, when possible, results will be compared to those of other researchers. Finally, one must assess the validity of theoretical models of composite damping.

To investigate the effects on damping of small non-uniformities in fiber volume, void content and fiber orientation, four specimens ($[0]_8$ -1, -2, -3, -4) were fabricated from the same laminate, so as to be as similar as possible. For tests conducted at the same frequency, the measured mean damping ratio and standard deviation of similar specimens are given in Table 4. In addition, the mean and standard deviations of all the tests are given. Note the extreme precision in the data. The standard deviations for each specimen range from 0.000047 to 0.000090 of critical. The standard deviation for the entire population is of the same order as that for the individual specimens. This implies that the scatter introduced by cutting specimens from the same laminate is comparable to the scatter of the measurement, which is very small. The damping of different composite specimens, at least those cut from the same laminate, is therefore much more uniform than might have been expected.

The next issue is the dependence of damping on peak specimen strain level, frequency and fiber orientation. To eliminate any scatter due to material non-uniformity, the frequency of the specimens was varied by cutting one specimen of each laminate type to successively shorter lengths. The dependence of damping on frequency is shown for $[0]_8$, $[90]_8$ and $[\pm 45]_2$ laminates in Figs. 4, 5 and 6, respectively. The damping in $[0]_8$ is independent of frequency. The mean damping level agrees well with the value of $\zeta = 0.00062$ found for $[0]_{12}$ graphite/epoxy in Ref. [11].

For both $[90]_8$ and $[\pm 45]_{28}$ a slight increase in damping with frequency are observed (note the different vertical scales in Figs. 5 and 6). No strong strain level dependence of damping was found in any of the graphite epoxy laminates. As can be seen by comparing Figs. 4, 5 and 6, there is an order of magnitude difference in damping between $[0]_8$ and the other two fiber orientations for the frequency and strain ranges tested. The values of damping versus fiber orientation for approximately the same frequency are shown in Fig. 7.

In an attempt to correlate the experimental damping data for graphite/epoxy, three analytic models of damping in nonhomogeneous anisotropic materials were applied. The first was a simple rule of mixtures, which states that the fibers and matrix contribute to the damping in proportion to their fractional volume

$$\zeta = V_f \zeta_f + V_m \zeta_m \quad (3)$$

where V is the fractional volume, and the subscripts f and m refer to fiber and matrix properties [16]. This model predicts damping which is independent of fiber orientation, which clearly fails to correlate with the strong dependence on fiber orientation shown in Fig. 7.

The second model was proposed by Hashin, and is based on a transformation of complex moduli [9]. This model assumes a unidirectional laminate, but the fiber orientation need not be aligned with the specimen longitudinal axis. It also assumes the fibers are brittle and therefore have only a real modulus, i.e., they do not contribute to the dissipation. By beginning with a rule of mixtures for the complex modulus and defining the loss tangent as the quotient of the imaginary and real part of the modulus, the expression for the damping ratio is

$$\zeta = \frac{\zeta_m E_m V_m}{E_f V_f + E_m V_m} \quad (4)$$

where E is the Young's modulus of the respective constituents.

A third model, also restricted to unidirectional laminates, was proposed by Adams and Bacon, and is based upon a combination of the complex modulus model for dissipation, supplemented by the additional dissipation in transverse shear [10]. However, the specimens used in this investigation were of sufficiently small thickness/length that the shear dissipation contribution was insignificant, and the damping predicted from this model with shear effects included was indistinguishable from that predicted by the simpler complex modulus model.

Having eliminated the simple rule of mixtures model as clearly inadequate, and the shear damping model as redundant (in this case), there remains only the complex modulus model, given in Eq. (4), for correlation

with the experimental results. Unfortunately, this correlation requires an a priori knowledge of the damping in the neat resin, to determine ζ_m . Tests were not performed on the resin and no data was available from the manufacturer. As an alternative, the model was used to back calculate the matrix damping from the experimental data. The value calculated from each specimen can be compared for consistency. Consistent values of matrix damping calculated from different tests in this manner would be a necessary condition for verification of the analytic model. Since the complex modulus model is limited to unidirectional laminates, the $[\pm 45]_2$ data will not be used.

Applying the complex modulus model to data from $[0]_8$ and $[90]_8$ specimens of similar frequencies yields the results listed in Table 5. Note that while the laminate damping ratios differ by an order of magnitude, the back-calculated matrix damping is remarkably consistent over the strain and frequency ranges tested. This level of matrix damping is not untypical of that found in similar epoxy materials. Thus, as best as can be determined, the complex modulus model appears to correlate well with the experimental data. One other significant result of the graphite/epoxy tests is that the real part of the laminate modulus as determined in flexure from these experimental data is approximately 15% lower than that measured in static tensile testing, both in the longitudinal and transverse fiber orientations. This result is in substantial agreement with previous experimental results for moduli in flexure measured for thin laminates [15].

Graphite/Metal Matrix

Preliminary measurements of material damping were made in three graphite/metal matrix specimens, and are shown on Fig. 8. The data for the two specimens with titanium foil, P100/AZ91C/Ti and P55/AZ91C/Ti, showed no strain level dependence. However, the strain range involved was fairly small, due to limitations of the TELM. The specimen with magnesium foil, P100/AZ91C/Mg, showed a very slight strain dependence over a strain range of 36 μs to 176 μs . Frequency dependence could not be tested for any of these specimens, since only one specimen was provided, and its geometry could not be altered. The order of magnitude of the damping ratio for all of these specimens is the same as in aluminum and $[0]_8$ graphite/epoxy.

The damping ratios for all of the specimens were compared to the theoretical Zener values for AZ91C magnesium, which is the matrix material being used. This was done by assuming the specimens are made entirely of magnesium, but have the same dimensions as the ones tested. The theoretical curve is plotted together with the actual damping ratio for each specimen in Fig. 8. The two specimens with a frequency above the relaxation frequency, P100/AZ91C/Ti and P55/AZ91C/Ti, exhibit the same characteristics as aluminum, that is, no strain dependence, and a damping value slightly above the Zener value. The specimen with a frequency below the relaxation frequency, P100/AZ91C/Mg, behaved in an irregular way. The

average value of damping is slightly below the predicted Zener value, but the lowest extreme is well below the Zener model value. The large standard deviation for this specimen cannot be adequately explained, but is statistically valid since over fifty measurements of damping in this specimen were made. The fact that the mean values of damping correlate so well with Zener model implies the damping is dominated by the matrix, and is similar in mechanism to that found in metals. Insufficient data was available on the metal matrix samples to allow any correlation with the complex modulus damping model.

Conclusions

The experimental data leads to the following conclusions:

1. Material damping in aluminum 2024-T3 follows the Zener curve for frequencies above the relaxation frequency. In this region the damping is independent of stress level up to approximately 16 KSI, or 1500 μ s.
2. For frequencies below the relaxation frequency, aluminum 2024-T3 does not appear to follow the Zener curve. There is a strong dependence on stress levels as low as 8 KSI, or 750 μ s, and a slight frequency dependence.
3. Material damping in graphite/epoxy $[0]_g$ was found to be independent of stress and independent of frequency. Damping ratios ranged from 0.049% to 0.064% with an average of 0.056%. The stress range tested was from 0.3 KSI to 12.8 KSI, or 20 μ s to 775 μ s, and the frequency range was from 45 Hz to 237 Hz.
4. Material damping in graphite/epoxy $[90]_g$ was independent of stress and slightly dependent on frequency, increasing with increasing frequency. Damping ratios ranging from .55% to .66% were obtained. The stress ranges were from 0.009 KSI to 0.84 KSI, 7 μ s to 675 μ s, and the frequency range was 43 Hz to 143 Hz.
5. Material damping in graphite/epoxy $[\pm 45]_{2g}$ was largely independent of stress, and slightly dependent on frequency, increasing with increasing frequency. Damping ratios ranged from .50% to .67%, in the frequency range of 18 Hz to 171 Hz, and in the stress range of 0.1 KSI to 6.5 KSI.
6. Dynamic modulus for graphite/epoxy $[0]_g$ was approximately 15% lower than static modulus. Dynamic modulus for graphite/epoxy $[90]_g$ was also approximately 15% lower than the static modulus.
7. Hashin's theory for damping in unidirectional composites gives consistent values for matrix damping when applied to graphite/epoxy $[0]_g$ and $[90]_g$. No conclusion can be made whether the addition of shear effects improves the level of correlation.

8. Damping ratio for metal matrix P100/AZ91C/Ti is independent of strain over the range 17 μ s to 47 μ s. A value of .039% damping ratio was found at a frequency of 494 Hz.

9. Damping ratio for metal matrix P55/AZ91C/Ti is independent of strain over the range 37 μ s to 61 μ s. A value of .039% damping ratio was found at a frequency of 401 Hz.

10. Damping ratio for metal matrix P100/AZ91C/Mg may be slightly dependent on strain over the range 36 μ s to 176 μ s. An average value of .099% was found at a frequency of 138 Hz.

11. The damping in metal matrix specimens correlated with the damping predicted by the Zener model for the matrix metal alone. This implies the damping is dominated by the matrix, and that the mechanism is similar to that in homogeneous metals.

Acknowledgements

This research was sponsored in part by NASA under grant #NAGW-21, with Mr. Samuel Venneri of NASA Headquarters serving as technical monitor, and in part by HR Textron, with Mr. Joseph Garibotti serving as monitor. In addition, HR Textron supplied the metal matrix specimens. Captain Sheen was supported by the U.S. Air Force.

References

1. Bert, C.W., "Material Damping: An Introductory Review of Mathematical Models, Measures and Experimental Techniques," Journal of Sound and Vibration, (1973), 29(2), pps 129-153.
2. Vorlicek, P.L., "Material Damping of Aluminum and Graphite/Epoxy in a Simulated Zero-Gravity Environment," M.I.T. Space Systems Laboratory #13-81, January 1981.
3. Mohr, D.G. and Crawley, E.F., "Experimental Measurements of Material Damping of Aluminum and Graphite/Epoxy in Free-Fall with Tuneable Excitation," M.I.T. Space Systems Laboratory #11-82, June 1982.
4. Crawley, E.F., Mohr, D.G., "Experimental Measurements of Material Damping in Free Fall with Tuneable Excitation," Presented at AIAA/ASME/ASCE/AHS Structures, Structural Dynamics and Materials Conference, Paper No.83-0858-CP, Lake Tahoe, NV, May 1983, to be published in AIAA Journal.
5. Sheen, R.L., Crawley, E.F., "Experimental Measurement of Material Damping for Space Structures in Simulated Zero-G," M.I.T. Space Systems Laboratory #1-84, January 1984.

AD-A152 547

VIBRATION DAMPING WORKSHOP PROCEEDINGS HELD AT LONG
BEACH CALIFORNIA ON 2... (U) AIR FORCE WRIGHT
AERONAUTICAL LABS WRIGHT-PATTERSON AFB OH L ROGERS

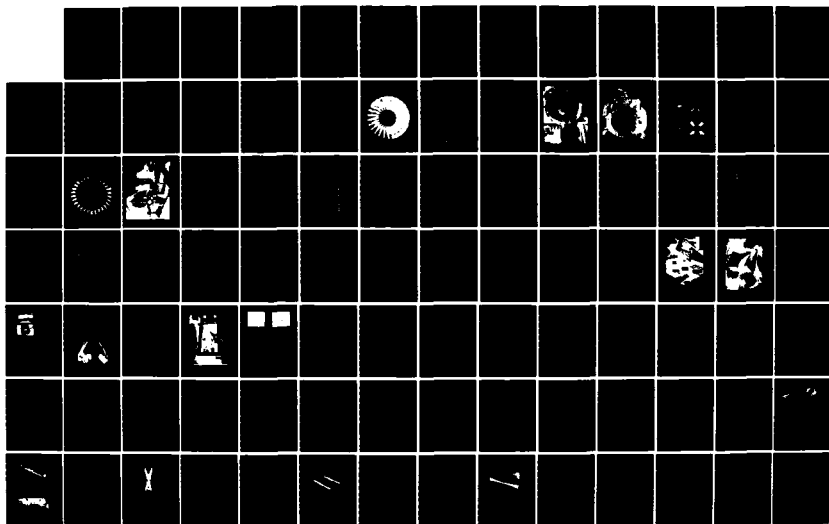
2/11

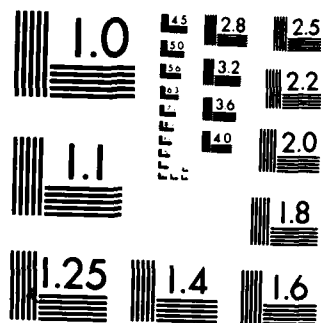
UNCLASSIFIED

11 NOV 84 AFMAL-TR-84-3864

F/G 20/11

NL





MICROCOPY RESOLUTION TEST CHART
NATIONAL BUREAU OF STANDARDS-1963-A

6. Granick, N., Stern, J.E., "Material Damping of Aluminum by a Resonant-Dwell Technique," NASA TN D-2893, August 1965.
7. Zener, C.M., Elasticity and Anelasticity of Metals, University of Chicago Press, Chicago, 1948.
8. Shultz, A.B., Tsai, S.W., "Dynamic Moduli and Damping Ratios in Fiber-Reinforced Composites," Journal of Composite Materials, Vol. 2, July 1963.
9. Hashin, Z., "Complex Moduli of Viscoelastic Composites-II. Fiber Reinforced Materials," International Journal of Solids and Structures, Vol. 6, 1970.
10. Adams, R.D., Bacon, D.G.C., "The Dynamic Properties of Unidirectional Fibre Reinforced Composites in Flexure and Torsion," Journal of Composite Materials, Vol. 7, January 1973.
11. Putter, S., Buchanan, D.L., Rehfield, L.W., "Influence of Frequency and Environmental Conditions on Dynamic Behavior of Graphite/Epoxy Composite," in Composite Materials: Testing and Design (Sixth Conference), ASTM STP 787, I.M. Daniel, Editor, ASTM, 1982, pp 414-424.
12. Timmerman, N.S., "Damping Characteristics of Metal Matrix Composites, Army Materials and Mechanics Research Center Report, AMMRC TR-82-19, April 1982.
13. Marquardt, D.W., "An Algorithm for Least Squares Estimation of Nonlinear Parameters," Journal of the Society for Industrial and Applied Mathematics, Vol. 11, No.2, June 1963.
14. Military Standardization Handbook, Metallic Materials and Elements for Aerospace Vehicle Structures, MIL-Hdbk-5C, Vol.1, September 1976.
15. Turner, M.D., "Comparison of Static and Dynamic Test Methods for Determining the Stiffness Properties of Graphite/Epoxy Laminates," S.M. Thesis, M.I.T., Cambridge, MA, June 1979.
16. Ashton, J.E., Halpin, J.C., Petit, P.H., Primer on Composite Materials: Analysis, Technomics Publishing Company, Westport, CT, 1969.

Table 1 Aluminum Specimens

Specimen	Length (in)	Width (in)	Thickness (in)	Mass (Slugs (10^{-3}))	Wire	Data Filter
Al-1	18.00	1.00	.062	3.409	C,N	F
Al-2	14.00	1.00	.062	2.652	C,N	F
Al-3	6.00	1.00	.062	1.136	C,N	F
Al-4	20.00	1.00	.062	3.789	C	F
Al-5	18.94	1.00	.031	1.794	N	U
Al-6	14.00	1.00	.031	1.326	N	U
Al-7	10.00	1.00	.031	0.947	N	U
Al-8	8.00	1.00	.031	0.758	N	U
Al-9	6.00	1.00	.031	0.568	N	F
Al-10	10.00	1.00	.061	1.894	C	F

In Tables 1, 2 and 3, C denotes strain gauge wire attached at the Center, N at the first free-free Node, F denotes Filtered data was analyzed, U denotes Unfiltered data.

Table 2 Graphite/Epoxy Specimens

Specimen	Length (in)	Width (in)	Thickness (in)	Mass (Slugs (10^{-3}))	Wire	Data Filter
[0] ₈ -1	17.75	1.01	.042	1.297	N	F
[0] ₈ -2	17.78	0.99	.041	1.245	N	F
[0] ₈ -3	17.75	1.01	.042	1.291	N	F
[0] ₈ -4	17.75	1.00	.043	1.301	C	F
[0] ₈ -5*	13.88	1.00	.043	1.020	C	F
[0] ₈ -6*	10.00	1.00	.043	0.735	C	F
[0] ₈ -7*	7.88	1.00	.043	0.579	C	F
[90] ₈ -1	9.66	1.00	.041	0.683	C	F
[90] ₈ -2§	7.34	1.00	.041	0.519	C	F
[90] ₈ -3§	5.31	1.00	.041	0.375	C	F
[±45] _{2s} -1	18.00	0.99	.041	1.320	C	F
[±45] _{2s} -2†	14.12	0.99	.041	1.035	C	F
[±45] _{2s} -3†	10.00	0.99	.041	0.733	C	F
[±45] _{2s} -4†	5.97	0.99	.041	0.438	C	F

* specimen [0]₈-4 cut to a shorter length

§ specimen [90]₈-1 cut to a shorter length

† specimen [±45]_{2s} cut to a shorter length

Table 3 Graphite/Metal Matrix Specimens

Specimen	Length (in)	Width (in)	Thickness (in)	Mass (Slugs (10^{-3}))	Wire	Data Filter
P100/AZ91C/T1	6.00	1.00	.044	0.624	C	U
P55/AZ91C/T1	6.10	1.00	.045	0.630	C	U
P100/AZ91C/Mg	8.00	0.96	.023	0.363	N	U

Table 4 Damping of Similar Specimens of $[0]_8$

Specimen	Frequency (Hz)	No. of Tests	Mean Damping Ratio (10^{-3})	Std Deviation (10^{-3})
$[0]_8-1$	46.0	23	0.622	0.048
$[0]_8-2$	45.2	23	0.512	0.082
$[0]_8-3$	45.9	23	0.642	0.047
$[0]_8-4$	47.8	23	0.514	0.090
Total Population		92	0.572	0.090

Table 5 Back-Calculated Matrix Damping

Laminate	Frequency (Hz)	Strain Range (10^{-6})	Laminate Damping Ratio (10^{-3})	Matrix Damping Ratio (10^{-3})
$[0]_8$	47	504-791	0.51	32.7
$[90]_8$	43	250-676	5.5	26.8
$[0]_8$	77	96-364	0.60	37.5
$[90]_8$	74	43-215	6.0	29.8
$[0]_8$	148	160-240	0.49	30.3
$[90]_8$	143	7-208	6.6	33.6

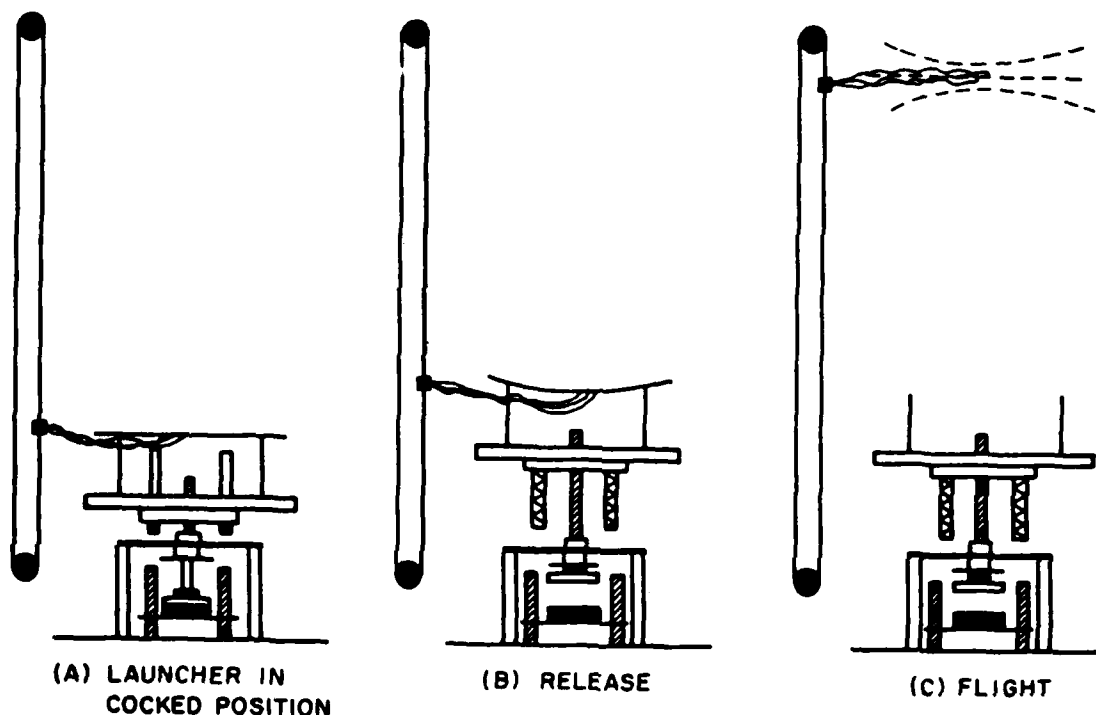


Fig. 1 Test Sequence of the Tunable Excitation Launch Mechanism, Showing the Launcher, Specimen and Signal Wire Carrier

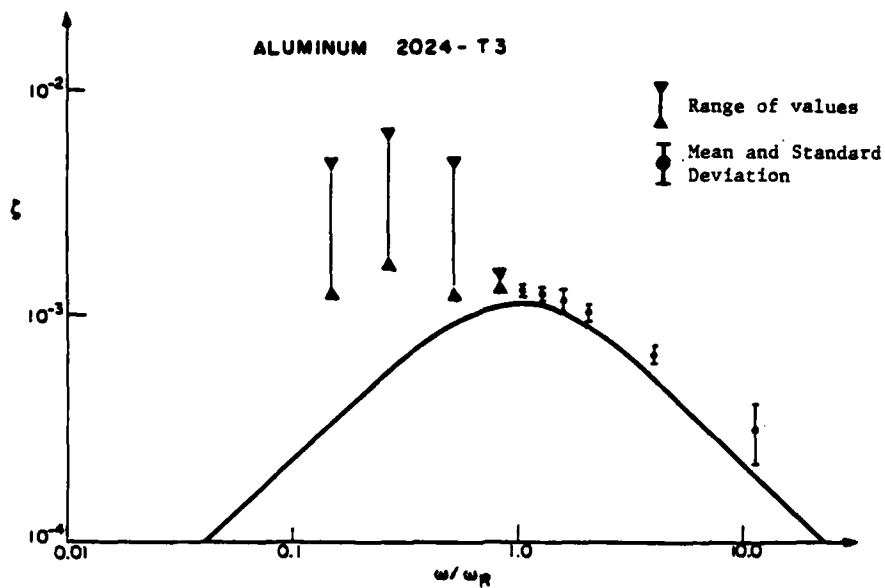


Fig. 2 Damping Ratio versus Frequency for Aluminum

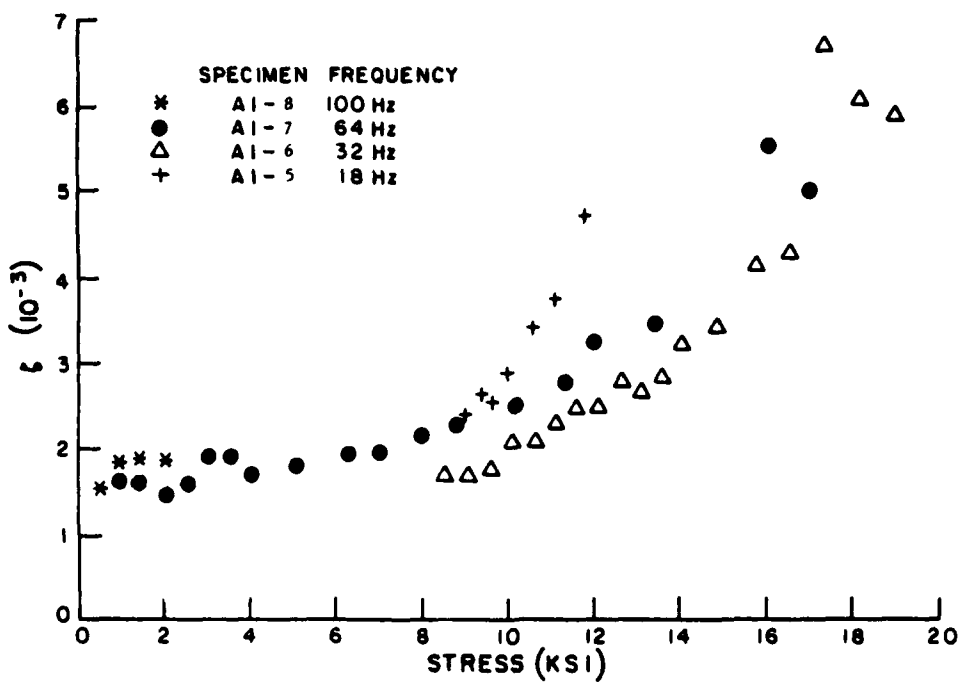


Fig. 3 Damping Ratio versus Stress for Specimens with First Free-Free Frequency Below Zener Relaxation Frequency

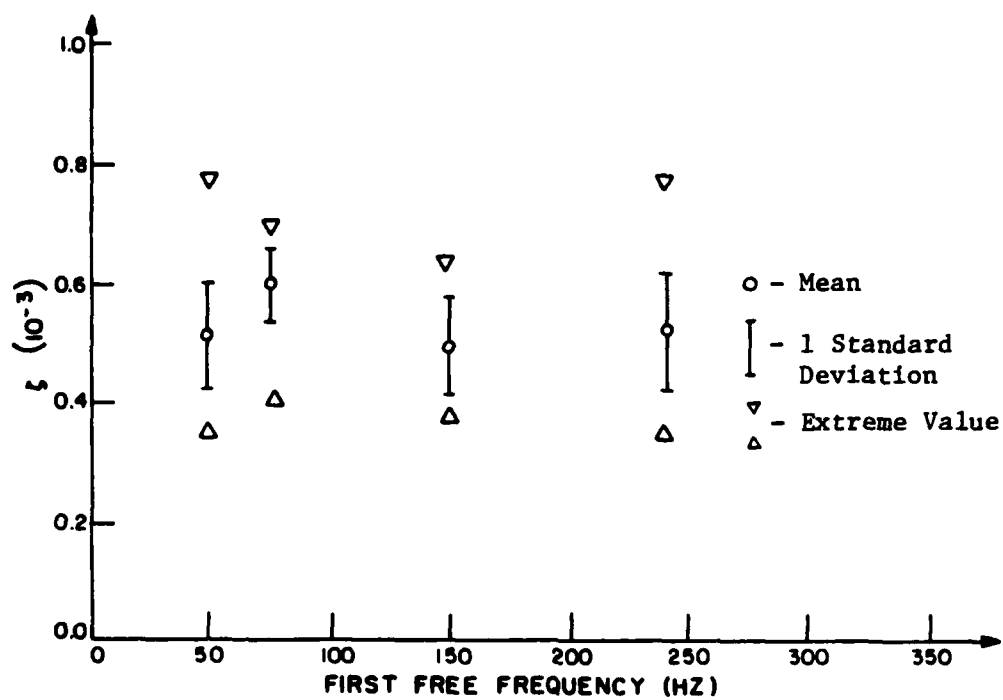


Fig. 4 Damping Ratio versus Frequency for $[0]_8$ Graphite/Epoxy

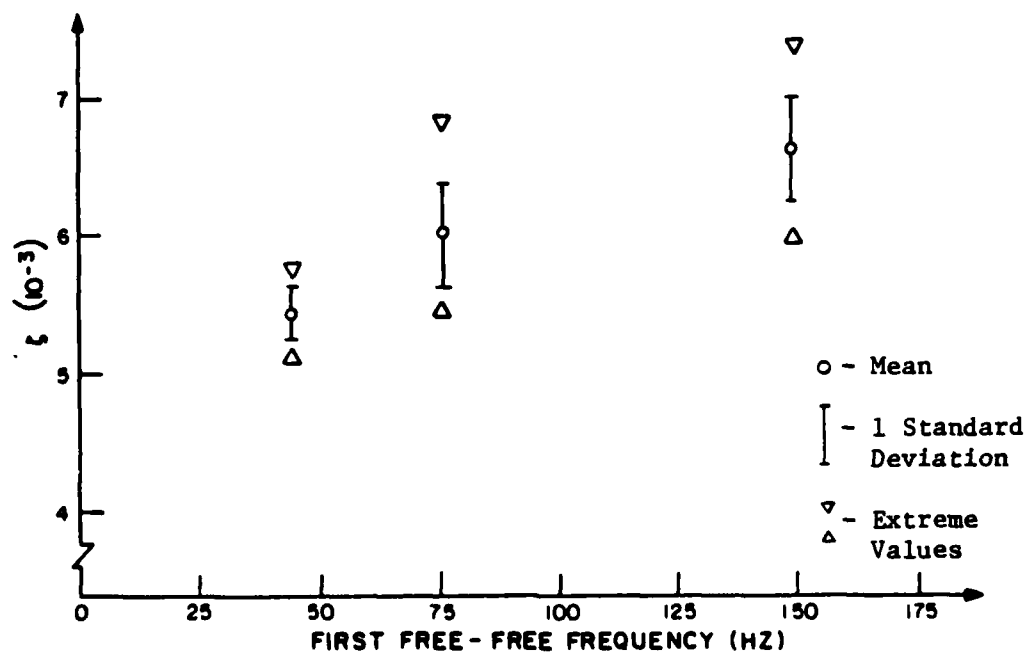


Fig. 5 Damping Ratio versus Frequency for $[90]_8$ Graphite/Epoxy

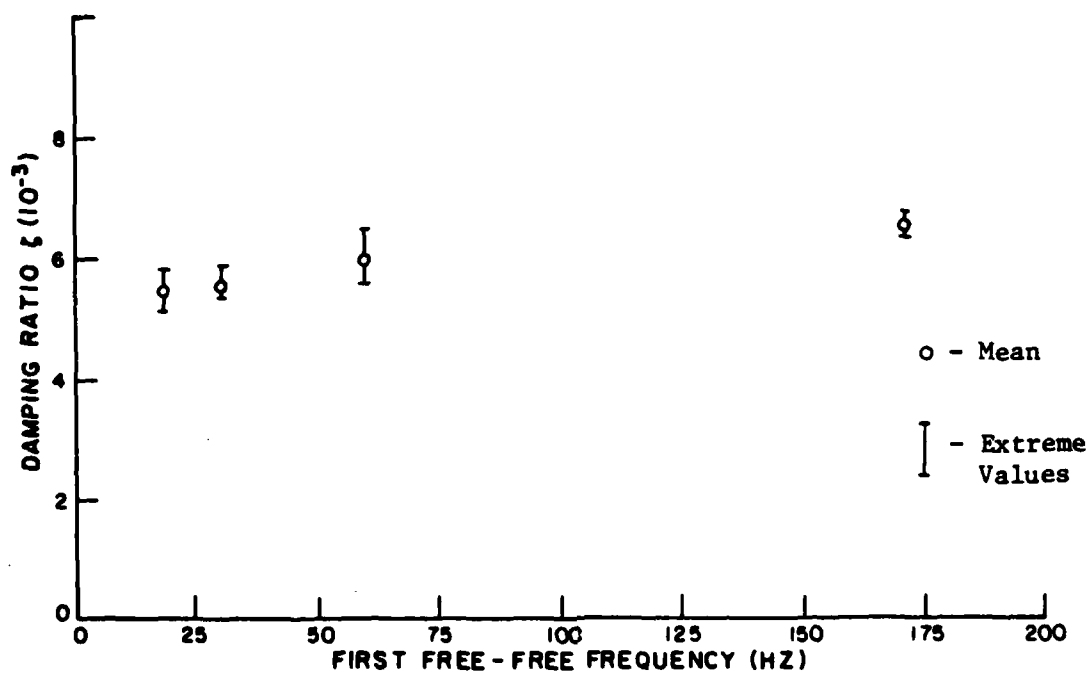


Fig. 6 Damping Ratio versus Frequency for $[\pm 45]_{2s}$ Graphite/Epoxy

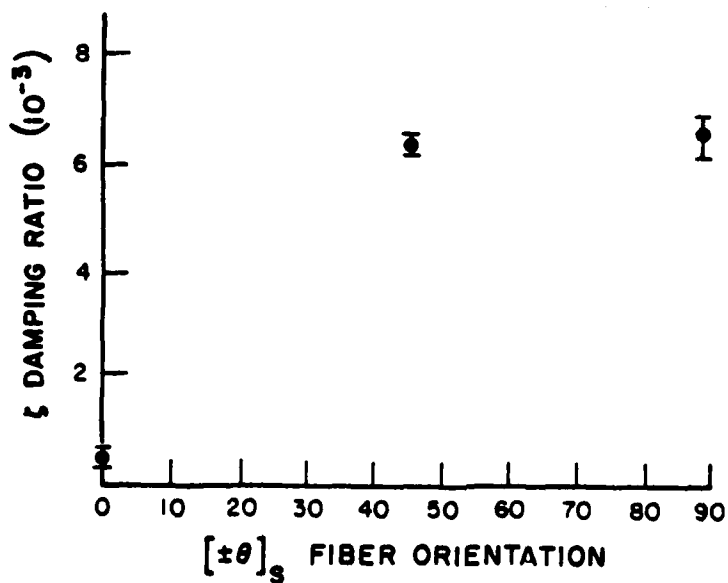


Fig. 7 Damping Ratio versus Fiber Orientation for Graphite/Epoxy (Frequency 140-170 Hz)

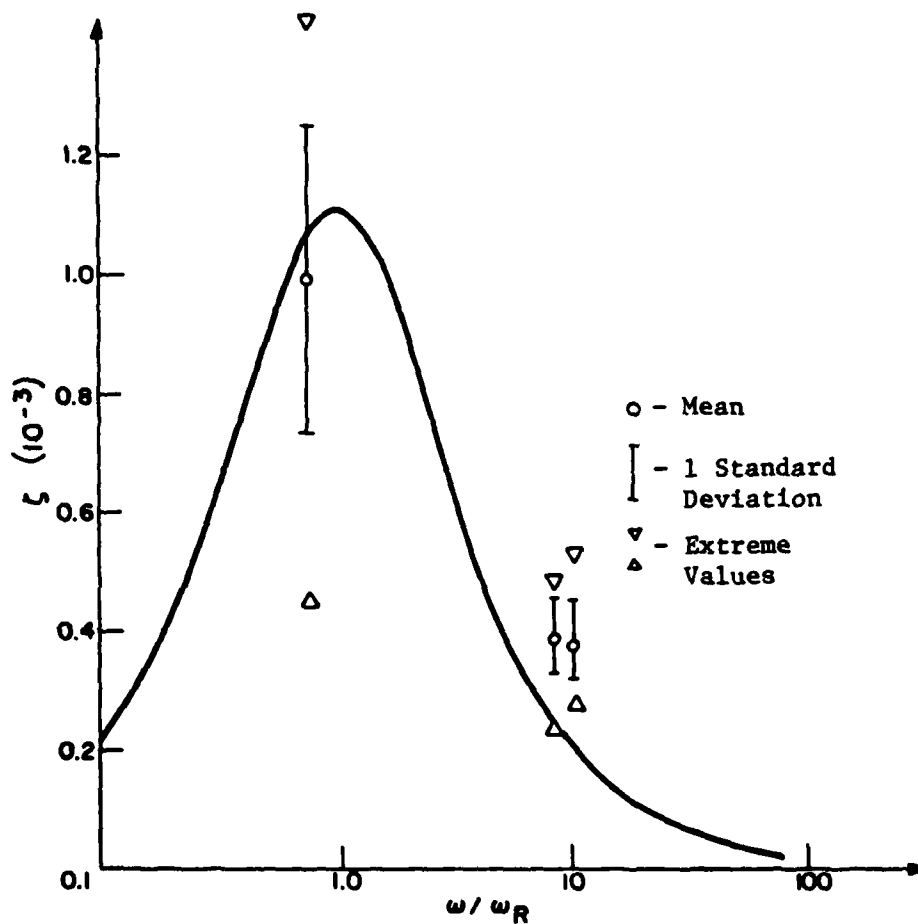


Fig. 8 Damping of Metal Matrix Specimens versus Frequency

Specimen	ω/ω_R
P100/AZ91C/Ti	10.2
P55/AZ91C/Ti	9.3
P100/AZ91C/Mg	0.9

Zener Curve for Mg AZ91C

COULOMB FRICTION APPLICATIONS

Professor H. A. Scarton
Rensselaer Polytechnic Institute
Troy, New York

Paper was not presented; not available for publication.

DAMPING APPLICATIONS IN TURBINE ENGINES

R. L. Jay and D. W. Burns
Allison Gas Turbine Operations
General Motors Corporation
Indianapolis, Indiana

DAMPING APPLICATIONS IN TURBINE ENGINES

R.L. Jay and D.W. Burns

Allison Gas Turbine Operations
General Motors Corporation

ABSTRACT

An evaluation of the application of damping treatments to turbomachinery rotating and static components based on measured response characteristics of compressor and turbine stages was performed. In the evaluation, data from a shrouded fan stage, an integral turbine stage, and two stator vane assemblies were used. From the data the contributions due to material damping, interface damping and aerodynamic damping comprising the total system damping were obtained. Based on these identifications a basis for the application of damping treatments which would be effective in controlling resonant response amplitudes is established.

INTRODUCTION

Forced vibration of both rotating and stationary blading in turbomachines occurs when one of the natural frequencies coincides with a periodic forcing function created by upstream generated blade wakes, inlet distortion or potential disturbances emanating from a downstream blade row. Accurate prediction of blade/disk frequencies and stator vane frequencies are well within the existing state of the art. However, the prediction of the amplitudes of dynamic stress which occur at resonance is beyond the current state of the art. The elements comprising an ideal forced vibration amplitude prediction system include an unsteady aerodynamic model, a structural dynamics model, and a knowledge of the inherent mechanical damping available in various modes of vibration. The unsteady aerodynamic model should be formulated such that both the forcing function in terms of complex pressures along an airfoil surface and the aerodynamic damping are available to be coupled into the structural model. However, these aerodynamic models are not currently available for the wide range of flows experienced by today's turbine engine blading, but are being pursued. As these unsteady aerodynamic models become available, the design of blading free of potential high cycle fatigue can be accomplished using available damping values obtained from in-vacuum static and rotating testing.

When this predictive methodology is firmly in place, attention will be more critically focused on the use of damping to control resonance response amplitudes. Currently, damping coatings and/or mechanical damping concepts to control response amplitudes are often the result of a major field or development problem. In lieu of the predictive methodology to assess forced vibration an assessment of the damping present in typical forced vibration problems will be made in order to characterize damping sources and magnitudes, thus furnishing information relative to the proper use of damping materials and/or devices in turbomachines.

In the discussion which follows, the results of testing a shrouded fan assembly, an integral turbine stage, and two compressor stator vane assemblies will be presented. For each component the damping attributable to the aerodynamics and to the structural sources will be defined. From these definitions, the range of damping which must be added to effectively control resonant amplitude can be established.

DISCUSSION

Shroud Fan Study

In recent aeroelastic investigations, a controlled study of the resonant response of a shrouded fan stage was accomplished. The fan stage investigated was an approximate one-fifth geometrical scale of the inlet stage of the TF-41 engine. The scaled version was constructed of steel rather than from the titanium used in the full size fan in order to allow magnetic excitation. The fan, shown in Figure 1, features 25 airfoils having part span shrouds. Testing of the fan was accomplished in-vacuum, both static and rotating, and in an aerodynamic component rig. Individual

blades were tested in-vacuum in order to determine modal damping for the first five modes of vibration. The blades were then bonded into the disk, the shrouds bonded at their contact faces, and the bladed disk assembly modal damping values obtained in-vacuum and in air in non-rotating testing. Following these bench tests, the fan assembly was installed in a vacuum facility and modal damping values obtained at varying rotor speeds.

To provide excitation for the assembly modes of the fan, shown in terms of a frequency versus speed chart in Figure 2, a preferential drive concept using small electromagnets was used. The magnetic excitation was required in the absence of air in the vacuum facility. The preferential drive concept is illustrated in Figure 3. In this concept, magnetic pulses or fields are generated by both the front and rear magnets simultaneously. Choice of the location and number of magnets used provided a preferential excitation so that a single assembly mode could be isolated and investigated. In the figure the set-up for a three diametral mode excitation is evident. The magnet drives were energized via computer control of the power delivered to each magnet. This feature enabled the magnets to provide a constant or alternating force field. In this discussion, a constant force field is termed DC excitation and the alternating force field is termed AC excitation.

The vacuum facility was designed to accommodate fan rotational speeds up to 45000 rpm while maintaining a working pressure of less than 5 mm of Mercury. The electromagnets comprising the preferential drive system utilized cores which extended through the front and rear plates of the vacuum chamber to within .050 inches from the fan blades. The cores were radially aligned with the shrouds to maximize the input energy into the blades. The vacuum was obtained using a high-volume vacuum pump attached to a 2 inch diameter hose mounted into the forward face of the vacuum chamber. Features of the vacuum facility and preferential drive system are shown in the photographs presented as Figures 4 and 5. Testing in the vacuum facility was accomplished by first determining the assembly mode of interest and configuring the preferential drive system accordingly. Excitation in the AC mode of operation of the magnets was used at varying rotor speeds up to the critical speed of the particular assembly or diametral mode. To investigate the behavior at the critical speed, the magnets were used in the DC mode. At the subcritical rotor speeds both dieaway and resonant width techniques were used to define the damping. The assembly modes investigated in this study included the third, fourth, fifth and sixth diametral patterns.

Following the in-vacuum rotating tests the fan assembly was placed in an aerodynamic component test rig so that resonant responses of the assembly modes could be established. In order to provide known order excitations to the fan, inlet distortion patterns were placed in the inlet duct immediately upstream of the fan. The distorters shown in Figure 6 were used to create disturbances for excitation of the 3, 4, 5, and 6 diametral modes of the fan. Testing in the aerodynamic rig was accomplished by inserting the chosen distorter and accelerating the fan through the critical speed range. In the testing, response data was obtained at varying pressure ratios so that effects of steady aerodynamic loading could be assessed.

In the testing two modifications of the fan were examined relative to the effect on overall damping. The first of these was accomplished in the aerodynamic rig and consisted of removing the bonding between the shroud faces which prevented shroud slippage, thus obtaining data on the effects of shroud slippage. The second modification involved coating one surface of the airfoil with a plasma spray which enhanced damping properties. The effect of this applied damping coating was evaluated in the vacuum facility.

Fan Test Results

The testing of the individual blades using die-away techniques indicated damping values ranging from 0.12% logarithmic decrement for the first torsional mode to approximately 0.6% for the first bending mode. The other three modes investigated had damping values of approximately 0.2%, thus an average damping for all blade alone modes was approximately 0.26% when tested in-vacuum.

A plot of all the vacuum data for the uncoated configuration is shown in Figure 7. This shows the effect of stress level on structural damping. The points below ± 0.8 ksi were obtained from AC magnet excitation of the fan and the die-away method was used to measure damping.

From ± 0.8 ksi to approximately ± 5 ksi the data was obtained from bench testing of the fan also using the die-away method. The data points above ± 5 ksi were obtained during DC magnet excitation of the fan with the resonance width method used to measure damping. This plot would imply average structural damping for this fan bladed-disk system of $0.5\% \delta$ at ± 1 ksi to $2\% \delta$ at ± 40 ksi.

Figure 8 is a similar plot for the baseline aerodynamic testing responses at the two compressor loadings. The average damping for the open throttle (O.T.) and near surge (5 N.C.) loadings are noted on Figure 9 as $4.45\% \delta$ and $4.1\% \delta$ respectively. This gives ratios of average aerodynamic damping to average structural damping from about 9 to 2 for stress levels of ± 1 to ± 40 ksi respectively.

The overall damping data for the various phases of the fan program is summarized in Figure 9. The ranges and the averages for each test are charted. Comparisons of the various test results for the vacuum and bench data for the 3 through 6 diametral modes indicate the changes in damping listed to the right of the figure. Effects of coating, speed and atmosphere are noted. Comparison of the aerodynamic data, bars F through I, indicates a slight increase in damping associated with unbonded shrouds. For both configurations there is a noted drop in overall damping with higher loading.

Tested in a static facility in the uncoated, shrouds-locked configuration, the system damping for the various diametral patterns ranged from approximately 0.45% to 0.8%. For the damped configuration this range increased to approximately 1.0% to 2.2%, an increase of over 2. Comparisons of the static in-vacuum and the rotating in-vacuum results indicate that the effects of rotation resulted in a damping increase of approximately 0.40% for both the uncoated and coated configurations.

This resulted in an average of the high and low values of damping for the uncoated configuration of 0.97% and for the coated configuration an average of 2.05%. Thus the addition of the damping coating resulted in a damping increase of over 2.

To quantify the aerodynamic damping, comparisons between data from the uncoated, locked shroud configuration tested in-vacuum and under aerodynamically induced conditions were made. From these comparisons, the incremental damping attributed to aerodynamics was approximately 3.3% logarithmic decrement. The effect of loose shrouds on the overall damping was to increase the uncoated, locked shroud system damping by approximately 0.57% logarithmic decrement.

Thus the total damping which can be expected in resonant responses in a front stage, shrouded fan stage can be broken down as follows:

	<u>Logarithmic Decrement</u>	<u>% of Total</u>
(a) Due to blade alone	0.26%	6
(b) Due to assembly	0.35%	8
(c) Due to rotational effects	0.40%	9
(d) Due to aerodynamic influence	3.30%	77
Total System Damping	4.31%	100

The addition of the plasma spray damping coating to the airfoil surfaces increased the system damping by 1%.

These results pertain specifically to the fan configuration tested. The largest influence on the total system damping is obviously the aerodynamic damping which is a result of the motion of the airfoils in the steady state flow field. It must be realized that this aerodynamic damping is influenced by airfoil geometry, number of airfoils, inlet relative velocities, and of course, frequencies and mode shapes.

Integral Turbine Study

The resonant response of an integrally machined turbine stage shown in Figure 10 was obtained in a turbine aerodynamic component rig. The excitation source which provided the aerodynamically induced forces on the turbine airfoils were generated by the wakes of an upstream vane row comprised of 26 vanes. The turbine rotor featured 30 blades. The interaction between the 26 vanes and the 30 airfoils created the potential to excite assembly modes of the four diametral family, a phenomena discussed by Jay, MacBain, and Burns in reference 1. Modal identifications were accomplished in-vacuum using holographic techniques in a laboratory set-up shown in Figure 11. Based on the results of the vibratory bench tests, a frequency versus speed diagram for the turbine stage was constructed and is presented in Figure 12.

Two resonances which were excited by the upstream vane row are of major interest. These assembly modes are labelled in Figure 12 as the 4D and 4D-1C modes, i.e., the fourth diametral, zero circumferential and the fourth diametral, first circumferential modes respectively. At the intersections of the excitation frequency and the assembly frequencies, responses measured by strain gages located on the rotor airfoils ranged from +10 ksi to +40 ksi. A typical waterfall chart in which response amplitudes as functions of rotor speed and frequency are denoted by the vertical height of the spectrum lines is shown in Figure 13 to indicate the modal identification technique. In Figure 14 a plot of dynamic stress as a function of rotor speed is presented. The response peaks at near 15000 and 25000 rpm are the resonant responses of the 4D and 4D-1C modes, respectively.

From the character of these responses it is readily apparent that the overall damping in either mode is quite small. Use of the resonant width techniques provided the overall damping. For the 4D-1C mode, the overall damping was calculated to range between 0.2 to 0.4% logarithmic decrement for all the test conditions investigated. The stress amplitudes of response used in this definition ranged from +10 to +40 ksi, the stress dependent on the spacing between the vane row and the rotor and the aerodynamic loading of the turbine. The low damping value obtained from the turbine test results implies that little or no aerodynamic damping was available in the modes investigated. The damping values were in the range of the blade alone damping obtained for the fan assembly. Thus it can be implied that the integral nature of the turbine results in inherent damping in line with material damping values.

Low Aspect Ratio Compressor Stator Vanes

The third turbomachinery component to be evaluated in terms of damping was that of stators. Rig testing of an advanced low aspect ratio compressor resulted in fatigue cracks of vanes in two separate rows. The source of the excitation which created these fatigue cracks were the adjacent rotating blade rows. The modes of vibration identified as the resonant responders are shown in Figure 15 and are high frequency bending modes.

After the fatigue cracking was noted and prior to a second build of the rig, a plasma spray coating was applied to both stator vane assemblies. The intent of this coating was to reduce the resonant responses of the vanes. As indicated in the table in Figure 15, the reduction in dynamic stress amplitude was accomplished. Bench testing of the vanes prior to rig operation indicated that with no damping coating applied the damping in the modes of interest was approximately 0.23% logarithmic damping. After application of the coating, this value increased to 1.63%, the coating contributing approximately 1.4%. This value is in line with the results noted from the fan testing previously discussed.

Using the response values for the vanes in the coating and uncoated states and the structural damping measured in the bench testing allowed the calculation of aerodynamic damping for these complex modes. For

Configuration A the implied aerodynamic damping was 1.68% logarithmic decrement while for Configuration B the damping was 1.9%. Thus, for these high frequency chordwise bending modes the aerodynamic damping of approximately 1.8% is larger than the inherent material damping but of the same order of magnitude as the damping added by the application of the plasma spray.

Assessment of Damping Treatments to Control Resonant Response

The necessity to quantify the aerodynamic damping has been shown in these examples. Effective and efficient application of damping treatments to control vibratory response requires a knowledge of the amount of aerodynamic damping involved in the response. From the three examples approximate aerodynamic values of damping are as follows:

Shrouded fan stage first bend mode	$\delta = 3\%$
Low aspect ratio compressor CWB mode	$\delta = 1.5\%$
Turbine inlet diametral disk mode	$\delta = 0\%$

Damping coatings in the case of the fan and LAR compressor vane examples gave a damping increase of about 1 to 1.5%. This order of magnitude implies that such treatments would be greatly effective in controlling the turbine diametral disk mode responses where aerodynamic damping is essentially zero. This coating has also been shown to be somewhat effective for the higher frequency compressor blade modes where aerodynamic damping is on the same order as the coated structural damping. However for the lower modes of compressor vibration the aerodynamic damping is of sufficient magnitude to make the use of this type of damping treatment of little effect.

Viscoelastic damping treatments which have the potential of equalling or exceeding the aerodynamic damping of the lower modes of response in compressor blading, are being considered for low mode compressor response control.

In conclusion, to effectively assess the use of damping treatments to control vibratory response an ability to calculate the amount of aerodynamic damping present in the response of interest is important. In lieu of the methodology to predict the aerodynamic damping, the results presented offer insight into typical aerodynamic damping in gas turbine engines and thusly, a baseline from which to establish design parameters for the effective use of damping to control forced vibration response.

REFERENCES

1. Jay, R., MacBain, J., and Burns, D. "Structural Response Due to Blade-Vane Interaction," Transactions of the ASME, Journal of Engineering for Gas Turbines and Power, Vol. 106, Jan. 1984.

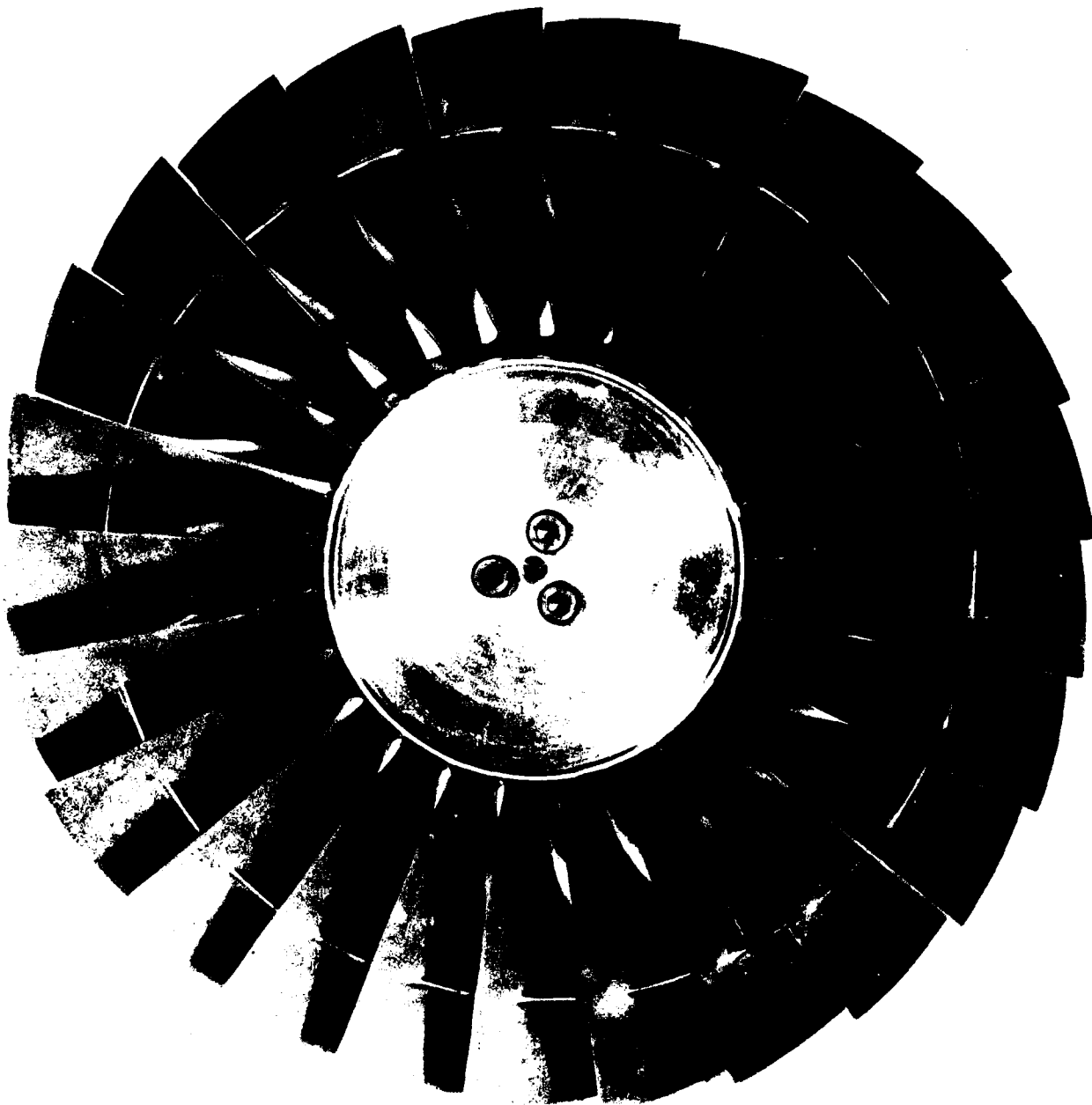


FIGURE 1. SCALED TF41-LP1 SHROUDED FAN STAGE

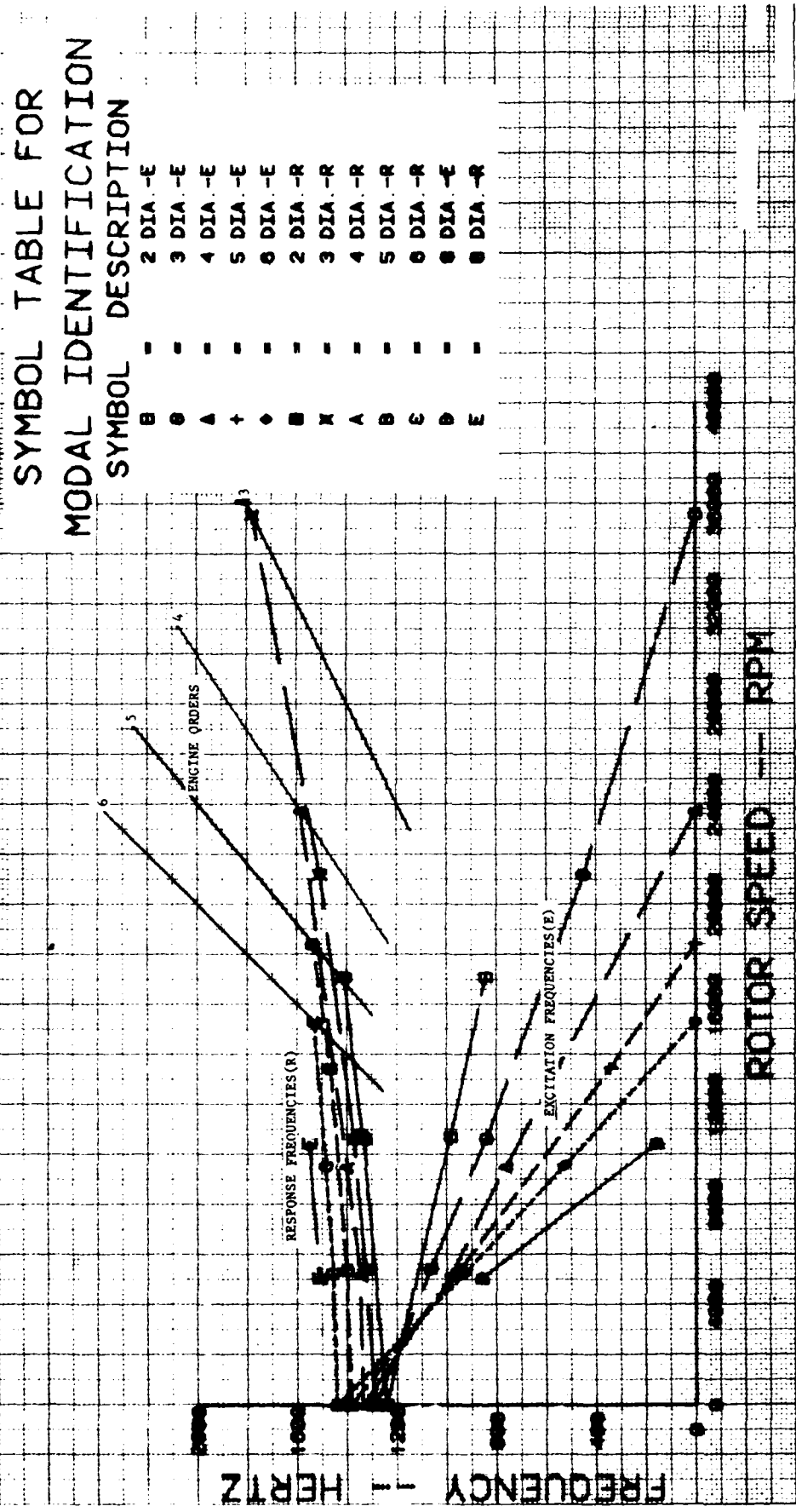


FIGURE 2. CAMPBELL DIAGRAM FOR FAN ROTATING VACUUM TESTING

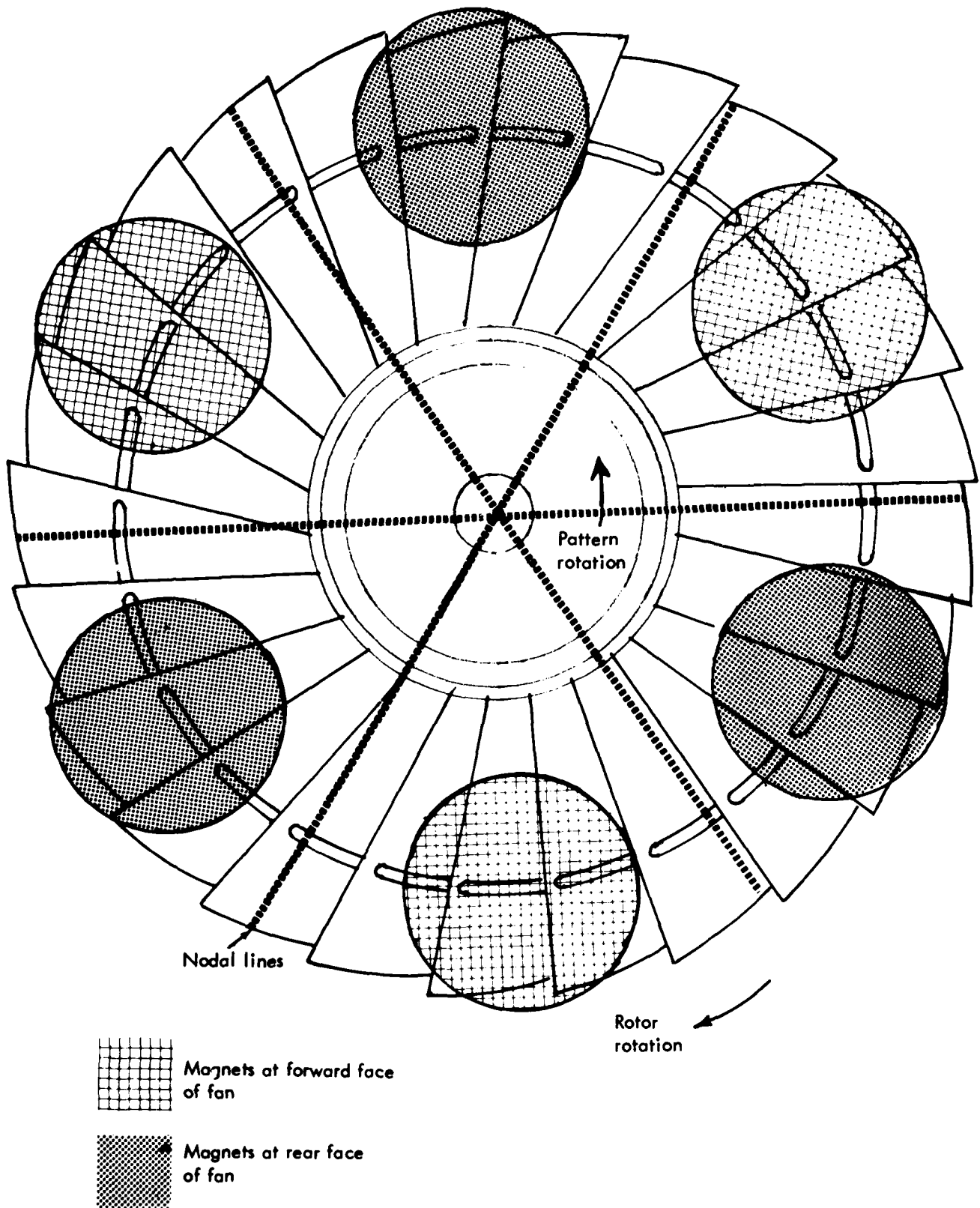


FIGURE 3. PREFERENTIAL DRIVER CONCEPT

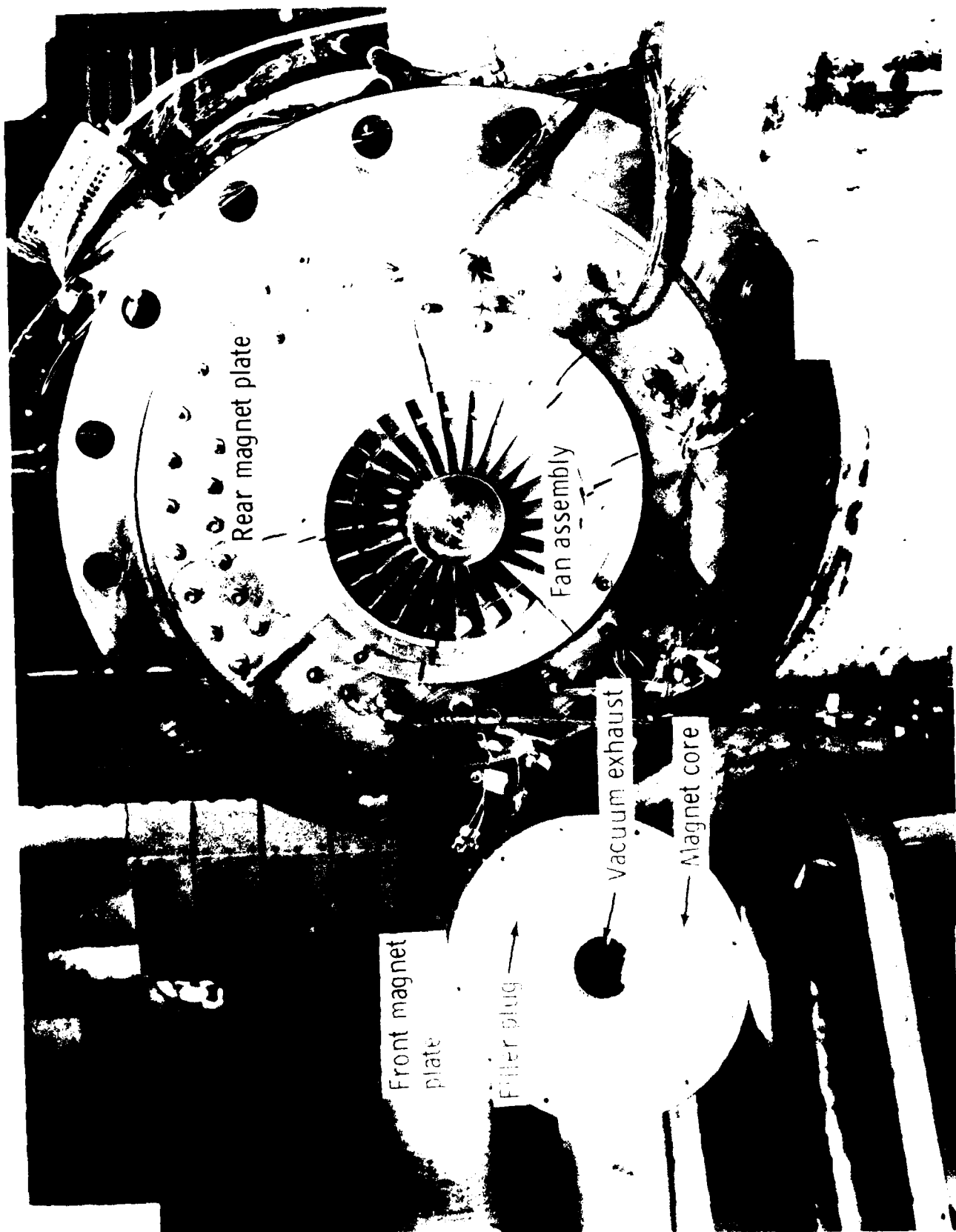


FIGURE 4. VIEW OF VACUUM FACILITY WITH FAN INSTALLED

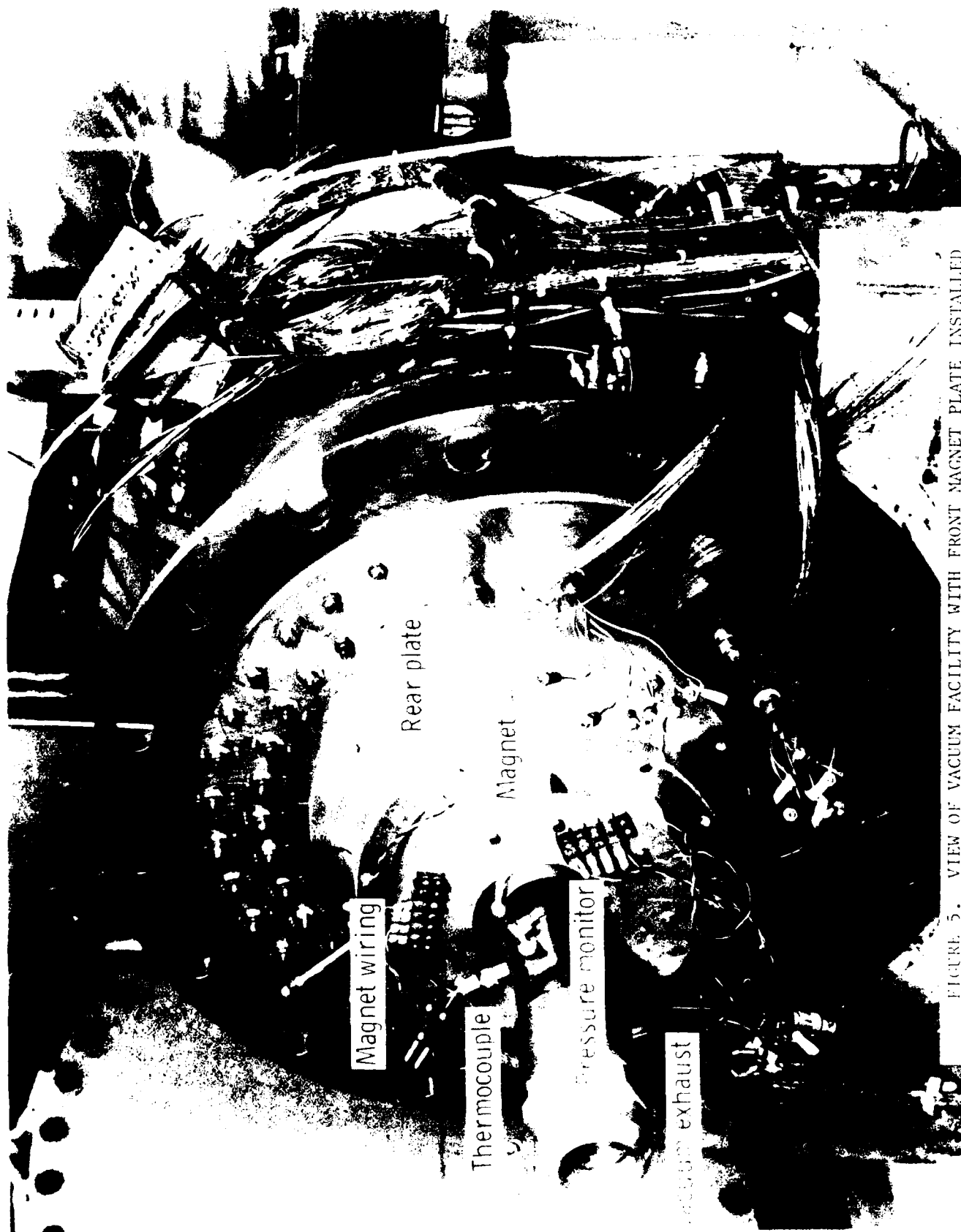


FIGURE 5. VIEW OF VACUUM FACILITY WITH FRONT MAGNET PLATE INSTALLED

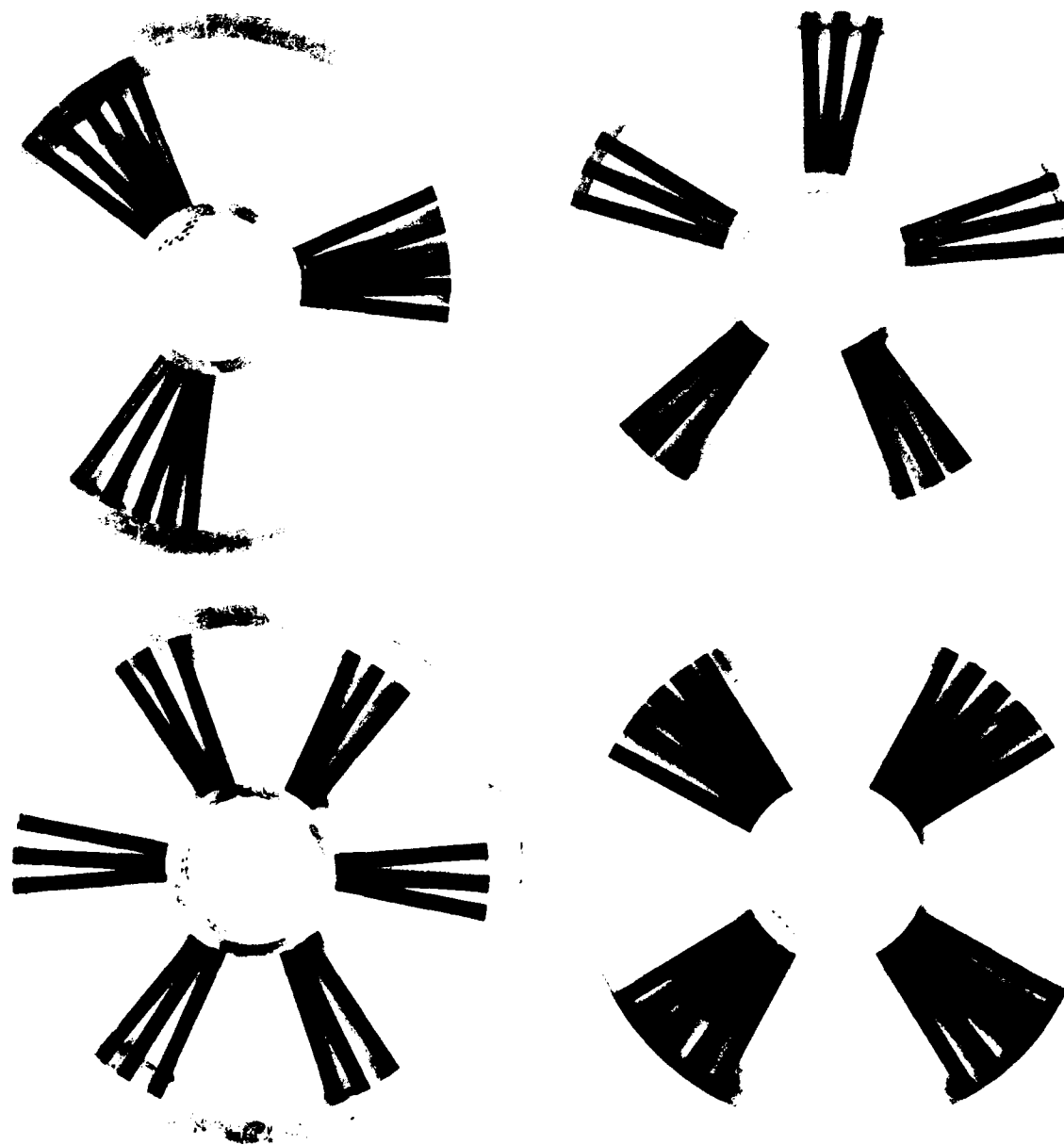


FIGURE 6. AERODYNAMIC DISTORTION EXCITER ASSEMBLIES

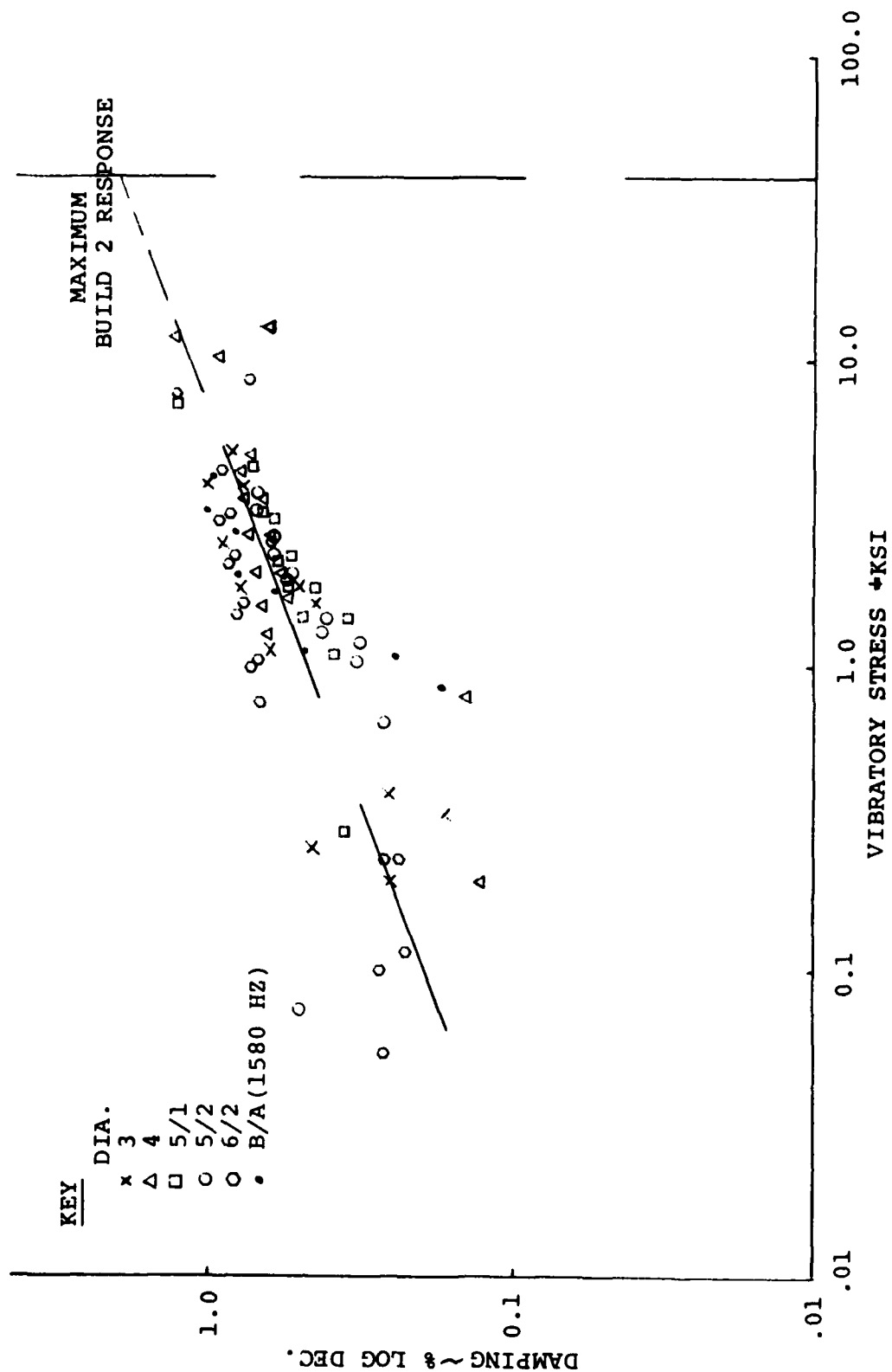


FIGURE 7. SCALED FAN DAMPING IN VACUUM

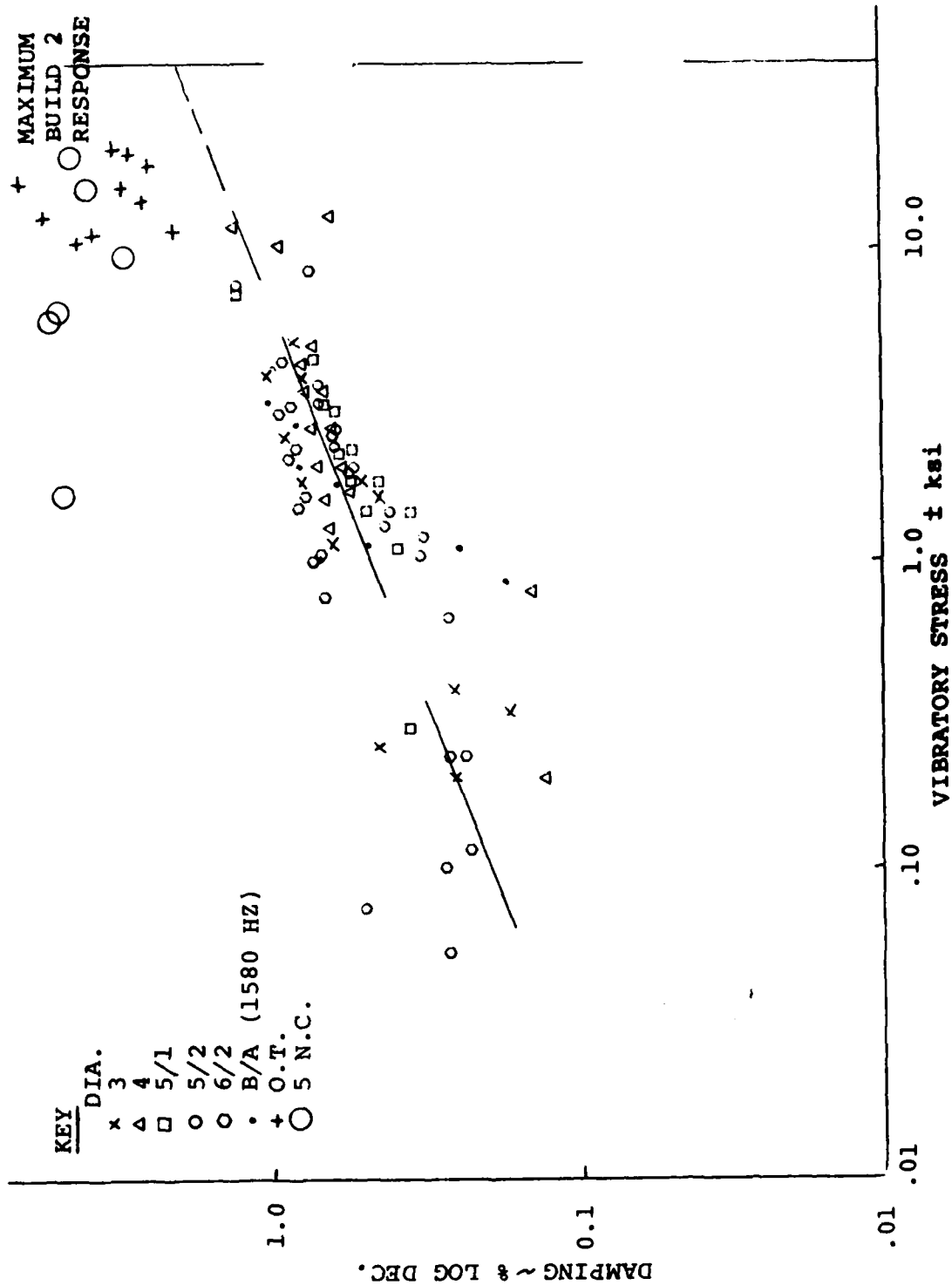


FIGURE 8. SCALED FAN DAMPING INCLUDING AERODYNAMIC TESTING

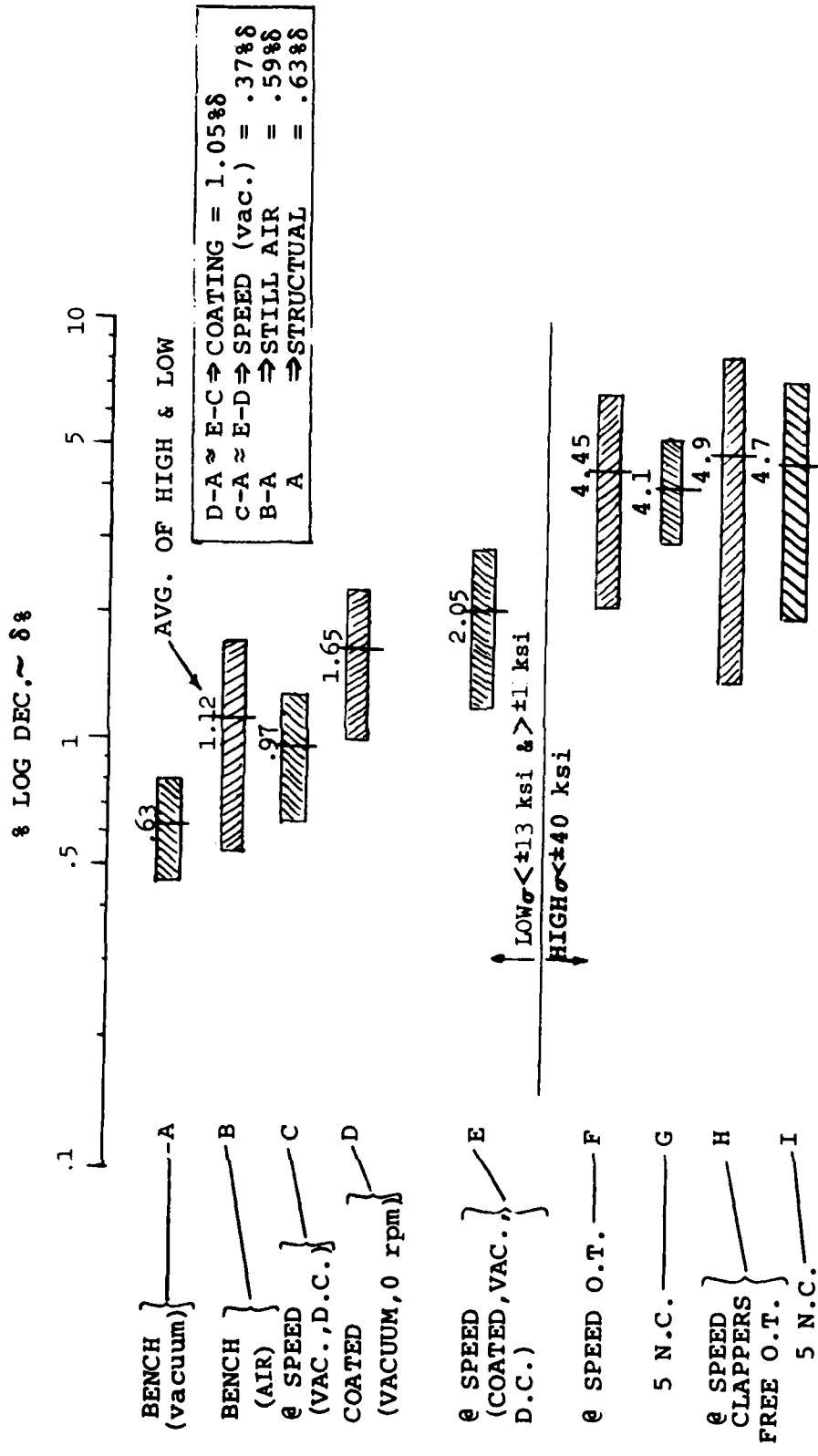


FIGURE 9. OVERALL FAN DAMPING RESULTS

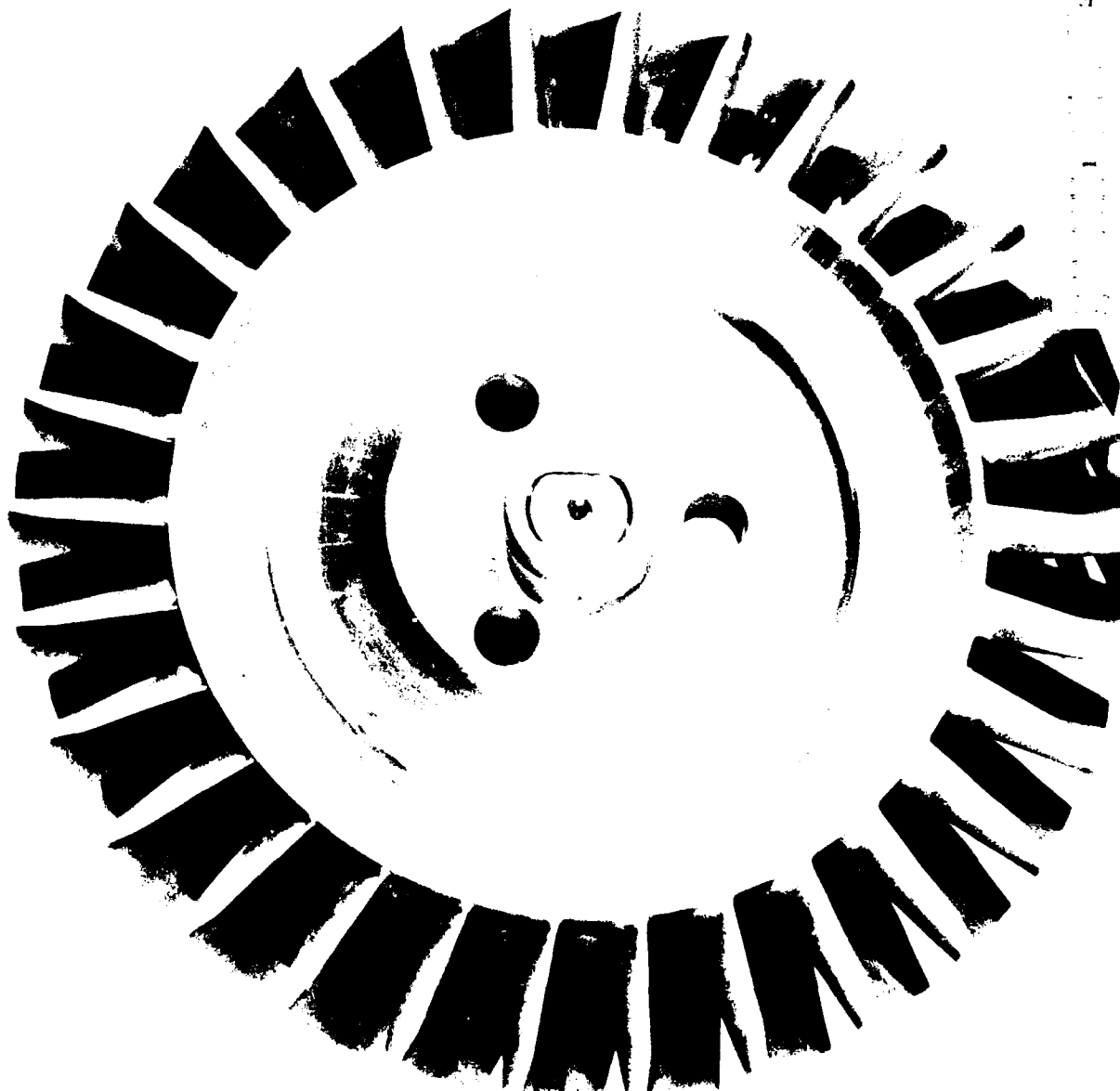


FIGURE 10. INTEGRALLY MACHINED TURBINE STAGE

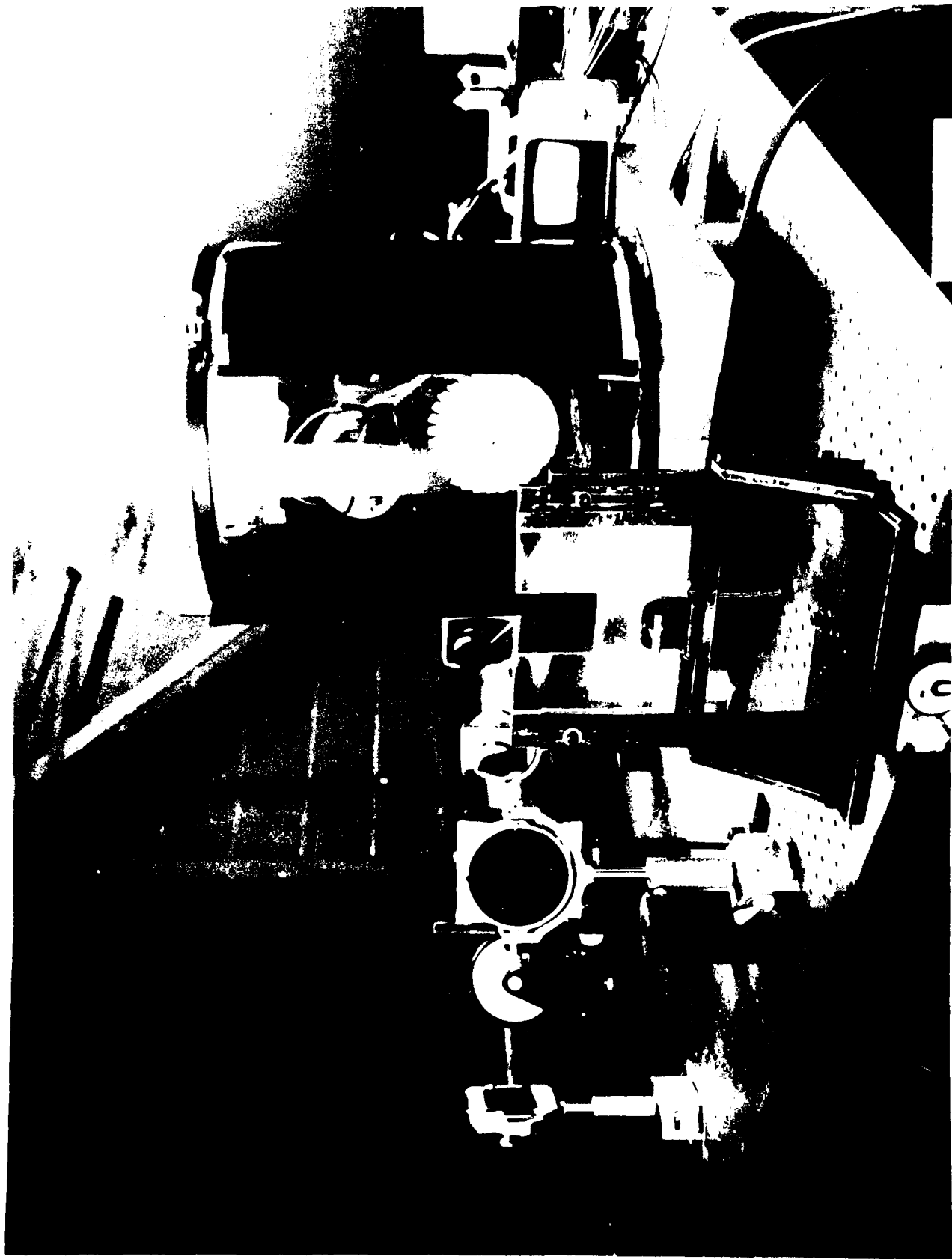


FIGURE 11. IN-VACUUM HOLOGRAPHIC TESTING OF TURBINE

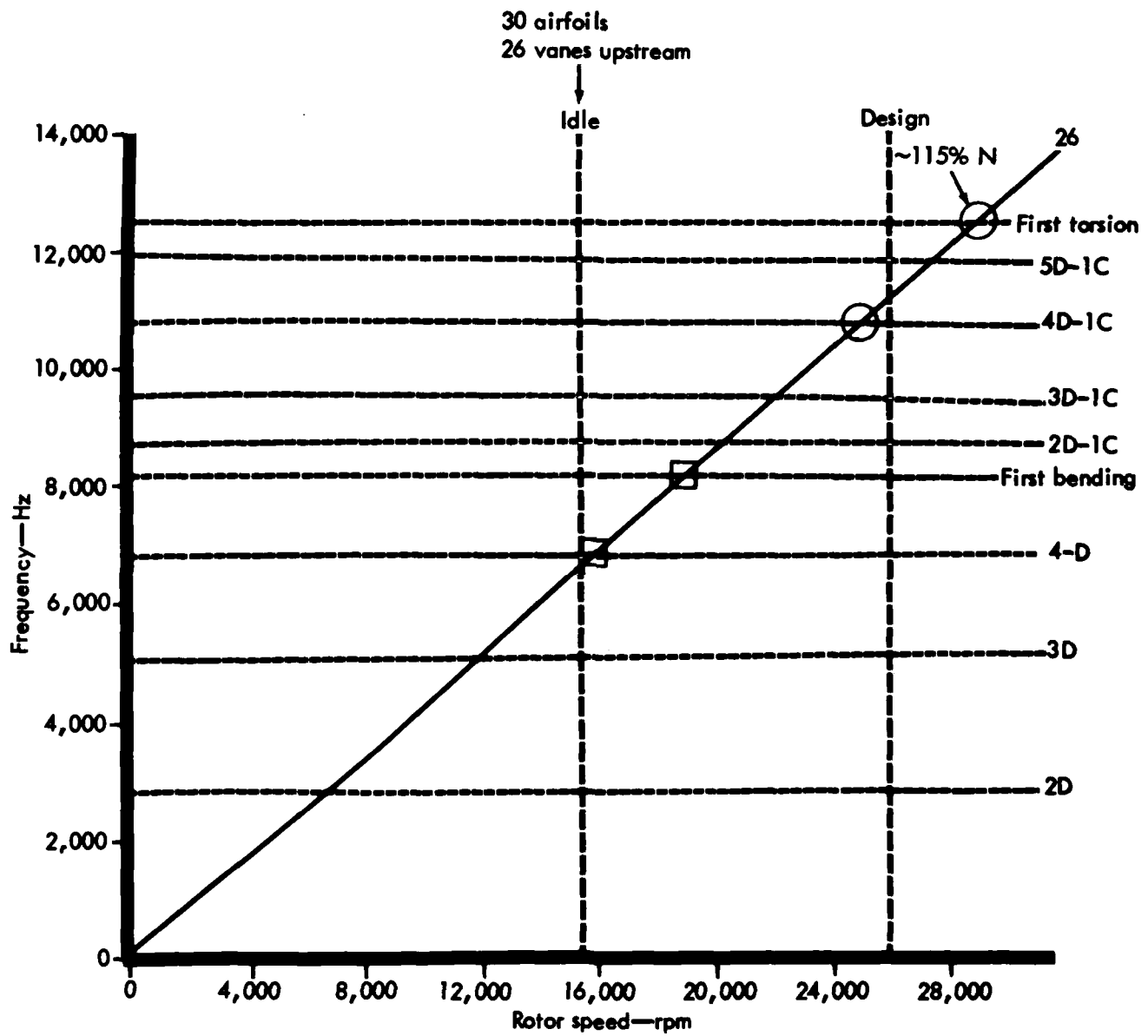


FIGURE 12. CAMPBELL DIAGRAM FOR TURBINE

.275 SPACING

EXPANSION RATIO = 2.25

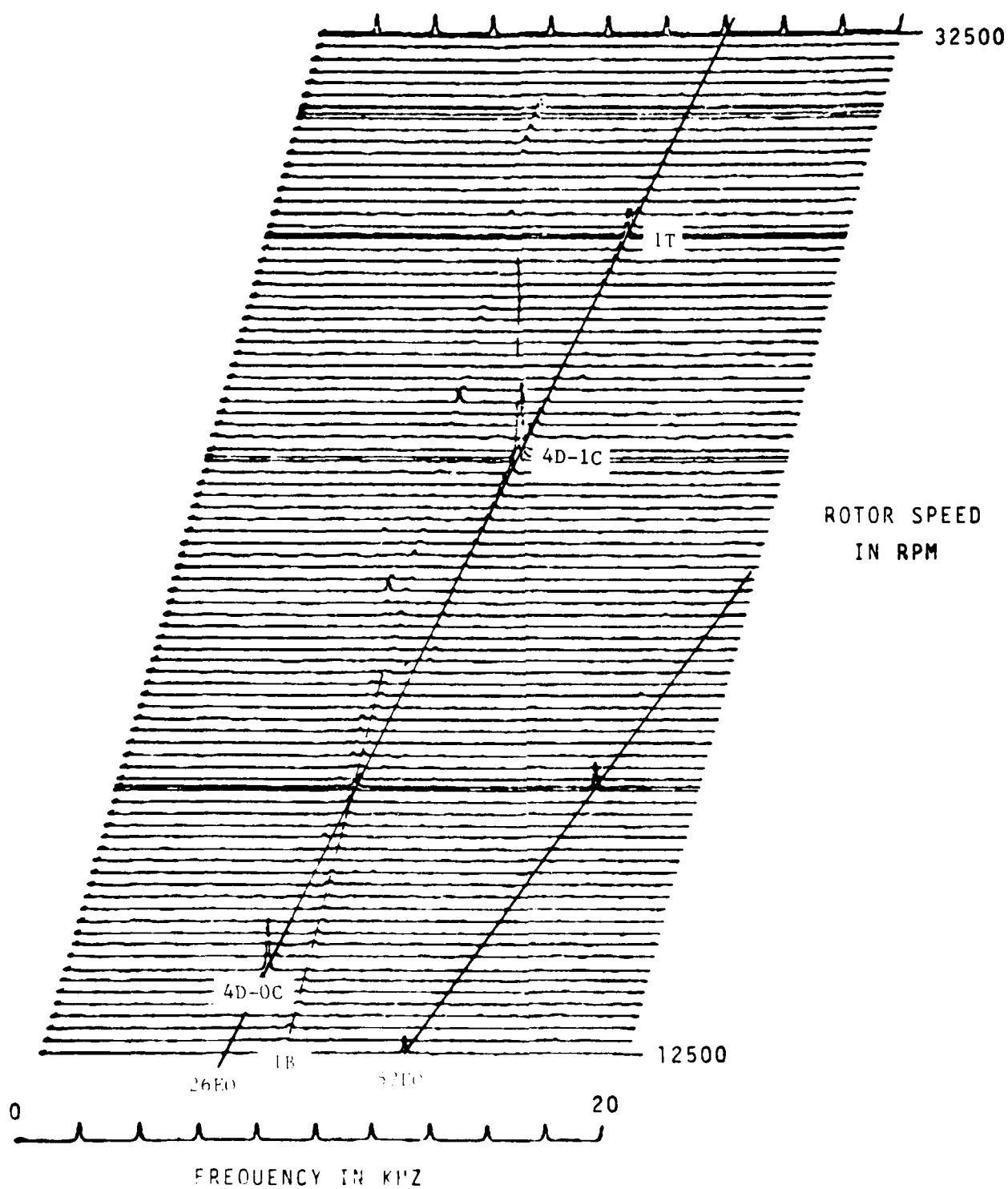


FIGURE 13. WATERFALL CHART OF TURBINE
RESPONSE DURING ACCELERATION

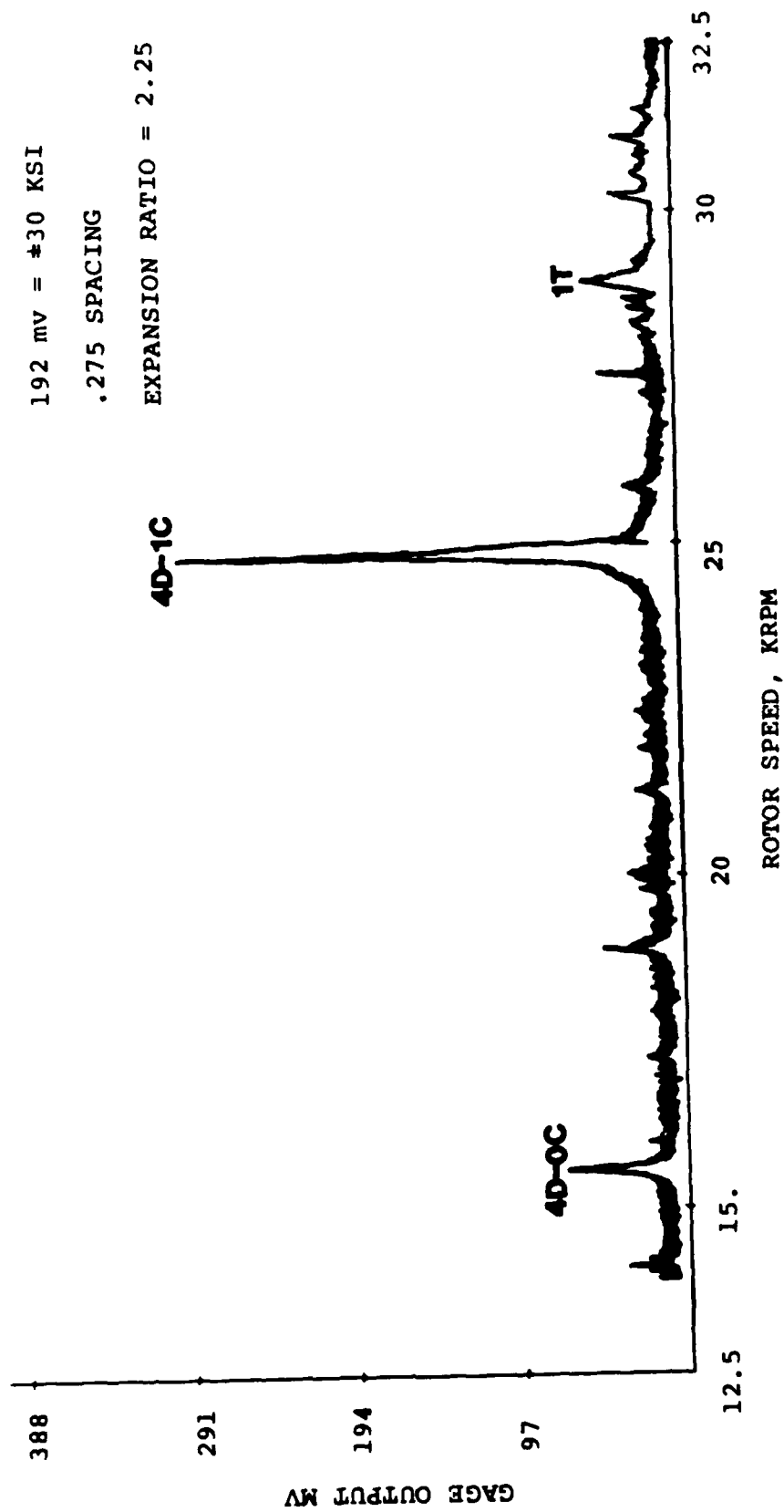
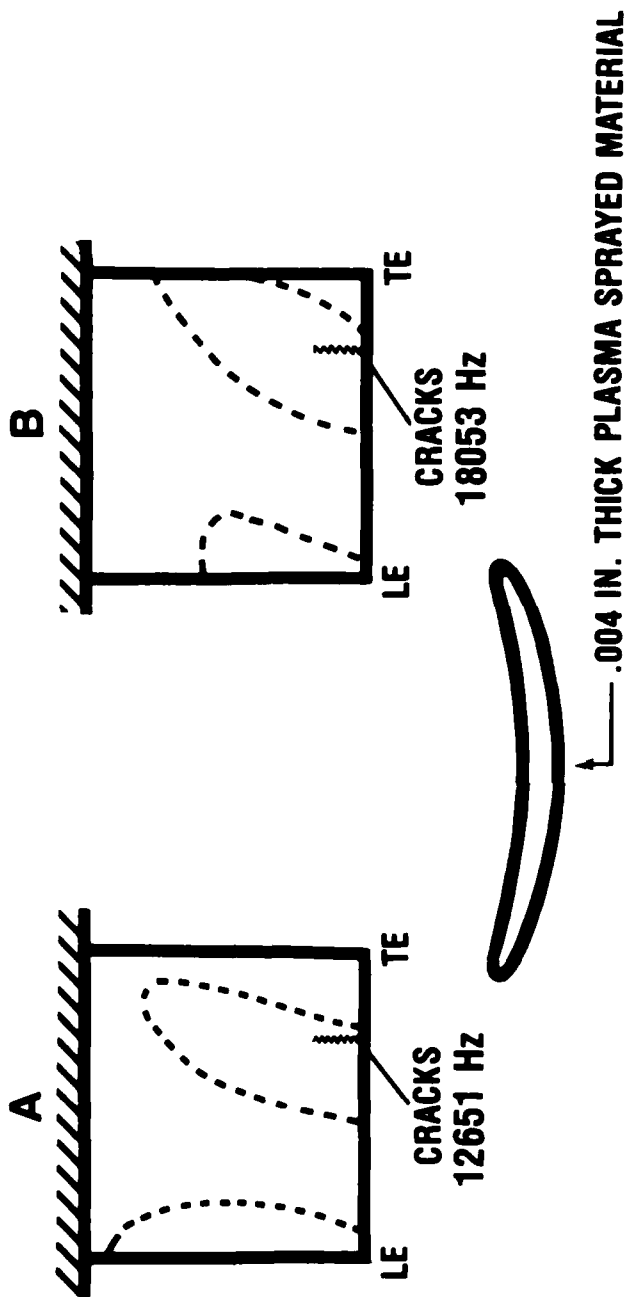


FIGURE 14. OVERALL RESPONSE VERSUS TURBINE ROTOR SPEED

DAMPING ADDED TO RESPONSIVE VANES

PLASMA SPRAYED



CONFIGURATION	STAGE A	STAGE B
UNCOATED	10200 PSI*	19000 PSI*
COATED	5900 PSI*	11500 PSI*

* **VIBRATORY RESPONSE IN COMPRESSOR TESTING**

FIGURE 15. RESULTS OF DAMPING APPLICATION ON RESPONSE OF LOW ASPECT RATIO COMPRESSOR VANES

CHARACTERISTICS OF DRY FRICTION DAMPING

A. V. Srinivasan
Manager

B. N. Cassenti
Senior Analytical Engineer

and

D. G. Cutts
Research Engineer

Applied Mechanics Research
United Technologies Research Center
East Hartford, Connecticut 06108

Characteristics of Dry Friction Damping

by

A. V. Srinivasan*

B. N. Cassenti**

D. G. Cutts***

United Technologies Research Center
East Hartford, CT 06108

ABSTRACT

This paper contains a summary of a literature survey pertaining to the overall problem of estimating damping due to dry friction forces induced at interfaces of vibrating components. The survey clearly indicated the complex processes involved during rubbing of one component relative to another bringing into play a host of parameters. Very limited data, especially of a fundamental nature, appears to be available in regard to dry friction in a vibratory environment.

The work reported herein was sponsored by the AFOSR, Contract F49620-83-C-0076 under the technical direction of Dr. A. Amos.

* Manager, Applied Mechanics Research

** Senior Analytical Engineer, Applied Mechanics Research

*** Research Engineer, Applied Mechanics Research

1. INTRODUCTION

The structural integrity of engineering systems depends to a large extent on the levels of energy dissipation that can occur when the system is subjected to time dependent forces. One of the most important sources of energy dissipation in built-up structures pertains to dry friction at joints and at interfaces in contact with each other. When materials with very low inherent damping are used in environments offering essentially no aerodynamic damping (such as, for example, in space structural systems), the ability of the structures to withstand resonant vibration depends almost entirely on the extent of friction damping. Even in the design of components which can generate certain levels of aerodynamic damping, it is essential to be able to estimate accurately the levels of non-aerodynamic sources of damping because unlike the latter, the former can be either positive or negative. For example, the aeroelastic instabilities of aircraft structures such as airplane wings or turbomachinery blades are attributed to negative aerodynamic damping developing in the system as a result of its interaction with the air forces causing the system to vibrate. In such situations, escalation of vibratory stresses to dangerous levels is prevented only through the contribution to damping from sources such as friction. In some instances, artificial devices are designed and introduced into the structural system with the sole purpose of developing friction forces leading to damping when the dynamics of the component demands it. Thus, there is a clear need to enhance the level of understanding in the broad area of dynamics of surfaces in contact.

Friction between contacting interfaces which undergo relative vibratory motion is known to dissipate the energy of vibration resulting in damped oscillations. The phenomenon of friction between contacting surfaces is probably the most elusive physical mechanism that defies clear comprehension. The complexity of the phenomenon of friction damping arises from the variations in the type of time dependent motions developing at an interface. These variations in the relative motion at the contacting surfaces span the extremes between microslip and gross motion and include local slip, stick-slip motion, chatter, etc. The parameters that control the resulting motion include the normal forces holding the surfaces together, their distribution, properties of materials in contact, surface treatments, temperature, frequency of vibration, level of vacuum, coefficient of dynamic friction, etc. The phenomenon is clearly nonlinear and the feasibility of linearization needs to be established.

In the context of vibration engineering, the basic requirements are to (a) quantify the nature and magnitude of friction forces that are manifest between contacting interfaces of vibrating components, (b) quantify the nature and magnitude of vibratory motion at these interfaces, and (c) predict the

extent of damping that may be present. Within this context, friction forces are considered to be useful, i.e. they control vibratory amplitudes which otherwise may escalate. On the other hand, any consideration of friction forces cannot ignore the influence of these forces on wear of the components resulting in loss of useful life of machines. The phenomena of friction and wear are thus inseparable. The emphasis in this study, however, is in outlining those aspects of friction forces that pertain to vibration damping.

2. REVIEW OF THE LITERATURE

In order to assess the state-of-the-art in the area of damping due to dry friction, a literature search was initiated. It became clear that the subject matter could be classified into at least three specialized disciplines comprising efforts in the areas of (a) surface science (b) characterization of friction forces at mating surfaces and (c) damping technology. Further, there appears to be very limited data, especially of a fundamental nature, obtained in a vibratory environment in which friction forces play a significant role. The developments in each of these areas have occurred somewhat independent of each other because each represents an area important in itself providing considerable research opportunities. Future developments must, however, attempt to integrate these efforts in order to be able to obtain accurate and reliable estimates of energy dissipation in vibrating systems.

An excellent treatment of the science of friction and wear is found in a book Friction and Wear: Calculation Methods (Ref. 1) by the Russian authors Kragelsky, Dobychin and Kombarov. The chapter on "Dry and Boundary Friction" should be of special interest to researchers in this field and has an excellent treatment of the subject beginning as far back as 1508 when Leonardo da Vinci established the simple law of friction which assumed the friction force to be proportional to the normal load. Researchers should also find the three volumes of the book on Friction, Wear, Lubrication (Ref. 2) edited by Kragelsky and Alisin. Another book, also by Russian authors Panovko and Gubanova entitled Stability and Oscillation of Elastic Systems (Ref. 3) treats the subject of self-induced oscillations with dry friction. In addition, the proceedings volume of a NASA-sponsored symposium on Interdisciplinary Approach to Friction and Wear (Ref. 4) edited by Ku contains material which covers the several aspects of surface topography, friction, and adhesion, wear, etc. These books along with the papers that will be referred to in the sections below have served as the basis for the viewpoints presented in this report. Because of the interdisciplinary nature of the subject matter, no claim will be made that all the relevant literature has been surveyed here. The reader may, therefore, draw to the authors' attention relevant books or papers not included in this preliminary survey so that a more complete list of references may emerge at the end of this research effort.

2.1 Interface Characteristics

Surfaces of real components used in engineering practice are never ideally smooth so that when they come into contact with each other, the contact cannot be continuous and only certain parts of the surface will carry the applied load (see Fig. 1). Thus, the true contact area is the sum of those parts of the surfaces where the interaction between the bodies is strong. The true contact area is the result of penetration or crushing of individual asperities, and, therefore, the contact area increases with

increasing deformation. The real contact area is much smaller than the apparent area of contact and can be as low as ".01 to .1% of the apparent contact area" (see Ref. 2).

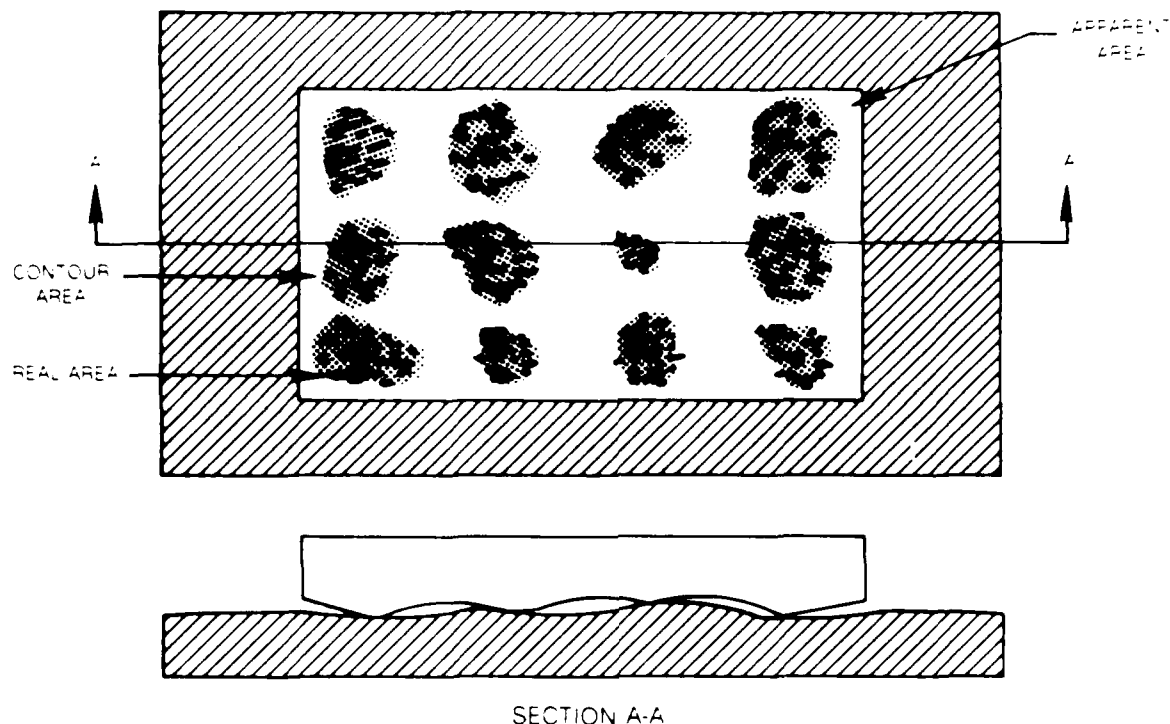


Figure 1. Contact Areas

The research pertaining to the mechanism governing the formation of true contact area goes back to 1939 when Bowden and Tabor (Ref. 5) determined, on the basis of measurement of electrical conductivity, that the true contact area changes in direct proportion to the normal load N . In elastic contact, this was shown to be $A \propto N^{2/3}$. Further generalization for practical application in all cases of contact between metallic surfaces led to the relationship $A = N/\sigma_y$ where σ_y = yield stress of the soft material. This law is considered to be applicable only when the tips of spherical asperities lie at the same level.

V. A. Zhuravlev, (Ref. 6) whose research work done during World War II remained unknown for a long time, calculated the true surface area in elastic contact of two rough bodies. He modeled spherical segments of equal radius for the microasperities whose tips were assumed to be linearly distributed and obtained

$$A = K \left(\frac{1-\nu^2}{\pi E} \right)^{10/11} N^{10/11} \quad (1)$$

where K is a coefficient, E is modulus of elasticity, and ν is Poisson's ratio. Greenwood and Williamson (Ref. 7) derived the following relationship assuming elastic contacts.

$$A = \pi \lambda A_a r \sigma F_1(h) \quad (2)$$

where

- λ = density of asperities
- A_a = nominal contact area
- r = radius of asperities
- σ = standard deviation of height distribution of asperities
- h = d/σ

$$F_1(h) = \int_h^{\infty} (s-h) n_{\psi}^*(s) ds \quad (3)$$

where ψ^* represents the normal density distribution of heights of asperities, (i.e. ψ^* is the height distribution scaled to make its standard deviation unity), and d represents the distance between the reference planes in each contacting surface (see Fig. 2). It is assumed that all asperity summits have the same radius r and their heights vary randomly. Figure 3 shows the manner in which the contact area may vary when the interfaces are under "very high pressure". It may be noted that the true area of contact under "moderate loads" can be less than 50% of the possible total area.

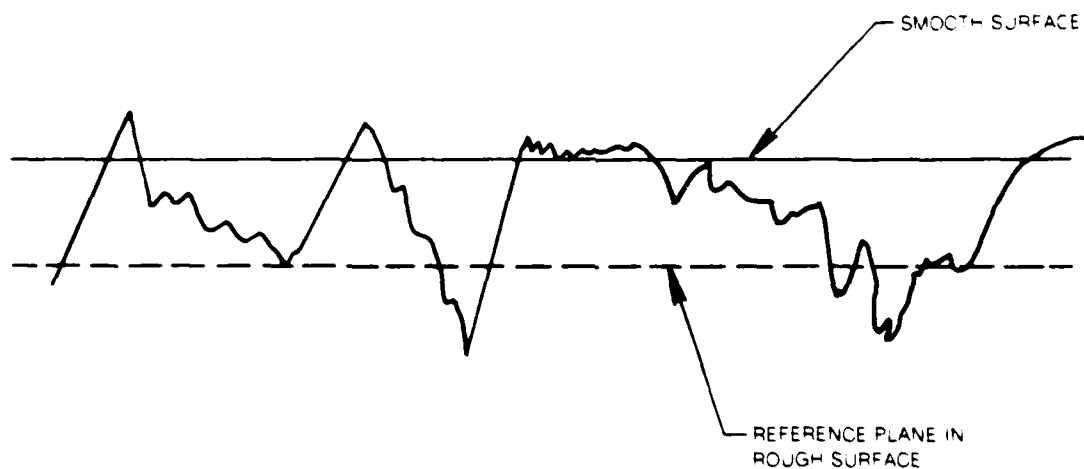
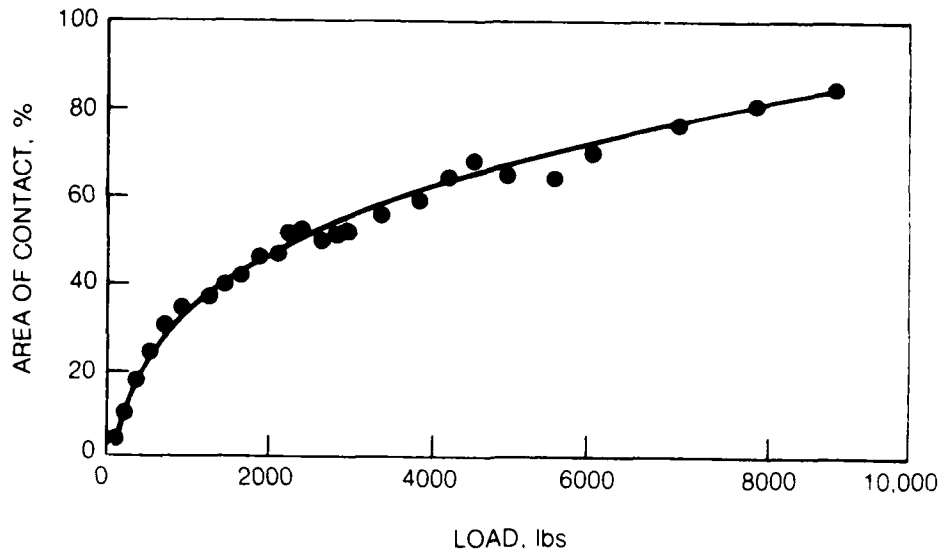


Figure 2. Surface Characterization



REF #4, PAGE 109

Figure 3. Behavior of Contact Under Very High Pressure

Oden and Pires, in Ref. 8 also present a simple argument to demonstrate that the contact area should vary, approximately, linearly with the normal load. In general, the contact pressure will be a constant independent of the deformation. The total contact area, A_c , can be represented as

$$A_c = A_1 + A_2 + \dots + A_n \quad (4)$$

where A_K is the contact area at point K and n is the total number of contact points. Then the normal force at point K is given by

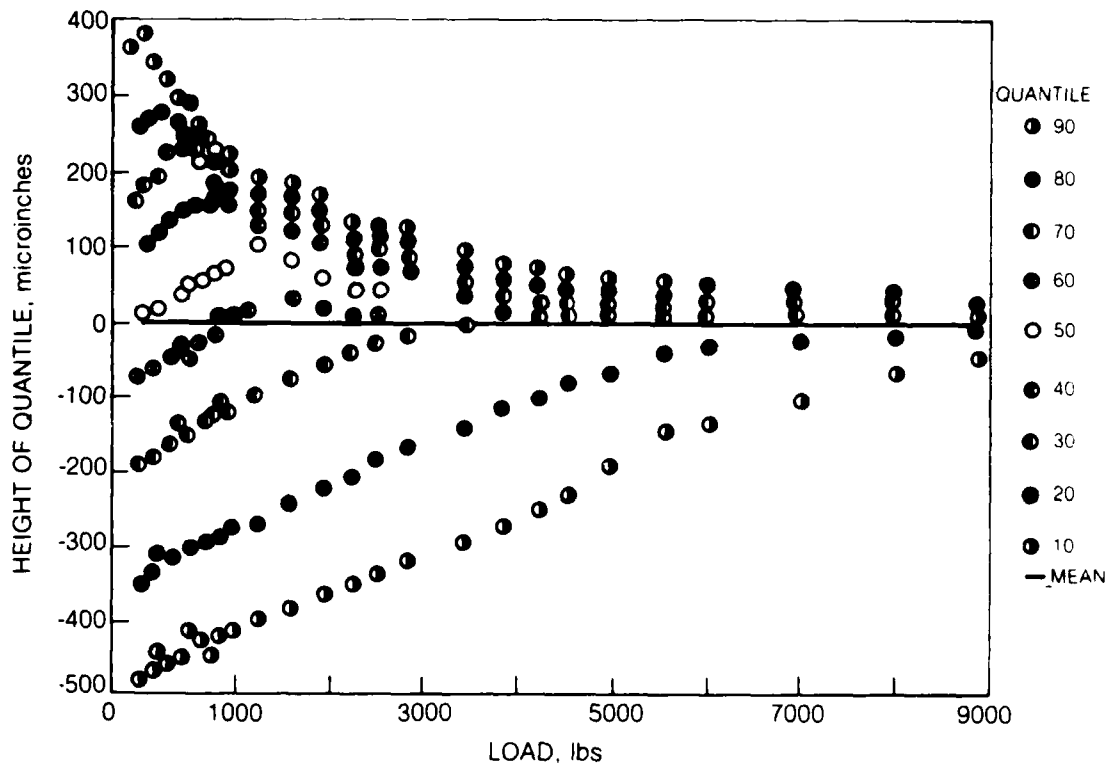
$$N_K = p_o A_K \quad (5)$$

where p_o is the yield pressure for the material. Substituting for the areas in Eq. (4),

$$A_c = \frac{N_1}{p_o} + \frac{N_2}{p_o} + \dots + \frac{N_N}{p_o} = \frac{N}{p_o} \quad (6)$$

where N is the total normal force.

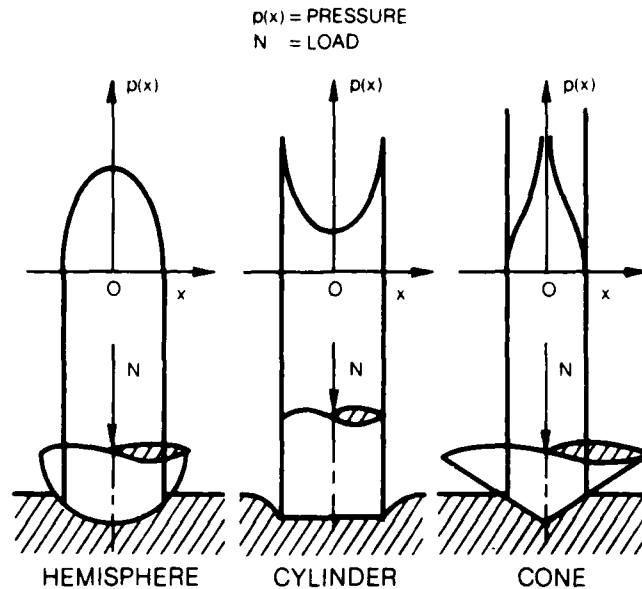
Figure 4 shows the nature of deformation of the asperities as the normal load increases. The symbols in Fig. 4 refer to the height of the asperities in microinches below which a certain percentage of the surface lies. As the load increases, the highest points at the interface flatten as expected. But the upward slopes in the data show that heights of asperities actually increase indicating an elastic deformation of the entire surface. Clearly, any law of friction at interfaces must account for the deformation taking place in the neighborhood of a point in question.



REF #4, PAGE 106

Figure 4. Behavior of Aluminum Surface Under High Pressure Contact

Most of the researchers who have tried to characterize the asperities appear to agree on the spherical segment as the most convenient geometry to model surface roughness. The preference for this simple geometry is obvious in view of indeterminate stress distribution calculated for other geometries examined, i.e. a bar model and a cone model as shown in Fig. 5.



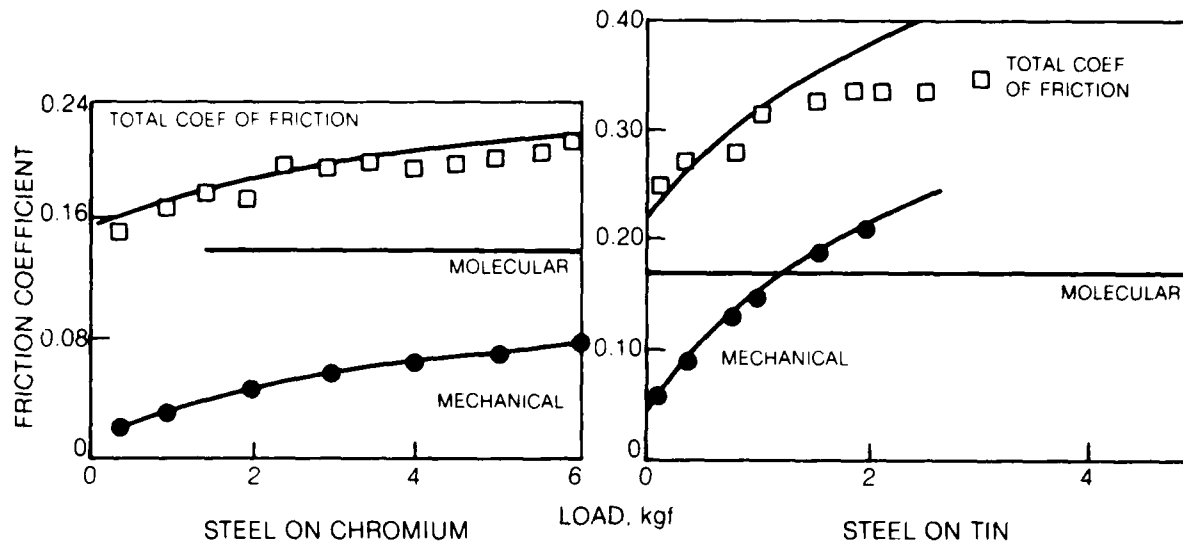
REF. #1. PAGE 57

Figure 5. Comparison of Pressure Distribution Curves Obtained in the Contacts of Various Geometric Shapes

If an ellipsoidal geometry is considered appropriate, a radius for an equivalent sphere is calculated from $r_{eq} = \sqrt{r_{long} r_{tran}}$.

2.2 Characteristics of Friction Forces

A great variety of phenomena occur in rubbing contact between surfaces of components. This is because of the dual nature of friction by which surface friction overcomes molecular interaction forces between surfaces and mechanical resistances associated with changes in the profile of the surface layer. Kragelsky et al (Ref. 1) point to data that indicates molecular attraction at an interface could contribute substantially to the observed frictional forces. As can be observed from Fig. 6, the contribution to friction from molecular forces can dominate particularly for lighter load conditions. It is assumed that a sublayer of decreased resistance is formed at the interface between rubbing components. One speaks of dry friction forces when the sublayer is in a solid phase.



REF #1 PAGE 192

Figure 6. Variation of Friction Coefficient Components with Normal Load

Mechanical deformation may occur due to either penetration of surfaces with ploughing or continuous formation and rupture of welds. As stated earlier, all these processes are influenced by the environment. As observed by Kragelsky, et al (Ref. 1) "in spite of the complex nature of mechanical, physical, and chemical processes involved, it is still possible to pinpoint certain principles which are common to all friction and wear processes". They are outlined below:

1. Three interconnected processes occur simultaneously in sliding contact
 - a) Interaction of the surfaces
 - b) Changes in the surface layers and films
 - c) Rupture of the surface layer.
2. The contact between solids occurs at discrete points because of surface roughness.
3. Increase in load leads to increase in contact area due to increase in number of contact points. Therefore, the real pressure at any point increases only slightly.

4. Tangential resistances are additive. Dissipation of energy in the formation and rupture of an individual frictional bond is determined by the resistance in overcoming molecular interaction at points of contact, and the mechanical ploughing effects.

5. Surface sliding requires formation and rupture of a thin layer (weakened layer of base material or films) whose shear strength must be less than the shear strength of the substrate.

The apparent simplicity of the relationship that friction force induced at a point on an interface is proportional to the normal load at that point has been the primary reason for its use in most studies of dry friction. However, in addition to the problem of obtaining a reliable estimate of the constant of proportionality, i.e. the coefficient of friction μ , the representation $F = \mu N$ leads to computational complications even when applied to the study of a single degree-of-freedom system (see Fig. 7), as shown by Den

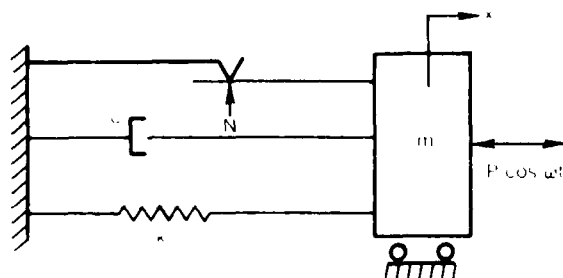


Figure 7. Den Hartog's Model

Hartog (Ref. 9). Oden and Pires (Ref. 8) have recently discussed the mathematical and physical difficulties associated with such a representation. Nevertheless, a substantial number of attempts have been made and continue to be made to use modifications of this basic model (Refs. 10 to 26). Such modifications are adaptations of the basic model to the analysis of particular components under study. Adding more degrees-of-freedom to the basic model leads to additional complexity (Ref. 10) which can be avoided by the use of linearized versions of the model. As shown by Jacobsen (Ref. 11), such linearization can provide a good representation of system behavior if the friction force is small so that it does not distort the motion appreciably. Subsequent analyses, many of which have been devised to represent specific

vibratory components, have generally relied upon the basic model in its linearized version. These developments have mainly involved more degrees-of-freedom and different configurations (Refs. 12, 13, 14, 15). Improved friction models have been tried, for example, making the friction force dependent on the vibration amplitude (Ref. 16) and by analyzing the interfacial slip in a vibrating beam (Ref. 17). However, there have been few studies which incorporate a detailed model of interface behavior into a model of a vibrating system.

In 1778, a two term formula was proposed by Coulomb according to which the friction force F was written as $F = AN + B$, where A can be identified as the familiar coefficient of friction. With such a representation, the coefficient of friction is not a property depending only on the materials in contact but also on the normal load.

Interface behavior is a difficult area of study which is why it is often avoided by invoking a constant overall coefficient of friction. Any discussion of friction in the context of vibratory rub must recognize the need to distinguish between the tangential forces of external static friction and those of external dynamic friction. The former exist in a region of small partially reversible displacements and peak at the boundary of such a region. Dynamic friction forces are not dependent on the magnitude of displacement. The fully developed static friction force is characterized by a coefficient which is different from that corresponding to the dynamic friction force. In the solution of vibration problems, prior to the initiation of any sliding motion, the static coefficient of friction should govern. The coefficient of friction is either chosen on the basis of practical experience or used as a disposable parameter to obtain the best agreement between theory and experiment. However, a deeper understanding of the effects of interface damping on vibrating systems can only be obtained by studying the friction processes in more detail.

Introducing the concepts of a local coefficient of friction and combining it with a study of stress distribution in the contact leads to a microslip solution in which only a part of the contact undergoes relative motion. Goodman (Ref. 18) has reviewed the basis of this approach which has since been applied to practical systems through the use of finite element techniques (Refs. 19, 20, 21).

Postulating an overall friction force, but allowing it to vary throughout each vibration cycle leads to the study of stick-slip behavior. Antoniou et al (Ref. 22) have reviewed this approach and show the degree of complication which this can add to a one degree of freedom system.

The classical mathematical model of dry friction, i.e.

$$F = \begin{cases} + F_0 & ; \dot{x} > 0 \\ - F_0 & ; \dot{x} < 0 \end{cases} \quad (6)$$

(where F_0 is the force of slipping friction, \dot{x} is the velocity of slipping) leads to a force-displacement relationship for alternating input displacement illustrated by two fixed horizontal lines and two vertical lines as shown in Fig. 8. Experimental observations, however, suggest that the transition from

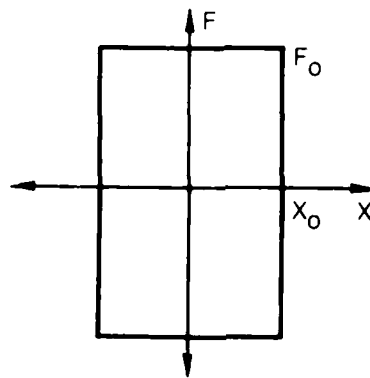


Figure 8

one equation of slip ($-F_0$) to the other ($+F_0$) is smoother than indicated by Eq. (6), and more like the characteristics shown in Fig. 9 (see Ref. 27).

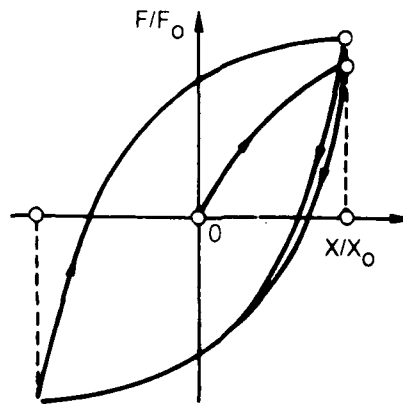


Figure 9. Hysteresis Characteristic of Dry Friction

This important observation allows the introduction of hysteresis characteristics of contact interaction and may serve as a basis of the analysis of friction damping. Accordingly, if x and F represent displacement and friction force respectively and x_0 , F_0 their maximum values, the hysteresis representation may be represented as

$$\alpha = \begin{cases} 1 - e^{-\beta(\xi - C_1)} & ; \dot{\xi} > 0 \\ -1 + e^{\beta(\xi - C_2)} & ; \dot{\xi} < 0 \end{cases} \quad (7)$$

where

$$\begin{aligned} \alpha &= F/F_0 \\ \xi &= x/x_0 \\ \beta &= bx_0 \\ b &= \text{is a material constant} \end{aligned}$$

The constants C_1 , C_2 can be shown to be equal and opposite to each other, i.e., $C_1 = -C_2$

$$\therefore \frac{d\alpha}{d\xi} = \begin{cases} \beta(1-\alpha) & ; \dot{\xi} > 0 \\ \beta(1+\alpha) & ; \dot{\xi} < 0 \end{cases} \quad (8)$$

Given initial values of ξ , α , the constants C_1 , C_2 can be generated for the ascending and descending parts of the loop. The procedure can be repeated for several vibration cycles.

An amplitude dependent model of friction can be derived as shown in Ref. 23 for any prescribed value of β . For example, for $\xi = A$, from Eq. (7)

$$\alpha_A = 1 - e^{-\beta(A - C_0)} \quad (9)$$

$$\alpha_{-A} = -1 + e^{\beta(-A + C_0)}$$

which leads to

$$C_0 = \frac{-1}{\beta} \ln (\cosh \beta A) \quad (10)$$

using which α can be shown to be

$$\alpha = \begin{cases} 1 - \frac{e^{-\beta\xi}}{\cosh \beta A} & \dot{\xi} > 0 \\ -1 + \frac{e^{\beta\xi}}{\cosh \beta A} & \dot{\xi} < 0 \end{cases} \quad (11)$$

Equation (11) is an amplitude dependent friction model. The area of the hysteresis loop due to friction can be shown to be equal

$$4\left(A - \frac{1}{\beta} \tanh \beta A\right) \quad (12)$$

from which β can be determined from tests. It may be noted that $4A$ in the above expression is the area of the loop consistent with the friction characterization shown in Eq. (6).

An appreciation of the continuum nature of bodies in contact leads to the concept of nonlocal laws of friction postulated by Oden and Pires (Ref. 8). With such a representation, the friction force at a point \bar{x} is the sum total of the influence of normal stresses over a neighborhood as shown schematically in Fig. 10. Thus, unlike the local law

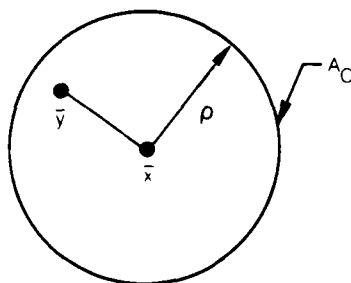


Figure 10. Nonlocal Nonlinear Laws of Friction (Oden & Pires)

$$\tau(\bar{x}) = \mu \sigma_n(\bar{x}) \quad (13)$$

a nonlocal law represents

$$\tau(\bar{x}) = \mu \int_{A_c} w_\rho(\bar{x}-\bar{y}) \sigma_n(\bar{y}) dA_c \quad (14)$$

where W_ρ is a weighting function that distributes the influence of σ_n in a circle of radius ρ . Recognition of the fact that the friction (shear stress) vector is always opposed to the direction of relative motion leads to the modification of Eq. (14) as follows,

$$\bar{\tau}(\bar{x}) = -\mu \bar{n}_f \int_{A_c} W_\rho(\bar{x}-\bar{y}) \sigma_n(\bar{y}) dA_c \quad (15)$$

$$\bar{n}_f = \frac{\bar{u}_f}{|\bar{u}_f|}$$

where \bar{u}_f is the vector of relative displacement along the surface. A more complete representation is achieved by introducing the requirement that the friction force be dependent on the motion (displacement or velocity) and leads to

$$\bar{\tau}(\bar{x}) = -\mu \bar{n}_f \phi_e(u_f) \int_{A_c} W_\rho(\bar{x}-\bar{y}) \sigma_n(\bar{y}) dA_c \quad (16)$$

Figures 11 and 12 show possible representation of W and ϕ .

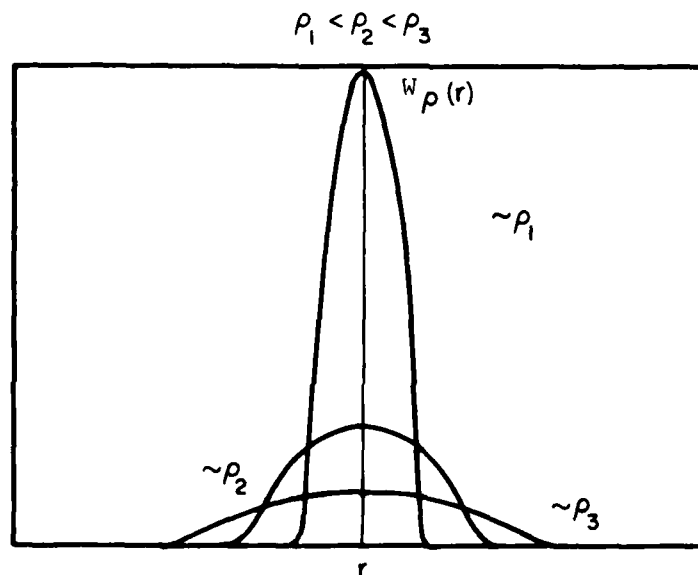


Figure 11. Nonlocal Effects

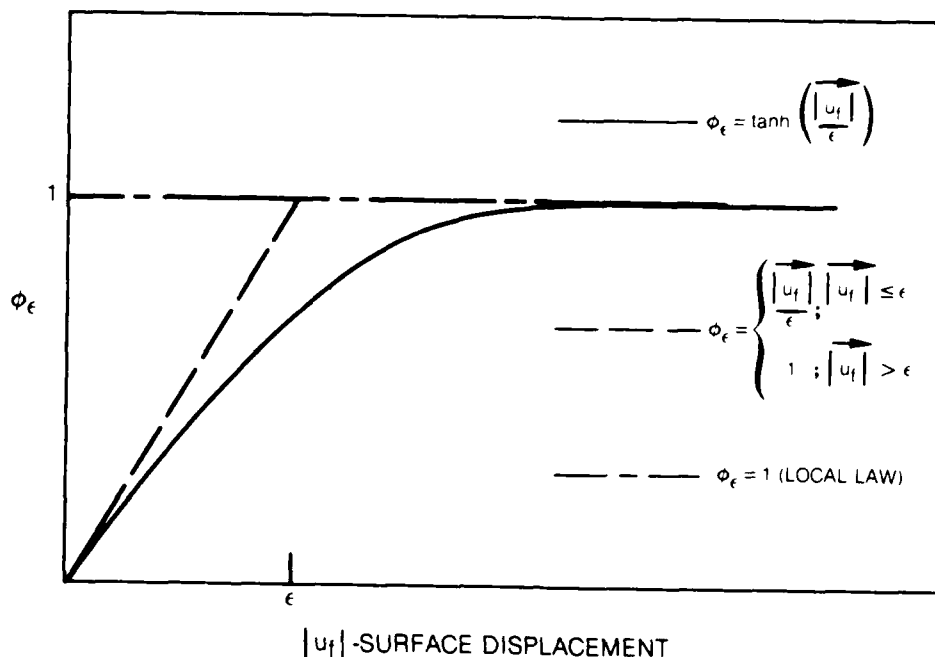


Figure 12. Nonlinear Effects

2.2.1 Coefficient of Friction

An accurate calculation of friction forces induced at interfaces in relative vibratory motion depends on the accuracy with which the coefficient of sliding friction can be estimated. As observed earlier, there appears to be no experimental data obtained in a vibratory environment from which the nature of the coefficient of friction can be obtained. The following is a summary of such an experiment performed at the United Technologies Research Center under contract to NASA LeRC (Ref. 14).

The approach that was chosen in that investigation was to provide sinusoidal relative motion between two test pieces which were held together with a constant normal force and to measure the resulting frictional forces directly. The range of normal loads, frequencies and relative velocities imposed were consistent with vibration of a jet engine fan in which resonant vibration is partly limited by damping available due to rubbing at shroud interfaces. The test pieces were a pair of titanium alloy (8-1-1) bars with their rubbing interfaces flame sprayed with tungsten carbide. The size of the rubbing surface was 22.35 x 6.35mm. The test assembly, shown in Figs. 13 and 14 uses an electrodynamic shaker to induce sinusoidal excitation of the lower test piece. The upper piece which rubs on the lower piece during test was held in such a way that longitudinal forces on the piece could be measured using a strain gaged load bolt, without any appreciable movement. The normal load on the joint was applied by setting the required weights on the loading platform. Testing consisted of setting the required frequency and input



Figure 13. Friction Test Assembly (Upper Arm Raised)



Figure 14. Friction Test Assembly

acceleration and recording the frictional force-slip loop on an oscilloscope for a range of normal loads.

The nominal condition for testing was defined as a displacement of 0.127mm DA at a frequency of 280Hz with normal loads ranging from about 250 to 700N. Three loads were used, based on the weights available and the dead load of the upper arm; these were 271, 492, and 672N. The displacement was varied from 0.056 to 0.132mm DA and frequencies of 80, 140, 280 and 420Hz were input. Two typical friction force-slip loops are shown in Fig. 15.

The equivalent friction coefficient was determined from the measured area of the recorded (photograph of oscilloscope picture) loop and a knowledge of the input frequency and displacement. The resulting values for friction coefficient are shown plotted against normal load, frequency and velocity, in Fig. 16. A least squares fit of an equation of the form: $\text{coef} = (A/\text{Load}) + B$ was attempted using all the data. The resulting curve is shown superimposed on the test data points in Fig. 16. An examination of the data in Fig. 16 indicates that there is no obvious correlation with either input frequency or maximum velocity.

2.3 Dry Friction Damping Technology

Control of resonant vibration in light, flexible structures has been found to be largely the result of damping available at mating surfaces. The potentials of such damping depends, as has been observed earlier, on a host of parameters that include the magnitude of normal force holding the surfaces in close contact and the characteristics of the surfaces. These and other parameters determine the nature and extent of slip at the interfaces so that an optimum in energy dissipation can be expected with an appropriate combination of normal load and relative motion (Ref. 23). Therefore, an understanding of the processes involved in relative vibratory motion at joints becomes a basic requirement that may influence the design of structures where friction becomes an important source of damping.

The analytical approaches for estimating friction damping can be broadly classified as follows: (1) macroslip approach and (2) microslip approach. In the macroslip approach, the entire interface is assumed to be either slipping or stuck. The friction mechanism is either replaced by an equivalent linear viscous model or assumed to be governed by some form of Coulomb's law of dry friction. The effect of friction damping is obtained by determining the forced response of the component. The analysis involved is relatively straightforward and the justification for wide-spread use of this approach is its effectiveness at predicting the actual response. However, there is some question as to the validity of the macroslip approach when the interface has a large area, and is subject to a nonuniform load distribution. In the microslip approach, a relatively detailed analysis of the stress distribution at the interface is carried out, typically via a finite-element procedure. The extent of local slip, not necessarily throughout the interface, between

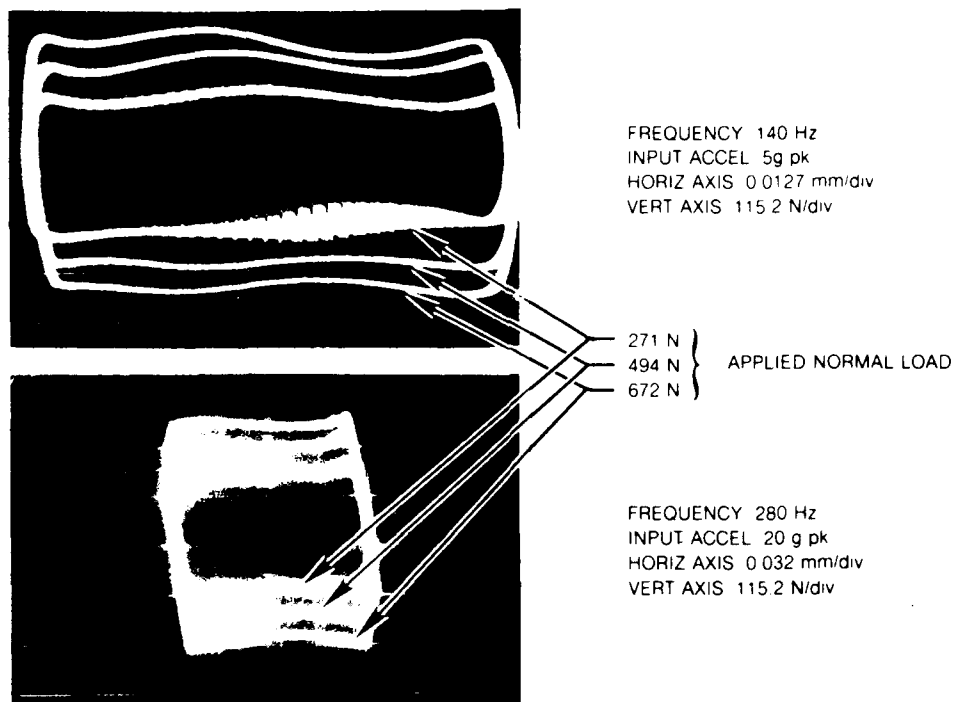


Figure 15. Typical Measured Friction Force—Slip Loops

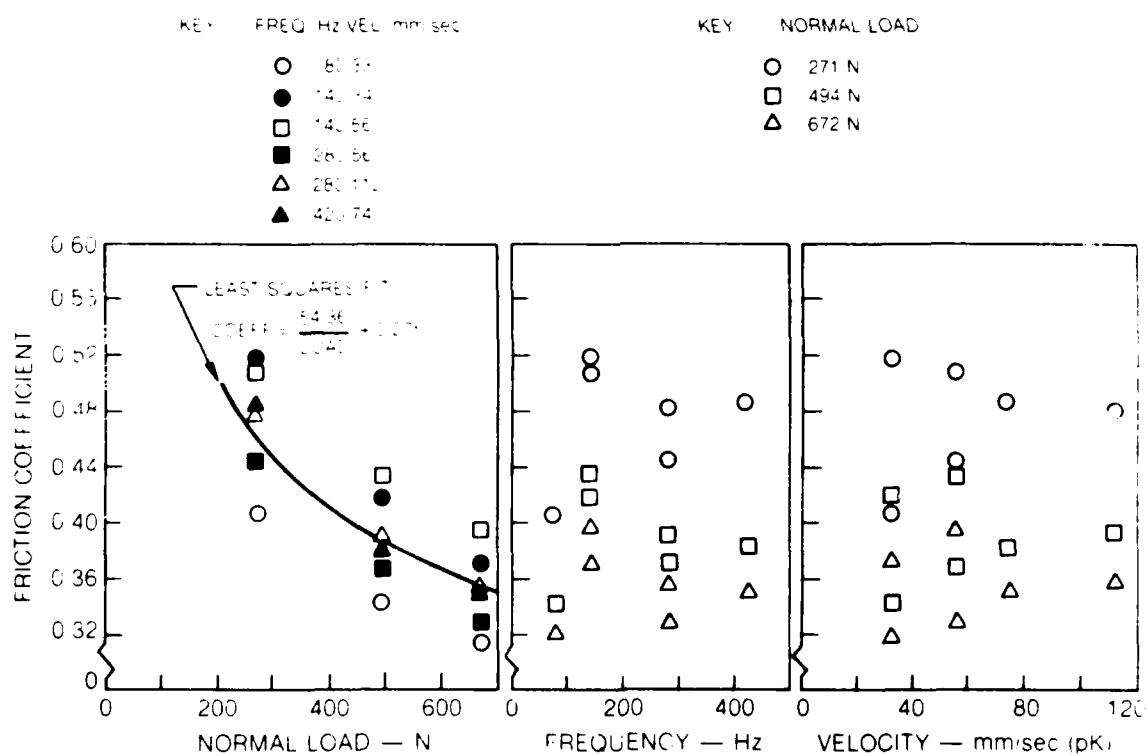


Figure 16. Variation of Equivalent Friction Coefficient During Sinusoidal Motion With Normal Load, Frequency and Maximum Relative Velocity

pairs of contacting points is determined by applying Coulomb's law of friction to the normal and tangential stresses. A detailed knowledge of interface slip dynamics can be obtained from this approach. Although much useful information can be gained in a linearized analysis, a fully nonlinear time history solution may be necessary and feasible with modern computational methods and equipment.

Calculation of energy dissipation over a period of vibration requires an accurate assessment of both the forces and motion of an interface. Much effort will be needed before satisfactory analytical models become available to calculate these parameters. In the meantime, the process of developing and calibrating analytical models requires advances in instrumentation that can measure extremely small vibratory motion at interfaces. A first step towards such development has been taken at the United Technologies Research Center and is described below.

The measurement system comprises a gallium arsenide photoemitting diode (Texas Instruments Type TIL24) and silicon position sensing detector (UDT Type PIN-SC/4D) pair mounted side by side in small aluminum block housings (see Fig. 17). The position reference is provided by the infrared LED emitting a light beam, the centroid of which is sensed by the UDT two-axes position sensing photo-detector. Each axis of the detector has two outputs which are amplified to provide adequate signal level. The voltage difference between the outputs of each axis provide the X and Y position information.

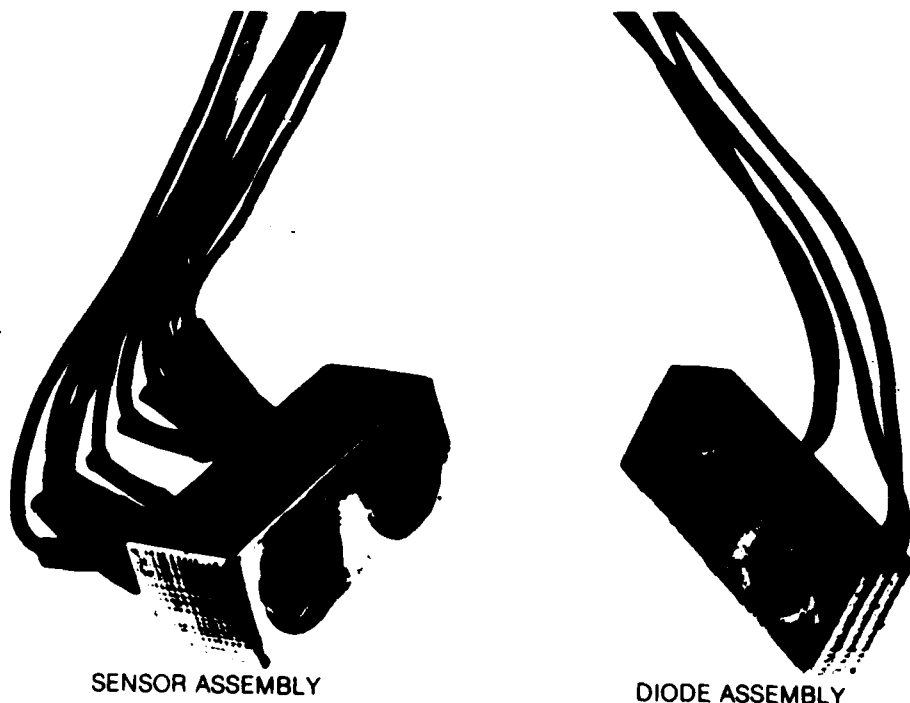


Figure 17. Shroud Motion Measurement Device

A feasibility study of this system was conducted to determine its potential for measuring extremely small motions at a shroud interface. A single part-span-shrouded fan blade was used and bench tests were conducted over a range of normal loads and frequencies. The installation is shown in Fig. 18.

The sensor assembly was glued using epoxy adhesive onto the shroud of a part span shrouded titanium fan blade which had its root welded into a massive titanium block. The test item was enclosed in an aluminum fixture. Application of the required normal loads on the shrouds was accomplished via loading platens mounted on a steel loading disk. The loads were set by applying a moment to the disk and then locking the disk in place. The diode assembly was mounted on the load platen opposite the sensors with a gap of 12 mils between the housings. The detector was oriented such that the Y-axis was radial and the X-axis directed along the shroud interface. The whole assembly was mounted on a slip plate attached to an electrodynamic shaker. Sinusoidal motion was applied to the blade horizontally in the direction of flap of the blade tip. The output from the motion detectors was passed through a low pass 3kHz filter and then displayed on a Tektronix DM 43 dual channel oscilloscope. Permanent records were made by photographing the resulting wave forms and Lissajous figures for each detector set.

The results of the blade tests show some interesting features of shroud motion for this particular test arrangement. The tests indicate that:

- a) Stick-slip or Coulomb damping is not evident from the traces. (A sample trace is included as Fig. 19.)
- b) Radial displacement generally exceeds that along the interface.
- c) The strain response of the blade increases with increase in shroud load indicating lower damping and yet the relative motion between the shrouds also increases.

The series of tests conducted on the single fan blade demonstrated that the optical system is very suitable for measuring small vibratory motions. It has been established that motions as small as 50×10^{-6} inch can be measured with this system in the frequency range of d.c. to 2kHz. The results of calibration indicate the system to be adequate for the range of frequencies and displacements that are of practical interest. This instrumentation system has been successfully used in measuring the extremely small vibratory motions at ten successive interfaces of a part-span shrouded fan. It is anticipated that in any experimental research in this area, this type of optical system will be found to be invaluable.

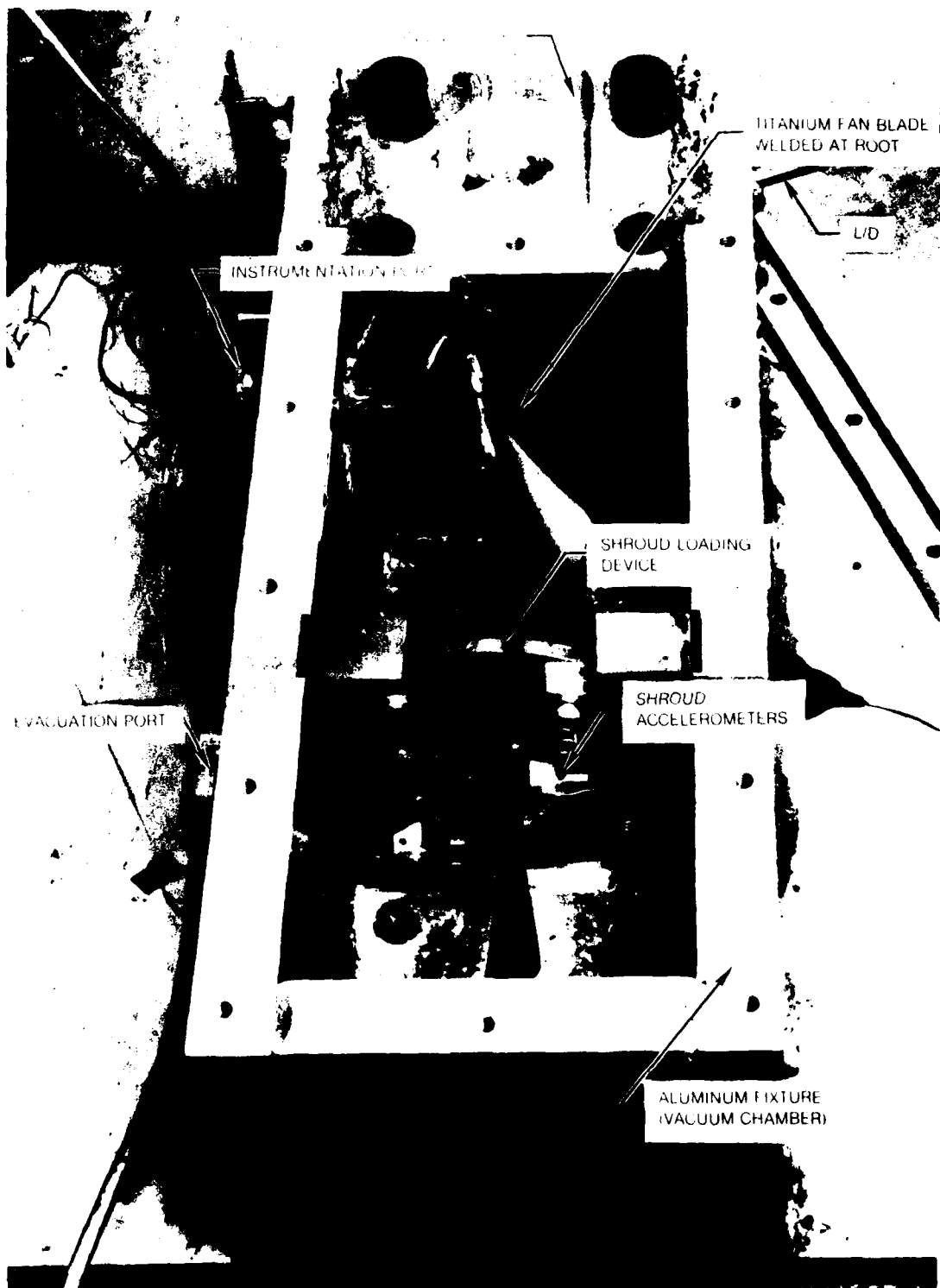


Figure 18. Test Set-Up for Shroud Damping Investigation

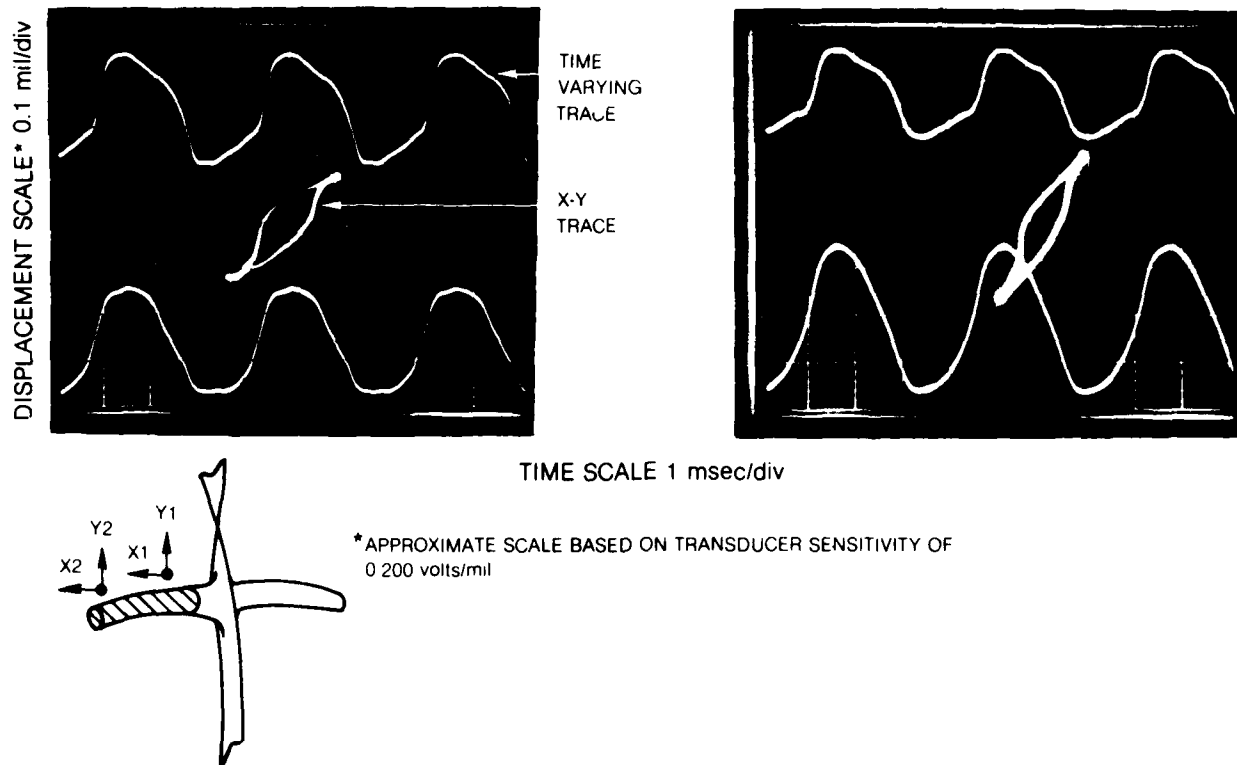


Figure 19. Recorded Shroud Motions for First Mode Blade Vibration and Applied Shroud Normal Load of 34 lbs

3. CONCLUDING REMARKS

An accurate assessment of damping due to friction will obviously depend upon the accuracy with which the interfaces and the environment are characterized. On the basis of observations made earlier, five important interdisciplinary aspects may now be outlined.

1. Surface Science: involving a definition of the interacting surfaces in terms of (a) geometry, (b) bulk material properties such as moduli of elasticity, hardness, etc., (c) surface topography and contact area, and (d) surface chemistry.
2. Environment: involving (a) definition of mechanical and thermal loading, (b) contaminants, gases and liquids present, (c) humidity, and (d) electrical and magnetic fields.
3. Laws of friction that relate 1 and 2 above.
4. Calculation of response of a machine element using 1, 2 and 3 above along with a knowledge of structural properties such as mass, stiffness, etc.
5. Calculation of energy dissipation using 2 and 4 above.

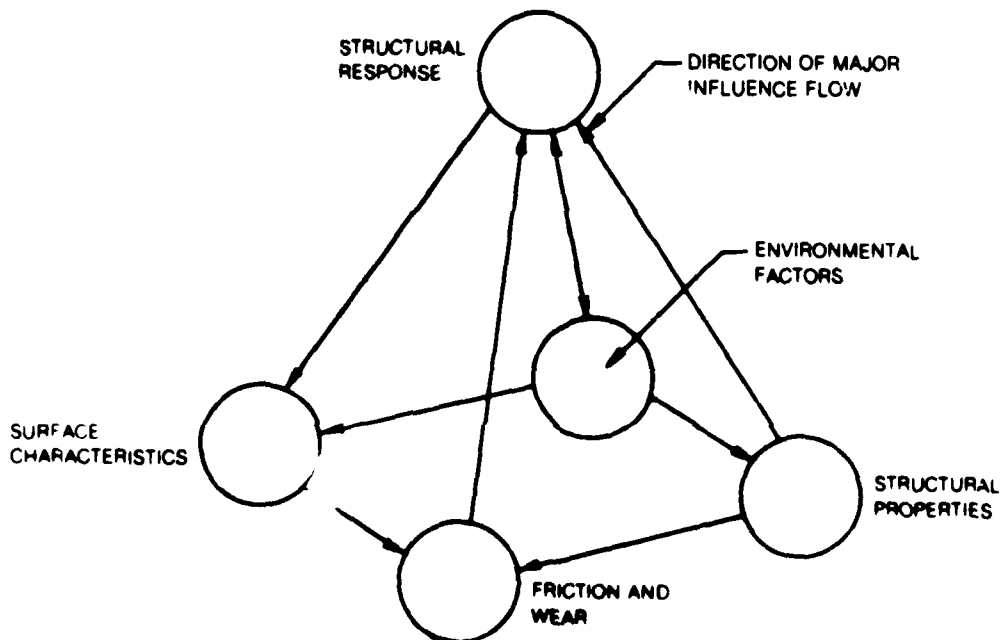


Figure 20. Factors Influencing Structural Response When Frictional Forces are Significant

These interdependent and influential factors may be represented in the form of a friction damping pyramid as shown in Fig. 20. Determination of those parameters that are most influential in a given application is an important task, although certain aspects of research in the technology of friction damping will be of a basic nature. For example, the general nature of the coefficient of friction may be established although its magnitude will vary from one pair of materials to another. Analytical modeling for both single degree of freedom and multiple degrees of freedom must be developed from first principles and calibrated on the basis of carefully planned experimental investigations.

As noted earlier, an important aspect of friction analysis is the determination of the law of friction that is valid and appropriate for application to a given vibrating component. The representation in the form of a nonlocal law affords the flexibility needed in this complex problem area. The representation suggested by Oden (Ref. 8) was primarily intended for the analyses of contact problems and therefore does not include provisions for gross sliding and vibratory motion. Further, in such a representation, the points on an interface of a vibratory component approach a zero relative velocity, and thus no provision is made for the velocity dependence of frictional forces. However, this concept provides a rational basis for deriving more general empirical descriptions which are appropriate to a vibratory environment.

REFERENCES

1. Kragelski, I. V., M. N. Dobychin and V. S. Kombalov: Friction and Wear; Calculation Methods. Pergamon Press, Inc. 1982.
2. Kragelski, I. V., and V. V. Alisin (ed.): Friction Wear Lubrication; Tribology Handbook. Mir Publishers, 1981.
3. Panovko, Y. G., and I. I. Gubanovo: Stability and Oscillations of Elastic Systems. Consultants Bureau, New York, 1965.
4. Ku, P. M. (ed.): Interdisciplinary Approach to Friction and Wear: NASA SP-181, 1968.
5. Bowden, F. P. and D. Tabor: Friction and Lubrication of Solids: Oxford Univ. Press (London), Pt. I, 1954 and Pt. II, 1964.
6. Zhuravlev, V. A.: On the Physical Basis of the Amontons-Coulomb Law of Friction. J. Tech. Phys. (USSR), Vol. 10, 1940, p. 1447.
7. Greenwood, J. A. and J. B. P. Williamson: The Contact of Nominally Flat Surfaces. Proc. 2nd Int. Conf. on Electric Contacts (Graz, Austria), 1964.
8. Oden, J. J. and E. B. Pires: Nonlocal and Nonlinear Friction Laws and Variational Principles for Contact Problems in Elasticity. J. App. Mech., Vol. 50, 1983.
9. Den Hartog, J. P.: Forced Vibrations with Combined Coulomb and Viscous Friction. Trans. ASME, APM-53-9, pp. 107-115, 1931.
10. Yeh, G. C. K.: Forced Vibrations of a Two-Degree-of-Freedom System with Combined Coulomb and Viscous Damping. J. Acoustical Soc. of America, Vol. 39, (1966), pp. 14-24.
11. Jacobsen, L. S.: Steady Forced Vibration as Influenced by Damping. Trans. ASME, Vol. 52 (1930), pp. 169-181.
12. Pratt, T. K. and R. Williams: Non-Linear Analysis of Stick/Slip Motion. J. Sound and Vibration, Vol. 74, No. 4 (1981), pp. 531-542.

REFERENCES (Cont'd)

13. Griffin, J. H.: Friction Damping of Resonant Stresses in Gas Turbine Engine Airfoils. ASME Paper #79-GT-109, March 1979.
14. Srinivasan, A. V., D. G. Cutts, and S. Sridhar: Turbojet Engine Blade Damping. NASA CR 165406, July 1981.
15. Mayer, R. L. and N. A. Mowbray: The Effect of Coulomb Damping on Multidegree of Freedom Elastic Structures. Earthquake Engineering and Structural Dynamics, Vol. 3 (1975), pp. 275-286.
16. Earles, S. W. E. and E. J. Williams: A Linearized Analysis for Frictionally Damped Systems. Jour. Sound and Vibration 24(4), pp. 445-458, 1972.
17. Pian, T. H. H.: Structural Damping of a Simple Built-up Beam with Riveted Joints in Bending. ASME J. Appl. Mechanics, Vol. 24 (1957), pp. 35-38.
18. Goodman, L. E.: A Review of Progress in Analysis of Interfacial Slip Damping (in Structural Damping papers from a colloquium - ASME annual meeting, December 1959), J. E. Ruzicka (ed.), Pergamon (1960).
19. Bielawa, R. L.: An Analytic Study of the Energy Dissipation of Turbo-machinery Bladed Disk Assemblies Due to Inter-Shroud Segment Rubbing. ASME Paper No. 77-DET-73 (1977).
20. Annigeri, B. S.: Finite Element Analysis of Planar Elastic Contact with Friction. ME Thesis, Graduate School of Illinois Institute of Technology (August 1976).
21. Rimkunas, D. A. and H. M. Frye: Investigation of Fan Blade Shroud Mechanical Damping. Wright-Patterson Air Force Base, Aero Propulsion Lab., Report No. FR-11065, 1979.
22. Antoniou, S. S., A. Cameron, and C. R. Gentle: The Friction Speed Relation from Stick-Slip Data. Wear, Vol. 36 (1976), pp. 235-254.
23. Beards, C. F.: The Damping of Structural Vibration by Controlled Interfacial Slip in Joints. ASME Paper 81-DET-86 (1981).

REFERENCES (Cont'd)

24. Levitan, E. S.: Forced Oscillation of a Spring-Mass System Having Combined Coulomb and Viscous Damping. J. Acoustical Soc. of America, Vol. 32, No. 10, (October 1960), pp. 1265-1269.
25. Earles, S. W. E. and M. G. Philpot: Energy Dissipation at Plane Surfaces in Contact. J. Mech. Eng. Sci., Vol. 9 (1967), pp. 86-97.
26. Goodman, L. E. and J. H. Klumpp: Analysis of Slip Damping with Reference to Turbine-Blade Vibrations. Trans. ASME, J. Appl. Mechs., Vol. 23 (1956), pp. 421-429.
27. Busarov, Y. P. and M. S. Ostrovskii: Mathematical Model of Hysteresis of Surface Friction. Mashinovedenic 1976, No. 5, pp. 82-87.

PRACTICAL ASPECTS OF DRY FRICTION DAMPING IN TURBINES

T. J. Oldakowski
General Electric Company
Lynn, Massachusetts

Paper was not presented; not available for publication.

DAMPING PROPERTIES OF STEAM TURBINE BLADES

**Neville F. Rieger
Stress Technology Incorporated
Rochester, New York**

DAMPING PROPERTIES OF STEAM TURBINE BLADES

Neville F. Rieger, Stress Technology Incorporated, Rochester, New York

ABSTRACT

Material hysteresis, attachment friction and gasdynamic effects are recognized sources of damping in turbomachinery blading. No comparison study of their relative effectiveness appears to have been made, although there are diverse opinions on this topic. This overview paper describes a series of tests which were made to examine the damping properties of several types of steam turbine blades. One objective was to determine the relative contributions from the above damping sources in these blade types. These studies were conducted in a non-rotating damping test rig which used real blades mounted in corresponding real disk root attachments. Simulated centrifugal loading was applied to the blades as a lengthwise axial pull along the blades, in a manner which simulated the rotational effect. The rig and the test program are described. The blade damping properties were found to conform primarily to effects associated with material hysteresis damping. For the blades studied, the influence of friction in the attachment region was found to be negligible for test loads and vibratory amplitudes encountered in practice. Gasdynamic damping from the surrounding medium was studied using an environmental chamber, and was found to be negligible. However, a small level of gasdynamic damping from fluid working appears to be possible for blades under operating loads.

INTRODUCTION

This paper describes a series of experiments which were undertaken to determine the nature and magnitude of damping in steam turbine blades. The test program included high-pressure blades, intermediate pressure blades, and low pressure blades. The program was undertaken using a special type of test rig, figure 1, which simulated the blade loading under rotating conditions, by the application of a known preload. A statistically-significant number of identical blades were involved in each test. This gave some indication of the amount of test scatter which could result in the damping data under controlled test conditions from differences between blades and their assembly conditions within their root attachments. The tests examined the influence of blade type, attachment root type, surrounding environment (air, steam, vacuum), axial load, mode of vibration, and other factors.

The objectives of this study were:

- To study the damping properties of several types of steam turbine blades in actual root attachments under simulated operating conditions.
- To examine the nature of the damping which is evident in the test results.
- To evaluate the magnitude of the damping from the decay traces for a variety of blade types, root attachment designs, blade lengths, and operating conditions.
- To determine the relative contributions of the various damping mechanisms to the total damping under these conditions.
- To evaluate the significance of applied root load, vibration amplitude, root type, blade length, and gas environment as possible contributing parameters in each case.

Details of the test rig used, and of the test conditions, and results achieved are given in the following sections.

PREVIOUS WORK

a. Steam Turbine Blades

There is surprisingly little information in the open literature on the damping properties of steam turbine blades. Blade manufacturers have developed extensive test data relating to materials performance, and to blades and blade group performance from vibration tests.

Grady [1] tested several dummy intermediate-pressure blades in disk attachments using a pull-test machine, and used a dynamic shaker to excite the blades to specified force levels. Attachment prestress conditions were changed by varying the root interference fits. It was shown that an optimum root flexibility condition could be developed which would result in dynamic stresses about 1/3 to 1/2 of those in a rigid (welded) joint. Where root stiffness is high, less damping is developed. Considerable variability existed in this optimum root flexibility condition, which was found to depend on blade assembly procedures and on blade vibration history.

Grady [2] performed tuning fork vibration tests in air to measure blade material damping under simulated centrifugal load conditions in a tensile test machine. Data was obtained at zero centrifugal load through a range of dynamic stress to 30,000 psi. The results showed that the material log. dec. values were highest with high dynamic stresses. A maximum test log. dec. value of 0.033 was obtained. Damping decreased with increase in centrifugal load, and increased with frequency of excitation.

Wagner [3] conducted a program of damping tests on rotating steam turbine blade groups in a test turbine. The magnitude of blade damping, the influence of root details and of blade sizes on damping, and the effectiveness of certain damping devices were studied. The test blade groups were rapidly rotated through axially-directed water jets which impulsively excited them into vibratory motion. The blade response was obtained with weldable strain gages and a slip-ring assembly. Substantial scatter was observed in the log. dec. results. The damping for impulse blade groups was found to be greater than for long reaction-type blades. Slightly higher damping with higher stress values was observed. In one test the damping remained substantially constant over 84,000 cycles at a maximum stress value of 30,000 psi. Undershroud welding caused an insignificant reduction in damping.

Rieger and Beck [4] found similar results to these of Grady and Wagner. Their tests were performed on blade pairs inserted in disk segments, with an axial pre-load during testing. Log. dec. values increased in a linear manner with increase in vibratory amplitude, and decreased with increase in root load in a linear manner, with increase in vibratory amplitude, and decreased with increase in root load. Values of log. dec. within the same general range as those obtained by Grady and Wagner were obtained ($\delta=0.01$ to 0.04) for similar blades, at similar vibration amplitudes. Rieger and Beck observed higher log. dec. values in axial vibration ($\delta=0.02$ to 0.08) than in tangential modes.

Brown [5] tested a blade row in a rotating test apparatus to determine the blade row damping values. A steam jet was used for excitation, and both impulse and harmonic excitations were used to excite the blades. The damping results were presented as a ratio between the log. dec. decay test results and the resonance bandwidth test results. No absolute data are given. Brown reported difficulty extracting the damping results due to beating, multiple resonances, etc. The impulse excitation could initiate several modes simultaneously.

Gotuda [6] studied the influence of damping on steam turbine blade vibrations. He identified damping contributions from the blade material, from structural effects, and from aerodynamic damping. Gotuda used the resonance decay method to obtain data, and showed that the log. dec. increased in proportion to dynamic stress. Tests were next conducted on tangential-entry tee-head steam turbine blades, tightly fitted as single blades into the disk root groove. Higher damping values were obtained in this case than in the tuning fork tests. Damping was again found to vary linearly with dynamic stress, and the increase in such values over the material test results was attributed to root friction. The scatter in results was attributed to individual differences between blades. At high stress this scatter was quite large, and the log. dec. vs. dynamic stress relationship was no longer linear, above $\sigma_d = 12 \text{ Kg/mm}^2$. Calculations by Gotuda demonstrated that the value of the damping stress index was 3, for the

blade material used. Further data was given for the variation of log. dec. with stress for simple blades, blade groups, and tuning forks. The form of the damping vs. stress relation was linear for the blades tested, except as noted above.

b. Gas Turbine Blades

An early study of enhanced damping in hollow blades was made by DiTaranto [7] who tested blades containing numbers of 0.005 in. diameter radial wires. The damping in a stationary blade with wires prestressed to 7,000 psi was an order of magnitude higher than that of the stationary hollow blade without wires for equal excitations. The damping in a blade rotating at 8,000 rpm was further found to be twice that of the stationary blade with wires stressed to 7,000 psi. DeTaranto discussed the following methods for enhanced damping: (a) Insertion of particles and/or wires of different sizes into hollow blades; (b) Use of two flat cantilevered plates under normal force, rubbing together as they vibrated; (c) Root damping of the vibrating blade, with normal force being the critical factor. Too great a force was found to prevent relative blade-root motion; (d) Tuned dampers, which were effective in narrow frequency bands.

Srinivasan, Cutts and Sridher [8] studied compressor fan blade damping. Root damping was found to be negligible at operating speeds for the dovetail root attachment structure. The material damping in the titanium alloy blades was also found to be very small. The shroud interface contacts were found to be the most useful source of damping in such fan blade structures, but the authors indicate that damping from shroud or platform rubbing may be difficult to define for consistent results. Material damping log. dec. values for titanium blades were found to range from 0.0006 to 0.0015.

Jones and Muszynska [9] investigated the influence of slip between components in the blade platform region. The purpose of this study was to determine the extent to which damping in a blade geometry could be optimized by allowing contact between the blade platform and the disk to occur at high speed. Approximate non-linear equations of motion were derived and solved using a harmonic balance procedure. It was found the high levels of slip damping could be achieved if the relative component stiffnesses were properly selected. This paper does not contain any significant experimental results, but testing is proposed together with a spin pit investigation, to validate the influence of practical platform dampers.

Muszynska, Jones, Lagnese and Whitford [10] analyzed the non-linear response of a set of compressor blades mounted on a rigid disk and interconnected with a dry friction coupling near each blade platform. Each blade consists of a discrete two-mass system connected to adjacent blades by a flexible link, with a dry friction contact. Effects from blade-to-blade dry friction contacts are also included. A single blade was initially investigated experimentally to obtain modal values for the blade models. Several system effects were examined, including blade mistuning and influences from the magnitude and distribution of exciting forces and phase differences between the exciting forces on adjacent blades. Conclusions concerning the influence of dry friction in reducing blade response amplitudes and on the influence of mistuning on the resulting blade amplitudes are given. The fundamental modes of the blades were accurately modeled and their parameters were precisely identified. An optimum value of

the friction parameter was found to exist for which response amplitudes are at a minimum for all blades. The effect of blade mistuning was to introduce blade-to-blade coupling through the stiffness elements connecting the blades. This lead to typical mistuned behavior in which several response peaks were observed, scattered on both sides of the tuned system resonant frequency.

c. Attachment Slip Studies

Hanson [11] described a rig for testing gas turbine and compressor blade damping properties, which consisted of a disk carrying a single blade which could be rotated at speeds up to 15,000 rpm. The blade could be excited by an air jet or by the impact of a small ball. Blade decay rates following impact were observed. Data is given on root friction damping coefficient vs. rpm, and on material damping vs. rpm, for several types of blade roots. For these blades fir-tree roots were found to give rates of amplitude decay. Pin-root and wedge-root blades gave smaller damping values. In all instances the damping increased as rpm increased.

Hanson, Meyer and Manson [12] investigated a proposed compressor blade friction-damping device. Using the same rotating blade apparatus, they demonstrated a 3:1 decrease in blade vibration amplitudes when this device was used on compressor blades. Similar platform-friction devices were recently developed and tested during studies of blade vibration associated with the space shuttle turbopump engines

Beards [13] evaluated the likely effectiveness of root slip damping for suppressing vibrations of compressor blades based on an examination of the results obtained by Hanson [11], Hanson, Meyer and Manson [12], and Goodman and Klumpp [14].

Jones and Muszynska [15] developed a simple two-mass analytical model to represent the vibrational behavior of a jet engine compressor blade in its fundamental mode, allowing for slip at the blade attachment interface. This work is an attempt to develop a theoretical basis for earlier work by Hanson, Meyer and Manson [12], and others. Vibration tests were carried out to experimentally verify the analysis using a particular blade geometry. A blade with a simple root geometry was inserted in a heavy fixture containing a matching axial-entry tee-head root. The blade was loaded with radial forces to simulate the centrifugal load on the root during operation. Tests were conducted to determine the response amplitude at various frequencies corresponding to several centrifugal loads. The nonlinear equations of motion with slip at the root were developed and solved by the method of matched parameters. Correlation between analysis and experiment showed that it is possible to model the blade response using a simple two-degree system with slip at the root level. Their response curves follow the response for a linear model until slip occurs at the loaded interface. Beyond this point the blade vibration amplitude ceased to grow, and remained constant over a substantial range of frequency.

Muszynska and Jones [16] investigated the dynamic response of blades on a rigid disk allowing for interface slip at the attachment interface and blade hysteretic damping. Two types of mass model of a single blade in a disk were used. The first model allowed for root slip and blade hysteresis, and the second model allowed a damper concept which incorporated platform slip to be

studied. Results were compared with experimental response data for a single blade in a test fixture under low level harmonic excitation. It was demonstrated that the contribution of root slippage to blade damping falls off with increasing rotational speed, but this was compensated with a suitably sized damper device in the second model.

d. Material Damping

Material damping has been studied by many investigators. This literature has been discussed comprehensively by Lazan [17]. Rowett [18] investigated the torsional damping properties of certain grades of steel shafting, and appears to have first suggested the stress-damping law $D = J\sigma^n$. Kimball [19] obtained log. dec. damping data for several grades of carbon steels and alloy steels. Lazan studied the general nature of material damping, and presented results for almost 2000 materials in his treatise on this subject. Lazan's results are presented in terms of the above material damping law in chart form and in a data glossary, in which specific damping energy is related to dynamic stress. An application of Lazan's procedure to first-mode vibration of a turbine blade is given.

Lazan's results again show that log. dec. values will increase with dynamic stress i.e., with vibration amplitude, where material damping is the dominant mechanism. Similar results were obtained by Robertson and Yorgiadis [20] in an early study of energy dissipation in several metals under torsional and axial loadings.

APPARATUS

a. Blade Test Rig

A blade test rig of the type used in this program is shown in figure 1. The principle of the rig is illustrated in figure 2. Several rigs of different sizes were built to accommodate different blade lengths. Damping properties of steam turbine blades in disk segments with actual root attachments were measured. Vibration decay tests were conducted using blades which had been welded together in pairs at their tips: see figure 3. The purpose of this blade-pair arrangement was to carry the lengthwise tensile preload which was intentionally developed using relative thermal shrinkage (initially) and pressured load cells (later) between the blade pairs and the rig frame to simulate the blade centrifugal loading which acts on the root attachments during operation. Damping data was obtained from the preloaded blade pairs when tested in their lowest mode of vibration, in both the tangential and the axial directions. Details of vane lengths, root attachment types, location in rotor, etc., which were included in this program are given in Table 1.

The primary requirements for the blade test apparatus were (a) to provide a rigid support for the blade and root attachment structure during testing, (b) to apply a simulated lengthwise load to the blade pairs during testing in a manner which simulates applied centrifugal loading on the blade, and (c) to isolate the blade pair from any rig or apparatus natural frequencies. It was also required that the natural frequencies and mode shapes of the preloaded blade pairs should

be reasonably similar to those of the grouped blades used in practice. This requirement was achieved by making a natural frequency calculation of the original blade, and by then adding a suitably proportioned flexure link between the blades, figure 3. The flexure link transmits the end-applied blade tensile load. This arrangement typically allowed the tangential and axial natural frequencies to be approximated to within 15 percent. Some inaccuracies remain between the relative mode shapes of these two conditions near the blade tips, and flexure link, but calculations showed that the mode shape in the attachment region, and in the lower portion of the vane are in good agreement.

A requirement of each test apparatus was that the natural frequencies and mode shapes of the rig should not influence, or interact significantly, with any mode of the blade pair. Prior to rig construction, a detailed finite element calculation was made to identify the first ten or more natural frequencies of the test rig, both with the blade pair inserted, and without blade pair inserted. Each rig was also tested by rapping, to locate actual natural frequencies. The test apparatus was finally modified as needed so that the required blade natural frequencies occurred in dynamically-inert frequency regions ("dead zones") of the test apparatus.

b. Environmental Chamber

The environmental chamber shown in figure 4 was built to investigate the influence of the surrounding gas environment on the blade-damping properties. Gas-dynamic damping effects from surrounding air, from steam (at various pressures and temperatures), and in vacuum were tested using this chamber. The chamber completely enclosed the blade pair and disk attachment segments. The design and construction of the environmental chamber used for evaluation of 25 inch vane, low pressure, curved axial-entry blades involved the following:

- A simulated low pressure stage environment between 0.8 and 1.5 inches of Hg and 100 degrees F.
- A steel tube which surrounded the blade pair and attachment, using a pair of flexible bellows at either end to accomodate rig thermal and other expansions, from the steam tests and applied preload.

The blade pairs were mounted in the rig in the usual manner and during testing were preloaded using hydraulic load cells. All blade and attachment components were contained within the environmental chamber during the test program.

The test arrangement consisted of five openings in the environmental test chamber: two for strikers to excite the blades, two for the transducers, and one for the vacuum draw-off connections. The location of the transducers and the strikers within the environmental test chamber is shown in figure 4.

c. Computer Aided Data Acquisition System

The amount of test data obtained from this program was substantial. Between ten and twenty-five blades of each type were tested, over a range of preload, initiating amplitude, environment, etc. conditions, and each test was repeated five to ten times, to ensure that representative statistical results had been

obtained. In anticipation, a computer-aided data acquisition system was developed and used to reduce the test data. This system is shown in figure 5. A calibrated decay signal from the blade transducer was captured on a spectrum analyzer, visually reviewed, and then processed. Accepted traces were then transmitted by a data link to the memory of a minicomputer. This data was then processed and printed as a tabulation of log. dec. vs. decreasing vibration amplitude, with test details.

TEST RESULTS

Seven blade configurations were tested to determine their damping properties. These included two high-pressure blade designs, three intermediate blade designs and two low-pressure blade designs. Statistical analyses were performed on the damping results for selected tests. The influence of root coatings, of root modifications, and of several operating environments on damping was also investigated, for low-pressure blades. The results obtained are described in this section, and their significance is discussed in the following sections.

a. High Pressure Blade Tests

2" Vane, Straddle Mounted, Tangential Entry Blade. Figure 6.

Sixteen blade pairs were tested in air for damping in the tangential and axial directions, each under four centrifugal load conditions (1000, 2000, 3000 and 5000 lb.). The results, figures 7 and 8, show that the log. dec. values increase with blade tip displacement in both axial and tangential modes. Damping is approximately linearly-related to the vibration amplitude. Increasing the centrifugal load decreased the damping value.

4" Vane, Ball and Shank, Axial Entry Blade. Figure 9.

Damping values were obtained from the tests conducted in air on two sets of eleven pairs of ball and shank blades, in the tangential and axial modes. Both long shank and short shank blades with 4 in. vanes were tested. Typical results for log. dec. vs. amplitude are shown in figure 10. Damping increased with increased blade tip displacement in the tangential mode, for both long and short shank blades. For long shank blades, the axial mode damping increased only slightly with increased load. For short shank blades, axial damping increased by an order to magnitude over axial damping of the long shank blades.

Comments on High Pressure Blade Results

High pressure blade damping appears to be related to vibration amplitude in a linear manner, and inversely related to centrifugal load.

b. Intermediate Pressure Blade Tests

6" Vane Fir Tree Root, Axial Entry. Figure 3.

Damping data was obtained for 23 blade pairs tested in air. Results for log.dec. values are shown in figure 11 for the tangential and axial directions, as a function of blade tip displacement and centrifugal load. Damping increased linearly with increased tip displacement, and decreased with increased centrifugal load.

9.5" Vane, Fir Tree Root, Axial Entry Blade

Twelve blade pairs were tested in air. Tests were conducted in both the tangential and axial modes. Damping values increased with blade tip displacement, and decreased with increased centrifugal load.

Comments on Intermediate Pressure Blade Results

Damping results for I.P. blades with fir tree roots again indicate the trends observed with the high-pressure blades, i.e., damping increased with tip displacement, and decreased with increase in centrifugal load.

c. Low Pressure Blades

25" Vane, Fir Tree Root, Curved Axial Entry Blade. Figure 12.

Twenty-two pairs of blades were tested in their disk root sections, for seven centrifugal load conditions. Trends for both tangential and axial modes are shown in figure 13. The curve showed a small negative hook followed by a shallow curve of positive slope. The spread of damping values for centrifugal loads of 5000, 9000, and 13,4000 lbs. were statistically analyzed.

Comments on Low-Pressure Blade Results

Tests on the curved axial-entry blades showed some interesting features. Initially, the blade damping decreased to a minimum value, from which it increased with centrifugal load. These blades differed from other blades tested in that they were much longer, the attachment was curved, and it was oriented across the disk rim at an angle. These results appear to be some combination of effects seen in tangential and axial modes of previous tests. The two-part curve may be an expanded version of the characteristic seen for stiffer blades, e.g. figure 11. Damping increases with larger tip amplitudes of vibration. The LP vane section is generally more flexible than other blade types, and so the damping which results from flexure occurs mostly toward the vane tip.

Environmental Effects: Low-Pressure Blades. Figure 14.

Ten pairs of 25" low-pressure blades were tested in air, in vacuum, and in steam. Statistical data was compiled from the multiple testing performed on each pair. Negligible differences were detected between the mean damping values obtained for the three environments.

Root Coating Effects. Figure 15.

The results from the root coating test on 25" low-pressure blades indicate that attachment coatings consisting of thin films of structural adhesives on the hook faces have only a small effect on the overall blade damping in the normal operating range.

Influence of Root Modifications. Figure 16.

Six 25" vane low pressure blades with the following relieved hook conditions were tested in their disk attachments. Two sets of conditions applied: (i) the two upper hooks were relieved (reduced contact loads), and the four lower hooks

were therefore equally loaded; and (ii) the two middle hooks were relieved, and the upper and lower hooks were equally loaded. Little difference was found between results obtained from these two test conditions. Under circumstances where the relieved upper hooks could slide, case (ii), the damping values were higher. This condition is not expected to occur under normal conditions.

DISCUSSION OF TEST RESULTS

The blade types and test conditions involved in this program are listed in tables 1 and 2. The high pressure blades showed tangential log. dec. values ranging between 0.012 and 0.18, and axial log. dec. values between 0.024 and 0.21. Corresponding values for the IP blades range from .008 to 0.09 in the tangential direction, and from 0.015 to 0.15 in the axial direction. Log. dec. values for the low pressure blades range from 0.005 to 0.030 in the tangential direction, and from 0.005 to 0.035 in the axial direction. The range of variation of log. dec. in each instance is due to variation of dynamic amplitude, i.e. to dynamic stress range values, and to test conditions, particularly applied preload values.

Damping data for short high-pressure blades are shown in figures 7 and 8, for a tangential entry root, and in figure 10 for a ball-type axial entry root. The general form of the curve in each instance is similar. For tangential entry blades, log. dec. increases with blade tip displacement in both the tangential and axial directions. Centrifugal load tends to decrease the damping for higher centrifugal load values. This trend is more pronounced for tangential vibrations than for axial vibrations. The ball-type roots repeat these trends, but for the short shank blades the axial vibration damping is almost constant with blade tip displacement and centrifugal force.

Results for 6-inch blades with axial entry fir tree roots are shown in figure 11, and these again show an increase in log. dec. with blade tip displacement. Data is given for tangential vibrations and for axial vibrations, in air. The damping relationship is seen to be almost linear in these instances, though the vibration test amplitudes were relatively small. Later tests established that damping continues to increase with higher vibration amplitudes. Increased centrifugal load causes the log. dec. values to decrease, as was found by Lazan [17] for damping which is related to material hysteresis.

Results from tests on 25-inch blades with curved axial entry attachments under a variety of conditions are shown in figure 13. Log. dec. vs. blade tip displacement is shown for several preload values, for axial vibrations, and for tangential vibrations. In this instance a higher mean stress appears to increase the blade damping, at loading values beyond a certain lower limit. The reason for the difference between these results and, for example, those in figures 7 and 11 is thought to lie in the interaction between the local preload and the dynamic stress. This causes local plastic deformations to occur at higher preloads, which would give higher material damping values. Higher amplitudes of vibrations were achieved for the tangential vibrations than for the axial vibrations.

Figure 14 shows the influence of gaseous environment on the test results, for tests involving new roots (assembled for the first time), and old roots (which

had been used in previous tests). Generally speaking there is little difference between the values obtained under vacuum and in air. Damping data with used roots in air gave somewhat lower values than air tests with new roots. These tests were conducted using a 25-inch blade loaded lengthwise with a force of 13,400 lbs. which is smaller than typical operating attachment loads carried by such blades.

Figure 15 shows the influence of root coatings on log. dec. for various amplitudes of vibration. Results for uncoated roots were compared with those obtained from roots coated with epoxy, and with loctite. It was found that the epoxy-coatings would smear throughout the attachment upon insertion, and were only present over portions of the root surface when the blades were removed. The influence of loctite appeared to decrease the overall damping by a small amount, probably because of its effectiveness in securing the blade into the disk attachment.

Figure 16 demonstrates the effect of severe mal-distribution of root tolerances in LP blade attachments. For similar applied loads, relief of the middle hook contact was found to increase the damping more than for relief of the upper hook. This is because the middle hook relief applied a greater load to the upper hook, where damping and movement is most likely to occur. The test data is consistent for loads between 5,000 lbs. and 13,400 lbs. These results may be compared with similar data for unmodified roots in figures 13 and 14.

Variation of log. dec. with centrifugal load increase is shown in figure 17. The vertical bars show in the data scatter limits for one standard deviation. This data applies to vibration amplitudes up to 3.7×10^{-3} inches in the tangential direction, and to 0.7×10^{-3} inches in the axial direction. It is seen that the log. dec. is almost constant for centrifugal load variation in the axial direction, but it decreases with load increase for vibrations in the tangential direction. These results are again in keeping with results obtained by Lazan [17] for material hysteresis.

Figure 18 shows additional damping data for a 30 inch LP blade, where log. dec. is plotted against vibratory stress. The blade pairs used had curved axial entry roots. Dynamic stress values were obtained with a strain gage attached on the vane near the root. It is seen that log. dec. decreases in the lower stress region, and then increases as the dynamic stress increases further. This is again due to the complex interaction between the dynamic stress, the mean stress under test conditions, and the material properties, as mentioned above.

CONCLUSIONS

- Blade damping increased with increase of vibration amplitude in most instances, for both tangential vibrations and axial vibrations. This trend was most evident for HP and IP blades.
- Damping in low-pressure blades increased with increase in vibration amplitude, but at a lower rate than in HP and IP blades. Average log. dec. values were moderately constant with vibration amplitude.
- No evidence was found of slip between components in the attachment region. Attachment loadings appear to be too high for slip damping to develop at the test amplitudes studied. This test condition is representative for the blading studied under operating conditions, where attachment loads are often much higher than the study loadings.
- Negligible differences in damping values were observed between tests in non-flowing steam, in air, and in vacuum. Gaseous environments appear to contribute no significant damping to steam turbine blades, unless the blades are doing work against the steam loadings.
- The above conclusions indicate that blade damping is mainly due to material hysteresis, because root friction and gasdynamic effects are both negligible.
- Adjacent hook modifications in the attachment region had no significant effect on damping in LP blades. Minor changes in damping values were observed with LP blades where root coatings were applied.
- Higher damping values were usually observed in modes occurring at higher frequencies of vibration.

ACKNOWLEDGEMENTS

The test programs described in this paper were undertaken by the author in collaboration with Patrick C. Johnson, Project Engineer of Stress Technology Incorporated, and with Louis C. Peck III, formerly of STI. The work was funded by the Electric Power Research Institute, Fossil Fuel Energy Division under the guidance and encouragement of John B. Parkes, Jr. (initially) and Thomas H. McCloskey, EPRI Program Managers. Grateful thanks are due to EPRI for this support.

REFERENCES

1. Grady, R.F., "Investigation of Dovetail Damping Contribution of Propulsion Steam Turbine Buckets", General Electric Co., Report NOB5-94390, Submitted to Bureau of Ships, Department of the Navy, November, 1967.
2. Grady, R.F., "Investigation of Material Damping Properties of Propulsion Turbine Blade Material", General Electric Co., Report NOB5-94390, Submitted to Bureau of Ships, Department of Navy, December, 1967.
3. Wagner, J.T., "Blade Damping Tests", Westinghouse Engineering Report, EC-401, NOBSN00024-67-C-5494, May, 1969.
4. Rieger, N.F. and Beck, C.M., "Damping Tests on Steam Turbine Blades". EPRI Project RP-1185-1, Palo Alto, California, 1980.
5. Brown, W.G., "Determination of Damping Value for Turbine Blades", ASME Design Engineering Technical Conference, 81-DET-131, Hartford, 1981.
6. Gotoda, Hidemi, "An Analysis on Resonant Stresses in Steam Turbine Blades", Technical Designing Department, Kawasaki Heavy Industries, Ltd., Kobe, Japan, 1974.
7. DiTaranto, R.A., "Blade Vibration Damping Device", Journal of Applied Mechanics, Trans. ASME, Vol. 80, pp 21-27, 1958.
8. Srinivasan, A.V., Cutts, D.G., Sridhar, S., "Turbojet Engine Blade Damping", United Technologies, Report No. R81-91441031. Submitted to NASA (Report No. CR-165406), July, 1981.
9. Jones, D.I.G., Muszynska, A. "Design of Turbine Blades for Effective Slip Damping", The Shock and Vibration Bulletin, Part 2. Washington, D.C., Sept. 1979.
10. Muszynska, A., Jones, D.I.G., Lagnese, T., and Whitford, L., "On Non-linear Response of Multiple Blade Systems" Shock and Vibration Symposium, San Diego, California, October, 1980.
11. Hanson, M.P., "A Vibration Damper for Axial Flow Compressor Blading", Proc. Sec. Exptl. Stress Analysis XIV, pp. 155-162, 1955.
12. Hanson, M.P., Meyer, A.J. and Manson, S.S. "A Method for Evaluating Loose Blade Mountings as a Means of Suppressing Turbine and Compressor Blade Vibrations", Proc. Soc. Exptl. Stress Analysis, 10 (2) pp. 103-116, 1953.
13. Beards, J.E., "Damping in Structural Joints", Shock Vibration Digest, (8), pp. 35-41, 1979.

14. Goodman, L.E. and Klumpp, J.H., "Analysis of Slip Damping with Reference to Turbine Blade Vibration", Journal of Applied Mech., Trans. ASME, 23, (3), pp. 421-429, Sept., 1956.
15. Jones, D.I.G., Muszynska, A., "Vibrations of a Compressor Blade with Slip at the Root", The Shock and Vibration Bulletin, Washington, D.C. Sept., 1978.
16. Muszynska, A., Jones, D.I.G., "On Discrete Modelisation of Response of Blades with Slip and Hysteretic Damping", Proc. of the Fifth World Congress on Theory of Machines and Mechanisms, 1979.
17. Lazan, B.J., "Damping of Materials and Members in Structural Mechanics", Pergamon Press, Inc., New York, 1968.
18. Rowett, F.E., "Elastic Hysteresis in Steel", Proceedings, Royal Society of London, Vol. 89, London, 1914.
19. Kimball, A.L., "Vibration Problems, Part 5 Friction and Damping in Vibrations", Trans. ASME, 63, pp. A-135 A-140, 1941.
20. Robertson, J.M. and Yorgiadis, A.L., "Internal Friction in Engineering Materials", Jnl. Appl. Mech., Vol. 13, No. 3, pp. A173-182, Sept. 1946.

<u>Root Type</u>	<u>Vane Length</u>	<u>Entry</u>	<u>Stage</u>
Straddle-mount	2.0	Tangential	First
Ball and Shank	3.5	Axial	L-3
Fir Tree	6.00	Axial	L-5
Fir Tree	9.50	Axial	L-1
Fir Tree	25.0	Curved Axial	Last

Table 1 **Details of Turbine Blades and Root Attachments Tested**

<u>Stage</u>	<u>Vane Size</u>	<u>Root Type</u>	<u>Range of Axial Log. Dec.</u>	<u>Range of Tangential Log. Dec.</u>	<u>Comment</u>
HP	2"	Tangential straddle mount	0.05-0.12	0.07-0.18	Air environment
HP	4"	Ball & shank short	0.12-0.21	0.012-0.021	Air environment
HP	4"	Ball & shank long	0.024-0.041	0.012-0.024	Air environment
IP	6"	Axial fir tree	0.015-0.035	0.008-0.055	Air environment
IP	9.5"	Axial fir tree	0.015-0.15	0.015-0.090	Air environment
LP	25"	Curved axial fir tree	0.005-0.035	0.008-0.030	Air environment
LP	25"	Curved axial entry	0.010-0.020	0.008-0.010	Air/Vaccum/Steam
LP	25"	Curved axial entry	0.020-0.024	0.005-0.010	Loctite & epoxy coatings
LP	25"	Curved axial entry	0.020-0.025	0.020-0.030	Adjacent root study
LP	25"	Curved axial	0.025-0.030	0.015-0.028	Modified root study

Table 2 **Range of Logarithmic Decrement Values**

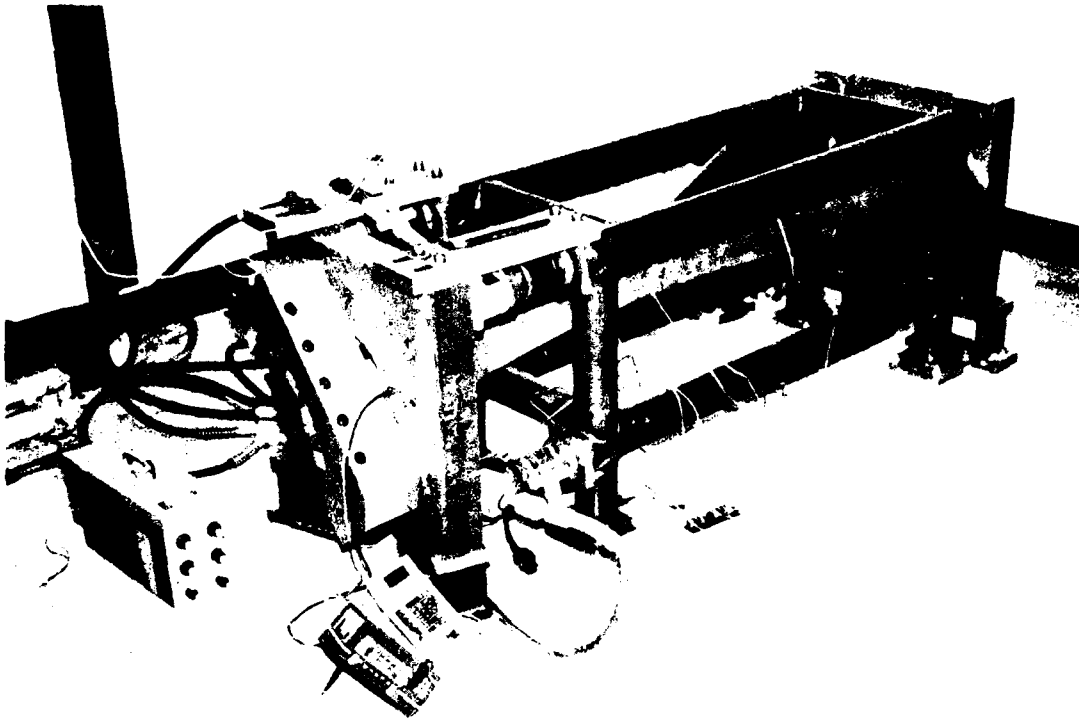


Figure 1 Blade Damping Test Apparatus

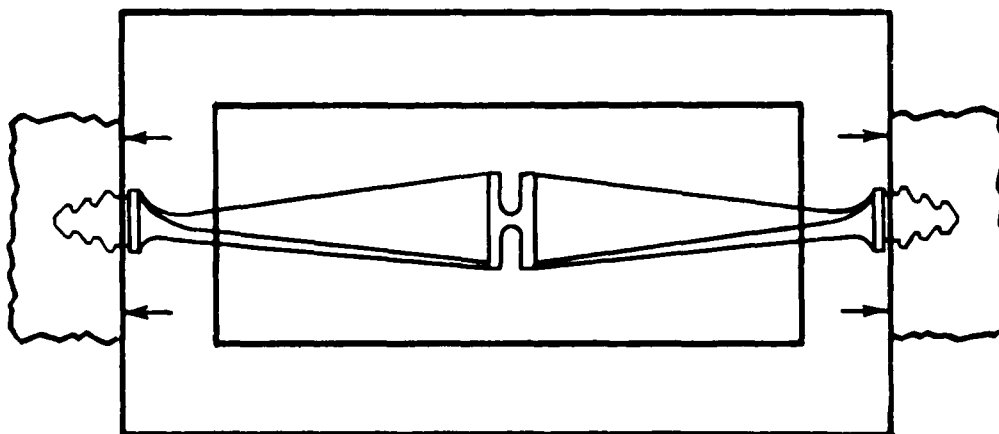


Figure 2 Principle of Test Rig

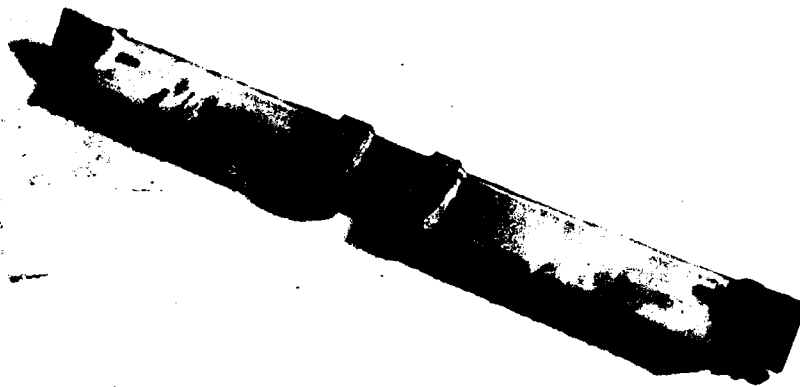


Figure 3 Welded Blade Pair Showing Flexure Link

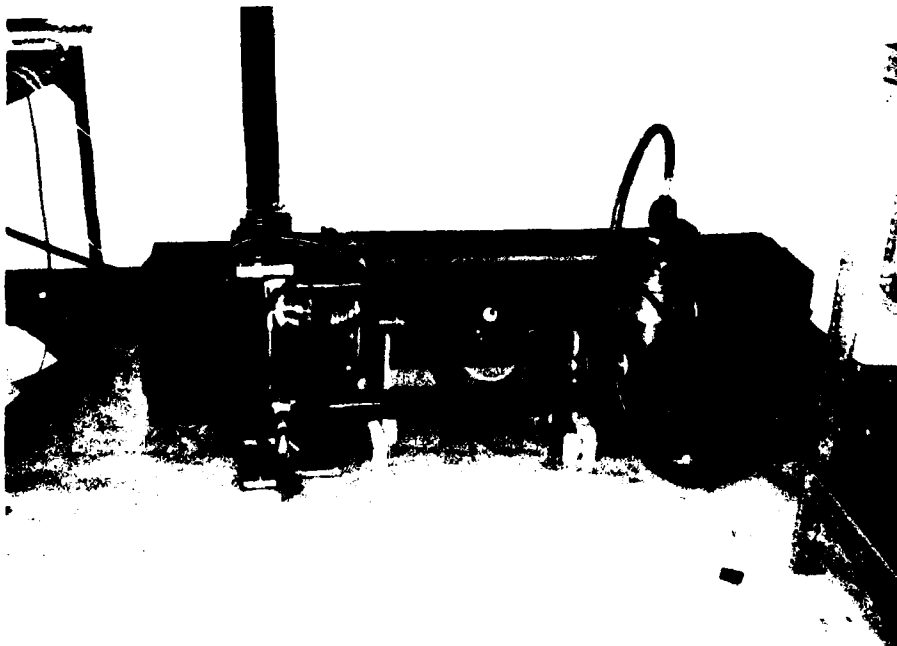


Figure 4 Test Rig With Environmental Chamber

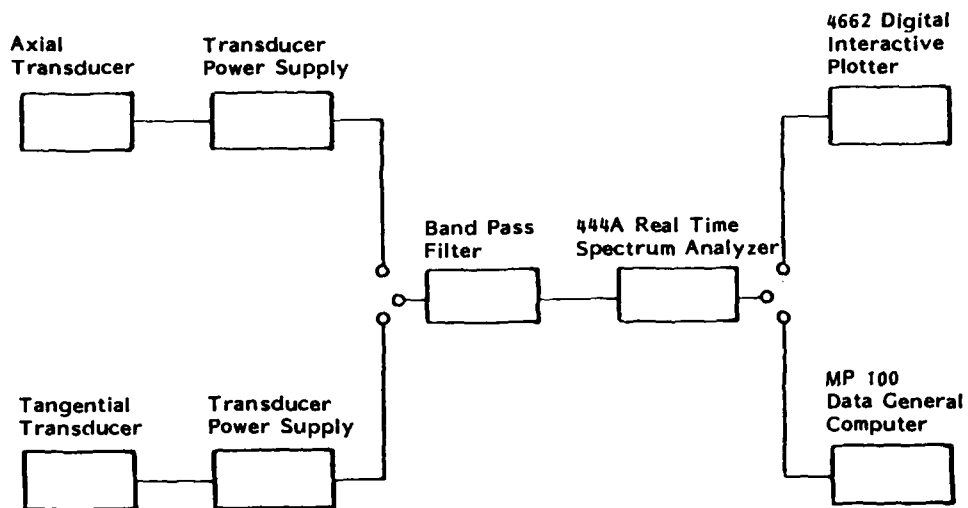


Figure 5 Computer Aided Data Acquisition System



**Figure 6 2" Straddle Mounted Tangential Entry
High Pressure Blade Pair**

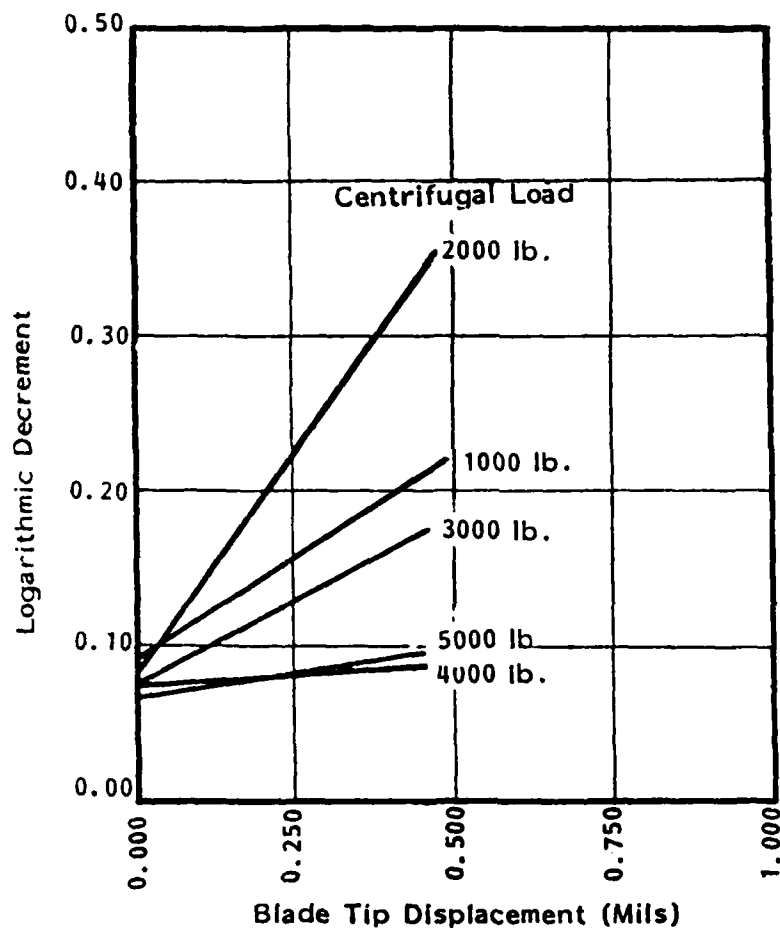


Figure 7 Logarithmic Decrement vs. Tip Displacements and Centrifugal Load. Tangential Mode 2" Straddle Mounted, Tangential Entry High Pressure Blade

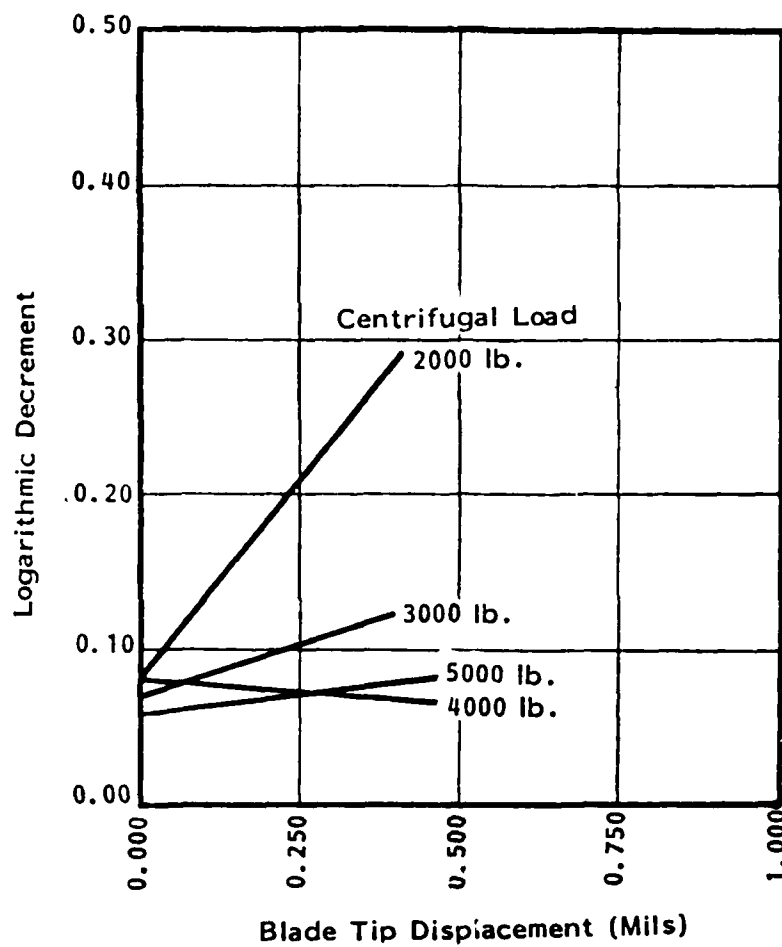
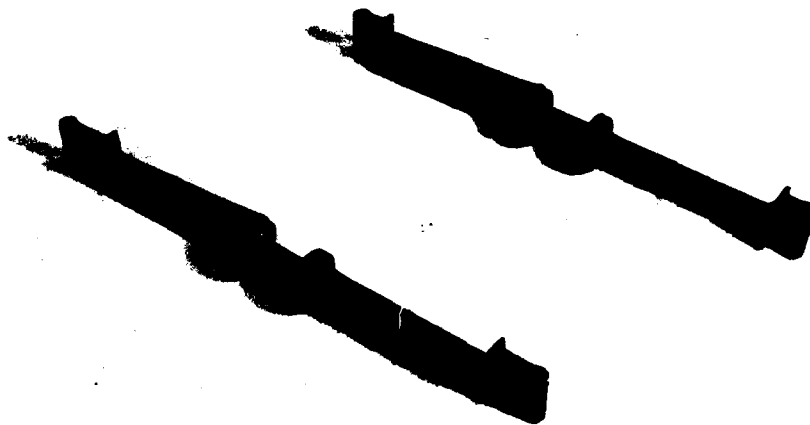


Figure 8 Logarithmic Decrements vs. Tip Displacements and Centrifugal Load (Axial) 2" Straddle Mounted, Tangential Entry High Pressure Blade



• Figure 9 4" Ball and Shank - Axial Entry High Pressure Blade Pairs

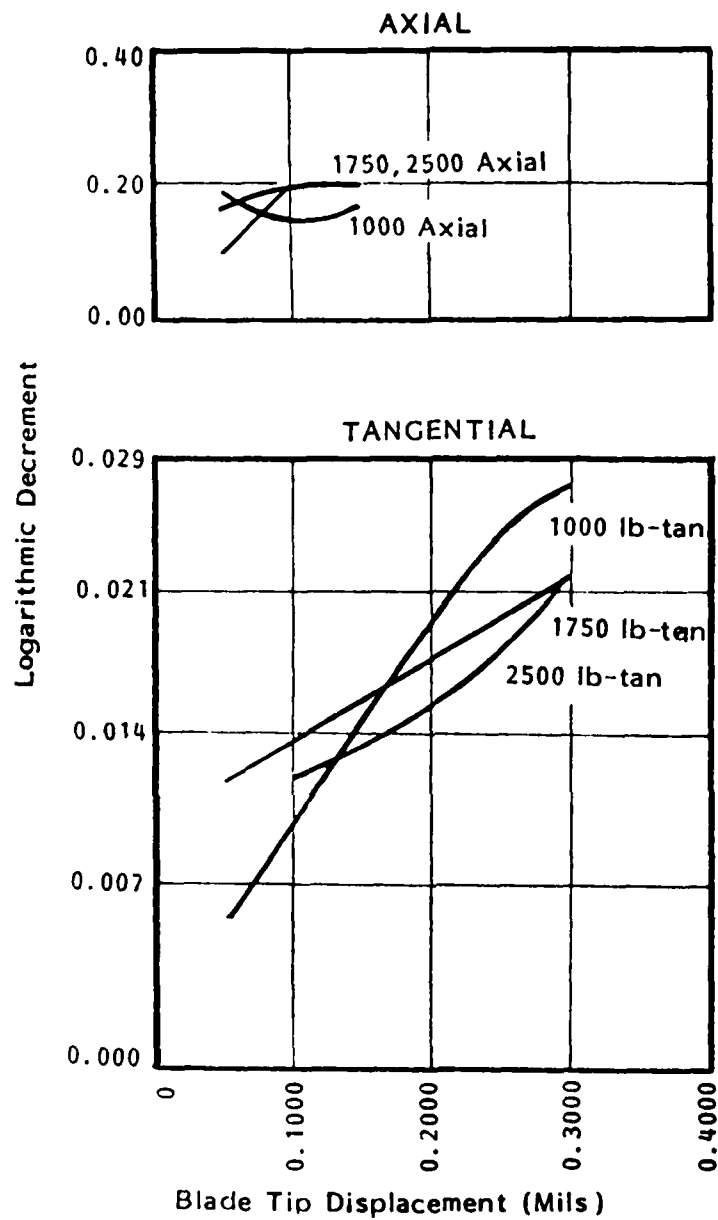


Figure 10 Logarithmic Decrement vs. Blade Tip Displacement and Centrifugal Load - Short Shank 4" High Pressure Blade Pairs

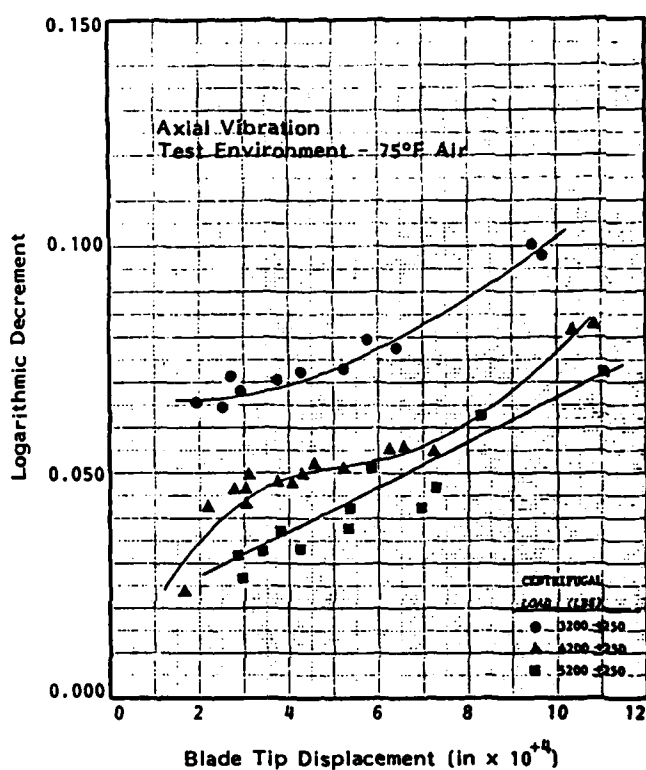
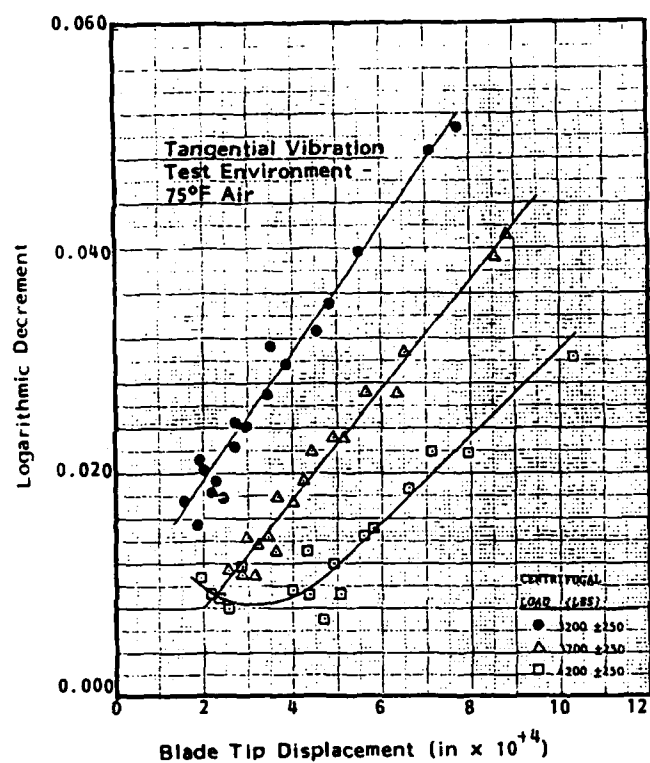


Figure 11 Logarithmic Decrement vs. Blade Tip Displacement and Centrifugal Load - 6" Axial Entry Fir Tree Root, Intermediate Pressure Blade



**Figure 12 25" Curved Axial Entry Fir Tree Root Low
Pressure Blade Pair**

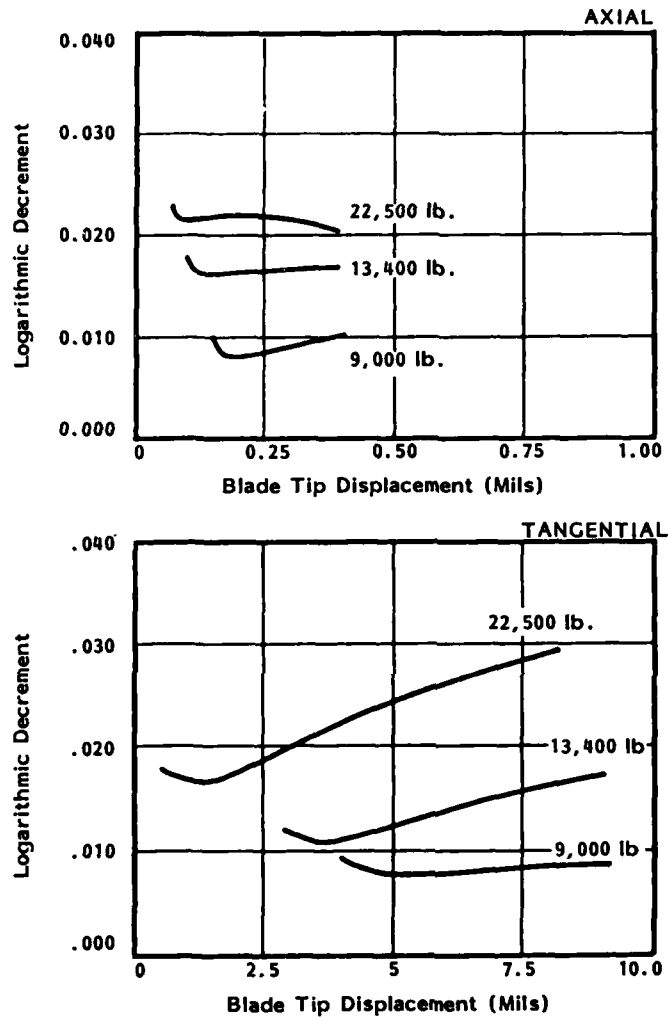


Figure 13 Logarithmic Decrement vs. Blade Tip Displacement and Centrifugal Load - 25" Fir Tree Root - Curved Axial Entry - Low Pressure Blade

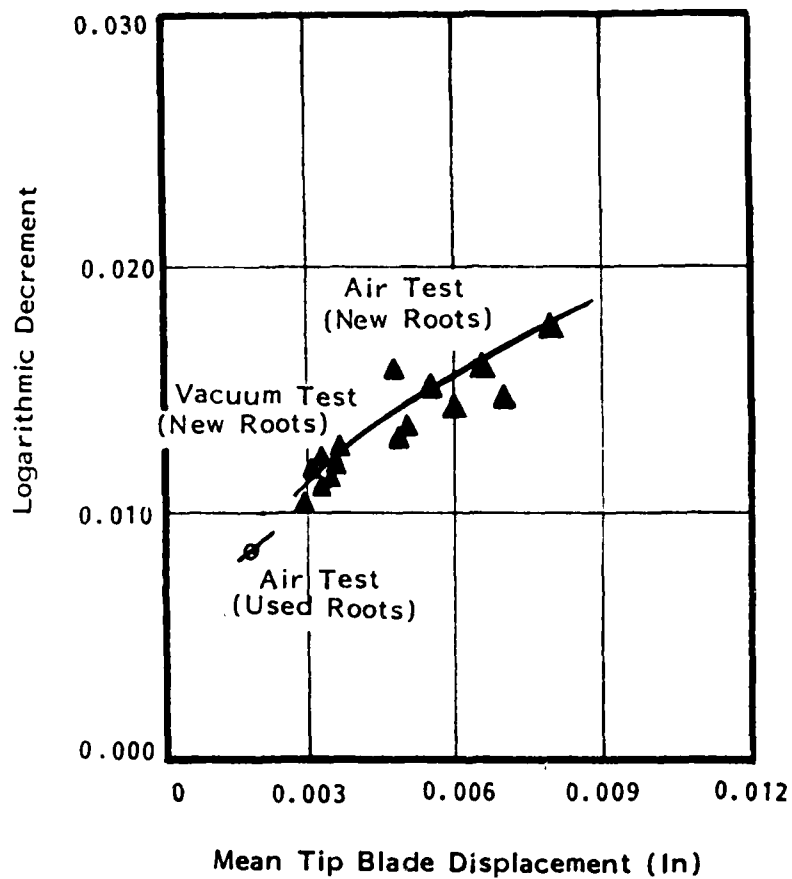


Figure 14 Environmental Effects - Log. Dec. vs. Tip Displacement - Tangential-Air/Vacuum/Steam - 9000 lbs. - 25" Curved Axial Entry, Fir Tree Low Pressure Blade

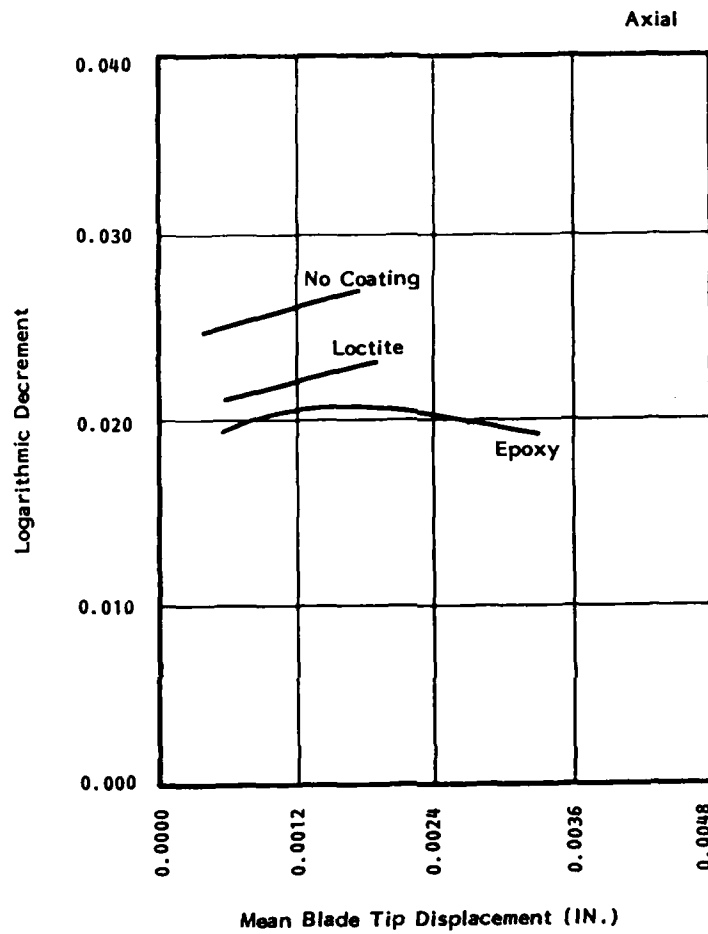


Figure 15 Root Coatings Comparison - Log. Dec. vs. Tip Displacement - Axial - 13,400 lb - 25" Curved Axial Entry, Fir Tree Root Low Pressure Blade

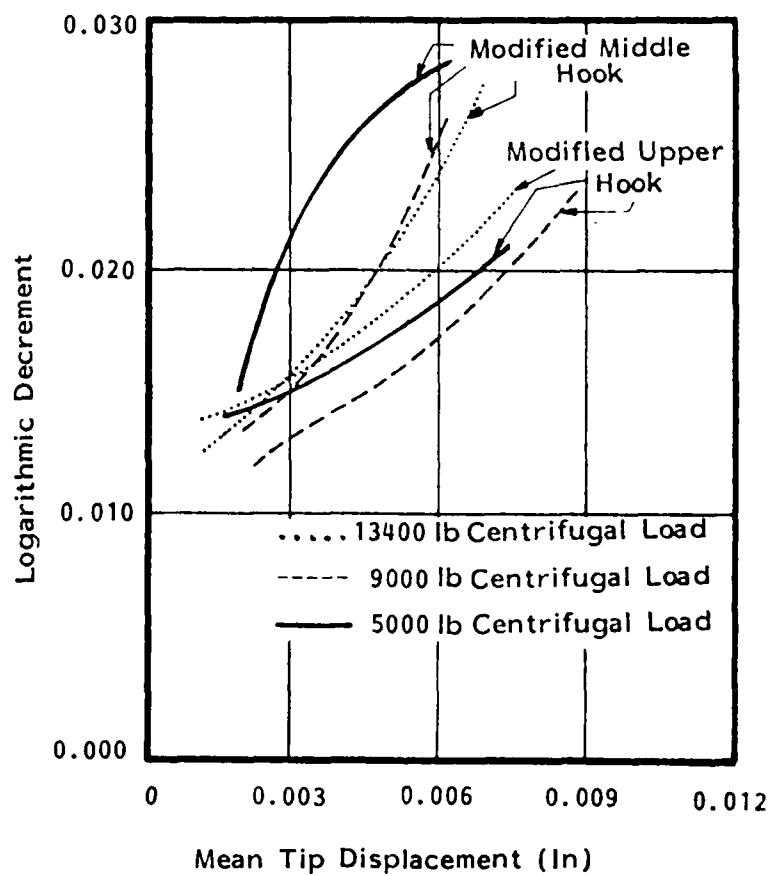


Figure 16 Modified Root Load Study - Log. Dec. vs. Tip Displacement Tangential 25", Curved Axial Entry, Fir Tree Root, Low Pressure Blade

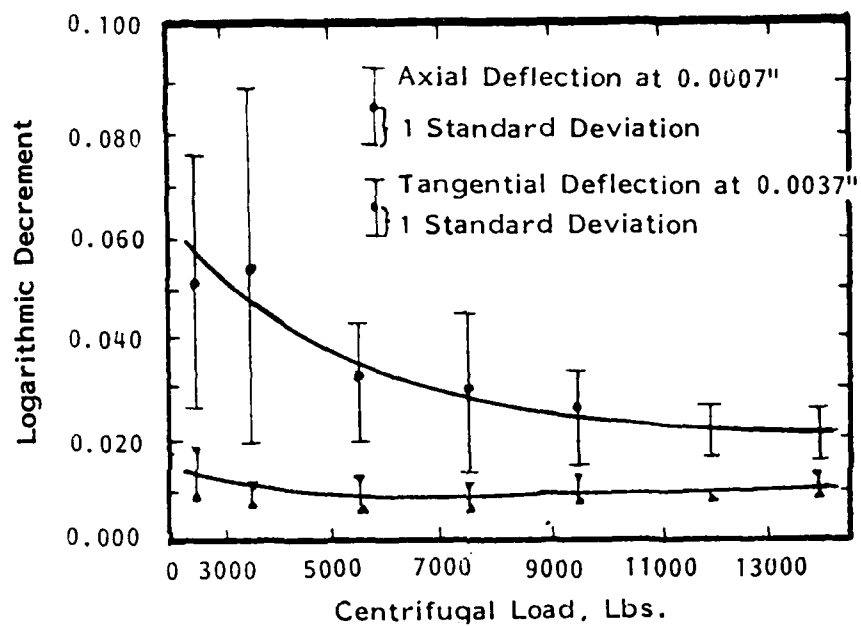


Figure 17 Variation of Damping with Preload Showing Limits of Data Scatter. 25 inch LP Curved Axial Fir Tree Entry Blade Pair. Specified Vibratory Amplitudes.

WD-A152 547

VIBRATION DAMPING WORKSHOP PROCEEDINGS HELD AT LONG
BEACH CALIFORNIA ON 2. (U) AIR FORCE WRIGHT
AERONAUTICAL LABS WRIGHT-PATTERSON AFB OH L ROGERS

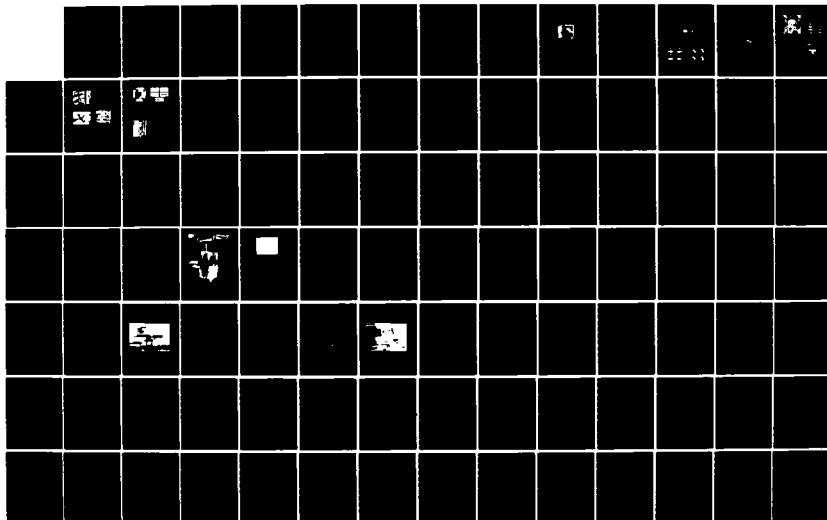
3/11

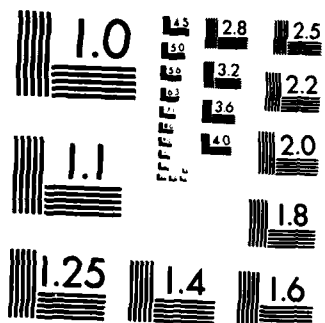
UNCLASSIFIED

11 NOV 84 AFMAL-TR-84-3064

F/G 20/11

NL





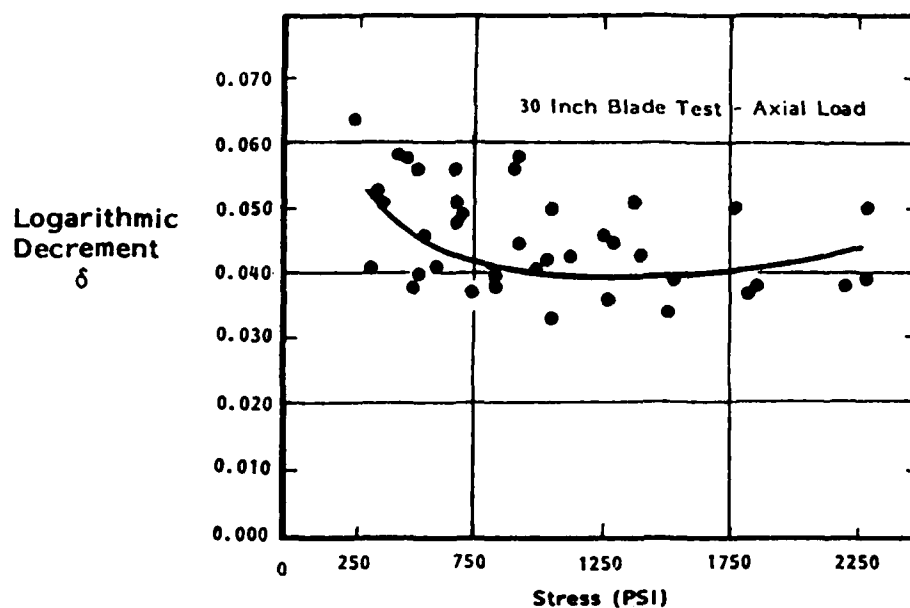


Figure 18 Variation of Damping with Vibratory Stress. 30 inch LP Blade Pair. Axial Vibration, Curved Axial Entry Root, Preload 22,500 lb.

CONCEPTS AND EFFECTS OF DAMPING IN ISOLATORS

James Kerley
NASA/Goddard Space Flight Center
Greenbelt, Maryland 20771

CONCEPTS AND EFFECTS OF DAMPING IN ISOLATORS

James Kerley
NASA/Goddard Space Flight Center
Greenbelt, Maryland 20771

ABSTRACT

The hallmark of engineering has always been creative, inventive design. This paper presents a series of innovative designs and inventions that has led to the solution of many aerospace vibration and shock problems through damping techniques. In particular, the design of damped airborne structures has presented a need for such creative innovation. The primary concern has been to discover just what concepts were necessary for good structural damping. Once these concepts were determined and converted into basic principles, the design of hardware followed.

INTRODUCTION

The concepts of damping in isolators were first arrived at through work with sandwich panels. The sandwich panels were formed into isolators and then bent into a form to give three-dimensional isolation. The solid metal in the sandwich was eliminated, and sandwich panels of steel wire and plastics were formed. The steel wire was replaced with cable in the plastic, and finally, the cable by itself was used as a medium of structural damping and isolation in three planes.

The concepts converted into basic principles were (1) heavy damping at low frequency with no damping at high frequency, (2) the structural damping medium to be formed in such a way to give isolation in all three planes, (3) the ability to take shock, vibration, and steady-state loads simultaneously without changing damping characteristics, and (4) designing the damped structure so that it could be analyzed and tested to ensure reliable performance in the service environment.

Based on these principles, the following hardware and techniques were developed in support of aerospace program requirements:

- Shipping containers
- Alignment cables for precision mechanisms
- Isolation of small components such as relays and flight instruments
- Isolation for heavy-flight equipment
- Coupling devices
- Universal joints

- Use of wire mesh to replace cable
- Isolation of 160-dB, 5000-lb horn
- Compound damping devices to get better isolation from shock and vibration in a high steady-state environment

DISCUSSION

As shown in Figure 1, in solving problems in the design of isolation systems, the designer must consider the entire vibration field. The isolation problems of an automobile are less difficult to solve than those of a spacecraft. The isolation of an automobile begins with the frame, and this fact solves many problems. An automobile does not have to fly upside down as does a spacecraft. The designer must use a different approach in the isolation of a spacecraft since its entire frame cannot be isolated. Therefore, it was decided to try first to isolate a complete compartment.

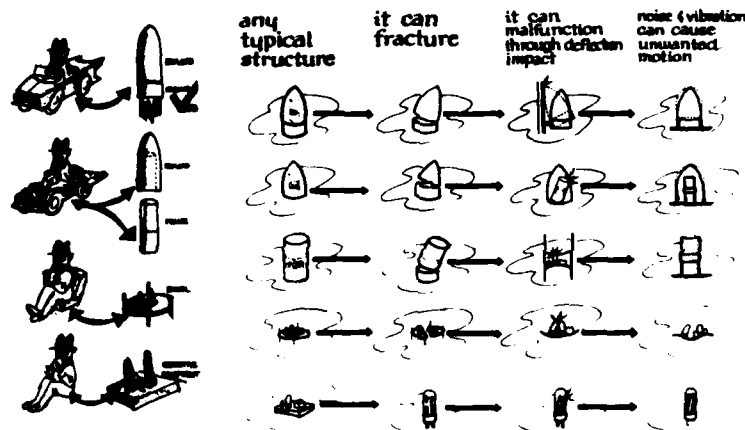


Figure 1. Overall problem of designing damping into a system.

Figure 1 is divided into entire structure, payload, frame, panel, and sensitive equipment. The problems of isolation are listed on the right side. The first attempt is to isolate the frame. As can be seen from the figure, the structure could fracture and break. It could also malfunction if it bangs against another piece of hardware. This is a major problem with isolators. If it is not designed properly, the isolator could cause this banging. Finally, noise and vibration can get through to the entire structure. The isolators must be three-dimensional and handle steady-state loads at the same time in order to isolate from shock and vibration loads.

The first attempt at isolation is shown at the top of Figure 2. Commercially available were sandwich panels composed of aluminum on the outside and plastic on the inside. A box structure was made of this configuration. The damping was good, but it was further improved by fabricating our own panels that were aluminum on the inside and a plastic called saran on the outside. Although the damping was very good, it was obviously too heavy for space flight. The next step was to form

a straight aluminum box and make a central panel of sandwich construction (aluminum on the inside and saran on the outside). This isolation was good except in the edge planes, and it was difficult to mount anything on the saran. Thus, the configuration was changed to that shown at the bottom of Figure 2, which shows a straight aluminum panel with equipment mounted on it. At the edges of the panel were quarter-round sandwich bent panels with aluminum in the center and saran on the outside.

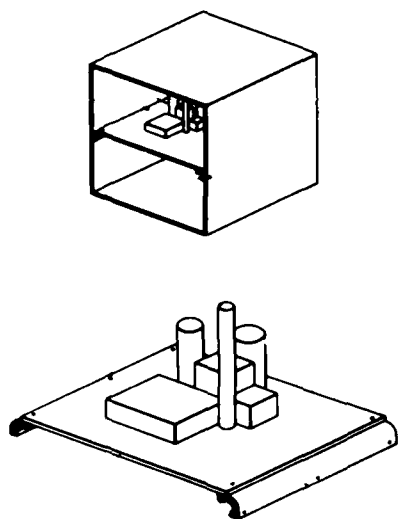


Figure 2. Sandwich damping in panels, frames, and curved mounts.

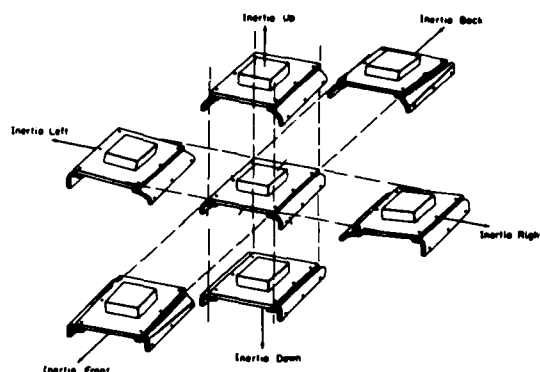


Figure 3. Dynamic motion of curved, mounted panels.

The motion of this system is indicated in Figure 3 by the lines drawn up and down, front and back, and sideways. The quarter-round sandwich-core material was always in bending, allowing for good isolation. However, two problems existed: the metal would fatigue, and vibration was still evident in the edge plane of the panel.

The internal stresses caused by this type of motion are shown in Figure 4. It is evident from these figures that the stress concentration at the end of the aluminum was quite high. To reduce this extreme motion at the edges, bumpers were constructed to slow this motion down. They are shown in Figure 5.

The motion was still too severe; therefore, other forms of sandwich core were constructed to get good isolation in all three planes and reduce the metal fatigue. The center row of Figure 6 shows all the quarter-round forms. On the left is the typical metal in the middle. Next is the metal on the inside and saran on the outside. Following this was the metal on the outside and saran on the inside. Last was the sandwich construction of metal on the outsides and saran on the inside. All of these types of sandwich-core materials were made in different forms: quarter round, question mark, and "W" formations. The question mark form was eliminated because it banged against the side too easily. The quarter round ended up where it started with the saran on the outside and the aluminum inside. Of the four "W" forms, the best was the saran on the outside and the aluminum inside.

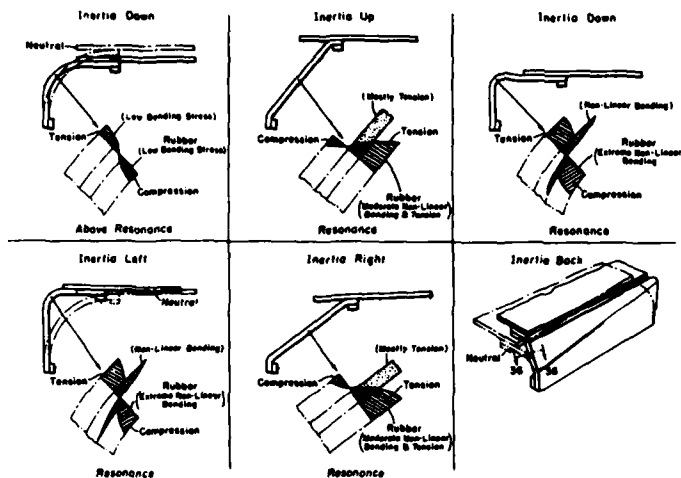


Figure 4. Internal stress condition of curved sandwich panels.

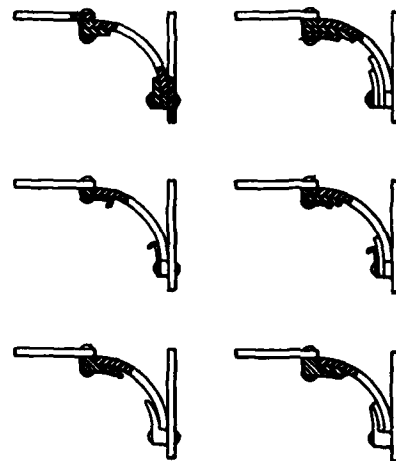


Figure 5. Bumpers to reduce deflections.

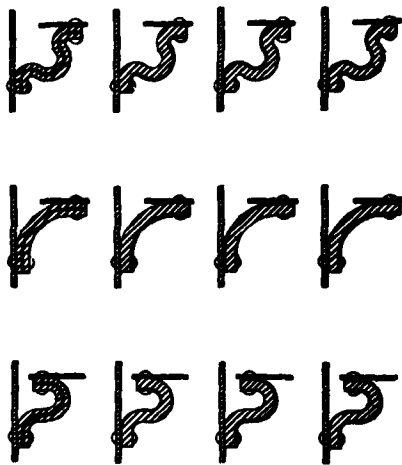


Figure 6. Special forms of sandwich mounts.

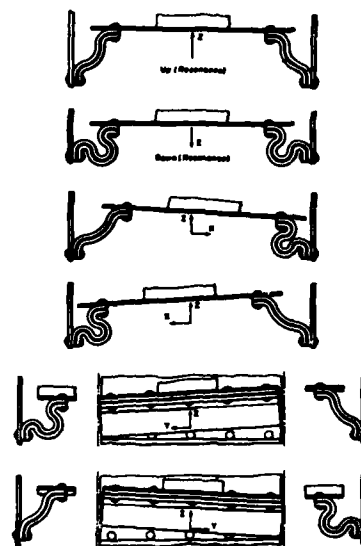


Figure 7. Dynamic motion of best mount.

This final solution was tested and is shown in Figure 7. The fatigue life was increased as the "W" form relieved the stress concentration at the edges. However, there were still problems because the metal would fatigue in the center.

It must be kept in mind that these were all good shock and vibration systems. The purpose of this study was to find a universal solution to any shock and vibration problem that could arise. The advantage of these first systems is that they could be bent up, glued together, and made overnight for a quick isolation job, particularly where a heavy-shock load was present.

To solve the fatigue problem, the metal was cut in the center into strips and was glued between two pieces of saran. Although this isolation worked well, it eventually developed fatigue problems. High-strength wire was substituted for the metal strips, but they would eventually fatigue. A piece of cable was chosen by chance; although not expecting it to work well, it was known that it could handle the fatigue problem. The cable was glued between two pieces of saran and mounted on the panel. It was immediately obvious that this was the motion that was under control (see the bottom of Figure 8).

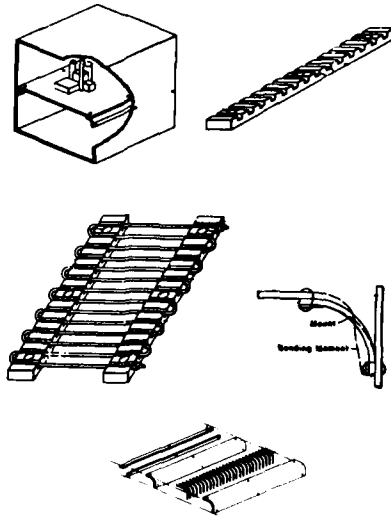


Figure 8. Cable sandwiched between two pieces of plastic.

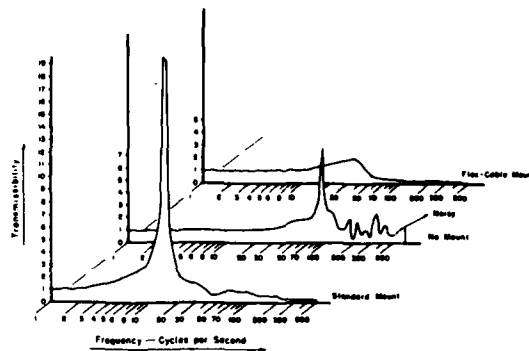


Figure 9. Dynamic response curves of rubber, plain, and cable mounts.

Because it was difficult to cut the individual cables, a frame was made to hold the cables as shown and was mounted at the end of the panels. The isolation is shown in Figure 9. In the front is the transmissibility function of a standard mount. Standard mounts worked well except at resonance where they would bottom out and cause a tremendous shock to the entire structure. The center transmissibility curve shows a frame without isolators with many resonant points. In the back is the saran cable isolation system. The transmissibility was 2 to 3 at resonance, and then it diminished gradually without rising again. The specification called for 4 g's from 20 to 35 Hz and 20 g's from 35 to 2000 Hz sine testing.

The foregoing system demonstrated the following:

- All three planes had good isolation.
- High damping existed at resonance and little or no damping at high frequencies.
- The isolator was good for both shock and vibration loads.
- Preliminary tests demonstrated that the isolation was good in the presence of high steady-state loads.

There were some problems that still had to be solved. The saran was too stiff at low frequencies and too limber at high frequencies. It was also subject to deterioration under many chemical contacts. Fabrication continued to cause problems. Many different types of plastics were used: natural rubber, Teflon, etc. It was known then that the only good universal solution was to make the isolators of cable without the saran.

For many months, many forms of all-cable isolators were made, but they failed one after the other, usually because they would be stable in two planes but would become unstable in the third plane. Finally, it was observed that the only system would be a cable system that had uniform geometry in all planes except in the front and back. This is illustrated in Figure 10.

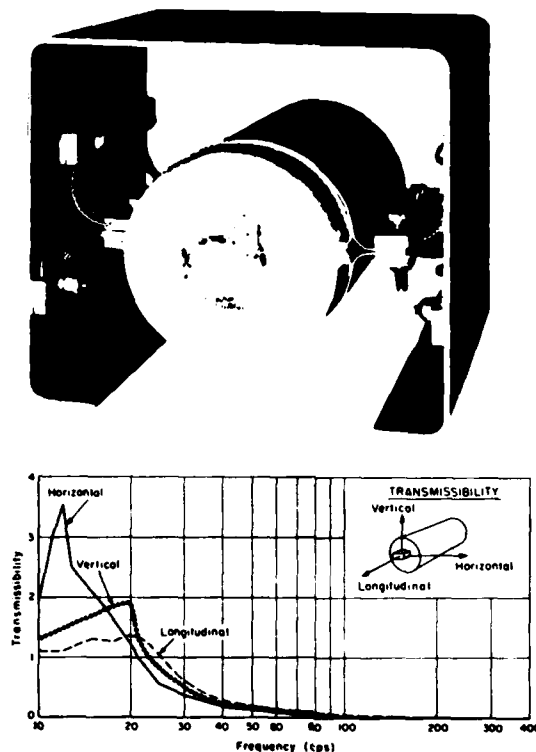


Figure 10. First and most recent use of all-cable mounts.

Quarter-round cable mounts were mounted top and bottom on both ends of the mounting panel. This was a symmetrical mounting system that provided good isolation in all three planes. The transmissibility response functions are plotted below the picture. This was the first all-cable isolator used in flight, and it mounted on a true air-speed indicator. It worked well during flight and was used in both spacecraft and airplanes. It is interesting to note that Aeroflex Laboratories, Inc., Plainview, Long Island, New York, has recently revived this invention, and they are using it for shelf mounting where difficult shock and vibration loads exist. It is cheaper to use cable isolators than to weld the shelves. This approach is published in the October 10, 1983, issue of "Design News."

Calculating the response with different weights and different specifications became a difficult task. Every job became a major design project. It was decided that a more uniform isolation system would have to be made of all cables and should be easily adapted to any shock, vibration, load, or difficult environment that could be found in space use.

After many trials with different forms of cable, a system was found that performed the job. It is shown in Figure 11. The upper left "A" shows a perspective of the overall system, and "B" is the end view showing the versatility of the system. The cables could be straight, or they could be stiffened to give a higher frequency, right on the spot. "C" shows the opposite as the cables can be crimped to give a low-frequency response. "D" shows the way the mounts could be constructed to give this versatility.

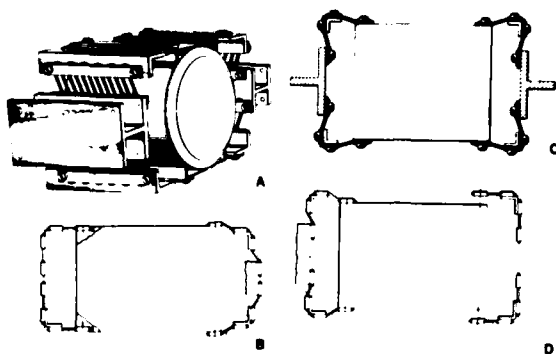


Figure 11. Use of corner angle with cable to control frequency and damping.

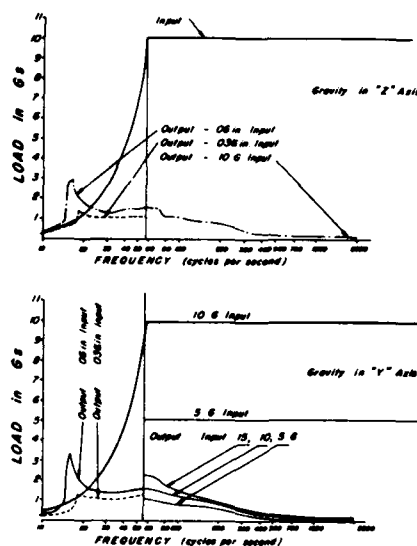


Figure 12. Vibration in two different planes noting the same natural frequency and the same damping.

By adjusting the cables in and out, it was possible to give the same amount of damping and the same natural frequency in all three planes. This is illustrated by the transmissibility curves shown in Figure 12. The natural frequency in two planes is about 16 Hz, and the magnification factor "Q" is about 3 in both planes. For the first time in the history of isolation, there was a damped spring system that had the same response in "Q," which meant the same damping and the same natural frequency in all three planes. This meant that no matter in what plane the structure was pushed, it would respond the same way. This simplified the mathematics and made day-by-day work an easy task to accomplish. It solved many problems such as rate gyros that had to respond the same in all three planes. This was the first isolation system which was a true "design tool."

Figure 13 shows a comparison of rubber response with cable response. The rubber responds differently in tension, compression, and shear. The cable mounts always bring about a shearing action that causes the cable to bend. Thus, it is possible to have the same response in all three planes.

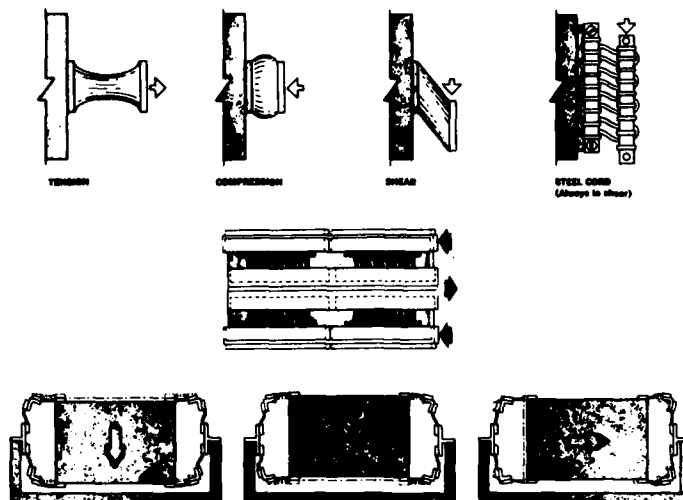


Figure 13. Deflections of rubber and steel cable (cord).

Figure 14 shows the first form of versatility for this type of configuration. With the cables pushed out as they are shown in "A," they are quite limber and have a low natural frequency and a considerable amount of damping. When the cables are pulled in as shown in "C," they become quite stiff with much less damping. This is a design tool since it is possible to adjust the natural frequency a full octave the night before testing. A few shims will adjust the cables and give the right natural frequency right on the flight line.

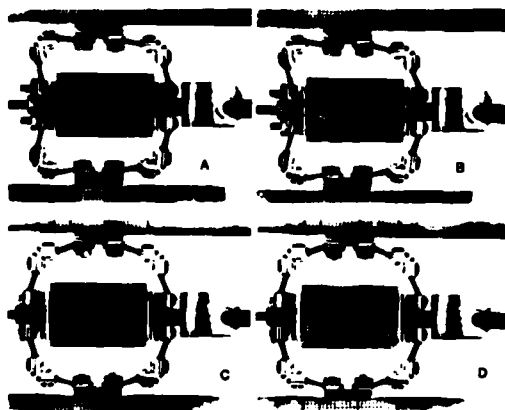


Figure 14. Different deflections caused by different preform.

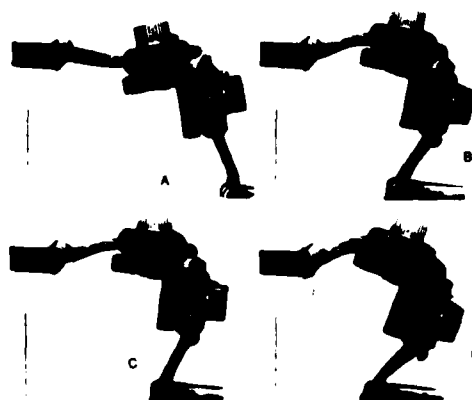


Figure 15. Angle rotation and damping during vibration.

Not illustrated here are the many cases in which the isolator can be made stiff in two planes and limber in the third plane. In this way, any motion in the stiff plane will be diverted into the third plane. This is controlled motion isolation. This is necessary when the designer is called in to isolate a black box already installed in a missile or airplane, and the motion is limited to one plane only. It can be isolated.

Figure 15 is an example of macrophotography used to study the motion of cable during isolation. Note the large rotation of the angle with motion to the cable. Many strands of cable rub against many more strands, and the damping controls the motion.

Figure 16 shows a typical hysteresis curve of the average isolation system. This response is nonlinear with respect to both stiffness and damping, but it is repeatable and consistent. The natural frequency can be predicted within ± 5 percent.

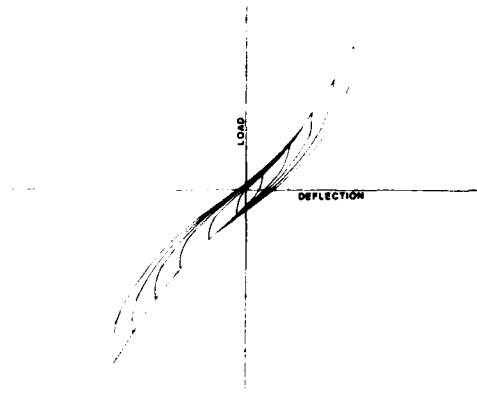


Figure 16. Load deflection curve for soft cable system.

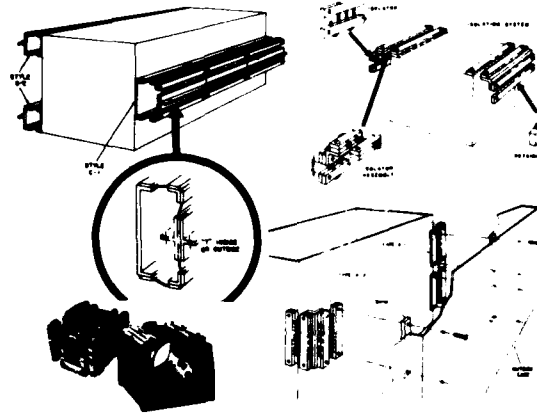


Figure 17. Applications of cable systems.

Figure 17 shows some of the installations of the systems that performed well in flight. The upper left shows rack-mounting systems. The upper right shows the top and bottom mounting system. The lower right shows side mounting. The lower left shows a field installation of a gyro and a radar altimeter for flight use. All performed well.

Figure 18 is a picture of the Goddard Space Flight Center (GSFC) noise horn weighing 5000 pounds. The frame weighs 5000 pounds, and both are mounted on Aeroflex cable isolators (see arrow).

Many ways were studied to increase the damping in the cable. Figure 19 shows a series of macrophotographs of cable under bending conditions. It was noted how the cable strands opened during this bending and ways were sought to prevent it. It was discovered that a slight twist to the cable while stringing it caused the outer strands to close and the independent wire rope core (IWRC) to expand. This action would force cables against cables and make more contact points. With more contact points, the damping increased considerably. Too much pretwist would cause the IWRC to pop out.

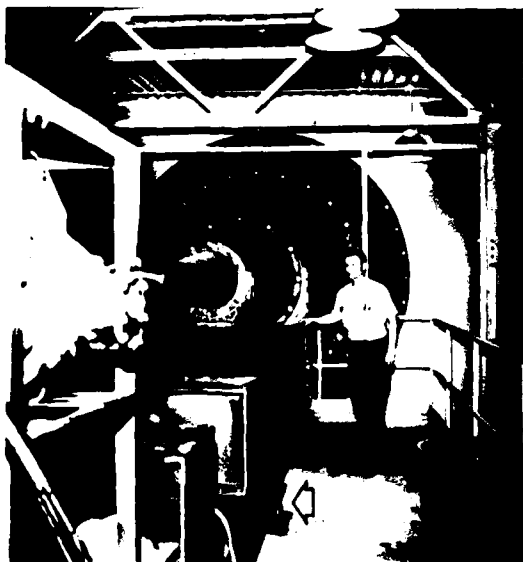


Figure 18. Mounting of 5000-lb horn and frame with cables.

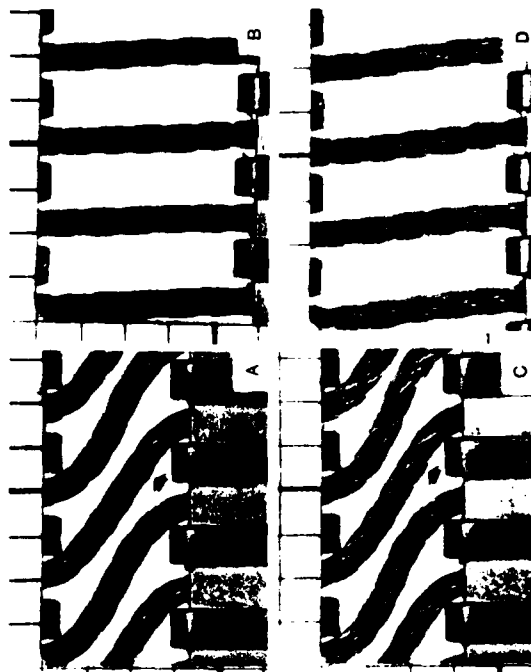


Figure 19. Cable opening during bending.

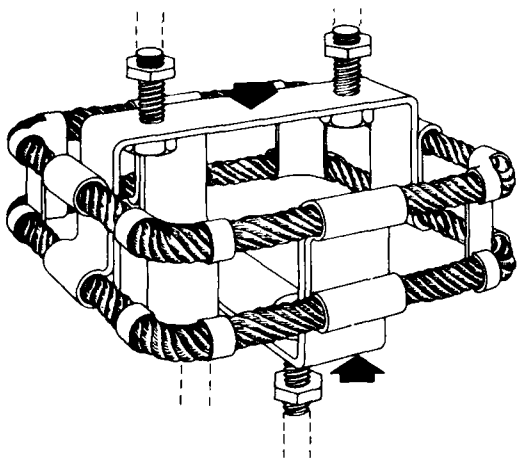


Figure 20. Single-cable mounting system.



Figure 21. Isolating with heavy preload.

For economy and efficiency, it was considered necessary to make a mount that would be easily installed anywhere. This new invention is shown in Figure 20. Note that the typical angles are still there. There are four corners to prestress the cables either in or out, etc. It is made of stamped metal for economy, and it is easily mounted under, over, or at the side of any piece of equipment.

Figure 21 shows an application of this mount. Relays were causing a problem at GSFC, and a method of isolation had to be worked out to prevent the chatter. Note that the finger is pushing down on the isolator while it is going through vibration. This push simulates the steady-state load that exists when a fast rocket takes off.

The response curves are shown in Figure 22. Note that the natural frequency without steady-state loads is approximately 23 Hz. With the 15-g load, the natural frequency jumped up to 28 Hz. There is only a slight change in the natural frequency with the addition of a severe steady-state load. Also note that the "Q" or magnification factor at resonance is less because more cables are rubbing against themselves to create better damping. This system performed quite well.

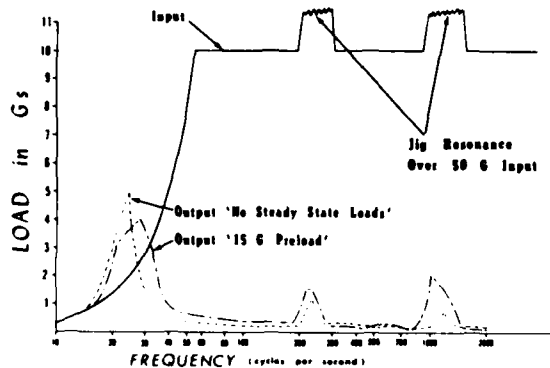


Figure 22. Response function of isolation with 15-g preload.

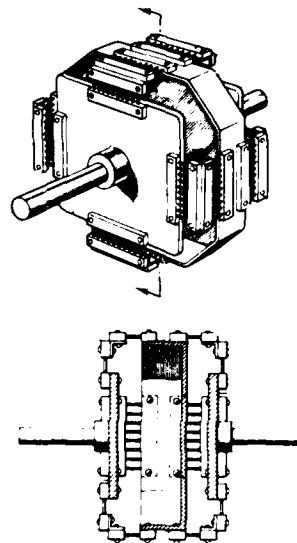


Figure 23. Heavily damped coupling systems.

Now that it could be established that the cable isolators could work just as well with or without steady-state loads applied at the same time, it became apparent that they could be used in coupling devices. Figure 23 shows such a coupling system of cable. This system not only corrects for misalignment but also isolates from shock and vibration any load that tries to get through the coupling. Note that there is a floating element in the center of the coupling. This floating element allows a greater degree of rotation, and it offers an additional barrier to vibration.

Another example is the use of Aeroflex isolators (Figure 24) to act as a coupling of the Launch Phase Simulator at GSFC. This coupling brings out a smooth motion where a metal coupling caused constant jerking.

Another use of couplings is shown in Figure 25. The upper coupling is quite flexible. It will take a lot of misalignment, but it will not take heavy loads. The lower couplings are not as well isolated, but they take much higher torque forces.

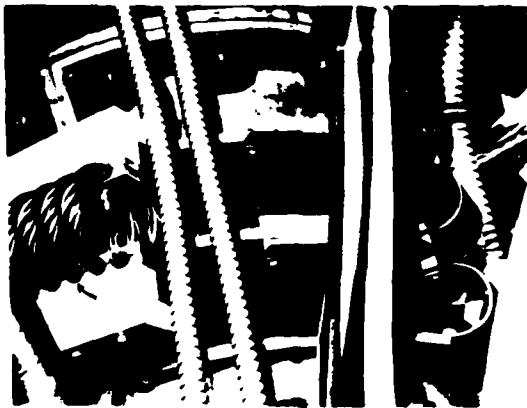


Figure 24. Application of coupling with good damping.

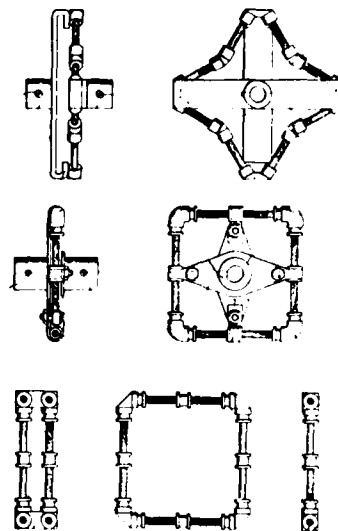


Figure 25. Coupling systems with damping.



Figure 26. Coupling system with damping.

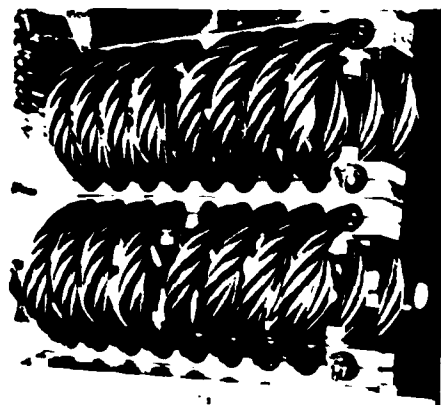


Figure 27. Compound cable systems.

Another coupling designed for GSFC is shown in Figure 26. This is the simplest of all the designs but must be designed by an engineer. This coupling is different from the rest in that it used a centering device.

Another need arose when it was discovered that compound systems were necessary for additional isolation. The compound isolation systems would lower the natural frequency and increase the damping. The one shown in Figure 27 is on the Launch Phase Simulator at GSFC.

Figure 28 shows another use of a compound system. The device is a g-negation device that is mounted in a spacecraft which goes into free fall to study component actions. After the free fall, it must be stopped without damaging the spacecraft. The cable compound system gave a simple single-degree-of-freedom well-damped motion.

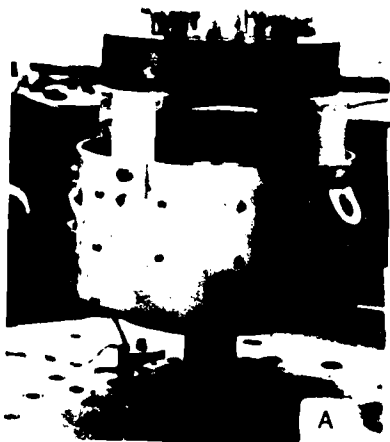


Figure 28. Compound cable systems.

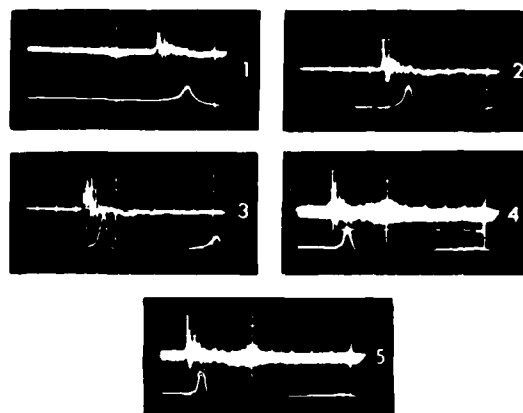


Figure 29. Shocks from 30 g's to 100 g's on cable systems.

Shock loads with the cable isolation system are shown in Figure 29. These shocks range from 30 g's in part 1 to over 100 g's in part 5. The scale on the oscilloscope has been changed to accommodate the signal. Note that the only response was a single-cycle, well-damped response. There is no bottoming out or any secondary responses.

Once it had been established that shocks could be mitigated, it was obvious that the shocks from an electric or pneumatic hammer could be isolated from the handle. Figure 30 shows such an installation. After a few years of use, the operators of these hammers complain of nerve loss in the wrists.

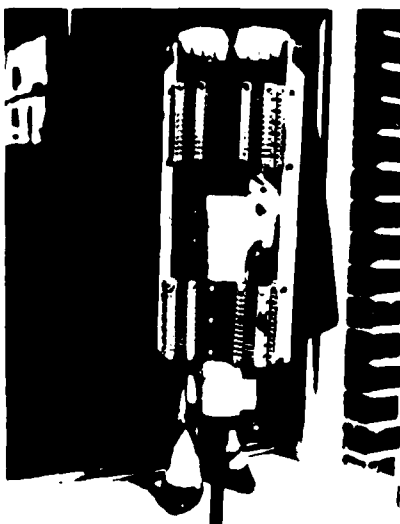


Figure 30. Isolation through damping of electric hammer.

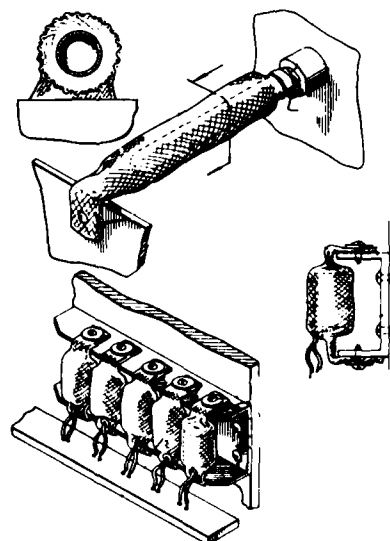


Figure 31. Damping isolation through wire mesh.

This isolation system takes the shock off the wrists. Furthermore, by pushing down on the handle (to simulate steady-state loads on top of shock), the chisel point is kept closer to the cement and drills through a concrete slab twice as fast as it would if the hammer were held loosely and allowed to bounce. This could be applied to gun mounts, drilling rigs for mines, or oil rigs.

When a sensitive piece of equipment to be flown the next day had to be isolated during the night, there was no time to build a cable isolator. A piece of wire mesh was opened up, the instrument placed inside, the ends crimped to simulate the motion of a cable isolator, and then was mounted on a small frame (see Figure 31). The principles of operation were that the wires were rubbing against each other as they would in a cable system. The wire mesh was formed in such manner to preload the mounted system. It worked well in flight. Figure 31 shows that any form of wire can be used (not necessarily cable). If wire rubs against wire, the resulting system gives restrained motion in all three planes.

Figure 32 is a sketch of the design tool of cable isolation systems. These curves represent the installations of Figures 11 through 17 and Figures 19 and 22. If the cable is kept in the neutral position, the damping curve is drawn from the original hysteresis curve as shown in Figure 16. If the cable is pulled tight, the hard curves are superimposed on the average system. If the natural frequency is raised, there is less damping because there is less motion and less rubbing of wire against wire. If the system is made more limber, the soft curves apply as shown in Figure 32. If there is more damping, the natural frequency goes down. The natural frequency of a system can be doubled by changing the form of the cable. It is easy to see now what a design tool the cable systems are. The cables can be stacked one isolator on top of the other as shown in Figure 17. Thus, if the designer desires the same natural frequency with more damping, he simply adds another layer of cables. They are all bolted together.

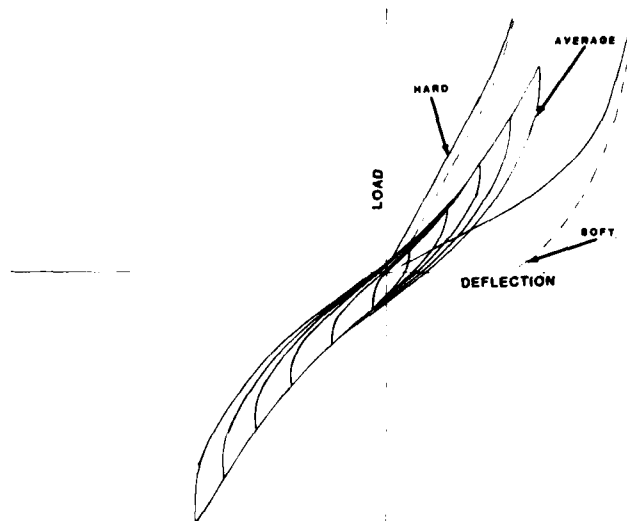


Figure 32. Damping and stiffness as a design tool.

RESEARCH ON FRICTION DAMPING IN JET ENGINES
AT CARNEGIE-MELLON UNIVERSITY

J. H. Griffin and J. Bielak

Carnegie-Mellon University
Pittsburgh, Pennsylvania 15213

RESEARCH ON FRICTION DAMPING IN JET ENGINES AT CARNEGIE-MELLON UNIVERSITY

by

J. H. Griffin and J. Bielak
Carnegie-Mellon University
Pittsburgh, Pennsylvania 15213

ABSTRACT

This paper discusses the results of recent research on friction damping at Carnegie-Mellon University. Topics include: mistuning/friction interaction, flutter stabilization, the use of the finite element method to calculate the forced response of structures containing friction interfaces, and improved methods for modeling friction.

1 INTRODUCTION

The the main objective of this paper is to summarize recent research at Carnegie-Mellon University on how friction can affect vibration in jet engines. Understanding friction is an important step in the development of the next generation of analytical tools that will be used by engine designers. These tools will serve to predict not only the frequency and mode shape of the response of an engine part but also its magnitude.

The work discussed in this paper falls into two categories: one is applications oriented and the other is more fundamental and seeks to improve our basic understanding of the nature of friction and its modeling. The first category deals, for instance, with the analysis of stage vibration, and uses very simple dynamic models consisting of springs, masses and dashpots to represent the various structural components of a system. These simple, lumped parameter models are used to address issues such as, how blade mistuning affects the selection of a friction damper slip load or to what extent friction dampers can be used to control flutter. The lumped parameter models are easy to analyze and in spite of their simplicity provide physical insight and a qualitative, and under certain conditions, even a quantitative measure of the behavior of actual systems.

The following basic issues will be addressed in the second part of the present work: (a) what are the limitations of such relatively simple models and (b) how can they be improved when this becomes necessary. Basically, improvements are of two types, improved models of the structure and improved methods of modeling the effect of the friction interface.

The paper is divided into the following sections. In Section 2 we consider applications to stage dynamics, including discussions of (a) how blade mistuning influences the design of blade-to-blade friction dampers when these are used to control resonant response and (b) how friction can be used to stabilize flutter. Several methods that can be used for improving the structural and friction interface models are considered in Section 3.

2 APPLICATIONS TO STAGE DYNAMICS

2.1 THE INFLUENCE OF MISTUNING ON THE DESIGN OF BLADE-TO-BLADE DAMPERS

2.1.1 PRELIMINARY DISCUSSION

Friction dampers are devices that are used to connect points that experience a significant amount of relative motion when the stage vibrates. They transmit a force through a friction contact which slips and dissipates energy if the motion is sufficiently large. If the normal load on the friction joint is increased, the vibration must also increase for slip to occur; however, more energy may then be dissipated. The normal load that results in the lowest resonant stress and the amount by which the stress will be reduced are the two most important issues faced by the engineer in designing these devices.

Two types of dampers are used in practice, blade-to-ground (BG) and blade-to-blade (BB). BG dampers link a point on the blade, such as the platform, to a point which experiences little or no motion, such as the coverplate. In this instance, each blade and damper can be analyzed as a subsystem independent of the other blades on the disk [1]. BB dampers, on the other hand, link each blade to its neighbors; energy then is dissipated only if the blades experience relative motion. Hence, in this case, the bladed disk must be analyzed as a system.

2.1.2 EQUIVALENT SINGLE DEGREE OF FREEDOM (SDF) SYSTEM

If a bladed disk is "tuned" each blade has identical dynamic properties. If, in addition, the disk is excited by static pressure fluctuations then it can be shown that all blades will have the same vibratory amplitude and that their response will differ only by a constant phase angle. Under these conditions the system exhibits the same behavior as a single blade with an equivalent BG damper [2]. The optimum slip load and how much the amplitude can be reduced are readily calculated using the techniques developed for BG dampers [1]. An important question is to find out to what extent these values apply if the blades are mistuned.

2.1.3 RESPONSE OF A MISTUNED DISK

In this study mistuning is simulated by allowing the blade frequencies to vary around the disk. When a bladed disk is mistuned the amplitudes and interblade phase angles are no longer uniform. Of particular interest is how the amplitude of the highest responding blade is affected as the damper slip load is changed since it is this "worst" blade that will fail first.

In these simulations the amplitude and phase of the blades are calculated at each frequency using the method of harmonic balance [2] which takes into account the nonlinear and linear forces acting on the blades. For a given slip load the frequency is incremented (representing a slow engine acceleration) until each blade experiences a maximum amplitude. This process is repeated over a range of slip loads until the optimum slip load is obtained; this is the slip load that minimizes the amplitude of the worst blade. These values of amplitude reduction and optimum slip load are then compared with values calculated from tuned system theory, the SDF model.

2.1.4 RESULTS AND CONCLUSIONS

Two cases were studied extensively, alternate mistuning and random mistuning of an eight-bladed disk. For each of these cases the amplitude reduction and optimum slip load were calculated for a range of system parameters. In all instances the tuned system values of amplitude reduction and optimum slip load from the SDF model provided a good approximation of amplitude reduction and optimum slip load corresponding to the worst blade on the mistuned disk.

This study suggests that mistuning may not directly alter the choice of optimum damper slip load used to suppress resonant response in bladed disks. *This means that a unique damper design may exist that would work equally well on any bladed disk of a particular nominal design, independently of how much blade frequencies vary around the disk.* Two points must be emphasized, however. First, mistuning must be taken into account in properly assessing the magnitude of the generalized force acting on the stage, since the optimum friction force is directly proportional to this quantity. Secondly, while the results of this study are encouraging, they are not definitive in that the response of only a few small systems has been studied. A more efficient computer code is currently being developed for studying assemblies with fifty to a hundred blades. It will be used to explore the extent to which the above result holds for larger systems.

2.2 THE USE OF FRICTION TO STABILIZE FLUTTER

2.2.1 SINGLE BLADE DYNAMICS

This work studies the feasibility of using a BG friction damper to stabilize flutter in blades. The response of an equivalent, single mode model in which the aerodynamic force is represented as negative viscous damping is determined in order to investigate the following issues: the range of amplitudes over which friction damping can stabilize the response, the maximum negative aerodynamic damping that can be stabilized in such a manner, the effect of simultaneous resonant excitation, and the determination of the optimum damping parameters for flutter control.

2.2.2 ANALYSIS AND RESULTS

Conceptually, this type of problem is quite different from those discussed in the previous sections since here we are dealing with a nonlinear eigenvalue problem in which both the frequency and the amplitude of the response are unknown (the phase of the response is arbitrary since the blade is self-excited).

However, the method of harmonic balance [3] can still be applied, and it is found that provided the aerodynamic damping is less than some maximum, there are two pairs of amplitude and frequency which satisfy the equations of motion. The solution corresponding to the larger amplitude is a stability limit. If this amplitude is exceeded during a transient the vibration increases in an unbounded fashion; otherwise the solution will damp out and approach the lower steady state solution. A non-dimensionalized plot which summarizes this result [3] is depicted in Figure 1. The quantity ζ_+ is the ratio of the negative aerodynamic damping to system critical damping, ϵ is the fraction of the system's stiffness due to the damper, and the amplitude, A , has been normalized so that the damper slips when A equals unity. As a result, the physical amplitude is proportional to the damper's slip load. Consequently, from a design point of view selecting the damper's slip load establishes the steady state amplitude of the blade (which must be limited to prevent high cycle fatigue) and the maximum transient response for which the blade will be stable (which should be as high as possible). Clearly, the selection of this parameter must be made by the designer with these trade-offs in mind. A second observation is that the maximum ζ_+ that can be stabilized is proportional to ϵ , the fraction of the system's stiffness due to the damper. As a result, increasing the dampers modal stiffness by either increasing its physical stiffness or by having it contact the blade at a point where there is more motion increases its effectiveness.

Lastly, the system is destabilized if the blade is simultaneously excited by an external harmonic excitation at the flutter frequency. Quantitative methods for assessing its effect are given in [3].

2.2.3 STAGE DYNAMICS

The analysis of how friction affects flutter in bladed disk assemblies, in which the blades are connected to their neighbors with friction dampers, is significantly more complex than the case of a single blade. Detailed procedures for analyzing

these systems are presented in [4] along with some results for three, four, and five bladed disks. As in the case of forced response, if the disk is tuned an equivalent SDF model exists for each tuned mode. However, additional solutions of the nonlinear eigenvalue problem also exist which are not associated with the tuned modes.

A primary goal of this work is to establish how large the vibration must be before the stage becomes unstable. Since a set of initial blade displacements and velocities is a vector which may be composed of many tuned modes it is not clear from the results of the nonlinear eigenvalue analysis whether or not an arbitrary set of initial conditions will result in a long-time solution that is stable or unbounded. This issue is addressed for a four bladed system by using a statistical simulation in the following manner. First, an approximate procedure is developed for calculating the maximum negative damping for which a specific initial condition leads to a bounded response. Initial conditions are then randomly generated and the associated maximum damping for which it can be stabilized is calculated. A measure of the vibration, the maximum amplitude of the worst blade on the rotor, can then be correlated with negative damping. It is shown that these data points correlate relatively well with stability curves of blade amplitude versus negative aerodynamic damping established from the nonlinear eigenvalue analysis. Thus, the results from the steady state analysis may be used to estimate how large the vibration in the blades must get before a stage with friction damping will become unstable. In fact, results from the four-bladed disk considered herein suggest that the least stable tuned mode provides a reasonable estimate of how large the amplitude of a blade must be for the response of bladed disks to become unstable (Figure 2).

3 IMPROVED METHODS

3.1 INTRODUCTION

This section deals with ways to improve the accuracy of the methods used to simulate friction effects in vibrating systems. The results of three studies are summarized. The first concentrates on improving the structural models of the linear subsystems by representing them with finite element models. The approach is to assume that the steady state response is essentially harmonic and keeps only the lowest frequency terms in a Fourier series expansion of the nonlinear force. It then uses receptances, calculated from a standard harmonic, finite element analysis of each substructure to reduce the problem to one involving only those degrees of freedom associated with the friction interface. The resulting set of nonlinear, algebraic equations for the interface unknowns are then solved by the method of harmonic balance. This is computationally an efficient approach since it isolates the nonlinear effects. Consequently, it offers a practical method for analyzing complex structures which require a finite element model to adequately simulate their structural behavior.

An important aspect of this approach is that the nonlinear friction force is accurately represented in terms of the interface degrees of freedom. As a first step the friction damper is modeled as a massless spring; in this case a Fourier series expansion for the friction force in terms of the interface motion is readily calculated which holds over the full range of possible damper slip loads. In order to generalize this approach so that multiple structures may be tied together with friction constraints it is necessary to remove the spring and consider the case in which the substructures are directly linked by friction constraints at some mutual nodes. Understanding how the systems behave when they are linked via a rigid slip joint is the subject of a second study.

In both of these cases the friction interface is modeled as a single point contact which slips when the magnitude of the force transmitted across the interface becomes equal to the coefficient of friction times the normal load. In the last study the possibility is considered that only part of the interface may be slipping. In this case "microslip" results in an altered force-deflection curve for the friction joint that, when expanded in a Fourier series, predicts quite a different response from that of a simple, single point contact joint. The microslip model is used to explain a number of experimental results that were previously not well understood.

3.2 STEADY STATE FINITE ELEMENT ANALYSES OF THE FORCED RESPONSE OF A FRICTIONALLY DAMPED BEAM

3.2.1 INTRODUCTION

This work includes two important features. The first is that it utilizes a linear, harmonic finite element analysis of the primary structure, with no friction element, to establish the beam's relevant response characteristics. The values are then used in a separate algorithm which solves the nonlinear problem as a function of the excitation frequency, slip load, and damper characteristics. This postprocessor can be made compatible with any standard finite element code and, consequently, forms the basis of a first generation of codes which can solve the steady state forced response problem of structures which incorporate friction interfaces.

A second feature of this work is that the approximate solution is compared with independently calculated "long-time" numerical solutions of the transient problem rather than with experimental data. There are two equally important points that need to be investigated when modeling nonlinear problems. Since solutions are nearly always approximate, one issue is whether or not they agree with an exact solution of the mathematical model. A second issue is whether or not the mathematical model accurately represents the physical system. Friction damping experiments are complicated, critical parameters frequently have to be inferred, and, yet, data rarely completely agree with the results predicted by analyses. One difficulty is that often it is not clear whether the discrepancy occurs because of inaccurate mathematical approximations or inaccurate physical models. This work

isolates the first issue by comparing solutions from the approximate method with "long-time" transient solutions of the same mathematical model which are exact except for negligible numerical round-off errors. A detailed description of this work is given in [5].

3.2.2 TECHNICAL APPROACH

A general linear structure is attached to a flexible friction element at a given point A. Using a finite element analysis of the structure without a damper the external excitation is calculated to produce a displacement at point A of u_E . Assuming that the total displacement at A is harmonic and given by u_T then the nonlinear friction force, f_N , is approximated by keeping only the first term in its Fourier series expansion. Thus, an expression is determined for f_N as a function of u_T , $f_N(u_T)$. This component of the nonlinear force is harmonic in time and, consequently, induces a simple sinusoidal response at point A. This can be evaluated by using the same finite element model of the linear structure and calculating the receptance of the structure at point A. Then the displacement induced by the damper reaction force is $u_N(f_N)$. Lastly, the fact that the total displacement is given by the sum of u_E and u_N gives the overall constraint, $u_T = u_E + u_N(f_N(u_T))$, which can be solved iteratively for u_T .

3.2.3 RESULTS AND CONCLUSIONS

Two cases were simulated corresponding to stiff and flexible dampers. Since the approximate method is exact for linear systems it yields the exact results for fully slipping and fully stuck conditions. It was found that the accuracy of the method was acceptable for the case of the essentially rigid damper and improved as the flexibility of the damper became more comparable to that of the test beam. Since the latter condition more closely represents engine hardware, this approach should prove accurate for analyzing frictionally damped turbine blades.

The results of the finite element analyses were also compared with those predicted by a single mode model [1]. It was found that the single mode model was accurate provided the damper is relatively flexible with respect to the blade and, consequently, the blade's mode shape does not change significantly as the slip load changes. Under these conditions an equivalent lumped parameter model of the system will adequately represent its behavior. However, if the mode shape changes significantly then a more sophisticated structural model such as that presented here is required.

3.3 THE GENERAL TWO BODY PROBLEM

3.3.1 INTRODUCTION

If two spring mass systems are linked by a rigid friction interface, then the masses will ride together when the joint is stuck and will slide relative to each other when the load across the joint equals the friction slip load. A number of current researchers simulate this effect by assuming that the friction force equals the slip load, μN , multiplied by the algebraic sign of the relative velocity. They then assume that the relative motion across the friction interface is harmonic. Together these assumptions imply that the friction force is an alternating square wave and that the joint is always slipping in one direction or the other. This study attempts to establish a better model for the friction force, f_N , which takes into consideration the sticking portion of the cycle during which time f_N varies gradually between its extreme values.

3.3.2 RESULTS

This work is still in progress and, consequently, only partial results are reported at this time. It has been found that for large amounts of slip the assumption that the friction force is an alternating square wave is, in fact, exactly correct. However, for moderate amounts of slip f_N has a jump when the relative velocity changes sign that may be only a fraction of μN and that it then varies as a smooth function to its other extreme value. Using this insight into f_N 's behavior a more accurate approximation for its Fourier series expansion has been established.

3.4 MICROSLIP

3.4.1 INTRODUCTION

In the previous discussions the friction contact either slips or sticks. In practice, however, the friction load is transmitted across an interface and it is possible, especially for large contact pressures, that only part of the interface may be slipping. Such a phenomenon is referred to as microslip or partial interface slip.

3.4.2 DISCUSSION AND RESULTS

In this work a new microslip model has been developed which allows partial slip on the contact interface. The interface model consists of two parallel elastic bars connected by a shear layer. The interface between the two bars can slip when the shear force magnitude is equal to the coefficient of friction times the normal pressure. This model is different from earlier microslip models in that it includes a shear layer which allows an initial elastic deformation of the structure. A typical response curve breaks into three regions: an elastic deformation, microslip or partial interface slip, and macroslip or total interface slip. By choosing various values of bar and shear layer stiffnesses the model can easily be varied from a total microslip model to a fully macroslip one.

Once the quasistatic behavior of the nonlinear joint element is established a

cyclic force deflection diagram can be computed. If the relative displacement, Δu , is then assumed to be harmonic the Fourier series expansion of the nonlinear force can be readily calculated and the Fourier coefficients of the fundamental harmonic terms expressed as functions of Δu . These terms are used via the method of harmonic balance in exactly the same way as for the macroslip models to establish the overall motion of the total structure. This approach was used to simulate two different experiments: 1) friction damping tests conducted at the University of Dayton (UDRI) and 2) shroud contact tests performed at the United Technologies Research Center (UTRC).

First, a simulation of the UDRI test was performed using the standard macroslip model. When the results of the simulation were compared with the experimental results it was found that the experiment did not lock up at high normal loads in the same way that the macroslip model did. There are two significant differences: near lock up the test results had much lower amplitudes than those calculated using the theoretical model. Secondly, the macroslip model predicted that near lock up the response curves for different normal forces should all lie on the linear response curve of the locked system until they started slipping (at which time they are nearly flat). The experimental data did not exhibit such behavior and showed shifted curves instead.

The UDRI blade was reanalyzed using the microslip model. The results qualitatively agree quite well with the test data in that they exhibited both attenuated and shifted response near lock up.

The second system that was analyzed represented shroud contact tests performed at UTRC. The test results of blade amplitude versus excitation force exhibited a gradual transition from an elastic response, which increased linearly with excitation, to a nearly flat response with a much lower slope (that was dominated by friction). A macroslip model predicted a bilinear curve which did not exhibit the gradual transition of the experimental data. However, when the microslip model of the friction interface was used it exhibited good agreement with the test data for a wide range of shroud contact pressures.

In summary, a new microslip model has been developed which accounts for the possibility of only partial slip along the interface. This model exhibits the three main characteristics required of such contact problems: initially only elastic deformation when the amplitude of the input force is small, followed by a region of microslip or partial interface slip when the amplitude increases and, lastly, total slip of the joint for really large forces. The model has three adjustable parameters, the stiffnesses of the two elastic bars and the stiffness of the shear layer. It has been shown for two quite distinct experiments that it is possible to select these parameters in such a way that the predictions from the analytical model correlate extremely well with the test results over a wide range of forces and frequencies.

4 REFERENCES

1. Griffin, J. H., "Friction Damping of Resonant Stresses in Gas Turbine Engine Airfoils," *ASME Journal of Engineering for Power*, April 1980, Vol. 102, pp. 329-333.
2. Griffin, J. H. and Sinha, A., "The Interaction Between Mistuning and Friction in the Forced Response of Bladed Disk Assemblies," accepted for publication in the *ASME Journal of Engineering for Power*. To be presented at the 29th International Gas Turbine Conference, Amsterdam, June 1984.
3. Sinha, A. and Griffin, J. H., "Friction Damping of Flutter in Gas Turbine Engine Airfoils," *Journal of Aircraft*, Vol. 20, No. 4, April 1983, p. 372.
4. Sinha, A. and Griffin, J. H., "Effects of Friction Dampers on Aerodynamically Unstable Rotor Stages," AIAA Paper No. AIAA-83-0848-CP, presented at the 24th Annual SDM Conference, Lake Tahoe, May 1983.
5. Menq, C. and Griffin, J. H., "A Comparison of Transient and Steady State Finite Element Analyses of the Forced Response of a Frictionally Damped Beam," presented at the 9th Biennial Design Conference on Mechanical Vibration and Noise, Dearborn, Michigan, September 1983.

ACKNOWLEDGEMENTS

This work was supported by the Air Force Office of Scientific Research, Grant AFOSDR-82-0134, under the direction of Dr. Anthony K. Amos, Program Manager, Aerospace Sciences and by the National Aeronautics and Space Administration, Grant NAG-367, under the direction of Dr. Robert E. Kielb, Program Manager, Lewis Research Center.

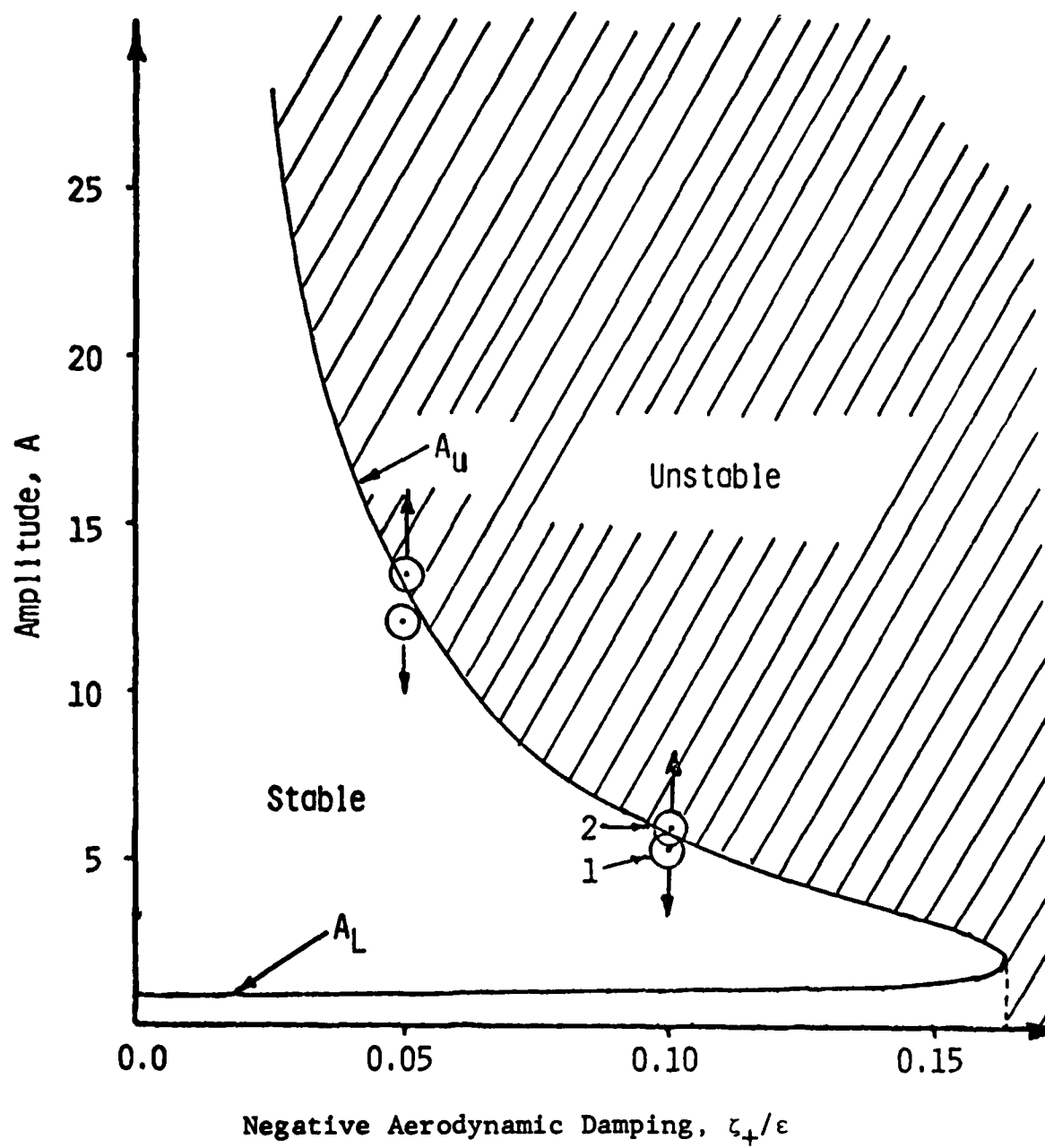
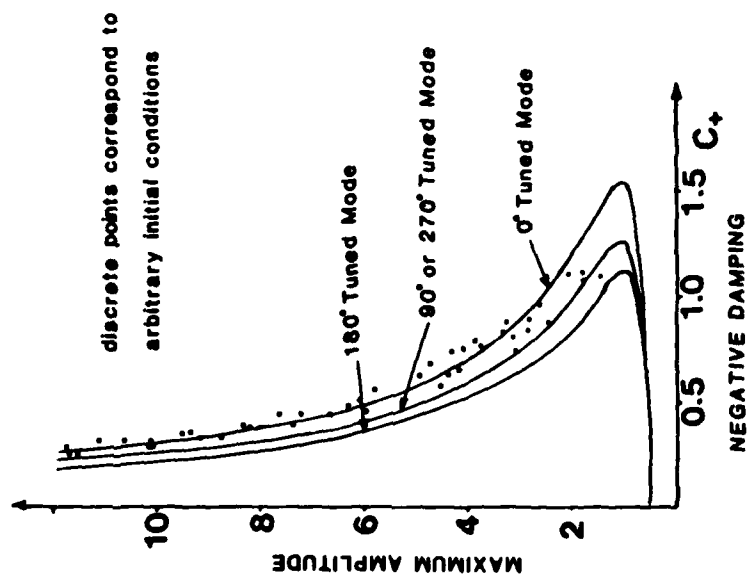
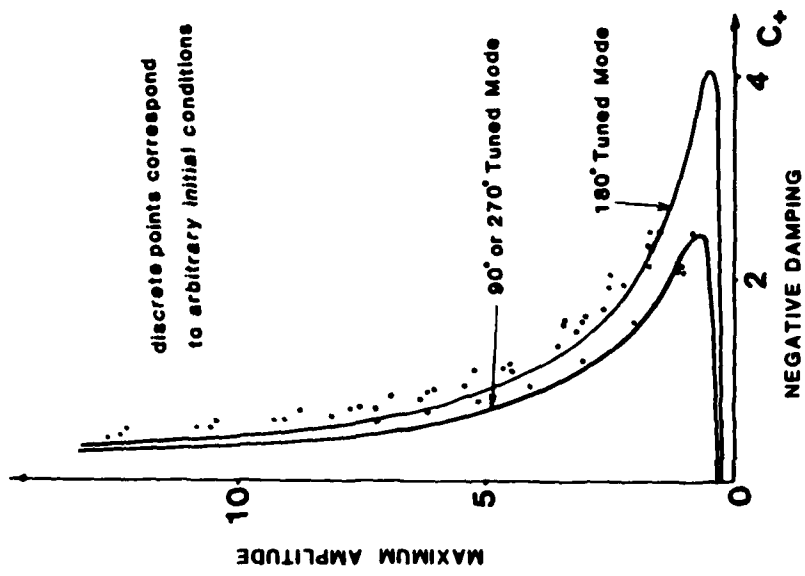


Figure 1. Stability Plot for Flutter Control



a) Blade-to-Ground Dampers



b) Blade-to-Blade Dampers

Figure 2. Maximum Amplitude Versus Negative Damping

FRICTION DAMPING STUDIES AT IMPERIAL COLLEGE

C. F. Beards
Imperial College
London, England

Paper was not presented; submitted for publication.

FRICION DAMPING STUDIES AT IMPERIAL COLLEGE

C.F. Beards

Imperial College

London

ABSTRACT

Force transfer by friction between joint elements, energy dissipation mechanisms, friction damping in joints and the effects of increased joint damping on the vibration response of structures are discussed.

INTRODUCTION

In most engineering structures considerable attention has to be given to the effects of dynamic loading. Although high damping is usually necessary to control structural response, current construction methods often produce structures with low damping. Since most inherent structural damping originates in the joints, this source of damping has been the subject of careful investigation.

Efficient use of this damping mechanism is rarely made because the small relative movements which are necessary between the joint interfaces can cause fretting corrosion, a loss in stiffness, and difficulties with design and analysis. These factors, together with joint damping and structural response, have therefore received particular attention in friction damping studies.

JOINTS

Friction effects and the mechanisms of force transfer by joint elements have been studied, and methods for surface roughness measurement and description have been investigated. A theory for stick-slip of real surfaces has been evolved. (1-3)

Vibrational energy dissipation by a lap joint subjected to interfacial slip has been studied and the optimum conditions determined. The energy dissipation mechanisms and controlling factors have been described. (4)

A range of surface preparations have been tested for reducing fretting corrosion whilst giving good energy dissipation. (5, 6) Cyanide hardened and electro-discharge machined steel surfaces were found to be particularly good in this respect.

Friction dampers have also been designed for adding to existing structures which had insufficient inherent damping. (7,8)

Current endeavours aim to give a better understanding of the different joint damping mechanisms, their relative magnitudes and circumstances under which they occur. Time and environmental effects are also under consideration.

STRUCTURES

The damping in structures has received considerable attention. (9-11) Because of the high energy dissipation levels possible in a joint wherein relative interfacial slip occurs, it is desirable to design this type of damping into a structure to increase the inherent damping. (12,13)

Application to beam type structures has been considered, by increasing the damping in the supporting joint or by using a laminated beam construction so that vibration promotes interfacial slip between layers. (14) The application of viscoelastic layers to this type of vibration problem has also been considered. (15) To achieve high damping with viscoelastic layers a high strain is necessary, which usually requires large vibration amplitudes: however this effect can be reduced by including elastic particles to act as stress raisers in the layer. (16)

Increased frame damping has been achieved by controlling the clamping force and hence the slip in one or more joints. Reductions in frame mobility of about 10 dB have been measured. Frame resonance frequencies can be changed by adjusting the end clamping of struts and ties: this is a useful technique for avoiding the excitation of resonance. (17,18)

Plate type structures can be damped by friction, either by controlled edge clamping or by using a laminated plate construction. (19, 20) This has been applied to the damping of a diesel engine oil sump and covers for reducing noise levels. (21)

Analysis methods used give a good qualitative prediction of the effects of increased joint damping in a structure. (12,14) This has been done by replacing the periodic friction force by a Fourier Series and using a finite element analysis of the structure. (17, 18) In laminated plate vibration the friction force has been associated with an in-plane shear force. (19, 20) Quantitative analysis is not yet possible because of the uncertainty regarding the value of the coefficient of friction, μ and possible changes during a cycle or over an interval of time; however some allowance can be made for the change in μ with slip velocity if macroslip occurs.

The provision of increased friction damping in the joints of real structures is currently being considered, and the accuracy of predictions is being improved by using more refined analytical models.

REFERENCES

1. Sayles R.S. and Thomas T.R.
"Computer Simulation of the Contact of Rough Surfaces".
Wear. 49. 1978.
2. Kaneta M. and Cameron A.
"Effects of Asperities in Elasto Hydro-Dynamic Lubrication".
ASLE/ASME Paper 79 - LUB - 6. 1979.
3. Sayles R.S. et al.
"Elastic Conformity in Hertzian Contacts".
Tribology Int. Dec 1981.
4. Beards C.F.
"The Damping of Structural Vibration by Controlled Interfacial Slip in Joints".
Trans ASME. Jnl Vibn, Acoustics, Stress and Reliab.
15 (3) 1983.
5. Beards C.F.
"Some Effects of Interface Preparation on Friction Damping in Joints".
Int. J. Mach Tool Des and Res. 15 p 77-83. 1975.
6. Beards C.F. and Neroutsopoulos A.A.
"The Control of Structural Vibration by Friction Damping in Electro Discharge Machined Joints".
Trans ASME. Jnl Mech Des. 102.1 Jan 1980.
7. Rosenberg R.H.
"The Structural Damping of Bridges by Friction at the Supports".
M.Sc Thesis. Imperial College, London 1973.
8. Wyatt T.A.
"Mechanisms of Damping".
Seminar on Dynamics of Bridges. TRRL. England May 1977.

9. Grootenhuis P.
"Damping Mechanisms in Structures and Some Applications of the Latest Techniques".
I Mech. E. Symp on Struc. Dyn. ISVR Southampton, England. April 1972.
10. Grootenhuis P
"The Use of Damping to Control Vibration in Structures".
Acoustics Bull. 4.4. October 1979.
11. Wyatt T.A.
"Structural Response".
Symp on Lattice Towers. Inst. Struc. England. 1979.
12. Beards C.F.
"Structural Vibration Analysis".
Pub. by Ellis Horwood Ltd, Distributed by John Wiley and Sons. 1983.
13. Beards C.F.
"Damping in Structural Joints".
Shock and Vibn Digest. 14. (6). 1982.
14. Beards C.F. and Bermingham P.J.
"The Effects of Frictional Damping on the Vibration of an Elastically Supported Beam".
Symp. Non-Linear Dyn. Loughborough, England. Paper El. 1972.
15. Ioannides E. and Grootenhuis P.
"An Integral Equation Analysis of the Harmonic Response of Three-Layer Beams".
Jnl Sound and Vibn. 82 (1). 1982.
16. Paipetis S.A. and Grootenhuis P.
"The Dynamic Properties of Particle Reinforced Viscoelastic Composites".
Fibre Science and Tech. 12.5. September 1979.

17. Beards C.F. and Williams J.L.

"The Damping of Structural Vibration by Rotational Slip in Joints".

Jnl. Sound and Vibn. 53 (3) 1977.

18. Beards C.F. and Woowat A.

"The Control of Frame Vibration by Friction Damping in Joints".

ASME DET Conf. Dearborn MI. USA. Paper 83 - DET - 76.
Sept 1983.

19. Beards C.F. and Imam I.M.A.

"The Damping of Plate Vibration by Interfacial Slip Between Layers".

Int. J. Mach. Tool. Des and Res. 18, p 131-137. 1978.

20. Beards C.F. and Robb D.A.

"The Use of Friction Damping to Control the Vibration of Plates in Structures".

Int. Conf. Adv in Struc Dynamics. I.S.V.R. Southampton.
England. July 1980.

21. Beards C.F.

"Disel Engine Sump Noise".

Inter-Noise 1983. IOA Conf. Edinburgh U.K. 1983.

A DERIVATION OF EQUIVALENT LINEAR VISCOUS AND ELASTIC CONSTANTS
FOR VISCOELASTIC MATERIALS

S. R. Dahl and R. B. Rice

Martin Marietta Corporation
Denver Aerospace Division
P. O. Box 179
Denver, Colorado 80201

A DERIVATION OF EQUIVALENT LINEAR VISCOUS AND ELASTIC CONSTANTS FOR VISCOELASTIC MATERIALS

S. R. Dahl and R. B. Rice
Martin Marietta Corporation, Denver Aerospace Division
P.O. Box 179, Denver, CO 80201

Abstract

A testing method was devised and implemented to directly measure the hysteresis characteristics of a viscoelastic material for shear displacements. Three commonly available materials were tested over a frequency range of 0.1 to 100 Hz. Though the materials are essentially non-linear, linear elastic and viscous damping parameters were approximated using an equivalent energy approach valid for specific frequencies and amplitudes. These linearized parameters can then be used in linear structural and control systems analysis programs for the analysis of structures having distributed discrete passive damping mechanisms.

Introduction

In the design of large space structures, some degree of passive damping will be necessary to alleviate the workload of the structural shaping control system. Since ground testing of these structures is difficult, accurate simulation and modelling must be performed. Whatever the passive damping mechanism is, the material properties which it is constructed of should be in a form that can be used with existing analysis tools. The damping materials should be as "lossy" as possible to conserve mass. However, the lossy materials tend to exhibit creep behavior, especially at the low modal frequencies expected of the structures. Creep is a non-linear phenomenon, and therefore difficult to model using linear analysis. We are interested in the amount of energy a passive damper can absorb from the structural modes, irrespective of the particular method by which it is accomplished. So if we can linearize the viscoelastic material's model and have the model accurate over a limited range of frequencies and amplitudes, while predicting the amount of energy absorbed, then linear analysis methods can be used to predict the behavior of a structure with efficient damping techniques.

A test fixture was designed and built to measure the force versus displacement characteristics of viscoelastic samples in shear. The apparatus was designed to contribute negligible friction to the measurements for as little data contamination as possible. The primary measurements were

frequency response and hysteresis data. Our frequency range of interest was from 0.1 Hz. to 100 Hz., since this is the region of the large displacement structural modes in large space structures. The shear amplitude range was between 10^{-4} and 10^{-1} to maximize energy dissipation. Temperature was not considered in this study, although it tends to have a frequency shifting characteristic and will change material properties in a space environment.

Equivalent Viscous and Elastic Constants

A simple Voigt model was chosen to represent a viscoelastic material in shear deformation. This model consists of a spring and viscous damper in parallel, as shown in Figure 1. The force across the material is the sum of the spring force and the dashpot forces:

$$F = F_S + F_D \quad (1)$$

where F_S is the spring force and F_D is the damper force. Since these forces are summed, they will be treated separately in the following discussion.

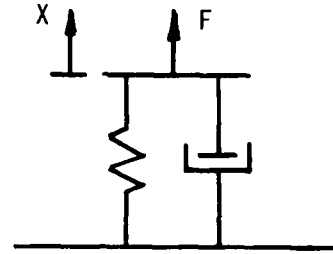


Figure 1: Viscoelastic Damper Model

Damping Force

A generalized non-linear damping force can be expressed as:

$$F_D = -F_D(x, \dot{x}) \operatorname{sgn}(\dot{x}) \quad (2)$$

where $\operatorname{sgn}(\dot{x})$ indicates that the sign of the damper force changes with the relative velocity \dot{x} , and the negative sign means that the damper force opposes the relative velocity. If we consider that energy is only dissipated by velocity, then the damper is represented by a velocity-nth power model given by:

$$F_D = -C_n |\dot{x}|^n \operatorname{sgn}(\dot{x}) \quad (3)$$

where C_n is the damping constant. Table 1 lists the first three integer powers of velocity and their respective force expressions.

Damping Type	Damping Force
Coulomb	$F_D = -C_0 \operatorname{sgn}(\dot{x})$
Viscous	$F_D = -C_1 \dot{x}$
Quadratic	$F_D = -C_2 \dot{x}^2 \operatorname{sgn}(\dot{x})$
Velocity-nth power	$F_D = -C_n \dot{x} ^n \operatorname{sgn}(\dot{x})$

Table 1: Damping Types

Figure 2 shows the hysteresis curves for these damping types with n , the velocity power, called out. Coulomb damping has a rectangular hysteresis curve. As n increases, the rectangle becomes more rounded, until $n=1$ (viscous damping) when the hysteresis curve becomes elliptical. For $n>1$, the maximum displacement points become increasingly pointed. Therefore, a cursory examination of a hysteresis curve gives a first approximation of the velocity power, n . A hysteresis curve can only be recorded for a given frequency and amplitude, and it may change for other input conditions. Only viscous damping is subject to linear analysis, so we want to approximate other velocity powers with an equivalent viscous damper.

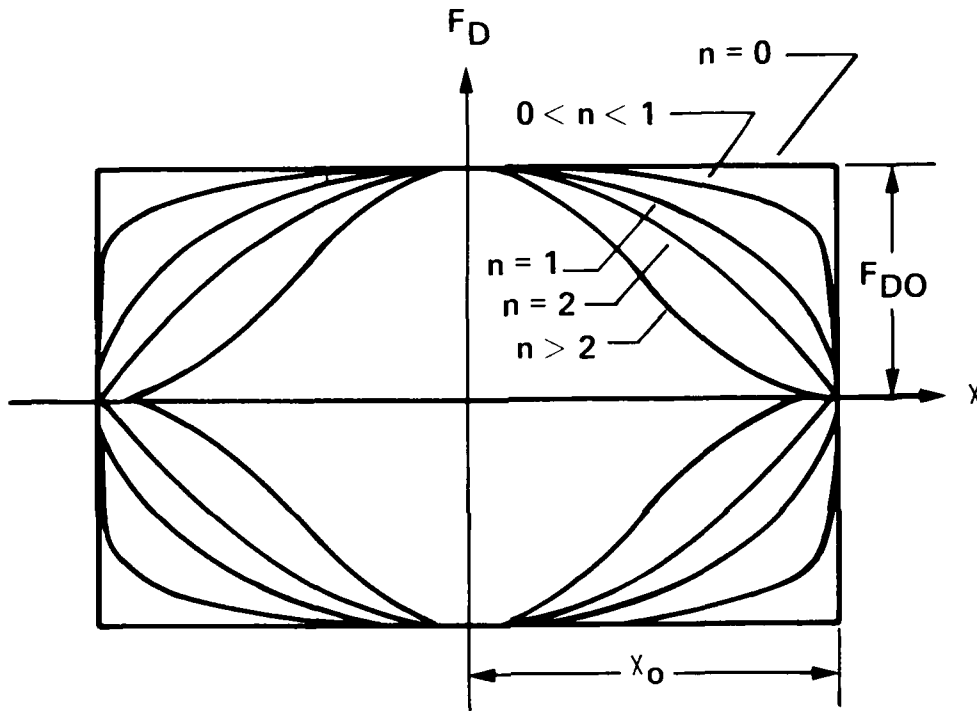


Figure 2: Hysteresis Variation With Velocity Power

The energy dissipated (or converted to heat) by a general damper per cycle is equal to the area of a hysteresis curve. The area of an elliptical hysteresis curve is:

$$D = \pi C_1 \omega x_0^2 \quad (4)$$

where D is the energy dissipated per cycle, C_1 is the viscous damping coefficient in Table 1, and x_0 is the maximum displacement from the origin, or half of the total displacement. If D is measured by experiment, and the hysteresis curve is not the ideal ellipse, then an equivalent viscous damping coefficient is defined as :

$$C_{eq} = D / \pi \omega x_0^2 \quad (5)$$

When this equivalent viscous damping coefficient is used with the viscous type damper ($F_D = -C_{eq}\dot{x}$), F_D varies less than 10 percent from its experimental value for $0.6 < n < 1.6$.

Elastic Force

When a viscoelastic damper experiences a harmonic relative displacement, the force in phase with the displacement is conservative and dissipates no energy. The ideal elastic element is the linear spring, and the elastic force is proportional to the displacement: $F_s = kx$. A non-ideal spring has a non-linear force versus displacement curve, and the spring constant is a function of displacement. More generally, the spring constant includes time as an independent variable, and is evident as creep behavior. An equivalent linear spring constant can be defined from an experimental hysteresis curve by the slope of the line connecting the maximum displacement, or zero velocity points, as shown in Figure 3. The linear equivalent spring constant is

$$k_{eq} = \Delta F / \Delta x \quad (6)$$

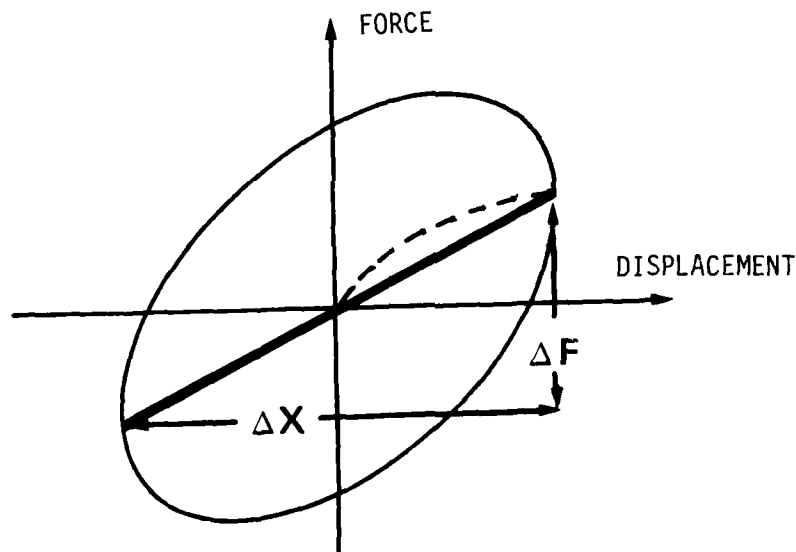


Figure 3: Equivalent Linear Spring Constant Determination

A linear spring constant is independent of amplitude. Experimental results indicate that for some materials, and especially at low frequencies, this is not true. The dashed line in Figure 3 shows a possible spring force decrease as amplitude increases. An explanation for the variable spring constant may be the creeping property of the materials tested. In any case,

the equivalent linear spring constant is valid for a narrow range of frequencies and amplitudes.

Frequency Domain Approach

The method presented thus far utilizes hysteresis data generated at discrete frequencies and amplitudes. The data taking process, unless automated, is slow and tedious. Data from a signal analyser, presented in the frequency domain, can be processed to yield the same equivalent spring and viscous damping coefficients through curve fitting. The frequency domain representation of the Voigt viscoelastic model is

$$\frac{F(j\omega)}{x(j\omega)} = k + j\omega C = k(1 + j\omega C/k) \quad (7)$$

The magnitude and phase of this transfer function is given by

$$\frac{F(\omega)}{x(\omega)} = k[1 + (\omega/\omega_0)^2]^{1/2} \quad (8)$$

$$\phi(\omega) = \tan^{-1} (\omega/\omega_0) \quad (9)$$

where $\omega_0 = k/C$, the Bode break frequency. The frequency response in Bode form (log magnitude versus log frequency and phase versus log frequency) is shown in Figure 4.

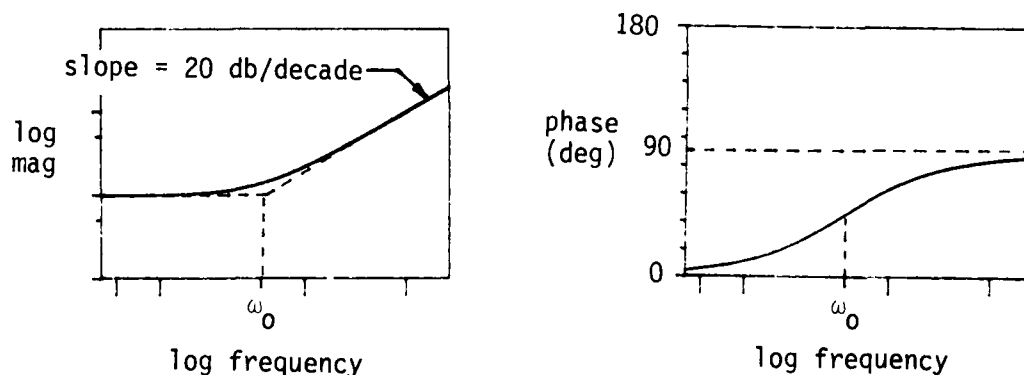


Figure 4: Bode Frequency Response of Voigt Viscoelastic Model

Similar to the hysteresis data curve fitting procedure, the Voigt model frequency response is curve fitted to experimental frequency response data. This is easily accomplished with a digital signal analyzer which has a transfer function synthesis feature. The gain and break frequency are varied by trial and error until there is a good fit for the frequency range of interest, which is usually less than a decade.

Another approach is to back out the gain, k , and break frequency, ω_0 , using the slope of the experimental transfer function at a specific

frequency, but this doesn't have any accuracy advantage over the synthesized fit approach. If the transfer function synthesis feature is not available, an accurately plotted Voigt model frequency response on semi-transparent paper which is fitted over the experimental frequency response plot gives equally reliable results.

Once the Voigt model parameters are found, the equivalent linear spring constant is equal to the Voigt model DC gain, and the equivalent viscous damping coefficient is found from the Bode break frequency and the equivalent spring constant:

$$C_{eq} = K/\omega_0 \quad (10)$$

These constants are dependent upon the geometrical form of the test apparatus. The spring and viscous damping constants for the material itself are calculated using the appropriate geometrical form factor.

Viscoelastic Material Test Apparatus

The test apparatus was designed to measure force and displacement directly across the viscoelastic material with negligible friction. The material was stressed in shear by a multiple plate shear sandwich construction. A strain gauge load cell sensed force, and a non-contacting linear variable differential transformer sensed displacement. An electromechanical shaker provided the force input. Figure 5 is a photo of the test apparatus. It proved rigid enough to not have any significant structural modes below 100 Hz.

Test Data

A hysteresis plot for variations in amplitude at frequency of 30 Hz is shown in Figure 6. The viscoelastic material was an uncured butyl rubber. Note the flattening of the equivalent spring constant as the amplitude increases. Figure 7 is a Bode frequency response plot for the same material with a linearized curve fit for the 5 Hz to 10 Hz range. The magnitude plot show good agreement, while the phase plot deviates more significantly. Also plotted on Figure 7 is the magnitude transfer function at a lower average amplitude, indicating that the spring constant is larger, reflecting the trend seen on the hysteresis plot in Figure 6.

Conclusions

Using a curve fitting procedure, linear equivalent spring and viscous damping constants can be approximated from viscoelastic material frequency response data. The spring constant appeared to be non-linear for the materials tested. This implies that if the equivalent constants are to be used with linear analysis, iterations may be needed to match the spring constant with the structural displacements. For a more accurate curve fit over a broader frequency range, a damper modeled by a fractional derivative of the velocity is necessary. The theoretical groundwork has been broken for this type of modeling of viscoelastic materials², but most linear analysis tools accept only integral derivatives.

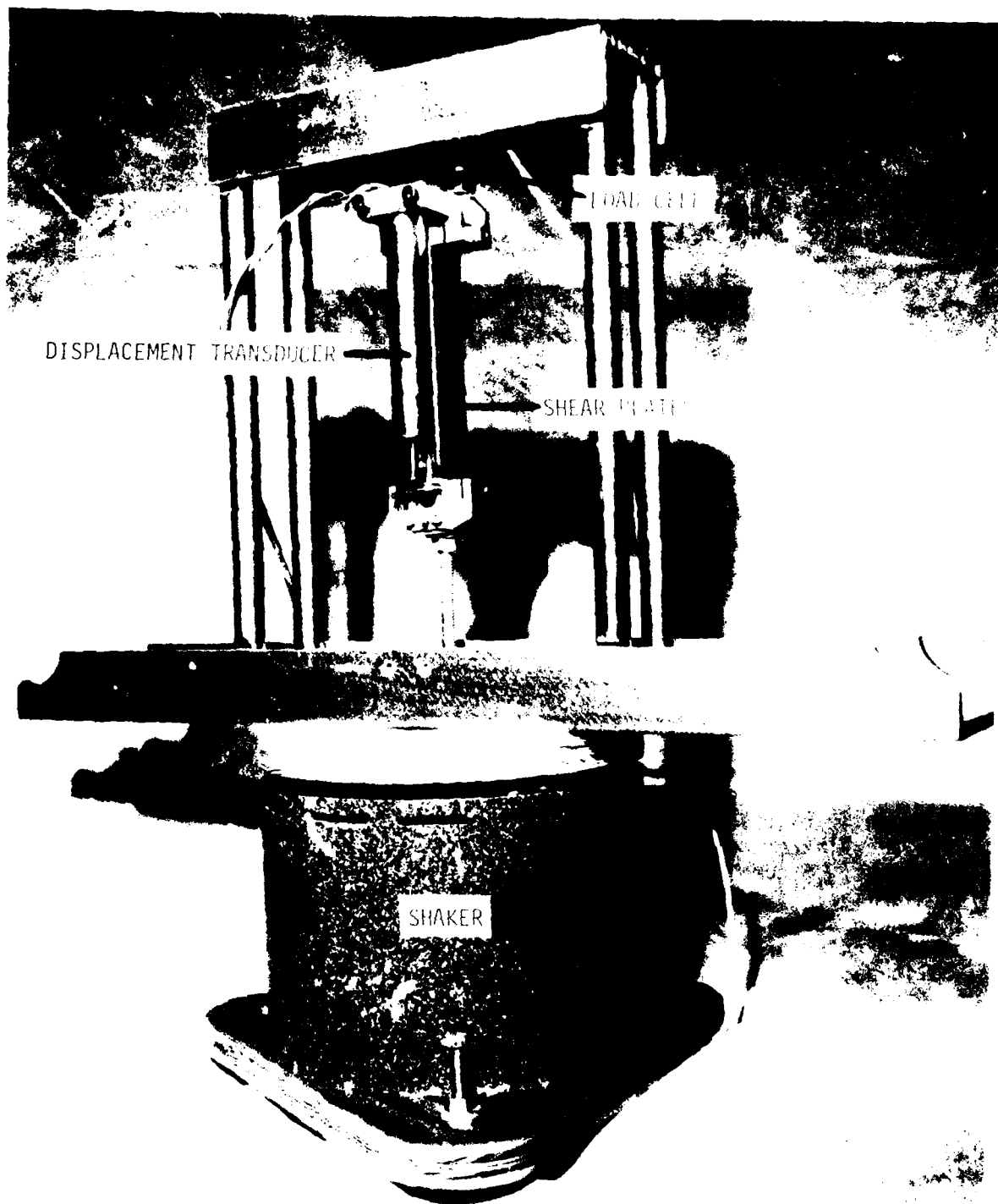


Figure 5: Viscoelastic Material Test Apparatus

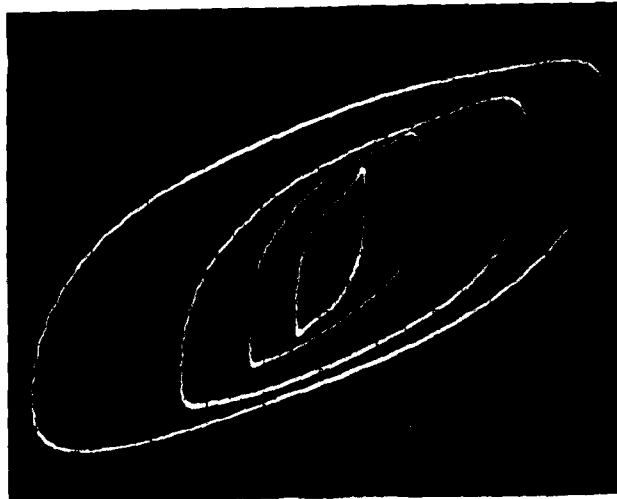


Figure 6: Hysteresis Curves with Amplitude Variation

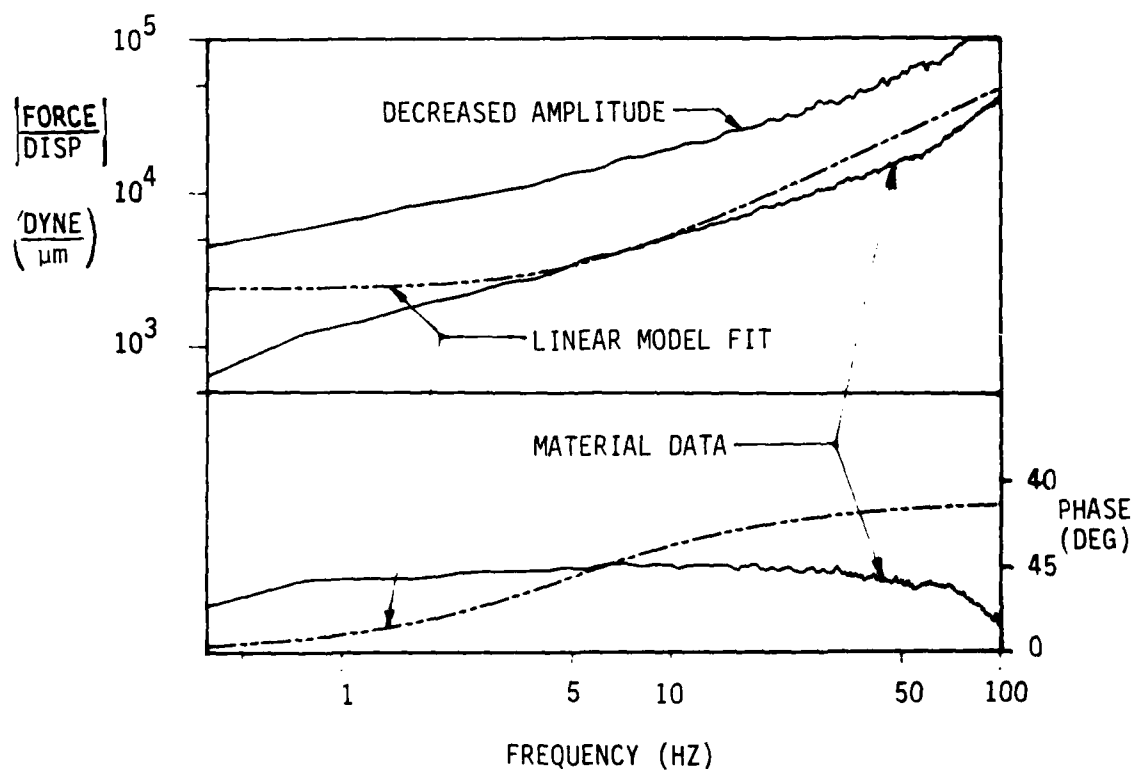


Figure 7: Bode Frequency Response Plots, Gain and Phase with Linear Approximation

COMPOSITE MATERIAL DAMPING USING IMPULSE TECHNIQUE

C. T. Sun and B. T. Lee
Department of Engineering Sciences
University of Florida
Gainesville, Florida 32611

and

S. K. Chaturvedi
Department of Engineering Mechanics
University of Missouri-Rolla
Rolla, Missouri 65401

Composite Material Damping Using Impulse Technique

by

C.T. Sun, B.T. Lee
Department of Engineering Sciences
University of Florida
Gainesville, Florida 32611

and

S.K. Chaturvedi
Department of Engineering Mechanics
University of Missouri-Rolla
Rolla, Missouri 65401

Abstract

An experimental technique known as the impulse technique is presented for measuring the internal damping of composite materials. In order to gain confidence on the experimental data measured from this technique some improvements have been made.

The improvements involve the following:

- (a) to replace a contact probe by a non-contact probe.
- (b) to use an amplifier to reduce the noise level.
- (c) to use a spring to control the magnitude, location and dwelling time of the applied force.
- (d) to use zooming technique to obtain more accurate data.

Introduction

Damping is a very important property for structural materials. It can reduce amplitude of vibration and hence reduce the maximum stress level and increase the service life of structures. In general to the authors' knowledge there exist two commonly used experimental techniques to measure material damping [1,2].

[A] Forced vibration technique:

In this method [1] the specimen is continuously excited with an electromagnetic shaker with a random input. The output (transfer function) in the frequency domain is obtained with the FFT (Fast Fourier Transform) analyzer. The random signal is generated by the noise source of the FFT analyzer. The advantages of using this technique are:

- (1) The force level is easily controlled.
- (2) The force spectrum can easily be shaped at modal points.
- (3) Extraneous noises can be easily controlled and non-linearities and distortion effects can be removed.

The disadvantages of using this technique are:

- (1) It can be used only in the fundamental frequency range.
- (2) It generally cannot be used for in-situ testing of engineering structures.
- (3) It cannot be used to detect micro-damages in structures.

[B] Impulse Hammer Technique.

The second method used in this program is known as the impulse hammer technique. The impulse hammer technique, discussed in this paper, has a distinct advantage of being able to generate all higher modes simultaneously. One of the major objectives of this research report is to assess the experimental results of damping measurement using impulse hammer technique and point out some problems associated with this technique which should be taken care of before reliable data can be obtained. A detailed description of this technique can be found in reference [2] and a schematic set-up of this technique is shown in Fig. 1. An impulse hammer kit (Model K291A) from Piezotronics, Inc., New York and a Fast Fourier Transform (FFT) analyzer (Model 5420, Hewlett Packard) was used in this study.

Impulse Hammer Technique

The fundamental idea of using the impulse technique was probably due to Halvorsen and Brown [2]. The objective of the experimental method described in [2] was much broader than just the damping measurement. It is used to determine the responses of a structure under dynamic loads. However, we can use this technique to measure damping. The general idea of this technique is to determine experimentally the structural frequency response under a given forcing function. The basic principle is to define a ratio $H(f)$ of the Fourier transforms of the system output or response $v(t)$ to the system input or excitation $u(t)$.

$$H(f) = V(f)/U(f)$$

(1)

where $V(f)$ = Fourier transform of the system output $v(t)$
 $U(f)$ = Fourier transform of the system input $u(t)$

The real part and the imaginary part of the complex function $H(f)$ can be obtained through the FFT analyzer. A typical experimental display of the real and imaginary part of $H(f)$ is shown in Fig. 2 for graphite-epoxy composite. From the imaginary part we can locate a particular mode (say the 2nd mode) and then from the corresponding real part (see Fig. 3) we can calculate the material damping η from the formula [3]

$$\eta = \frac{1 - (f_a/f_b)^2}{1 + (f_a/f_b)^2} \quad (2)$$

It should be pointed out that from Eq. (2) η is very sensitive to the experimental data of f_a and f_b for the case of small damping i.e. $f_a/f_b \approx 1$. Method of obtaining accurate data of f_a and f_b will be discussed in the next section.

Experimental Results and Improvements

The different materials, as shown in Table 1, were chosen in this study. In the original set-up an accelerometer, screwed to a small highly polished anodized aluminum nut (known as adhesive mounting base) which was glued to the tip of each specimen, was used to obtain the output response of the beam specimens. This added mass was shown to have large effect on the natural frequencies of the specimens and the measured material damping was too high as compared with some well-known results. This observation is specially true for lightweight specimens of composite materials. In order to eliminate the effects of the added mass, we used a non-contact probe, known as motion transducer, operated under the principle of eddy current (KD - 2310-3U, Kaman Sciences Corp. Colorado) placed about 1.5 to 3 mm below the tip of each specimen. A schematic drawing of the modified experimental set-up is shown in Fig. 4 and a photographic overview is shown in Fig. 5. We believe that the replacement of a contact accelerometer by a non-contact motion transducer is a major improvement of the impulse hammer technique.

A comparison between the experimental results using contact and non-contact probe is shown in Table 2 for five different specimens and the first three fundamental modes of vibrations. Table 2 shows consistently that the results using accelerometer contact probe differ significantly than those obtained using the non-contact probe.

In principle the input signal by using a contact accelerometer probe is much stronger than the input signal by using a non-contact displacement probe. Therefore, the replacement of contact probe by non-contact probe creates a

coherence problem. In general, the coherence between input and output signals by using non-contact probe is not as good as obtained using the contact probe. Coherence is a function of many parameters; such as signal to noise ratio, mass of the hammer, hardness of striking tip, stiffness and mass of the specimen, input force and frequency. We believe that the coherence problem of using non-contact probe is primarily attributed due to the effect of noise, or due to low signal to noise ratio. In Fig. 6 we can clearly observe the difference in coherence using contact and non-contact probes.

In order to improve the coherence we introduce an octave filter (4302 dual 24dB) which was connected to the force transducer in hammer tip on one end and to the FFT analyzer on the other end as shown in Fig. 4. By using this filter the input signal can be magnified by 100 times. A comparison of coherence with and without the filter is shown in Figs. 7 and 8. The interference by the noise level on the magnitude of the transfer function (Fig. 7) is particularly important when the technique of half power point is used to measure damping.

After an amplifier is introduced we still find the following additional problems which affect the accuracy of the experimental data.

- The exact location of impulse of the hammer on the specimen and the force level cannot be accurately controlled.
- Measured data sometimes is several orders of magnitude higher than the well-known existing data.

In order to further improve the experimental technique the following steps were taken into consideration

1. We connect the hammer to a fixed spring so that the magnitude, location and the dwelling time of the impact load can be controlled. The detailed set-up is shown in Fig. 9. A comparison of the experimental display of the transfer function is shown in Figs. 10 and 11. In Figs. 10 and 11 the imaginary part of the transfer function and the coherence (the real part) are presented with and without the control by the spring. It is clearly indicated that by using a spring to control the impulse characteristics the resolution and coherence are indeed improved. It should, however, be realized that such a special hammering technique may not be very useful for field - testing of structures.
2. In order to improve the accuracy of the experimental data of damping associated with a particular mode of vibration we first determine approximately the values of natural frequencies within the frequency range of our interest (say from 0 to 1600 Hz). Then we use zooming technique to increase the resolution of the response in the neighborhood of this particular frequency. By using this technique we are able to obtain the experimental data of material damping of aluminum

alloy and some other composites and compare closely with values documented in existing literature. The experimental results of each kind of specimens are presented in Table 3, for the first three modes. In the last column of Table 3 BW represents the band width used in each experiment. For each material the value of damping appeared in the first row is corresponding to the first mode and the second row corresponding to the second mode etc. Table 3 shows clearly that the experimental data of damping obtained from zooming measurement are more reasonable than the original base-band measurement. We also observe from Table 3 that the band width associated with higher modes is relatively large. A possible explanation of this phenomenon is that at higher modes of vibration the displacement (or the input signal) is small and the effect of noise level becomes important in small band width range.

Finally after taking into account of all the above mentioned improvements the damping values for each material are presented in Table 4.

Concluding Remarks

(1) Impulse technique appears to be reliable technique for measuring internal material damping of composite materials as well metallic materials.

(2) The replacement of a contact accelerometer probe by a non-contact displacement transducer is an important step to improve the accuracy of the experimental results.

(3) Some other improvements ~~made~~ such as the reduction of the effect of noise level and the introduction of a spring to control the magnitude, location and the dwelling time of the applied impact force by the hammer have been encouraging.

(4) Zooming technique have shown to improve the experimental data considerably but it has certain limitation on the band width. This situation is particularly true for the higher modes.

(5) Based upon the experimental data, damping characteristics of aluminum shows a stronger dependence on maximum stress level (or maximum displacement level) as compared to the damping of composite materials.

Acknowledgement

This research is supported by the AFOSR under Grant No. AFOSR-83-0154 monitored by Dr. D.R. Ulrich, Program Manager, Director of Chemical and Atmospheric Sciences AFOSR, Bolling Air Force Base, Washington D.C.

References

- [1] R.F. Gibson and R. Plunkett "A Forced Vibratin Technique for Measurement of Material Damping" Experimental Mechanics 11 (8) Aug. 1977 p. 297.
- [2] W.G. Halvorsen and D.L. Brown "Impulse Technique for Structural Frequency Response Testing" Sound and Vibration Nov. 1977 p. 8.
- [3] G.F. Lang "Understanding Vibration Measurements" Sound and Vibration, March 1976 p. 26.

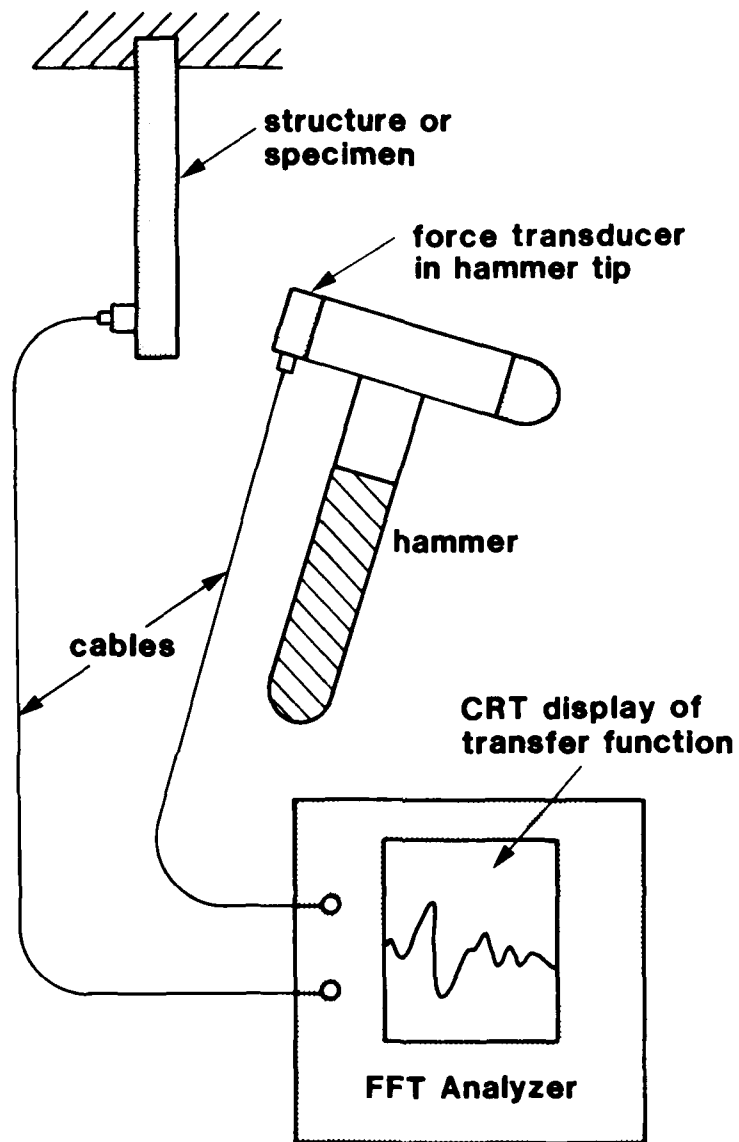


Figure 1. Original Schematic Drawing of the Impulse Hammer Technique.

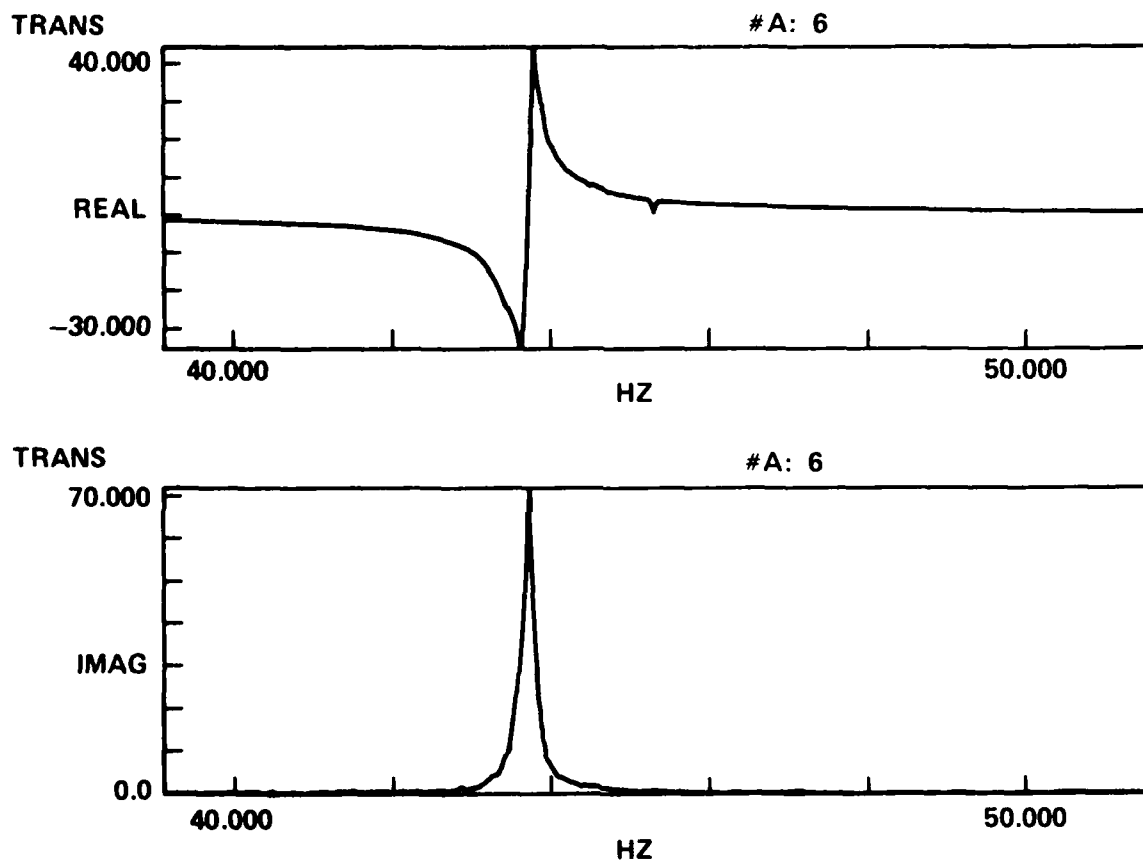
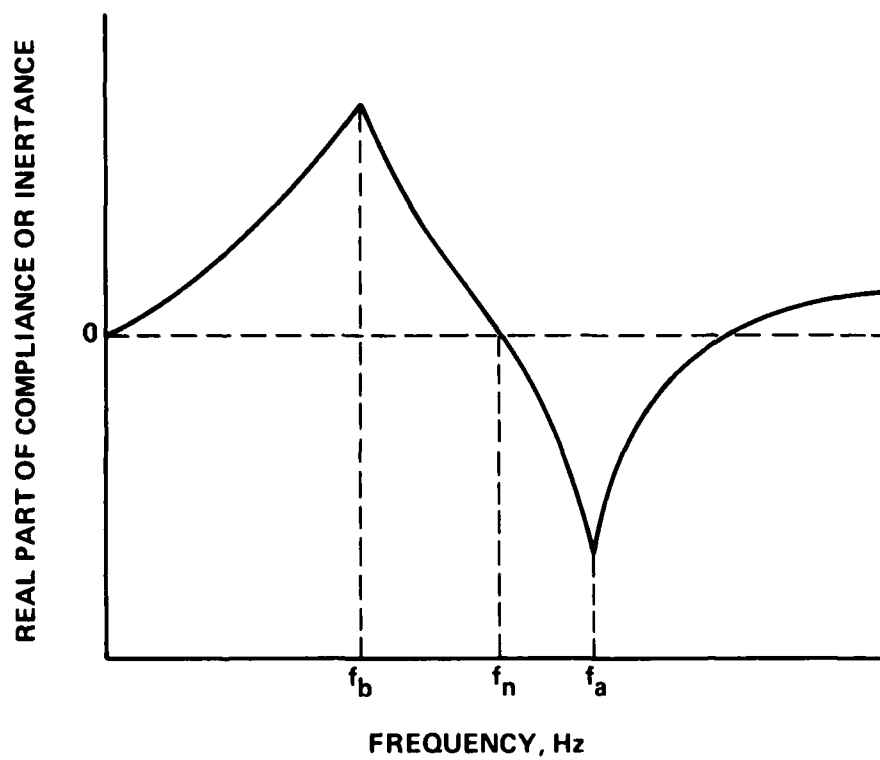


Figure 2. Typical Imaginary and Real Part of the Transfer Function.



$$\eta = \frac{(f_a/f_b)^2 - 1}{(f_a/f_b)^2 + 1}$$

Figure 3. Definition of f_a and f_b used for Damping Calculation.

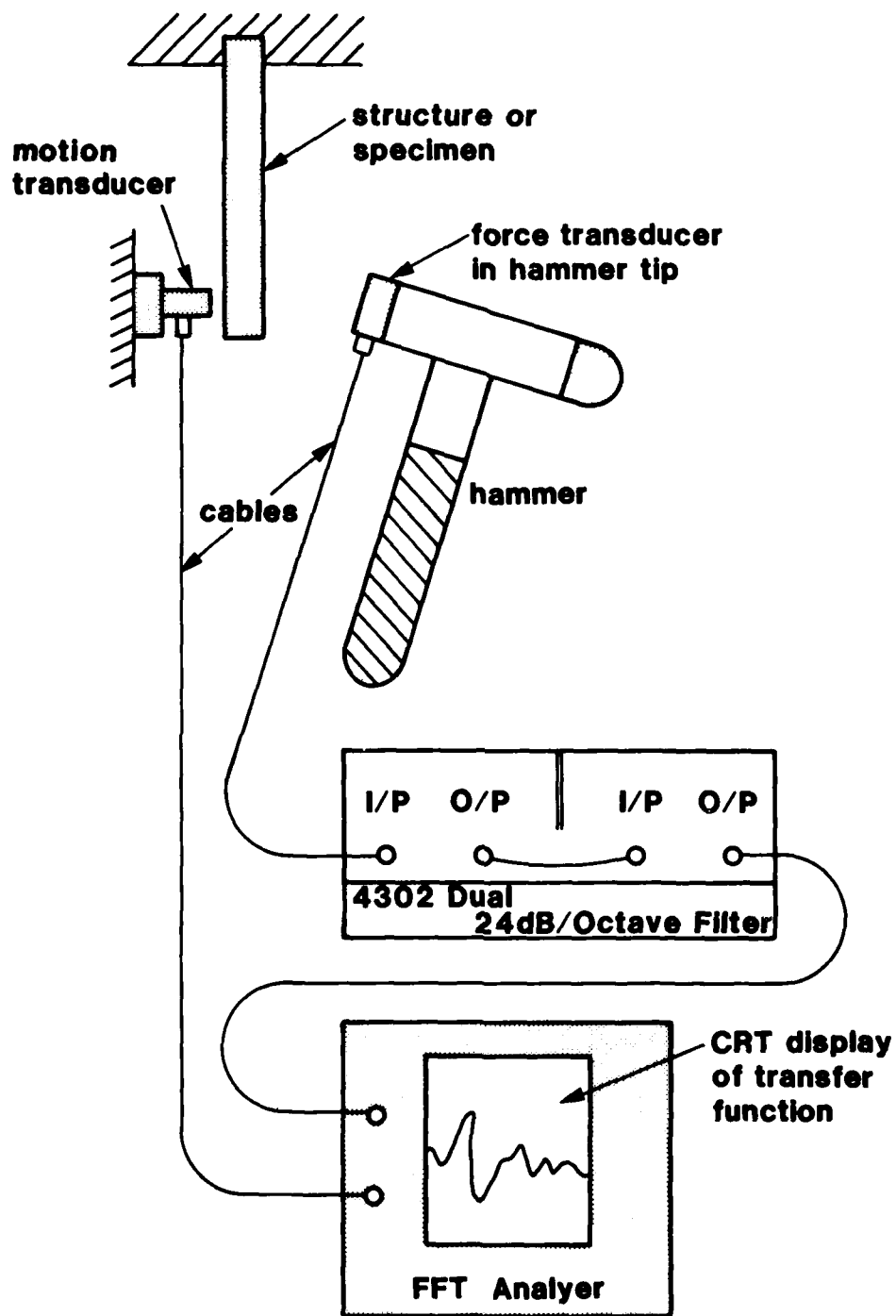


Figure 4. Schematic Drawing of the Modified Impulse Hammer Experimental Set-up.

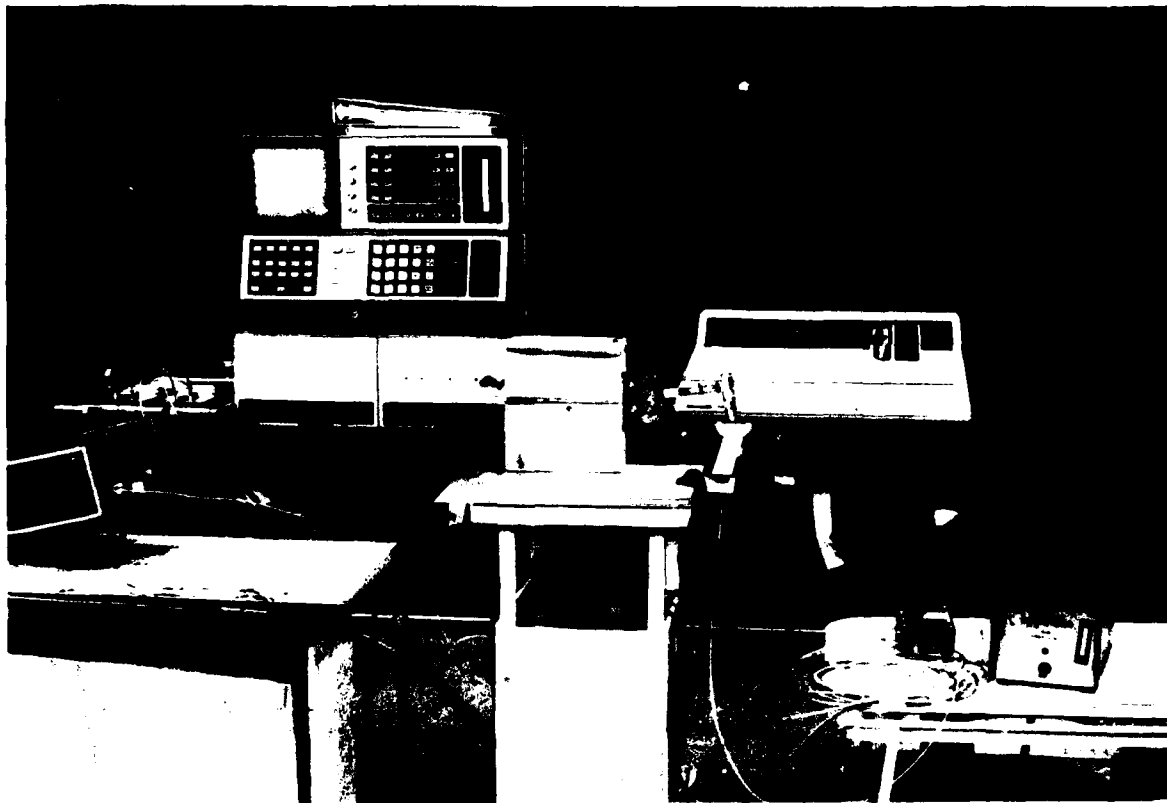
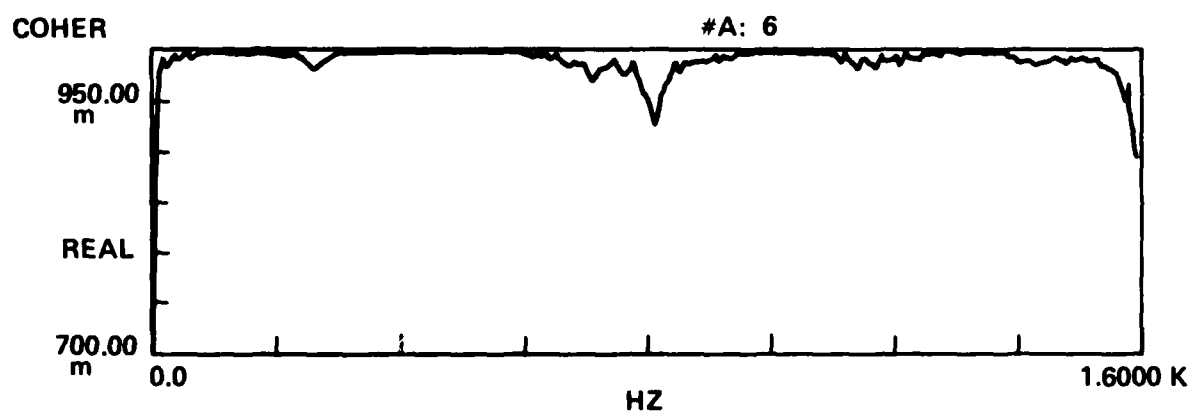


Figure 5. A Photographic View of the Experimental Set-up.

A. Coherence of Graphite/Epoxy Composite (Contact)



B. Coherence of Graphite/Epoxy Composite (Non-Contact)

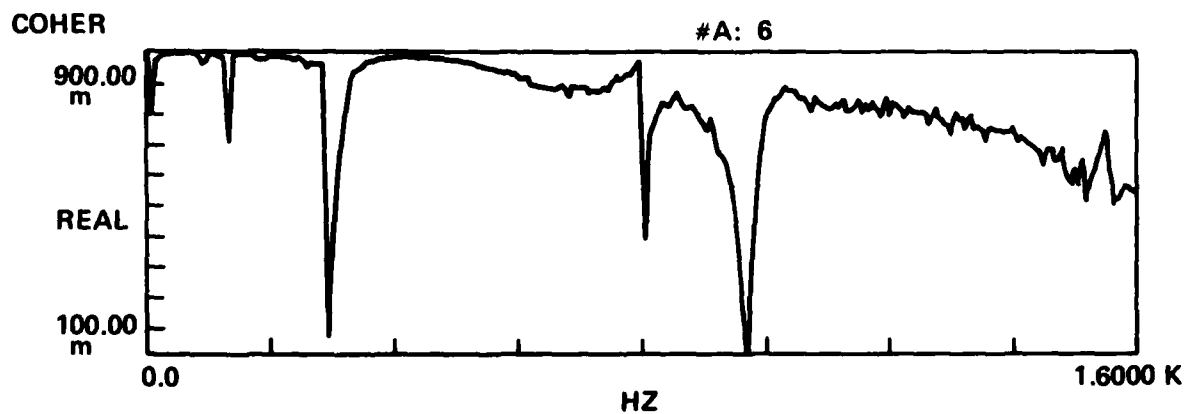
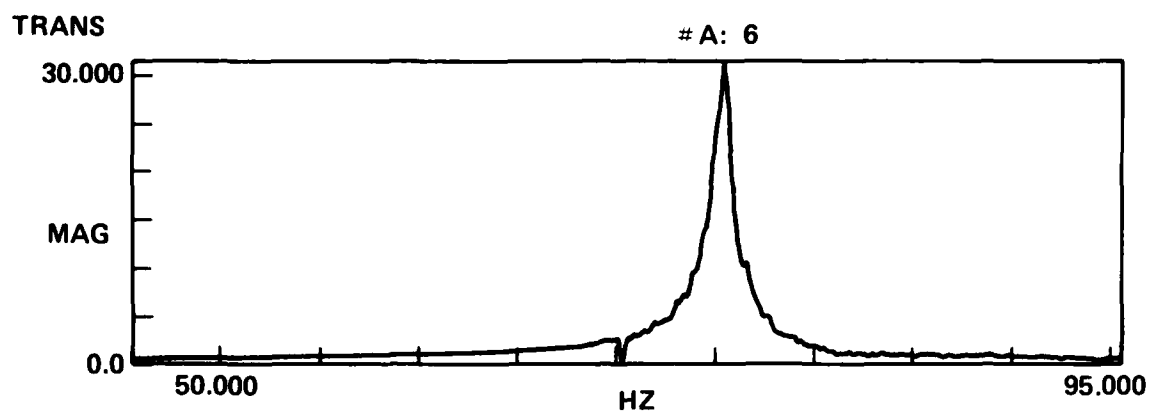


Figure 6. Comparison of Coherence using Contact and Non-Contact Probe.

A. Hammer signal amplified



B. No hammer signal amplified

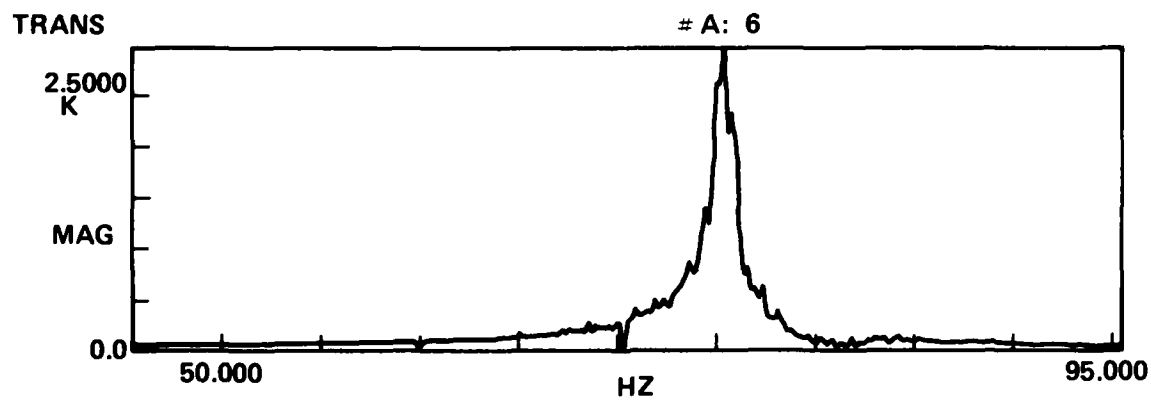
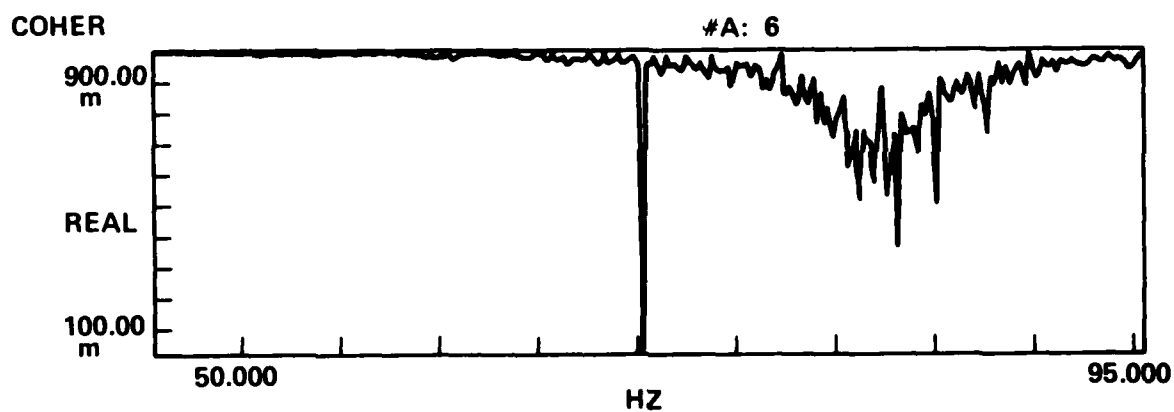


Figure 7. Comparison of Hammer Signal with and without Amplifier.

A. Hammer Signal Amplified



B. No Hammer Signal Amplified

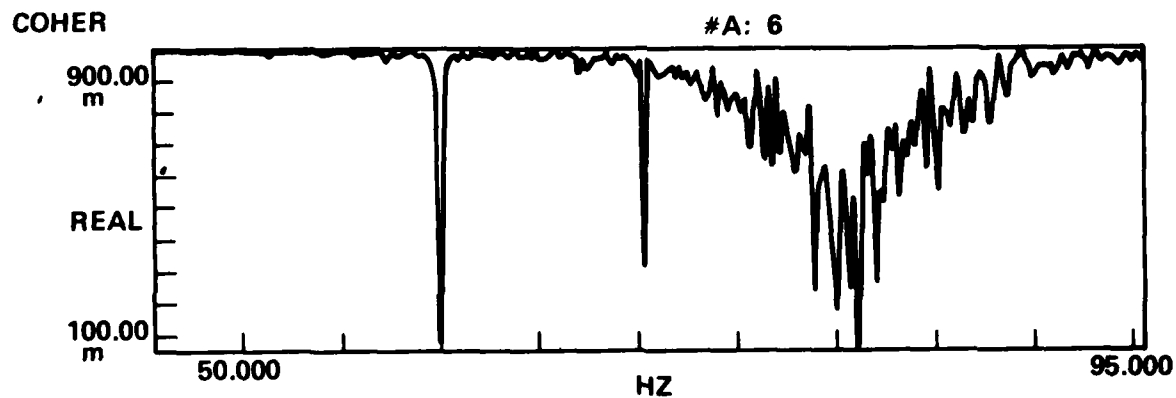


Figure 8. Comparison of Coherence with and without Amplifier.

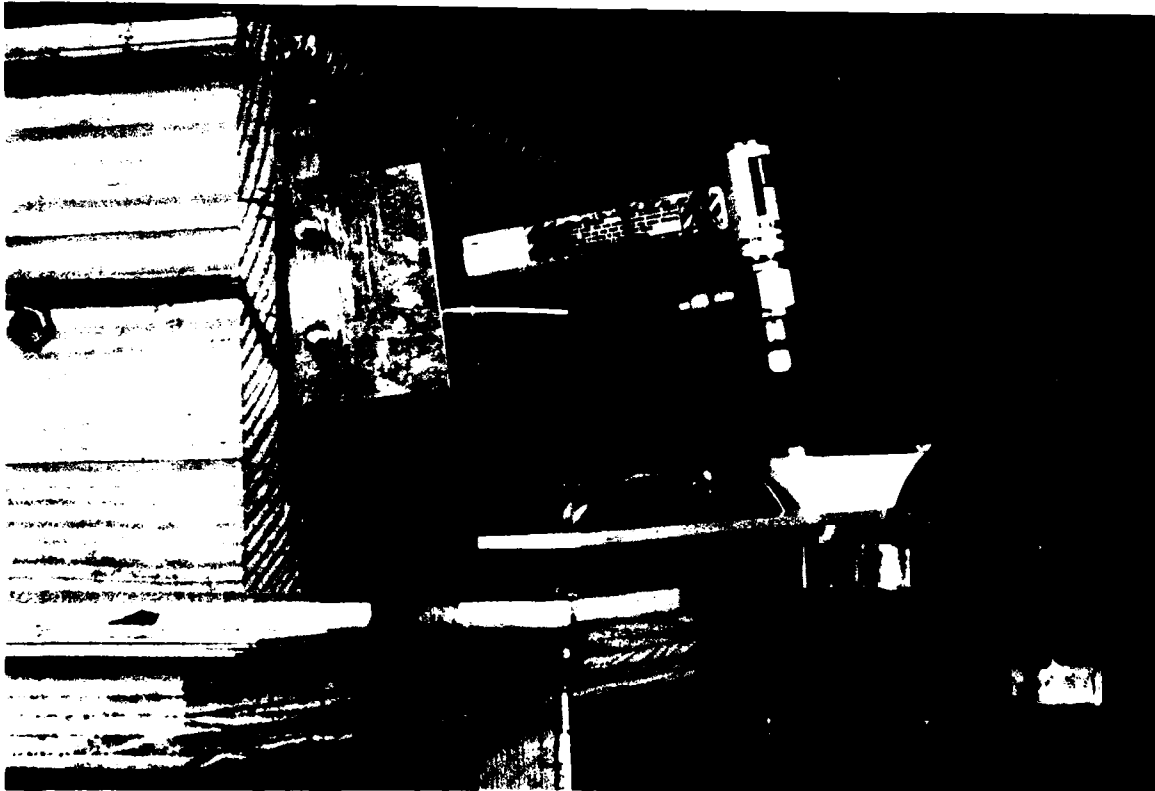
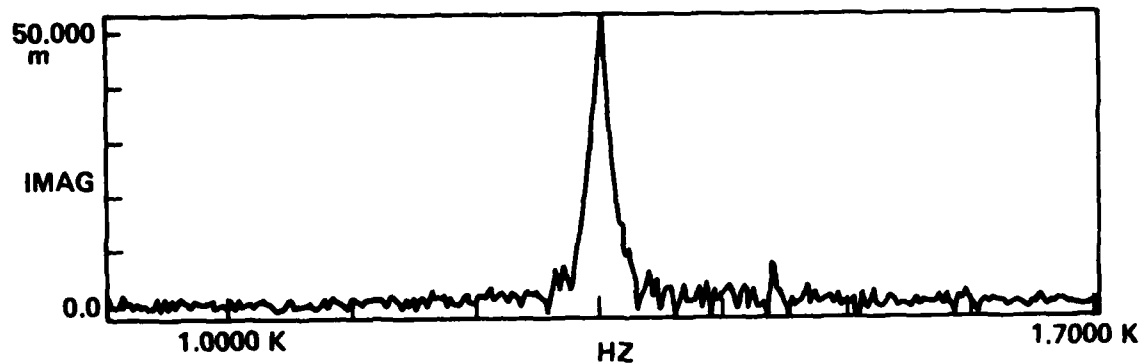


Figure 9. Photographic View of Spring Attached to the Hammer.

A. With spring

TRANS

A: 6



B. No spring

TRANS

A: 6

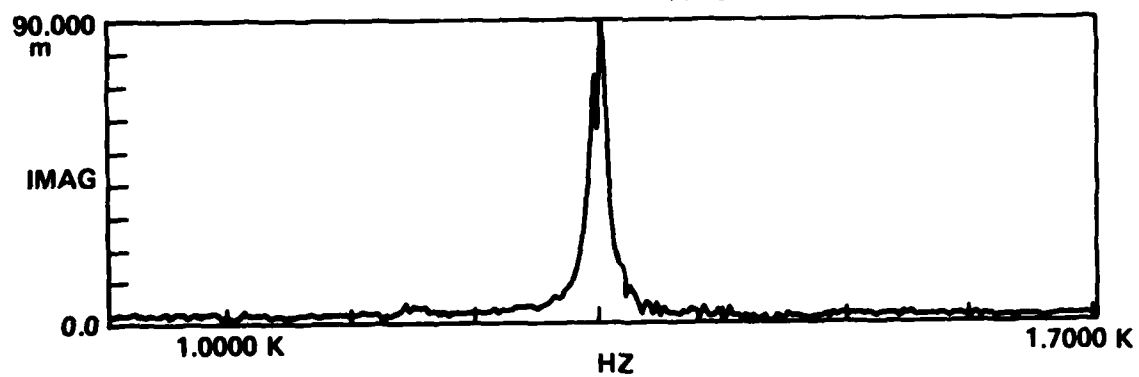
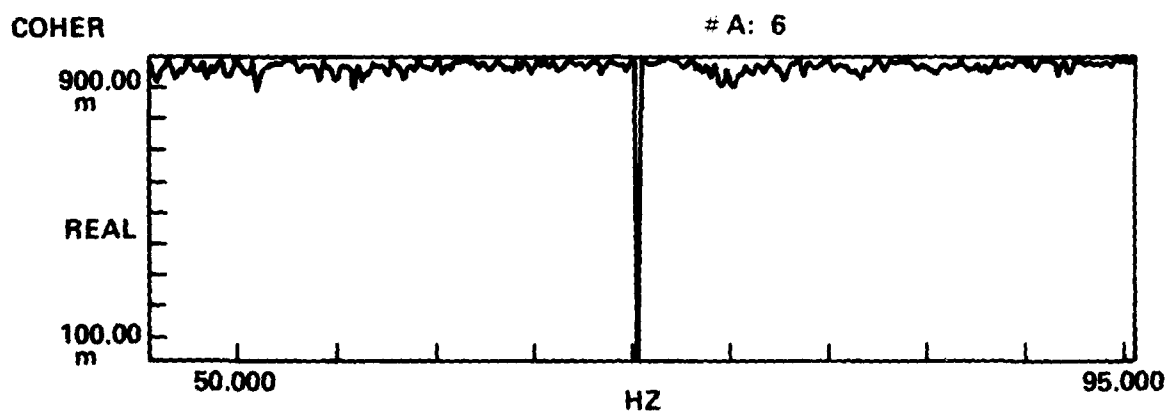


Figure 10. Imaginary Part of the Transfer Function with and without Spring Control.

A. With spring



B. No spring

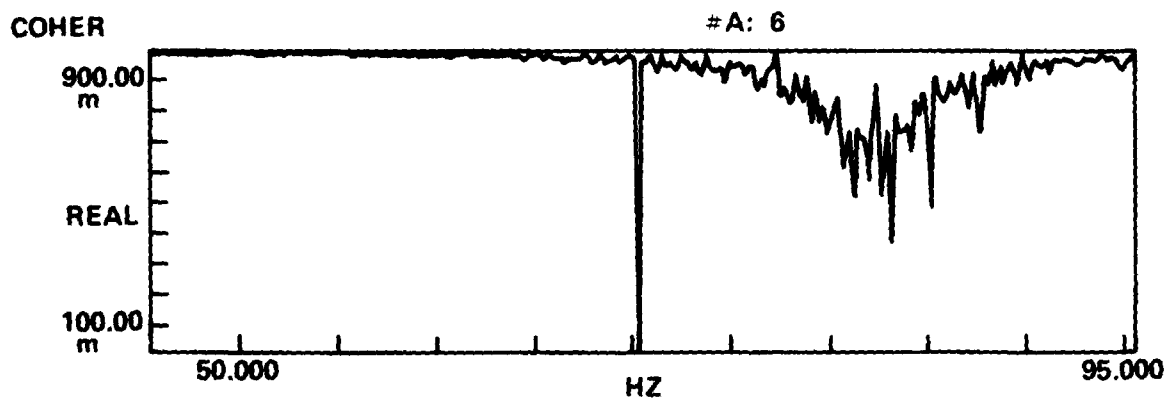


Figure 11. Coherence Function with and without Spring Control.

Table 1: Specimen Dimensions

Specimen	Length (in)	Width (in)	Thickness (in)	Mass (gram)
Aluminum 2024 - T3	9.5	0.75	0.125	42.9
E-Glass/Polyester PPG-SMC R65	5.5	1.0	0.112	20.2
Graphite/Epoxy HY-E 1034C [90 ₂ /0 ₆ /90 ₂] s	9.5	1.0	0.115	28.4
Kevlar/Epoxy HY-E 1734A2 [Unidirectional]	9.6	1.0	0.12	26.75
Hybrid Composite Owens-Corning G4 [O/R/O/R/O]	9.625	1.5	0.178	91.6
Mass of Transducer + Nut + Connector				4.1

Table 2: Comparison of Experimental Results using Contact and Non-Contact Probe.

Specimen	Mode	Non-Contact	Contact
		$\eta \times 10^{-4}$	$\eta \times 10^{-4}$
Aluminum 2024 - T3	1st	14.33	33.61
	2nd	3.28	7.65
	3rd	2.46	2.83
E-Glass/Polyester PPG-SMC R65	1st	77.83	204.1
	2nd	100.22	155.6
	3rd	71.79	178.5

(2a)

Specimen	Mode	Non-Contact	Contact
		$\eta \times 10^{-4}$	$\eta \times 10^{-4}$
Graphite/Epoxy HY-E 1034C [90 ₂ /0 ₆ /90 ₂] _s	1st	33.85	52.9
	2nd	40.83	61.5
	3rd	31.32	33.3
Kevlar/Epoxy HY-E 1734 A2 [Unidirection]	1st	43.59	62.5
	2nd	44.36	50.7
	3rd	31.95	53.4
Hybrid Composite Owens-Corning G4 [O/R/O/R/O]	1st	32.86	46.8
	2nd	42.16	59.8
	3rd	40.47	65.3

(2b)

Table 3: Comparison of Experimental Results using Base – Band Measurement and Zoom Measurement.

Specimen	Base-band Measurement (0 – 1.6 KHz)	Zoom Measurement	
	$\eta \times 10^{-4}$	$\eta \times 10^{-4}$	BW (Hz)
Aluminum 2024 - T3	1529.4	14.33	8
	229.9	3.28	25
	83	2.46	50
E-Glass/Polyester PPG-SMC R65	798.7	77.83	50
	266.6	100.22	400
	96.2	71.79	800

(3a)

Specimen	Base-band Measurement (0 – 1.6 KHz)	Zoom Measurement	
	$\eta \times 10^{-4}$	$\eta \times 10^{-4}$	BW (Hz)
Graphite/Epoxy HY-E 1034C [90 ₂ /0 ₆ /90 ₂] _s	1529.4	33.85	12.5
	219.8	40.83	100
	78.4	31.32	200
Kevlar/Epoxy HY-E 1734 A ₂ [Unidirection]	1172.4	43.59	12.5
	176.9	44.36	100
	---	31.95	400
Hybrid Composite Owens-Corning G4 [O/R/O/R/O]	1327.4	32.86	12.5
	224.7	42.16	100
	161.3	40.47	400

(3b)

Table 4: Final Experimental Results.

Specimen	Loss Factor, $\eta \times 10^{-4}$ (1st Mode)		
	Signal Amplified	No Amplified	Existing Values*
Aluminum (43 Hz) 2024 - T3	14.33	14.34	10.5
E-Glass/Polyester (75 Hz) PPG-SMC R65	77.83	103.46	90.0
Graphite/Epoxy HY-E 1034C (43 Hz) [90 ₂ /0 ₆ /90 ₂] _s	33.85	33.85	--
Kevlar/Epoxy HY-E 1734A ₂ (56 Hz) [Unidirection]	43.59	42.92	--
Hybrid Compoiste Owens-Corning G4 (45 Hz) [O/R/O/R/O]	32.86	41.93	--

*Suarez, Gibson and Deobald: "Development of Experimental Techniques for Measurement of Damping in Composite Materials", SESA 1983 Fall meeting, Salt Lake City, Utah, Nov. 6-10, 1983.

(4a)

Loss Factor, $\eta \times 10^{-4}$ (2nd Mode)			
Specimen	Signal Amplified	No Amplified	Existing Values*
Aluminum (275 Hz) 2024 - T3	3.28	3.29	3.0
E-Glass/Polyester (467 Hz) PPG-SMC R65	100.22	100.55	98.0
Graphite/Epoxy HY-E 1034C (287 Hz) [90 ₂ /0 ₆ /90 ₂] _s	40.83	40.83	---
Kevlar/Epoxy HY-E 1734 A ₂ (354 Hz) [Unidirection]	44.36	44.42	---
Hybrid Composite Owens-Corning G4 (277 Hz) [O/R/O/R/O]	42.16	42.22	---

*Suarez, Gibson and Deobald: "Development of Experimental Techniques for Measurement of Damping in Composite Materials", SESA 1983 Fall meeting, Salt Lake City, Utah, Nov. 6-10, 1983.

(4b)

Loss Factor, $\eta \times 10^{-4}$ (3rd Mode)			
Specimen	Signal Amplified	No Amplified	Existing Values*
Aluminum (771 Hz) 2024 - T3	2.46	2.46	2.3
E-Glass/Polyester (1296 Hz) PPG - SMC R65	71.79	71.88	99.0
Graphite/Epoxy HY-E 1034C (794 Hz) [90 ₂ /0 ₆ /90 ₂] _s	31.32	39.04	---
Kevlar/Epoxy HY-E 1734 A ₂ (976 Hz) [Unidirection]	31.95	32.16	---
Hybrid Composite Owens-Corning G4 (773 Hz) [O/R/O/R/O]	40.47	40.47	---

*Suarez, Gibson and Deobald: "Development of Experimental Techniques for Measurement of Damping in Composite Materials", SESA 1983 Fall meeting, Salt Lake City, Utah, Nov. 6-10, 1983.

(4c)

IMPROVED EXTENSIONAL MODULUS MEASUREMENTS
FOR POLYMERS AND METAL MATRIX COMPOSITES

Walter Madigosky
Naval Surface Weapons Center
White Oak
Silver Spring, Maryland 20910

Improved Extensional Modulus Measurements
for Polymers and Metal Matrix Composites

MADIGOSKY, Walter

Naval Surface Weapons Center
White Oak, Silver Spring, MD 20910

ABSTRACT

An improved resonance apparatus for rapid and reliable materials characterization is described. The apparatus accurately determines the propagation constants of an extensional acoustic wave by exciting a bar of material at one end by a noise source while the other is allowed to move freely. Miniature accelerometers measure the accelerations at the two locations. A dual channel Fast Fourier Transform (FFT) spectrum analyzer is used to obtain the amplitude and phase response as a function of frequency from which the complex Young's modulus can be obtained. Young's modulus and loss factor measurements have been successfully measured in materials ranging from soft polymers to rigid metal matrix composites. For viscoelastic materials the method of fractional derivatives is found to successfully model the complex modulus throughout the transition region, and suggests that the four independent constants used are indeed related to the measurable physical properties and chemical composition of the material.

INTRODUCTION

Various methods ¹⁻³ have been used to determine the mechanical properties of materials. Recently, an apparatus employing progressive waves has been refined by computer automation and reported by us in the literature.⁴ However, this apparatus has a number of disadvantages. (a) It is limited to measuring the mechanical properties of "rubber like" viscoelastic materials (with a modulus between 5×10^6 to 5×10^9 dynes/cm²). (b) A loss factor lower than 0.2 can not be accurately measured. (c) The long test sample that is required is found to be cumbersome and difficult to manufacture, and is not always available. (d) Even with long test samples (60 cm), resonance can not be prevented in materials with high modulus and/or low loss factor. (e) Finally, the apparatus requires a well trained operator.

The purpose of this paper is to describe an improved resonance apparatus and to demonstrate its superiority to others. Unlike the progressive wave apparatus, this apparatus is capable of characterizing a wide range of materials from soft polymers to rigid metals and stiff composites. The test sample size is relatively small and is easily mounted on the test fixture of the apparatus. Finally, the measurement procedure is simple, direct and less prone to operator error. We have successfully measured materials having moduli from 10^5 to 10^{13} dynes/cm² and loss factor from 0.004 to 5. With special care, a wider range may be possible.

APPARATUS

The apparatus consists of the following: (1) An electromagnetic shaker (Bruel & Kjaer type 4810) is used to drive a test specimen at one end while the other end is allowed to move freely. (2) Miniature accelerometers (Bruel & Kjaer type 8307) are mounted on each to measure the driving point acceleration and the acceleration at the free end. An important new feature of the apparatus is the use of random noise source to drive the test specimen. (3) Finally, the output signals from the accelerometers are then analyzed by a dual channel Fast Fourier Transform Spectrum Analyzer (Hewlett-Packard Spectrum Analyzer 3582A). The analyzer performs the following: digitizes and displays the measured signals as the amplitude of the acceleration ratio and the phase difference of the two accelerometers, and provides a noise source to drive the shaker. The amplitude and phase of acceleration ratio are continuously measured over a frequency range of five decades (.25 to 25,000 Hz). The individual measurement amplitude and phase accuracy of the 3582A is at least 0.4 dB and ± 2 degrees respectively, however, the data are always sampled at least 32 times and

RMS averaged which reduces the instrumentation error to a level below the error associated with the mechanical aspects of the apparatus. The acquisition of the data is further automated with mini-computer (Hewlett-Packard 9825A calculator). The calculator is programmed to initiate and control the frequency range and to collect and store data from the analyzer for later calculations. Typically, the length of the specimen is 15 cm, although much shorter and longer specimens have been used successfully. A typical lateral dimension is between 0.25 and 0.5 cm. The correction for "shape factor" was negligible and this was verified by an experimental study.

The output of the spectrum analyzer shows that at certain frequencies the amplitude of the acceleration ratio goes through a local resonant peak. In general, a number of peaks are observed. The lowest frequency peak is usually due to the classical resonance of both the added mass of the accelerometer and the distributed mass of the sample with the compliance of the sample. Higher frequency peaks are due to standing wave effects in which the length of the sample is an integral multiple of the wavelength. This data, peak amplitude and frequency, are used to calculate the Young's modulus and loss factor.

Finally, for viscoelastic materials measurements may be made at several temperatures, typically between -50 and 100°C, and a family of modulus and loss factor curves is obtained over a range of frequencies at a constant temperature. The data are then processed in one of two ways: as a temperature plot or as a frequency plot. In the traditional plot, only the first resonant peak data are used and plotted as a function of temperature. In this case the data points actually vary with frequency. In a frequency plot, modulus and loss factor curves are mechanically shifted until they partially overlap in a well-known procedure called time-temperature superposition. The final result is a constant temperature plot (master curve) over a wider frequency range than actually measured. The equations describing longitudinal forced vibration of a viscoelastic bar with added end mass have been presented in technical reports by Norris and Young⁵.

DISCUSSION

As an illustration of the use of the apparatus, the Young's modulus and loss factor of a commercially available polyurethane (Witco Chemical Company, New Castle, Delaware, density = 1.16 g/cm³, sample number 24-8-1) were determined. Typical amplitude and phase of the acceleration ratio, plotted against frequency at 17°C, are shown in Figure 1. From this plot, Young's modulus and loss factor

are determined. By repeating the measurements at different temperatures, a family of modulus and loss factor curves, each over a range of frequencies, is obtained. From this data, a temperature or frequency plot can be made.

The modulus and loss factor versus temperature is shown in Figure 2. From the peak of the loss factor curve, the glass transition temperature is 40°C at approximately 400 Hz. Also, the modulus and loss factor can be plotted against frequency (master curve) as shown in Figure 3 by mechanically shifting the data until they overlap. The shifted data span approximately eight decades of frequency, although the actual measurements are made over two decades. Just how far the time temperature-superposition principle may be used is not known. The reliability of the shifted data two decades above and below the measurement range is well established with older techniques. The data shifted beyond that range using this improved apparatus appears reasonable. Finally, we compare the data with a current viscoelastic model based on fractional operators.⁶ It can be shown that the model, in its simplest form, gives a complex Young's modulus

$$Y^* = Y_{\infty} + (Y_0 - Y_{\infty}) / (1 + (i f/f_0)^{\beta})$$

where Y_0 and Y_{∞} are the low and high frequency limiting moduli, f_0 is the frequency at which the imaginary part of Y is a maximum, and β is the slope of the real part of Y in the transition region. In general β is a number less than one.

In the case of polyurethane, to fit the data the model assumes three transition regions. The fractional operator model is extended to include the slopes β_r and β_g in the rubber and glass region. The solid curve in Figure 3 is the result of such a fit. The fit is relatively good. The advantage of the fractional operator model is that all of the parameters have physical meaning.

As a demonstration of the use of the apparatus for materials other than polymers, the modulus and loss factors of twelve metal matrix composite materials and six alloys were determined. Modulus values of 1.63×10^{12} and 9.93×10^{11} dyne/cm² were obtained, respectively, for a unidirectional reinforced graphite aluminum (DWA Composite Specialties, Inc., Chatsworth, CA, density = 2.49 g/cm³) and a short fiber silicon carbide aluminum (Exxon Enterprises, Greer, SC, density = 2.85 g/cm³). These moduli are in excellent agreement with measurements determined by an

ultrasonic method: 1.61×10^{12} and 9.79×10^{11} dyne/cm², respectively, as shown in Table 1. The remaining ten samples were composites of reinforced lead, carbon-carbon and silicon carbide. The results are shown in Table 2 and represent original data on these materials. Similar data for six alloys are given in Table 3. The three Nitinol (55% Ni, 45% Ti) alloys were formed as follows: (I) Hot formed, heat treated 1/2 hr at 1000°, water quenched, aged 650° for 1 hr, cooled. (II) Hot formed, extruded, heat treated 1 hr at 1000°. (III) Blended elemental composition (not an alloy), sintered density 90%.

REFERENCES

1. W. S. Cramer, "Propagation of stress waves in rubber rods," J. Polym. Sci. XXVI, 57-65 (1957).
2. R. S. Witte, B. A. Mrowca and E. Guth, "Propagation of audiofrequency sound in high polymers," J. Appl. Phys. 20, 481-485 (1949).
3. T. M. Lee, "Method of determining dynamic properties of viscoelastic solids employing forced vibration," J. Appl. Phys. 34, 1524-1529 (1963).
4. W. M. Madigosky and G. Lee, "Automated dynamic Young's modulus and loss factor measurements," J. Acoust. Soc. Am. 66, 345-349 (1979).
5. D. M. Norris, Jr. and Wun-Chung Young, "Complex Modulus Measurement by Longitudinal Vibration Testing," Experimental Mechanics, 10, 93-96 (1970).
6. L. Rogers, "Operators and Fractional Derivatives for Viscoelastic Constitutive Equations," to be published, J. Rheology.

Table 1 Measured Young's Moduli (dynes/cm²) of two
Metal Matrix Composites

Sample	Resonance Technique	Ultrasonic Method
Unidirectional Graphite- Aluminum ^a ($\rho = 2.85 \text{ gm/cm}^3$)	1.63×10^{12}	1.61×10^{12}
Short Fiber silicon carbide-aluminum ^b ($\rho = 2.85 \text{ gm/cm}^3$)	9.93×10^{11}	9.79×10^{11}

(a) DWA Composites Specialties, Inc. Chatsworth, CA.

(b) Exxon Enterprises, Greer, SC.

Table 2 Dynamic Elastic Young's Moduli

Sample	f (Hz)	E	δ
		(10^{10} dynes/cm ²)	
Aluminum (6061-T6)	5764	70.8	.004
	17470	71.7	.004
Chemical Lead (Pb)	1891	23.8	.028
	5717	24.2	.025
	9462	23.9	.014
	13209	23.7	.011
	16962	23.7	.017
	20651	23.5	.015
	24317	23.3	.014
Reinforced Lead (FP-05)	2735	33.0	.010
	7873	30.3	.008
	13417	31.2	.003
	18773	30.9	.003
	24497	31.5	.004
Reinforced Lead (FP-10)	2652	30.6	.008
	8198	32.1	.009
	13386	30.6	.005
	18702	30.3	.006
	24338	30.6	.011
Nextel/Pb 10% (NE-10)	2183	30.9	.008
	6834	33.6	.008
	11079	31.8	.006
	15414	31.7	.008
	19637	30.6	.006
Nextel/Pb 20% (NE-20)	3102	44.4	.007
	8761	39.3	.024
	14595	39.3	.006
	20599	39.9	.004
Carbon/Carbon (CC-15)	14900	167.	.29
Carbon/Carbon (CC-17)	11,100	146.	.011
Glass Roving/Pb 10% (SG-10)	2270	26.6	.013
	6806	26.5	.006
	11415	26.9	.004
	15889	26.6	.007
	20378	26.4	.008

Dynamic Elastic Young's Moduli (Con't)

Sample	f (Hz)	E	
		(10 ¹⁰ dynes/cm ²)	δ
Glass Roving/Pb 20% (SG-20)	2412	34.2	.010
	7314	34.8	.024
	12231	35.1	.011
	16751	33.6	.008
	21564	33.6	.005
SiC Reinforced Pb (SG-15)	4052	38.7	.005
	11998	37.8	.007
	19967	37.5	.009
SiC Reinforced Pb (SC-30)	4844	49.8	.045
	14164	47.4	.006
	23405	46.5	.008

Table 3 Measured Viscoelastic Properties

	Young's Modulus (10 ⁶ psi)	Loss Factor
Cu ^{54.2} -Mn ⁴⁴ -Al ^{1.8}	12.5	.04
Fe ⁸⁵ -Cr ¹² -Al ³	10.5	.08
Mn ^{54.5} -Cr ³⁶ -Al ^{4.5} -Ni ² -Fe ³	7.7	.12
Ni ⁵⁵ -Ti ⁴⁵ (I)	8.4	.01
Ni ⁵⁵ -Ti ⁴⁵ (II)	8.2	.04
Ni ⁵⁵ -Ti ⁴⁵ (III)	13.8	.05

(superscript indicates percentage)

FIGURE 1. Typical measured amplitude ratio and phase data versus frequency for the polyurethane sample at 17°C. Five resonant peaks can be identified.

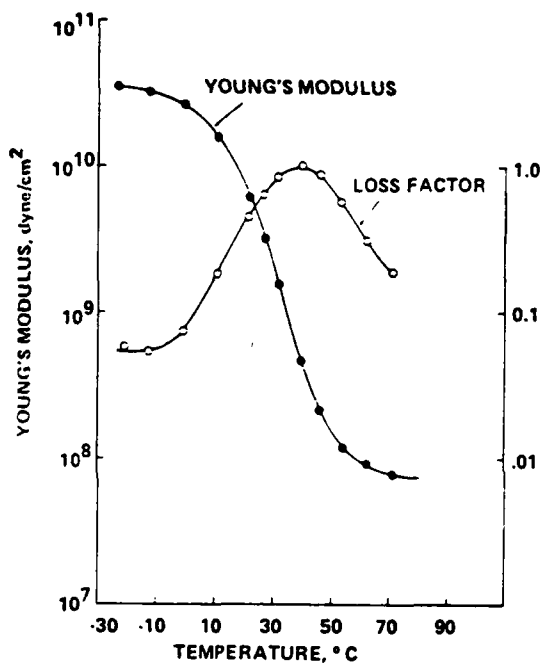
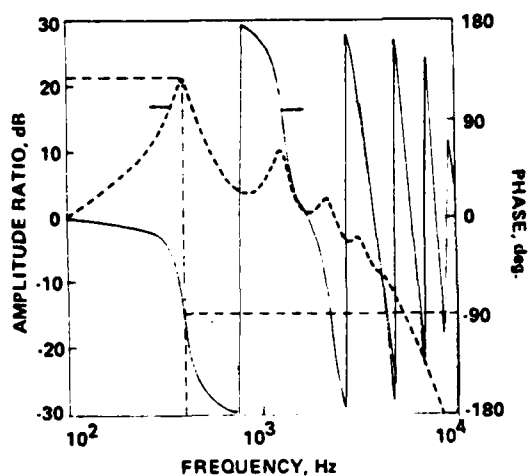
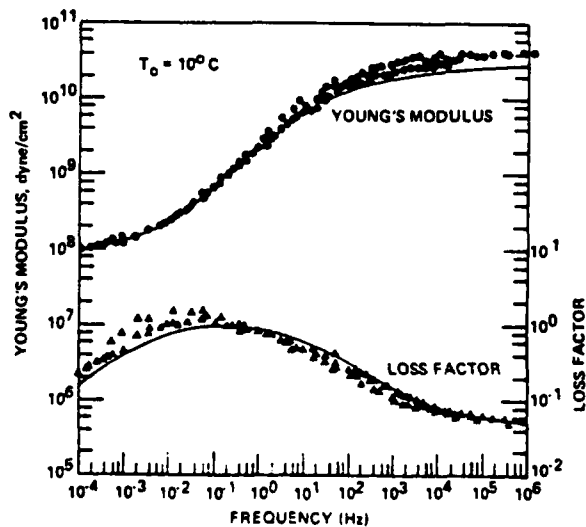


FIGURE 2. Young's modulus and loss factor for the polyurethane sample, as determined from the first resonant mode, versus temperature.

FIGURE 3. Master curve of the Young's modulus and loss factor for the polyurethane sample versus frequency at 10°C. Solid curve is the Fractional Operator model fit.



MATERIAL DAMPING OF CARBON/EPOXY COMPOSITES
BY MEANS OF FREE-FREE BEAM RESONANCE TESTS

Daniel W. Haines
Mechanical Engineering Department
Manhattan College
Riverdale, New York 10471

Paper was not presented; submitted for publication.

MATERIAL DAMPING OF CARBON/EPOXY
COMPOSITES BY MEANS OF
FREE-FREE BEAM RESONANCE TESTS

Daniel W. Haines
Mechanical Engineering Department
Manhattan College
Riverdale, N. Y. 10471

ABSTRACT

Results are presented of a testing program which characterizes the principal (0° and 90°) damping properties of unidirectional composites incorporating Celion carbon fibers. Data for $0/\pm 45/90_s$ specimens are also presented. Use of free-free beam resonance tests eliminated errors introduced by support conditions. This test method also enables the determination of Young's moduli and the shear modulus in the plane of bending.

INTRODUCTION

A total of 35 specimens supplied by the Celion Carbon Fibers Division, Celanese Corporation, were tested dynamically to determine damping and other material properties. The specimens were rectangular strips measuring 15 x 1.3 x 0.2cm. (6 x 0.5 x 0.08 in., nominal). All were carbon fiber-reinforced composites except for two aluminum specimens used for control tests. Damping of flexural vibration at a resonance frequency was the material property of central interest. Also obtained for each strip were Young's modulus and velocity of sound in the lengthwise direction of the strip and the material density. Four specimens were selected for which we obtained, in addition, damping at all resonance frequencies in the audio range (20-20,000 Hz) and the shear modulus for deformation in the plane of bending (bending occurred about the weak axis). The strips were tested as beams with free end conditions, subjected to forced sinusoidal excitation.

SPECIMEN DESCRIPTION

Five systems of fiber-resin combinations were supplied. These are designated as 3KO8, 6KO8, 3K13, 6K13, GY70, and identified as follows:

3KO8:	Celion 3000 fiber, Narmco 5208 resin (350° F. Cure)
3K13:	Celion 3000 fiber, Narmco 5213 resin (250° F. Cure)
6KO8:	Celion 6000 fiber, Narmco 5208 resin
6K13:	Celion 6000 fiber, Narmco 5213 resin
GY70:	Celion GY-70 fiber, Fiberite 934 resin (350° Cure)

The Celion 3000 and 6000 carbon fibers have identical elastic modulus (34×10^6 psi, 234 GPa, typically) but differ in filament count, 3000 and 6000 filaments per yarn, respectively. The elastic modulus of the Celion GY-70 carbon fiber is typically 75×10^6 psi, 517 GPa.

The test specimens consisted of eight plies, each ply nominally ten mils thick. From unidirectional plates, both 0° and 90° strip specimens were removed for testing, the 0° specimens being the stiffest and the 90° specimens being the least stiff. A third set of strip specimens were prepared from a plate with 0/±45/90 symmetric ply arrangement, the 0° direction coinciding with the length of the beam. Note that all strips were symmetric with respect to their neutral axis of bending.

At least two specimens were provided for each system-orientation combination. Accordingly, we have the following table showing the number of specimens provided for each combination.

System	0°	90°	0/+45/90 _s
3KO8	2	2	6
3K13	2	2	
6KO8	2	2	
6K13	2	2	
GY70	3	2	6
Aluminum (Isotropic)	2		

The specimens were A-B-C coded such that A indicated replicate number, B the system, and C the fiber orientation, e.g. 1-3KO8-0 and 2-GY70-45.

TEST PROCEDURE

Our method of determining material properties requires the excitation of the strips at a low flexural resonance frequency and recording that resonance frequency to determine the velocity of sound and Young's modulus. To find the damping, we record either or both the decay of free vibration at the resonance frequency or by means of forced sinusoidal excitation, the frequencies on both sides of the resonance peak which correspond to a 3dB reduction in amplitude from the peak value. Since damping is often strongly dependant on frequency, these procedures can be repeated for all resonance frequencies in the audio range. The theory for these test principles can be found in the texts of Timoshenko¹ and Thomson².

A block diagram of the experimental apparatus is shown in Figure 1. The strip is suspended at two of the calculated nodes on two fine, taut threads. A small ferrous armature attached to one end of the strip permits the strip to be excited into vibration by means of the electromagnetic transducer driven by the oscillator. The amplitude of vibration is detected at the other end of the strip by the small microphone placed close to the surface at an antinode. The detected signal is filtered, if necessary, and amplified before its amplitude is measured on the meter. Purity of signal is best checked by observation on the screen of the real time analyzer. When damping is measured by means of the decay method, the high speed level recorder measures the decay rate when the oscillator circuit is abruptly broken. All single (low) frequency tests were performed in this manner.

EXPERIMENTAL APPARATUS

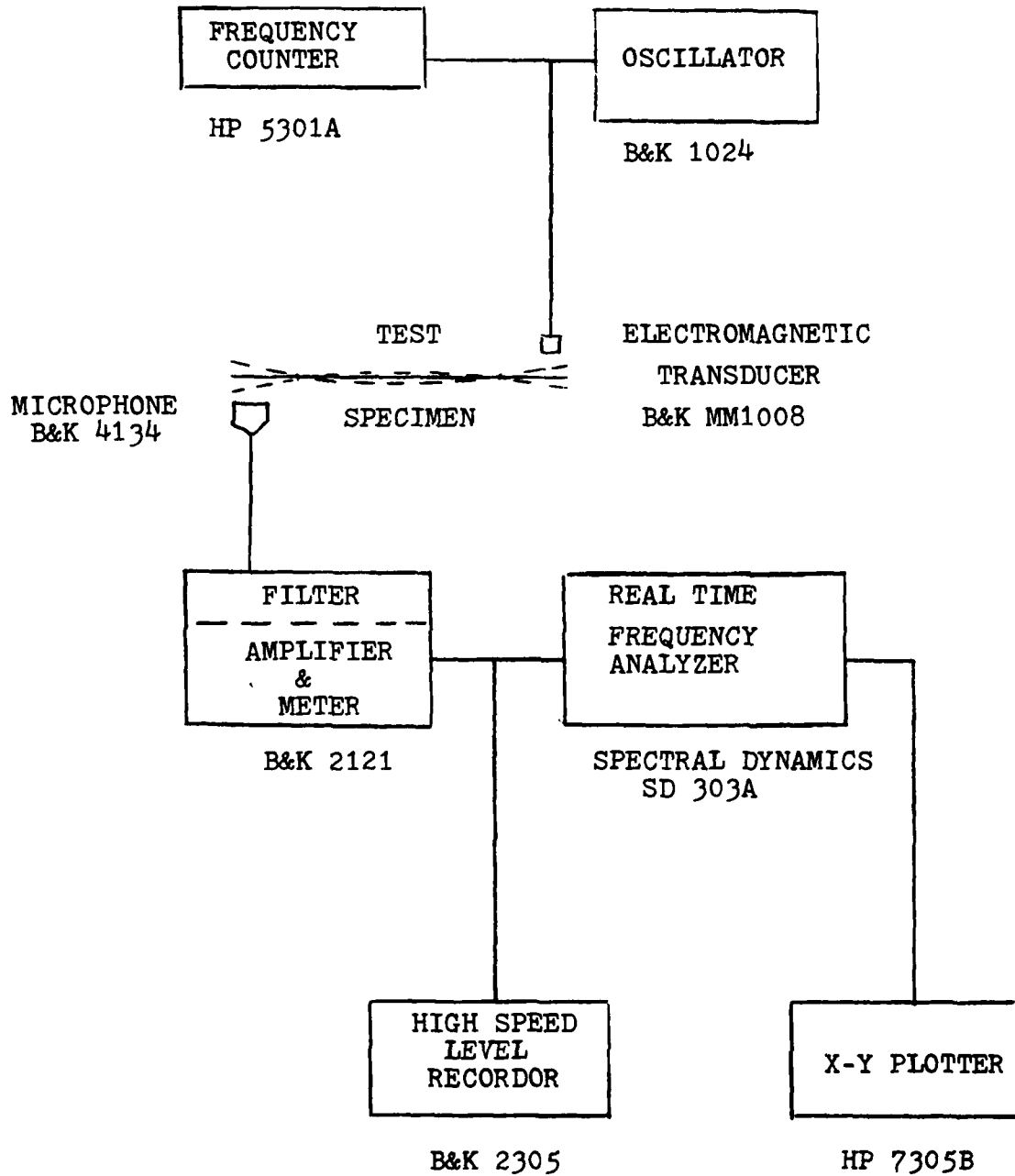


FIGURE 1

The multiple frequency tests required the use of a heavier armature to produce a sufficiently strong signal at high frequencies to overcome the background noise, even when filtered. The band width method was used to measure damping at high frequencies. The heavier armature lowers the resonance frequencies significantly, so to obtain an accurate spectrum of resonance frequencies, the armature was removed and the specimen lightly tapped to produce a "ring" (transient capable of being captured and analyzed by the real time analyzer (See Figure 2).

BASIC EQUATIONS

For the lower resonance frequencies, Bernoulli-Euler beam theory is sufficiently accurate. The velocity of sound, c , may be calculated from

$$c = \frac{0.974 f_1 L^2}{H} \quad (1)$$

where f_1 is the lowest resonance frequency of the free-free beam, L is its length, and H is its thickness. If the next lowest resonance frequency is used the equation is

$$c = \frac{0.553 f_2 L^2}{H} \quad (2)$$

where f_2 is the frequency. Young's modulus, E , is found from

$$E = \rho c^2 \quad (3)$$

where ρ is the material density.

The distance of a node from the end is $0.224L$ for the fundamental mode (lowest resonance frequency) and

$$\frac{0.661 L}{2n+1}, \quad n > 1 \quad (4)$$

for the higher modes.

For the band width method of damping measurement the quality factor

$$Q = \frac{f}{f_H - f_L} \quad (5)$$

where f is the resonance frequency and f_H and f_L are the nearest higher and lower frequencies, respectively, at which the measured amplitude is 3dB less than at f . When the decay method is used the reverberation time, T_{60} , is easily measured from the slope of the decay curve. The reverberation time is defined to be the time required for the amplitude to diminish 60 dB. It can be shown that

$$Q = \frac{T_{60} f}{2.2} \quad (6)$$

SPECIMEN 1-GY70-45
FREE VIBRATION FREQUENCY
ANALYSIS BY TRANSIENT
CAPTURE ON REAL TIME
ANALYZER - SD330A

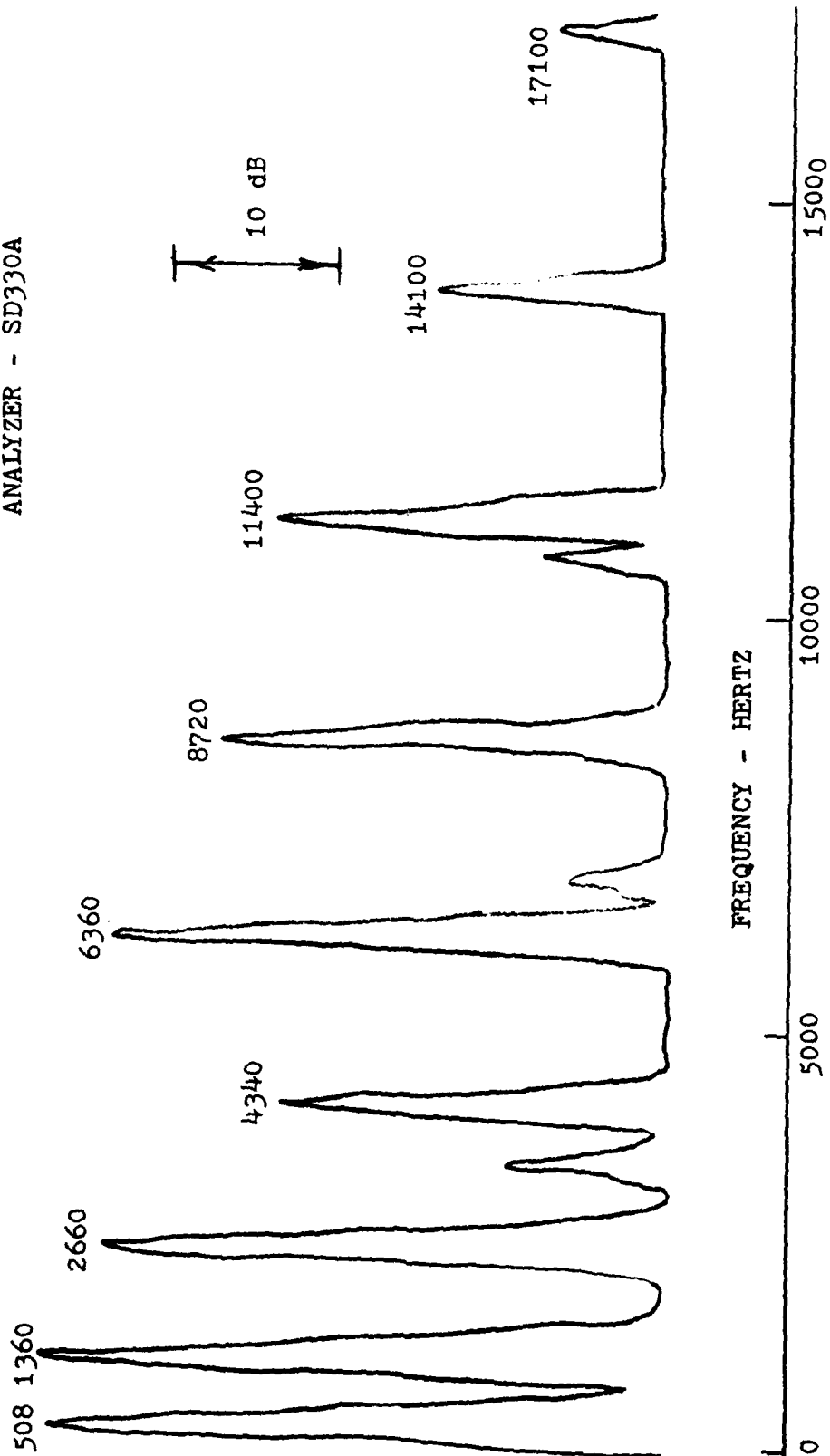


FIGURE 2

if the damping is viscous. Viscous damping occurs if the decay curve is a straight line on a plot with a logarithmic vertical scale such as that on the high speed level recorder. The records obtained in this series of tests confirmed that the assumption of viscous damping for this material is valid.

The shear modulus cannot be found from a simple explicit formula with this resonance method. The effect of shear deformation and rotatory inertia is to lower the resonance frequencies from their values as predicted by the elementary Bernoulli-Euler beam theory which neglects these effects. This phenomenon grows more and more pronounced as one obtains higher and higher resonance frequencies; in our tests the elementary theory is adequate for the lowest frequencies. The more complex Timoshenko beam theory incorporates the effects of shear deformation and rotatory inertia. We used the equations of this theory to calculate the shear modulus from the data provided by all resonance frequencies in the audio range for the specimen. A computer program incorporating a least squares technique was used to find the shear and Young's moduli which produced the best match with the eight or so experimentally determined frequencies.

SAMPLE CALCULATIONS

Specimen 1-6K13-0

$$H = 0.226 \text{ cm}$$

$$\rho = 1.54 \text{ g/cm}^3$$

$$L = 15.30 \text{ cm}$$

$$f_1 = 922 \text{ Hz}$$

From Eq. 1,

$$C = \frac{0.974 \times 922 \times 15.30^2}{0.226}$$

$$C = 9.30 \times 10^5 \text{ cm/sec} \quad (9300 \text{ m/sec})$$

From Eq. 3,

$$E = 1.54 (9.30 \times 10^5)^2$$

$$E = 13.3 \times 10^{11} \text{ d/cm}^2 \quad (133 \text{ GPa}, 19.3 \text{ Mpsi})$$

From Eq. 6,

$$Q = \frac{4.4 \times 922}{2.2}$$

$$Q = 1800$$

Specimen 1-3K08-90

$$H = 0.204 \text{ cm}$$

$$\rho = 1.60 \text{ g/cm}^3$$

$$L = 15.28 \text{ cm}$$

$$f_1 = 249 \text{ Hz}$$

$$f_2 = 679 \text{ Hz}$$

From Eq. 1,

$$C = \frac{0.474 \times 249 \times 15.28^2}{0.204}$$

$$C = 2.78 \times 10^5 \text{ cm/sec} \quad (2780 \text{ m/sec})$$

From Eq. 2,

$$C = \frac{0.353 \times 679 \times 15.28^2}{0.204}$$

$$C = 2.74 \times 10^5 \text{ cm/sec} \quad (2740 \text{ m/sec})$$

Use the higher value.

From Eq. 3,

$$E = 1.60 (2.78 \times 10^5)^2$$

$$E = 1.23 \times 10^{11} \text{ d/cm}^2 \quad (12.3 \text{ GPa}, 1.79 \text{ Mpsi})$$

From Eq. 6,

$$Q = \frac{0.24 \times 679}{2.2}$$

$$Q = 74$$

Specimen 1-GY70-45

(Multiple frequency test)

This specimen was also tested in the single frequency test series.
For damping at mode 3 from Eq. 5,

$$Q = \frac{2576}{2580 - 2568}$$

$$Q = 210$$

RESULTS AND DISCUSSION

The material properties as calculated from each single frequency test are given in Tables 1, 2, and 3. Average values are shown in Table 4. The damping information obtained from the four multiple frequency tests is displayed in Figure 3 and the shear moduli from these tests is given in Table 5.

TABLE 1
MATERIAL PROPERTIES FROM SINGLE
FREQUENCY TESTS - 0° ORIENTATION

Specimen Identi- fication	Density g/cm ³	Velocity of Sound m/sec	Yeung's Modulus		Damping Q	Resonance Frequency Hz
			GPa	Mpsi		
Alum 1	2.76	5130	73	10.5	3100	466
Alum 2	2.76	5160	74	10.7	3200	471
1-3KO8-0	1.59	9630	147	21.3	1500	859
2-3KO8-0	1.58	9530	144	20.9	1500	808
1-3K13-0	1.56	9380	137	19.9	2100	896
2-3K13-0	1.56	9270	134	19.4	2000	866
1-6KO8-0	1.57	9480	141	20.4	1300	897
2-6KO8-0	1.55	9400	137	19.9	1300	867
1-6K13-0	1.54	9300	133	19.3	1800	922
2-6K13-0	1.54	9240	131	19.0	2000	896
1-GY70-0	1.66	13300	294	42.6	850	1052
2-GY70-0	1.68	13100	289	41.9	1000	1128
3-GY70-0	1.67	12900	276	40.0	690	1089

The primary purpose of this series of tests was to obtain damping data for the composites. Values for the other material properties had previously been obtained by means of static tests. Examination of Table 4 verifies that all composite specimens tested are more highly damped (lower Q) than aluminum. The data in Table 4 is grouped to display the evidence that the damping of 0° specimens is essentially fiber controlled and damping of 90° specimens is essentially resin controlled.

The first observation is that the Q of all 0° specimens is significantly higher than for any of the 90° specimens, indicating as expected that the carbon fiber material is less damped than the resin. All values of Q for the 0° and 90° specimens verify that the resins may be listed in decreasing order of Q as: Narmco 5213, Narmco 5208, Fiberite 934, while a similar listing for the fiber gives Celion 3000, Celion 6000, GY70. Note that the low temperature cured 5213 resin produced the highest Q's by far even though its stiffness appeared to be less than the 5208 resin. Generally, stiffer materials produce higher Q's. Exceptions such as we seem to find here are not rare however.

As a guide to the use of these results for predicting the damping of panels made of these materials, we suggest taking the average of 0° and 90° results for two dimensional modes in the 400-1100 Hz frequency range. For example, $Q = 800$ is suggested for two dimensional panel vibrations of the 3K08 aligned material. If one dimensional modes occur in a panel then the values of Q in Table 4 may be used directly. The Q's obtained for the $0^\circ/45^\circ/90^\circ$ specimens are closer to those of corresponding 90° specimens than 0° specimens. This may be due to the orientations (90° and $\pm 45^\circ$) of the inner layers of this laminate where the shear deformation is greater.

Our original plan was to obtain these material properties by means of vibrating the specimens as cantilever beams in a commercially available complex modulus fixture. The data we recorded for these tests had to be discarded when it was discovered that the stiffnesses calculated from these test results were obviously too low from comparison with results of static tests³. The cantilever beam method gave Q values which were also far too low. The cause of these errors was traced to the inability to achieve full fixity at the clamped end and the inevitable absorption of vibrational energy at this location.

Use of the free-free beam concept with non-contacting excitation (electromagnetic) and response (microphone) minimize support damping and allows for highly accurate determination of material damping.

TABLE 2
MATERIAL PROPERTIES FROM SINGLE
FREQUENCY TESTS - 90° ORIENTATION

Specimen Identi- fication	Density g/cm ³	Velocity of Sound m/sec	Young's Modulus GPa Mpsi		Damping Q	Resonance Frequency Hz
1-3KO8-90	1.60	2780	12.3	1.79	74	679
2-3KO8-90	1.61	2790	12.5	1.81	85	667
1-3K13-90	1.56	2590	10.5	1.52	130	686
2-3K13-90	1.57	2600	10.6	1.54	140	684
1-6KO8-90	1.58	2720	11.6	1.68	70	701
2-6KO8-90	1.58	2710	11.6	1.68	73	696
1-GK13-90	1.55	2580	10.3	1.49	120	703
2-6K13-90	1.55	2570	10.3	1.49	130	697
1-GY70-90	1.68	2040	7.0	1.02	63	432
2-GY70-90	1.67	2040	6.9	1.00	60	441

TABLE 3
MATERIAL PROPERTIES FROM SINGLE
FREQUENCY TESTS
0/45/90 ORIENTATION

Specimen Identi- fication	Density g/cm ³	Velocity of Sound m/sec	Young's Modulus		Damping Q	Resonance Frequency Hz
			GPa	Mpsi		
		*	*	*		
1-3KO8-45	1.52	5220	41.4	6.00	230	461
2-3KO8-45	1.57	5560	48.4	7.02	250	522
3-3KO8-45	1.61	5850	55.1	7.99	270	546
4-3KO8-45	1.57	5680	50.0	7.34	300	542
5-3KO8-45	1.57	5530	47.9	6.95	250	519
6-3KO8-45	1.55	5220	42.1	6.10	250	468
1-GY70-45	1.57	6060	57.5	8.34	300	504
2-GY70-45	1.63	6920	77.9	11.3	330	613
3-GY70-45	1.63	6920	78.2	11.3	370	626
4-GY70-45	1.64	6910	78.3	11.4	370	619
5-GY70-45	1.61	6860	75.9	11.0	260	629
6-GY70-45	1.62	6560	69.7	10.1	310	560

* Values listed for velocity of sound and Young's Modulus must be considered as "effective", useful only when the mechanism of deformation is flexural for laminates of 0.200 cm thickness.

TABLE 4
AVERAGE MATERIAL PROPERTIES
ALL SINGLE FREQUENCY TESTS

Specimen Identi- fication	Density g/cm ³	Velocity of Sound m/sec	Young's Modulus		Damping Q	Resonance Frequency Hz
			GPa	Mpsi		
Alum	2.77	5150	73	10.6	3200	469
3KO8-0	1.59	9580	146	21.1	1500	833
3K13-0	1.55	9330	136	19.7	2100	881
6KO8-0	1.56	9440	139	20.2	1300	882
6K13-0	1.54	9270	132	19.2	1900	909
GY70-0	1.67	13100	292	42.3	850	1090
3KO8-90	1.61	2790	12.4	1.80	80	673
3K13-90	1.56	2590	10.6	1.53	140	685
6KO8-90	1.58	2670	11.6	1.68	72	699
6K13-90	1.55	2570	10.3	1.49	130	700
GY70-90	1.67	2040	7.0	1.01	62	437
3KO8-45	1.56	5510*	47.6*	6.90*	260	510
GY70-45	1.62	6710*	72.9*	10.6*	320	670

* Effective values, valid only for flexure of laminates of 0.200 cm thickness.

DAMPING OF FLEXURAL VIBRATIONS
FOR SPECIMENS OF CELION
FIBER REINFORCED COMPOSITES

FREE-FREE BEAM TESTS

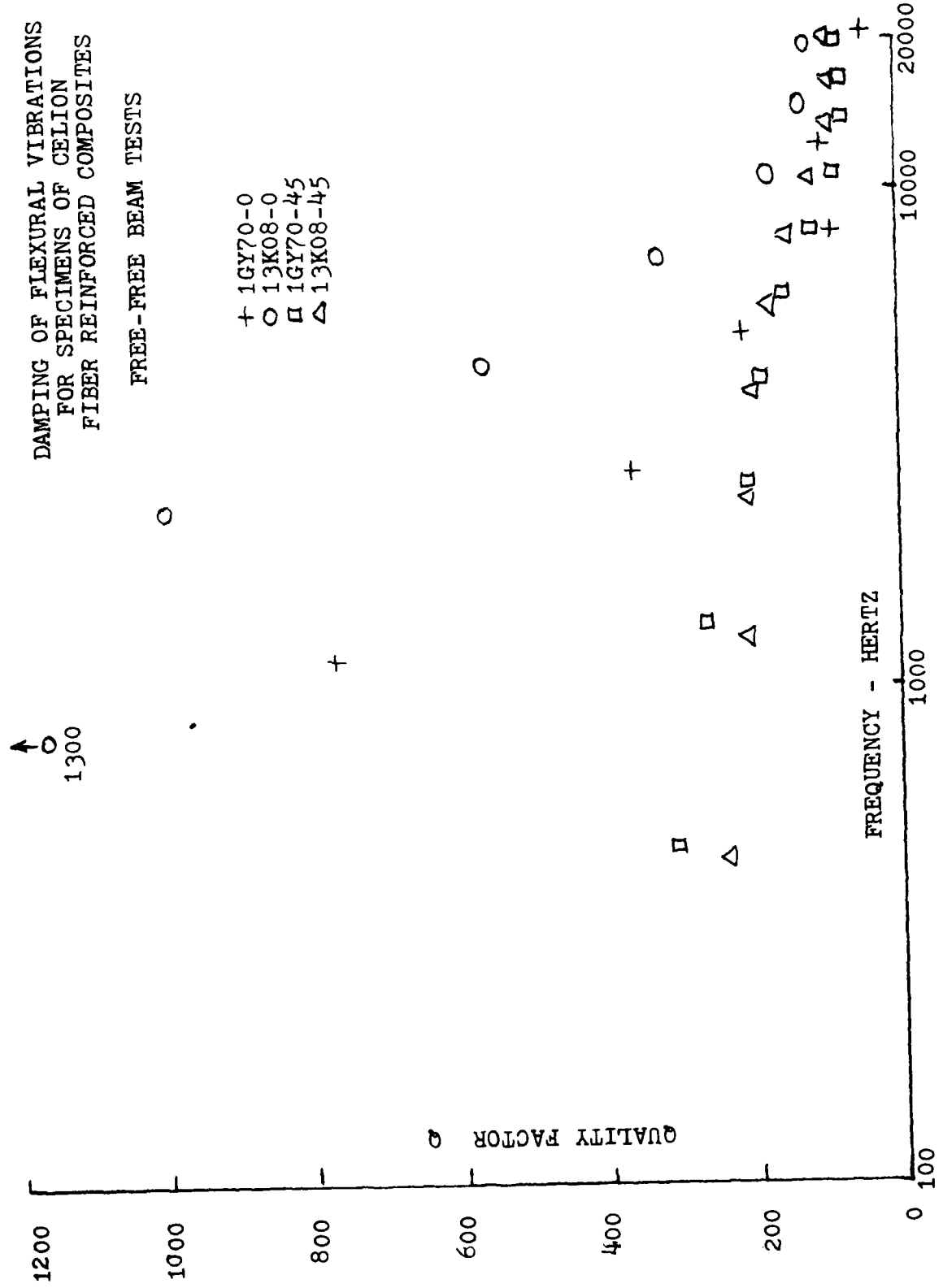


FIGURE 3

AD-A152 547

VIBRATION DAMPING WORKSHOP PROCEEDINGS HELD AT LONG
BEACH CALIFORNIA ON 2.. (U) AIR FORCE WRIGHT
AERONAUTICAL LABS WRIGHT-PATTERSON AFB OH L ROGERS

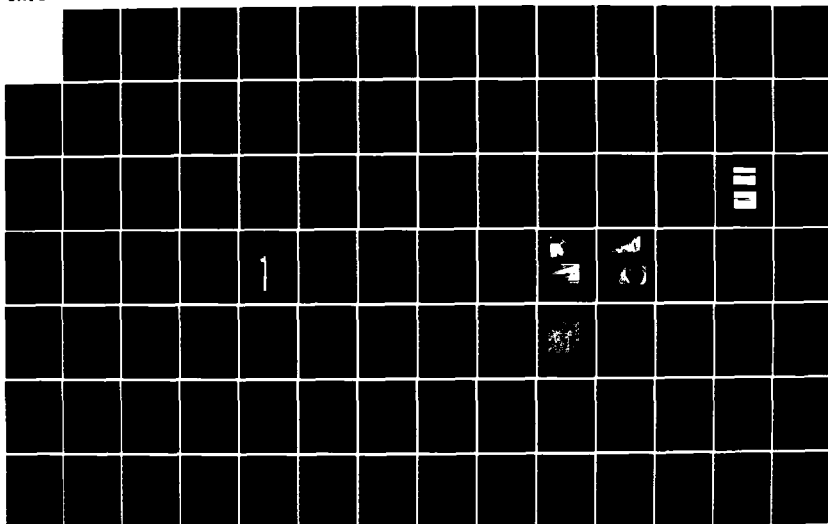
4/11

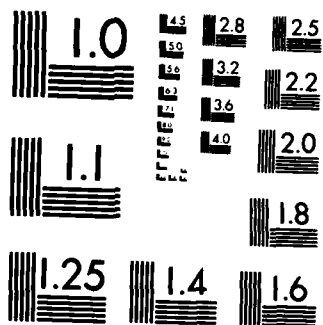
UNCLASSIFIED

11 NOV 84 AFMAL-TR-84-3064

F/G 20/11

NL





MICROCOPY RESOLUTION TEST CHART
NATIONAL BUREAU OF STANDARDS-1963-A

TABLE 5

SHEAR MODULI FROM MULTIPLE
FREQUENCY TESTS

Specimen Identification	$K^2 G (\text{lb/in}^2)$	Shear Modulus $G (\text{lb/in}^2)$
1-3KO8-0	0.45×10^6	0.5×10^6
1-GY70-0	1.0×10^6	1×10^6
1-3KO8-45	$0.47 \times 10^6 *$	$0.6 \times 10^6 *$
1-GY70-45	$0.26 \times 10^6 *$	$0.3 \times 10^6 *$

- NOTES:
1. The factor K^2 is Timoshenko's shear coefficient, taken to be $\pi^2/12$ to give the values of the shear modulus shown.
 2. Those values indicated by "*" can be considered only as "effective" values, valid only for shear of laminates of 0.200 cm thickness.

REFERENCES

1. S. Timoshenko and D. H. Young, Vibration Problems in Engineering, 3rd ed., Van Nostrand, New York, 1955.
2. W. T. Thomson, Theory of Vibration, Prentice Hall, Englewood Cliffs, N. J., 1972.
3. "Celion Carbon Fibers - Material Properties Composites", Celion Data Sheet, Celanese Corporation, April 1982.

ACKNOWLEDGEMENT

The support received from Celanese Corporation, in particular Dr. Howard S. Kliger, is gratefully acknowledged.

IMPROVEMENT OF DAMPING IN FIBER REINFORCED POLYMER COMPOSITES

R. F. Gibson, S. A. Suarez, and L. R. Deobald
Mechanical Engineering Department
University of Idaho
Moscow, Idaho 83843

IMPROVEMENT OF DAMPING IN
FIBER REINFORCED POLYMER COMPOSITES

R. F. Gibson, S. A. Suarez and L. R. Deobald

Mechanical Engineering Department
University of Idaho
Moscow, Idaho 83843

April 1984

ABSTRACT

This paper presents preliminary experimental results from a study of damping in aligned discontinuous fiber reinforced polymer composites. The experiments were conducted in order to verify a previously developed theoretical model, which predicted that discontinuous fiber reinforcement should enhance the shear-induced linear viscoelastic damping effect in the polymer matrix material. Data for graphite/epoxy and aramid/epoxy composites show that, as predicted, very low fiber aspect ratios are required to produce significant improvements in damping, and that damping also increases markedly with increasing vibration frequency at these low aspect ratios.

INTRODUCTION

In a recent paper by one of the authors, it was concluded that the use of discontinuous fiber reinforcement appears to be a very attractive approach to the problem of improvement of internal damping in fiber reinforced polymer composite materials [1]. This conclusion was based primarily on a study of the different damping mechanisms operating in these materials and on the results of an earlier theoretical analysis of damping in aligned discontinuous fiber reinforced composites [2]. In Reference [2], it was shown that there is a theoretically optimum fiber aspect ratio where the loss modulus in a discontinuous aligned fiber composite is maximized. Since the predicted optimum aspect ratios were very low ($L/D < 20$, where L is fiber length and D is fiber diameter), it was expected that only greater-than-optimum values would be practically attainable. The primary goal of the work discussed here was to fabricate and test composite specimens having fiber aspect ratios which were at least low enough that significant increases in damping could be measured. Graphite/epoxy, Kevlar/epoxy and boron/epoxy are currently being tested, but only the results for graphite/epoxy and Kevlar/epoxy were available at the time of preparation of this paper. Since many of the details regarding fabrication and testing have been published elsewhere, this paper will be concerned primarily with the presentation of current experimental results.

SPECIMEN FABRICATION

The procedure used to fabricate small beam-type specimens for the damping tests was similar to that reported in Reference [2], except that only 12 plies were used and the autoclave curing process was simulated in a laminating press. Fiberite* hy-E1034C (T-300 graphite fibers/934 epoxy resin) and Fiberite hy-E1734A2 (Kevlar 49 fibers/934 epoxy resin) pre-preg tapes 12 inches (304.8 mm) wide were cut into strips of different lengths and the strips were placed end-to-end in a staggered 12 ply lay-up sequence to form laminated plates 12 inches (304.8 mm) square. A standard utility knife was used to cut the tapes. The plates were then cured by using an autoclave cure cycle (Table 1) with a specially designed vacuum mold in a standard laminating press (Figure 1). Once the plates were cured, the beam specimens were machined by using either carbide or diamond cut-off wheels in a precision reciprocating grinder. Specimen dimensions are given in Table 2. Densities, fiber volume fractions, and void fractions were determined by using ASTM standards D-792 and D 3171-76, Procedure A. The autoclave-style press cure yielded autoclave-quality plates having void fractions of well below 1%. Neat resin specimens were also needed, since the micromechanics model required input data on the dynamic properties of the matrix resin [2]. Fiberite 934 resin castings 12 inches (304.8 mm) square by 1/8 inch (3.18 mm) thick were produced in an aluminum mold by using the procedure outlined in Table 3, and beam specimen dimensions are given in Table 2. Testing of all specimens was done within a few days after fabrication, so that moisture absorption was negligible.

* Fiberite Corporation, 501 W. 3rd St., Winona, Minnesota 55987.

EXPERIMENTAL TECHNIQUE

The forced vibration technique used to measure damping previously in Reference [2] was replaced by a faster, more accurate impulse technique described in References [3] and [4]. A detailed comparison of damping measurements from the old forced vibration technique with those from the new impulse technique and with those from a random excitation technique showed that the impulse method gives valid results [3,4]. Cantilever beam specimens were excited in flexural vibration with an electric solenoid-actuated hammer which had a force transducer in its tip, while the response was detected with an eddy current displacement transducer. The excitation and response signals were fed into a Fast Fourier Transform (FFT) analyzer, which computed and displayed the frequency-domain transfer function in real time. A desktop computer was interfaced with the FFT analyzer for data acquisition and reduction. The loss factor, η , was found from the half-power bandwidths of the resonant peaks of the transfer function, as described in [3] and [4]. Storage moduli were found from measured resonant frequencies and the frequency equation for a cantilever beam. All of the results reported here are in terms of the complex modulus, which is completely specified by the storage modulus and the loss factor. Alternatively, the results can be expressed in terms of the storage and loss moduli [1]. Due to the reduced response in the higher modes, only the first three flexural modes provided useful data.

EXPERIMENTAL RESULTS

In this section, current experimental results will be compared with predictions from the micromechanics analysis in Reference [2]. A micromechanics analysis is one in which the mechanical properties of the composite (in this case the storage and loss moduli) are expressed in terms of the corresponding properties of the constituent materials and their respective volume fractions. As shown in Reference [2], the following equation for the complex extensional modulus of an aligned discontinuous fiber reinforced composite may be derived by using a force-balance approach in combination with the elastic-viscoelastic correspondence principle:

$$E_c^* = E_f^* \left(1 - \frac{\tanh \beta^* L/2}{\beta^* L/2} \right) v_f + E_m^* v_m \quad (1)$$

where E_c^* , E_f^* , E_m^* = complex extensional modulus of composite, fiber and matrix, respectively,
 v_f , v_m = volume fractions of fiber and matrix, respectively,
 and β^* = function of matrix and fiber properties and volume fractions (defined in Reference [2]).

By separating real and imaginary parts and neglecting higher order terms in the loss factors, the equations for predicting storage and loss moduli may be found (equations 21 and 22 in Reference [2]). These equations were then used to generate the predicted curves in Figures 2 through 7 in this paper. In Figures 2 and 3, the dimensionless ratio of the composite loss modulus E_c''

to the matrix loss modulus E'' is plotted versus the fiber aspect ratio, L/D for the two materials tested^m. Figures 4 and 5 show the variation of the composite loss factors with fiber aspect ratio, while Figures 6 and 7 show the variation of the storage moduli with aspect ratio. Figures 8 through 11 show the raw data for loss factor and storage modulus versus frequency for the first three flexural modes. Each experimental data point in Figures 2 through 7 represents the average value based on six specimens at the first flexural mode frequency, and the corresponding predicted curves are based on measured matrix data at the same frequency. Curve fits to matrix resin data similar to that shown in Figures 8-11 were used to estimate the matrix properties at the frequencies corresponding to the composite first mode frequencies.

It is interesting to note that the predicted loss factor continually increases with decreasing fiber aspect ratio, whereas the predicted loss modulus goes through a maximum at the optimum aspect ratio. Significant improvements in damping and corresponding reductions in stiffness are evident as the fiber aspect ratio is reduced. Experimental composite damping is consistently greater than predicted, whether we look at the loss factor or the loss modulus. On the other hand, experimental composite storage moduli are always less than predicted. All predicted curves are based on the assumption that the fibers are nondissipative, and that all damping is due to the polymer matrix. As shown in Reference [2], however, the predicted loss modulus curves can be made to fit the experimental data by assuming the proper value for the fiber loss factor. Although this has not been done here, it is obvious that a greater assumed fiber loss factor would be required for Kevlar than for graphite. Thus, it appears that either the Kevlar fibers have much better damping than the graphite fibers, or the Kevlar/epoxy interfacial region contributes more damping than the corresponding interfacial region for graphite/epoxy. It also appears that the experimental data could be made to fall closer to the predicted curves if the experimental fiber aspect ratio were based on something other than a single fiber, as it is in the figures. This is particularly true for the storage modulus data shown in Figures 6 and 7. For example, a larger effective fiber diameter (possibly based on a fiber bundle) might explain the difference. Work is continuing on the selection of curve-fitting parameters to improve the accuracy of the predictions. Additional insight is expected from the experimental data on boron/epoxy, because the relatively large boron fiber diameter will make it possible to fabricate specimens with near-optimum aspect ratios.

Figures 8 and 9 show that the composite loss factor does not change very much with increasing frequency for continuous fiber reinforcement, but increases markedly with increasing frequency as the fiber aspect ratio is reduced. On the other hand, Figures 10 and 11 show that the storage modulus appears to be essentially independent of frequency, regardless of fiber aspect ratio. These findings have important implications for structures subjected to high frequency vibrations. The exact mechanism for the increased dissipation in low aspect ratio composites at high frequencies is not known, but the increased shear deformation associated with shorter vibrational wavelengths may be partly responsible. Here again, the experimental results for boron/epoxy should provide additional insight at the lower aspect ratios.

ACKNOWLEDGEMENTS

The authors are grateful for the financial support of U.S. Air Force Office of Scientific Research Grant No. AFOSR-83-0156, monitored by Dr. Donald R. Ulrich. We would also like to give credit to John Sterner and Carolyn Ahern, undergraduate assistants, and Darrel Brown, machinist, for their valuable contributions to this research program.

REFERENCES

1. Gibson, R.F., "Development of Damping Composite Materials," 1983 Advances in Aerospace Structures, Materials and Dynamics, AD-06, American Society of Mechanical Engineers (1983).
2. Gibson, R.F., Chaturvedi, S.K. and Sun, C.T., "Complex Moduli of Aligned Discontinuous Fibre-Reinforced Polymer Composites," Journal of Materials Science, 17, 3499-3509 (1982).
3. Suarez, S.A., Gibson, R.F. and Deobald, L.R., "Development of Experimental Techniques for Measurement of Damping in Composite Materials," Proc. Soc. for Experimental Stress Analysis 1983 Fall Meeting, Salt Lake City, Utah (Nov. 1983).
4. Suarez, S.A., Gibson, R.F. and Deobald, L.R., "Random and Impulse Techniques for Measurement of Damping in Composite Materials," Experimental Techniques, in print.

TABLE 1

Cure Cycle for Fiberite Hy-E1034C (graphite/epoxy) and Hy-E1734A2
(Kevlar/epoxy) prepregs (both have same resin system)

-
1. Apply vacuum to mold-bag assembly.
 2. Heat to 245°F @ 3°-5°F/minute.
 3. Hold 15 min. @ 245°F.
 4. Apply 100 psi pressure.
 5. Hold 45 minutes.
 6. Heat to 350°F @ 3°-5°F/minute.
 7. Hold @ 350°F for 2 hours.
 8. Cool to 150°F under vacuum and pressure.
-

TABLE 2
Description of Specimens

Number of Specimens	Fiber Length (in.)	Specimen Length (mm)	Width (in.)	Thickness (in.)	Density lb/in ³	Density (g/cc)
<u>GRAPHITE/EPOXY</u>						
6	7.5	(190.5)	7.5	(18.948)	0.062	(1.575) 0.0571 (1.584)
6	1/2	(12.7)	7.5	(19.304)	0.0588	(1.494) 0.0571 (1.584)
6	1/4	(6.35)	7.5	(18.618)	0.06	(1.523) 0.0572 (1.586)
6	1/8	(3.175)	7.5	(19.025)	0.061	(1.554) 0.0568 (1.574)
6	1/6	(1.588)	7.5	(19.126)	0.0625	(1.588) 0.0567 (1.573)
<u>KEVLAR/EPOXY</u>						
5	7.5	(190.5)	7.5	(19.177)	0.0528	(1.341) 0.0492 (1.362)
5	1/2	(12.7)	7.5	(19.177)	0.0542	(1.377) 0.0487 (1.348)
6	1/4	(6.35)	7.5	(18.796)	0.0521	(1.323) 0.0477 (1.323)
6	1/8	(3.175)	7.5	(19.025)	0.053	(1.346) 0.049 (1.357)
6	1/16	(1.588)	7.5	(18.948)	0.0553	(1.405) 0.0498 (1.382)
<u>934 RESIN</u>						
6	N/A	7.5	0.744	(18.898)	0.123	(3.134) 0.0469 (1.298)

TABLE 3

Cure Cycle for Fiberite 934 Resin 350°F (177°C) Cure

-
1. Let resin warm overnight to room temperature.
 2. Heat in oven at 80°C for 1 hour.
 3. Heat in vacuum oven at 80°C for 1/2 hour.
 4. Coat mold inner surfaces with Frekote 33 mold release, then preheat mold to 125°C, then pour resin in mold.
 5. Cure in 100°C for 16 hours, then 177°C for 2 hours.
 6. Cool to room temperature.
-

AUTOClave-STYLE PRESS CURE

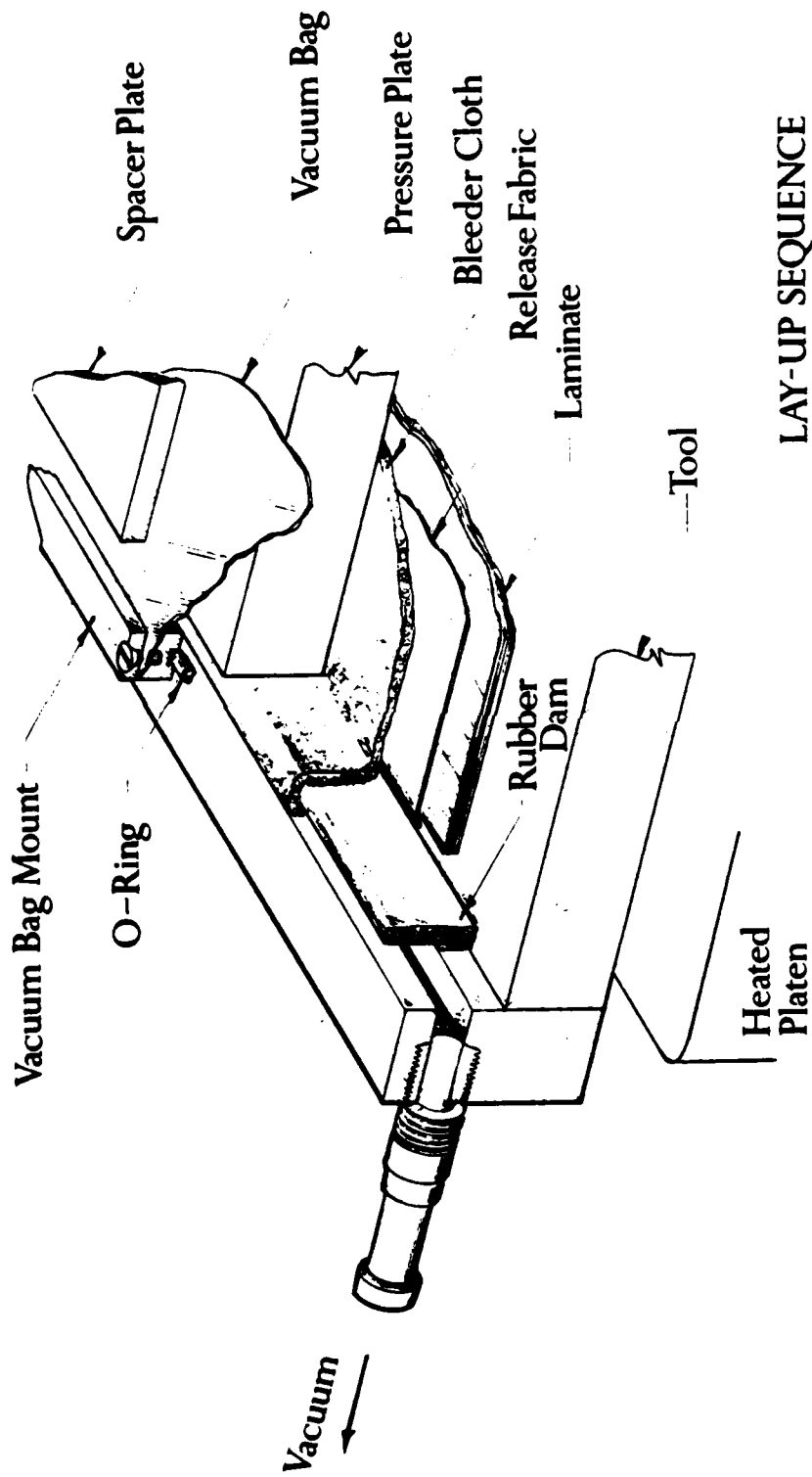


Figure 1. Cutaway view of autoclave-style press cure system.

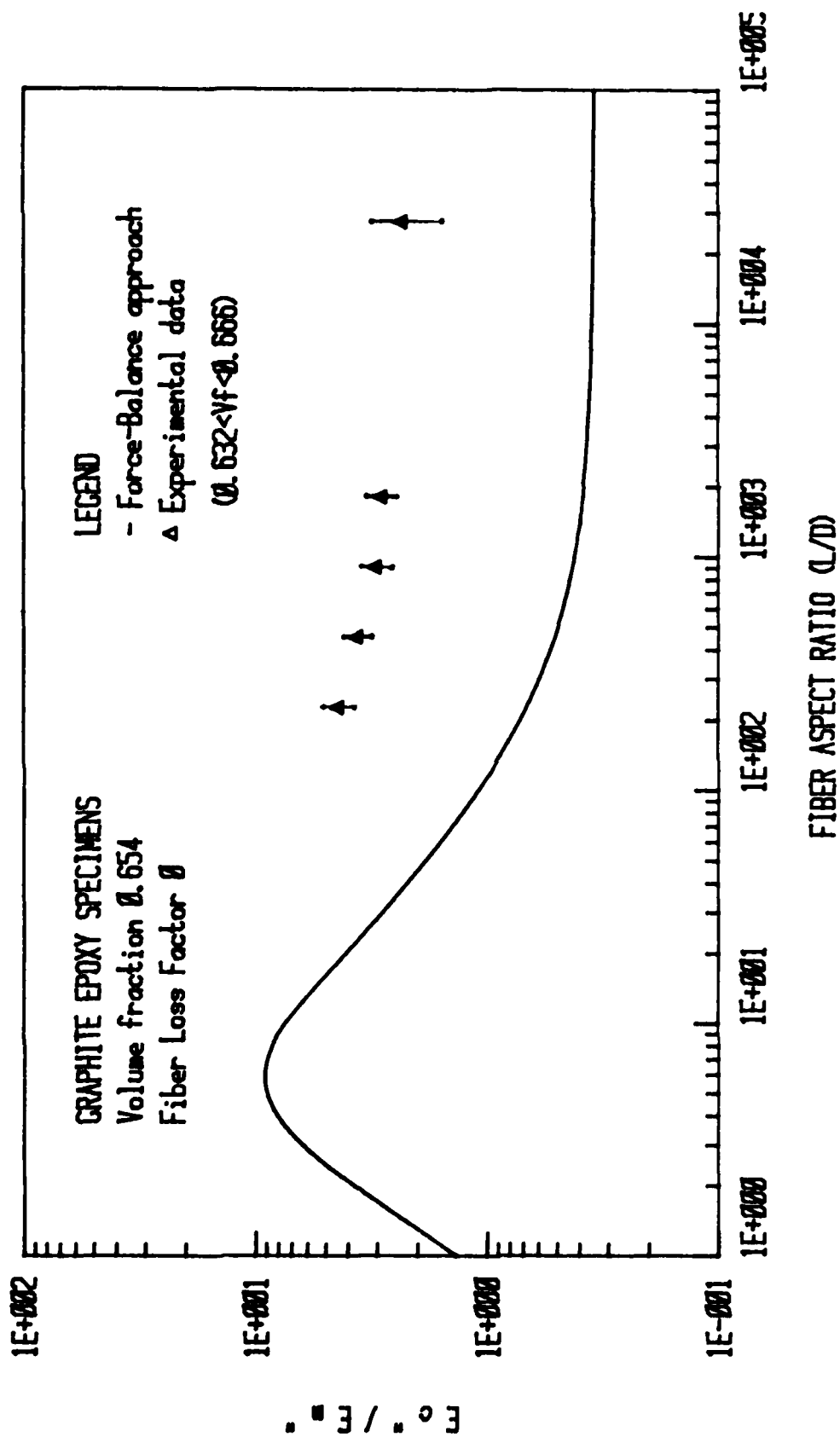


Figure 2. Ratio of composite loss modulus to matrix loss modulus versus fiber aspect ratio for graphite/epoxy.

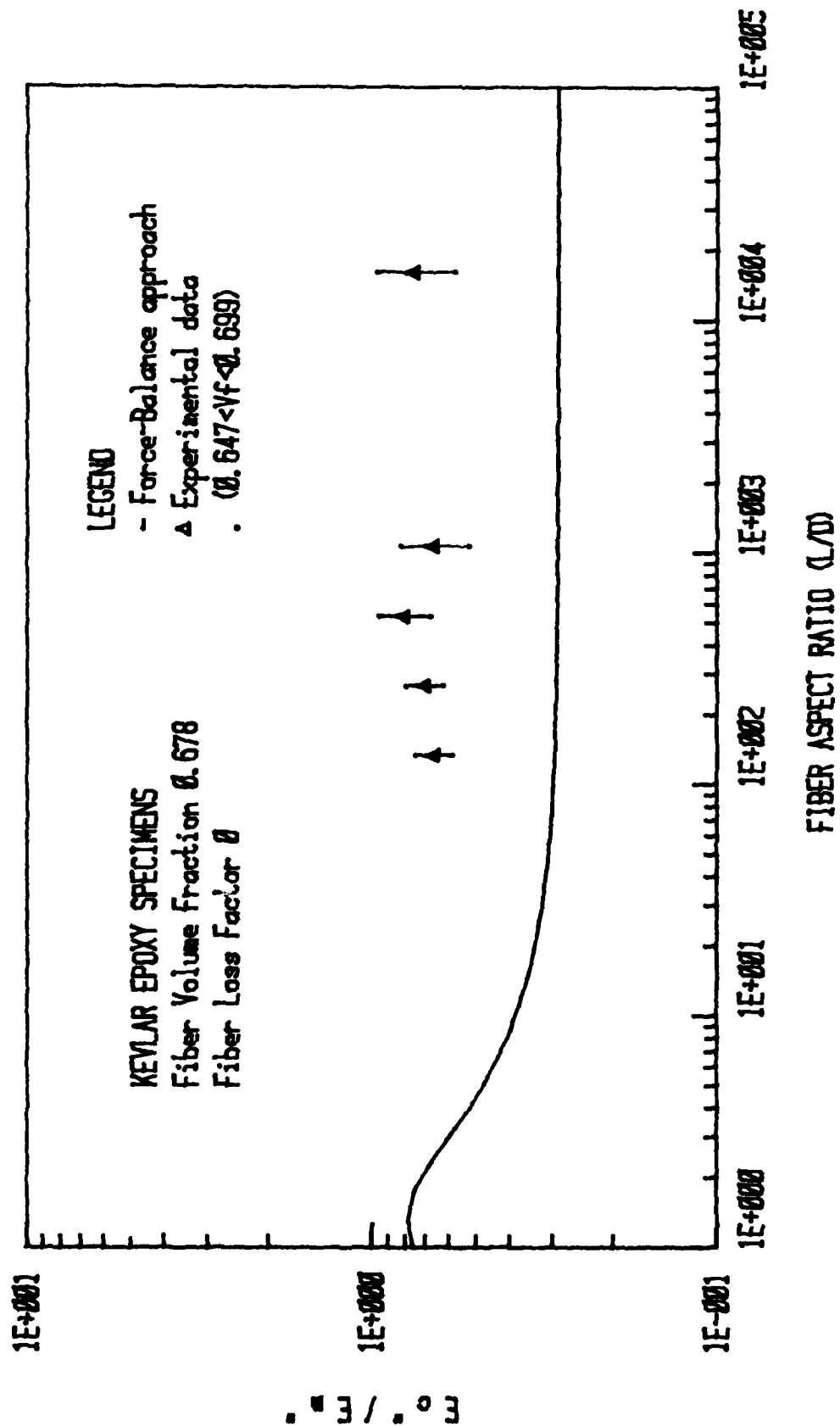


Figure 3. Ratio of composite loss modulus to matrix loss modulus versus fiber aspect ratio for Kevlar/epoxy.

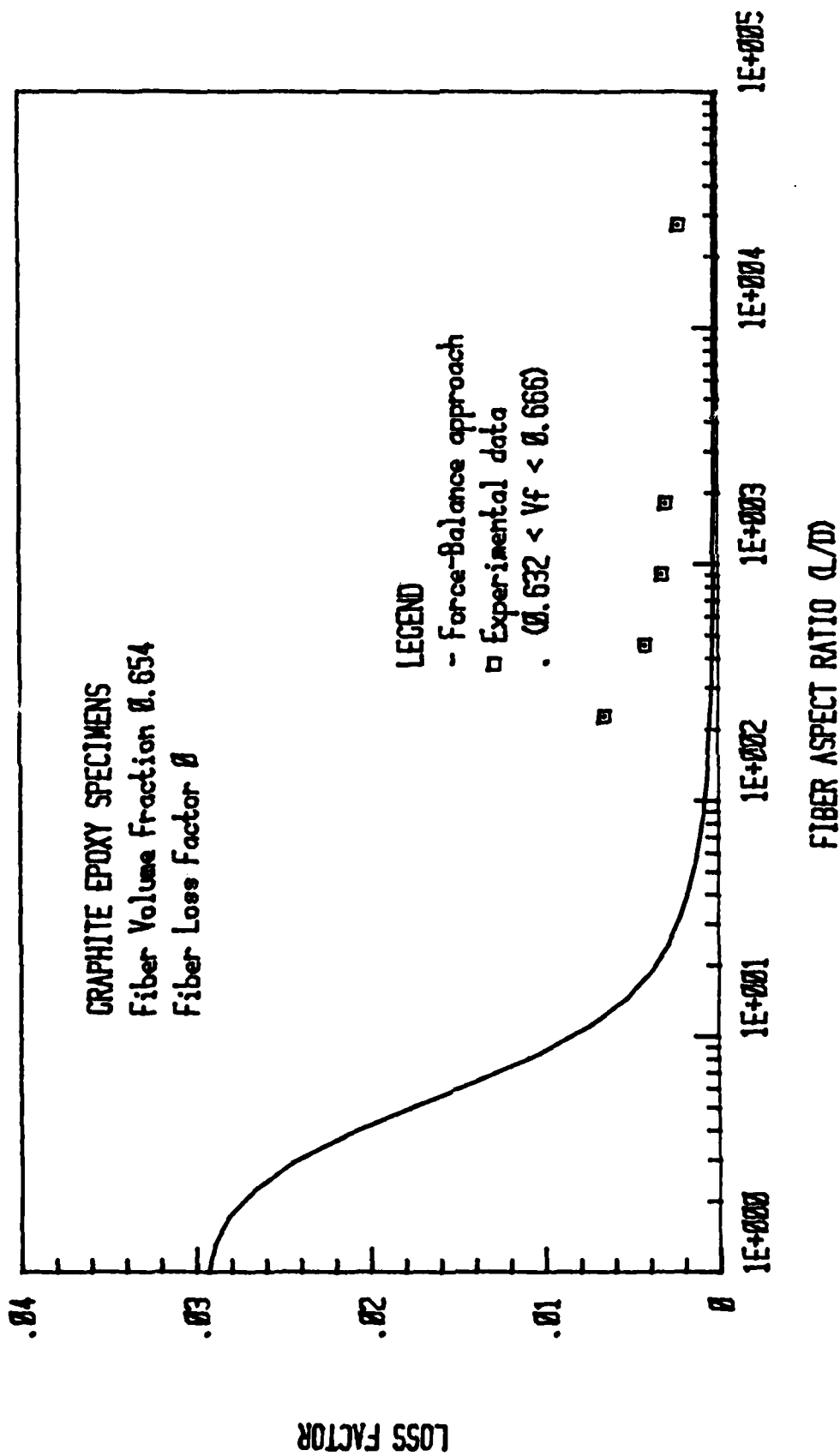


Figure 4. Composite loss factor versus fiber aspect ratio for graphite/epoxy.

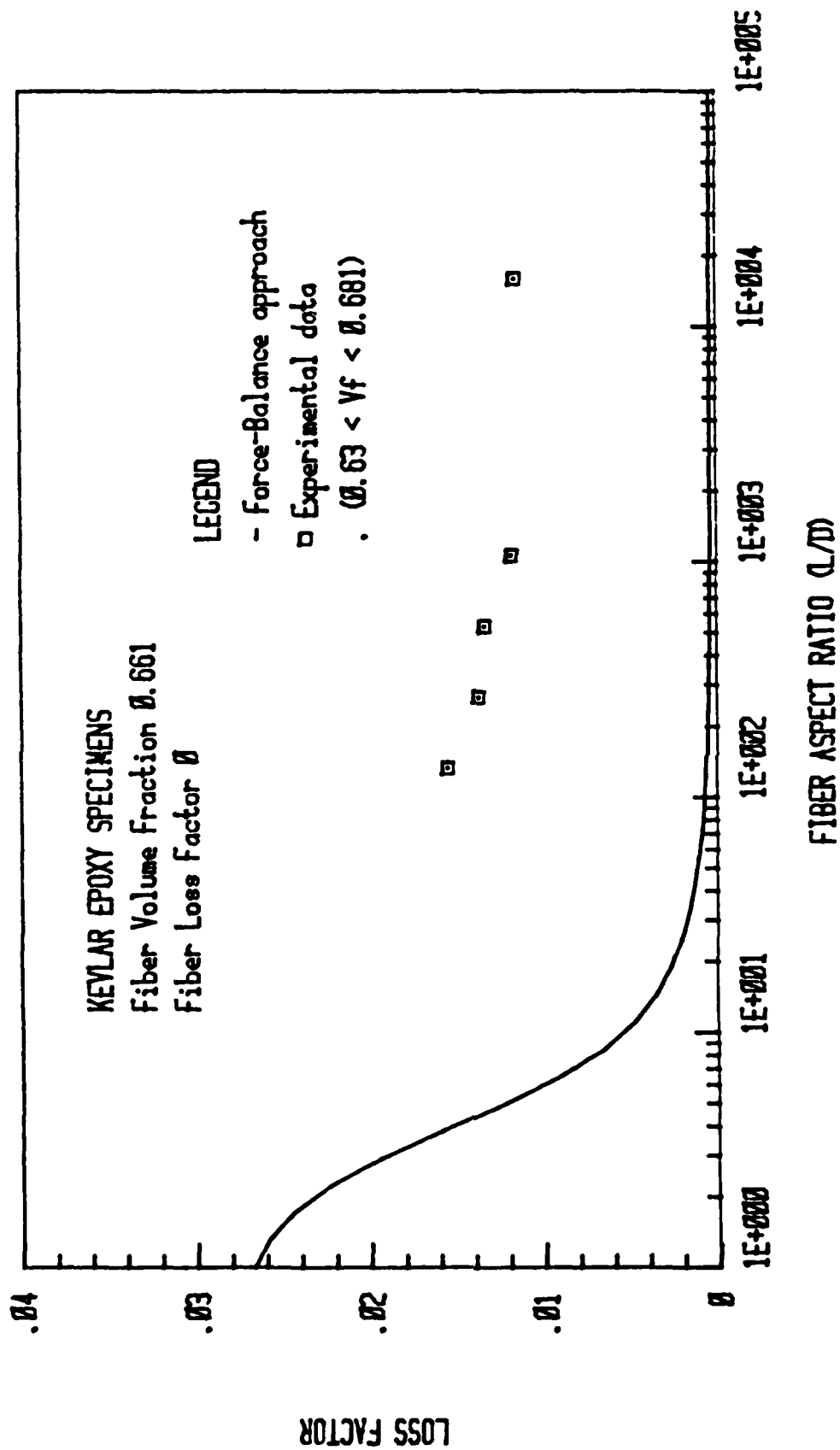


Figure 5. Composite loss factor versus fiber aspect ratio for Kevlar/epoxy.

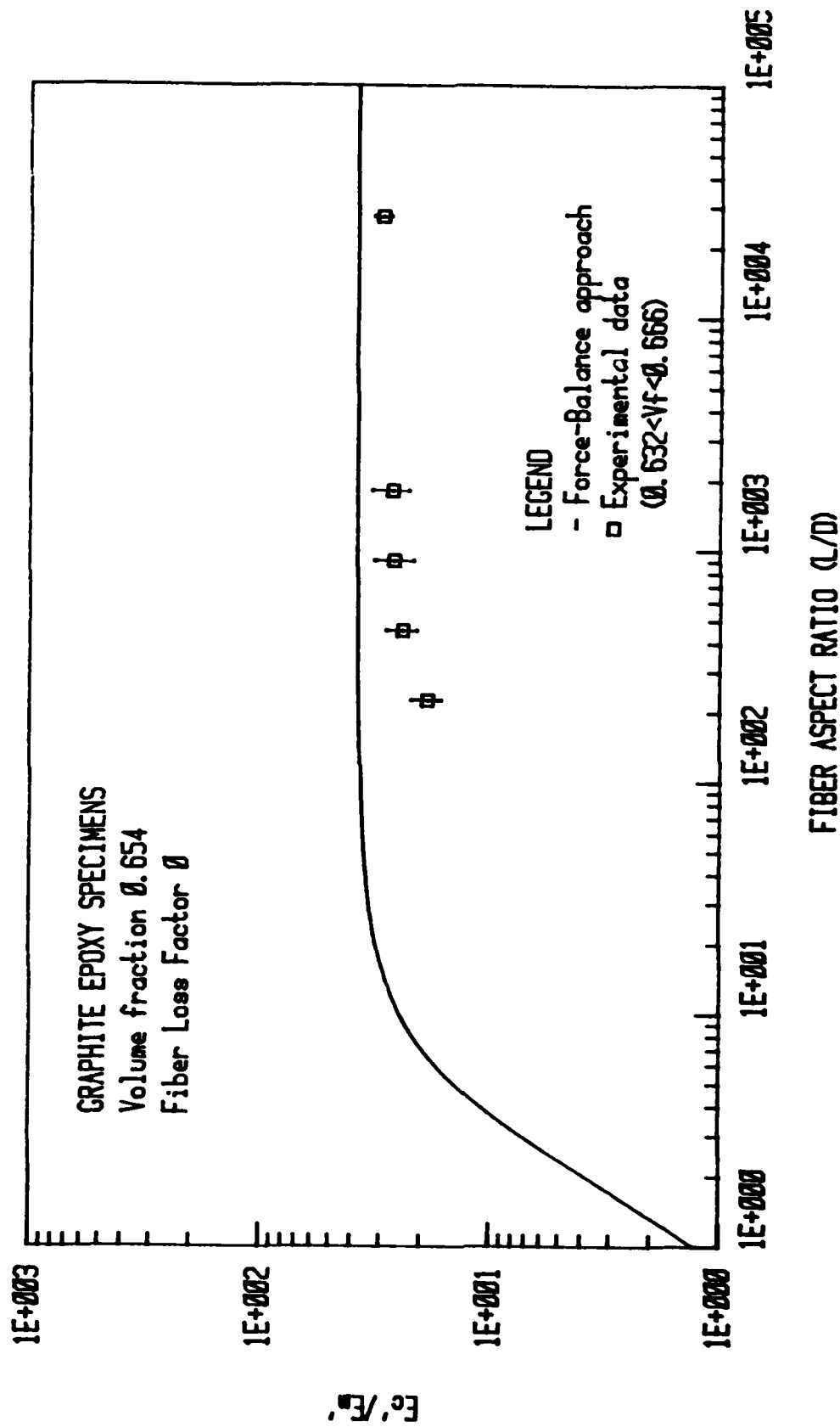


Figure 6. Ratio of composite storage modulus to matrix storage modulus versus fiber aspect ratio for graphite/epoxy.

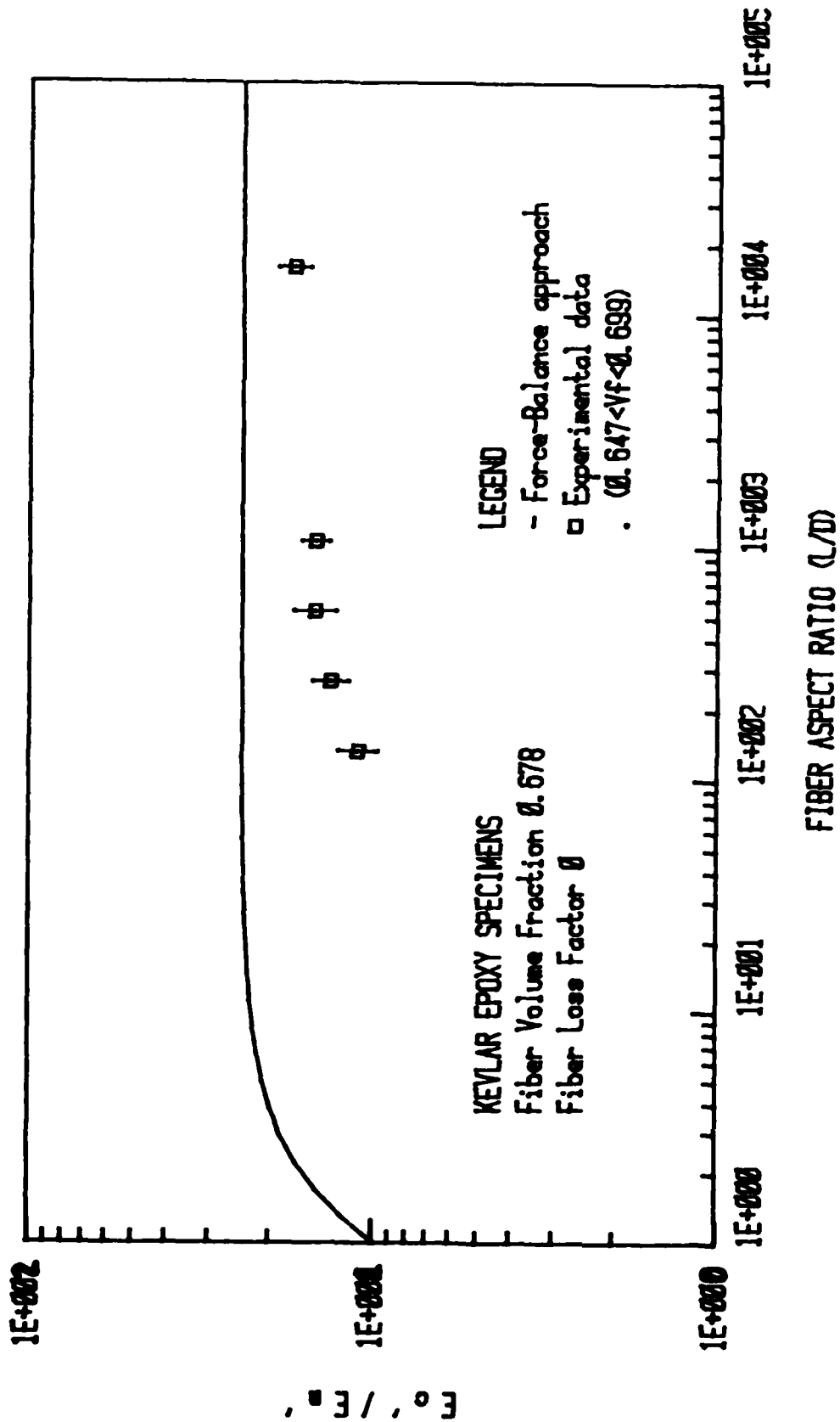


Figure 7. Ratio of composite storage modulus to matrix storage modulus versus fiber aspect ratio for Kevlar/epoxy.

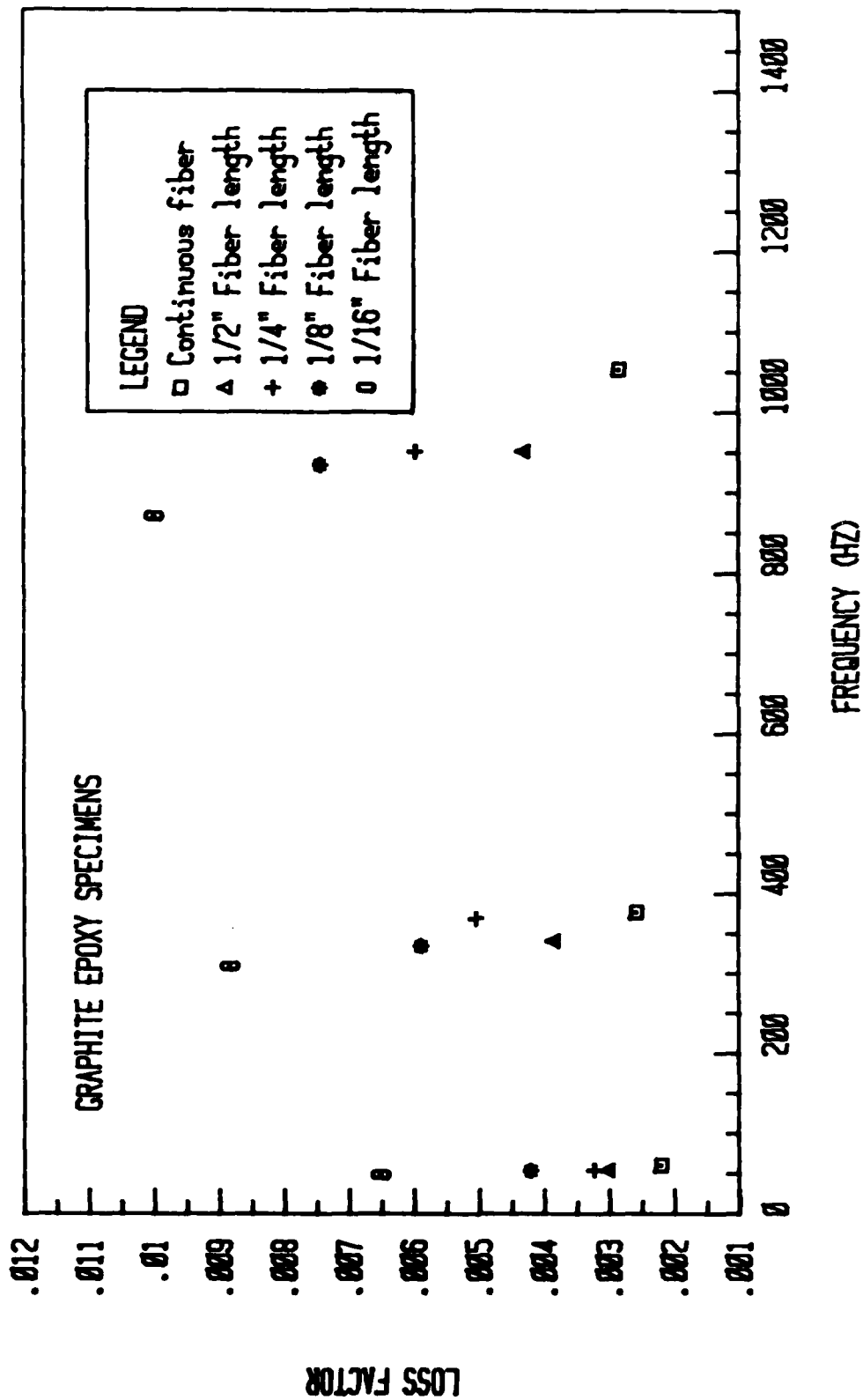


Figure 8. Graphite/epoxy composite loss factor versus frequency for different fiber lengths.

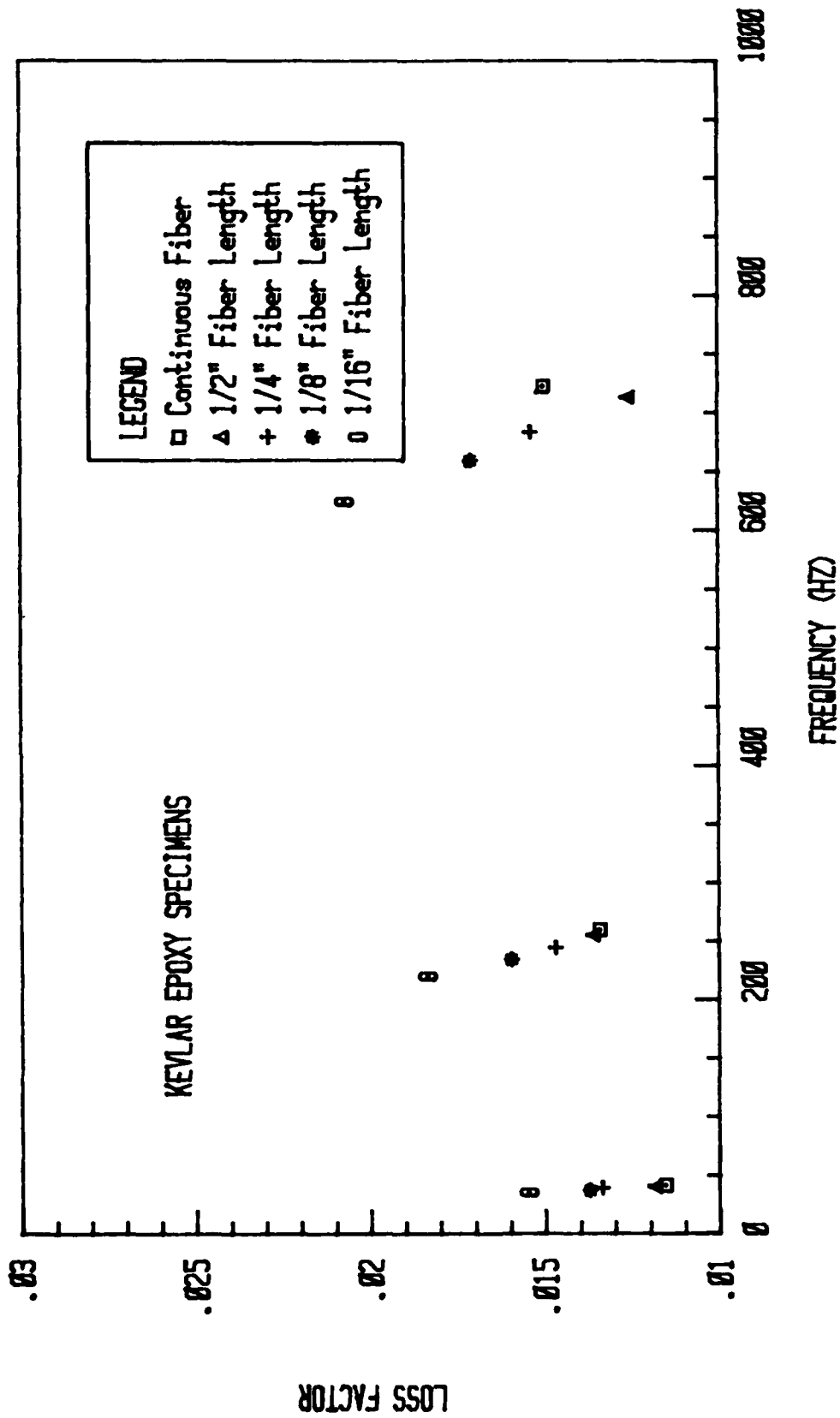


Figure 9. Kevlar/epoxy composite loss factor versus frequency for different fiber lengths.

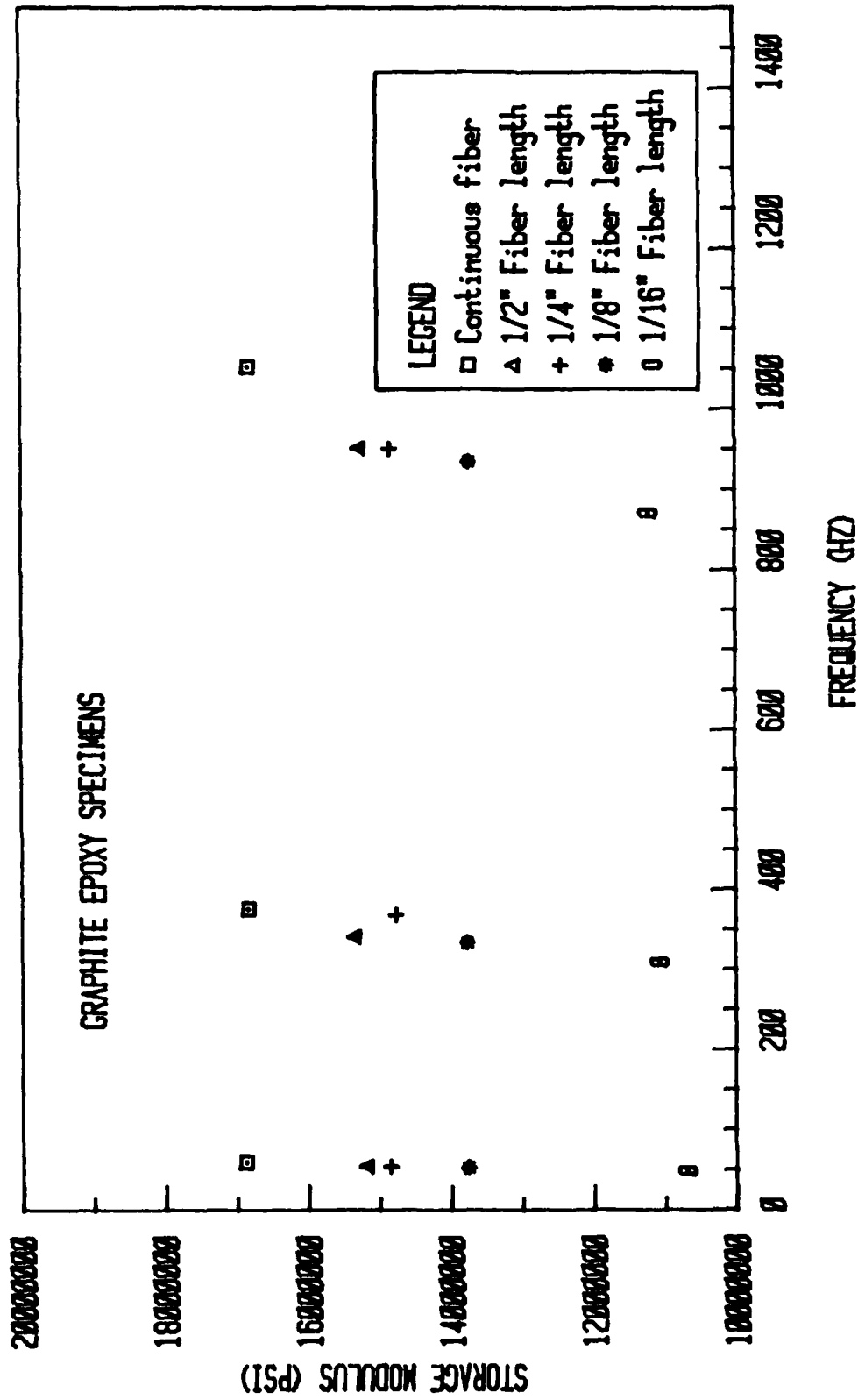


Figure 10. Graphite/epoxy composite storage modulus versus frequency for different fiber lengths.

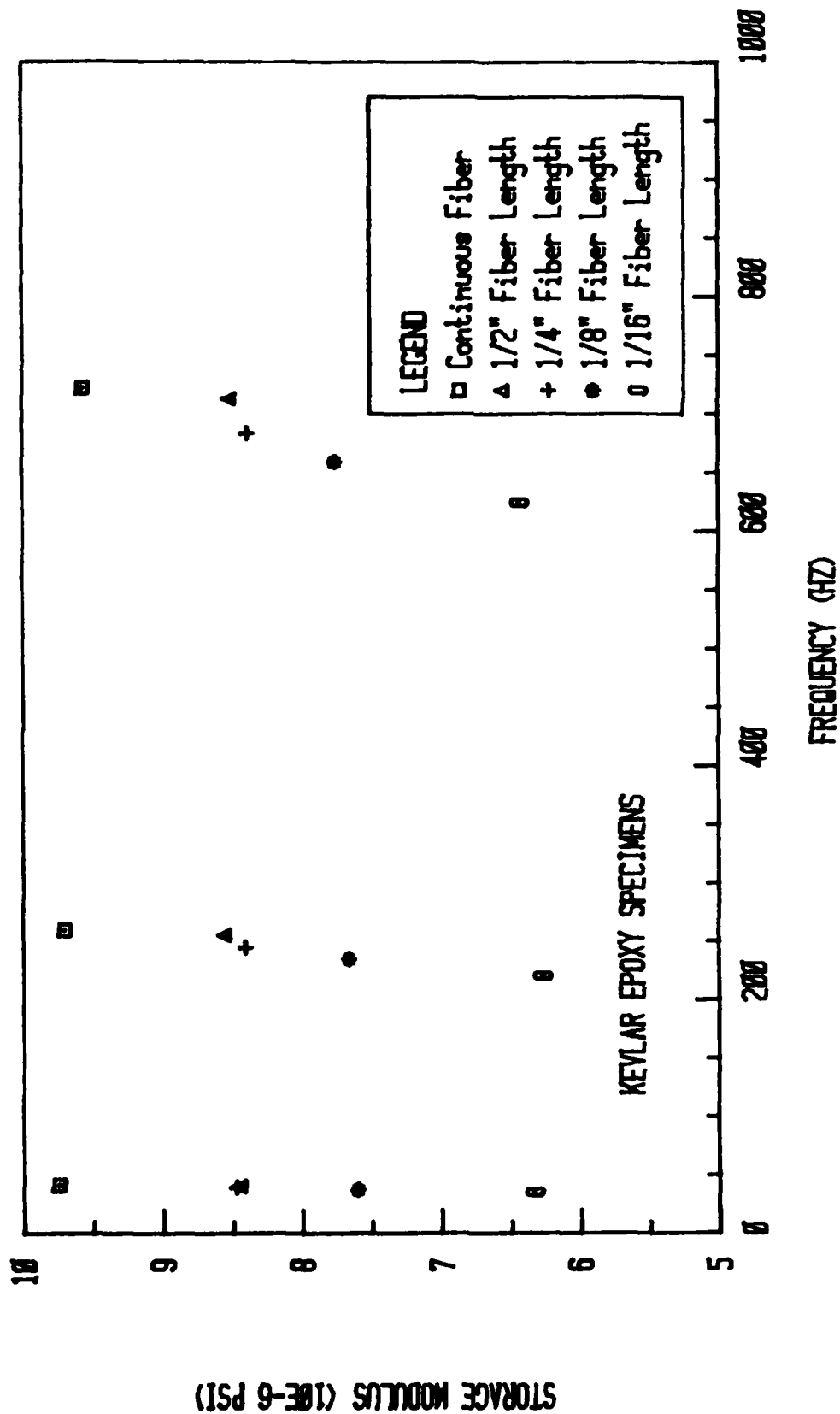


Figure 11. Kevlar/epoxy composite storage modulus versus frequency for different fiber lengths.

DYNAMIC MECHANICAL PROPERTIES OF GRAPHITE/ALUMINUM WIRES AT
AUDIO-FREQUENCIES

Gilbert F. Lee and Clifford W. Anderson
Naval Surface Weapon Center, White Oak
Silver Spring, Maryland 20910

ABSTRACT

Twenty graphite/aluminum wires used in this study have been shown by x-ray to have voids due to poor impregnation of aluminum in the graphite fibers. The dynamic mechanical properties of these wires were also determined. It was found that the dynamic mechanical properties correlated with the x-ray results. The following properties were determined at room temperature; torsional properties - logarithmic decrement and shear modulus at approximately 0.5 Hz and flexural properties - logarithmic decrement and bending stiffness over a frequency range of 10 to 500 Hz. From the torsional results, good impregnated wires were shown to have logarithmic decrements less than 0.6 dB and shear moduli greater than 1.3×10^{10} Pa while poorly impregnated wires have logarithmic decrements greater than 2.0 dB and shear moduli less than 0.9×10^{10} Pa. From the flexural results, good impregnated wires have logarithmic decrements less than 1.1 dB and bending stiffnesses greater than 1.3×10^{-3} Pa-m⁴, while poorly impregnated wires have logarithmic decrements greater than 1.1 dB and bending stiffnesses less than 1×10^{-3} Pa-m⁴. Thus these two nondestructive methods are viable means of investigating the effects of poor aluminum impregnation on the dynamic mechanical response of graphite reinforced aluminum precursor wires.

INTRODUCTION

Presently, one fairly reliable method used to identify voids in graphite/aluminum wires is x-ray. However, x-ray is particularly cumbersome method on a production line, since small samples of the wire are cut off from a continuous length of wire to be examined by x-ray and voids can still go undetected in the rest of the wire not examined. Thus the purpose of this paper is to demonstrate two dynamic mechanical methods can be used instead of x-ray. Good wires (no voids) can be distinguished from poorly impregnated wires based on the measured dynamic mechanical properties. The following properties are determined: torsional properties - shear modulus and logarithmic decrement; flexural properties - bending stiffness and logarithmic decrement; and density. A comparison will be made to determine the correlation, if any, between the dynamic mechanical properties and the x-ray results.

Twenty graphite/aluminum wires were studied. They were obtained from Material Concept Inc., Columbus, Ohio. The type of graphite fiber is VSB 32 and the aluminum is 6061. The fiber is oriented along the length of the wire. A liquid metal infiltration process is used to make the wires.

EXPERIMENTAL

TORSIONAL MEASUREMENTS

The shear modulus and logarithmic decrement are determined by using a torsional pendulum.¹ A test specimen is excited into free oscillation at approximately 0.5 Hz. A damped sine wave is recorded on a strip-chart recorder from which the shear modulus and logarithmic decrement are determined by reducing the damped sine wave data by hand. The shear modulus, G is calculated from

$$G = 8\pi I L f^2 / r^4, \text{ Pa} \quad (1)$$

where I is the moment of inertia of the inertia member of the apparatus, kg-m^2 , f is the frequency of oscillation, Hz, and r is the radius of test specimen, m. The logarithmic decrement, Δ , is calculated from

$$\Delta = (8.686/n) \ln A(r)/A(r+n), \text{ dB} \quad (2)$$

where $A(r)$ is the reference peak amplitude and $A(r+n)$ is the peak amplitude n cycles later.

FLEXURAL MEASUREMENTS

Flexural measurements are made by driving one end of the wire while the other end is free to oscillate which is known as a cantilever type measurement. The apparatus consists of an electromagnetic shaker (Bruel & Kjaer Type 4809), a power amplifier (Bruel & Kjaer 2706), and a frequency generator (Hewlett Packard 3330B). The frequency generator is manually set

at discrete frequencies between 10 to 500 Hz. The resonances of the wires are observed by visually noting when the largest displacement on the free end of the wire occurs as the frequency is changed at 0.1 Hz steps. Three resonant modes are observed. The 3 dB down from the peak resonance amplitude points are obtained by adjusting the power amplifier to a given displacement at resonance then changing the frequency until the displacement is exactly one half at resonance. The displacement of wire is measured by using a linear caliper. The bending stiffness is the product of the Young's modulus and moment of inertia of the wire. The Young's modulus can not be determined accurately because the moment of inertia of the wire is too difficult to determine with confidence. The bending stiffness, B is calculated from

$$B = f_n^2 w L^4 / C_n^2, \text{ Pa-m}^4 \quad (3)$$

where f_n is the resonance frequency, Hz; w is the weight per length, kg/m, L is the length, m, and C_n is a characteristic constant for each mode ($C_1 = .56$, $C_2 = 3.51$, and $C_3 = 9.82$ for mode 1, 2, and 3, respectively). A more detailed description of equation 3 is described by Skudrzyk.² The logarithmic decrement Δ is calculated from

$$\Delta = 8.686 \pi b / f_n, \text{ dB} \quad (4)$$

where b is the bandwidth at the 3 dB down from the peak amplitude, Hz. It was found that the bending stiffness did not vary much from mode to mode, but logarithmic decrement did vary considerably. Thus the results to be presented are from analyzing the first mode.

The wires are trimmed to one arbitrary length of 24.2 cm, so the resonance frequencies can be compared from wire to wire and any differences are due to the property of the wires and not on the length.

DENSITY MEASUREMENTS

The density measurements are made somewhat crudely. The weight of the wires is determined in a Metler balance where the accuracy is high, where the volume of the wires is determined from dimensional measurements, less accurate than the weight measurement. The cross section of a wire is not circular but an average diameter is used to calculate the volume.

TORSIONAL RESULTS

Wires, that have no voids, should have low values of logarithmic decrement, high shear modulus and oscillation frequency. The opposite trend is true for wires with poor impregnation. The logarithmic decrement are presented in Table 1 from low to high values along with the shear modulus and oscillation frequency. From this ordering, the good wires are on the top of the list and poor wires on the bottom. The accuracy of each measurement is listed on the bottom of the columns. Good wires appear to have modulus greater than 1.3×10^{10} Pa, oscillating frequency greater

than 0.5 Hz, and logarithmic decrement less than 0.6 dB. The logarithmic decrement seems to be the most sensitive to voids. A plot of logarithmic decrement versus shear modulus is shown in Figure 1. Good wires are found in the lower right hand corner, while the poor wires are found in the upper left hand corner. Thus there is some correlation between the two properties.

FLEXURAL RESULTS

It is also expected from flexural measurements that good wires have lower logarithmic decrement and higher bending stiffness than poor wires. These results are recorded in Table 2 in order of good to poor wires based on the logarithmic decrement. The accuracy of the three measurements are presented at the bottom of the table, where the least accurate measurement is the logarithmic decrement. A plot of logarithmic decrement versus bending stiffness is shown in Figure 2. Good wires are again in the lower right and the bad wires in the upper left of figure. It is interesting to see that wire #11, 13, and 16 are in a group by themselves, because the graphite fibers in these wires are of higher modulus than the others. Also this difference in the wires is not noted by the shear measurements in Figure 1. The resonance frequencies are reported in Table 3. The average frequency for mode 1 is about 18.6 Hz excluding wire # 13 and #18 for reason of shorter wire length than the other wires. For mode 2 and 3, the average frequencies are approximately 113 Hz and 317 Hz, respectively. The accuracy of the frequency measurements is about one percent. The resonance frequency for the same mode varied somewhat from wire to wire where the differences are small, that to make a distinction between good or poor wires is difficult. However, for wire #12 the frequencies for mode 2 and 3 are much lower than the average values: 67 Hz and 200 Hz, respectively.

DENSITY RESULTS

The densities of the wires are listed in Table 4. Wires with high density are considered good and low density poor. Wire # 3 and 12 have low densities as expected. The accuracy of these measurements is about 5%. The logarithmic decrement determined in torsion is plotted against density in Figure 3 which is similar in appearance to Figure 1. The logarithmic decrement determined in bending is also plotted against density in Figure 4. Both figures show that good wires are found on the bottom right and poor wires in the upper left of figure. Thus, there is a correlation between the two logarithmic decrements and density.

COMPARING WITH X-RAY RESULTS

Typical x-ray results are shown in Figure 5, which represent a small length of two different wires. The top picture depicts a wire with good infiltration of aluminum while the lower picture is a poorly impregnated wire. The void is the dark area running along the length of the wire.

The ranking of the wires as good, fair, and poor according to x-ray results is presented in Table 5. Making a comparison between the dynamic mechanical results and the x-ray ratings the following observations are made:

1. The results of Figure 1, 2, 3, and 4 are in agreement with the x-ray results (Table 5) for wires rated as good.
2. There are partial disagreements in the fair category. Wires # 6, 7, and 8 are considered good by the two dynamic mechanical measurements, but are rated fair by x-ray.
3. There are also disagreements in the bad category. Wire #18 is rated good in this work, but is rated bad by x-ray.

CONCLUSIONS

The graphite/aluminum wires can be rated good, fair and poor from the dynamic mechanical properties. Based on the results, the following conclusions have been reached:

1. Torsional Properties

Good wires usually have shear moduli greater than 1.3×10^{10} Pa and logarithmic decrements less than 0.6 dB. Fair wires have shear moduli between 0.9 and 1.28×10^{10} Pa and logarithmic decrements between 0.6 and 2 dB. Poor wires have shear moduli less than 0.9×10^{10} Pa and logarithmic decrements greater than 2.0 dB.

2. Flexural Properties

Good wires usually have bending stiffnesses greater than 1.3×10^{-3} Pa-m⁴ and logarithmic decrements less than 1.1 dB. Fair wires have bending stiffnesses between 1 and 1.3×10^{-3} Pa-m⁴ and logarithmic decrements less than 1.1 dB also. Poor wires have bending stiffnesses less than 1×10^{-3} Pa-m⁴ and logarithmic decrements greater than 1.1 dB.

3. It seems apparent that the torsional properties are matrix dominated while the flexural properties are sensitive to both the matrix and fiber.

4. Density

Good wires usually have densities greater than 1500 kg/m³. Fair wires have densities between 1400 and 1500 kg/m³. Poor wires have densities less than 1400 kg/m³.

5. There is a fair agreement between the dynamic mechanical results and the x-ray results.
6. Both torsional and flexural vibrational methods provide a useful means of quantifying the mechanical effects of poor infiltration in finite lengths of graphite aluminum precursor wire.

REFERENCES

1. Nielsen, L. E., Mechanical Properties of Polymers and Composites, Marcel Dekker, Inc., 1974, Vol. 1, p. 11.
2. Syudrzyk, E., Simple and Complex Vibratory Systems, The Pennsylvania Stat University Press, 1968, p. 208.

TABLE 1: TORSIONAL RESULTS: LOGARITHMIC DECREMENT, SHEAR
MODULUS AND OSCILLATION FREQUENCY OF GRAPHITE/ALUMINUM WIRES

WIRE #	LOGARITHMIC DECREMENT dB	SHEAR MODULUS $\times 10^{10}$, Pa	OSCILLATION FREQUENCY Hz
10	0.12	1.5	.62
15	0.14	1.4	.61
2	0.16	1.5	.68
6	0.17	1.4	.62
17	0.19	1.3	.54
7	0.21	1.4	.62
13	0.21	1.5	.64
8	0.24	1.4	.58
19	0.24	1.5	.64
16	0.26	1.5	.64
11	0.28	1.3	.61
18	0.30	1.5	.58
14	0.31	1.3	.62
20	0.49	1.4	.66
5	0.69	1.3	.49
4	1.0	1.1	.48
9	1.2	1.2	.46
1	1.4	1.1	.46
3	3.0	0.56	.41
12	3.6	0.16	.17
ACCURACY	10%	5%	2%

TABLE 2: FLEXURAL RESULTS: LOGARITHMIC DECREMENT, AND
BENDING STIFFNESS OF GRAPHITE/ALUMINUM WIRES

WIRE #	LOGARITHMIC DECREMENT dB	BENDING STIFFNESS $\times 10^{-3}$, Pa-m ⁴
15	.54	1.7
20	.56	1.9
6	.58	1.6
5	.61	1.3
8	.61	1.6
7	.62	1.7
9	.68	1.3
10	.69	1.6
16	.72	2.7
19	.73	2.0
11	.74	2.4
2	.76	1.8
13	.76	2.5
4	.77	1.2
18	.81	1.5
17	.91	1.4
14	.92	1.9
1	.92	1.2
3	1.76	1.1
12	3.90	0.47
ACCURACY	20%	5%

TABLE 3: RESONANCE FREQUENCIES FOR THREE MODES OF
GRAPHITE/ALUMINUM WIRES

WIRE #	RESONANCE FREQUENCIES, Hz			
	MODE	1	2	3
1		17	107	294
2		18	114	323
3		20.1	108	298
4		17.7	109	299
5		17.8	108	306
6		18.8	114	318
7		17.6	113	320
8		18	114	320
9		16.1	103	298
10		19.8	112	315
11		22	144	392
12		15.4	67	200
13*		50.4	306	***
14		17.7	115	323
15		20.4	116	323
16		22.7	143	401
17		18	110	312
18**		26.8	159	438
19		18.8	119	336
20		19.4	119	335

*SAMPLE #13 WIRE LENGTH ONLY 14.9 CM AS COMPARED TO OTHER WIRE LENGTH OF
24.7 CM

**SAMPLE #18 WIRE LENGTH ONLY 18.7 CM

***DID NOT DETECT, AMPLITUDE TOO SMALL

TABLE 4: DENSITY OF GRAPHITE/ALUMINUM WIRES

WIRE #	DENSITY, kg/m ³
1	1450
2	1670
3	1240
4	1470
5	1500
6	1600
7	1620
8	1550
9	1500
10	1640
11	1500
12	1270
13	1470
14	1640
15	1620
16	1600
17	1480
18	1560
19	1670
20	1670
ACCURACY	5%

TABLE 5: RANKING OF GRAPHITE/ALUMINUM WIRES FROM X-RAY RESULTS

GOOD	FAIR	POOR
2	1	3
10	4	9*
11	5	12
13	6	18
14	7	
15	8	
16	9*	
17		
19		
20		

*WIRE #9 IS DESIGNATED AS 1/2 FAIR, 1/2 BAD

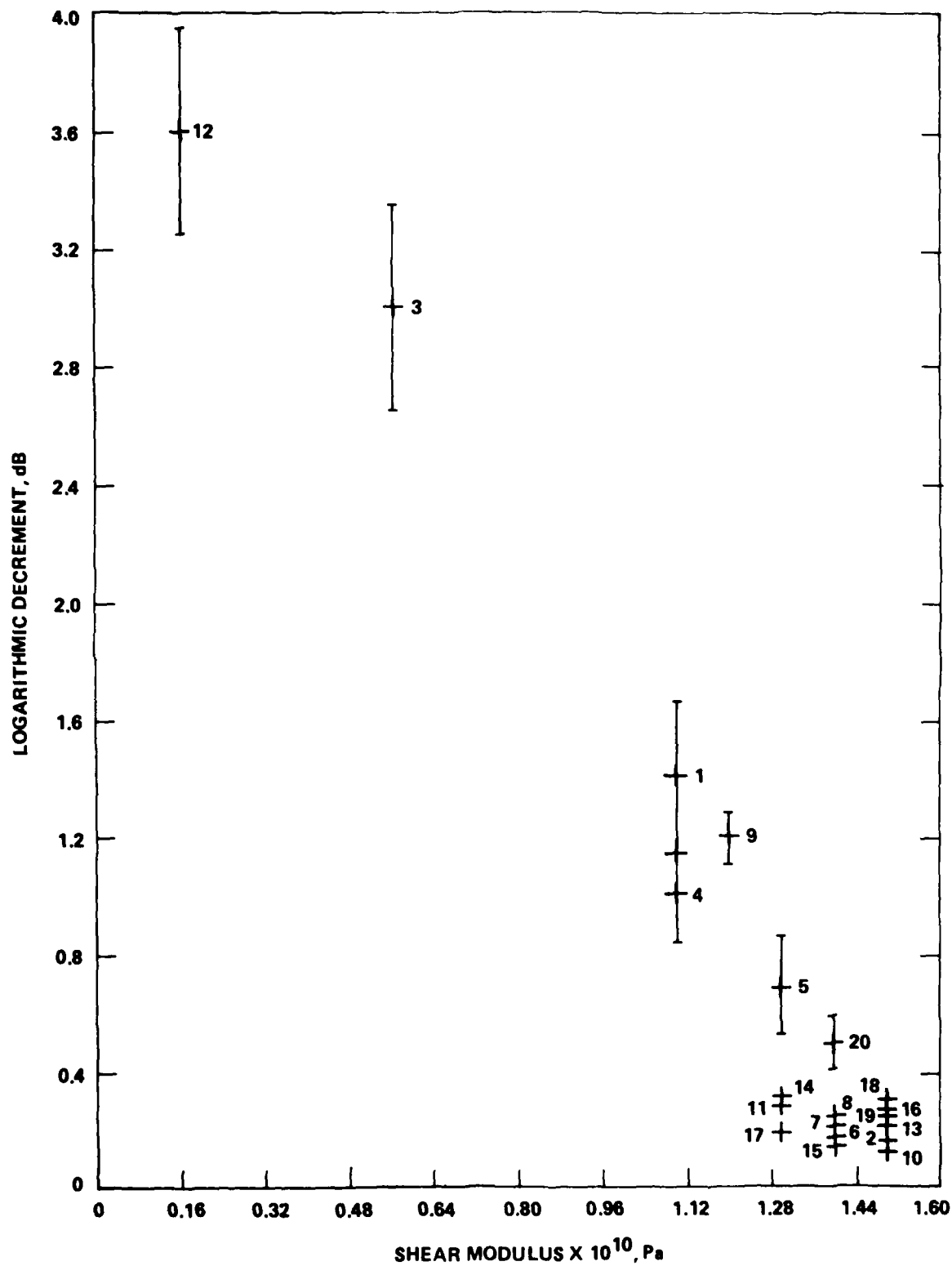


FIGURE 1. LOGARITHMIC DECREMENT VERSUS SHEAR MODULUS FOR GRAPHITE - ALUMINUM WIRES

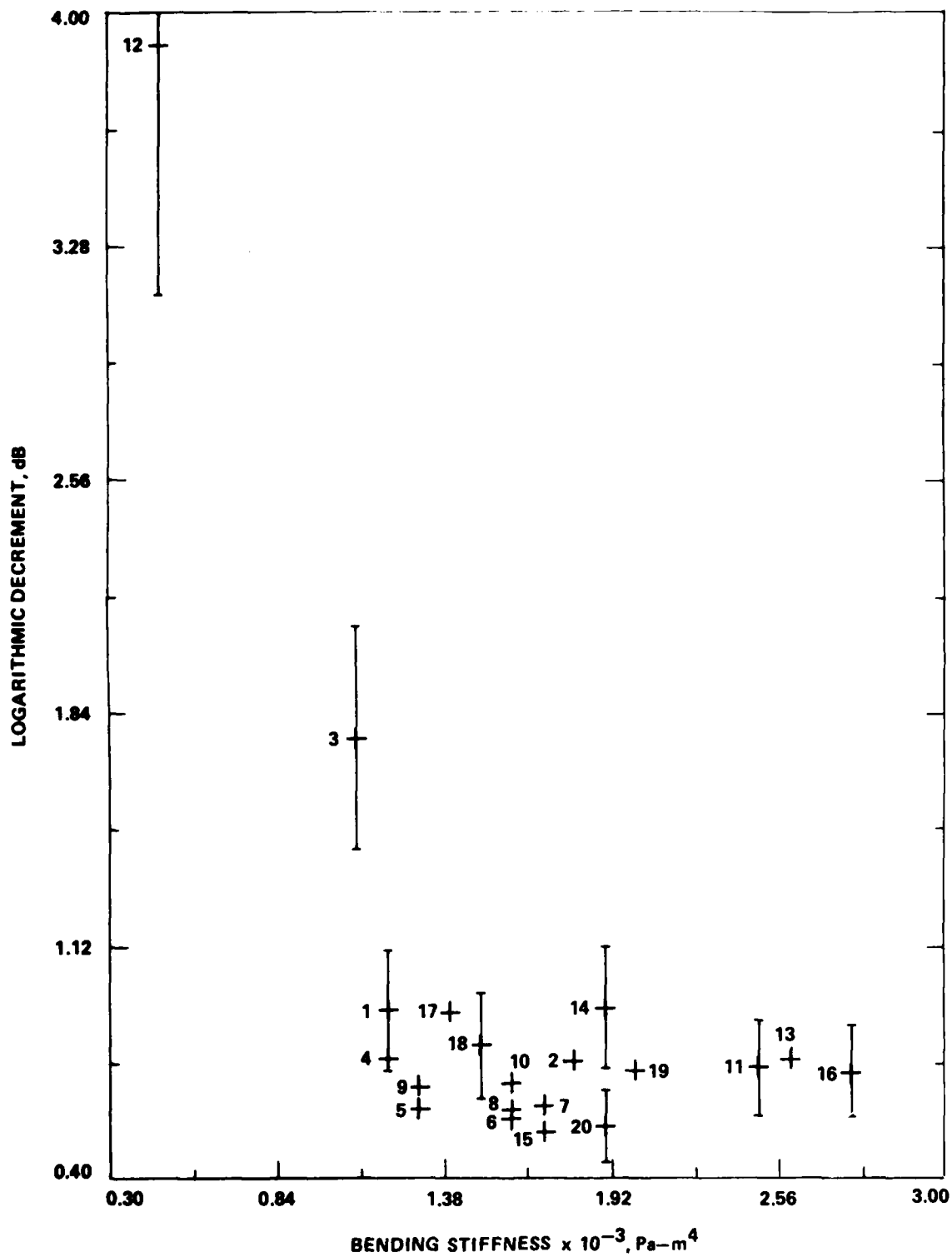


FIGURE 2. LOGARITHMIC DECREMENT VERSUS BENDING STIFFNESS OF GRAPHITE-ALUMINUM WIRES

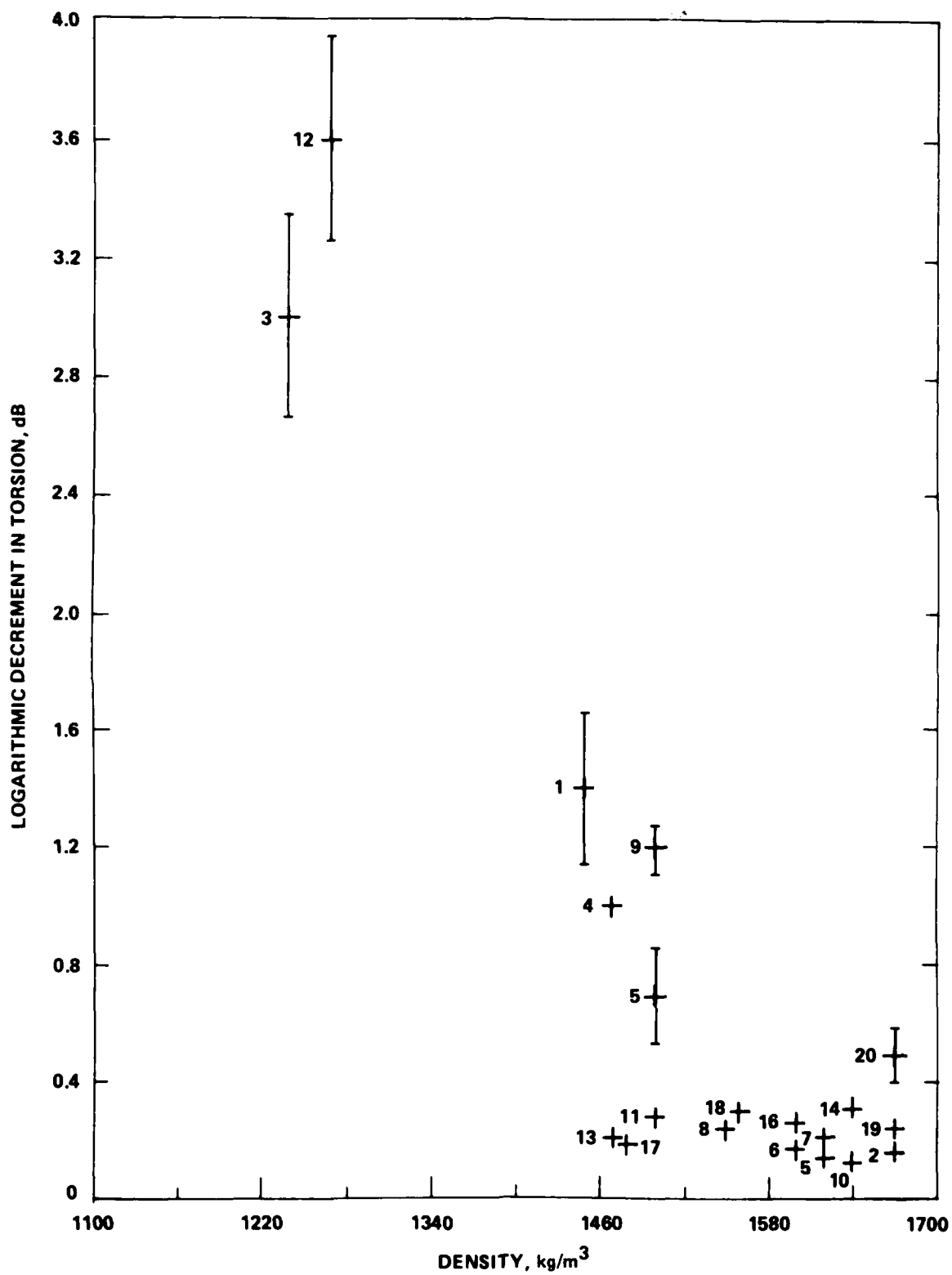


FIGURE 3. LOGARITHMIC DECREMENT IN TORSION VERSUS DENSITY FOR THE GRAPHITE - ALUMINUM WIRES

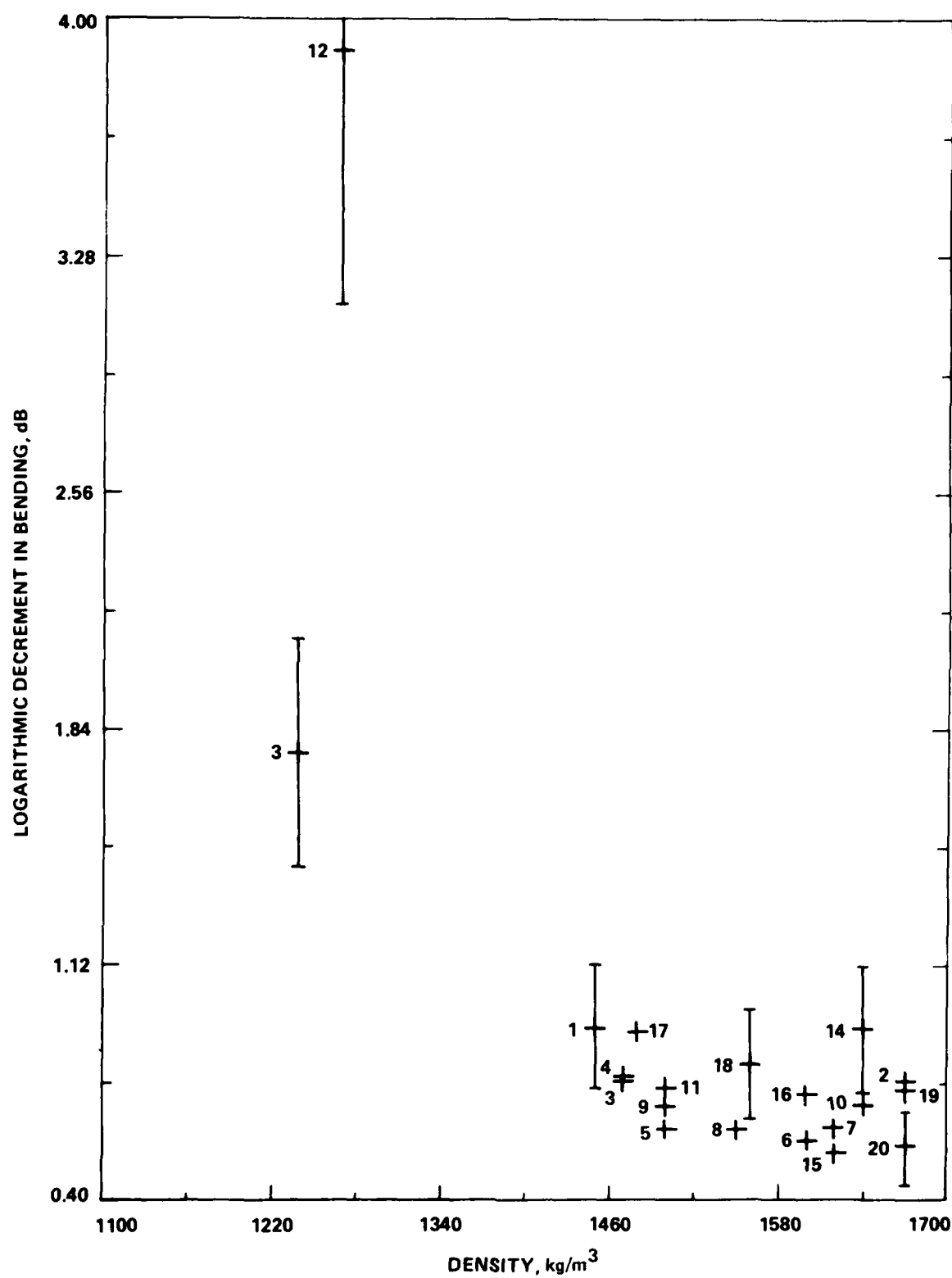
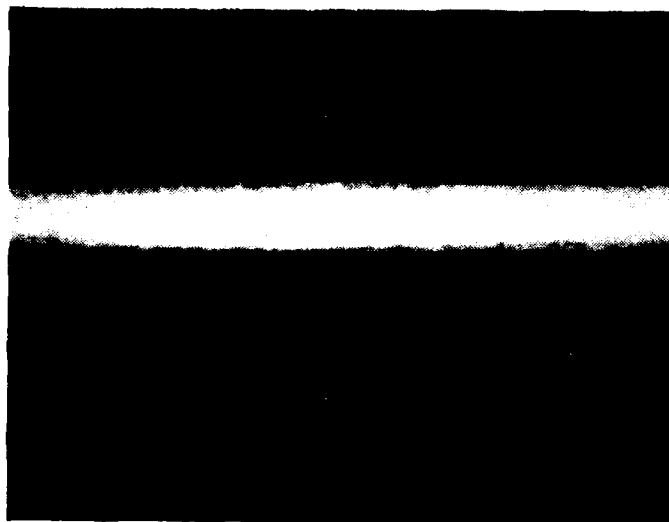
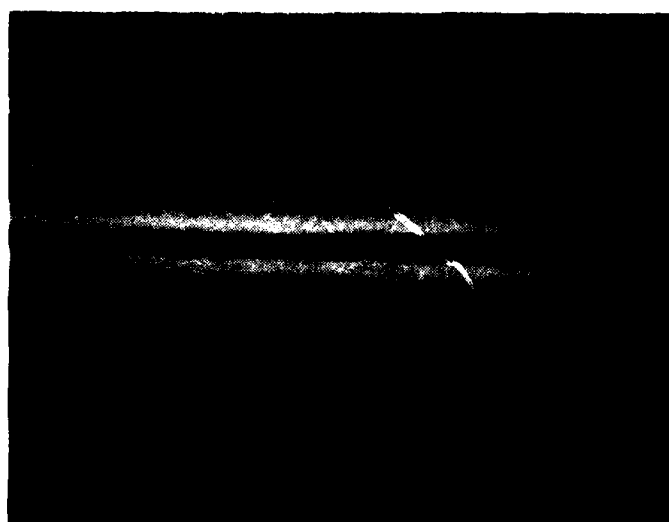


FIGURE 4. LOGARITHMIC DECREMENT IN BENDING VERSUS DENSITY FOR THE GRAPHITE - ALUMINUM WIRES



GOOD WIRE



NON-INFILTRATION

FIGURE 5 RADIOGRAPHS OF GRAPHITE/ALUMINUM WIRES

DAMPING BEHAVIOR OF METAL MATRIX COMPOSITES

M. S. Misra and P. D. LaGreca
Martin Marietta Aerospace
Denver, Colorado 80201

Damping Behavior of Metal Matrix Composites

M.S. Misra
P.D. LaGreca
Martin Marietta Aerospace
Denver, CO 80201

ABSTRACT

Discontinuous and continuous fiber reinforced composites were evaluated for their damping capacities and elastic moduli. In the case of Gr/Al and Gr/Mg, the damping factor increases significantly in the transverse direction and slightly in the longitudinal direction whereas the longitudinal elastic modulus of the composite has increased by a factor of 3 or more. The damping behavior of the SiC particulate reinforced aluminum composite was similar to that of the matrix aluminum alloy. Efforts were made to explain the observed behavior to the fiber matrix and the diffusion bonded interfaces present in these composites. If the interface strength is higher than that of the matrix alloy, the damping capacity remains the same. However, if the interfaces are the weaker areas, i.e., areas of metallurgical imperfection, the damping capacity increases.

INTRODUCTION

In large structures damping is normally controlled by active control systems or by the application of passive dampers. Natural damping of the structural materials is seldomly considered of any significance, primarily due to the fact that material damping is not a very well understood phenomenon. Many investigators have related damping to the microstructural and macrostructural changes in crystalline materials and also with the mechanisms causing anelastic deformation. However, the prediction and analyses of material damping can be extremely complicated due to the fact that there are so many physical mechanisms involved such as microstructural changes, grain boundary sliding, internal friction, mechanical and magnetic hysteresis, and interface structures. In a particular system, any or all may be significant parameters for vibrational energy dissipation.

Most structural alloys such as aluminum, titanium, and steels exhibit very poor damping, i.e., specific damping capacities of less than 1%. However, during recent years several new alloys with higher damping capacities have been developed. "Silent alloy" (Fe-Cr-Al-System) developed in Japan (Reference 1) exhibits higher damping due to the interaction between the acoustic waves and the ferromagnetic domain boundaries. Small alloying additions of Ni, Fe, Al, etc., to the Cu-Mn binary alloys are also known to change the damping behavior (Reference 2), specifically for the alloys known as "Sonaston" (37Cu-54Mn-5Al-3Fe-1Ni) and "Incramate" (58Cu-40Mn-2Al). The improved damping in these alloys is attributed to magnetoelastic effects. Other alloys such as Ni-Ti, and Cu-Ni-Al show higher damping capacities because of the vibration induced transformation to a thermo-elastic martensitic structure. It is also very well known that changing the microstructure of a grey cast iron to a coarse graphite flake structure increases the damping capacity by a factor of 100. Similarly, changing the grain size in alpha brass and plastic deformation in zinc can significantly increase their specific damping capacities.

As discussed above, several processes have been identified to improve the damping behavior, however due to a lack of systematic investigations, the exact mechanism for the energy dissipation in specific alloy systems is still speculative. Nevertheless, it is certain that the damping characteristics of structural materials can be modified by altering a number of metallurgical parameters.

Metal matrix composites are a new class of structural materials that have been developed during recent years. These composites are ideal materials for space structures because of their high specific stiffness and potentially zero thermal expansion coefficient. It has been a common observation for crystalline materials that the specific damping capacity decreases as modulus increases. Therefore, the question is raised whether metal matrix composites will follow a similar trend.

The objective of this ongoing study is to evaluate and to fundamentally understand the damping behavior of several metal matrix composites.

TEST MATERIAL

Both discontinuous and continuous fiber reinforced composites were selected for the damping study. These materials are listed in Table 1. For discontinuous composites, silicon carbide particulate reinforced 6061 aluminum alloys are probably the most advanced and therefore were selected as the test material. The composites were fabricated by powder metallurgy technology using vacuum consolidation. The particulate volume fraction (v/o) was varied from 20 to 30 v/o to characterize the effect of increased particulate-matrix interfaces.

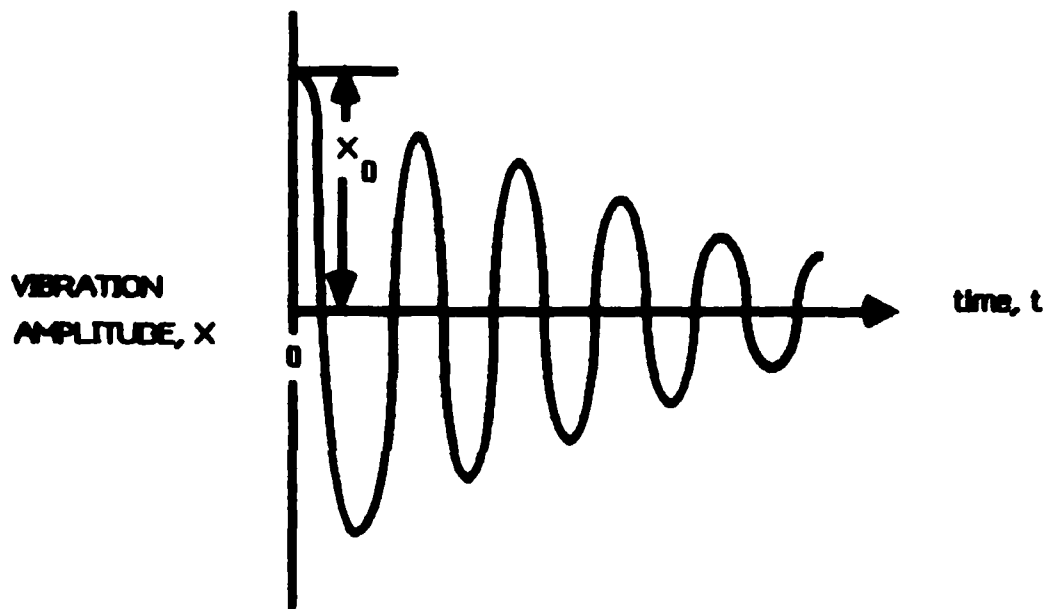
Table 1 - Test Materials

<u>DISCONTINUOUS REINFORCED</u>	
O	17 v/o SiC _w /6061
O	20 v/o SiC _p /6061
O	30 v/o SiC _p /6061
<u>CONTINUOUS REINFORCED</u>	
O	PITCH 55/AZ91C/AZ31B (Gr/Mg)
O	PITCH 100/AZ91C/AZ31B (Gr/Mg)
O	PITCH 100/6061/6061 (Gr/Al)

Similarly for continuous fiber reinforced composites, the most common Graphite/Aluminum (Gr/Al) and Graphite/Magnesium (Gr/Mg) composites were selected. Again, the v/o of the graphite fibers was increased from 12.7 to 26.5 to study the effects of fiber-matrix interfaces. Both Gr/Al and Gr/Mg panels were fabricated by the hot pressing-diffusion bonding process.

EXPERIMENTAL PROCEDURE

The damping factors (ζ) were calculated by determining the logarithmic decrement (δ) from the time response curve as shown in Figure 1. Approximately 6.0 in long specimens were used in a cantilever set-up with an accelerometer placed on one end to record the deflection. The test set-up is shown schematically in Figure 2. The time-response curve was continuously recorded by an HP1000/5451c computer equipped with a Fourier Analyzer to calculate the damping factor, frequency, and one-half life cycle.



$$\zeta = \frac{\delta}{2\pi} \quad \text{where } \delta = \frac{1}{n} \ln \frac{x_0}{x_n} \quad f = \frac{n}{t}$$

- ζ = DAMPING FACTOR
- δ = LOGARITHMIC DECREMENT
- x = VIBRATIONAL AMPLITUDE
- n = NUMBER OF CYCLES ELAPSED
- f = AVERAGE FREQUENCY OF OSCILLATION
- t = TIME TO COMPLETE n CYCLES

Figure 1 - Damping Factor Calculation

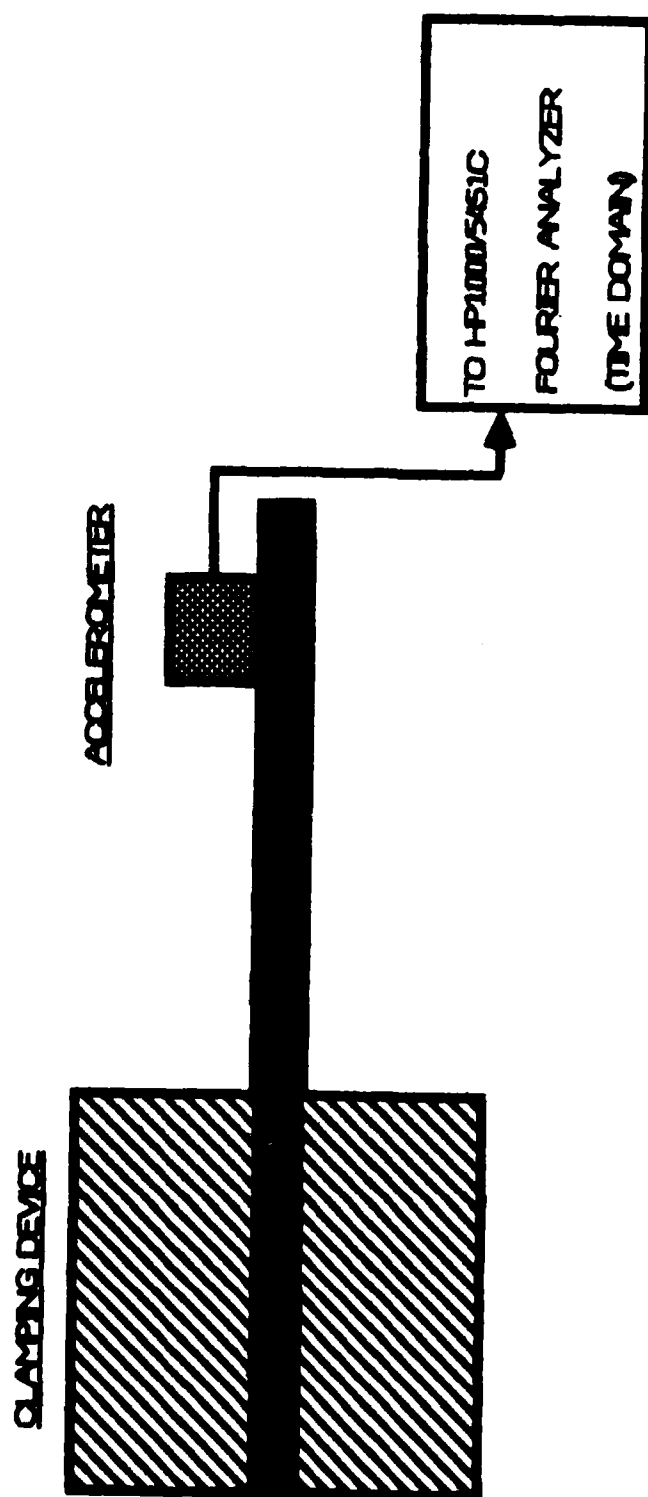


Figure 2 - Schematic of Test and Recording System

RESULTS AND DISCUSSIONS

Typical tensile properties of the selected composites are presented in Table 2. It should be noted that the transverse properties of the continuously reinforced composites are lower than the matrix alloy, and this will be discussed further, later in this section. For the aluminum alloy 6061-T6, the average damping factor was determined to be 0.27% (Table 3)₂, while in the case of 34.0 volume percent (v/o) Gr/Al, there was a significant increase in the damping factor to an average value of 1.25% for the transverse specimen, i.e., the fibers oriented 90° to the damping axis, as presented in Table 4. Since the transverse modulus of the Gr/Al composite is only 5.4 Msi compared to 10.5 Msi for the matrix alloy, the increase in the damping factor is consistent with the established theories.

Table 2 - Typical Properties of Metal-Matrix Composites

MATERIAL	VOLUME-PERCENT REINFORCEMENT (v/o)	ELASTIC MODULUS (Msi)	ULTIMATE STRENGTH (Ksi)	0.2% YIELD STRENGTH (Ksi)	ELONGATION TO FAILURE (%)
SiC _w /6061-T6	17	14.7	73	56	2.1
SiC _p /6061-T6	20	15.2	70	55	4.5
SiC _p /6061-T6	30	17.5	77	60	3
PITCH 55/AZ91C/AZ31B	12.7				
LONGITUDINAL		12.4	53.2	-	0.29
TRANSVERSE		4.6	18.2	14.6	1.28
PITCH 100/AZ91C/AZ31B	26.5				
LONGITUDINAL		32.4	83.2	-	0.42
TRANSVERSE		4.8	14.6	9.9	0.89
PITCH 100/6061/6061	34.0				
LONGITUDINAL		37.1	92.8	-	-
TRANSVERSE		5.4	8.4	6.5	-
AZ31B-H24*	-	6.5	42	32	15
6061-T6*	-	10.0	45	40	12

*Metals Handbook, Vol. 2, Ninth Edition

Table 3 - Damping Properties - 6061-T6 Al Alloy

MATERIAL	OSCILLATION FREQUENCY-f(Hz)	DAMPING FACTOR (%)	ONE-HALF LIFE CYCLE
6061-T6	15.2	0.29	38.0
6061-T6	53.9	0.25	45

For the longitudinal direction, the modulus is 37.1 Msi, and the damping factor is still increased to 0.51% as shown in Table 4. For 12.7 v/o Gr/Mg the average transverse damping factor is 0.7%, while that in the longitudinal direction is 0.49% (Table 5). When the volume fraction of the composite is increased to 26.5%, the damping factors both in the transverse and longitudinal directions increased to 0.94% and 0.61% respectively (Table 6). One of the direct effects of the higher v/o fiber should be a higher fiber-matrix interface volume. Consequently, these interfaces may be a source for dissipation of the vibrational energy.

Table 4 - Single-Ply Unidirectional Pitch 100/6061/6061
(34v/o Graphite)

SPECIMEN ORIENTATION	OSCILLATION FREQUENCY-f(Hz)	DAMPING FACTOR (%)	ONE-HALF LIFE CYCLE
LONGITUDINAL	35.5	0.46	25
LONGITUDINAL	47.6	0.57	20
TRANSVERSE	38.6	0.93	12
TRANSVERSE	37.4	1.53	8

- O 6.1 inch x 0.35 inch x 0.036 inch specimens
- O Face sheet thickness = 0.005 inch

Table 5 - Singly-Ply Unidirectional Pitch 55/AZ91C/AZ31B
(12.7 v/o Graphite)

SPECIMEN ORIENTATION	OSCILLATION FREQUENCY-f(Hz)	DAMPING FACTOR (%)	ONE-HALF LIFE CYCLE
TRANSVERSE	11.4	0.54	20.5
TRANSVERSE	10.8	0.71	15.5
TRANSVERSE	11.0	0.79	14.0

LONGITUDINAL	13.2	0.34	32.5
LONGITUDINAL	12.6	0.42	26.0
LONGITUDINAL	13.1	0.71	15.5

O 4.0 inch x 1.0 inch x 0.038 inch specimens
O Face sheet thickness = 0.011 inch

Table 6 - Damping Properties
Single-Ply Unidirectional Pitch 100/AZ91C/AZ31B
(26.5 v/o Graphite)

SPECIMEN ORIENTATION	OSCILLATION FREQUENCY-f(Hz)	DAMPING FACTOR (%)	ONE-HALF LIFE CYCLE
TRANSVERSE	8.8	0.67	16.5
TRANSVERSE	8.8	0.79	14.0
TRANSVERSE	8.6	1.30	8.5
TRANSVERSE	8.4	1.10	10.0

LONGITUDINAL	13.6	0.61	16.5

O 4.0 inch x 1.0 inch x 0.032 inch specimen
O Face sheet thickness = 0.008 inch

In order to understand the damping mechanism, the microstructure of the single ply Gr/Mg composite was studied by optical and electron microscopy. Two distinct interfaces are clearly observed from the scanning electron microscope micrograph in Figure 3; (i) a fiber-matrix interface; and (ii) a diffusion bonded interface between the precursor wires. If the composite is stressed in the transverse direction, the final fracture occurs at the diffusion bonded interface (Figure 4) with no plasticity in the adjacent matrices. It could be concluded that all the elastic and plastic deformation is localized at these interfaces. Consequently, the vibrational energy dissipation may also be concentrated at these locations. The fracture at the diffusion bonded interface also explains the lower transverse properties of the composites compared to those of the matrix alloys as previously reported in Table 2, since the interface is weaker than the matrix. The role of the fiber-matrix interface was not very clear in this test program and needs to be studied further.

In the longitudinal direction, the fracture mode, as shown in Figure 5 is attributed to the failure of the fibers when their strain-to-failure limit is exceeded, however, matrix plasticity between the precursor wires is also clearly observed. The diffusion bonded interfaces could not be clearly identified with the limited optical and scanning electron microscopic examinations performed. Since the damping factor has increased, it is assumed that the damping mechanisms involve these interfaces.

For the SiC_p/Al composites, the damping factor is similar to that measured for the matrix alloy as reported in Table 7. The fracture mode in this case is in the matrix alloy (Figure 6), and not at the fiber-matrix interface, indicating that the interface strength is higher than that of matrix alloy 6061-T6. Consequently, all the elastic and anelastic strains are concentrated in the matrix and the damping factor is also similar to the matrix alloy.

Table 7 - Damping Properties of SiC/Al

MATERIAL	OSCILLATION FREQUENCY-f(Hz)	DAMPING FACTOR (%)	ONE-HALF LIFE CYCLE
			PT.
17v/o SiC _w /6061-T6 ^a (L)	32.1	0.25	44.0
20v/o SiC _p /6061-F ^b (L)	120.0	0.46	24.0
30v/o SiC _p /6061-F ^b (L)	20.1	0.37	29.5
30v/o SiC _p /6061-F ^b (L)	104.7	0.13	87
30v/o SiC _p /6061-F ^b (T)	105.4	0.15	74

a - Extruded and Cross-Rolled Sheet (L = Longitudinal to the Extrusion Direction)

b - Rolled Sheet

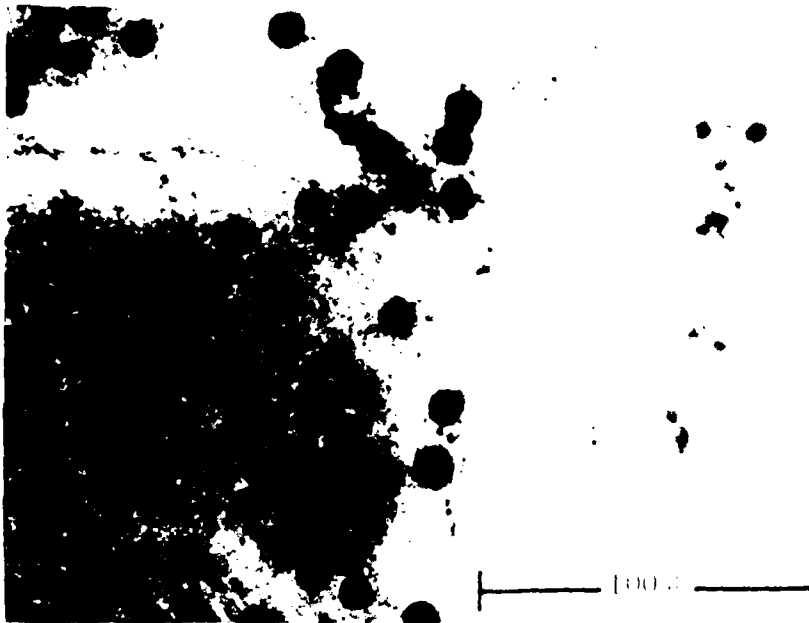


Figure 3 - Microstructure of Single-Ply Gr/Mg Composite Showing Fiber-Matrix Interface and Diffusion Bonded Interface

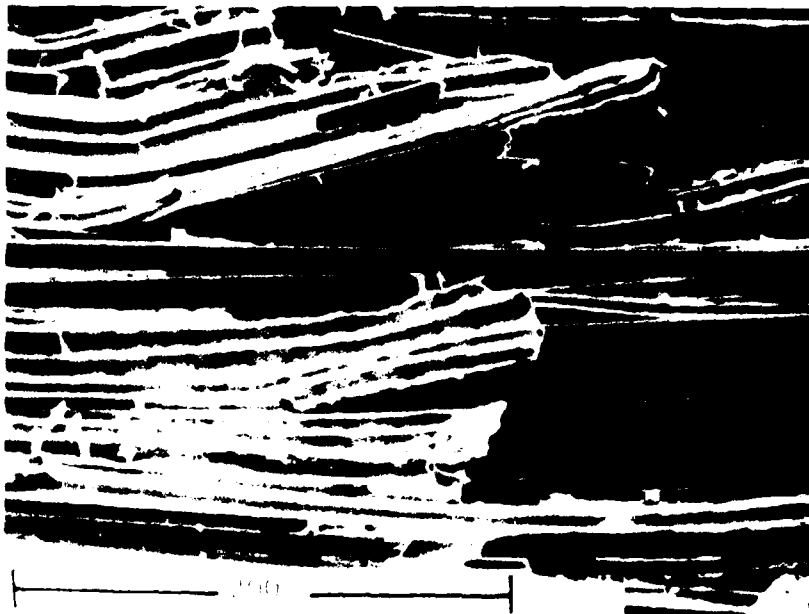


Figure 4 - Transverse Specimen Showing Final Fracture at Diffusion Bonded Interface

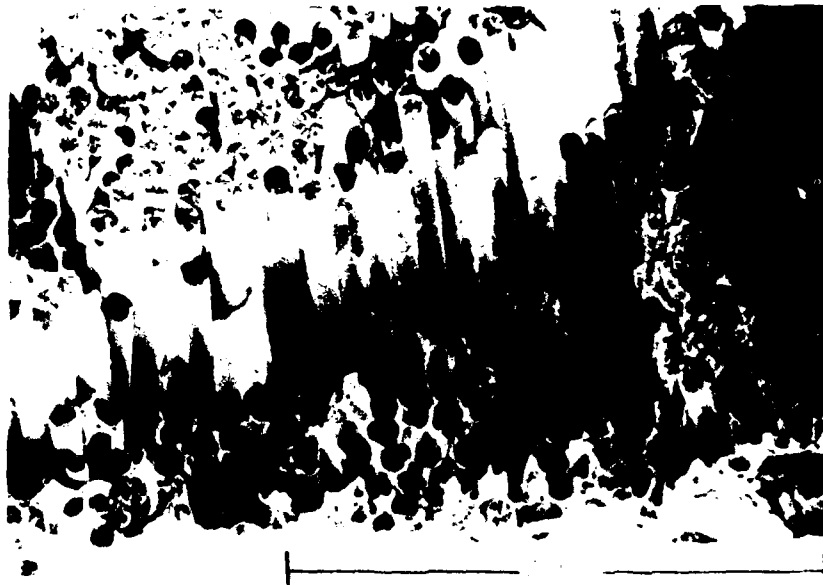


Figure 5 - Longitudinal Specimen Showing Fibers and Matrix Plasticity



Figure 6 - Fracture Surface of SiC_w/6061 Aluminum

A large data scatter in the damping factor for all the metal matrix composites is noted, which is very similar to the data scatter observed for the tensile properties in these materials. The latter effect has been attributed to the variance in material fabricability which strongly affects the bond strength. Damping behavior is also probably strongly influenced by the variation in the interface structure and strength.

SUMMARY

Normally for crystalline material, the damping capacity decreases if the elastic modulus is increased. However, continuous fiber reinforced Gr/Al composites exhibit a factor of 2 improvement in the damping factor along with a factor of 3 improvement in the elastic modulus when compared to the matrix aluminum alloy. A similar behavior is observed for Gr/Mg composites. In addition, both the modulus and damping factors are improved for the higher volume fraction of the fiber-matrix and diffusion bonded interfaces. Since the interfaces are the regions of metallurgical imperfections, vibrational energy could be absorbed by the microstructural changes in these regions.

For discontinuous SiC reinforced composites the particulate-matrix interface is stronger than the matrix as confirmed by the fracture mode. Consequently, damping mechanisms are controlled by the matrix and not by the interfaces.

It is certain the fiber-matrix diffusion bonded interfaces play a dominant role in the damping behavior of the metal matrix composites. The present study is continuing to fundamentally understand these interfaces and subsequently optimize the damping capacity without sacrificing the stiffness.

ACKNOWLEDGMENTS

This work was supported in part by Martin Marietta Aerospace, Denver Division IR&D funds, and by Air Force Contract F33615-82-R-3222 Passive and Active Control of Space Structures (PACOSS).

We would like to thank Ms. Paula Shaeffer for the graphics and typing of this manuscript.

REFERENCES

1. K. Amano, et. al., Proc. 6th Int. Conf. Internal Friction and Ultrasonic Attenuation in Solids, July 1977, Tokyo, pp. 763-767
2. J.C. Fister and S. Shapiro, Final Report, INCRA Project No. 221, Sept. 1974

DAMPING IN METAL MATRIX COMPOSITES

Dr. G. L. Steckel
The Aerospace Corporation
Los Angeles, California

Paper was not presented; not available for publication.

DAMPING IN METAL-MATRIX COMPOSITES: MEASUREMENT AND MODELING

H. M. Ledbetter
Fracture and Deformation Division
Center for Materials Science
National Bureau of Standards
Boulder, Colorado 80303

and

S. K. Datta
Department of Mechanical Engineering
University of Colorado
Boulder, Colorado 80309

Damping in Metal-Matrix Composites: Measurement and Modeling

H. M. Ledbetter
Fracture and Deformation Division
Center for Materials Science
National Bureau of Standards
Boulder, Colorado 80303

S. K. Datta
Department of Mechanical Engineering
University of Colorado
Boulder, Colorado 80309

Abstract

Both experimentally and theoretically, we consider attenuation, α , of elastic waves in a composite consisting of elastic reinforcing particles dispersed in an elastic matrix. We consider only geometrical attenuation caused by scattering from particles. Our model contains the effects of particle volume fraction, particle shape, particle size, particle elastic constants, matrix elastic constants, measurement frequency, and elastic-wave polarization. Concerning the particles, we make several assumptions: arbitrary-shape ellipsoids (spheres, discs, rods), uniform distribution, random orientation. Thus, the model composite is macroscopically both homogeneous and isotropic. Calculations relate only to long wavelengths. In this limit, both α_l and α_t are proportional to ω^4 , where ω denotes circular frequency, l longitudinal wave, and t transverse wave. The self-consistent approach taken here predicts that both α_l and α_t tend to zero when the particle concentration tends to zero. As a particular example, we consider a composite consisting of a 6061-aluminum-alloy matrix reinforced with 5- μm silicon-carbide particles. We model the particles as prolate spheroids. For this composite, we give preliminary α_l results measured by a pulse-echo-decay method.

Intended for Vibration Damping Workshop, Long Beach, California,
27-29 February 1984.

Introduction

In composites, internal friction, or attenuation, arises from four sources:

1. particle, intrinsic;
2. matrix, intrinsic;
3. interface, considered either as a defect or as a third phase; and
4. geometrical, scattering from particles.

Here we consider the fourth source: geometrical. It depends on several variables:

1. particle volume fraction;
2. particle shape;
3. particle size;
4. particle elastic constants;
5. matrix elastic constants;
6. vibrational frequency; and
7. polarization of sound wave (longitudinal or transverse, for example).

Our preliminary studies described here consider these seven variables. Beyond these, other important variables remain unstudied:

8. particle orientations;
9. particle-size distribution; and
10. nonhomogeneity.

Many authors studied the attenuation of elastic waves caused by scattering from particles in a composite material. Reviews are given by Ishimaru [1] and Bhatia [2]. Earlier studies considered only single scattering. Recent studies consider multiple scattering, but mostly for only spherical particles. Particle-shape effects on phase velocities in an elastic composite were considered by Kuster and Toksoz [3], Berryman [4], and Willis [5].

The present approach to attenuation in composites follows our earlier studies [6-8] and differs from those used by others [3-5]. We consider scattering from a random distribution of randomly oriented ellipsoids and take the ensemble average of the scattered field by using the quasi-crystalline approximation. In the long-wavelength limit, we calculate the

effective phase velocities of coherent plane longitudinal and shear waves. The particles modeled as ellipsoids can have arbitrary shape (spheres, discs, rods), but are confined to a single size. Bose and Mal [9] also used this approach to consider the attenuation of a coherent plane wave due to viscous bonding between spherical particles and their surrounding matrix. To derive the attenuation factor, α , we assume

$$\alpha = n\bar{\sigma} \quad (1)$$

where n denotes number of particles per unit volume and $\bar{\sigma}$ denotes the average scattering cross-section of a single particle embedded in a matrix with the effective composite properties. The derived expressions are most correct in the dilute limit where geometrical attenuation vanishes. Above a particle volume fraction of 30 percent, the expressions probably break down.

Formulation

We consider the spatial attenuation of a coherent elastic wave propagating through a particle-reinforced composite in terms of energy dissipation:

$$E = E_0 \exp(-\alpha x) \quad (2)$$

where E is the energy flux per unit area perpendicular to the plane-wave front averaged over one period. Suppressing the harmonic time factor, $\exp(-i\omega t)$, we express the coherent plane wave as

$$u_x = a \exp(i k^* x) \quad (3)$$

where a denotes polarization and k^* denotes the effective wave vector. The effective wave velocity is

$$c^* = \omega / \text{Re } k^* \quad (4)$$

where Re denotes the real part, and the amplitude attenuation is

$$\alpha = 2 \text{Im } k^* \quad (5)$$

On the other hand, if $\bar{\sigma}$ denotes the scattering cross-section of a single particle embedded in a matrix with the overall macroscopic composite properties, then Eq. (1) applies.

Several studies [2,3,9-12] use the scattering approach to calculate α for elastic waves. Brinji et al. [13] report related studies.

For the longitudinal wave, our model leads to the following relationship for internal friction, or attenuation [14]:

$$Q^{-1} = \alpha/k = 3\bar{c} \text{abc} (\omega/c_l)^3 F_l \quad (6)$$

where

α = attenuation per unit length

k = wavenumber = ω/c_l

ω = angular frequency

c_l = longitudinal-wave velocity

a, b, c = semiaxes of ellipsoidal particle

\bar{c} = particle volume fraction

$F_l = F_l[\bar{c}, c/a, C_{ij}(p), C_{ij}(m), \text{wave speed}(p), \text{wave speed}(m)]$

where p and m denote particle and matrix. For the transverse wave, a similar relationship emerges [14], except that F_l is replaced by a similar function, F_t .

In summary, our model for predicting geometrical internal friction possesses the following characteristics:

1. Considers scattering of a plane harmonic wave from an ellipsoidal particle embedded in a matrix.
2. Matrix has effective elastic constants of macroscopic composite.
3. Limited presently to isotropic elastic constants.
4. Total scattering determined by summing over all scatterers; particle interactions neglected.
5. Valid for all wavelengths and frequencies; but here we consider the long-wavelength limit where $\lambda \gg d$ (λ = wavelength, d = particle diameter); thus, present results refer only to Rayleigh region.

Model Results

As an example material, we consider a 6061-aluminum alloy reinforced with thirty-volume-percent 5- μ m silicon-carbide particles. See Fig. 1.

Figures 2-6 show some graphed results obtained from Eq. (6). Figure 2 gives α/k (attenuation/wavelength) versus particle volume fraction. We realize that our model breaks down somewhere below $\bar{c} = 0.5$. At both ends, $\bar{c} = 0.0$ and $\bar{c} = 1.0$, geometrical attenuation must vanish. Figure 2 shows several features: a maximum attenuation at relatively low volume fractions, S (or t) waves attenuate more than P (or l) waves. Basically, S waves attenuate more than P waves because they move with lower velocities; the shear elastic constant is typically about three-eighths of the longitudinal elastic constant.

Figure 3 shows the effect of particle shape. it gives results for three cases: spheres ($c/a = 1$), fat discs ($c/a = 1/3$), and short rods ($c/a = 3/1$). We see that spherical particles exhibit highest attenuation, that small deviations in either direction from $c/a = 1$ drastically reduce the attenuation, and that rods attenuate less than discs. However, we did not yet study the full range of aspect ratios. Conceivably, more extreme aspect ratios may show that discs attenuate less than rods.

Figure 4 shows effects of particle size. Larger particles attenuate more. This is a well-known classical result related to the scattering cross-section. For the present case, submicrometer-size particles contribute practically nothing to geometrical attenuation.

Figure 5 shows the effect of increasing the particle's relative elastic stiffness. The figure shows curves for the unperturbed case (1.0), an increase of 50 percent (1.5), and a decrease of 50 percent (0.5). Higher particle stiffness causes higher attenuation. Basically, this increase arises because we are increasing the difference between particle and matrix elastic properties. No geometrical scattering occurs if the two phases have identical elastic properties.

Figure 6 represents a companion to Fig. 5. Here the matrix properties are perturbed plus and minus 50 percent. Again, attenuation increases (decreases) as the particle-matrix elastic-constant difference increases (decreases).

In summary, for geometrical internal friction we list the variable changes that increase attenuation:

1. higher particle volume fraction (up to a limit past which attenuation decreases);
2. spherical particles;
3. large particle sizes;
4. high-elastic-stiffness particles;
5. low-elastic-stiffness matrix material;
6. higher vibrational frequencies; and
7. S waves rather than P waves.

Preliminary Measurements

For the SiC/Al composite, we have obtained preliminary internal-friction measurements by two methods (1) resonance of circular-cylinder specimens at kHz frequencies in a Young-modulus (extensional) vibrational mode, and (2) decay of a longitudinal-polarization plane-wave pulse in cube-shaped specimens at MHz frequencies.

For the resonance studies, we used a Marx-oscillator method [15] where from the resonance peak one obtains

$$Q^{-1} = (f_2 - f_1)/f_0 \quad (7)$$

where f_0 denotes resonance frequency and f_1 and f_2 denote the frequencies corresponding to $1/2$ of the maximum strain amplitude at f_0 .

For the decay studies, we measured the attenuation, α , occurring in our usual [16] pulse-echo-overlap method for determining sound velocities. Here, we determine attenuation by the amplitude, A , decay of a stress wave detected by a piezoelectric transducer:

$$A = A_0 \exp(\alpha_t t) \quad (8)$$

where t denotes time. One obtains attenuation per unit length by invoking the sound velocity, v :

$$\alpha_l = \alpha_t / v \quad (9)$$

Table 1 gives Young moduli and internal friction measured in the composite's three principal directions. No significant difference appeared in the Young moduli measured at different frequencies: kHz and MHz. Our scattered-plane-wave ensemble-average model [17] explains the Young-modulus anisotropy, which arises from the aligned aluminum-matrix-material oblate spheroids (see Fig. 1).

Table I. Young's moduli and internal friction of a 30-volume-percent SiC-particle-reinforced 6061-Al-alloy-matrix composite.

Axis	E(kHz) GPa	E(MHz) GPa	Q^{-1} 10^{-6}
Observed:			
x_1	120	125	75
x_2	121	124	75
x_3	112	111	60

Concerning internal friction, composites contain four separate sources: reinforcement, matrix, interfaces, and geometry. Several previous studies on metal-matrix composites show that interfaces contribute negligibly to internal friction [18,19]. One expects a high-stiffness material such as SiC to possess low Q^{-1} . Our present model indicates that, at kHz frequencies, geometrical scattering in these materials is negligible. Thus, most of Q^{-1} should arise from the matrix material: 6061 aluminum alloy. One must consider whether the aligned oblate spheroids shown in Fig. 1 explain

the Q^{-1} anisotropy displayed in Table I, particularly the lower Q^{-1} in the soft-Young-modulus direction. Igata and Kohyama [19] gave an expression for the rule-of-mixture internal friction of a fiber-reinforced composite. But, as yet, no similar model exists for the present case. We now study this problem and plan to report on it later.

The low Q^{-1} values present a puzzle. They suggest not only that the SiC particles, the interfaces, and the geometry contribute insignificantly to Q^{-1} , but also that the 6061-aluminum-alloy matrix possesses a low Q^{-1} , even lower than the alloy alone. Explanation of this puzzle requires further study. Arsenault and Fisher [20] showed that thin foils of this material contain enormous dislocation densities ($2 \cdot 10^{10}/\text{cm}^2$) that arise from the particle-matrix thermal-expansion difference. Presumably, these dislocations are pinned and contribute only slightly to internal friction. The lower dislocation density in the alloy alone may consist mainly of unpinned dislocations that contribute significantly to internal friction. Thus, here lies an embryonic explanation. To test this idea, we just obtained a new plate of this material with identical thermal-mechanical processing, but without SiC particles. Very soon, we shall measure its directional elastic-constant and internal-friction properties. Opportunities exist also to study the effects of heat treatment on dislocation density and damping.

Figure 7 shows the decay of a MHz-frequency pulse reverberating through an SiC/Al specimen (a 1-cm cube). Fitting Eq. (8) to such measurements yields the attenuation α_{ω} . Measurements at several frequencies reveal the frequency dependence of Q^{-1} shown in Fig. 8.

In conclusion, we developed a model to describe geometrical damping in particle-reinforced composites. In progress, we have preliminary measurements to test the model. In the near future, we hope to extend the model to include intrinsic-particle, intrinsic-matrix, and interface damping. Also, we hope to develop improved measurement methods for studying damping. Here, contactless transducer methods seem most appealing.

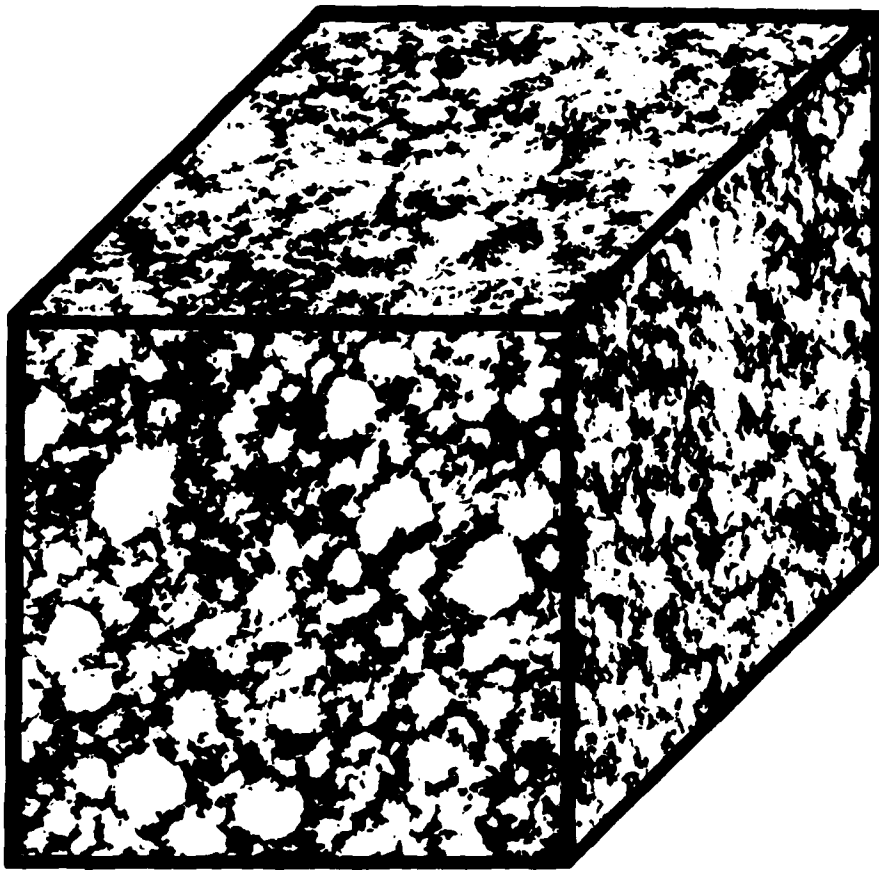
Acknowledgment

This study arose from research sponsored by DARPA. Dr. R. D. Kriz of NBS contributed computer calculations. Dr. R. J. Fields of NBS contributed quantitative metallography. M. W. Austin of NBS contributed measurements.

References

1. I. Ishimaru, Wave Propagation and Scattering in Random Media (Academic, New York, 1978).
2. A. B. Bhatia, Ultrasonic Absorption (Oxford U. P., Oxford, 1967).
3. G. T. Kuster and M. N. Toksöz, "Velocity and attenuation of seismic waves in two-phase media: Part I. Theoretical formulations; Part II. Experimental results", Geophysics 39, 587-618 (1974).
4. J. G. Berryman, "Long wavelength propagation in composite elastic media; II. Ellipsoidal inclusions", J. Acoust. Soc. Am. 68, 1820-1831 (1980).
5. J. R. Willis, "A polarization approach to the scattering of elastic waves; II. Multiple scattering from inclusions", J. Mech. Phys. Solids 28, 307-327 (1980).
6. S. K. Datta, "A self-consistent approach to multiple scattering by elastic ellipsoidal inclusions", J. Appl. Mech. 44, 657-662 (1977).
7. S. K. Datta, "Scattering by a random distribution of inclusions and effective elastic properties", in Solid Mechanics Study Series Number 12 (Univ. Waterloo P., 1978), pp. 149-208.
8. S. K. Datta, "Wave propagation in the presence of a random distribution of inclusions", in Solid Mechanics Study Series Number 15 (U. Waterloo P., 1980), pp. 565-582.
9. A. K. Mal and S. K. Bose, "Dynamic elastic moduli of a suspension of imperfectly bonded spheres", Proc. Cambr. Philos. Soc. 76, 587-600 (1974).
10. J. E. Gubernatis and E. Domany, Effects of microstructure on the speed and attenuation of elastic waves in porous materials, Report LA-UR-83-2611, Los Alamos National Laboratory.
12. A. J. Devaney, H. Levine, and T. Plona, "Attenuation due to scattering of ultrasonic compressional waves in granular media", in Elastic Wave Scattering and Propagation (Ann Arbor Science, Ann Arbor, 1982).
13. V. N. Brinji, T. A. Seliga, V. K. Varadan, and V. V. Varadan, "Bulk propagation characteristics of discrete random media", in Multiple Scattering and Waves in Random Media (North-Holland, Amsterdam, 1981).
14. S. K. Datta, H. M. Ledbetter, and R. D. Kriz, "Attenuation of elastic waves in a particle-reinforced composite", J. Acoust. Soc. Amer., to be submitted to.
15. H. M. Ledbetter, "Dynamic elastic modulus and internal friction in G-10CR and G-11CR fiber-glass-cloth-epoxy composites", Cryogenics 20, 637-640 (1980).

16. H. M. Ledbetter, N. V. Frederick and M. W. Austin, "Elastic-constant variability in stainless-steel 304, J. Appl. Phys. 51, 305-309 (1980).
17. S. K. Datta and H. M. Ledbetter, "Effective wave speeds in an SiC-reinforced Al composite", J. Acoust. Soc. Am., submitted to.
18. H. M. Ledbetter, unpublished measurements on B/Al fiber-reinforced composites.
19. N. Igata and A. Kohyama, "Tensile strength and ductility of Cu-Mo composite", Trans. Jap. Soc. Compos. Mater. 2, 30 (1976).
20. R. J. Arsenault and R. M. Fisher, "Microstructure of fiber and particulate SiC in 6061 Al composites", Scripta Metall. 17, 67 (1983).



=====
100 μm

Fig. 1. Photomicrograph of particle-reinforced SiC/Al-alloy composite formed from powders of SiC and Al. Randomly oriented SiC particles exist nonhomogeneously in a "sea" where the SiC volume fraction is approximately double that of the macroscopic average volume fraction. Our present model considers nonhomogeneous particle distribution for elastic constants of composite but neglects it for composite's internal friction.

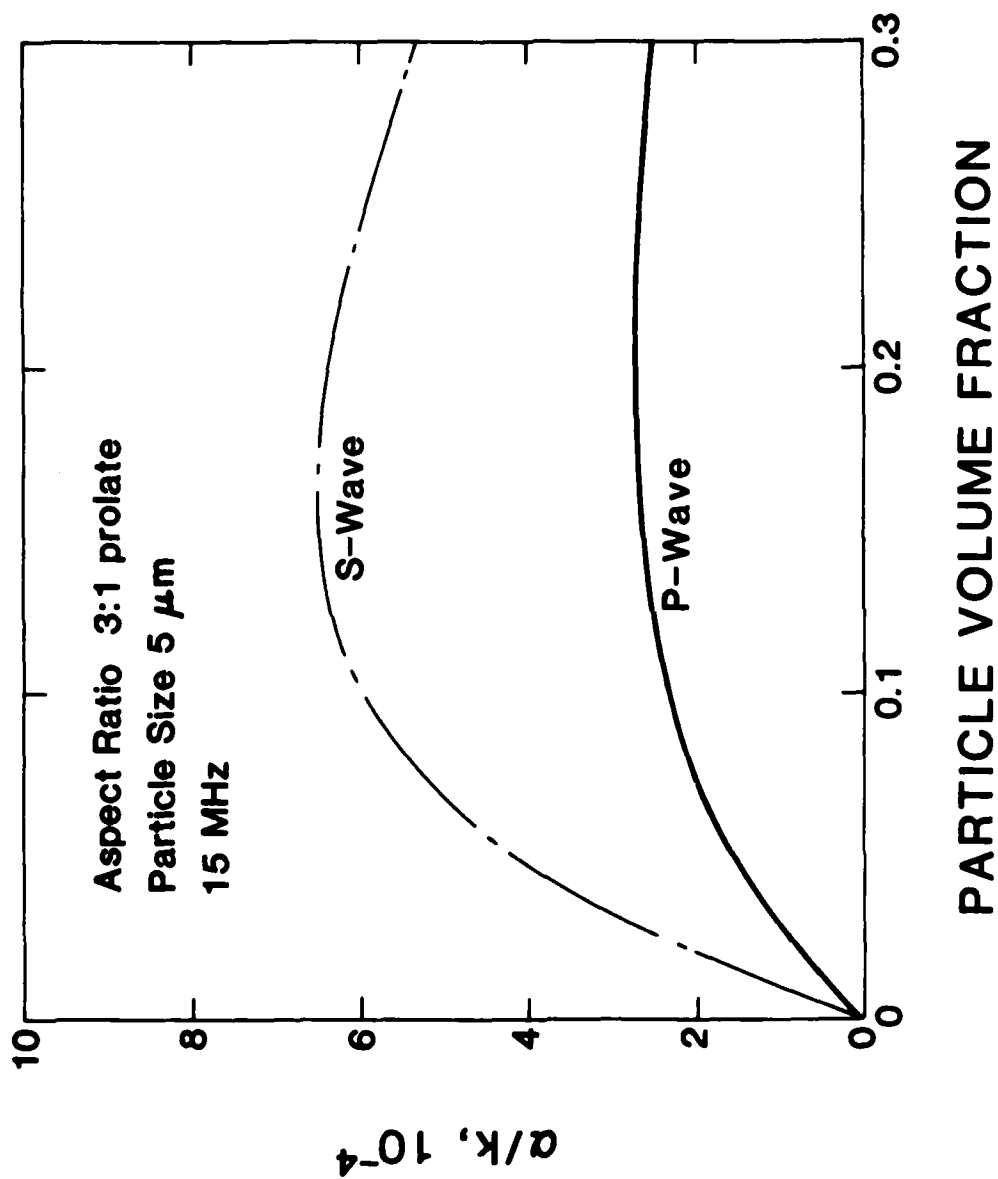


Fig. 2. Internal friction $Q^{-1} = \alpha/k$ versus particle volume fraction, where α denotes attenuation and $k = \pi/\lambda$, where λ denotes wavelength. Model invalid at higher volume fractions.

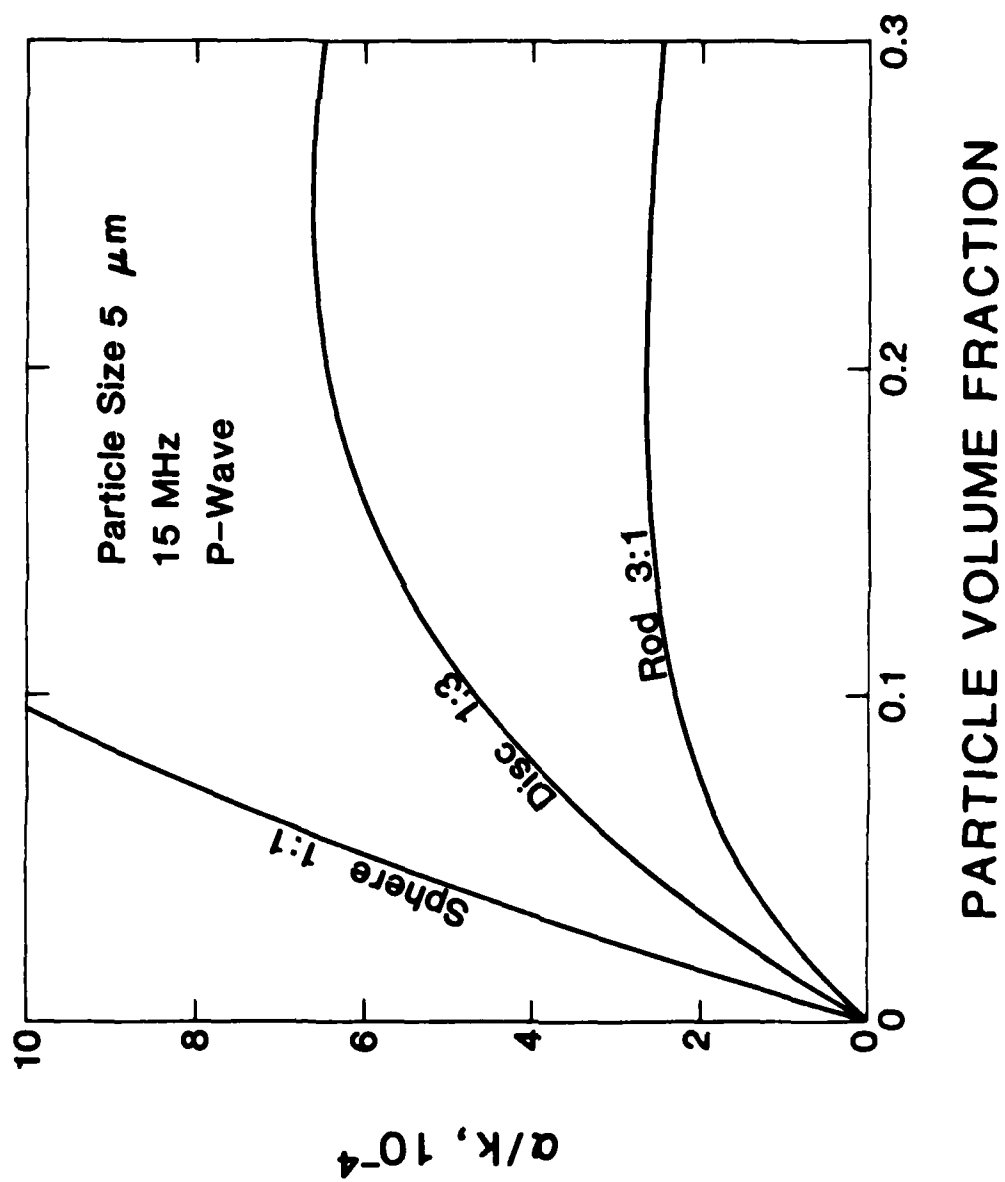


Fig. 3. Internal friction versus particle volume fraction for various particle shapes: sphere, fat disc, short rod.

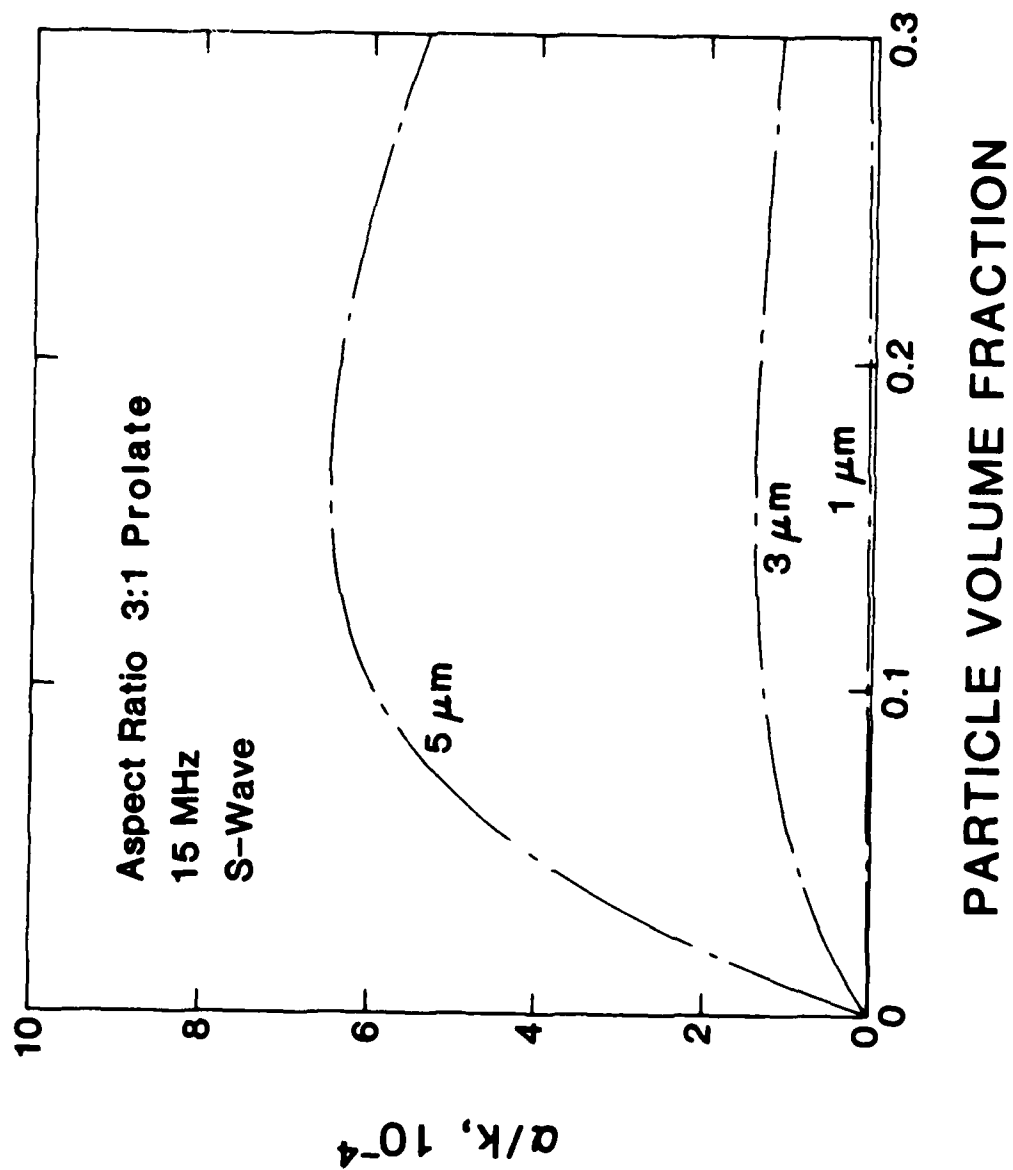


Fig. 4. Internal friction versus particle volume fraction for various particle sizes.

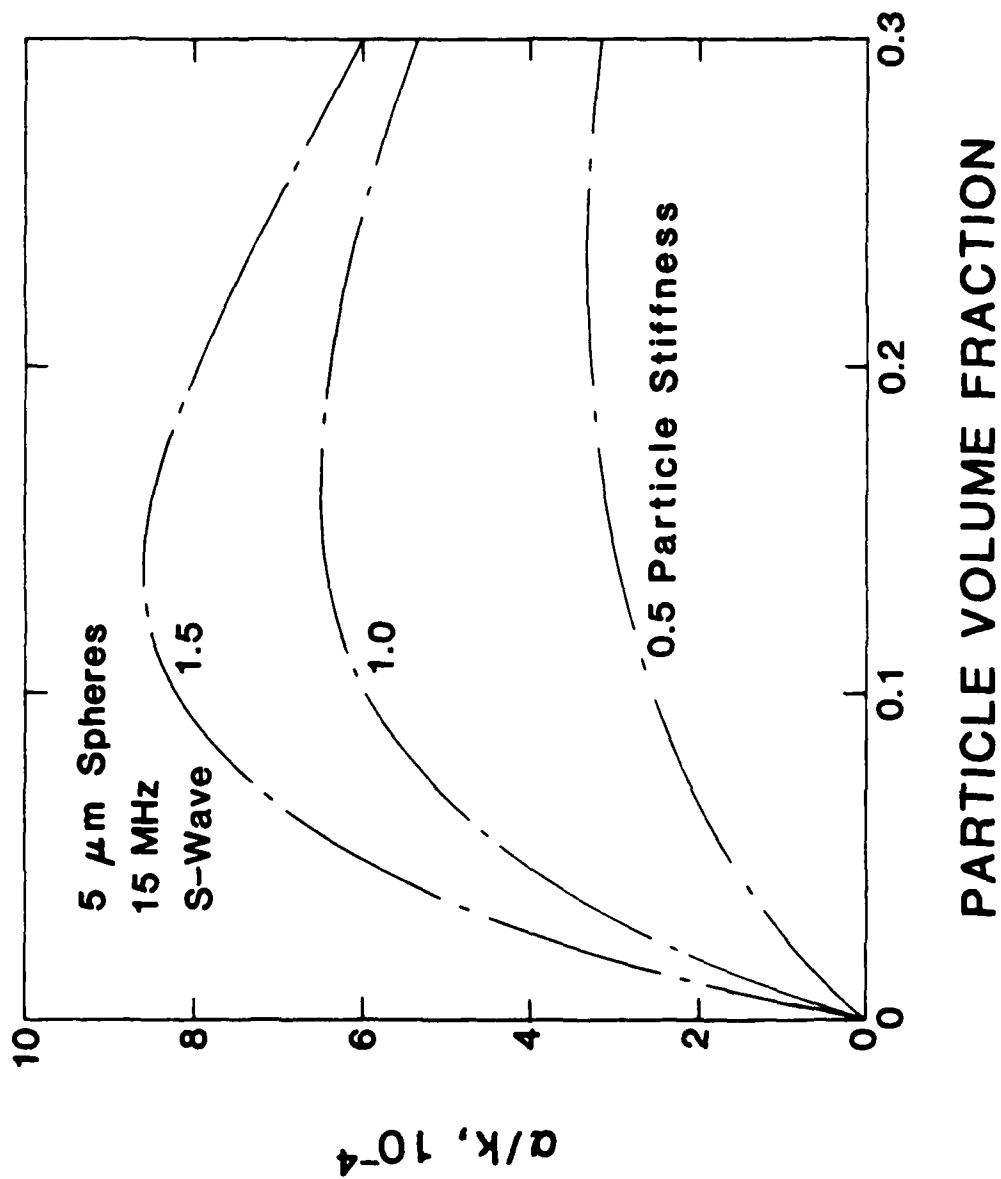


Fig. 5. Internal friction versus particle volume fraction for relative particle elastic stiffnesses.

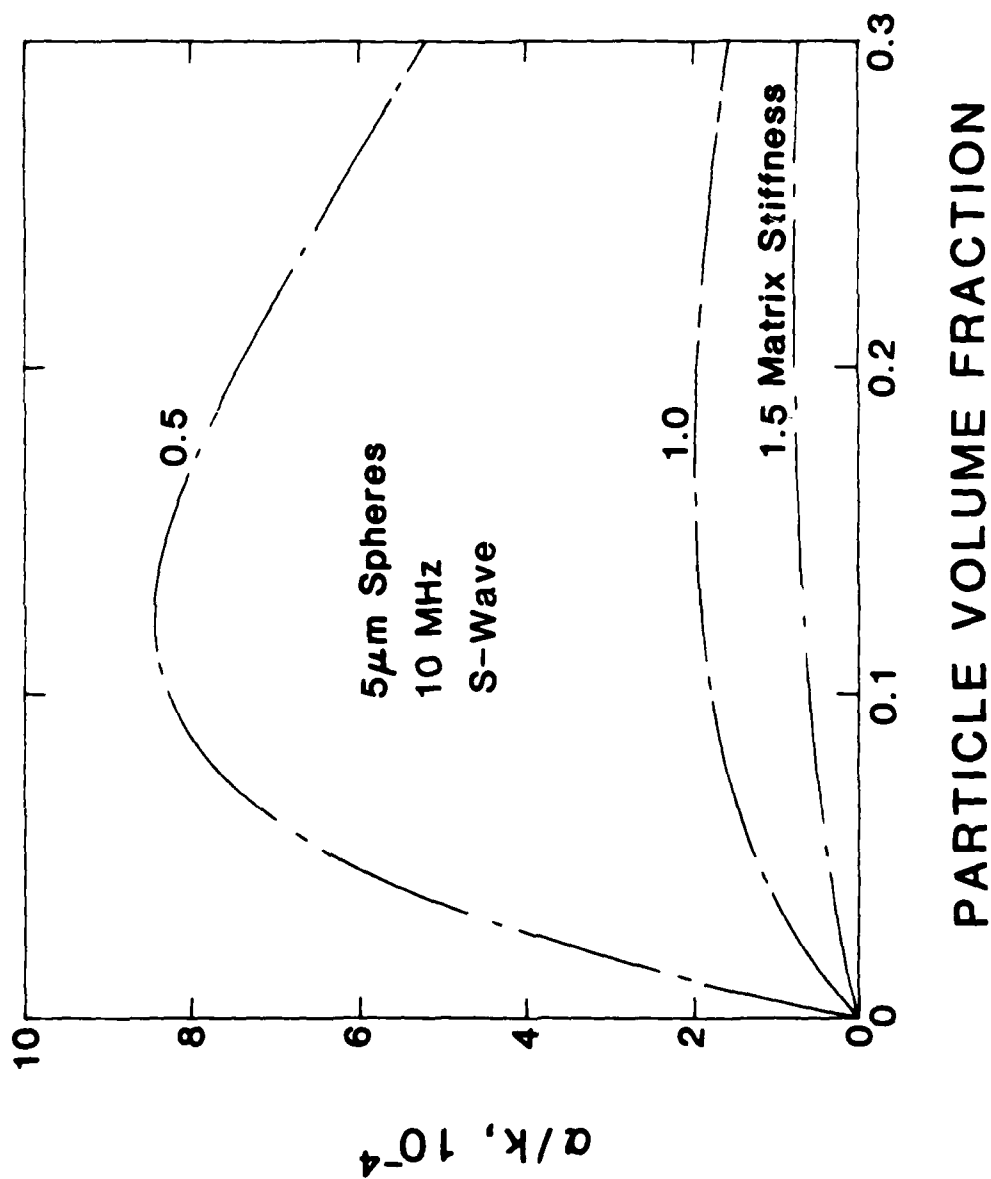


Fig. 6. Internal friction versus particle volume fraction for relative matrix-material elastic stiffnesses.

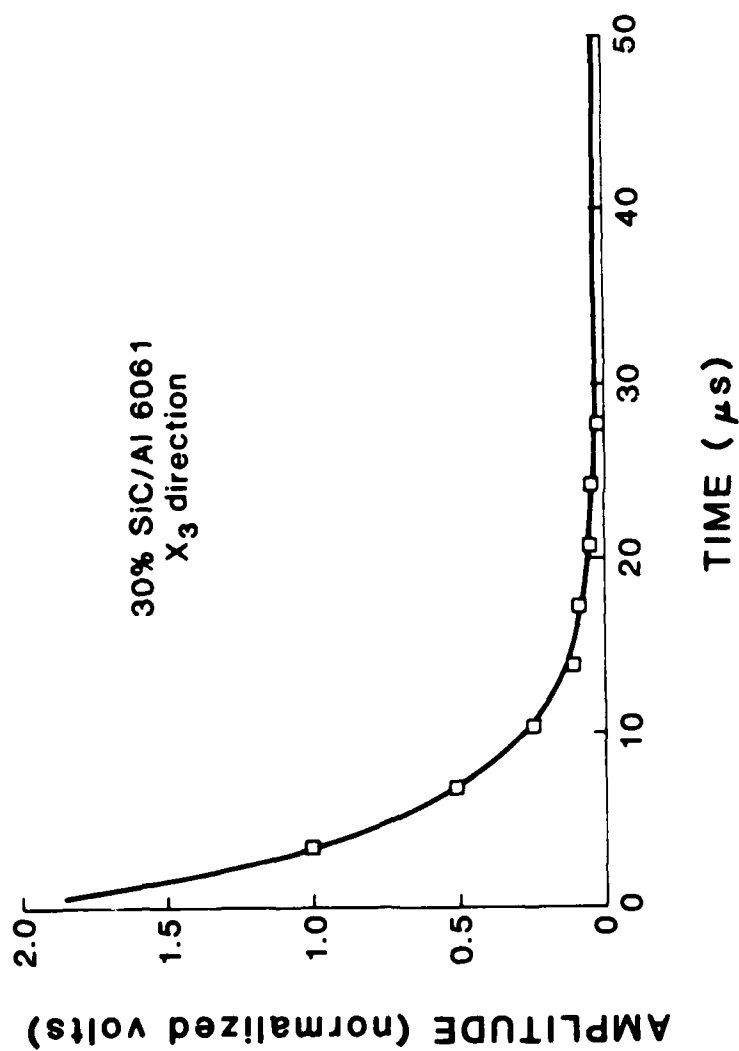


Fig. 7. Amplitude of a MHz-frequency stress wave reverberating through a 1-cm-cube specimen of SiC/Al.

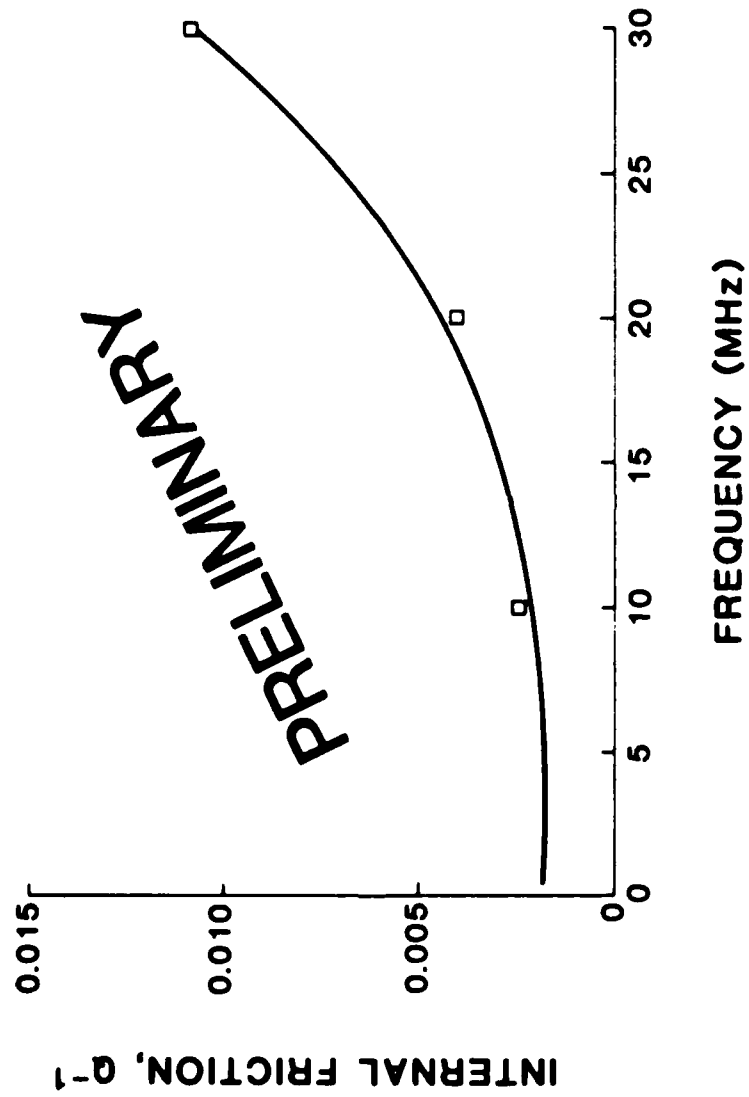


Fig. 8. Internal friction versus frequency for a SiC/Al composite. Curve represents best fit to equation $y = a + bx$.

DAMPING MEASUREMENT BY DYNAMIC STIFFNESS METHODS

David I. G. Jones
Materials Laboratory (AFWAL/MLLN)
Wright-Patterson Air Force Base, Ohio

and

Agnes Muszyńska
Bently Rotor Dynamics Research Corporation
Minden, Nevada

DAMPING MEASUREMENT BY DYNAMIC STIFFNESS METHODS

by

David I.G. Jones

Materials Laboratory (AFWAL/MLLN)
Wright-Patterson Air Force Base, Ohio

and

Agnes Muszyńska

Bently Rotor Dynamics Research Corp.,
Minden, Nevada

ABSTRACT

In this paper, the problem of determining the mass, stiffness and damping parameters of a structure from measured modal response data is addressed. The modal mass shape and damping parameters are determined from both receptance and dynamic stiffness approaches. Complex normal modes are used in the representation of non-proportional damping, localized in specific parts of a structure, whereas real normal modes are sufficient to represent the behavior of a system with damping proportional to stiffness. The inversion of the receptance matrix to obtain the dynamic stiffness matrix, and some unique properties of the elements of the dynamic stiffness matrix, are discussed. Two examples, one from dynamics of a discrete structure and the other for a rotor-bearing system, illustrate the methodology.

1. INTRODUCTION

The dynamic stiffness matrix $[\kappa]$ is the inverse of the well known receptance matrix $[\alpha]$, which is the usual form in which modal test data is stored and displayed [1-6]. A great deal of information concerning the modal parameters of a system can be inferred from the reciprocal, $\kappa'_{pq} = 1/\alpha_{pq}$, of each element of the receptance matrix, including modal masses, resonant frequencies, modal functions, both real and complex, and modal damping. This, together with the mass, stiffness and damping parameters obtained from the dynamic stiffness matrix, allows one to identify the system parameters from the test data [7,8]. The advantages and disadvantages of this approach will be discussed with reference to several examples, including (a) a two degree of freedom structural model with distributed and discrete damping, (b) a single degree of freedom rotor system driving a bearing, for which one may determine some of the bearing parameters which would otherwise be difficult to measure [9-11].

2. ANALYSIS

2.1 Point and Transfer Receptance

In any linear structure under harmonic excitation, the response vector component amplitude W_p in any selected direction, at any point p , resulting from an applied force of amplitude F_q in any selected direction at any point q is defined by:

$$W_p = \alpha_{pq} F_q \quad (1)$$

For structures with linear damping uniformly distributed throughout its spatial zone, the dynamic receptance can be represented as a series of real normal modes:

$$\alpha_{pq} = \sum_{n=1}^N \frac{\phi_n(p) \phi_n(q)}{M_n \{ \omega_n^2 (1 + i\eta_n) - \omega^2 \}} \quad (2)$$

where $\phi_n(p)$ is the n -th modal function at point p , M_n is the n th modal mass, ω_n is the n th resonant frequency and η_n is the n -th modal loss factor.

If the damping is not uniformly distributed, a "distortion" of the modal arrangements take place and the real modes ϕ_n are replaced by complex modes $\phi_n(1 + i\mu_n)$ with $\mu_n \ll 1$, which may not be fully orthogonal. The modal expansion then can be written:

$$\alpha_{pq} \doteq \sum_{n=1}^N \frac{\phi_n(p) \phi_n(q) \{1 + i(\mu_{np} + \mu_{nq})\}}{M_n \{ \omega_n^2 (1 + i\eta_n) - \omega^2 \}} \quad (3)$$

This can be shown to be equivalent to the sum of the conjugate series:

$$\alpha_{pq} = \sum_{n=1}^N \frac{\phi_n(p) \phi_n(q) (1 + i\mu_{np})(1 + i\mu_{nq})}{2\omega_n M_n \{ \omega_n (1 + i\beta_n) - \omega \}} + \sum_{n=1}^N \frac{\phi_n(p) \phi_n(q) (1 - i\mu_{np})(1 - i\mu_{nq})}{2\omega_n M_n \{ \omega_n (1 - i\beta_n) + \omega \}} \quad (4)$$

where $\beta_n = \eta_n \omega_n / 2\omega$, and must be small,

and $\pm \omega_n + i \omega_n \beta_n$ are a pair of singularities in the complex- ω plane which lie above the $\text{Im}(\omega) = 0$ line. Both of the representations (3) and (4) may be used to model the behavior of a dynamic system, the additional parameters μ_{np} and μ_{nq} being needed to model the effects of non-ideally distributed damping. The modal parameters $M_n, \omega_n, \eta_n, \phi_n(p), \phi_n(q)$, μ_{np} and μ_{nq} are determined by fitting to experimental data. The modes $\phi_n(p)$ and $\phi_n(q)$ are determined for any points (p) and (q) from relative peak response amplitudes at various points on the basis of selecting any

one point, for each mode, for normalization. The resonant frequencies are determined from peak amplitudes and modal loss factors from half-power bandwidth measurements. The modal masses can then be determined from equations (2) for $\omega = \omega_n$: at the point 1, for which $\phi_n(p) = 1$:

$$M_n = \frac{1}{\omega_n^2 \eta_n |\alpha_{pp}|_{\max}} \quad (5)$$

The parameters μ_{np} and μ_{nq} can be determined by varying these parameters and comparing the calculated values of α_{pq} with the measured, the other modal parameters having been determined. If the modes are closely spaced or the system is highly damped, this process is not simple because some coupling of effects arises between each modal term $n = 1, 2, \dots, N$. It is not, however, impossible.

2.2 Point and Transfer Dynamic Stiffness

The inverse of the point receptance α_{pq} is defined as the corresponding point or transfer dynamic stiffness, or perhaps more properly, the pseudo-dynamic stiffness [7]:

$$\kappa'_{pq} = 1 / \alpha_{pq} \quad (6)$$

By examining these point dynamic stiffnesses we can obtain the modal parameters in an alternate way, which may be more useful in some cases. In the vicinity of the n -th mode, modal coupling being assumed small:

$$\kappa'_{pq} = M_n \left\{ \omega_n^2 (1 + i\eta_n) - \omega^2 \right\} / \left\{ \phi_n(p) \phi_n(q) \right\} \quad (7)$$

for point p , if this is the point where $\phi_n(p) = 1$, then, M_n is given by the slope of the κ'_{pp} vs. ω^2 line at $\omega = \omega_n$. The modal loss factor can be determined from the quadrature component of κ'_{pp} at $\omega = \omega_n$, i.e.

$$\eta_n = \kappa'_{ppQ} / M_n \omega_n^2 \quad (8)$$

Again, the complex modal terms μ_{np} and μ_{nq} are best determined by varying these parameters and observing the effect on the predicted values of κ'_{pp} .

2.3 Receptance and Dynamic Stiffness Matrices

The full set of receptances α_{pq} form a matrix of order $n \times n$, where n is the number of points at which the receptances are measured. The relationship between the set of forces and resulting displacements at each point form the matrix equation:

$$\begin{bmatrix} \alpha \end{bmatrix} \begin{Bmatrix} F \end{Bmatrix} = \begin{Bmatrix} W \end{Bmatrix} \quad (9)$$

The inverse relationship is given by:

$$\begin{bmatrix} \kappa \end{bmatrix} \begin{Bmatrix} W \end{Bmatrix} = \begin{Bmatrix} F \end{Bmatrix} \quad (10)$$

where:

$$\begin{bmatrix} \kappa \end{bmatrix} = \begin{bmatrix} \alpha \end{bmatrix}^{-1} \quad (11)$$

The dynamic stiffness matrix $[\kappa]$ is also of order $n \times n$ and each element κ_{pq} appears to behave, ideally, in the manner:

$$\kappa_{pq} = k_{pq} (1 + i\eta_{pq}) - m_{pq} \omega^2 \quad (12)$$

The complex stiffness term $k_{pq} (1 + i\eta_{pq})$ may be frequency dependent if the damping mechanism is frequency dependent, as for a polymeric damping material, but in most practical structures k_{pq} , η_{pq} and m_{pq} are often independent of frequency. Note that the κ_{pq} terms in the $[\kappa]$ matrix are not the same as the transfer dynamic stiffness $\kappa'_{pq} (=1/\alpha_{pq})$ i.e., $[\kappa] \neq [1/\alpha]$.

2.4 Discrete Model

It is sometimes useful to use the dynamic stiffness matrix to create a discrete model of the system. If, as in Figure 1, the real structure is replaced by a set of masses and springs located at points where receptance measurements were made, then an equation of motion can readily be set up of the form:

$$\left[k_{p0} + k_{p1} + k_{p2} + \dots - m_p \delta_{pq} \omega^2 \right] \{W\} = \{F\} \quad (13)$$

where δ_{pq} is the Kronecker Delta.

Comparing each term of the dynamic stiffness matrices in equations (12) and (13), one can determine the complex stiffness k_{p0} , k_{p1} , ... and the masses m_1 , m_2 , m_3 , Note that the masses m_{pq} are zero in equation (13), so full equivalence of the model is possible only if $m_{pq} = 0$, in equation (12), for $p \neq q$.

This can only occur if the number of mass points selected for the model is exactly equal to the number of modes of vibration to be considered, and hence the number of degrees of freedom of the discrete model. Also, it is necessary that the points be selected so that $m_{pq} = 0$ ($p \neq q$), and this can only happen at particular sets of points, i.e., a search procedure is necessary. For some types of structures, the elements of the discrete model can be attributed to specific areas of the actual structure, and hence the discrete model can be used to study the distribution of mass and stiffness in the structure and evaluate the area where changes may be needed to achieve improved dynamic response behavior. In other types of structures, particularly those where large areas are highly continuous, the discrete model may be of little direct value. Only in each specific problem can this determination be made.

3. ILLUSTRATIONS

3.1 Two-Degree of Freedom System

Consider the two-degree of freedom system shown in Figure 2. The response is given by:

$$\begin{bmatrix} K_1(1+i\eta_1) + K_2(1+i\eta_2) - m_1\omega^2 & -K_2(1+i\eta_2) \\ -K_2(1+i\eta_2) & K_2(1+i\eta_2) + K_3(1+i\eta_3) - m_2\omega^2 \end{bmatrix} \begin{Bmatrix} W_1 \\ W_2 \end{Bmatrix} = \begin{Bmatrix} F_1 \\ F_2 \end{Bmatrix} \quad (14)$$

From this equation it is simple to calculate the receptances

$\alpha_{pq} = \partial W_p / \partial F_q$, ($p, q = 1, 2$). Hence, the direct and quadrature parts of the receptance matrix terms, α_{pqD} and α_{pqQ} , can be determined and the $[\alpha]$ matrix inverted. Since the purpose of the example is to illustrate the errors inherent in the modal approach, however, we must first create a modal model of α_{pq} , and then invert that matrix. The identification of terms in the modal model is best accomplished by examining the transfer dynamic stiffness κ'_{pq} ($= 1/\alpha_{pq}$), for each p and q , and especially the direct and quadrature terms:

$$\kappa'_{pqD} = \frac{\alpha_{pqD}}{\alpha_{pqD}^2 + \alpha_{pqQ}^2} \quad (15)$$

$$\kappa'_{pqQ} = \frac{\alpha_{pqQ}}{\alpha_{pqD}^2 + \alpha_{pqQ}^2} \quad (16)$$

Figure 3 shows the variation of α_{pq} with frequency for two cases (a) $\eta_1 = \eta_2 = \eta_3 = 0.1$ and (b) $\eta_1 = \eta_2 = 0$, $\eta_3 = 0.10$. Figures 4 to 6 show the variation of κ'_{pqD} and κ'_{pqQ} with frequency squared for the same cases. For case (a), where the damping is uniformly distributed, the modal parameters can be chosen to fit the initial (directly calculated from Eq 14), values quite readily with μ_{np} and $\mu_{nq} = 0$. For case (b), μ_{np} and μ_{nq} are not zero but must be selected to give the best fit. The modal parameters selected from Figures 4 to 6 for cases (a) and (b) are summarized in Table 1. Some aspects of these figures are particularly interesting. For the uniformly distributed damping case, note that κ'_{11Q} and κ'_{22Q} both vary qualitatively in the same way as a function of frequency squared but, for damping concentrated in the link k_3 the value of

κ'_{22Q} is independent of frequency, perhaps providing some clue as to which link is providing the damping. The other matter of interest is the difficulty encountered in fitting the curves exactly by means of the complex mode model in the case of concentrated damping. Further iterations could improve the fit, but that obtained here was sufficient for the present purposes. The calculation of α_{pq} from equation (3) is now quite straightforward for the two modes involved here, as is the inversion of the $[\alpha]$ matrix. The variation of each κ_{pq} term in the dynamic stiffness matrix, as a function of frequency squared, is illustrated in Figures 7-9.

With each κ_{pq} term identified, it is not difficult to re-derive the corresponding discrete model by comparison with equation (14). The results are summarized in Table 2. It is seen that the mass and stiffness parameters are recovered quite well, but the damping is not recovered so well, although the qualitative aspects are. It would seem that this difficulty will always arise as a result of experimental error, which is in turn reflected as an imperfect modal model.

3.2 Oil Bearing Identification by a Perturbation Test

In this problem, a model rotor system was used to evaluate the dynamic properties of an oil bearing [9-11]. The system is illustrated in Figures 10 and 11. The main rotor shaft was run at various rotational speeds ω_R and independently the perturbation shaft was run at various perturbation speeds ω_p , all at various temperatures which led to changes in the hydrodynamic characteristics of the bearing as a result of viscosity changes. Figure 12 shows a set of typical plots of bearing response amplitude and phase versus perturbation speed at one main rotor speed $\omega_R = 200$ rad/sec. Similar plots were obtained at other rotor speeds [9]. It is seen that the temperature affects the response significantly, and the goal of the investigation was to determine some of the bearing properties as a function of viscosity from the tests. In order to do this, an equation describing the rotor response, on the basis of a one-degree of freedom model, was set up. This equation is:

$$(m + M)\ddot{z} + (d_r - id_T)\dot{z} + (K + K_r - i\omega_R K_T)z = U \omega_p^2 e^{i\omega_p t} \quad (17)$$

$$z = x + iy \quad (18)$$

where M is the effective mass of the main and perturbing shafts (with $M = I_1 / \ell_4^2 + I_2 / \ell_1^2$), I_1 and I_2 are the moments of inertia of the main and perturbing shafts, ℓ_4 is the length of the main shaft and ℓ_1 is the length of the perturbing shaft, $U = (\ell_4 - \ell_2) \ell_5 m_p r / \ell_1 \ell_4$ is the perturbing excitation parameter, x and y are the horizontal and vertical deflections of the main shaft, respectively, as seen by the measuring probes. Other symbols are defined in Figure 10. If the excitation is harmonic then the solution has also the harmonic form $z = Z e^{i(\omega_p t + \gamma)}$. The equation (17) is solved to give:

$$\frac{Z}{U \omega_p^2} = \frac{1}{-(m + M)\omega_p^2 + (d_r - id_T)i\omega_p + K + K_r - i\omega_R K_T} \quad (19)$$

In principle one might determine the unknown bearing coefficients, m , d_r , d_T , K_r , K_T from a comparison of plots of Equation (19) with Figure 12, but examination of the dynamic stiffness $U \omega_p^2 / Z$ is much easier to interpret: In this case

$$\kappa = U \omega_p^2 / Z = -(m + M)\omega_p^2 + i(d_r - id_T)\omega_p + K + K_r - i\omega_R K_T \quad (20)$$

From this equation, we see that the relationship between the various coefficients and the direct and quadrature components of the dynamic stiffness are given by:

$$\kappa_D = K + K_r + d_T \omega_p - (m + M)\omega_p^2 \quad (21)$$

$$\kappa_Q = d_r \omega_p - \omega_R K_T \quad (22)$$

From which we see that the relationship between κ_D and ω_p is an offset parabola which may be converted to a straight-line relationship between and $(\omega_p')^2$ by the transformation:

$$\omega'_p = \omega_p - \frac{d_T}{2(M+m)} \quad (23)$$

Furthermore, the relationship between κ_Q and ω_p gives d_r , the slope, and $-K_T \omega_R$, the intercept. The measured values of Z and γ , plotted in Figure 12, give the measured direct and quadrature receptances κ_D and κ_Q by the simple relationships:

$$\kappa_D = U\omega_p^2 \cos\gamma / Z \quad (24)$$

$$\kappa_Q = -U\omega_p^2 \sin\gamma / Z \quad (25)$$

Figure 13 shows a typical plot of κ_D and κ_Q , calculated from equations (24) and (25), for several temperatures at $\omega_R = 200$ radians/second, versus the perturbation speed ω_p . Further plots of κ_D versus $(\omega'_p)^2$, according to equation (23), can be used to determine J_T and the parameters m and K_r . The graph of κ_Q versus ω_p gives d_r and K_T . For the known values of m_p , r and ℓ_1 through ℓ_5 , giving the excitation parameter U , all the needed bearing parameters have been determined. Further information is given in reference [9], for other main rotor speeds. The results indicate the strong influence of viscosity on all the bearing parameters. One exception, however, is the very important average oil speed ratio:

$$\lambda = K_T / d_r$$

which was found to be about 0.48 (nearly 1/2) over the range of viscosities and the type of bearing considered in the investigation. The dynamic stiffness approach, in this case, provided a very simple and effective means of obtaining subsystem (bearing) parameters.

4. SUMMARY AND CONCLUSIONS

In the two problems examined, it has been shown (a) that the transfer dynamic stiffness, being the inverse of the transfer receptance, can be used to evaluate the parameters of real and complex modal expansions of structural response behavior, (b) that the elements of the dynamic stiffness matrix, being the inverse of the receptance matrix, possess simple stiffness, damping and inertia characteristics which may be used to create a discrete model of the structure for use in further analysis and for structural modification purposes, (c) that a structure with well distributed damping possesses more nearly real modes than a structure with localized damping, for which complex normal modes are needed to obtain an adequate model, (d) that the accuracy of recovery of the mass, stiffness and damping terms in the dynamic stiffness matrix depends strongly on the accuracy of the initial receptance data, which is a particularly important matter when experimental data is being evaluated, and that the greatest sensitivity to error lies in the damping terms.

ACKNOWLEDGMENTS

The support and encouragement of the research work on dynamic stiffness applied to rotor-system dynamic behavior by D. Bently, President, Bently Nevada Corporation, is gratefully acknowledged. Thanks are especially due to R. Fields-Payne and R. Lemaster for typing the many versions of the manuscript.

NOMENCLATURE

D	Subscript denoting direct component
d_r, d_t	Radial and tangential bearing damping parameters
e	Exponential function
F_q	Harmonic force amplitude at point q
{F}	Column vector of force amplitudes
i	$\sqrt{-1}$

I_1, I_2	Moments of inertia of main and perturbing shafts, respectively, about x or y axis
K_r, K_t	Radial and tangential bearing stiffness parameters
K	Equivalent stiffness of additional springs ($K = 33100 \text{ N/m}$)
k_{pq}	Effective stiffness of element p,q of κ matrix
k_p	p th stiffness element of discrete model
ℓ_1	Length of perturbing shaft (0.241 m)
ℓ_2	Distance from center of bearing to probe (0.0159 m)
ℓ_3	Distance from bearing center to pulling force section (0.0508 m)
ℓ_4	Length of main shaft (0.298 m)
ℓ_5	Distance to position of perturbing force (0.195 m)
m_p	Perturbing unbalance mass (0.004 kg) p th discrete mass element
m	Radial bearing fluid inertia parameter
m_{pq}	Effective mass of element p,q of $[\kappa]$ matrix
M_n	n th modal mass (kg)
M	Effective mass of rotor shaft
Q	Subscript denoting quadrature component
r	Radius of controlled unbalance (0.0262 m)
U	Excitation parameter (unbalance)
W_p	Harmonic response amplitude at point p
$\{W\}$	Column vector of displacement amplitudes
x	Rotor displacement in x direction
y	Rotor displacement in y direction
z	Complex displacement ($x + i y$)
α_{pq}	Transfer receptance: p,q element of $[\alpha]$ matrix
$[\alpha]$	Receptance matrix
β_n	Damping parameter ($\beta_n = \eta_n \omega_n / 2 \omega$)
$\phi_n(p)$	n th modal function at point p
δ_{pq}	Kronecker Delta
$[\kappa]$	Dynamic stiffness matrix
κ_{pq}	Element p,q of $[\kappa]$ matrix
κ'_{pq}	Pseudo- dynamic stiffness ($= 1/\alpha_{pq}$)

μ_{np}	Complex mode parameter at point p for mode n
η_n	n th modal loss factor
η_{pq}	Effective loss factor of element p,q of $[\kappa]$ matrix
η_p	Loss factor of p th stiffness element of discrete model
ω	Frequency (radians/second)
ω_n	n th resonant frequency

REFERENCES

1. D.J. Ewins, "Why's and Wherefores of Modal Testing", SEE Journal, 18(3), 1979.
2. N. Miramand, J.F. Billand, F. Leleux and J.P. Kernevez, "Identification of Structural Modal Parameters by Dynamic Tests at a Single Point", Shock and Vibration Bulletin, 46(5), pp 197-212, 1976.
3. J.M. Leuridan, D.L. Brown, R.J. Allemang, "Direct System Parameter Identification of Mechanical Structures with Application to Modal Analysis", AIAA Paper 82-0767-CP, Proc. 23rd AIAA/ASME/ASCE/AHS Symposium, New Orleans, 1982.
4. A.L. Klosterman, "On the Experimental Determination and Use of Modal Representations of Dynamic Characteristics", PhD. Thesis, University of Cincinnati, 1971.
5. H.G.H. Goyder, "Methods of Application of Structural Modelling from Measured Structural Frequency Response Data", J. Sound & Vib., 68(2), pp 209-230, 1980.
6. R.J. Allemang, "Experimental Modal Analysis Bibliography", Proc. 1st Int. Modal Analysis Conf., Orlando FL, pp 714-726 (Sponsored by Union College, Schenectady, NY) 1982.
7. G.J. O'Hara, "Mechanical Impedance and Mobility Concepts", J. Acoust. Soc America, 41(5), pp 1180-1184, 1967.
8. D.I.G Jones and A. Muszyńska, "On the modal identification of Multiple Degree of Freedom Systems from Experimental Data", Shock and Vibration Bulletin, 53(2), pp 191-110, 1983.
9. D.E. Bently and A. Muszyńska, "Oil Whirl Identification by Perturbation Test", Advances in Computer-Aided Bearing Design, Proc. ASME/ASLE Lubrication Conference, Washington DC, Oct 1983.
10. D.E. Bently and A. Muszyńska, "Stability Evaluation of Rotor/Bearing System by Perturbation Test" Rotordynamic Instability Problems in High Performance Turbomachinery, NASA CP2250, Proc. Workshop at Texas A&M University, College Station TX 1982.

11. D.E. Bently and A. Muszyńska, "Perturbation Tests of Bearing/Seal for Evaluation of Dynamic Coefficients," Rotor Dynamical Instability, AMD - Vol 55, Applied Mechanics, Proc Bioengineering and Fluids Engineering Conference, Houston TX, June 1983.

TABLE 1
Identified Parameters for
Two Degree of Freedom System

<u>MODAL PARAMETERS</u>	<u>From Figs 4-6(a)</u> <u>CASE (a)</u>	<u>From Figs 4-6(b)</u> <u>Case (b)</u>	<u>From Eq 14, Case (a)</u> <u>Theory</u>
$m_1 - \text{Kg}$	0.238	0.238	0.254
$m_2 - \text{Kg}$	0.910	0.910	0.946
$f_1 - \text{Hz}$	402	402	401
$f_2 - \text{Hz}$	770	770	774
$\eta_1 - \text{n.d.}$	0.1	0.0329	0.1
$\eta_2 - \text{n.d.}$	0.1	0.0300	0.1
$\phi_1(1) - \text{n.d.}$	1.000	1.000	1.000
$\phi_1(2) - \text{n.d.}$	0.701	0.701	0.732
$\phi_2(1) - \text{n.d.}$	1.000	1.000	1.000
$\phi_2(2) - \text{n.d.}$	- 2.608	- 2.608	- 2.732
$\mu_{11} - \text{n.d.}$	0	+ 0.015	0
$\mu_{12} - \text{n.d.}$	0	- 0.045	0
$\mu_{21} - \text{n.d.}$	0	- 0.025	0
$\mu_{22} - \text{n.d.}$	0	+ 0.015	0

TABLE 2
Re-Identified Discrete Parameters of
Two-Degree of Freedom System

Model	Case Parameter	(a)		(b)		
		Direct	Real Modes	Direct	Real Modes	Complex Modes
Modal	m_{11}	0.200	0.189	0.196	0.189	0.189
	m_{12}	0	0	0	0.002	0
	m_{22}	0.100	0.105	0.099	0.100	0.106
	k_{11}	2.000E6	1.899E6	2.013E6	1.899E6	1.915E6
	$-k_{12}$	1.000E6	0.973E6	1.000E6	9.730E5	9.862E5
	k_{22}	2.000E6	2.084E6	2.003E6	1.891E6	2.113E6
	η_{11}	0.100	0.0999	0	0.0317	0.008
	η_{12}	0.100	0.103	0	0.0298	0.012
	η_{22}	0.100	0.100	0.0499	0.033	0.0436
Discrete	m_1	0.200	0.189	0.196	0.189	0.189
	m_2	0.100	0.105	0.099	0.100	0.106
	k_1	1.000E6	9.267E5	1.013E6	9.260E5	9.289E5
	k_2	1.000E6	9.726E5	1.000E6	9.730E5	9.826E5
	k_3	1.000E6	1.111E6	1.003E6	9.176E5	1.127E6
	η_1	0.100	0.0967	0	0.034	0.004
	η_2	0.100	0.103	0	0.030	0.012
	η_3	0.100	0.0973	0.100	0.037	0.072

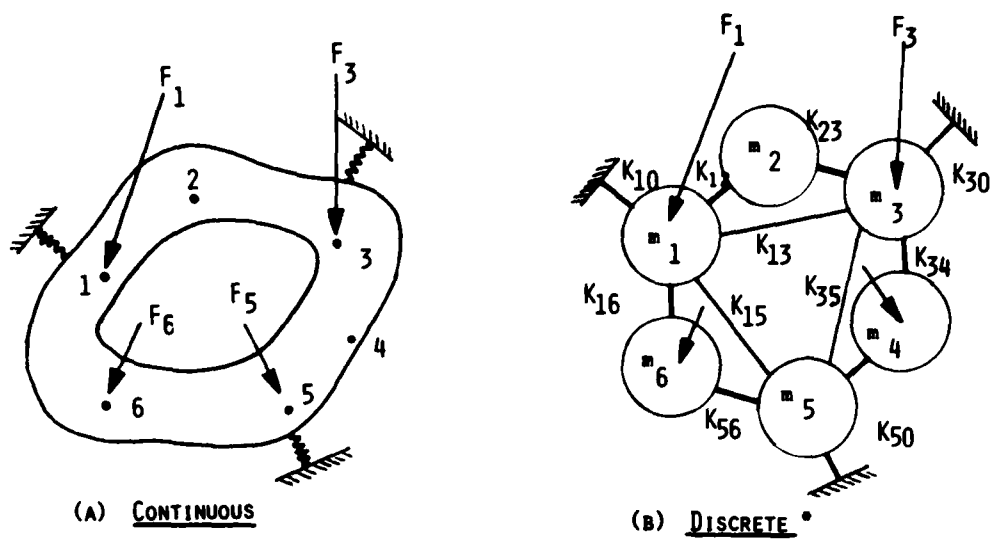


Figure 1. A structure and its corresponding discrete model
(* some stiffnesses omitted for clarity)

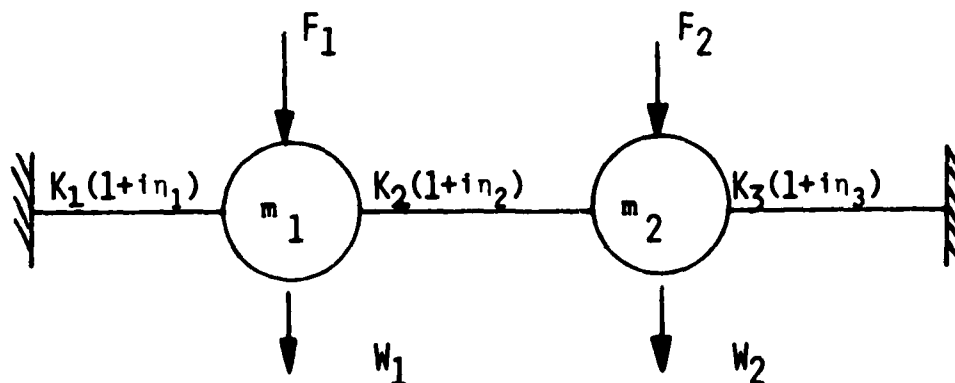


Figure 2. Two- degree of freedom system

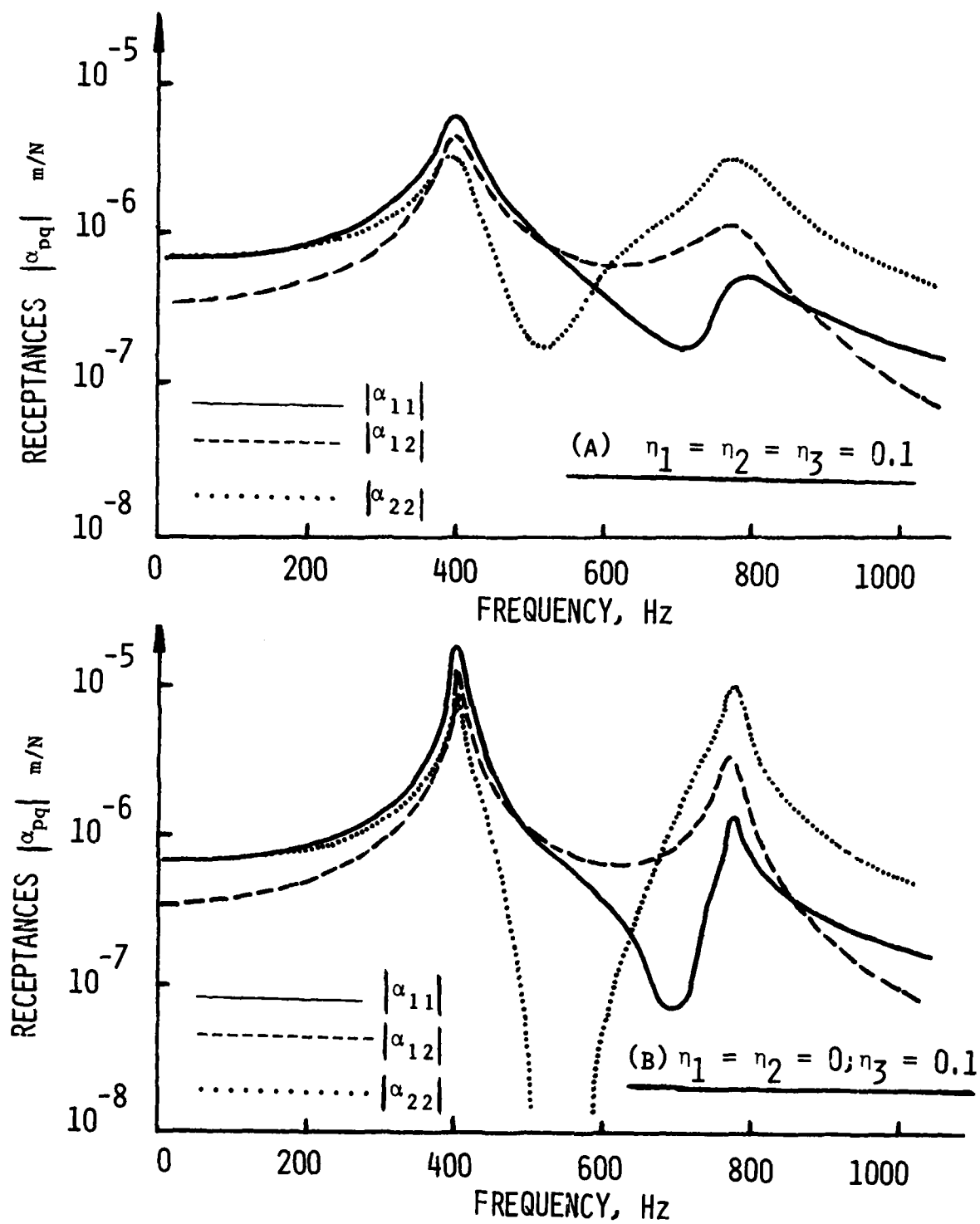


Figure 3. Typical receptance vs. frequency plots

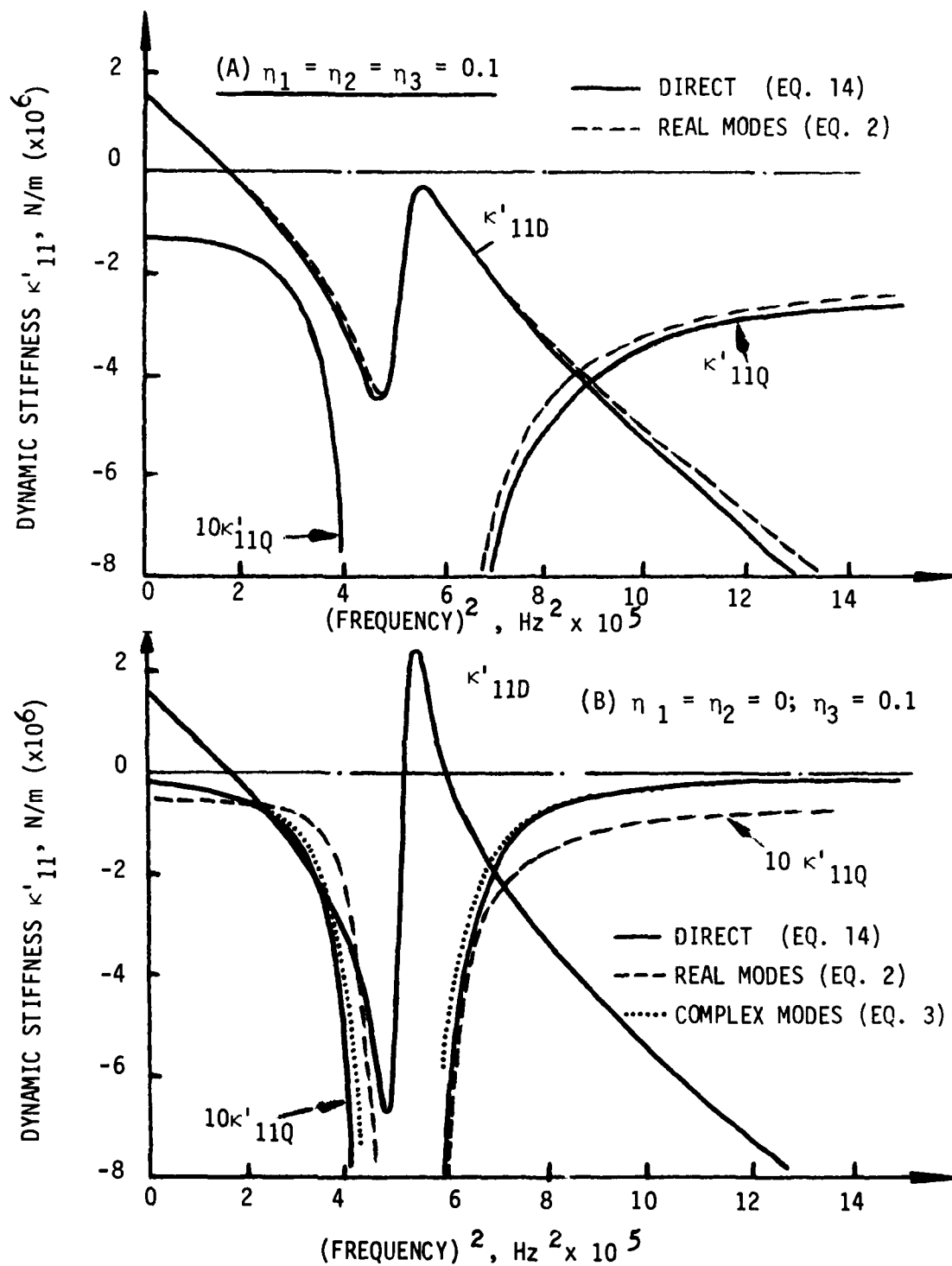


Figure 4. Dynamic stiffness κ'_{11} versus (frequency)²

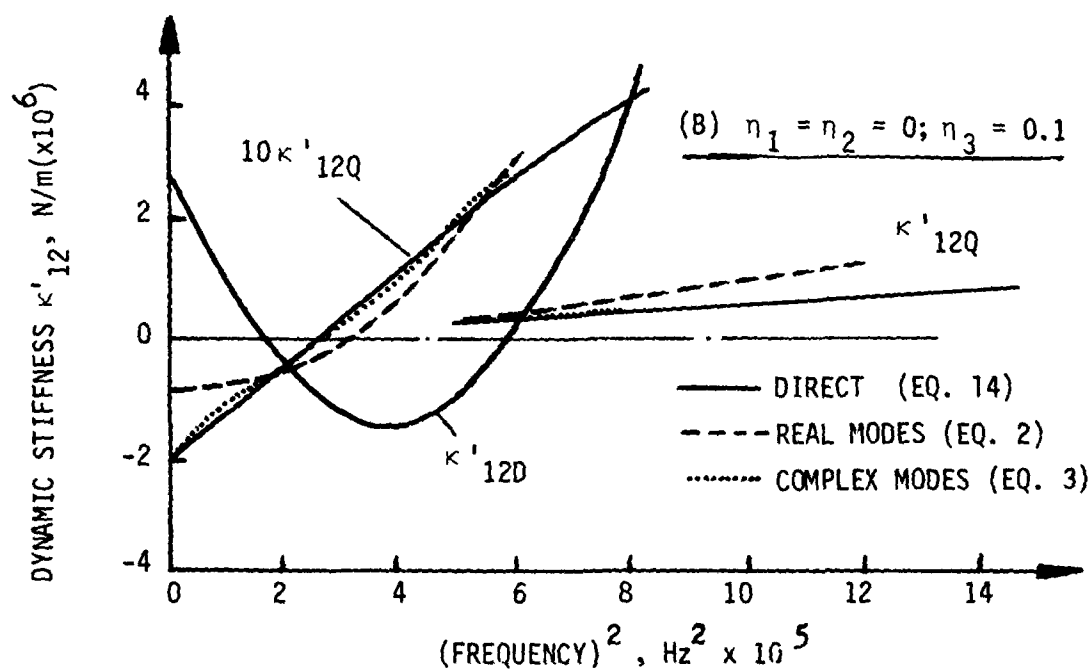
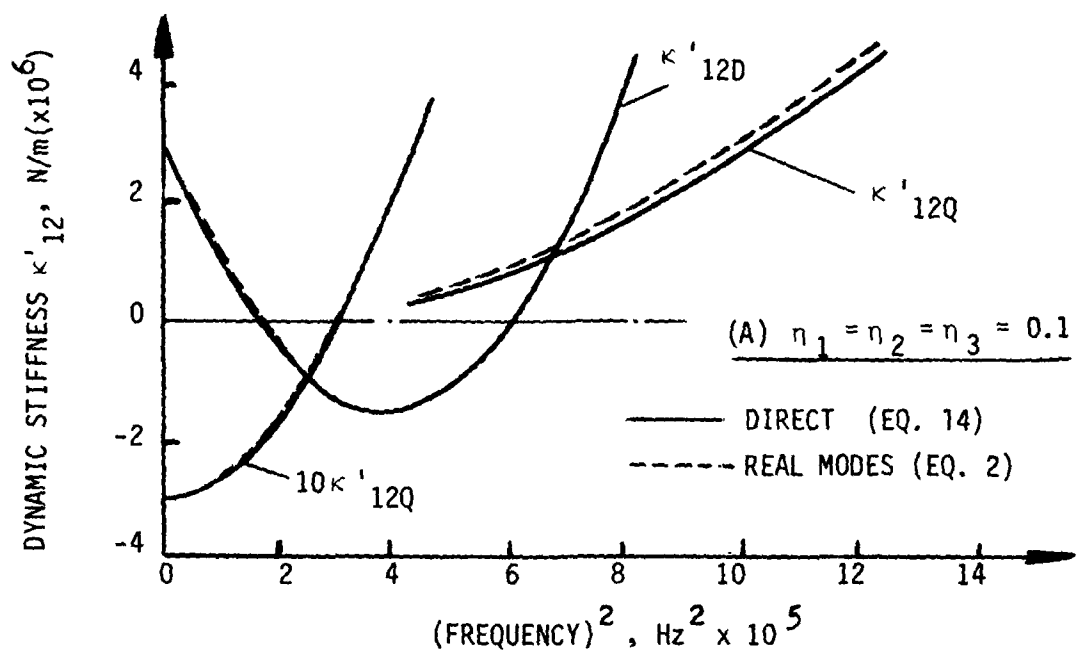


Figure 5. Dynamic stiffness κ'_{12} versus $(\text{frequency})^2$

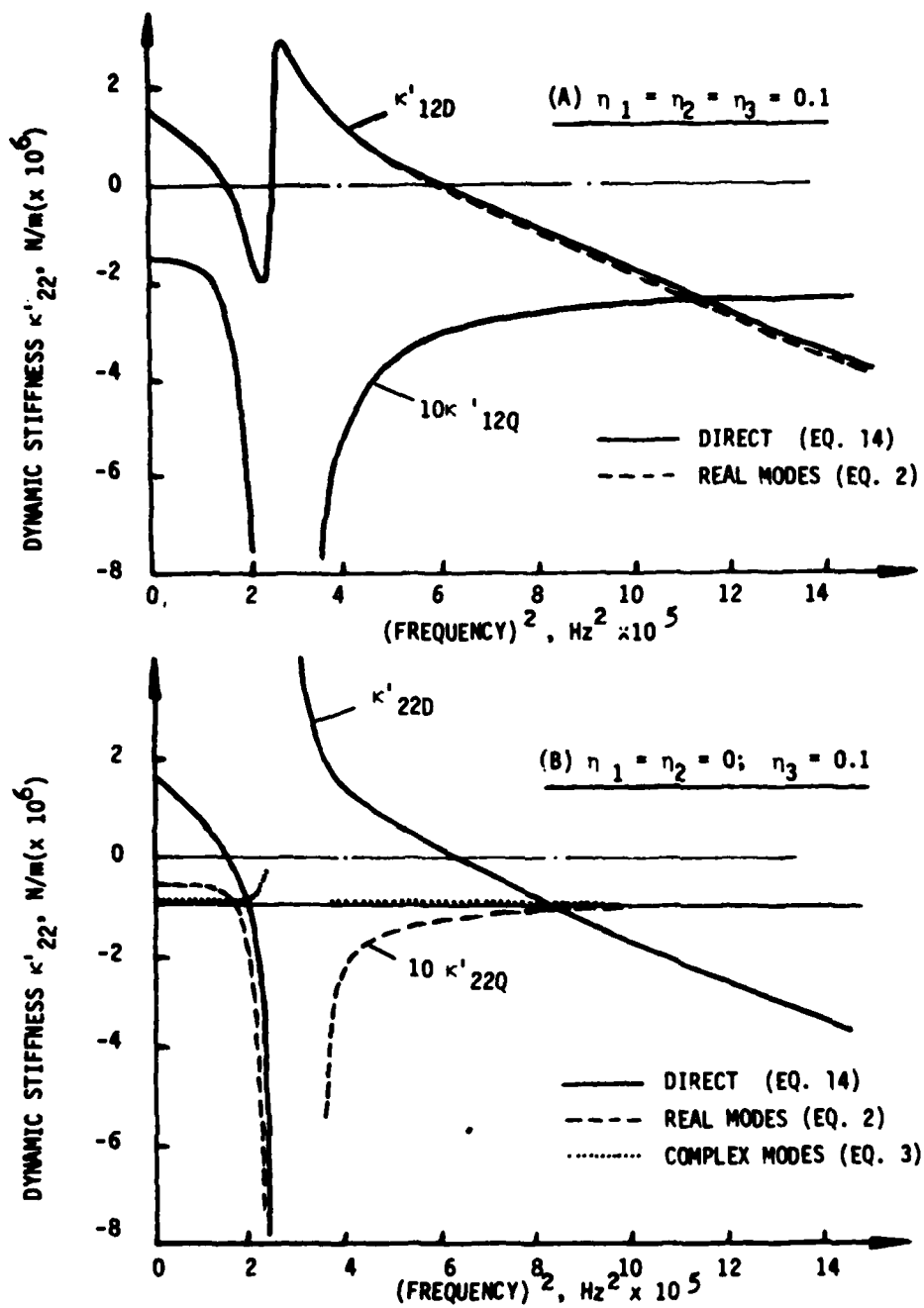


Figure 6. Dynamic Stiffness κ'_{22} versus $(\text{frequency})^2$

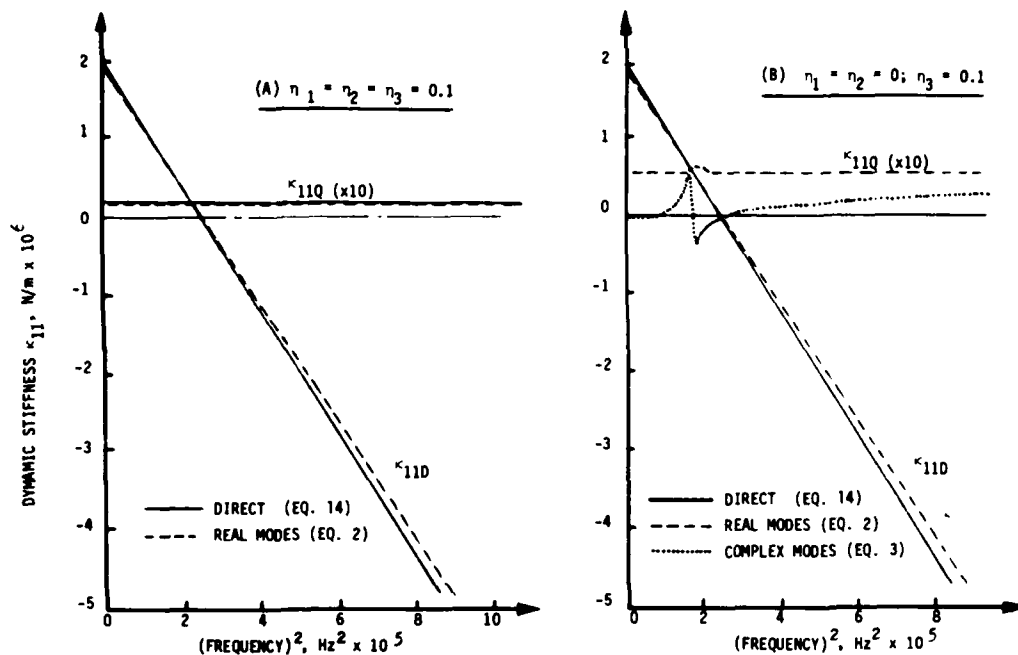


Figure 7. Dynamic stiffness κ_{11} versus $(\text{frequency})^2$

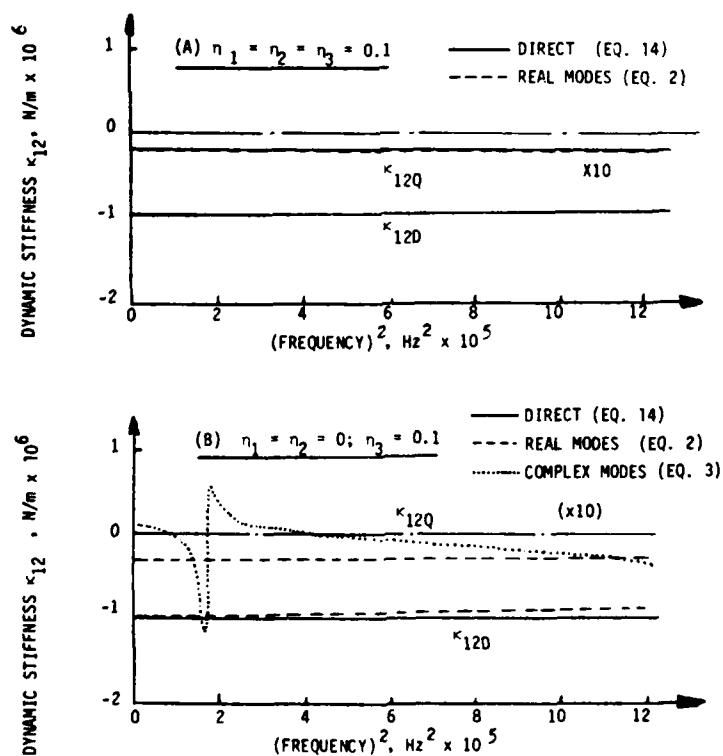


Figure 8. Dynamic stiffness κ_{12} versus $(\text{frequency})^2$

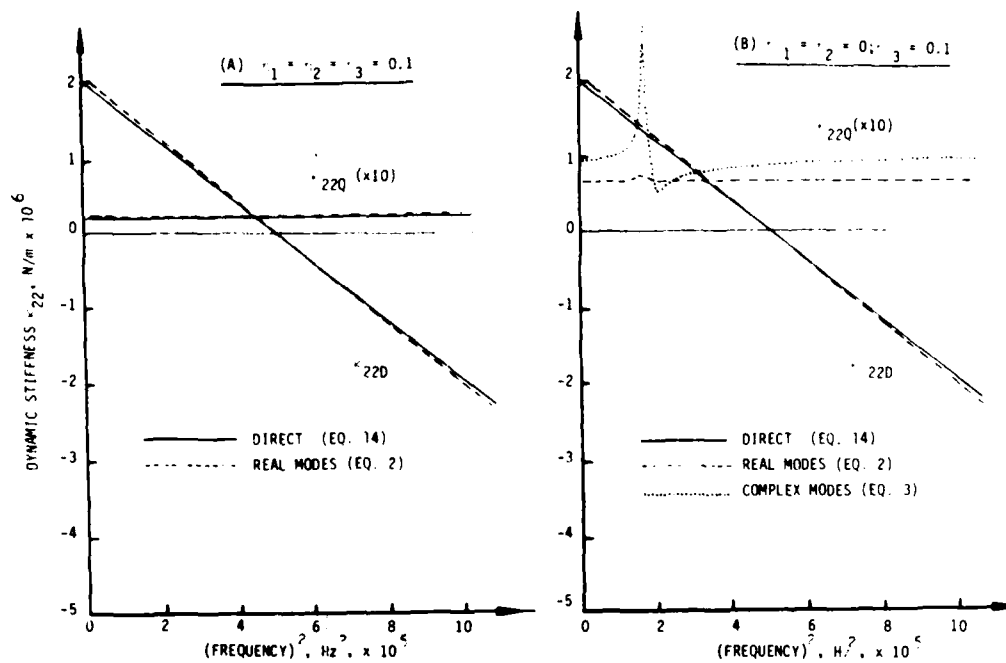


Figure 9. Dynamic stiffness κ_{22} versus (frequency)²

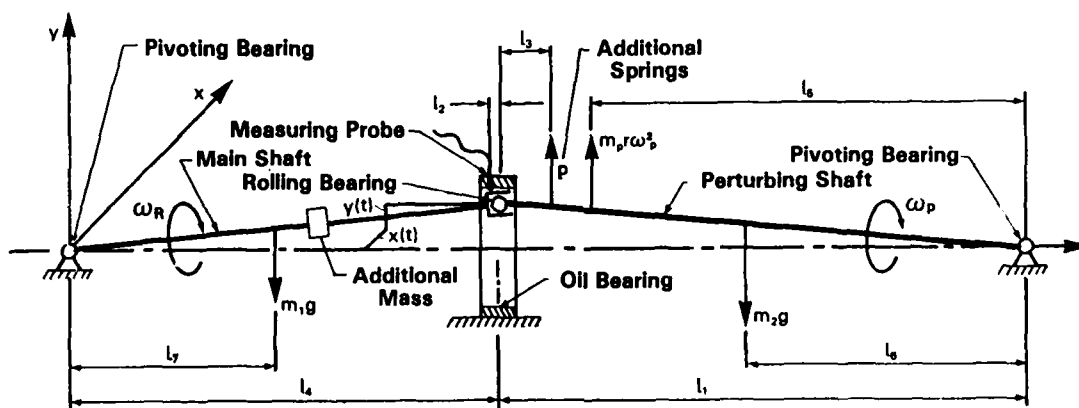


Figure 10. Rotor- bearing system

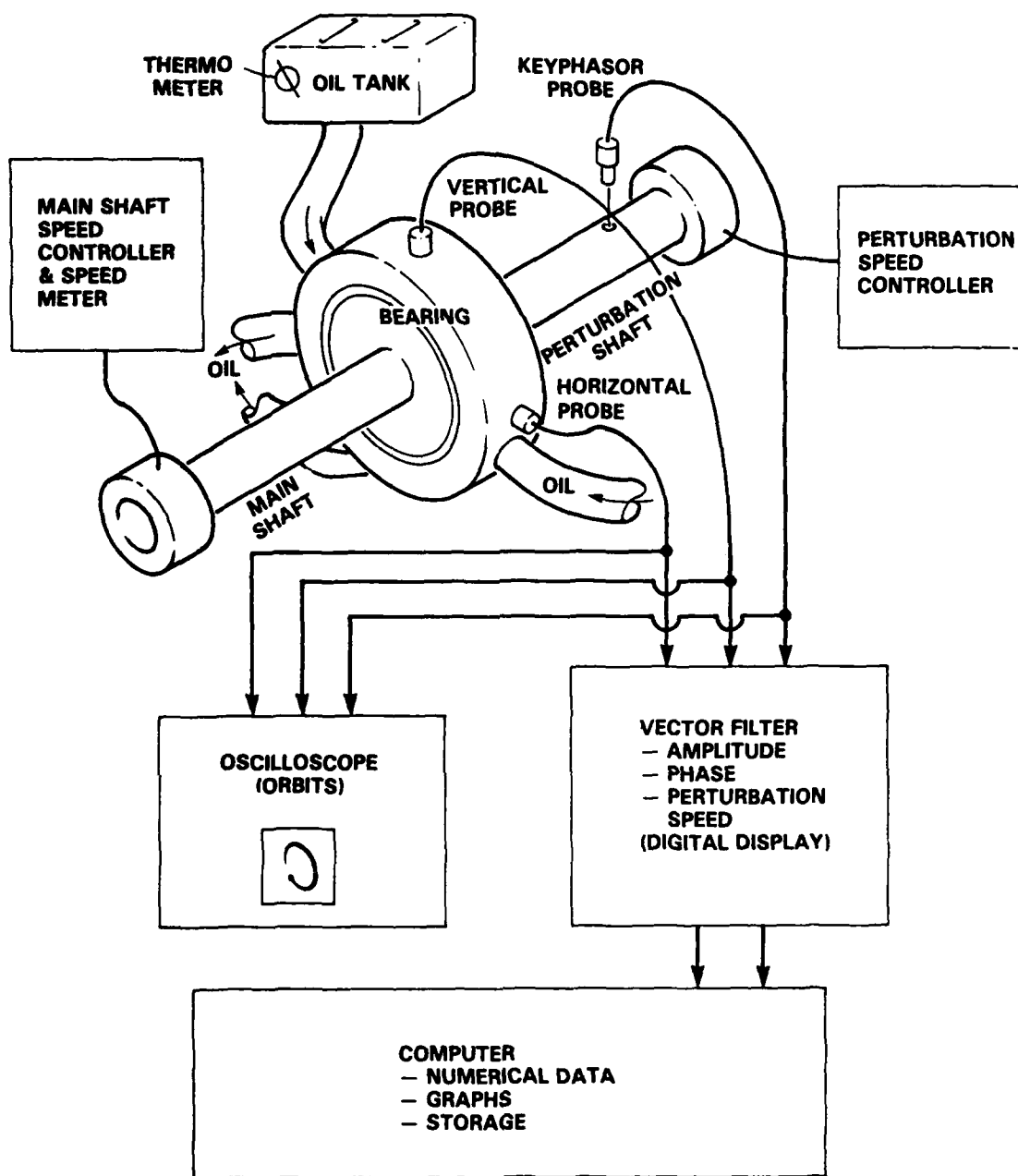


Figure 11. Test system

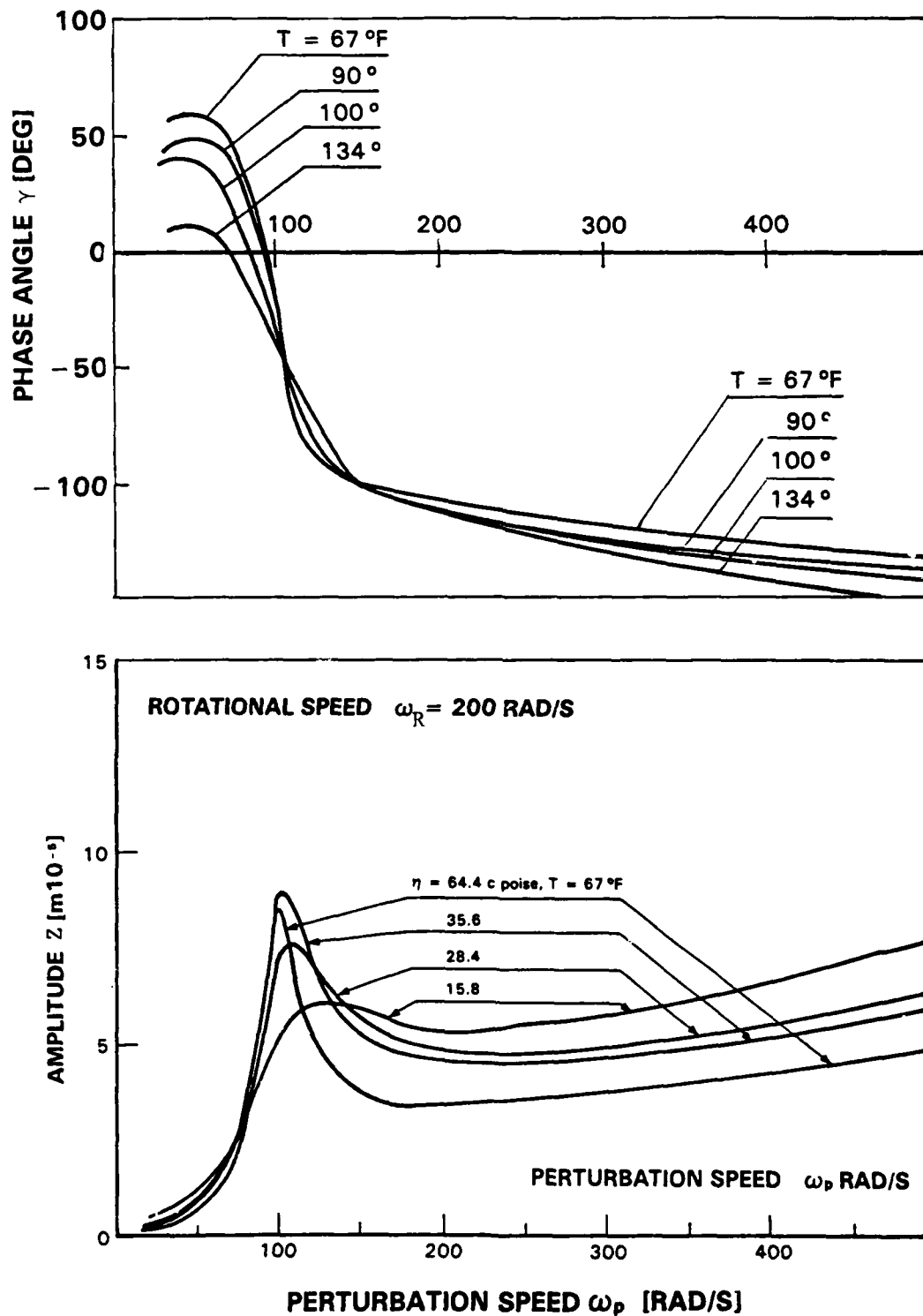


Figure 12. Amplitude and phase versus perturbation speed ω_p

NO-A152 547

VIBRATION DAMPING WORKSHOP PROCEEDINGS HELD AT LONG
BEACH CALIFORNIA ON 2.. (U) AIR FORCE WRIGHT
AERONAUTICAL LABS WRIGHT-PATTERSON AFB OH L ROGERS

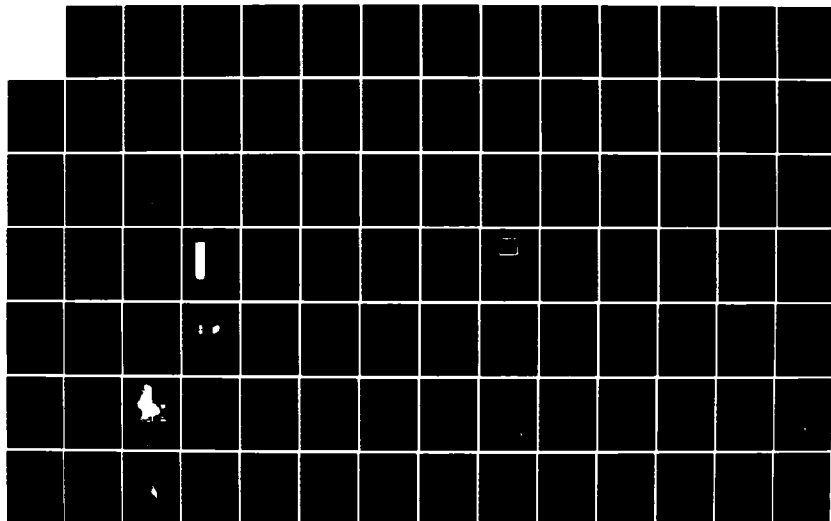
5/11

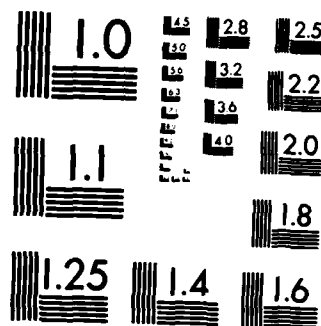
UNCLASSIFIED

11 NOV 84 AFWAL-TR-84-3064

F/G 20/11

NL





MICROCOPY RESOLUTION TEST CHART
NATIONAL BUREAU OF STANDARDS-1963-A

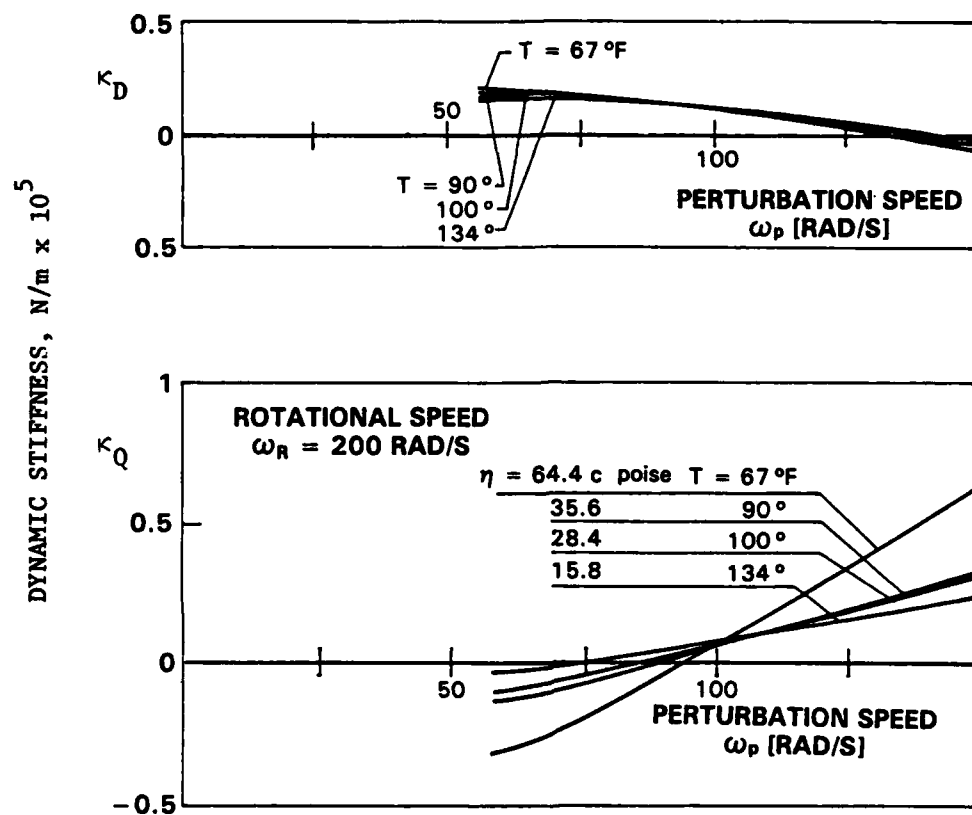


Figure 13. Dynamic stiffness κ vs. perturbation speed ω_p

A COMPARISON OF MEASURED SPACECRAFT MODAL DAMPING VALUES

**B. K. Wada and J. C. Chen
Jet Propulsion Laboratory
California Institute of Technology
Applied Mechanics Technology Section
Building 157/Room 507
4800 Oak Grove Drive
Pasadena, California 91109**

A COMPARISON OF MEASURED
SPACECRAFT MODAL DAMPING VALUES

B. K. WADA
J. C. CHEN

JET PROPULSION LABORATORY
CALIFORNIA INSTITUTE OF TECHNOLOGY
APPLIED MECHANICS TECHNOLOGY SECTION
BUILDING 157/ROOM 507
4800 OAK GROVE DRIVE
PASADENA, CA 91109

ABSTRACT

The presentation summarized the experiences at the Jet Propulsion Laboratory in the prediction and the measurement of modal damping values of spacecrafts for use in the determination of design loads. The initial recognition of the uncertainty in the prediction of damping and the direct dependence of damping on the design loads when subjected to slowly swept sinusoidal input resulted in an effort to use realistic transient forcing functions.

Experiences in the solution of complex eigenvalue response solutions resulting from modal synthesis of subsystems, each subsystem assigned modal damping values, were also discussed. Damping data on both the Voyager and the Galileo spacecrafts using up to 8 different types of techniques to analyze modal data were presented. The preliminary conclusions are that difficulty exists in estimating the "true" damping of a structure and the "measured damping values" are dependent on the analysis method of the data. A large quantity of damping data is available and further analysis and evaluation is warranted in order to help predict damping and establish the confidence in the measured damping values.

ACKNOWLEDGEMENT

The paper presents the results of one phase of research carried out at the Jet Propulsion Laboratory, California Institute of Technology, under Contract NAS7-100 sponsored by NASA.

REFERENCES

Modal Testing

Heer, E. and Trubert, M. R.: Analysis of Space Vehicle Structures Using the Transfer-Function Concept. Technical Report No. 32-1367, Jet Propulsion Laboratory, Pasadena, CA, April 1, 1969.

Gayman, W. H., Trubert, M. R., and Abbott, P. W.: Measurement of Structural Transfer Functions Significant to Flight Stability of the Surveyor Spacecraft. Technical Memorandum No. 33-389, Jet Propulsion Laboratory, Pasadena, CA, May 1, 1969.

Trubert, M. R.: A Practical Approach to Spacecraft Structural Dynamics Problems. Journal of Spacecraft and Rockets, Vol. 9, No. 11, November 1972, pp. 818-824.

Leppert, E. L., Wada, B. K., and Miyakawa, R.: Modal Test of the Viking Orbiter. The Shock and Vibration Bulletin, No. 44, Part 2, Naval Research Laboratory, Washington, DC, pp. 165-175; also published as JPL Technical Memorandum 33-688, July 15, 1974.

Fortenberry, J. and Brownlee, G.: Viking Mars Lander 1975 Dynamic Test Model/Orbiter Developmental Test Model Forced Vibration Test: Summary Report, Technical Memorandum 33-6589, Jet Propulsion Laboratory, Pasadena, CA, November 15, 1974.

Brownlee, G. R., Day, F. D., and Garba, J. A.: Analytical Prediction and Correlation for the Orbiter During the Viking Spacecraft Sinusoidal Vibration Test. The Shock and Vibration Bulletin, Bulletin 45, Part 3, Washington, DC, June 1975, pp. 37-57.

Garba, J. A., Wada, B. K., and Chen, J. C.: Experiences in Using Modal Synthesis within Project Requirements. The Shock and Vibration Bulletin, Bulletin 46, Part 5, August 1976. Also Technical Memorandum 33-729, Jet Propulsion Laboratory, Pasadena, CA, July 1, 1975.

Wada, B. K.: Modal Test: Measurement and Analysis Requirements. SAE Paper No. 751066, Los Angeles, CA, November 17-20, 1975.

Wada, B. K. and Garba, J. A.: Dynamic Analysis and Test Results of the Viking Orbiter. ASME 1975 Winter Annual Meeting, ASME Paper 75-WA/Aero 7, Houston, TX, November 30-December 4, 1975.

Leppert, E. L., Lee, S. H., Day, F. D., Chapman, C. P., and Wada, B. K.: Comparison of Modal Test Results: Multipoint Sine Versus-Single-Point Random. SAE Paper No. 760879, San Diego, CA, November 29-December 2, 1976.

Hanks, B., Ibrahim, S. R., Miserentino, R., Lee, S. and Wada, B. K.: Comparison of Modal Test Methods on the Voyager Payload. SAE Paper No. 781044, San Diego, CA, November 1978.

Wada, B. K., "Required Developments in Structural Dynamics", The Shock and Vibration Bulletin, Bulletin 52, Part 1 of 5, May 1982.

Chen, J. C. and Stroud, R. C., "Analysis Techniques for Support of Modal Testing", presented at 1st International Modal Analysis Conference, Orlando, FL, November 10, 1982.

Chen, J. C., "Planning the Galileo Spacecraft Modal Test", presented at Modal Analysis Seminar sponsored by the Institute of Environmental Sciences, Los Angeles, CA, March 17, 1983.

Chen, J. C., "Response of Large Space Structure with Stiffness Control", to be presented at 1983 AAS/AIAA Astrodynamics Conference at Lake Placid, NY, August 22-24, 1983.

Wada, B. K., and Freeland, R. E., "Technology Requirements for Large Flexible Space Structures", 34th International Astronautical Federation Meeting, Budapest, Hungary, October 9-15, 1983.

Wada, B. K., Garba, J. A., and Chen, J. C., "Modal Test and Analysis Correlation", Modal Testing and Model Refinement, AMD-Vol. 59, ASME Winter Annual Meeting, Boston, MA, November 14-18, 1983.

Chen, J. C., and Trubert, M. R., "Galileo Modal Test and Pre-Test Analysis", Proceedings of the 2nd International Modal Analysis Conference, Orlando, FL, 1984.

Trubert, M. R., "Galileo Modal Test/Multiple Sine Dwell", Proceedings of the 2nd International Modal Analysis Conference, Orlando, FL, 1984.

Stroud, R. C., Coppolino, R. N., Hunt, D. L., and Ibrahim, S. R., "Advanced Methods Used on the Galileo Spacecraft Modal Survey", Proceedings of the 2nd International Modal Analysis Conference, Orlando, FL, 1984.

Chen, J. C., "Comparison of Various Modal Analysis Test Results", Proceedings of the 2nd International Modal Analysis Conference, Orlando, FL, 1984.

Wada, B. K., and Chen, J. C., "Comparison of the Modal Damping Values Determined by Various Modal Test Techniques on the Galileo Spacecraft", presented at the Vibration Damping Workshop, Long Beach, CA, February 27-29, 1984.

Modal Test/Analysis Correlation

Ross, R. G.: Synthesis of Stiffness and Mass Matrices from Experimental Vibration Modes. SAE Paper 710787, Los Angeles, CA, September 1971.

Bamford, R. M., Wada, B. K., and Gayman, W. H.: Equivalent Mass System for Normal Modes. Technical Memorandum 33-380, Jet Propulsion Laboratory, Pasadena, CA, February 1971.

Wada, B. K., Bamford, R., and Garba, J. A.: Equivalent Spring Mass System: A Physical Interpretation. The Shock and Vibration Bulletin, Bulletin 42, Naval Research Laboratory, Washington, DC, January 1972, pp. 215-225.

Caughey, R. K.: Matrix Perturbation Techniques in Structural Dynamics. Technical Memorandum 33-652, Jet Propulsion Laboratory, Pasadena, CA, September 1, 1973.

Wada, B. K., Garba, J. A., and Chen, J. C.: Development and Correlation: Viking Orbiter Analytical Dynamic Model with Modal Test. The Shock and Vibration Bulletin, Bulletin 44, Part 2, Naval Research Laboratory, Washington, DC, pp. 125-164, also published as JPL Technical Memorandum 33-690, June 1, 1974.

Chen, J. C. and Garba, J. A.: Determination of Propellant Effective Mass Properties Using Modal Test Data. The Shock and Vibration Bulletin, Bulletin 45, Naval Research Laboratory, Washington, DC, 1975.

Chen, J. C. and Wada, B. K.: Matrix Perturbation for Structural Dynamic Analysis. AIAA Journal, Vol. 15, August 1977, pp. 1095-1100.

Garba, J. A. and Wada, B. K.: Application of Perturbation Methods to Improve Analytical Model Correlation with Test Data, SAE paper 770959, November 1977.

Chen, J. C., and Garba, J. A.: Analytical Model Improvement Using Modal Test Results, AIAA Journal, Vol. 18, No. 6, June 1980.

Chen, J. C., Garba, J. A., and Kuo, C. P.: "Direct Structural Parameter Identification by Modal Test Results", AIAA Paper No. 83-0812, to be presented at the 24th AIAA/ASME/ASCE/AHS Structures, Structural Dynamics and Materials Conference, May 2-4, 1983, Lake Tahoe, NV.

Criteria For Correlation

Chen, J. C. and Wada, B. K.: Criteria for Analysis-Test Correlation of Structural Dynamic Systems. Journal of Applied Mechanics, June 1975.

Chen, J. C., "Analytical Model Accuracy Requirements for Structural Dynamic Systems", AIAA Paper No. 82-0734, presented at the AIAA/ASME/ASCE/AHS 23rd Structures, Structural Dynamics and Materials Conference at New Orleans, LA, May 10-12, 1982.

General Dynamics/Loads

Wada, B. K.: Viking Orbiter - Dynamics Overview. The Shock and Vibration Bulletin, Bulletin 44, Part 2, Naval Research Laboratory, Washington, DC, February 12, 1962.

Hurty, W. C.: Dynamic Analysis of Structural System by Component Mode Synthesis. Technical Report No. 32-530, Jet Propulsion Laboratory, Pasadena, CA, January 15, 1964.

Trubert, M. R.: A Fourier Transform Technique for the Prediction of Torsional Transients for a Spacecraft from Flight Data of Another Spacecraft Using the Same Booster. Technical Memorandum 33-350, Jet Propulsion Laboratory, Pasadena, CA, October 15, 1976.

Garba, J. A., Wada, B. K., Bamford, R. and Trubert, M. R.: Evaluation of a Cost-Effective Loads Approach. Journal of Spacecraft and Rockets, Vol. 13, No. 11. November 1976, pp. 675-683.

Chen, J. C., Wada, B. K., and Garba, J. A.: Launch Vehicle Payload Interface Response. Journal of Spacecraft and Rockets, Vol. 15, No. 1, January-February 1978, pp. 7-11.

Chen, J. C., Garba, J. A., and Wada, B. K.: Estimation of Payloads Loads Using Rigid-Body Interface Accelerations. Journal of Spacecraft and Rockets, Vol. 16, No. 2., March-April 1979, pp. 74-80.

Wada, B. K.: Design of Space Payloads for Transient Environments. Paper presented at the ASME 1979 Winter Annual Meeting, December 2-7, 1979, New York, NY.

Chen, J. C., Zagzebski, K. P., and Garba, J. A.: Recovered Transient Load Analysis for Payload Structural Systems. AIAA/ASME/ASCE/AMS - 21st Structures, Structural Dynamics, and Materials Conference, Seattle WA, May 12-14, 1980.

Trubert, M. R., and Salama, M.: A Generalized Shock Spectra Method for Spacecraft Loads Analysis. JPL Publication 79-2, Jet Propulsion Laboratory, Pasadena, CA, March 15, 1979; to be published in AIAA Journal, Vol. 18 (September 1980) and in the Journal of Space and Rockets.

Wada, B. K.: Design of Space Payloads for Transient Environments. Survival of Mechanical Systems in Transient Environments, AMD-Vol. 36, ASME.

Chen, J. C., Garba, J. A., Salama, M., and Trubert, M. R.: A Generalized Shock Spectra Method for Spacecraft Loads Analysis. JPL Publication 79-2, Jet Propulsion Laboratory, Pasadena, CA, March 15, 1979; to be published in AIAA Journal, Vol. 18 (September 1980) and in the Journal of Space and Rockets.

Wada, B. K.: Design of Space Payloads for Transient Environments. Survival of Mechanical Systems in Transient Environments, AMD-Vol. 36, ASME.

Chen, J. C., Garba, J. A., Salama, M., and Trubert, M. R.: A Survey of Load Methodologies for Shuttle Orbiter Payloads. JPL Publication 80-37.

Inverse Solution

Trubert, M. R.: Use of Ranger Flight Data in the Synthesis of a Torsional Acceleration Transient for Surveyor Vibration Qualification Testing. Technical Memorandum 33-237, Jet Propulsion Laboratory, Pasadena, CA, April 19, 1966.

Sperling, F. and Garba, J. A.: A Treatise on the Surveyor Lunar Landing Dynamics and an Evaluation of Pertinent Telemetry Data Returned by Surveyor I. Technical Report 32-1035, Jet Propulsion Laboratory, Pasadena, CA, August 15, 1967.

Trubert, M. R.: A Fourier Transform Technique for the Prediction of Torsional Transients for a Spacecraft from Flight Data of Another Spacecraft Using the Same Booster. Technical Memorandum 33-350, Jet Propulsion Laboratory, Pasadena, CA, October 15, 1967.

Trubert, M. R., Chisholm, J. R., and Gayman, W. H.: Use of Centaur/Spacecraft Flight Data in the Synthesis of Forcing Functions at Centaur Main Engine Cutoff During Boost of Mariner 1969, OAO-II, and ATS Spacecraft: Analysis, Evaluation, and Computer Plots. Technical Memorandum 33-487, Volumes I and II, Jet Propulsion Laboratory, Pasadena, CA, June 21, 1971.

Day, F. D. and Wada, B. K.: Unique Flight Instrumentation/Data Reduction Techniques Employed on the Viking Dynamic Simulator. The Shock and Vibration Bulletin, Bulletin 45, Part 3, Naval Research Laboratory, Washington, DC, 1975, pp. 25-35.

Day, F. D. and Wada, B. K.: Strain Gaged Struts and Data Reduction Techniques to Maximize Quality Data from Spacecraft Flight Measurements. 21st International Instrumentation Procedures, Philadelphia, PA 1975.

STRUCTURAL DAMPING OF SHUTTLE ORBITER AND ASCENT VEHICLES

D. L. Jensen, M. S., P.E.
Member Technical Staff
Rockwell International
Downey, California 90241

STRUCTURAL DAMPING OF SHUTTLE ORBITER AND ASCENT VEHICLES

D. L. Jensen, M.S., P.E.
Member Technical Staff
Rockwell International

Abstract

Experimental structural mode damping factor data are presented for an actual full size vehicle structure. These data were obtained from vibration test programs conducted during development of the shuttle orbiter vehicle. Results show average values of structural damping factor range from 0.017 to 0.032. Theoretical analysis indicates a primary source of energy dissipation due to air mass displacement is directly dependent on amplitude of motion. An analysis of frictional energy loss develops a relation between viscous damping factor and coulomb friction. The theoretical and analytical development provides a basis for understanding and interpreting the test results.

Nomenclature

C = Viscous damping factor, lb/ft/sec.
 C_F = Aerodynamic force coefficient, N.D.
F = Force, lbs.
K = Displacement force factor, lb/ft.
M = Mass, Slugs
N = Normal Force, lbs.
S = Surface area, square ft.
t = Time, sec.
Q = Generalized forcing function, lbs.
X = Amplitude, ft or in.
Y = Displacement, Ft or In.

 δ = Logarithmic decrement, N.D.
 ζ = Damping factor, N.D.
 ϵ = Mode displacement function, ft or in.
 ω = Frequency, rad/sec
 ρ = Air density, slugs/ft³
 ϕ = Mode shape factor, N.D.
 μ = Coefficient of friction, N.D.

Subscripts

K = Finite element
j = Mode number
D = Dissipation
n = Element or cycle number
N = Normal
V = Vertical
O = Initial value

Introduction

Valuable experimental damping factor data were obtained from the Mated Vehicle Ground Vibration Tests conducted in June and November 1978 and February 1979. The data are presented herein versus frequency of occurrence and vehicle mass. It should be kept in mind these values include aerodynamic effects (air damping) as well as friction and internal structure energy losses. Therefore, they are not directly comparable with values normally used for flight control system synthesis and design since they are intended to represent only the latter effects. The damping factor values obtained for various modes of flexible vibration motion as measured during vibration testing at discrete frequencies from around 12 rad/sec to beyond 90 rad/sec.

Theoretical Considerations

The differential equation governing the vibratory motion of a single structural mode of motion is given below along with standard definition of the mode frequency and damping factor

STRUCTURAL DAMPING

GIVEN STRUCTURAL MODE DYNAMICS EQUATION

$$m\ddot{\epsilon}_i + C_i\dot{\epsilon}_i + K_i\epsilon_i = Q(t)$$

AND DEFINING

$$\omega_i^2 = K_i/m, 2\zeta_i\omega_i = C_i/m$$

THEN

$$\zeta_i = C_i/2m\omega_i = C/2\sqrt{K_i m}$$

There are three modes of energy dissipation which enter into the damping of the flexible structure vibratory motion. These are:

- . Air Mass Displacement ($\dot{\zeta}_A$)
- . Friction ($\dot{\zeta}_F$)
- . Inelastic Deformation (Fatigue) ($\dot{\zeta}_D$)

The damping factor is a composite of all three effects, i.e.,

$$\zeta = \zeta_A + \zeta_F + \zeta_D$$

The internal energy dissipation and friction would manifest themselves as heat given off from the structure. Since inelastic deformation is very small (nearly infinitesimal) it may be considered as included in the frictional energy losses, i.e.,

$$\zeta_F (1 + \epsilon) = \zeta_F + \zeta_D$$

where ϵ is an arbitrarily small amount to account for, losses due to infinitesimal inelastic deformation within the structure.

The remaining sources of damping (air mass displacement and friction) can then be developed or characterized as follows:

AIR RESISTANCE TO FORCED BENDING VIBRATION

BENDING MODE DIFFERENTIAL EQUATION IS

$$m\ddot{\epsilon}_i + C\dot{\epsilon}_i + K\epsilon_i = F_v(t)$$

BY DEFINITION

$$C_i/m = 2\zeta_i\omega_i$$

THEREFORE,

$$\zeta_i = C_i/2m\omega_i$$

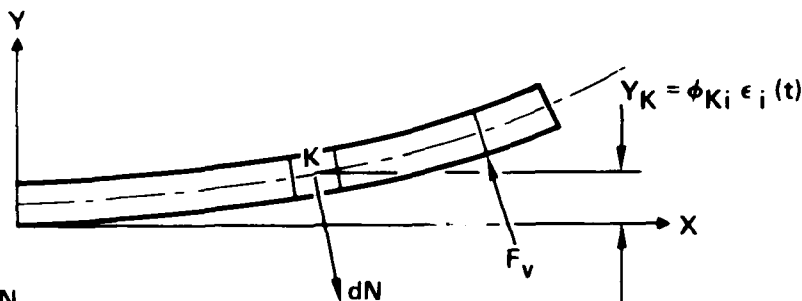
IT CAN BE SHOWN

$$C_i \approx \sum_{K=1}^n 2C_{NK} \rho \phi_{Ki}^2 \epsilon_{oi} \omega_i S_K / \pi$$

SUBSTITUTING

$$\zeta_i = (\rho \epsilon_{oi} / \pi m) \sum_{K=1}^n C_{NK} \phi_{Ki}^2 S_K$$

EQUALS AMPLITUDE DEPENDENT DAMPING FACTOR



The amplitude dependence of the air mass displacement damping factor is an important factor in understanding and interpreting the test results which are presented and discussed later. Turning to the friction dependent damping factor, a relationship between viscous damping factor and coulomb type friction can be established as indicated below.

STRUCTURAL DAMPING — ENERGY LOSS CAUSED BY COULOMB FRICTION

THE EQUIVALENT VISCOUS FRICTION THAT
DISSIPATES THE SAME AMOUNT OF ENERGY
PER CYCLE AS COULOMB FRICTION IS

$$C_i = 4F_D / \pi \epsilon_i \omega_i$$

WHERE F_D IS DISSIPATION FORCE TO OVERCOME
FRICTION. SUBSTITUTING

$$\zeta_i = 2F_D / \pi \epsilon_i K_i$$

THE AVERAGE DISSIPATION FORCE IS A PORTION
OF AVERAGE DISPLACEMENT FORCE

$$\bar{F}_D = \mu K_i \epsilon_i / 2$$

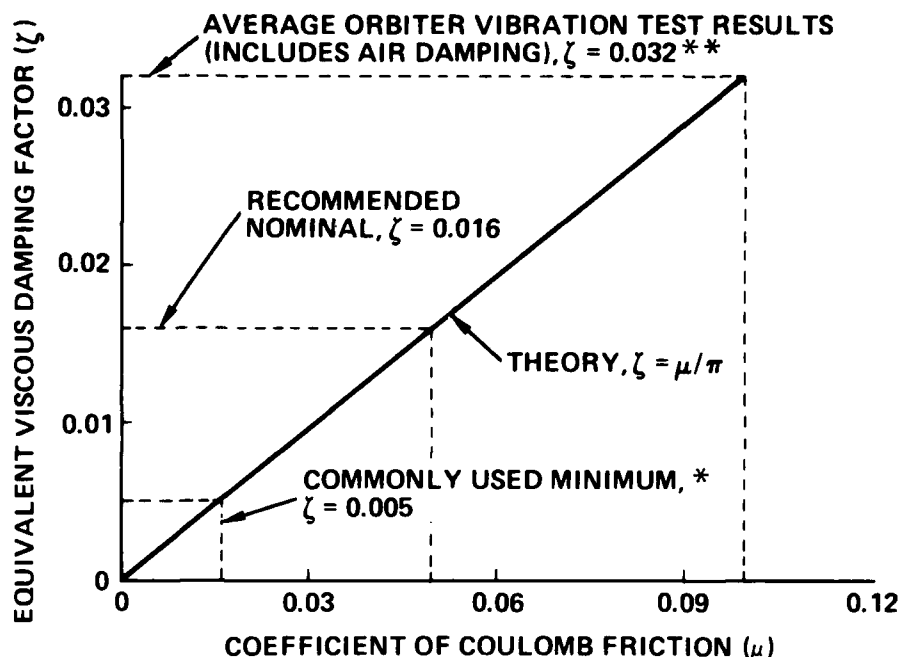
WHERE μ IS COEFFICIENT OF FRICTION. THEREFORE,

$$\boxed{\zeta_i = \mu / \pi}$$

This fundamental relationship is plotted in Figure 1 which follows.

Figure 1

STRUCTURAL MODE DAMPING VARIATION WITH FRICTION



* INTERPRETED TO REPRESENT A MEAN VALUE MINUS THREE STANDARD DEVIATIONS: $\zeta (\text{MINIMUM}) = \bar{\zeta} - 3\sigma_{\zeta}$

** BASED ON DATA IN VERIFICATION ANALYSIS REPORT OF OV-101 HGVT, ROCKWELL INTERNATIONAL, SD 76-SH-0228 (JAN. 1977).

The preceding development provides a theoretical basis which could be used to estimate the amount of damping present for a structure deployed in the vacuum of space from test data obtained within the earth's atmosphere.

$$\zeta_F (1 + \epsilon) = \zeta (\text{ATMOSPHERIC TEST}) - \zeta_A (\text{CALCULATED})$$

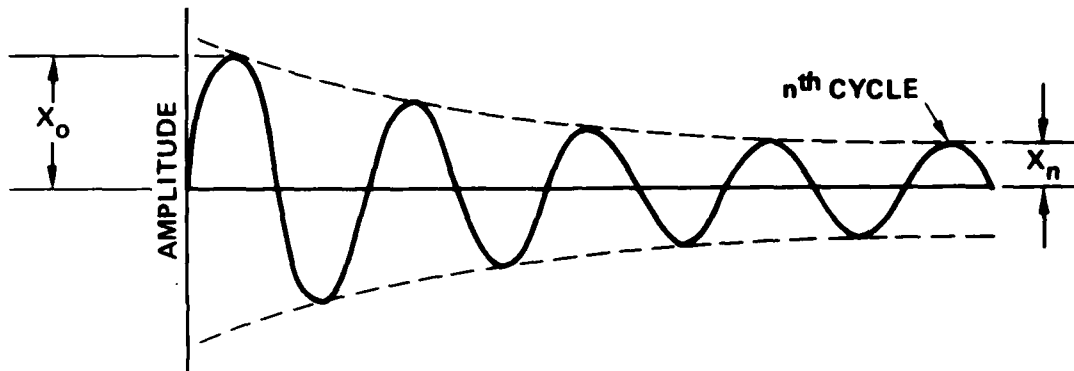
Also, since the air damping factor is shown to be amplitude dependent, it is a significant element in interpreting ground based test results. Ground based test results presented in this report were obtained as outlined by the following procedure.

Procedure

The procedure was to excite modes at particular discrete frequencies and record the output from various accelerometers via the shuttle Modal Test and Analysis System. This automated data reduction system was programmed to compute subsidence, logarithmic decrement, and damping factors "on-line" from the recorded test data. Figure 2 shows the familiar definitions and basic calculations for measuring and computing the various factors involved.

Figure 2

ESTIMATION OF STRUCTURAL DAMPING FACTOR



$$\text{LOGARITHMIC DECREMENT: } \delta = (1/n) \ln (X_0/X_n)$$

$$\text{DAMPING FACTOR: } \zeta = \delta / (\delta^2 + 4\pi^2)^{1/2}$$

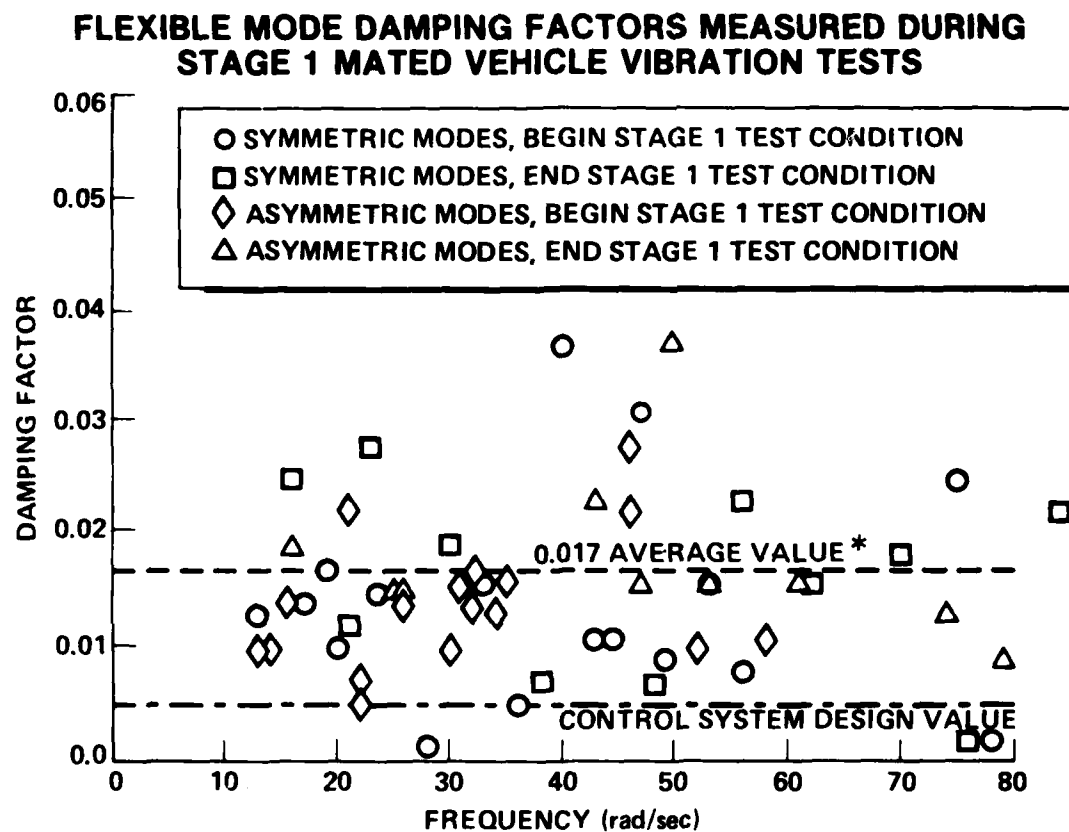
Tests were performed on three vehicle configurations. These were:

- A. Stage one shuttle ascent vehicle (orbiter, external tank and two solid propellant booster rockets).
- B. Stage two shuttle ascent vehicle (orbiter and external tank).
- C. The orbiter alone.

Results

Results from the stage one tests are shown in Figure 3.

Figure 3



* INCLUDES DATA NOT SHOWN BEYOND 80 rad/sec

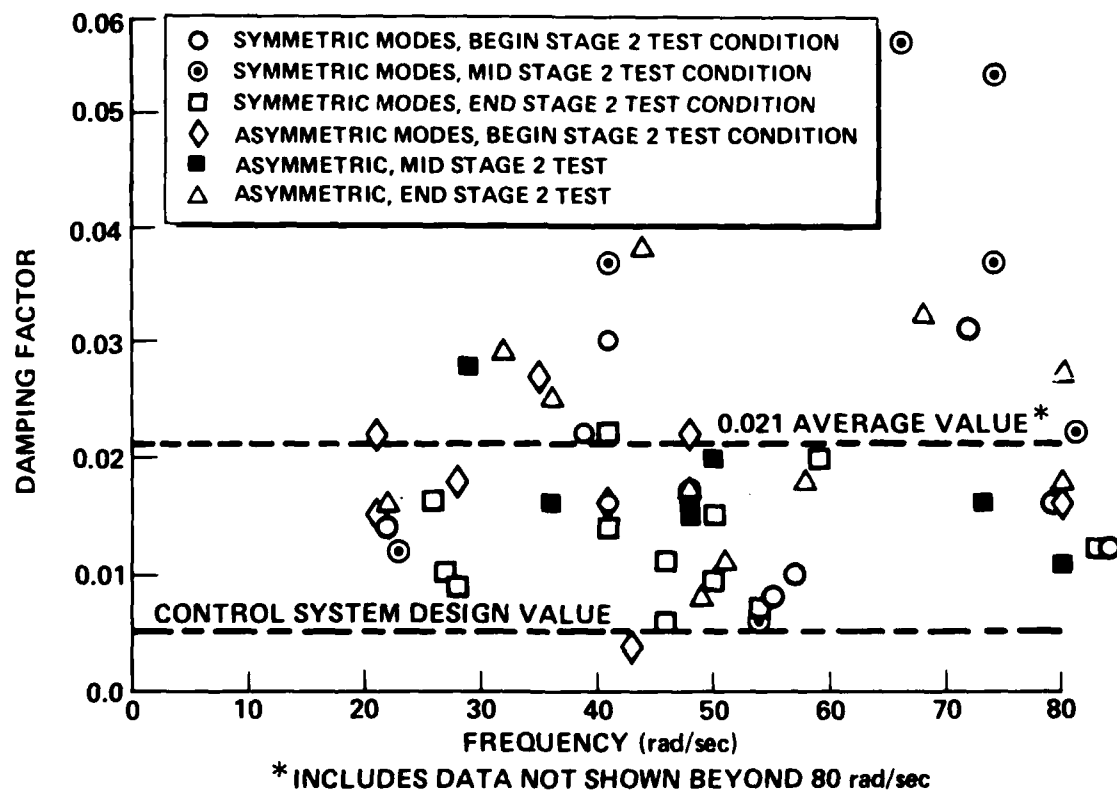
The data are identified as to symmetric or asymmetric modes as well as whether they correspond to the beginning or end of stage one test condition. The Begin Stage One test condition corresponds to the vehicle at rocket ignition with a full load of propellants using an inert material in the booster rockets. The End Stage One test condition represented rocket "burn-out" with empty booster rocket cases. Water was present in the external tank to simulate liquid oxygen.

The average value of measured damping during these test was 0.017 which is substantially greater than the value of 0.005 used for control system design. The data show no correlation with frequency. It can be conjectured the fluctuating values are the result of varying amplitudes at which the individual modes responded to the test vibration. To demonstrate this requires further work to present these data versus amplitude of response and see if the expected correlation materializes.

Stage Two test condition results are shown in Figure 4 similar to the Stage One test data. Three test conditions are presented corresponding to the beginning, middle, and end of stage two flight with the orbiter and external tank. Water of various amounts was used as ballast in the oxidizer tank to simulate the three flight conditions.

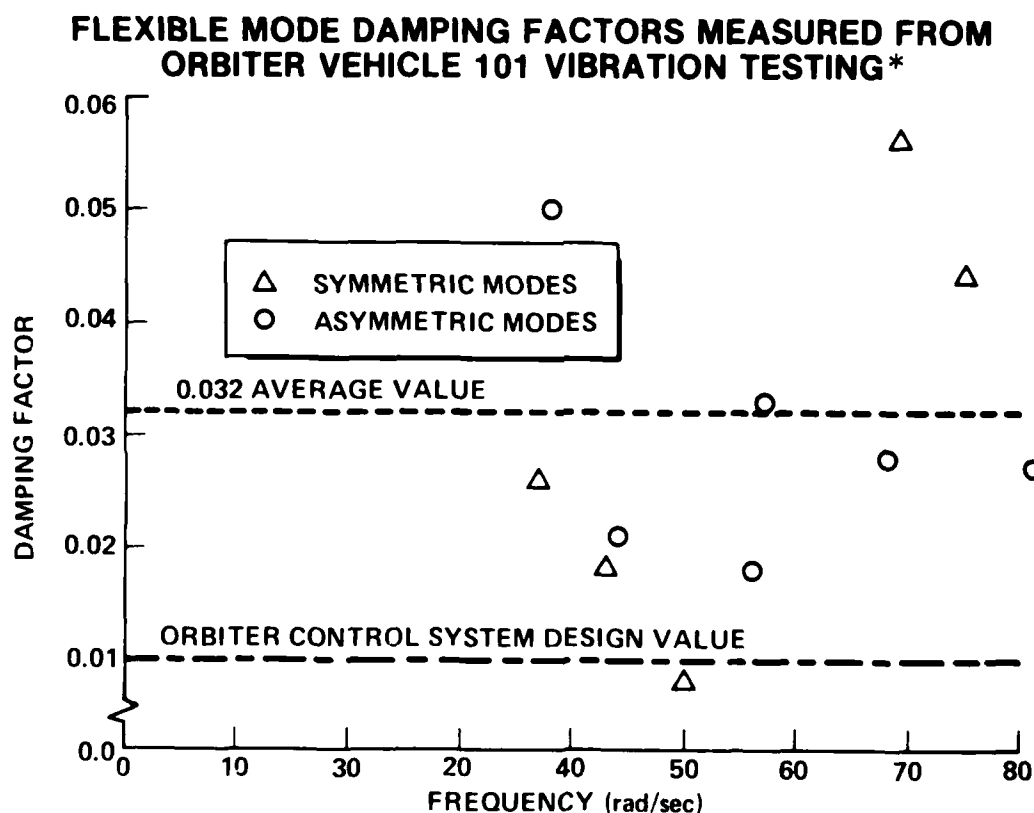
Figure 4

FLEXIBLE MODE DAMPING FACTORS MEASURED DURING STAGE 2 MATED VEHICLE VIBRATION TESTS



The average value of these tests was 0.021 which is substantially greater than the first stage tests. Again there is no correlation with frequency, but the speculation about the dependence of the damping factor on the amplitude of excitation may be applied to these results also. The difference between the average value of the tests results may be explained because the average amplitude of response was greater for the lighter weight stage two tests than for the more massive stage one tests. This trend was continued for the orbiter test as shown in Figure 5 below:

Figure 5



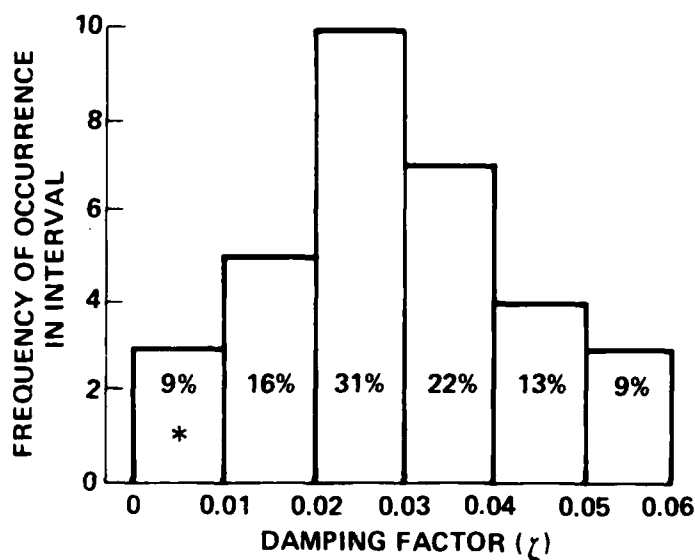
* REFER TO VERIFICATION ANALYSIS REPORT OF OV 101 HGVT,
ROCKWELL INTERNATIONAL, SD 76-SH-0228 (JAN. 1977).

Here the average value of damping factor has increased to 0.032, nearly twice that for stage one tests.

As a matter of interest the frequency of occurrence for damping factors was plotted from these test data as shown in Figure 6.

Figure 6

DAMPING FACTOR FREQUENCY OF OCCURRENCE FOR 32 MODES



* NO DATA SHOWED LESS THAN $\zeta = 0.005$
REFER TO VERIFICATION ANALYSIS REPORT OF THE OV 101 HGVT,
ROCKWELL INTERNATIONAL, SD 76-SH-0228 (JAN. 1977).

The results of all three tests are summarized for comparison in Table 1 shown below as well as in Figure 7 which follows.

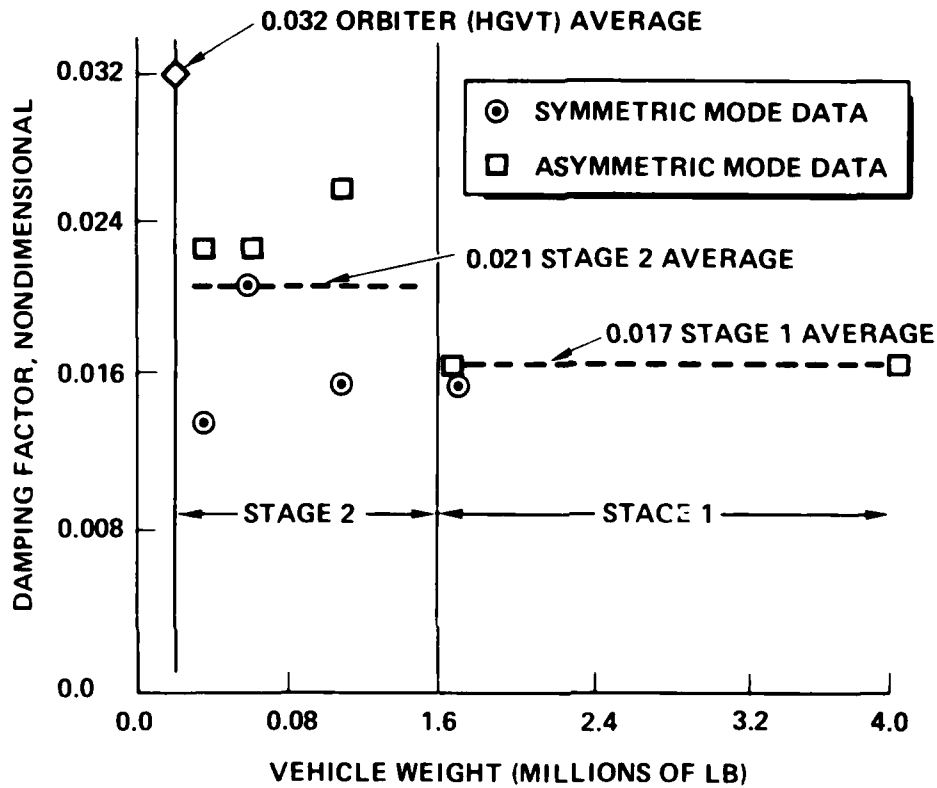
Table 1

STRUCTURAL DAMPING OF SPACE SHUTTLE ORBITER AND ASCENT VEHICLES

VEHICLE CONFIGURATION	AVERAGE VALUE OF DAMPING FACTOR
STAGE 1 (MVGVT)	0.017
STAGE 2 (MVGVT)	0.021
ORBITER VEHICLE (HGVT)	0.032

Figure 7

COMPARISON OF AVERAGE VIBRATION DAMPING FACTORS FOR THREE TEST CONFIGURATIONS (STAGE 1, STAGE 2, AND ORBITER ALONE)

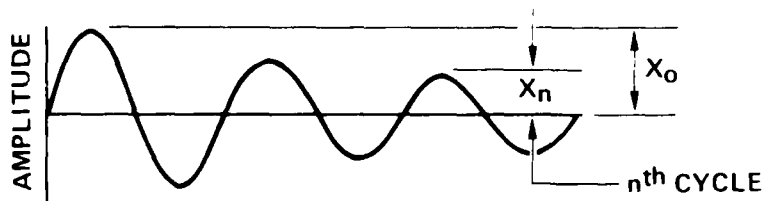


Further corroborating data on vibration damping factors was obtained from accelerometer data recorded during launch of STS-3. An obvious oscillatory mode of response appeared on the output of the accelerometers and calculations were made by making direct measurement from the strip chart recording of this trace. The results of this computation are tabulated below.

Table 2

DAMPING FACTOR CALCULATED FROM ACCELEROMETER DATA DURING STS-3 LAUNCH

CYCLES (n)	AMPLITUDE (X ₀)	AMPLITUDE (X _n)	LOGARITHMIC DECREMENT (δ)	DAMPING (ζ)
7	19.5	7+	0.15	0.024
8	19.5	7-	0.13	0.021
11	20.0	4.5	0.14	0.022
12	19.0	6.0	0.10	0.016
AVERAGE				0.021



$$\text{LOGARITHMIC DECREMENT: } \delta = (1/n) \ln (X_0/X_n)$$

$$\text{DAMPING FACTOR: } \zeta = \delta / (\delta^2 + 4\pi^2)^{1/2}$$

The results range from 0.016 to 0.024 with the mean at 0.021. This compares favorably with the value of 0.017 from the stage one tests.

Conclusion

Valuable and useful damping factor data were obtained from various test programs for actual full size vehicle structure. The data appear to depend on the amplitude of response, but further work is needed to verify this. Also, some unique analytical work has provided some insight and basis for understanding the sources and nature of observed damping factors.

Acknowledgement

Data presented in this paper are partial results of a large and complex test program which depended on the knowledge and expertise of numerous individuals. Mr. Bohdan Bejmuk and Mr. John De Yulia are two who were substantially involved in obtaining and reporting damping factor data from the Mated Vertical Ground Vibration test at the NASA/MSFC facility near Huntsville, Alabama in 1978 and 1979.

References

1. Thomson, W. T., Mechanical Vibrations, Second Edition, Prentice-Hall, Inc., 1956.
2. Wylie, C. R., Jr., Advanced Engineering Mathematics, McGraw-Hill Book Co., Inc., 1951.
3. Jensen, D. L., Flight Control Frequency Response Testing of the Shuttle Ascent Vehicle, Journal of Guidance, Control and Dynamics, Vol. 5, No. 3, May-June 1982, Page 243.

MEASURED DAMPING OF SHUTTLE ACOUSTIC TEST STRUCTURES

C. E. Wallace and Mark Mielke
Mechanical and Aerospace Engineering
Arizona State University
Tempe, Arizona 84827

and

Jack Joanides
Rockwell International
Space Division
12214 Lakewood Boulevard
Downey, California 90241

Measured Damping of Shuttle Acoustic Test Structures

by

C.E. Wallace
Mark Mielke

Mechanical and Aerospace Engineering, Arizona State University
Tempe, Arizona 84827

Jack Joanides
Rockwell International, Space Division, 12214 Lakewood Boulevard
Downey, California 90241

Abstract

Damping measurements have been made on ten shuttle structural test specimens which were constructed for acoustic testing. These specimens include the cargo bay doors, the OMS/RCS pod, the wing leading edge section, the wing elevon section, the body flap, the tail section, three fuselage panels and one wing panel. The damping of each natural mode of vibration for each specimen is plotted versus the natural frequency. Statistical analysis, including the mean, standard deviation and probability density for the damping data is presented. The analysis demonstrates that the damping ratio decreases with increasing frequency and that the logarithm of the damping ratio has a normal distribution.

Introduction

Structural damping is an important parameter in the analysis of dynamic response and acoustic fatigue. During the design of the structure, and before the structural test specimens are constructed, the engineer must rely on estimates of the structural damping. If the engineer is developing a probabilistic analysis of the structural response, then estimates of the damping probability distribution function are also required. In this paper, the measured values of these damping parameters are presented for ten Space Shuttle acoustic test structural specimens.

Discussion

The damping of each natural mode for ten acoustic test structural specimens was measured as a part of the acoustic fatigue and dynamic response test program. The structural damping was obtained through the circle fit procedure associated with the modal modeling vibration tests which preceded the acoustic tests. The structural test specimens included in this study are shown in Figure 1 and are described as follows:

Fuselage Panel FFA-04.¹ The FFA-04 panel is a ten foot by ten foot rectangular curved aluminum skin riveted to aluminum hat stiffeners. The exterior is covered with real or simulated TPS tile. The curved shape is set by five transverse frames about 30 inches apart.

Fuselage Panel DAI.¹ This panel is a rectangular aluminum panel with integrally machined stiffeners, and is covered with TPS tile or simulated TPS tile. It is located aft of the FFA-04 panel on the Space Shuttle under the cargo bay.

Wing Panel C20D.¹ This panel is a flat rectangular skin with riveted hat stiffeners. It is only about one third the size of the previous two panels. It is located about half way out on the underside of the wing. It was covered with real or simulated TPS tile during the test.

Lower Vertical Tail Aft Fairing.² This tail section is a roughly triangular section of skin riveted to aluminum bulkheads about 100 by 100 by 160 inches when viewed from the side. Near the center of the section is a 20 by 40 inch access door made of a honeycomb sandwich panel.

Wing Elevon Section WA18.³ This test specimen is an approximately 13 by 14 foot section consisting of a portion of the wing with the elevon attached on hinges and an overlapping rub panel with flipper doors at the elevon root. The elevon is constructed of honeycomb skin panels with ribs and frames and is covered with TPS tile from one half inch to one inch thick on the upper surfaces and 2.7 inches thick on the lower surfaces. The wing section was covered with Neoprene sponge from one half to one inch thick on the upper surface and two to three inches thick on the lower surface.

Cargo Bay Doors.⁴ The cargo bay doors are graphite epoxy honeycomb panels over curved frames. The doors are supported on an aluminum fixture simulating the longeron and side panel.

Wing Leading Edge Section WA-19.⁵ This test specimen is a roughly triangular eleven foot length of the leading edge and supporting structure of the outboard portion of the wing. The structure is riveted hat stiffeners on aluminum skin supported by aluminum ribs and spars; aluminum spars and tubular trusses connect the upper and lower surfaces. The specimen is about 11 by 8 by 8 feet and covered with TPS tiles on the upper surface and simulated tiles on the lower surface. The leading edge consists of two monocoque carbon-carbon panels and three simulated panels.

OMS/RCS POD.⁶ The OMS POD has a graphite-epoxy shell, aluminum waffle and honeycomb panels, and aluminum and titanium sheets over graphite-epoxy frames and aluminum sheet ribs with add on stiffeners.

Body Flap.⁷ The body flap is a wedge shaped rectangular plane form aluminum structure. The forward 2/3 of the body flap are thin aluminum honeycomb sandwich skin panels over ribs. The aft 1/3 is full depth aluminum honeycomb. The trailing edge is attached to the forward section by piano hinges which extend the full width of the flap top and bottom.

Aft Fuselage Sidewall Panel AFAll.⁸ This test specimen is an external flat aluminum integrally machined waffle skin approximately 8.5 by 5.5 feet. It is attached to three aluminum frames about eighteen inches apart and running parallel to the long side of the panel. Most of the external surface is covered with real or simulated TPS tile. A flash evaporator exhaust port is included on the test panel structure.

The measured damping data for each test specimen is presented in Figures 2 through 7. Both linear and logarithmic plots of the damping ratio ζ vs. the frequency f are shown. Least square fits and \pm one standard deviation about the fit are also included on each graph.

The probability density function for the damping of panels FFA-04 and DA-11 are shown in Figures 2 and 3. In order to better define the probability density distributions, the average distributions for the three panels FFA-04, DA-11 and C-20-D are shown in Figure 8. These three panels were selected because they have provided the most data points, 267 in all, and demonstrate very similar damping trends. It should be emphasized that the damping values for these three panels were not combined, but that the probability density distributions for each panel were averaged to obtain the results in Figure 8. These results clearly show a skewness in the probability density distribution of the damping ratio ζ . This skewness is not present when the damping is represented by $\log_{10} \zeta$. In fact, the probability density distribution of $\log_{10} \zeta$ appears to have a normal or gaussian distribution. Thus it is recommended that the logarithm of the damping ratio be used to represent the damping as a random variable.

Table 1 provides the damping constants for all ten specimens, and the average values for the three panels FFA-04, DA-11 and C-20-D. The ratios of the standard deviations σ_2/σ_1 and σ_4/σ_3 demonstrate the advantage of considering the damping to be a function of frequency. While the advantage is very small for the panels AFA-11, FFA-04, DA-11 and the Body Flap, it is more significant for the other structural specimens.

Summary

The damping data for each natural mode of ten structural test specimens are presented. These plots of the damping ratio demonstrate the great variation in damping from mode to mode and the variation in damping averages and trends from one kind of structure to another.

When damping is to be represented as a random variable it is observed that the damping ratio is not normally distributed, but that the logarithm of this ratio is so distributed.

Conclusions

The structural damping can be estimated for structures similar to those in Table 1 and in the associated figures showing the damping plots. When damping is considered to be a random variable, it is best represented through the logarithm of the damping ratio rather than the damping ratio itself, since the logarithm of the damping ratio demonstrates a normal distribution while the damping ratio is skewed.

References

1. Brillhart, R., "Modal Testing of Space Shuttle Enterprise (OV-101) Forward and Mid-Fuselage and Wing Panels To Identify Critical Modes and Boundary Condition Effect," Prepared For Rockwell International Corp., February 6, 1981.
2. Johnson Space Center Vibration and Acoustic Test Agency Report #24, "VSA-17 Lower Vertical Stabilizer," November 1982.
3. Rockwell International, NAAO Test Facility Report STS-82-0052, "Wing/Elevon (WA-18) Acoustic Test," February 1982.
4. Johnson Space Center Vibration and Acoustic Test Agency Report, JSC-16194 Vol. I, "PBAOT-2 Aft Payload Bay Doors Acoustic Test," March 1980.
5. Johnson Space Center Vibration and Acoustic Test Agency Report, JSC-14724 Vol. I, "WA-19 Wing Leading Edge Acoustic Test," April 1979.
6. Johnson Space Center Vibration and Acoustic Test Agency Report, JSC-17491 Vol. I, "AFA-26 OMS Pod Acoustic Test," August 1981.
7. Johnson Space Center Vibration and Acoustic Test Agency Report, JSC-17349 Vol. I, "AFA-15 Body Flap Acoustic Test," May 1981.
8. Johnson Space Center Vibration and Acoustic Test Agency Report, JSC-17937 Vol. I, "AFA-11 Aft Fuselage Sidewall Acoustic Test," May 1982.

Table 1. Damping Constants for 10 Structural Test Specimens

STRUCTURE	No. Points	ζ_{ave}	σ_1	σ_2	σ_3	σ_4	σ_2/σ_1	σ_4/σ_3
FFA-04	78	0.0219	0.0171	0.0170	0.3054	0.3019	0.990	0.989
DALL	94	0.0221	0.0163	0.0162	0.2785	0.2717	0.998	0.976
C20D	95	0.0238	0.0217	0.0214	0.3425	0.3201	0.987	0.935
TAIL	19	0.0331	0.0199	0.0116	0.2898	0.1981	0.583	0.684
ELEVON	19	0.0433	0.0206	0.0131	0.2033	0.1280	0.634	0.630
BAY DOORS	35	0.0131	0.0092	0.0067	0.2805	0.1876	0.728	0.669
WING LDG EDGE	24	0.0180	0.0145	0.012	0.2861	0.2385	0.887	0.834
OMS POD	26	0.0201	0.0090	0.0080	0.1909	0.1694	0.896	0.887
BODY FLAP	10	0.0341	0.00642	0.0063	0.0921	0.0889	0.984	0.966
AFA-11	17	0.0196	0.00654	0.0067	0.1884	0.1938	0.990	0.996
FIRST THREE PANELS COMBINED	267	0.0226	.0186	0.018	0.3093	0.2983	0.991	0.964

where ζ_{ave} = average value of ζ

σ_1 = standard deviation of ζ about ζ_{ave}

σ_2 = standard deviation of ζ about the linear fit of ζ vs. f .

σ_3 = standard deviation of $\log_{10} \zeta$ about $(\log_{10} \zeta)_{ave}$

σ_4 = standard deviation of $\log_{10} \zeta$ about the linear fit of $\log_{10}(\zeta)$ vs. $\log_{10}(f)$

Test Specimens

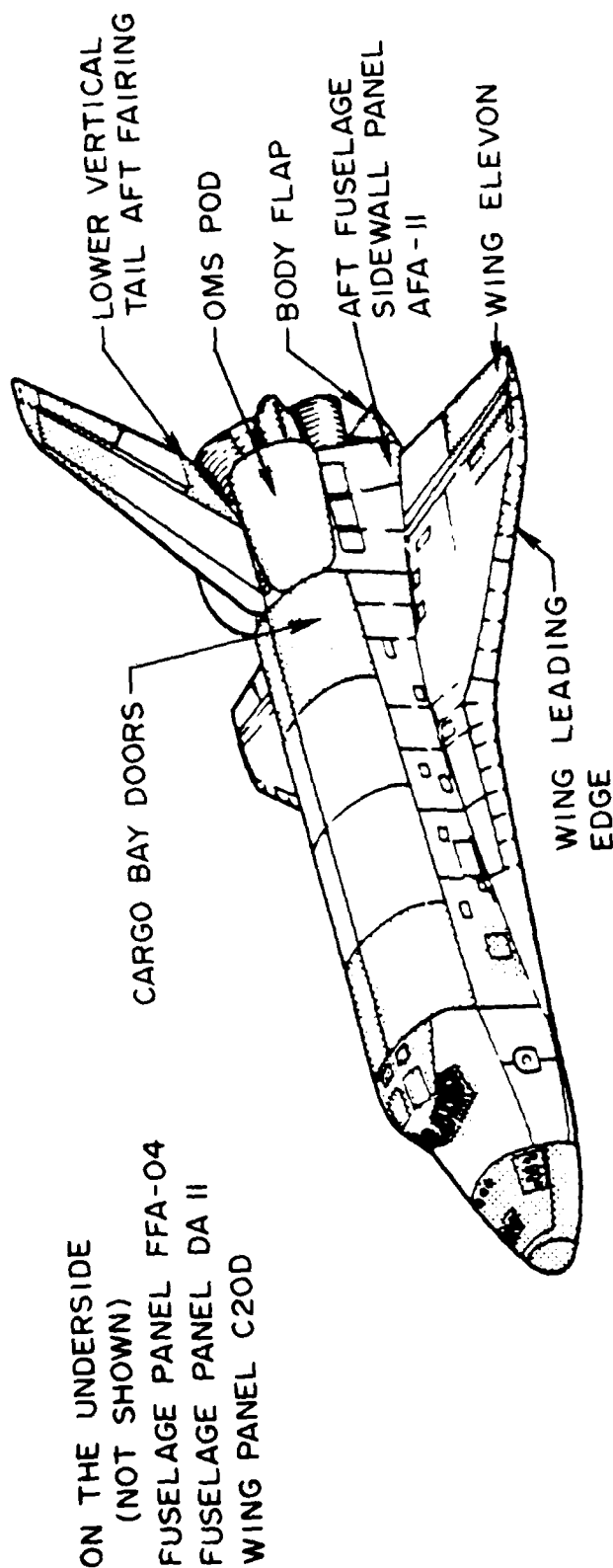


Figure 1. Shuttle locations of the structural least specimens.

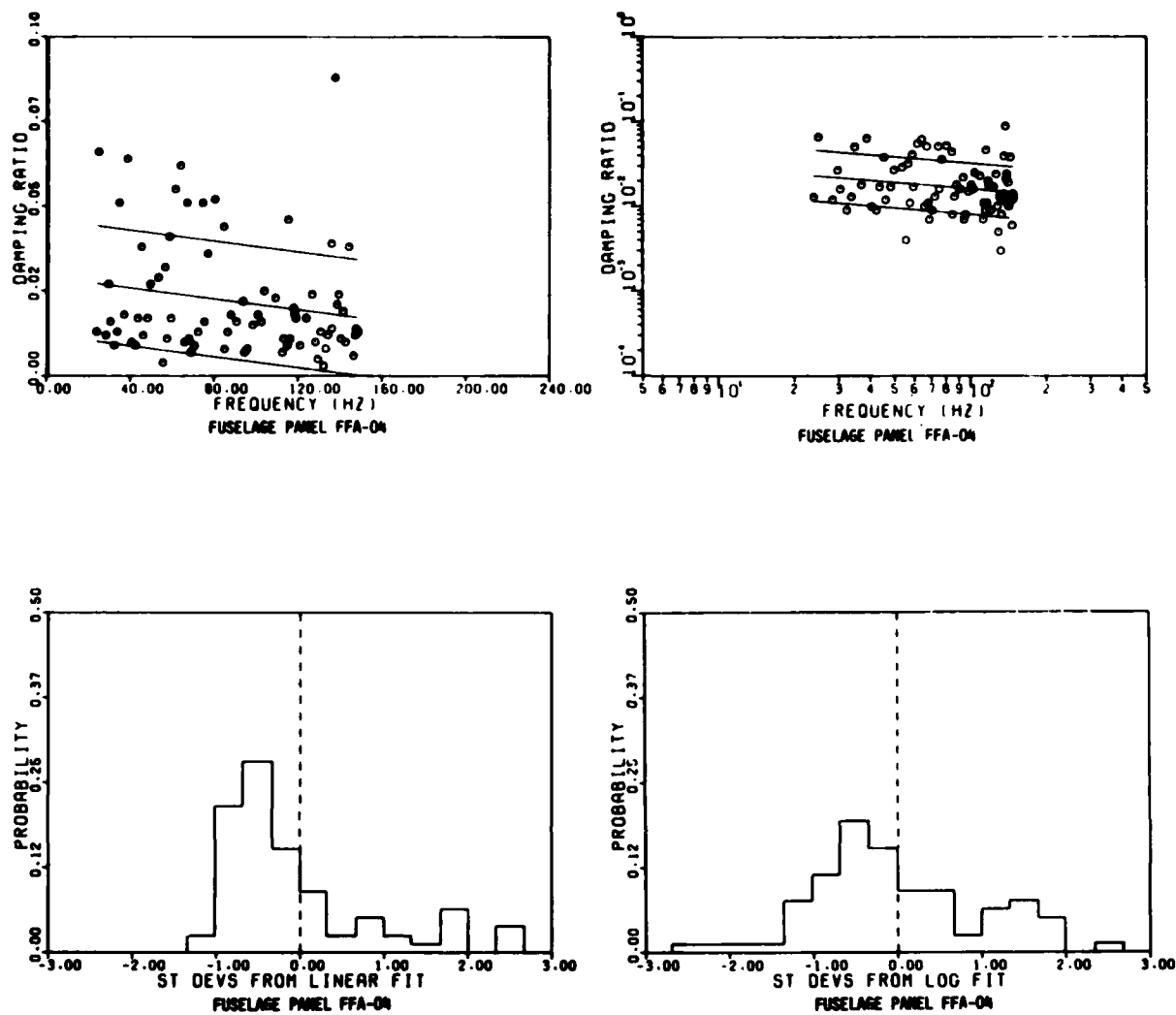


Figure 2. Fuselage Panel FFA-04 damping data.

Upper: Linear and logarithmic plots of the damping ratio ζ vs. frequency
 Lower left: Probability density distributions of the damping ratio ζ .
 Lower right: Probability density distributions of the logarithm of the damping ratio $\log_{10}\zeta$.

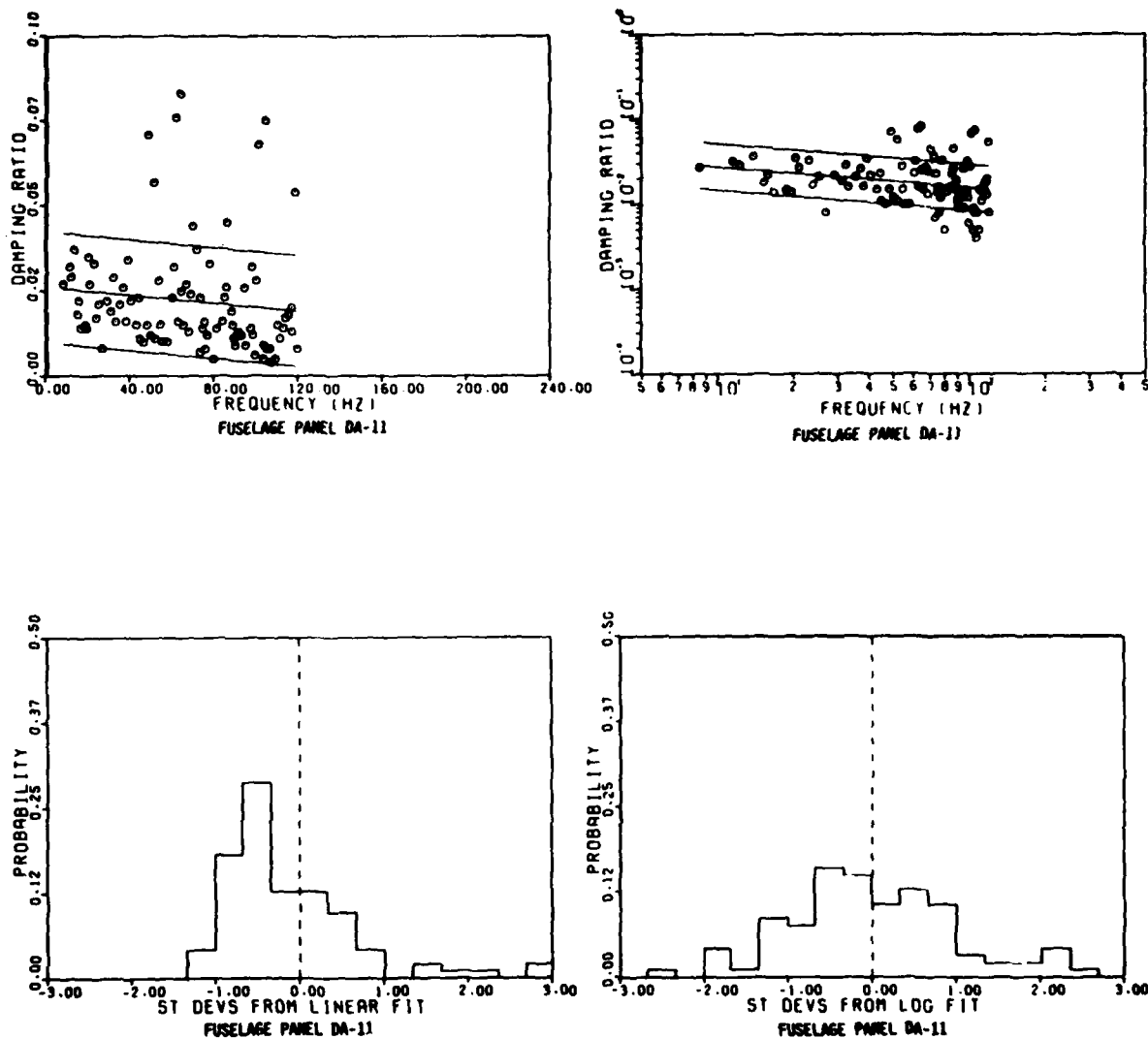


Figure 3. Fuselage Panel DA-11 damping data.

Upper: Linear and logarithmic plots of the damping ratio ζ vs. frequency
 Lower left: Probability density distributions of the damping ratio ζ .
 Lower right: Probability density distributions of the logarithm of the damping ratio $\log_{10}\zeta$.

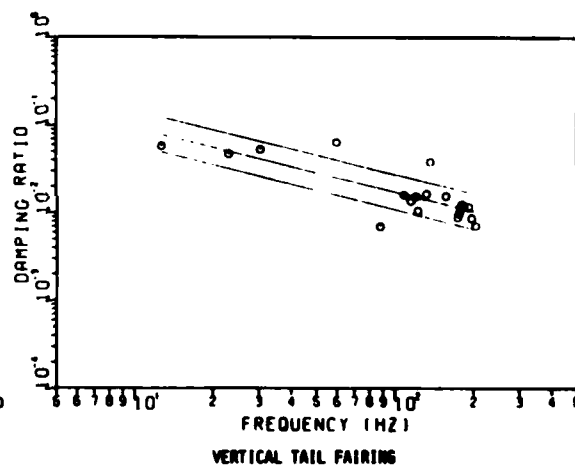
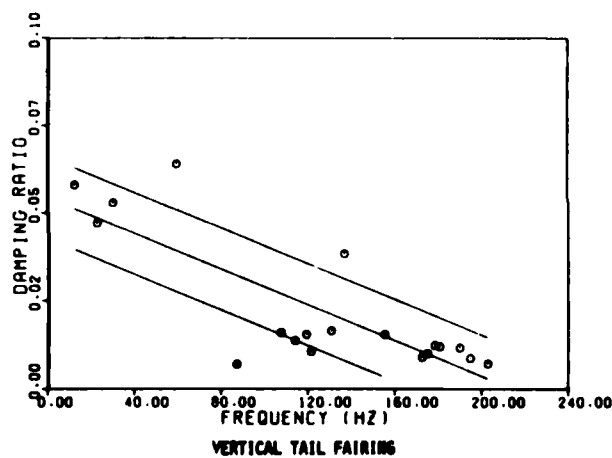
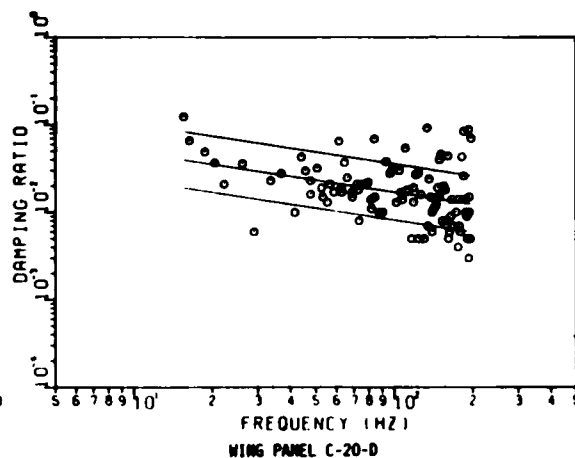
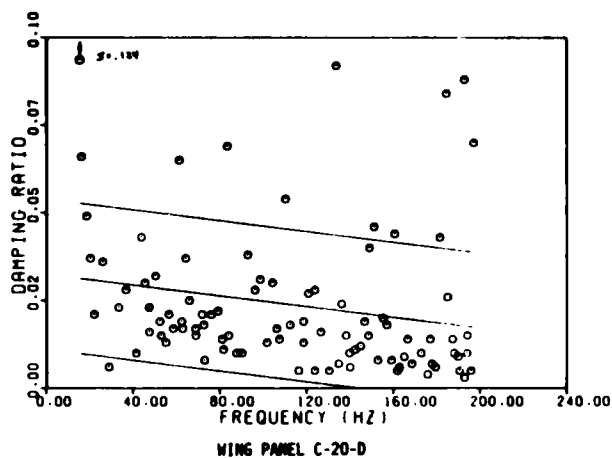


Figure 4. Linear and logarithmic plots of the damping ratio ζ vs. frequency.

Upper: Wing Panel C-20-D.

Lower: Vertical Tail Fairing.

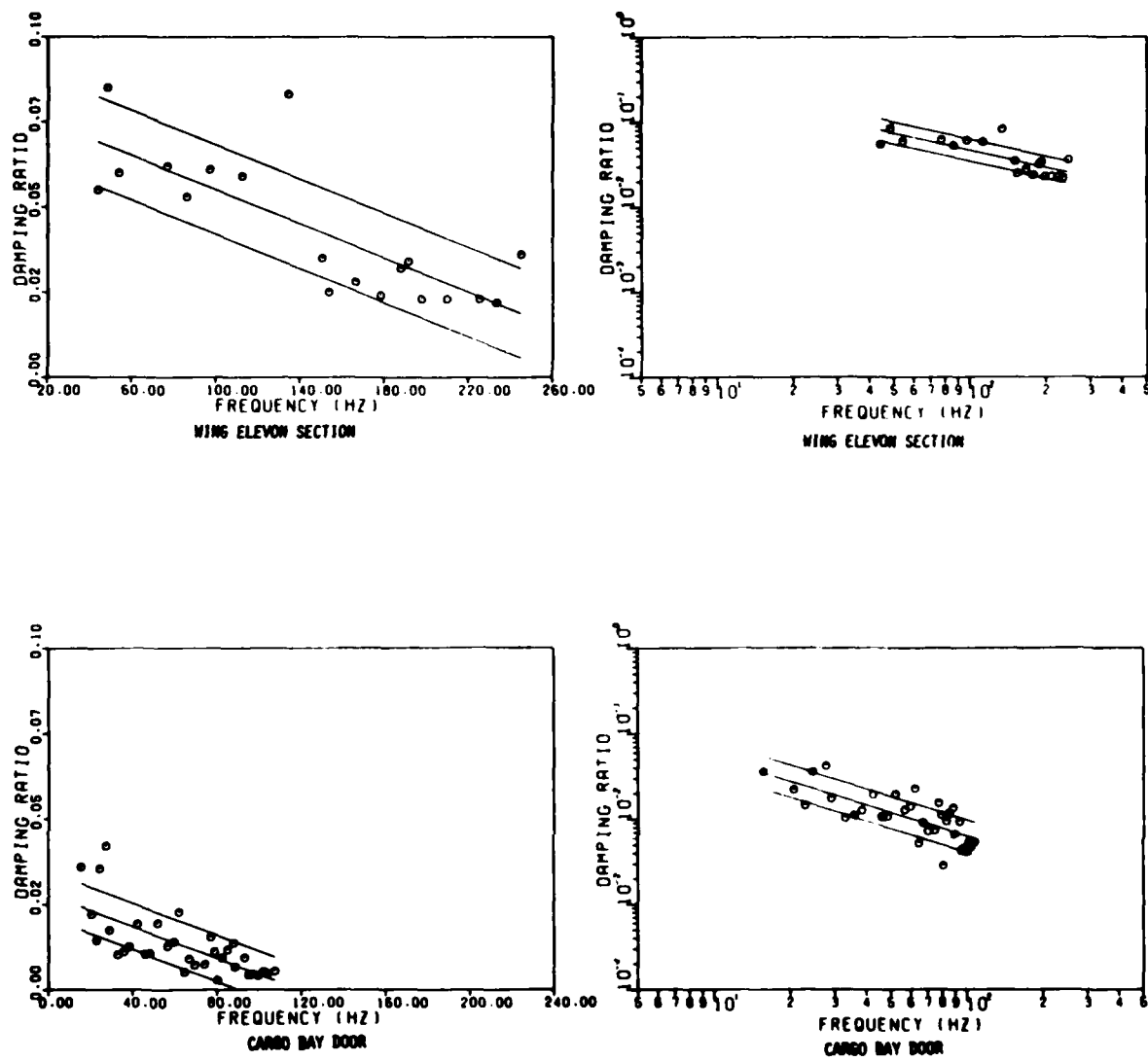


Figure 5. Linear and logarithmic plots of the damping ratio ξ vs. frequency.

Upper: Wing Elevon Section WA-18.

Lower: Cargo Bay Doors.

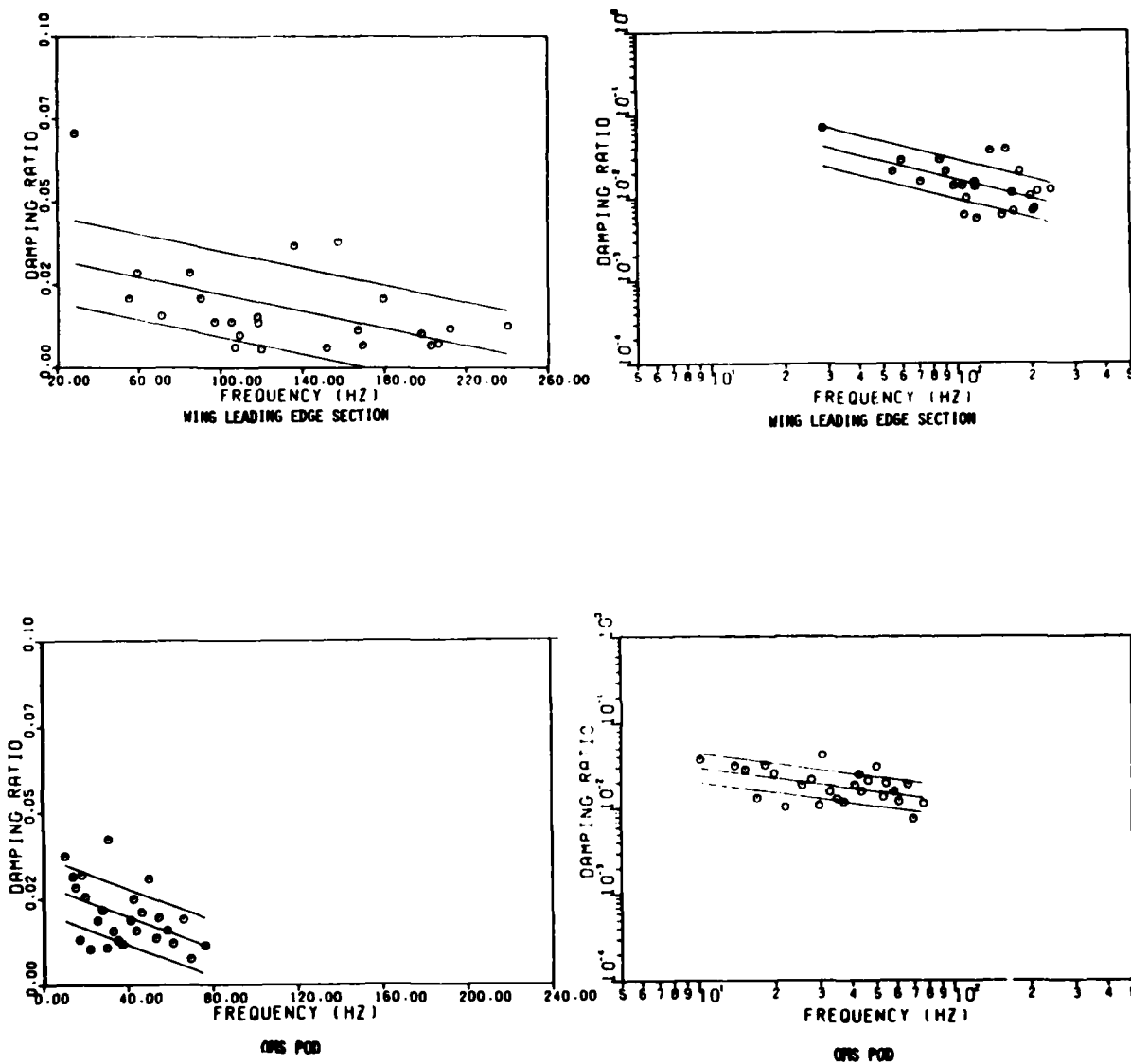


Figure 6. Linear and logarithmic plots of the damping ratio ξ vs. frequency.

Upper: Wing Leading Edge Section WA-19.

Lower: OMS/RCS POD.

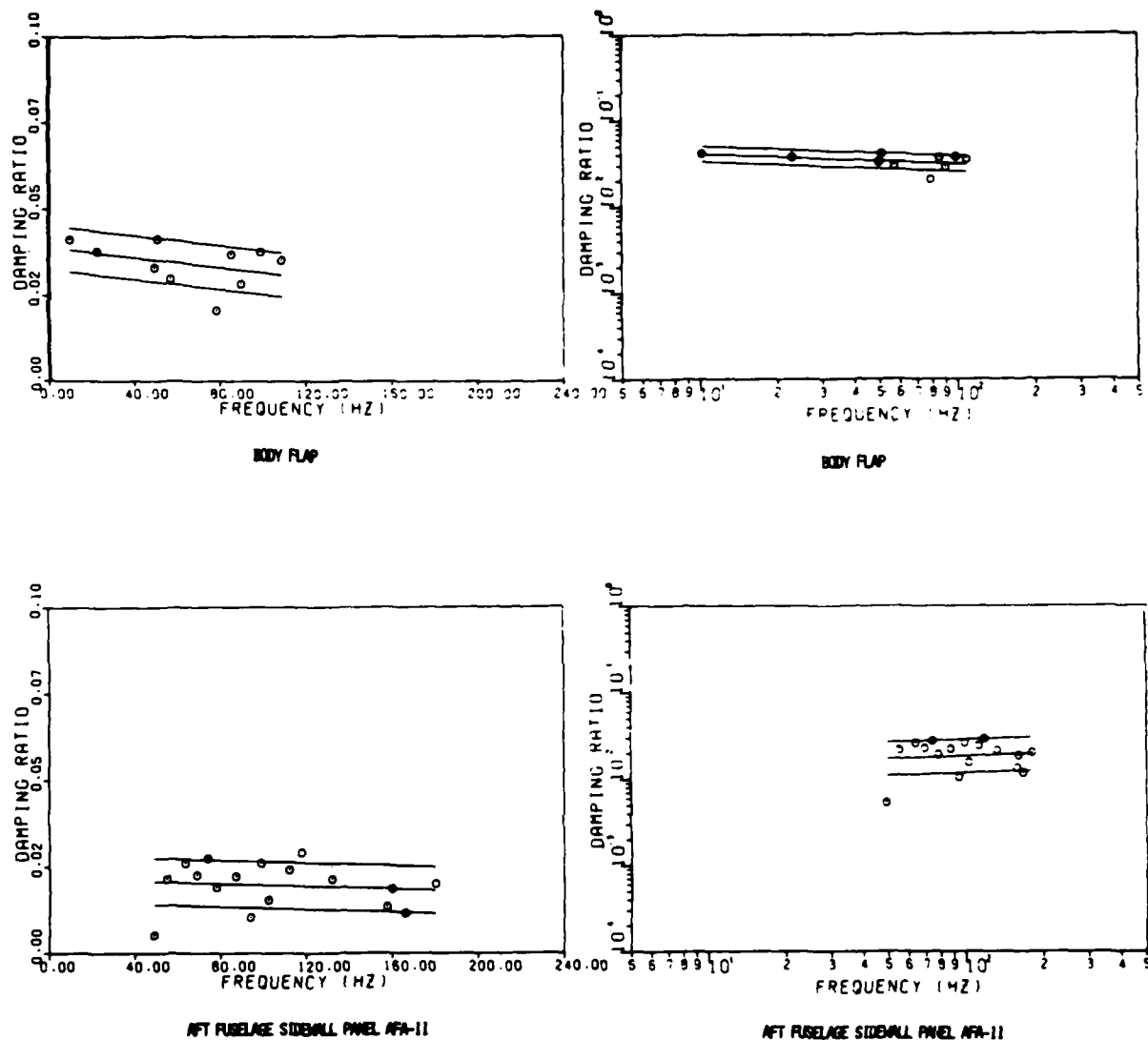


Figure 7. Linear and logarithmic plots of the damping ratio ξ vs. frequency.

Upper: Body Flap. Lower: Aft Fuselage Sidewall Panel AFA-11.

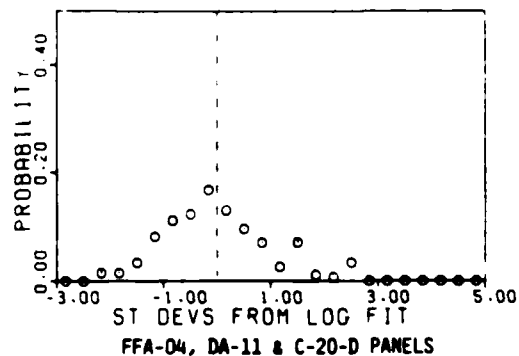
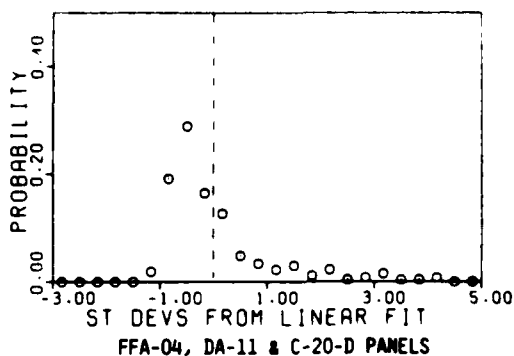
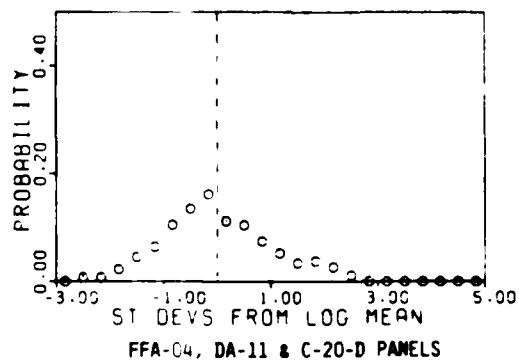
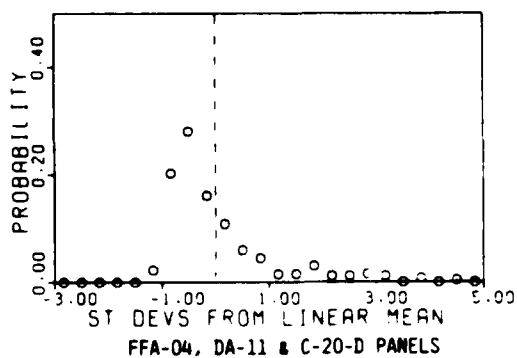


Figure 8. Average probability density distributions.

Each plot represents the probability density distribution averaged over the distributions for the panels FFA-04, DA-11, and C-20-D.

Upper left: Distribution about the mean value of z .

Upper right: Distribution about the mean value of $\log_{10} z$.

Lower left: Distribution about the least square fit of z .

Lower right: Distribution about the least square fit of $\log_{10} z$.

AVERAGE LOSS FACTORS FOR USE IN STATISTICAL ENERGY ANALYSIS

K. T. Brown
Institute of Sound and Vibration Research
The University
Highfield
Southampton, England

and

B. L. Clarkson
The Principal
University College of Swansea
The Abbey
Singleton Park
Swansea

AVERAGE LOSS FACTORS FOR USE IN STATISTICAL ENERGY ANALYSIS

by

K.T. Brown* and B.L. Clarkson**

*Institute of Sound and Vibration Research
The University, Highfield, Southampton

**The Principal, University College of Swansea
The Abbey, Singleton Park, Swansea

Abstract

This paper describes a new technique for the measurement of frequency band and space averaged loss factors of uniform structural components. Values are obtained by an energy measurement technique which is shown to give good results over a wide range of loss factor values. The results obtained can be used in Statistical Energy Analysis prediction programs, or simply to study the frequency dependence of loss factors in components or materials.

Introduction

The prediction of the response of a structure to external forces is of prime concern to the designer. The classical methods predict the response of each mode of a structure. As the frequency range of interest and the modal density rise, this becomes more and more difficult, not to say expensive. The technique known as Statistical Energy Analysis, which was originally developed by R.H. Lyon [1] for use in room acoustics, has in recent years been adapted for use with high frequency structure borne sound.

The Statistical Energy Analysis (S.E.A.) method is used to estimate the frequency band average energy for each structural component in response to random excitation. A frequency band has to be wide enough to contain sufficient modes to reduce the variance of the result. Depending on the modal overlap factor [2] a band typically contains 5-10 modes. As a result of the acoustical heritage of the technique, bands are sometimes expressed in one or one-third octaves. Since the typical structural components under investigation have modal densities which are constant or have generally increasing trends with increasing frequency, it is current practice to use constant bandwidth analysis.

A number of computer based prediction programs are now in use which are based on the S.E.A. method. These programs require knowledge of certain structural parameters, namely modal density, loss factor, and the coupling loss factor between components. Since these techniques are being applied to spacecraft structures, the types of component involved are usually of extremely innovative and radical construction. This being the case there are very limited theoretical models

available for these structures and little in the way of experience to draw on. It has therefore been necessary to develop measurement techniques which can be used to determine these parameters. Methods for measuring modal density and coupling loss factor are described elsewhere [3,4]. This paper describes the technique which has been developed to measure average loss factor (η) in frequency bands.

The Measurement Technique

The technique used is developed directly from the definition of loss factor which is:-

$$\text{Loss factor } (\eta) = \frac{\text{Energy dissipated / cycle}}{\text{Energy stored / cycle}} \quad (1)$$

For random excitation and a stationary system this can be written as

$$\eta = \frac{\text{Average Power Input}}{\omega \times \text{Average Energy Stored}} \quad (2)$$

where ω = frequency of excitation.

The power input for a point input can be expressed as the product of the force and velocity at the point and the average energy stored in a uniform structural component can be expressed in terms of the spatial average of the velocity squared ($\langle v^2(t) \rangle$), which leads to the form:-

$$\eta = \frac{\overline{f(t) v(t)}}{\omega m A \langle v^2(t) \rangle} \quad (3)$$

where $f(t)$ = force at a point
 $v(t)$ = velocity response at that point
 ω = angular frequency of the force
 m = mass per unit area of the structure
 A = Area of the structure
 $\overline{\quad}$ = time average
 $\langle \quad \rangle$ = space average

This can be implemented in a form suitable for use with transient excitation and Fourier Transform techniques. The expression (for each band) then becomes:-

$$\eta_b = \frac{\int_{f_1}^{f_2} \text{Re}\{Z\} v^2 df}{2\pi f_0 m_A < \int_{f_1}^{f_2} v^2 df >} \quad (4)$$

where f_0 = band centre frequency

f_2 = band upper frequency

f_1 = band lower frequency

$\text{Re}\{Z\}$ = Real part of Impedance (F/V)

V = Fourier Transform of $v(t)$

The real part of Impedance is used in the calculation of power input since it does not require to be mass cancelled for the effect of the added mass at the mounting point.

The technique used for the tests was the rapid swept sine testing technique, which is fully described by White and Pinnington [5]. Figure 1 shows an example of a time history and the modulus of the transform of a typical swept sine from 40Hz to 2040Hz as used in the following tests. Figure 2 shows the instrumentation used. The ISVR Sweep Oscillator is described in [5]. Note that six accelerometers were used to estimate the spatial average velocity of the structure. They were placed randomly on the structure, without being placed too close to boundaries. The response of the excitation point must not be included in the space average due to the presence of reactive (nearfield) waves, which are not part of the reverberant energy field of the structure. The signal processing was all carried out in the Data Analysis Centre of the ISVR. The test was repeated at a number of different driving points and the results from each test were averaged. Sufficient test should be carried out in order that the results converge. In the results presented here only four tests were necessary.

On structures with low damping, additional precautions were taken in testing. Note in Figure 2 the relay in the power lead. This disconnects the output of the power amplifier from the coil of the exciter immediately the excitation has finished. If left connected the low impedance output shorts the coil and acts as a point damper on the structure. The coil and magnet exciter also reduces added mass and stiffness and particularly introduces no rotational constraints. The structure should, of course be suspended by a light elastic system which decouples the structure under test from the supporting frame. The transient nature of the testing technique also means that extremely long transforms are sometimes necessary. This has the additional advantage that extremely fine frequency resolution is achieved in the initial measurement. It is important that the finest resolution possible should be used to measure the power input in Equation 4 before frequency averaging takes place, because of the extreme dynamic range of response in a lightly damped structure.

Results

One of the main reasons for developing this method has been the difficulties encountered using the traditional methods. Figure 3 shows a typical decay record achieved by exciting a structure in the band 900-1000Hz and measuring the rms response following the switching off of the excitation. As can be seen, the initial decay is dominated by a heavily damped mode with a loss factor of 0.017. The lower part clearly indicates that other, more lightly damped modes are present. In fact the energy average result using the new method gives a result of 0.0041. The decay method always tends to give a result which is dominated by the more heavily damped modes.

A second series of tests was performed on a flat aluminium plate. The dimensions of the plate were 0.9m x 0.45m x 0.0015m. The plate was tested undamped, partially damped and fully damped. In the partially damped case two strips of self adhesive visco-elastic damping tape 0.05m wide were attached along two opposite edges of the plate. In the fully damped case two further strips of damping tape were added to the other two sides. Figures 4, 5 and 6 show the point mobility of the plate in the three cases. The damping values were calculated by the half power point method for each of the modes which were discernible. These were compared with the values obtained for the same frequency band by the energy method. The comparison is shown in Figure 7. As can be seen the energy method shows a good progression of loss factor, and agrees well in the undamped case and in the fully damped case. The partially damped case is more confused, but the point to notice is that the number of modes which are measurable by the half power method decreases with added damping. It is also clear that any average of half power point estimates is going to be dominated by the more lightly damped modes, since the most heavily damped modes cannot be measured.

A further experiment considering only the energy method was conducted to investigate the sensitivity of the method to changes in damping on a typical spacecraft structure. The structure chosen was a flat aluminium face-plated honeycomb panel with a central circular cut-out, as shown in Figure 8. It was tested undamped, partially damped and fully damped, when the whole surface was covered in tape. The mass of the damping tape was assumed to be evenly distributed over the whole area for the partially damped case. The results of the experiment can be seen in Figure 9. A panel of this type has fairly high loss factors above a frequency of about 600-800Hz. Also there is very little modal behaviour discernable above these frequencies because the wave propagation is mostly by shear waves. This also explains the limited effect of the damping tape. However, at low frequencies there are very lightly damped modes formed by bending waves, and the effect of the damping tape on them can be quite clearly seen. The result shows good sensitivity to changes in the average loss factor, even when the changes are small, over a wide frequency range.

The emphasis in this work has been on the measurement of low loss factors because these are typical of many structural configurations. As the loss factor increases the power flow into the structure is greater and is therefore easier to measure. In the extremes of high damping traditional methods break down because the modes become indistinct. In the energy method it is easy to measure the power flow but the technique is also limited at very high levels of damping because the vibration level will decay with distance from the infinite point. Thus the concept

of a uniform spatial average velocity breaks down. Neither method is suitable for the measurement of very high damping values.

Conclusions

A new technique for the measurement of the loss factor of structural components has been described. Frequency average values of loss factor have been compared favourably with more traditional methods. Average values obtained with decay methods have been shown to be over-estimates and those obtained by Nyquist or half power point methods have been shown to be under-estimates.

By using Fourier techniques of this type, average values of loss factor are easily obtained which are usable directly in statistical energy analysis prediction techniques.

The technique also shows promise as a method for investigating the frequency dependence of loss factors for other reasons. Techniques are available for the use of the rapid swept sine to control any variation in the level of excitation with frequency [6]. This should enable frequency trends to be examined without interaction with effects which are dependent on excitation level.

Acknowledgements

The authors would like to acknowledge the contract support of the European Space Agency for this work. They would also like to thank Mr D.C.G. Eaton of ESTEC for his help and Mr M.F. Ranky of the Hungarian Institute for Physics who carried out some of the experiments included here, whilst on secondment to the ISVR.

REFERENCES

1. R.H.LYON, 1975, Statistical Energy Analysis of the Dynamical Structures: Theory and Applications, MIT Press.
2. H.G.DAVIES, M.A.WAHAB. 1981. Ensemble averages of power flow in randomly excited coupled beams. Journal of Sound and Vibration 76(3) pp311-321.
3. B.L.CLARKSON and R.J. POPE, 1981. Experimental Determination of modal densities and loss factors of flat plates and cylinders, Journal of Sound and Vibration (1981) 77(4) pp535-549.
4. B.L.CLARKSON and M.P.RANKY, 1984. On the measurement of the coupling loss factor of structural connections. Journal of Sound and Vibration, to be published.
5. R.G.WHITE and R.J.PINNINGTON, 1982. Practical application of the rapid frequency sweep technique for structural frequency response measurement. Aeronautical Journal, May 1982, pp179-199.
6. R.G. WHITE, 1982. Shock testing using a controlled oscillatory waveform. Journal of the Society of Environmental Engineers, December.

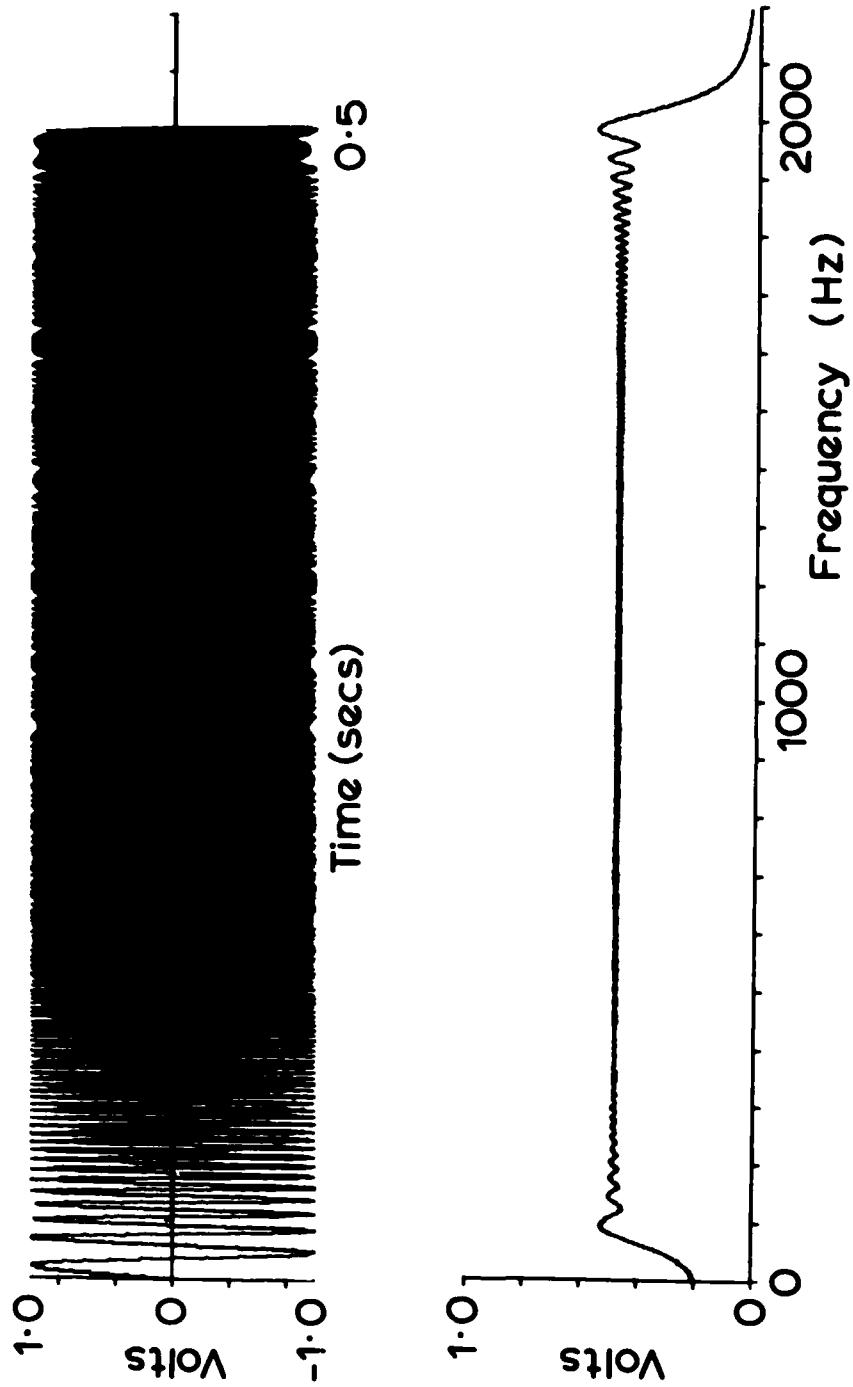


FIGURE 1: Time history and modulus of rapid swept sine (40 - 2040 Hz)

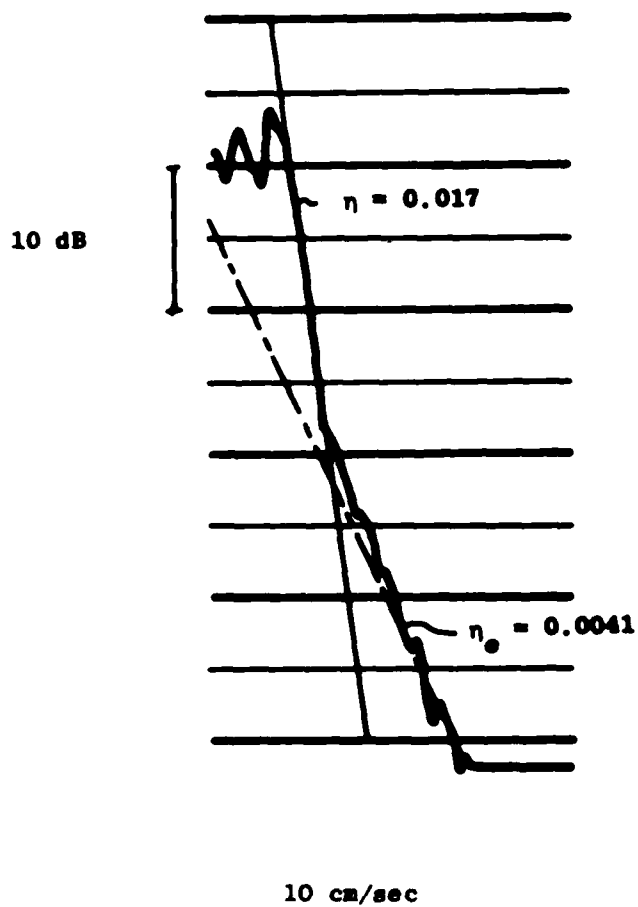
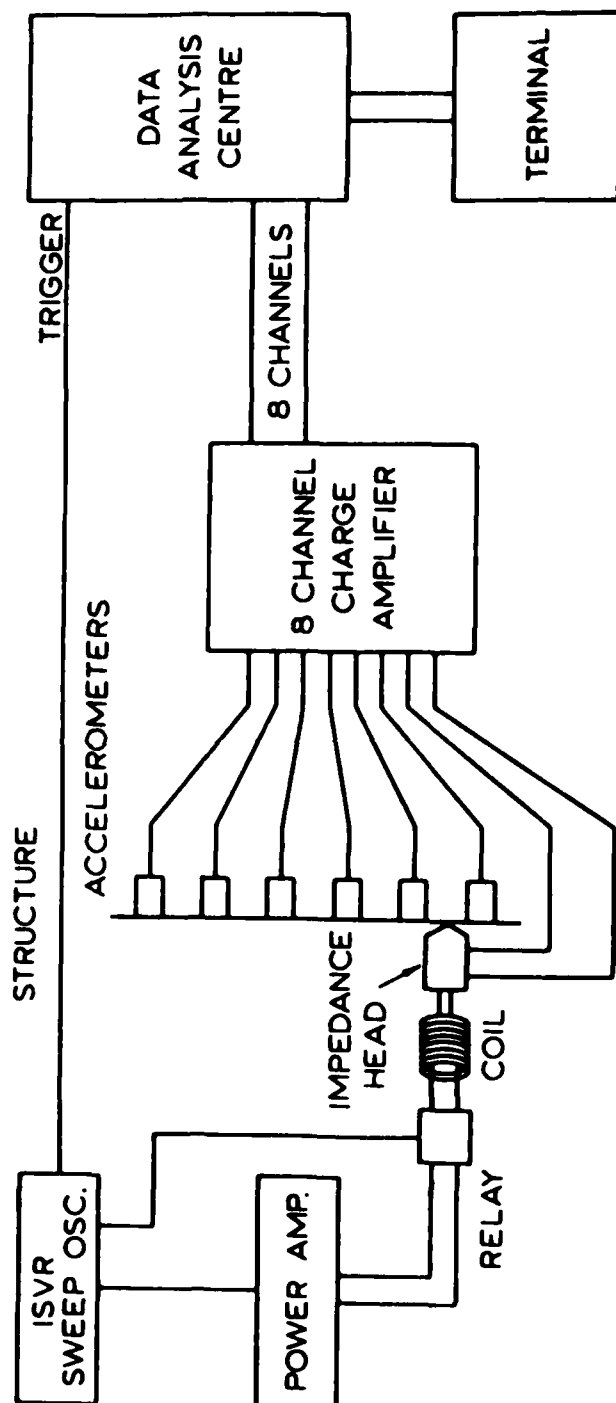


FIGURE 2: Comparison of a decay record made at a single point on a plate, and the energy method derived loss factor (η_e)



INSTRUMENTATION SET-UP

FIGURE 3: Instrumentation set-up

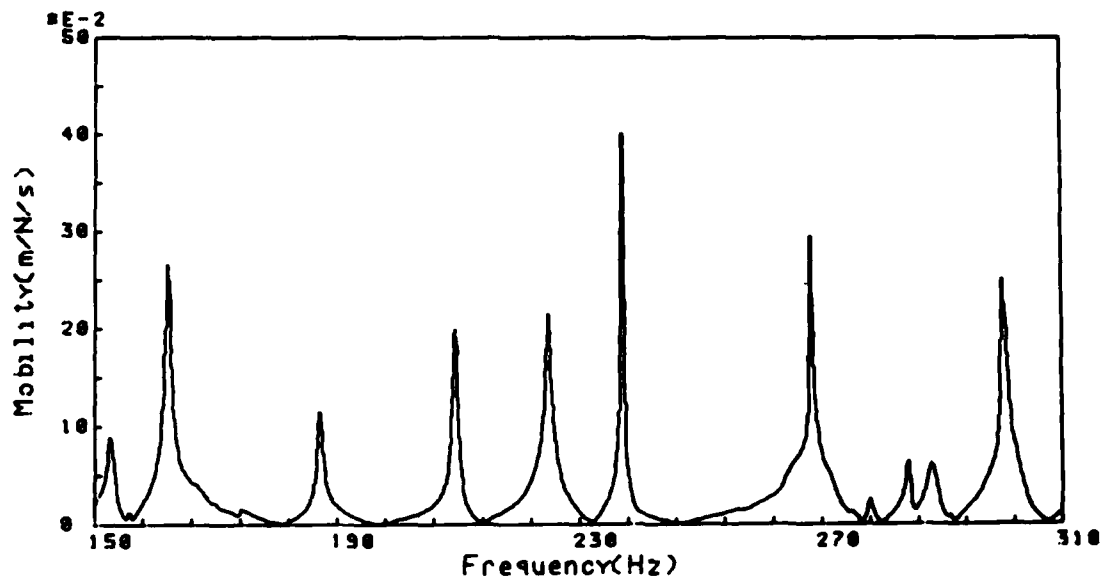


FIGURE 4: Frequency response of undamped flat plate
in range 150 - 300 Hz

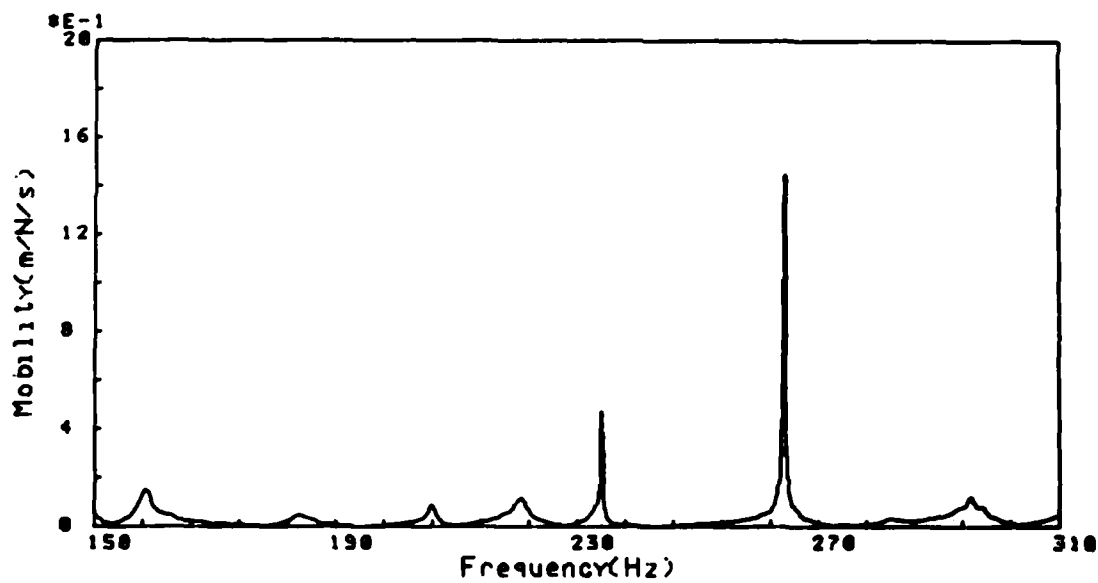


FIGURE 5: Frequency response of partially damped plate
in range 150 - 300 Hz

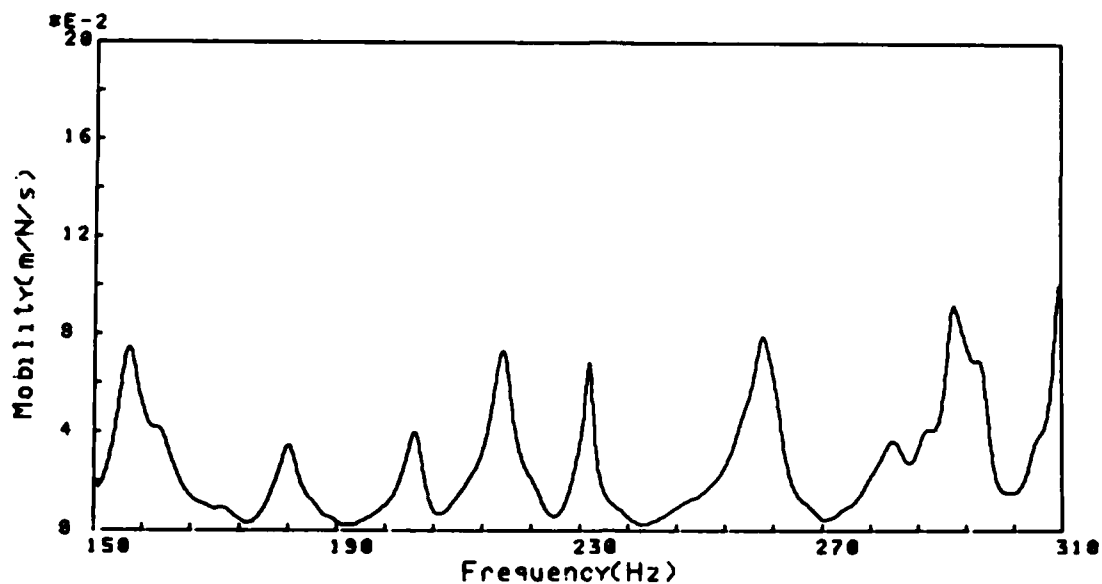


FIGURE 6: Frequency response of damped flat plate in range 150 to 300 Hz

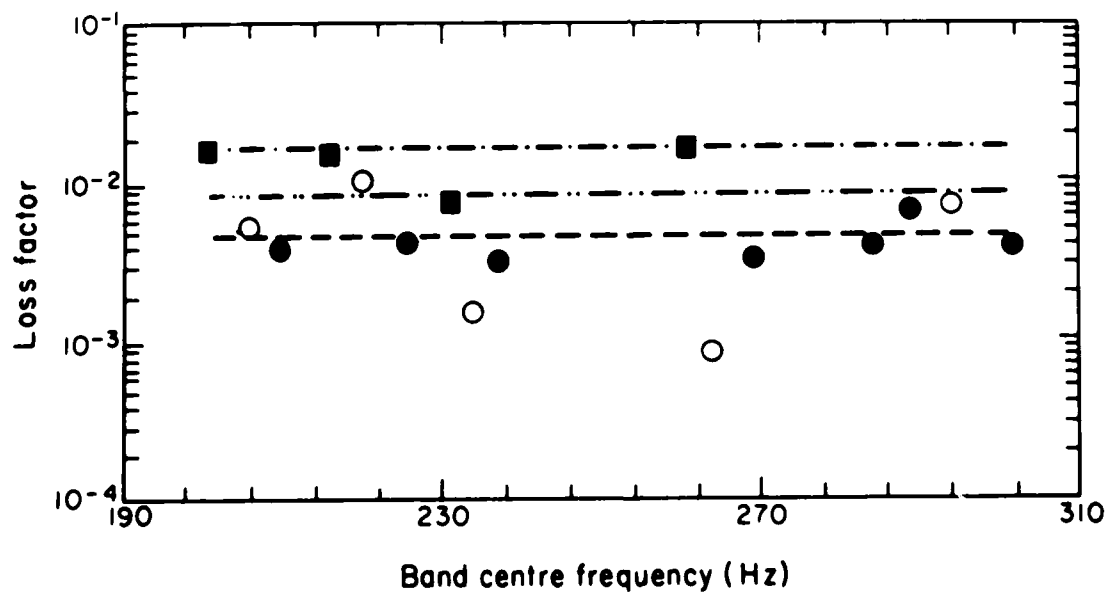
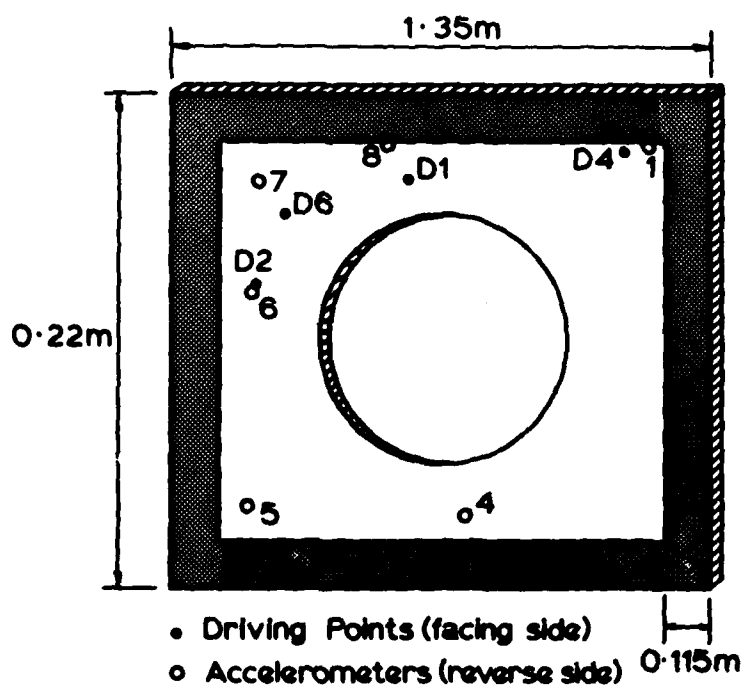


FIGURE 7: A comparison of loss factor estimates in 200-300Hz band on a flat plate. Individual modes: ●, undamped plate; ○, partially damped; ■ damped. Energy method band average: --- undamped; -.- partially damped; - - - damped.



ATTACHMENT OF DAMPING TAPE IN THE PARTIAL DAMPING CASE

FIGURE 8: Aluminium face plated honeycomb panel

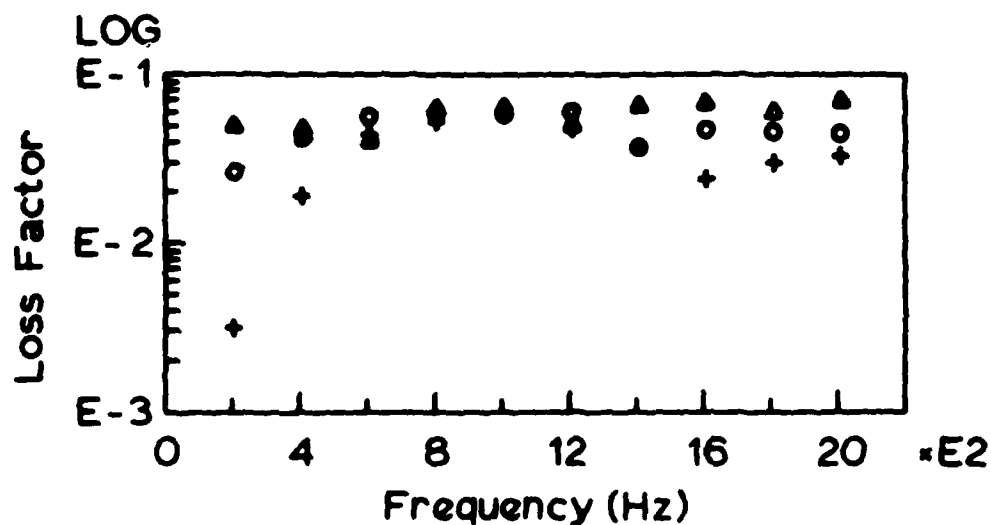


FIGURE 9: Comparison of loss factors of above panel with no damping (+), Partial damping (O) and total damping (Δ)

STRUCTURAL DAMPING POTENTIAL OF WAVEGUIDE ABSORBERS

Eric E. Ungar and Leonard G. Kurzweil
Bolt Beranek and Newman Incorporated
Cambridge, Massachusetts

STRUCTURAL DAMPING POTENTIAL OF WAVEGUIDE ABSORBERS

Eric E. Ungar and Leonard G. Kurzweil
Bolt Beranek and Newman Inc., Cambridge, MA

ABSTRACT

Results of a preliminary study indicate that waveguide absorbers - structural elements that extract energy from vibrating structures in the form of traveling waves - may serve as effective vibration reduction means.

Expressions are presented that indicate how the damping effectivenesses of waveguide absorbers attached to structures depend on absorber and structural parameters. Realizations of waveguide absorbers in terms of damped tapered rods and beams are described. Data are presented that illustrate that suitable waveguide absorber installations can provide considerable damping, even of massive structures, with relatively little weight penalty. The damping of a thin plate by means of a waveguide absorber is compared to that of viscoelastic layer treatments of the same weight.

INTRODUCTION

Background

Aircraft and spacecraft include a multitude of components which may be adversely affected by vibrations. For example, vibrations may cause airframe or engine parts to suffer premature fatigue fracture, images in optical systems to blur, instrumentation to malfunction, and laser weapons to become ineffective. The control of vibrations and their effects therefore is a significant aspect of aerospace system design and development.

Much work has been done on the design of vibration-resistant structures, as well as on techniques for vibration reduction. These techniques include the well-known vibration isolation approach, detuning (i.e., selecting configurations with small vibration responses to the excitations of concern), the more recently developed methods for increasing the vibratory energy dissipation capabilities (structural damping) of components, and local additions of vibration-suppressing masses or dynamic spring-mass systems. All of these classical approaches have been studied rather thoroughly, and the limits on their effectiveness and ranges of applicability are reasonably well known.

However, there has recently been developed the concept of waveguide vibration absorbers (Refs. 1,2), which promises to provide simple and practical vibration control means that not only are highly effective over a broad frequency range, but also relatively easy to apply in practice, including in retrofit situations. The present paper presents an introduction of this promising vibration reduction means, in the hope of spurring further investigations and applications.

The Waveguide Absorber Concept

A "waveguide" is simply a structural component - such as a beam, torsion bar or plate - along which vibrational waves can travel. If one end of a waveguide is attached to a vibrating structure and the other is provided with a suitable energy dissipation arrangement (as shown schematically in Fig. 1), then the waveguide may be expected to remove vibratory energy from the structure, thus acting as an energy absorber.

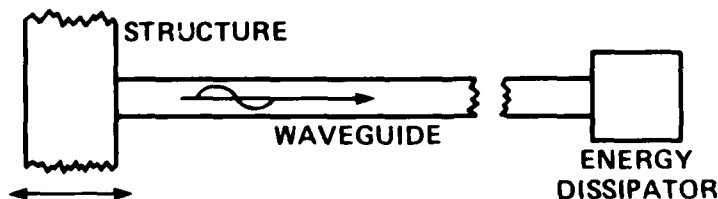


FIGURE 1. SCHEMATIC DIAGRAM OF WAVEGUIDE ABSORBER ACTION.

One may readily visualize that a semi-infinite rod (Fig. 2) constitutes a waveguide absorber in concept, because such a rod accepts energy from the structure to which it is attached while reflecting no energy from its far end back to the attachment (energy injection) point. It is also interesting to note that a finite rod behaves essentially like an infinite one with respect to energy injected to it at one end, provided that the rod is damped so highly that only an insignificant fraction of the injected energy is returned to the attachment point.* Thus, one may for the present visualize waveguide absorbers in terms of highly damped rods. Some practical realizations of such absorbers are discussed later.

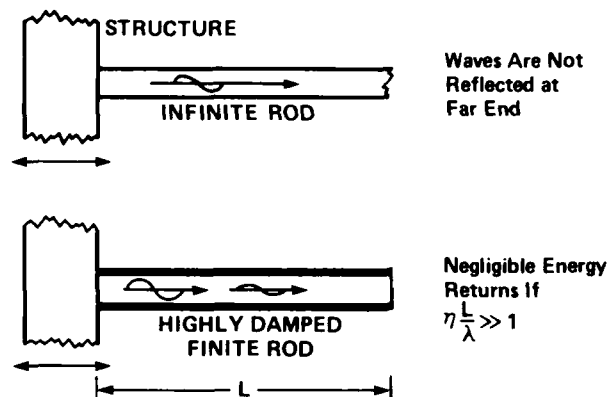


FIGURE 2. CONCEPTUAL WAVEGUIDE ABSORBERS.

It should be noted that waveguide absorbers are considerably different from the classical dynamic absorbers or "tuned dampers." The latter depend on resonant action of an attached dynamic system, are effective only at the system's resonance frequency, may increase vibrations at other frequencies, and do not act primarily by removing energy from vibrating structures to which they are attached. In contrast, waveguide absorbers do not rely on resonant action, are effective over wide ranges of frequency, never produce increase in vibrations, and work by extracting energy from the vibrating structures.

STRUCTURAL LOSS FACTORS DUE TO ATTACHED SYSTEMS[†]

The loss factor η_A that an attached system, such as a waveguide absorber, contributes to a structure, is given by

$$\eta_A = D/2\pi W \quad (1)$$

*This situation exists if $\eta L/\lambda \gg 1$, where η denotes the loss factor, L the length of the rod, and λ the wavelength.

[†]Based on Ref. 2.

(e.g., see Refs. 3,4). Here D denotes the energy that the attached system removes from the structure per cycle and W represents the structure's "energy of vibration."

For the case where the structure vibrates so that all points on it move either in phase or out of phase, and thus reach their greatest absolute velocities simultaneously, the energy of vibration is equal to the kinetic energy at the instant at which this energy is at a maximum. For example, for a plate with nonuniform mass per unit area $\mu(x,y)$,

$$W = \frac{1}{2} \iint \mu(x,y) v^2(x,y) dx dy = \frac{1}{2} M_S \bar{v}^2 \quad (2)$$

where $v(x,y)$ denotes the vibratory velocity distribution on the plate at the aforementioned instant and the integrations extend over the entire plate area. If M_S represents the total mass of the structure, then \bar{v}^2 is defined by the foregoing equation and is the mass-weighted spatial average value of $v^2(x,y)$.

If one writes the impedance of a waveguide absorber (or other attached system) as

$$Z_A = R_A + jX_A \quad (3)$$

in terms of a resistance (real part) R_A and reactance (imaginary part) X_A , one may express the energy D that the absorber accepts at its attachment point as

$$D = V_0^2 \pi R_A / \omega \quad (4)$$

where V_0 denotes the velocity amplitude of the attachment point and ω denotes the radian frequency.

Once the absorber is attached to the structure, the velocity amplitude V_0 of the attachment point on the absorber is equal to the velocity amplitude of the point on the structure to which the absorber is attached. However, attachment of an absorber may be expected to change the velocity of the structure, so that the velocity amplitude V_0 of the attachment point with the absorber connected in general is different from the velocity amplitude V_S of that point on the structure without the absorber attached. If Z_S denotes the structure's impedance at the attachment point, then

$$V_0^2 = \frac{V_S^2}{|1 + Z_A/Z_S|^2} \quad (5)$$

By combining the foregoing equations one finds that

$$\eta_A = \frac{R_A}{\omega M_S} \frac{V_S^2 / \bar{v}^2}{|1 + Z_A/Z_S|^2} \quad (6)$$

From this equation one may observe that the loss factor contribution η_A made by an attached absorber depends on:

- (a) the ratio of the structure's velocity V_S at the attachment point (without the attached absorber) to the structure's mass-weighted spatial average velocity \bar{v} ,
- (b) the ratio of the absorber impedance Z_A to the structure's impedance Z_S at the attachment point, and
- (c) The ratio of the absorber's resistance R_A to ωM_S , which is equal to the magnitude of the structure's impedance if the structure acts as a rigid mass.

In order to obtain a large loss factor contribution η_A one clearly needs to attach an absorber at a point on the structure where the vibration velocity V_S is relatively large.

If the structural impedance is much greater than the absorber impedance, so that $|Z_A/Z_S| \ll 1$, as is generally the case when one deals with very massive structures, then η_A is proportional to R_A and one needs to select an absorber with the greatest obtainable resistance R_A in order to achieve the greatest loss factor contribution. However, if the foregoing condition on the impedances does not apply, then one obtains the largest value of η_A by matching the impedance of the absorber to that of the structure - i.e., by making

$$R_A = R_S, \quad X_A = -X_S \quad (7)$$

where the structure's impedance at the attachment point is $Z_S = R_S + jX_S$. The loss factor contribution due to such an impedance-matched absorber is given by

$$(\eta_A)_{\text{matched}} = \frac{V_S^2/\bar{v}^2}{4\omega M_S R_S / |Z_S|^2} \quad (8)$$

At a structural resonance, where $Z_S = R_S$, the foregoing reduces to

$$(\eta_A)_{\text{matched resonance}} = \frac{V_S^2/\bar{v}^2}{4\omega M_S / R_S} \quad (9)$$

TAPERED ROD AND BEAM WAVEGUIDES*

In order to save weight, and also in order to enhance the effectiveness of damping treatments or terminations, one may

*Based on Refs. 1 and 2.

consider use of a tapered rod instead of the uniform one indicated in the lower part of Fig. 2.

For a rod whose cross-sectional area A varies exponentially,

$$A = A_0 e^{-x/\delta} \quad (10)$$

one finds that there exists a cutoff frequency

$$f_c = c_L / 4\pi\delta \quad (11)$$

below which the rod does not support traveling waves and acts like a pure mass. However, as indicated in Fig. 3, for increasing frequencies above f_c , the reactance X_A of the rod tends toward zero whereas the resistance R_A approaches that of an infinitely long rod with uniform cross-sectional area A_0 ,

$$R_\infty = \rho c_L A_0 \quad (12)$$

where ρ denotes the density of the rod's material and c_L the speed of longitudinal waves in that material. Since the reactance of an infinitely long rod is zero, one may conclude that the impedance of a tapered rod approaches that of an infinitely long uniform rod at high enough frequencies.

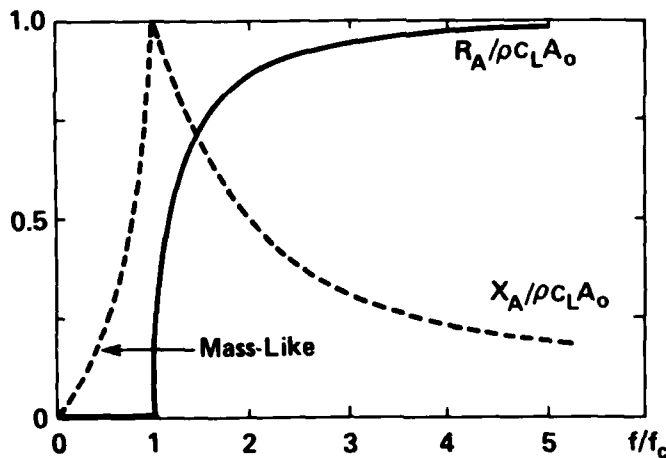


FIGURE 3. DRIVING-POINT IMPEDANCE OF TAPERED ROD (COMPRESSIONAL MOTION).

Flexural Waveguides

Although rod-like waveguides that propagate compressional (longitudinal) waves are relatively easy to visualize and analyze, the comparatively high wavespeeds associated with compressional waves in commonly available materials restrict the utility of compressional waveguide absorbers to relatively high frequencies. Because the speeds of flexural (bending) waves tend

to be much lower than those of compressional waves, waveguide absorbers that rely on bending motions may be expected to be better suited to lower-frequency applications.

A flexural waveguide absorber may be visualized as a beam that is attached to a vibrating structure in such a way that structural vibrations give rise to bending motions that carry energy away from the structure. Just as an infinitely long rod (or one that is finite and highly damped) carries energy away from its structural attachment point in the form of compressional waves, an infinitely long beam (or one that is finite and highly damped) carries energy away from its structural attachment point in the form of flexural waves.

The behavior of tapered beams turns out to be analogous to that of tapered rods. For beams with exponentially tapered moments of inertia I and cross-sectional areas A , that is, with

$$I = I_0 e^{-x/\delta}, \quad A = A_0 e^{-x/\delta} \quad (13)$$

there exists a cutoff frequency f_c below which a tapered beam does not support propagating flexural waves. For such a tapered beam this cutoff frequency obeys

$$f_c = rc_L / 8\pi\delta^2 \quad (14)$$

where $r = \sqrt{I_0/A_0}$ denotes the radius of gyration of the beam cross-section at the attachment point ($x=0$). Above this cutoff frequency, the impedance $Z_A = R_A + jX_A$ of a tapered beam approaches that of an infinite uniform beam with cross-sectional area A_0 and moment of inertia I_0 :

$$Z_\infty = R_\infty + jX_\infty, \quad R_\infty = X_\infty = 2A_0\rho/rc_L\omega \quad (15)$$

The dependence of R_A and X_A on f/f_c is indicated in Fig. 4.

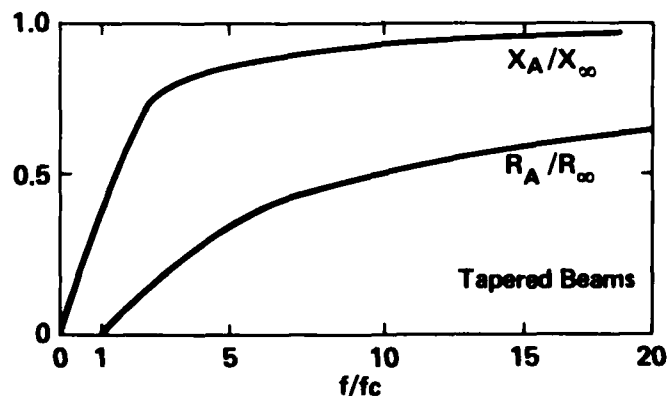


FIGURE 4. DRIVING-POINT IMPEDANCE OF TAPERED BEAM (BENDING MOTION).

ABSORBER MODELS TEST RESULTS, TREATMENT COMPARISONS

Experimental Models

Figure 5 shows two experimental absorber configurations developed at Messerschmitt-Boelkow-Blohm (MBB).^{*} One consists of a tapered steel beam which is coiled and twisted to fit into a cylindrical volume of 53 mm (2.1 in) diameter and 40 mm (1.6 in) height, and which is potted in a damping material; the resulting cylindrical arrangement weighs 0.23 kg (0.5 lb). The other consists of a folded tapered beam of cast aluminum, again potted in damping material, resulting in a brick-shaped assembly measuring 38 x 68 x 120 mm (1.5 x 2.7 x 4.7 in) and weighing 0.8 kg (1.8 lb).

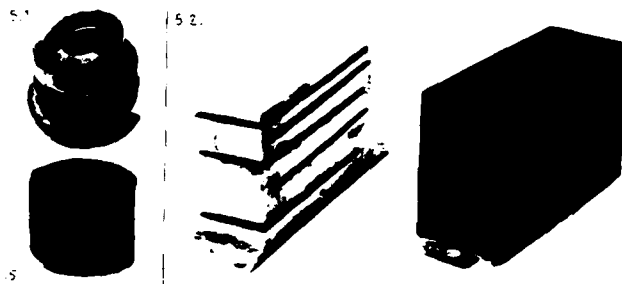


FIGURE 5. TWO EXPERIMENTAL ABSORBERS DEVELOPED BY MBB.

Figure 6 shows another experimental absorber configuration constructed on the basis of similar ones described by MBB (Ref. 5). This absorber consists of a 1.6 mm (1/16 in) aluminum disk of 162 mm (6 3/8 in) diameter, with a layer of damping material bonded to it, and with spiral-shaped cuts that in effect divide the disk into 8 skew tapered beams. This absorber weighs a mere 0.15 kg (0.3 lb).

Measured Loss Factors

Figures 7 and 8 illustrate the results of loss factor measurements made on two rather massive steel beams with several judiciously attached absorbers of the coiled beam type shown in Fig. 5. The numbers and locations of the absorbers are shown in the diagrams, which also indicate the beam dimensions in millimeters. As noted in the figures, the mass of the absorbers amounts to only about 3% of the beam masses; nevertheless, the measured damping may be seen to be quite considerable (compared to loss factors of less than 10^{-3} without the absorbers in place) over wide ranges of frequency.

^{*}Figures 5-8 are adapted from Ref. 1.

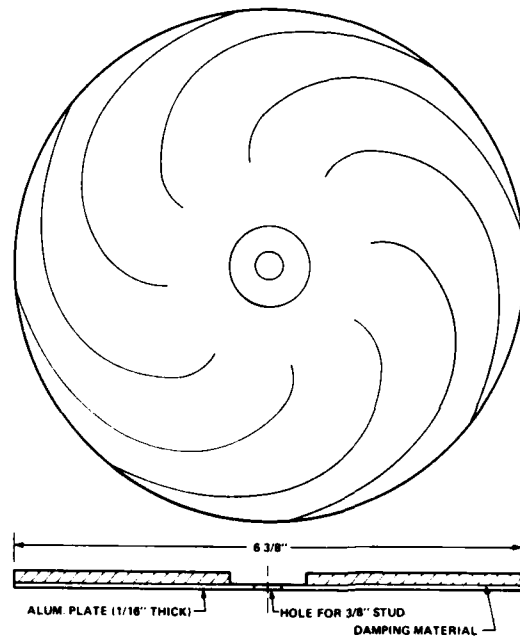


FIGURE 6. EXPERIMENTAL SPIRAL DISC ABSORBER.

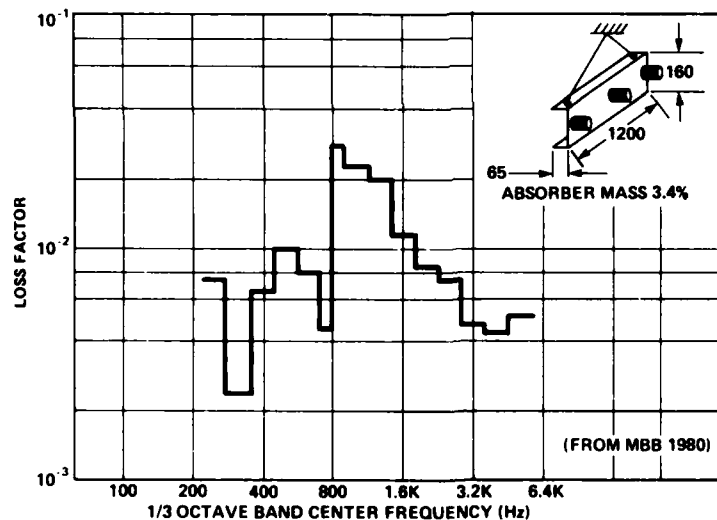


FIGURE 7. LOSS FACTOR OF 20.5 kg (45 lb) CHANNEL OF 8 mm (0.3 in) THICK STEEL WITH THREE EXPERIMENTAL COILED-BEAM ABSORBERS.

Figure 9 shows the results of loss factor calculations, based on measured impedances, for a thin aluminum plate with one or two spiral-disk absorbers attached (in different ways that were explored) and compares these to the theoretical maximum given by Eq. 8. It is apparent that these simple, light-weight

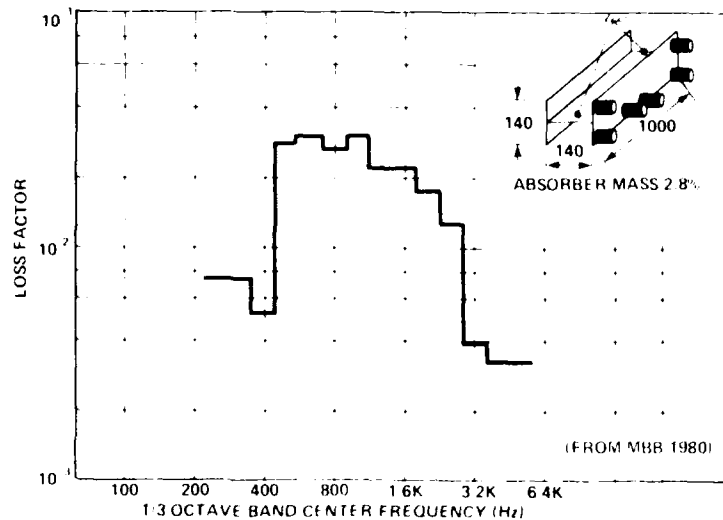


FIGURE 8. LOSS FACTOR OF 50.4 kg (111 lb) STEEL I-BEAM, 12 mm (0.47 in) WALL THICKNESS, WITH SIX EXPERIMENTAL COILED-BEAM ABSORBERS.

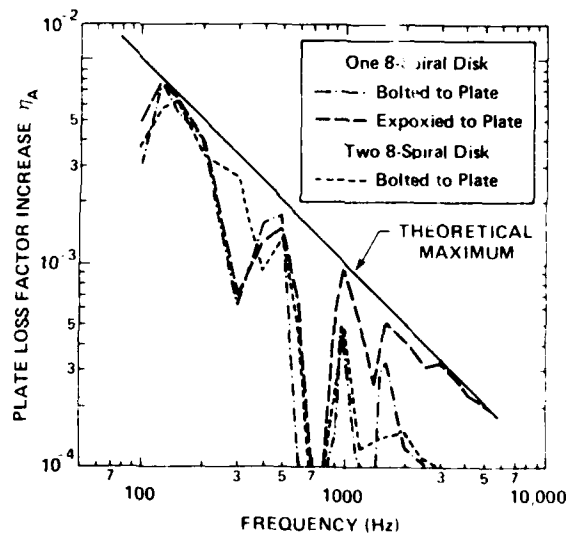


FIGURE 9. LOSS FACTORS MEASURED ON IRREGULARLY SHAPPED 2 mm (0.08 in) THICKNESS ALUMINUM PLATE OF 1.16 m² (1800 in²) AREA AND 6.37 kg (14 lb) MASS, WITH ONE AND TWO SPIRAL DISC ABSORBERS ATTACHED.

absorbers, which are not yet well developed, come close to achieving the maximum performance that is theoretically possible.

Comparison of Damping Treatments on This Plate

Figure 10 presents a comparison of the (calculated) loss factor increases achievable by means of four different damping treatments of the same weight on the thin plate to which Fig. 9 refers:

- (1) a spiral-disk or other comparable waveguide absorber,
- (2) a thin layer of a highly effective extensional damping material with assumed frequency-independent loss modulus,*

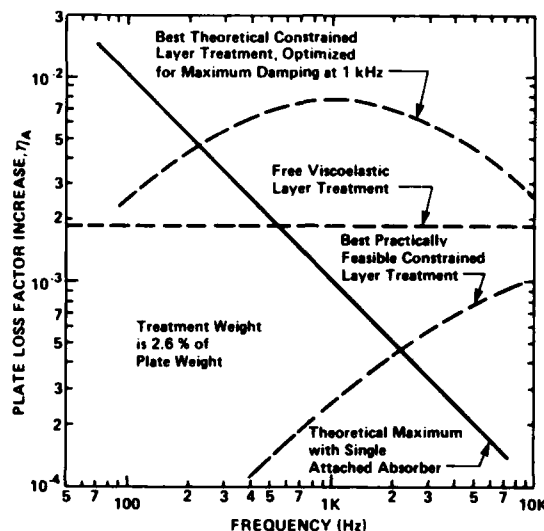


FIGURE 10. COMPARISON OF EFFECTIVENESSES OF WAVEGUIDE ABSORBER AND OF VISCOELASTIC LAYER TREATMENTS OF THE SAME WEIGHT FOR DAMPING OF 2 mm (0.08 in) THICK ALUMINUM PLATE.

- (3) a theoretical optimized constrained layer treatment consisting of an aluminum covering layer of about 0.05 mm (2 mil) thickness attached to the plate via an extremely thin (0.002 mm or 0.1 mil) ideal viscoelastic material with a frequency-independent loss factor of 0.5 and very low shear modulus, designed for optimum damping at 1 kHz,*
- (4) a more practical constrained layer treatment consisting of a 0.04 mm (1.8 mil) thick covering layer and an 0.01 mm (0.5 mil) thick viscoelastic layer, again of a

*Performance calculated according to methods from Refs. 3 and 4.

material with a frequency-independent loss factor of 0.5 and a low shear modulus.

It appears that for a thin plate like that studied experimentally, optimized waveguide absorbers can provide greater damping at low frequencies than even ideal free or constrained viscoelastic layer treatments of the same weight. At high frequencies, these ideal treatments can in theory outperform waveguide absorbers; however such ideal treatments are extremely difficult to implement and waveguide absorbers that can be constructed relatively simply may provide better damping than practically achievable viscoelastic layer treatments of the same weight.

CONCLUDING REMARKS

Summary

Expressions have been developed that indicate how the structural damping provided by point-attached dynamic systems, including waveguide absorbers, depend on the structural and system parameters. The ratio of absorber resistance to structural mass was found to play a major role, as well as the ratio of the absorber impedance to the structural impedance. Damping was also found to vary as the ratio of the structural vibration velocity at the absorber attachment point to the average mass-weighted structural vibration velocity, indicating the importance of selecting a suitable attachment point.

The results of analyses have been summarized showing the dynamic behavior of tapered rods and beams, which may serve as the basis for the design of practical waveguide absorbers.

Some experimental results have been displayed that demonstrate that waveguide absorbers have the potential of providing considerable damping with relatively small weight penalty.

Conclusions and Recommendations

The brief preliminary study that served as the essential basis for this paper sufficed to indicate the potential utility of waveguide absorbers for providing significant damping with comparatively little added weight and complication. The general nature of these absorbers also leads one to conclude that they tend to be relatively insensitive to temperature and damage, that they can be made in compact form, that they lend themselves to retrofit applications with relatively little difficulty, and that they can be readily encapsulated for environmental or outgassing protection.

It is clear, however, that good damping performance requires that an absorber must be impedance-matched to the structure on which it is to be employed; one should not expect to achieve good

results in general by attaching an arbitrary waveguide absorber configuration to a particular structure. In general, considerable effort is required to develop an absorber that has attachment details, structural elements and damping means that are suitable for an application under consideration.

REFERENCES

1. O. Bschorr and H. Albrecht, "Schwingungsabsorber zur Reduzierung des Maschinenlaerms" (Vibration absorbers for the reduction of machinery noise), VDI-Zeitschrift, 121 (1979), pp. 253-261.
2. E.E. Ungar and L.G. Kurzweil, "Preliminary Evaluation of Waveguide Absorbers," Air Force Flight Dynamics Laboratory Report AFWAL-TR-83-3125, January 1984. *
3. L. Cremer, M. Heckl, E.E. Ungar, Structure-Borne Sound, Springer-Verlag, New York, 1973.
4. E.E. Ungar, "Damping of Panels." Chapter 14 of Noise and Vibration Control, Ed. by L.L. Beranek. McGraw-Hill Book Co., New York, 1971.
5. P.J. Van den Brulle, "Entwicklung von Schwingungsabsorbern zur Herabsetzung von Vibrationsbelastung" (Development of Vibration Absorbers for the Reduction of Vibratory Loading," Messerschmitt-Boelkow-Blohm Report No. MBB/FE 17/2TL/R/12 (31 Jan. 1980).

*Copies of this report are available from the Defense Technical Center, Cameron Station, Alexandria, Virginia 22314, Document Number ADA140743.

NEW PROPOSED DYNAMIC VIBRATION ABSORBERS FOR EXCITED STRUCTURES

**Helmut F. Bauer
Professor, Institute of Spacetechnology
University of the German Armed Forces
8014 Neubiberg, FRG
Munich, Germany**

New Proposed Dynamic Vibration Absorbers For Excited Structures

by Helmut F. Bauer*

University of the German Armed Forces, Munich
Germany, 8014 Neubiberg, FRG

Abstract

Structural systems are very susceptible to oscillations. There exist not too many effective systems to dampen the dangerous motion of the structure. The more effective vibration absorbers have some disadvantages such as the adjustment, blockage and servicing. They can therefore not be employed in space structures. The following suggests a new damping device consisting of a completely filled liquid container filled with two immiscible liquids, in which the motion of the interface is able to effectively dampen the structure. The effectiveness is exhibited for the coupled structure-liquid system. In addition an active motion prevention system is proposed, consisting of a control system with a control accelerometer and a cold-gas jet system as a control force. Both systems show good results in preventing structural motion.

* Professor, Institute of Spacetechnology

1. Introduction

An elastic structure may vibrate under the action of a variety of causes, stemming from steady, oscillatory or even random sources. If the body exhibits a bluff shape a broad wake is produced, which is bound by the two shear layers that separate from the body and represent the source of flow induced vibrations. One important effect, arising from the instability of the shear layers, is their tendency to roll up and form alternating vortices, which create an oscillatory pressure upon the body thus generating the so-called v.Kármán-vortex shedding [1]. Actually there exist two motions, namely one in the direction perpendicular to the flow direction (vortex shedding motion) and one in flow direction which is due to the fluctuating drag component. Wind- or waterflow induced vibrations are one of the most severe excitation sources have been painfully experienced by the failure of missiles on the launchpad, of smoke stacks, bridges, cooling towers and other civil structures. The relatively small structural damping inherent in the excited structure is therefore not able to prevent large amplitudes for possibly long periods of durations. Another type of motion can arise when the shear layers may exhibit asymmetry as caused by the body shape through a small translational or torsional motion. This creates a pressure distribution upon the body which forces it into the direction of the initial small motion, thus resulting in an ever-growing galloping instability [2-9]. Not only structures with circular cross section are susceptible to vortex-induced vibrations but also those of non-circular cross section as well as tube arrays, in-line and staggered tube banks, tow cables, transmission lines and high-rise buildings. In general the problem is the interaction and feedback between a vibrating structure and an oscillating flow field, which requires the knowledge of the aeroelastically or hydroelastically excited time dependent forces upon the structure, which actually is a formidable nonlinear problem. More thought should for practical purposes be given to the reduction or avoidance of such vibrations. For the reduction of vibrations the engineer has responded only by a few rather impractical methods, such as the increasing of the damping of the system, the avoidance of resonance, the change of the cross section and/or orientation of the structure and even the stiffening of the structure. All these methods certainly provide in their realization great difficulties and in many cases major redesign problems. Increasing the damping, which decreases the resonant amplitude of the vibration, may be achieved by using some other building material or some kind of composite materials or external dampers, if possible. A variety of damping devices have been suggested [10,11]. Other devices for energy dissipation were used such as draping chains over tubes [12] or permitting scraping and the incorporation of energy absorbing materials such as rubber, plastics, wood etc. [13,14] or a viscous oil in a container, which is subdivided by perforated plates, through which the oil is flowing during the motion [15]. The avoiding of resonance is quite difficult to realize, since it usually requires a stiffening of the structure, by increase of the diameter, increase of stiffness or the reduction of the flow velocity, which usually are impossible. A shortening of the structure, which would (due to the influence of the length l in form of $1/l^2$), have a strong effect upon the magnitude of the natural frequency of the structure, is usually, however, not possible. Finally one may be able to change the cross section to a more stream-lined version, where vortex shedding is avoided. This is in most cases

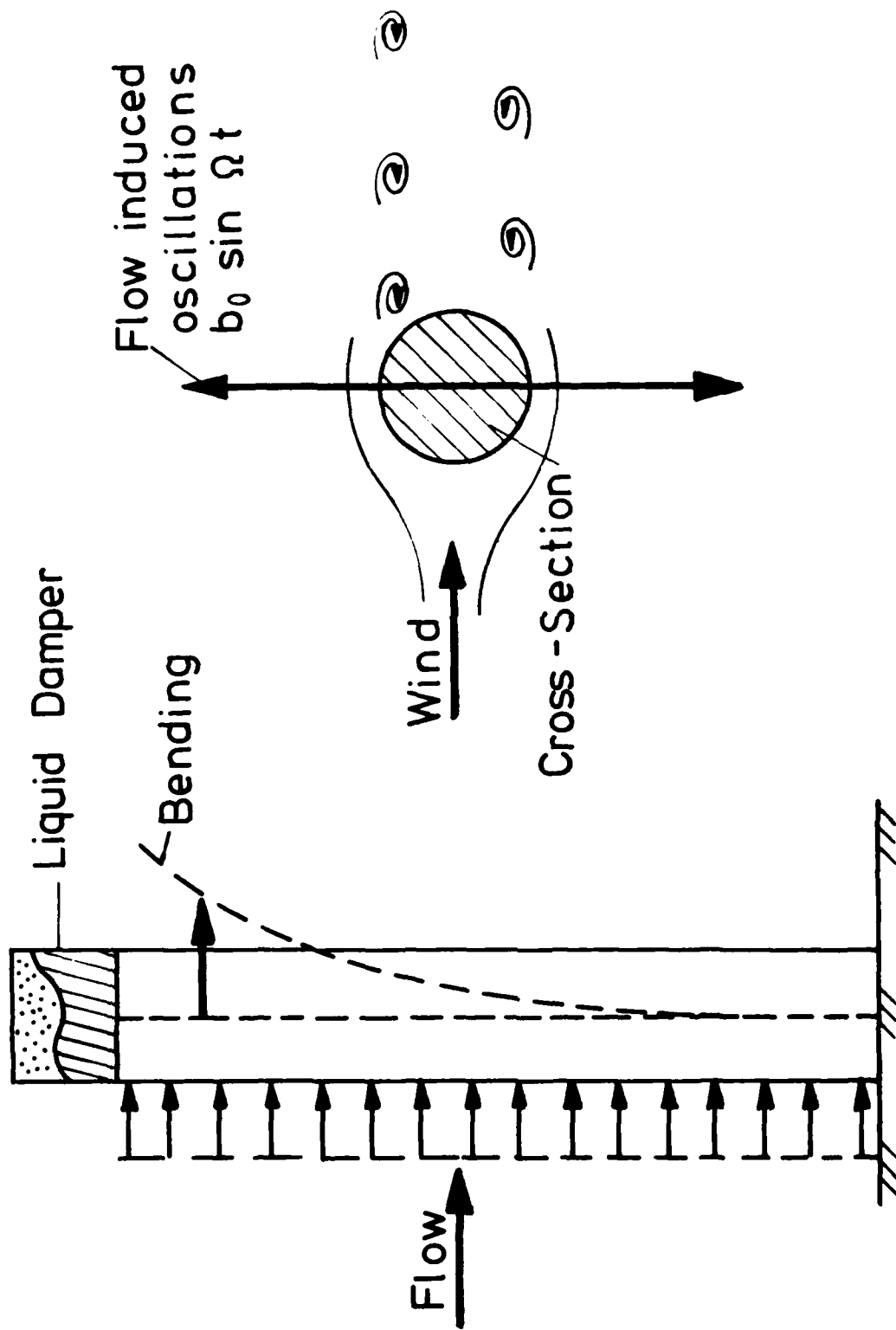
impractical since a large taper ratio is required to achieve this and since the flow direction is mostly not predictable. For missiles on the launch-pad spoiler wires along the sides of the vehicle have been tried to break up the vortex-shedding, but proved to be not too efficient. Most dampers cannot be used in aerospace structures, such as satellite booms or space stations. For this reason new dynamic (passive and active) vibration absorbers are proposed. The passive damper consists of an additional container of a certain geometry filled completely with two immiscible liquids of different densities. This density ratio will provide an additional parameter to geometry and filling heights of the container to shift the natural frequencies of the liquid system to the desired magnitude for an effective operation of the dynamic damper-system. The motion of the interfacial liquid surface may be tuned to the structural system to counteract its motion, thus providing a strong vibration absorber effect. In addition an active damper system is proposed and investigated theoretically. It consists of an accelerometer as a sensor and a closed loop control system, for which a coldgas-jet system provides the necessary thrust force. By a proper design of the control system, i.e. a proper choice of the gain values, the structure may be damped in a very satisfactory way. (Fig.1).

2. Relevant physical and geometrical parameters and conditions for excitation

The most relevant physical parameters for flow-induced oscillations are the size and geometrical form of the after-body behind the point of flow separation. The load due to the pressure which causes vortex-induced or galloping oscillation acts principally on the afterbody surface, from which we may conclude that a structure with a short afterbody shall not be easily susceptible to such excitations. This means that a semi-circular cylinder of opposite orientation definitely oscillates. The flow separates at the edges and acts on the circular afterbody. The length of the afterbody, however, exhibits with its increase the effect of stream lining, thus decreasing again the violence of the oscillations. So it could be detected that sharp trailing edges of the cross-sectional profile result in practically no oscillation amplitude. Some of the basic parameters for the vortex-induced oscillations is the flow velocity V and the diameter of the cross-section, which essentially determine the frequency of the vortex-shedding. This frequency may be determined by

$$f_s = S \frac{V}{D}$$

where S is the Strouhal-Number, which exhibits over a large range of Reynolds-numbers $100 < Re = V \frac{D}{\nu} < 10^5$ a nearly constant value of $S \approx 0.2$. This Strouhal-Number is a function of geometry and Reynoldsnumber for small flow velocities. For noncircular sections, in which the length D is defined as the maximum width of the section normal to the free stream [16 through 25], the Strouhal-Number ranges between $S = 0.12$ and 0.29 in the range of Reynolds Numbers $50 < Re < 10^5$. The treated bodies were of the form of plates in and across the flow direction, rectangular bodies, triangular and bluff circular (i.e. large circular segment) geometry. For in-line and staggered tube banks [26-27] or in other profile structures [28] the Strouhal-Number varies in the range of $0.12 < S < 0.7$ depending on geometrical spacing ratios, such as width distances to diameter ratios across and in flow direction, where only for rare ratios the value of the Strouhal-Number is larger than 0.25 .



DD-5

Figure 1 H.F. Bauer

The fluctuating drag component exhibits a frequency twice as large as that of the oscillating lift. This is due to the fact that one vortex is shed from the body for each cycle. Thus the structure may execute a combined oscillation and describe a Lissajous figure motion. It may also be noticed that for piles in water an apparent mass effect of the surrounding medium will lower the natural frequency of the structure considerably. There also may be additional damping due to the medium, but it is well known that the large amplitude vortex-induced oscillations of marine cables will fatigue cables quite rapidly, which may lead to breakage within a few hours. Even for high-rise buildings, which should not exhibit a dynamic response which may disturb the occupants of the buildings low frequencies in the range of 0.45 to 0.7 cps have been obtained and a very low damping of roughly $\zeta = 0.01$ and less has been measured. For solid circular tower structures of a height of about 70 m and a tip diameter of 3 m the lowest natural structural frequency is about 1 cps while the damping factor $\zeta = 0.01$. Such a structure will easily oscillate with a tip amplitude of 8 cm. It may be noticed that a wind speed of about 15 m/sec. will excite the tower to vortex-induced oscillations. Such a wind speed of about 55 km/h is in such a height expected several times in a year. It is therefore quite important, that whatever the cause of such detrimental oscillations are, a means should be provided to avoid them.

3. New Proposed Passive Dynamic Vibration Absorber

The incorporation of the liquid dynamic absorber (Fig.2) system requires its description as a mathematical model and therefore first the theory of liquid motion of two immiscible liquids in a completely filled container [29]. The natural frequencies are

$$\frac{\omega_{mn}}{\sqrt{\frac{g}{a}}} = \left\{ \frac{E_{mn} \left(1 - \frac{\rho_1}{\rho_2}\right) \tanh\left(E_{mn} \frac{h_2}{a}\right)}{\left[1 + \frac{\rho_1}{\rho_2} \cdot \frac{\tanh\left(E_{mn} \frac{h_2}{a}\right)}{\tanh\left(E_{mn} \frac{h_1}{a}\right)}\right]} \right\}^{1/2} \quad (1)$$

For a cylinder of circular cross-section the values E_{mn} are the roots of $J_m'(E) = 0$, of which for translational excitation of the container only those of $m=1$ appear. The basic natural frequency ω_{11} is presented in Fig.3 for various density ratios ρ_1/ρ_2 of the two immiscible liquids.

The mathematical model has to satisfy

$$m = m_0 + \sum_{n=1}^{\infty} m_n \quad (2)$$

In addition the center of mass law yields

$$\frac{1}{2}[m_2 h_2 - m_1 h_1] = m_0 h_0 - \sum_{n=1}^{\infty} m_n h_n \quad (3)$$

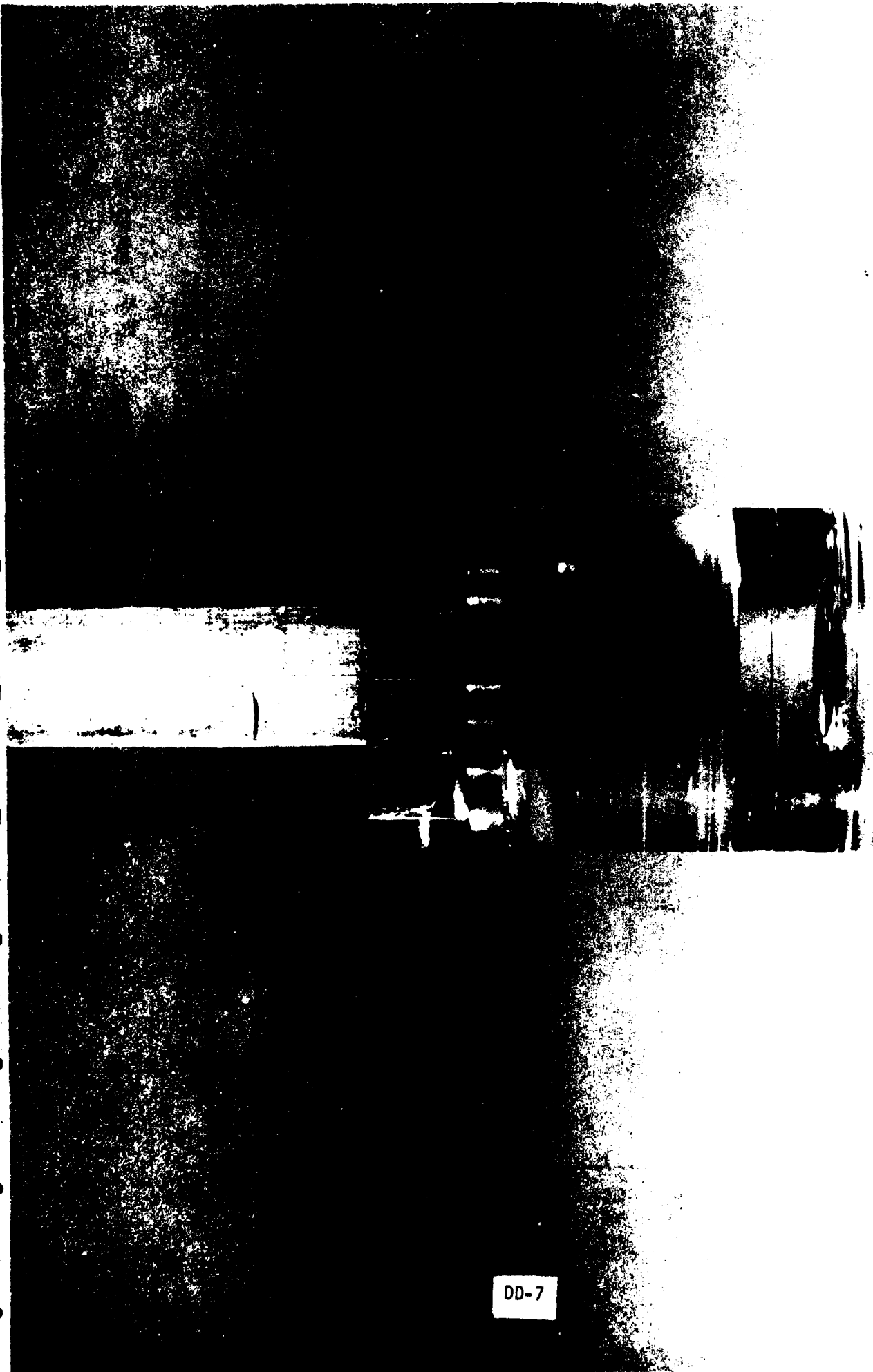


Figure 2 H.F. Bauer

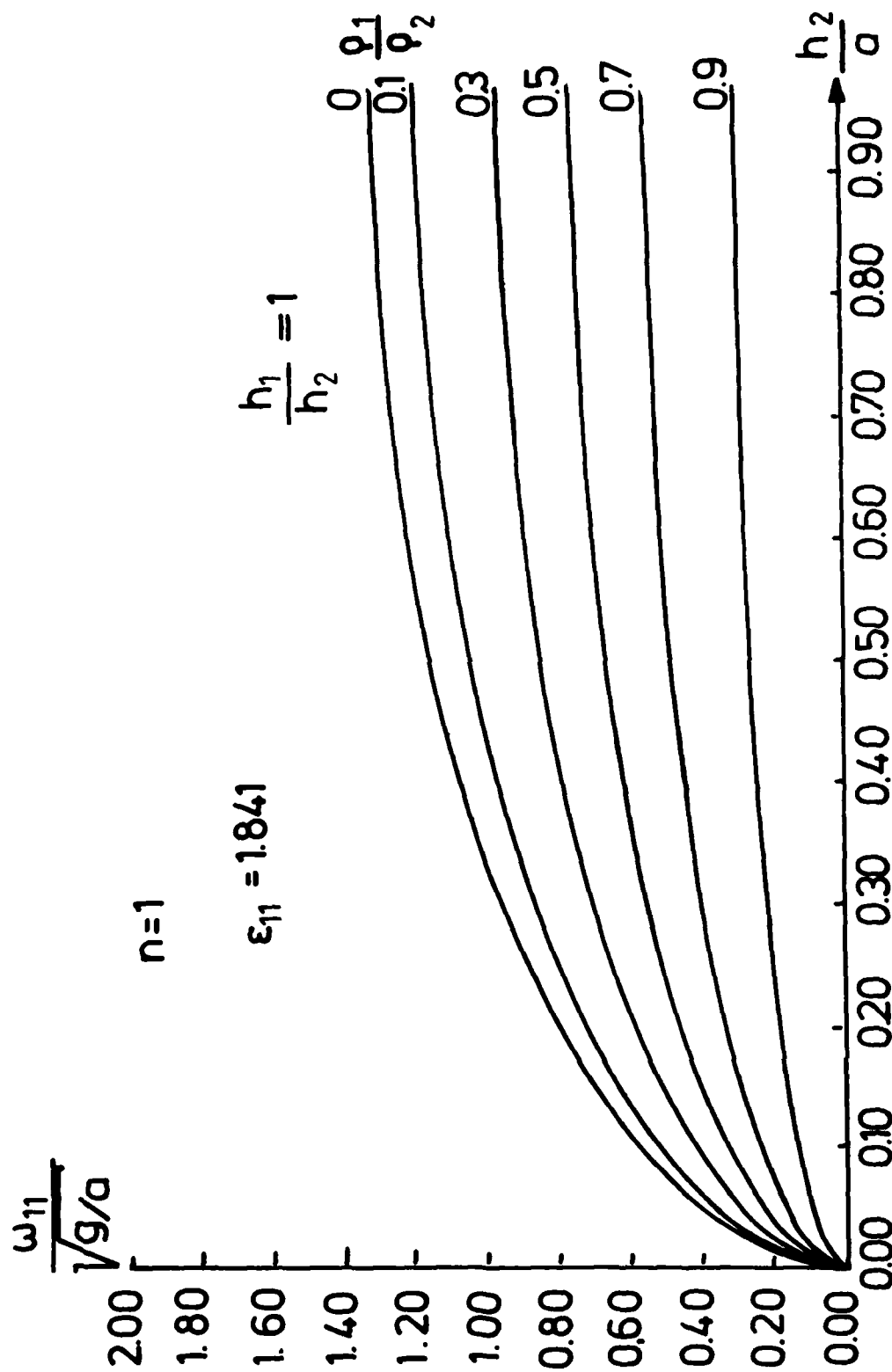


Figure 3 H.F. Bauer

Assuming for the non-sloshing mass m_0 , a moment of inertia I_0 and for the sloshing masses a motion ξ_n relative to the container results with the kinetic and potential energy

$$T = \frac{m_0}{2} (\dot{x} - h_0 \dot{\vartheta})^2 + \frac{1}{2} I_0 \dot{\vartheta}^2 + \frac{1}{2} \sum_{n=1}^{\infty} m_n (\dot{x} + \dot{\xi}_n + h_n \dot{\vartheta})^2 \quad (4)$$

$$V = \frac{1}{2} m_0 h_0 g \vartheta^2 - \frac{1}{2} g \vartheta^2 \sum_{n=1}^{\infty} m_n h_n - g \vartheta \sum_{n=1}^{\infty} m_n \xi_n + \frac{1}{2} \sum_{n=1}^{\infty} k_n \xi_n^2 \quad (5)$$

after application of the Lagrange equations for translational excitation (rotation about the angle $\vartheta=0$) in the equation

$$m \ddot{x} + \sum_{n=1}^{\infty} m_n \ddot{\xi}_n = -F_x, \quad (6)$$

the moment equation

$$\sum_{n=1}^{\infty} m_n (h_n \ddot{\xi}_n - g \xi_n) + \ddot{x} \sum_{n=1}^{\infty} (m_n h_n - m_0 h_0) = -M_y, \quad (7)$$

and the slosh equations

$$\ddot{\xi}_n + \omega_n^2 \xi_n = -\ddot{x} \quad \text{for } n=1, 2, \dots \quad (8)$$

With $r_n = \frac{\Omega}{\omega_n}$ as the frequency ratio of the forcing frequency Ω and the natural frequency ω_n and $x = x_0 e^{i\Omega t}$, the force equation of the model reads

$$F_x = -\ddot{x} [m_1 + m_2 + \sum_{n=1}^{\infty} m_n \left(\frac{r_n^2}{1 - r_n^2} \right)] \quad (9)$$

and yields by comparison with the liquid force [29] the sloshing masses

$$m_n = \left(2\pi a^3 \rho_2 \left(1 - \frac{\rho_1}{\rho_2}\right)^2 \tanh\left(\epsilon_n \frac{h_2}{a}\right) / \epsilon_n (\epsilon_n^2 - 1) \left\{ 1 + \frac{\rho_1}{\rho_2} \frac{\tanh\left(\epsilon_n \frac{h_2}{a}\right)}{\tanh\left(\epsilon_n \frac{h_1}{a}\right)} \right\} \right) \quad (10)$$

(ϵ_n are roots of $J_1'(\epsilon_n) = 0$)

for the circular cylindrical container. The moment of the model is given by

$$M_y = -\ddot{x} \left\{ -m_0 h_0 + \sum_{n=1}^{\infty} m_n h_n + \sum_{n=1}^{\infty} m_n \left(\left(h_n r_n + \frac{g}{\omega_n^2} \right) / (1 - r_n^2) \right) \right\} \quad (11)$$

The inclusion of a linear damping in the model requires with the dissipation function

$$D = \frac{1}{2} \sum_{n=1}^{\infty} c_n \dot{\xi}_n^2 = \sum_{n=1}^{\infty} m_n \omega_n \zeta_n \dot{\xi}_n^2 \quad (12)$$

the introduction of the imaginary term $2i\zeta_n \omega_n \Omega$ into the resonance terms, we

have to write instead of $(1 - r_n^2)$ the terms $[(1 - r_n^2) + 2i\zeta_n r_n]$. It may be noticed that only the basic sloshing mass $n=1$ contributes (for all engineering purposes) to the motion, since higher masses $n>1$ render only a mass, which is only less than 4% of that of the first (basic) sloshing mass. Figure 4 exhibits this basic sloshing mass as a function of the liquid height h_2/a with the density ratio ρ_1/ρ_2 as a parameter. With decreasing container height the sloshing mass decreases, while with decreasing density ratio its magnitude shows larger values. To exhibit the effectiveness of the damper on the motion of a structure, we use the simple mechanical model of a completely filled container mounted at the end of a cantilever beam performing a vibration the coupled equations of motion

$$\ddot{\eta} + g_B \omega_B \dot{\eta} + \omega_B^2 \eta + \frac{m_s}{M_B} Y_s \ddot{\xi} = 0 \quad (13)$$

$$\ddot{\xi} + 2\zeta_s \omega_s \dot{\xi} + \omega_s^2 \xi + \ddot{\eta} Y_s = 0 \quad (14)$$

where ω_B is the bending frequency, ω_s the sloshing frequency, η the generalized displacement and ξ the sloshmass displacement. ζ_s represents the slosh damping factor and g_B the structural damping, represented here as an equivalent viscous damping. Y_s is the modal displacement at the location of the sloshing mass. The characteristic equation of the above system reads

$$\left[1 - \frac{m_s}{M_B} Y_s^2 \right] s^4 + [2\zeta_s \frac{\omega_s}{\omega_B} + g_B] s^3 + \left[1 + \frac{\omega_s^2}{2} + 2\zeta_s g_B \frac{\omega_s}{\omega_B} \right] s^2 + [2\zeta_s + g_B \frac{\omega_s}{\omega_B}] \frac{\omega_s}{\omega_B} s + \frac{\omega_s^2}{\omega_B^2} = 0 \quad (15)$$

This equation has been evaluated for constant structural damping $g_B = 0.01$ in order to exhibit the influence of the various parameters upon the coupled roots $s_{\omega_B} = \sigma + i\omega$ (Fig. 5, 6). An increase of the frequency ratio ω_s/ω_B below unity yields first an increase of the coupled frequencies with enhanced stability. It also shows that the coupled bending frequency reaches for a ratio ω_s/ω_B of about 0.9 optimal stability.

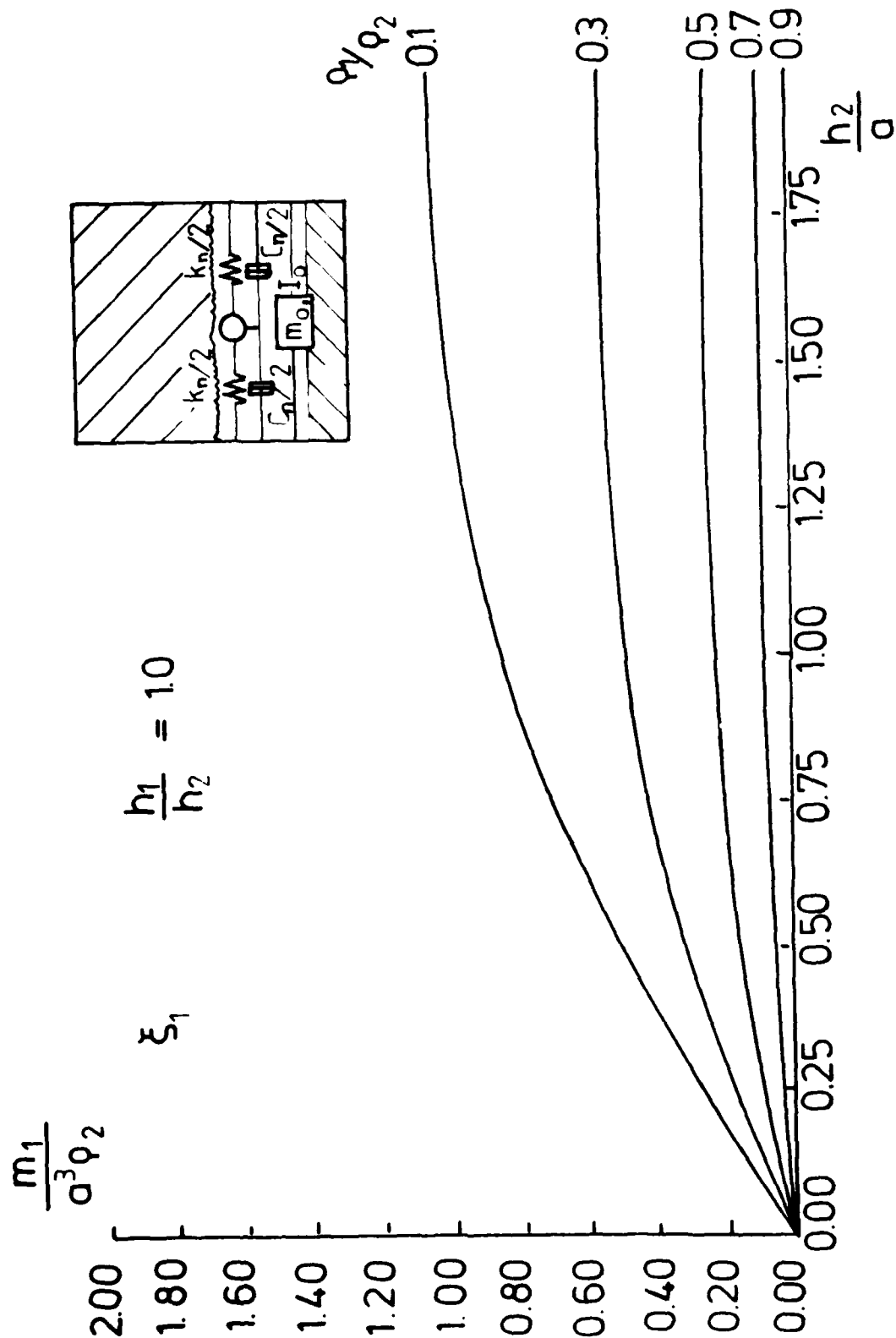


Figure 4 H.F. Bauer

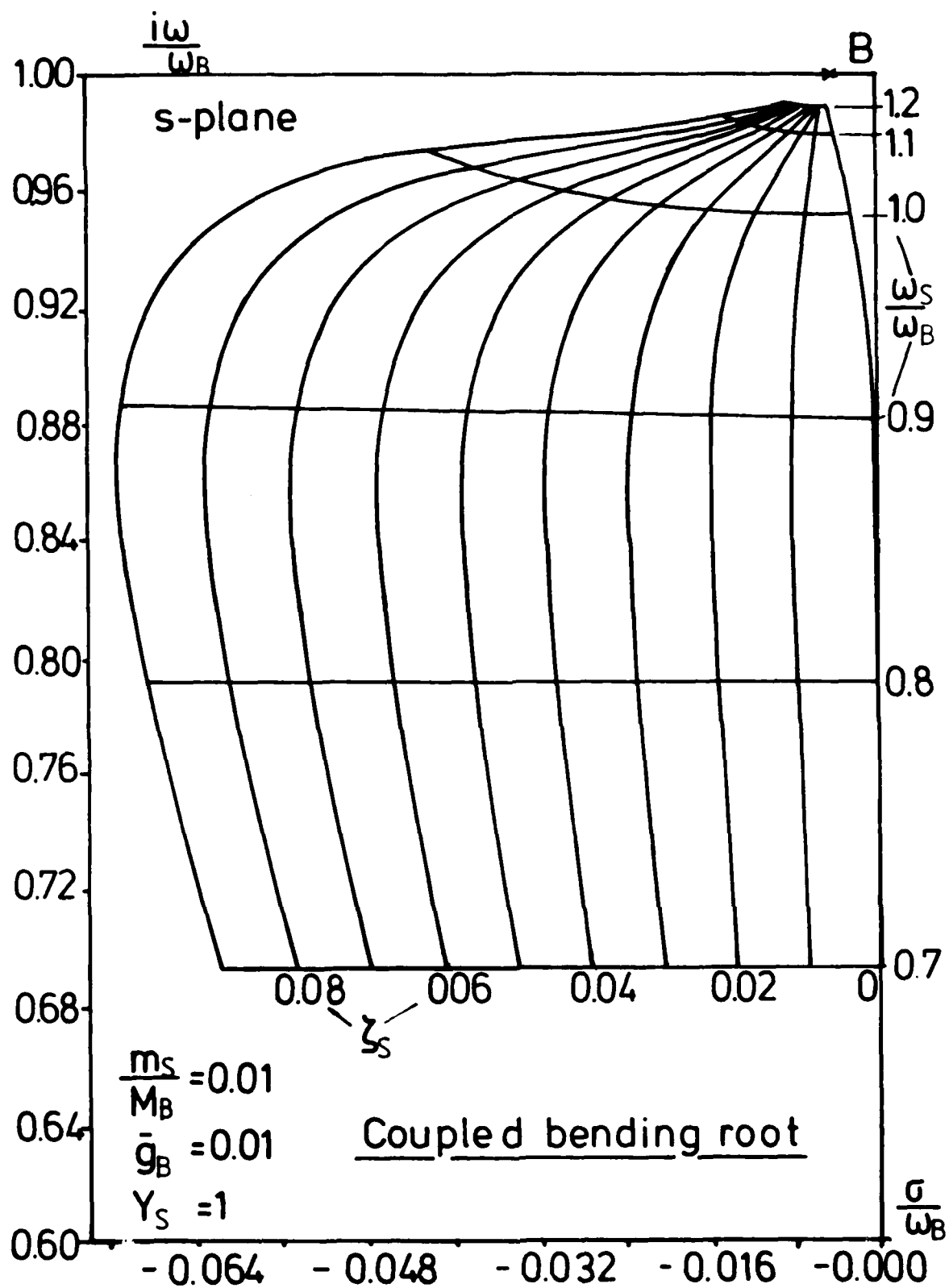


Figure 5 H.F. Bauer

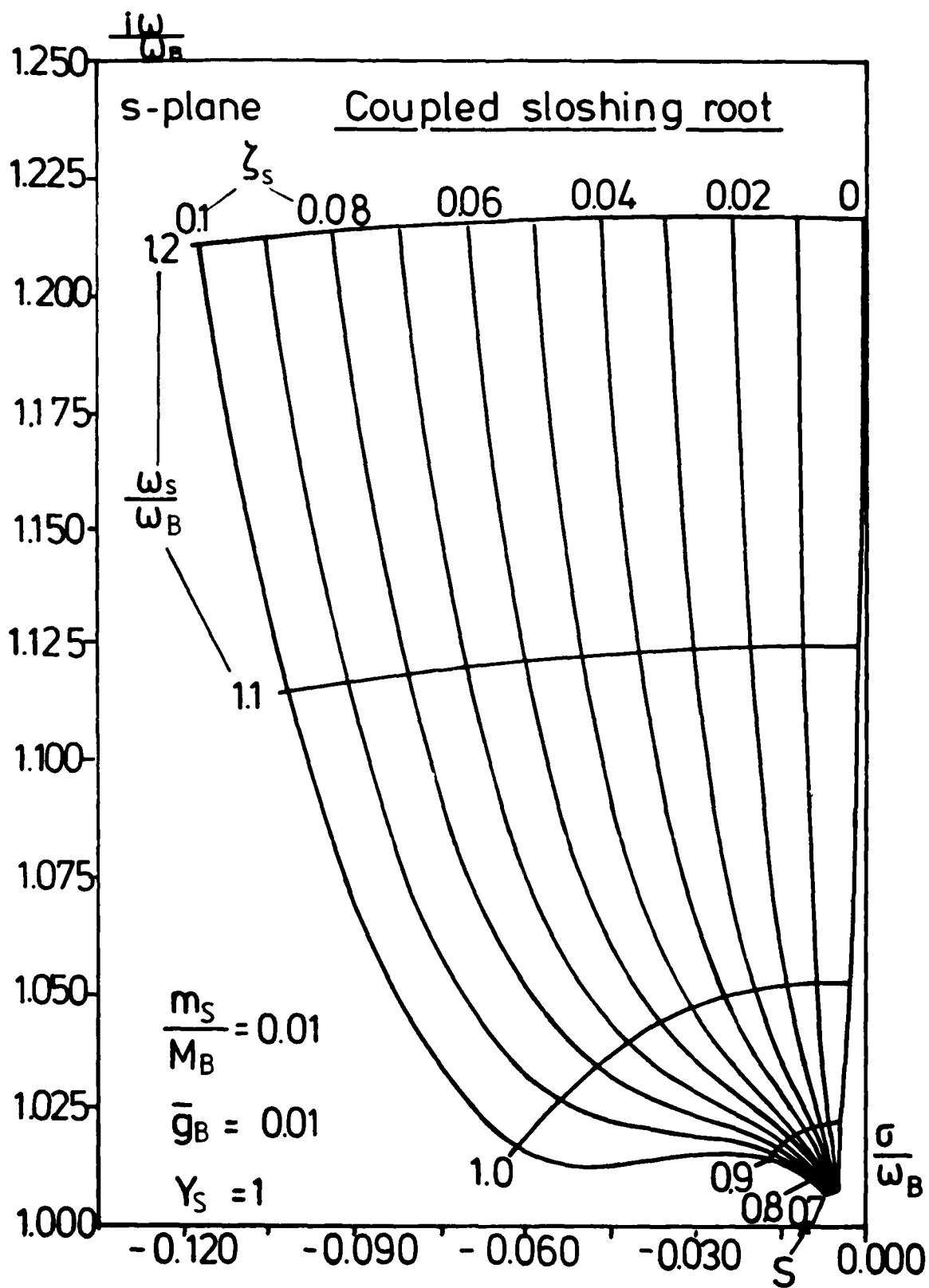


Figure 6 H.F. Bauer

The coupled sloshing frequency yields with increasing frequency ratio ω_s/ω_B larger oscillation frequency and increasing stability, i.e. a stronger decay of the oscillatory motion. The uncoupled bending- and sloshing frequencies are presented by B and S respectively. It may be noticed that for $0.7 < \omega_s/\omega_B < 1.2$ the coupled bending frequency exhibits increased stability, i.e. a stronger decay of the oscillation of the beam. For increasing ratio m_s/M_B , i.e. increased sloshing mass the oscillation frequency of the coupled bending root decreases and loses some damping effect, while the coupled sloshing root exhibits increased frequency and more damping. The maximum damping for the coupled bending root shows up at a slightly smaller frequency ratio ω_s/ω_B . The coupled bending root may be damped further by the inclusion of additional liquid damping as obtained for instance by baffles inside the container. A doubling of the liquid damping factor ζ_s yields for the bending motion of the cantilever beam a little more than twice the decay magnitude at about the same oscillation frequency (for $\omega_s/\omega_B = 0.9$). The already lowered stability of the sloshing root will be enhanced accompanied by a slight decrease of the oscillation frequency. We conclude from the above results that a cantilever beam can be made to perform a much heavier damped (decaying) motion by introducing at its end a liquid damper of proper dimensions. Thus the uncoupled frequency ratio ω_s/ω_B should be in the vicinity of 0.9 and the liquid should have sufficient damping, while the ratio of the sloshing mass m_s to the generalized mass M_B of the beam should be small. Both of those parameters may be influenced by the geometric size of the liquid damper and the density ratio ρ_1/ρ_2 of the employed liquids, thus providing an efficient means to dampen and restrict the amplitudes of a system.

4. New Proposed Active Damper

The active damper system consists of a control system, a cold-gas jet system and of an accelerometer as sensor of the motion of the structure (Fig.7). Due to the magnitude of the signal of the accelerometer one of the cold-gas jets shall yield a thrust to counteract the structure's motion. The basic equations are

$$\ddot{\eta} + g_B \omega_B \dot{\eta} + \omega_B^2 \eta = \frac{BF}{M_B} Y_F, \quad (16)$$

the bending equation

$$\frac{\ddot{A}_i}{\omega_a^2} + \frac{2\zeta_a}{\omega_a} \dot{A}_i + A_i = \ddot{\eta} Y_a, \quad (17)$$

the accelerometer equation, and

$$\beta = a_0 A_i + \left(\frac{a_1}{\omega_B}\right) \dot{A}_i \quad (18)$$

the control equation. The stability boundary is obtained from the Hurwitz determinant

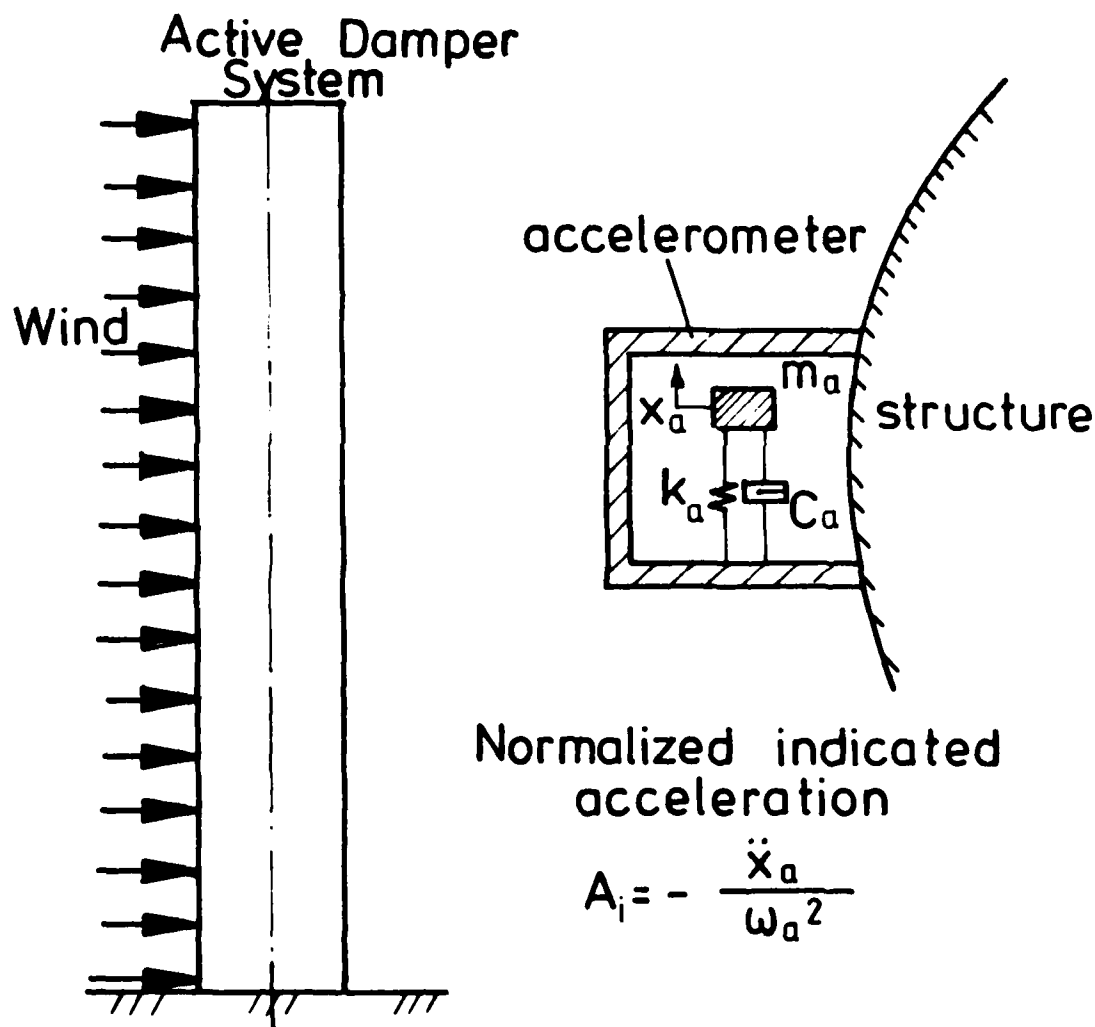
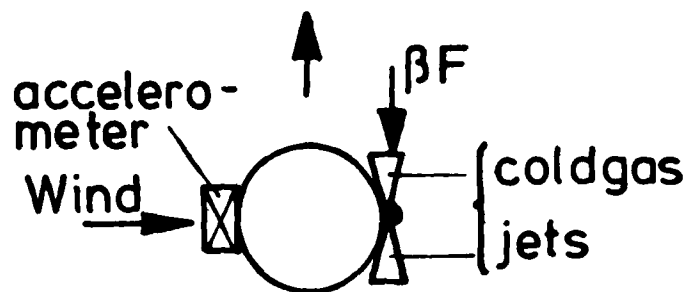


Figure 7 H.F. Bauer

$$H_3 = \begin{vmatrix} A_1 & A_3 & 0 \\ A_0 & A_2 & A_4 \\ 0 & A_1 & A_3 \end{vmatrix} = A_1 A_2 A_3 - A_1^2 A_4 - A_3^2 A_0 = 0$$

and renders the equation ($Y_a Y_F F / M_B = f$)

$$\begin{aligned} a_0 f \left(\frac{\omega_B}{\omega_a} \right) \left[g_B + 2\zeta_a \left(\frac{\omega_B}{\omega_a} \right) \right] \left[g_B \frac{\omega_B}{\omega_a} + 2\zeta_a \right] + a_1 f \left\{ \left(g_B + 2\zeta_a \frac{\omega_B}{\omega_a} \right) \left(1 + 2\zeta_a g_B \frac{\omega_B}{\omega_a} + \frac{\omega_B^2}{\omega_a^2} \right) - \right. \\ \left. - 2 \frac{\omega_B}{\omega_a} (2\zeta_a + g_B \frac{\omega_B}{\omega_a}) \right\} - a_1^2 f^2 + a_0 a_1 f^2 \left(g_B + 2\zeta_a \frac{\omega_B}{\omega_a} \right) + \left\{ \left(1 + 2\zeta_a g_B \frac{\omega_B}{\omega_a} + \frac{\omega_B^2}{\omega_a^2} \right) \left(g_B + \right. \right. \\ \left. \left. + 2\zeta_a \frac{\omega_B}{\omega_a} \right) (2\zeta_a \frac{\omega_B}{\omega_a} + g_B \frac{\omega_B^2}{\omega_a^2}) - \frac{\omega_B^2}{\omega_a^2} \left(g_B + 2\zeta_a \frac{\omega_B}{\omega_a} \right)^2 - \frac{\omega_B^2}{\omega_a^2} (2\zeta_a + g_B \frac{\omega_B}{\omega_a})^2 \right\} = 0 \end{aligned} \quad (19)$$

The stable regions for the gain values a_0 , a_1 are presented in Fig. 8 for a structural damping $g_B = 0.01$, a frequency ratio $\omega_B/\omega_a = 0.5$ and various accelerometer damping factors ζ_a . The roots in the s -plane are presented as a mesh created by the variation of the gain values $a_0 f$ and $a_1 f$ of the control system. These may be chosen freely for the particular structural system (cantilever) at hand. The coupled structural- and accelerometer roots are presented in consecutive Figures 8. For the parameters $g_B = 0.01$, $\zeta_a = 0.7$ and $\omega_B/\omega_a = 0.5$ Figure 9a represents the coupled bending root, while Figure 9b exhibits the corresponding coupled accelerometer root. All roots must, of course, be stable roots. It may be noticed that the system shows for a large range of positive $a_1 f$ -values instability in the structure, while for negative $a_1 f$ -values the structure is quite stable, but the root corresponding to the accelerometer (coupled accelerometer root) is unstable for $a_1 f < -0.52$. The value $a_0 f = a_1 f = 0$ exhibits in the cantilever only a damping of $\sigma = -0.01$ ($g_B = 0.01$) and in the accelerometer a magnitude of about $\sigma = -1.5$. To optimize the response of the system with these given parameters ζ_a , ω_B/ω_a and g_B the magnitude of $a_1 f$ should be negative, say $a_1 f = -0.7$ with $a_0 f = 0$. This would yield (see Figure 9a) maximum decay ($\sigma = -0.37$) for the cantilever structure. Unfortunately the accelerometer root is instable for this parameter configuration (see Figure 9b). If the magnitude of the accelerometer frequency is only one fifth of that of the cantilever beam ($\omega_B/\omega_a = 5$), it may be noticed that the structure exhibits after proper choice of the gain values $a_0 f$ and $a_1 f$ of the control system a damping which may be 50 to 70 times as large as without the control system. This is about 5 to 7 times larger as could be obtained by the proposed liquid damper (Fig. 10a,b).

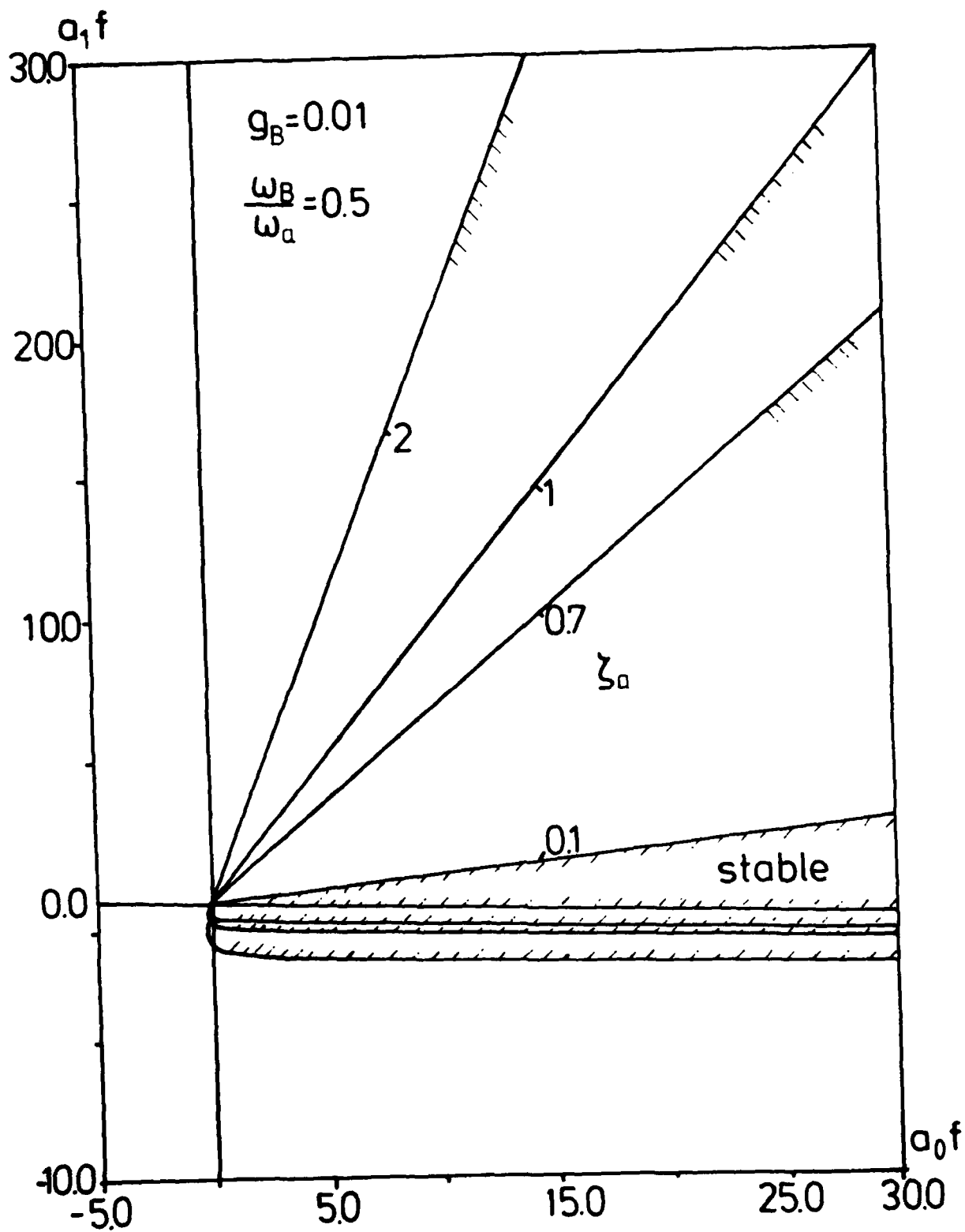


Figure 8 H.F. Bauer

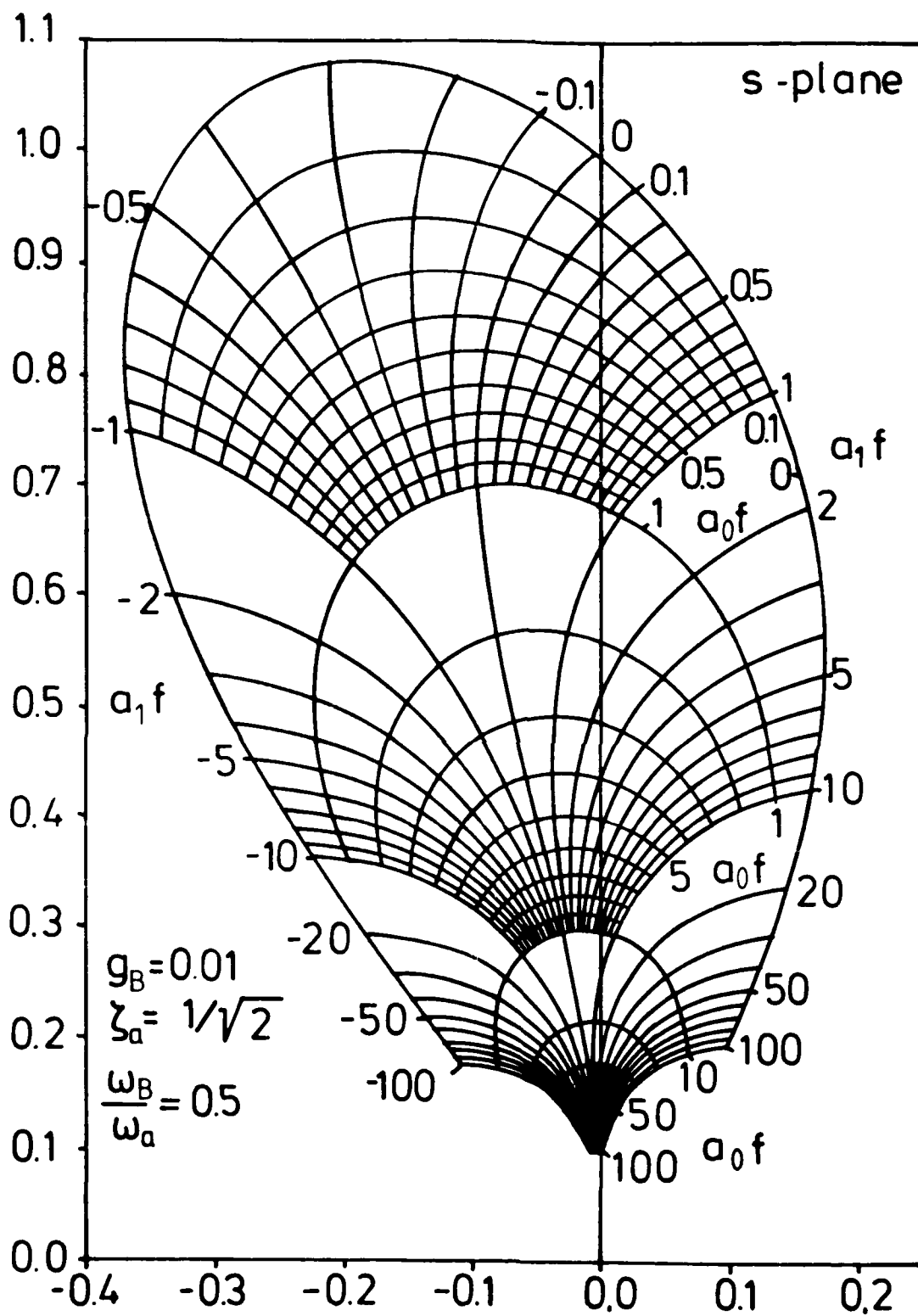


Figure 9a H.F. Bauer

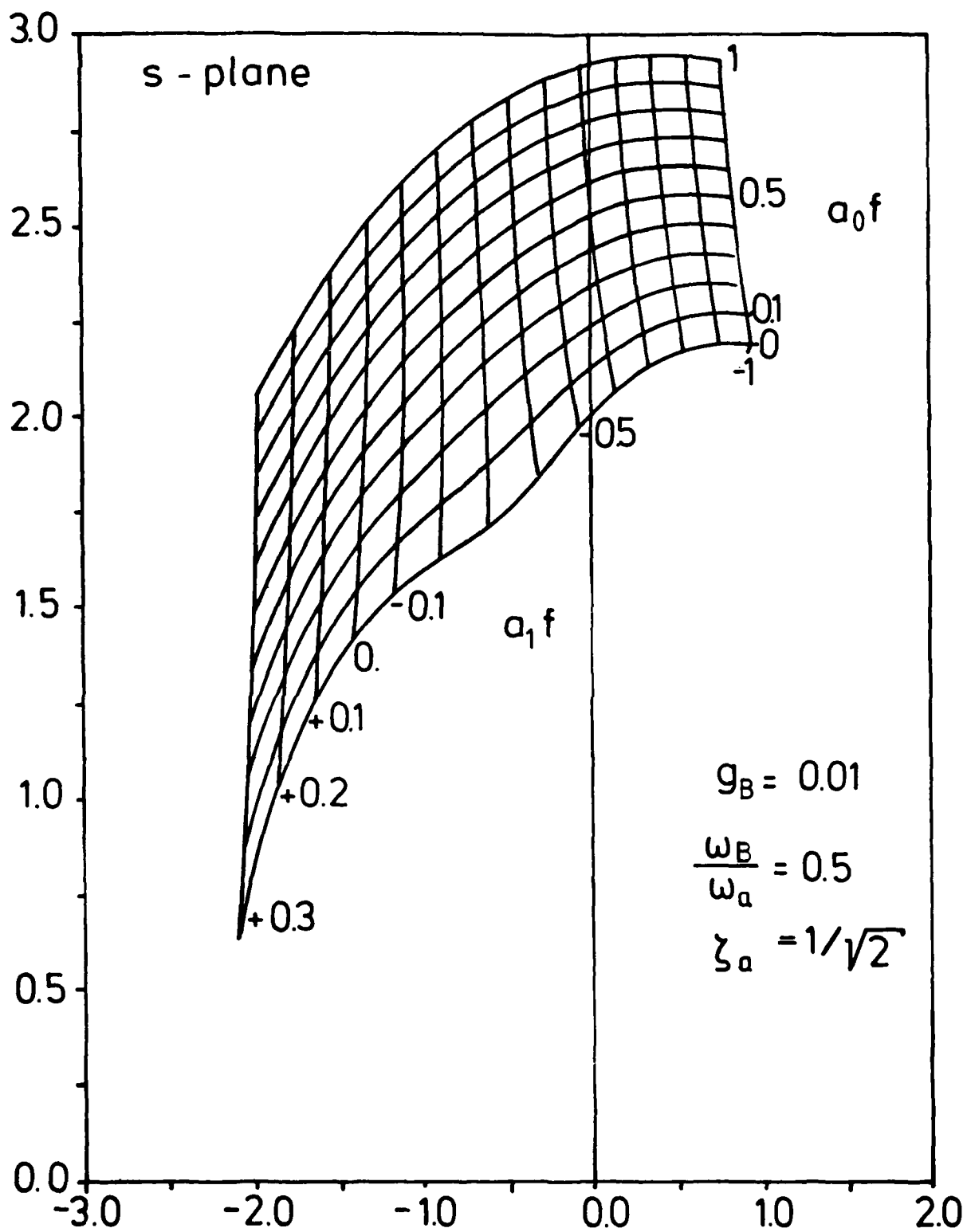


Figure 9b H.F. Bauer

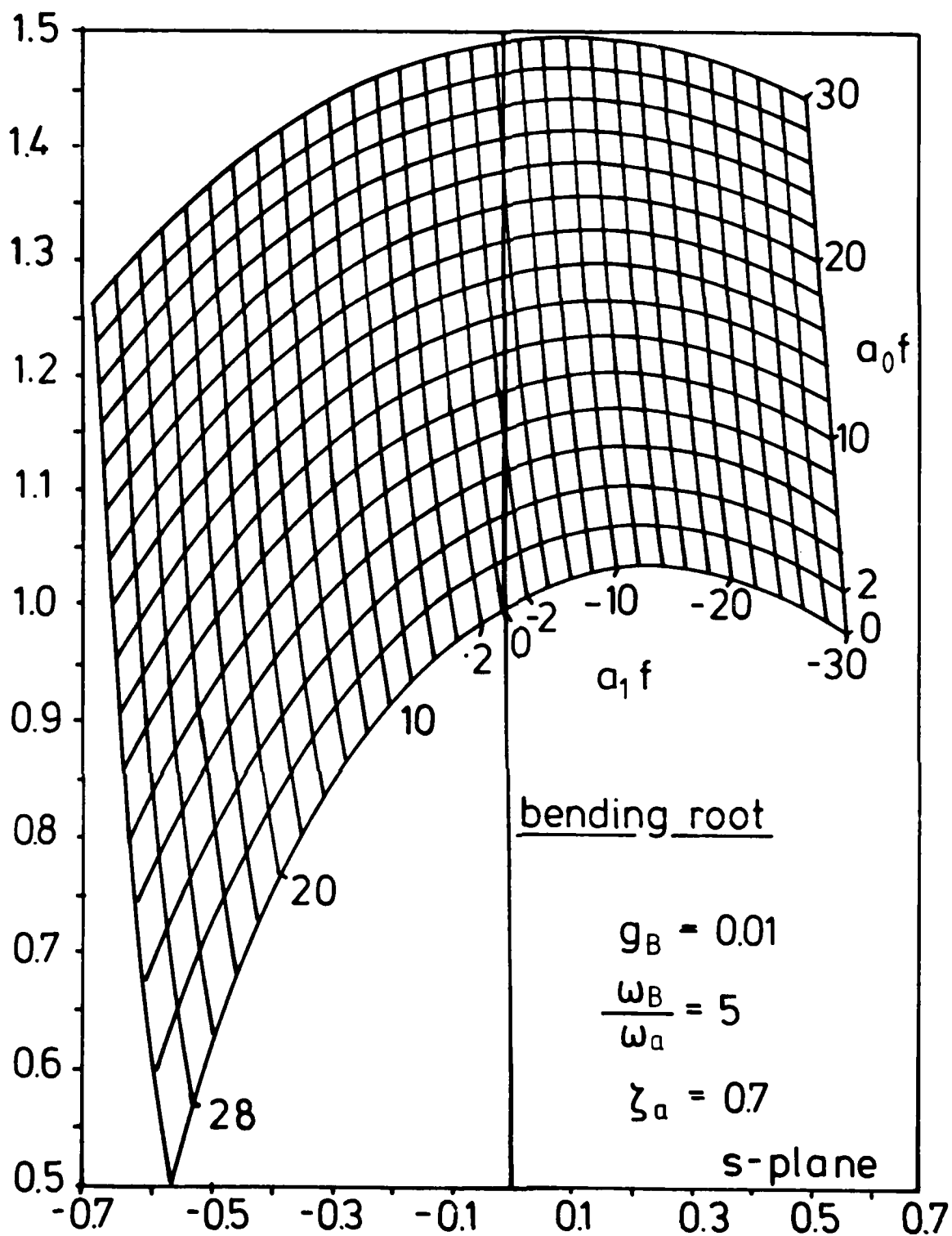


Figure 10a H. F. Bauer

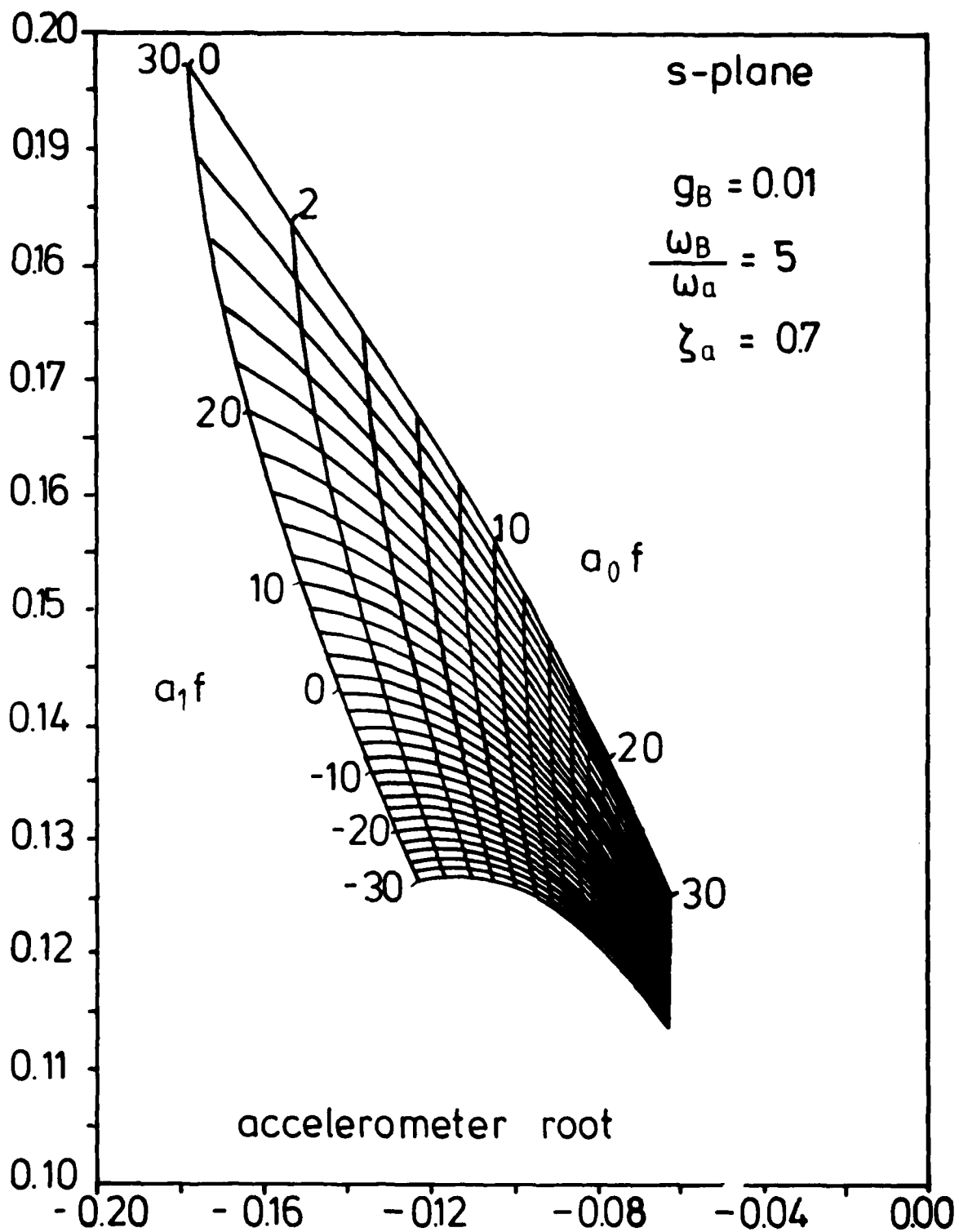


Figure 10b H.F. Bauer

5. Conclusions

In conclusion we are able to state. A liquid damper consisting of two immiscible liquids is a very effective means for damping vibrations of structures. This may be achieved by proper choice of the interface damping and the frequency ratio of the liquid-system and the structural frequency. It is preferably a passive damping system which may need no particular servicing once it is in action, and yields a damping of ten times that of the original structure without the damper. The active damping system consisting of a cold-gas-jet couple and a control system with a sensing accelerometer plus a differentiating network is an extremely effective damping system, if the magnitude of the accelerometer frequency is low compared to the structural frequency and if the damping factor of the accelerometer is large, possibly critical or supercritical. The system will damp the excited motion in an extremely small time period, 50-70 times as strong as without it .

List of Symbols

A_1	indicated acceleration
a	radius of circular cylindrical container
a_0, a_1	gain values of the control system
c_n	model damping coefficient
D	dissipation function
F	thrust of cold-gas jet system
$f = F \cdot \frac{Y_a Y_F}{M_B}$	thrust control coefficient
F_x	liquid force in x-direction
g	gravity constant
g_B	structural damping factor
h_1, h_2	liquid height of liquid 1 and 2 resp.
J_m	Besselfunction of m^{th} order and first kind
k_n	model spring stiffness
M_B	generalized mass of beam
M_Y	liquid moment about y-axis
m_1, m_2	liquid mass of liquid 1 and 2 resp.
m_s	sloshing mass
m	total liquid mass
m_0	non-sloshing mass
r, ϕ, z	polar coordinate system
$r_n = \frac{\Omega}{\omega_n}$	frequency ratio of forced to natural frequency
$s = \sigma + i\omega$	complex frequency
$S = \frac{D}{V} f_s$	Strouhal number
t	time
T	kinetic energy

V potential energy, wind speed
 x_0 excitation amplitude in x-direction
 Y mode shape (subscript "a" indicating at location of accelerometer, "s" at sloshing mass location, "F" at thrust location)
 E_{mn} zeros of $J'_m(\xi) = 0$
 E_n relative motion of sloshing mass m_n to container
 θ_0 pitch excitation amplitude
 ρ_1, ρ_2 density of liquid 1 and 2 resp.
 ζ_s, ζ_a slosh-damping factor, accelerometer damping factor
 η generalized bending displacement
 ω_{mn} natural frequencies of liquid system
 ω_s, ω_b slosh- and bending frequency resp.
 ω_a natural frequency of accelerometer

References

- [1] v. Kármán, Th.; "Über den Mechanismus des Widerstands, den ein bewegter Körper in einer Flüssigkeit erfährt", Göttinger Nachrichten, Math. Phys. Kl. (1911) pp. 509-519
- [2] Edwards, A.T. and Madeyski, A.; "Progress Report on the Investigation of Galloping", Trans. AIEE 75, (1956) pp. 666-683
- [3] Parkinson, G.V. and Brooks, N.P.H.; "On the Aeroelastic Instability of Bluff Cylinders", J. Appl. Mech. 28, (1961) pp. 252-258
- [4] Parkinson, G.V. and Smith, J.D.; "The Square Prism as an Aeroelastic Non-Linear Oscillator", Quart. J. Mech. Appl. Math. 17, (1964) pp. 225-239
- [5] Richardson, A.S., Martucelli, J.R. and Price, W.S.; "Research Study on Galloping of Electric Power Transmission Lines", in Proceedings of the First International Conference on Wind Effects on Buildings and Structures II, Teddington, England 1965, pp. 612-686
- [6] Novak, M.; "Aeroelastic Galloping of Prismatic Bodies", J. Eng. Mech. Div. ASCE 96 (1969) pp. 115-142
- [7] Novak, M.; "Galloping and Vortex Induced Oscillations of Structures", in Proceedings of the Third International Conference on Wind Effects on Buildings and Structures, Tokyo, Japan (1971), Paper IV - 16, p. 11
- [8] Novak, M. and Tanska, H.; "Effect of Turbulence on Galloping Instability", J. Eng. Mech. Div. ASCE 100, (1974) pp. 27-47
- [9] Blevins, R.D. and Iwan, W.D.; "The Galloping Response of a Two-Degree-of-Freedom System", J. Appl. Mech. 41, (1974) pp. 1113-1118
- [10] Walsh, D.E. and Woolton, L.R.; "Preventing Wind Induced Oscillations of Structures of Circular Section", Proc. Inst. Civil Engrs. (London) 1970
- [11] Scanlan, R.H. and Wardlaw, R.L.; "Reduction of Flow Induced Structural Vibrations", in Isolation of Mechanical Vibration, Impact and Noise, Snowdon and Ungar (eds.), American Society of Mechanical Engineers, New York, 1973
- [12] Funakawa, M.; "Vibration of Tube Banks by Wake Force", Symposium on Flow Induced Vibrations in Heat Exchangers Held in Keswick, England, April 1973
- [13] Kunert, K.; "Schwingungen schlanker Stützen im konstanten Luftstrom", Bauingenieur 37, (1962), 168-173

- [14] Novák, M.; "Über winderegte Querschwingungen der Ständer der Bogenbrücke über die Moldau", *Der Stahlbau* 37 (1968), 340-346
- [15] Bounner, A.; "Amortisseur d'Oscillations hydraulique pour cheminées", *Société Hydrotechnique de France. VIII umes Journées de Hydraulique (Lille, 1964), Quest III, Rapp. 5, 1-8, 1964*
- [16] Roshko, A.; "On the Drag and Shedding Frequency of Two-Dimensional Bluff Bodies", *NACA-TN-3169* (July 1954)
- [17] Fung, Y.C.; "An Introduction to the Theory of Aeroelasticity", *John Wiley and Sons, Inc., New York 1955*
- [18] Toebes, G.H. and Eagleson, P.S.; "Hydroelastic Vibrations of Flat Plates Related to Trailing Edge Geometry", *J. Basic Eng.* 83, (1961) pp. 671-678
- [19] Wardlaw, R.L.; "On Relating Two-Dimensional Bluff Body Potential Flow to the Periodic Vortex Wake", *DME/NAE Quarterly Bulletin* (1966)
- [20] Vickery, B.J.; "Fluctuating Lift and Drag on a long Cylinder of Square Cross-Section", *J. Fluid Mech.* 25 (1966) pp. 481
- [21] Jones, G.W., Cincotta, J.J. and Walker, R.W.; "Aerodynamic Forces on a Stationary Oscillating Circular Cylinder at High Reynolds Numbers", *NASA-TR-R-300*, (Febr. 1969)
- [22] Nakaguchi, H., Hashimoto, K. and Muto, S.; "An Experimental Study in Aerodynamic Drag of Rectangular Cylinders", *J. Japan Soc. Aero and Space Sciences* 16, (1968) pp. 168
- [23] Bearman, P.W. and Trueman, D.W.; "An Investigation of the Flow around Rectangular Cylinders", *Imperial College Aero Report 71-15* (1971)
- [24] Bostock, B.R. and Mair, W.A.; "Pressure Distributions and Forces on Rectangular and D-shaped Cylinders", *Aero Quarterly*, 1-6 (Febr. 1972)
- [25] Mujumdar, A.S. and Douglas, W.J.M.; "Vortex Shedding from Slender Cylinders of Various Cross-Sections", *J. Fluids Eng.* 95, 1973, pp. 474-476
- [26] Fitz-Hugh, J.S.; "Flow Induced Vibration in Heat Exchangers", *Oxford University Report RS 57 (AERE-PF 238)* (Jan. 1973)

- [27] Zdravkovich, M.M. and Nuttall, J.A.; "On the Elimination of Aerodynamic Noise in a Staggered Tube Bank", J. Sound and Vibration 34, (1974), pp. 173-177
- [28] Task Committee on Wind Forces; "Wind Forces on Structures", Trans. Am. Soc. Civil Engrs. 126, (1961) pp. 1124-1198
- [29] Bauer, H.F.; "Schwingungen nichtmischbarer Flüssigkeiten mit Anwendung auf einen neuen Dämpfer für Satellitenausleger", Ingenieur-Archiv 49, (1980), pp. 119-136

EXTENSIONS OF THE RITZ-GALERKIN METHOD FOR THE FORCED,
DAMPED VIBRATIONS OF STRUCTURAL ELEMENTS

A. W. Leissa, Professor and
T. H. Young, Graduate Student
Department of Engineering Mechanics
Ohio State University
Columbus, Ohio

EXTENSIONS OF THE RITZ-GALERKIN METHOD FOR THE FORCED,
DAMPED VIBRATIONS OF STRUCTURAL ELEMENTS

of

A.W. Leissa, Professor
T.H. Young, Graduate Student

Department of Engineering Mechanics
Ohio State University
Columbus, Ohio

ABSTRACT

The classical method for analyzing the forced vibrations of structural elements such as beams, plates and shells is to express the displacements as superpositions of the responses of the free vibration modes. This is only possible for those relatively few problems where exact eigenfunction solutions exist, and often only with considerable difficulty. Ritz-Galerkin methods are widely used to obtain approximate solutions for free undamped, vibration problems. The present paper demonstrates how these same methods may be used straightforwardly to analyze forced vibrations with damping. This is done directly without requiring the free vibration eigenfunctions.

The Galerkin method has been shown previously to be an effective technique for these types of problems. The Ritz method has the further advantage of not needing to satisfy the force-type boundary conditions, which is particularly important for plates and shells. But proper functionals representing the forcing and damping terms must be developed, and this is done in the present work.

The present paper considers two types of damping--viscous and material (hysteretic). Both distributed and concentrated exciting forces are treated. Numerical results are obtained for cantilevered beams and rectangular plates. Studies showing the rates of convergence of the solutions are made. In the case of the cantilever beam, approximate solutions from the present methods are compared with the exact solutions.

I. INTRODUCTION

The Rayleigh-Ritz methods are probably the best known and most widely used methods for analyzing the free, undamped vibrations of more complicated structural elements, such as beams (e.g., variable thickness), plates and shells. The Rayleigh method, which has been in existence for over a century [1], takes advantage of the fact that a system vibrating in one of its normal modes, interchanges its energy completely between potential and kinetic forms. That is, the maximum potential energy (V_{\max}) equals the maximum kinetic energy (T_{\max}) which occurs in a cycle of vibration. Assuming a trial function for the mode shape, one which satisfies at least the geometric boundary conditions of the structural element, and assuming simple harmonic motion, setting T_{\max} equal to V_{\max} yields the vibration frequency. Unless one is fortunate enough to have assumed the exact eigenfunction (i.e., mode shape) of free vibration for the trial function, the resulting frequency is too high, and is consequently an upper bound on the exact solution.

In 1908 Ritz [2] improved upon the Rayleigh procedure by assuming a set of admissible trial functions, each having independent amplitude coefficients. He was able to show that a closest upper bound for the frequency could be achieved by minimizing the functional $T_{\max} - V_{\max}$ with respect to the coefficients. Indeed, he applied this method to the completely free square plate [2] for which no exact solution is possible. Since then literally hundreds of references may be found which apply the method to free vibration problems (cf. [3,4]). In some cases such as shells, an exact solution may exist, but it is so complicated to use that a Ritz procedure may be employed more easily to obtain accurate results (e.g., [5-9]). But in most cases no exact solution exists, and an approximate, properly convergent technique such as the Ritz method becomes essential.

The classical method for solving forced vibration problems for structural elements is to expand both the forcing function and the displacement response in terms of the free vibration eigenfunctions. This requires first solving the free vibration problem and finding an orthogonal set of eigenfunctions. Further, the forced vibration response typically requires the tedious (and computationally expensive) evaluation of integrals of products of the eigenfunctions with themselves and the loading functions. If the eigenfunctions are complicated (for example, combinations of the regular and modified Bessel functions in the case of a circular plate) the integrals may have to be evaluated numerically. In many cases (e.g., beams) large roundoff errors are easily generated during the procedure.

It can be shown that the method of Galerkin [10] is equivalent to the Ritz method, and is some ways more general (it may be applied even when no energy functionals exist for the problem). This equivalent method has also been frequently used to analyze the free vibrations of structural elements such as beams, plates and shells (cf., [3,4]). Several years ago a method of applying the Galerkin method to forced vibration problems of continuous systems having viscous damping was demonstrated [11,12]. The method is a direct one; that is, the forced response is found without first having to solve for the free vibration eigenfunctions. The method was demonstrated for the one-dimensional, second order differential equation of the vibrating

string, and the two-dimensional, fourth order differential equation of the vibrating plate.

However, the Galerkin method has one disadvantage in comparison with the Ritz method. Both methods require satisfaction of only the geometric boundary conditions. However, if the force-type boundary conditions are not also satisfied, the Galerkin method requires the use of additional terms. For a plate having free edges, for example, these additional terms consist of two line integrals taken along each free edge which must be added to the orthogonalizing integrals. In the case of a shell, four line integrals would have to be added for each free edge. Thus for a cantilevered plate or shell of rectangular planform, the Galerkin method becomes quite cumbersome.

The Ritz method has been demonstrated in recent years to be an efficient, accurate technique for the analysis of free vibrations of cantilevered shells having rectangular planform [13-16]. Such configurations may be used for turbomachinery blade vibration studies. The method is particularly useful for preliminary design stages, or for making parameter studies, where finite element methods have been found to be very costly and unreliable.

The present paper summarizes recent research in extending the Ritz method to forced vibration problems where damping is present. This eliminates the aforementioned disadvantages of the Galerkin method when free edges are encountered. The crux of the problem is to find a dissipation functional accounting for the damping forces which are 90 degrees out of phase with the exciting, restoring and inertia forces of the system, which may be added to the kinetic, strain and load potential energies in a suitable manner to give the correct solution. The extension is demonstrated in the present work for systems having either viscous or material damping, distributed or concentrated exciting forces, and one-dimensional (beam) or two-dimensional (plate) structural elements. The convergence of the extended method to exact solutions is demonstrated for a set of cantilever beam problems. A similar method was developed by Siu and Bert [17] for laminated composite plates having material damping, subjected to distributed forcing pressure.

II. BEAM ANALYSIS - VISCOUS DAMPING

2.1 Distributed Forcing Function

Consider first a beam of length ℓ subjected to a distributed transverse load \bar{q} (force/unit length) which varies sinusoidally with time,

$$\bar{q}(x,t) = q(x)e^{i\Omega t} \quad (2.1)$$

where Ω is the forcing frequency and x is the coordinate measured along the length. The kinetic energy during vibratory motion is

$$T = \frac{1}{2} \int_0^{\ell} \rho A \left(\frac{\partial w}{\partial t} \right)^2 dx \quad (2.2)$$

where w is the transverse displacement, ρ is the mass per unit length and A is the cross-sectional area. The strain energy of the beam due to bending deformation is

$$V = \frac{1}{2} \int_0^l EI \left(\frac{\partial^2 w}{\partial x^2} \right)^2 dx \quad (2.3)$$

where E is the modulus of elasticity and I is the second moment of the cross-sectional area with respect to the neutral axis of bending.

Define a dissipation functional \mathcal{D} by

$$\mathcal{D} = \frac{1}{2} \int_0^l c \frac{\partial w}{\partial t} w dx \quad (2.4)$$

where c is the viscous damping coefficient. It should be noted that \mathcal{D} differs from the well-known dissipation function of Rayleigh [1]. The work done by the exciting force is

$$\mathcal{W} = \int_0^l \bar{q} w dx \quad (2.5)$$

To apply the Ritz method, assume that the vibratory displacement $w(x,t)$ may be expressed as

$$w(x,t) = W(x) e^{i\Omega t} \quad (2.6)$$

$$= \sum_{j=1}^J C_j \phi_j(x) e^{i\Omega t} \quad (2.7)$$

where the $\phi_j(x)$ are trial functions which satisfy at least the geometric boundary conditions (zero displacement and/or zero slope) which exist for the beam, and the C_j are complex coefficients which may be separated into real and imaginary parts as

$$C_j = C_j^R - iC_j^I \quad (2.8)$$

where $i = \sqrt{-1}$. The real part (C_j^R) may be regarded as the vector component of the response in phase with the exciting force, and the imaginary part (C_j^I) is the response component which lags the exciting force by 90 degrees.

Define further a generalization of the functional $T_{\max} - V_{\max}$ used in free, undamped vibration analysis by the Ritz method. That is, let

$$L_{\max} = (T_{\max} - \mathcal{D}_{\max}) - (V_{\max} - \mathcal{W}_{\max}) \quad (2.9)$$

where the separate terms on the right-hand-side of Eq.(2.9) are the maximum values of the functionals previously given by Eqs.(2.2) through (2.5), obtained by substituting Eq.(2.6) into them and setting $|e^{2i\Omega t}| = 1$. That is,

$$T_{\max} = \frac{\Omega^2}{2} \int_0^l \rho A W^2 dx \quad (2.10a)$$

AD-A152 547

VIBRATION DAMPING WORKSHOP PROCEEDINGS HELD AT LONG

BEACH CALIFORNIA ON 2... (U) AIR FORCE WRIGHT

AERONAUTICAL LABS WRIGHT-PATTERSON AFB OH L ROGERS

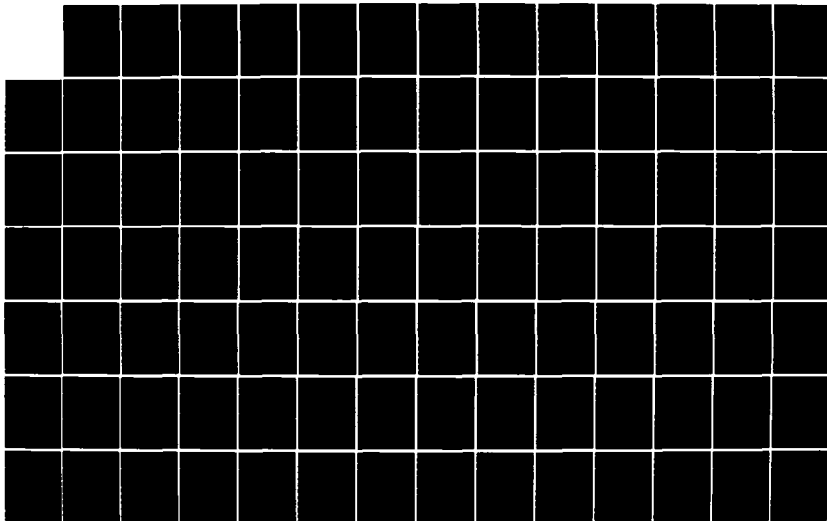
UNCLASSIFIED

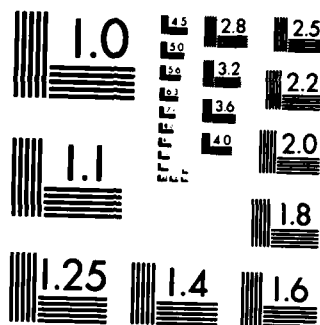
11 NOV 84 AFMAL-TR-84-3064

F/G 20/11

NL

6/11





MICROCOPY RESOLUTION TEST CHART
NATIONAL BUREAU OF STANDARDS-1963 A

$$V_{\max} = \frac{1}{2} \int_0^{\ell} EI \left(\frac{d^2 w}{dx^2} \right)^2 dx \quad (2.10b)$$

$$D_{\max} = \frac{i\Omega}{2} \int_0^{\ell} c w^2 dx \quad (2.10c)$$

$$W_{\max} = \int_0^{\ell} q w dx \quad (2.10d)$$

The Ritz method is applied by substituting Eq. (7) into Eqs. (2.10) and by using the minimizing equations

$$\frac{\partial L_{\max}}{\partial C_j} = 0 \quad (j=1,2,\dots,J) \quad (2.11)$$

which results in a set of J linear simultaneous equations in the unknown coefficients C_j . Setting the real and imaginary parts of each equation equal to zero yields a set of $2J$ equations in the unknowns C_j^R and C_j^I , with coupling between the C_j^R and the C_j^I coefficients arising from the damping. The right-hand sides of the equations evolve from the forcing function (q). Solution of this set of equations completely determines the forced, damped response.

2.2 Example. Cantilever Beam with Uniform Pressure

Consider the uniform, homogeneous, cantilever beam of length ℓ clamped at the end $x=0$ and free at the end $x=\ell$ (see Fig. 1), subjected to a uniformly distributed pressure

$$q(x,t) = q_0 e^{i\Omega t} \quad (2.12)$$

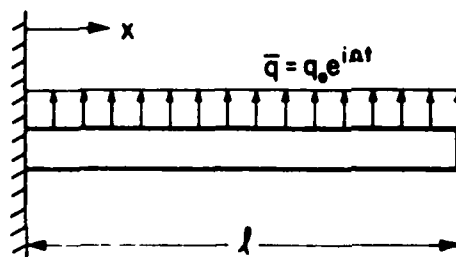


Figure 1. Cantilever beam with uniformly distributed forcing pressure.

where q_0 is a constant. Let the trial functions ϕ_j to be used in Eq.(2.7) be expressed as simple algebraic polynomials,

$$\phi_j(x) = x^j \quad (j=2,3,\dots,J) \quad (2.13)$$

which, by beginning with $j=2$, guarantees that the boundary conditions at the clamped edge

$$w(0,t) = \frac{\partial w}{\partial x}(0,t) = 0 \quad (2.14)$$

are satisfied exactly. Substituting Eqs.(2.12) and (2.13) into Eqs.(2.7), (2.9) and (2.10), carrying out the minimization indicated by Eqs.(2.11) and the necessary integrations over x , and separating the real and imaginary parts, yields the following set of equations:

$$\sum_{j=2} \left\{ \left[\frac{EI}{\ell^4} \frac{j(j-1)k(k-1)}{j+k-3} - \frac{\rho A \Omega^2}{j+k+1} \right] C_j^R + \left[\frac{c\Omega}{j+k+1} \right] C_j^I \right\} = \frac{q_0}{k+1} \quad (2.15a)$$

$$\sum_{j=2} \left\{ - \left[\frac{c\Omega}{j+k+1} \right] C_j^R + \left[\frac{EI}{\ell^4} \frac{j(j-1)k(k-1)}{j+k-3} - \frac{\rho A \Omega^2}{j+k+1} \right] C_j^I \right\} = 0 \quad (k=2,3,\dots,J) \quad (2.15b)$$

These $2(J-1)$ equations may be solved for the $2(J-1)$ unknowns C_j^R and C_j^I . The Galerkin method [11,12] was applied in the present work for purposes of comparison, and yielded Eqs.(2.15) identically.

The response of the beam at a typical point may now be obtained by adding the in-phase and out-of-phase components separately, and combining them vectorially. That is,

$$w(x,t) = \bar{w}(x) e^{i(\Omega t - \phi)} \quad (2.16)$$

with the amplitude of the response given by

$$\bar{w}(x) = \sqrt{\left[\sum_{j=2}^J C_j^R \phi_j(x) \right]^2 + \left[\sum_{j=2}^J C_j^I \phi_j(x) \right]^2} \quad (2.17)$$

and the phase angle lag by

$$\phi(x) = \tan^{-1} \frac{\sum_{j=2}^J C_j^I \phi_j(x)}{\sum_{j=2}^J C_j^R \phi_j(x)} \quad (\text{in radians}) \quad (2.18)$$

2.3 Exact Solution of the Previous Problem

The preceding problem of the cantilever beam subjected to uniformly distributed, sinusoidally oscillating exciting pressure has an exact solution. The equation of motion for the problem is

$$EI \frac{\partial^4 w}{\partial x^4} + \rho A \frac{\partial^2 w}{\partial t^2} + c \frac{\partial w}{\partial t} = q(x) e^{i\Omega t} \quad (2.19)$$

Assume a solution to Eq.(2.19) in the form

$$w(x,t) = \sum_{m=1}^{\infty} X_m(x) T_m(t) \quad (2.20)$$

where $X_m(x)$ is a typical eigenfunction of the free, undamped vibration problem. That is,

$$X_m(x) = \cosh \alpha_m \xi - \cos \alpha_m \xi - \gamma_m (\sinh \alpha_m \xi - \sin \alpha_m \xi) \quad (2.21)$$

where $\xi = x/l$ and $\alpha_m l$ is the nondimensional frequency parameter given by

$$(\alpha_m l)^2 = \omega_m l^2 \sqrt{\frac{\rho A}{EI}} \quad (2.22)$$

which are the eigenvalues of the equation

$$\cos \alpha_m l \cdot \cosh \alpha_m l = -1 \quad (2.23)$$

The coefficient γ_m is determined from

$$\gamma_m = \frac{\cosh \alpha_m l + \cos \alpha_m l}{\sin \alpha_m l + \sinh \alpha_m l} \quad (2.24)$$

Values of $\alpha_m l$ and γ_m are given in Table 1.

Substituting Eq.(2.20) into Eq.(2.19), multiplying through by a typical eigenfunction χ_n , integrating over the length, using the orthogonality relationships

$$\int_0^l \chi_m \chi_n dx = 0 = \int_0^l \frac{d^4 \chi_m}{dx^4} \chi_n dx \quad (2.25)$$

(when $m \neq n$) and the equation of motion for free vibrations

$$EI \frac{d^4 \chi_m}{dx^4} - \rho A \omega_m^2 \chi_m = 0 \quad (m=1, 2, \dots) \quad (2.26)$$

Table 1. Eigenfunction parameters for clamped-free beams.

m	$\alpha_m \ell$	γ_m
1	1.8751041	0.7340955
2	4.6940911	1.01846644
3	7.8547574	0.99922450
4	10.9955407	1.00003355
5	14.1371684	0.99999855
...
∞	$(2m-1)\pi/2$	1

yields the equation for the response of the mth mode:

$$\rho A \ddot{T}_m + c \dot{T}_m + \rho A \omega_m^2 T_m = q_m e^{i\Omega t} \quad (2.27)$$

where the dots represent time derivatives, and where

$$q_m = \frac{\int_0^\ell q_0 \chi_m dx}{\int_0^\ell \chi_m^2 dx} \quad (m=1,2,\dots) \quad (2.28)$$

The solution to Eq.(2.27) is

$$T_m(t) = (A_m - iB_m) e^{i\Omega t} \quad (m=1,2,\dots) \quad (2.29)$$

where A_m and B_m are given in nondimensional form as

$$\begin{aligned} A_m &= \frac{\delta_m}{\Delta} \left(1 - \frac{\Omega^2}{\omega_m^2} \right) \\ B_m &= \frac{\delta_m}{\Delta} \left(2 \frac{c}{c_{cm}} \frac{\Omega}{\omega_m} \right)^2 \\ \Delta &= \left(1 - \frac{\Omega^2}{\omega_m^2} \right)^2 + \left(2 \frac{c}{c_{cm}} \frac{\Omega}{\omega_m} \right)^2 \end{aligned} \quad (2.30)$$

Here δ_m is the static amplitude of the mth mode (i.e., A_m when $\Omega/\omega_m=0$) and c_{cm} is the critical damping constant of the mth mode. In detail,

$$\delta_m = \frac{q_m}{\rho A \omega_m^2}, \quad c_{cm} = 2\rho A \omega_m \quad (2.31)$$

The total response at a typical point on the beam is given by

$$w(x,t) = C e^{i(\Omega t - \phi)} \quad (2.32)$$

$$\text{where } C^2 = \left[\sum_{m=1}^{\infty} A_m \chi_m(x) \right]^2 + \left[\sum_{m=1}^{\infty} B_m \chi_m(x) \right]^2 \quad (2.33)$$

$$\text{and } \phi = \tan^{-1} \frac{\sum_{m=1}^{\infty} B_m \chi_m(x)}{\sum_{m=1}^{\infty} A_m \chi_m(x)} \quad (\text{in radians}) \quad (2.34)$$

It is observed that C and ϕ are both functions of x .

The classical solution procedure shown above is exact in that explicit expressions for responses of the free vibration modes (i.e., Eqs.(2.30)) may be written, even though the total response requires infinite summations of terms. The crux of the problem is the evaluation of the integrals of Eq.(2.28). For this purpose the tables calculated by Young and Felgar [18] are useful.

2.4 Numerical Results for the Uniform Pressure Loading

Table 2 presents numerical results for the amplitude response C/δ_0 of a cantilever beam subjected to uniform pressure varying sinusoidally with time, where δ_0 is the static displacement ($\Omega=0$) of the point considered. In this case the viscous damping is small ($c/c_{c1}=0.01$), and response at the free end ($x=l$) is evaluated. The frequency ratio (Ω/ω_1) is varied from 0 to 2, and data are given also for excitation at the second and third natural frequencies ($\Omega/\omega_1 = 6.267$ and 17.547). Solutions using the Ritz method are obtained using 2, 4 and 7 polynomial terms of the type given by Eq.(2.13), yielding 4, 8 and 14 simultaneous equations from Eqs.(2.15). Comparison is made with the results of the exact solution, described in Section 2.3.

It was found that, to at least five significant figure accuracy, the exact solution is the same as the 7-term Ritz solution for all Ω/ω_1 except at the third resonance and that (again, except near the third resonance) a 4-term solution would be sufficiently accurate for engineering purposes. If 9 terms are used, five significant figure agreement with the amplitude at the third resonant point is also found. Results for the response at the middle of the beam ($x=0.5l$) yielded nearly identical comparisons.

Table 2. Amplitude response C/δ_0 at the end ($x=l$) of a cantilever beam; uniformly distributed load, viscous damping ($c/c_{c1}=0.01$).

$\frac{\Omega}{\omega_1}$	Number of trial functions in Ritz method			Exact Solution
	2	4	7	
0.0	1.00000	1.00000	1.00000	same
0.5	1.33134	1.33759	1.33759	"
0.9	5.06759	5.29616	5.29622	"
0.99	28.6556	36.0870	36.0896	"
1.0	45.8860	50.6697	50.6694	"
1.01	44.5984	35.5744	35.5715	"
1.1	5.04832	4.81325	4.81315	"
1.5	0.82658	0.82473	0.82472	"
2.0	0.34731	0.35276	0.35276	"
6.267	0.03837	1.27647	4.48085	"
17.547	0.00001	0.02056	0.83682*	0.93829

*9-term solution yields 0.93829

The static solution ($\Omega/\omega_1=0$) in this case is exactly expressible as a polynomial of 4th degree. Thus a 3-term Ritz solution would be exact at this frequency, while the "exact" method must laboriously sum up an infinite set of eigenfunctions. Table 2 shows the 2-term solution to be also exact at the particular point $x=l$. At $x=0.5l$, it would yield 0.941176, instead of unity.

Interestingly enough, the exact solution procedure gave numerical difficulty in obtaining accurately converged results for Table 2, even with the use of double-precision (i.e., 16 significant figure) arithmetic. This was largely for large $\alpha_m l$, the γ_m are very close to unity, and $\cosh \alpha_m \xi$ and $\sinh \alpha_m \xi$ are nearly identical. However, the Ritz method proceeded straightforwardly without difficulties.

2.5 Point Loading

Consider next the case of excitation by a concentrated transverse force $\tilde{F}_1 = F_1 e^{i\Omega t}$ acting at an arbitrary point $x=x_1$ along the beam. Solution of the problem by the Ritz method is simple and straightforward. Instead of Eq.(2.5), the work done by the exciting force is

$$W = \tilde{F}_1 w(x_1) \quad (2.35)$$

and the appropriate functional for use with the Ritz method is

$$W_{\max} = F_1 W(x_1) \quad (2.36)$$

instead of Eq.(2.10d). When two or more point loads are present, or if a point load is acting in addition to a distributed load, then superposition applies.

In the case of a point load acting at the free end of a cantilever beam, the right-hand-side of Eq.(2.15a) is simply replaced by F_1 .

To obtain an "exact" solution to the problem in terms of free vibration modes when a concentrated force is present, either of two methods may be used. One method would represent the concentrated force as a Dirac-delta function for $q(x,t)$, and expand this function in terms of the eigenfunctions as in Eq. (2.28). However, this procedure would be extremely tedious, for it would require many terms in the series (Eq.(2.20)) to determine a reasonably accurate representation.

Another exact procedure introduces a change of variables. For example, consider the end loaded beam. The equation of motion is homogeneous:

$$EI \frac{\partial^4 w}{\partial x^4} + \rho A \frac{\partial^2 w}{\partial t^2} + c \frac{\partial w}{\partial t} = 0 \quad (2.37)$$

But one of the boundary conditions is nonhomogeneous; i.e.,

$$w(0,t) = \frac{\partial w}{\partial x}(0,t) = \frac{\partial^2 w}{\partial x^2}(\ell,t) = 0 \quad (2.38a)$$

$$EI \frac{\partial^3 w}{\partial x^3}(\ell,t) = F_1 e^{i\Omega t} \quad (2.38b)$$

Let $w(x,t)$ be replaced by

$$w(x,t) = v(x,t) + g(x) e^{i\Omega t} \quad (2.39)$$

where $g(x)$ is chosen so that

$$g(0) = \frac{\partial g}{\partial x}(0) = \frac{\partial^2 g}{\partial x^2}(\ell) = 0 \quad (2.40a)$$

$$EI \frac{\partial^3 g}{\partial x^3}(\ell) = F_1 \quad (2.40b)$$

Then $g(x)$ is found to be

$$g(x) = -\frac{F_1}{2EI} x^2 + \frac{F_1}{6EI} x^3 \quad (2.41)$$

Substituting Eqs.(2.39) and (2.41) into (2.37) transforms the problem into one having a nonhomogeneous equation of motion, with homogeneous boundary conditions; viz.

$$EI \frac{\partial^4 v}{\partial x^4} + \rho A \frac{\partial^2 v}{\partial t^2} + c \frac{\partial v}{\partial t} = (\rho A \Omega^2 - i c \Omega) g(x) e^{i\Omega t} \quad (2.42a)$$

$$v(0,t) = \frac{\partial v}{\partial x}(0,t) = \frac{\partial^2 v}{\partial x^2}(l,t) = \frac{\partial^3 v}{\partial x^3}(l,t) = 0 \quad (2.42b)$$

and the solution proceeds as in Section 2.3.

III. BEAM ANALYSIS - MATERIAL DAMPING

3.1 Incorporation of Complex Stiffness

In the case of material damping (also called "structural" or "hysteretic" damping), it is possible to use an equivalent viscous damping representation under certain conditions, the viscous damping coefficient being chosen so as to dissipate an equivalent amount of energy per vibratory cycle. The most important condition to be met is that, for the given forcing function and the range of frequency ratio under consideration, a single normal mode is strongly dominant among the modes excited. While it is possible to represent any single mode response adequately by equivalent viscous damping, especially in the vicinity of resonance and if the damping is reasonably small, the individual modes respond differently. Therefore, strong normal mode coupling makes the representation less accurate.

The preferred method of treating material damping is by means of a complex modulus of elasticity (cf. [19]). That is, let the modulus be

$$E^* = E(1 + i\eta) \quad (3.1)$$

where $i = \sqrt{-1}$ and η is the loss factor.

To apply the Ritz method to a forced vibration problem with material damping, the energy dissipation due to friction is combined with the elastic strain energy in complex form, and the functional to be minimized is

$$L_{\max} = T_{\max} - V_{\max}^* + \dot{W}_{\max} \quad (3.2)$$

In the case of a beam, for example, V_{\max}^* is given by

$$V_{\max}^* = \frac{1}{2} \int_0^l E(1+i\eta) I \left(\frac{\partial^2 w}{\partial x^2} \right)^2 dx \quad (3.3)$$

whereas T_{\max} and \dot{W}_{\max} remain as given previously by Eqs. (2.10a) and (2.10d), respectively.

The exact solution uses the equation of motion expressed in complex form, which is

$$E(1+i\eta) I \frac{\partial^4 w}{\partial x^4} + \rho A \frac{\partial^2 w}{\partial t^2} = q(x) e^{i\Omega t} \quad (3.4)$$

Assuming that the displacement (w) and the transverse loading (q) can both be represented as summations of the eigenfunctions of free vibration, a procedure similar to that employed in Section 2.3 may be followed, leading to the solution forms given by Eqs.(2.29) and (2.32), except that in the case of material damping the coefficients A_m and B_m become

$$\begin{aligned} A_m &= \frac{\delta_m}{\Delta_s} \left(1 - \frac{\Omega^2}{\omega_m^2}\right) \\ B_m &= \frac{\delta_m}{\Delta_s} \eta \\ \Delta_s &= \left(1 - \frac{\Omega^2}{\omega_m^2}\right)^2 + \eta^2 \end{aligned} \quad (3.5)$$

with δ_m given by Eq.(2.31), and the amplitude and phase angle again given by Eqs.(2.33) and (2.34), respectively.

3.2 Example. Cantilever Beam with Uniform Pressure

The uniform, homogeneous, cantilever beam subjected to sinusoidally varying, uniform pressure, as described previously in Section 2.2, is again taken as an example; however, in this case the damping is hysteretic. Using algebraic polynomial trial functions as in Eq.(2.13) with the Ritz method, the following set of equations arises for the determination of the coefficients C_j^R and C_j^I associated with the real and imaginary parts of the solution:

$$\sum_{j=2}^J \left\{ \left[\frac{EI}{\ell^4} \frac{j(j-1)k(k-1)}{j+k-3} - \frac{\rho A \Omega^2}{j+k+1} \right] C_j^R + \left[\eta \frac{EI}{\ell^4} \frac{j(j-1)k(k-1)}{j+k-3} \right] C_j^I \right\} = \frac{q_0}{k+1} \quad (3.6a)$$

$$\sum_{j=2}^J \left\{ - \left[\eta \frac{EI}{\ell^4} \frac{j(j-1)k(k-1)}{j+k-3} \right] C_j^R + \left[\frac{EI}{4} \frac{j(j-1)k(k-1)}{j+k-3} - \frac{\rho A \Omega^2}{j+k+1} \right] C_j^I \right\} = 0 \quad (3.6b)$$

Application of the Galerkin method to the problem yielded Eqs.(3.6) identically. The displacement $w(x,t)$ of an arbitrary point is again given by Eqs. (2.16), (2.17) and (2.18).

Numerical results for the nondimensional amplitude ratio C/δ_0 at the free end of the beam as a function of the frequency ratio Ω/ω_1 are presented in Table 3 for a loss factor representative of many metals ($\eta=0.001$), and in Table 4 for a large loss factor ($\eta=0.1$). Once again it is seen that the Ritz method converges rapidly to the exact solution as polynomial terms are added to the displacements. A 7-term solution is accurate to 6 significant figure accuracy except in the vicinity of the third resonance.

In studying Tables 3 and 4, the data is seen to exhibit certain characteristics similar to those for a single degree of free system having material damping (e.g., [20], p. 230). That is,

Table 3. Amplitude response C/δ_0 at the end ($x=l$) of a cantilever beam; uniformly distributed load, material damping ($\eta=0.001$).

$\frac{\Omega}{\omega_1}$	Trial functions-Ritz method		Exact Solution
	4	7	
0.0	0.999999	0.999999	same
0.5	1.33770	1.33770	"
0.9	5.31980	5.31986	"
0.99	50.8387	50.8463	"
1.0	1013.39	1013.39	"
1.01	50.3766	50.3686	"
1.1	4.83954	4.83944	"
1.5	0.834967	0.824959	"
2.0	0.352793	0.352792	"
6.267	1.32170	14.3001	"
17.547	0.025578	0.925293*	1.06942

*9-term solution yields 1.06942

Table 4. Amplitude response C/δ_0 at the end ($x=l$) of a cantilever beam; uniformly distributed load, material damping ($\eta=0.1$).

$\frac{\Omega}{\omega_1}$	Trial functions-Ritz method		Exact Solution
	4	7	
0.0	0.995037	0.995037	same
0.5	1.32593	1.32593	"
0.9	4.70715	4.70719	"
0.99	9.93494	9.93498	"
1.0	10.13252	10.13249	"
1.01	9.93658	9.93649	"
1.1	4.36873	4.36865	"
1.5	0.822066	0.822058	"
2.0	0.352364	0.352362	"
6.267	0.148371	0.145056	"
17.547	0.009427	0.010733	0.010730

- (1) At $\Omega/\omega_1=0$, C/δ_0 is not unity (as in viscous damping), but $C/\delta_0 = [1/(1+\eta^2)]^{1/2}$.
- (2) Damping does not shift the first resonant peak - it remains at $\Omega/\omega_1=1$.
- (3) The first resonant amplitude ratio (C/δ_0) is very nearly equal to $1/\eta$.

That C/δ_0 at $\Omega/\omega_1=0$ is not exactly $1/\eta$ is due to the slight influence of the higher modes. Comparing Tables 3 and 4, it is seen that increased material damping causes greater contribution from the first mode at the second and third resonant frequencies, as might be expected.

IV. PLATE ANALYSIS

4.1 Ritz Method

Except for the fortuitous case of a plate having at least its two opposite sides simply supported, no exact solution for the free vibration eigenfunctions is possible [3]. Nevertheless, the Ritz method may be generalized from the preceding beam analysis to deal with the forced vibrations of plates having arbitrary edge conditions, including point supports.

To be somewhat specific, let us consider a rectangular plate having dimensions $a \times b$, such as the cantilever shown in Fig. 2. The exciting force

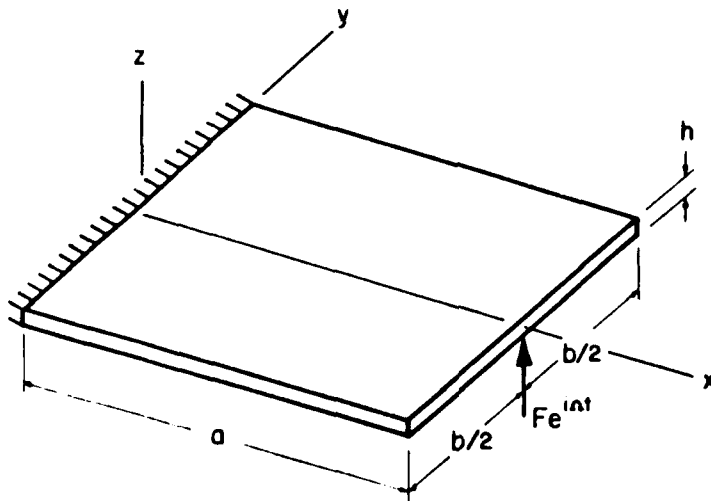


Figure 2. Cantilever plate with concentrated exciting force.

may be either distributed or concentrated. A sinusoidally varying distributed load will, in general, be of the form

$$\tilde{q}(x,y,t) = q(x,y)e^{i\Omega t} \quad (4.1)$$

where now q is force per unit area, whereas a point load is of the form

$$\tilde{F} = F e^{i\Omega t} \quad (4.2)$$

The transverse displacement is taken as

$$w(x, y, t) = W(x, y) e^{i\Omega t} \quad (4.3)$$

$$= \sum_{j=1}^J \sum_{k=1}^K C_{jk} \phi_{jk}(x, y) e^{i\Omega t} \quad (4.4)$$

where the ϕ_{jk} satisfy the geometric boundary conditions exactly, and the C_{jk} are complex coefficients given by

$$C_{jk} = C_{jk}^R - i C_{jk}^I \quad (4.5)$$

The functionals for the plate, which are the generalizations of the beam functionals given by Eqs. (2.10), are:

$$T_{\max} = \frac{\Omega^2}{2} \int_0^a \int_{-b/2}^{b/2} \rho h W^2 dx dy \quad (4.6a)$$

$$V_{\max} = \frac{1}{2} \int_0^a \int_{-b/2}^{b/2} D \left\{ (\nabla^2 W)^2 - 2(1-\nu) \left[\frac{\partial^2 W}{\partial x^2} \frac{\partial^2 W}{\partial y^2} - \left(\frac{\partial^2 W}{\partial x \partial y} \right)^2 \right] \right\} dx dy \quad (4.6b)$$

$$D_{\max} = \frac{i\Omega}{2} \int_0^a \int_{-b/2}^{b/2} c W^2 dx dy \quad (4.6c)$$

$$W_{\max} = \int_0^a \int_{-b/2}^{b/2} q W dx dy \quad (4.6d)$$

In these expressions the flexural rigidity (D) is

$$D = \frac{Eh^3}{12(1-\nu^2)} \quad (4.7)$$

with h being the plate thickness and ν being Poisson's ratio. In the case of material damping, the integrand for V_{\max} is simply multiplied by $(1+i\eta)$.

The functional L_{\max} is constructed as in Eq. (2.9) and minimized as

$$\frac{\partial L_{\max}}{\partial C_{jk}} = 0 \quad (j=1, \dots, J; k=1, \dots, K) \quad (4.8)$$

yielding a set of 2JK simultaneous equations in the coefficients C_{jk}^R and C_{jk}^I . Solution of these equations determines the forced, damped response.

4.2 Example. Cantilever Square Plate with Point Load

To demonstrate the Ritz method, a cantilever plate of square planform ($a/b=1$) is chosen, and is excited by a concentrated force F acting at the center of the outer edge, the force varying sinusoidally with time (Fig. 2). Assume viscous damping affects the plate uniformly (i.e., c is a constant). Let Poisson's ratio (ν) be 0.3.

A set of polynomials for use in Eq.(4.4) may be chosen as

$$\phi_{jk}(x,y) = x^j y^k \quad (j=2,3,\dots,J; k=0,1,\dots,K) \quad (4.9)$$

which satisfy the geometric boundary conditions

$$w(0,y,t) = \frac{\partial w}{\partial x}(0,y,t) = 0 \quad (4.10)$$

exactly. Moreover, for the present example problem where the exciting force preserves the geometric symmetry already present, the antisymmetric modes are not excited, and the index k may be taken as $k=0,2,4,\dots$ with no loss of generality.

Accurate numerical results were obtained by taking 6 terms in the x -direction (i.e., $j=2,3,\dots,7$) and 4 terms in the y -direction (i.e., $k=0,2,4,6$). This yields $6 \times 4 = 24$ polynomial terms ϕ_{jk} and, hence, 24 modal degrees of freedom to the problem. Considering the in-phase and out-of-phase components of motions, the resulting problem consists of solving $2 \times 24 = 48$ simultaneous equations for the C_{jk}^R and C_{jk}^I .

Numerical results for a small damping ratio ($c/c_{c1}=0.01$) are shown in Table 5. Here, as in the beam analysis $c_{c1} (=2\phi h\omega_1)$ is the critical damping coefficient for the first free vibration mode of the square cantilever plate. In Table 5 the nondimensional displacements WD/Fa^2 of three significant points are given, as functions of Ω/ω_1 . These points are the plate center ($x=0.5a$, $y=0$), the point of loading ($x=a$, $y=0$) and the corner points ($x=a$, $y=\pm 0.5b$). In addition to the first resonant frequency ($\Omega/\omega_1=1$), data is also given for the next three frequencies of symmetric modes ($\Omega/\omega_1=6.1317$, 7.8307 and 15.6165). $\omega_3/\omega_1=7.8307$ corresponds to a chordwise bending free vibration mode, whereas the other three are spanwise (i.e., flapwise) bending modes (cf., [3,131]).

Comparing Table 5 for the plate with Table 2 for the beam, both having the same damping ratio ($c/c_{c1}=0.01$), one observes that the amplitude responses at the second and third spanwise bending frequencies is considerably greater for the plate than the beam. This is mainly due to two differences:

- (1) The concentrated end force excites the higher spanwise bending modes more than a uniformly distributed force.

Table 5. Displacements WD/Fa^2 of a cantilever plate with a sinusoidally varying point load (P) at the center of the outer edge; viscous damping ($c/c_{c1}=0.01$).

$\frac{\Omega}{\omega_1}$	Plate center $\frac{x}{a} = 0.5, \frac{y}{b} = 0$	Load point $\frac{x}{a} = 1, \frac{y}{b} = 0$	Corner point $\frac{x}{a} = 1, \frac{y}{b} = 0.5$
0.0	0.111	0.360	0.329
0.5	.150	.473	.440
0.9	.601	1.798	1.744
0.99	4.153	12.209	11.982
1.0	5.755	16.887	16.597
1.01	3.992	11.690	11.507
1.1	.548	1.574	1.572
1.5	.096	.247	.268
2.0	.043	.089	.114
6.1317	1.714	3.997	1.843
7.8307	1.193	1.254	2.865
15.6165	.736	1.258	1.307

- (2) The concentrated force is not along the entire free end of the plate, but only at its center, thereby causing a significant contribution of the first chordwise bending mode.

It is interesting to observe the change in chordwise bending effects in Table 5 as Ω/ω_1 is swept from zero to the fourth natural frequency. At $\Omega/\omega_1 = 0$ one has static loading, and the plate exhibits significant anticlastic curvature; that is, the center of the free edge deflects more than the corner points. The anticlastic curvature is greater here than for a uniformly loaded square cantilever [22], as might be expected. As Ω/ω_1 is increased, the curvature remains anticlastic until slightly past the first resonance ($\Omega/\omega_1 \approx 1.1$). The curvature is strongly anticlastic at the second resonance, but reverses itself for the third and fourth resonances.

Table 6 gives the results for the same problem when the damping coefficient is ten times greater ($c/c_{c1}=0.1$). The responses at the resonant peaks are all very similar to those with small damping, except with amplitudes essentially one-tenth as large, except for the fourth resonance.

V. CONCLUDING REMARKS

An extension of the Ritz method has been developed for analyzing the forced vibrations of structural elements such as beams, plates and shells in a straightforward and efficient manner. Both viscous and material damping may be accounted for. The exciting forces may be distributed and/or concentrated. Convergence to the exact solutions for a set of cantilever beam problems was demonstrated.

Table 6. Displacements WD/Fa^2 of a cantilever plate with a sinusoidally varying point load (P) at the center of the outer edge; viscous damping ($c/c_{c1}=0.1$).

$\frac{\Omega}{\omega_1}$	Plate center $\frac{x}{a} = 0.5, \frac{y}{b} = 0$	Load point $\frac{x}{a} = 1, \frac{y}{b} = 0$	Corner point $\frac{x}{a} = 1, \frac{y}{b} = 0.5$
0.0	0.111	0.360	0.329
0.5	.148	.469	.436
0.9	.438	1.309	1.268
0.99	.578	1.700	1.669
1.0	.576	1.690	1.660
1.01	.567	1.662	1.636
1.1	.381	1.094	1.093
1.5	.093	.240	.261
2.0	.042	.088	.113
6.1317	.172	.404	.187
7.8307	.119	.129	.287
15.6165	.117	.200	.207

Although the method was demonstrated for homogeneous beams and plates of uniform thickness, the energy functionals presented are in more general form, capable of accounting for variable cross-sections (i.e., A, I, h) and nonhomogeneous material (E, ρ). Work is currently progressing to extend the method further to shell problems. The method will also be developed for analyzing the free, damped response of structural elements, and other types of damping will also be considered.

ACKNOWLEDGEMENT

This work was carried with the support of the National Aeronautics and Space Administration, Lewis Research Center, under Grant No. NAG3-424.

REFERENCES

1. Lord Rayleigh, Theory of Sound, Vol. 1, Macmillan (1877) (reprinted by Dover Publications, 1945).
2. Ritz, W., "Theorie der Transversalschwingungen, einer quadratischen Platte mit freien Randern," Ann. Physik, Vol. 28, pp. 737-786 (1909).
3. Leissa, A.W., Vibration of Plates, U.S. Govt. Printing Office, NASA SP-160, 353 pp. (1969).
4. Leissa, A.W., Vibration of Shells, U.S. Govt. Printing Office, NASA SP-288, 428 pp. (1973).

5. Arnold, R.N. and Warburton, G.B., "The Flexural Vibrations of Thin Cylinders," Inst. Mech. Engineers (ser. A), Proc. 167, pp. 62-80 (1953).
6. Gontkevich, V.S., "Natural Oscillations of Closed Cylindrical Shells with Various Boundary Conditions," Prikl. Mekh., Vol. 9, No. 2, pp. 216-220 (1963).
7. Gontkevich, V.S., "Natural Vibrations of Plates and Shells," A.P. Filipov, ed., Nauk Dumka (Kiev), Transl. by Lockheed Missiles and Space Co. (1964).
8. Sewall, J.L. and Naumann, E.C., "An Experimental and Analytical Vibration Study of Thin Cylindrical Shells With and Without Longitudinal Stiffeners," NASA TN D-4705 (Sept. 1968).
9. Sharma, C.B. and Johns, D.J., "Vibration Characteristics of a Clamped-Free and Clamped-Ring-Stiffened Circular Cylindrical Shell," J. Sound Vib., Vol. 14, No. 4, pp. 459-474 (1971).
10. Kantovovich, L.V. and Krylov, V.I., Approximate Methods of Higher Analysis (English translation). Groningen: P. Noordhoff Ltd. (1958).
11. Leissa, A.W., "A Direct Method for Analyzing the Forced Vibrations of Continuous Systems Having Damping," Journal of Sound and Vibration, Vol. 56, pp. 313-324 (1978).
12. Leissa, A.W., "The Analysis of Forced Vibrations of Plates Having Damping," Developments in Theoretical and Applied Mechanics, Vol. 9, pp. 183-193 (1978).
13. Leissa, A.W., Lee, J.K. and Wang, A.J., "Vibrations of Cantilevered Shallow Cylindrical Shells Having Rectangular Planform," Journal of Sound and Vibration, Vol. 78, No. 3, pp. 311-328 (1981).
14. Leissa, A.W., Lee, J.K. and Wang, A.J., "Rotating Blade Vibration Analysis Using Shells," presented at the ASME Gas Turbine Conference, Houston, Texas, March 8-12, 1981 (Paper No. 81-GT-80), Journal of Engineering for Power, Vol. 104, No. 2, pp. 296-302 (1982).
15. Lee, J.K., Leissa, A.W. and Wang, A.J., "Vibrations of Cantilevered Circular Cylindrical Shells: Shallow versus Deep Shell Theory," International Journal of Mechanical Sciences, Vol. 25, No. 5, pp. 361-383 (1983).
16. Leissa, A.W., Lee, J.K. and Wang, A.J., "Vibrations of Cantilevered Doubly-Curved Shallow Shells," International Journal of Solids and Structures, Vol. 19, No. 5, pp. 411-424 (1983).
17. Siu, C.C. and Bert, C.W., "Sinusoidal Response of Composite-Material Plates with Material Damping," Jour. Engrg. Industry, pp. 603-610 (1974).
18. Felgar, R.P., "Formulas for Integrals Containing Characteristic Functions of a Vibrating Beam," Univ. of Texas, Circular No. 14 (1950).
19. Snowdon, J.C., Vibration and Shock in Damped Mechanical Systems, John Wiley and Sons, 486 pp. (1968).

20. Ruzicka, J.E. and Derby, Thomas F., Influence of Damping in Vibration Isolation, The Shock and Vibration Information Center, 269 pp. (1971).
21. Leissa, A.W., "The Free Vibration of Rectangular Plates," Journal of Sound and Vibration, Vol. 31, No. 3, pp. 257-293 (1973).
22. Leissa, A.W. and Nietenfuhr, F.W., "A Study of the Cantilevered Plate Subjected to a Uniform Loading," J. Aerospace Sciences, pp. 162-169 (February, 1962).

FINITE ELEMENT DESIGN OF VISCOELASTICALLY
DAMPED STRUCTURES--METHODS

Drs. C. D. Johnson and D. A. Kienholz
CSA Engineering Incorporated
Palo Alto, California 94306

Published as one paper; see Section HH.

**FINITE ELEMENT DESIGN OF VISCOELASTICALLY
DAMPED STRUCTURES--APPLICATIONS**

**Dr. D. A. Kienholz, Dr. C. D. Johnson,
E. M. Austin, and M. E. Schneider
CSA Engineering Incorporated
Palo Alto, California 94306**

Published as one paper; see Section HH.

**FINITE ELEMENT DESIGN OF
VISCOELASTICALLY DAMPED STRUCTURES**

**Conor D. Johnson, David A. Kienholz,
Eric M. Austin and Michael E. Schneider
CSA Engineering, Incorporated
Palo Alto, California 94306**

Presented as two papers; published as one paper.

FINITE ELEMENT DESIGN OF
VISCOELASTICALLY DAMPED STRUCTURES

Conor D. Johnson, David A. Kienholz,
Eric M. Austin and Michael E. Schneider

CSA Engineering, Inc.
Palo Alto, CA 94306

ABSTRACT

This paper describes four methods for the finite element analysis of structures containing a viscoelastic material. These methods fall into the categories of methods for damping treatment selection or methods for response prediction. The main emphasis of this paper is directed towards the Modal Strain Energy (MSE) method. The MSE method uses normal mode techniques and, therefore, is an efficient method for the design of viscoelastically damped structures. The MSE method, implemented by finite element techniques, will aid the analyst in 1) selecting the location of the damping treatment, 2) selecting the damping treatment, 3) predicting the modal damping factors, and 4) predicting the responses of the structure. A discussion of finite element modeling methods for structures containing viscoelastic materials is included. Two structures are discussed for which viscoelastic damping treatments were designed using the MSE technique. Comparisons of predicted and measured modal damping and frequencies are given.

1.0. INTRODUCTION

Increasing the damping of a structure can often improve performance under dynamic load. A rational design process requires a method for predicting the damping values that can be expected for a given structural configuration. However, the prediction of damping has historically been largely an art, or at best, a specialized science requiring a greater investment of time and effort than is practical within most design projects.

Predictions of dynamic response in finite element analysis are most often made by the simple expedient of choosing a single structural loss factor to characterize all modes of vibration or, at most, assigning loss factors based on the natural frequency of each mode. The values themselves are obtained empirically or are otherwise based on the judgement and experience of the user. Uncertainties in loss factor are simply ignored or are accounted for by running the analyses for a range of values.

This approach is probably reasonable for situations where the damping is accidental, i.e. due to mechanisms not under the control of the designer. Phenomena such as hysteretic losses in metals, air pumping and friction in joints, or acoustic radiation invariably lead to some measurable amount of damping. However, it is often too little and too unpredictable to produce a satisfactory design. In these cases the addition of damping by the use of viscoelastic materials (v.e.m.) can be highly effective. Damping-by-design has proven valuable in many applications, particularly in the aerospace industry. Methods have recently been developed for predicting damping in structures with integral or add-on viscoelastic treatments.

Since much of the difficulty of analyzing damping in structures stems from complicated geometries, it is natural to look to finite element methods for solutions, just as they are used for analysis of general undamped structures. Several mathematical techniques for dynamic analysis of structures containing viscoelastic materials have been implemented using finite elements. All make use of the correspondence principal of viscoelasticity. That is, the Young's modulus and shear modulus of the v.e.m. are treated as complex quantities. The ratio of the imaginary part to the real part is called the loss factor or loss tangent and is a measure of the materials ability to dissipate vibrational energy.

In this paper, the approaches to damped structural design are examined in the context of implementation by finite element

techniques. A modeling method suitable for three layer sandwiches and other configurations is described and details of its use are discussed.

One technique in particular, the modal strain energy (MSE) method, has been developed by the authors with design work in mind. It has proven to be accurate and flexible in both theoretical studies and practical applications. This method uses normal mode techniques and is therefore cost effective for design analysis.

The authors have applied the modal strain energy method to the design of damping treatments for a number of structures. This paper presents two such examples - a high velocity gas duct and a space truss structure.

2.0 ANALYSIS OF DAMPED STRUCTURES BY FINITE ELEMENT METHODS

Current methods for finite element analysis of damped structures can generally be placed in one of two categories. These categories deal with 1) damping treatment selection and 2) response prediction methods. The damping treatment selection category is subdivided into the complex eigenvalue method and the modal strain energy method. The response prediction category is subdivided into the direct frequency response method and the modal frequency response method with a corrected modal damping versus frequency table. The four methods are briefly described in this section along with the advantages and disadvantages of each for design purposes.

All four of the methods use, to some extent, the idea of treating the elastic constants of a viscoelastic material as complex quantities. This very useful notion is often misunderstood. It derives simply from the use of complex arithmetic to keep track of relative phase between stress and strain under deformations that vary sinusoidally in time. The idea is obviously extendible to non-sinusoidal motion for linear systems by the use of Fourier transform theory to represent arbitrary time histories as sums of sinusoids. Crandall [1,2] has shown that the notation can, if taken too literally, lead to implications that are physically impossible. The point is a subtle one and is mentioned here only in passing.

2.1 METHODS FOR DAMPING TREATMENT SELECTION

The two methods that fall within this category are 1) the complex eigenvalue method and 2) the modal strain energy (MSE) method. The modal strain energy method is an approximation to the more expensive complex eigenvalue method. It has been developed by the authors with the intent of producing a tool which is accurate, flexible, and yet usable in day-to-day design analysis.

2.1.1 Complex Eigenvalue Method

Suppose the discretized equations of motion take one of the following two forms

$$[M]\{\ddot{x}\} + [C]\{\dot{x}\} + [K]\{x\} = \{l(t)\} \quad (1)$$

or

$$[M]\{\ddot{x}\} + [K_1]\{x\} + i[K_2]\{x\} = \{l(t)\} \quad (2)$$

where

$[M], [C], [K]$ = physical coordinate mass, damping and stiffness matrices (all real and constant)

$[K_1], [K_2]$ = real and imaginary parts of the stiffness matrix calculated with complex material constants

$\{x\}, \{\dot{x}\}, \{\ddot{x}\}$ = vectors of modal displacements, velocities, and accelerations

$\{l(t)\}$ = vector of applied node loads

The solution for either form of the equations of motion can be carried out in terms of damped normal modes [3,4]. Both the eigenvalues and eigenvectors will in general be complex but the method is nonetheless quite standard in that the modes obey an orthogonality condition and thus allow uncoupled equations of motion to be obtained.

The complex eigenvalue method has three important drawbacks. It is computationally expensive; typically greater than three times the cost of an undamped solution of the same order [5]. In most finite element codes, one does not have the same

sophisticated spill logic as for real eigenvalue analysis and thus the maximum problem size is smaller. Finally, for a structure to be described by Eq. (1) or (2), its materials, including any viscoelastics, must have dynamic stress-strain behavior of a certain type. Eq. (2) implies that both storage and loss moduli are constant. Eq. (1) requires that storage moduli be constant and loss moduli increase linearly with frequency [2]. Real viscoelastic materials simply do not behave in such accommodating ways. Storage moduli tend to increase monotonically while loss moduli exhibit a single, mild peak [6].

2.1.2 Modal Strain Energy Method

The essence of the modal strain energy (MSE) method is that it does not attempt to calculate the damping matrix $[C]$ of Eq. (1) nor the imaginary stiffness $[K_2]$ of Eq. (2). Rather, it avoids the use of complex matrices entirely by assuming that the real mode shapes obtained by suppressing the term $[C]\{x\}$ in Eq. (1) or $[K_2]\{x\}$ in Eq. (2) are approximations to the true complex mode shapes.

The discretized version of a partial differential equation for free vibration of a structure is:

$$[M]\{\ddot{x}\} + [K]\{x\} = [0] \quad (3)$$

where the stiffness matrix $[K]$ is taken initially to be constant but complex if the structure contains a viscoelastic material. Equation (3) is converted to an eigenvalue problem by assuming a solution of the form

$$\{x\} = \{\theta^*(r)\} e^{ip_r^* t} \quad (4)$$

where p_r^* and $\{\theta^*(r)\}$ are the r th complex eigenvalue and eigenvector; that is

$$\{\theta^*(r)\} = \{\theta_R^{(r)}\} + i\{\theta_I^{(r)}\} \quad (5)$$

$$p_r^* = p_r \sqrt{1 + i\eta^{(r)}} \quad (6)$$

where $\{\theta_R^{(r)}\}$, $\{\theta_I^{(r)}\}$, $\eta^{(r)}$, and p_r are real. The term $\eta^{(r)}$ is the loss factor for the r th mode. It has been shown in Ref. [7] that an approximate value for $\eta^{(r)}$ can be calculated by approximating the complex eigenvector by the real eigenvector,

which is calculated from purely elastic analysis, i.e., by suppressing the imaginary part of $[K]$. This approximation has the form

$$\eta^{(r)} = \eta_i (SE_i^{(r)} / SE^{(r)}) \quad (7)$$

where the new symbols are

η_i = material loss factor for the i 'th material

$SE_i^{(r)}$ = strain energy in the i 'th material when the structure deforms in its r 'th mode

$SE^{(r)}$ = total strain energy for the r 'th mode

In a finite element formulation, this becomes

$$\eta^{(r)} = \sum_{j=1}^N (\eta_j SE_j^{(r)} / SE_j^{(r)}) \quad (8)$$

where the summation is over the number of elements in the model. Examination of Eqs. (7) and (8) shows that the fraction of the total strain energy in each element is desired, and not the dimensional magnitude. Therefore, the method of normalization for the eigenvectors has no effect. In words, the modal loss factor for the r th mode is equal to the summation over all elements of the product of each element's material loss factor and the fraction of the strain energy in that element. A standard output option of many finite element codes is the percent strain energy in each element for each mode of interest.

Equation (8) leads to a simple approximate method for calculating structural loss factor for each mode using the undamped mode shapes and the material loss factor for each material. This general approach was first suggested by Ungar and Kerwin [8] in 1962. Its application by finite element methods was first suggested by Rogers [9]. The basic advantages of the method are that only undamped normal modes need be calculated and that the energy distributions are of direct use to the designer. They serve to guide the choice of viscoelastic material as well as the optimum location for it. The disadvantage is that some approximation is required to accommodate frequency-dependent material properties.

Material loss factors for metals and other primary structure materials are usually very small compared to those for viscoelastic materials. Therefore, for structures that contain viscoelastic materials, a good approximation is to sum over only the elements that represent those viscoelastic materials.

Comparisons with true complex eigenvalue solutions, both differential and finite element, have shown the approximation to be reasonable even for values of material loss factor in excess of unity [7,9]. A comparison of results between the MSE method and the complex eigenvalue method (constant complex stiffness), both implemented in MSC/NASTRAN, is shown in Table 1. It is for a cantilever beam seven inches long with sixty mil aluminum face sheets and a 300 psi, five mil viscoelastic core. The complex eigenvalue results indicate that $\eta^{(r)}$, the modal loss factor, and η_v , the viscoelastic material factor, are almost exactly proportional over a wide range of η_v . Modal loss factors agree quite well between the methods. Computation cost for eigenvalue extraction in the complex stiffness, complex eigenvalue method was found to be about 5 times greater than for real eigenvalue extraction in the corresponding MSE run. The Hessenberg method was used in the former and the Givens method in the latter.

TABLE 1
Comparison of Loss Parameter for a Sandwich Beam
Calculated by the Modal Strain Energy and
Complex Stiffness Eigenvalue Methods

Mode	Type	MSE	Complex Eigenvalue Method	
			$\eta_v = 0.3$	$\eta_v = 1.3$
1	1B	0.214	0.216	0.210
2	2B	0.280	0.287	0.276
3	1T	0.025	0.025	0.025
4	3B	0.213	0.223	0.218
5	4B	0.134	0.142	0.141
6	2T	0.026	0.026	0.026
7	5B	0.081	0.093	0.092
8	3T	0.031	0.031	0.031
9	6B	0.057	0.062	0.062

Comparisons have been made between the results of closed form solutions and the modal strain energy method for beams, plates, and rings. These comparisons have been made for

predicted frequencies, modal damping, and mode deformations. For beams, the sixth order theory of Rao [10] and the MSE results for damping and frequencies were, for practical purposes, identical for the first six modes. Results from the fourth order theory [11,12] differed somewhat for certain boundary conditions as would be expected based on the assumptions of the theory. The MSE results for simply-supported, damped plates agreed quite well with the sixth order theory of damped plates by Abdulhadi [13]. The frequencies and modal damping for rings predicted by the MSE method also agreed with those predicted by the sixth order theory of Lu [14].

2.2 RESPONSE PREDICTION METHODS

The two methods that fall within this category are 1) the direct frequency response (DFR) method and 2) the modal frequency response (MFR) method. The DFR method permits the stiffness matrices to be functions of frequency. This is not the case for the uncoupled modal frequency response method. In the latter method, the solution is obtained using modal coordinates obtained from matrices constant with respect to frequency. Damping is introduced into the solution in the form of modal damping versus frequency.

2.2.1 Direct Frequency Response Method

If the applied load varies sinusoidally in time, energy dissipation in the structure can be accounted for by treating the elastic constants of any or all of the materials as complex quantities which are functions of frequency and temperature. These material properties are presumably available from sinusoidal tests. If the structure is linear, its response will be sinusoidal with frequency equal to the driving frequency, and the steady-state equations of motion will have the form:

$$[-[M]\omega^2 + [K_1(f)] + i[K_2(f)]] \{X(f)\} = \{L(f)\} \quad (9)$$

where

$[K_1(f)], [K_2(f)]$ = stiffness matrices calculated using the real and imaginary parts of the material properties, respectively

ω = radian frequency of excitation

$\{L(f)\}$, $\{X(f)\}$ = complex amplitude vectors of applied node loads and responses, respectively

There are several drawbacks to the direct frequency response (DFR) method. It is computationally expensive because a general sinusoidal solution requires that the displacement impedance matrix (the long bracketed quantity in Eq. (9)) be recalculated, decomposed, and stored at each of many frequencies. Further, the method does not give information of direct use in improving a candidate design. The costliness of the direct frequency response method indicated by Eq. (9) is a direct result of the restriction to physical coordinates (as opposed to modal coordinates). This restriction is caused by the form of the corresponding time domain representation. General convolution integral relations between forces and displacements must be admitted in order to accommodate the variation of $[K_1]$ and $[K_2]$ with frequency that is observed in real viscoelastic materials. Since not even the form, let alone the parameter values, of the convolution relation is generally known, it must be represented numerically in the frequency domain in terms of its Fourier transform. A tabular frequency representation can be arbitrarily accurate as long as the underlying stress-strain operator is linear. However, the use of such a data format is costly, particularly if a high level of frequency resolution is required. The most reasonable application of the DFR method in design work is in making final predictions of frequency response after the materials and geometry of the damping treatment have been selected using the modal strain energy method. The ability to account exactly for the frequency dependence of material properties will generally yield some improvement in accuracy over the modal frequency response method. This may justify its higher cost if only a small number of functions with moderate frequency resolution are required.

Direct frequency response analysis with variable material properties is possible in several finite element codes. The procedure for MSC/NASTRAN is explained in Section 2.11-2 of the Applications Manual [5]. A frequency-dependent complex shear modulus may be specified in terms of tables. These are prepared in a particular format to include both frequency dependent damping for each element material as well as additional damping which is constant with frequency.

2.2.2 Modal Frequency Response Method

The modal frequency response method represents the damped structure in terms of its undamped mode shapes with appropriate damping terms inserted into the uncoupled modal equations of

motion. It is implied that the physical coordinate damping matrix $[C]$ of Eq. (1) need not be explicitly calculated but that it can be diagonalized, at least approximately, by the same real modal matrix that diagonalizes $[K]$ and $[M]$. That is:

$$\ddot{\alpha}_r + \eta^{(r)} \omega_r \dot{\alpha}_r + \omega_r^2 \alpha_r = l_r(t) \quad (10)$$

$$\{x\} = \sum_r \{\phi\}^{(r)} \alpha_r(t) \quad (11)$$

$$r = 1, 2, 3 \dots$$

where

α_r = r'th modal coordinate

ω_r = natural radian frequency of the r'th mode

$\{\phi\}^{(r)}$ = r'th mode shape vector of the associated undamped system

$\eta^{(r)}$ = loss factor of the r'th mode

When the modal frequency response method is used, the modal properties are obtained from system matrices that are assumed to be constant. Viscoelastic materials, however, have storage moduli which vary significantly with frequency. There is no theoretically correct way of resolving this contradiction. Nonetheless, normal mode methods have great practical advantages, both for making response predictions and for suggesting design improvements. Real normal modes, uncoupled but with damping, have been found to be reasonably accurate if a simple correction is made to the modal loss factors obtained by Eq. (7). The correction is obtained as follows.

For broadband excitation, most of the response of a given mode occurs within a narrow band around the mode's natural frequency. It is natural then to require that the energy distribution used to compute the loss factor for a given mode be obtained using a stiffness matrix evaluated for material properties taken at that mode's frequency. Because the natural frequencies themselves depend on material properties, an iterative solution of two simultaneous relations (the eigenvalue problem for each mode

number and the material property vs. frequency relation) is required. However, the final modal coordinate representation of the structure must come from a single stiffness matrix evaluated using a single value of storage modulus for the viscoelastic material. Natural frequencies, mode shapes, and modal masses will be correct for, at most, one mode. A correction to the modal loss factor, obtained as follows, has been found to give some improvement. Each modal equation of motion has the form given in Eq. (10). At resonance the first and last terms on the left cancel each other. The response magnitude is inversely proportional to the product $\eta^{(r)}\omega_r$, the coefficient of the modal velocity. If $\eta^{(r)}$ is altered to correct for the error in ω_r , an improvement in peak response may be expected although resonance will still occur at a slightly shifted frequency and some small error will remain due to l_r which depends on modal mass. In test cases run for sandwich beams [9], it was found that taking ω_r to be proportional to the square root of G_2 (G_2 = core shear modulus) would improve the agreement between the MSE method and the direct frequency response method. This is of course an approximation since ω_r depends on properties of the face sheets as well as the core. The modal damping ratios are adjusted according to

$$\eta^{(r)'} = \eta^{(r)} \sqrt{G_2(f_r)/G_{2, \text{ref}}} \quad (12)$$

where

$\eta^{(r)}$ = adjusted modal damping ratio for the r'th mode

$\eta^{(r)}$ = modal damping ratio for the r'th mode obtained by equation (8)

$G_{2, \text{ref}}$ = viscoelastic shear modulus used in calculation of the mode set used in the response calculation

$G_2(f_r)$ = viscoelastic shear modulus at $f = f_r$ where f_r is the r'th mode frequency calculated with $G_2 = G_{2, \text{ref}}$

3.0 FINITE ELEMENT MODELING METHODS FOR SANDWICH STRUCTURES

Flexural vibration of plates or panels can often be suppressed by constructing the plate as a three layer sandwich with metal outer layers and a viscoelastic core. Techniques for finite element modeling of this important class of damped structures are discussed in this section.

Regardless of the solution method to be employed, modeling of sandwich structures requires that the strain energy due to shearing of the core be accurately represented. To be practical, a modeling method must do this without incurring an unacceptable increase in computation cost relative to a uniform, single layer model. A modeling method is described in this section which is reasonably efficient and can be readily implemented in MSC/NASTRAN, a commercially available and widely used finite element code.

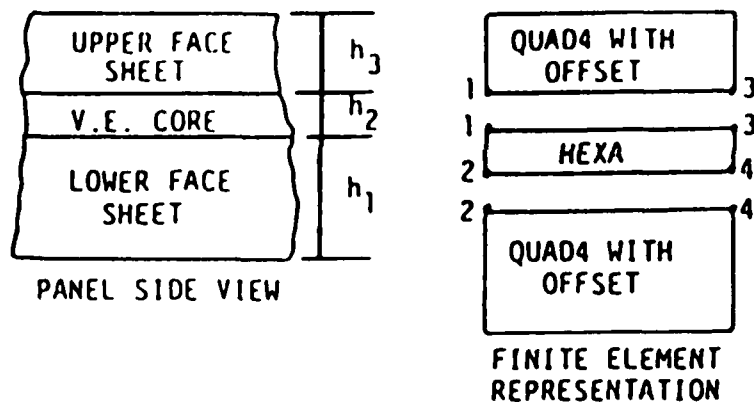


Figure 1 Finite Element Modeling of a Sandwich Panel with Viscoelastic Core

Figure 1 shows the arrangement for modeling of a three layer sandwich. The face sheets are modeled with quadrilateral or triangular plate elements producing stiffness at two rotational and three translational degrees of freedom per node. The viscoelastic core is modeled with solid elements producing stiffness at three translational degrees of freedom per node. All nodes are at element corners. The plate elements used are TRIA3's, TRIA6's, QUAD4's, and QUAD8's, and the solid elements are PENTA's and HEXA's. A key feature of the plate elements in the present

application is their ability to account for coupling between stretching and bending deformations [5]. This allows the plate nodes to be offset to one surface of the plate, coincident with the corner nodes of the adjoining solid elements. In this way a three layer plate can be modeled with only two layers of nodes. The technique is explained in the Applications Manual under the TRIA3 and QUAD4 elements. Alternatively, one may use the PCOMP property card normally employed for layered composites. A two-layer composite is defined but with a near-zero modulus specified for one layer. The other layer then represents the offset plate element. In MSC/NASTRAN Version 63, a new and recommended method of offsetting the plate elements is employed. This method is implemented by using the field Z-OFF on the element connection cards. Table 2 is a comparison between an analytical solution and the MSE method using various offset methods for frequencies and percent strain energies in the viscoelastic for a simply supported plate. Also included in this Table is the RBAR method. Although correct, this method requires an additional layer of GRID's plus RBAR rigid elements for each face sheet and is therefore not recommended. This example was for a symmetric sandwich. Experience has shown that for non-symmetric sandwiches, care must be used in selecting the offset method.

Table 2
Comparison of Frequencies and Percent Strain
Energy in the Viscoelastic for a Simply
Supported Plate Using Different Offset Methods

Mode Number	Analytical [Abduhalil]	Offset Quad's (MID4 & PCOMP)	Offset Quad's (Z-OFF)	RBAR Offset Method
1	60.3 Hz	56.8 Hz	56.3 Hz	56.5 Hz
	38.0 %SE	36.8 %SE	36.2 %SE	36.6 %SE
2	115.5 Hz	112.2 Hz	110.5 Hz	111.0 Hz
	40.6 %SE	39.1 %SE	38.2 %SE	38.9 %SE
3	130.6 Hz	127.8 Hz	125.3 Hz	126.3 Hz
	39.8 %SE	38.4 %SE	37.3 %SE	38.1 %SE

Very large aspect ratios (in-plane dimension/thickness dimension) may be used for the solid elements in the core layer because the strain field is usually quite simple. Values as high as 5000/1 have been used successfully and are in fact necessary since core layers are often only a few mils thick. Poisson's ratio for the core material is normally set to 0.49. However, in studies of curved elements, the authors have found that Poisson's ratio has a major effect on the predictions of frequency and modal damping [15]. For the important transition region and the rubbery region, using a value of Poisson's ratio of 0.49 is valid. However, in the glassy region, care must be exercised to ensure that Poisson's ratio is correct.

In all but the smallest problems, some form of dynamic reduction must be employed to reduce the number of degrees-of-freedom in the analysis. Either Guyan reduction or generalized dynamic reduction may be used. In Guyan reduction, the d.o.f. to be retained are selected by the user prior to calculation of eigenvalues. As usual in vibration analysis, some care is warranted in this selection. Some displacements should be retained for both face sheets, although it is not necessary to keep both upper and lower face displacements at any single in-plane location on the model. This result is somewhat surprising in that virtually all sandwich panel theories assume the transverse displacements of the face sheets to be equal.

4.0 DESIGN OF DAMPED STRUCTURES

Figures 2 and 3 show a simplified flow chart of the logic that might be used in designing a viscoelastically damped structure using MSC/NASTRAN. The initial design effort (left part of Figure 2) is usually concerned with basic issues such as static stiffness, strength, and insuring that the normal modes of vibration will be acceptable, once adequate damping is obtained. When these issues are settled, the model is modified to account for additive damping, either in the form of damping inserts, integral damping, or add-on constrained layer damping treatments. The geometry and material properties of the treatment are selected by an iterative process using the results of a modal strain energy analysis to guide each succeeding trial.

Once the engineer believes his damped design is close to optimum, he performs his final response calculations with NASTRAN using either the adjusted MSE method or the DFR method (see Figure 3). These simulations are based on the best available

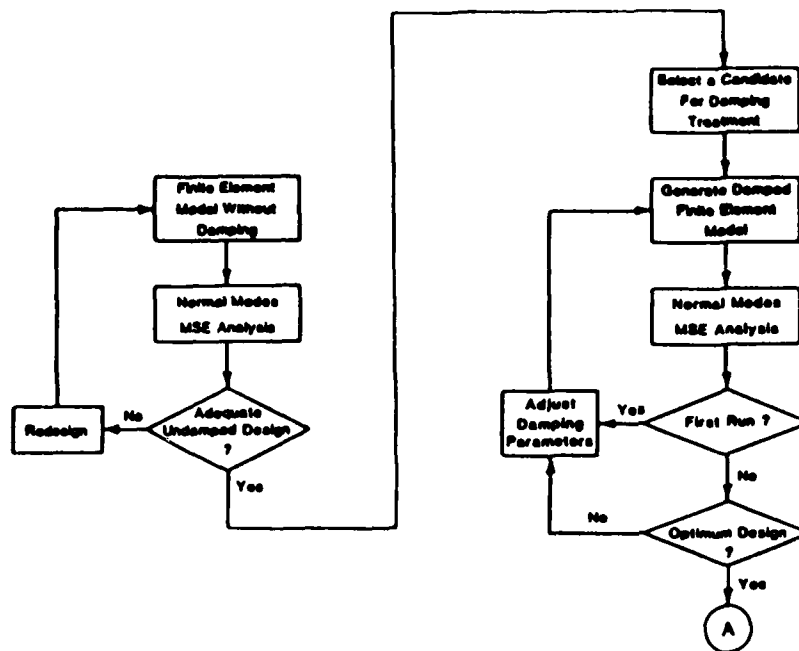


Figure 2 Flow Chart for the Selection of the Damping Treatment

From Part 1
Selection of Damping Treatment

Part 2
Response Prediction

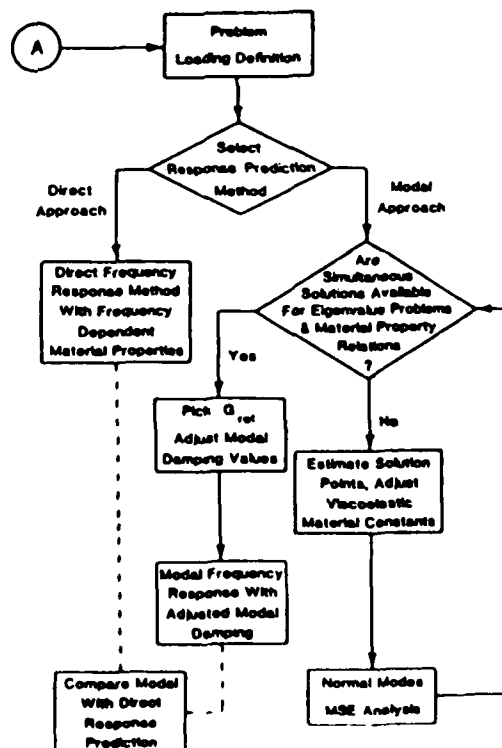


Figure 3 Flow Chart for Responses Prediction of Damped Structures

estimate of the in-service dynamic load. The choice of methods would depend on the type of load (transient, periodic, or random), the number of load cases, the frequency range, the properties of the viscoelastic, and the required accuracy.

4.1 CASE STUDY - HIGH VELOCITY HELIUM DUCT

Figure 4 shows a structural part for which an add-on damping treatment was designed by the modal strain energy method. The part is an annular hollow plate with many internal passages which carry coolant at high velocity. Gas under pressure flows radially outward from the hub and exhausts through the cavity between the lips at the outer circumference of the plate. Calculations indicated that unstable flow induced vibration, or flutter, could occur in the lips of the plate if the damping of a certain mode was below a critical value.

The plate was tested in its original undamped form and the damping was found to be well below the desired value. The authors were asked to design a damping treatment subject to the following requirements:

1. The damping of the critical mode had to be increased to at least 1.0% (structural).
2. Static stiffness at the plate rim in the axial direction could be increased by no more than 10%.
3. The damping treatment had to be effective over a temperature range of 75 deg F. to 400 deg F. and was to withstand short term exposure to 650 deg F.
4. The treatment had to be designed, fabricated, and applied within a few weeks with no major machining of the original plate.

Based on these requirements, it was decided that a viscoelastic insert installed between the lips of the plate was the most desirable approach. The insert was to take the form of an O-ring which would be forced into the space between the lips of the plate around its entire circumference. The design was later changed to include several O-rings.

One of the finite element models used in the design process is shown in cross section in Figure 5. The structure and symmetry of the plate were such that modeling of only a small azimuthal sector of one lip was necessary along with half of the

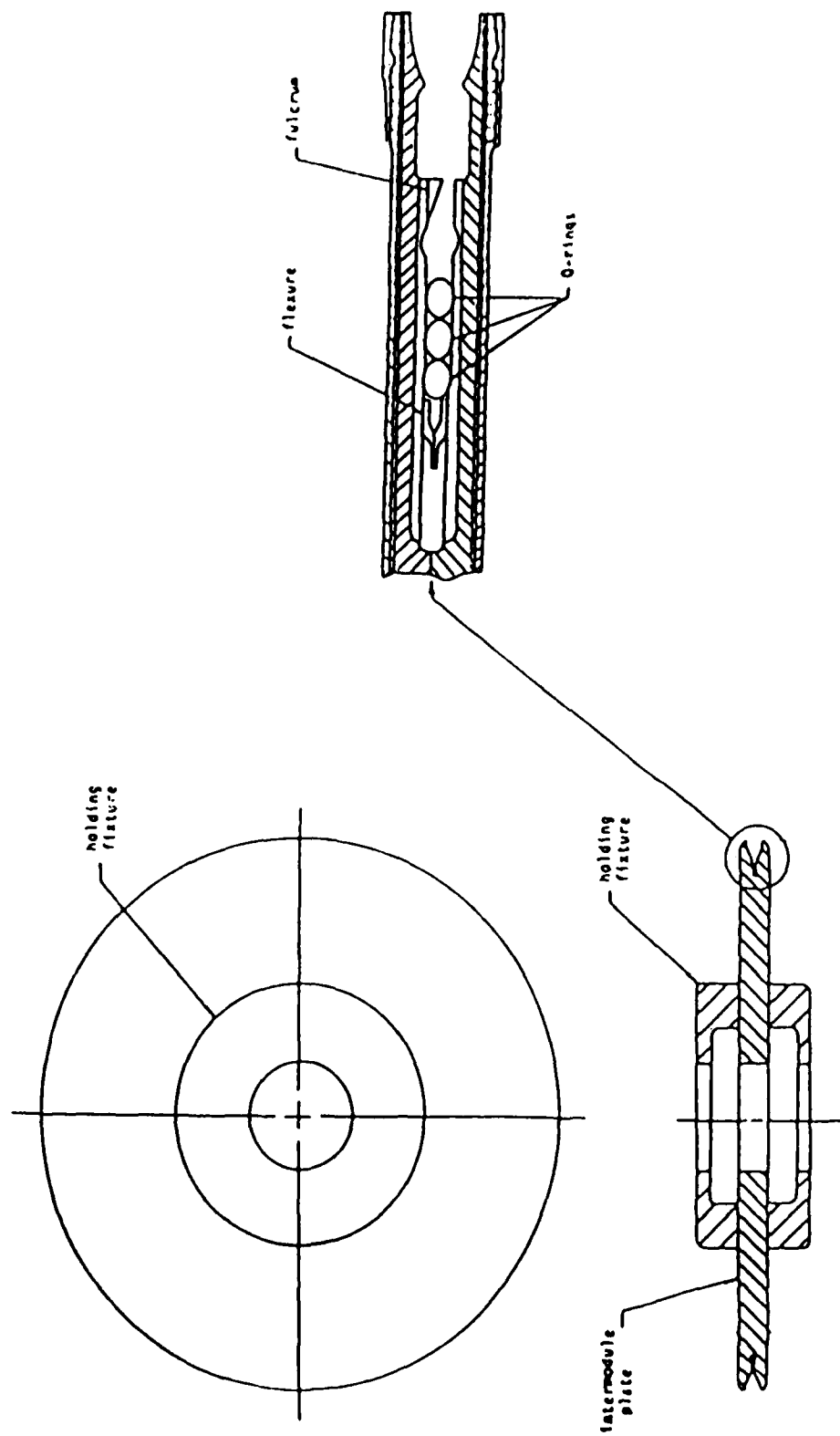


Figure 4 Plan and Cross-Section Views of High Velocity Helium Duct

O-ring(s) as shown. The model was composed entirely of solid elements. Calculations of modal properties, including energy distributions, were made for a range of values of material stiffness of the O-ring. Based on these calculations, a value was found that would allow the plate to meet both the damping and static stiffness requirements.



Figure 5 Single O-Ring Model, Undeformed Shape

The next step was finding a viscoelastic material with the required properties. After some searching, a form of fluorosilicon rubber was identified as a likely candidate. Arrangements were made with a manufacturer to have some fabricated into the required O-ring shape. The finished product, resembling a strand of spaghetti, was installed and the plate was retested.

Figure 6 shows, for the single O-ring configuration, predicted damping as a function of temperature along with measured values at two temperatures. The predicted natural frequency of the critical mode and the increase in static stiffness are also shown. Agreement between predicted and measured damping was excellent and the value was well above that needed to assure stability.

Figure 7 shows measured driving point frequency response functions between acceleration response and force input at the plate rim in the axial direction. The upper trace is for the plate with no damping insert and the lower trace is with two O-rings installed. The critical mode is at 2353 Hz. (without O-rings) and is characterized by out-of-phase motion of the plate lips, i.e. they move in opposite directions as they vibrate. The increase in damping due to the viscoelastic inserts is quite dramatic and results in a decrease of response at resonance of about 30 dB. The numerous modes of vibration that occur below 2353 Hz. are only slightly affected by the O-ring. They are in-phase modes in which the lips of the plate move together and therefore produce no strain in the viscoelastic.

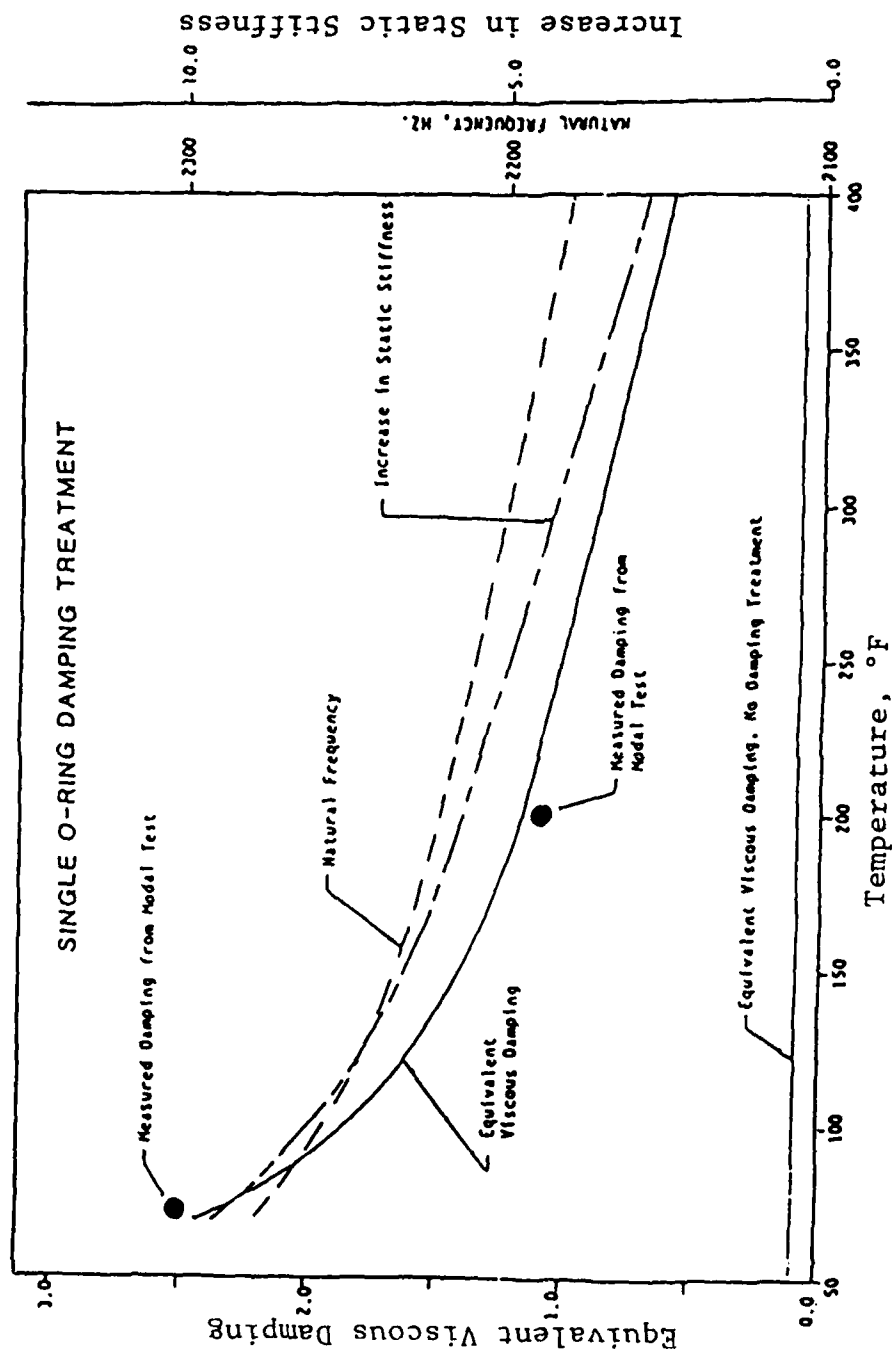
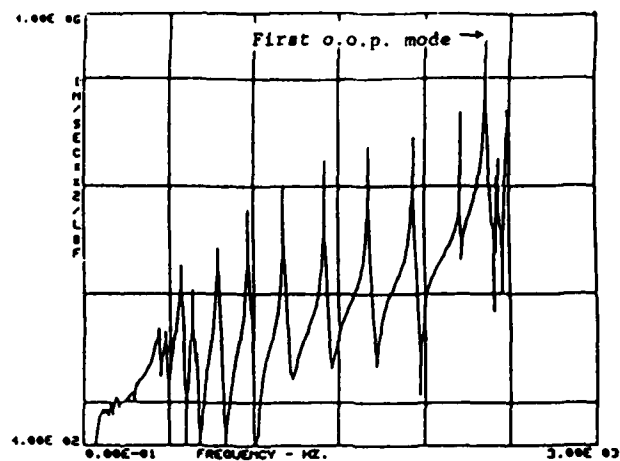
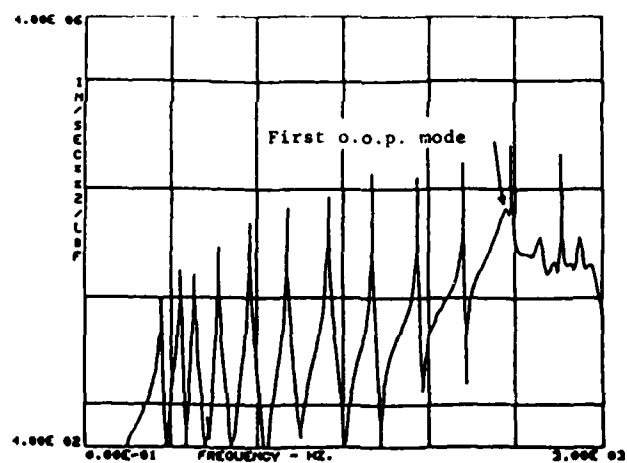


Figure 6 Properties of the High Velocity Helium Duct with Single O-Ring Damper



a) Without Added Damping



b) With Two O-Ring Inserts

Figure 7 Measured Acceleration/Force Frequency Response of High Velocity Helium Duct

4.2 CASE STUDY - SCALE MODEL DAMPED TRUSS

A small damped truss was designed and built as part of the PACOSS (Passive and Active Control of Space Structures) program. Its purpose was to graphically demonstrate the difference in behavior between two truss structures that differed in their damping characteristics but were otherwise similar. A finite element model of the truss is shown in Figure 8a.

The damped truss is constructed of 1/4" plexiglass rod. It is mounted in cantilever fashion to a fixed horizontal base. Horizontal dimensions are approximately 4" by 4". It is constructed in two 24" sections joined together at a 1" thick plexiglass plate. Discrete, extensional dampers are incorporated into the laces in the bottom four bays of the truss.

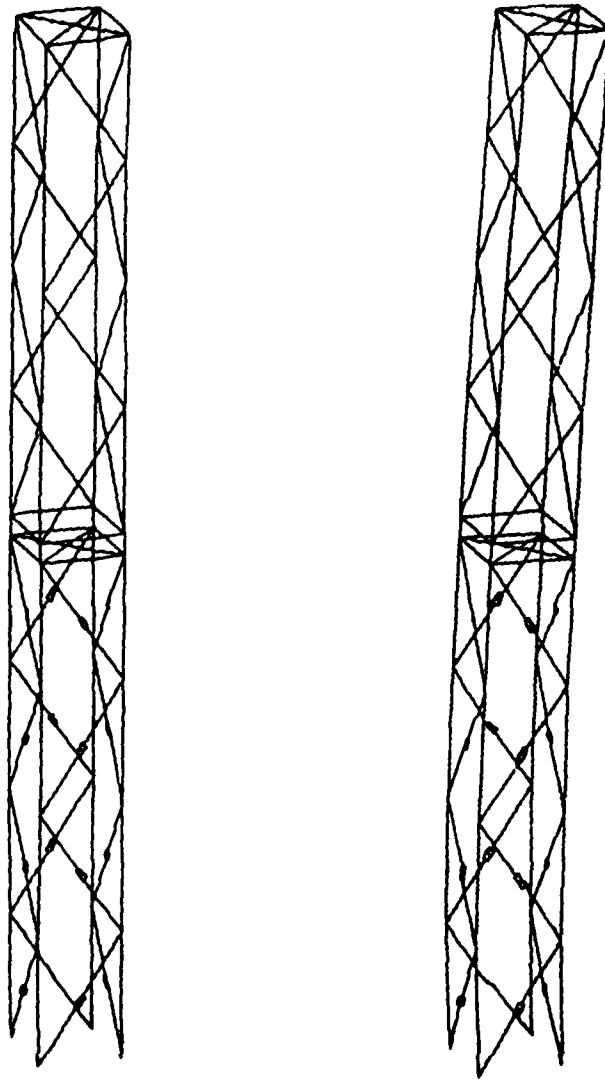
The undamped truss is constructed of Lexan and has solid laces without the damping links. The two trusses are mounted side by side and are excited by displacing the tip laterally and releasing them simultaneously. The transient vibration of the damped truss decays much more rapidly. Since most of the motion is produced by the lowest mode of vibration, the damping links were optimized for that mode. The links are arranged in a "K" pattern to obtain maximum flexibility and thus to make the motion as visible as possible.

Mode shapes of the undamped and damped truss are essentially the same. The first mode is shown in Figure 8b.

Damping was incorporated into one of the trusses in two ways. The first was the choice of structural material. Plexiglass has a material loss factor of about 0.04 compared to about 0.005 for Lexan. The second, more important, method was the inclusion of discrete, extensional damping elements in the laces of the lower truss section. Figure 9 shows a cross section of the damping element.

The links are loaded only in tension or compression when the truss vibrates in its first mode. Thus the extensional stiffness of the viscoelastic annulus in the dampers is a damping design parameter. This stiffness is GA/t where G = viscoelastic storage modulus, A = area of viscoelastic "ribbon", and t = radial thickness of the viscoelastic.

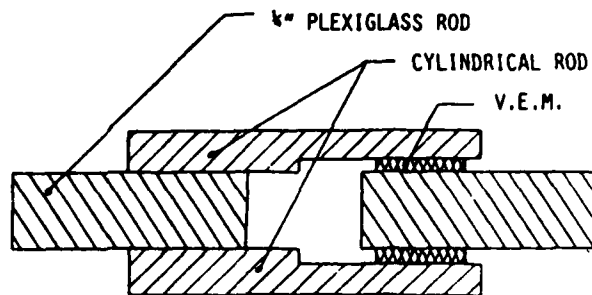
Figures 10 and 11 show the natural frequency and energy fraction in the viscoelastic for the first mode as functions of GA/t . The energy fraction is proportional to the modal loss



a) Undeformed Shape

b) First Mode of
Vibration

Figure 8 Undeformed and First Mode of Damped Truss



(B) CYLINDRICAL SHEAR CONFIGURATION

Figure 9 Schematic of Damping Link

factor. The curve of damping versus GA/t shows a peak, but at a value of GA/t too low to be practical. The limit on obtained damping is set in this case by the allowable shear stress in the viscoelastic and overall stability. The final choice was $GA/t = 250$, which was obtainable using ISD 112 viscoelastic at a thickness of 0.030".

A truss was fabricated with only the bottom bay damped to check out the fabrication process. This truss was tested and the damping obtained was considered satisfactorily for the desired purposes. Therefore, a model of a truss with dampers only in the bottom bay was executed. Table 3 shows excellent agreement between predicted and measured values for this configuration. The predictions include energy dissipation in the plexiglass as well as the viscoelastic. It is felt that the 8 pound weight added at the tip of the truss caused some non-linear behavior in the viscoelastic.

Table 4 illustrates an interesting point about the behavior of a damped truss, in this case a four bay damped truss. It lists the strain energy stored in each of the bottom four bays for the first mode shape. They are essentially equal, contrary to the behavior of a classical cantilever beam of uniform cross section. There is no contradiction; the same extensional compliance that causes significant energy storage in the laces (and thus significant damping) allows longitudinal displacement of the chords relative to each other. This is in contrast to a beam of solid cross section where bending does not produce significant shear deformation. The obvious conclusion is that damping links in a cantilever truss need not be located near the root to provide a worthwhile increase in damping.

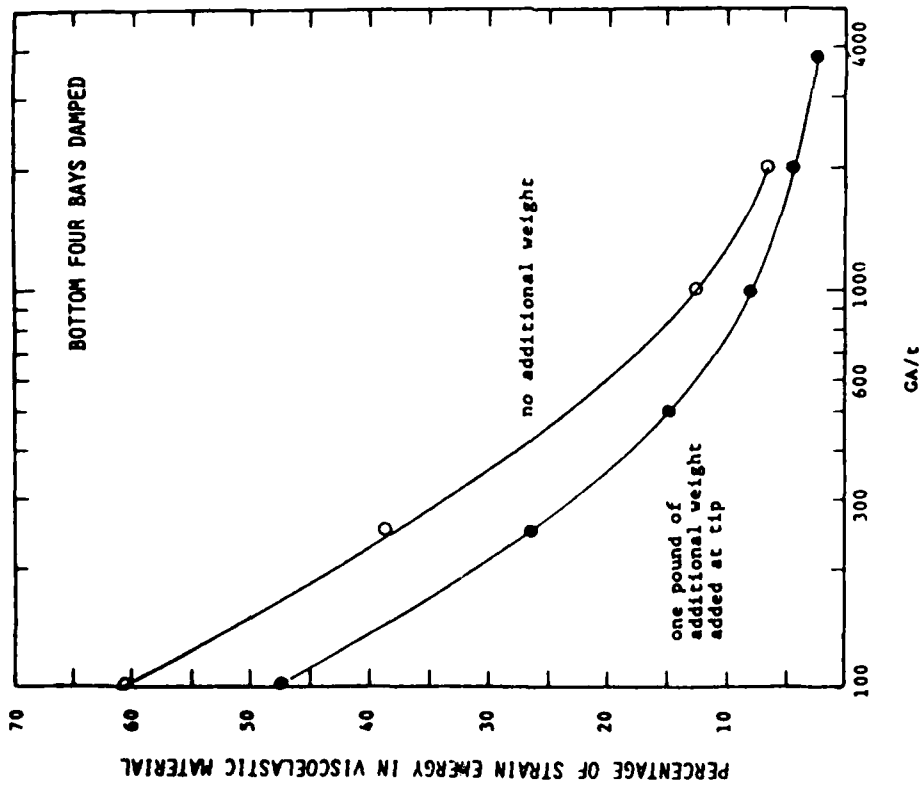


Figure 10 Damping of First Mode of Subscale Truss

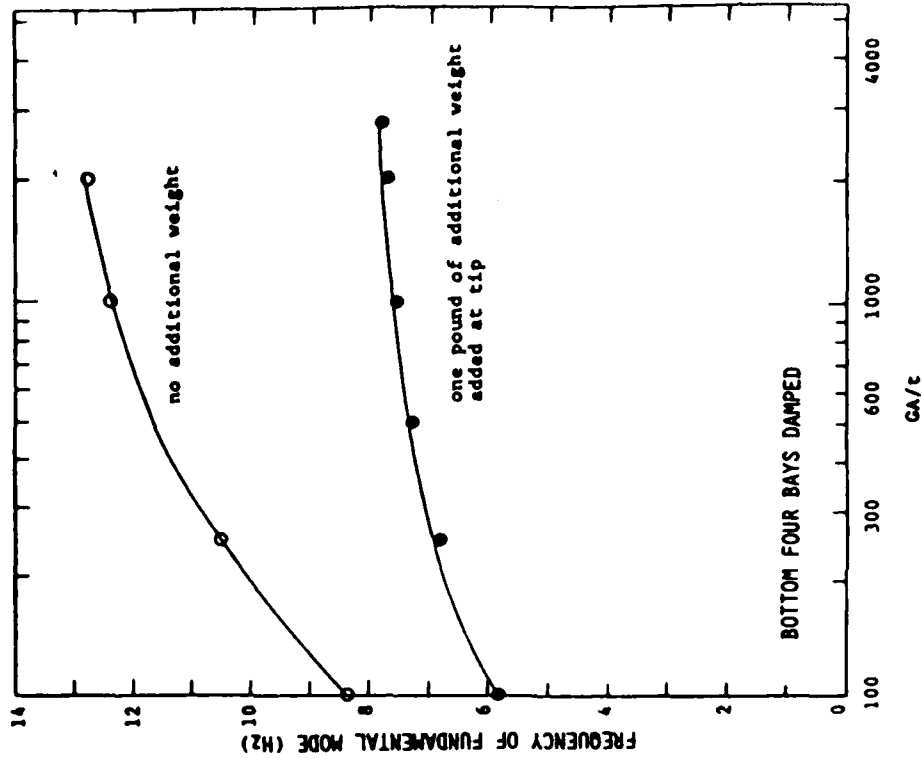


Figure 11 Frequency of First Mode of Subscale Truss

TABLE 3
Predicted and Measured Frequencies and Damping for First
Mode of the Subscale Truss - Dampers in Bottom Bay Only

	No Additional Weight Added		8 Pound Weight Added at Tip	
	Frequency (Hz)	Structural Damping	Frequency (Hz)	Structural Damping
Analysis	14.6	11.2 % *	3.2	6.4 % **
Experiment	15.5	11.5 %	3.1	4.9 %

* Assumes .046 for material loss factor of plexiglas @ 14.6 hz
 ** Assumes .035 for material loss factor of plexiglas @ 3.2 hz

TABLE 4
Strain Energy Distribution in the Viscoelastic
Links for the Four Damped Bay Truss (Mode 1)

Bay No.	Diagonal 1	Diagonal 2	Diagonal 3	Diagonal 4	Total
1 (Root)	0.425	2.752	0.490	2.725	6.110
2	0.541	3.059	0.539	2.937	6.775
3	0.482	2.848	0.482	2.964	7.073
4	0.425	2.587	0.493	2.537	6.392

ACKNOWLEDGEMENT

A portion of this work was sponsored under the PACOSS (Passive and Active Control of Space Structures) Contract. The prime contractor is Martin Marietta Aerospace, Denver Division. This contract is issued by the Air Force Wright Aeronautical Laboratories, Flight Dynamics Laboratory, Air Force Systems Command, United States Air Force, Wright-Patterson AFB, Ohio 45433.

REFERENCES

1. Crandall, S.H., "The Role of Damping in Vibration Theory," J. Sound and Vibration, Vol. 11, No.1, Jan. 1970, pp. 3-18.
2. Crandall, S.H., "Dynamic Response of Systems with Structural Damping," Air, Space, and Instruments, Draper Anniversary Volume, 1963, S. Lees, Editor, McGraw-Hill, also M.I.T. AFOSR No. 1561, Oct. 1961.
3. Foss, K.A., "Coordinates Which Uncouple the Equations of Motion in Damped Linear Dynamic Systems," Journal of Applied Mechanics, Vol. 25, 1958, pp. 361-364.
4. Duncan, W.J., Elementary Matrices, MacMillan & Co., New York, 1946.
5. Joseph, J.A. (Ed.) MSC/NASTRAN Applications Manual, MacNeal-Schwendler Corp., Los Angeles, Calif., April, 1977.
6. Rogers, L., (Ed.), "Conference on Aerospace Polymeric Viscoelastic Damping Technology for the 1980's," Air Force Flight Dynamics Laboratory, TM 78-78-FBA, Feb. 1978.
7. Johnson, C.D. and Kienholz, D.A., "Finite Element Prediction of Damping in Structures with Constrained Viscoelastic Layers," AIAA Journal, Vol. 20, No. 9, Sept 1982.
8. Ungar, E.E. and Kerwin, E.M. Jr., "Loss Factors of Viscoelastic Systems in Terms of Energy Concepts," Acoustic Society of America, Vol. 34, July 1962, pp. 954-957.
9. Johnson, C.D., Kienholz, D.A. and Rogers, L.C., "Finite Element Prediction of Damping in Beams with Constrained Viscoelastic Layers," Shock and Vibration Bulletin, No. 51, May 1981, pp. 71-82.
10. Rao, D.K., "Frequency and Loss Factors of Sandwich Beams Under Various Boundary Conditions," Journal Mech. Eng. Science, Vol. 20, No. 5, May 1978, pp. 271-282.

11. DiTaranto, R.A., "Theory of Vibratory Bending for Elastic and Viscoelastic Layered Finite Length Beams," Journal of Applied Mechanics, Vol. 32, Dec. 1965, pp. 881-886.
12. Ross, D., Ungar, E.E., and Kerwin, E.M., "Damping of Plate Flexural Vibrations by Means of Viscoelastic Laminates," Section 3 of Structural Damping, ASME, 1959.
13. Abdulhadi, F. "Transverse Vibrations of Laminated Plates with Viscoelastic Layer Damping," Shock and Vibration Bulletin, No. 40, part 5, Dec. 1969.
14. Lu, Y.P., Douglas, B.E. and Thomas, E.V., "Mechanical Impedance of Damped Three-Layer Sandwich Rings," AIAA Journal, Vol. 11, No.3, March 1973, pp. 300-304.
15. Austin, E.M., Johnson, C.D., and Kienholz, D.A., "Analysis and Design of Curved and Built-up Damped Structures using the Modal Strain Energy Method," CSA Engineering Report 83-10-02, October 1983.

ON VIBRATION DAMPING ANALYSIS
USING THE FINITE ELEMENT METHOD

R. A. Brockman
University of Dayton
Research Institute
Dayton, Ohio 45469

Supplementary paper for publication; was not presented.

ON VIBRATION DAMPING ANALYSIS USING THE FINITE ELEMENT METHOD

R. A. Brockman
University of Dayton
Research Institute

ABSTRACT

This paper describes some of the current solution methodology for finite element analysis of problems in vibration damping, and addresses several common questions regarding the differences between methods and computer programs. The discussion is intended for non-specialists in finite element methods, and focuses on basic questions and principles in the use of finite elements for damping design and analysis.

INTRODUCTION

The finite element method has been used for several years as a means of analyzing the effects of viscoelastic damping materials upon the steady-state vibration behavior of complex structures. A variety of programs and methods have been used by analysts at different organizations, with varying degrees of success. In the process, our collective experience has produced a large body of information on the relative merits of the many methods and software packages which have been used in such studies. We have learned a great deal from this experience; still, a great deal of myth and misconception persists regarding different methods and programs for performing vibration damping analysis. This note represents an attempt to clarify a few of these questions.

We begin by reviewing the three most common methods for finite element vibration damping analysis, defining their common theoretical basis, and noting some important distinctions between them. Next, we address briefly the differences between two general purpose finite element codes which have been used for damping analyses, and the impact which these dissimilarities have upon their ability to solve viscoelastic damping problems.

THEORETICAL CONSIDERATIONS

In the following, we outline the underlying theory which is common to all three of the solution methods to be described. The following basic assumptions are adopted:

- (a) displacements and strains are infinitesimal;
- (b) material behavior is linear and viscoelastic;
- (c) the steady-state viscoelastic behavior of all materials of interest can be characterized by three parameters: bulk and shear moduli and a damping coefficient; and
- (d) the applied loading, if any, varies sinusoidally with time.

With the above assumptions, our problem is described by the kinematic relationships and balance equations of linear elasticity: the strain-displacement equations,

$$\epsilon_{ij} = \frac{1}{2} \left(\frac{\partial u_i}{\partial x_j} + \frac{\partial u_j}{\partial x_i} \right) \quad (1)$$

the momentum and moment of momentum equations,

$$\partial \sigma_{ji} / \partial x_j + \rho \bar{b}_i = \rho \dot{v}_i \quad (2)$$

$$\sigma_{ji} = \sigma_{ij} \quad (3)$$

and the displacement and force boundary conditions,

$$u_i = \bar{u}_i \quad \text{on } \partial V_u \quad (4)$$

$$\sigma_{ji} n_j = \bar{t}_i \quad \text{on } \partial V_f \quad (5)$$

In the case of free vibration, or for forced vibration at a single frequency, it is assumed that each of the components of displacement varies sinusoidally with time at a common frequency,

$$u_i(x_k, t) = A_i(x_k) \sin[\omega t - \phi_i(x_k)] \quad (6)$$

or

$$u_i(x_k, t) = U_i(x_k) e^{i\omega t} \quad (7)$$

With the latter notation, which we use hereafter, the displacement amplitudes $U(x)$ may be complex-valued. For free vibration the frequency is unknown, while for forced motion the frequency is the same as the frequency of the prescribed forces during steady-state motion.

The material model consists of a linear relationship between strain and stress,

$$\sigma_{ij} = C_{ijkl} \epsilon_{kl} \quad (8)$$

in which the tensor C for an isotropic material is obtained from the bulk and shear moduli (K and G , respectively),

$$C_{ijkl} = (k - \frac{2}{3} G) \delta_{ij} \delta_{kl} + 2G \delta_{ik} \delta_{jl} \quad (9)$$

In turn, these moduli may be complex-valued, to account for the dissipative behavior of the material; with a common damping factor for both moduli, we take:

$$G = G'(1 + i\eta) \quad (10)$$

$$K = K'(1 + i\eta) \quad (11)$$

Both strains and stresses may assume complex values, with real and imaginary components denoting, for example, in-phase and out-of-phase contributions. It is important to note that, in most materials, the dissipative bulk and shear characteristics are different; however, the use of a single damping factor above reflects the practical limitations of most current applications software.

The finite element discretization of the system follows familiar procedures, resulting in a system of simultaneous equations:

$$([K] - \omega^2 [M]) \{U\} = \{F\} \quad (12)$$

in which

- $[K]$ = system stiffness matrix (complex-valued)
- $[M]$ = system mass matrix (real-valued)
- $\{U\}$ = nodal displacements (complex-valued)
- $\{F\}$ = nodal force amplitudes (usually real-valued)
- ω = frequency of vibration

For the case of forced vibration, $\{F\}$ and ω are known, $\{U\}$ are the unknowns, and the response is determined by solving a system of complex-valued simultaneous linear equations. In free vibration, $\{F\} = \{0\}$ and the frequency ω is unknown, as are the nodal displacements $\{U\}$; the numerical problem is a generalized eigenvalue problem with complex coefficients, whose solutions consist of frequency-mode shape pairs $[\omega, \{U\}]$ corresponding to natural frequencies and mode shapes of the system.

The theoretical formulation sketched above is common to virtually all finite element treatments of the vibration damping problem. Each finite element code contains a unique library of finite elements, which determine the contents of the system matrices $[K]$ and $[M]$. Furthermore, a particular

program may not include all of the numerical solution methods outlined in Section 3, thereby restricting the choice of an approach to be used in problem-solving.

SOLUTION TECHNIQUES

Three distinct types of solution techniques for damped vibration response are in widespread use at present. Below we outline the important features of these three methods, and point out some of their most important differences. It is important to note that for each method, differences in the solution methodology between finite element programs arise chiefly due to the choice of numerical algorithms and programming techniques, whose primary influence is on efficiency rather than the numerical results produced.

Complex Eigenvalue Solution. This technique is used less commonly than the others because of the technical complexity and expense of solving the numerical problem. We consider the unforced motion of the system,

$$([K] - \omega^2[M]) \{U\} = \{0\} \quad (13)$$

The frequencies and mode shapes of the damped system are determined directly by the solution of a complex eigenvalue problem.

Frequency Response Solution. This method considers a forced vibration at a known frequency,

$$([K] - \omega^2[M]) \{U\} = \{F\} \quad (14)$$

and obtains the corresponding displacement shapes by solving a system of complex-valued linear equations. The behavior of the system over a range of frequencies (and therefore, the identification of resonant points) is analyzed by using several frequency values, and plotting the resulting amplitudes and phase quantities versus forcing frequency.

Real Eigenvalue Solution. The third technique involves an additional assumption: the influence of damping action on the natural frequencies and mode shapes of the model is small. The solution is based upon the unforced vibration of the undamped system,

$$([K'] - \omega^2[M]) \{U\} = \{0\} \quad (15)$$

Here $[K']$ is the real part of the stiffness matrix, ω is the (unknown) frequency of vibration, and $\{U\}$ are the corresponding nodal displacements, which are now real-valued. The real eigenvalue problem is solved for frequency

and mode shape data which describe the undamped system. We assume that the natural frequencies of the damped system are nearly the same as those obtained for the undamped system. Damping information (such as system loss factors) are based upon the assumption that the mode shapes of the damped system are also similar to the undamped system: relative amounts of strain energy stored in each of the materials present should therefore also be similar. With this data, and the damping factors for each material, one can compute an approximation to the system loss factor.

None of the above solution techniques presents fundamental difficulties which render them incapable of representing a particular physical system; even the real eigenvalue method, which involves additional simplifying assumptions, is generally regarded as good methodology. We should note, however, that the way in which these methods are applied and the way in which results are interpreted are crucial if realistic results are to be obtained.

The first source of difficulty involves the proper choice of material properties. The variation of shear and damping properties with frequency is often quite pronounced, and in the two eigenvalue-based methods the frequency of vibration is not known a priori. Representative properties (based, for example, on rough estimates of the natural frequencies) must be assumed in order to carry out the analysis. Once the frequencies are estimated from these properties, new property values may be introduced and the analysis repeated. Typically, three or four such iterations are needed to match material properties with the frequency and mode shape data. Rogers, Johnson and Keinholz [1] have outlined the necessary procedures in detail.

At present, the general-purpose finite element packages do not include such an iterative procedure as a standard feature, and the task of performing the solution in this way is the responsibility of the user. If the iterative process is used, the real eigenvalue method (commonly called the modal strain energy method) is quite reliable, and in fact produces a wealth of information which is useful for design purposes. In many instances, however, damping calculations are performed without iterating material properties, and produce correspondingly poor results. The improvement in damping predictions which is obtained with the iterative procedure (which normally involves the modification of a few lines of materials data) is well worth the small effort involved.

The frequency response solution, for which the frequency of vibration is known exactly before the equations are solved, eliminates the need for property iteration but introduces new pitfalls of its own. Since the forcing frequencies are predefined, the system natural frequencies

may not correspond precisely to those used for the solution. Thus, although those values which are obtained are consistent as regards material property variation with frequency, it may be difficult or expensive to obtain damping data exactly at the resonant frequencies. Often it is necessary to perform sweeps over frequency ranges of interest, in order to isolate amplitude peaks at which critical damping data are required.

A second type of difficulty arises due to the differences in computed response obtained with the forced vibration technique and the eigenvalue-based methods. Some debate has focused on the question of "which is better?", when in fact the choice of the most appropriate technique is dependent upon the problem to be solved. Consider, for example, two vibration experiments performed on a single test specimen; for simplicity, we can think of a simple beam, although the differences are more significant for more complex structures. In experiment 1, the root of the beam is clamped tightly and forced sinusoidally by a shaker; in experiment 2, a piezoelectric element at the tip of the beam is used to apply a sinusoidal force, with the root section remaining stationary. In experiment 1, the first resonant point corresponds to a pure, classical first mode of the clamped-free beam; experiment 2 gives a first resonance which excites a similar (but not identical) mode: the force boundary conditions are different. For the simple beam, the resonant frequencies and corresponding system damping values are not radically different, but certainly they are not quite the same. More complicated geometries lead to more pronounced differences between methods; for example, the first few natural mode shapes of a clamped cylindrical shell are quite different in character from the resonances predicted by forcing the shell at a single point.

The choice of method is usually a matter of modeling the true physical situation faithfully, a fundamental but too-often-neglected consideration. This point is no more or less important in vibration damping analysis than in any other exercise in dynamic analysis; however, the adoption of "pet" methods for damping analysis within individual organizations has sometimes made the choice of method a point of contention.

We can best emphasize the differences in the modal (eigenvalue-based) and frequency response solution methods by noting the situations in which each is appropriate. Most often, the modal approach is preferred for design, because of the more basic and general information it provides about the behavior of the damped structure. The modal data is more likely to provide useful information about damping performance over wide ranges of forcing frequency, without detailed knowledge of the in-service loading. When detailed information is needed about dynamic behavior under specified

forces at definite frequencies of interest, the frequency response method provides this data directly.

Occasionally, differences in damping predictions have been attributed solely to differences in implementation between computer programs. We wish to emphasize that, while differences in eigenvalue solution methods do exist in the codes in general use for damping analysis, disagreement between their numerical results is most often a function of modeling technique, choice of method, and interpretation of results. Given identical eigenproblems, the variation in results between programs is extremely small.

In practice, the most significant differences between damping predictions occur due to such factors as:

- the decision of the analyst to iterate, or not to iterate, the eigenvalue-based solution until material properties used in the analysis are in agreement with the frequencies obtained;
- the comparison of forced vibration solutions at a pre-specified frequency with natural frequency results obtained at somewhat different frequencies; and
- the comparison of analytical and/or experimental data which represent subtly different physical problems.

Each of these issues arises as a result of the way in which computer programs are applied to the solution of a problem, or of the interpretation of computed results. Improved numerical methods, better programs, and more detailed finite element models will never eliminate the need for stating the problem correctly and interpreting the results with care.

MODELING PROCEDURES

Significant differences in damping predictions can result purely from differences in finite element modeling; normally these are the result of the choice of finite element types and the degree of model refinement in otherwise similar models. Choice of a finite element type is dictated both by the analyst (and his opinion of the expected dynamic behavior) and by the particular finite element program which is used. In the following, we discuss two specific programs, NASTRAN and MAGNA, to indicate the kinds of modeling decisions which are dictated by the choice of computer program.

In discussing NASTRAN, it is important to distinguish between the MacNeal-Schwendler (MSC) proprietary version and the public domain version of NASTRAN distributed by COSMIC.

Although COSMIC NASTRAN contains a large library of structural elements and solution procedures, it is largely unsuitable for practical vibration damping analysis. The finite elements available in the COSMIC program are much less sophisticated than the newer elements in MSC/NASTRAN, particularly when solid continua (such as shear-flexible damping layers) or curved thin shells must be modeled. Furthermore, the COSMIC version of NASTRAN does not contain the necessary strain energy calculations for performing damping solutions by the real eigenvalue (modal strain energy) approach.

MSC/NASTRAN [2] includes a wide variety of specialized structural elements, including plates, thin shells, beams, rings, etc. Three dimensional solids are included as well. The structural elements are widely used and, in this author's experience, quite reliable. The variety of elements of this type which are available in MSC/NASTRAN are certainly a strong point. Some difficulties may arise in modeling beams, plates, or shells with damping layers, since such shear-flexible layers must be modeled with three dimensional elements. However, HEXA and QUAD4 finite elements (which are incompatible but may be joined at node points) have been used with success in modeling damping treatments. The breadth of solution techniques available in MSC/NASTRAN for linear dynamics is unparalleled, and analysis paths exist in the program for each of the numerical methods discussed previously. Most of the NASTRAN work performed to date in the area of vibration damping analysis appears to be based on the modal strain energy (real eigenvalue) method.

MAGNA [3] is strongly oriented toward solid continua, and contains a wide variety of 3-D solid elements; the number of nodes is highly flexible, and several integration options (selective, non-Gaussian, etc.) are available to improve element performance. However, MAGNA offers a more limited choice of structural elements than some other general purpose codes. The shell elements in MAGNA are unique in that they involve only translational degrees of freedom and are therefore displacement-compatible with solids, so that difficulties in joining dissimilar types of elements are minimized. When fully three dimensional behavior is expected in all or part of a model, MAGNA may offer some advantages; however, the complete range of element types available is far less than that of NASTRAN. MAGNA includes two of the solution methods outlined in the previous section (the complex eigenvalue technique is not available), each one the equivalent of the corresponding MSC/NASTRAN solution branch. Material damping factors may be specified in equation form as functions of temperature and frequency in MAGNA, but properties are not iterated automatically during a natural frequency solution.

The choice of a computer program raises similar questions to the choice of solution method, in that the appropriate choice is problem-dependent. For this reason the author, also the developer of MAGNA, is and will continue to be a user of NASTRAN (and several other finite element codes) as well: each finite element problem is different, and requires an appropriate method of solution.

ACKNOWLEDGEMENTS

The author is grateful to Mr. Michael L. Drake of UDRI for suggesting the preparation of this manuscript, and to Dr. Lynn Rogers, AFWAL/FIBA, Wright-Patterson Air Force Base, Ohio and Drs. Conor Johnson and David Keinholz of CSA Engineering, Palo Alto, California, for their comments and suggestions on its content and presentation.

REFERENCES

1. L. Rogers, C. D. Johnson, and D. Keinholz, "The Modal Strain Energy Finite Element Analysis Method and its Application to Damped Laminated Beams," proc. 51st Shock and Vibration Symposium, October 21-23, 1980, San Diego, California.
2. R. H. MacNeal (editor), MSC/NASTRAN User's Manual, The MacNeal-Schwendler Corporation, Los Angeles, California, 1981.
3. R. A. Brockman, MAGNA (Materially And Geometrically Nonlinear Analysis) User's Manual, Part I: Finite Element Analysis Manual, UDR-TR-82-111, University of Dayton Research Institute, Dayton, Ohio, 1983.

RESULTS OF FINITE ELEMENT ANALYSIS
OF DAMPED STRUCTURES

Matthew F. Kluesener, P. E.
Associate Research Engineer
University of Dayton Research Institute
Dayton, Ohio

RESULTS OF FINITE ELEMENT ANALYSIS OF DAMPED STRUCTURES

Matthew F. Kluesener, P.E.
Associate Research Engineer
University of Dayton Research Institute
Dayton, Ohio

ABSTRACT

Finite Element Analysis (FEA) is being used increasingly to model passive damping configurations on integrally damped structures. However, the modeling of passive damping designs on complex structures poses two problems. First of all, the thin damping layers generally result in high aspect ratios (length ÷ thickness) of the 3D solid elements representing the damping system. Secondly, if a multilayered damping system is modeled, there are a large number of degrees-of-freedom (DOF) which results in a costly computer run. This paper discusses ways to reduce the number of elements representing the damping system and the accuracy of the damping prediction using high aspect ratios. Experimental tests and corresponding FEA of a double constrained layer damped cantilever plate show that aspect ratios up to 1000:1 yield very accurate results. The experimental FEA comparison also shows that FEA modeling techniques such as using membrane elements for the constraining layers or using an "equivalent" element to represent several layers of the damping system yield good results and save considerable computer time.

INTRODUCTION

The University of Dayton Research Institute (UDRI) has been involved in the area of vibration damping for over twenty years with much of the research being sponsored by the Air Force Materials Lab (AFWAL/MLLN) at Wright-Patterson Air Force Base.

One joint research effort between UDRI and Allison Gas Turbine Operations is the Dynamic Behavior of Advanced Fan Materials program (F33615-82-C-5022) sponsored by AFWAL/MLLN. The overall objective of this program is to develop and evaluate techniques and materials for introducing high levels of intrinsic damping into fan or compressor blades of a gas turbine engine with a view toward eliminating the need for a shroud and to quantify the design changes and performance advantages that would arise from the incorporation of the damping.

One of the major tasks in this program is the analytical evaluation of the damping configuration on the fan blade. The analytical evaluation of the modal loss factors was to be accomplished by the finite element method. The blade chosen for study in this program is the TF41-A-100 first stage clapperless fan blade from the Rolls-Royce Allison TF41 Turbofan engine. A finite element model of the undamped blade is shown in Figure 1.

The damping configuration to be analyzed was a double constrained layer damping system on each side of the airfoil. It became apparent during the construction of the FE model that two problems could develop. First, the number of degrees-of-freedom (DOF) for a complex model such as this would be quite large. Secondly, the aspect ratio (length : thickness) of the 3D solid elements could approach 1000 to 1; the recommended limit for these element types is 100 to 1.

To investigate these concerns, tests and FEA were conducted on two cantilever plates with a double constrained layer damping system (on one side). The cantilever plate (shown in Figure 2) was 12" long x 3.5" wide x 0.25" thick.

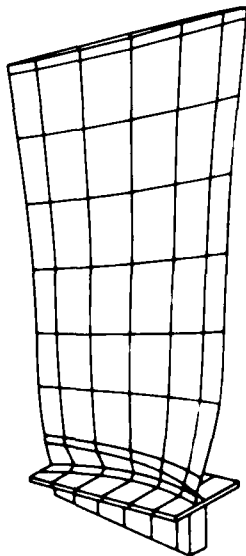


Figure 1. FE Model of Undamped TF41-A-100 Blade.

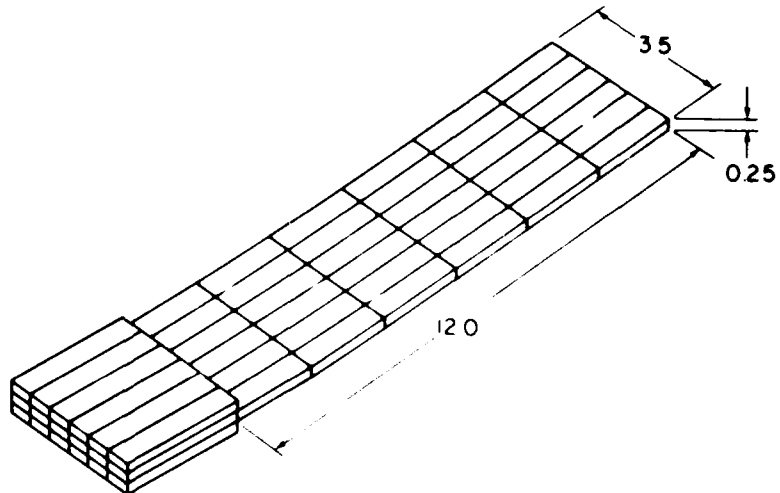


Figure 2. Cantilever Plate FE Model.

Before discussing the finite element model and results it is instructive to consider the methods by which the modal loss factors can be determined by FEA. This involves performing a forced vibration analysis (forced harmonic response) of the structure in which a load is imposed on the structure at the natural frequency of interest. Using the forced vibration analysis, the modal damping can be calculated by either of two methods: the half-power bandwidth method or the strain energy method.[1,2,3,4]

When using the half-power bandwidth method, a forced vibration analysis is performed at a number of discrete frequencies centered about the natural frequency. The displacement amplitude of a point on the structure (usually a point of high displacement) is plotted versus forcing frequency to generate the frequency response plot. The loss factor is then calculated as the ratio of the bandwidth defined by the half-power points (maximum response) to the natural frequency, as shown in Figure 3.

The advantage of this method is that a frequency response plot is generated which, when compared to other plots, allows one to observe the effect of damping as represented by the lower broader peaks. However, a large number of computer runs (10 to 15) is required to generate the data for a single mode at a single temperature, making this procedure expensive for large models.

When using the strain energy method, the output desired from the forced vibration response is the strain energy in each element caused by the load applied to the structure at the frequency of interest. The loss factor is then determined as the ratio of the total energy dissipated to the total strain energy stored in the structure. The energy dissipated is equal to the summation over all the elements of the product of the loss factor for each element and the strain energy stored in each element (see Figure 4). The loss factor is thus calculated from one forced response run, rather than from several runs.

The strain energy can also be calculated based on the normal mode shape deflection rather than the deflection from the forced response.[2] Using the normal mode saves the additional expense of the forced response run. It is felt that either the normal mode shape or the forced response can be used in the strain energy method, but that one approach might match the test conditions or end use of the structure more closely than the other. It should be noted that normal modes are associated with proportional damping [5] and the damping

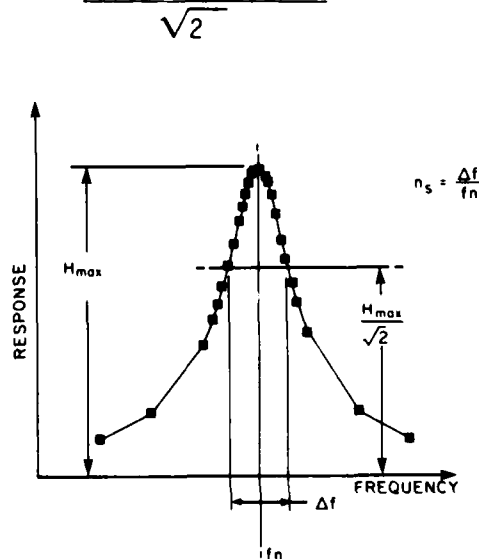


Figure 3. System Loss Factor by Half-Power Bandwidth.

$$\text{SYSTEM LOSS FACTOR, } \eta_s = \frac{\text{ENERGY DISSIPATED}}{\text{TOTAL STRAIN ENERGY}}$$

$$= \frac{\sum_{i=1}^n \eta_i \times SE_i}{\sum_{i=1}^n SE_i}$$

SE_i = STRAIN ENERGY IN i^{th} ELEMENT

η_i = MATERIAL LOSS FACTOR FOR i^{th} ELEMENT

Figure 4. System Loss Factor by Strain Energy Method.

treatment being considered here generally lead to non-proportional damping.[6]

Also, in highly non-proportionally damped structures, the use of normal modes to predict damping may become a moot point because there is increased participation of other modes (i.e. more modal coupling). [6]

Results Using High Aspect Ratios

Figure 5 shows the cross section of one of the damping configurations tested and analyzed. This configuration, referred to as Plate 1, consisted of the 0.25" plate with 0.002" 3M ISD-110, damping material, 0.007" stainless steel middle constraining layer, 0.003" Soundcoat MN damping material, and 0.007" stainless steel outer constraining layer. All layers in the FE model were modeled with 3D solid-thick shell elements. Since the elements were 2" long and some elements were as thin as 0.002", the aspect ratios on some elements were 1000 to 1.

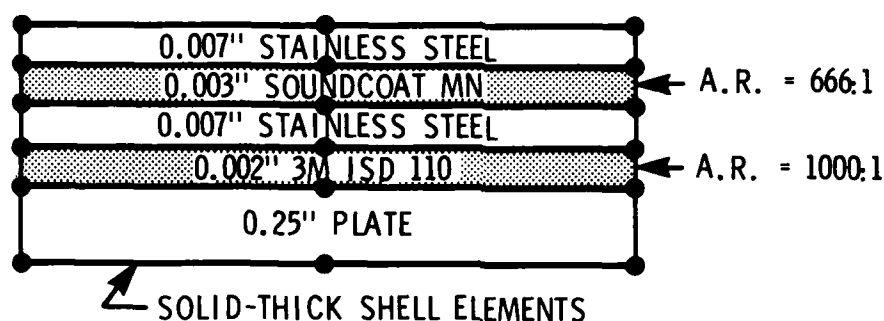


Figure 5. Plate 1 Damping Configuration.

The results of the FEA and test of Plate 1 are shown in Figure 6, for the second bending mode. It can be seen that there is very good agreement between the test results and the FE forced vibration results. The results from the FE normal mode are considerably higher than the test results. It is felt in this case that the strain energy method using the forced response more closely matches the test. In both the test, and the forced response analysis the plate was subjected to a small tip load. Another cause of the discrepancy could be that the tip load does not excite a pure mode. Indeed damping couples modes together. Perhaps if the test had been conducted with the clamped end of the cantilever mounted on a shaker the mode shape of the cantilever plate may have been more nearly a pure mode than exciting the cantilever at the tip. Then perhaps the normal mode method would more closely match the shaker test.

The second damping configuration evaluated, referred to as Plate 2, is shown in cross section in Figure 7. This damping system had two layers of the same damping material (0.002" 3M ISD-112) separated by a 0.003" middle constraining layer. The outer constraining layer was 0.007" stainless steel. All layers were modeled with 3D solid-thick shell elements. The aspect ratios of the damping layers were 1000 to 1.

The results of the FEA and test of Plate 2 are shown in Figure 8 for the second bending mode. Again there is very good agreement between the test results and the FE forced vibration results. As for the Plate 1, the normal mode results are higher than the test results; the same explanation given for

Plate 1, holds here as well.

Results for the first torsion mode are shown in Figure 9. The forced vibration results agree well with the test results, as do the normal mode results. In this instance, driving at the tip of the cantilever for the forced response (and test results) yields approximately the same results as the normal mode.

The reader may have noticed in the Plate 1 and Plate 2 results presented so far, that although the magnitude of the peak damping and the shape of the loss factor curve predicted by the FE forced vibration is nearly identical to the test results, the forced vibration curve is shifted 25°F to the left of the test data. This temperature shift could be due to two causes. The finite element model of the cantilever plate could be stiffer than the actual specimen; this is in fact the case, with the second bending mode frequency approximately 8 percent high. The other cause could be that the actual damping material is stiffer than the properties being input into the FEE model. It is likely that the cause is a combination of the above two factors, and this point is still being investigated.

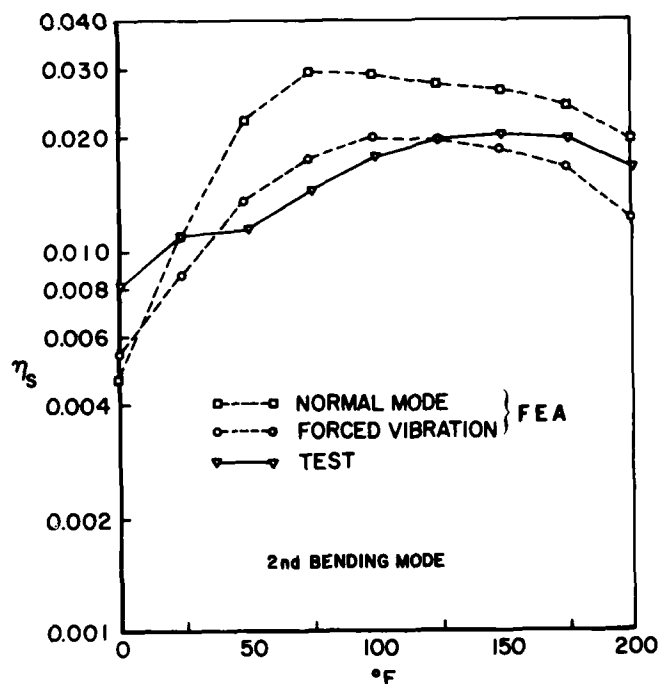


Figure 6. Plate 1 FEA and Test Results.

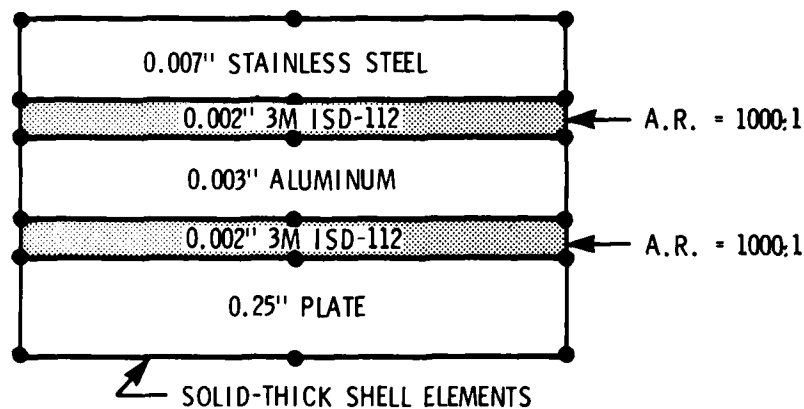


Figure 7. Plate 2 Damping Configuration.

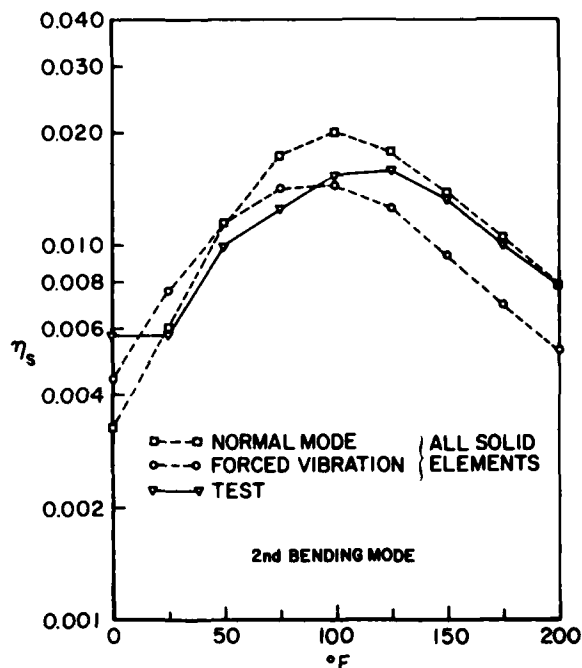


Figure 8. Plate 2 FEA and Test Results.

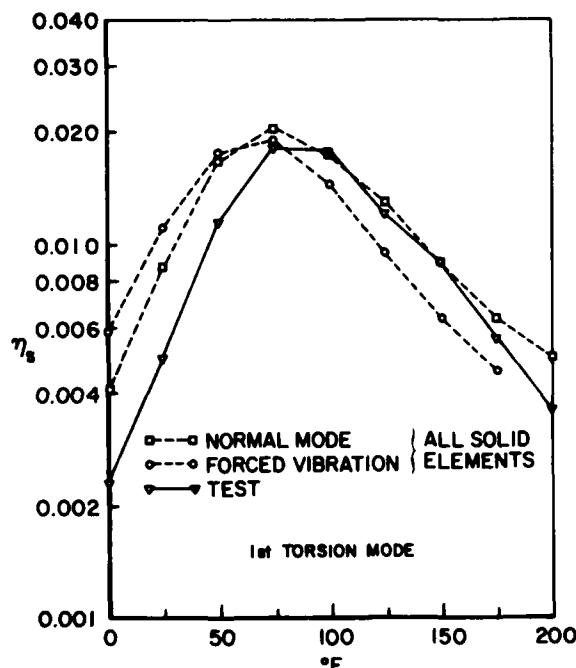


Figure 9. Plate 2 FEA and Test Results.

The results presented so far have been for aspect ratios up to 1000 to 1. To see if the prediction of loss factors could be improved, the FE model was changed. Twelve elements were used up the length of the cantilever instead of six and the aspect ratio was correspondingly cut by a factor of two. The change in the results due to the lower aspect ratio was insignificant. Therefore, the use of aspect ratios up to 1000 to 1 was acceptable. The use of aspect ratios greater than 1000 to 1 is still being investigated.

Modeling Techniques to Reduce the DOF

The large number of DOF in the FE model of the TF41-A-100 blade with a double constrained layer damping system on both sides of the airfoil was a concern; there was a risk that the FE job would be too large to run on the computer or would run only with a weekend priority. Therefore, two means of reducing the number of DOF were investigated. The first method involves the use of membrane elements to model the constraining layers. The second approach is to replace several layers in the damping system by an "equivalent" element.

Use of Membrane Elements for Constraining Layers

The purpose of the constraining layer in a constrained layer damping system is, as its name implies, to constrain the damping material. During bending the constraining layer places the damping material in a state of shear stress and thus dissipates energy. The constraining layer being stiff, and usually very thin, undergoes very little shear deformation and is subjected to in-plane loading. Thus it has the characteristics of a membrane and can be represented by a membrane element. The damping layer on the other

hand undergoes considerable shear deformation and therefore must be modeled with shear deformable elements such as 3D solid-thick shell (solid) elements.[4]

The use of membrane elements for constraining layers as applied to the Plate 1 damping configuration is shown in Figure 10. The nodes of the membrane elements are coincident with the nodes on the upper surface of the damping layers. Therefore, the membrane elements do not add any DOF to the three solid elements used for the damping layers and plate. Thus the damping system shown in Figure 5 which was modeled by five solid elements through the thickness is modeled by three solid elements and two membrane elements, resulting in a 33 percent reduction in DOF.

Figure 11 shows the FE forced vibration results using the membrane and solid elements model. Also shown are the FE forced vibration results using all solid elements, previously shown in Figure 6. It is seen that the two methods compare very favorably. Notice that the damping predicted by the use of the membrane elements is nearly uniformly lower than the results using all solid elements. This is probably due to the fact that the outer damping material and outer constraining layer are not as far away from the neutral bending axis because the membrane elements have no physical thickness.

For structures with constraining layers that are thin relative to the base structure, such as Plate 1, this introduces a small error. Thick constraining layers would result in more error.

Use of Equivalent Solid Element

The other means of reducing the number of DOF became apparent by studying the Plate 2 configuration (see Figure 7). Since the two damping layers are the same thickness and of the same material and are separated by a thin middle constraining layer, it seemed that the overall behavior of the three layer system would be governed by the soft damping materials.

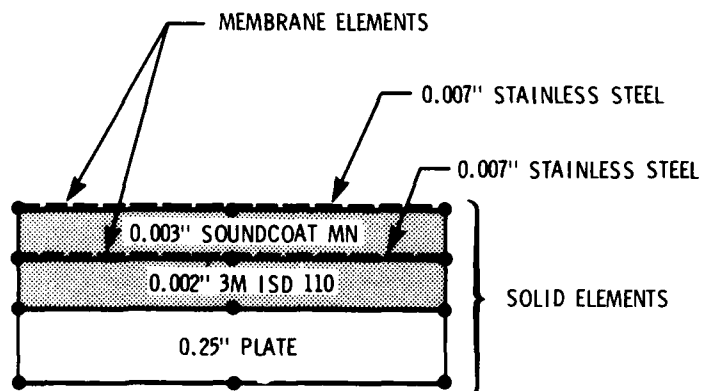


Figure 10. Plate 1 Using Membrane and Solid Elements

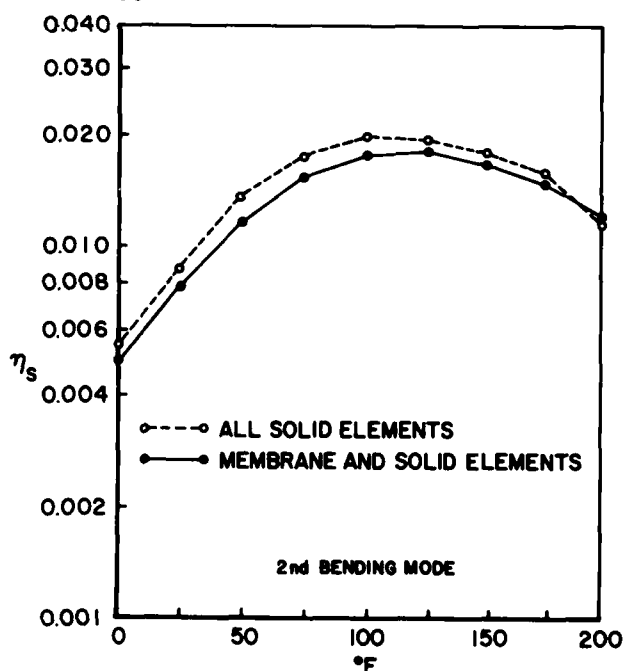


Figure 11. Plate 1 FEA Results.

Furthermore, it seemed that the three layers could be represented by a single "equivalent" layer. It only remained to determine the dynamic properties of the three layers. The properties were determined from a symmetric sandwich beam test. Usually to determine the properties of a constrained layer damping material, the material is placed between symmetric sandwich beams and tested over a broad temperature and frequency range, [7,8] as is shown in Figure 12. In the present case, the three layer system was placed between symmetric sandwich beams, as shown in Figure 13, and tested as if it were a typical damping material. The properties could have been determined analytically and the test procedure avoided if the suitable equations had been operational on our computer.

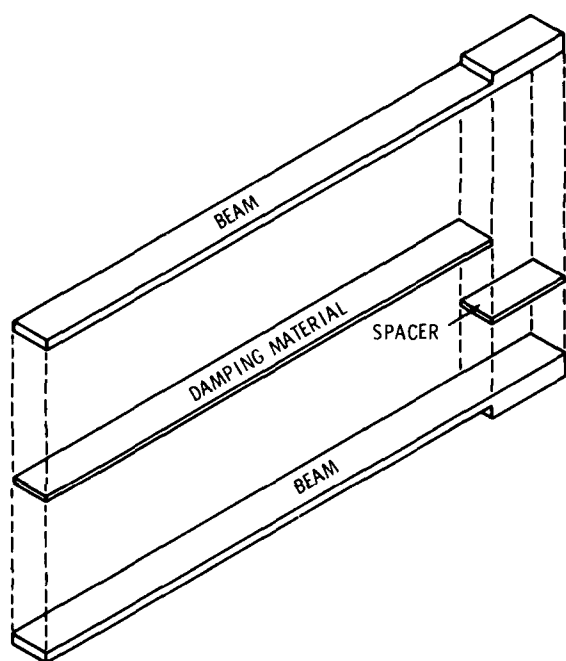


Figure 12. ASTM Beam Test for Damping Material Properties.

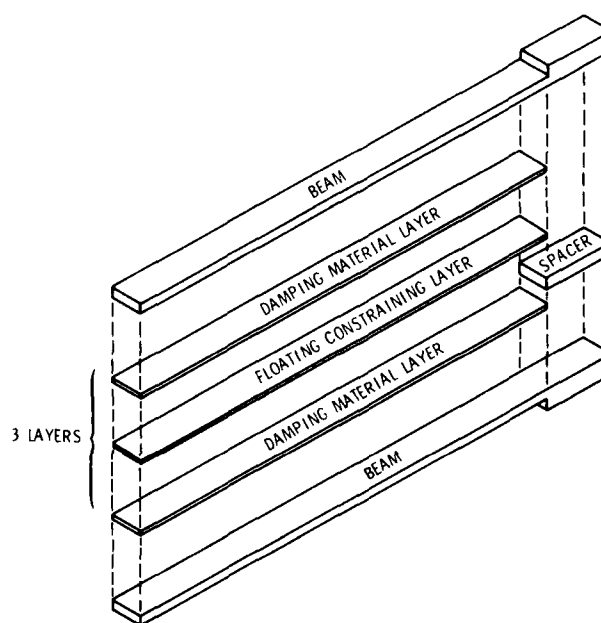


Figure 13. Damping Material Test of 3 Layers.

The application of this modeling technique to the Plate 2 configuration is shown in Figure 14. Figure 15 shows the second bending mode FE forced vibration results using all solid elements (previously shown in Figure 8) and the equivalent solid element. The results are nearly identical. The same is true for the first torsion mode shown in Figure 16.

Summary and Conclusions

It was seen from tests and analysis of a cantilever plate that aspect ratios up to 1000 to 1 on the solid-thick shell elements used to represent the damping can be used and still get a good prediction of the system loss factor. The prediction of the magnitude of the peak damping was very good, although, there was a temperature shift associated with the loss factor versus temperature curve.

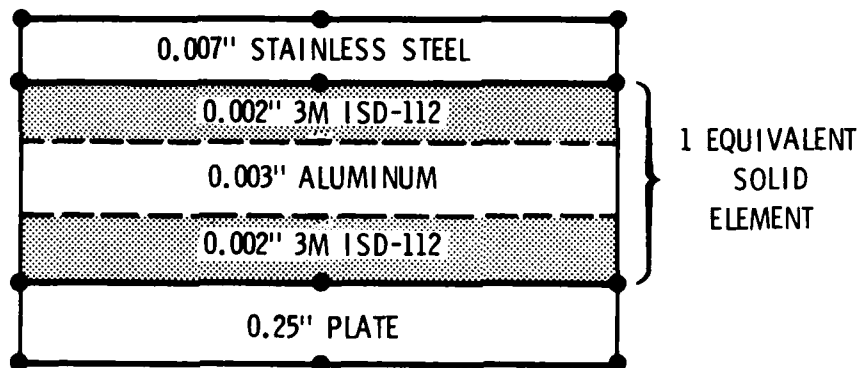


Figure 14. Plate 2 Using Equivalent Solid Element.

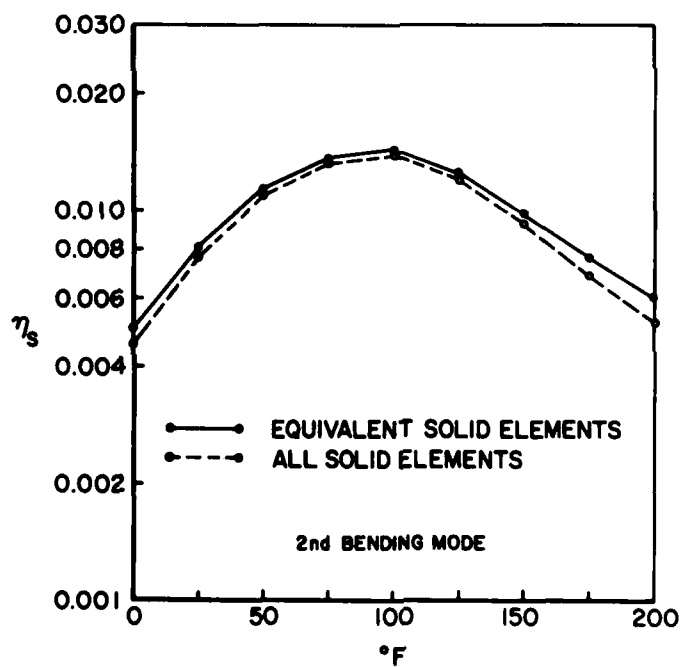


Figure 15. Plate 2 FEA Results.

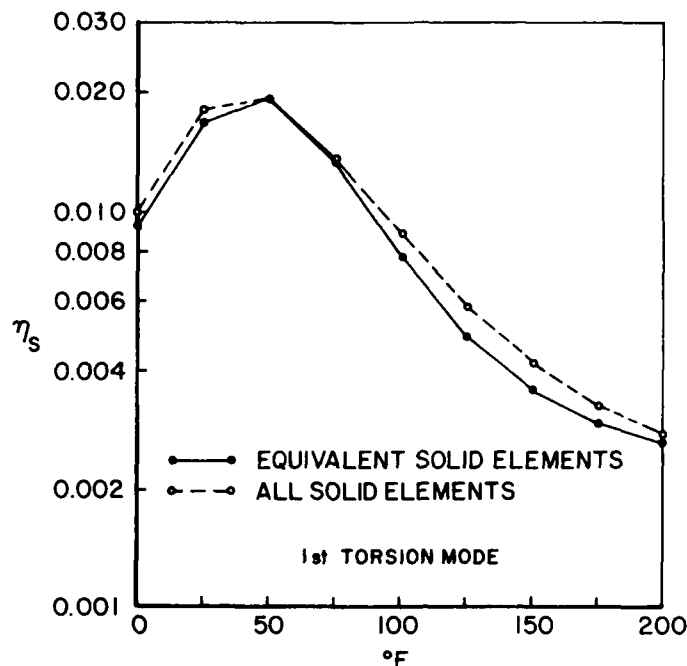


Figure 16. Plate 2 FEA Results.

The modeling techniques for reducing the DOF were found to be accurate. The use of membrane elements for constraining layers predicts a slightly lower value of damping than the standard approach and reduced computer costs 44 percent in the present analyses. An equivalent solid element replacing the two damping materials and middle constraining layer gave nearly identical results as the standard modeling approach. This technique reduced computer costs 60 percent.

Most importantly, the modeling techniques for reducing the DOF make modeling complex structures with multi-constrained layer damping systems easier and less costly to run.

Acknowledgements

The author wishes to acknowledge the following people for their contributions to this work. To Dave Oeth of Allison and Mike Drake of UDRI for their comments and suggestions. To Dave Hopkins and Rick Nash for assisting in the FEA and to Pam Brown for typing the paper.

This work was sponsored by the Air Force Materials Laboratory (AFWAL/MLLN) at Wright Patterson Air Force Base with Dr. D.I.G. Jones as contract monitor.

References

1. Kluesener, Matthew F., and Drake, Michael L.; "Damped Structure Design Using Finite Element Analysis," The Shock and Vibration Bulletin 52, part 5, (May 1982): 1-12.
2. Johnson, Conor D., Kienholz, David A., and Rogers, Lynn C., "Finite Element Prediction of Damping in Beams with Constrained Viscoelastic Layers," The Shock and Vibration Bulletin 51, part 1 (May 1981): 71-82.
3. Vibration Damping Short Course (mimeographed), June 1982, University of Dayton Research Institute, Dayton, Ohio.
4. Soni, M.L., "Finite Element Analysis of Viscoelastically Damped Sandwich Structures," The Shock and Vibration Bulletin 51, part 1 (May 1981): 97-109.
5. Hurtz, Walter C., and Rubenstein, Moshe F.; Dynamics of Structures, Englewood Cliffs, New Jersey: Prentice-Hall, Inc. 1964.
6. Soni, M.L., University of Dayton Research Institute, Dayton, Ohio. Interview, March 1984.
7. Drake, Michael L., Terborg, Gary E., Polymeric Material Testing Procedures to Determine Damping Properties and the Results of Selected Commercial Materials, AFWAL-TR-80-4093; University of Dayton Research Institute, July 1980, for Materials Laboratory, Air Force Wright Aeronautical Laboratories, Wright-Patterson Air Force Base, Ohio.

SEGMENTING AND MECHANICAL ATTACHMENT OF CONSTRAINED
VISCOELASTIC LAYER DAMPING TREATMENTS FOR FLEXURAL AND
EXTENSIONAL WAVES

Edward M. Kerwin, Jr. and P. W. Smith, Jr.
Bolt Beranek and Newman Incorporated
Cambridge, Massachusetts

SEGMENTING AND MECHANICAL ATTACHMENT OF CONSTRAINED
VISCOELASTIC LAYER DAMPING TREATMENTS FOR FLEXURAL AND
EXTENSIONAL WAVES

Edward M. Kerwin Jr. and P.W. Smith Jr.
Bolt Beranek and Newman Inc.
Cambridge, Massachusetts

Abstract

Segmenting (periodic interruption) increases the effectiveness of a constrained-layer damping treatment for flexural waves at frequencies below the peak damping for the continuous system (G.G. Parfitt, 4th ICA, 1962). The interruption of the constraining layer results in "induced" strains in the viscoelastic layer, giving higher dissipation than for the continuous system. There is an optimum segment length for a given treatment. In this paper we discuss the application of segmented constrained layers to the damping of extensional waves. There are significant parallels with the flexural wave case; the optimum segment length for a given damping treatment is essentially the same. As with flexural waves, the results apply below an upper frequency limit. Achievable loss factors for extensional waves are lower than for flexural waves for a given system cross section.

Mechanical attachment of the constrained-layer damping treatment is sometimes required. Damping performance is compromised to the extent that the constraining layer lateral deflection is inhibited. Here we report quantitative results on the effect of a "point" fastener. Results are given for the treatment effective area lost due to a rigid fastener, and for a fastener of finite lateral stiffness. These results can guide the design of fasteners to minimize their effect on performance.

1. INTRODUCTION

The constrained viscoelastic layer treatment is well known for flexural wave damping.¹⁻⁴ For a continuous constraining layer the loss factor exhibits a broad peak as a function of frequency. As Parfitt⁵ has shown, cutting or segmenting the constraining layer improves the damping at frequencies below the peak. The enhanced performance is the result of induced shear strain in the viscoelastic layer around the discontinuities in the constraining layer. There is an optimum segment length for which the low-frequency damping is raised approximately to the level of the peak for the continuous system, and the high-frequency behavior is essentially unaffected.

In the work reported here, the segmented constraining layer concept is applied to the damping of extensional waves. In this case the continuous constraining layer, if of the same material as the base plate, would also carry extensional waves. Thus the induced strains generated by segmenting are essential to effective damping. We determine the distribution of strain and strain energy in the viscoelastic layer, finding again an optimum segment length which is essentially the same as that for flexural waves. That this should be the result is reasonable in that the excitation of the segmented constrained layer is via surface strain in the base plate for both wave types. However, because of the higher base plate elastic strain energy (for the same surface strain), a given treatment provides lower damping in the case of extensional waves.

The effect of a localized constraint, as by a "point" fastener, is evaluated in terms of the reduction of the shear strain field in the viscoelastic layer. An effective area of cancellation of the strain energy is determined for a rigid fastener, and this loss in treatment effectiveness is found to be significant. In addition, the lateral input stiffness of the constraining layer, as seen by the fastener, is determined. Thus the effect of fastener compliance and the attendant mitigation of the loss in shear strain is evaluated, so that fasteners can be designed for minimum impact on system performance. Some limitations of the present analysis are noted.

2. SEGMENTED CONSTRAINED LAYERS FOR FLEXURAL WAVES

2.1 Continuous Treatment

The constrained viscoelastic layer is a familiar treatment for damping flexural waves in beam and plates.¹⁻⁴ At a given temperature, the characteristic performance of a continuous treatment (see Fig. 1) yields a loss factor that rises at low frequencies, reaches a maximum value, and decreases at high frequencies. The height of the curve (η_{\max}) and the frequency at

which occurs are determined by the system geometry and the dynamic properties of the viscoelastic layer.

A basic parameter is α , the shear spatial decay parameter. As Fig. 2 shows, in a one-dimensional system a localized lateral displacement of the constraining layer decays in space as $e^{-\alpha x}$. The relative disturbance amplitude decays to e^{-1} in a distance $1/\alpha$. The decay constant α is defined as follows:

$$\alpha^2 = \frac{G_2}{H_2} \left(\frac{1}{K_1} + \frac{1}{K_3} \right) \quad (1)$$

where G_2 = shear modulus,

H_2 = layer thickness,

$K = EH$ = extensional stiffness of a unit length and width, and

E = extensional modulus of the layer, taken as Young's modulus E for beams, or as the "plate modulus" $E/(1-\nu^2)$ for plates.

Subscripts 1, 2, and 3 refer to the baseplate, the viscoelastic layer, and the constraining layer, respectively.

In a spatially harmonic wave field, the same decay parameter is useful in describing the behavior in combination with the flexural wavelength λ_p and wavenumber $k_p = 2\pi/\lambda_p$. An important combined parameter is the "shear parameter":

$$\gamma = \frac{\alpha^2}{k_p^2} = \left(\frac{\alpha \lambda_p}{2\pi} \right)^2 \quad (2)$$

For a range of "practical" treatment parameters, the maximum loss factor occurs for

$$\gamma \doteq 0.5$$

or equivalently

$$\frac{\alpha \lambda_p}{2\pi} \doteq 0.7$$

and the corresponding decay distance is

$$1/\alpha \doteq \lambda_p/4.4$$

i.e., roughly one quarter of a flexural wavelength. This result make intuitive sense in that the wave generates stress and strain reversals every half wavelength, and the maximum damping occurs when the shear strain energy in the viscoelastic layer is maximized.

The "weight" or potential effectiveness of a constrained layer treatment is determined by a geometric parameter Y with a simple physical interpretation in terms of the uncoupled and coupled bending stiffnesses:³

$$Y = \frac{B_{\text{coupled}} - B_{\text{uncoupled}}}{B_{\text{uncoupled}}} \quad (3)$$

For a thin viscoelastic layer $H_2/H_1 \ll 1$ and for H_3/H_1 small, one finds

$$Y \doteq 3 H_3/H_1$$

Figure 3 shows η_{max} versus Y with η_2 as parameter.

As a reference example we see that

$$\text{for } H_3/H_1 = 0.2$$

$$\text{and } \eta_2 = 1.0$$

$$\text{one finds } Y \doteq 0.7$$

$$\eta_{\text{max}} \doteq 0.1$$

(the same material is assumed for base plate and constraining layer; and H_2/H_1 is taken to be small). Here the treatment weight and thickness are about 20% of that of the baseplate. For lighter treatments η_{max} is roughly proportional to $(H_3/H_1)\eta_2$.

2.2 Segmented Treatment

As frequency decreases below that for maximum damping for a continuous treatment, the flexural wavelength becomes progressively longer than the shear decay distance $1/\alpha$. Thus, the distance between reversals of curvature (i.e., of surface strain) becomes greater and greater, and shear strain in the viscoelastic layer can relax by generating extensional strain in

the constraining layer. Such relaxation decreases the strain energy in the viscoelastic layer, and thus decreases the loss factor of the composite plate laminate.*

In this longer wavelength region, cuts made in the constraining layer generate induced strains in the viscoelastic layer and an increase in the system loss factor. Parfitt and Lambeth^{5,6} showed this effect both experimentally and analytically. Their results appear in Fig. 4 which shows the effect of various numbers of cuts in the constraining layer of a treatment applied to a beam. As the number of cuts increases, the low-frequency performance rises, passes through a more-or-less flat maximum value comparable to the maximum loss factor for the continuous treatment, and then falls. These results clearly show that there is an optimum length of constraining layer segments for the system tested. Parfitt's analysis, carried out for "light" treatments, $H_3/H_1 \ll 1$,† shows that the optimum segment length is given by

$$\alpha L_{\text{opt}} = 3.28 \quad (4)$$

independent of the properties of the base plate. Here α is the shear decay constant of Eq. (1). Parfitt's results have been confirmed and extended to a multiple-layer configuration by Plunkett and Lee⁷.

Later experimental work by Zeinetdinova et al.⁸ confirms the utility of a segmented constraining layer for heavier (thicker) treatments as well. They state that the optimum segment length is just about the same as that for light treatments, i.e., $\alpha L_{\text{opt}} \approx 3$ to 4.

The existence of an optimum value of αL indicates a best combination of the shear stiffness of the viscoelastic layer and the extensional stiffness of the constraining layer. The curves of Fig. 5 illustrate the point. There we show the distribution of shear energy density in the viscoelastic layer, here treated as an elastic layer. As in Fig. 1, uniform extension of the base plate is used as the input. The strain energy density is normalized to the maximum value occurring in the optimum patch, and results are shown for values of α that are 1/2 and 2 times

*Note that as the flexural wavelength increases for constant wave amplitude, the curvature and surface strain drop, with corresponding proportional decreases in the strain energy in baseplate flexure and viscoelastic-layer shear. The relaxation described above is in addition to these effects and, therefore, reduces the loss factor.

†And presumably also $H_2/H_1 \ll 1$.

the optimum, corresponding to values of shear modulus $1/4$ and 4 times the optimum. As the curves show, the higher shear modulus increases the maximum energy density, but results in a more rapid spatial decay with distance from the edge of the patch. On the other hand, the lower shear modulus results in a lower maximum energy density but a lower spatial decay rate. The maximum damping will occur when the integrated energy is greatest, i.e., at αL_{opt} .

3. APPLICATION TO EXTENSIONAL WAVES

In the control of structureborne sound, wave types other than flexural can be of practical importance. Extensional waves are an obvious example; and in shells one can encounter a range of waves from those that are nearly pure flexural to extensional or membrane waves, for which "in-plane" stresses dominate. The latter wave types involve higher wave speeds, impedances, and energies (in appropriate senses); and damping them by applied treatments is more difficult.

Let us consider purely extensional waves in a flat plate as a limiting case, and determine the utility of segmented constrained layer treatments for damping such waves. Further, if we take the constraining layer to be made of a material having the same extensional wave speed as the base plate, it is clear that a continuous constrained viscoelastic layer treatment provides negligible damping. Consider that near any point of excitation or discontinuity the viscoelastic layer will bring the constraining layer into the same extensional motion as the base plate, so that relative tangential motion between the two essentially disappears. In this "spatial steady state" a continuous treatment is ineffective. The plane extensional stiffness of the viscoelastic layer is assumed to be much less than the corresponding combined stiffnesses of the base plate and constraining layer, so that the extensional component of damping is also negligible; i.e., $E_2 H_2 \ll E_1 H_1 + E_3 H_3$.

Thus, if a constrained layer treatment is to be at all effective for extensional waves, ways must be found to introduce shear strains into the viscoelastic layer. Cutting the constraining layer into segments is a good, low-mass means to this end. When the segments are small relative to the extensional wavelength, they will respond to the tangential displacement field on the surface of the baseplate quasi-statically, i.e., elastically, without carrying waves. There are strong parallels to the case of flexural wave damping discussed above, including essentially the same optimum segment length, and approximately constant damping in the lower frequency, long wavelength region. There are also differences between the cases, namely--lower levels of damping for a given treatment, and different high-frequency limitations.

For extensional waves the simple model of Figure 1 is appropriate in describing the behavior of a segment in the low-frequency, long wavelength range. Although the baseplate is wavebearing, we take the segment to be (much) smaller than a wavelength, so that the extensional strain in the baseplate is nearly constant over a segment length. Also, since the segment is small relative to a wavelength, its response is dependent principally on the elastic properties of the system; and its inertial properties may be ignored.

Figure 6 shows the fraction of total strain energy stored in the viscoelastic layer for a purely elastic system, as a function of αL for various "weights" of treatment (i.e., for constraining layer thickness ratios H_3/H_1 from 0.1 to 1.0). Each of the curves shows a maximum for $L = 3.5$.

When the viscoelastic nature of layer 2 is included, the effective loss factor for a segment of constrained-layer treatment on a baseplate of the same length can be determined. Figures 7 and 8 shows such results for $H_3/H_1 = 0.2$ and 1.0, respectively: effective loss factor η_{eff} versus the real part of αL for viscoelastic layer loss factors ranging from 0.1 to 2.0. Here again the maximum system loss factor, and thus the optimum value of $Re(\alpha L)$, is found for $Re[\alpha L_{opt}] = 3$ to 4.

This range of values indicates essentially the same result as given by Parfitt for light constrained layer treatments for flexural waves. The analogy to extensional waves holds surprisingly well, even for heavy treatments ($H_3/H_1 = 1$).

The above results show the strong similarity between the optimum segment length for flexural and extensional wave damping. A comparison of Figure 3 with Figures 7 and 8, however, indicates that a given treatment produces significantly lower damping for extensional waves. Specifically, for the "reference" case $H_3/H_1 = 0.2$, $\eta_2 = 1.0$, Figure 3 (flexural waves) shows a maximum system loss factor $\eta = 0.1$ while Figure 7 (extensional waves) shows $\eta = 0.032$ as the loss factor for the optimum segment length. Thus, the same treatment produces only about 1/3 the damping for extensional waves as for flexural waves.

Let us consider whether this result is consistent with expectations. In a thin plate in flexure the extensional strain varies linearly through the plate thickness, passing through zero at the center. On the other hand, the corresponding strain is uniform through the thickness of a plate undergoing simple extension. Thus, for a given surface strain ϵ_s in a plate of thickness H one has the following:

	<u>Flexure</u>	<u>Extension</u>
Strain	$\epsilon_s \cdot z/(H/2)$	ϵ_s
Mean-Square Strain	$\epsilon_s^2/3$	ϵ_s^2

(z is the coordinate in the thickness direction, $-H/2 < z < H/2$.)

Since the strain energy density is proportional to the mean-square strain, the strain energy for a given surface strain is three times as great for extension as for flexure. Further, because surface strain is the "driving quantity" for a segmented constrained layer treatment (for long wavelengths), the loss factor for extensional waves should be about 1/3 of that for flexural waves, as was found for our reference case above. This simple, rule-of-thumb argument ignores flexural energy in the constraining layer, and is, therefore, appropriate for light treatments. Also for light treatments, the extensional energy in the constraining layer should be comparable (and small) for the two wave types.

The high-frequency performance of a segmented constrained layer treatment is limited by various system resonances. In particular, the first extensional wave resonance will occur when $L_{opt} = \lambda_{ext}/2$; and this extensional wavelength λ_{ext} will be the same in the base plate and the constraining layer if the wavespeeds are the same. Thus, we would expect the optimum segments to provide approximately constant damping up to about $L_{opt} = \lambda_{ext}/4$, with irregular and decreasing performance at higher frequencies. (The frequency dependence of the properties of the viscoelastic material must of course be considered in performance calculations.) Other resonances that may occur include the lateral and normal resonance of the constraining layer on the viscoelastic layer. These are estimated to occur at about 1.0 and 1.7 times the frequency where $L_{opt} = \lambda_{ext}/2$.

4. EFFECT OF A FASTENER ON CONSTRAINED LAYER TREATMENT PERFORMANCE

It is sometimes necessary that a localized fastener be placed through a constrained-layer damping treatment. Such a fastener might be required, for example, to retain the constraining layer or to serve as an attachment for some auxiliary structure or device. Such a fastener restricts the lateral motion of the constraining layer in its vicinity. As a practical matter we want to determine the quantitative measure of "vicinity". We therefore determine the constraining-layer displacement field for a localized applied force, and also find the input stiffness. These results are then applied to

calculate the reduction in energy stored in the viscoelastic layer. The integral of the reduction in relative energy density is then interpreted as an "area defect" i.e., an area of the damping treatment that is removed from service by the fastener.

4.1 Constraining Layer Displacement Around a Local Input Force

In developing an understanding of the effect of a fastener we first consider the displacement that is generated by a force applied in the plane of the constraining layer. The force is assumed applied uniformly at a circle of radius a ; see Figure 9. The constraining layer is treated as a thin plate in plane stress, bonded to an elastic layer (layer 2, the viscoelastic layer). For the purposes of this first approach to the problem several simplifying assumptions have been made:

- a) The traction stress at the interface between the constraining layer and the viscoelastic layer is taken to act at the neutral plane of the constraining layer: bending moments are neglected.
- b) The baseplate is treated as a rigid foundation.
- c) Within the constraining layer, see Figure 10, an annular element is allowed to have strains representing radial compression ϵ_{rr} and shear $\epsilon_{r\theta}$, but not circumferential extension $\epsilon_{\theta\theta}$. This assumption was made for analytical convenience: to allow for a simple closed-form solution with which to assess the phenomenon. It is a conservative assumption in that it makes the plate appear somewhat stiffer to the localized force.

Under these assumptions, the lateral displacement of the constraining layer in the direction of the applied force (taken as the x-direction) is

$$\frac{u_x(r)}{u_a} = \frac{K_0(kr)}{K_0(ka)} \quad (5)$$

Here, $K_0(kr)$ is the modified Bessel function⁹ which decreases monotonically with increasing argument and:

$$k^2 = 4 \left(\frac{1-\nu^2}{3-\nu} \right) \alpha^2 \quad (6)$$

where ν = Poisson's ratio of the constraining layer material, and

$$\alpha^2 = \frac{G_2}{H_2 K_3} = \frac{G_2}{H_2 E_3 H_3} \quad (7)$$

The spatial decay constant α is the same as that discussed earlier (See Eq. (1), noting that here we have set $(1/K_1) = 0$ for a rigid baseplate). For a typical value of $\nu = 0.3$ for steel, aluminum, etc.,

$$k \doteq 1.16\alpha, \quad (\nu = 0.3) \quad (8)$$

so that the spatial decay constant k for the two-dimensional field around the localized force is about 1/6 larger than that for the one-dimensional cases treated previously.

The response described by Eq. (5) is such that all displacements are in the x direction, with a magnitude dependent on the radial distance from the location of the force. That is: circular contours around the force remain circular but are displaced relative to each other in the x -direction. See Figure 10.

4.2 Input Stiffness

The solution of the fastener problem requires K_{in} the input stiffness to the constraining layer as seen by the fastener. Under the assumptions listed above we find:

$$K_{in} = \frac{F}{u_a} = \frac{\pi}{a} \left(\frac{3-\nu}{1-\nu^2} \right) E_3 H_3 \, ka \frac{\mathcal{K}_1(ka)}{\mathcal{K}_0(ka)} \quad (9)$$

To illustrate the behavior of this function, Figure (11) presents the normalized input stiffness κ_{in} as follows:

$$\kappa_{in} = \frac{K_{in}}{\frac{\pi}{2} \left(\frac{3-\nu}{1-\nu^2} \right) E_3 H_3} = ka \frac{\mathcal{K}_1(ka)}{\mathcal{K}_0(ka)} \quad (10)$$

The stiffness varies relatively slowly with ka (i.e., with fastener radius) over the range shown.

To develop some quantitative feeling for the magnitude of the input stiffness, consider the following example:

Estimate ka :

- assume that the segment length is the optimum.

- note:

$$ka = kL_{\text{opt}} \cdot \frac{a}{L_{\text{opt}}}$$

$$kL_{\text{opt}} = 1.16 \alpha L_{\text{opt}} \quad , \quad \text{for } \nu = 0.3 \\ \doteq 4$$

- assume $\frac{a}{L_{\text{opt}}} \doteq 1/200$

e.g., 0.1 in. diameter fastener for a 10-in. segment length

- Then $ka \doteq 4/200 = 0.02$

- whence $\kappa_{\text{in}} \doteq 0.2$ (see Figure 11)

$$K_{\text{in}} = (0.2) \frac{\pi}{2} \left(\frac{3-\nu}{1-\nu^2} \right) E_3 H_3 \\ \doteq E_3 H_3 \quad \text{for } \nu = 0.3.$$

That is, the input stiffness for the parameters chosen is approximately $K_3 = E_3 H_3$, the in-plane stiffness of a square piece of the constraining layer, with force applied normal to opposite edges. This result is not very sensitive to the assumed fastener radius. As we noted above, the input stiffness varies rather slowly with ka , specifically we find from Figure 11:

$$K_{\text{in}} \sim (ka)^{0.255} \quad (0.01 < ka < 0.07) \quad (11)$$

Thus, a doubling of fastener radius increases the input stiffness by only about 20%.

In order to determine the effect of a local fastener, let us assume that a uniform lateral displacement u_0 , say in the x direction, would have existed everywhere in the vicinity of the fastener in the absence of the fastener (see Figure 12). Then for a fastener having lateral stiffness K_f and a constraining layer input stiffness K_{in} as determined above, we can show that the actual x -displacement at the fastener is u_a :

$$u_a = \frac{u_o}{(1 + K_f/K_{in})} \quad (12)$$

whereas the perturbation or localized displacement induced in the constraining layer by the fastener is (at $r = a$)

$$u_o - u_a = \frac{u_o}{1 + K_{in}/K_f} = \frac{u_o}{1 + C_f} \quad (13)$$

where $C_f = K_{in}/K_f$, is the relative compliance of the fastener.

The total lateral displacement of the constraining layer as a function of position (r) measured from the fastener is then

$$u_x(r) = u_o \left[1 - \frac{1}{(1 + C_f)} \frac{\mathcal{K}_o(kr)}{\mathcal{K}_o(ka)} \right], \quad r > a \quad (14)$$

4.3 Fastener Induced Area Defect

The shear strain energy density is proportional to $u_x^2(r)$. Figure 13 shows the spatial (radial) variation of relative energy density around a fastener for values of fastener compliance C_f of 0 (rigid) and 1.0 (equal stiffness in fastener and constraining layer). The relative energy density is reduced near the fastener and rises to unity in the far field. The radial coordinate is given as r/a , i.e., the number of fastener radii. For the rigid fastener, the energy density falls to zero at the fastener, rises to half the far field value at $r/a = 15$, and to about 3/4 at $r/a = 30$. In the case of unity fastener compliance, the relative energy density at the fastener is 1/4 (equal stiffness means half the far-field displacement, Eq (12), and thus 1/4 the energy density), and it rises to about 0.87 at $r/a = 30$.

In considering the quantitative importance of the fastener in reducing the strain energy in the viscoelastic layer, we should remember that Figure 13 is a polar plot. Thus, although the energy density defect (the difference from 1.0) decreases with increasing r/a , the associated area is increasing. The energy density fractional defect is defined as follows:

$$D(r) = \frac{u_o^2 - u_x^2(r)}{u_o^2} = 1 - \left(\frac{u_x(r)}{u_o} \right)^2 \quad (15)$$

That is, $D(r)$ represents the fractional decrease in the local energy density caused by the presence of the fastener. Thus, the total area defect S_d (i.e., the area of the damping treatment that is rendered ineffective by the fastener) is

$$\begin{aligned}
 S_d &= \pi a^2 + \int_a^\infty D(r) 2\pi r dr \\
 &= \pi a^2 + \frac{2\pi}{k^2} \int_{ka}^\infty \frac{1}{(1+C_f)} \frac{\mathcal{K}_o(kr)}{\mathcal{K}_o(ka)} \left[2 - \frac{1}{(1+C_f)} \frac{\mathcal{K}_o(kr)}{\mathcal{K}_o(ka)} \right] kr d(kr)
 \end{aligned}
 \tag{16}$$

Figure 14 shows the dependence of the area defect S_d on fastener radius a for various values of fastener compliance C_f . The results are given in dimensionless form as $k^2 S_d$ versus ka . (Strictly, the quantity calculated from Eq. (16) is $S_d - \pi a^2$, but the fastener cross section πa^2 is assumed small). Here again it is useful to refer to the result for the optimum segment length L_{opt} , i.e.,

$$kL_{opt} \doteq 1.16 \quad aL_{opt} \doteq 4, \text{ for } \nu = 0.3; \tag{17}$$

so that

$$\begin{aligned}
 k^2 S_d &= (kL_{opt})^2 S_d / L_{opt}^2 \\
 &\doteq 16 S_d / L_{opt}^2
 \end{aligned}
 \tag{18}$$

On this basis, Figure 14 has its right-hand ordinate scale the quantity S_d / L_{opt}^2 , the area defect expressed as a fraction of the area of a square patch of optimum size. Such a measure lets one draw some quantitative conclusions about the adverse effects of fasteners.

It is clear that rigid fasteners are bad for a constrained layer damping treatment. For example, for $ka \doteq 0.02$ ($a \doteq L_{opt} / 200$), Figure 14 shows $S_d \doteq 0.2 L_{opt}^2$, i.e., a single rigid fastener would disable an area of the treatment equal to 20% of the area of an optimum-size patch! (However, see the discussion below.) Smaller fasteners are less disruptive, but not by significant factors.

Clearly, fastener compliance is desirable. In the above case for $C_f = 1$, the area defect drops to $0.1 L_{opt}^2$, and for $C_f = 4$, to about $0.04 L_{opt}^2$. One can imagine a number of ways of achieving compliance including through choice of fastener material or configuration (height, slenderness, etc.), or alternately through the use of compliant sleeves, washers, and so forth.

In view of the magnitude of the bad effects of a fastener, some qualifying comments are in order.

The analysis presented here is most appropriate for a localized effect, i.e., one in which the fastener-induced perturbation has an extent small relative to the wavelength and small relative to the segment size. The assumption of a more-or-less uniform "far-field" displacement field u_0 for the constraining layer would be appropriate for the low-frequency long wavelength case, but only if the segment size were large relative to the extent of the fastener-induced displacement field. However, this extent is not negligible with respect to the optimum segment length. Thus, for constraining layer segments of optimum size, the present analysis provides guidance rather than precise answers.

In addition, of course, the results for the area defect are based on the actual local displacement of the constraining layer. This displacement would vanish in the center of a segment (low-frequency case where $\lambda_p \gg L$), and a fastener in the center would not affect the damping. However, it is more likely that fasteners would be placed near the edges of a segment, where the constraining layer displacement is near its maximum value. The present analysis does not apply near an edge or corner. But one could estimate fastener effects by a) reducing the area defect by a factor 2 or 4 for edge or corner locations, respectively, and b) approximating the input stiffness K_{in} of the constraining layer by smaller values for edge or corner locations.

Further, because the extent of the fastener-induced displacement field is significant, the simplifying assumption of no hoop strain $\epsilon_{\theta\theta}$ in the constraining layer should be reassessed. Qualitatively at least, such hoop strain would reduce the constraining layer input stiffness and would also decrease the spatial extent of the fastener-induced disturbance. The quantitative importance of this effect is yet to be determined.

5. SUMMARY

We have shown that segmented constrained layer damping treatments can be effective for extensional waves in plates and

beams in the low-frequency, long wavelength regime. There is an optimum segment length (for a given treatment), which is essentially the same as that found by Parfitt⁵ for flexural waves. However, the loss factor for extensional waves is about 1/3 that for flexural waves, because of the higher strain energy in the extensional waves for the same surface strain in the base plate.

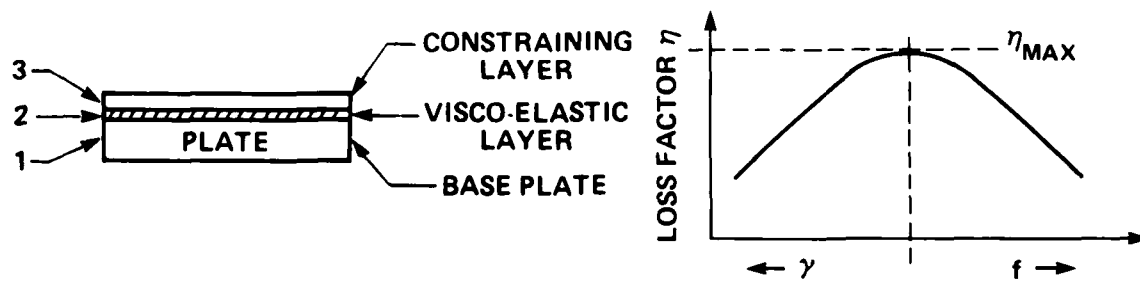
The extent of the influence of a local fastener is comparable to a significant fraction of the optimum segment length. Thus a single rigid fastener will disable an appreciable portion of the area of the damping treatment - say $S_d = 0.2 L_{opt}^2$ relative to the local unperturbed energy density. This approximate result refers to a situation removed from boundaries. Adjustments are required in the general case of a fastener near the edge or the corner of an optimum-size segment to account for:

- a. the input stiffness to the constraining layer
- b. the relative compliance of the fastener
- c. the fraction of 2π of the constraining layer surrounding the fastener
- d. the average shear energy density over the segment (see, for example, Fig. 5 for the shear energy density distribution in an optimum size segment).

The results indicate that fastener compliance is indeed desirable. Further analysis and experiment are required to define precise results, but the present analysis gives approximate guidance.

REFERENCES

1. E.M. Kerwin, Jr., "Damping of Flexural Waves by a Constrained Viscoelastic Layer," J. Acoust. Soc. Amer. 31-7, 952-962 (1959).
2. D. Ross, E.E. Ungar, and E.M. Kerwin, Jr., "Damping of Plate Flexural Vibrations by Means of Viscoelastic Laminae," Section III in Structural Damping, J.E. Ruzicka, Ed., Am. Soc. Mechanical Engrs., New York (1959).
3. E.E. Ungar, "Damping of Panels," Ch. 14 in Noise and Vibration Control, L.L. Beranek, Ed., McGraw Hill Book Co., New York (1971).
4. In addition to the historical references on constrained layer damping noted above, there have been many papers on both analysis and applications. For example see the following Meeting Programs:
J. Acoust. Soc. Amer., 65 S-1, S109-S111 (1979) and
J. Acoust. Soc. Amer., 68, S-1, S11-S13 (1980).
5. G.G. Parfitt, "The Effect of Cuts in Damping Tapes," Proc. Fourth International Congress on Acoustics, Copenhagen (1962).
6. G.G. Parfitt and D. Lambeth, "The Damping of Structural Vibrations," Aeronautical Research Council, Report A.R.C. 22,250 (N.P.L. Teddington, Middlesex, UK) (1960).
7. R. Plunkett and C.T. Lee, "Length Optimization for Constrained Viscoelastic Layer Damping," J. Acoust. Soc. Amer., 48-1 (Part 2) 150-161 (1970).
8. R.Z. Zeinetdinova, N.I. Naumkina, and B.D. Tartakovskii, "Effectiveness of a Vibration Absorbing Coating with a Cut Constraining Layer" Soviet Physics-Acoustics, 24-4 (1978).
9. M. Abramowitz and I.A. Stegun, Handbook of Mathematical Functions, Applied Mathematics Series No. 55, National Bureau of Standards, Washington, DC (1964).



$$\text{SHEAR PARAMETER } \gamma = \frac{\alpha^2}{k^2} = \frac{1}{k^2} \frac{G_2}{H_2} \left(\frac{1}{K_1} + \frac{1}{K_2} \right)$$

Fig. 1 Characteristic damping performance of a continuous constrained viscoelastic layer.

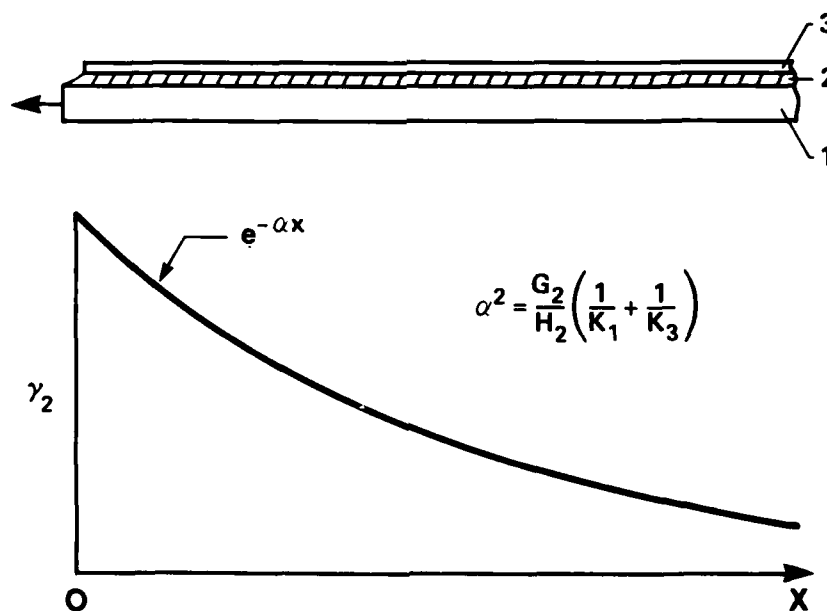


Fig. 2 Shear relaxation in a constrained viscoelastic layer.

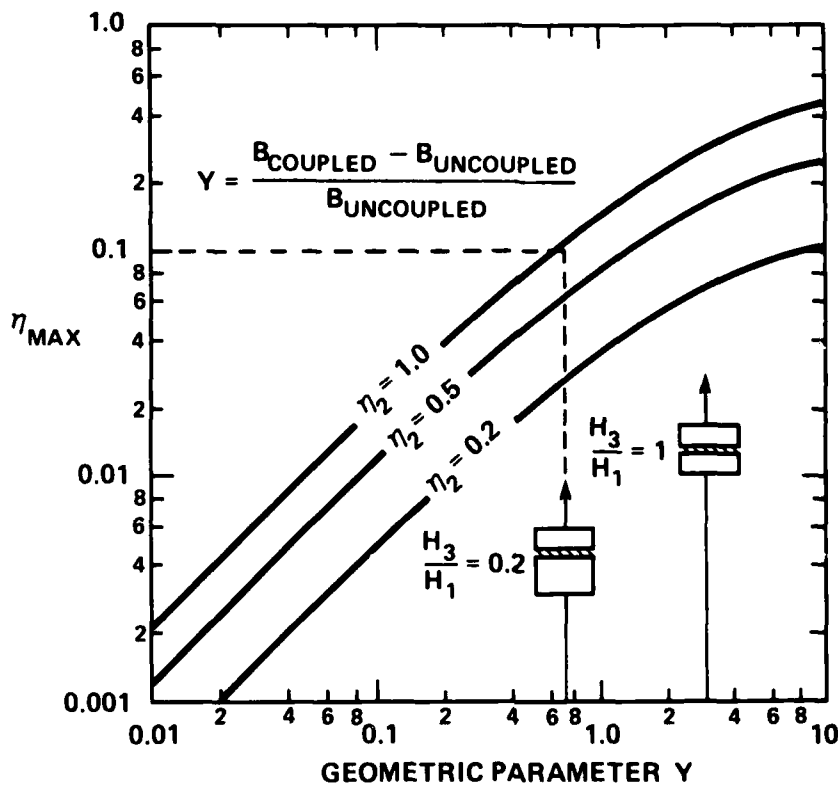


Fig. 3 Maximum damping of constrained layers.

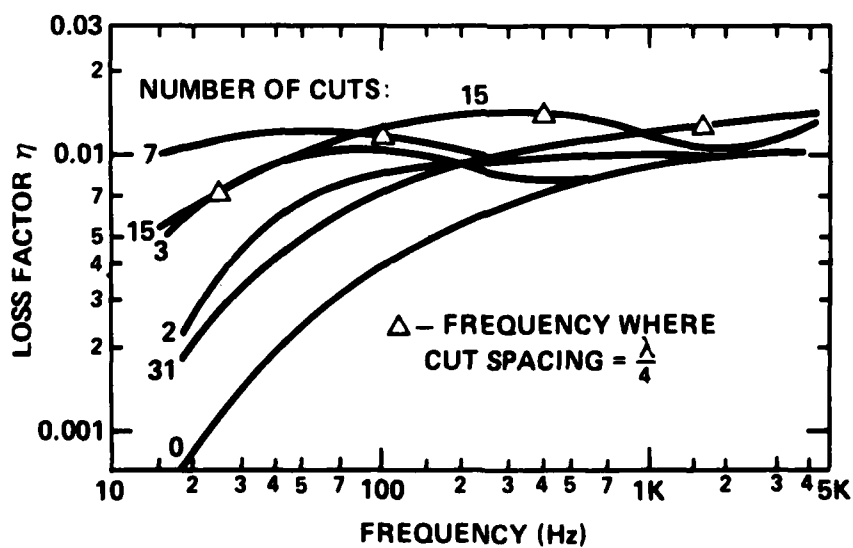


Fig. 4 Effect of cuts in constraining layer (after Parfitt and Lambeth)

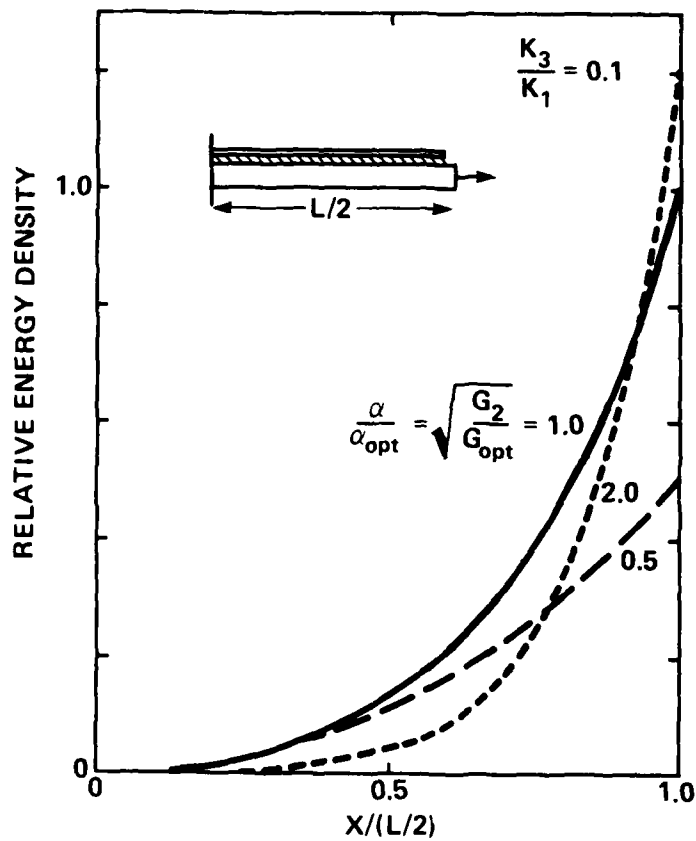


Fig. 5 Shear strain energy density distribution under a constraining layer segment.

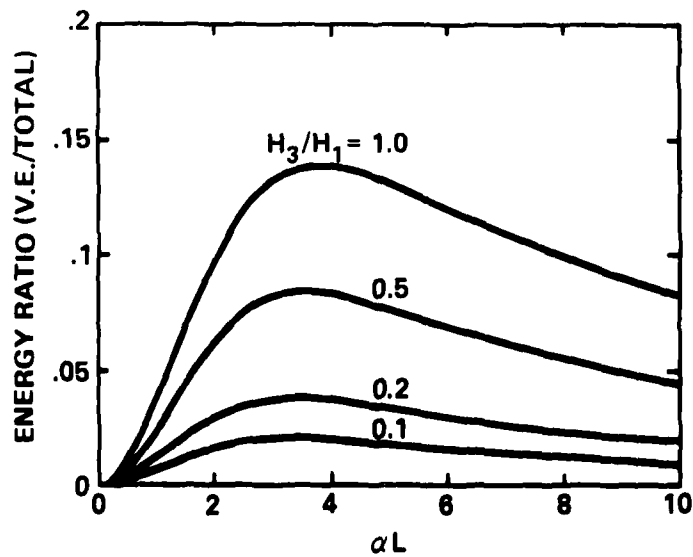


Fig. 6 Integrated viscoelastic layer shear energy as a fraction of total extensional wave strain energy vs segment length.

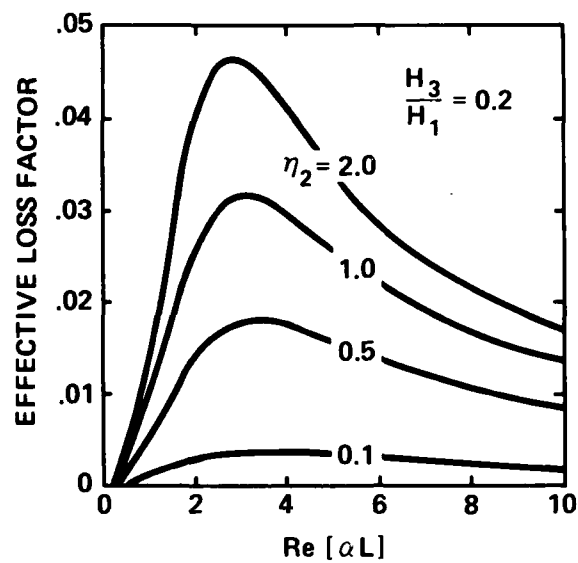


Fig. 7 Extensioal wave loss factor for a segmented constrained layer; $H_3/H_1=0.2$.

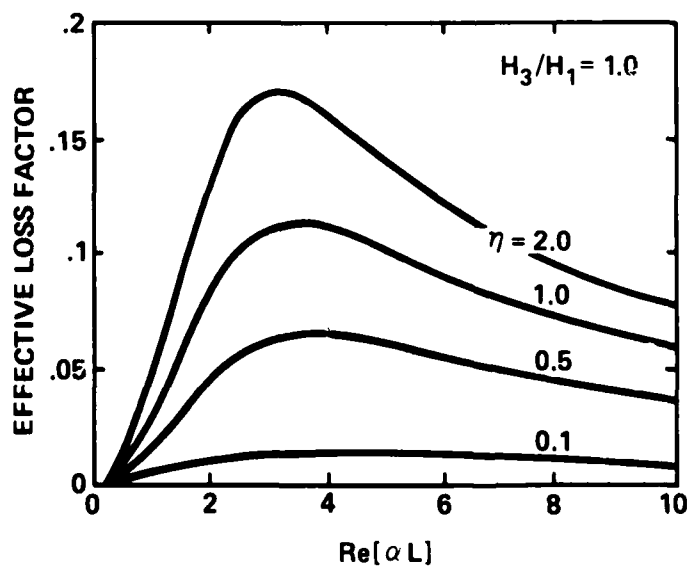


Fig. 8 Extensioal wave loss factor for a segmented constrained layer; $H_3/H_1 = 1.0$.

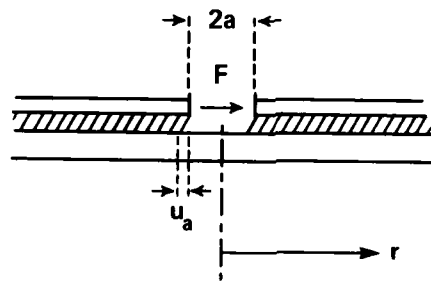


Fig. 9 Lateral force applied to a constraining layer.

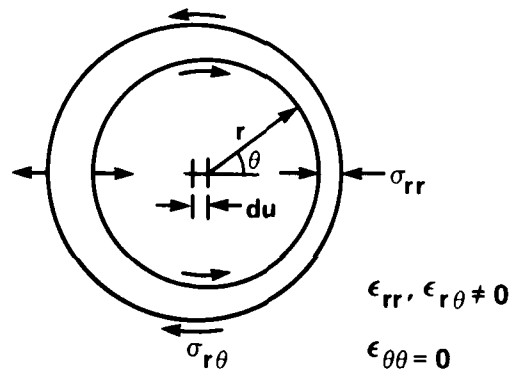


Fig. 10 Annular element of constraining layer.

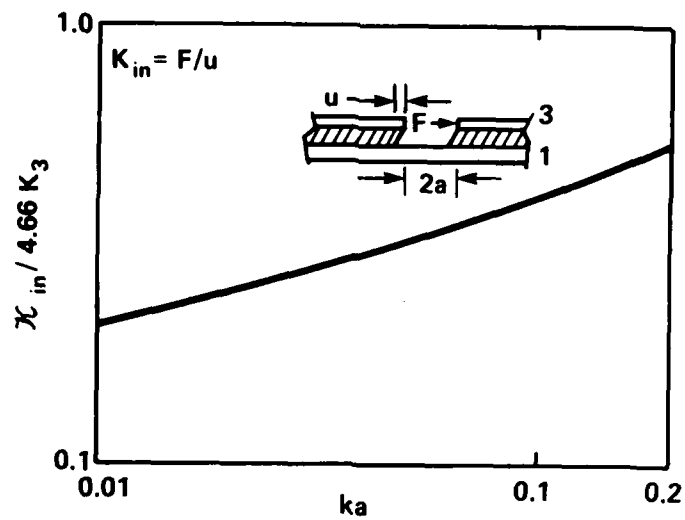
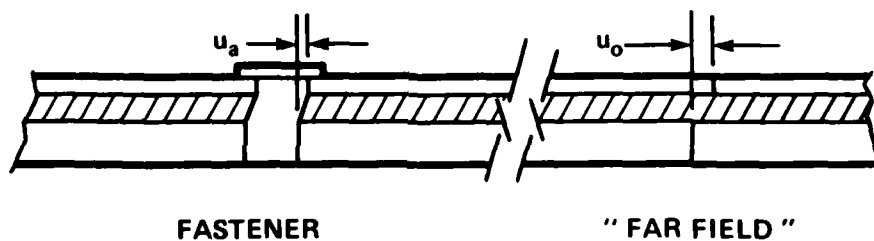


Fig. 11 Normalized lateral stiffness of constraining Layer.



$$\frac{u_o - u_a}{u_o} = \frac{1}{1 + C_f} = \frac{1}{1 + K_{in}/K_f}$$

Fig. 12 Reduction of lateral displacement by a fastener.

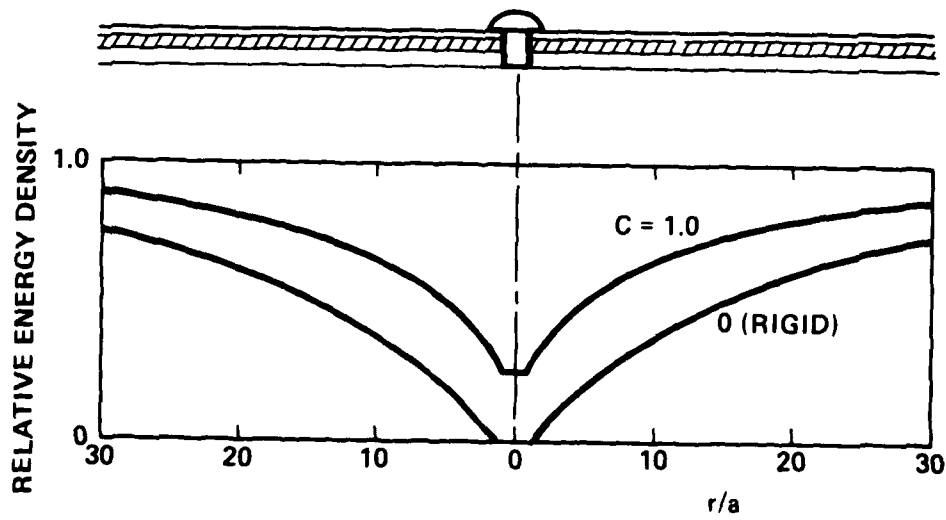


Fig. 13 Shear energy density distribution around a fastener having compliance C_f .

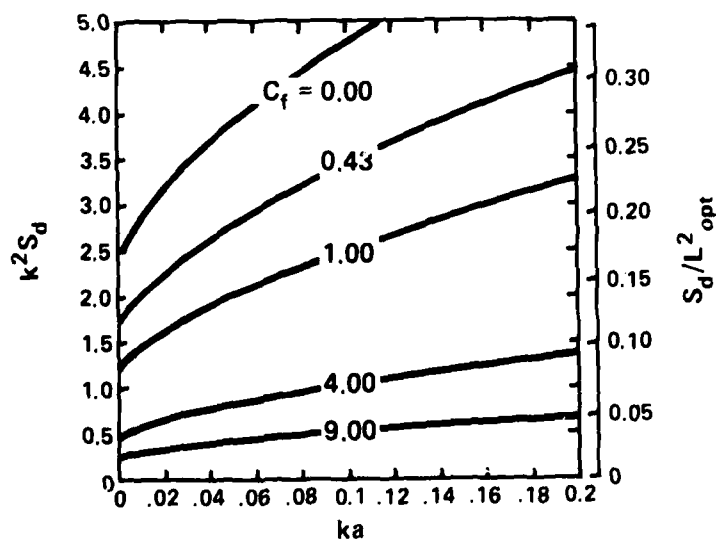


Fig. 14 Damping area defect due to a fastener of radius a and compliance C_f .

VIBRATION ISOLATION OF AN ELEVATOR SYSTEM

H.-S. Tzou
Assistant Professor
Department of Mechanical Engineering
North Carolina A&T State University
Greensboro, North Carolina
and
A. J. Schiff
Professor
School of Mechanical Engineering
Purdue University
West Lafayette, Indiana

VIBRATION ISOLATION OF AN ELEVATOR SYSTEM

By H.-S. Tzou¹ and A. J. Schiff²

ABSTRACT: The vulnerability of elevator system has been demonstrated from recent earthquake reports. An elevator counterweight/ frame/ guide rails system is modeled by beam finite elements. Because of large structural vibration, parts of the system may come in contact if their relative displacement exceeds the gap. Due to the fact that large dynamic force resulting from contact often causes the damage of the elevator system, the study of viscoelastic damper being used as vibration isolator is introduced. System with viscoelastic dampers which are modeled by standard linear model is evaluated in the dynamic analysis.

INTRODUCTION

In recent earthquake damage reports, it is observed that elevator systems were damaged significantly even though there was almost no structural damage to buildings. Among the elevator failures, the damage modes include permanent deformation of guide rails, failure of roller guides, derailment of counterweights, crash of passenger car roof by counterweights, etc... The most vulnerable mechanical part in an elevator system was the counterweight system which consists of frame, weights, roller guides, and guide rails(3).

In order to improve the earthquake resistance of the elevator systems, several investigators have proposed different design modifications(1,7). In Japan, Hitachi Elevator Corporation proposed a design modification in which a large gap is provided between the counterweights and the frame. Ideally, the weights, initially centered in the frame, would stay fixed in space as the structure and the frame vibrate. This would continue as long as the relative displacement of the weights and the frame is smaller than the gap. However, when the relative displacement exceeds the gap, the weights would contact the frame and apply a large contact force to the frame and the guide rail. The dynamic response, should contact occur, was not analyzed.

In this study, a finite element model representing a full-scale counterweight system with a large gap provided between the weights and the frame is constructed by using beam elements. The dynamic behavior of the counterweight and the rails is evaluated in a numerical analysis. To improve the dynamic response of this configuration, viscoelastic dampers are then introduced into the system to absorb vibration energy and reduce the contact load. A counterweight system with viscoelastic dampers is evaluated in the dynamic analysis.

-
1. Assistant Professor, Department of Mechanical Engineering, North Carolina A&T State University, Greensboro, NC.
 2. Professor, School of Mechanical Engineering, Purdue University, West Lafayette, IN.

FINITE ELEMENT MODELING

A full-scale elevator counterweight system consists of counterweights secured inside a pair of deep steel channels which form sides of the counterweight frame. The weights are located in the lower two thirds of the frame; and the frame is hung between a pair of guide rails by a steel rope. The guide rail is usually supported by building floors. The position of the counterweight system is assumed to be centered between two floors. Thus, the finite element model only uses one span simply supported rail to simplify the problem.

The counterweight frame and the guide rail would contact first when the relative displacement exceeds the small gap between them; and they would stay in contact for a half-cycle of the excitation frequency which would be the fundamental frequency of the structure. The effect of the small gap might not be as significant as that of the large gap between the weights and the frame. Thus, the frame and the rail are modeled by a single beam, referred to as the combined-beam.

To model the contact between the weights and the combined-beam, a bi-linear spring is used to connect the corresponding nodes in the model. The spring constant is very small when these two nodes are separate and its effect to the dynamics is negligible. However, this spring becomes very stiff when these two nodes come in contact. A contact force is generated and applied to these two nodes. The stiff spring is referred to as a contact spring.

Two cases are studied in the forced vibration analysis. The first case representing the original configuration has been discussed above. In the second case a number of viscoelastic dampers are introduced into the system. Each damper connects the weights and the combined-beam. The viscoelastic damper is modeled by three parameters viscoelastic model which consists of a primary stiffness, K_1 , a secondary stiffness, K_2 , and a viscous damping, $C(2)$. The complex stiffness for a given damper is determined by K_1 , K_2 , C , and excitation frequency.

Since the response of a high-rise building top would be a sinusoidal-like motion when it is excited by an earthquake, thus, the base excitation used in dynamic analysis will be a sinusoidal acceleration with different frequencies.

A full-scale elevator counterweight system with 7,400 lb counterweights, C8-18.75 steel channels, and 12 lb guide rails is modeled in Figure 1 in which the counterweights are divided into five lumped masses, the frame and the rail are simplified as a combined-beam which has six elements.

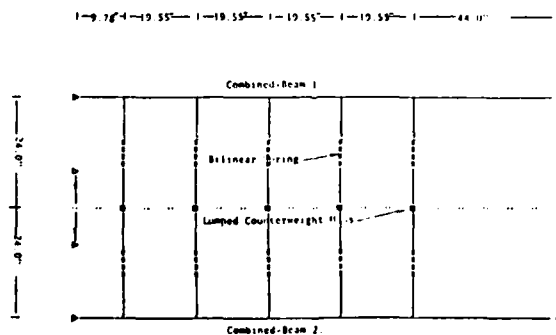


Figure 1. Finite Element Model of A Full-Scale Counterweight System

NO-A152 547

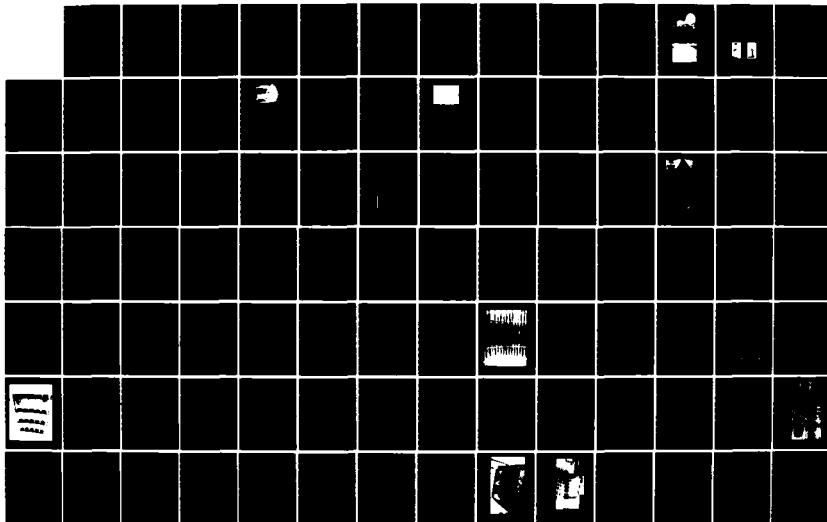
VIBRATION DAMPING WORKSHOP PROCEEDINGS HELD AT LONG
 BEACH CALIFORNIA ON 2... (U) AIR FORCE WRIGHT
 AERONAUTICAL LABS WRIGHT-PATTERSON AFB OH L ROGERS
 11 NOV 84 AFMAL-TR-84-3864

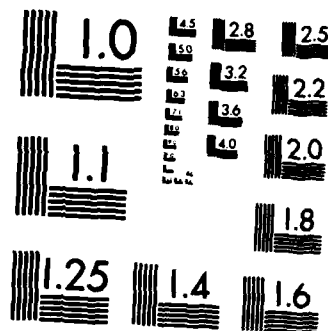
7/11

UNCLASSIFIED

F/G 28/11

NL





MICROCOPY RESOLUTION TEST CHART
NATIONAL BUREAU OF STANDARDS-1963-A

FREE VIBRATION ANALYSIS

An eigenvalue analysis is first conducted to study the natural frequencies and mode shapes of the system. The natural frequencies can be determined by solving eigenvalue equations

$$\{[K] - \omega^2 [M]\} \{X\} = \{0\} \dots\dots\dots(1)$$

where $[K]$ and $[M]$ are the system stiffness and mass matrices respectively; $\{X\}$ is the generalized coordinate vector; and ω is the natural frequency.

The first natural frequency of the combined-beam is 14.9 Hz by using lumped mass formulation and 15.2 Hz by using consistent mass formulation. The analytical solution is 15.2 Hz. Because there are two identical combined-beams in the model, two repeated natural frequencies are found in the analysis, which represent the out of phase and the in phase motions of the two beams.

FORCED VIBRATION ANALYSIS

The equations of motion for a system excited by an imposed motion can be written as

$$[M]\{\ddot{X}\} + [C]\{\dot{X}\} + [K]\{X\} = -[M]\{\ddot{Y}\} \dots\dots\dots(2)$$

in which $[C]$ represents the system damping matrix; $\{X\}$, $\{\dot{X}\}$, and $\{\ddot{X}\}$ indicate the relative displacement, velocity, and acceleration vectors. $\{\ddot{Y}\}$ is the base acceleration vector. The system damping matrix is assumed to have Rayleigh's formulation which is the linear combination of the mass and the stiffness matrices, i.e.,

$$[C] = \alpha[M] + \beta[K] \dots\dots\dots(3)$$

where α and β are Rayleigh's coefficients(4).

After the system equations are formulated, the Wilson- θ method is used to determine the dynamic response in the time domain(4,5). In this study, a time step of 0.001 sec is used in the direct integration, and a 2% damping is assigned to the combined-beam. A sinusoidal acceleration of 0.4g with different excitation frequencies is applied to the base of the model. Since the fundamental natural frequency of a high-rise building is generally low, only low excitation frequency is considered in the study.

RESULTS

The dynamic responses of the center mass and the two adjacent nodes on each combined-beam are plotted. Figures 2 and 3 show the displacement responses for the system excited by 0.75 Hz and 0.5 Hz sinusoidal acceleration respectively.

The contact between the counterweight mass and the combined-beam, the ringing of the beam after break the contact can be observed in both figures. A two percent beam damping is calculated from the beam ringing by logarithmic decrement method. There are five separate "peaks" in the response curve of beam 1, which can be observed in Figure 2. The first three peaks are three

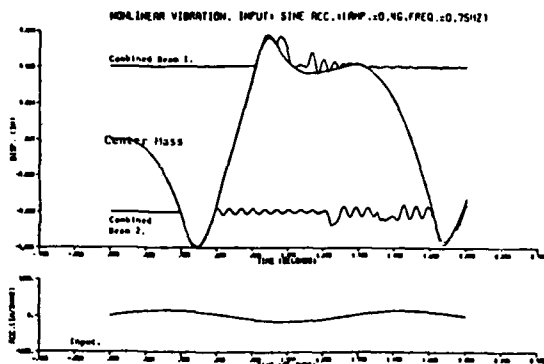


FIGURE 2: MODEL (F36SRU) (12.8 FT RAIL + CB-18.75 CHANNEL FRAME)
DT=0.00101 RAIL BEARS=19E-4 INPUT=0.75HZ,0.4G
NONLINEAR REMOVAL=1.99E-4 C (NON)=0.5E-1 (LUMP MASS) (34 D.O.F...)

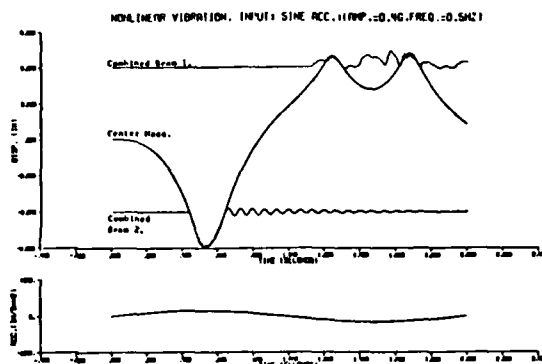


FIGURE 1: MODEL (F36SRU) (12.8 FT RAIL + CB-18.75 CHANNEL FRAME)
DT=0.00101 RAIL BEARS=19E-4 INPUT=0.5HZ,0.4G (RUBBER K1=0.01)
NONLINEAR REMOVAL=1.99E-4 C (NON)=0.5E-1 (LUMP MASS) (34 D.O.F...)

separate contacts due to different masses in the system. The last two peaks are the oscillation of the combined-beam at its natural frequency of 15 Hz. There is another minor contact on beam 2 at approximately 1.25 sec. The beam 1 also shows lifting prior to the contact with the center mass. This lifting is caused by the contact of other mass.

In order to improve the dynamic response and reduce the contact load, viscoelastic dampers are introduced into the system. A series tests using different dampers are performed. The primary stiffness, K_1 , of the damper is assumed to be 50 lb/in, 100 lb/in, 150 lb/in, and 200 lb/in in different test. Figure 4 shows all the response curves in which the original curves are also included. It can be observed that the contact is reduced when $K_1 = 50$ lb/in, and that is prevented when $K_1 = 100, 150$, and 200 lb/in. The maximum deflection, relative to the base, of the center mass for different K_1 is summarized in Table 1.

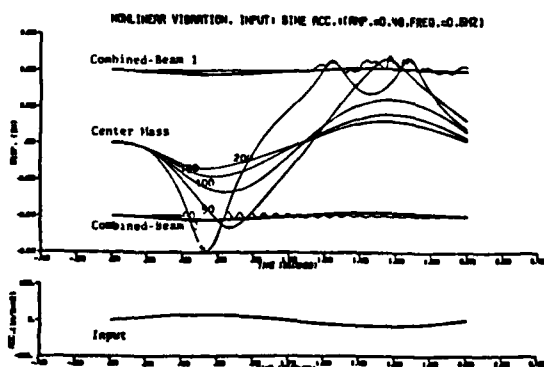


FIGURE 4: MODEL (F36SRU) (12.8 FT RAIL + CB-18.75 CHANNEL FRAME)
DT=0.00101 RAIL BEARS=19E-4 INPUT=0.5HZ,0.4G
NONLINEAR REMOVAL=1.99E-4 C (NON)=0.5E-1 (LUMP MASS) (34 D.O.F...)

Table 1.
Maximum Deflection of the Center Mass

Primary Stiffness: K_1 (lb/in)	Max. Deflection (in)*	Contact †
00.0	8.89	Yes
50.0	7.04	Yes
100.0	3.98	No
150.0	2.72	No
200.0	2.08	No

* : The Deflections are Measured Relative to the Base.

† : Six-inch gap is provided.

DISCUSSION

Referring to Table 1, the motion of the center mass is reduced when the primary stiffness, K_1 , of the viscoelastic damper is increased. To prevent the contact means to eliminate the vital contact force from the system. This has been demonstrated from the above analysis. However, continuously increasing the primary stiffness does not imply that the system response could be continuously improved. The reason is that when the mass is further constrained by the damper, the force, due to the imposed motion, applied to the combined-beam would increase again. Thus, the best selection of viscoelastic damper would be the one which just prevents the contact, eliminates the vital contact force, but does not add extra constrained force into the system.

ACKNOWLEDGMENT

This research was supported by the National Science Foundation.

REFERENCES

1. ANCI A17.1-1978, "American National Standard Safety Code for Elevators, Dumbwaiters, Escalators and Movingwalks," ASME, 1978, pp58-65, and Appendix F, 1980.
2. Anderson, A.D., "Testing and Parameterization of Elastomers for Modeling of Linear Vibration System," SAE Paper 730266, SP-375, 1973.
3. Ayres, J.M. and Sun, T.Y., "Nonstructural Damage," from "San Fernando, California, Earthquake of February 9, 1971," U.S. Department of Commerce, National Ocean and Atmospheric Administration, 1973, Vol.1, Part B, pp. 736-742.
4. Bathe, K.J. and Wilson, E.L., "Numerical Methods in Finite Element Analysis," Prentice Hall, Inc. 1976.
5. Bathe, K.J. and Wilson, E.L., "Stability and Accuracy Analysis of Direct Integration Methods," International J. of Earthquake Engr. and Structural Dynamics, Vol.1, 1973, pp. 283-291.
6. Guran, R.J., "Reduction of Stiffness and Mass Matrices," AIAA J., Vol.3, No.2, 1965, pp.380.
7. Schiff, A.J., Tzou, H.S. and Chu, Y.H., "Earthquake Response of Elevator Counterweights," Proc. 7th World Conference on Earthquake Engr., Sept. 1980, pp. 483-486.
8. Tzou, H.S., "A Nonlinear Dynamic Analysis Finite Element Program with an Application to Elevator Counterweight Systems," Thesis presented to Purdue University at 1983, in partial fulfillment of the requirements for the Degree of Doctor of Philosophy.
9. Yang, T.Y., et al, "Dynamic Response Analysis of Elevator Model," J. of Structural Engr., ASCE, Feb. 1983, pp.1194-1210.

DESIGN EVALUATION AND FIELD QUALIFICATION
OF A DAMPING SYSTEM FOR AN
AUXILIARY POWER UNIT

Michael L. Drake
Research Engineer
University of Dayton Research Institute
Dayton, Ohio

DESIGN EVALUATION AND FIELD QUALIFICATION
OF A DAMPING SYSTEM FOR AN
AUXILIARY POWER UNIT

Michael L. Drake
Research Engineer
University of Dayton Research Institute
Dayton, Ohio

ABSTRACT

A turbine engine used to operate an auxiliary power unit was incurring resonant vibration induced fatigue failures in the inlet guide vanes (IGV). Field test data from the IGV's revealed high stress levels at frequencies corresponding to the second bending and second torsional resonances. The operational environment required a damping system to be functional over the temperature range of -50°F to 150°F. The damping system had to survive the high air-flow and erosion environment associated with the inlet of the engine and also had to be field installable. A computer aided design procedure was used to develop the required damping design. The final design was proof tested in the laboratory and demonstrated an 86 percent stress reduction. Engine test stress reductions agreed well with the laboratory results. After successful engine test evaluations, a one year field evaluation successfully demonstrated the field installation procedures and the durability of the damping system.

I. INTRODUCTION

An industrial power system is shown in Figure 1. The power system is designed to provide power at remote sites around the world. The heart of the system is a gas turbine engine. The first vanes in the engine are the inlet guide vanes (IGV). The original design IGV was a solid cast aluminum structure as shown in Figure 2. The IGV case was approximately 3.5 feet in diameter and weighed over 300 pounds. There are eighteen vanes in the IGV case. The physical blade dimensions are given in Figure 3. Since the IGV was a solid casting, and therefore, no interfaces or joints provide additional damping, the inherent system damping would be approximately equal to the material damping of aluminum. As a result, if a vane resonant frequency occurred in the excitation spectrum one would anticipate a high cycle fatigue (HCF) failure.

In service, the IGV's were developing high cycle fatigue cracks at the inner diameter on the trailing edge. A frequency analysis of engine test data revealed high strain readings in the 1200 Hz's range and in the 2000 Hz's range. Modal analysis of the IGV showed that the two high strain readings corresponded to the second bending mode (1269 Hz) and the second torsional mode (2036 Hz), respectfully. The mode shapes determined from holograms are shown in Figure 4. There were two possible solutions to the problem studied: 1) Replace the current aluminum IGV with a steel IGV; 2) Add a damping system to the aluminum IGV to reduce the vibratory stress levels. The primary emphasis in the paper will be the passive damping design and evaluation.

II. DAMPING DESIGN AND EVALUATION

The initial step in the development of an operational damping design, for this system, was to demonstrate that at room temperature a damping system could control the problem resonant modes and could be applied in an acceptable thickness from an aerodynamic point of view.

The damping design was developed using a flat plate model of the vane analyzed with damped 4th order plate theory [1,2]. The model was based on the physical dimensions of the vane using an averaged overall thickness. In order to obtain accurate model frequency predictions, a modified blade density was used. The density modification to adjust the predicted frequency was used instead of dimensional changes because density does not effect the strain energy stored by the vane in the analysis. The need for accurate frequency prediction is obvious since damping material properties are functions of frequency as well as temperature [3,4]. The damping design called for a room temperature damping material (ISD-112, see Figure 5 for the reduced temperature nomogram) in a 0.010 inch thickness with a 0.020 inch aluminum constraining layer. It has been demonstrated that in a multiple layer damping system where each damping layer contains the same damping material and the constraining layers are all the same that the total system damping is coming from the damping layer closest to the structure.[5,1] In other words, a single material multi-layer damping system acts like a single constrained layer damping system where the thickness of the bottom most damping layer is the same as the single damping layer and the thickness of the single constraining layer is equal to the total thickness of all the constraining layers in the multiple layered system. (See Figure 6)

Using this fact, the final room temperature design was the multi-layered system shown in Figure 7. The application of four layers of 0.005 inch aluminum to the double curved blade was much easier than applying a single 0.020 inch aluminum layer.

The room temperature damping system was applied to an IGV case and tested on a shaker in the laboratory. The results are shown in Figures 8 and 9. Note in Figure 8 the largest stress occurs near 600 Hz. This is the first bending mode of the blade; however, it is not excited during engine operations. The second bending mode had stresses reduced from approximately 7 KSI to 2 KSI.

After successfully demonstrating that damping was a viable design alternative for the problem, the next step was to develop an operation compatible and effective damping design. The operational temperature requirements were placed at -50°F to 150°F for damping and survivability. The design modes were the second bending(1269 Hz) and second torsional (2036 Hz). The anticipated structural loss factor (η_s) required was 0.01. The overall thickness of the damping design could not be greater than 0.45 inch per side of the vane. The damping design also had to survive the harsh airflow environment of the engine inlet and the damping system had to be installed on the IGV's with the engine in place in the field.

The basic damping configuration was once again developed using a simple flat plate model of the vane. It was necessary to use two different damping materials in order to provide effective damping across the entire temperature range. The final design consisted of a layer of ISD-830 0.015 inch thick with a constraining layer of 0.010 inch of stainless steel on one side of the vane and a layer of 0.015 inch ISD-112 with a 0.010 inch stainless steel constraining layer on the other side of the vane. The ISD-830 damping system had peak

damping at -20°F and the ISD-112 damping system had peak damping at 60°F . The structural loss factor versus temperature for each of these damping designs is shown in Figure 10. The reduced temperature nomogram for ISD-830 is shown in Figure 11. (ISD-112 see Figure 5)

The next step in the design development was to determine the application method for the damping configuration. To ensure that the damping wrap would not debond and go into the engine, a design was developed where an outer wrap of aluminum covered the entire vane and was epoxied directly to the vane[6]. Since fixing the constraining layer to the vane reduces the effectiveness of the damping system, a second damping layer was added with the sole purpose to "float" or disconnect the main steel constraining layer from the bonded outer wrap. The floating constraining layer concept is illustrated in Figure 12. Also shown in Figure 12 is the epoxy bond between the outer aluminum retaining layer at the leading and trailing edges. A plan view of the wrap (see Figure 13) further illustrates the areas of the outer aluminum wrap that bond to the vane. The center line of the wrap bonds to the leading edge of the vane, the top and bottom of the wrap bonds to the outer diameter and inner diameter of the vane respectively, and the outer edges of the wrap bonds to the trailing edge of the vane. The epoxy bond formed a frame of support around the entire damping treatment preventing any damping material bond failure from going into the engine.

Note in Figure 13 that the damping layers are cut in 1 inch wide strips. This cut was required in order to enable the 0.010 inch steel floating constraining layer to conform to the curved surface of the vane.

After developing a damping system meeting all the operational requirements, a laboratory proof test was needed. Because of limitations of chamber sizes available, it was necessary to cut out a section of the IGV case as a test specimen to evaluate the damping design over the entire temperature range of operation. For convenience, a single vane specimen was chosen. The test article is shown in Figure 14. A mandatory requirement for the laboratory test article is that it be dynamically similar to the IGV case. The dynamic characteristics of the test article were established using digital Fourier modal analysis techniques [7]. Figure 15 shows the measured second bending mode of the test article which occurred at 1191 Hz. The other dynamic evaluation required was the level of inherent damping in the test article. Figure 16 shows the modal damping to be in the range of 0.0015 to 0.005.

Once the dynamic test article was established, the damping design was applied and evaluated over the operational temperature range. Figure 17 shows that the goal of achieving $0.01 \eta_s$ was accomplished for the second bending mode. In Figure 18, it is seen that even higher values of damping were achieved for the second torsional mode.

The successful laboratory evaluation led to a field test. All eighteen vanes were strain gaged and measurements were made for both the undamped and damped cases. The field wrap application procedure used is listed in Figure 19. Using this application procedure, it took eight man-hours to install all eighteen damping wraps. Figure 20 shows a close-up of the IGV with the damping wraps installed. Figures 21 and 22 show the minimum stress reduction (76.1%) and maximum stress reduction (90.3%) seen from all eighteen blades on the field test IGV.

The final evaluation phase was a year long field durability test conducted on six engines. The wraps successfully completed this test with no erosion or any other durability problems.

III. SUMMARY AND CONCLUSIONS

The design procedures followed resulted in an effective damping design which:

- 1) provided sufficient damping across the temperature range of -50°F to 150°F;
- 2) provided sufficient damping for both the second bending and second torsional modes;
- 3) provided a maximum stress reduction of 90%;
- 4) provided an application procedure which required eight man-hours to install all 18 wraps in the field;
- 5) did not sufficiently effect the aerodynamics of the flow around the IGV's;
- 6) proved to be durable in field tests;
- 7) eliminated the IGV cracking problem.

As was stated earlier, there were two approaches studied to solve the cracking problem. The all steel IGV case from an economic stand point cost four times as much as the aluminum case and would require replacing all the IGV's in the field. The damped aluminum case cost only one-third of the steel case and the damping system could be applied to the cases already in the field.

The damping solution was seen to be the best overall fix to this cracking problem.

IV. ACKNOWLEDGEMENTS

The author wishes to acknowledge Mr. Mark Ruddell's significant contribution in the design and evaluation of the damping system. Thanks are also due to Ms. Pam Brown for typing the manuscript.

REFERENCES

1. Vibration Damping Short Course Notes, University of Dayton Research Institute, Dayton, Ohio.
2. Ross D., Kerwin, E.M., Ungar, E.E., "Damping of Plate Flexural Vibrations by Means of Viscoelastic Laminaes," Proc. Colloq. Struct. Damping, ASME, pp. 49-87, 1959.
3. Nashif, A.D., "Control of Noise and Vibration with Damping Materials," Sound and Vibration, July 1983.
4. Drake, M.L., Terborg, G.E., "Polymeric Material Testing Procedures to Determine Damping Properties and the Results of Selected Commercial Materials," AFWAL-TR-80-4093.
5. DiTaranto, R.A., "Summary of Constrained Damping Literature," in Conference on Aerospace Polymeric Viscoelastic Damping Technology for the 1980's (Roger, L., ed.), AFFDL-TM-78-78-FBA.
6. Henderson, J.P., Rogers, L.C., Parin, M.L., Paul, D.P., "Engine Evaluation of a Vibration Damping Treatment for Inlet Guide Vanes," ASME paper #79GT-163.
7. University of Cincinnati Modal Analysis Short Course, Dave Brown, Director.

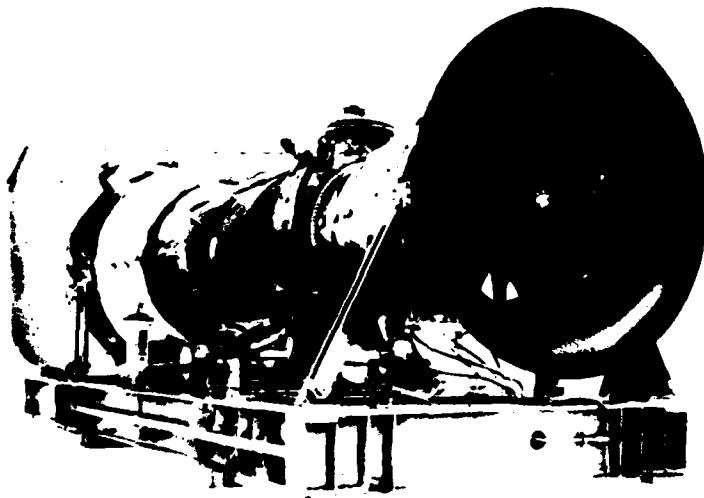


Figure 1. An Industrial Turbine Driven
Electric Power System.

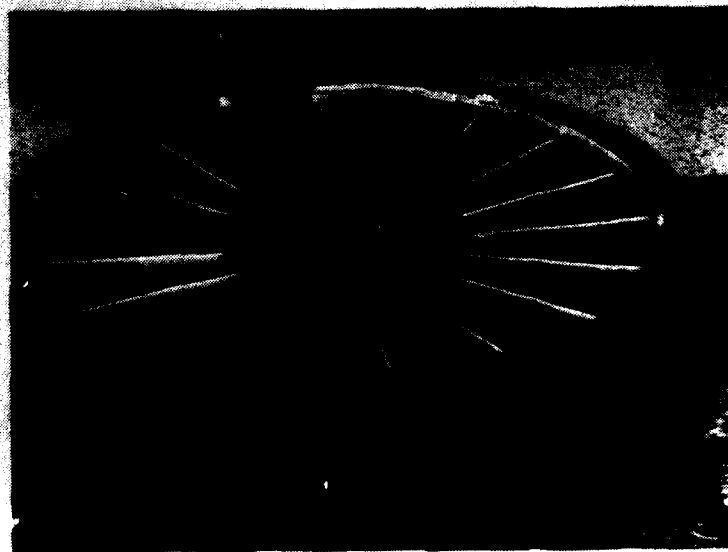


Figure 2. The Inlet Guide Vane Case.

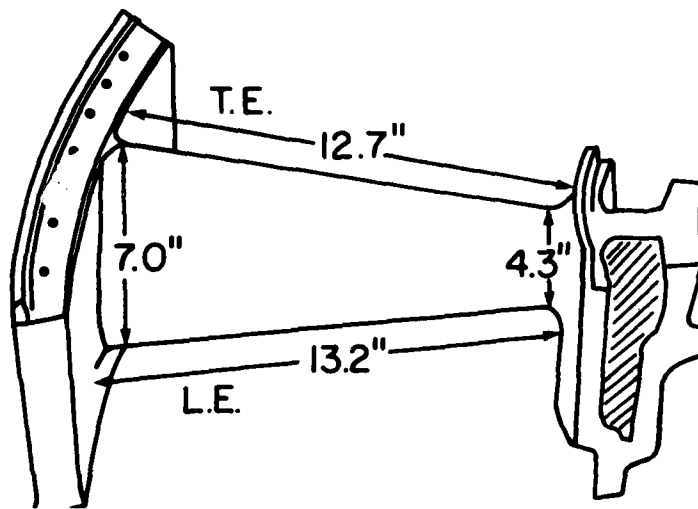
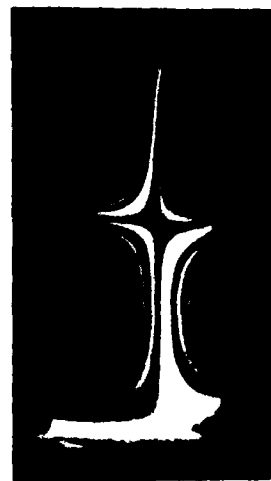


Figure 3. The Dimensions of the Vanes.



1269 Hz



2036 Hz

Figure 4. Mode Shapes of the Second Bending (1269 Hz) and Second Torsional (2036 Hz) Resonant Modes.

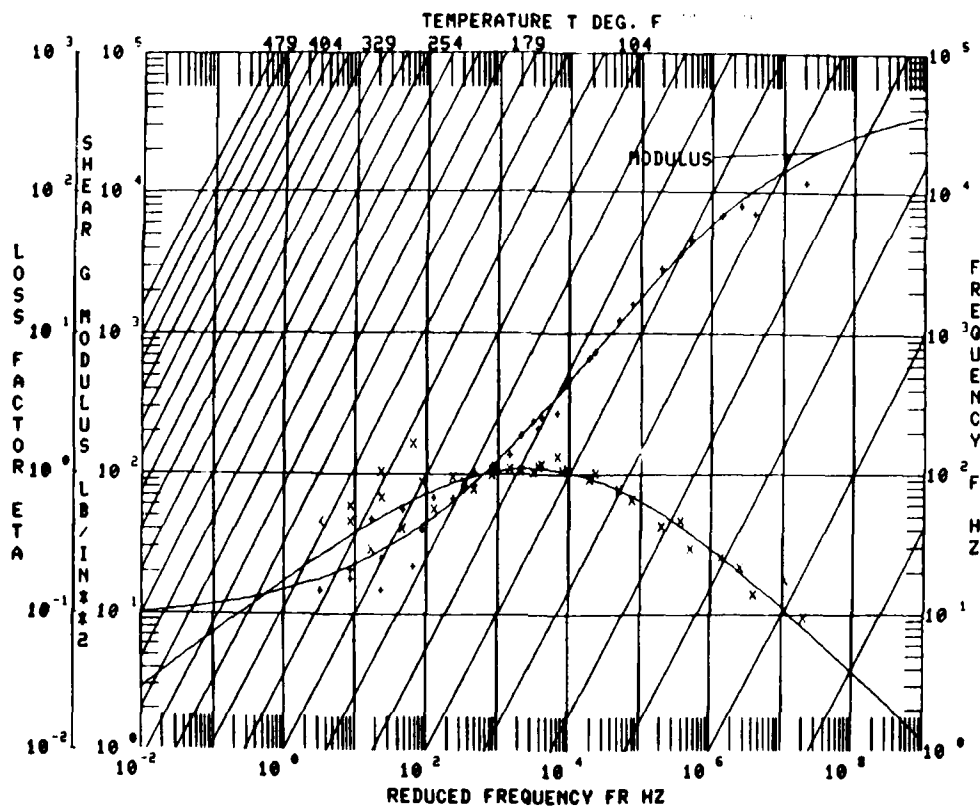


Figure 5. Reduced Temperature Nomogram for ISD-112.

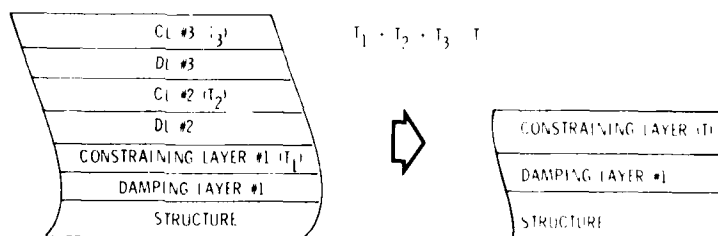


Figure 6. Illustration of a Single Material Multi-Constrained Layer Damping System Equivalence to a Single Layer System.

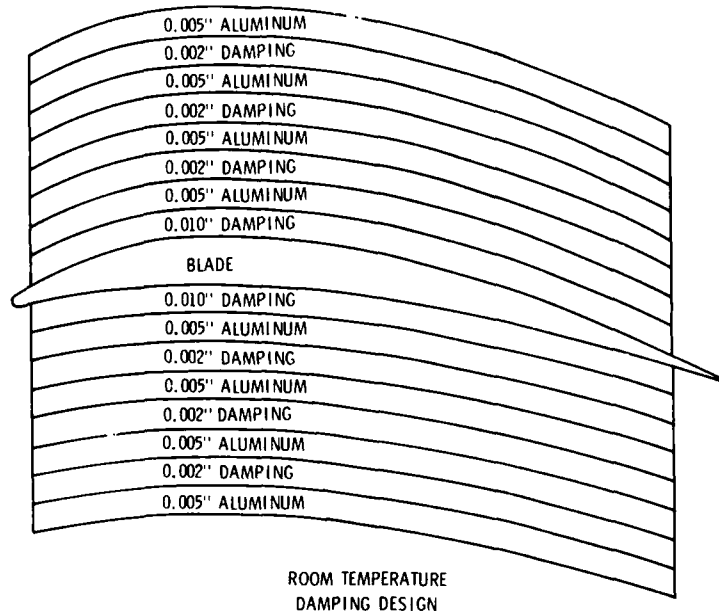


Figure 7. Room Temperature Damping Design.

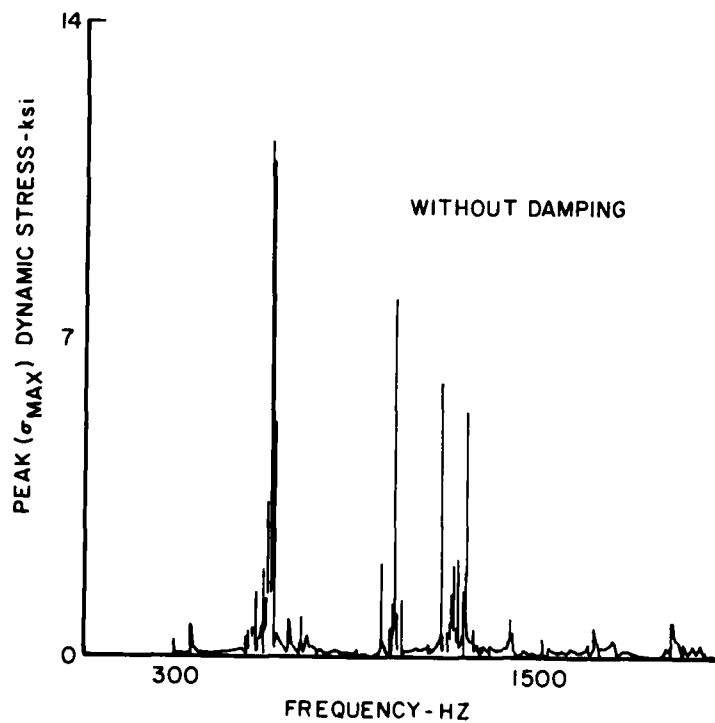


Figure 8. Shaker Test of IGV Before Damping Wrap was Applied.

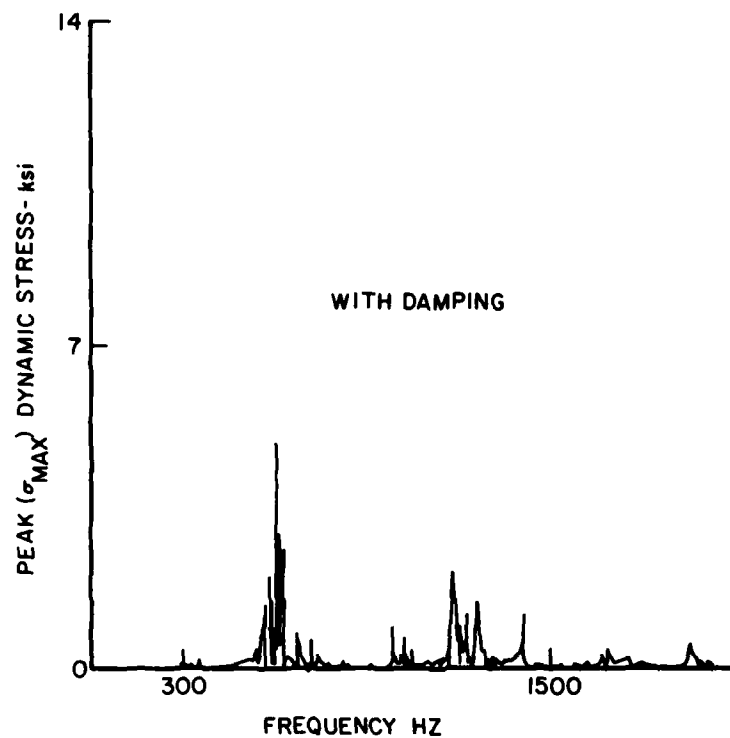


Figure 9. Shaker Test of IGV After Damping Wrap was Applied.

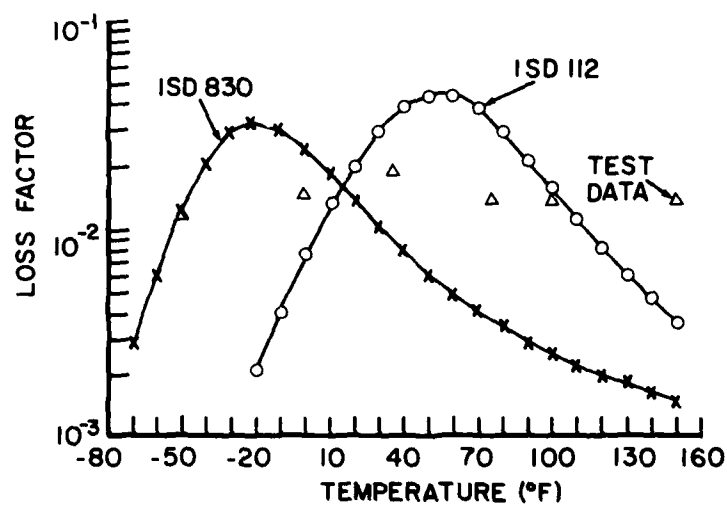


Figure 10. Computer Predicted System Loss Factor Versus Temperature for ISD-112 and ISD-830.

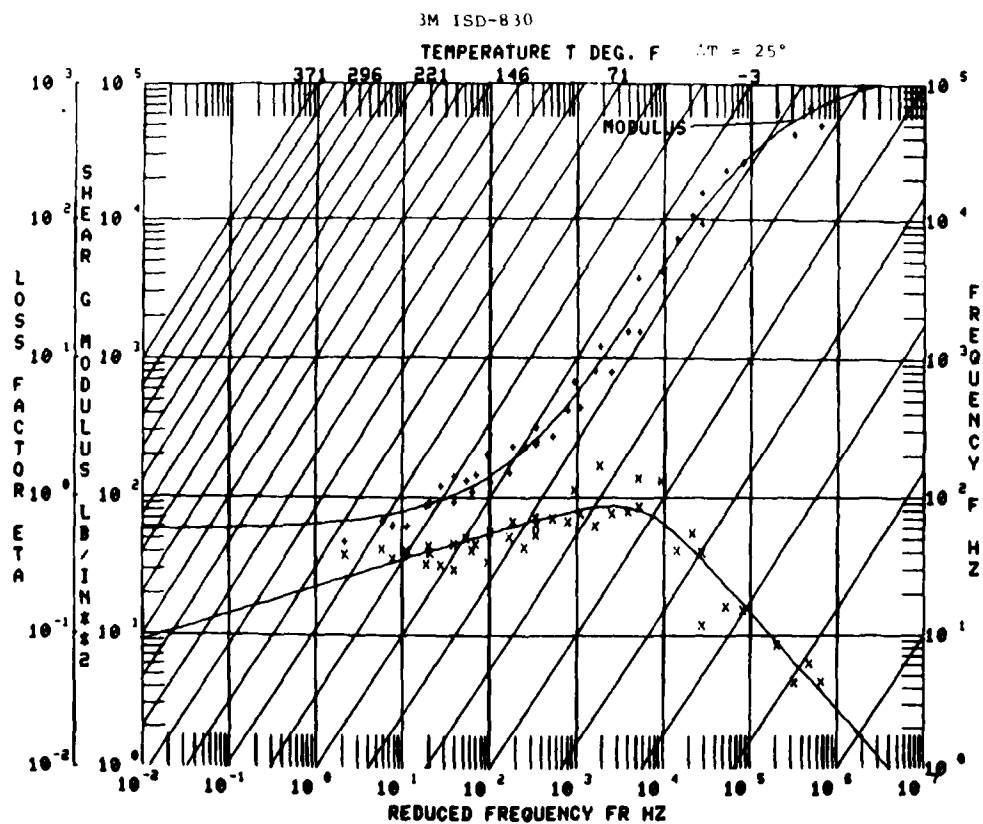


Figure 11. Reduced Temperature Nomogram for ISD-830.

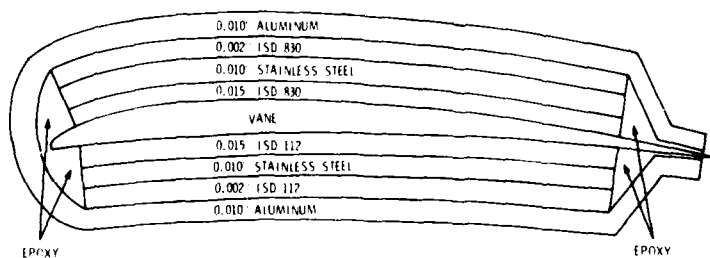
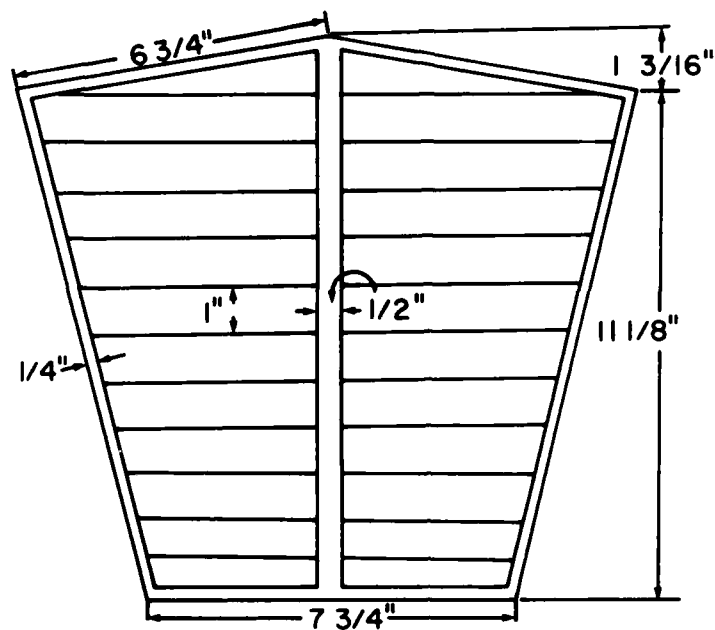


Figure 12. Cross-Section of Operational Damping Design.



EDGE VIEW OF DAMPING WRAP

LAYER A - ALUMINUM
 B - DAMPING MATERIAL
 C - STAINLESS STEEL
 D - DAMPING MATERIAL

Figure 13. Plan View of Damping System.

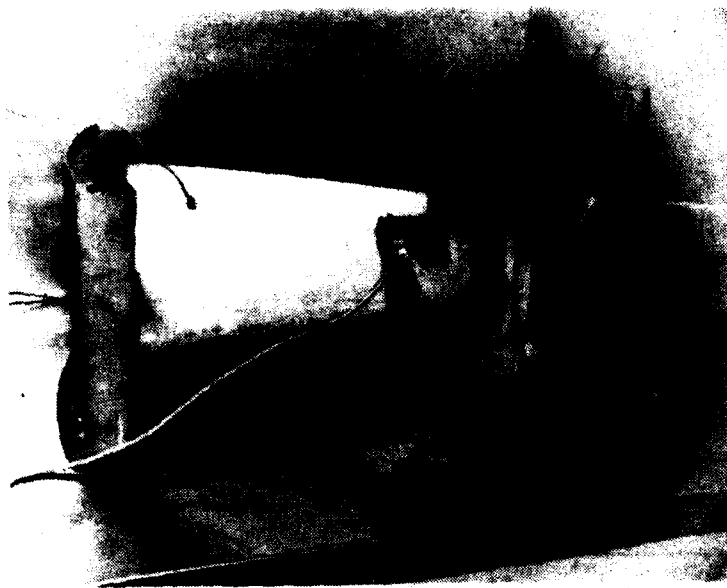


Figure 14. Laboratory Test Article.

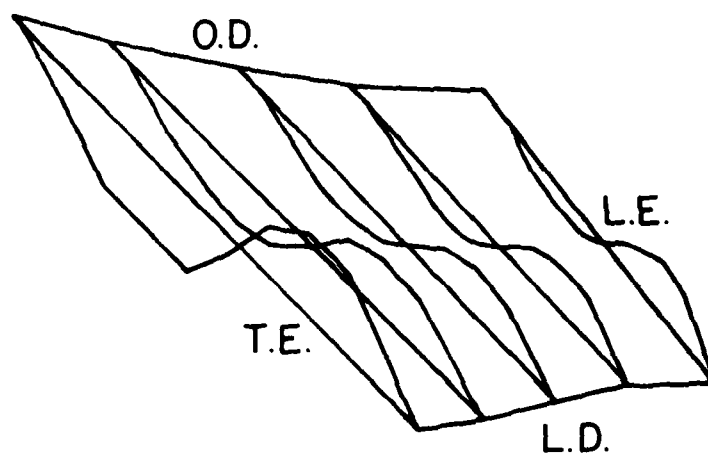


Figure 15. Second Bending Mode (1191 Hz) of Laboratory Test Article.

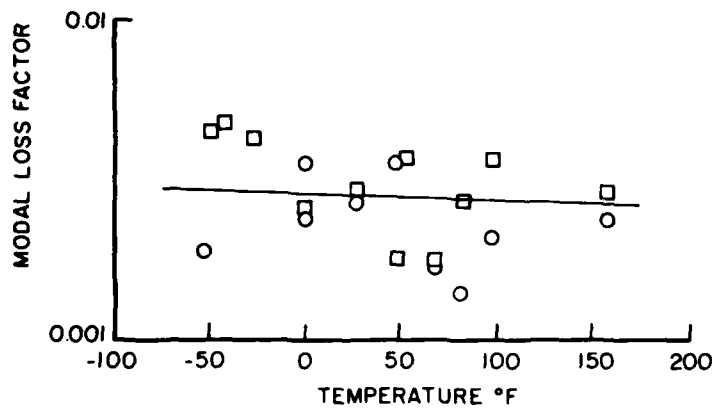


Figure 16. Modal Damping from Laboratory Test Article.

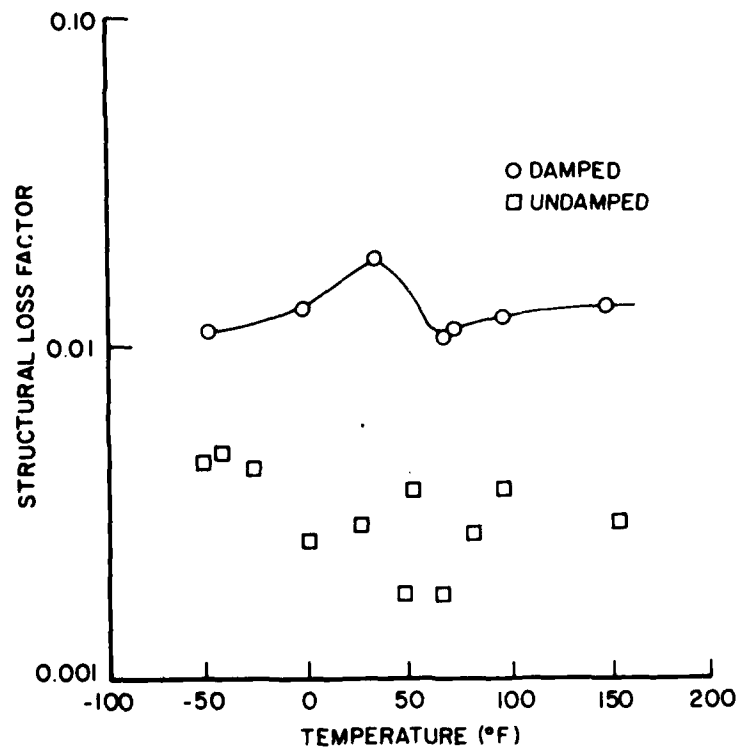


Figure 17. Modal Damping for the Laboratory Test Article for the Second Bending Mode With and Without the Damping Wrap.

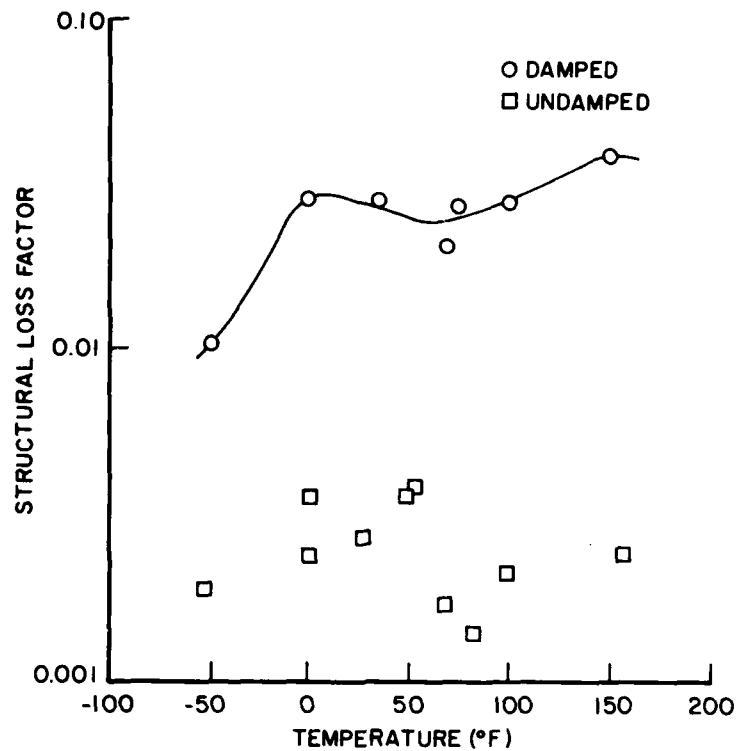


Figure 18. Modal Damping for the Second Torsional Mode With and Without the Damping Wrap.

WRAP APPLICATION PROCEDURE

- CLEAN GUIDE VANE
- APPLY TAPE PRIMER
- MIX AND APPLY EPOXY
- REMOVE BACKING PAPER
- POSITION DAMPING TREATMENT
- APPLY WRAP WORKING FROM L.E. TO T.E.
- AVOID ENTRAPPED AIR
- ROLL WRAP SURFACE
- WIPE OFF EXCESS EPOXY

Figure 19. Damping Wrap Application Procedure.

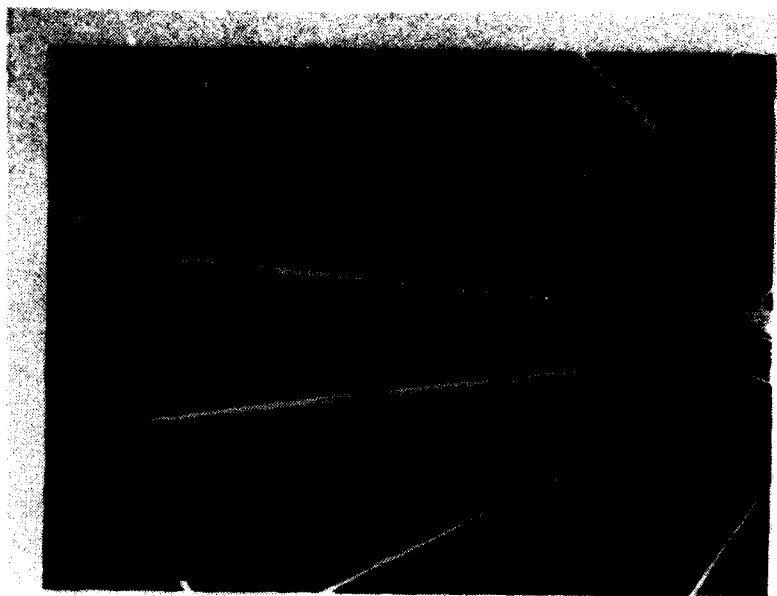


Figure 20. IGV Vane With Wrap Applied.

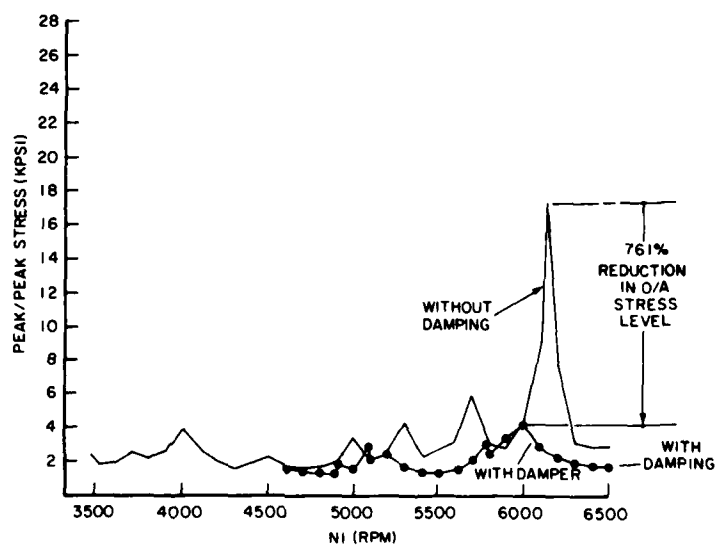


Figure 21. Field Test Data With and Without the Damping Wrap.

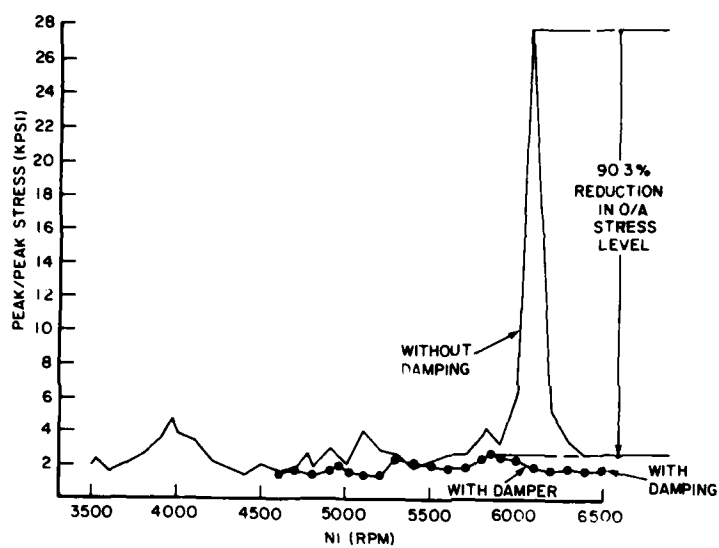


Figure 22. Field Test Data With and Without Damping Wrap.

DAMPING APPLICATIONS IN MASS PRODUCTION

A. D. Nashif
Anatrol Corporation
Cincinnati, Ohio

Paper presented; not available for publication.

LAMINATED DAMPED FUSELAGE STRUCTURES

Richard A. Ely
LTV Aerospace and Defense Company
Dallas, Texas

LAMINATED DAMPED FUSELAGE STRUCTURES

Richard A. Ely

LTV Aerospace and Defense Company

ABSTRACT

This paper discusses the application of constrained layer damping, in the form of laminated skins, frames, and equipment racks, to control of acoustical fatigue of structures and vibration of equipment in the aft fuselage sections of large aircraft. Discussions of applications of constrained layer damping go beyond conventional skin-stringer configurations to include honeycomb structures. It is shown that the influence of constrained layer damping on the response of a honeycomb panel at its critical frequency is very different from the influences on its resonant responses. A discussion of baseline data and background methodology includes laboratory characterization of materials, acoustical fatigue tests of baseline and laminated structures, peculiarities of structures with high damping, influences of various boundary conditions on damped panels, dynamic versus static stiffness of damped panels, and comparisons of predicted and measured stresses in damped and undamped panels that are representative of aircraft structures.

Most of the information that is reported in this paper resulted from the "Structural Improvement of Operational Aircraft Program," under the sponsorship of the Flight Dynamics Laboratory, Wright-Patterson Air Force Base, Ohio 45433. Lt. Col. W. R. Bassett, AFWAL-FIBAA, is the Air Force Project Engineer for that contract (No. F33615-81-C-3219). As part of that program, advanced metallic technology and constrained layer damping are being utilized to redesign the A-7 center section leading edge flap and the F-111 outboard spoiler to achieve large increases in their acoustical fatigue lives.

LAMINATED DAMPED FUSELAGE STRUCTURES

Richard A. Ely
LTV Aerospace and Defense Company

1. INTRODUCTION

The exhaust from jet engines on some large aircraft generates broad band random sound at overall sound pressure levels in the neighborhood of 170 decibels (re 20 μ Pa) at the outer surfaces of components of the aft fuselage. Such intense sound places narrow constraints on the design of conventional structures. Skins and substructures must be designed to ward off acoustical fatigue for the lifetime of the aircraft, and internal equipment must be protected from structural-borne acoustically-induced vibrations and from direct impingement by air-borne sound that is transmitted through the skin of the fuselage. Constrained layer damping provides increased options in design that result in decreased weight of structure and in reductions in the amount of space that is occupied by vibration isolators within equipment bays.

2. BACKGROUND

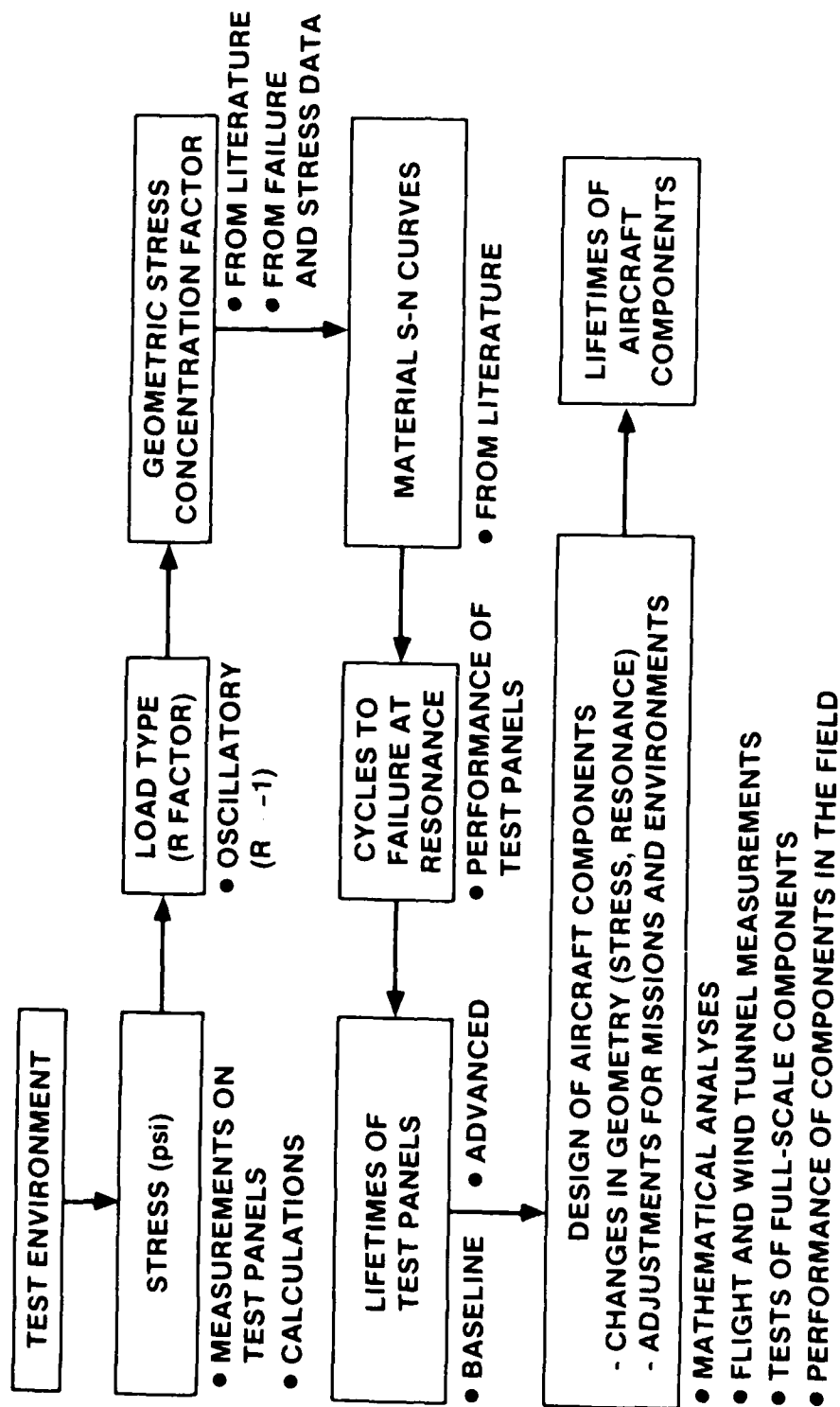
The role of damping in controlling acoustically induced stresses and acoustical fatigue life has been recognized for over twenty years. For example, seven detailed papers on the subject were presented at the Second International Conference on Acoustical Fatigue in Aerospace Structures, in 1964 (Reference 1). Design equations, characterization of damping materials, optimization techniques, and results of experiments were discussed at that conference. One author at the conference reported laboratory measurements which showed that a thin layer of viscoelastic material bonded to a test panel reduced acoustically induced stresses in the panel by a factor of four.

Although there have been some demonstrations of practical applications of viscoelastic materials to control vibrations and fatigue of structures, such applications to aircraft structures have been sporadic, largely because suitable materials were not available, or had not been identified and characterized. Advancements within materials science within the last decade provide viscoelastic materials that are excellent candidates for damped aircraft structures.

Figure 1 shows the elements of a methodology that encompasses the studies that are reported in this paper. Many applications of that methodology to designing for durability, predicting durability, and measuring the durability of laboratory specimens and of components of flying aircraft have demonstrated that elements of the methodology are in mutual agreement.

The test environment that is noted in Figure 1 can be an acoustical excitation that is arbitrarily chosen to explore the fundamental characteristics of a test specimen, or it can be a simulation of a known operational environment. For studies of acoustical fatigue, an oscillatory load of zero mean ("R" factor = -1) usually is considered. (Although a superimposed static stress modifies resonant frequencies of a structure, the existence of a corresponding shift in the mean stress that influences

DURABILITY METHODOLOGY



AP4-448-1

Figure 1

acoustical fatigue is debatable.) Geometric stress concentration factors in such regions of structure as rivet lines or bend radii can be found in publications (e.g., Reference 2), or they can be derived from measured strain and measured time to failure if the lifetime versus stress (S-N) characteristics of the test material are known. S-N characteristics often can be found in publications (e.g., Reference 2). The observed cycles to failure of a test panel provide a check of mathematical predictions if one is confident of the S-N characteristics of the test material; otherwise, an observed failure provides one point towards characterizing the S-N characteristics of the material. (If one doubts available S-N data or has no such data, then it is best to obtain the required data with an uncomplicated configuration such as a cantilevered reed vibrated at its base.)

Many applications of the same mathematical analysis to laboratory specimens and to corresponding aircraft components have generated confidence in the analysis. Therefore, results of laboratory tests can be mathematically transformed to account for any differences in configuration or in acoustical excitation between a laboratory specimen and its corresponding aircraft component.

The durability methodology includes predictions of acoustical excitations in service. The mathematical techniques for predicting those excitations have been found to be consistent with measurements on wind tunnel models and on full-scale flying aircraft. Laboratory procedures for simulating the service environments have been shown to be consistent with performance of components in service. For example, structural failures that are caused by random noise in service can be duplicated in the laboratory by using an equivalent pure tone excitation (References 3, 4). This paper discusses only noise generated by the exhaust of a jet engine, but the methodology includes predictions of noise generated by air flow. The latter often is overlooked, yet the magnitudes that have been documented by the author for such noise (Reference 5) are sufficient to drive the design of some aircraft components.

3. CHARACTERIZATION AND SELECTION OF DAMPING MATERIAL

Figure 2 is a plot of the frequency-dependence of the shear modulus and of the associated loss factor of the structural adhesive that is discussed in this paper. The data in Figure 2 were extracted from measurements that were made by U.S. Air Force materials specialists at the Wright-Patterson Materials Laboratory. They utilized a device for placing a strip of cured adhesive in oscillatory torsion. They extended low frequency measurements to higher frequencies by varying the temperature of the test sample during low frequency oscillation, and mathematically relating temperature and frequency (Reference 6). Their data also define the variation of the material coefficients with temperature at a given frequency.

Jones (Reference 7a) discussed several laboratory devices, other than those for inducing torsional oscillation, for characterizing damping materials. Figure 3 is a sketch of one such device that was used to assure that the desirable properties of 3M Company's AF-32 structural adhesive that are shown in Figure 2 were maintained throughout the studies that are described in this paper. The resonance-dwell apparatus that is shown in that figure was used to oscillate the base of a cantilevered beam consisting of two

DYNAMICAL SHEAR MODULI OF AF-32 ADHESIVE

FROM AFML DATA, CONFIRMED BY LTV FOR EACH BATCH

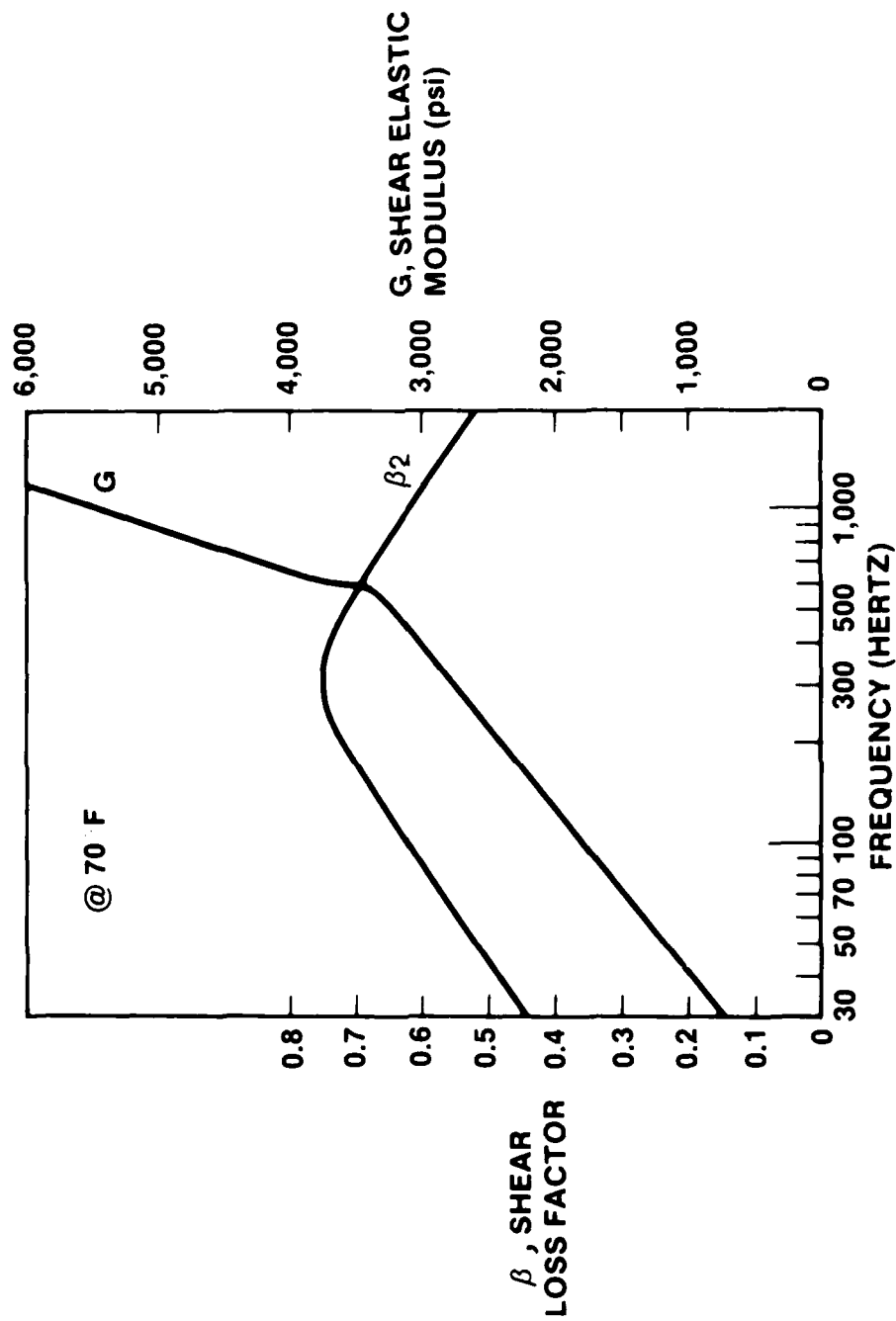


Figure 2

AP4-448-2

VIBRATING BEAM APPARATUS FOR MEASURING FREQUENCY — DEPENDENT DYNAMICAL MECHANICAL MODULI

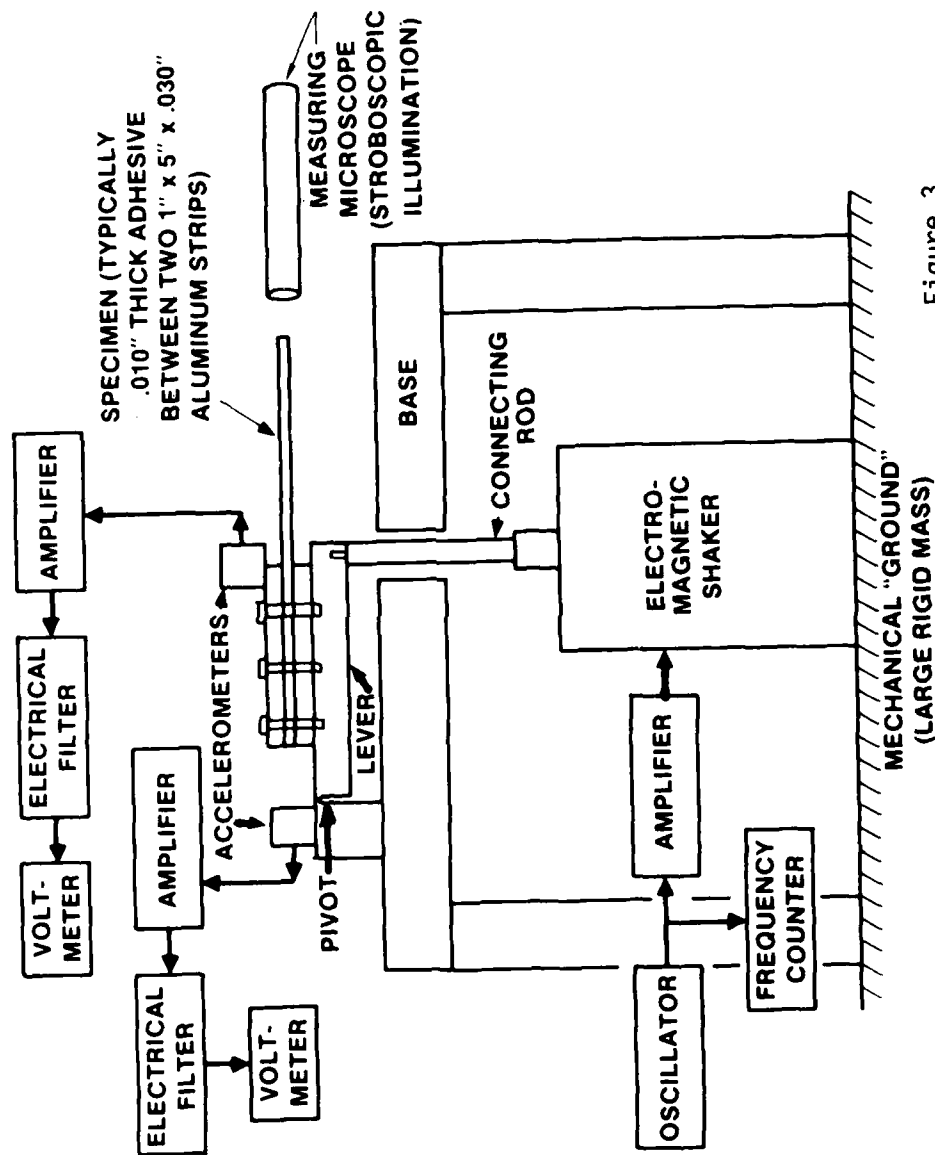


Figure 3

AP4-448-3

layers of aluminum with a layer of AF-32 bonded between them. The beam was oscillated sinusoidally at its first resonant frequency. The sample damping factor was calculated from the measured sinusoidal acceleration at the base of the beam, the measured resulting oscillatory displacement of the tip of the beam, and the measured resonant frequency. That technique was employed by Heine (Reference 8). The characteristics of the adhesive were obtained for various frequencies by progressively decreasing the length of the sample. The frequency-dependent loss factor and the frequency-dependent shear modulus of the adhesive that was used in these studies were calculated from the measured sample loss factor and the measured resonant frequency, using Abdulhadi's (Reference 7b) specialization of the equations of References 10 and 11 to account for the finite length of a cantilever beam.

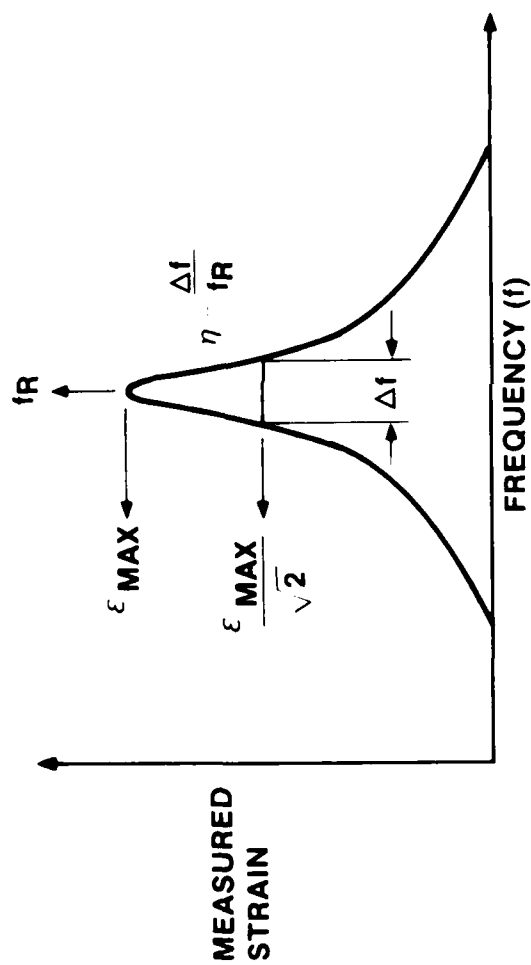
One might question the suitability of obtaining the sample loss factor of a laminate with a shear layer from Heine's mathematical equation that was derived for a monolithic beam. However, Heine's sample loss factor is in good agreement with the sample loss factor that was predicted from the known properties of the adhesive from the equations of Reference 7b. Use of Heine's equation to determine sample loss factor from resonance dwell data allowed some difficulties with broadness of tuning that are discussed in the next section to be avoided. Since measurements were at a single frequency, rather than over a band of frequencies as is involved in measurements of broadness of tuning, the extreme sensitivity of damping factor to frequency did not complicate the measurements. Further, the resonance dwell measurements were made at fixed amplitude, so there were no changes in amplitude to cause changes in damping during a single measurement, as there are when damping is determined from broadness of tuning.

4. BASELINE PANELS

Figure 4 shows the method that was used to measure the loss factor of panels that are discussed in this paper. The method that is shown in that figure is widely-used (Reference 9). However, when one applies the method to highly-damped structures, one should remember the caveats that are listed in Figure 4.

"C" in Figure 4 is a viscosity coefficient. Although popular thought connects it with a liquid, or at least with a viscoelastic solid, the author has shown (Reference 12) that it also describes conventional structural damping such as sliding friction. "C" is generally strongly frequency dependent, especially for highly-damped structures, and high damping broadens resonant peaks like the one that is sketched in Figure 4. Therefore, the quantity " $C\omega^2$ " does not change by a small amount to the "one-half power points", as it must for the associated theory to be strictly applicable (Reference 13).

ONE MEASUREMENT OF LOSS FACTOR



POWER = FORCE X VELOCITY

$$(C\dot{X})^T X$$

$C_{\omega^2} X^2$

$$\text{POWER} = C\omega^2 \left(\frac{X}{2} \right)^2$$

**VALID ONLY FOR SMALL
CHANGES IN $C\omega^2$ THROUGH
RESONANCE. ($\omega = 2\pi f$)**

APPROXIMATE FOR HIGH DAMPING

- ☐ **FREQUENCY—DEPENDENT DAMPING**
- ☐ **DEFINITIONS OF RESONANCE AND MODE BREAKDOWN**
- ☐ **SAME PROBLEMS WITH COMPUTER ANALYSES OF MEASUREMENTS**

Figure 4

The concept of resonance begins to break down for high damping. For high damping, the off-diagonal terms in the matrix formulation of a vibrating structure become significantly different from zero (Reference 13), so classical normal modes do not exist (Reference 14). Since added damping materials generally are nonlinear, the natural tendency of a thin panel to hysteresis, "jumps", and subharmonic responses (Reference 15) will be exacerbated when damping material is added to a panel.

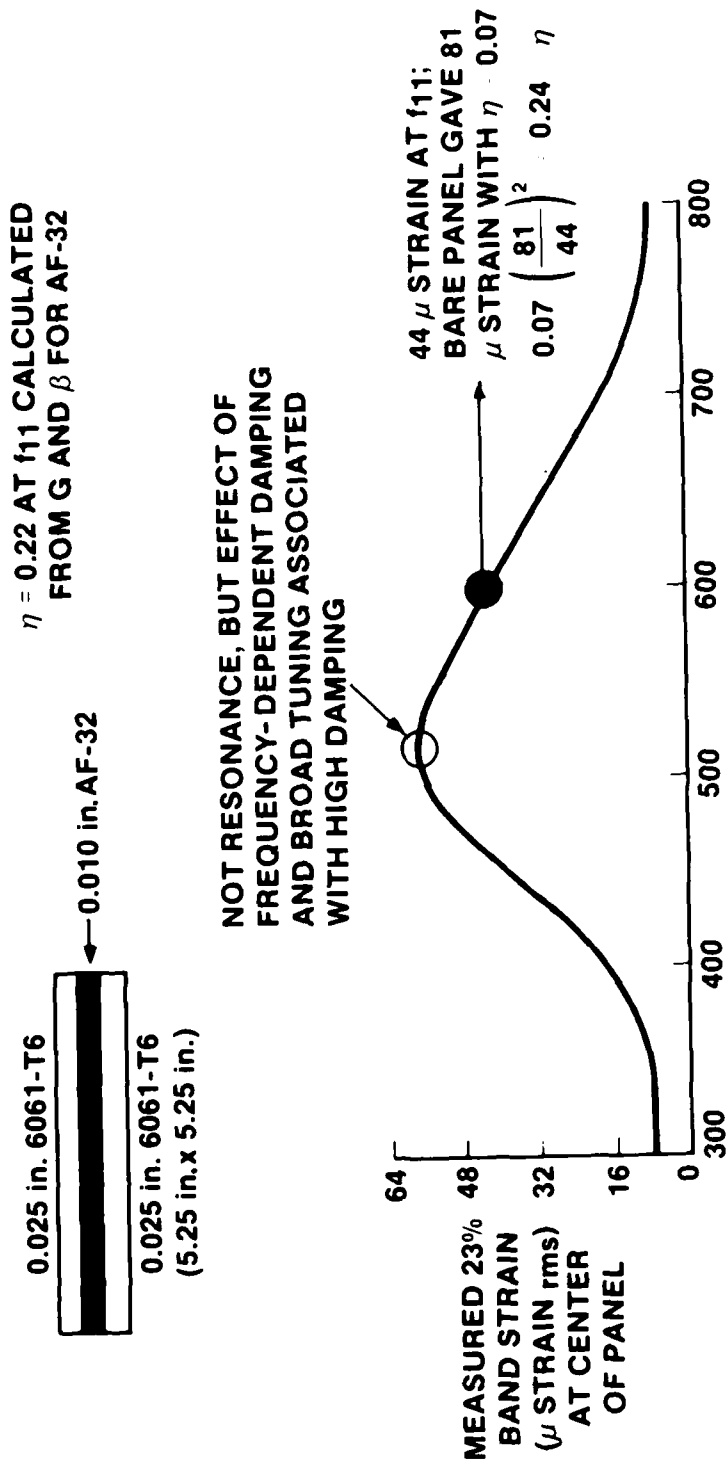
The following discussion will show that the non-ideal, non-classical aspects of test panels that are described in this paper did not interfere with a consistent application of the methodology that was described in connection with Figure 1. However, it was important to keep those aspects in mind as tests of panels were planned, performed, and interpreted.

Figure 5 shows measured values of root-mean-square (rms) strain at the center of a square aluminum panel with a constrained layer of AF-32 adhesive. The output of a strain gage at the center of the panel was recorded while the panel was excited with random noise in a frequency band with a bandwidth equal to 23 percent of a continuously progressing center frequency. The sound pressure level for that moving band was 150 decibels (re 20μ Pa). The peak in the curve in Figure 5 is not a resonant peak like the peak that is shown in Figure 4. Rather, it is due to the changes in the material coefficients of AF-32 with frequency that are evident in Figure 2. The strain levels shown in Figure 5 are the result of a competition between increases in strain due to the increasing bandwidth of excitation with increasing frequency, and decreases in strain due to the rapidly changing loss factor, δ , and shear modulus, G , of AF-32 with increasing frequency. The resonant frequency f_{11} of the test panel that was observed with pure-tone excitation was about 600 Hertz. The strain that was measured with random excitation centered about the resonant frequency was compared with the strain that was measured in a bare panel for which the loss factor was measured in the way that is shown in Figure 4. As shown in Figure 5, the resulting loss factor was in good agreement with the loss factor that was independently calculated by means of the equations that will be presented in Section 5. The loss factor for the bare panel is a little higher than is usually observed for that type of structure (Reference 16). The reason for that will be explained below.

Figure 6 shows measured values of the loss factor for three square, flat panels and one built-up structure as a function of the level of pure-tone excitation. The measured loss factor for a typical built-up aircraft structure, an A-7 flap without added damping, was at the expected level.

The three square panels that are described in Figure 6 were rigidly bolted at their edges, through clamping bars, to an acoustical progressive wave tube. The bare panel (without added damping) is known to have undergone cyclic slipping at its clamped edges, because wear marks were visible, and the resonant frequency of the panel varied with the level of acoustical excitation. The panel with a constrained layer of American Cyanamide Company's FM-73 structural adhesive showed less evidence of slipping at the edges, probably because the slightly compressible FM-73 improved clamping at the edges, so it manifested the low loss factor that was expected from independent measurements of the material characteristics like those that are shown in Figure 2 for AF-32 structural adhesive.

COMPARISON OF CALCULATED AND MEASURED DAMPING

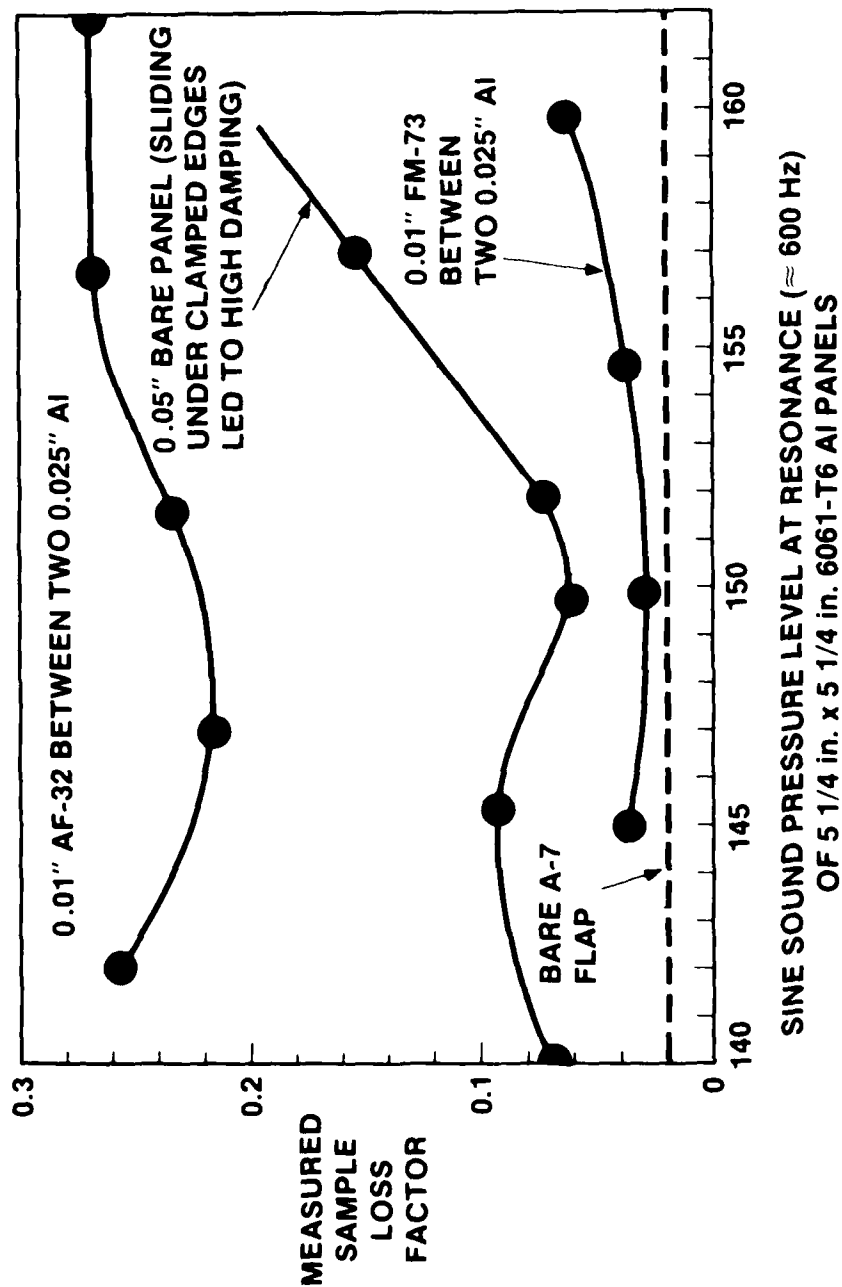


23% BAND CENTER FREQUENCY AT 150 dB 23% BAND SPL

AP4-448-5

Figure 5

COMPARISON OF PANEL LOSS FACTORS



AP4-448-6

Figure 6

The loss factors for the bare panel, the panel with FM-73, and the A-7 flap were measured in the way that is described in Figure 4. It was not possible to measure the loss factor for the panel with AF-32 in that way, because the high damping of the AF-32 led to the complications that are listed in Figure 4 and in the above discussion of Figure 4. The values of the loss factor were obtained for the panel with AF-32 by comparing measured stress levels with stress levels that were calculated from independent measurements of the characteristics of AF-32, as is shown in Figure 5, except Figure 5 applies to random excitation, and Figure 6 applies to pure-tone excitation. The mathematical equations that were used in the calculations will be presented in Section 5. The non-linear behavior of AF-32 is evident in Figure 6, since the panel loss factor varies with the level of acoustical excitation.

5. ANALYTICAL TECHNIQUES

The mathematical analyses that were used in this study go beyond descriptions of unstiffened panels like those that are described in Section 4, to describe rectangular panels like the one that is sketched in Figure 7, with stiffeners attached to them. Ungar's equations (Reference 9) were used to predict sample loss factors for structures like the one in the figure. The resonant frequency was determined by the coupled stiffness, as expected. However, the loss factor was determined by the uncoupled stiffness, probably because of the influence of membrane forces in the two constraining sheets that are not accounted for in Ungar's one-dimensional equations. Maximum stress at the center of the long edge of a skin bay and at the end of a stiffener were calculated by means of equations published by Ungar, et al (Reference 17).

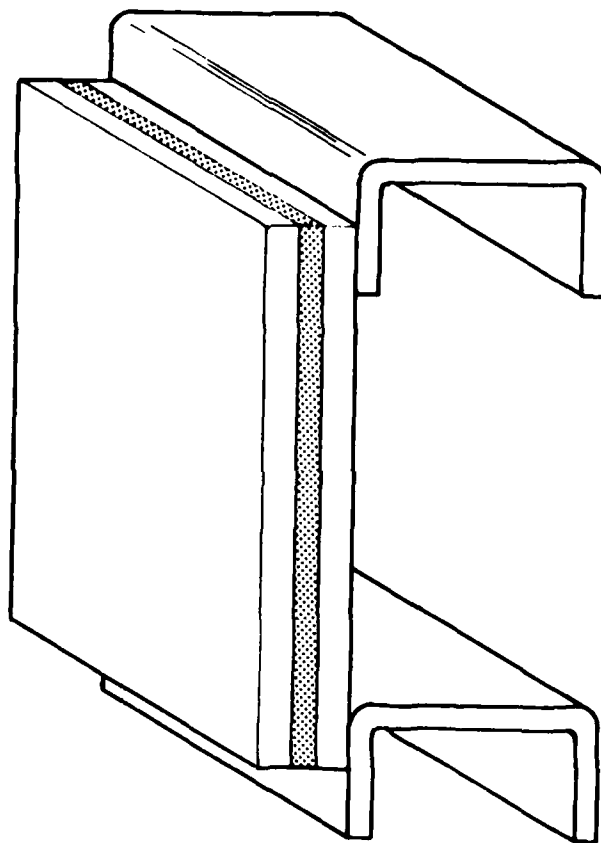
The acoustical fatigue life of a skin or attached stiffener was predicted from the maximum stress in those structural elements by entering the value of the acoustically-induced stress in the log-log equation for S-N plots like those that are published in Reference 2, as shown in Figure 8. Comparisons of calculated life, strains that were measured in structural elements and full-scale airplane components in a laboratory, and observations of performance of airplane components in the field have provided no evidence of a "threshold stress" (e.g., Reference 18) below which "infinite life" is achieved for aluminum alloys. Such comparisons are part of the consistent methodology that is summarized in Figure 1 and discussed in Section 2.

The effects of multiple levels of acoustical excitation of varied durations were predicted by means of Miner's rule (Reference 19) of accumulative damage. Other mathematical formulations have been proposed for low-cycle high-stress accumulative fatigue associated with propagation of cracks from initial flaws (Reference 20). However, Miner's rule is consistent with the methodology of Figure 1 for high-cycle low-stress acoustical fatigue.

6. SKIN-STRINGER PANELS

Figure 9 is a photograph of a stiffened sheet metal panel that is typical of those that were tested in the studies that are described in this paper. Such panels (one at a time) were rigidly bolted through edge doublers to the acoustical test fixture. Complications due to fastening an airplane component to flexible frames were intentionally avoided so that well-defined test conditions could be maintained. The effects of fasteners and flexible

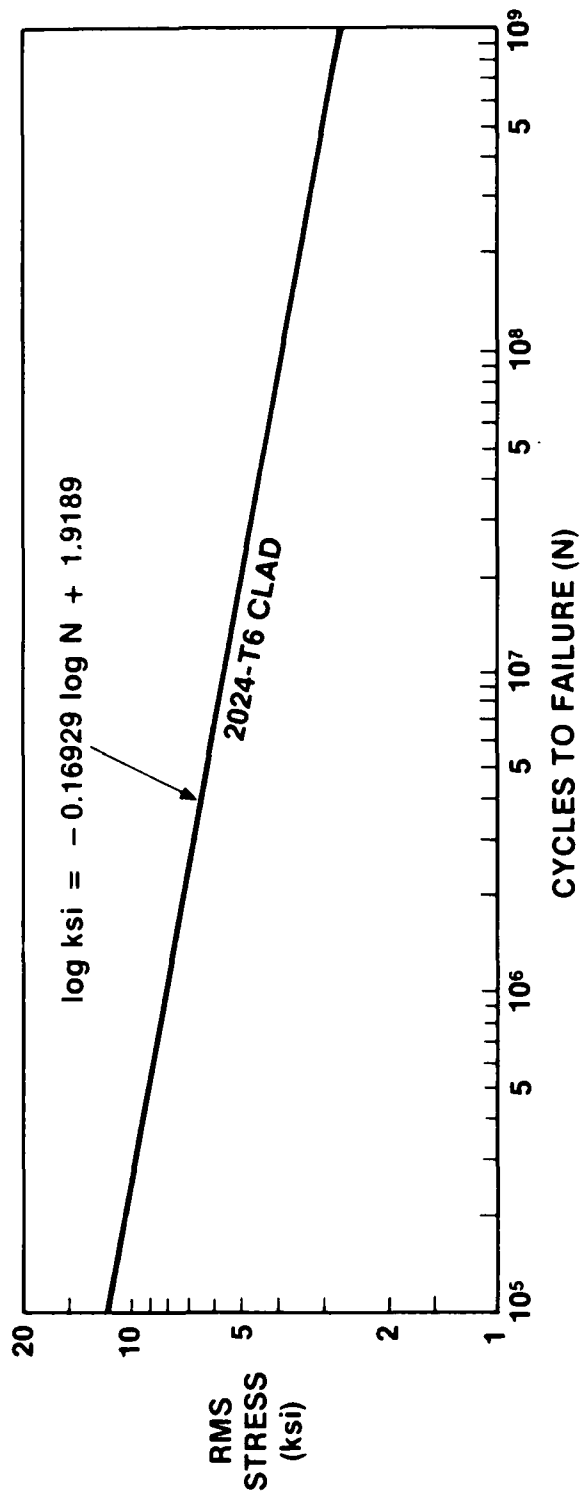
GEOMETRY FOR DURABILITY CALCULATIONS



AP4-448-7

Figure 7

TYPICAL S-N DATA



AP4-448-8

Figure 8

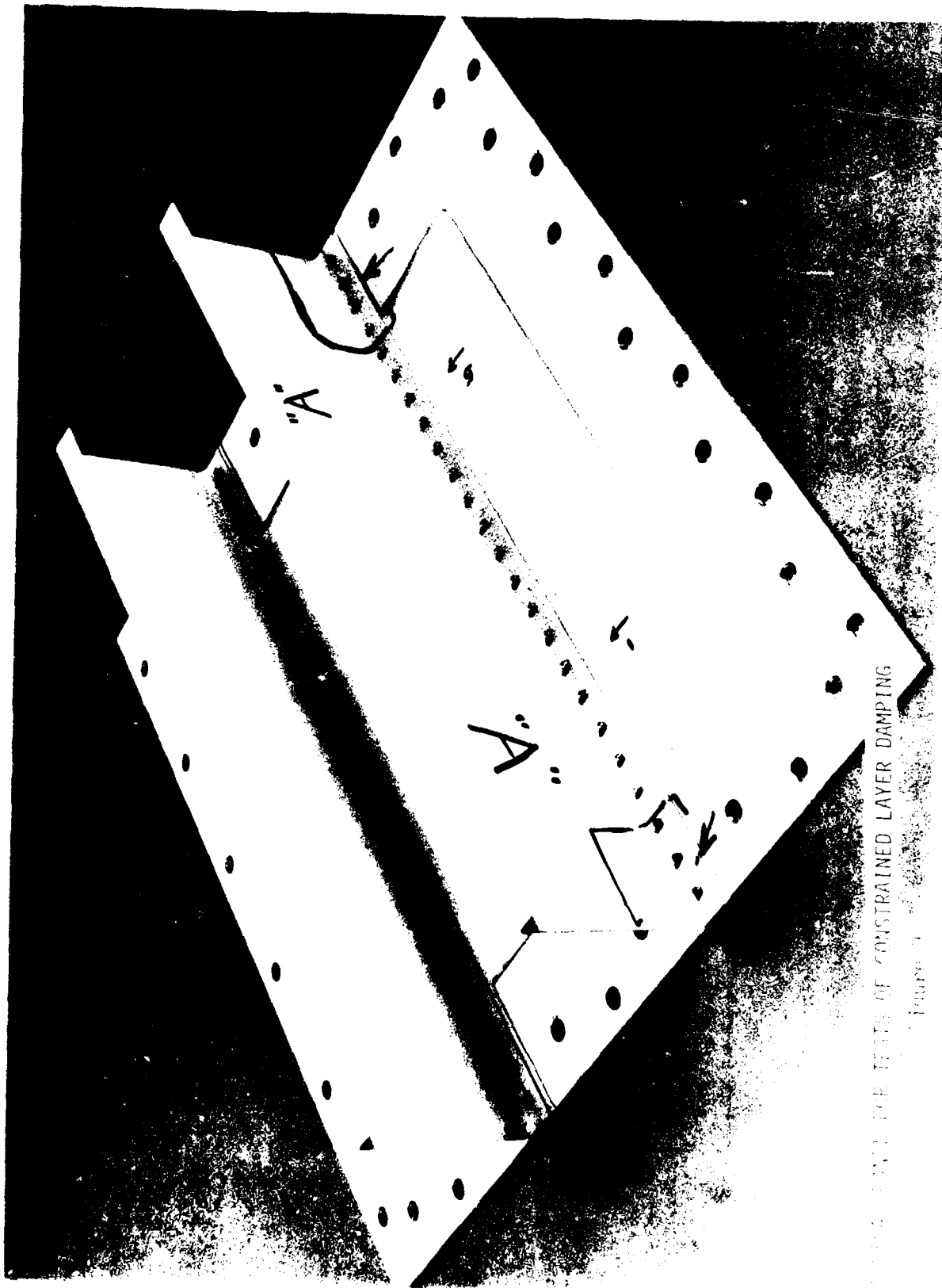


Figure 1. TESTS OF CONSTRAINED LAYER DAMPING

substructure were studied by attaching stiffeners to the skin within the clamped boundary of each test panel. The web of each stiffener was not clipped to supporting structure as it would be in an aircraft component, so the equation for maximum stress in a rib from Reference 17 does not apply to the test configuration. Nevertheless, the stiffeners on the test panels provided valuable data; by substituting observed cycles to failure of the ribs in log-log S-N equations, calculating a stress, and relating that stress to strain that was measured in the skin, stress concentration factors for the bend radius of the ribs and for a line of rivets that are in good agreement with Reference 2 were calculated. Measurements of the acoustical fatigue lives of panels with and without bonding material at the rivets showed that rivet-bonding eliminates the usual 74 percent increase in stress at a line of rivets.

The panel shown in Figure 9 is 18 inches by 18 inches. That is smaller than some acousticians prefer. However, Clarkson (Reference 21) showed that Lassiter, Hess, and Hubbard (References 22 and 23) obtained good agreement between theory and measurements for even smaller unstiffened panels. The tests of baseline panels that are described in Section 4 of this paper extended that early work to high values of damping and to high sound pressure levels with the same success.

7. COMPARISON OF CALCULATED AND MEASURED STRAINS

Figure 10 shows that tests of panels like the one that is shown in Figure 9 extended the early work on unstiffened panels to stiffened panels with good success. Figure 10 shows a comparison of strains that were measured at the center of a panel (or of a bay between stiffeners for a stiffened panel) with strains that were calculated by means of the analytical techniques that are described in Section 5 of this paper. Random excitations and sinusoidal excitations were related through the damping factor in the way that is shown in Figure 10 and discussed in References 3 and 4. Damping factors were measured as shown in Figure 4 and discussed in Section 3.

Perfect agreement between calculated and measured strains would cause each datum of comparison to fall on the straight line that is plotted in Figure 10. Panel "A" that is referred to in the Figure is shown in Figure 9. Panels "X", "Y", and "K" were variations of "A". Since the plot in Figure 10 is a log-log plot, some of the deviations of an individual datum are transformed by log-log stress-strain equations like the one in Figure 8 into large uncertainties in acoustical fatigue life. However, the agreement between predicted and measured strains is good for the built-up panels ("X", "Y", "K", and "A") for excitation with random noise, and that is how similar panels are exposed during flight of a parent aircraft.

The damping factors that were used in the calculations for Figure 10 were obtained by measuring the broadness of tuning of the first resonance of a panel. (See Figure 4, and Section 3.) The deviations from the straight line in Figure 10 of some baseline points for random excitation and of some points for built-up panels for sine excitation are both related to non-linear responses of the panels at high sound pressure levels.

COMPARISONS OF CALCULATED AND MEASURED STRAINS

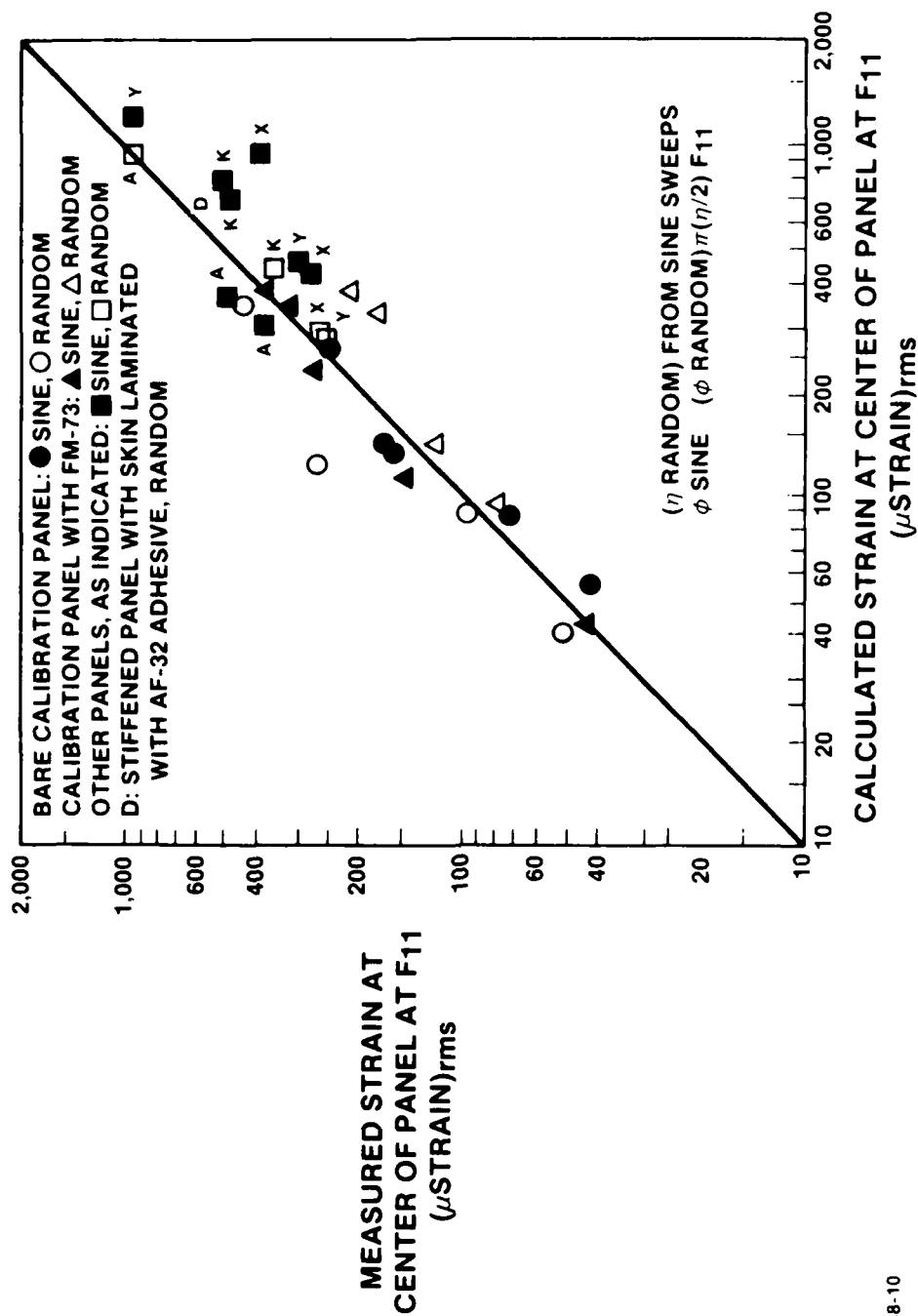


Figure 10

AP4-448-10

Excitation of the baseline panels with a sinewave that was equivalent to the highest strains that are shown for the baseline panels in Figure 10 pushed the panels into a region of non-linear response that was not evident in the responses of the panels to the equivalent random excitation. Therefore, the damping factor that was measured with sine excitation was not strictly applicable to the random excitation that was chosen. The data for the baseline panel with AF-32 damping material that are shown in Figures 5 and 6 and discussed in Section 4 are not shown in Figure 9 for a similar reason. The damping was so high that the problems that are listed in Figure 4 and discussed in Section 4 arose -- the resonant peak became asymmetric in frequency. The loss factor for the panel with AF-32 was determined by comparing measured strains with strains that were measured for the equivalent panel without added damping material. As is shown in Figure 5 and discussed in Section 4, the agreement of the loss factor that was calculated in that manner with the loss factor that was calculated independently is good.

The reason for the deviation of the points for built-up panels for sine excitation from the straight line in Figure 10 is the same as the reason that is given above for the deviation of the points for baseline panels for random excitation from that line--non linearity. At the high sound pressure levels that were used to obtain the points for the built-up panels that are shown in the figure, the resonant peak became highly asymmetrical in frequency. Therefore, damping factors that were obtained from sine sweeps of the same panels at low sound pressure levels were used in predictions of strain at high sound pressure levels.

Regardless of the complications that are discussed above, the analytical techniques that are presented in Section 5 predict acoustical fatigue lives for airplane components that agree well with lifetimes that are observed for service on flying aircraft in the fleet. That probably is because even high-amplitude, non-linear responses to random noise are better behaved than high-amplitude responses to pure tone excitation, as is evident in Figure 10 for the built-up structures.

The datum labeled "D" in Figure 10 is for a highly-damped, stiffened panel. That panel comprised two .025 inch skins bonded together with a layer of AF-32 adhesive approximately .01 inch thick, with .040 inch "C" stiffeners rivet-bonded to the laminated skin. As Figure 10 shows, the predicted value for the strain in the center of a bay between ribs agreed well with the measured value. In this case, a sine sweep of the panel provided a peak for the first resonance that was well enough defined to allow the damping factor to be obtained from the width of that peak. That damping factor, which was used in the calculations of the acoustically-induced strain for random excitation, was in good agreement with the value that was calculated from independently measured material coefficients for AF-32 (Figure 2, and Section 3) by means of the equations that are discussed in Section 5.

Tests of panel "D" and of similar panels showed that damping and rivet bonding caused a bay between stiffeners to resonate at a frequency that corresponded to rigidly clamped boundaries, yet Ungar's (Reference 17) equation for stress at the edge of a bay with mixed boundary conditions applied. The tests also revealed that the strain at the center of a bay of highly-damped skin between stiffeners is equal to the strain at the edge of

the bay, rather than being approximately one-half of the strain at the edge as classical theory predicts (References 2, 21). However, if the strain at the edge of the bay had been plotted in Figure 10, then the datum for panel "D" would fall at a much lower value of strain (for a given excitation) than any of the other built-up panels, because all of the points except for "D" would be raised by a factor of two. That shows that the maximum stress in panel "D" was greatly reduced by the damping AF-32 in the laminated skin, even though the ratio of stress at the center of a bay to stress at the edge of the same bay was increased.

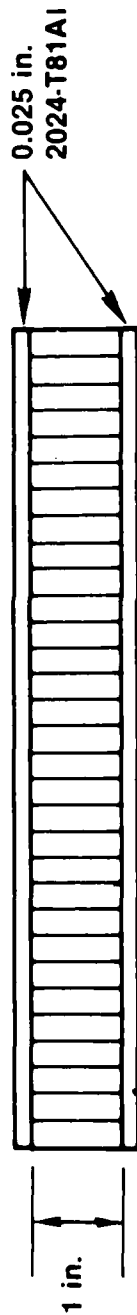
8. HONEYCOMB PANELS

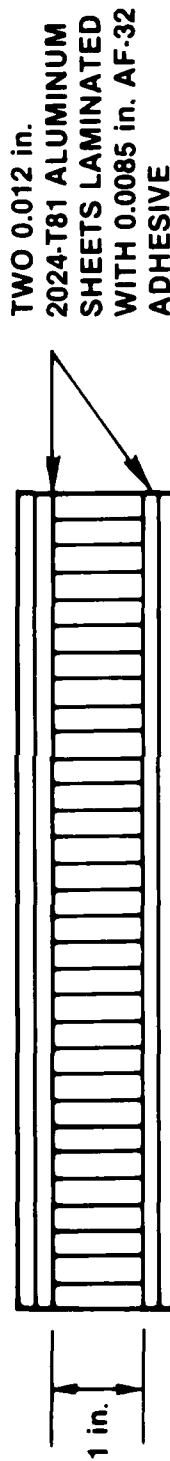
Figure 11 shows sketches of some of the honeycomb panels that were tested in the studies that are described in this paper. The top panel in the figure is representative of some control surfaces on high performance jet fighter aircraft. Such components are being destroyed in small fractions of the lifetimes of their parent aircraft by fluctuating pressures associated with localized separation of boundary layer flow. The tests that are described below indicate that the initial failure is caused by induced stresses that exceed the ultimate strength of the adhesive bond between a skin and a honeycomb core; cracking of skins, and destruction of the core follow.

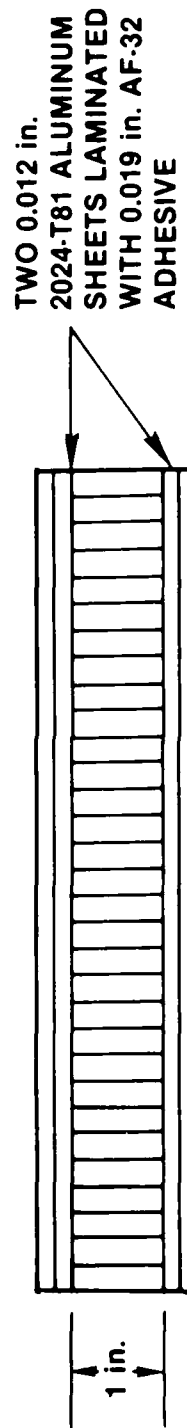
The purpose of the studies that are described below was to utilize laminated skins for honeycomb panels, to reduce the levels of induced resonant vibrations, thereby reducing the stress in the adhesive bond-line between two skins and a core. Ungar (Reference 9) reported that the benefits from such damping layers that are spaced above the neutral bending plane of a structure are enhanced, and "...honeycomb portions of practical honeycomb sandwich panels often behave nearly like ideal spacers."

Figure 12 summarizes some qualitative differences in induced responses of a honeycomb panel that is excited at a resonance and the same panel that is excited at its critical frequency (where the speed of bending waves in the panel equals the speed of sound in air--Reference 24). The critical frequency is a function only of the thickness of a panel (for a given material), while the resonant frequency of a panel depends on its length, width, and boundary conditions as well as its thickness. A panel radiates sound only from its edges at resonance, while it radiates sound from its entire surface at and above its critical frequency (Reference 24). Since a conventional honeycomb panel has low internal damping, re-radiation of sound is the dominant damping mechanism for a rigidly clamped panel. The tests that are described below produced responses at the critical frequency of a panel that mimicked resonance, with induced vibrations decreasing above the critical frequency, so attention was focused on the critical frequency and the resonant frequencies of each panel.

Figure 13 summarizes the results of acoustical fatigue tests of the panels that are sketched in Figure 11. Each test panel was bolted to the test fixture through filled-edges of the honeycomb core, to establish well-defined boundary conditions. The measured resonant frequencies and critical frequency for each panel agreed with values that were predicted from the calculated stiffness and mass of the panel. While the well-defined (clamped) boundary conditions were maintained, with no attempt to simulate edge conditions of







AP4-448-11

Figure 11

VIBROACOUSTICAL PROPERTIES OF HONEYCOMB STRUCTURES

AT CRITICAL FREQUENCY	AT RESONANCE
<ul style="list-style-type: none"> • Proportional to $\sqrt{\text{mass} \div \text{stiffness}}$ • Independent of length and width • Naturally high damping, due to re-radiation of sound • Increased viscoelastic damping interferes with re-radiation of sound, increases stress 	<ul style="list-style-type: none"> • Proportional to $\sqrt{\text{stiffness} \div \text{mass}}$ • Sensitive to length and width • Naturally low damping (limited re-radiation of sound, low internal friction) • Increased viscoelastic damping converts vibration to heat, decreases stress

Figure 12

AP4-448-12A

RESULTS OF ACOUSTICAL FATIGUE TESTS OF HONEYCOMB PANELS

(167.5 dB SINUSOIDAL EXCITATION)

BASELINE HONEYCOMB

RESONANT FREQUENCY (Hz)	DAMPING FACTOR	STRESS AT CENTER OF PANEL (ksi)*	LIFE
394 (f _{CLAMPED})	0.056	8.2	DEBONDED IN 25 MINUTES

LAMINATED HONEYCOMB (THIN ADHESIVE)

370 (f _{CLAMPED})	0.064	7.1	CRACKED IN 3.4 HOURS
--------------------------------	-------	-----	-------------------------

LAMINATED HONEYCOMB (DOUBLE ADHESIVE)

370 (f _{CLAMPED})	0.17	1.5	3.5 HOURS
320 (f _{CRITICAL})	—	7.3	DEBOND AND CRACK IN 2.5 HOURS

* HOLES WITH $K_T = 1.74$ ADDED TO SIMULATE FASTENERS AND
CHEM-MILLED STEPS.

AP4-448-13

Figure 13

aircraft components, holes were added to simulate stress concentrations due to fasteners and chem-milled steps in the skin of an aircraft component.

No stress values are given in Figure 13 for the critical frequency of the panel with no added damping or for the panel with a thin layer of added damping material (in laminated skins), because the acoustically-induced response of each of those panels was negligible at its critical frequency. The figure shows that a single layer of damping material prevented debonding, indicating that the threshold stress in the skin for debonding was above 7.1 Ksi. It also shows that a double layer of damping material decreased the stress in the skin at resonance by more than a factor of five, at the expense of increasing the stress at the critical frequency until it nearly offset the benefits at resonance. The mode of failure of the panel with double damping agrees with the earlier conclusion that the threshold stress in the skin for debonding is just above 7.1 Ksi for the particular adhesive that was studied. That result agrees with studies of failures of failed components in service.

Data that were presented in Section 6 for skin-stiffener panels showed that it is the uncoupled stiffness of a laminated skin that determines how much damping is achieved from a constrained layer of viscoelastic material. The measured damping factors that are listed in Figure 13 for honeycomb panels are close to values that were calculated with the value for coupled stiffness that is defined in Reference 9.

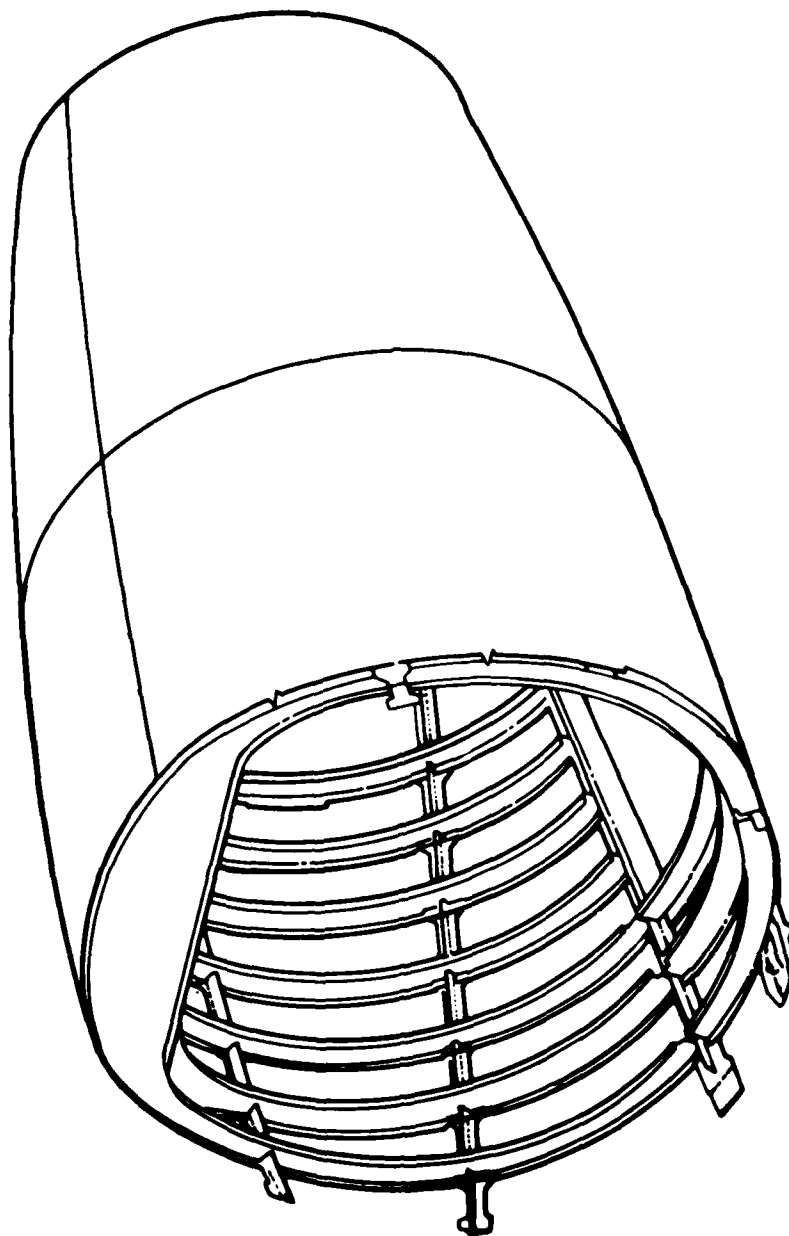
The test results that are summarized above demonstrate that great care must be exercised in designing a damped honeycomb panel, to avoid adverse influences of added damping material at the critical frequency of the panel. A panel can be designed to keep the critical frequency well-separated from resonant frequencies, and a damping material and configuration can be selected to be effective at resonant frequencies, without adversely affecting responses at the critical frequency.

9. APPLICATION OF CONSTRAINED LAYER DAMPING TO AFT FUSELAGE COMPONENTS

The studies of laminated skin on stiffeners or on honeycomb that are discussed above were directed at redesigning aircraft control surfaces to increase their acoustical fatigue life. The demonstrated principles are equally applicable to fuselage skin and substructure and to controlling vibration of equipment within a fuselage.

Figure 14 is a sketch of a typical structural component of the aft fuselage of a large aircraft. It is assembled from the usual "C" channel stiffeners, riveted to a sheet metal skin. The engines of the parent aircraft for such components expose them to broad-band random noise at overall sound pressure levels in the neighborhood of 170 decibels (re 20 μ Pa) during takeoff. The damping of acoustically-induced resonant vibrations of such structures is very low. Therefore, the conventional approach to meeting the required acoustical life of a component is to make it as stiff as possible, to raise the resonant frequency (which reduces stress for a given spectral level of acoustical excitation, plus often moves the frequency into a region in which the intensity of the acoustical excitation is decreasing). Increasing stiffness usually involves increasing weight, which, besides its usual penalties, partially offsets the advantage of increased stiffness.

TYPICAL SKINS AND FRAMES IN THE AFT FUSELAGE OF A LARGE AIRCRAFT



AP4-448-14

Figure 14

Figure 15 shows sketches of typical cross-sections of the skin and attached frames for a typical component like the one that is sketched in Figure 14. Application of the technology that is summarized in the first eight sections of this paper indicates that frames can be simplified in configuration and reduced in thickness and weight by the application of a constrained layer of viscoelastic damping material, as shown in Figure 15. Experimental data have been presented which support calculations that show that the pockets a skin like the one that is sketched in Figure 15 can be reduced from .083 inches thick to two .025 inch layers bonded together with approximately .01 inch of adhesive, if the adhesive is carefully selected and fully characterized. Similar reductions could be made in the stepped lands, and chem-milling could be eliminated by adhesively bonding successive layers to form lands. The mission profile of operating temperatures of a treated component must be considered, to evaluate the influence of the temperature dependency of material characteristics like those that are shown in Figure 2.

The same external acoustical excitation that threatens to fatigue the skin and frames of a component of an aft fuselage induces vibrations of rack-mounted equipment within the component. Those vibrations can result either from air-borne transmission of sound through the skin to the equipment, or from acoustically-induced vibrations of the skin and attached frames that are transmitted through the rack and shelves that holds the equipment.

Figure 16 is a sketch of the envelope of a typical assembly of rack and shelves to hold equipment in an aft fuselage component. Any portion of the rack or any shelf could be "L", "I", or "C" channels, stiffened sheet metal, or honeycomb. Any or all of those structural elements can be damped through applications of the technology that is presented in this paper, so that reduced weight and space would be required for racks and shelves to keep levels of vibration at equipment within permissible limits.

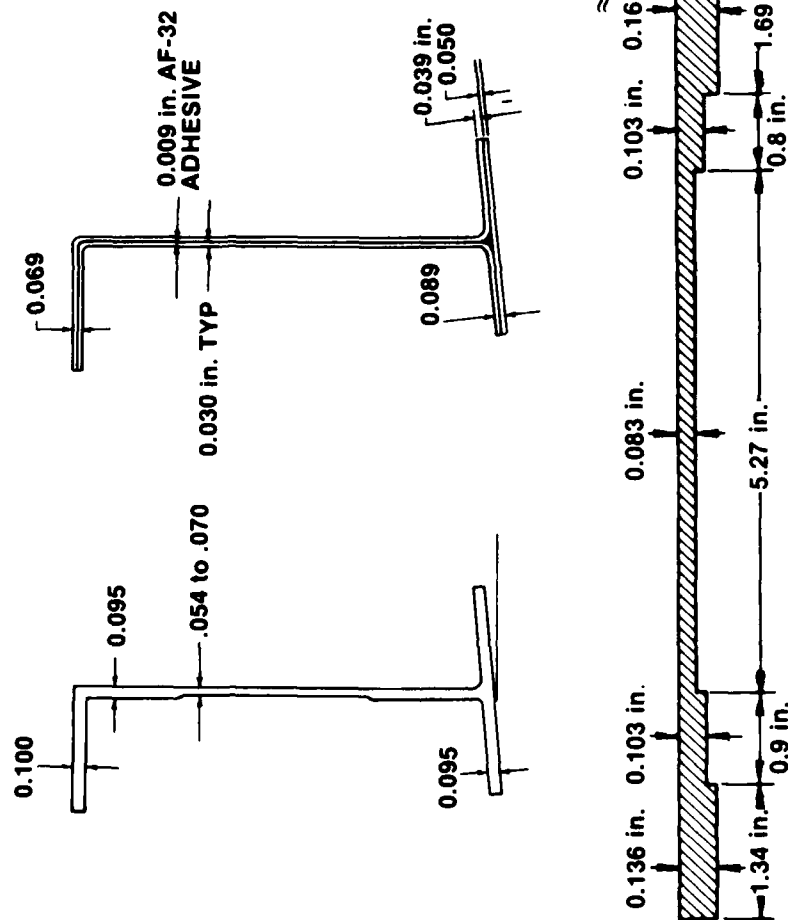
A constrained layer of damping adhesive may be beneficial even when a structure is driven off-resonance, because a laminate can be designed to exhibit a dynamic stiffness that is greater than the static stiffness of the same amount of metal (a sheet of metal twice as thick as one of the constraining layers of the laminate). To demonstrate that point, notice that the equations of Reference 9 show that the dynamic stiffness of a

$$\text{laminate is } E \left[1 + \frac{XY}{1+X} \right] \frac{2(h/2)^3}{12} ,$$

where h is the thickness of the original solid metal that is divided into two equal constraining layers, Y is a stiffness and geometric parameter, and X is related to the shear wavelength in the constrained damping material, and is, therefore, frequency dependent. The stiffness of the original solid metal = $Eh^3/12$. Comparison of the two expressions for stiffness shows that the dynamic stiffness of the laminate is greater than the stiffness of the original

$$\text{metal if } \left[1 + \frac{XY}{1+X} \right]$$

TYPICAL SKIN AND FRAME FOR THE AFT FUSELAGE OF A LARGE AIRCRAFT



AP4-448-15

Figure 15

TYPICAL EQUIPMENT RACK IN THE AFT FUSELAGE OF A LARGE AIRCRAFT

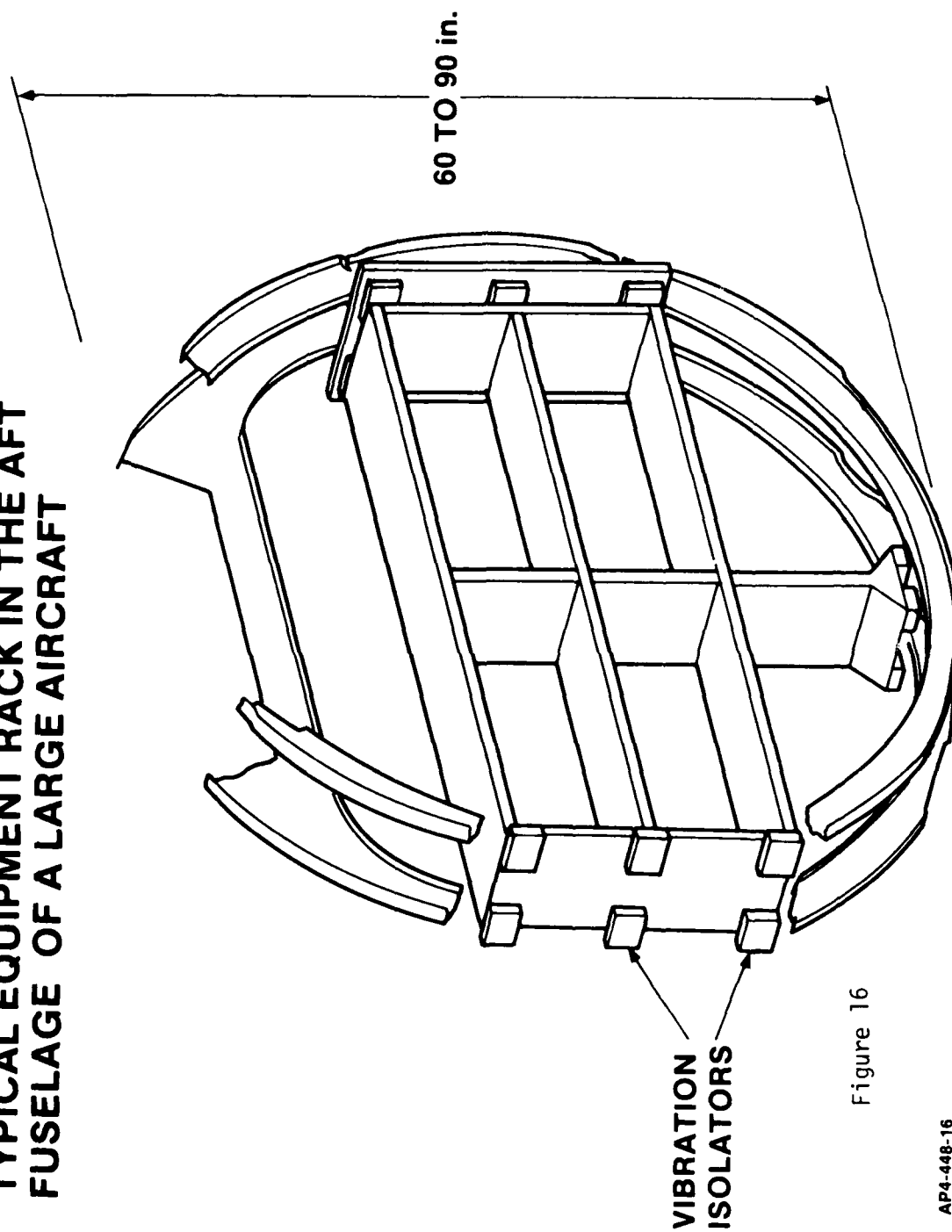


Figure 16

AP4-448-16

is greater than four, which can be achieved in some frequency ranges. Further benefits can be obtained at resonance and off-resonance by the 74 percent reduction in stress that accompanies rivet bonding (Section 6).

Vibration isolators between an equipment rack and fuselage structure especially provide an opportunity to reduce the space, weight, and cost that is required to meet specifications for limits on levels of vibration of equipment. Those isolators usually are bulky, expensive, rubber-like elements. The principles of application of constrained layers of viscoelastic material that have been discussed in this paper in connection with skins, frames, stiffeners and racks are applicable to the interface between an equipment rack and surrounding fuselage structure. The configuration of the constrained damping material probably will be more complicated than a single layer of viscoelastic material, and materials different from those that are useful in other structural members may be required.

10. SUMMARY AND CONCLUSIONS

Figure 17 summarizes the advantages of applying the damping technology that is described in this paper to controlling fatigue and vibrations of components of the aft fuselage of a large aircraft. Existing required restrictions on levels of vibration of equipment and on acoustical fatigue can be met with less weight (and probably lower cost) than is required by conventional technology.

While the theory of constrained-layer damping is well developed, well established, and verified by laboratory measurements, application of damping technology to flight hardware requires precision, care, thoroughness, and documentation. The temperature and frequency dependent elastic and damping moduli must be measured. The sensitivity of those moduli to variations in cure cycles, change in feed stock at the supplier's manufacturing plant, storage conditions, aging, exposure to moisture, and contaminants must be known. The dependence of the properties of the constrained layer on different combinations of constraining materials and processes for preparing the surfaces of the constraining material must be known. The formability of laminated parts must be determined. If they are not formable in the form of the final laminate, then procedures for bonding two pre-formed elements of a part must be developed. Potential problems with alignment of a laminated part upon installation in aircraft or with creep of the part after installation must be assessed. Finally, it is essential that development tests be performed. The performance of laminated structural elements such as "C" channels should be measured. Built-up elements, such as stiffened panels and portions of equipment racks should be tested. Segments of components large enough to allow measurements of acoustical transmission loss through the skin, acoustical fatigue life of the skin and frames, and transmissibility of vibrations through the structure should be assembled. A full-scale, instrumented component should be fabricated and flight-tested. At every level of assembly, direct measurements of vibrations should be made with strain gages and accelerometers during acoustical excitation or direct excitation with a shaker. Fast Fourier Transform modal analyzers (or equivalent) should be used to augment local

TYPICAL BENEFITS OF CONSTRAINED-LAYER DAMPING IN FUSELAGE STRUCTURES

SAVE WEIGHT WHILE MEETING DURABILITY REQUIREMENTS

<u>SKIN</u>	<u>FRAMES</u>	<u>EQUIPMENT RACKS</u>
<ul style="list-style-type: none">• REDUCE FROM 0.083 in. TO TWO 0.025 in.	<ul style="list-style-type: none">• REDUCE FROM ~ 0.1 in. TO TWO 0.030 in.	<ul style="list-style-type: none">• LAMINATED FRAMES• LAMINATED HONEYCOMB• LAMINATED SHEET METAL• REDUCE EQUIPMENT VIBRATION• REDUCE SPACE & WEIGHT FOR VIBRATION ISOLATORS

AP4-448-17

Figure 17

measurements of strain and acceleration by providing "global" representations of the motions of the structure. Sound pressure levels, and induced strains and accelerations should be recorded during flight tests of a full-scale component, and parameters such as temperature, altitude, air speed, and maneuver modes should be recorded at the same time. The data that are recorded in flight should be electronically reduced in a laboratory in such a way that they provide checks of predicted behavior of the component and guidelines for any required modifications.

REFERENCES

1. Acoustical Fatigue in Aerospace Structures, edited by Walter J. Trapp and Donald M. Forney, Jr., Syracuse University Press, Syracuse, New York (1965)
2. "Sonic Fatigue Design Guide for Military Aircraft," AFFDL-TR-74-112, Air Force Flight Dynamics Laboratory (May, 1975)
3. "Development of Aircraft Structure to Withstand Acoustic Loads," P. M. Belcher, A. L. Eshleman, Jr., and J. D. Van Dyke, Jr., Aerospace Engineering, 18, No. 6 (June, 1959)
4. "A Procedure for Designing and Testing Aircraft Structures Loaded by Jet Engine Noise," P. M. Belcher, A. L. Eshleman, Jr., and J. D. Van Dyke, Jr., ASME Paper No. 59-AV-48 (March 1959)
5. "Flow Regimes Underlying Aeroacoustical Excitation of Airplane Wings," R. A. Ely, Proceedings of the Institute of Environmental Sciences (April, 1976)
6. "A Reduced-Temperature Nomogram for Characterization of Damping Material Behavior," D. I. G. Jones, 48th Shock and Vibration Symposium (October 1977)
- 7a. "Temperature-Frequency Dependence of Dynamic Properties of Damping Materials," D. I. G. Jones, Journal of Sound and Vibration, 33, No. 4 (1974)
- 7b. "Determination of Damping Properties of Soft Viscoelastic Materials", F. Abdulhadi, Sound and Vibration Bulletin, No. 41, Part 2 (1970)
8. "The Stress and Frequency Dependence of Material Damping on Some Engineering Alloys," J. C. Heine, Ph.D. Dissertation, Massachusetts Institute of Technology (1966)
9. "Damping of Panels," Eric E. Ungar, Chapter 14 of Noise and Vibration Control, edited by Leo L. Beranek, McGraw-Hill Book Company, New York (1971)
10. Damping of Plate Flexural Vibrations by Means of Viscoelastic Laminae," D. Ross, E. E. Ungar, and E. M. Kerwin, Jr., in Structural Damping, edited by J. E. Vuzicka, American Society of Mechanical Engineers, New York (1959)
11. "Loss Factors of Viscoelastically Damped Beam Structures," Eric E. Ungar, J. Acous. Soc. Am., 34, No. 8 (August 1962)
12. "Use of the Complex Shear Stiffness of a Viscolastic Liquid to Illustrate the Origins of Structural Damping," R. A. Ely, 92nd Meeting of the Acoustical Society of America, San Diego, California (November 1976)
13. Mechanics, John C. Slater and Nathaniel H. Frank, McGraw-Hill Book Company, Inc., New York (1947)

REFERENCES (Cont.)

14. "Effect of Damping on the Natural Frequencies of Linear Dynamic Systems," T. K. Caughey and M. E. J. O'Kelly, J. Acoust. Soc. Am., 33, No. 11 (November 1961)
15. "Non-Linear Response of a Simple Clamped Panel," P. W. Smith, Jr., C. I. Malme, and C. M. Gogos, J. Acoust. Soc. Am. 33, No. 11 (November 1961)
16. "The Damping of Stiffened Plate Structures," Denys J. Mead, in Acoustical Fatigue in Aerospace Structures, Proceedings of the Second International Conference, edited by Walter J. Trapp and Donald M. Forney, Jr., Syracuse University Press, Syracuse, New York (1965)
17. "Excitation, Response, and Fatigue Life Estimation Methods for the Structural Design of Externally Blown Flaps," Eric E. Ungar, K. L. Chandiramani, and J. E. Barger, NASA CR-112216 (October 1972)
18. "Experimental Methods in Acoustical Fatigue," Alan P. Berens and Blaine S. West, AFFDL-TR-71-113 (March 1972)
19. "Cumulative Damage in Fatigue," M. A. Miner, J. Appl. Mech., 12 (September 1945)
20. "The Role of Similitude in Fatigue and Fatigue Crack Growth Analyses," B. N. Leis and D. Brock, Shock and Vibration Digest, 13, No. 7 (July 1981)
21. "Stresses in Skin Panels Subjected to Random Acoustic Loading," Brian L. Clarkson, AFML-TR-67-199, Air Force Materials Laboratory (June 1967)
22. "An Experimental Study of the Response of Simple Panels to Intense Acoustical Loading," L. W. Lassiter, R. W. Hess, and H. H. Hubbard, J. Aero. Sciences, 24 (1957)
23. "Calculated and Measured Stresses in Simple Acoustic Panels Subject to Intense Random Acoustic Loading Including the Near Field Noise Field of a Turbojet Engine," L. W. Lassiter and H. H. Hubbard, NACA TN4076 (1957)
24. "Interaction of Sound Waves with Solid Structure," Istvan L. Ver and Curtis I. Holmer, in Noise and Vibration Control, edited by Leo L. Beranek, McGraw-Hill Book Company, New York (1971)

BEAM DAMPERS FOR SKIN VIBRATION AND NOISE REDUCTION IN THE 747

R. N. Miles
The Boeing Company
P. O. Box 3707
Seattle, Washington 98124

BEAM DAMPERS FOR SKIN VIBRATION AND NOISE REDUCTION IN THE 747

R. N. Miles
The Boeing Company
P.O. Box 3707
Seattle, Washington 98124

ABSTRACT

A special constrained layer damper has been incorporated into the Boeing 747 upper deck fuselage structure. This damper replaces a rivetted stiffener which was installed to reduce noise levels inside the cabin. It has been found that the damper installation produced a noise reduction equal to that achieved by the stiffener and resulted in an \$8000 per airplane cost savings and a 130 pound per airplane weight savings. A brief review is presented of the analysis and test that led to this design.

I. INTRODUCTION

In most commercial aircraft, structural vibration of the fuselage sidewall caused by the turbulent boundary layer is the main cause of noise in the passenger cabin. Methods of reducing the cabin noise include blocking the sound by adding fiberglass insulation or mass to the interior panels, or reducing the vibration of the structure by adding stiffeners to the airplane skin or increasing the damping of the structure. In this paper a program is described in which a skin panel stiffener installation for reducing cabin noise was replaced by a novel constrained layer damper design in the 747 upper deck. The damper produced cabin noise levels that are equivalent to those of the stiffener and resulted in an \$8000 per airplane cost savings and a 130 pound per airplane weight savings.

The development effort that led to this design began with a careful study of the vibration characteristics of the 747 upper deck fuselage structure. Structural mode shapes were measured to determine the resonant modes that were the primary cause of the cabin noise in the frequency region of interest. Since conventional constrained layer dampers such as sound damping tape did not sufficiently damp the important modes, a new damper was developed ¹ which proved to be extremely effective. This "beam damper" concept utilizes thickness deformation in the damping adhesive instead of shear deformation as in conventional designs. Since this light-weight damper is bonded to the skin with a pressure sensitive adhesive it is considerably easier to install than the rivetted stiffeners and a substantial manufacturing cost savings was achieved. Flight test results showed that the beam dampers achieved cabin noise reductions that are equal to those of the stiffener installation.

II. ORIGINAL STIFFENER INSTALLATION FOR NOISE CONTROL IN 747 UPPER DECK

Cabin sound levels obtained in flight in a 747 upper deck without any special sound proofing concepts are shown in figure 1. Also shown in the figure are the sound levels obtained when the skin of the upper deck structure is treated with two layers of 3M Y436 Sound Damping Tape. The figure shows that while the damping tape achieved significant reductions at high frequencies the peak in the spectrum in the 300 - 600 Hz common octave band was not significantly affected.

In order to reduce the noise in this frequency region, stiffeners were added to the structural design as shown in Figure 2. These stiffeners reduced the vibration of the low order skin panel modes which were predicted to be the major cause of the noise between 200 and 700 Hz. As shown in the figure, the stiffeners consisted of hat sections rivetted to each skin panel parallel to the stringers. The addition of these stiffeners produced a noise reduction of approximately 4 dB in the 300 -600 Hz octave band.

Though this noise reduction yielded an acceptable noise environment in the upper deck, the stiffener and damping tape installation caused a 220 pound weight penalty and was extremely time consuming to install. A program was then initiated to develop a constrained layer damper that could achieve the same noise reductions as the stiffener with less cost and weight.

III. BEAM DAMPER DEVELOPMENT PROGRAM

The first task in the damper development program was to obtain measured data that showed which mode needed to be damped. To accomplish this, mode shapes were measured on the upper deck fuselage structure in flight and cabin sound levels were measured to determine which modes contribute to the cabin noise.

The measured mode shapes are shown in Figure 3 along with skin panel vibration spectra. It was found that three modes dominate the response in the 300 - 600 Hz frequency range. The solid curve of the skin panel acceleration was obtained when the skin panel was exposed to the cabin with no fiberglass insulation or trim panel in place. The dashed curve shows the effect of replacing the fiberglass insulation over the skin. In this case the damping in the first two modes has been increased substantially. Note that the fiberglass is installed such that there is a 1.25 inch airgap separating it from the skin panel. For the two lowest modes there is a strong coupling between the skin and the fiberglass through the airgap.

The third mode shown in the figure is not significantly damped by the fiberglass. This mode consists of three half waves between the frames and one-half wave between the stringers. Since the two lower modes have substantial damping when the fiberglass insulation is in place it would be very difficult to achieve further vibration reduction of these modes by increasing the damping.

Figure 4 shows the effect of adding two layers of 3M Y436 Sound Damping Tape to the skin panels. In this case the modes above 700 Hz are heavily damped but the vibration of the first three modes is not reduced significantly more than it was by the fiberglass insulation. Since neither the fiberglass or the damping tape achieved significant reductions for the third mode it was felt that to reduce the vibration and noise in this frequency range a damper could be developed for the third mode.

Since the relation between vibration response and noise radiation is rather complicated for a periodic skin/stringer/frame structure that is excited by a turbulent boundary layer, cabin sound pressures were measured to ensure that the third mode contributes to the cabin noise. Figure 5 shows a comparison of the sound spectrum with the spectrum of the skin panel vibration. This figure shows that the three modes below 700 Hz contribute to the cabin sound levels.

Damper Design

Having determined that the first three modes were the most important and that the mode with three half waves between the frames was a very important one to damp, the next task consisted of selecting the appropriate damper. To select the damper we conducted an analytical study, laboratory tests, and manufacturing and durability studies.

Conventional constrained layer dampers work by creating shear deformation in the adhesive when the structure bends. Unfortunately at low order modes when there isn't much curvature there is very little shear and hence very little damping in damping tape treatments. To overcome this, spacers have been suggested such as shown in Figure 6. This spacer is designed to have infinite shear stiffness and no bending stiffness.

Rather than build a spacer as shown in Figure 6, a constraining layer could be used that is stiff in bending such as a very light I section. In this case if the adhesive is thick enough and flexible enough the constraining layer will cause thickness deformation in the adhesive along with shear. As can be seen from Figure 7 if the I beam is continuous over three half waves as in our third mode the constraining layer will have substantial "leverage" on the adhesive. The damper could be expected to be very effective on this mode.

To investigate the performance of this "beam" damper, laboratory tests were conducted on a skin/stringer/frame test panel as shown in Figure 8. Experimental modal analysis was performed on this panel to ensure that it responded with the same mode as observed on the airplane. Figure 9 shows the mode shape of the 3-1 mode, the third mode observed in flight as measured on test panel. Note that since the test panel was not subjected to tensile pressurization loads this mode occurred at 441 Hz rather than at approximately 600 Hz as on the airplane in flight.

With this simple laboratory test panel a very large number of configurations of the beam damper could be tested with minimal cost. The vibration of the panel with various treatments applied was measured with accelerometers and the panel was excited either with a light weight instrumented hammer or with a sound field.

Based on these laboratory tests, it was felt that the configuration shown in Figure 10 would have a good chance of achieving vibration and noise reductions equivalent to those of the stiffener. This configuration consists of a single layer of 3MY436 Sound Damping Tape and two I sections bonded with 3MISD113 adhesive parallel to the stringers. The I beams are made of .02 gage Kevlar. This installation weights a fraction of the weight of the stiffener and is extremely easy to install.

Since one of the major motives in this program was manufacturing cost savings, the manufacturing organization was consulted to ensure that the

damper would not be prohibitively difficult to build. Because of the substantial cost savings potential of replacing the stiffeners, manufacturing personnel enthusiastically responded with test parts made out of aluminum, fiberglass, Kevlar, graphite, extruded thermoplastics, nomex honeycomb, aluminum honeycomb and rigid foams. This coordination with manufacturing people proved to be very valuable in this program.

Laboratory tests were also conducted to study the durability of the installation shown in Figure 10 in the environment of the airplane skin. Since the major concern was reduction in adhesion due to moisture, test panels with the dampers applied were exposed to condensing humidity at 160°F for two weeks and to continuous water submersion for two weeks. As a result of these tests it was found that the dampers with 3M ISD 113 adhesive are not significantly affected by moisture.

Flight Test Verification

Once a configuration was considered acceptable based on laboratory tests, a flight test program was conducted to measure the effectiveness on the airplane. Figure 11 shows the skin panel vibration in flight when the dampers are installed as in Figure 10. The figure shows that the vibration level of the third mode is reduced by more than 10 dB. This is considerably more reduction than obtained by a conventional damping tape installation.

Figure 12 shows the cabin sound levels measured in flight with the beam dampers installed. The figure shows that the dampers achieved sound level reductions that are equivalent to those of the stiffener.

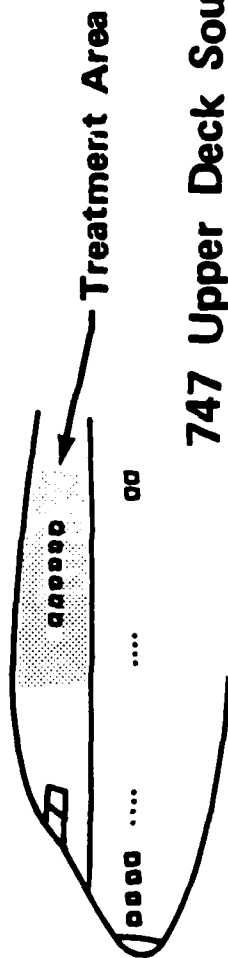
IV. CONCLUSIONS

As a result of these efforts the beam damper configuration shown in Figure 10 has replaced the stiffeners shown in Figure 2 in the 747 upper deck. The stiffener installation weighed 220 pounds and the beam damper installation weighs 90 pounds, giving a 130 pound weight savings. Also, because of the substantial reduction in installation time the damper resulted in an \$8000 per airplane cost savings.

REFERENCE

- (1) United States Patent 4,425,980, "Beam Dampers for Damping the Vibrations of the skin of Reinforced Structures," January 17, 1984, R. N. Miles.

Damping Tape Installation - 747 Upper Deck



747 Upper Deck Sound Levels
.84 Mach, 35,000 ft

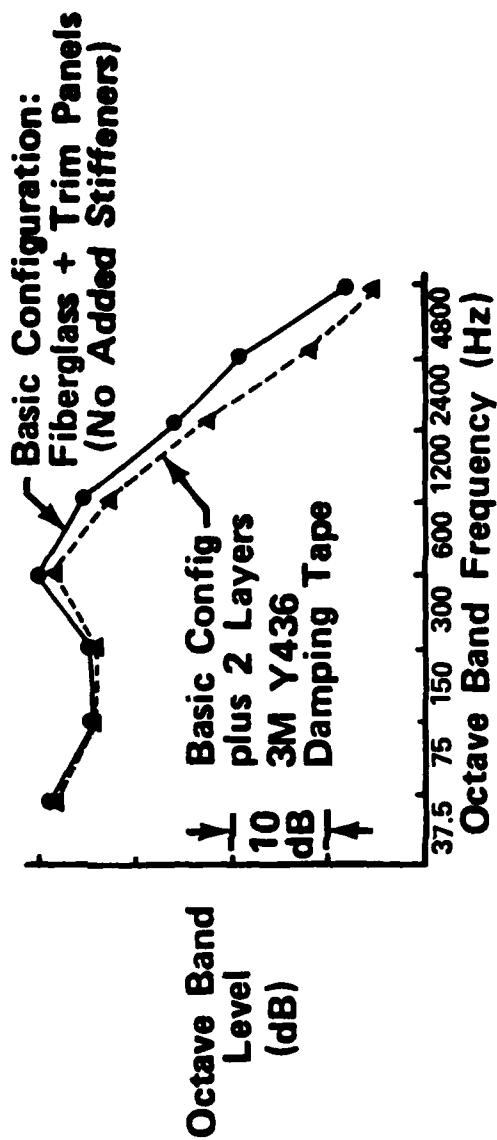
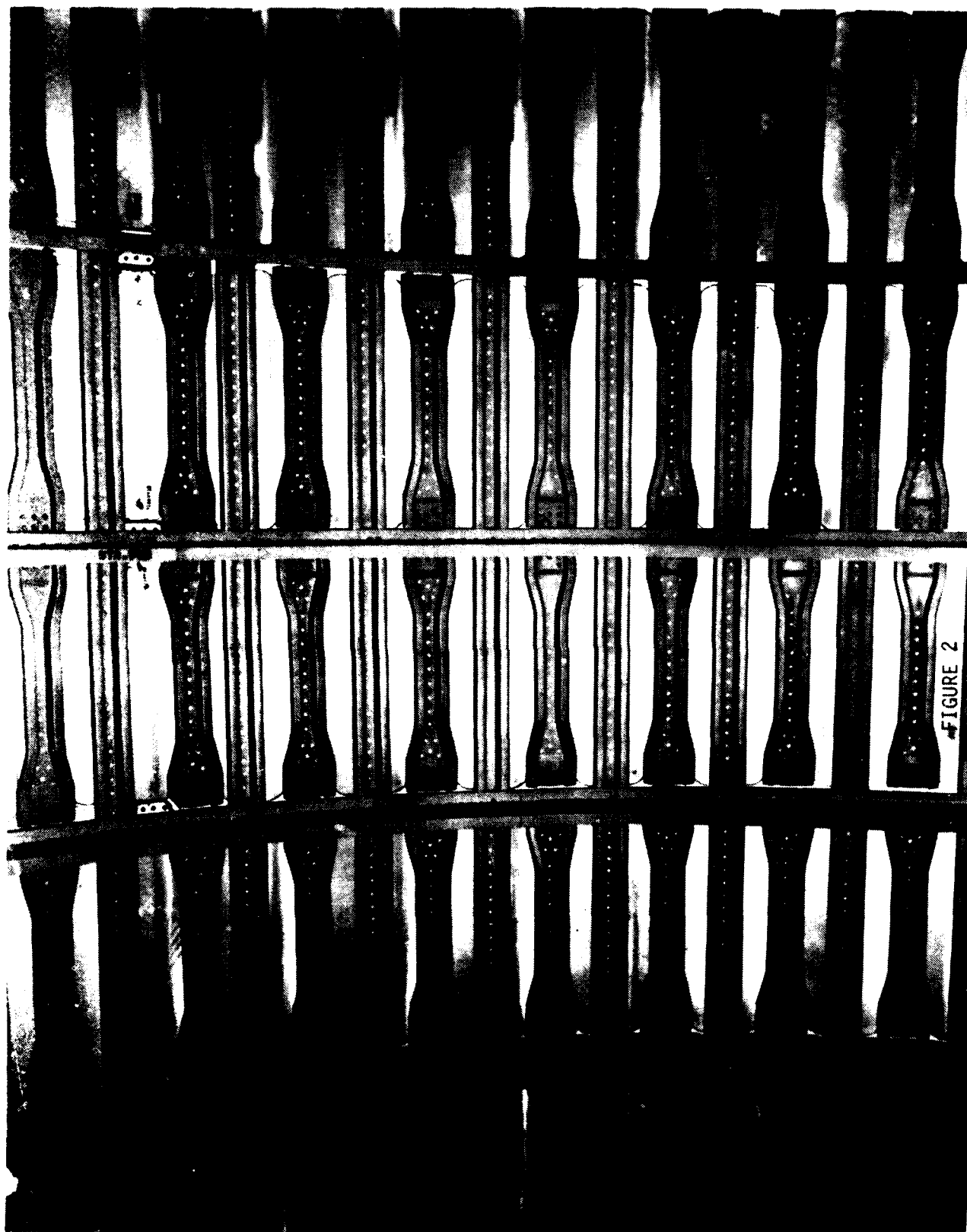


FIGURE 1



Flight Test Vibration Data 747 Upper Deck

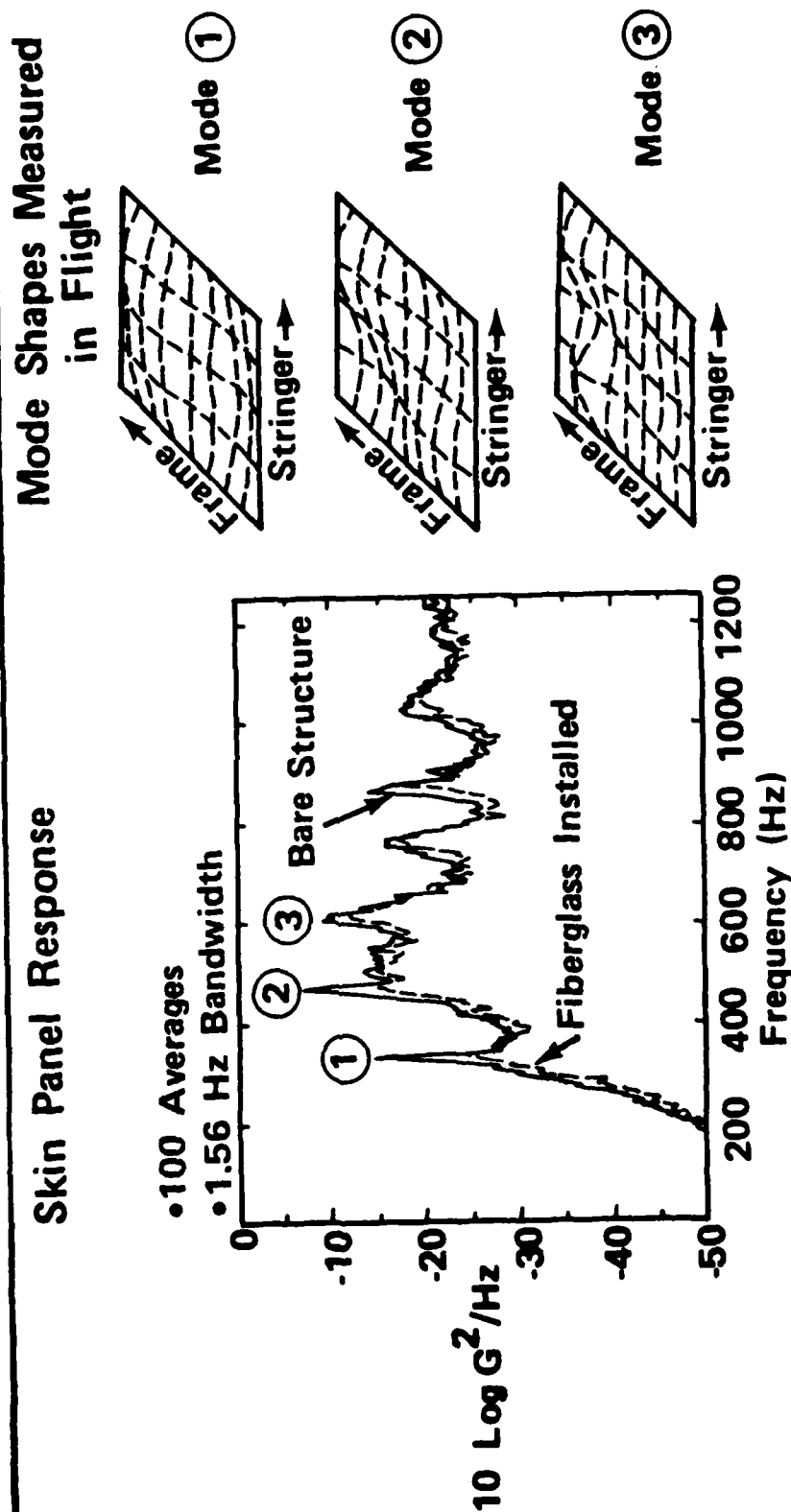


FIGURE 3

Flight Test Vibration Data 747 Upper Deck

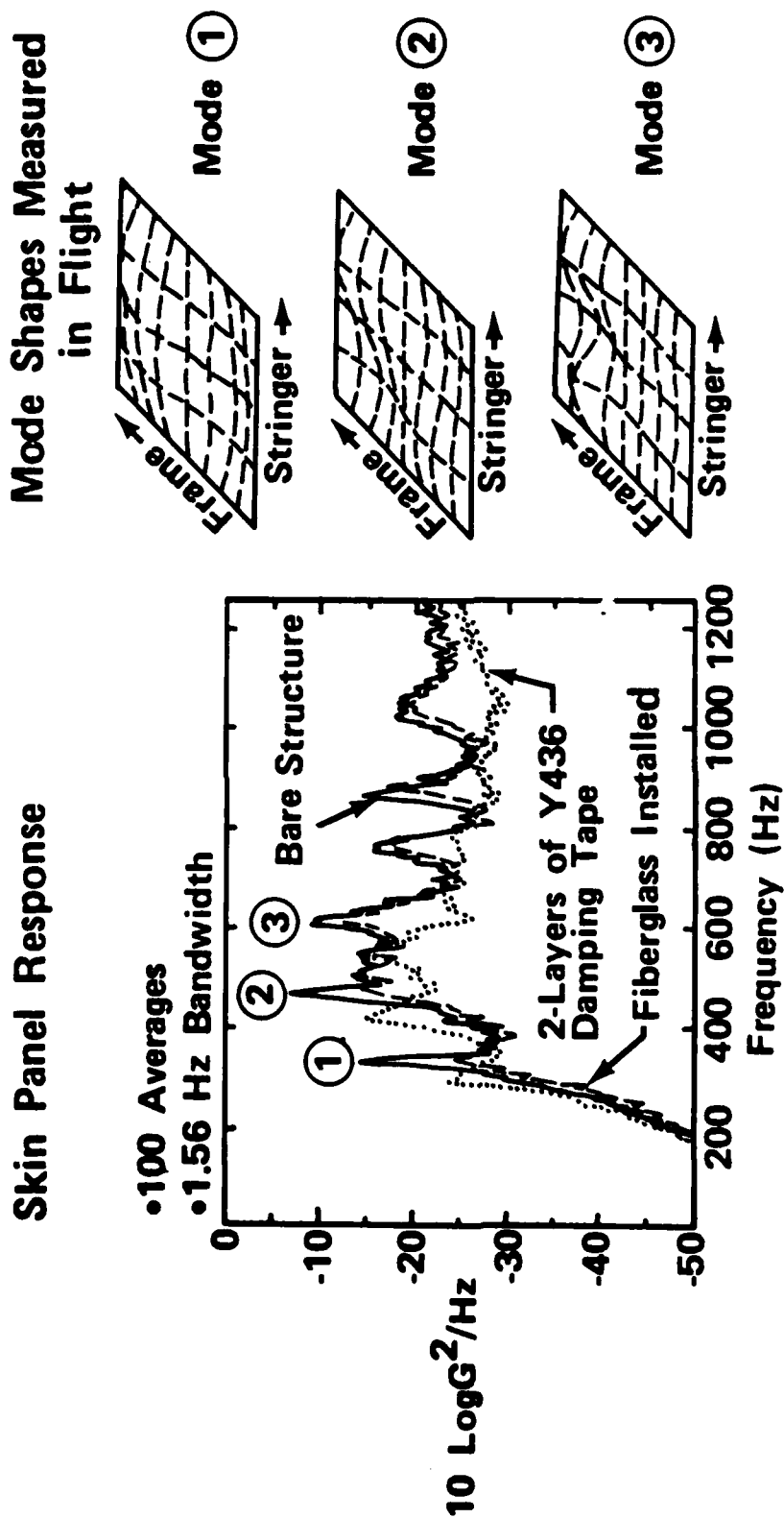


FIGURE 4

Comparison of Skin Panel Response and Cabin Sound Pressure

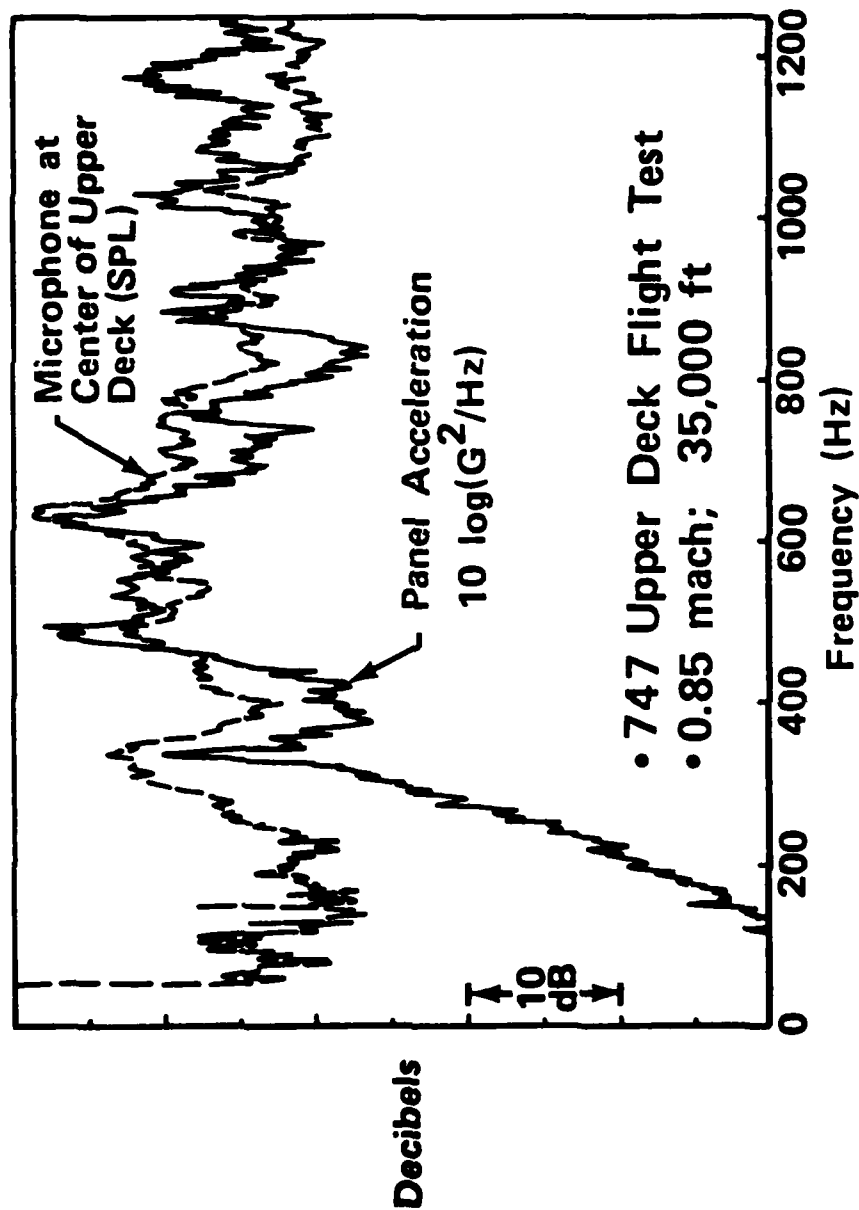


FIGURE 5

Shear Deformation In Conventional Constrained Layer Dampers

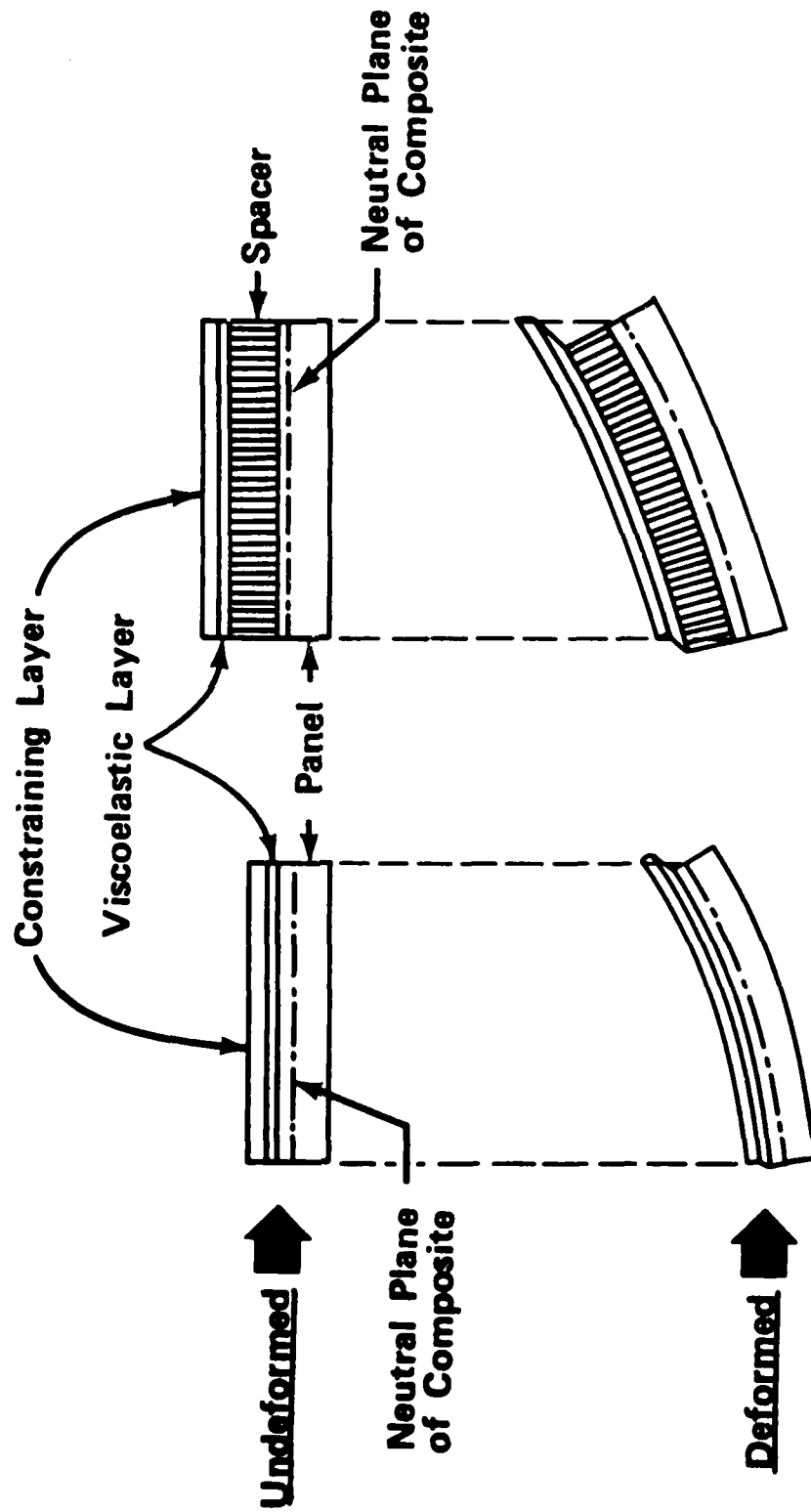


FIGURE 6

Thickness Deformation in Stiff Constrained Layer Dampers

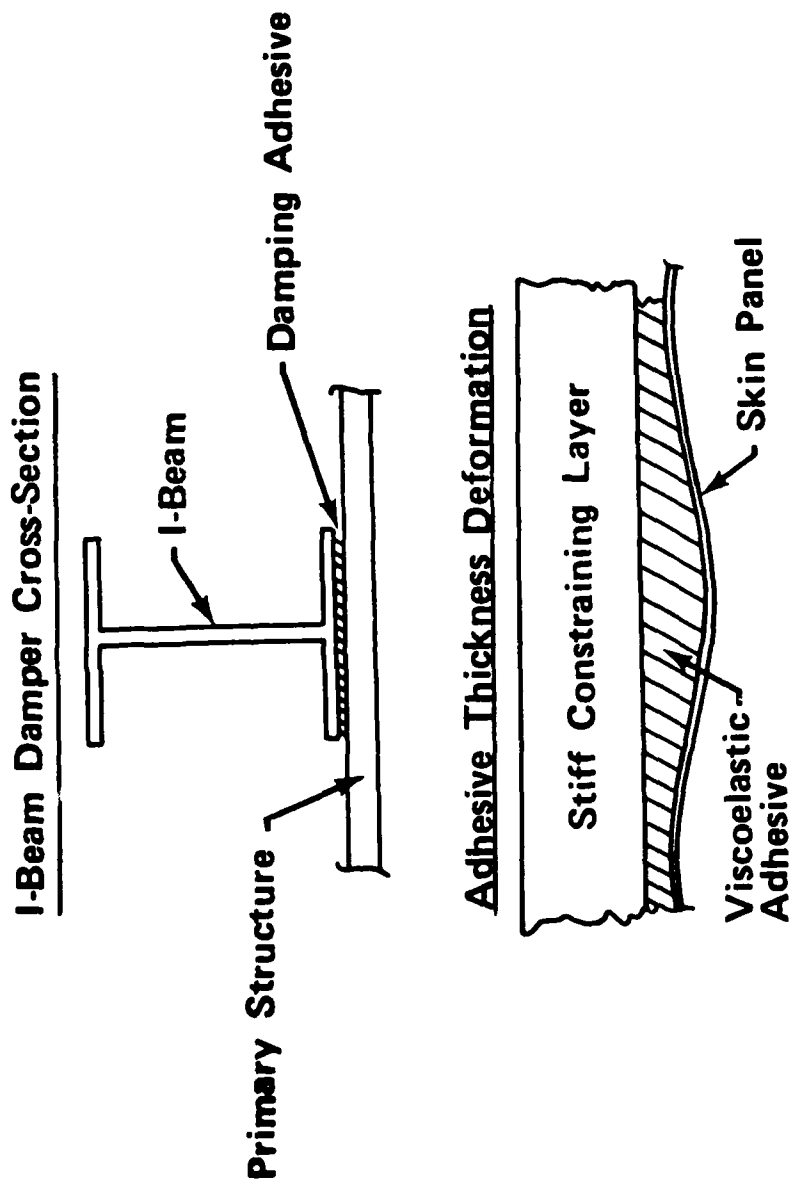


FIGURE 7



FIGURE 8

Measured Mode Shape in a Laboratory Test Panel

441 Hertz

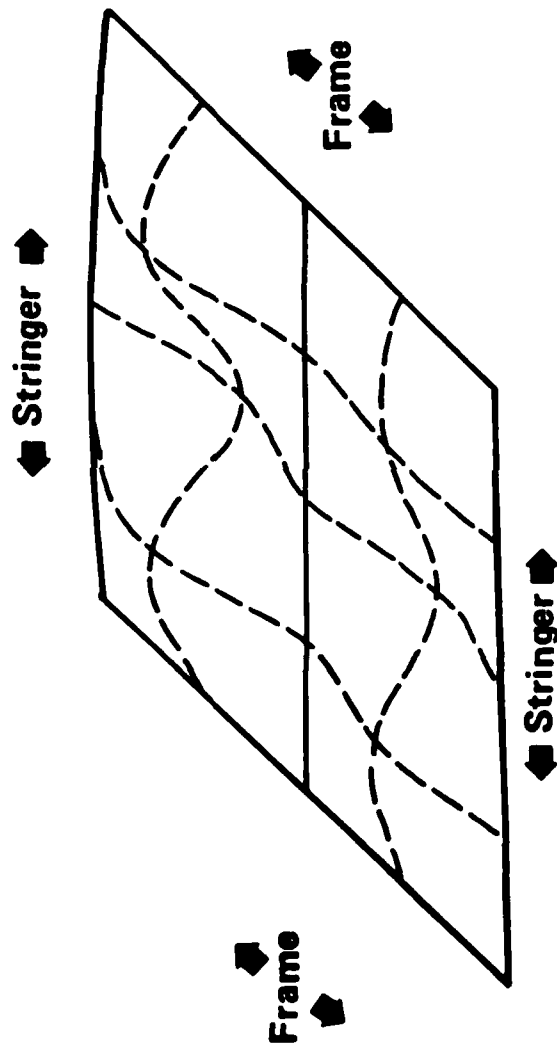
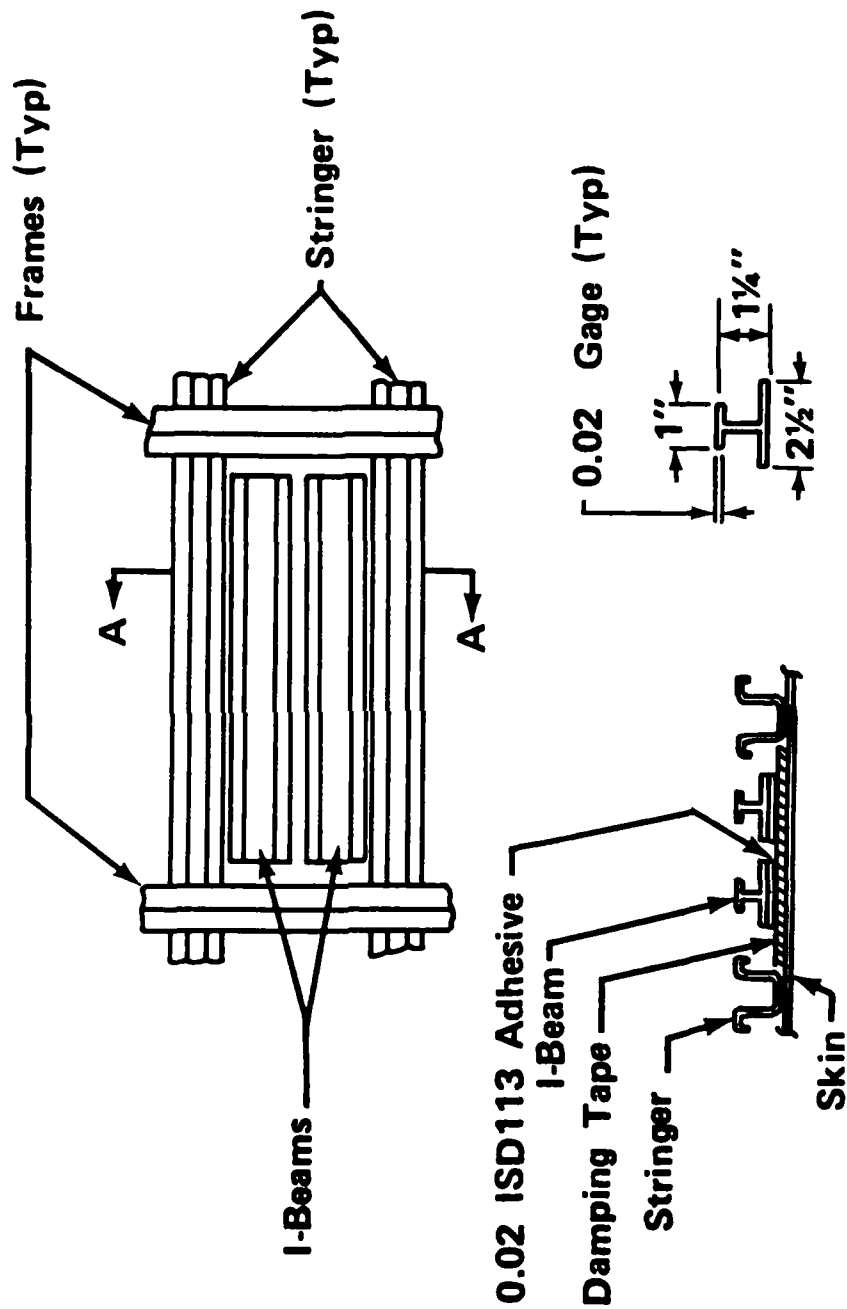


FIGURE 9

747 I-Beam Damper Installation



Section A-A
(Rotated 90° CW)
■ Up

I-Beam Section
(Kevlar)

FIGURE 10

I-Beam Damper Program

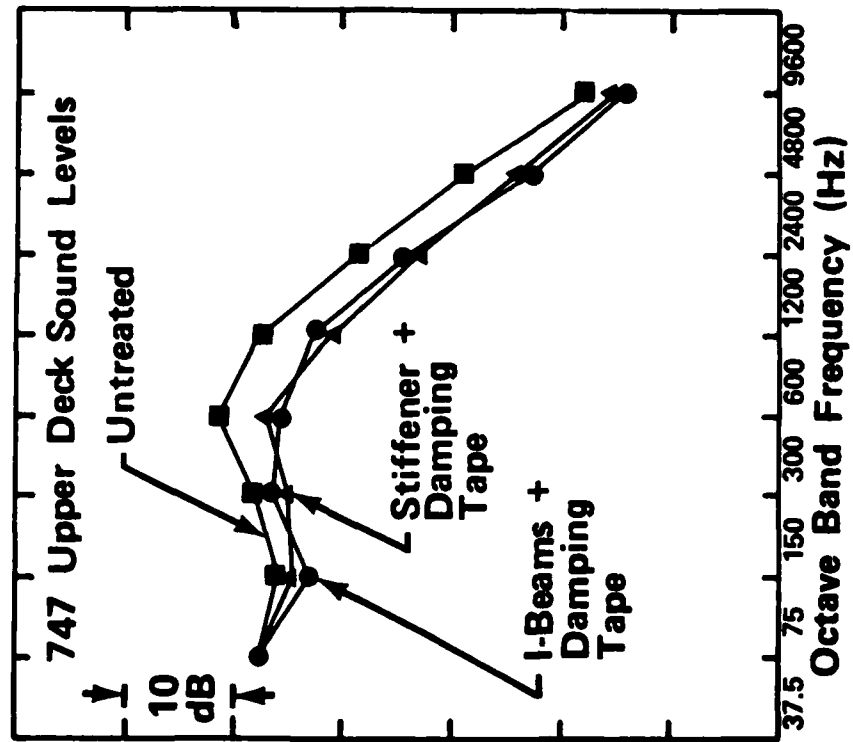


FIGURE 12

INTEGRATED DAMPED FUSELAGE STRUCTURE

Dr. L. M. Butzel
Boeing Military Airplane Company
Seattle, Washington 98124

SUMMARY OF PRESENTATION ON "INTEGRATED DAMPED FUSELAGE STRUCTURE"

Overviews

This presentation (23 slides) describes a program, largely funded under U.S. Air Force Contract F33615-79-C-3206, aimed at developing design guidelines for viscoelastic damping applied to skin-stringer-frame type aerospace structure. Periodic structure type response models developed as a first part of the program are discussed. Two procedures for assigning values of the damping parameters required in these models are presented. Results of test efforts to develop and verify the damping parameter assignment procedure and response prediction models are also discussed. The current status of these efforts is:

- Response models are yielding predictions in agreement with test results.
- The damping parameter assignment procedures are working, but more work is needed to bring them up to the confidence level of the response models.

Comments on Figures:

The organization and extent of the reference contract are indicated in Figure 1. Response prediction models developed in Phase I are (once validated in Phase II and in part in Phase IV) to support trade studies aimed at developing design charts and design guidelines (per Phase V).

Phase III has in large part been aimed at characterizing damped structural arrangements/damping treatments in terms of input parameters of the Phase I models. In particular, these include loss factors of characteristic (fuselage) structural elements used in these models as, skin, stringers (or longerons) and frames.

Phase IV has also been spent in part evaluating (via tests) loss factors, etc., associated with various damping treatments proposed in Phase III.

Figure 2 illustrates the type of structure of interest in this investigation. The very regular, periodic sense of the structure led us to apply so called "periodic structure" methods to analyzing it with regard to predicting its response behavior. Response quantities of interest were structure vibration, dynamic stress, and structure radiated acoustic intensity. These were desired for space (and time) random excitations as aerodynamic turbulent boundary layer (TBL), near field jet noise, and diffuse acoustic noise.

Desired and actual idealizations of the structure of Figure 2 are shown in Figure 3. The idealization used (b) neglects highly complicating curvature effects. This tends to limit resulting predictions to frequencies above the ring frequency.

The basic solution approach uses a series format in which the spatial functions are referred to as "Space Harmonics," following the work of Mead and Pujara (Fig. 4). The series can also be interpreted as a modulated complex Fourier series in which the modulating function is the excitation travelling wave. The coefficients of the series solution format are determined using the method of "Virtual Work," as implemented by Pujara and Mead. This implementation requires a knowledge of the differential equations of motion of the skin element, of the stiffener elements, and of the compatibility relations amongst the elements. Structural parameters appearing in the solution are hence those appearing in the various differential equations of motion.

The basic solution approach gives deterministic response to a single travelling wave characterized by a wave vector with components (k_x, k_s) . The power spectrum of response, S_w , to a space (and time) random excitation is evaluated through an integration of the basic solution over all wave vector space. The weighting function in the integral is the wave vector distribution function, f , describing the space random nature of excitation field. The time random part is characterized by the pressure auto power spectrum, S_p .

Related basic responses (acceleration, stresses and intensity) are indicated in Figure 5. Their spectra re a random field are obtained by the same type of infinite integration as for displacement. The acoustic radition law is that for radiation into a semi-infinite half-space.

A computer program incorporating the space harmonic and wave vector inegration approach has been developed. At present, it predicts only radiated acoustic intensity. Efforts to check the prediction are suggested on Figure 6. Data from two test efforts has been applied.

- A reverberant-reverberant room test of a large four-frame bay by nine stringer bay panel (approximately 80" x 81" in extent).
- A cruise flight test of a Boeing 727 jet transport with all the interior sound insulating system removed.

Agreement has been on the order of +3 dB. More validation is in progress.

A simplified version of the just-described general model has also been developed. Their relationship is indicated in Figure 7. The specialized model is simpler to understand (in principle) and also is more appropriate to predicting responses of test panels built as part of our contract effort.

The nature of the specialized model is suggested in Figure 8. The x-direction is the cross panel (parallel to periodic stiffeners axes) direction. The acoustic radiation law used is that for radiation into a hardwall slot.

Structural parameters required in the above models are suggested in Figure 9. These support a detail of skin-stringer-frame structure as:

- The skin element as a uniform thin plate of specified thickness, length and breadth, and with uniform material properties as one Young's modulus, one loss factor and one density.

- The one or two stiffener elements each as a line element characterized by a single set of cross section geometric properties, and with material properties as one Young's modulus and associated loss factor, one shear modulus and associated loss factor, and one shear modulus and associated loss factor, and one density.

This complexity generally does not support a dynamic description of most of the damping treatments we do deal with. However, the range of used (or anticipated) treatments is sufficient that a model incorporating a minimal complexity covering the range appears beyond the scope of the current effort. Instead we have opted to delineate strategies--separate from the response models--allowing us to "assign" parameter values to use in the response models which "capture" the nature of a specific damping treatment or treatment concept. This viewpoint is suggested (with regard to loss factors) in Figure 10.

One hardware realization of the viewpoint is the "coupon" of Figure 11(a). It is viewed as a representative segment out of the structure of Figure 11(b). That is, loss factors, as example, evaluated for a damped coupon, can be used in (one of) the response models to estimate the effect of the same damping arrangement on the response of the structure of Figure 11(b).

Two approaches to evaluating element composite loss factors have been tried (Fig. 12). The first uses measured data from an impact excited coupon. This is processed through a "strain energy" type model of the coupon in which loss factors of skin and stringer elements are the unknowns. Effectively, values of loss factors are selected which give in some sense a best agreement between measured and predicted coupon responses.

The second approach used is a finite element model of coupon and damping treatment. The "model strain energy" approach of John and Keinholz was applied to yield element loss factor values. Figure 13 gives examples of finite element models created as part of the above effort.

Finite element model results have been mixed (Fig. 14). Up to 800 Hz the mode frequency/mode shape agreement between model and physical coupons have been quite good. However, predicted modal loss factors have been from 100% to 300% below measured modal loss factors. The cause is still unknown.

The strategy behind the test efforts conducted during the contract effort are suggested in Figure 15. In addition to validating the prediction model(s)/loss factor assessment approach, the test program was also aimed at ranking tested damping treatments with regard to assigned loss factors, and with regard to panel response effectiveness.

Figures 16 and 17 show a stringer strip damped coupon and correspondingly damped panel. In all some six coupons with up to five different damping treatments applied (or designed in) were impact tested. Four panels and all damping treatments were also tested under reverberant acoustic excitation. Figure 18 indicates the extent of acceleration and strain gage instrumentation applied to each panel. Panel acoustic radiation was measured using Boeing's "Portable Acoustic Wattmeter System," (PAWS).

Current results from the coupon "strain energy data processor" (shown in Fig. 15) are listed in Figure 19. Results are shown for three coupons:

- Coupon 101 has a .063" skin to which is bonded a (type 142) stringer.
- Coupon 201 has a .063" skin to which is riveted a (type 142) stringer.
- Coupon 102 has a .080" skin to which is bonded a (type 142) stringer.

Note that the processor evaluates Yong's moduli as well as loss factors of skin and stringer elements. We question the results for the stringer; we would anticipate modulus values similar to aluminum, loss factor values in the range of .01 to .20. This matter is still being pursued.

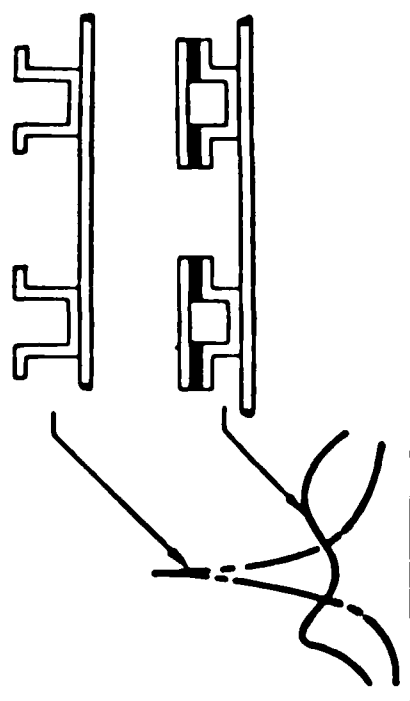
Figure 20 compares the measured and predicted (per specialized model) radiated acoustic intensity behavior of the panel 102--shown in Figure 18--except without the stringer damper strips installed. Figure 21 compares the measured and predicted effect of the stringer damper strips. Note that the measured curves have been raised 20 dB! The shaded-in areas indicate the effect of the stringer strip dampers. Our contention is that the predicted trends (and levels) quite closely follow the measured trends.

Figure 22 summarizes where we feel we are now. Overall, our response prediction models seem to be capturing well the trends we see in our test data. We still have some work to do to get good damping oriented input parameters. We have two approaches for getting these and some experience in applying them but more is needed. Although not discussed, we are starting work on elucidating design guidelines and method for effectively incorporating viscoelastic damping into fuselage (and aerospace) type skin-stringer-frame structure.

REFERENCES

L. M. Butzel, et al, "Reduction of Aerospace Structure Vibration Stress and Interior Noise Through the use of Integral Damping Techniques," AFWAL Technical Report (to be published), Contract No. F33615-79-C-3206, 1984.

INTEGRATED DAMPED FUSELAGE STRUCTURE

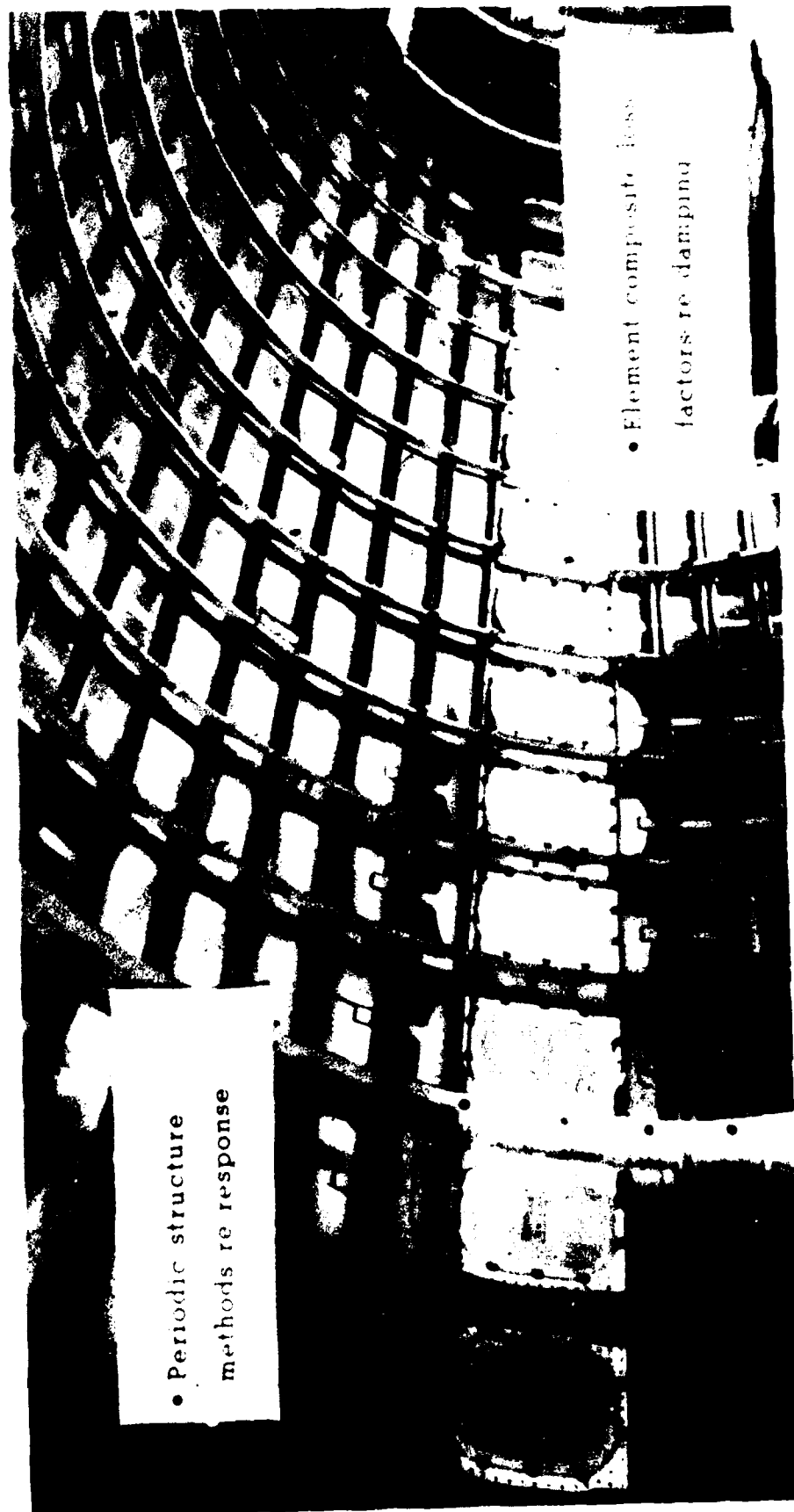


CONTRACT PHASES

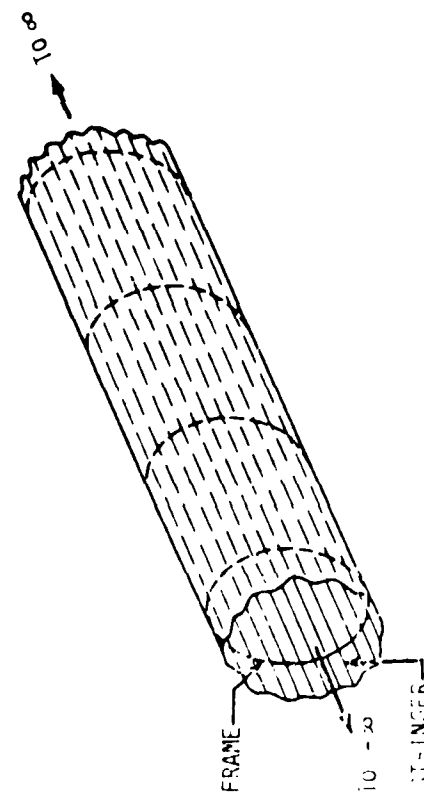
- I - DEVELOP PREDICTION METHODS
- II - CORRELATE WITH EXISTING TEST DATA
- III - FORMULATE / ANALYZE DAMPERS
- IV - TEST
- V - DEVELOP DESIGN METHODS

- CONTRACT F33615-79-C-3206
- \$425,000 EFFORT FOR AFWAL
- START = AUG., '79 . . . END = APR., '84

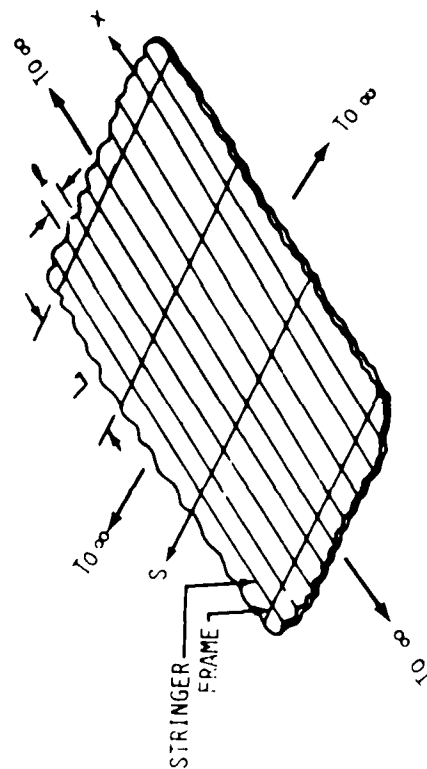
ANALYSIS APPROACH FOR SKIN-STRIDER-FRAME STRUCTURE



Skin-Stringer-Frame Structure Idealizations



(a) Basic Desired Idealization



(b) Actual Idealization (SH/VW Model)

BASIC SOLUTION APPROACH

- Determine response to single traveling wave

$$P_{exc} = e^{i\omega t} e^{-ik_x x} e^{-ik_y y}$$

- Use response format as

$$W = P_{exc} \cdot \left(\sum_{nm} A_{nm} e^{i2\pi m \frac{x}{L}} e^{i2\pi n \frac{y}{L}} \right)$$

- Evaluate A_{nm} 's using

- Virtual work method
 - Galerkin method
 - (Ritz method)
- Need DEQ's, Compat's

- Integrate to determine space random response

$$S_w(\omega) = S_p(\omega) \int_{k_y} \int_{k_x} |W|^2 \cdot f(k_x, k_y, \omega) dk_x dk_y \dots (!)$$

RELATED SOLUTIONS

- $\ddot{W} \longleftrightarrow S_{\ddot{W}}(\omega)$
- $\sigma_x, \sigma_s \longleftrightarrow S_{\sigma_x}(\omega), \dots$
- Radiated acoustic intensity (I) $\longleftrightarrow S_I(\omega)$

$$I = \frac{1}{2} \rho \omega^3 \sum_n \sum_m |A_{nm}|^2 \text{Real} \left\{ \frac{1}{K_{nm}} \right\}$$

$$K_{nm} = \sqrt{\left(\frac{\omega}{c}\right)^2 - \left(\frac{2\pi m}{L} - k_x\right)^2 - \left(\frac{2\pi n}{\ell} - k_s\right)^2}$$

- Different A_{nm} 's needed if acoustic insulation present . . . use transfer matrix techniques

VALIDATION EFFORTS ...

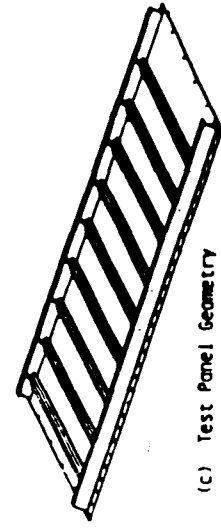
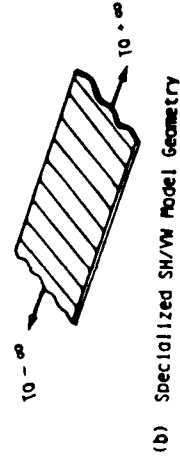
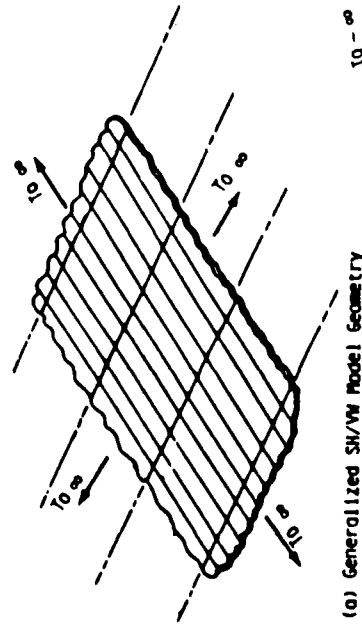
- Intensity checks

- "Reverberation room panel test . . . 4FB x 9SB

- 727 Flight Test . . . $M = .85$

- More in progress

Relation Between Generalized & Specialized SH/VW Models & Test Panels



SOLUTION APPROACH FOR SPECIALIZED SH/VW MODEL

- Essentially same as for generalized model
 - ... except ...
 - Different set of expansion functions in x-direction
 - Different acoustic radiation law used

PARAMETERS ... FOR MODELS

- Dimensions

- Element properties

- Geometric (section)

- Material "constants"

- .
 - :
 - .

- Element Composite Loss Factors

- .
 - :
 - .

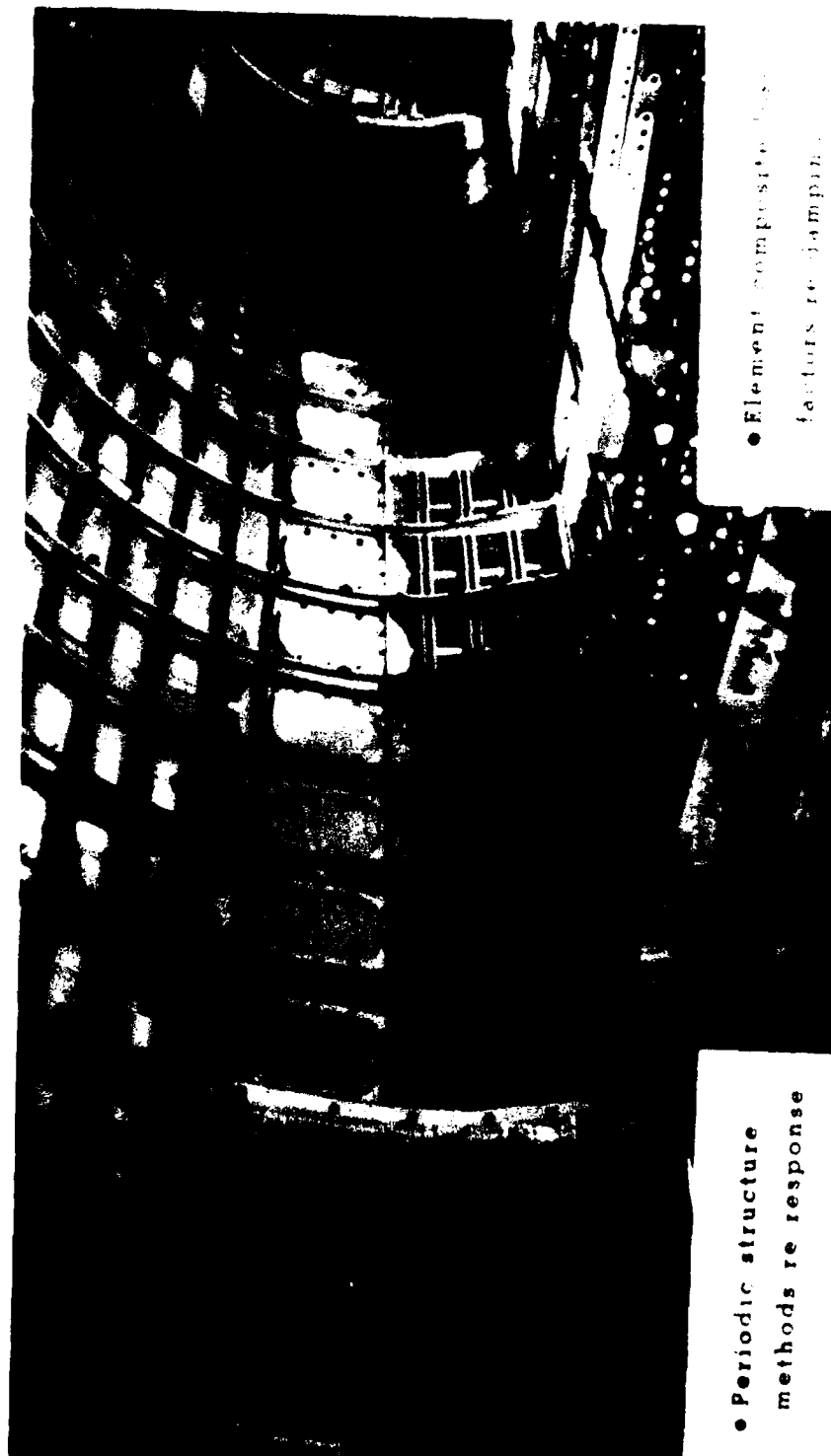
APPROACH

- Evaluate Loss Factors For
Simple Structure/Model . . . “Coupon”
- Use In Complex Models

"COUPON" ..IN SUPPORT FRAME



ANALYSIS APPROACH FOR SKIN-STRINGER-FRAME STRUCTURE



- Periodic structure
methods re response

- Element composite basis
factors re damping

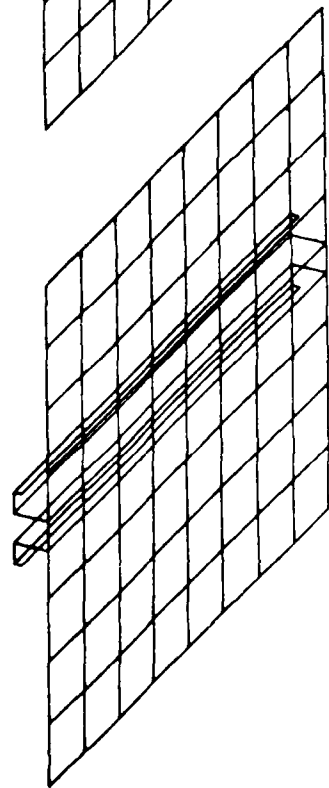
TWO APPROACHES BEING TRIED

(1) "Process" via "SE" approach using measured coupon data

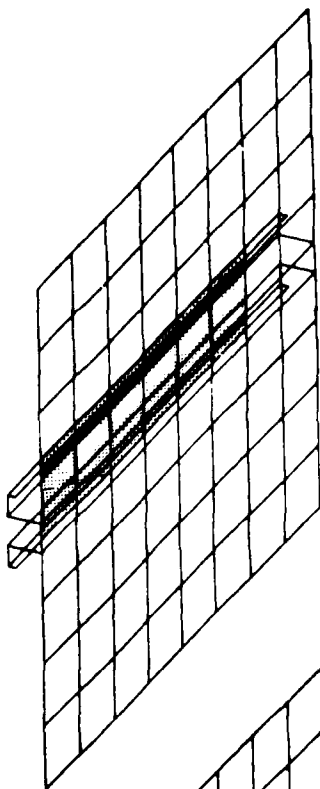
(2) "Predict" via "MSE" approach
using Finite Element Models

... Approach (1) requires analytic model of coupon

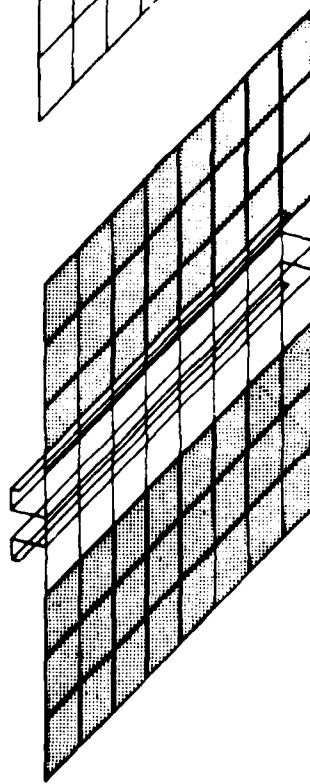
Coupon Finite Element Models



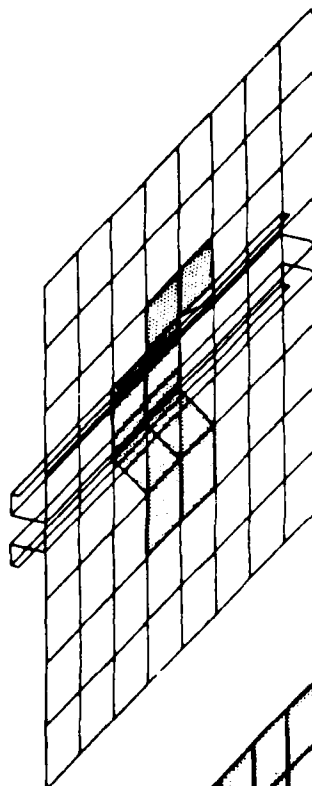
BARE



STRINGER DAMPER STRIP



SKIN DAMPING TAPE



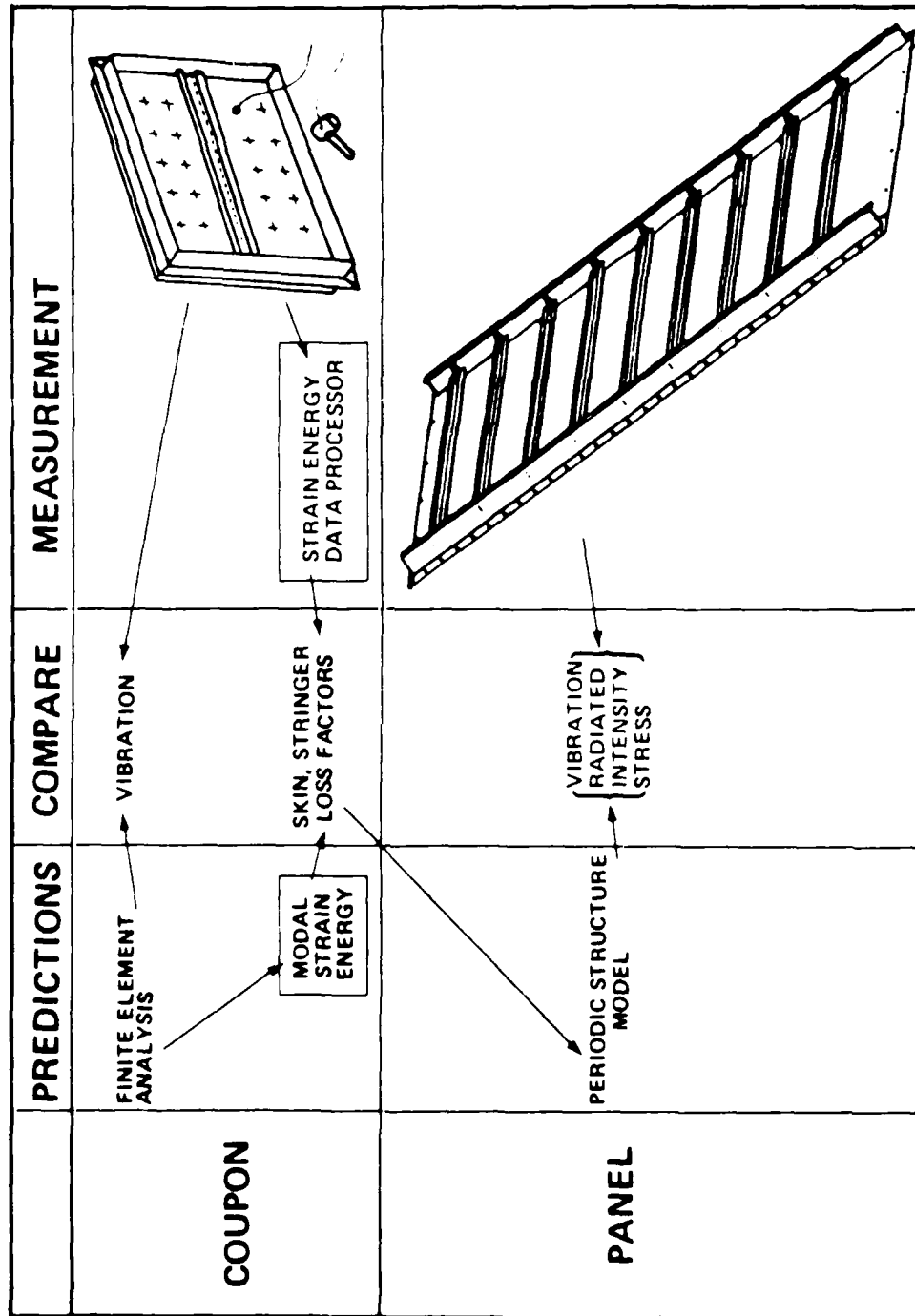
ACOUSTIC TILE

Finite Element Model Results

- Good mode shape/modal frequency agreement with tests
- Not so good modal loss factor agreement

... "Predicted" values less by 100-300%

TEST EFFORTS



AD-A152 547

VIBRATION DAMPING WORKSHOP PROCEEDINGS HELD AT LONG
BEACH CALIFORNIA ON 2. (U) AIR FORCE WRIGHT
AERONAUTICAL LABS WRIGHT-PATTERSON AFB OH L ROGERS

8/11

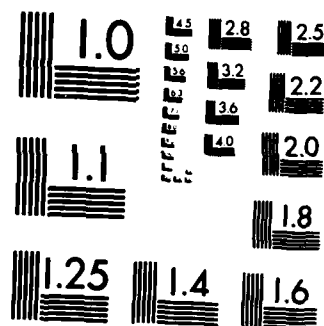
UNCLASSIFIED

11 NOV 84 AFMAL-TR-84-3064

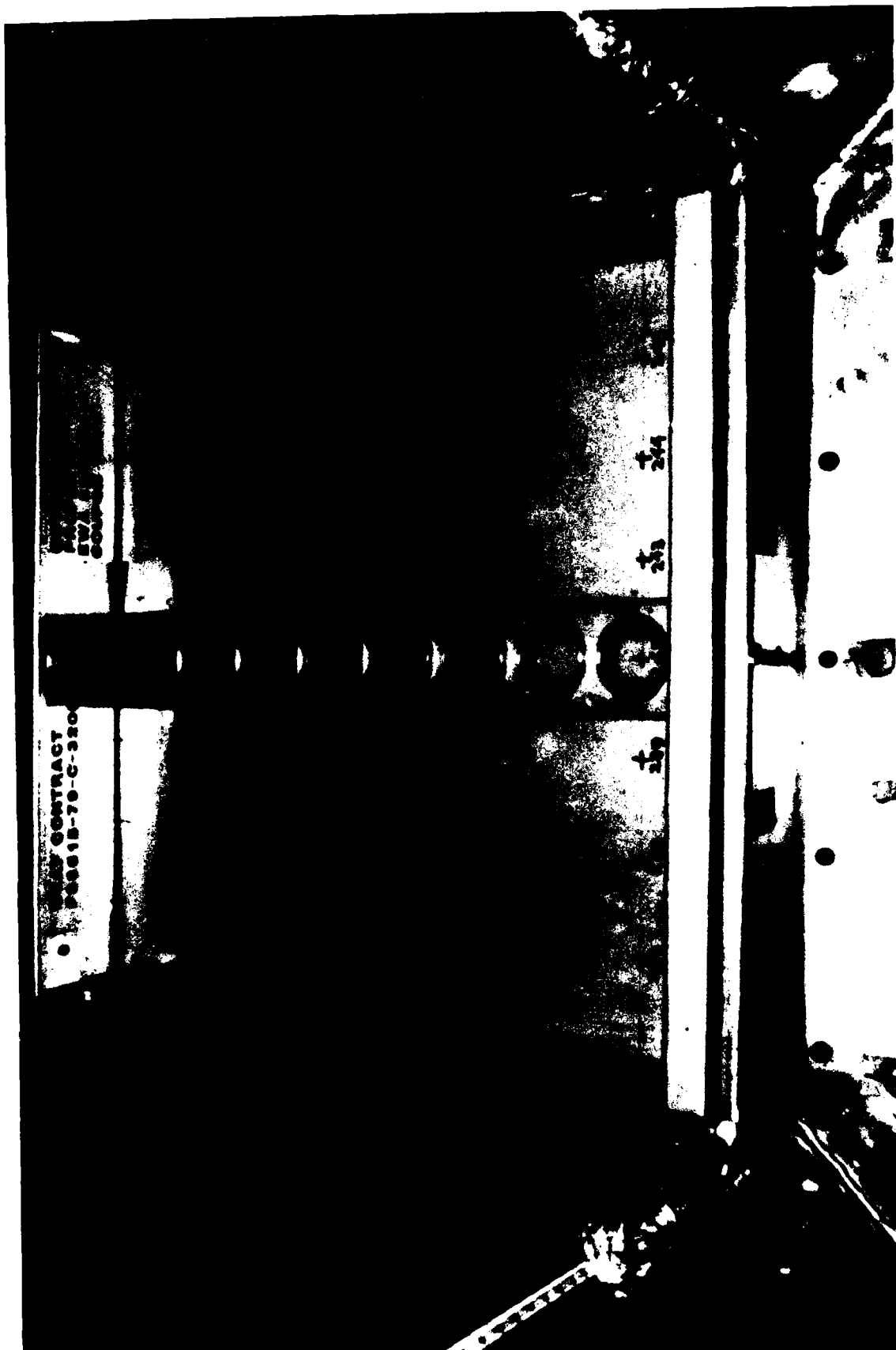
F/G 20/11

NL





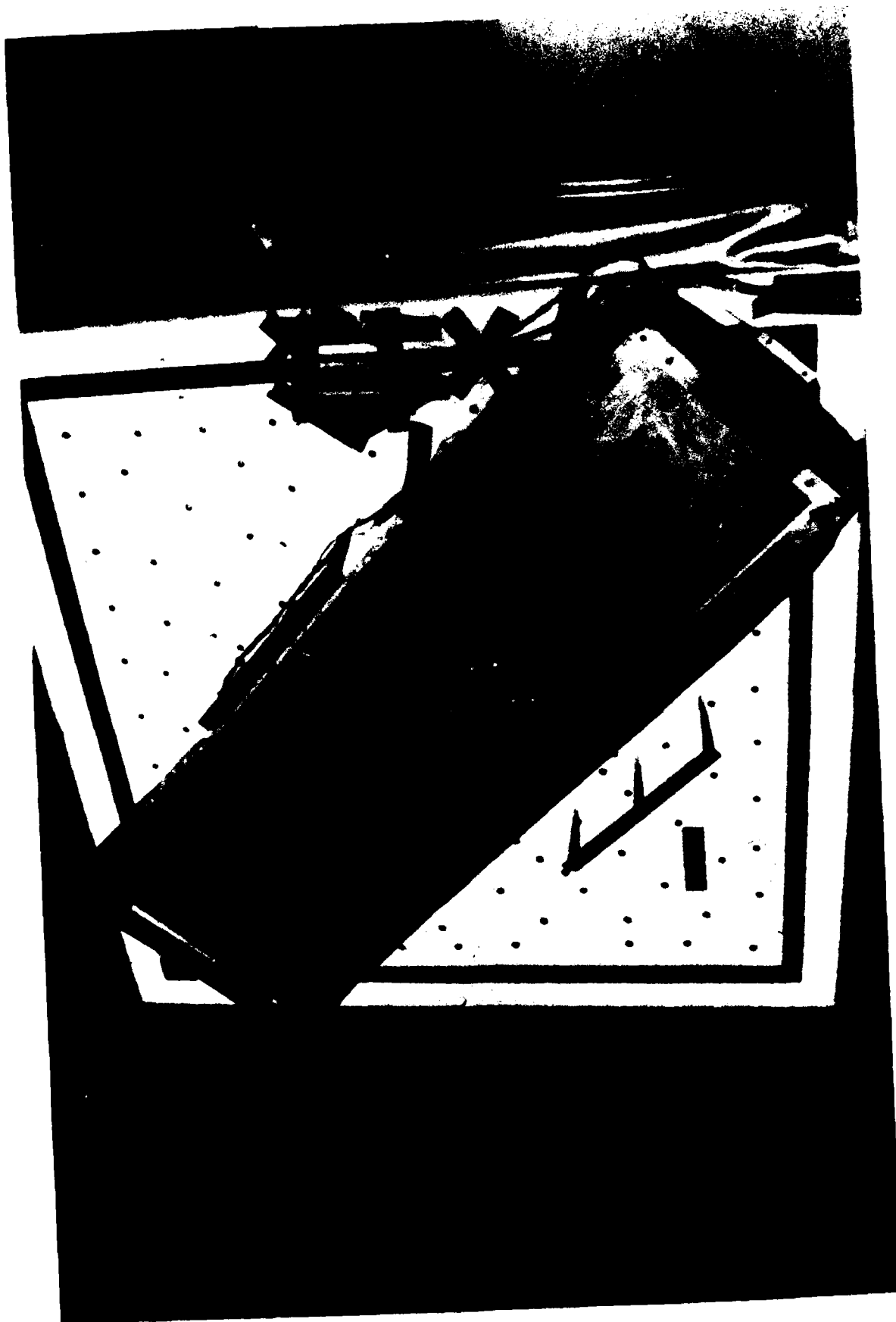
MICROCOPY RESOLUTION TEST CHART
NATIONAL BUREAU OF STANDARDS-1963-A



QQ-24



QQ-25



QQ-26

Current Strain Energy Processor Results

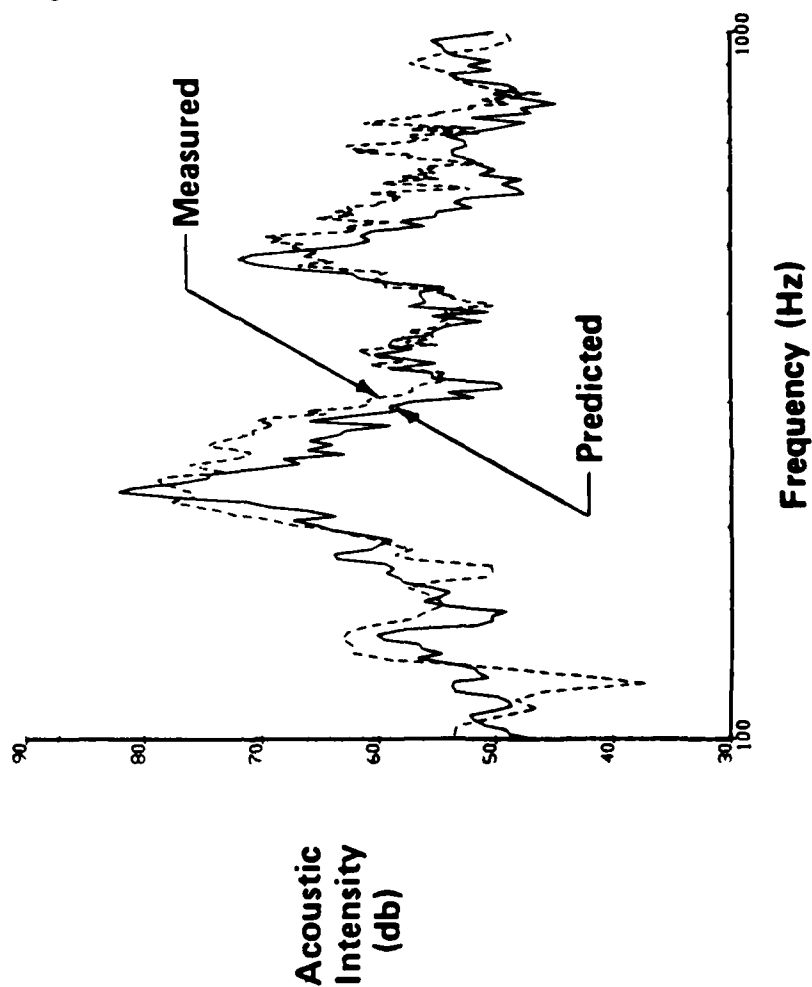
CASE	E _{SKIN} (PSI)	η_{SKIN}	E _{STR} (PSI)	η_{STR}	NOTE
COUPON 101 BARE	11.1×10^6	.022	12.1×10^6	.009	
COUPON 102 BARE	9.7×10^6	.016	6.3×10^6	.004	
COUPON 201 RVT'D STR	10.1×10^6	.013	3.8×10^6	.006	?
COUPON 101 STR DAMPING	11.3×10^6	.024	1.8×10^6	.952	?
COUPON 101 SKN DAMPING	11.3×10^6	.104	5.8×10^6	-.02	?

... E_{ALUM} $\cong 10 \times 10^6$...

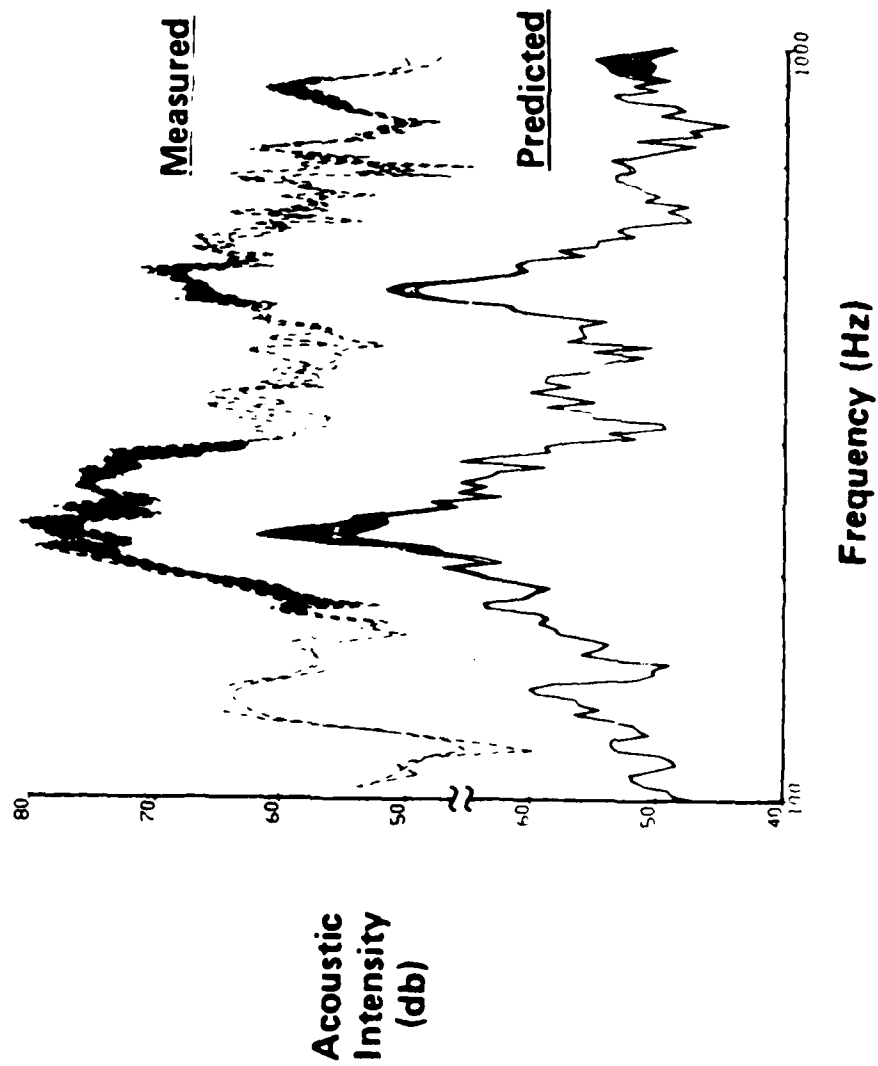
COMPARISON OF MEASURED & PREDICTED PANEL RESPONSE

Panel 102

- 6" stringer spacing
- No damping



MEASURED VS PREDICTED EFFECT OF STRINGER DAMPING



WHAT WE HAVE . . . WHERE WE ARE GOING

- Generalized skin-stringer-frame model . . . predicting
- Validation . . . encouraging/on-going
- Specialized (simpler) model . . . predicting
- Validation . . . good re current test efforts
- Characterizing damping re element composite loss factors
 - Coupon testing/SE based processing
 - FEM/MSE based processing
- Development of design guidelines/methods . . .

USE OF SKIN DAMPING TREATMENTS TO CONTROL AIRFRAME
DYNAMIC RESPONSE FOR INTERIOR NOISE CONTROL

C. I. Holmer
E-A-R Division/Cabot Corporation
7911 Zionsville Road
Indianapolis, Indiana 46268

Use of Skin Damping Treatments to Control Airframe Dynamic Response for Interior Noise Control

by

C. I. Holmer
E-A-R Division/Cabot Corporation
7911 Zionsville Road
Indianapolis, IN 46268

I. INTRODUCTION

The objectives of the project that this paper reports were to:

1. Define the role of structural damping treatments applied to the skin of aircraft for control of interior noise in the outfitting of the aircraft.
2. Develop some new materials for use in this particular application.
3. Demonstrate the role of these materials in actual aircraft flight tests.

II. BACKGROUND

Let us begin exploring the background to this problem by considering a conceptual model for the dynamics of the airframe structure. We will consider a representation of the airframe of interest as a cylindrical shell of relatively thin aluminum stiffened by longitudinal stringers and circumferential frames. These frames and stringers sub-divide the cylindrical shell into sub-panels of skin. The audio frequency dynamics of this structure involves many resonant modes. One group of these modes that are of interest can be defined as lying in a frequency range above what we will call the first sub-panel resonance. For frequencies below the first sub-panel resonance the sub-panel motion is controlled by the gross structure motion (i.e., the frame, stringers, and skin move more or less together in modes that correspond to those of a cylinder with an equivalent smeared stiffness and mass per unit area). For frequencies at and above the first sub-panel resonance the sub-panels can move more or less independently from the frames and the stringers (but with correlation of motion with adjacent sub-panels) with frames and stringers defining boundary conditions of the sub-panels.

The skin responds to many forcing functions which exist in flight. These forcing functions include: the turbulent boundary layer (TBL), vibration propagating away from the propulsion system attachment points on the fuselage, other on-board vibration sources, and finally the propulsion system sound field. The skin response is, of course, influenced by the presence of large in-plane stresses due to pressurization and other quasi-static aerodynamic forces.

Let us now examine what the potential effects of a damping treatment applied to the skin could have on the fuselage dynamics. First we observe that the treatment must add mass, stiffness, and damping to the system. The added mass and stiffness in each sub-panel can move the sub-panel first resonant frequency up or down depending upon the relative addition of each. We would expect this first resonance to shift in proportion to the change in $(B/M)^{1/2}$ for the skin. A treatment which adds stiffness at a greater rate than it adds mass per unit area will increase the first resonant frequency (and other sub-panel resonant frequencies as well). Below the first sub-panel resonance, the stiffness modification of the gross structure is typically negligible, and the major impact is on the change in total structure mass per unit area. These changes in mass are also usually small. This discussion has been limited to the consideration of cylindrical shells. The impact on non-cylindrical shells is more complex and beyond the scope of this investigation.

Due to the negligible change in stiffness below the first sub-panel resonance, the change in damping in the structure can, on strain energy grounds, be expected to also be relatively small. Above the first sub-panel resonance the change in sub-panel damping can be expected to be large or small, depending upon the treatment performance under actual temperature conditions and the amount of damping already present in the system. The expected influence on system dynamic response due to the addition of damping include:

First a reduction in resonant response of the skin to TBL forces in proportion to the change in:
[10 log (system loss factor)]

Attenuation of vibration propagating in the skin
in proportion to the change in:
[13.6 x (system loss factor) dB/wavelength]

The dynamics of an outfitted aircraft in the audio frequency range is also of interest since the outfitting treatments can be expected to influence the system properties. We will explore a conceptual model for this dynamic performance as well. Figure 1 shows a simplified cross-section of an outfitted aircraft at the fuselage. Note that the cross-section includes the skin and frames with stringers not shown. In-board of the fuselage structure are glass fiber bats, a weighted layer with all penetrations sealed, a second fiberglass layer, and an inner trim panel which is attached to the frames via mechanical connections. It is appropriate to invoke a double-wall model for the description of the dynamics of this system that are relevant for interior noise (1, 2, 3)*.

The trim system dynamics are characterized by a double-wall resonance (that frequency where the skin or fuselage structure and the weighted layer structure move in opposite phase). Above this frequency we expect increasing isolation of average velocity at the weighted layer surface and trim panel compared to average velocity at the fuselage surface. This increasing isolation will approach a limit at mid and high frequencies which is determined by structureborne transmission from the fuselage side of the structure to the interior trim panels through mechanical attachments. (A second double wall resonance between the weighted layer and the trim panel will also occur, but is less likely to significantly alter the dynamics already described.) The limit due to structureborne transmission is the item of primary interest. It can be presumed that the structureborne limit will typically occur in the frequency range between 250 and 1000 Hz depending upon the details of the specific construction. The first sub-panel resonance of the fuselage is also expected to occur in this frequency range. Thus we expect the sub-panel motion to contribute to the motion of frames in and above this frequency range, and that damping of fuselage sub-panels will have an impact on frame motion.

*Numbers in parentheses refer to references at the end of the text.

Also of interest is the damping produced by the presence of the glass fiber materials installed adjacent to the fuselage of a completed aircraft. Air pumping in the glass fiber is expected to be the dominant damping mechanism which is competing with any additive structural damping treatment. In the absence of good data on magnitude of this mechanism in flight, we can only look for differences in effects.

At this point we can identify some additional detail for project objectives. Our first objective for material design is to define a constrained layer treatment which operates effectively in the temperature regime of cruise flight for pressurized aircraft. We would expect to be able to rank order performance under laboratory conditions by comparison of the amount of damping produced in a sample representative of aircraft skin. To identify the contribution of such a system to actual in-flight performance, we would expect that a measure of the change in vibration velocity of frame surfaces at trim panel attachment points should be an appropriate metric.

III. SKIN DAMPING TREATMENTS

A typical skin damping treatment is constructed in the form of a constrained layer system of damping material and constraining layer, in order to give a high performance to weight ratio. Such constructions are known to be inherently frequency-dependent in the amount of damping produced (4). Perhaps less well appreciated by the airframe design community is the fact that these constructions will also be inherently temperature sensitive due to the changing properties of the damping material with temperature. These types of skin damping treatments are commercially available from several manufacturers and have been widely used for many years on virtually all multi-engine propeller and executive aircraft. Their appearance is less frequent on commercial aircraft and light, private aircraft where, more frequently, cabin load is considered to be a more important design parameter than interior noise level.

The temperature dependence of the skin damping treatment derives from the fact that the damping material properties change as a function of temperature. Also less well appreciated is the empirical observation that the level of damping achieved in a given material is associated with the rate at which the material properties change with temperature (5).

Figure 2 shows measured system loss factor data versus temperature, at several test frequencies, for two different treatments of 0.040 inch thick aluminum (a common skin thickness for aircraft in this class). The new E-A-R material is optimized to produce high system loss factor at a lower temperature than other commercially available materials. It produces significantly more damping at the low temperatures expected to be representative of cruise flight.

Upon presentation of this laboratory data we were challenged by a customer to design and execute an experiment to verify the laboratory findings in-flight. Two experiments were suggested to this airframe manufacturer. The first experiment addresses the question: "Is the performance difference indicated in the laboratory data verifiable in flight?" This will be addressed below under the heading "EXPERIMENT 1". The second experiment addresses the larger question of whether or not an effective damping treatment can influence the damping of the structure in the presence of damping mechanisms of an outfitted aircraft.

IV. EXPERIMENT 1 - Comparison of Two Skin Damping Treatments

The experiment was undertaken with the considerable assistance of Gulfstream Aerospace Corporation, the airframe manufacturer, and the data are used with permission. The test aircraft was Model G-III s. n. 357. Skin damping treatments were applied in the mid-cabin area (covering the region from fuselage Station 272 through Station 336) and from centerline to floor. E-A-R C-3201-25-ALPSA was applied to the righthand side of the aircraft. A mirror image installation of a commercially available damping treatment was installed on the left side. The cabin interior was partitioned with a flexible blanket across the fuselage fore and aft of the treated area and along the aircraft centerline to reduce the influence of acoustic coupling with either side or with the untreated area. The treatments were applied directly to the aircraft skin by GAC personnel with about 60% coverage of the sub-panel area in accordance with GAC internal procedures. No other interior outfitting was installed in the aircraft.

The data acquisition system consisted of phase and amplitude matched transducer channels feeding a two channel tape recorder. Two channel data were acquired simultaneously from designated measurement locations during the flight. These locations included (1) and (2) two light stringer locations (midway between frames, on stringers about 60 degrees from overhead), (3) one skin location (centered between frames and stringers), and (4) at the intersection of a frame and light stringer. Data at measurement location 4 (frame) were not acquired due to loss of the accelerometer mounting stud attachments in flight. Accelerometers were mounted by attachment to pre-applied mounting studs. Measurement locations were carefully matched for equivalent locations on either side of the aircraft. Positioning accuracy was estimated to be ± 0.1 centimeter. Light-weight (two gram) accelerometers were used to minimize mass and moment loading by the transducer on the measured structure. Temperature data were acquired using a digital thermometer.

The experiment protocol called for recording accelerometer output at one location pair through the climb profile and then several times during cool-down at normal cruise. Following this cool-down period recordings were made at each measurement location during normal cruise.

Data were reduced by tape playback through a dual channel spectrum analyzer (Nicolet 660B) to permit simultaneous evaluation of both channels of data. Segments of the tape recording were analyzed through climb as well as in steady cruise. The accelerometer signals from both channels were processed simultaneously and then recorded on digital disk for archival storage. The average spectrum was integrated to produce a velocity spectrum and summed over nominal octave band intervals to obtain octave band velocity levels estimates. The overall system record/playback frequency response and gain were calibrated before and after the flight. The response to simultaneous excitation of both transducers with a common input produced and overall record/playback response equality within ± 0.3 dB with an average bias of $+0.2$ dB. On the basis of this calibration, no correction was made to the data for inter-channel record/playback response.

Figure 3 shows a representative pair of spectra from the measurements. The upper spectrum in this plot represents the velocity level on a stringer flange on the side with E-A-R treatment. The lower curve represents the velocity level at the corresponding position for the alternate treatment. The central curve shows the difference between the two spectra with the center hash marks as 0 dB difference. The scale for the two spectra are shown on the left-hand side of the plot and with 10 dB per division hash marks. The scale for the difference curve is shown on the right-hand side and is plotted with a 10 dB per major division resolution. Notable in the two curves is the very strong resemblance between the response of the two sides. Significant features include two prominent engine-associated tones below 250 Hz, and a broad response maximum between 500 Hz and 1250 Hz which is attributed to a superposition of numerous sub-panel and stringer resonances. This feature also contains the estimated shell ring frequency. The broad peak in the vicinity of 2750 Hz may be associated with a stringer flange resonance.

Table 1 presents octave band velocity level data for all tape intervals analyzed, together with associated flight and temperature data. Of significance in this data presentation is first the stabilization of skin temperature in range of -19 to -24° C., in spite of an outside air temperature of approximately -60° C. It should be noted that the flight path followed during this test involved orbiting with 10 minute legs which exposed alternate sides of the aircraft to solar radiation providing uniform heat input to both sides. Averaging the results of measurements and positions at test points 11, 12, and 13 result in an average reduction in velocity level of 1.3 dB at 500 Hz and 4.9 dB at 1000 Hz, which fully support the differences in loss factor suggested by the laboratory data shown in Figure 2. Our inability to make accurate laboratory measurements at 2000 and 4000 Hz precludes us from speculating on the differences observed there.

Our conclusions from this brief experimental program are three:

(1.) Actual temperatures of an aircraft skin, at cruise altitudes of FL450 at speeds near M0.80, are on the order of -20 to -25° C. in spite of outside air temperatures in the range of -65° to -55° C. A mechanism supporting this observation is that the air temperature near the skin is influenced by aerodynamic compressability effects at these high cruise speeds.

(2.) Differences in the performance of skin damping treatments can affect a response on attached structures such as stringers in the frequency range of 500 Hz through 1500 Hz.

(3.) Differences in response velocity level observed in flight are comparable with differences expected from laboratory data at corresponding test temperatures.

V. EXPERIMENT 2 - Comparison with Other Damping Mechanisms

This second experiment was undertaken in conjunction with a larger series of experiments evaluating the influence of several parameters of new interior outfitting concepts. The data were acquired in a manner similar to the first experiment, with the support and assistance of Gulfstream Aerospace, and is used with permission. The test aircraft was another Model G-III, s. n. 389. The aircraft was outfitted with standard glass fiber blankets between frames and over frames, but with a free-standing interior shell which simulated in location and weight, the standard interior trim panel system. The data were acquired on two separate flights of the aircraft during May 1983. In the first flight, no skin damping treatments were installed, while for the second flight, E-A-R C-3201-25-ALPSA skin damping treatment was applied in accordance with normal installation procedures.

Acceleration level data was acquired at two locations on circumferential frame flanges on opposite sides of the aircraft near mid-cabin, using the same recording and analysis systems as for Experiment 1. Accelerometers were mounted on the frame inboard flange in direction normal to the flange at position approximately 60° from overhead. Accelerometers were attached with mounting studs adhered to the frame to permit accurate relocation for the repeat flight.

The experiment protocol called for recording of measurements at FL310 at speeds of M0.75 and M0.80, followed by similar recordings at FL450 at several alternate speeds. Difficulties with recording equipment and interference from radio transmissions prevented reduction of useful data at FL450 for one or the other of the two flights.

Figure 4 (at M0.75) and Figure 5 (at M0.80) present the velocity level data acquired in these tests. In each plot the upper curve represents the velocity level spectrum for data acquired at a measurement location for flight 2 (with skin damping treatment). The lower curve presents the corresponding data acquired on flight 1 without the skin damping treatment. The center curve presents the difference data. The data acquisition and reduction procedures were similar to those used in experiment 1 except that the data were corrected for tape recorder record-playback frequency response.

Distinct from the previous experimental procedure these data have been acquired in a relatively short time interval, less than one minute duration. Because of this difference in acquisition technique, it is appropriate to combine the velocity level on each side of the aircraft to determine an average response. Table 2 presents the average corrected velocity level data for each measurement location and speed. Velocity level on each side of the aircraft for each measurement configuration has been summed on an energy basis to give an average velocity level. The difference in average velocity level for the two flights, also shown in this table, is the influence of the damping treatment. As can be clearly seen, the addition of the skin damping treatment has significantly lowered frame velocity level by amounts as large as 6.5 dB in the frequency range of interest in spite of the presence of additional damping mechanisms such as is produced by the presence of glass fiber insulation.

We infer from these changes in frame response that a skin damping treatment, which is effective in the operational temperature range, will introduce sufficient damping to the system, in the presence of other damping mechanisms, such that vibration levels will be reduced. Alternately, damping treatments which produce significantly less additional system loss factor than those of the material described here could indeed have the effect of their addition masked by the damping mechanisms provided by other parts of the construction.

PART VI - SUMMARY AND CONCLUSIONS

The following paragraphs provide a summary of the significant information generated in this study program:

1. We have described a conceptual model for airframe and interior trim dynamic response. This model suggests that skin response in the frequency range of interest may be affected by skin damping treatments. Further, this skin response plays a role in producing response at other portions of the airframe such as trim panel attachment points. It is additionally suggested that this motion is of significance in producing interior noise.

We have presented observations of skin temperature data for aircraft in high speed sub-sonic flight that are substantially warmer than outside air temperature. For an outside air temperature of -60° , actual skin temperatures observed at speeds of $M0.8$ are on the order of -24 to -19° C.

2. Laboratory data of system loss factor for a new constrained layer, skin damping treatment have been presented which show improved damping performance at lighter weight than other commercially available skin damping materials.

3. We have presented experimental data on an effective skin damping treatment which evidently produces system loss factors which contribute significantly to total losses in the airframe in the presence of other loss mechanisms associated with the outfitted airframe.

This effective skin damping treatment does reduce airframe motion at representative trim panel attachment points, which, when interpreted in conjunction with the conceptual model, clearly suggests a role in reducing aircraft interior noise.

REFERENCES:

1. I. L. Ver and C. I. Holmer. "Interaction of Sound Waves and Solid Structures". Chapter 11 of Noise and Vibration Control, L. L. Beranek, ed. McGraw Hill, N. Y. (1971).
2. C. I. Holmer. "Investigation of Acoustic Properties of a Rigid Foam with Application to Noise Reduction in Light Aircraft". NASA CR132333 (1973).
3. L. D. Pope and E. G. Wilby. "Analytical Prediction of the Interior Noise for Cylindrical Models of Aircraft Fuselages for Prescribed Exterior Noise Fields. Phase II." NASA CR 165869 (1982).
4. E. M. Kerwin, Jr., "Damping of Flexural Waves by Constrained Viscoelastic Layer". J. Acous. Soc. Am. 31 (7), pp. 952-962, (July 1959).
5. Personal observation of the author in detailed study of several compendia of material properties such as "Damping Materials, Finite Elements and Special Projects". AFWAL-TR-82-4167, University of Dayton Research Institute, December 1982.
6. C. I. Holmer. "Reduction and Analysis of Data from an In-Flight Comparison of E-A-R and Alternate Skin Damping Treatments". E-A-R Technical Report 83-7/NC, February 1983 (Available from the author on request).

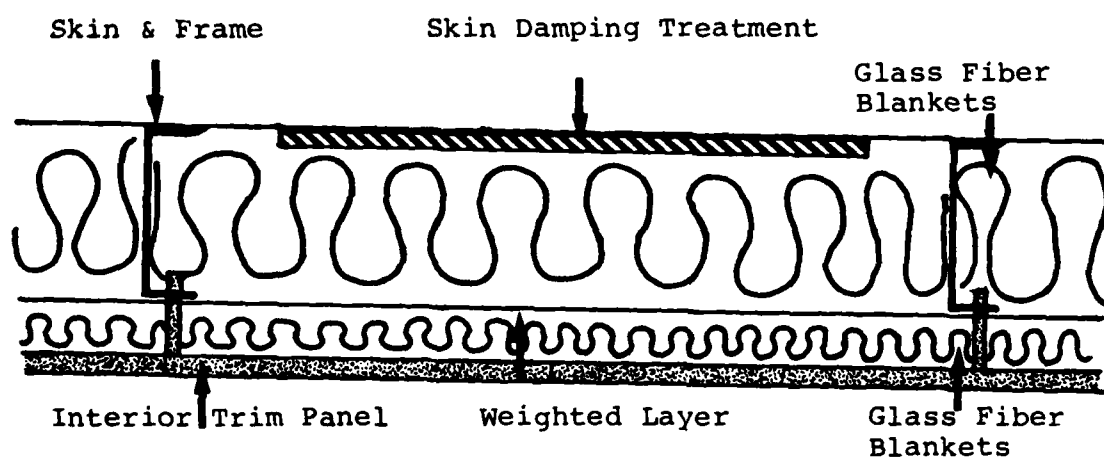


FIGURE 1. Conventional Aircraft Interior Treatment

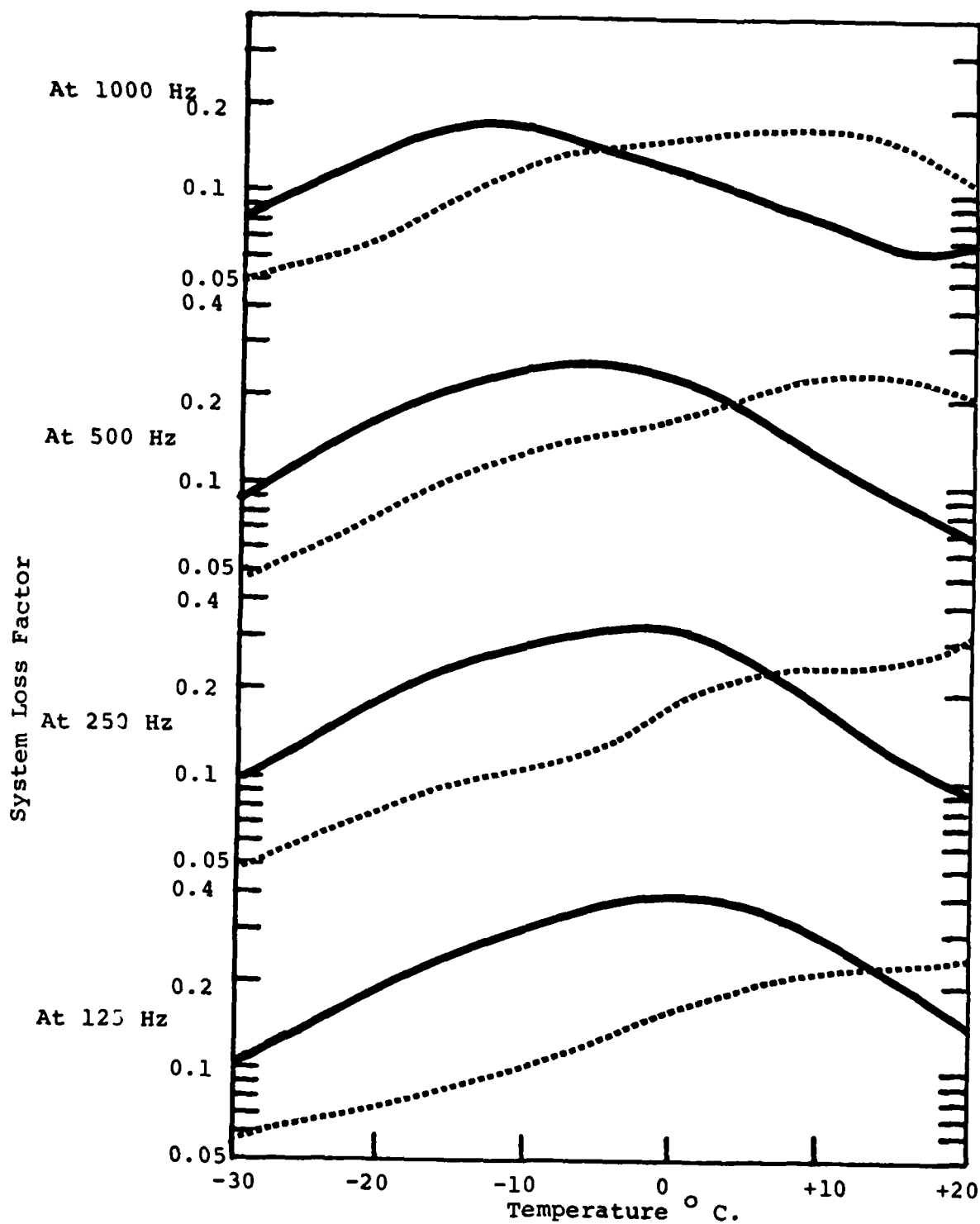


FIGURE 2. System Loss Factor vs Temperature for four frequencies.
 — E-A-R C-3201-25-ALPSA
 Commercially Available Material

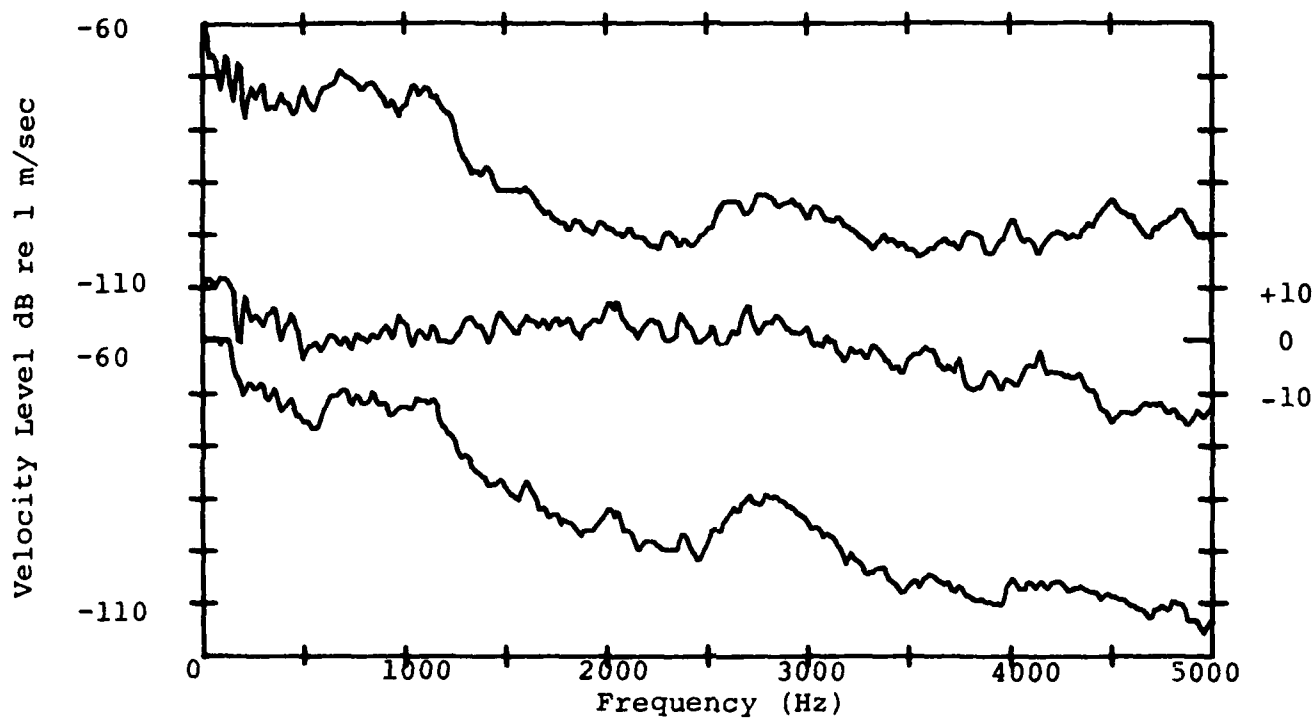


FIGURE 3. Velocity level vs frequency on stringer at M0.80, FL450, for two different skin damping treatments. Upper curve: E-A-R C-3201-25 ALPSA; lower curve: commercially available material; middle curve: (lower curve - upper curve) x 2; scale at right.

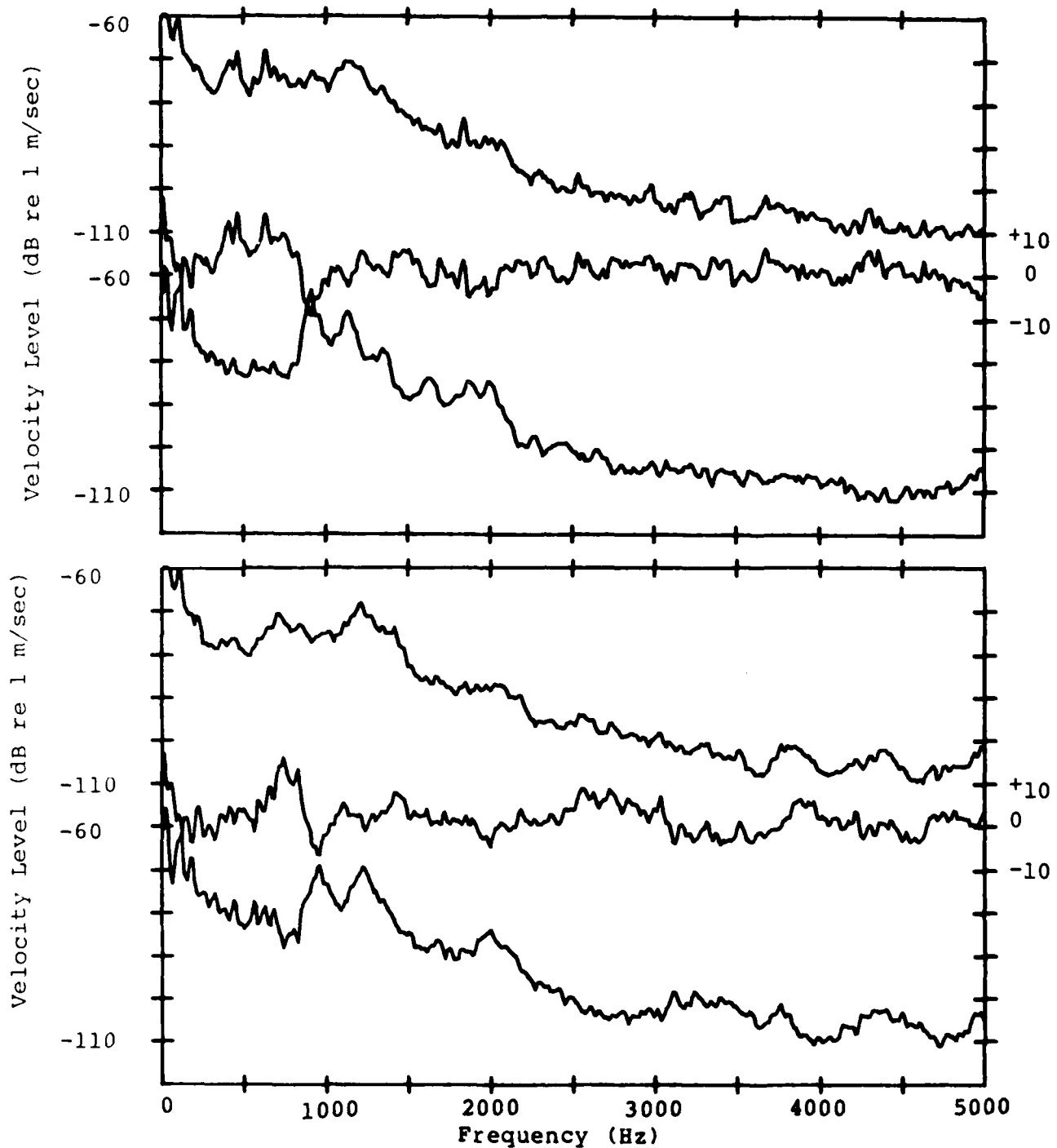


FIGURE 4. Velocity level on frame flange vs frequency speed M0.75, FL310. Upper plot - left side of airframe at mid cabin; lower plot - right side (with temporary outfitting). In each plot: upper curve (with skin damping); lower curve (without skin damping); middle curve - difference (upper - lower) x 2.

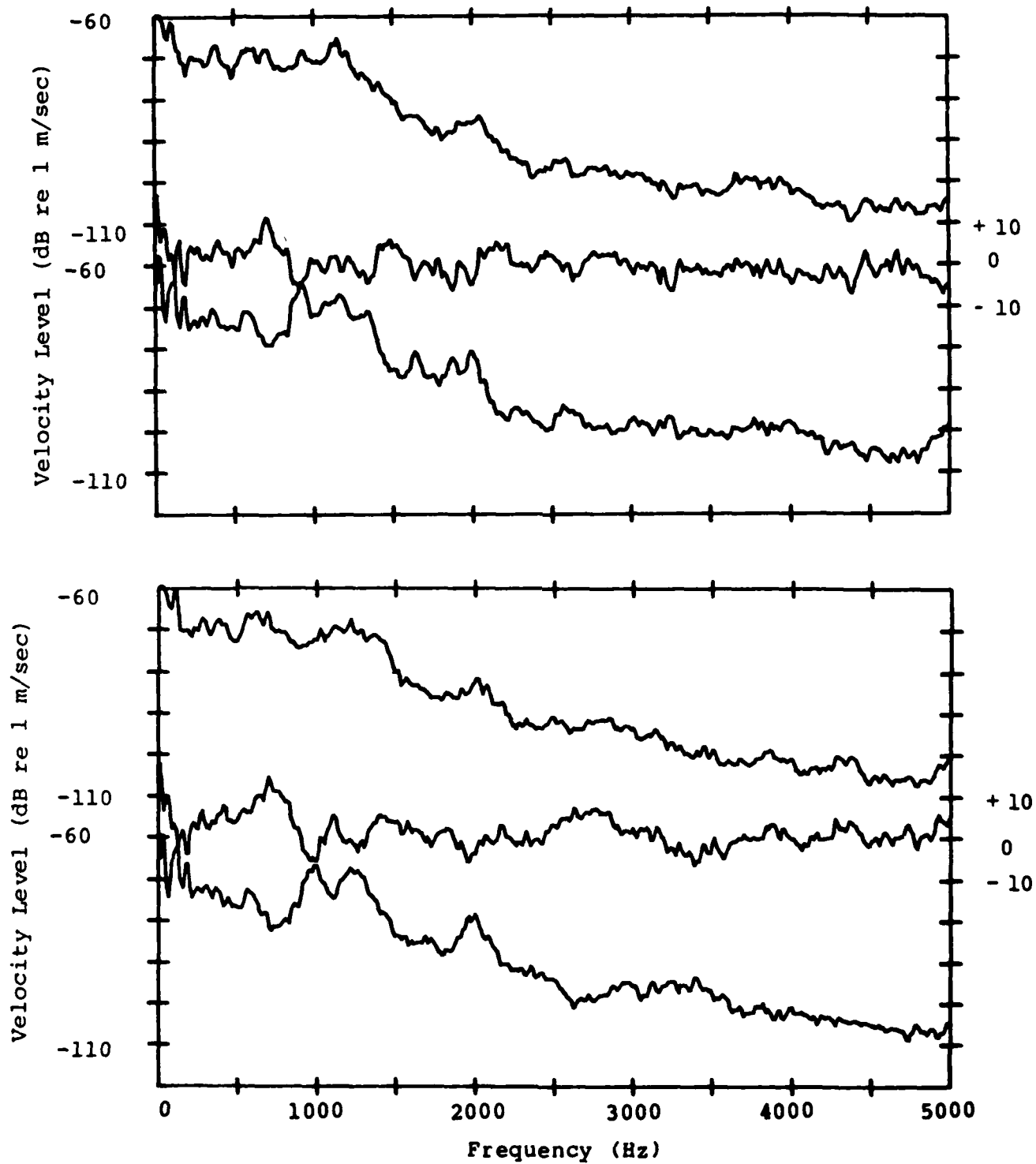


FIGURE 5. Same as FIGURE 4 except speed M0.80.

Table 1

Octave Band Velocity Level vs Frequency (db re 5 - 10⁻⁸ m/sec) +
from Experiment 1 (Comparison of Two Damping Treatments)

TP	Tape Interval	Disc ID	Event	Temp ° C Skin/Cabin/OAR	Ch*	Octave Band Center Frequency, Hz						
						250	500	1000	2000	4000	SIL	
						168 3/4- 356 1/4	343 3/4- 718 3/4	706 1/4- 1418 3/4	1406 1/4- 2831 1/4	2818 3/4- 5006 1/4	(500-4k)	
1.	036-049	008.238.208	0-10K climb, Loc. 1, Stringer	-/+15/+20	A	78.6	77.6	73.6	58.5	61.8		
					B	85.1	77.5	77.0	67.0	53.2		
					Δ	-6.5	1.0	-3.4	-8.5	8.6	-0.6	
2.	065-078	009.233.208	0-10k ft climb, Loc. 1, Stringer	-/+15/+-	A	77.0	84.3	81.2	59.2	54.8		
					B	78.5	84.4	84.7	64.1	52.4		
					Δ	-1.5	-0.1	-3.5	-4.9	2.4	-1.5	
3.	125-135	006.238.206	10k-20k ft climb, Loc. 1, Stringer M0.68	-/+14/+1	A	81.3	89.4	88.6	67.7	57.8		
					B	80.5	89.6	91.2	71.4	58.4		
					Δ	0.8	-0.2	-2.6	-3.7	-0.6	-1.8	
4.	165-176	007.238.207	20k, climb, M0.68, Loc. 1, Stringer	-/-/-19	A	80.6	89.4	89.1	68.9	59.6		
					B	80.5	89.4	91.3	71.8	61.6		
					Δ	0.1	0.0	-2.2	-2.8	-2.0	-1.8	
5.	195-207	010.238.209	20k, Level, Loc. 1, Stringer	-/+8/-	A	82.1	90.9	91.1	70.6	61.5		
					B	83.6	91.0	93.3	74.0	65.0		
					Δ	-1.5	-0.1	-2.2	-3.4	-3.5	-2.5	
6.	245-255	011.238.210	30-40k ft, climb, Loc. 1, Stringer M0.74	-/+7/-40	A	82.9	88.8	88.6	68.5	63.5		
					B	82.8	88.1	88.7	70.4	60.8		
					Δ	0.1	0.7	-0.1	-1.9	2.7	-0.4	
7.	315-324	012.238.211	40-45k ft, climb, Loc. 1, Stringer M0.75	-/+6/-59	A	82.5	82.4	84.6	66.5	65.5		
					B	79.6	83.2	84.6	67.2	58.8		
					Δ	2.9	-0.8	0.0	-0.7	6.7	+1.3	

*Channel Designation: A - E-A-R Treated Side; B -
Commercial alternate; Δ - Difference (E-A-R-Alternate)

+ Note: At reference velocity of 5 x 10⁻⁸ m/sec velocity
level is numerically equal to sound level radiated at the
surface by a structure with unit radiation efficiency.

Table 1 (continued)

TP	Tape Interval	Disc ID	Event	Temp ° C Skin/Cabin/OAT	Ch	250		500		1000		2000		4000		SIL
						168 3/4- 356 1/4	343 3/4- 718 3/4	706 1/4 1418 3/4	706 1/4 1418 3/4	2831 1/4 5006 1/4	1406 1/4 2831 1/4	2818 3/4- 5006 1/4	4000 1/4- 5006 1/4			
8.	360-368	013.238.212	40-45k ft, climb, Loc. 1, Stringer M0.75	-/+6/-60	A	81.7	82.4	85.5	67.7	68.0						
					B	80.4	81.5	84.1	67.5	60.4						
					Δ	1.3	0.9	1.4	0.2	7.6						+2.5
9.	385-393	001.238.213	45,000 ft, Level, 5 min. Loc. 1, Stringer M0.80	-9/+5/-58	A	81.2	84.1	86.2	67.9	67.0						
					B	80.4	83.9	86.7	70.3	63.5						
					Δ	0.8	0.2	-0.5	-2.4	3.5						+0.2
10.	431-439	001.238.223	45,000 ft Level 15 min Loc. 1, Stringer M0.80	-19/+3/-59	A	83.1	84.8	87.7	69.4	68.9						
					B	(87.5)*	86.1	86.4	69.4	62.9						
					Δ	--	-1.3	1.3	0.0	6.0						+1.5
11.	485-493	002.238.224	45,000 ft Level 25 min Loc. 1, Stringer M0.80	-/+2/-59	A	82.5	85.0	86.5	68.3	67.4						
					B	(85.8)*	85.8	87.4	71.3	65.6						
					Δ	--	-0.8	-1.1	-3.0	1.8						-0.6
12.	508-516	009.238.221	45,000 ft, Level, 37 min. Loc 1, Stringer M0.80	-21/-5/-60	A	82.2	84.8	82.2	69.7	69.0						
					B	(87.3)*	85.4	86.8	69.6	63.1						
					Δ	--	-0.6	-4.6	0.1	5.9						+0.2
13.	539-546	010.238.222	45,000 ft, Level, 54 min. Loc. 2, Stringer M0.81	-24/-5/-60	A	83.5	85.3	83.5	71.8	66.3						
					B	(85.1)*	87.3	88.8	72.0	63.5						
					Δ	--	-2.0	-5.3	-0.2	2.8						-1.2
14.	572-580	006.238.218	45,000 ft, Level, 69 min. Loc. 3, Skin M0.79	-20/-5/-60	A	78.3	85.0	84.3	77.5	67.4						
					B	78.4	84.2	83.7	79.0	60.4						
					Δ	-0.1	0.8	0.6	-1.5	7.0						+1.7

*Data in parentheses probably contaminated by extraneous instrument system noise.

TABLE 2. Octave Band Velocity Level (dB re 5×10^{-8} m/sec)
vs Frequency from Experiment 2 (Undamped vs
Damped Airframe; with Trim)

Position	Band Center Frequency (Hz)					
	125	250	500	1000	2000	4000
1. Mach 0.75, FL310, undamped fuselage (Flight 1)						
Left Frame	87.6	80.7	85.5	87.6	74.7	60.5
Right Frame	86.8	80.3	82.1	87.7	76.7	62.5
Avg (=Sum-3 dB)	87.7	80.5	84.1	87.7	75.8	61.6
2. Mach 0.75 FL310, damped fuselage (Flight 2)						
Left Frame	90.4	80.0	76.2	88.2	73.9	58.8
Right Frame	90.6	81.4	77.5	86.0	74.1	61.8
Avg (=Sum-3 dB)	90.5	80.7	76.9	87.2	74.0	60.6
Change (M0.75)	+2.8	+0.2	-7.2	-0.5	-1.8	-1.0
3. Mach 0.80, FL310, undamped fuselage (Flight 1)						
Left Frame	87.1	83.9	88.6	90.2	77.1	63.8
Right Frame	87.7	85.3	89.7	89.8	79.4	66.9
Avg (=Sum-3dB)	87.5	84.7	89.2	90.0	78.4	65.6
4. Mach 0.80 FL310, damped fuselage (Flight 2)						
Left Frame	90.6	83.0	84.3	90.5	76.2	65.0
Right Frame	91.0	83.8	82.7	89.4	78.1	66.3
	90.8	83.4	83.5	90.0	76.3	65.7
Change (M0.80)	+3.4	-1.3	-5.7	-0.0	-1.1	+0.1
Average Change (M0.75 & M0.80)	+3.1	-0.6	-6.5	-0.3	-1.5	-0.5

DAMPING APPLICATION TO SPACECRAFT

T. S. Nishimoto
Rockwell International, SSD
Seal Beach, California

DAMPING APPLICATION TO SPACECRAFT

T. S. Nishimoto
Rockwell International, SSD
Seal Beach, CA

The purpose of this note is to present various cases of design application of damping technology to spacecraft development. These cases illustrate various vibration problems for which damping was used as a design tool. The relative success and difficulties encountered are presented.

Damping technology in application to spacecraft addresses several design problem areas. Vibroacoustics environment associated with launch vehicle noise is an area of interest of long standing. On-orbit S/C controls problems have also emerged as candidates for damping technology. Problems associated with precision pointing and constrained settling time from controls reorientation are finding simpler controls design solutions from damping concepts. The cases presented are a progression from smaller elements to system design applications.

Case 1:

Recently on the GPS NAVSTAR program, the LCU (load control unit) failed during vibration qualification. The circuit elements which failed were 2-amp electromechanical relays. Constrained layer damping strips were incorporated on the circuit boards to control the resonances at 180 and 550 Hz. Simple development testing on a development article shows the performance gain at the subject resonances, Figure 1. Various damping strip configurations were studied. The constrained layer modification provided marginally acceptable performance, Figure 2.

The difficulty with this design situation was, as always, schedule and the constraint of only minor change could be tolerated. The behavior of the chassis and the relay's sensitivity should be addressed with an isolation system. The modifications and time required to implement this design approach precluded its consideration.

Case 2:

The second example illustrates a problem occurring at one level higher. The P80-1 program did not have an acoustic development test vehicle originally to develop the vibration requirements for the electrical boxes. The environment specifications were predicted values. Opportunity arose to run an acoustic development test on the flight spacecraft.

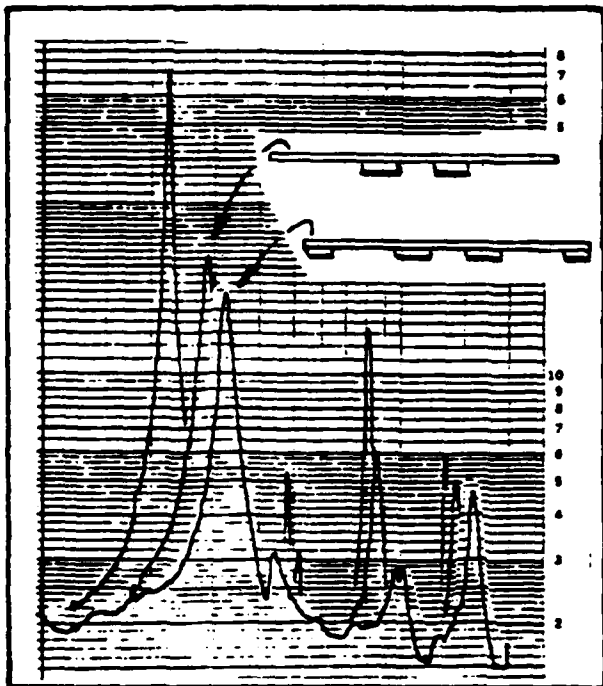


Figure 1
Sine Sweep Data

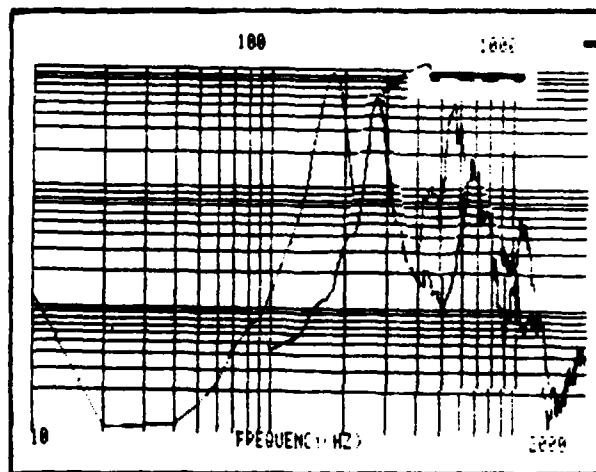


Figure 2
Qual Vibration PSD at Relay

Vibration responses showed an exceedance of specification for the shunt regulator. The shelf resonant response exceeded the qual requirement. A system of constrained damping layers was introduced to the waffled rib side of the shelf. The geometry is shown in Figure 3. The performance of the damping fix is seen in Figure 4.

Subsequent to the scheduled-constrained activities of the development testing, NASTRAN models and modal strain energy methods for predicting damping performance was used. The analysis pointed to a superior solution by placing the constraint strips at the three central ribs set instead of the set immediately beneath the box.

Case 3:

The third example illustrates an attempt to damp the system within the primary load path. As the NAVSTAR program developed from Block I to Block II, several issues associated with vibroacoustics became critical. First the carrier was changed from the Atlas to the Shuttle with changes in the acoustic environment. Second, many subsystem elements would remain unchanged going from Block I to Block II. The design goal was to provide dynamic characteristics in the new design which would not force requalification of the unchanged subsystem elements.

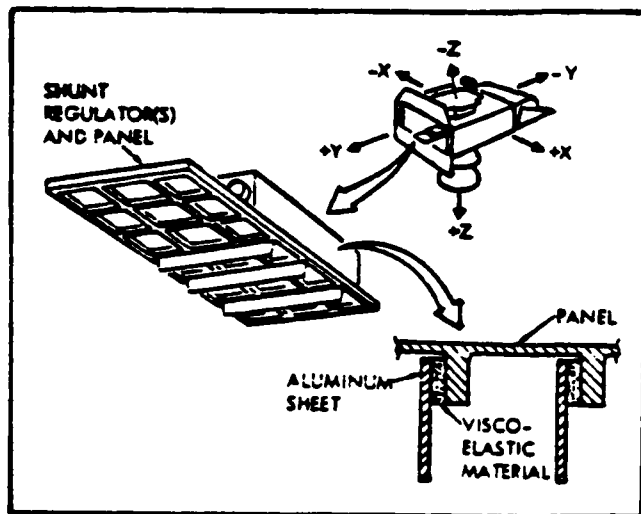


Figure 3
Damping Concept

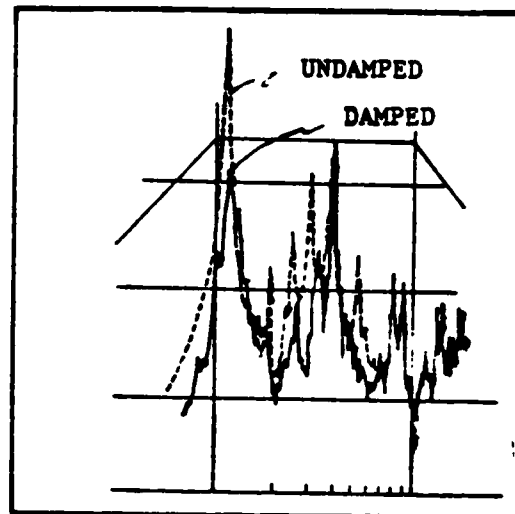


Figure 4
Response PSD

Concepts for introducing damping into structural joints were considered. The typical bulkhead shear panel joint configuration is shown in Figure 5. The partial-pinned characteristic was introduced in order to develop energy loss in rotation at the joint with damping shear pads. A development test was conducted to ascertain performance, see Figure 6. Vibration control of panel first mode can be seen.

During the Block II DTV acoustic testing, to develop equipment vibration levels, it was planned to implement the damped joints if the design goals could not be met. The results of the DTV testing precluded damping design modification.

Case 4:

Damping has been used to enhance control margins. The Teal Ruby program involves a large sensor system gimballed on the spacecraft. The step-stare operational sequence requires a complex controls system. An Earth albedo shield was placed on the sensor to control thermal input to the sensor. As requirements and thermal performance became better understood, the shield grew in dimension. The rotational inertia in the stepping DOF and the flexibility of the shield in this mode became increasingly a problem. One of the attempts to create greater margin was to provide greater damping in the objectionable vibration mode. A simply symmetric constrained layer damper system was used as the supporting strut system for the shield, Figure 7.

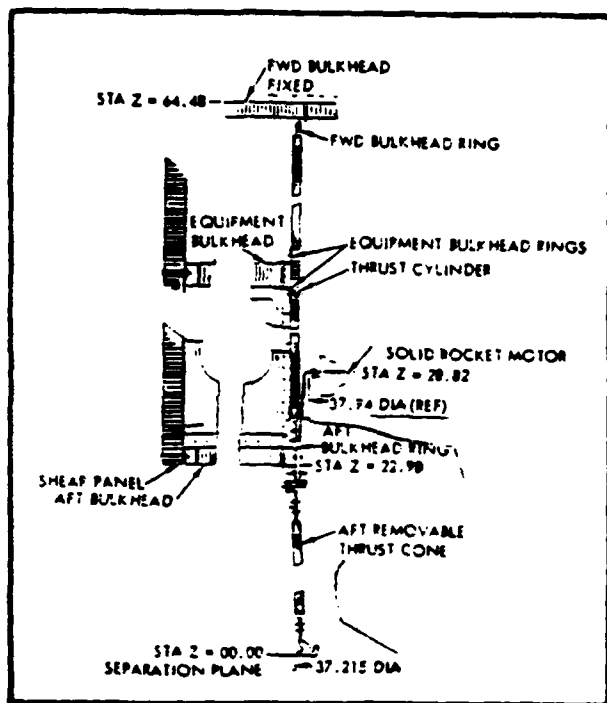


Figure 5
Spacecraft Structural Geometry

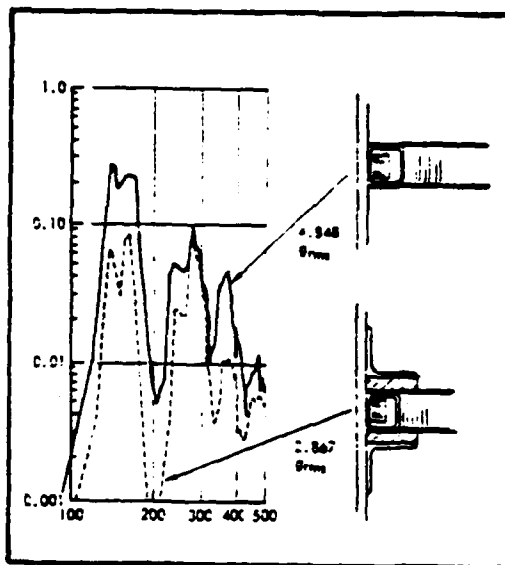


Figure 6
Development Test Performance

NASTRAN model and modal strain energy methods were used to size the design modification. The strut was fabricated and vibration testing established performance. Approximately 5% of critical damping was predicted. The controls simulation projected acceptable performance and margins.

This modification ultimately went by the wayside and the shield is currently mounted on the spacecraft instead of the sensor. Partly at fault is the uncertainty of performance of the damping design and also the limited margin projected.

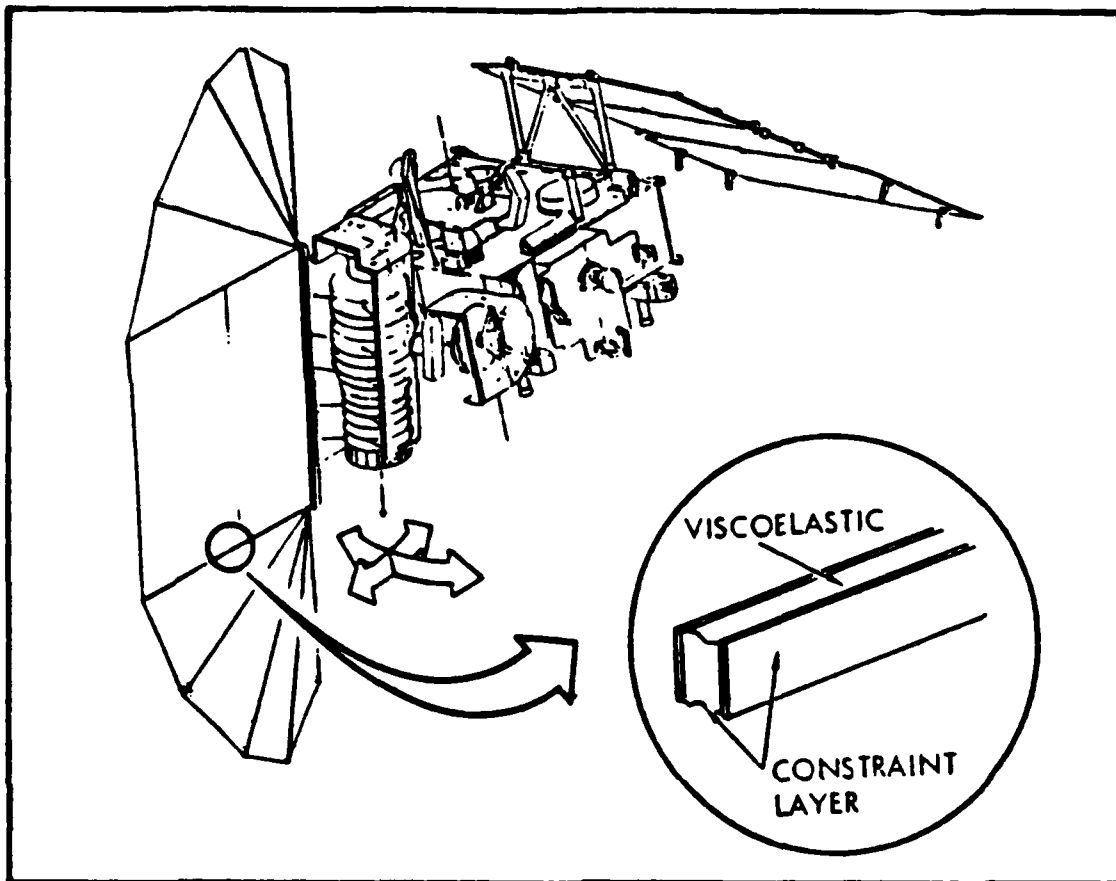


Figure 7
Earth Shield Damping Concept

Case 5:

Damping technology holds a promise of large payoffs in future systems. This example is the system design study of a Space-Based Laser. The design issue is the articulation of a very large optical element - namely, the primary and secondary mirror system. The settling time associated with retargeting has major system implications.

Parametric development of the design was conducted. Stiffness of the secondary mirror support truss was developed without available geometry, see Figure 8. Damping influence parametrically shown in Figure 9. System damping of 4 to 5% provided performance within the range of other system requirements.

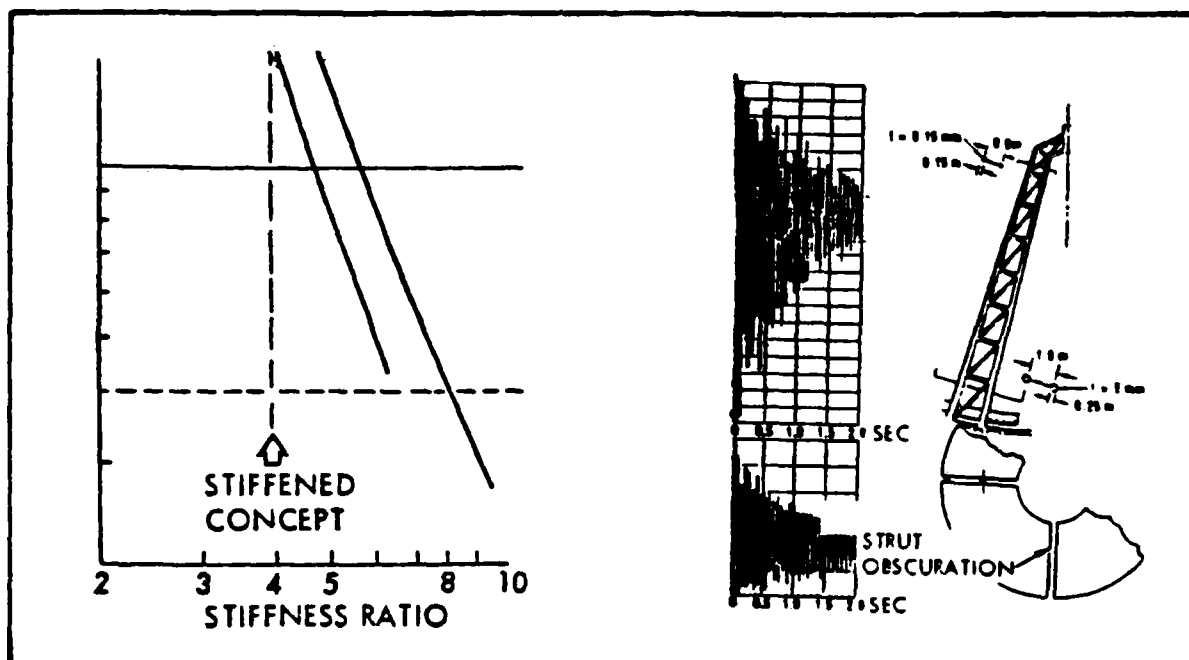


Figure 8
Stiffness Parameterization

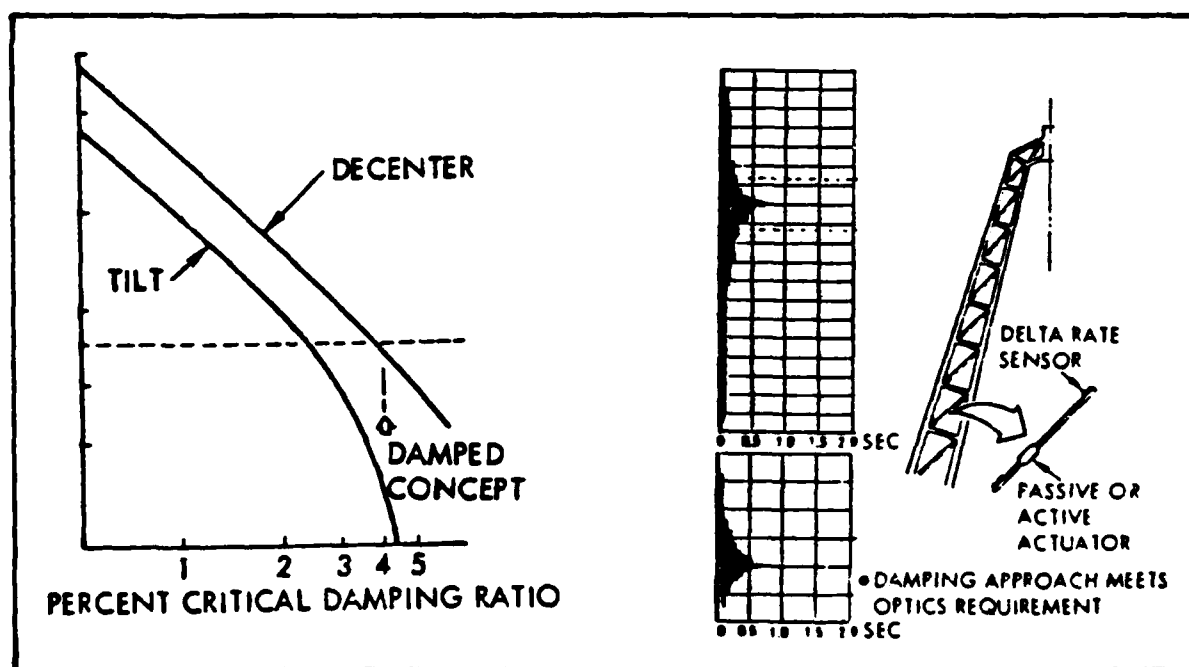


Figure 9
Damping Parameterization

Although this appears to be a design solution, many questions associated with implementation require further development. Several are: (a) materials or mechanisms to effect the required energy loss and meet the other environments, e.g., thermal, contamination, life, (b) loss mechanism behavior at micro strain. Geometry stability required may be so small that the strain associated may affect energy loss characteristics, and (c) the hysteresis may be outside the optically correctable range.

Summary

The examples of damping applications are a succession of spacecraft hardware design problems from the component level to the spacecraft system. These examples illustrate typical confining constraints which work to the detriment of the engineering effort. Late fixes to qual vibration failure necessarily leads to less than desirable design solutions. Late test failures will be avoided with the development of more reliable prediction techniques.

The example of integrating damping into the preliminary design process for system solutions points to the technology requirements necessary. Damping will become a more useful integrated design option as the technology matures.

APPLICATION OF DAMPING TO IMPROVE RELIABILITY OF IUS-TYPE
SATELLITE EQUIPMENT - RELSAT PROGRAM

Dr. Roy Ikegami
Mr. Clark J. Beck, and
Mr. William J. Walker
The Boeing Aerospace Company
Seattle, Washington 98124

APPLICATION OF DAMPING TO IMPROVE RELIABILITY OF IUS-TYPE
SATELLITE EQUIPMENT - RELSAT PROGRAM

by:

Dr. Roy Ikegami

Mr. Clark J. Beck

Mr. William J. Walker

The Boeing Aerospace Company

Seattle, Wash. 98124

Abstract

A review of the status of the Boeing Aerospace Company (BAC) RELIability of SATellite Equipment in Environmental Vibration (RELSAT) Program is presented. The program objectives, approach, goals and schedule are discussed. The work performed to date includes the selection of the BAC Inertial Upper Stage (IUS) as the baseline system for development in the RELSAT program. A description of work currently being performed is included. This contains typical passive damping design concepts currently under consideration, and component developmental testing and finite element modeling results.

INTRODUCTION

The need for sophisticated military surveillance and scientific observations in space have placed new and increasingly stringent design requirements on satellite systems. These systems must endure the rigors of the launch vibroacoustic environment and then operate precisely in space. In many cases, sophisticated equipment has not survived the high mechanical and acoustically induced vibration levels experienced during launch. These vibroacoustic environments impose severe qualification requirements on satellite equipment. However, current aerospace design practices do not identify critical avionics equipment vibration problems until late in the vehicle design process. The RELiability for SATellite Equipment in Environmental Vibration (RELSAT) program objective is to develop and validate the application of passive damping technology for vibration control to increase satellite equipment reliability. The challenge that is posed to the program is to demonstrate that the early incorporation of viscoelastic damping technology into standard aerospace vehicle design practice can reduce vibration levels and increase equipment reliability without significantly affecting the vehicle weight or program costs and schedules.

The application of viscoelastic material (VEM) has the potential to provide cost effective minimum weight solutions to vibration problems. Recent advances in this field have been numerous and cover a wide variety of disciplines. In particular, RELSAT technology will examine new materials having improved damping properties which can be accurately characterized to enable engineers to select the best, most efficient material for any particular application. Further, modern structural analysis theories will be applied to model structures containing viscoelastic materials (VEM's). In the study of design approaches, the best methods of using these materials will be identified. Although recent advances in materials technology have produced VEM's with greater potential for vibration control, two additional elements are needed to employ them effectively. First, it must be possible to characterize the VEM in a way which is accurate and repeatable. Data must be produced in a readily usable form. Secondly, it must be possible to predict the behavior of real structures which include VEM damping treatments. Both of these elements are RELSAT program goals. The program approach is to design, fabricate, analyze, and test selected damping treatments for structural components and assemblies. This information will be used to develop a damping design for a total system which will be optimized at the systems level for interdisciplinary synergism.

The purpose of this paper is to provide a description and status review of the Boeing Aerospace Company RELSAT Program. This program is funded by AFWAL Flight Dynamics Laboratories under the direction of Dr. Lynn Rogers and Mr. Robert Gordon.

PROGRAM DESCRIPTION

The RELSAT program effort is being conducted in seven major tasks which are scheduled to accomplish the program objectives in a timely and economic fashion.

Task 1 is the complete planning of the program, including details of schedules, tasks, and resources.

Task 2 is the selection of an existing satellite system as a baseline for development in this program. Systems level design requirements and performance goals for launch and satellite operation will be established. A Dynamic Test Article (DTA) will be selected from the baseline system.

Task 3 is a design development activity which will establish a damping design for the DTA. Passive damping concept generation, technology integration, structural analysis and element testing will be performed.

Task 4 is the fabrication of the DTA, and includes the design and construction of all necessary tooling, fixtures, and jigs necessary to fabricate and test it.

Task 5 is the ground test of the Dynamic Test Article to fully characterize its dynamic performance.

Task 6 is an assessment of the impact of the ground test results on the reliability and performance of future space systems. Technology issues requiring further work will be identified.

Task 7 is technology transfer. It consists of timely oral, visual, and written presentations of program progress and results to the United State government and aerospace industry.

The Boeing Aerospace Company (BAC) has the prime responsibility for the conduct of the RELSAT Program. CSA Engineering, Inc., Anatrol Corp., and the Boeing Commercial Airplane Company (BCAC) will assist BAC in accomplishing the program. Figure 1 illustrates the approach that will be used to combine the efforts of BAC, CSA, Anatrol, and BCAC to achieve the program goals.

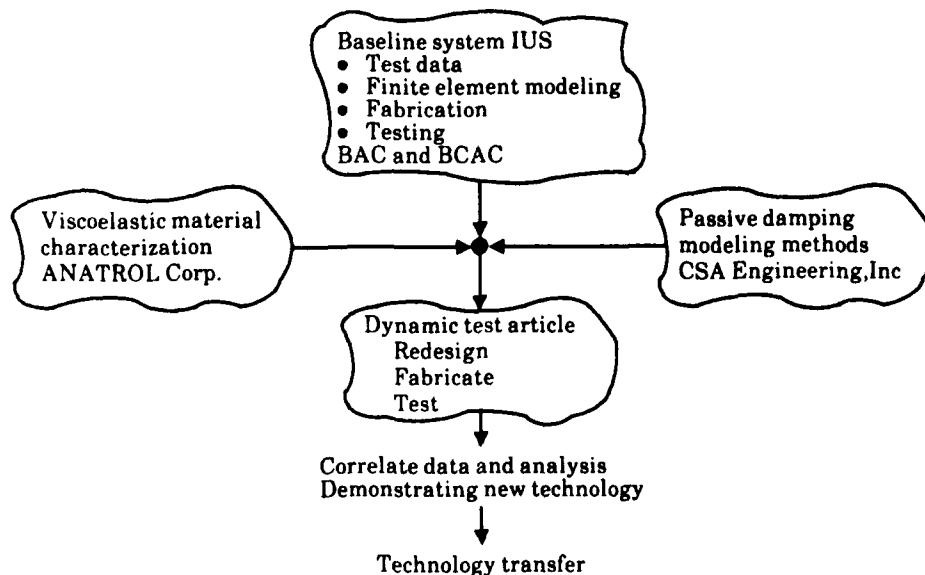


Figure 1: RELSAT Program Approach

Figure 2 illustrates the RELSAT program schedule. This schedule delineates the time allocated for each task and indicates the major milestones critical to the program. The contract was started in March 1983, with a total performance period of five years. The following sections of this paper will describe the current status of the program and some of the technical results obtained to date.

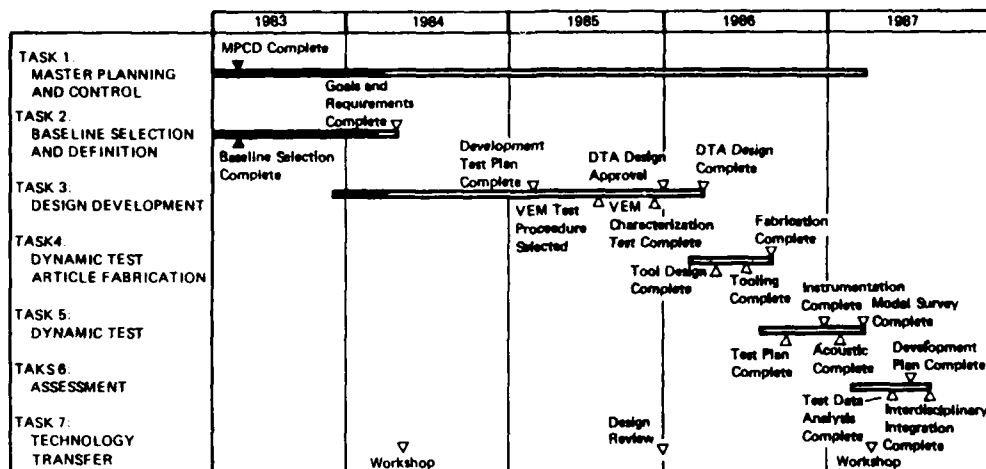


Figure 2: RELSAT Program Schedule

BASELINE SYSTEM SELECTION

The BAC Inertial Upper Stage (IUS) was selected as the baseline system. The following rationale was used for selecting the IUS: 1) the IUS structure is similar to other satellite systems; 2) there exist more than 500 IUS vibration and acoustic measurements which define equipment environments for a variety of structural configurations; 3) the IUS is designed to operate in the Space Shuttle and the Titan launch vehicles; 4) the IUS vibration data are characteristic of other satellite systems; 5) the measured IUS vibration levels are of the magnitude that degrade avionics equipment reliability and performance.

The IUS is shown in figure 3. Like most satellites, it contains avionics mounted on an equipment support section (ESS), propulsion devices and interstage structure. It also has

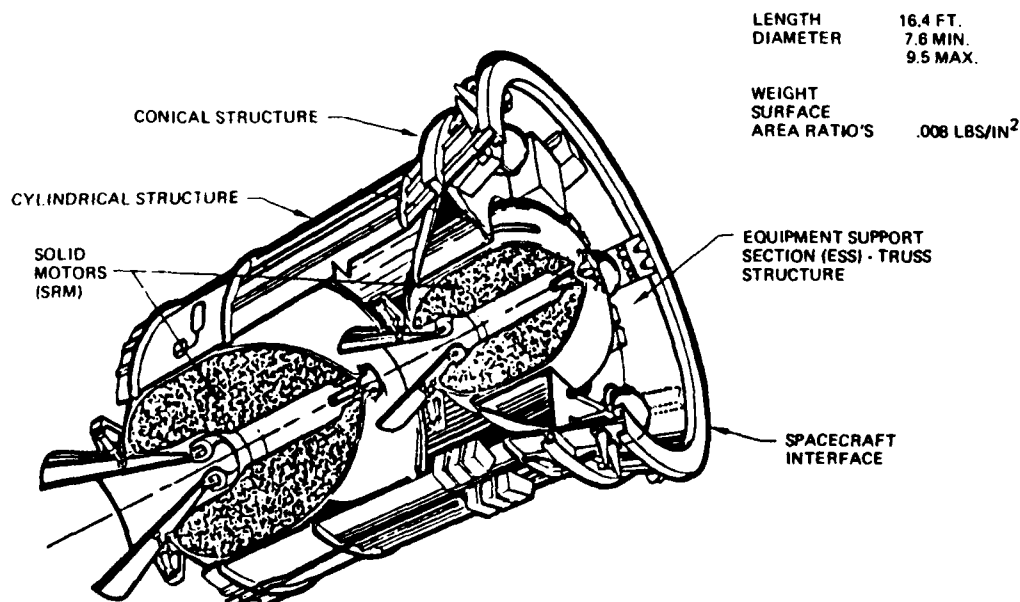


Figure 3: Internal Upper Stage (IUS) Selected for Baseline System

separation devices and structure for interfacing with other vehicles. The interstage and ESS structures are significant structural components for the RELSAT program because they support equipment items and provide vibration environments to the equipment. These structures are lightweight but have large surface areas, which results in high vibration response to noise. The ESS and interstage structure weight-to-surface area ratio is approximately 0.008 pounds per square inch. Other satellites such as the Tracking and Data Relay Satellite (TDRS), the Defense Support Program (DSP) Satellite, and the Defense System Communication Satellite (DSCS) have similar weight-to-area ratios. This type of structure can effectively utilize VEM damping treatments.

Another important reason for choosing the IUS as a baseline was the large amount of available vibroacoustic data. More than 500 vibration and acoustic measurements were made to define the equipment vibration environments. These measurements were made during acoustic tests performed on an IUS Dynamic Test Vehicle (DTV).

The 145 dB noise level applied during the DTV acoustic tests was the design level for payloads carried in the Space Shuttle and the Titan launch vehicle. This acoustic noise environment occurs during launch vehicle liftoff and flight. The IUS vibration response to this noise environment was the highest vibration environment encountered during the IUS mission and defined the equipment design vibration levels. The IUS design vibration levels are in the order of 10 gs rms.

The equipment design vibration levels for other satellite systems are also the result of launch vehicle noise. Since the IUS structure is similar to other satellite structures, the design vibration requirements for equipment are similar. This similarity supports the choice of the IUS as a good baseline system for generic demonstration of vibration control for satellite equipment.

Launch induced vibration levels of the magnitude experienced by the IUS can degrade equipment performance and reliability. Reliability data from MIL-STD-756 indicate that boost vehicle induced environments for satellites are 80 times more severe than orbital environments. This difference is attributed to the vibration and shock environments at launch (reference 1).

The IUS Dynamic Test Vehicle (DTV) was selected as the Dynamic Test Article (DTA) for the RELSAT Program. The IUS DTV has been selected as the DTA for the following reasons: 1) the DTV configuration and structure simulates the operational vehicle static and dynamic characteristics; 2) five vibroacoustic tests and a modal survey were conducted on the DTV to define equipment design vibration requirements; 3) the DTV is available for use in this study.

The DTV was fabricated during the development phase of the IUS program to serve as a static and dynamic test article for development of the production vehicle. A picture of the DTV assembled for an acoustic noise test is shown in figure 4. The configuration and major structural components of the DTV are similar to the IUS flight vehicles. The equipment vibration design and test requirements were obtained from acoustic tests on the DTV.

The five vibroacoustic tests summarized in figure 5 were conducted to define the vibration design requirements for IUS equipment. More than one test was conducted because the magnitude of the noise induced vibration levels created an avionics equipment design problem. During the tests, modifications were made to the IUS structure in an effort to reduce the vibration environment and to understand the interaction between the structure response and the applied noise excitation. Viscoelastic damping material was

applied during test 3. The damping material reduced the vibration response. A modal survey was conducted as part of test 3. The test examined significant vibration modes in the 50 to 300 Hz frequency range. Test 4 was conducted to determine whether IUS vibration response was affected by the acoustic test facility characteristics. Test results showed that the IUS vibration response was independent of the test facilities. Test 5 was conducted as part of a study to design an IUS simulator for use in satellite acoustic tests. The test consisted of measuring the vibration response to 145 dB overall sound pressure level noise excitation. This was done with and without the IUS interstage installed. The test results indicated that the interstage is a significant contributor to the IUS ESS vibration environment.

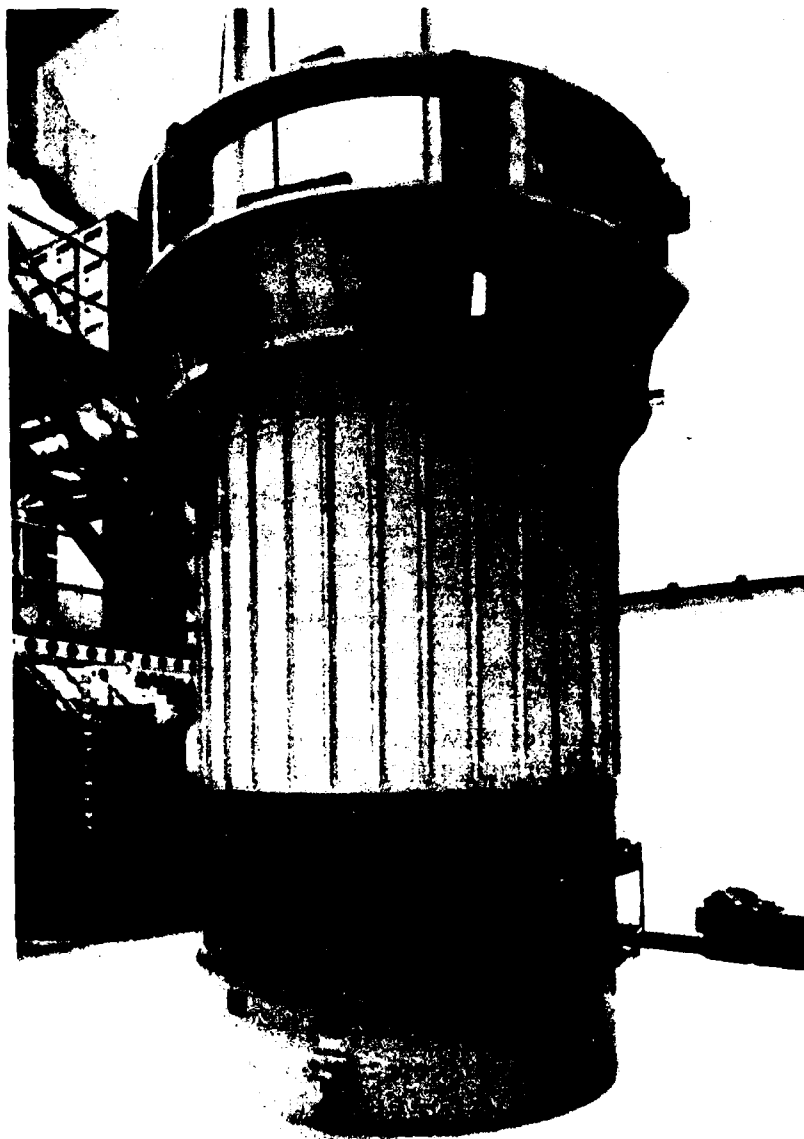


Figure 4: IUS DTV Assembled for Acoustic Noise Testing

TEST NO.	PURPOSE	MEASUREMENTS		TEST LEVEL OVERALL SPL dB
		VIBRATION 1	NOISE 2	
1	Determine equipment vibration response	42	5	139 145 3
2	Determine equipment vibration response on a modified equipment support section	17	5	145 3
3	Determine equipment vibration response 1) One stage configuration 2) Two stage configuration 3) With and without viscoelastic damping Conduct modal survey	53	8	145 3
4	Determine equipment vibration response in a larger acoustic test facility	53	13	145 4
5	Determine equipment vibration response with and without the IUS interstage	38	5	145 3

- 1 Vibration measured 20 to 2000 Hz 2 Noise measured 31.5 to 10,000 Hz
 3 Tested in Boeing 16 ft x 24 ft x 20 ft reverberation room
 4 Tested in Lockheed 88 ft x 50 ft x 44 ft reverberation room

Figure 5: IUS DTV Vibroacoustic Tests

A number of simulated components were installed on the DTV. Five have been selected to represent different structural configurations for studying damping design concepts. These five components are:

1. a 50 pound computer mounted on the conic shell structure;
2. a 5 pound reaction engine mounted near the spacecraft attachment ring;
3. a 20 pound battery mounted on the ESS deck;
4. a 3 pound encrypter mounted on the ESS deck;
5. a 45 pound battery mounted on the interstage.

SYSTEM REQUIREMENTS

Testing conducted on the DTV indicates VEM will reduce vibration, but this advantage may be offset by degradation of performance and reliability in another part of the system. System requirements which are likely to impose constraints on the DTA vibration control designs are contamination (outgassing), thermal and electrical conductivity, hardening (electromagnetic compatibility and electromagnetic interference), structural strength, structural deflection, and weight. Vibration control designs considered for the DTA will be reviewed to ensure that maximum damping is obtained with a minimal impact on other system requirements.

PERFORMANCE GOALS

Performance goals for the vibroacoustic response of the redesigned DTA include the following:

- o Reduce overall vibration levels (0 to 2000 Hz) at IUS equipment locations to 6 grms or less.
- o Limit acceleration power spectral density levels in the 100 to 300 Hz frequency range to $0.1 \text{ g}^2/\text{Hz}$.

Figure 6 compares these goals with measured vibration spectra from the DTV. The spectra were measured at IUS avionics support points during a 145 dB acoustic noise test.

These performance goals were chosen because the vibration reduction should be large enough to increase avionics reliability. Also, the 6 grms level corresponds to the minimum vibration design level specified in MIL-STD-1540A. Reducing satellite vibration to this level would make it possible to incorporate MIL-STD-1540A qualified equipment into a new satellite system with no additional qualification testing. This could greatly reduce the cost of future aerospace programs.

The $0.1 \text{ g}^2/\text{Hz}$ limit over the 100 to 300 Hz frequency range was chosen because of avionics and IUS vibration response characteristics. Avionics chassis and internal circuit boards characteristically have first mode resonant frequencies in the 100 to 300 Hz frequency range (reference 2). Since vibration induced failure is likely to occur in the first mode, it is beneficial to limit vibration input to the avionics box over this frequency range. Figure 6 shows that in the 100 to 300 Hz range the IUS DTV vibration input to avionics is high. Therefore, reducing these high levels will significantly increase avionics reliability. These goals will require spectral peak reductions of approximately 10 dB.

DESIGN DEVELOPMENT

The BAC RELSAT Program is currently involved in the performance of the Task 3 Design Development. This task includes all activities necessary to establish the detailed design

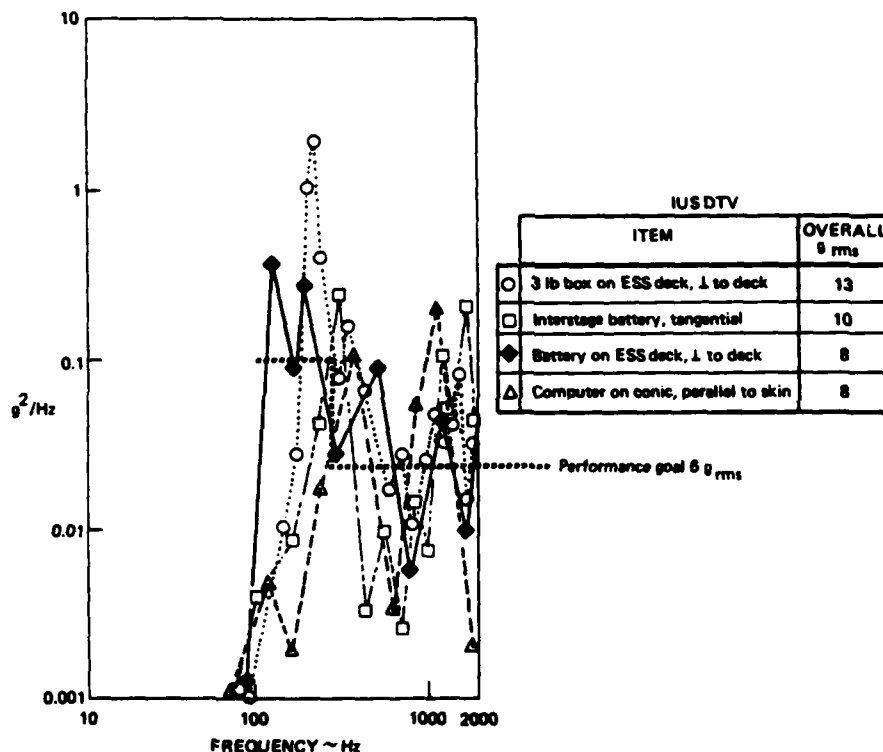


Figure 6: Performance Goals for Redesigned DTA Compared with Baseline Vehicle Vibration Environment

of a damping treatment for application to the DTA. Current efforts are being focused on the development of passive damping design concepts, component developmental testing and finite element analyses, and VEM characterization. The results of these efforts will provide the preliminary data required to initiate the analysis and design activities for the DTA.

DESIGN CONCEPTS

One of the reasons for selecting the IUS as the baseline system was that it contained representative structural components on which a wide variety of VEM damping design concepts could be studied. The design concepts activity is being performed by BAC with support from BCAC, CSA Engineering, and Anatrol. Design concepts are currently being developed which will lead to a full understanding of the benefits and limitations of applying viscoelastic damping to the baseline system. Anatrol is reviewing data on available VEM's and will select the most promising for incorporation into the design concepts. CSA Engineering is conducting analyses to support the damping design concept studies. BAC has fabricated a representative test structure on which the effectiveness of the damping concepts can be assessed. Promising concepts are being fabricated and applied to the test structure which is then subjected to vibration, shock and acoustic testing to determine the effects of the addition of the damping treatment. The detailed knowledge of the IUS baseline system structure and system requirements is aiding in the proper selection of VEM's for development testing and the generation of damping concepts which can be efficiently incorporated into the DTA design.

Some promising design concepts that are currently being considered are shown in figure 7. The concepts shown in figures 7a, b, and c are additive constrained layer treatments that can be applied to the IUS skin panels. Figure 7d shows link and web dampers or integral damping treatments that may be applied to the frame members of the equipment support section shelf. A type of link or axial damper is shown in figure 7e wherein

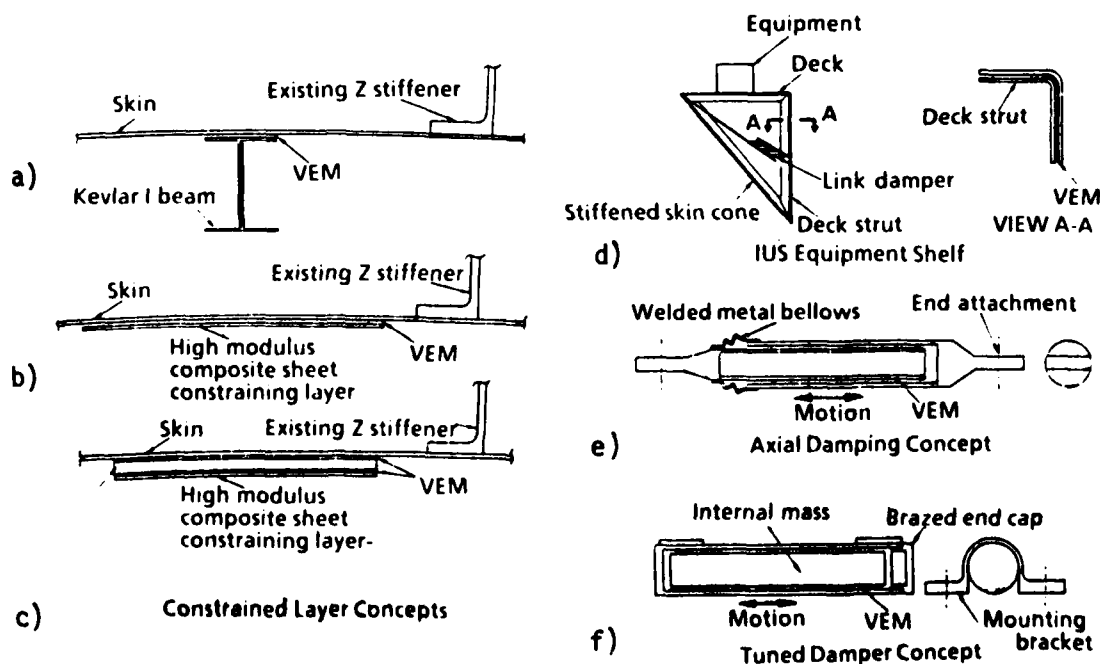


Figure 7: Typical VEM Damping Design Concepts

two close fitting cylindrical sleeves cause shearing motion in the VEM as they move in response to the relative axial motion between the two points of attachment. A tuned damper concept in which a cylindrically shaped free mass on the inside of a sealed unit would cause shearing of the VEM is shown in figure 7f. Other design concepts which are being considered are the use of vibration isolation or composite and injection molded structural components using lossy matrix materials.

The selection and characterization of the VEM that will be used with the damping concepts is currently being performed by Anatrol Corporation. Figure 8 illustrates the procedure that is being followed in determining which VEM will be used with the DTA design. Data from the existing literature is being screened according to two criteria. First, their relevance for satellite application in general will be assessed, and then their applicability to the IUS in particular. From this data list, four materials will be selected for consideration on the RELSAT program. One of these materials will have been sufficiently characterized in the literature so that further testing will not be required. Two other materials will be selected for use in establishing a well defined characterization procedure. Following establishment of a procedure, it will be used to characterize the two materials. Characterization tests will be conducted on the one remaining material to complement the existing data and to verify the recommended characterization procedure. The VEM data will be used to evaluate design concepts using component testing and Finite Element Analysis (FEA) and eventually in the development of the DTA design.

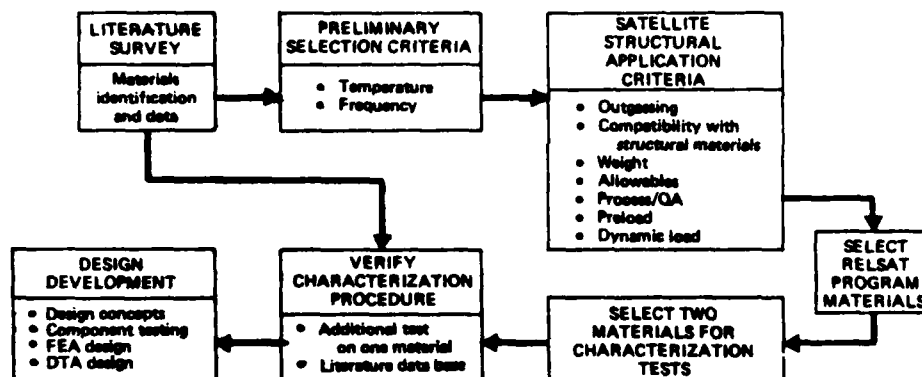


Figure 8: VEM Evaluation Procedure

COMPONENT TESTING

From previous testing performed on the DTV, it was known that the IUS interstage and equipment support section transmitted acoustically induced vibration to the avionics equipment. Therefore, a component test structure which represents a segment of the IUS second stage, second stage motor support cone, and equipment support deck between two spacecraft support longerons was designed and fabricated. A drawing of the component test structure is shown in figure 9. A picture of the test structure with a simulated electronic component mounted on the equipment deck is shown in figure 10. The structure is aluminum skin/stringer construction with all rivets replaced by bolts to facilitate future removal of portions of the structure to add damping treatments.

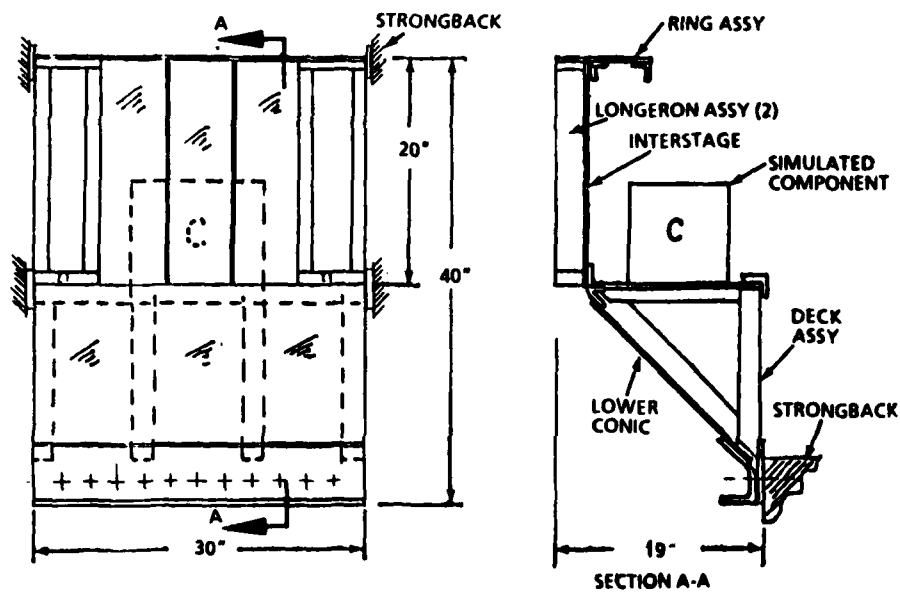


Figure 9: Test Article



Figure 10: RELSAT Component Test Structure

A modal survey test was performed to determine the mode frequencies and corresponding mode shapes and modal damping values for the test structure. A steel strongback test fixture was fabricated to fix the test structure at the upper and lower rings and along the motor support ring at the bottom end of the lower conic. Figure 11 shows the test article in the vibration test fixture. An electromagnetic vibration exciter was attached to a corner of the simulated electronic component and used to excite the structural modes which contained dominant component motions. The electromagnetic shaker was used to drive the box in the axial, radial and tangential directions. Sine sweeps were run in a frequency range between 50 to 400 Hz. Modal frequencies, damping ratios and shapes were obtained for all of the dominant modes of the test article in that frequency range. This test data is being used as a baseline for the comparison of the effectiveness of the various applied damping treatments, and to compare the results of the analytical finite element modeling.



Figure 11: RELSAT Component Test Structure in Vibration Test Fixture

FINITE ELEMENT ANALYSIS (FEA)

Finite Element Analyses are being performed by BAC and CSA Engineering, Inc. FEA will be the primary analytical modeling tool because it is appropriate for the complex structural geometry of the DTA. Also, recent advances in the use of FEA for modeling viscoelastically damped structures make the method particularly applicable for the RELSAT program (reference 3). The primary computer code for all FEA work will be the NASTRAN program.

The analysis tasks are broadly divided into two groups: those dealing with modeling the entire DTA structure and those dealing with smaller DTA structural components. It is anticipated that not only will the design concepts be developed by first applying them to structural components and subassemblies, but also efficient analytical modeling methods. New ideas will be tried first with models of easily manageable size so that problems can be isolated and solved one at a time. The design concepts and the FEA modeling techniques developed will then be applied to the detailed design development of the DTA.

A NASTRAN finite element model of the component test structure was developed by BAC to correlate with the results of the modal survey testing. An exploded view of the model is shown in figure 12. This model consisted of 708 nodes and 725 elements. A normal modes analysis was performed in NASTRAN using generalized dynamic reduction. Several major revisions to the model were made before an acceptable correlation with the modal survey tests results were achieved. A visual comparison between predominant electronic component test and analysis modes is shown in figure 13. Although a fairly good correlation with the test results was finally obtained, it was apparent that the finite element modeling would have to be greatly simplified to be practical for modeling the entire DTA. This model is currently being used by CSA Engineering to model the damping treatments to be applied to the component test structure and to develop more efficient modeling techniques.

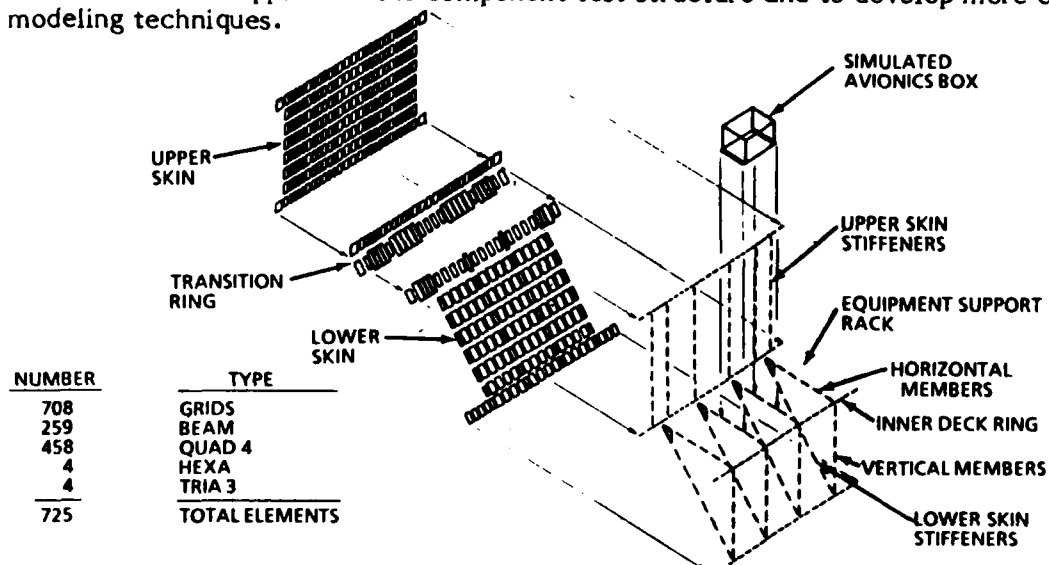


Figure 12: Exploded View of RELSAT Component Test Structure NASTRAN Model

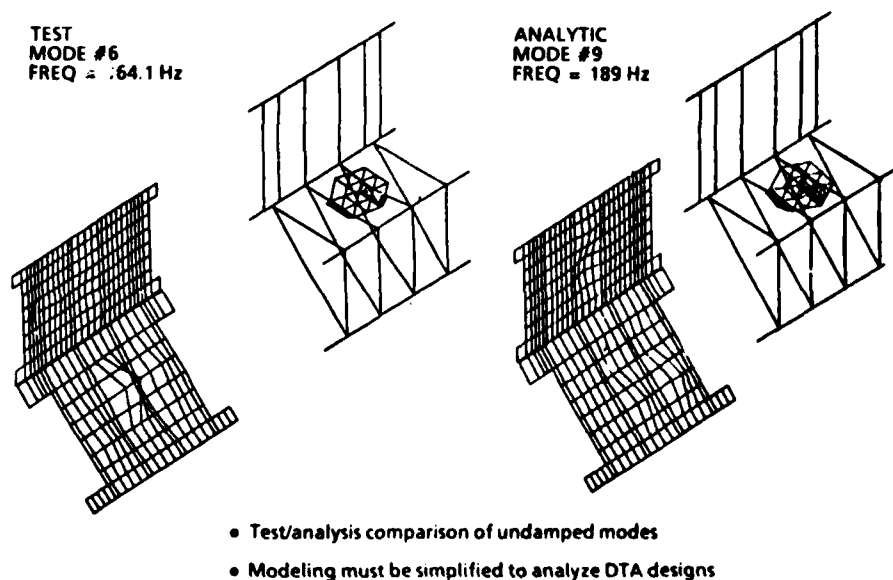


Figure 13: RELSAT Component Development Testing Results

SUMMARY

The BAC RELSAT program is a long term effort that is structured to effectively demonstrate recent advancements in passive damping technology. The application and validation of VEM vibration control techniques on a typical aerospace satellite system will demonstrate that damping design can be considered early in the design process for future satellite systems with a minimal effect on the overall system cost and weight. However, before this can happen, the impact of the design damping treatments on the other system level requirements must be addressed. It is anticipated that data developed in the RELSAT program will serve this purpose. During this program, an aggressive effort will be made to transfer the technology to the design community. It is felt that there will be a large potential payoff for future systems in the form of lower avionics equipment costs, savings in the time and cost of qualification testing, and an increase in overall system reliability.

REFERENCES

1. "Avionics Reliability", Swett, B. H., Shock and Vibration Bulletin 45, Part 2, June 1972, pg. 30.
2. "Vibration Analysis for Electronic Equipment", D. S. Steinberg, 1973, John Wiley and Sons, New York, pp. 49, 260.
3. "Finite Element Prediction of Damping in Structures with Constrained Viscoelastic Layers", Johnson, C. D., and Kienholz, D. A., AIAA Journal, Vol. 20, No. 9, pp. 1284-1290, Sept. 1982.

DAMPING IN SUPPORT STRUCTURES
FOR
SATELLITE EQUIPMENT RELIABILITY - RELSAT

J. A. Staley and C. V. Stahle
General Electric Space Systems Division
Valley Forge Space Center
P. O. Box 855
Philadelphia, Pennsylvania 19101

DAMPING IN SUPPORT STRUCTURES
FOR
SATELLITE EQUIPMENT RELIABILITY - RELSAT

J.A. Staley
and

C.V. Stahle

General Electric Space Systems Division
Valley Forge Space Center
P.O. Box 855, Philadelphia, PA 19101

ABSTRACT

This paper presents a discussion of the General Electric RELSAT (Reliability for Satellite Equipment in Environmental Vibration) program. This program is sponsored by the Flight Dynamics Laboratory, Air Force Wright Aeronautical Laboratories. The need for and benefits from applying damping treatments to satellite equipment panels to reduce component vibration during launch and ground vibration tests are discussed. Application of the same technology would directly benefit efforts to provide very stable platforms to meet high pointing accuracy requirements of satellites. The technology used to develop damped panel designs is discussed briefly, and a cost-reliability model used to assess the cost benefit of reduced vibration is described. The RELSAT program to demonstrate this technology for vibration reduction of damped satellite equipment panels is described.

DISCUSSION

The objective of the GE RELSAT program is to generically demonstrate passive damping control of panel mounted component vibration. The approach is to design, fabricate, and test damped representations of bay three of the Defense Satellite Communication System (DSCS) III spacecraft transponder panel. The DSCS III is designed to be launched in pairs using the Space Shuttle and Inertial Upper Stage (IUS). Some of the major activities involved include evaluating candidate damping material properties, developing and implementing damped panel design concepts, and performing vibration, acoustic, shock and static tests of damped panels. The payoffs from this effort will include:

- 1) A 20 percent increase in reliability through a 50 percent reduction in vibration environment;
- 2) A reduction in the large number of vibration test failures by 50 percent;
- 3) A reduction in a global communication satellite system development/operating cost by \$40M

A review of available data provides a qualitative evaluation of damping pay-offs. The flight and ground test failures experienced in the past indicate the significance of the vibroacoustic environment on spacecraft reliability and development cost. Recent specifications with increased equipment test levels show a trend which continues to emphasize the need for vibration control.

A significant number of on-orbit failures or malfunctions have been observed during the initial month of spacecraft operation which are believed to be traceable to the vibration environment. Data obtained from the evaluation of early flight failures from a number of NASA spacecraft are shown in Figure 1 (1). Each failure/malfunction was evaluated relative to its origin. As indicated by the bar graph, approximately half of the failure/malfunctions are considered to be traceable to vibration.

Satellite qualification and acceptance test data indicate that the vibroacoustic environment is a major cause of ground test failures. The data from four spacecraft programs using MIL-STD-1540 environmental tests was examined to determine test effectiveness (2). The vibroacoustic failures per satellite are summarized in Figure 2. During qualification testing, there was an average of 98 test failures per satellite of which 64 percent were vibroacoustic test failures. Subsequent acceptance tests of the qualified satellite designs exposed an average of 25 failures per satellite of which 30 percent occurred during vibro-acoustic testing. This high rate of acceptance test failures tends to indicate that an inherent susceptibility to dynamic stress exists even after a design has been qualified. These recent test data show the vibro-acoustic testing to be a major cost driver during spacecraft environmental development and acceptance testing.

The general trend in the recent past has been to increase the vibration requirements for satellite components and to revise equipment designs until they pass increased vibration test levels. Figure 3 shows a history of increasing component test levels and a decreasing portion of components passing vibration tests. At current test levels approximately 40 percent of components require design changes during development to meet increasing vibration test requirements.

A comparison of current, past and damped panel vibration requirements indicates that the damped panel requirements are less than past requirements. Figure 4 shows maximum expected random vibration requirements for Space Transportation System (shuttle) launched spacecraft. The "Past Small Spacecraft" levels are representative of spacecraft which could be launched on either large expendable boosters or on the shuttle. The "Current Large Spacecraft" levels are representative of large spacecraft designed specifically for shuttle launch. The lower "Damped Spacecraft" requirement represents levels which can be obtained by damping equipment panel mounting structure. The damped levels are almost within the requirements used for past spacecraft equipment. On the otherhand, the "Large Spacecraft" requirements are well above those used in the past in the low frequency range of major equipment resonances. The damped panel provides requirements compatible with current equipment designs and saves the cost of component redesign and development for the higher vibration levels. This obviously enhances the vibroacoustic reliability of the equipment.

Damping materials have been used for controlling satellite vibration levels during launch for the past ten years. Damping treatments have been extensively applied to printed wiring boards in the electronic components to increase reliability and to reduce deflections and thus allow more compact component designs (3). Damping treatments have also been applied to a limited number of secondary structures (4). Damping materials for use in spacecraft applications have been available and have been used for some time (5). These materials have high damping capability, result in low damping treatment weight and are space compatible. Figure 5 shows the viscoelastic material properties of interest for damping treatment designs. These properties may be expressed in terms of a complex modulus:

$$G^* = (1 + i\eta)G \quad (1)$$

where η is referred to as the damping material loss factor (damping characteristic) and G is the real part of the complex shear modulus. Both η and G are temperature and frequency dependent. The temperature/frequency dependence are related and this relationship may be shown on a reduced frequency plot as in Figure 5 for a damping material designated SMRD 100F90. This approach to presenting damping material properties was developed by D.I.G. Jones (6). Any temperature/frequency combination corresponds to a reduced frequency. A unique pair of values of shear modulus G and loss factor η is assumed to exist at each value of reduced frequency.

Table 1 shows the reduction in vibration previously achieved by adding damping to spacecraft structures. Applications have been made to ERTS, VIKING, IUE satellites as well as the BSE and ETS-III Japanese satellites. Table 1 shows results for vibration amplification factors before and after damping applications. Amplification factors were reduced nearly an order of magnitude from values as high as 65 to as low as 2.5.

Practical methods available for damping treatment designs using viscoelastic materials generally fall into two categories: a) simple "closed form" methods (7), and b) finite element modal strain energy (MSE) methods (8). Both methods make use of damping material shear modulus and loss factor in the treatment design.

In the modal strain energy approach, the composite loss factor for the damped structure is computed by first analyzing a finite element model of the structure without damping. The modal strain energy is computed for the damping material and for the total structure (including the damping material strain energy) for a given mode. The ratio of these two is multiplied by the damping material loss factor to obtain the system or composite loss factor for a particular mode:

$$\eta_c = \eta \frac{MSE(v)}{MSE(total)} \quad (2)$$

Since the damping material properties are frequency and temperature dependent, the material loss factor used will depend on the temperature for the particular application and on the computed undamped modal frequency. The shear modulus is also frequency dependent, but the modal analysis is done with a representative shear modulus at the temperature of interest and at the nominal frequency of interest.

Any iteration on the design parameters will require re-running the finite element modal strain energy analysis. The cost of iteration on the design depends on the complexity of the finite element model of the structure being analyzed.

Figure 6 shows an equipment panel which supports two electronic components. The panel was treated with a constrained layer damper strip running in the long direction near the center of the panel. The panel was assumed to be simply supported. Figure 6 shows the fundamental mode shape computed using the finite element model.

Figure 6 also shows the effect of varying the graphite/epoxy constraining layer and the viscoelastic material (SMRD 100F90) thicknesses on the percent of modal strain energy in the viscoelastic material for the fundamental panel mode. With this approach, a damping treatment design was obtained which was expected to give a composite loss factor of about 0.2 for a damping material loss factor of about 1.0 (see Figure 5 at 25 Deg C and 100 to 200 Hz where the composite loss factor is approximately 1.0). Since the amplification factor Q at resonance is the inverse of the composite loss factor, a maximum amplification factor of 5 would be expected.

Figure 7 shows test results for the panel shown in Figure 6. Results are for response in acoustic tests of two similar panel structures except for the addition of the damper strip. The random vibration response shown near one of the components is seen to be significantly reduced with the addition of the damper strip. Significant reduction is shown at the fundamental resonance and higher frequencies.

A method of quantification of damping payoffs is the OCTAVE code which focuses on the key elements of candidate space systems and provides an estimate of the reliability and dollar benefits derived from vibration control. The evaluation of the effects of the vibroacoustic environment on the cost and reliability of space systems is a difficult task that has been studied in depth at GE Space Systems Division. The need to prepare for the Space Shuttle from the standpoint of payload vibroacoustic testing was recognized early in the STS program. GE subsequently performed an extensive four year investigation of cost effective vibroacoustic test methods for STS payload development which resulted in the OCTAVE code and numerous publications (9 to 16). The approach in the study was to use Statistical Decision Theory to evaluate the expected costs of selecting alternate test programs and various test levels. This is shown schematically by the Decision Tree or action space in Figure 8.

The expected cost resulting from the selection of a particular test option is the sum of the direct and probabilistic costs. All costs during the life of the spacecraft are considered. The direct and probabilistic cost elements are summarized in Figure 8. The probabilities are based on stress-strength statistical analysis using component test data and spacecraft reliability models at the component "black box" level of assembly.

The damping payoffs are estimated at a savings of approximately \$40M and a significant increase in the reliability after being exposed to the launch vibroacoustic environment for a typical satellite system requiring four spacecraft operating simultaneously and planned for extended life. The damping payoff was estimated using OCTAVE with the vibroacoustic changes being reflected in a reduction in the environment. For a reference, the OCTAVE code was used to estimate the Expected Program Cost using a 145 dB acoustic environment. The damping effect was included by reducing the vibration and acoustic environment by 6 db, i.e., to a 139 dB environment. The flight failure probability is estimated to be reduced by approximately 20% (.0048 to .0040). The expected cost is shown to be reduced by \$2.8M per spacecraft. Considering this savings to be applicable to all of a complete series of 14 spacecraft, a total savings of \$40M is estimated.

Figure 9 shows the GE RELSAT program plan. This figure indicates that the program consists of seven major tasks. Two of these comprise about 60 percent of the effort: design development and dynamic/static testing. The remaining tasks include planning and control, baseline system selection, fabrication of the dynamic test article, and technology assessment and transfer. The program is currently in the design development task which should be concluded in the middle of calendar year 1985.

Figures 10 through 14 show the DSCS III system selected for demonstrating the effectiveness of damping technology to reduce equipment panel vibroacoustic environments. Figure 10 shows two DSCS III spacecraft on the IUS in the Space Shuttle prior to injection into orbit. Figure 11 shows the DSCS III with solar arrays stowed. The North panel is shown in Figure 12. Figure 13 shows an add-on damper treatment for Bay 3 of the DSCS III North panel. Two constrained layer damper strips are added to two existing panel stiffeners. Figure 14 shows Bay 3 of DSCS III North panel with five integrally damped stiffeners. A Dynamic Test Article will be built which will accommodate two panels representative of Bay 3 of the DSCS III North Panel. During acoustic testing two Dynamic Test Articles will be used to test three damped panel designs and one reference panel. A total of six damped panel designs will be tested.

Figure 15 shows a road map of the subtasks making up the design development task of the GE RELSAT program. Three major categories of effort are design, analysis, and materials selection/evaluation. Efforts which are currently being worked include preliminary design and analysis of damped panel designs and development of a test plan to determine a viscoelastic materials test procedure and to measure viscoelastic material properties for candidate panel damping materials for the dynamic test article. As indicated previously, all the design development effort indicated in Figure 15 is expected to be completed by the middle of calendar year 1985. Figure 16 shows some results obtained from preliminary analysis efforts aimed at obtaining optimum designs. What is desired is a damped panel design which provides adequate damping at least weight. Figure 16 shows two damped panel stiffener concepts which provide the same fundamental panel mode frequency and an objective damping level of a minimum loss factor of .3 for the first four panel modes. Configuration 2, however, provides the required damping at approximately half the weight for the panel structure. Note that the damping level at frequencies out to 500 Hz may be too low for Configuration

2 since we are interested in damping acoustic response which may require higher damping than shown for frequencies to 500 Hz. The requirement for damping in this frequency range will be established to provide adequate criteria for damping treatment design.

Figure 17 shows the subtasks associated with testing the damped panel designs which will be developed. Six damped panel designs will be developed. These panels along with baseline undamped panels will undergo modal survey, sine vibration, pyro-shock, static load and acoustic tests. Two series of acoustic tests will be conducted. Three damped panel designs and one reference panel will be tested in each series.

CONCLUSIONS

Satellite and ground vibration test histories indicate a significant number of vibration related anomalies. Past history has indicated a progressive increase in the severity of launch vibroacoustic environments. With the available viscoelastic damping technology, significant cost and reliability improvements can be achieved by applying damping to satellite equipment panels. The GE RELSAT program will generically demonstrate passive damping control of panel mounted component vibration and will establish by appropriate material and damped panel testing the confidence in damped panel design techniques required to make extensive applications in satellite secondary structure design.

REFERENCES

1. A.R. Timmins and R.E. Heuser, A Study of First Day Space Malfunctions, NASA TND-6474, 1971.
2. R.B. Laube, Methods to Assess the Success of Test Programs, Proc. of the 3rd Aersp. Testing Sem., Oct. 1982.
3. J.M. Medaglia, Dynamic Integrity Methods Including Damping for Electronic Packages in Random Vibration, 50th Shock and Vib. Bull., 1980.
4. J.M. Medaglia and C.V. Stahle, SMRD Damping Applications, SAMPE Series Volume 25, 1980, pp. 90-102.
5. C.V. Stahle, A.T. Tweedie, and T.M. Gresko, Viscoelastic Epoxy Shear Damping Characteristics, Shock and Vib. Bull. No. 43, 1973.
6. D.I.G., Jones, A Reduced-Temperature Nomogram for Characterization of Damping Material Behavior, 48th Shock and Vib. Symp., Oct. 1977.
7. F. Abdulhadi, Transverse Vibrations of Laminated Plates with Viscoelastic Layer Damping, Shock and Vib. Bull. No. 4, Dec. 1969.
8. L.C. Rogers, C. Johnson, and D.A. Kienholz, Finite Element Predictions of Damping in Beams with Constrained Viscoelastic Layers, Proc. of 22nd Struct., Struct. Dyn. and Mat. Conf., May 1981.
9. C.V. Stahle, H.R. Gongloff, J.P. Young, and W.B. Keegan, Shuttle Payload Minimum Cost Vibroacoustic Tests, Proc. 1977 Annual Reliab. and Maint. Symp.
10. C.V. Stahle, Cost Effectiveness of Spacecraft Vibration Qualification Testing, Proc. of Inst. of Env. Sci., 20th Annual Mtg., May 1974.
11. C.V. Stahle and H.R. Gongloff, Vibroacoustic Test Plan Evaluation Study on Component Environmental Specification Development and Test Techniques, Vol. 2, GE Doc. No. 76SDS4223, 1976.
12. C.V. Stahle and H.R. Gongloff, Vibroacoustic Test Plan Evaluation, Study on Development of Cost Effective Alternate Approaches to Creating Shuttle Spacelab Payload Environmental Test Requirements, Vol. 3, GE Doc. No. 76SDSD4223, 1976.
13. C.V. Stahle and H.R. Gongloff, Vibroacoustic Test Plan Evaluation, Parameter Variation Study, GE Doc. No. 76SDS4285, 1976.
14. C.V. Stahle and H.R. Gongloff, Shuttle Payload Vibroacoustic Test Plan Evaluation, Free Flyer Payload Applications and Sortie Payload Parametric Variations, GE Doc. No. 77SDS4250, 1977.
15. C.V. Stahle and H.R. Gongloff, Vibroacoustic Test Plan Evaluation, OCTAVE Computer Program, Program Manual, GE Doc. No. 78SDS4227, 1978.
16. C.V. Stahle and H.R. Gongloff, Vibroacoustic Test Plan Evaluation, OCTAVE Computer Program, User's Manual, GE Doc. No. 78SDS4226, 1978.

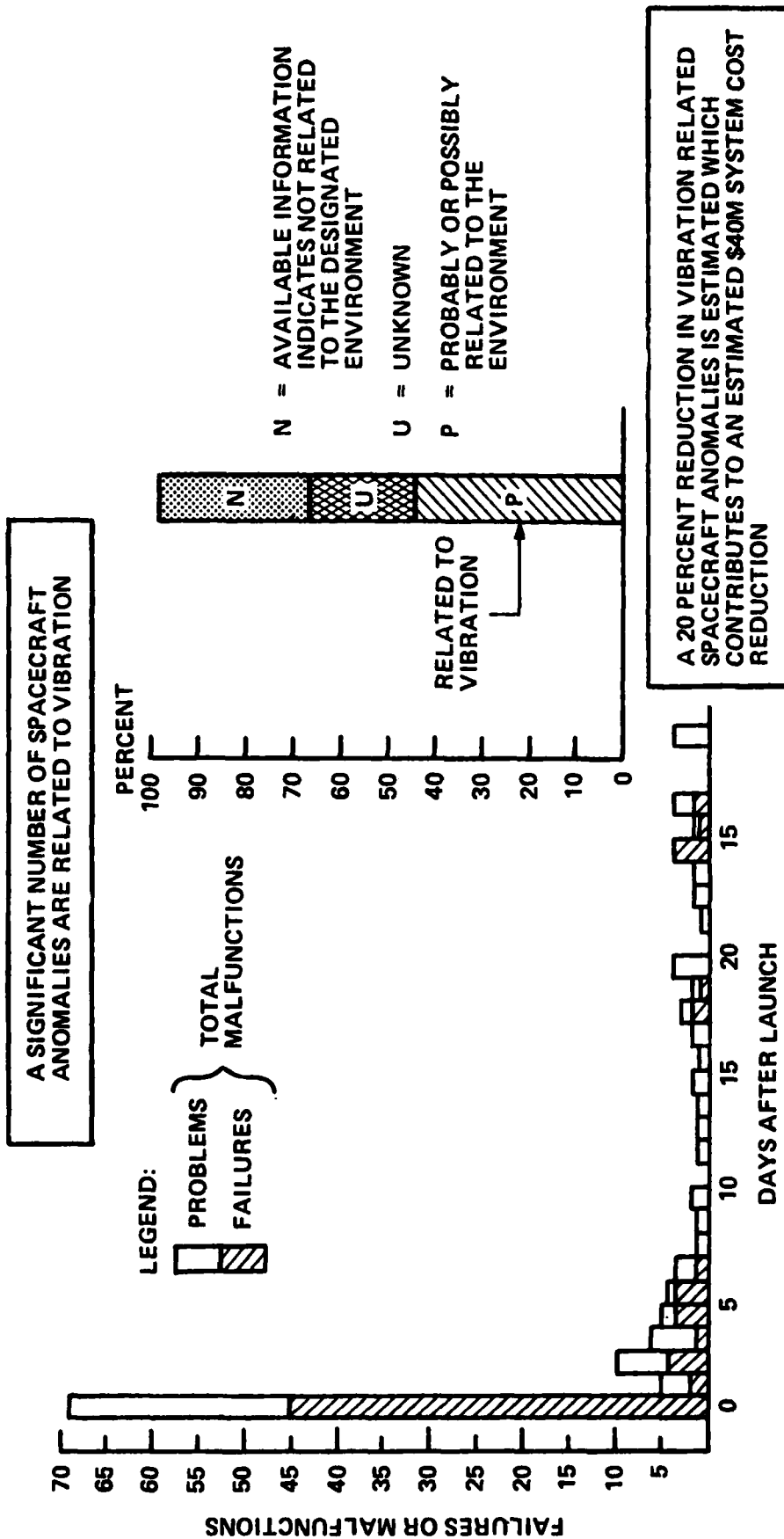
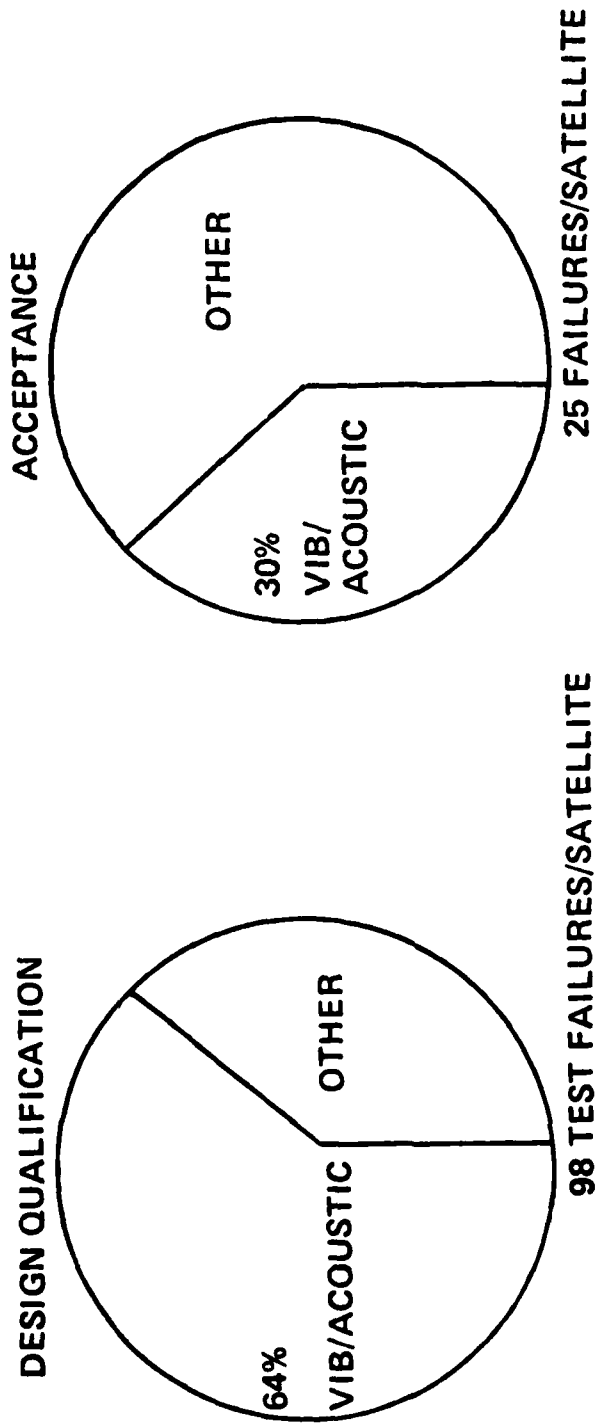


Figure 1. Summary of Early Satellite Anomalies



A 50% REDUCTION IN VIB/ACOUSTIC
GROUND TEST FAILURES IS ESTIMATED

REF: OCT 82 AEROSPACE TESTING SEMINAR

Figure 2. Summary of Vibroacoustic Test Failures

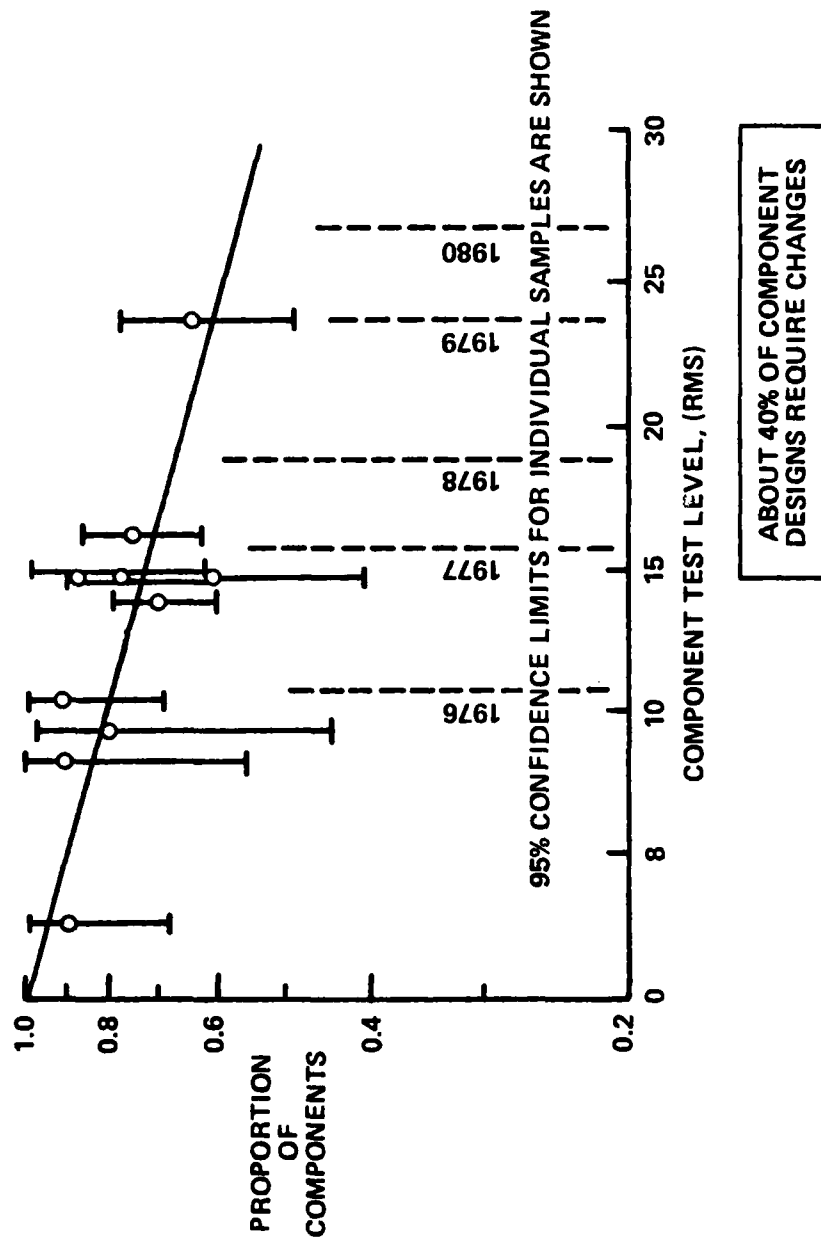


Figure 3. Components Passing Vibration Tests

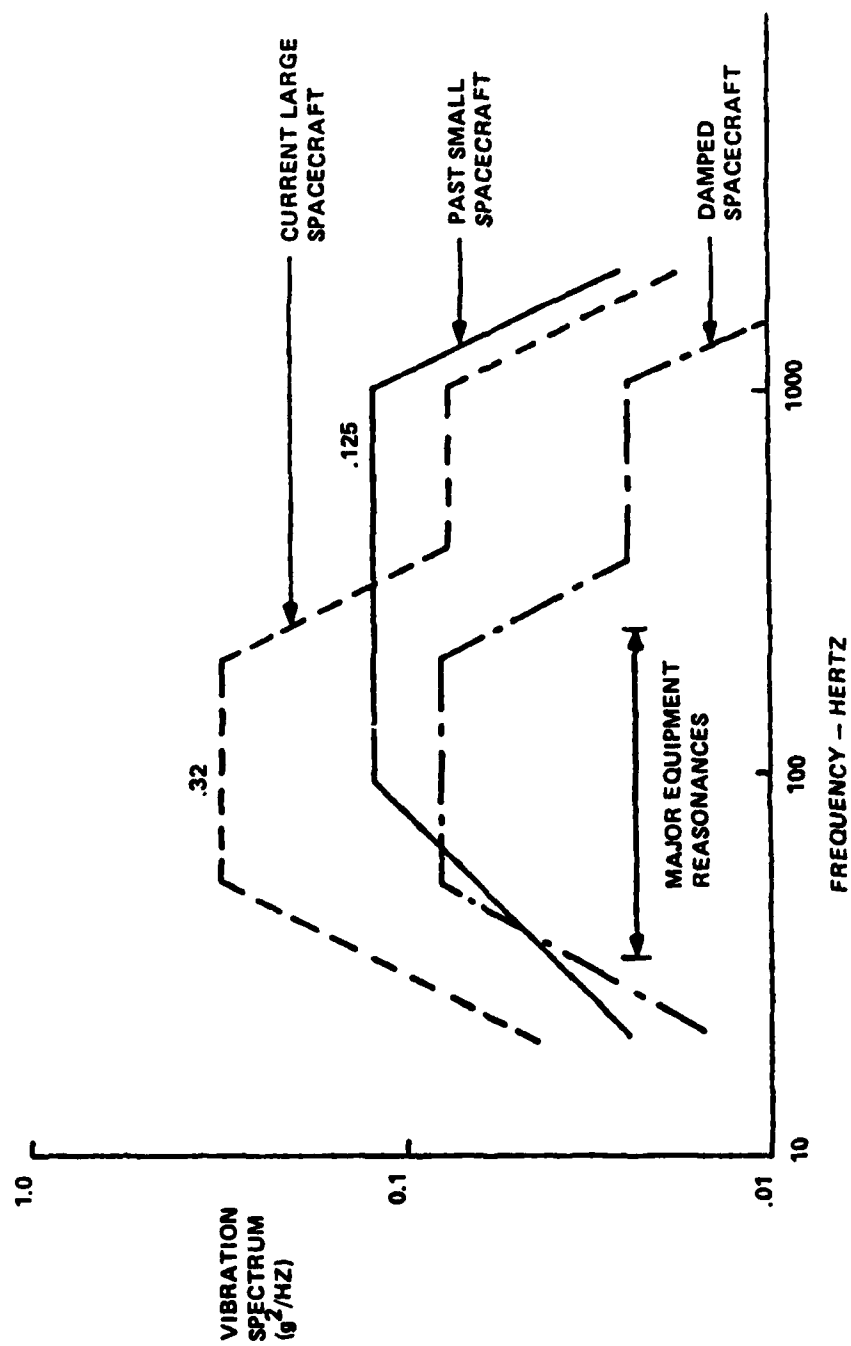


Figure 4. Equipment Random Vibration Requirements

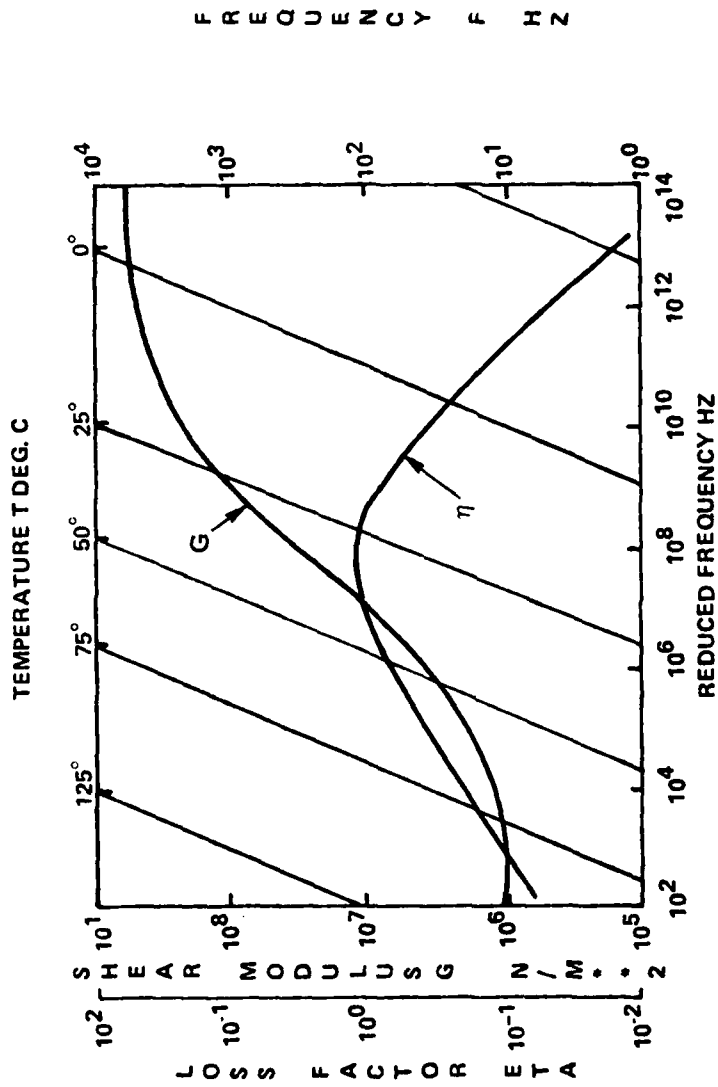
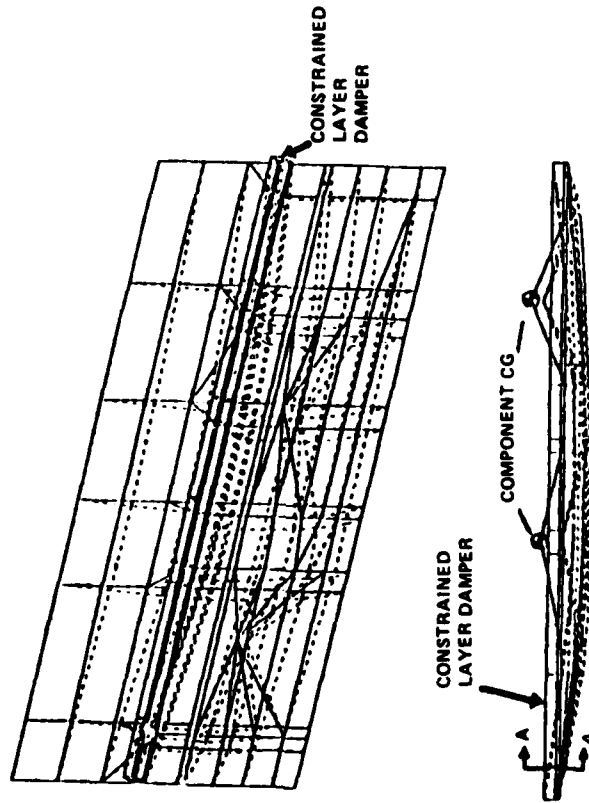


Figure 5. Damping and Stiffness Properties for SMRD 100F90

• JLE NASTRAN MODEL
AND FIRST MODE SHAPE



• NASTRAN PARAMETRIC OPTIMIZATION OF DAMPER DESIGN

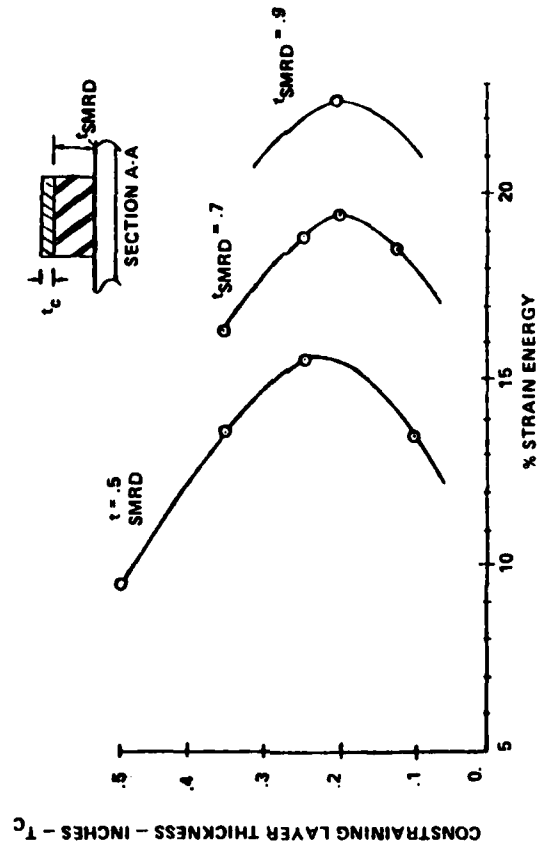


Figure 6. Optimization of Damping Treatment
Using the Modal Strain Energy Method and NASTRAN

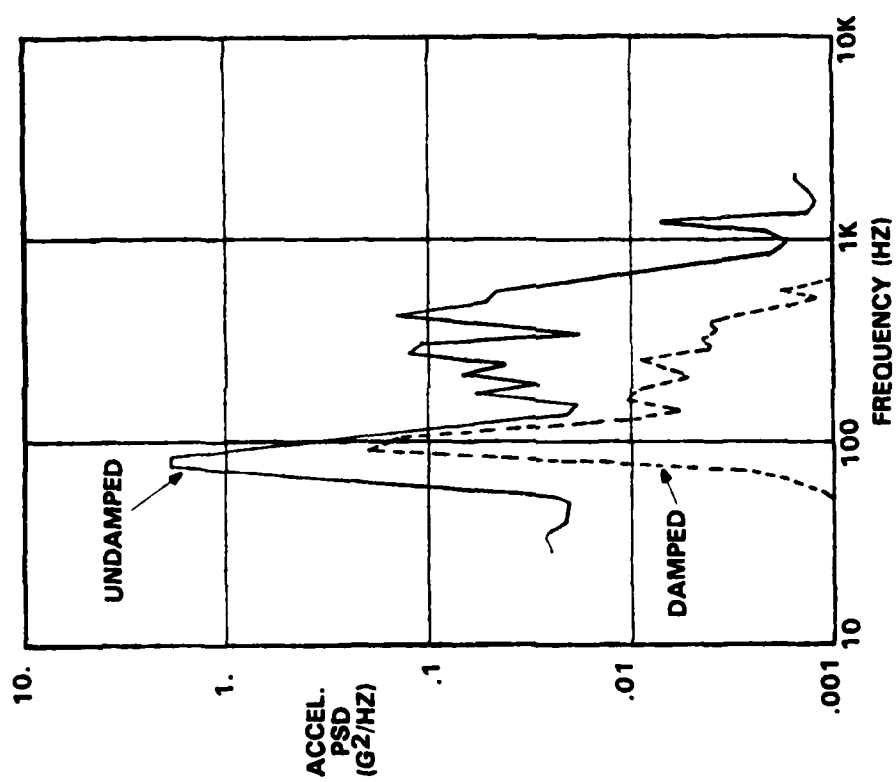
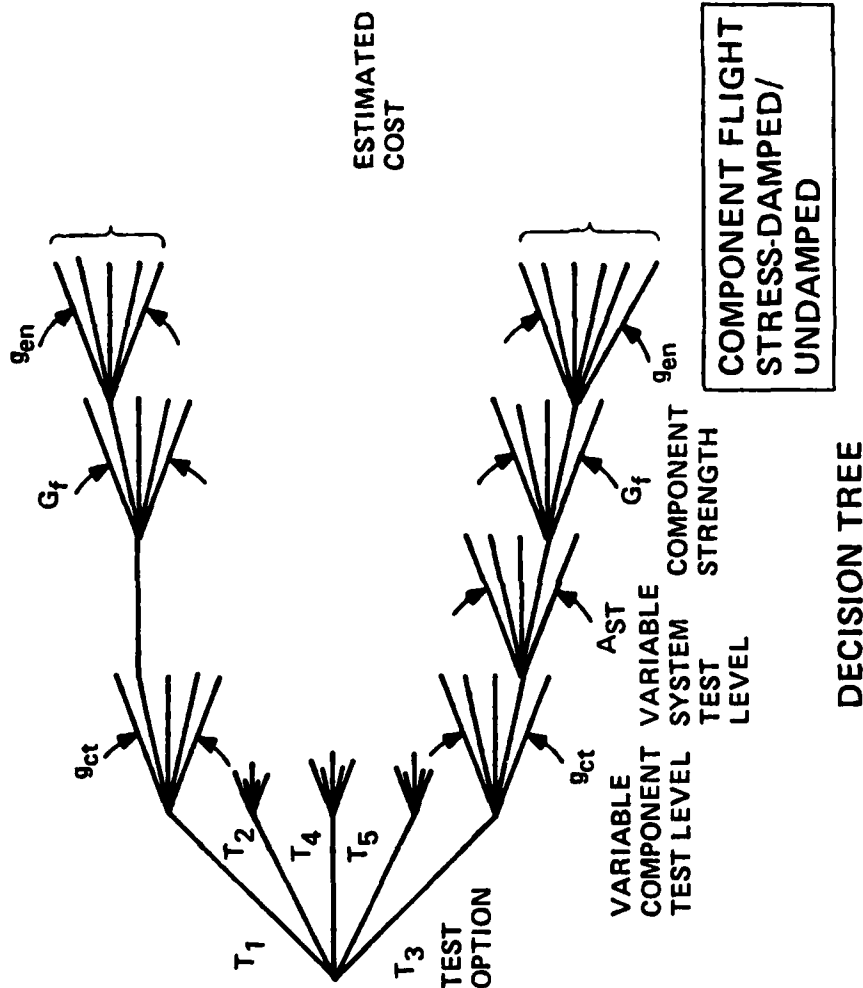


Figure 7. Panel Acoustic Response
With and Without a Viscoelastic Damper

COST TYPE	COST PARAMETER
DIRECT	PROTOTYPE COMPONENTS
	COMPONENT TESTS
	SUBASSEMBLY TESTS
	SDM AND SDM TEST
	PROTOFLIGHT SYSTEM TEST
PROBABILISTIC	STRUCTURAL WEIGHT
	DESIGN COST
	COMPONENT TEST FAILURES
	SUBASSEMBLY TEST FAILURES
	STRUCTURAL TEST FAILURES
	SYSTEM TEST FAILURES
	FLIGHT FAILURES



A \$40M REDUCTION IS ESTIMATED FOR A OPERATIONAL SPACECRAFT DESIGN

Figure 8. Cost Model to Estimate Vibroacoustic Effects

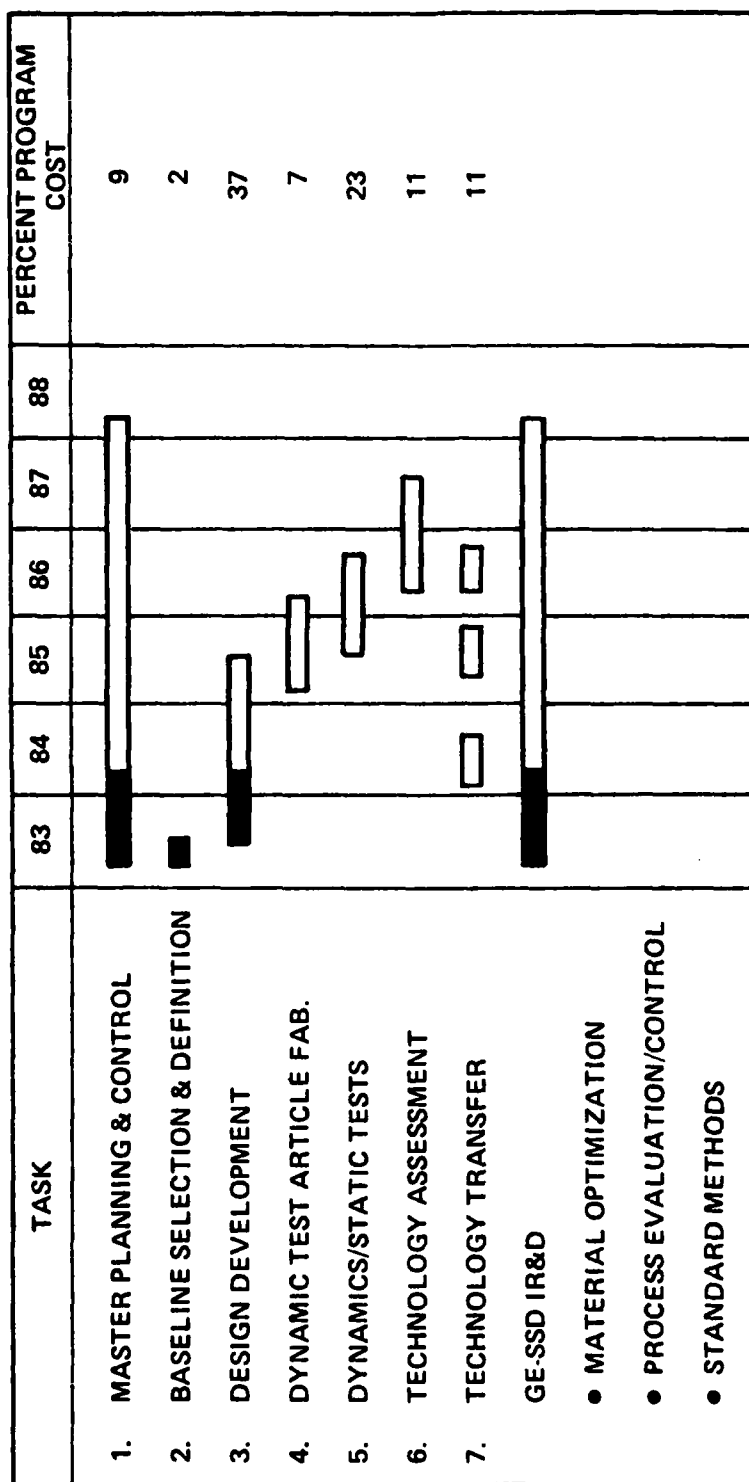


Figure 9. GE RELSAT Program Plan



Figure 10. DSCS III-III/IUS/Space Shuttle



GENERAL ELECTRIC
SPACE SYSTEMS DIVISION



Figure 11. DSCS-III with Solar Arrays Stowed Concealing North Panel

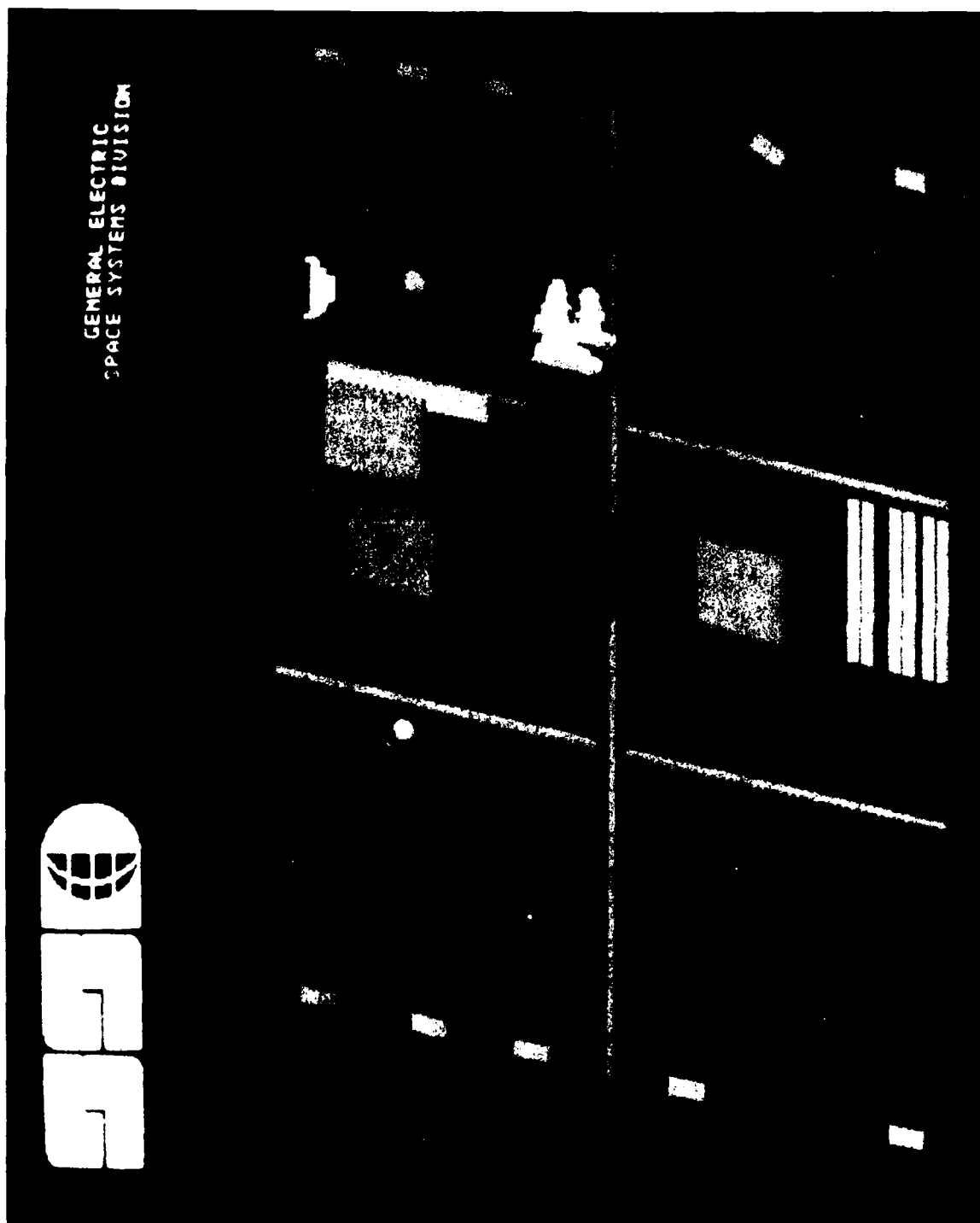


Figure 12. DSCS-III North (Transponder) Panel



Figure 13. DSCS-III North Panel Bay 3 with Two Add-on Damper Strips

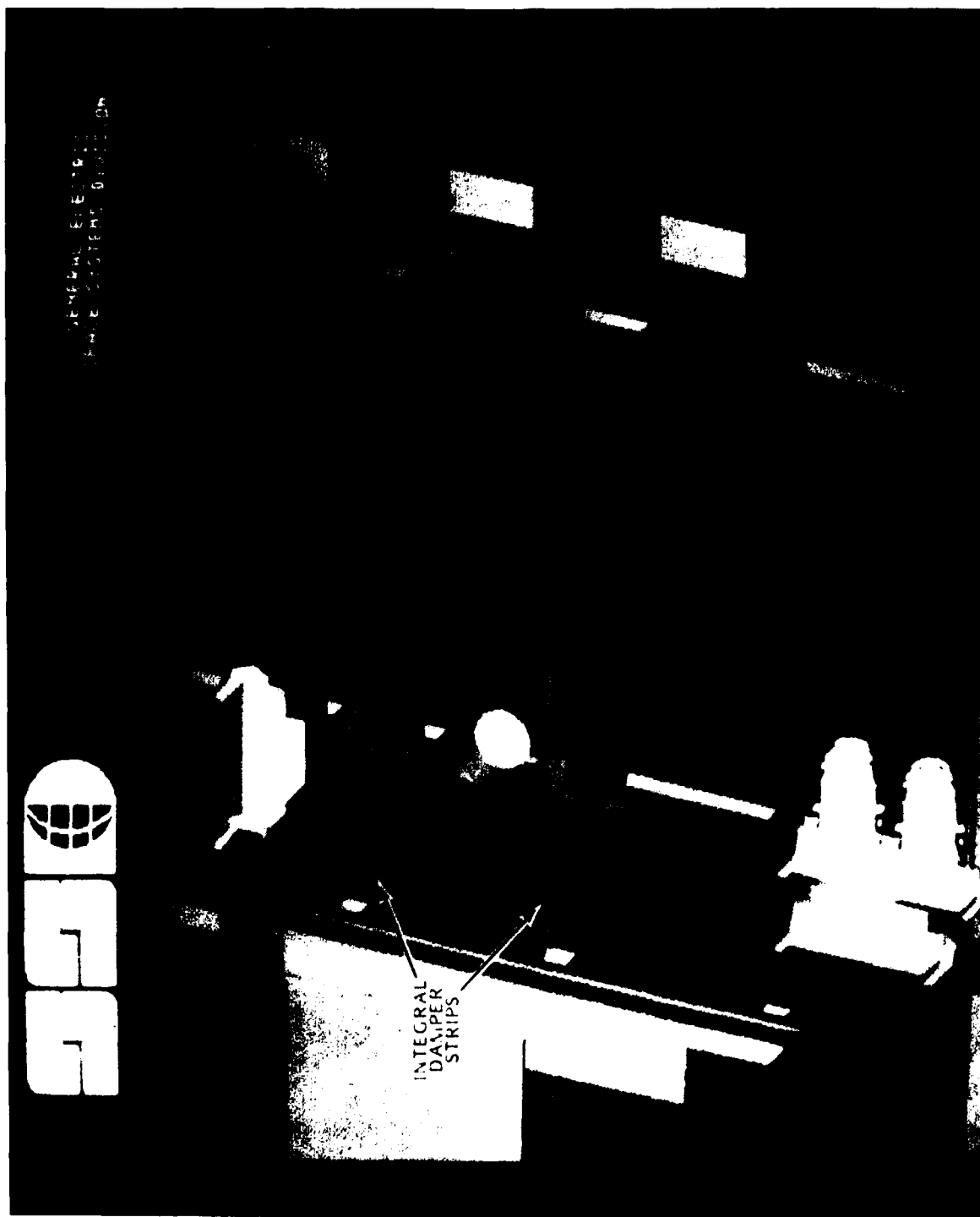


Figure 14. DSCS-III North Panel Bay 3 with Five Integral Damper Strips

- OPTIMUM SECTIONS SECTIONS CAN BE DEVELOPED WHICH PROVIDE ADEQUATE DAMPING, STIFFNESS, AND STRUCTURAL CAPABILITY AT MINIMUM WEIGHT

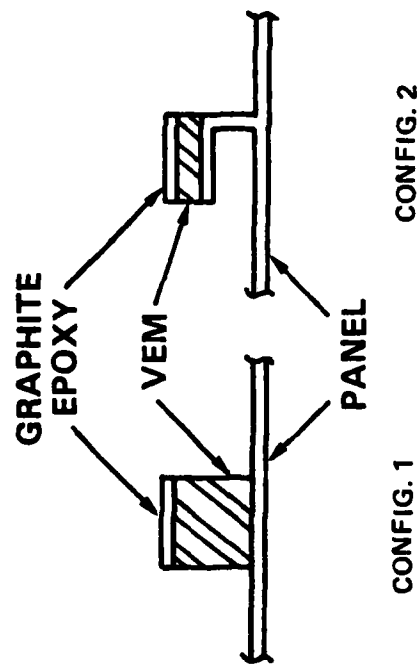
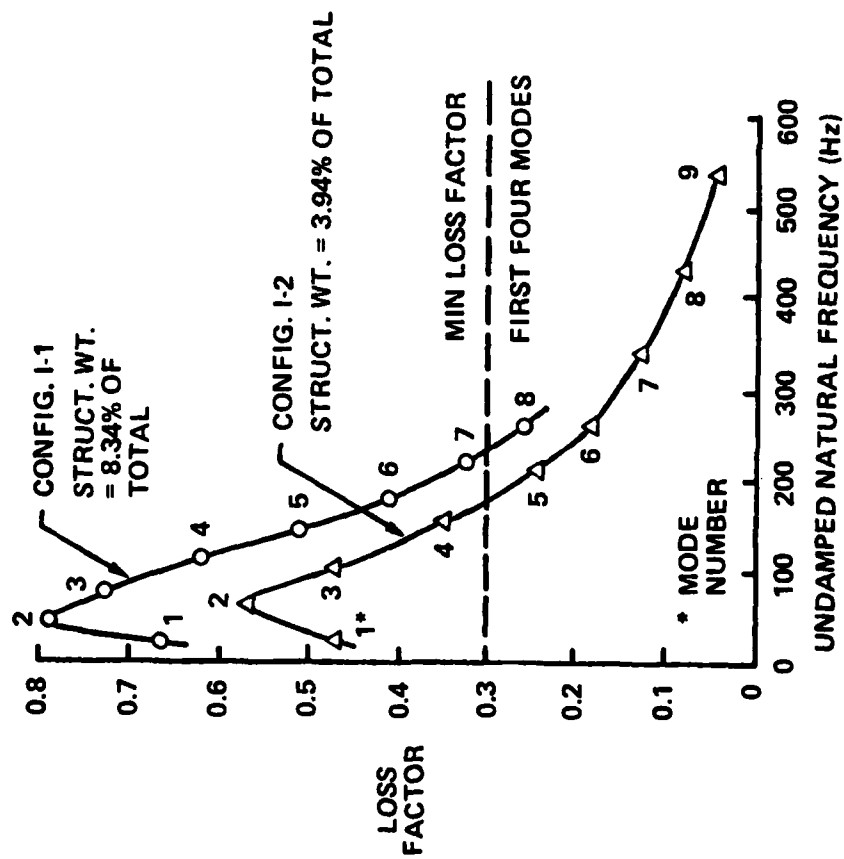


Figure 16. Optimization of Damping Designs

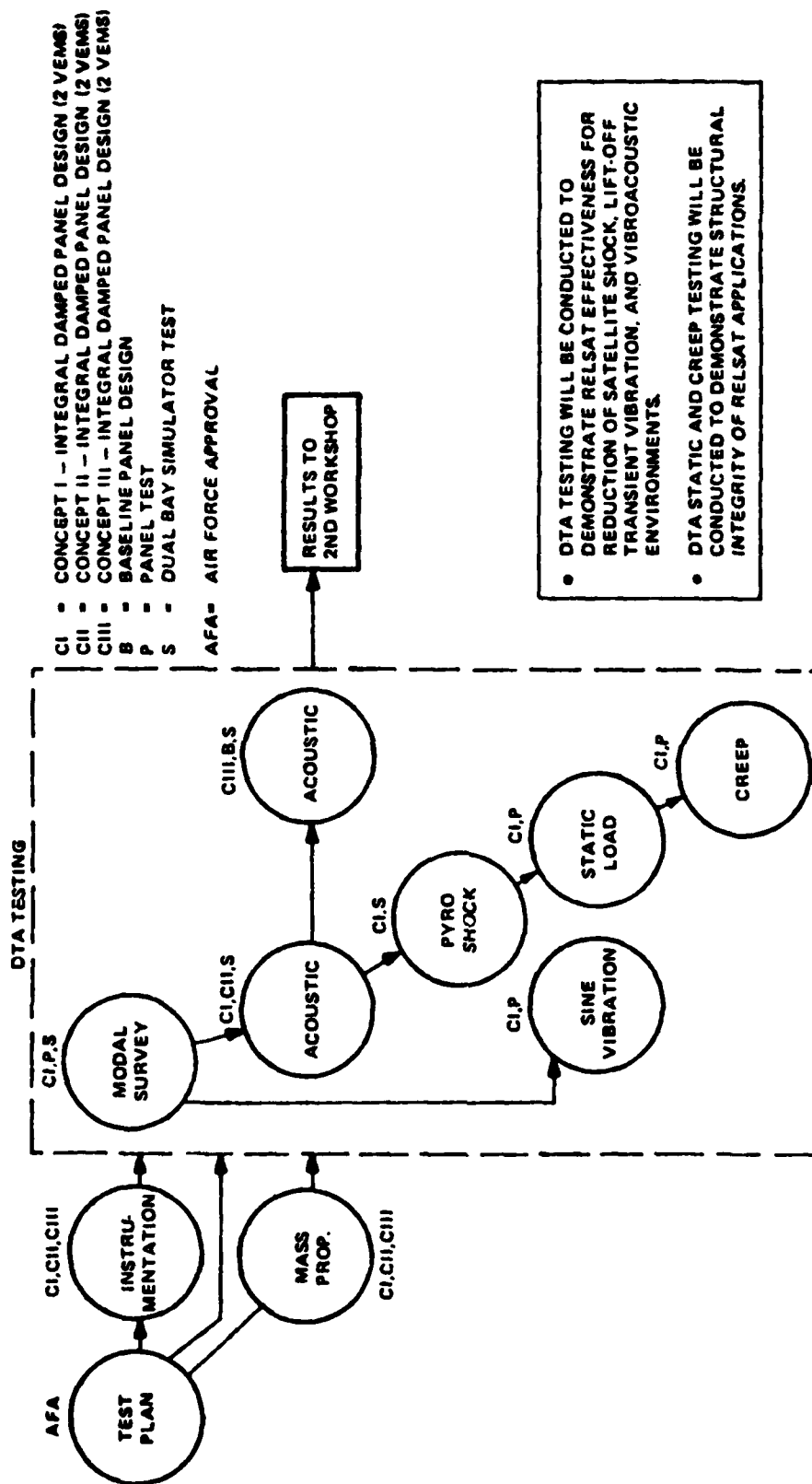


Figure 17. Flow Chart of Task 5 - Dynamic Test

Table 1. Typical Damping Applications

	VIBRATION AMPLIFICATION	
	BEFORE	AFTER
ERTS PSM RELAY PANEL (GE-SD)	40 @ 160 HZ	6 @ 180 HZ
ERTS AMS (QUANTIC)	44 @ 675 HZ	16 @ 1950 HZ
ERTS WBFM (GE-SD)	58 @ 480 HZ	7.6 @ 1600 HZ
VIKING DAPU (MARTIN MARIETTA)	50 @ 190 HZ	3 TO 6 @ 320 HZ
VIKING IRU - (HAM-STD)	50 @ 200 HZ	2 1/2 TO 4 @ 200 HZ
PC BRD DAMPING STRIP (MARTIN MARIETTA)	45 @ 230 HZ	3.2 @ 275 HZ
STEEL BAR COMPARISON (GE-IR&D)	39-49 @ 15-280 HZ	1.5-6 @ 48-550 HZ
20" DIA. BULKHEAD (GE-IR&D)	65 @ 400-3500 HZ	2.5 @ 350-3000 HZ
IUE CAMERA BRACKET - (NASA-GSFC)	15-20 @ 100-2000 HZ	1.5 TO 5 @ 77-400 HZ
IUE CAMERA DECK (NASA-GSFC)	7 TO 35 @ 80 - 2000 HZ	1.4 TO 4.8 @ 80-2000 HZ
TRIDENT GUIDANCE GIMBALL (CS DRAPER LAB)	40 AT 165 HZ	8 AT 125 HZ
BSE EQUIPMENT PANEL	32 @ 110 HZ	14 @ 150 HZ
ETS-III EQUIPMENT PANELS (TOSHIBA)	30 @ 55 HZ	<10 @ 55 HZ

A DESIGN GUIDE FOR DAMPING OF AEROSPACE STRUCTURES

J. Soovere
Lockheed - California Company
Burbank, California

M. L. Drake
University of Dayton Research Institute
Dayton, Ohio

and

V. R. Miller
Air Force Wright Aeronautical Laboratories
Flight Dynamics Laboratory
Wright-Patterson Air Force Base, Ohio

A DESIGN GUIDE FOR DAMPING OF AEROSPACE STRUCTURES

J. Soovere*, M.L. Drake**, and V.R. Miller***

ABSTRACT

The effectiveness of polymeric damping materials in controlling resonant vibration problems has been established through many successful applications. The area of these applications range from aircraft structures to jet engine structures. An effort is underway to develop a viscoelastic damping design guide for use by designers. This paper provides a brief outline of this effort.

1. INTRODUCTION

Aerospace structures and equipment mounted in these structures are required to operate under a wide range of dynamic loads. When structural resonances are excited, the dynamic loads can produce excessive vibration levels in the structures and equipment. These vibration levels can be significantly reduced by increasing the damping in the dominant modes through the application of viscoelastic damping technology.

The above vibration problems are often encountered following some initial in-service exposure. The high cost of subsequent structural changes has made the application of viscoelastic damping technology both attractive and cost-effective in solving these problems. In many instances the reduction in resonant vibration response has been quite dramatic (Figure 1), exceeding that possible with stiffening for the same weight increment [1]. The need for greater accuracy and reliability has extended the application of this technology to guidance systems, optical systems, and circuit boards to name a few. It has been used to reduce the vibration in stiffened aircraft structures and jet engine parts, the cabin noise in the aircraft, the noise emitted by diesel engines, and the noise transmission in buildings. The use of viscoelastic (passive) damping is also expected to increase in space applications, in conjunction with active damping, since the inherent damping is very low in aerospace metals and high modulus graphite/epoxy composites. These latter materials are being used in increasing quantities in space structures.

Vibration testing and data analysis capability has increased dramatically in recent years. The resonant frequencies and damping in structures can now be determined much quicker and with a greater accuracy. The dynamic loads and vibration environments encountered by aerospace structures and equipment are reasonably well known. Damping materials covering a temperature range from -65°F to 1500°F have been developed. The theory [2,3] for simultaneously curve fitting the measured modulus and loss factor for improved accuracy and consistency has been developed for these materials. The basic Ross-Kerwin-Ungar [4] analysis methods for application of viscoelastic damping to beams

* Lockheed-California Company

** University of Dayton Research Institute

*** Air Force-Wright Aeronautical Laboratory

and plates and the subsequent work by many authors [5,6] have been complimented by the development of finite element methods [7,8] which enable the damping technology to be applied to more complex structural designs. Many successful applications of the viscoelastic damping technology have been reported in the literature. Consequently, it should be possible to anticipate resonant vibration problems and apply the damping technology at the design stage. This approach would not only reduce the cost relative to a subsequent design change, but could also result in a lighter design (Figure 1). This need is becoming more evident as limits of current technology are being approached.

To fully capitalize on this viscoelastic damping technology, it is first necessary to bring all of the pertinent information together in a damping design guide. For a wide appeal, the design guide must be suitable for use by designers. This paper provides a brief outline of such a program, performed in three phases, over a period of 34 months. The program will be completed in July 1984.

2. TECHNOLOGY SURVEY

A technological survey was conducted, primarily in the United States, to identify the aerospace companies, government agencies, research institutes, and individuals active in the field of viscoelastic damping technology. A questionnaire was developed to identify the scope of this activity. An eighteen percent response was obtained to the mailed questionnaires. The results indicate a wide field of application (Figure 2) for the damping technology, primarily for vibration control, followed closely by noise control and fatigue suppression (Figure 3). The data in these figures have not been normalized since many of the respondents were involved in more than one field of activity. The classifications of the individuals involved in this activity is indicated in Figure 4. The research and development (R&D) and the management columns combined represent 93 percent of the individuals active in the field. Consequently, most of the design and production activity is also being supported by the R&D engineers. This result indicates a need for greater dissemination of the damping technology, a primary objective of the damping design guide.

3. DAMPING DESIGN GUIDE FORMAT

The damping design guide has been organized into three volumes.

Volume 1 is intended to be a reference volume summarizing the work performed to date on the application of damping technology and the allied fields. It also contains a bibliography of the published articles in these fields and an assessment of future needs.

Volume 2 is intended to be the user oriented design guide. This volume contains a brief introduction to vibration and damping, and a general discussion on how to identify potential vibration problems and how to select the appropriate damping treatment. One chapter will feature design equations/nomograms for predicting the dynamic response of common structural members, both with and without damping treatment. This will be followed by a

chapter on worked examples based on successful applications of damping technology. The worked examples are divided into the major fields of application, each introduced by a summary of the problems encountered in that field and followed by a single example for each type of problem.

All of the worked examples and analysis methods have been obtained from literature. The worked examples include a comparison of predicted and measured results such as illustrated in Figures 5 to 7 for circuit boards [9], bolts [10] and exhaust ducts [11], respectively, to name a few. Finite element methods, and results of finite element analysis, involving application of damping, are also included. A typical finite element model of a turbine blade [12] damped with a surface glass treatment is illustrated in Figure 8. A total of 234 elements were used to define the damped blade. The cross-section of the blade (Figure 8b) consisted of fifteen elements for the blade and twelve elements each for the nickel and glass layers. The analysis was performed at temperatures of 800, 925 and 1000° Fahrenheit (427, 296 and 538° Centigrade). The peak damping was obtained at the temperature of 925°F (see Figure 9) in the first mode.

This volume also contains a brief summary of other case histories available in literature for which complete information is not available. The purpose is to broaden the scope of application beyond the worked examples. Measured damping levels in typical aerospace structures and materials are included for use in the analysis when measured damping data on the actual structures are not available.

Volume 3 contains the damping material data required by the designer. The damping material modulus and loss factor are presented in the form of the reduced temperature nomogram [13] (See Figure 10) which is accompanied by a data sheet, Table 1, containing other pertinent information. The use of this standardized data format is explained in the introduction of this volume. The organizations from which these damping materials can be obtained are also listed in this volume.

The damping application can be designed using Volumes 2 and 3. These volumes are intended for use in loose-leaf binders to permit updating of the design methods, in light of experience gained, and of the damping materials which are subjected to change from the normal market pressures.

4. CONCLUSIONS

A design guide is being developed to encourage and permit the application of viscoelastic damping technology at the design stage. It is recognized that the designers will require assistance from dynamicists in the initial use of Volumes 2 and 3 of the design guide until they become familiar with dynamics and viscoelastic damping. They will also require help with finite element analysis, dynamic loads/vibration levels/test specifications, and test methods/data analyses required to verify the performance of the damping treatments, which are usually the responsibility of the dynamics engineer. The widespread use of this relatively specialized, but essential technology is, therefore, dependent upon the assimilation of this technology by dynamics engineers outside the R&D classification. The damping design guide, it is hoped, will speed up this process.

REFERENCES

1. L.C. ROGERS 1978 Conference on Aerospace Polymeric Viscoelastic Damping Technology for the 1980's (L.C.Rogers Editor) Wright-Patterson Air Force Base Report - AFFDL-TM-78-78-FBA. Damp It: A proposed advanced development program.
2. R.L. BAGLEY 1979 Air Force Materials Lab. TR-79-4103. Application of Generalized Derivatives to Viscoelasticity.
3. L.C. ROGERS 1981 The Shock and Vibration Bulletin, No. 51, Part 1, 55-69, Damping: On modeling viscoelastic behavior.
4. D. ROSS, E.E. UNGAR and E.M. KERWIN, Jr. 1959 Structural Damping, American Society of Mechanical Engineers (J.E. Ruzicka Editor) Damping of plate flexural vibrations by means of viscoelastic laminae.
5. B.C. NAKRA 1976 The Shock and Vibration Digest 8, 3-11. Vibration control with viscoelastic materials.
6. B.C. NAKRA 1981 The Shock and Vibration Digest 13, 17-20. Vibration control with viscoelastic materials - II.
7. M.S. KLUESENER, M.L. DRAKE 1982 The Shock and Vibration Bulletin No. 52, Part 5, Mathematical Modeling: Damped Structure Design Using Finite Element Analysis.
8. C.D. JOHNSON, D.A. KIENHOLZ, and L.C. ROGERS 1981 The Shock and Vibration Bulletin No. 51, Finite Element Prediction of Damping in Beams with Constrained Viscoelastic Layers.
9. J.M. MEDAGLIA 1978 Conference on Aerospace Polymeric Viscoelastic Damping Technology for the 1980's, Wright-Patterson Air Force Base Report AFFDL-TM-78-78-FBA, SMRD Damping.
10. R.C. PELLER, General Dynamics Convair Division Report, Damping in Mirror Mounts and Composite Structure.
11. J. J. DeFELICE, A.D. Nashif 1978 The Shock and Vibration Bulletin, No. 48, Part 2, 75-84, Damping of An Engine Exhaust Stack.
12. Same as Ref 7.
13. D.I.G. JONES 1981 Journal of Aircraft 18, 644-649. An attractive method for displaying material damping data.

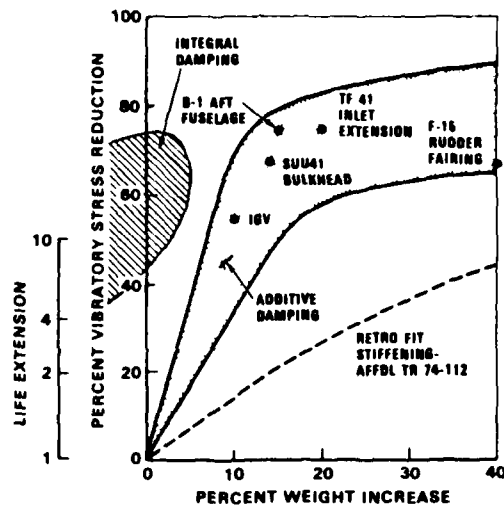


FIG. 1 LIFE EXTENSION OBTAINED WITH ADDITIVE DAMPING ON EXISTING HARDWARE

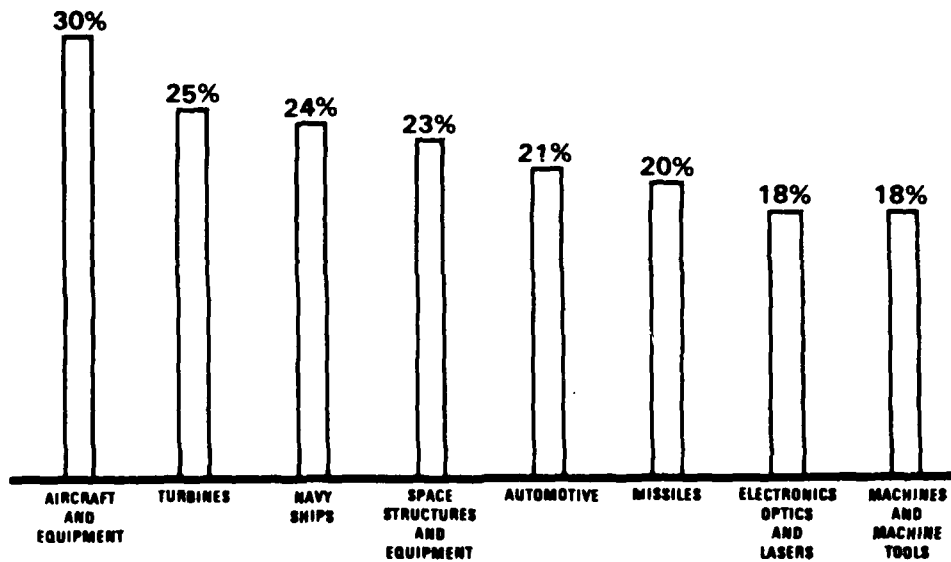


FIG. 2 APPLICATION OF DAMPING TECHNOLOGY

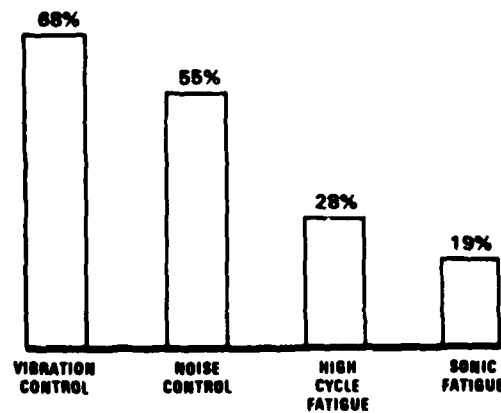


FIG. 3 PURPOSE FOR USE OF DAMPING TECHNOLOGY

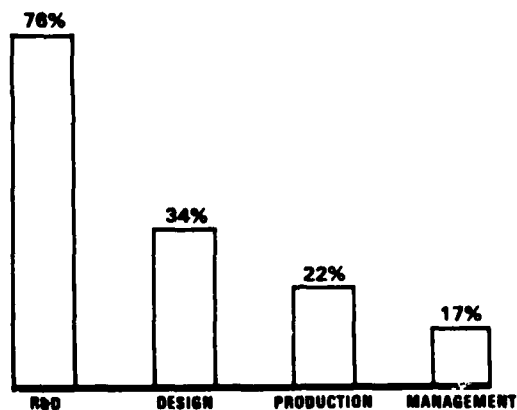


FIG. 4 CLASSIFICATION OF INDIVIDUALS ACTIVE IN THE APPLICATION OF DAMPING TECHNOLOGY

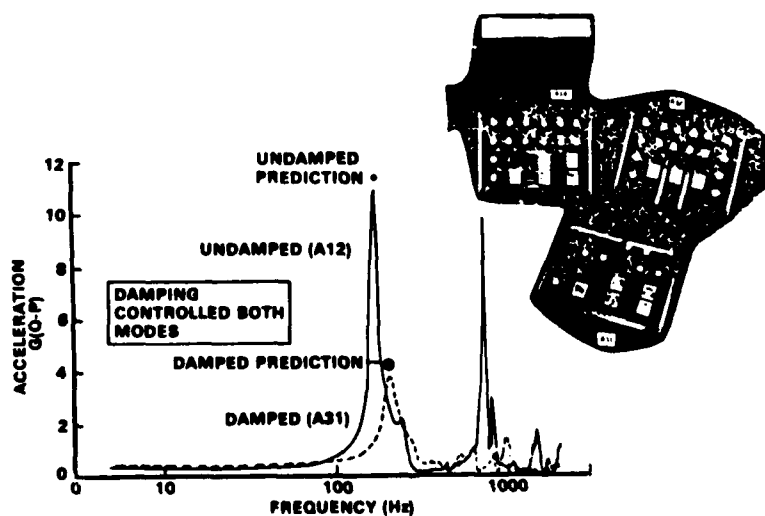


FIG. 5 REDUCTION IN CIRCUIT BOARD VIBRATION WITH ADDITIVE DAMPING

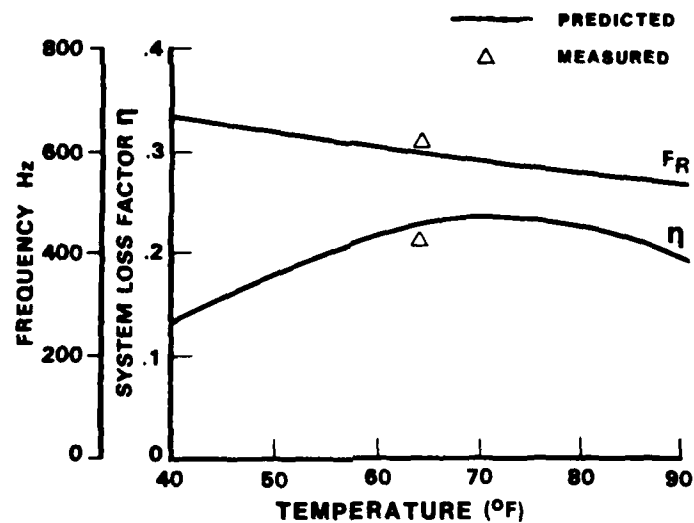
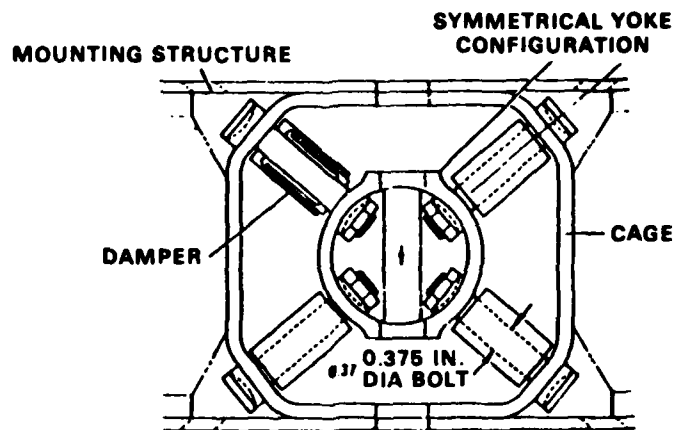


FIG. 6 INCREASE IN LOSS FACTOR OBTAINED WITH DAMPED BOLTS

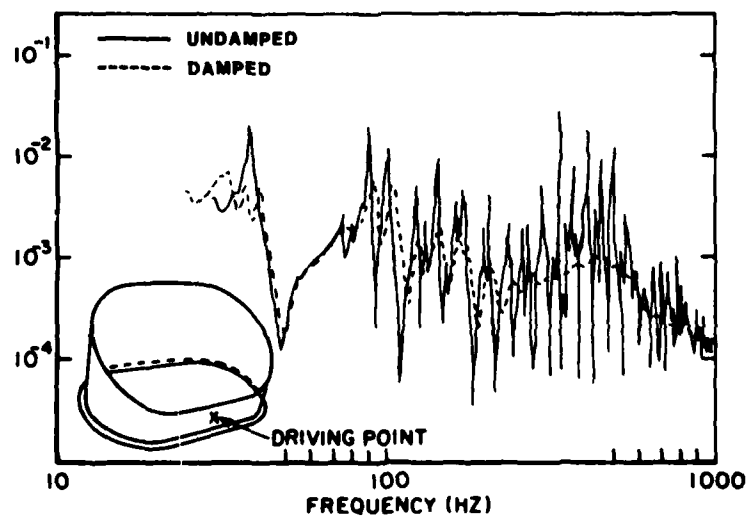


FIG. 7 EFFECT OF DAMPING ON HELICOPTER EXHAUST DUCT VIBRATION

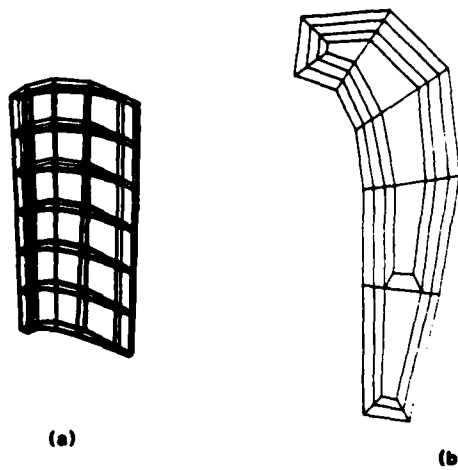


FIG. 8 FINITE ELEMENT MODEL OF TURBINE BLADE

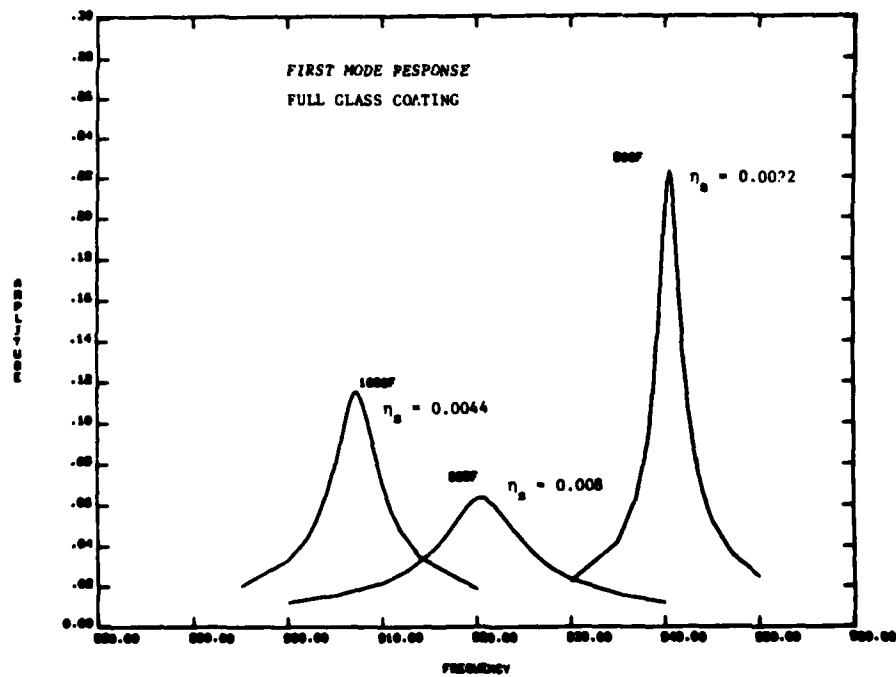


FIG. 9 FIRST MODE BLADE RESPONSE WITH FULL GLASS COATING AT THREE TEMPERATURES

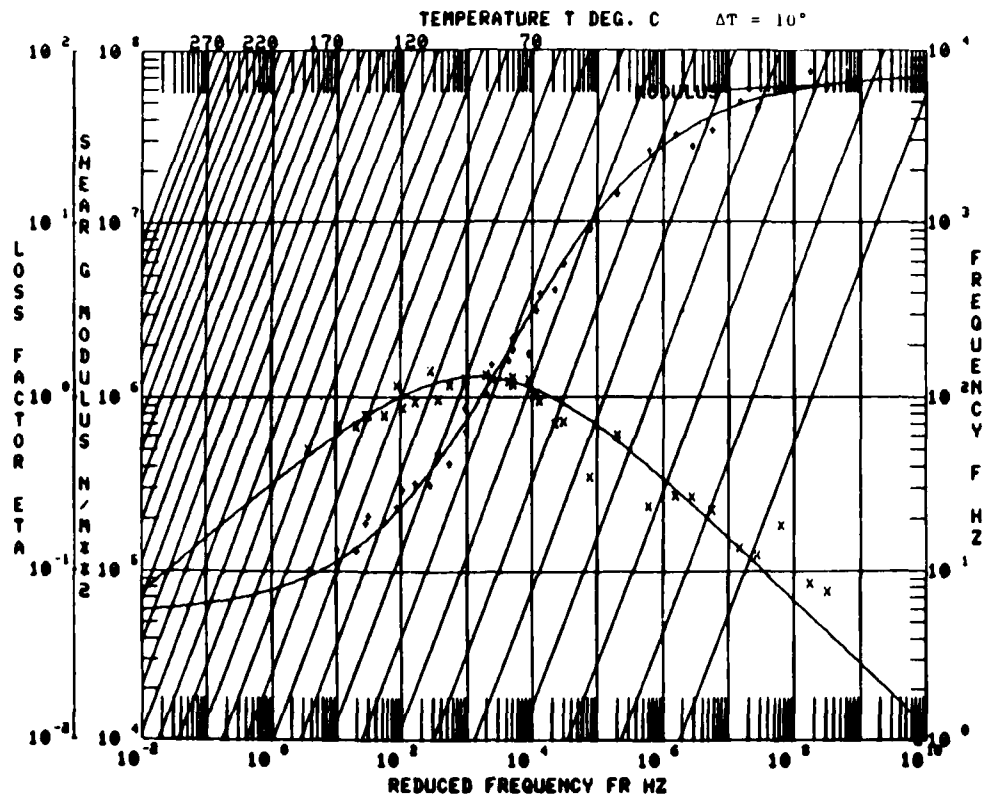


FIG. 10 TYPICAL REDUCED FREQUENCY DAMPING MATERIAL NOMOGRAM

TABLE 1 TYPICAL DAMPING MATERIAL DATA SHEET

MATERIAL MN MANUFACTURER THE SOUNDCOAT COMPANY
 MAX LOSS FACTOR η_p 2.1494 MODULUS μ SHEAR (1) YOUNG S
 MODULUS AT η_p 08 PSI 4.13E2 PASCALS
 MAX MODULUS 1.94E5 PSI 1.34E9 PASCALS
 MIN MODULUS 3.77 PSI 2.6E4 PASCALS
 MAX SURVIVAL TEMP LONG TERM NA OF $^\circ$ C
 MAX SURVIVAL TEMP SHORT TERM NA OF $^\circ$ C FOR MINUTES
 ULTIMATE TENSILE STRENGTH NA PSI PASCALS
 DENSITY 0.30 LBS/IN³ 0.83 G/CC
 POISSON'S RATIO NA
 MAX ALLOWABLE STRAIN LEVEL NA
 EFFECTS OF CONTAMINANTS NA
 EFFECTS OF RADIATION NA
 OUTGASSING NA
 THERMAL CONDUCTIVITY NA BTU IN/FT² HR OF $^\circ$ C
 CONFORMABILITY EXCELLENT
 SUPPLIED AS (FORM) AVAILABLE AS SOUNDFOIL - DAMPING MATERIAL WITH ALUMINUM CONSTRAINING LAYER
 BONDING AND/OR APPLICATION PROCEDURE MN IS SELF-ADHESIVE AT ROOM TEMPERATURE. CLEAN SURFACES TO BE BONDED WITH SOLVENT AND APPLY WITH MODERATE PRESSURE

FREQ Hz	TEMP FOR η_p OF $^\circ$ C	LOWER LIMIT FOR $\geq 70\% \eta_p$ OF $^\circ$ C	UPPER LIMIT FOR $\geq 70\% \eta_p$ OF $^\circ$ C	MODULUS AT LOWER LIMIT PSI Pa	MODULUS AT UPPER LIMIT PSI Pa
10	21 29.4	-48 -43.3	10 -12.2	1.80E3 1.241E7	8.7E1 6.0E5
100	13 10.6	16 -26.1	61 10.6	1.82E3 1.255E7	8.4E1 5.79E5
1000	64 12.2	21 -6.1	99 37.2	1.83E3 1.262E7	8.4E1 5.79E5

TEST NUMBER 81 01

T₀ 10 $^\circ$ C 12.2

MODULUS CURVE PARAMETERS

FROM 2.0E3

FROM 5.9E6

N 0.3

ML 2.8E4

ADDITIONAL COMMENTS

LOSS FACTOR CURVE PARAMETERS

ETAFROL 2.1

SL 0.4

SH -0.8

FROL 1.3E3

C 1.0

DAMPED OPTICS FOR PULSED LASER APPLICATIONS

R. G. Jaeger and M. J. Laughlin
United Technologies Research Center

Paper was not presented; not available for publication.

DISTRIBUTED PIEZOELECTRIC-POLYMER
ACTIVE VIBRATION CONTROL OF A
CANTILEVER BEAM

Thomas Bailey
Research Assistant

and

Dr. James E. Hubbard, Jr.
Assistant Professor of Mechanical Engineering
Massachusetts Institute of Technology
Cambridge, Massachusetts 02139

**DISTRIBUTED PIEZOELECTRIC-POLYMER
ACTIVE VIBRATION CONTROL OF A
CANTILEVER BEAM**

Thomas Bailey
Research Assistant

Dr. James E. Hubbard, Jr.
Assistant Professor of Mechanical Engineering

Massachusetts Institute of Technology
Cambridge, MA 02139

ABSTRACT:

An active vibration damper for a cantilever beam was designed using a distributed-parameter actuator and distributed-parameter control theory. The distributed-parameter actuator was a piezoelectric polymer, poly(vinylidene fluoride). Lyapunov's second method for distributed-parameter systems was used to design a control algorithm for the damper. If the angular velocity of the tip of the beam is known, all modes of the beam can be controlled simultaneously. Preliminary testing of the damper was performed on the first mode of the cantilever beam. A linear, constant-gain controller and a nonlinear constant-amplitude controller were compared. The baseline damping of the first mode was $\eta=0.003$ for large amplitude vibrations (± 2 cm tip displacement) decreasing to $\eta=0.001$ for small vibrations (± 0.5 mm tip displacement). The constant-gain controller provided more than a factor of 2 increase in the modal damping with a feedback voltage limit of 200 VRMS. With the same voltage limit, the constant-amplitude controller achieved the damping same damping as the constant-gain controller for large vibrations, but increased the damping by a factor of 40 to at least $\eta=0.040$ for small vibration levels.

INTRODUCTION

Satellites and other large spacecraft structures are generally lightly damped due to low structural damping in the materials used and the lack of other forms of damping, such as air drag. In large structures, these vibrations have long decay times which can lead to fatigue, instability, or other problems with the operation of the structure [Ref. 1]. Flexible structures are distributed-parameter systems having a theoretically infinite number of vibrational modes. Current design practice often is to model the system with a finite number of modes and to design a control system using lumped-parameter control theory. 'Truncating' the model may lead to performance tradeoffs when designing a control system for distributed-parameter systems [Ref. 2].

There exists a wealth of distributed-parameter control theory in the literature. References 3 through 8 are a small sampling of what is available. However, there are very few applications in the literature. One reason may be the difficulty of using distributed-parameter control theory with spatially discrete sensors and actuators. The goal of this study is to design and evaluate an active vibration damper for distributed-parameter systems using a distributed-parameter actuator and to show some advantages of distributed-parameter control theory.

At the Charles Stark Draper Laboratory, a scale model of a flexible satellite has been designed and built as a test structure for active vibration control schemes [Ref. 1](see Figure 1)¹. This test structure consists of a hub mounted on an air bearing table with four perpendicular arms (1.2 m long) extending radially from the hub. The arms have either thrusters or weights for the tip mass. Accelerometers at the tip of the arms monitor the vibrations of the structure. The damper is to be applied to the flexible arms. For the development work, an arm was modeled as a cantilever beam with a tip mass and tip inertia. A smaller dynamically scaled model of one of the arms (including the use of a tip accelerometer) was used for the preliminary testing. The design and analysis of an active damper for a thin cantilever beam is presented in the second section. The third section describes the apparatus and procedures used in the preliminary testing of the damper. The results are presented and discussed in the fourth section.

¹Figures and tables are included after the body of the paper.

DESIGN AND ANALYSIS

The Distributed-Parameter Actuator

The active element being used is a piezoelectric polymer, poly(vinylidene fluoride) or PVF₂. PVF₂ is a polymer that can be polarized or made piezoelectrically active with the appropriate processing during manufacture. In its non-polarized form, PVF₂ is a common electrical insulator, among many other uses. In its polarized form, PVF₂ is essentially a tough, flexible piezoelectric crystal. Polarized PVF₂ is commercially available as a thin polymeric film from the Pennwalt Corp., King of Prussia, PA. The film generally has a layer of nickel or aluminum deposited on each face to conduct a voltage or field across its faces.

A sketch of the PVF₂ is shown in Figure 2. For uniaxially polarized PVF₂, a voltage or field applied across its faces (y-direction) results in a longitudinal (x-direction) strain. This is the d₃₁ component of the piezoelectric activity. (Biaxially polarized PVF₂ would strain in both the x- and z-directions. This study uses uniaxial PVF₂.) The strain occurs over the entire area of the PVF₂ making it a distributed-parameter actuator. Note that if the field is varied spatially, the strain will also vary spatially. This gives the added possibility of varying the control spatially as well as with time.

Modeling the Active Damper

The simplest possible damper configuration was used for this study; a layer of PVF₂ bonded to one side of the cantilever beam. A sketch of the resulting two layer beam is shown in Figure 3. Only transverse vibrations of the beam, w(x,t), will be analyzed. A subscript (·)₁ refers to the original cantilever while a subscript (·)₂ refers to the PVF₂ layer.

The effect of a voltage applied to the PVF₂ is to introduce a strain, ϵ_p in the PVF₂ layer given by

$$\epsilon_p(x) = V(x) \cdot \frac{d_{31}}{h_2} \quad (1)$$

where V is the applied voltage, d₃₁ is the appropriate static piezoelectric constant, and h₂ is the thickness (y-direction) of the PVF₂ layer. This strain gives rise to two kinds of motion in the beam. One is a longitudinal strain, ϵ_l , to keep a force equilibrium in the axial (x) direction. The steady state value of ϵ_l is found by solving the force equilibrium and is given by

$$\epsilon_l(x) = - \frac{E_2 h_2}{E_1 b_1 + E_2 h_2} \cdot \epsilon_p(x) \quad (2)$$

where E is the modulus of elasticity and b is the thickness of the layers. The result of these strains is a net force in each beam layer due to the applied voltage. The net force in each layer acts through the moment arm from the mid-plane of the layer to the neutral axis of the beam, producing a torque given by

$$T(x) = E_1 h_1 b \epsilon_1 \left(\frac{h_1}{2} - D \right) + E_2 h_2 b (\epsilon_p + \epsilon_1) \left(\frac{h_2}{2} + h_1 - D \right) \quad (3)$$

where b is the width of the beam (assumed that $b_1 = b_2$) and D is the location of the neutral axis of the composite beam and is given by

$$D = \frac{E_1 h_1^2 + E_2 h_2^2 + 2 h_1 h_2 E_2}{2(E_1 h_1 + E_2 h_2)} \quad (4)$$

See Figure 4 for a detail of the cross-section of the composite beam. Combining Eqns. 1-4 and reducing yields

$$\begin{aligned} T(x) &= V(x) \cdot d_{31} \left(\frac{h_1 + h_2}{2} \right) \frac{E_1 h_1 E_2 b}{(E_1 h_1 + E_2 h_2)} \\ &= V(x) \cdot c \end{aligned} \quad (5)$$

where c is a constant (for a given beam material and geometry) expressing the torque per volt. If we assume that the longitudinal strain, ϵ_1 , settles much faster than the applied voltage is changing then

$$T(x,t) = V(x,t) \cdot c \quad (6)$$

Combining Eqn. 6 with a conventional Bernoulli-Euler beam analysis yields the equations of motion for transverse vibrations, $w(x,t)$, of the composite beam. The governing equation is

$$\frac{\partial^2}{\partial x^2} \left(EI \frac{\partial^2 w}{\partial x^2} - c V(x,t) \right) + \rho A \frac{\partial^2 w}{\partial t^2} = 0 \quad \text{for } 0 < x < L \quad (7)$$

with boundary conditions

$$\begin{aligned} w &= \frac{\partial w}{\partial x} = 0 && \text{for } x=0 \\ \left. \begin{aligned} EI \frac{\partial^2 w}{\partial x^2} &= -I_1 \frac{\partial^3 w}{\partial t^2 \partial x} + c V(x,t) \\ EI \frac{\partial^3 w}{\partial x^3} &= M_1 \frac{\partial^2 w}{\partial t^2} + c \cdot \frac{\partial V(x,t)}{\partial x} \end{aligned} \right\} && \text{for } x=L \end{aligned} \quad (8)$$

where $EI = E_1 I_1 + E_2 I_2$. I is the area moment of inertia of the layer about the z -axis,

$\rho A = \rho_1 A_1 + \rho_2 A_2$, ρ is the density of the layer, A is the cross-sectional area of the layer, and M_t and I_t are the tip mass and tip inertia, respectively.

For the development work, the simplest damper would have uniform geometry and have a spatially uniform voltage applied along its length. Making this assumption, the spatial derivatives for the input voltage drop out of the system described by Eqns. 7 and 8 leaving

$$EI \frac{\partial^4 w}{\partial x^4} + \rho A \frac{\partial^2 w}{\partial t^2} = 0 \quad \text{for } 0 < x < L \quad (9)$$

with boundary conditions

$$\left. \begin{aligned} w &= \frac{\partial w}{\partial x} = 0 && \text{for } x=0 \\ EI \frac{\partial^2 w}{\partial x^2} &= -I_t \frac{\partial^3 w}{\partial t^2 \partial x} + c V(t) \\ EI \frac{\partial^3 w}{\partial x^3} &= M_t \frac{\partial^2 w}{\partial t^2} \end{aligned} \right] \quad \text{for } x=L \quad (10)$$

Notice that the control voltage only appears in one of the boundary conditions. Eqns. 9 and 10 describe a linear distributed-parameter system that only has boundary control. Since we have a distributed-parameter actuator, we are able to easily include it in the equations of motion without nonlinear terms (e.g., spatial delta functions). This allows us to keep a linear distributed-parameter model throughout the analysis, avoiding any problems that may be caused by 'truncating' the model.

Deriving a Distributed-Parameter Control Algorithm

Distributed-parameter control theory was used to design a control algorithm for the active damper. This allows one the possibility of controlling all the modes of vibration at once, provided that the system is controllable through the actuator. Hence, we may avoid problems with spillover of the uncontrolled modes [Ref. 2].

The control problem is to damp the vibrations of the system described by Eqns. 9 and 10 using the input voltage to the PVF₂, $V(t)$, as the control variable. We shall assume that there is some practical limit on the magnitude of $V(t)$, i.e.

$$|V(t)| \leq V_{\max} \quad (11)$$

For the moment, assume there is no restriction on the type of sensors available.

Lyapunov's second or direct method for distributed-parameter systems is a straight-forward design method that can easily deal with bounded inputs [Refs. 4, 9]. With this method, one defines a functional that may resemble the energy of the system and chooses the control to minimize the time rate of change of the functional at every point in time. An appropriate functional for the system described by Eqns. 9 and 10 is the sum of the squares of the displacement and velocity, integrated along the length of the beam, or

$$F = \frac{1}{2} \int_0^L (w^2 + \left(\frac{\partial w}{\partial t}\right)^2) dx \quad (12)$$

Taking the time derivative of the functional yields

$$\frac{\partial F}{\partial t} = \int_0^L \left(w \cdot \frac{\partial w}{\partial t} - \frac{\partial w}{\partial t} \cdot \frac{\partial^2 w}{\partial t^2} \right) dx \quad (13)$$

Substituting from the governing equation, Eqn. 9, gives

$$\frac{\partial F}{\partial t} = \int_0^L \left(w \cdot \frac{\partial w}{\partial t} - \frac{EI}{\rho A} \cdot \frac{\partial^4 w}{\partial x^4} \cdot \frac{\partial w}{\partial t} \right) dx \quad (14)$$

Integrating the second term by parts twice to introduce the boundary conditions yields

$$\begin{aligned} \frac{\partial F}{\partial t} = & \int_0^L \left(w \cdot \frac{\partial w}{\partial t} - \frac{EI}{\rho A} \cdot \frac{\partial^3 w}{\partial t \partial x^2} \cdot \frac{\partial^2 w}{\partial x^2} \right) dx \\ & - \frac{M_t}{\rho A} \cdot \frac{\partial^2 w}{\partial t^2} \cdot \frac{\partial w}{\partial t} \Big|_L - \frac{I_t}{\rho A} \cdot \frac{\partial^3 w}{\partial t^2 \partial x} \cdot \frac{\partial^2 w}{\partial t \partial x} \Big|_L \\ & + \frac{c \cdot V(t)}{\rho A} \cdot \frac{\partial^2 w}{\partial t \partial x} \Big|_L \end{aligned} \quad (15)$$

The input voltage, $V(t)$, only appears in one term. Therefore, to minimize Eqn. 15, the feedback voltage should be chosen so that the term it appears in is always as negative as possible, or

$$V = - \operatorname{sgn} \left(\frac{\partial^2 w}{\partial t \partial x} \Big|_L \right) \cdot V_{\max} \quad (16)$$

where $\frac{\partial^2 w}{\partial t \partial x} \Big|_L$ is the angular velocity at the tip of the beam. This means that the control voltage should be chosen with as large a magnitude as possible and should generate a torque ($c \cdot V$) that opposes the angular motion of the tip of the beam.

This control law has several desirable characteristics. First, no modes have been truncated. This control law will (theoretically) work with any and all modes of vibration of a cantilever since every mode has some angular motion at the tip of the beam. Secondly,

the control law depends only on the angular velocity at the tip of the beam, not an integral along its length. This is a feature of Lyapunov's second method when applied to systems that only have boundary control and makes it possible to implement a distributed-parameter control law with a discrete sensor.

There are also several disadvantages with this control law. The $\text{sgn}(\cdot)$ function is nonlinear and discontinuous when its argument is zero. This nonlinear control law could lead to problems such as limit-cycling and/or sliding modes [Ref. 4]. A practical drawback is that the angular velocity of the tip is not readily available. However, the accelerometer at the tip of the beam measures the linear acceleration which can be integrated to find the linear velocity of the tip. For any given mode of vibration, the linear velocity is directly proportional to the angular velocity, although this relation does not hold if more than one mode of vibration is present. It was decided to perform the preliminary testing of the damper on only one mode of vibration. The first mode was chosen because it was the easiest to isolate.

Two other control algorithms were compared against the Lyapunov control law in the preliminary testing of the damper. Written in terms of the linear velocity at the tip of beam, the three are

1. Lyapunov;

$$V(t) = - \text{sgn} \left(\left. \frac{\partial w}{\partial t} \right|_L \right) \cdot V_{\max}$$

2. Constant-gain negative velocity feedback;

$$V(t) = -k \cdot \left(\left. \frac{\partial w}{\partial t} \right|_L \right); \quad |V(t)| \leq V_{\max}$$

3. Constant-amplitude negative velocity feedback;

$$V(t) = -k(t) \cdot \left(\left. \frac{\partial w}{\partial t} \right|_L \right); \quad |V(t)| \leq V_{\max}$$

where k is a feedback gain. As mentioned previously, the Lyapunov controller is nonlinear and discontinuous. The constant-gain controller can be derived from physical insight (negative velocity feedback tends to stabilize the system) or more rigorously from a modal control viewpoint. The constant-gain controller is linear and continuous, but as the velocity amplitude decays, so does the feedback voltage amplitude. This will reduce the effectiveness of the damper at low vibration levels, for a given voltage limit. The constant-amplitude controller compensates for the decaying velocity amplitude by adjusting the feedback gain.

$k(t)$, to keep the amplitude of the feedback voltage constant. This controller is continuous but nonlinear, and will be less effective (approx. 20%) than the Lyapunov controller since a square wave has more area than a sine wave if they have equal amplitude. However, the constant-amplitude controller may be more practical since the control circuitry does not have to produce high voltage step changes.

APPARATUS AND PROCEDURES

The dimensions and physical properties for an arm of the test structure and for the scaled model are given in Table 1. The scale model was used for the preliminary testing. A sketch of the beam and clamping fixture is shown in Figure 5. Included as part of the tip mass was a 2 gm accelerometer to monitor the vibrations of the tip of the beam. The leads to the accelerometer were made from a pair of small wires shielded inside a layer of aluminium foil and were extended above the beam from the clamping fixture to the accelerometer at the tip. This configuration provided the best shielding and had the least effect on the vibration of the beam.

The PVF₂ film used was uniaxially polarized. Table 2 gives the dimensions and some physical properties of the film. The PVF₂ was bonded to the steel beam using Eccobond 45LV, a low viscosity two-part epoxy. The average adhesive thickness was about 10 μ m. The leads to the PVF₂ consisted of wires soldered to tabs of copper foil. The copper tabs are clamped against the nickel plating on the appropriate face of the PVF₂.

Impact testing was used to identify the natural frequencies and modal damping of the uncontrolled beam. A schematic of the equipment used in this test is shown in Figure 6. The Hewlett-Packard 5423A spectrum analyzer applies a curve fit to the experimental data points near a resonance and uses the half-power bandwidth method to determine the modal damping. For the low levels of vibration used in impact testing, the loss factor, η , for the first mode was $\eta=0.001$.

A schematic of the equipment used to implement the constant-gain and constant-amplitude controllers is shown in Figure 7. (A controller to implement the Lyapunov control law is currently being assembled.) The accelerometer signal is integrated to give the tip velocity, phase-shifted, amplified through an audio amplifier and a step-up transformer, and applied to the PVF₂. The phase shift is necessary because the first mode of the cantilever beam is around 6 Hz, much below the linear region of an audio amplifier. The logarithmic plotter was used to determine the damping via the log decrement method. The plotter allowed a determination of how the damping changed with amplitude of vibration, especially with the nonlinear feedback of the constant-amplitude controller.

NO-A152 547

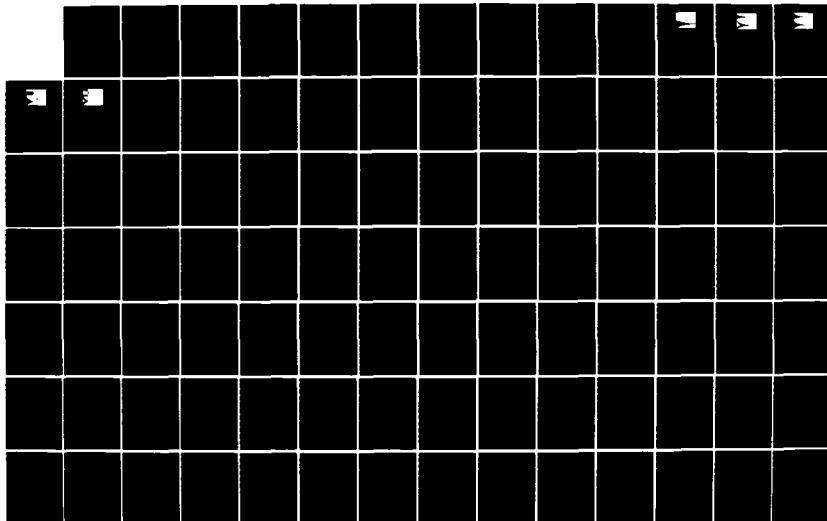
VIBRATION DAMPING WORKSHOP PROCEEDINGS HELD AT LONG
BEACH CALIFORNIA ON 2... (U) AIR FORCE WRIGHT
AERONAUTICAL LABS WRIGHT-PATTERSON AFB OH L ROGERS
11 NOV 84 AFMAL-TR-84-3064

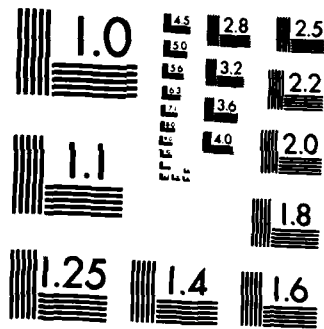
9/11

UNCLASSIFIED

F/G 20/11

NL





MICROCOPY RESOLUTION TEST CHART
NATIONAL BUREAU OF STANDARDS-1963-A

The test procedure was to hold the tip of the beam at 2 cm displacement, release it, and observe the decay. By holding the tip of the beam and then releasing it, very little of the second and higher modes were introduced in the initial conditions. For the constant-gain controller, the gain was set so that the maximum voltage amplitude would not exceed the voltage limit, V_{\max} . The maximum gain allowed was easily determined experimentally since the maximum voltage occurred when the beam was first released. For the constant-amplitude controller, the initial gain was determined in the same manner, but the gain was increased after the beam was released to keep the amplitude of the feedback voltage constant. This was done manually by turning the gain adjustment on the audio amplifier while watching the feedback voltage on the oscilloscope. The gain was increased until the gain limit of the amplifier was reached.

Two voltage limits were chosen; 100 and 200 VRMS. These limits were dictated by safety and control circuitry limitations, not by the breakdown voltage of the PVF₂. Note in Table 2 that the breakdown voltage of the film is over 1000 volts.

RESULTS AND DISCUSSION

The typical decay of an uncontrolled beam (a baseline test) is shown in Figure 8 in an oscilloscope photograph and a logarithmic plot. The upper trace in the oscilloscope photo is the feedback voltage, the lower trace is the tip displacement. Even though the decay envelope of the displacement looks exponential, the logarithmic plot shows a slight change in the slope. (The logarithmic plot should be a straight line for exponential decay.) This indicates that the loss factor, η , changes with amplitude. The loss factor at the large initial amplitudes (± 2 cm tip displacement) is slightly more than $\eta=0.003$ decreasing to about $\eta=0.001$ for small amplitudes (± 0.5 mm tip displacement). This confirms the damping value obtained for small amplitude vibrations from the impact testing.

The results for the constant-gain controller for the two voltage limits are shown in Figures 9 and 10. Since this is a linear controller, one expects the decay envelope to be exponential. As for the uncontrolled case, though, the slope of the logarithmic plots change slightly. However, this is probably due to the amplitude dependence of the loss factor in the beam itself. For $V_{\max} = 100$ VRMS, the average loss factor is slightly less than $\eta=0.006$, and slightly more than $\eta=0.007$ for $V_{\max} = 200$ VRMS. This is an improvement over the baseline damping in the beam, but, as noted previously in the analysis, the feedback voltage drops as the vibrations decay indicating that better damping could be achieved at the smaller vibration amplitudes.

The results for the constant-amplitude controller, shown in Figures 11 and 12, show a

dramatic improvement over the constant-gain controller. With $V_{\max} = 100$ VRMS, the vibrations are totally damped in 18 seconds. For $V_{\max} = 200$ VRMS, the vibrations are damped in 15 seconds. The decay envelopes are nearly linear, which is expected for a nonlinear control of constant amplitude. The logarithmic plots show how dramatically the damping changes. For both voltage limits the loss factor starts at the value achieved with the constant-gain controller and steadily increases to at least $\eta = 0.040$ for small amplitudes of vibration. This is at least a factor of 40 increase in the damping at small vibration levels. These results indicate that while an active damper of this type may not work well for large amplitudes of vibration, it may provide a way to keep resonant vibration from building up since the highest level of damping is achieved for very small vibration levels. It may be possible to use this kind of active damper in conjunction with another, more powerful actuator that will control the large amplitude vibrations. Powerful actuators often have problems such as limit-cycling or need a deadband at small vibration levels, providing a good complement to the active damper described here.

CONCLUSIONS

The control of distributed-parameter systems with discrete actuators and sensors and using lumped-parameter control theory may lead to performance tradeoffs. Using distributed-parameter control theory and distributed-parameter actuators one can avoid some of the tradeoffs, such as truncation of the model. An active distributed-parameter damper for a cantilever beam was designed and evaluated. The distributed-parameter active element was a piezoelectric polymer, poly(vinylidene fluoride). A control law was developed using Lyapunov's second method for distributed-parameter systems. Since no modes were truncated in the analysis, this control law will theoretically control all the modes of vibration. This avoids any structural problems with uncontrolled modes.

Preliminary testing of the active damper was done on the first mode of vibration of a small cantilever beam because the angular velocity of the tip of the beam was not available. The baseline damping for the first mode was $\eta = 0.003$ for large vibrations (± 2 cm tip displacement) decreasing to $\eta = 0.001$ for small vibrations (± 0.5 mm tip displacement). Three controllers were developed to test the damper on the first mode. Testing was performed using two of these controllers; the constant-gain and constant-amplitude controllers. The constant-gain controller was a linear controller and provided approximately double the baseline damping. The constant-amplitude controller was nonlinear and provided nonlinear damping; double the baseline damping for large vibrations increasing by a factor of 40 to at least $\eta = 0.040$ for small vibrations. These results were achieved with a simple damper configuration, simple control algorithms, and moderate voltage levels compared to the breakdown voltage of the PVF₂.

FUTURE WORK

The work presented here has only begun to examine the use of distributed-parameter control theory and distributed-parameter actuators on a very basic level. A distributed-parameter actuator opens many new possibilities. Some of the topics to be examined in the near future are

- Testing the active damper with continuous excitation rather than free decay.
- Attempting to control all modes at once by using an angular velocity sensor.
- Evaluate different damper designs;
 - * Use of viscoelastic materials to provide nominal passive damping which can be actively adjusted higher or lower,
 - * Use of spatially varying control.
- Use of distributed-parameter optimal control theory to design control algorithms.

REFERENCES

- [1] Kelley, M. G., "Mechanical Design and Dynamic Scaling Considerations of a Flexible Spacecraft Test Model", B.M./M.S. Thesis, Massachusetts Institute of Technology, June 1983.
- [2] Balas, M., "Feedback Control of Flexible Systems", *IEEE Trans. Automat. Contr.*, Vol. AC-23, pp 673-679, August 1978.
- [3] Ahmed, N. U. and K. L. Teo, *Optimal Control of Distributed Parameter Systems*, Elsevier North Holland, New York, 1981.
- [4] Buhler, E. and D. Franke, "Topics in Identification and Distributed Parameter Systems", *Advances in Control Systems and Signal Processing*, Vol. 1, Friedr. Vieweg & Sohn, Wiesbaden, Germany, 1980.
- [5] Komkov, V., *Optimal Control Theory for Damping of Vibrations of Simple Elastic Systems*, Springer-Verlag, Berlin, 1972.
- [6] Lions, J. L., "Some Aspects of the Optimal control of Distributed Parameter Systems", *Society for Industrial and Applied Mathematics*, 1972.
- [7] Stavroulakis, P., ed., "Distributed System Theory: Part 1, Control", *Benchmark Papers in Electrical Engineering and Computer Science*, Vol. 26, Hutchinson Ross Publ. Co., Stroudsburg, PA, 1983.
- [8] Tzafestas, S.G., *Distributed Parameter Control Systems: Theory and Applications*, Pergamon Press, Elmsford, NY, 1982.
- [9] Kalmann, R.E. and J.E. Bartram, "Control Systems Analysis and Design Via the 'Second' Method of Lyapunov", *ASME J. of Basic Eng.*, pp 371-400, 1960.

Table 1. Beam properties.

	<u>Test structure</u>	<u>Scaled model</u>
Material	Aluminum	Steel
Modulus, E (Nm^2)	76×10^9	210×10^9
length, L (m)	1.22	0.146
thickness, h (mm)	3.18	0.381
width, b (cm)	15.2	1.27
tip mass, M_t (kg)	2.04	6.73×10^{-3}
tip inertia, I_t (kgm^2)	1.1×10^{-2}	5.0×10^{-7}
density, ρ (kgm^{-3})	2840	7800

Table 2. PVF₂ Properties.

Modulus, E (Nm^2)	2.0×10^9
Static piezoelectric constant, d_{31} (mV^{-1})	22×10^{-12}
length, L (m)	0.146
thickness, h (mm)	28×10^{-3}
width, b (cm)	1.27
density, ρ (kgm^{-3})	1800
breakdown voltage, (V)	1400+

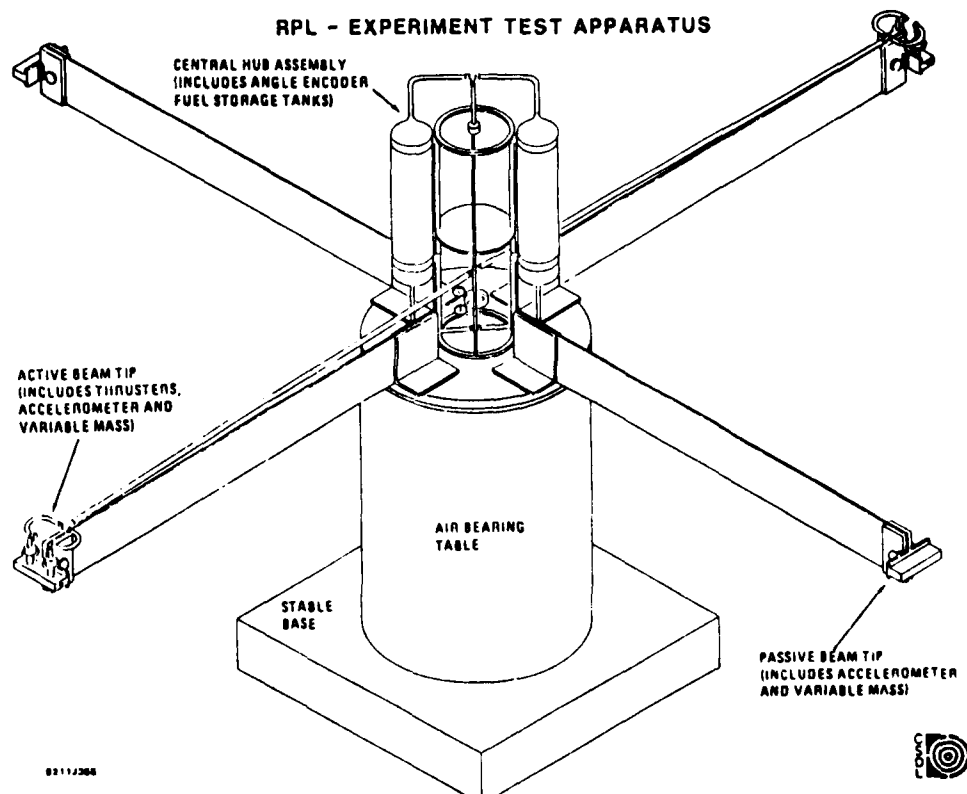


Figure 1. Flexible test structure at the Charles Stark Draper Laboratory.

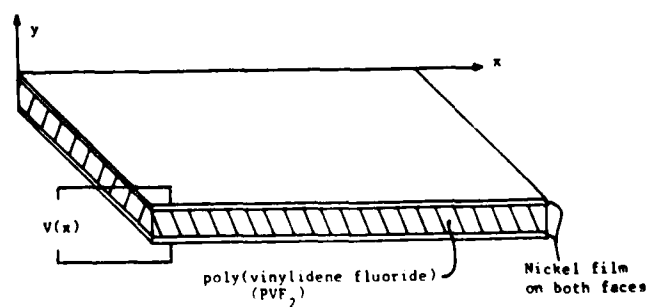


Figure 2. Coordinate system for the PVF₂ film.

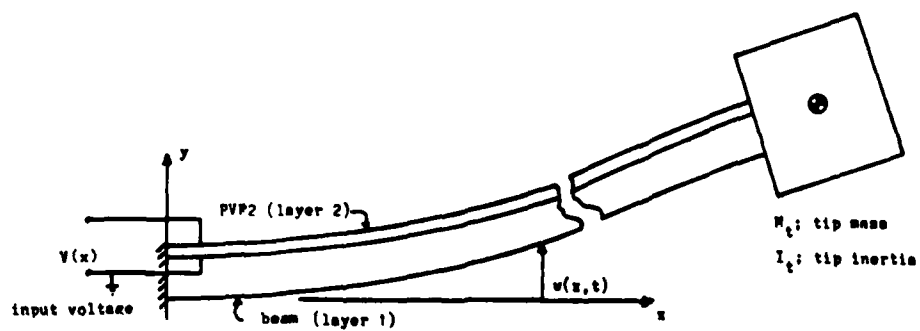


Figure 3. Active damper configuration.

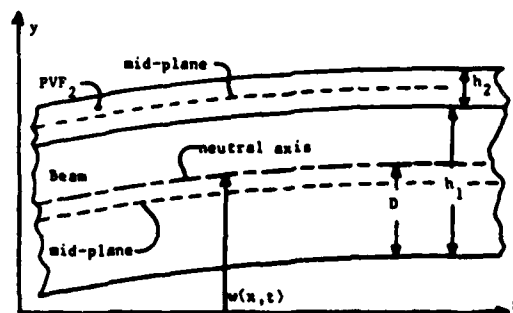
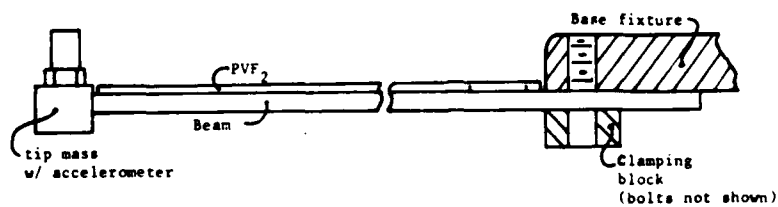
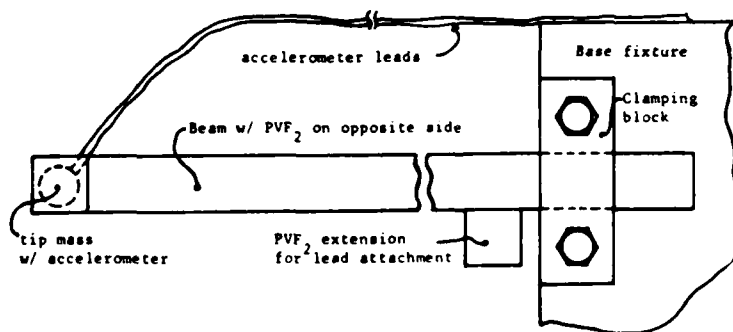


Figure 4. Detailed cross-section of beam with PVF₂ layer.



(a). Top view of steel beam in fixture.



(b). Side view of steel beam in fixture.

Figure 5. Experimental beam and fixture.

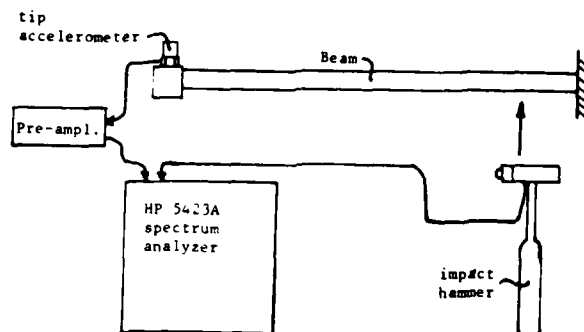


Figure 6. Schematic of apparatus used for impact testing.

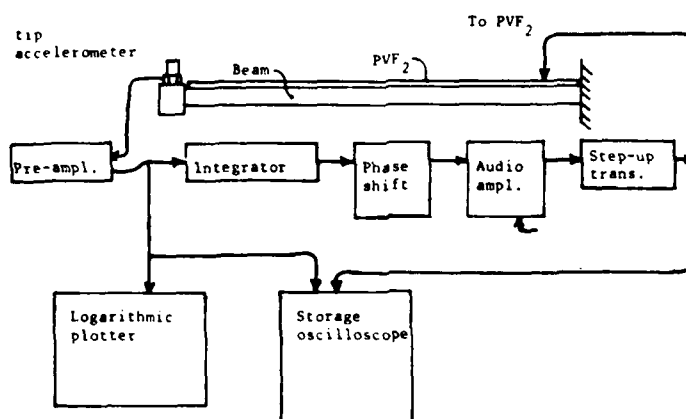
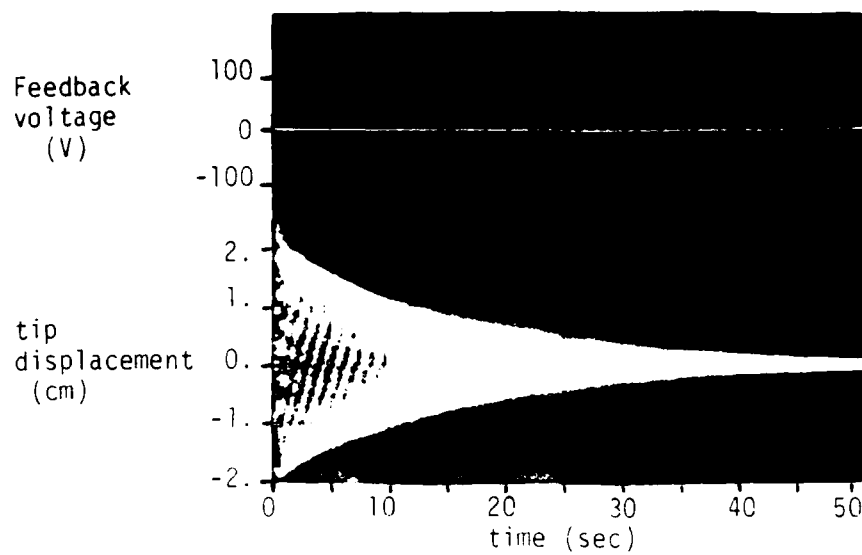
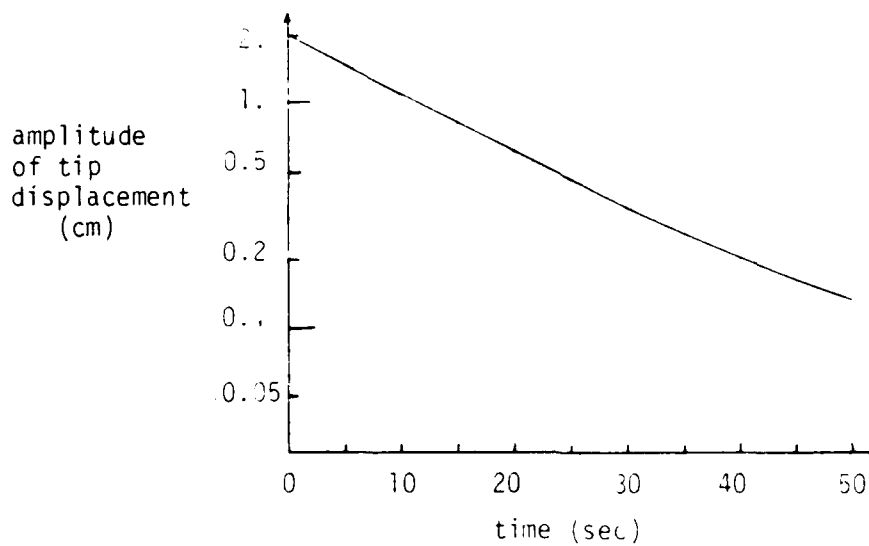


Figure 7. Schematic of apparatus used for preliminary testing of the active damper.

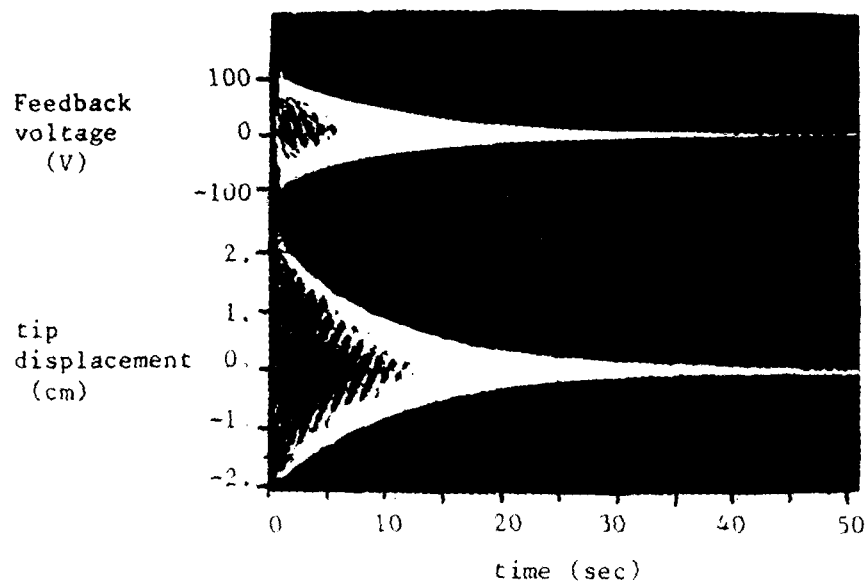


(a). Feedback voltage and tip displacement for the uncontrolled beam.

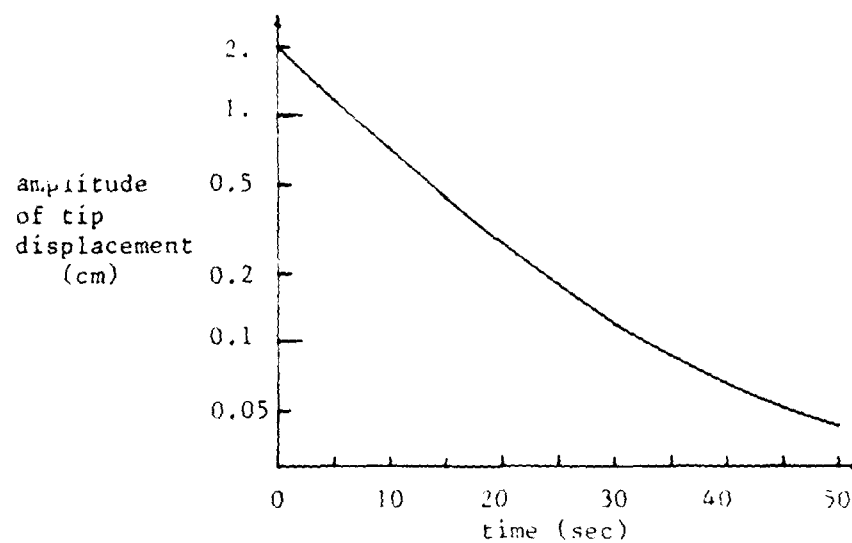


(b). Logarithmic plot of tip displacement decay.

Figure 8. First mode test results for uncontrolled beam.

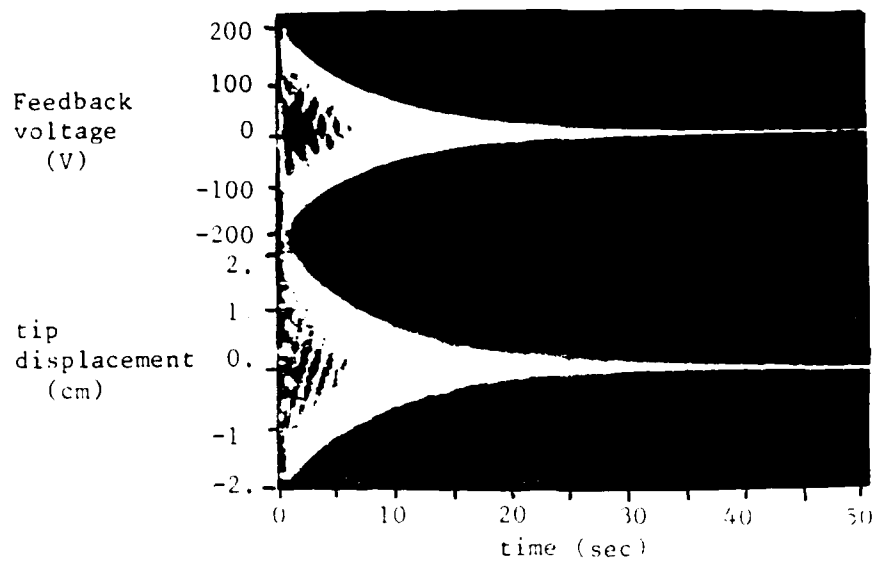


(a). Feedback voltage and tip displacement for the constant gain controller.

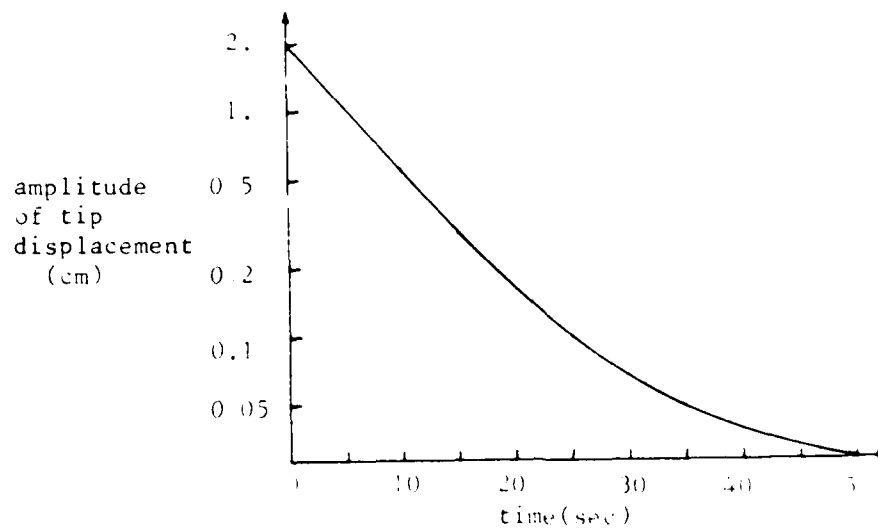


(b). Logarithmic plot of tip displacement decay.

Figure 9. First mode test results for the constant-gain controller, $V_{\max} = 100$ VRMS

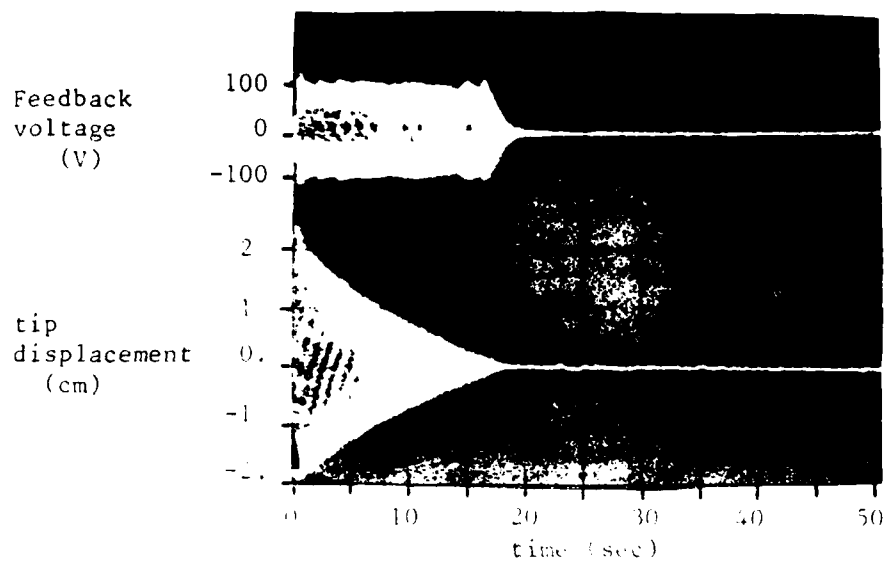


(a). Feedback voltage and tip displacement for the constant-gain controller.

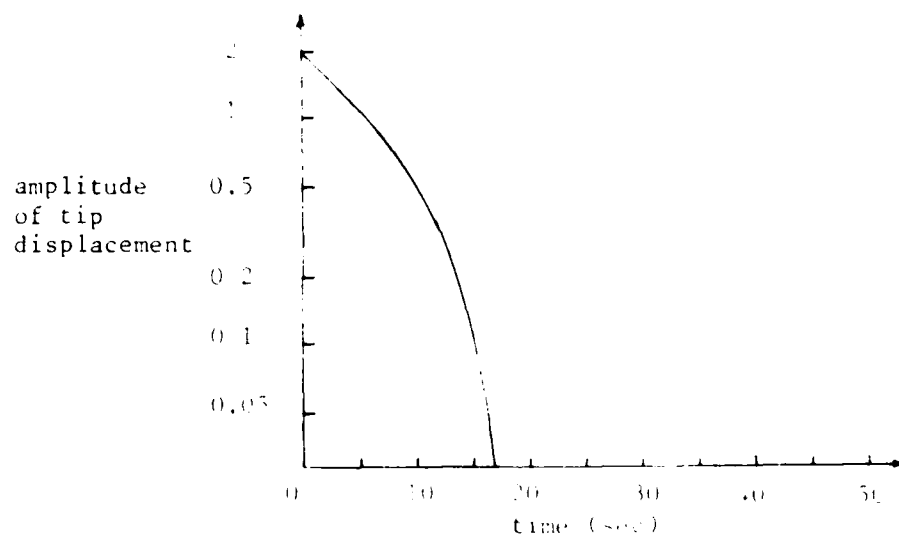


(b). Logarithmic plot of tip displacement decay

Figure 10 First mode test results for the constant-gain controller. $V_{\max} = 200$ VRMS.

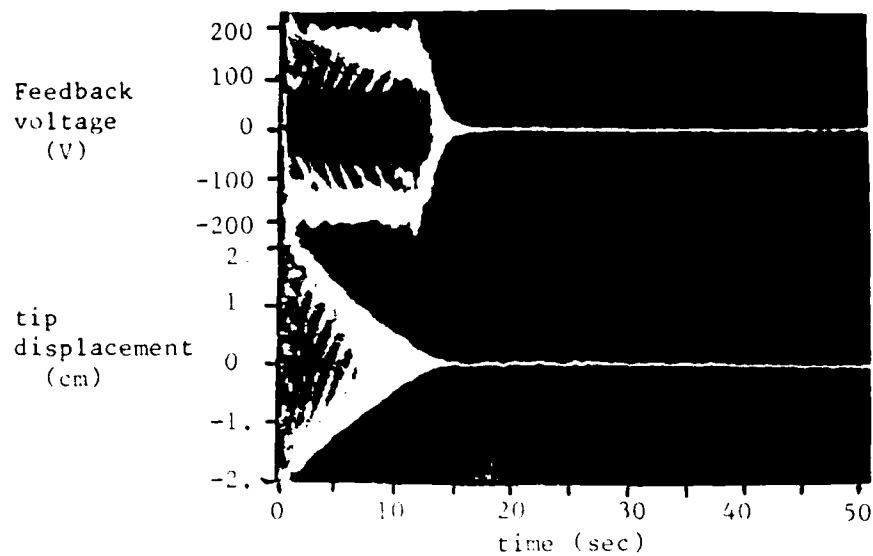


(a). Feedback voltage and tip displacement for the constant-amplitude controller

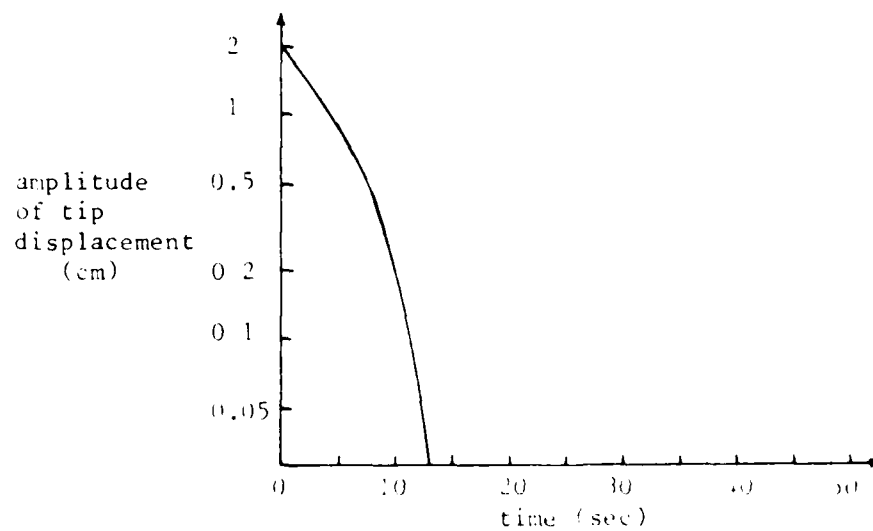


(b). Logarithmic plot of tip displacement decay

Figure 11. First mode test results for the constant-amplitude controller $V_{\max} = 100$ VRMS



(a). Feedback voltage and tip displacement for the constant-amplitude controller



(b). Logarithmic plot of tip displacement decay

Figure 12 First mode test results for the constant-amplitude controller $V_{\text{max}} = 200 \text{ VRMS}$

**AN EXPERIMENTAL STUDY OF PASSIVE DAMPING AND
ACTIVE CONTROL OF LARGE SPACE STRUCTURES**

**Dr. S. S. Simonian
Engineering Mechanics Laboratory
Dynamics Department**

**C. S. Major
Control and Sensor Systems Laboratory
Control Systems Engineering Department**

and

**Dr. R. Gluck
Engineering Mechanics Laboratory
Dynamics Department
TRW Space and Technology Group
Redondo Beach, California**

AN EXPERIMENTAL STUDY OF PASSIVE DAMPING AND
ACTIVE CONTROL OF LARGE SPACE STRUCTURES

by

Dr. S. S. Simonian
Engineering Mechanics Laboratory
Dynamics Department

C.S. Major
Control and Sensor Systems Laboratory
Control Systems Engineering Department

Dr. R. Gluck
Engineering Mechanics Laboratory
Dynamics Department

ABSTRACT

This report presents a methodology for incorporating passive dampers in large space systems (LSS) design. The methodology focuses on modular, discrete viscoelastic dampers which are integrally designed into the structure. The report describes the application of the methodology to the TRW LSS Experiment, a laboratory demonstration of a structure supporting a simulated optical mirror and subject to active and passive vibration control. Performance evaluation of the damped structure design was obtained using the Modal Strain Energy technique, based on finite element models in Program NASTRAN. A parameter variation study of the dampers' performance was conducted, yielding, for the first three modes of a nominal damper configuration, an augmented modal damping ratio of 9 percent of critical damping. This amount of passive damping, which is an order of magnitude larger than the residual damping present in the original structure, was obtained with a mere 8 percent penalty in structural weight.

1. INTRODUCTION

1.1 GENERAL CONSIDERATIONS

Current trends in satellite technology have been toward significantly larger spacecraft than those designed in the recent past. The advent of the Space Transportation System (STS) has made possible deployable and erectable structures of very large dimensions and extensive flexibility, the latter being a direct outcome of the requirement to minimize weight. Since the performance of these systems relies, in many cases, on precise pointing requirements and/or a precise structural configuration, it is necessary to minimize their structural/dynamic response to disturbances.

Examples of typical pointing requirements of large space structures can be drawn from two spacecraft now being developed for NASA. One is a 110-meter diameter antenna, and the other is the Large Space Telescope. The antenna must point to within 1 microradian of the intended direction and precisely maintain that position while it is in operation. The surface of the antenna must stay within 1 millimeter of the intended configuration. Additional deformation of the structure will misdirect the line of sight and/or degrade system performance. Even more precise performance is required of the Large Space Telescope. The system must limit the motion of optical-element surfaces to 0.2 microns, and can allow only 0.05 microradians of pointing error. Clearly such systems can tolerate little structural disturbance.

The control of structural disturbances at the source is impractical when these disturbances extend over a wide frequency band (as in the case of laser plume of high energy laser systems). The control of structural response can be affected, however, by invoking both active and passive damping techniques.

The advent of flexible large space structures with high precision pointing requirements and figure control has made the integral design of passive damping into these systems indispensable. Passive damping is not only important in its own right but also plays a major role on those spacecraft which employ active structural control. Passive damping is very cost effective in increasing the stabilization bandwidth as required for high precision control systems [1]. It also acts to reduce the possibility of closed-loop instabilities due to observation and control "spillover" [2].

The incorporation of passive damping in an actively controlled spacecraft must be done in such a way that the deficiencies of one technology be compensated by the strengths of the other. To design this dual source of damping application, one must determine an optimal blend of the two damping mechanisms in terms of dollar cost, weight, and power consumption penalties, simplicity of design, and, above all, reliability. Significantly, there is a noticeable absence of attempts to optimize the blending of passive damping and active control of large structures. Moreover, there are no experimental data available on structures with integrally designed passive damping which are also equipped with active control systems. The work described herein was undertaken with a view toward partially filling this void.

1.2 TRW LARGE SPACE STRUCTURE EXPERIMENT

This paper describes the design phase of a laboratory demonstration of a space structure reflecting and/or transmitting electromagnetic radiation, where the relative position of the structural components must be held to tolerances measured in fractions of a wavelength. The experimental structure was designed to use:

- 1) Viscoelastically damped mechanical joints
- 2) Noncolocated sensors and actuators
- 3) Optical sensing devices providing measurements akin to those which will be available on large space structures (LSS).

The viscoelastic (VE) joints are but one example of a class of passive dampers which include other entities such as viscous and coulomb dampers and piezoceramic devices. VE dampers have been widely used in recent years for structural and engine vibration reduction in the aircraft industry, but received very little application in spacecraft design due to the prevalent semirigid character of the latter.

The TRW LSS experiment (illustrated in Figure 1-1) is a scaled-down model of a single truss cell typical of a large space-based benchless optics mission. Such a space vehicle might carry a mirror measuring 8 x 8 meters with a mass distribution of 180 kg/square meter. The experimental structure consists of two rectangular plates of aluminum honeycomb, 4 inches thick, connected to each other near their corners by four 1-inch diameter aluminum tubes. The square plates are 55 inches in length and 115 inches apart. The bottom plate is securely clamped to a rigid platform mounted on the ground. The control actuators are placed along the length of four 1-inch diameter diagonal tube members which transmit actuator induced reactions to the plate (see Figure 1-2). Disturbances are applied through two momentum exchange actuators and electromagnetic actuators for excitation in the horizontal plane and in the axial direction, respectively. The horizontal displacement and rotation of the simulated mirror will be sensed by a Surface Accuracy Measurement System (SAMS) developed at TRW [11].

This paper is divided into five sections. The current development status of the TRW LSS experiment controller is described in Section 2. A more in-depth discussion of the controller will appear in [3]. Section 3 describes the proposed methodology for the near optimal blend of active control and passive damping and in Section 4 an in-depth design analysis of a viscoelastic damping device is presented. A brief summary of the results appear in Section 5.

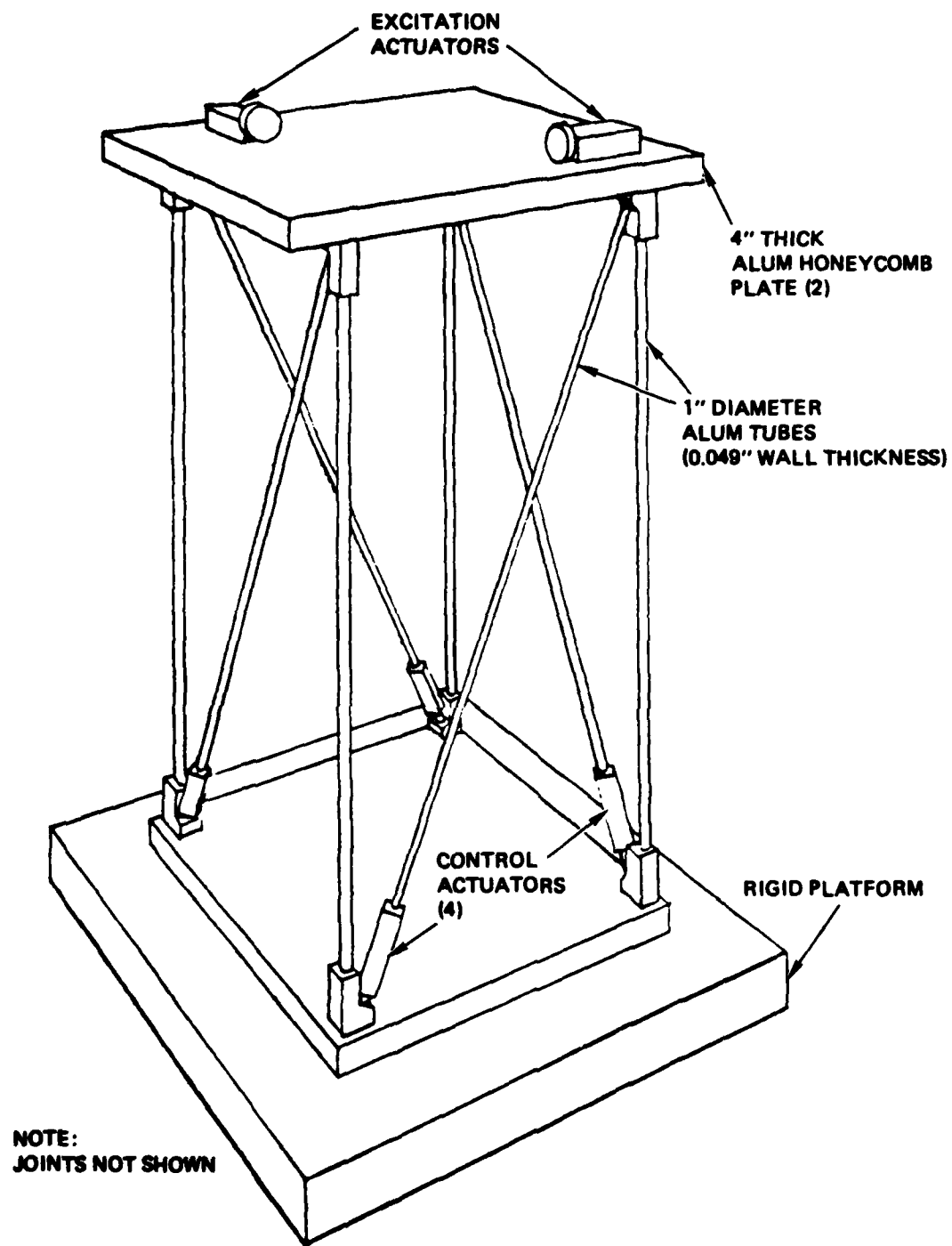


Figure 1-1. TRW LSS Experiment

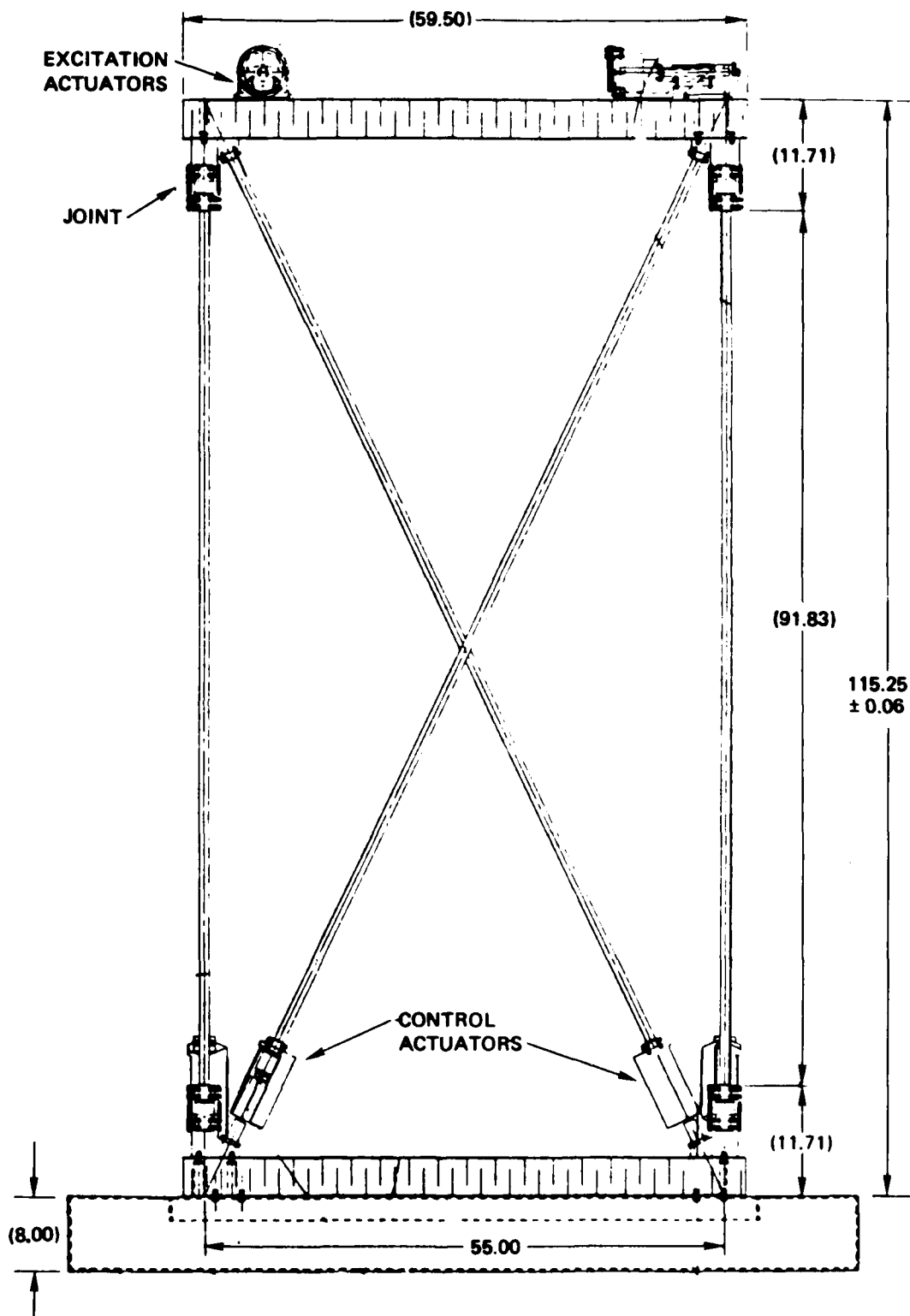


Figure 1-2. TRW Experiment Structure Side View

2. ACTIVE CONTROL DESIGN

An active control system design for the truss structure is in progress. The control design objective is to reduce the position error of the top plate of Figure 1-1 by a factor of 100, given a 15 Hz bandlimited disturbance input on the top plate. The top plate will be controlled to a position accuracy of 20 microns.

Three flexible modes of the structure are within the bandwidth of the controller, as shown by the magnitude (Bode) plot in Figure 2-1. Twenty-six additional modes are in the 15 to 60 Hz range. Those with the greatest influence on sensor and actuator outputs are indicated in the figure. These modes are of the greatest concern for designing the crossover of the controller.

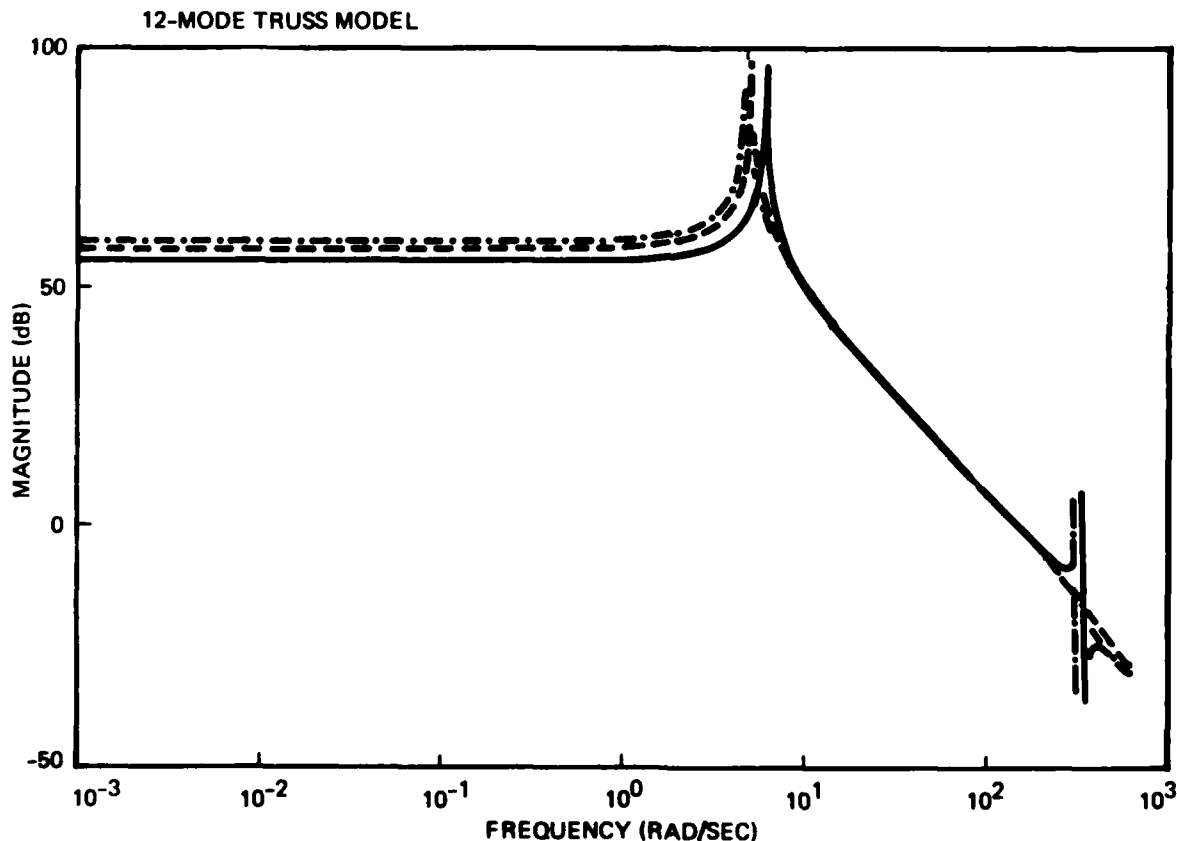


Figure 2-1. Magnitude Plot of Structural Dynamic Model with 0.005 Modal Damping Ratio and 200 Hz Sample Rate

A typical optics mission will require accurate positioning of one optical component with respect to another. Accordingly, in this experiment, 3 degrees of freedom (DOF) of the top plate will be controlled relative to the bottom plate. These DOFs are lateral motion in two directions (x and y) and rotation in the plane of the plate (θ_z). The TRW Surface Accuracy

Measurement System (SAMS) will be used to optically sense the relative position of the top plate. An unbroken line-of-sight for the sensor was therefore a structural design constraint.

Actuators for structural vibration control will typically be placed on portions of the structure away from the mirrors themselves for several reasons. First, it is important not to obstruct the line of sight required by the mission. Second, actuators should be placed so that modes with low controllability or observability do not have frequencies near the controller bandwidth. For the experimental structure, this requirement avoided placement of the control actuators near the top plate. Finally, it is important to be able to use relative actuation (between structural members) to avoid problems arising from the limited throw in momentum exchange devices.

To satisfy these constraints and, at the same time, to control the flexible modes which strongly affect the top plate position error, the actuators will be placed in the diagonal truss members. The actuators' force and displacement requirements were defined using finite element model analysis results.

The active control system is being designed with three controller channels, corresponding to the 3 plate DOF to be controlled. The control system design process follows the procedure described in [4]. First, alignment of the dynamic model of the structure is performed using the technique of [5]. Identical controllers are then inserted on each channel. Characteristic gain analysis is being used to improve the design in an iterative fashion. Finally, non-colocation of sensors and actuators implies a need for careful stability analysis, since control system stability will be sensitive to flexible modes within the controller bandwidth.

A preliminary design is now complete and has been simulated in conjunction with a 20-mode structural dynamic model. Each flexible mode in this case was modeled with a damping ratio of 0.005 to simulate the structure without the passively damped joints. Note the controller's effectiveness as demonstrated in the simulated sensor output shown in Figure 2-2 as a function of time.

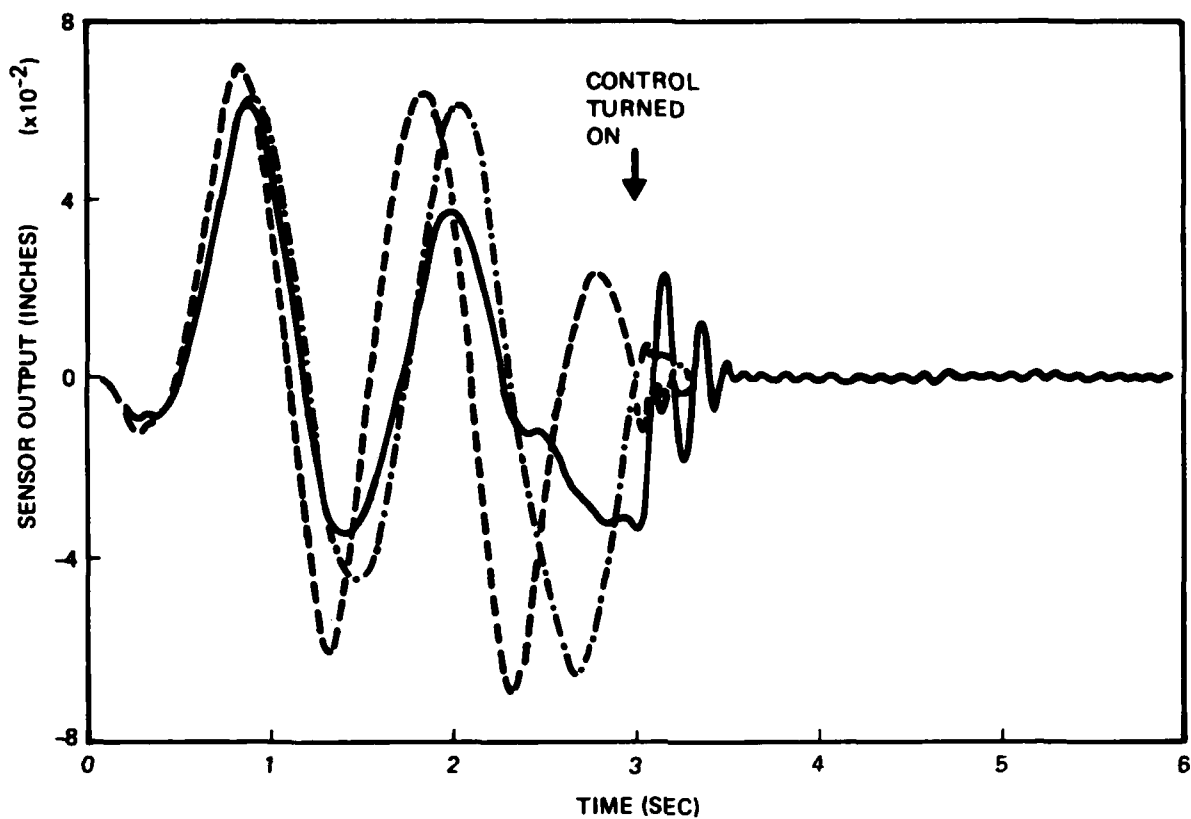


Figure 2-2. Simulated Sensor Outputs in Response to a 15 Hz Bandlimited Disturbance (The controller is turned on at $t=3$ seconds.)

3. A NEAR OPTIMAL BLEND OF PASSIVE DAMPING AND ACTIVE CONTROL DEVICES

An analytical treatment of the optimization of appropriate cost functions involving the important attributes of active control and passive damping of LSS (i.e., dollar cost, weight, power consumption, reliability, simplicity of design, etc.) is extremely complicated and leads to a multi-criteria optimization problem of high complexity. There are, at present, no practical methods to treat this problem when formulated in this fashion. Instead, a methodology is proposed herein which exploits the great sensitivity of any weighted cost function of an active control damping system to the system's frequency bandwidth. The methodology requires a dual track analysis as shown in Figure 3-1.

The procedure begins with the development of a finite element model of the spacecraft which is subjected to modal analysis yielding the vehicle's natural mode shapes and associated frequencies. The next step entails a detailed analysis, in the frequency domain, of the system requirements for a representative mission maneuver which may encompass vibration suppression, slewing, settling time, line-of-sight accuracy, and shape tolerance requirements. The mission requirements, when combined with a disturbance frequency spectrum analysis, permit the identification of the spacecraft natural modes which require damping augmentation. By tracking the strain energy stored in the finite elements of the structural model, a modal participation factor analysis yields an optimal nodal list for the incorporation of damping in the model.

At this point the passive and active damping design procedures branch apart. A multivariable frequency domain analysis identifies the amount of damping which must be introduced by each of the controllers in order to satisfy the mission requirements. A weighted cost function in the form:
$$\text{WEIGHTED COST} = a_1 (\$ \text{COST}) + a_2 (\text{WEIGHT}) + \dots + a_n (\text{RELIABILITY}),$$
can now be established and plotted against the bandwidth frequency.

For the viscoelastic damping design, the Modal Strain Energy methodology ([6], [7]) will provide realistic estimates of the maximum amount of damping which can be added to each of the natural modes of the structure, using the optimal nodal list obtained from the modal participation factor analysis. If the added viscoelastic damping meets the mission requirements, then a weighted cost function for the passive damping design can be established and compared to the active control cost function in the frequency domain. This is shown schematically in Figure 3-2. The intersection of the two curves will establish an optimal division of the frequency band of interest between the passive and active damping systems.

If the passive damping design cannot supply the amount of damping necessary, then the passive system cost function will be augmented by the cost function of the active system supplying the fractional damping necessary to meet the system requirements. A comparison of this hybrid cost function to that of a purely active system will determine the optimal amount of viscoelastic damping which should be added to the structure.

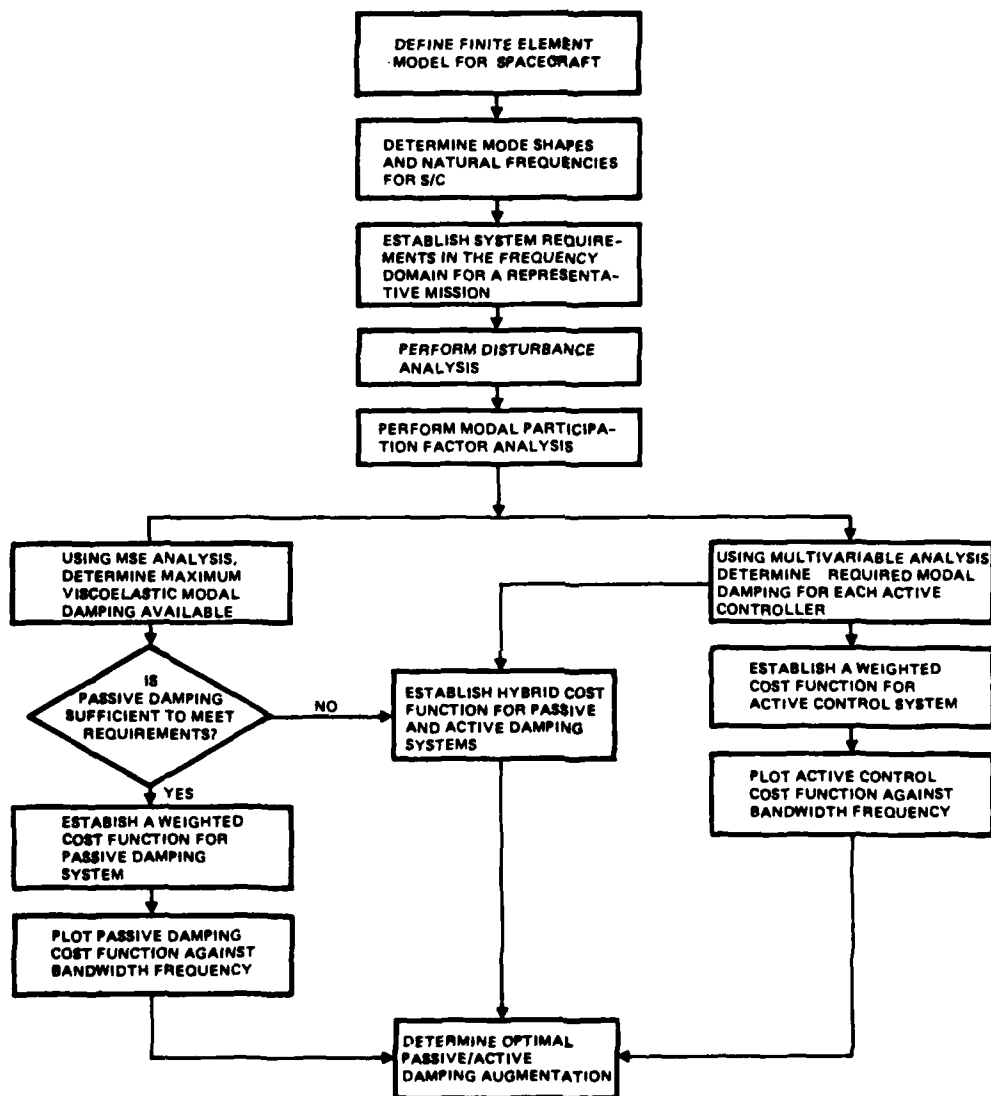


Figure 3-1. A Methodology for Trading Passive Damping and Active Control

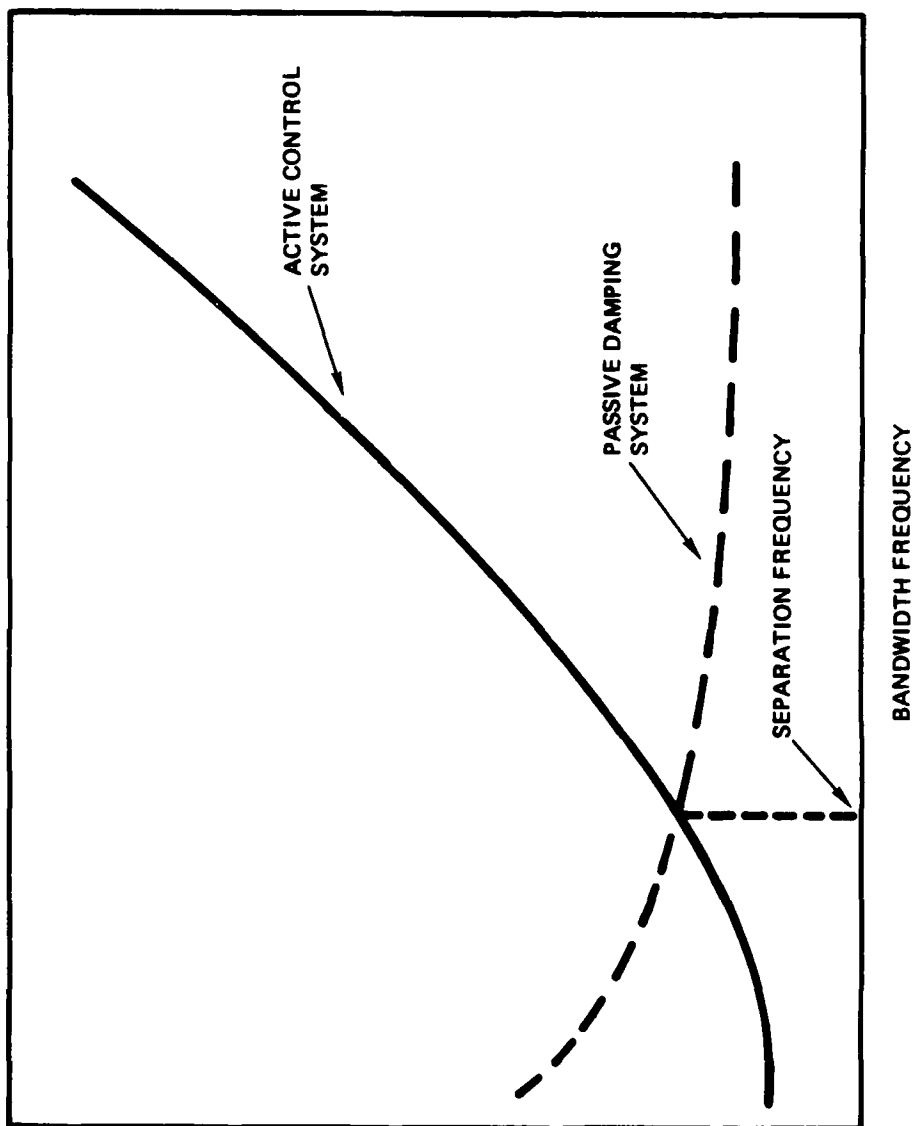


Figure 3-2. Optimal Passive and Active Damping System Augmentation

This straightforward procedure is based on an approach developed at TRW in the course of the ACOSS and VCOSS studies ([4], [8]), where passive damping was assumed to be a local rate feedback. Therefore, the passive-active trade became equivalent to establishing which method is most cost, weight, and power efficient in realizing rate feedback. The procedure is based on the recognition that any representative cost function of an active control system will rise sharply at high frequencies. In contrast, the loss factors of viscoelastic materials are, in many cases, only weak functions of frequency. As a result, the corresponding cost function is not expected to vary significantly with this parameter. In any case, this tradeoff methodology when applied to an actual spacecraft design is expected to require several iterations. These will stem from the constraints applied to the system which will necessitate more than one version of a damped structure design. The constraints include geometrical and strength consideration, line-of-sight interference as well as intrinsic requirements; for example, the desire to induce shearing rather than extensional strain in the viscoelastic material in order to increase its dissipation efficiency.

4. DESIGN AND ANALYSIS OF VISCOELASTICALLY DAMPED STRUCTURES

4.1 DESIGN CONCEPTS

In this section, some basic design aspects of VE dampers are examined. These provide guidelines for determining the optimal locations of VE material in a structure, as well as the selection between discrete and distributed type dampers and their integration in the structure in relation to the prevailing structural load path.

4.1.1 Damper Location and Characteristics

The ability of VE dampers to dissipate significant amounts of energy depends on their geometries, the VE material loss factor, and the dampers presence at structural regions where a significant amount of strain energy is being stored when the structure is subjected to its prescribed external loads. To place the dampers at their proper locations in the structure requires that they be integrally designed into it, rather than added later as an afterthought.

Two methodologies were applied to determine the proper placement of VE dampers in the TRW LSS experiment. These are:

- a) The modal strain energy (MSE) distribution in the structure
- b) A quasi-static force-distortion analysis of a structure under expected loads/deformations.

The MSE approach, as described in [6] and [7] is by far the more general of the two. Yet, it provides much less detailed information than can be obtained from the quasi-static force-distortion analysis. The latter is a more intuitive approach, and therefore applicable only to relatively simple structures. An example of the application of methodology (b) to the TRW LSS experiment is given below, whereas the application of the MSE methodology to this structure is discussed in Section 4.3.

Because of its relative simplicity, the deformed shapes of the TRW LSS experiment, due to the applied forces, can be drawn by inspection. This is shown in Figure 4-1. It can be clearly seen that in-plane lateral motions of the simulated mirror induce predominantly bending moments in the columns. The bending moment distribution along the column is depicted in Figure 4-1(f). Similarly, rocking and vertical motion of the simulated mirror induce predominantly axial forces in the columns (see Figure 4-1(g)).

A cursory examination of Figure 4-1 reveals that a significant amount of strain energy, obtained from the product of reaction force (moment) and distortion, can be found near the columns' boundaries, and that only a small amount of strain energy is stored at the columns' central regions. This suggests that an indiscriminate application of VE material along the entire length of the columns will be very wasteful, a vital piece of information for the effective design of the damped structure. The effective damping of the first three modes can be best accomplished by concentrating VE material near the columns' boundaries. Similarly, the rocking and axial modes of the

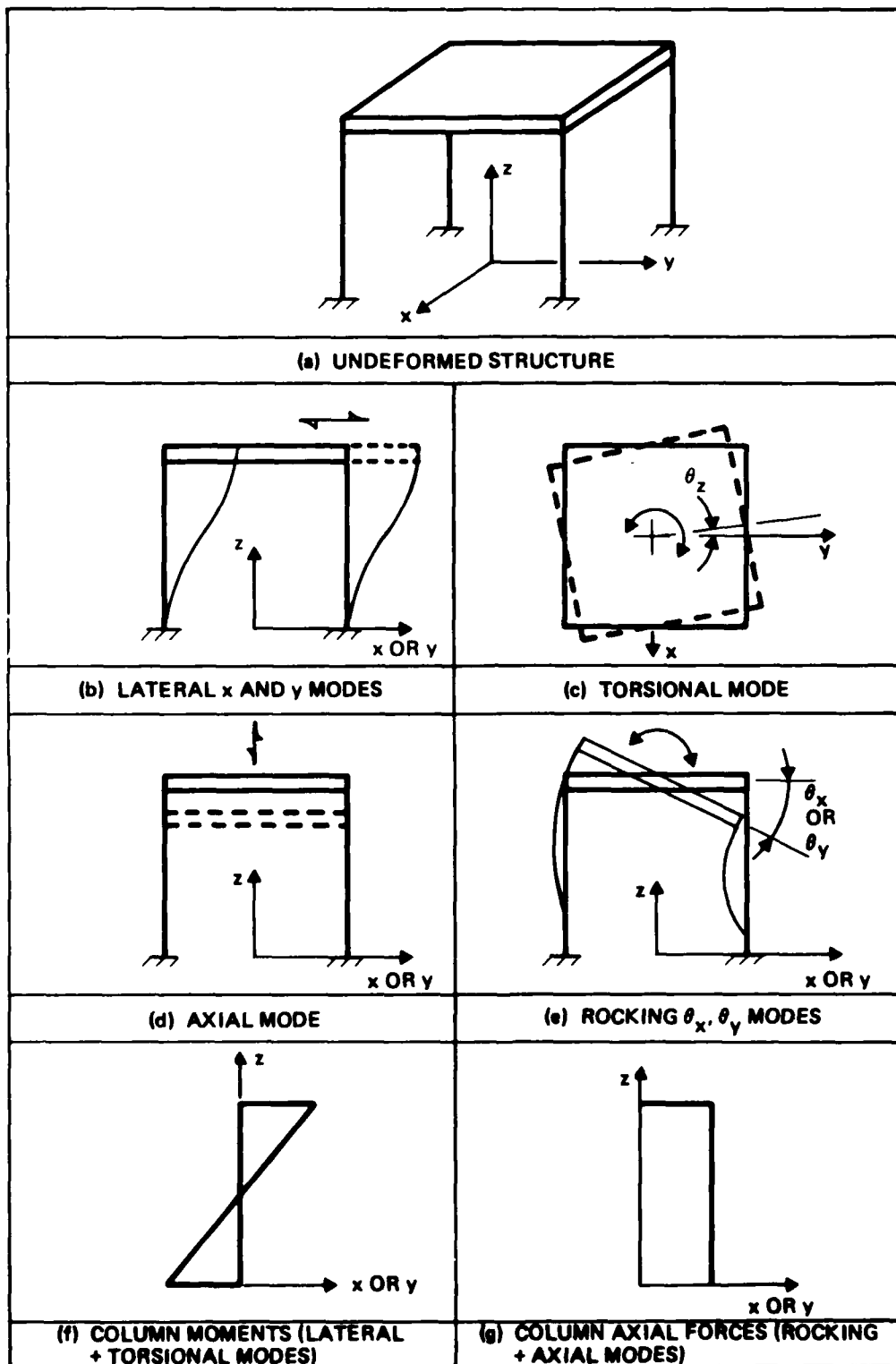


Figure 4-1. Predominant Force-Deflection Characteristics of Experiment Structure

simulated mirror translate directly into axial reaction forces in the columns. Hence, to introduce damping in these modes, the VE material must be so configured as to absorb some of the energy due to the axial motion of the columns.

The desire to concentrate VE material near the columns' boundaries leads naturally to the concept of a discrete VE "joint." A VE joint, or dashpot, possesses several important advantages over distributed damper concepts. For the generic class of structures proposed for LSS, there are a number of important considerations which favor discrete damper concepts, as they:

- a) Maximize the efficiency of material usage, hence minimize weight penalty.
- b) Maximize quality control, since these devices can be manufactured as independent components.
- c) Modularize the design and thus minimize design and manufacturing costs.
- d) May be readily designed to store axial, bending and torsional strain energies, singly or in combination. This is dictated by the desired structural action (truss or frame behavior).
- e) Can be readily incorporated into mathematical, finite element models as general elements, after their stiffness matrices are derived by detailed 3D finite element models.
- f) Effectively encapsulate the VE material, thus minimizing direct radiation and outgassing effects.
- g) Lend themselves to optimization/trade studies, since each joint may be assigned a cost factor as a fraction of the overall damping contribution per mode.
- h) Can be analyzed in a very cost effective way, since the detailed finite element modeling of only a single joint is required (using a two-step approach), regardless of how many similar joints there are in the structure.

2.1.2 VE Dampers and the Structural Load Paths

Following the selection of a VE damper configuration (a discrete joint) and its location (at the columns' boundaries), there remains to be determined the relation of the damper to the structural load path. Intuitively, there are three possibilities:

- a) A parallel load path arrangement
- b) A series load path arrangement
- c) A combination of a) and b).

Past applications of VE damping have utilized, almost exclusively, the parallel load path approach. This is not surprising, since, in the majority of cases, VE damping was applied as an afterthought -- to correct an existing severe vibration problem. In these cases, a free or constrained layer VE application was used, placing the damper in parallel to the prevailing structural load path.

The main deficiency of a parallel load path arrangement is the high weight penalty associated with it when a significant amount of VE damping is introduced into the structure. This is shown in Figure 4-2. The figure shows the ratio of achievable strain energy in a VE spring when this spring is combined with a metal spring, first in series and then in parallel. It can be shown that, for equal damping efficiency of the two configurations ($R=1$), the two spring rates must be equal ($r=1$). For $r<1$, a series configuration yields higher damping, but for $r>1$, the opposite is true. However, analysis of these results reveals that it is extremely weight inefficient to design a parallel load path with $r>1$, where the VE material carries more than 50 percent of the imposed load. Hence to introduce significant damping into the system with minimal weight penalty, the series load path must be preferred, even in cases where $r>1$. It should be noticed, however, that the preferred design region in Figure 4-2 (for $r<1$) is normally constrained by the existence of a minimum stiffness requirement for precision LSS, as well as potential on-orbit creep effects for applications where a static preload may exist in the structural link (such as in tensioned cables).

4.2 DESIGN OF A DISCRETE VISCOELASTIC JOINT

Several candidate joint designs were considered for the TRW LSS experiment. Because of practical considerations and the load path requirements discussed above, two competing constrained viscoelastic damping layer concepts emerged. These are the double-shear action rectangular joints depicted in Figure 4-3 and the spherical ball-and-socket joint shown in Figure 4-4. Due to time and budgetary limitations, the relative merits of these two concepts, and possibly others, were not investigated. The rectangular joint was chosen for application to the TRW LSS experiment -- a choice based largely on its relatively simple fabrication procedures. The finite element modeling details of this VE joint are discussed in the next section.

4.2.1 Finite Element Modeling of a Viscoelastic Joint

A NASTRAN finite element model of the joint depicted in Figure 4-3 was constructed for a set of nominal joint parameters determined from approximate analytical considerations. The model of the joint shown in Figures 4-5 and 4-6 includes 202 grid points. It is composed of 64 solid CHEXA elements, half of which are used to model the viscoelastic elements and the rest to model the central aluminum constraining layer. The outer aluminum constraining layers are modeled by 32 offset CQUAD elements. The rigid aluminum blocks to which the central and outer aluminum constraining layers are attached are modeled by 72 relatively rigid CBAR elements. The free-free unconstrained model of the single joint has two planes of symmetry and a total of 876 degrees of freedom.

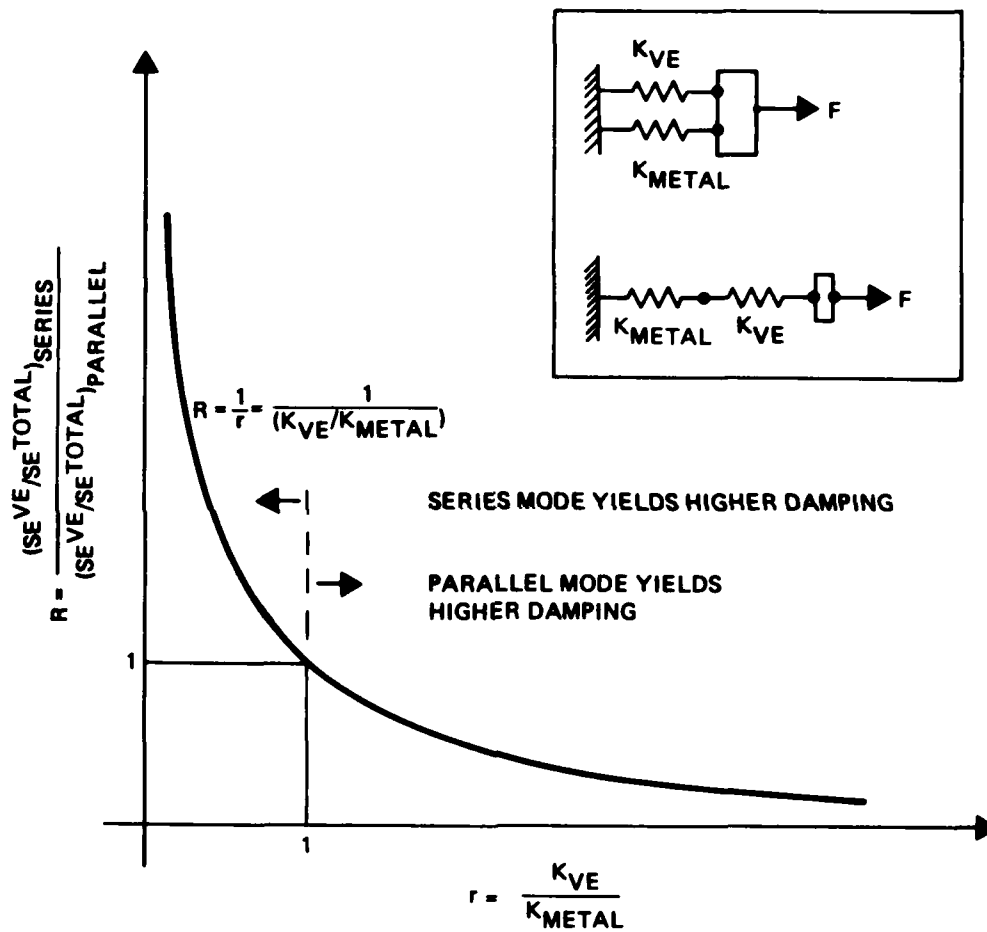


Figure 4-2. Comparative Study of Series and Parallel Load Paths

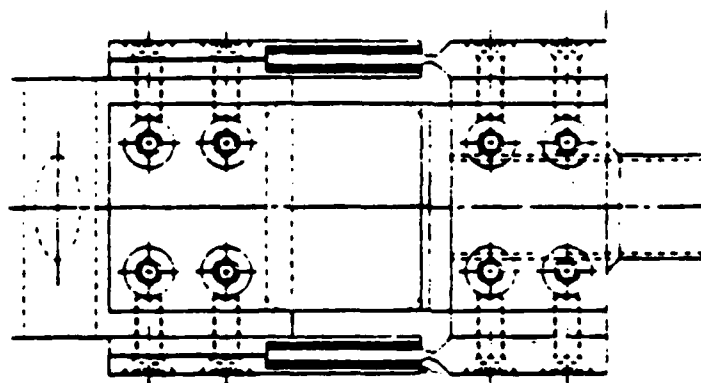


Figure 4-3. Rectangular Viscoelastic Joint in Double Shear

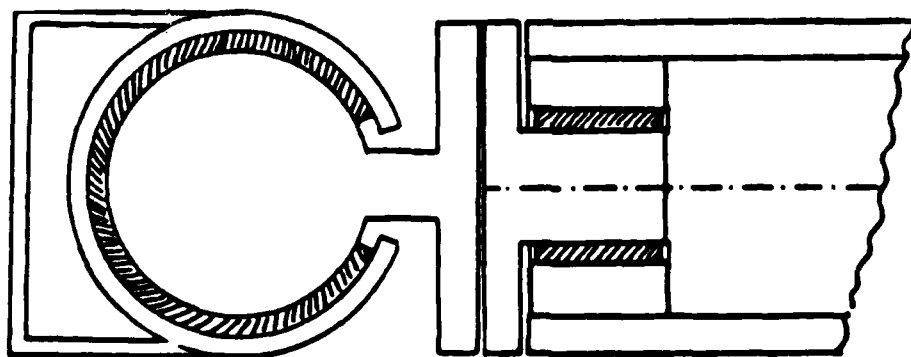


Figure 4-4. Spherical Ball and Socket Viscoelastic Joint

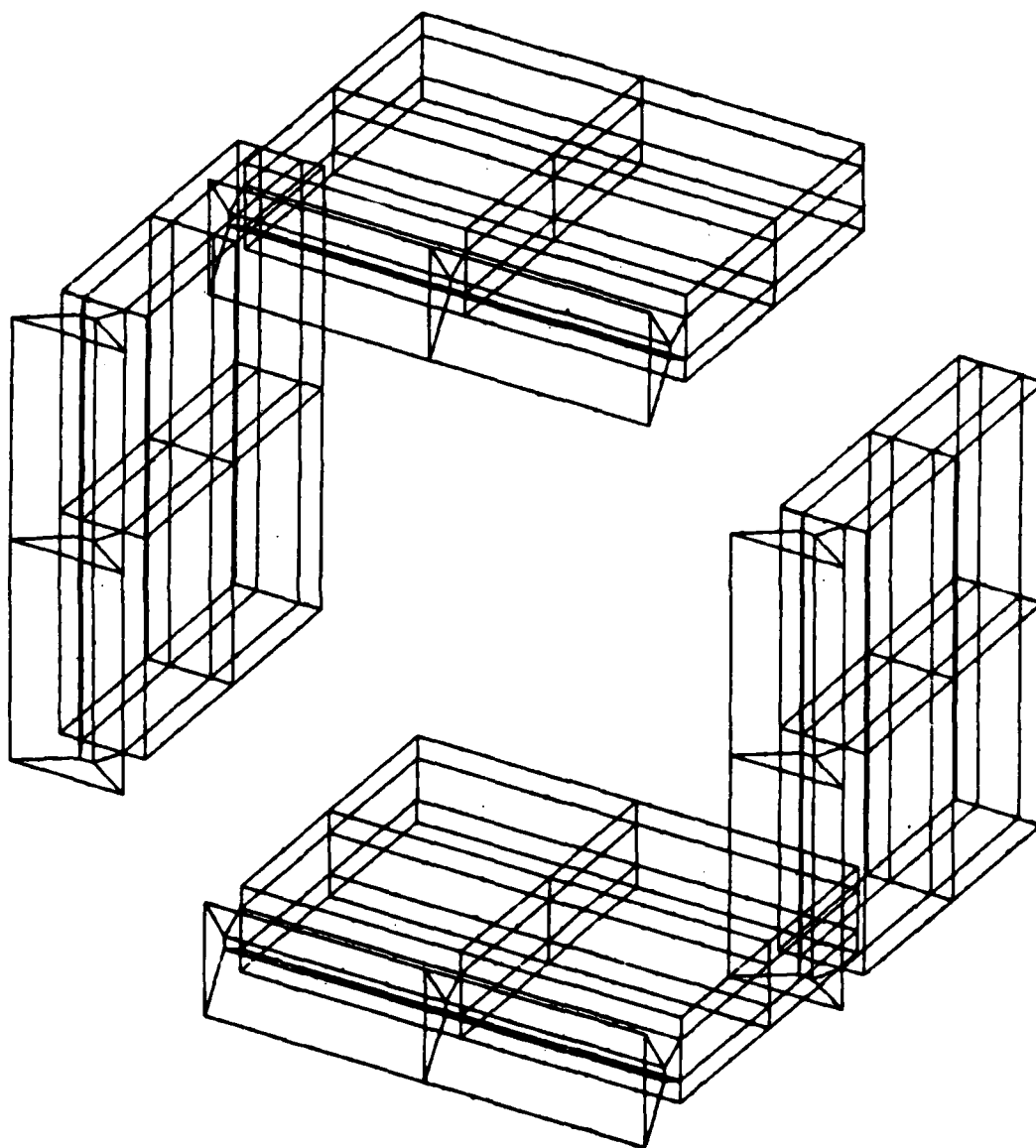


Figure 4-5. NASTRAN Finite Element Model of Viscoelastic Joint

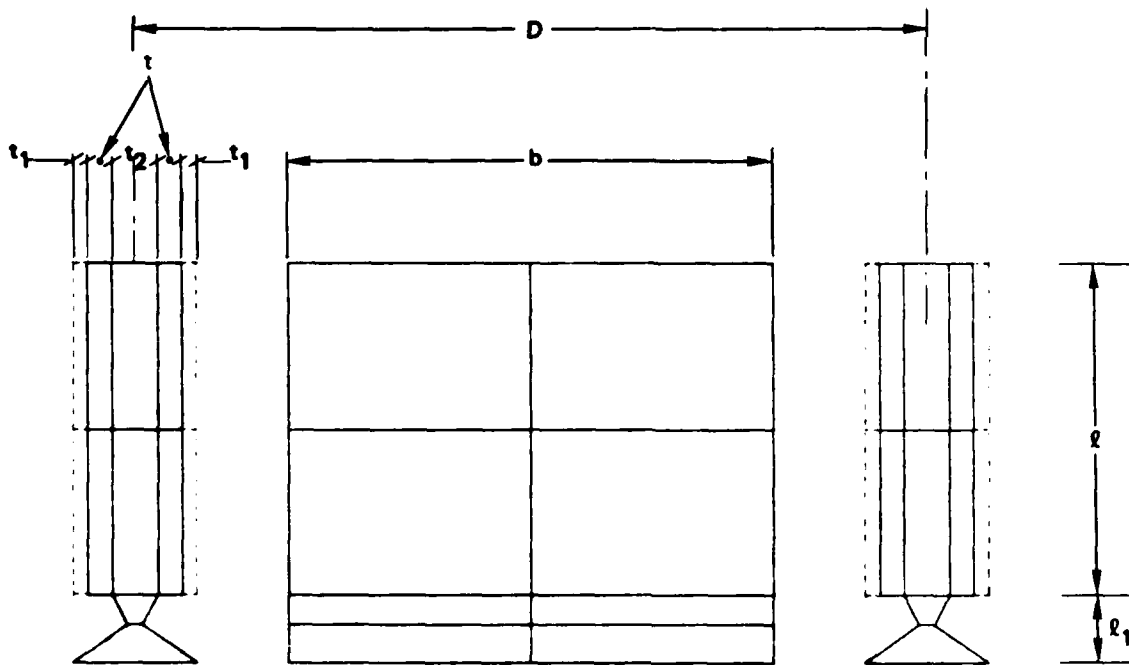


Figure 4-6. Design Parameters of Viscoelastic Joint

4.2.2 Joint Flexibility and Strain Energy Analysis

The joint model shown above was cantilevered at grid point 6 and subjected to unit forces and moment, applied one at a time. See Figure 4-7 for the grid locations. The resulting deflections and strain energy distribution in the joint were calculated. The percentages of the strain energy stored in the VE material out of the total joint strain energy was found to be 74 percent, 74 percent, 99 percent, 94 percent, 94 percent, and 88 percent in the x , y , z , θ_x , θ_y , and θ_z directions, respectively. These percentages provide a measure of the efficiency of the joint, i.e., a 100 percent efficiency indicating that all the elastic energy in the joint is stored in the VE material. For the present application, it was noted earlier (see Figure 4-1) that the damper stiffness components in the θ_x , θ_y , and z directions play a major role in the dynamics of the structure. Therefore, as the above stated efficiency values indicate, the initial design of the joint damper appears to be quite satisfactory. The VE material selected for the damper's design was Scotchdamp SJ-2015X Type 110, manufactured by the 3M Company. Since the structure is to be tested in a laboratory environment, material properties at room temperature were used in the computations. The dynamic properties of this material are shown in Figure 4-8.

Some of the deflected shapes of the joint damper under unit force and moment loading conditions are shown in Figures 4-9 through 4-12.

----- } CBAR ELEMENTS IN x-y PLANE

NODE 6: CLAMPED

NODE 1: UNIT LOADS AND MOMENTS APPLIED

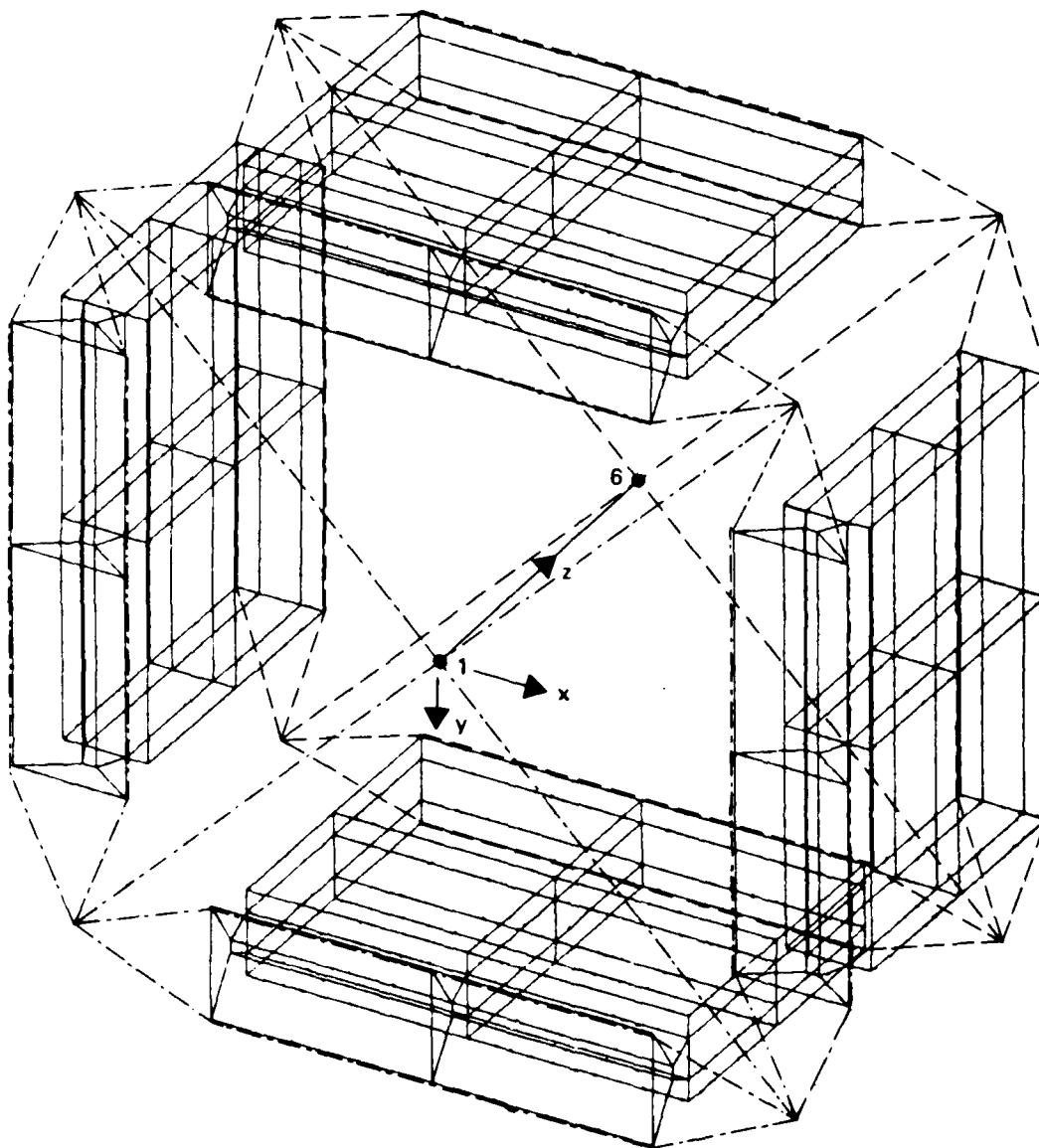


Figure 4-7. Joint Flexibility Calculation

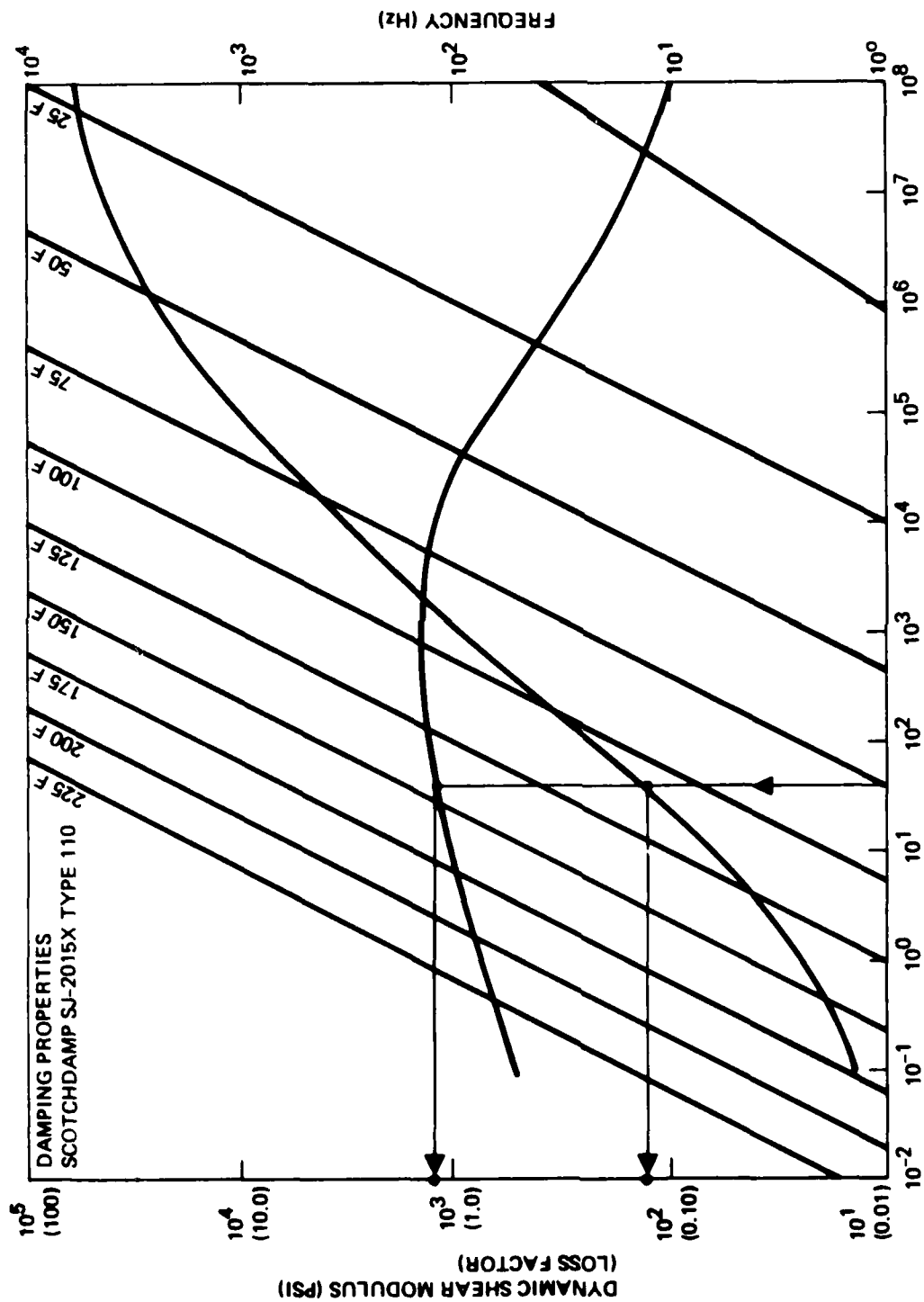


Figure 4-8. Damping Properties of Viscoelastic Material
 (Ref: Scotchdamp SJ-2015 x Type 110,
 Manufactured by 3M Company)

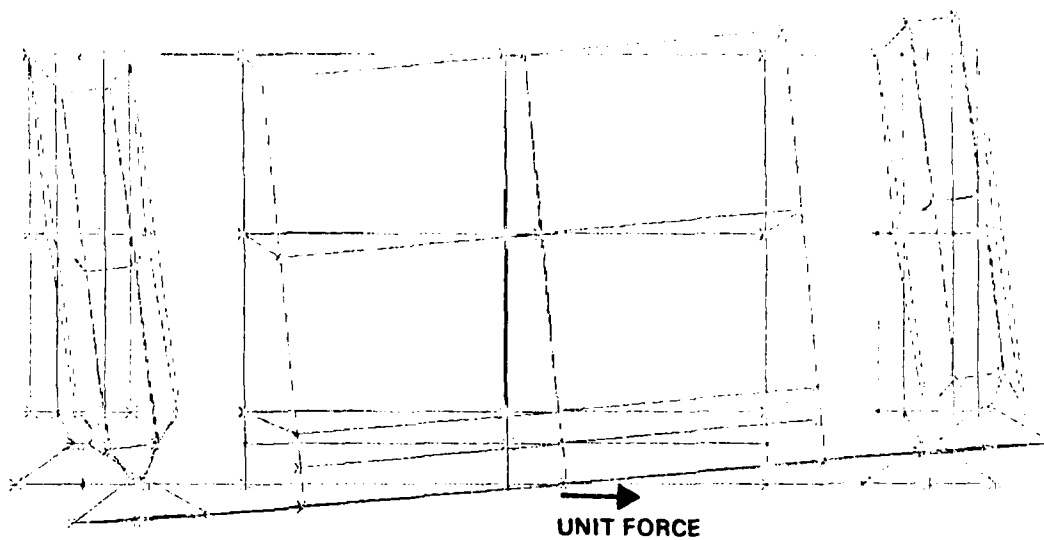


Figure 4-9. Joint Deformation Due to Unit Force Along x or y Axis

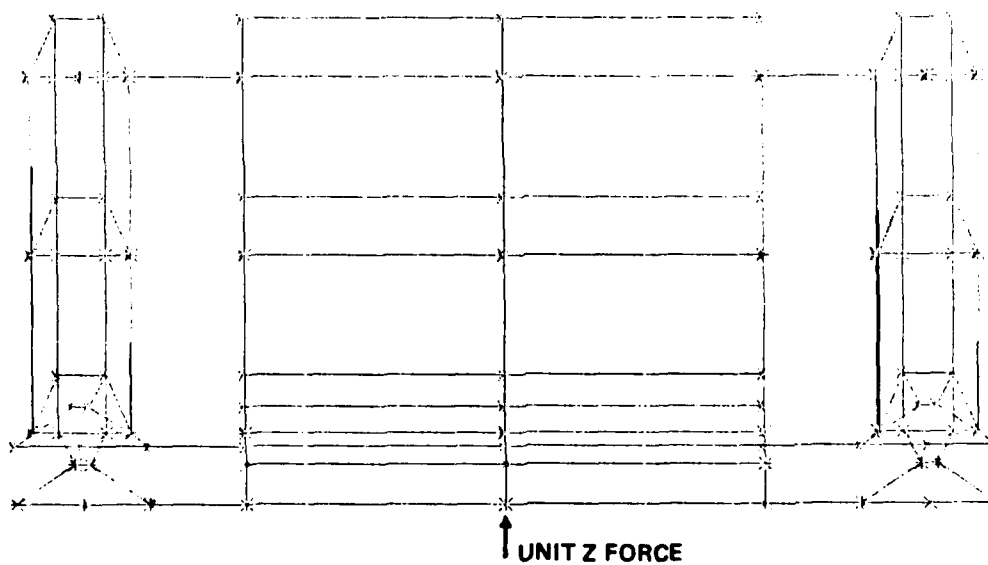


Figure 4-10. Joint Deformation Due to Unit Force Along z Axis

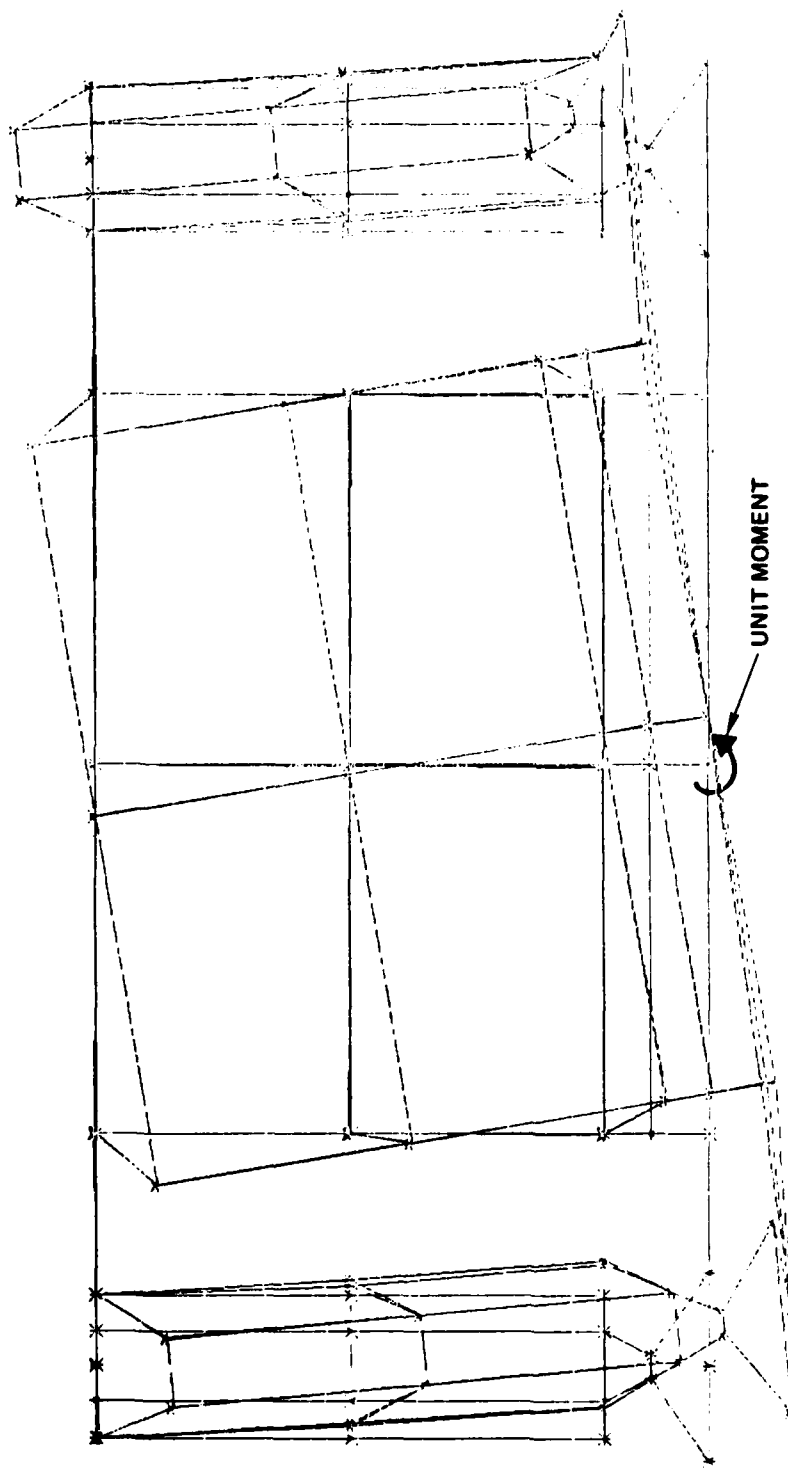


Figure 4-11. Joint Deformation due to Unit Applied Moment About x or y Axis

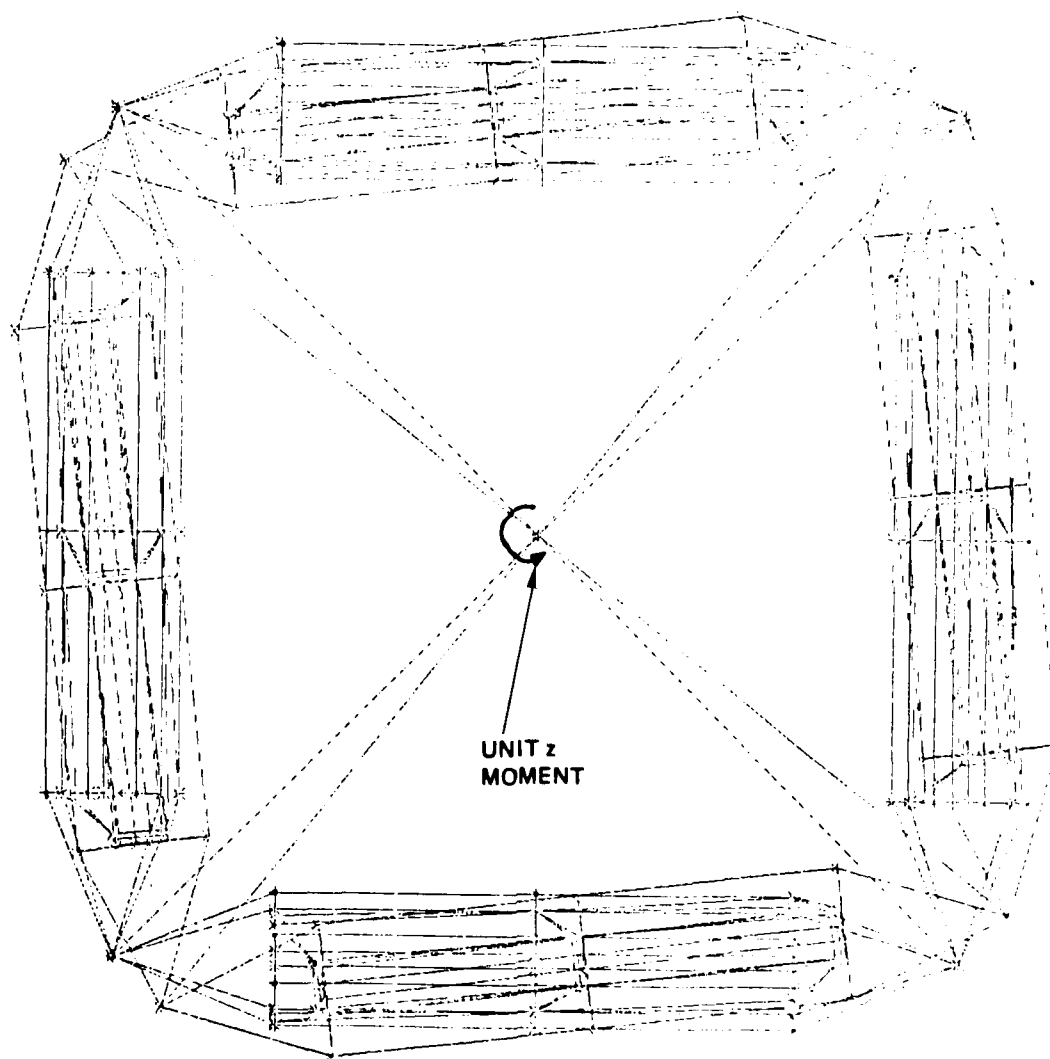


Figure 4-12. Joint Deformation Due to Unit Applied Torque About z Axis

Once the joint flexibility is considered satisfactory, a 12 x 12 free-free stiffness matrix of the joint is calculated and saved for future use. This stiffness matrix is then integrated into the composite structure finite element model (through DMIG card images) for each joint damper in the system. This is described in the following section.

4.3 DYNAMIC ANALYSIS OF A STRUCTURE INCORPORATING VISCOELASTIC JOINTS

As described in Section 1.1, the purpose of the TRW LSS experiment is to yield information leading to the optimization of the blending of passive damping and active control of LSS. To this end, the actively controlled structure must be tested with and without augmented passive damping, requiring an interchangeable set of damped and undamped joints. The geometry of an undamped joint designed for the experiment is depicted in Figure 4-13 and that of a damped joint is shown in Figure 4-14. Note that the two joints are completely interchangeable.

A finite element model and a modal analysis of the undamped experiment structure were described in detail in [9]. This section is devoted to a description of the analysis of the damped structure, yielding realistic estimates of modal loss factors which may be used to evaluate the structure's response to imposed external loads.

4.3.1 A Finite Element Model of the Composite Damped Structure

A finite element model of the damped TRW LSS experiment (see Figures 1-1 and 1-2) was constructed on Program NASTRAN utilizing 78 grid points. The top plate was modeled by eight CTRIA3 2D honeycomb shell elements and the aluminum tubes and linear actuators by 64 1D CBAR elements. The model has 33 mass-loaded points, with 434 DOF of which 335 are Gaussian eliminated, thus leaving a total of 99 dynamic DOF. As mentioned earlier, the eight VE joints are represented in the model by direct stiffness entry DMIG card images.

The design methodology which facilitates representing the VE joints in the overall structure as 12 x 12 stiffness matrices has a major impact on the computational efficiency of the modeling procedure. The savings accrued from this technique are twofold:

- a) In the initial modeling of the structure, where the introduction of hundreds of finite element joint models in a full size LSS model is very time-consuming
- b) In the computational cost for model reduction.

As an example of the latter's cost savings, consider the relatively simple structure presented herein. If the full finite element models of the 8 VE joints were included in the model of the composite structure, the latter would have possessed 7442 structural DOF which would then require Gaussian elimination to the aforementioned 99 dynamic DOF. Assuming, conservatively, that the computational cost is proportional to the cubic power of the number of DOF in the model, then the stiffness matrix representation translates into a computational cost-saving factor of $(7442/434)^3 = 5000$ per run. This cost reduction factor will undoubtedly become much larger for a full-size LSS model which contains tens of thousands of structural DOF.

UNDAMPED FLEXURE
(4 PER JOINT)

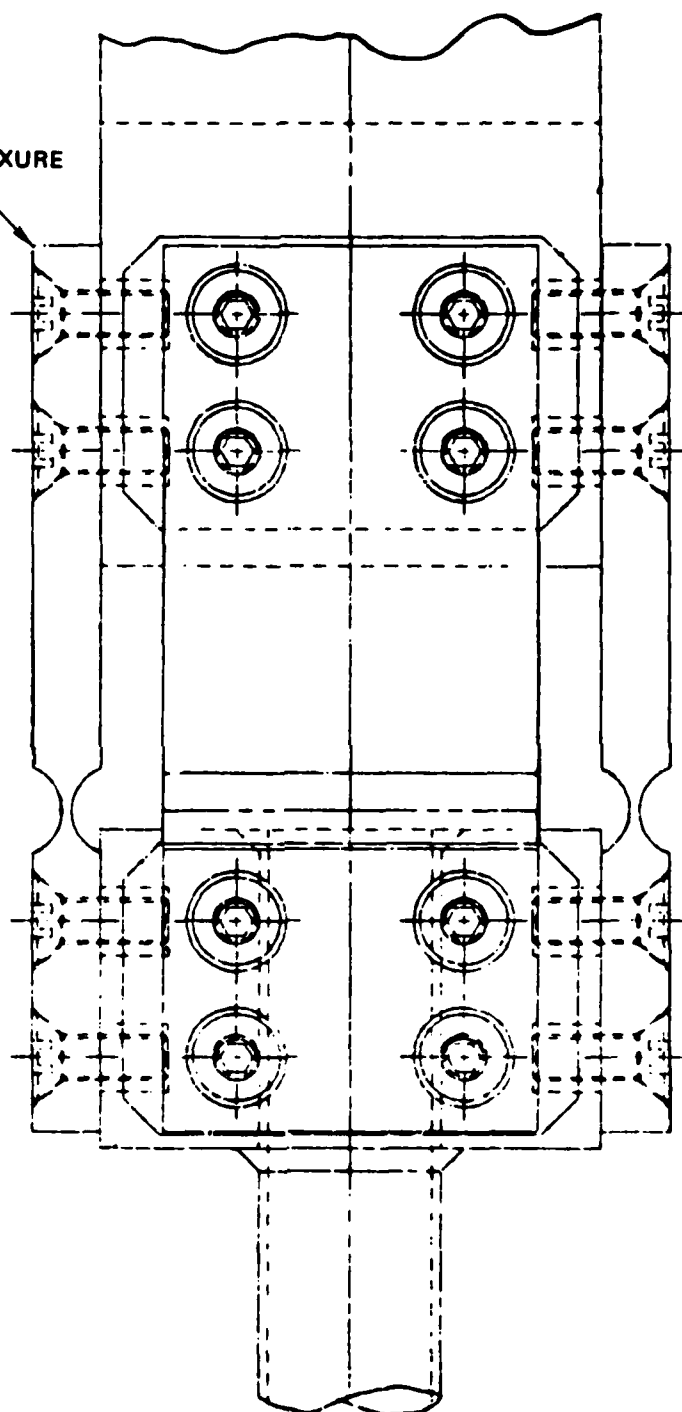


Figure 4-13. Undamped Joint

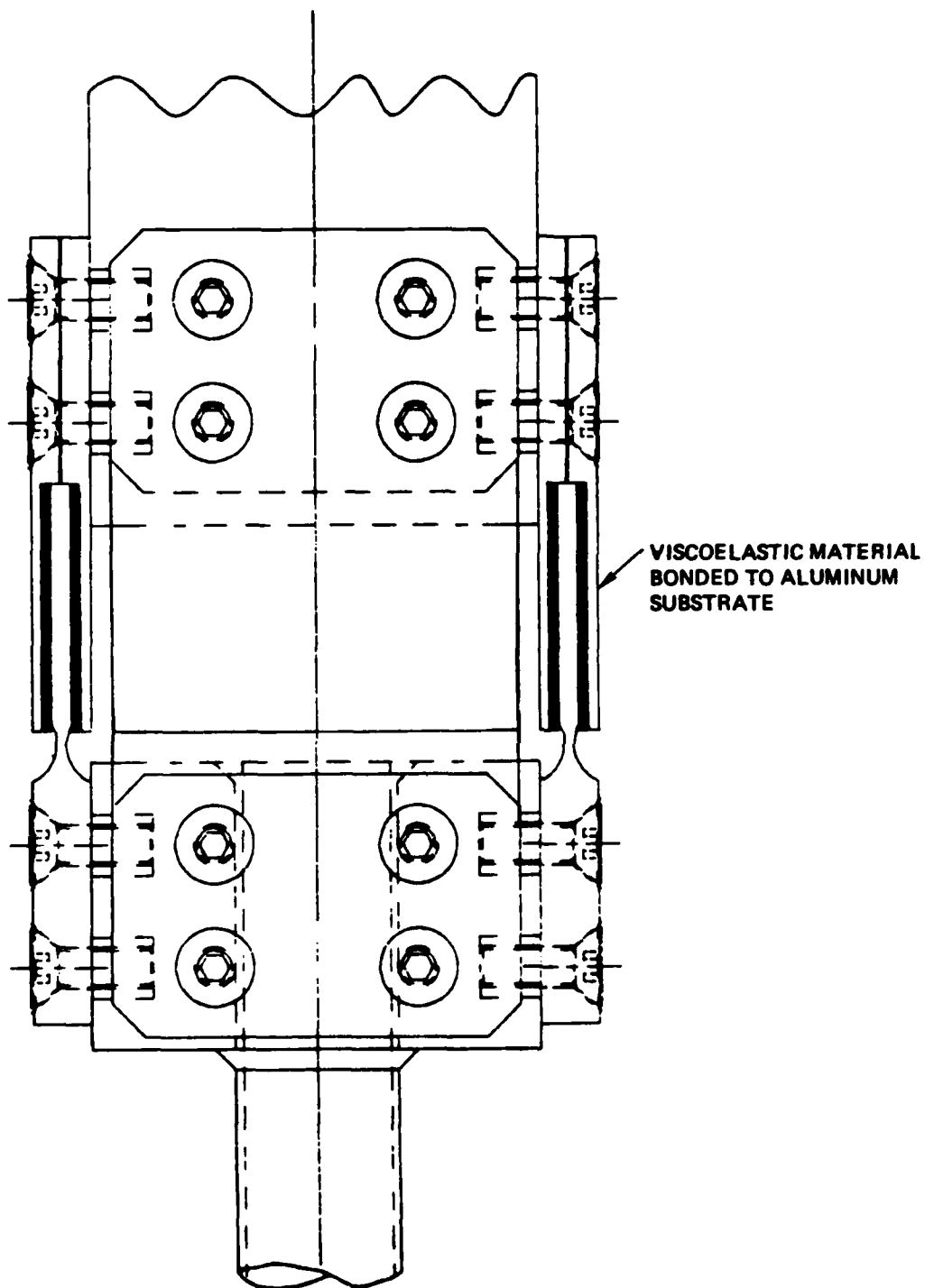


Figure 4-14. Detail of Viscoelastic Damper

4.3.2 Modal Strain Energy Analysis

There are a number of analytical approaches applicable to the modeling of viscoelastically damped structures which have been reported in the literature [6]. These include:

- a) Modal strain energy (MSE) approach
- b) Direct frequency response approach
- c) Complex eigenvalue -- eigenvector approach
- d) Fractional calculus approach
- e) Operational methods -- based on numerical inversion of Laplace transforms.

The pros and cons of some of these approaches have been briefly discussed in the literature (see [7]). The MSE method, although heuristic in nature, appears to be the most straightforward and, at the same time, compatible with finite element modeling tools. This method consists of (see [6] and [7] for details):

- a) Finite element modeling of the undamped structure
- b) Modal analysis (modes + modal strain energies)
- c) Selection of damping parameters and locations
- d) Development of finite element models for the structure including viscoelastic materials
- e) Modal analysis of d) (modes + strain energy)
- f) Calculation of system loss factors (here an iterative process may be exercised to approximately incorporate the VE material frequency dependence)
- g) Damped vibration response analysis
- h) Assessment of compliance data, if satisfactory, completes the design; otherwise, steps c) through h) are repeated until design requirements are satisfied.

In [7], the above process is carried out for a simple example with acceptable engineering accuracy. The reference also clearly indicates the tradeoff between accuracy of results and model simplicity for the MSE method and the direct frequency response approach.

The MSE method is based on the principle that the ratio of composite structural loss factor to VE material loss factor for a given mode of

vibration can be estimated as the ratio of elastic strain energy in the VE material to the total strain energy in the entire structure when it deforms into the particular undamped mode shape. Denoting the system loss factors by η_i , these may be calculated from:

$$\frac{\eta_i}{\eta_{VE}} = \frac{1/2 \phi_{VE}^{(i)T} K_{VE} \phi_{VE}^{(i)}}{1/2 \phi^{(i)T} K \phi^{(i)}} = \frac{SE_{VE}^{(i)}}{SE_{Total}^{(i)}} = \frac{2 SE_{VE}^{(i)}}{\omega_i^2} \quad (1)$$

Where:

$\eta_i = 2\xi_i$ = The i-th mode system loss factor

ξ_i = The i-th mode critical damping ratio

η_{VE} = Loss factor of VE material (Figure 4-8)

$\phi_{VE}^{(i)}, \phi^{(i)}$ = The i-th mode shape associated with VE material DOF and total structure, respectively

K_{VE} = Stiffness matrix due to VE material

K = Global stiffness matrix of total structure

$\phi^{(i)}$ = i-th structural mode shape vector

$(SE)_{VE}^{(i)}, (SE)_{Total}^{(i)}$ = i-th modal strain energy stored in VE material and total structure, respectively

ω_i = The i-th undamped natural frequency in (rad/sec)

Since η_{VE} is frequency dependent, it must be evaluated at the frequency of interest. Then, the i-th mode critical damping ratio ξ_i is obtained from:

$$\xi_i = \frac{(SE)_{VE}^{(i)}}{\omega_i^2} \eta_{VE}(\omega_i) \quad (2)$$

The damped structure's response to external loads is calculated in the conventional manner, using the uncoupled modal equations of motion, where the critical damping ratios ξ_i of equation (2) multiply the velocity terms.

The utilization of Program NASTRAN in the MSE methodology, as outlined above, has the disadvantage of not being able to extract the stiffness matrix K_{VE} in equation (1) from the total structure's finite element model. This is because the joint dampers are not modeled there as finite elements, but instead are represented by their 12 x 12 stiffness matrices. To remedy this deficiency, one may return to the detailed finite element of the joint damper and generate another stiffness matrix which does not include the VE material

contribution. By subtracting the latter matrix from the original one, the desired partitioned matrix K_{VE} can be obtained. Note also that in computing the strain energy of a structure, Program NASTRAN provides only the composite (total) strain energy for a given mode, making it difficult to differentiate among the strain energy components contributed by local bending, torsion, axial deformation, etc. As this information is vital in optimizing the damper's configuration, it may be obtained from Program NASTRAN by evaluating the generalized forces acting on the structure.

4.4 PREDICTION OF MODAL DAMPING RATIOS BASED ON MSE TECHNIQUE RESULTS

This section presents the analytical results obtained for the TRW LSS experiment in the form of modal damping ratios using the methodology described above. As seen in Figure 4-6, the joint damper may be defined by seven geometric parameters. However, only two of these, the thickness of the VE layer t and its width b were varied for the present study. The results reported herein cover four different combinations of these parameters whose numerical values are depicted in Table 1.

Table 1. Combinations of Joint Parameters

Case	Joint Parameters*		
	Viscoelastic Layer Thickness t (in.)	Viscoelastic Layer Width b (in.)	$\frac{t}{b}$
Nominal	0.100	2.000	0.05
1	0.100	1.000	0.10
2	0.050	2.000	0.025
3	0.050	1.000	0.05

* See Figure 4-6 for joint dimensions.

In Figure 4-15 (the nominal case), the loci of the first three natural modes of the simulated mirror are displayed as functions of the shear modulus of the VE material. A similar plot, for the axial, rocking, and first mirror-bending modes follow in Figure 4-16. Also shown in these two figures are the frequency variations of the shear modulus of the VE material. The intersection of the shear modulus curve with the locus of any natural mode defines the VE shear modulus, which is appropriate for calculating the damping of that mode at the indicated frequency. These frequencies are used together with Figure 4-8 to obtain the VE material loss factors $n_{VE}(\omega_i)$. As can be seen from Figure 4-8, the VE material chosen for the present study exhibits high loss factor ($n_{VE} > 1.2$) in the frequency range of interest (1-80 Hz) and at ambient conditions (75°F).

In Figure 4-17, the expression given for n_i/n_{VE} in equation (1) is plotted as a function of: (1) t , (2) b , and (3) t/b . It is observed that for case (3), a log-log plot resulted in straight lines for the seven structural modes of mirror motion studied (2 lateral, 1 torsional, 1 axial, 2 rocking, and 1 bending). These lines thus summarize the results obtained for the four different parameter combinations of Table 1. Figure 4-17, together with

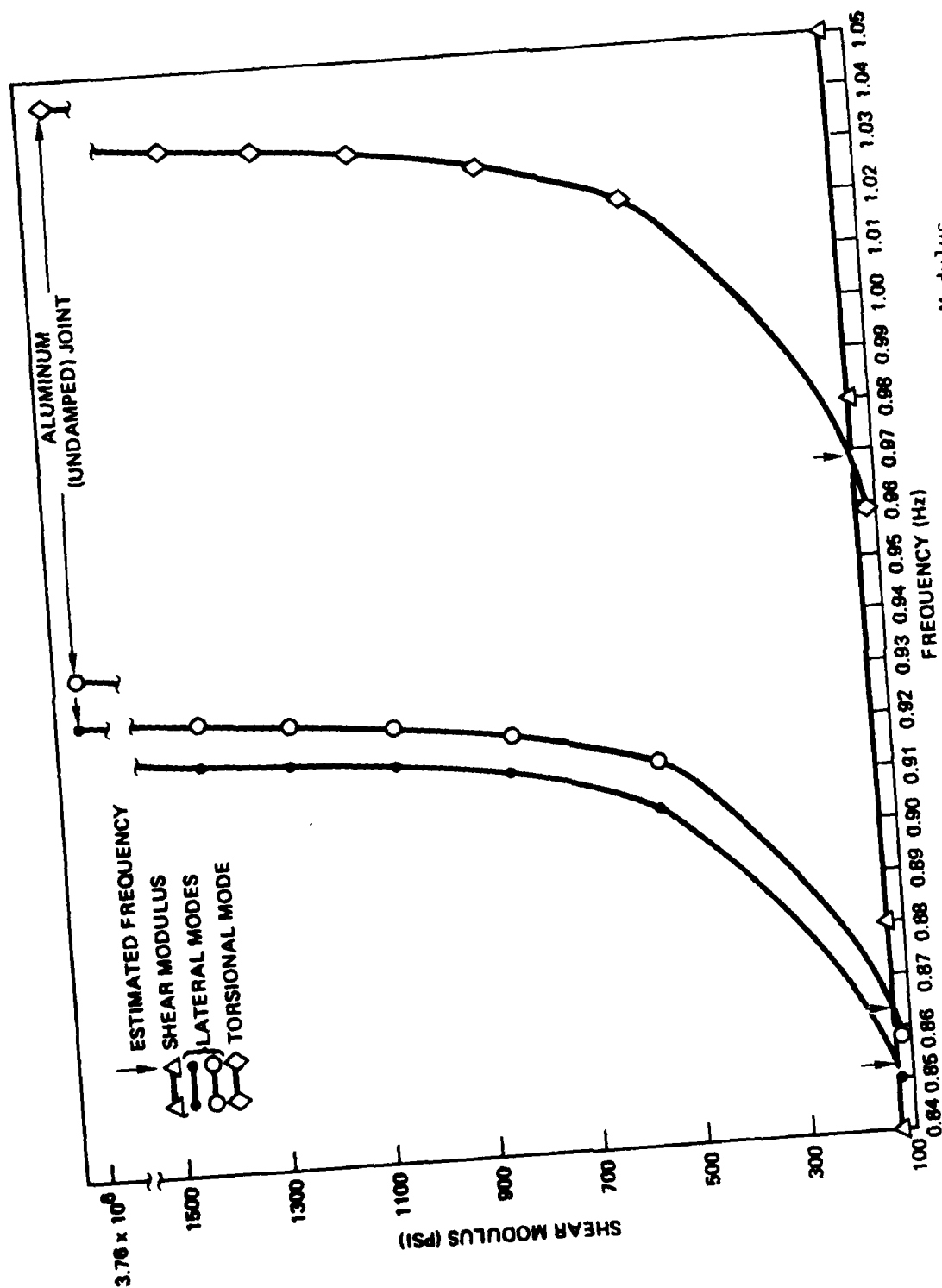


Figure 4-15. Frequency Variations Versus VE Shear Modulus

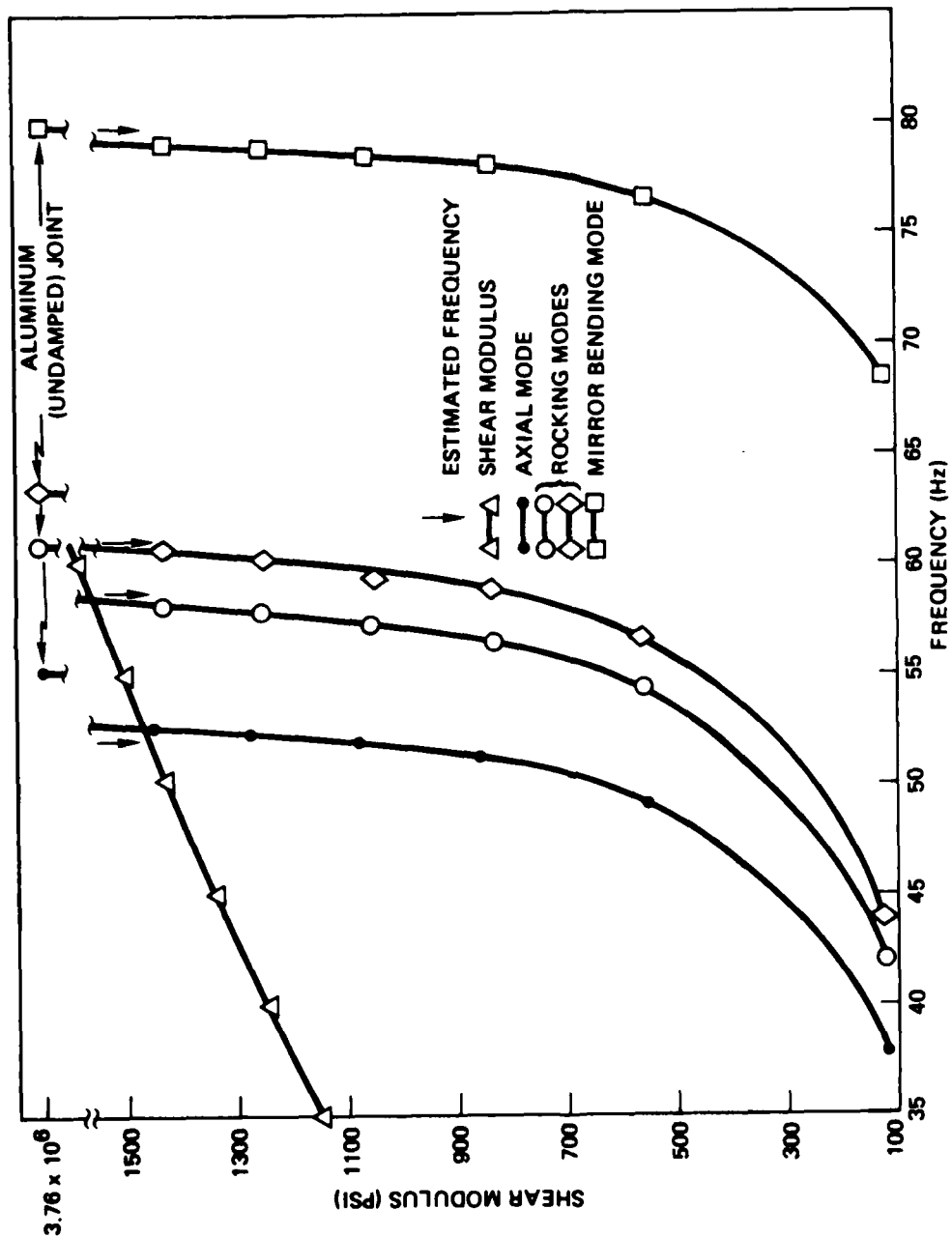


Figure 4-16. Frequency Variations Versus VE Shear Modulus

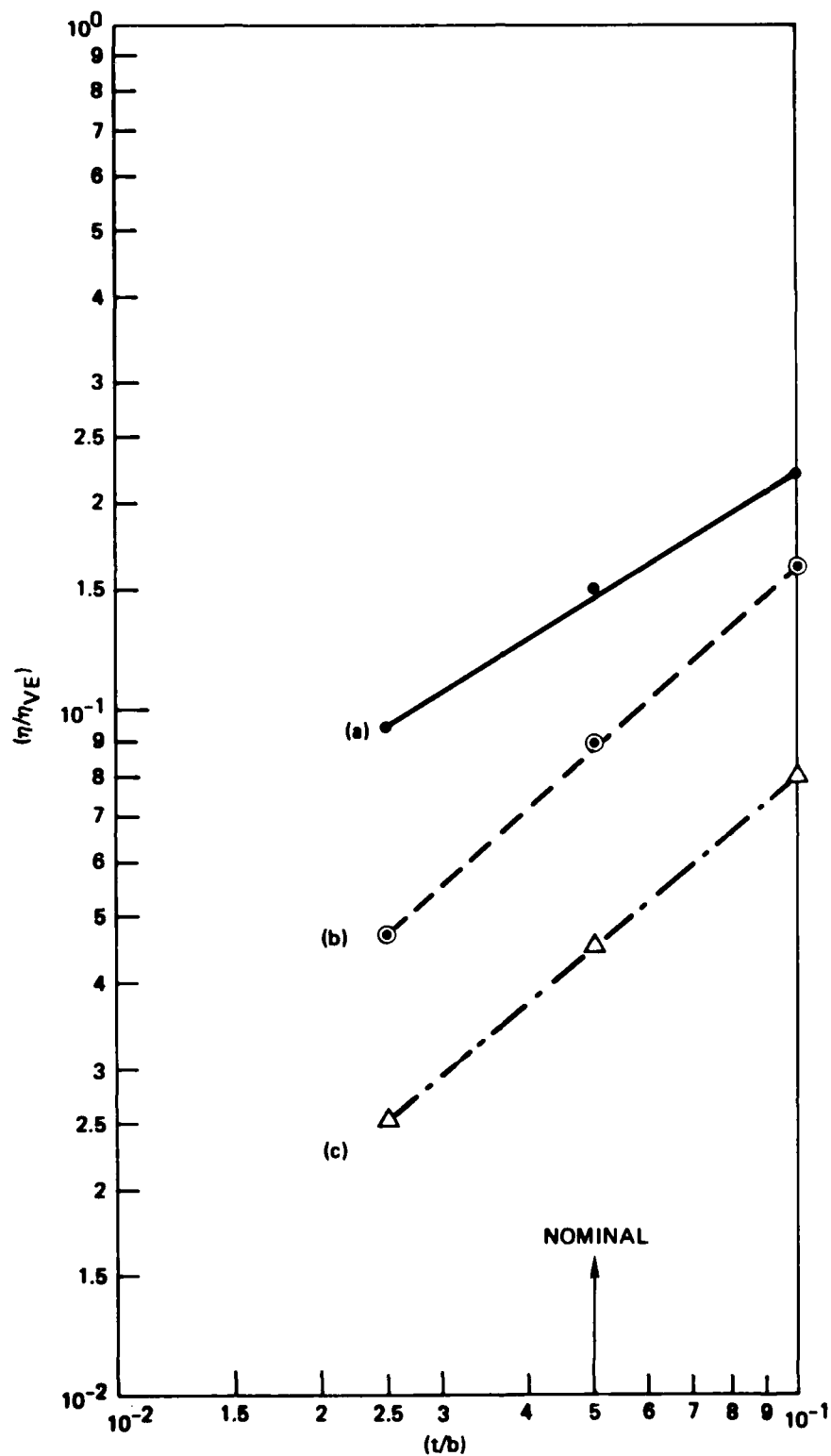


Figure 4-17. Ratio of Loss Factors Versus Nondimensional Joint Parameters: (a) Mirror Lateral and Torsional Modes, (b) Mirror Axial and Rocking Modes, (c) Mirror Bending Mode

Figures 4-8, 4-15, and 4-16, contains all the information necessary to establish the designed damping characteristics of the seven important modes of the simulated mirror. These damping values are summarized in Table 2. It should be noted that for the nominal case ($t = 0.1$ inch, $b = 2$ inches), 9 percent of critical damping is predicted for the in-plane mirror modes at frequencies close to 1 Hz. This value of augmented damping is an order of magnitude greater than can be expected from the undamped structure and was obtained at a weight penalty of 8 percent of the total structural weight. Lower values of damping were calculated for the two mirror rocking modes (5.4 percent), the axial (defocus) mode (5.4 percent), and the bending mode (2.7 percent).

Table 2. Summary of Damping Results

Mode	Description	Frequency** (Hz)	Modal Damping Ratio, ξ (%)		
			$t/b = 0.025$	$t/b = 0.050^{**}$	$t/b = 0.100$
1	Mirror lateral mode 1	0.85 (0.93) ^(†)	5.6	9	13
2	Mirror lateral mode 2	0.86 (0.94)	5.6	9	13
3	Mirror torsional mode	0.97 (1.05)	5.6	9	13
28	Mirror axial mode	53 (55)	2.8	5.4	9.6
29	Mirror rocking mode 1	58 (61)	2.8	5.4	9.6
30	Mirror rocking mode 2	61 (63)	2.8	5.4	9.6
47	Mirror bending mode	79 (80)	1.5	2.7	4.8

* For intermediate values of (t/b) use Figure 19.

** Nominal case.

(†) Values in parenthesis relate to the undamped structure.

A substantial amount of analytical effort was undertaken to substantiate the results obtained from the finite element tools described herein. The relatively simple structural geometry of the TRW LSS experiment lent itself to closed form analytical prediction of damping which was in good agreement with the finite element results. As can be seen in Figure 4-18, the damping in the first three structural modes is governed by the nondimensional parameter $k_\theta/(6EI/L)$, where k_θ is the bending stiffness of the VE joint and $6EI/L$ is the bending stiffness of the column. The good agreement between the analytical and finite element results validates the structural deformation postulates shown in Figure 4-1. It is noteworthy that for a given joint damper stiffness, k_θ structural damping in the first three modes increases with EI , the column bending rigidity.

A separate analytical effort verified the static stability of the TRW LSS experiment, accounting for the expected disturbances to the simulated mirror and the control forces in the diagonal rods.

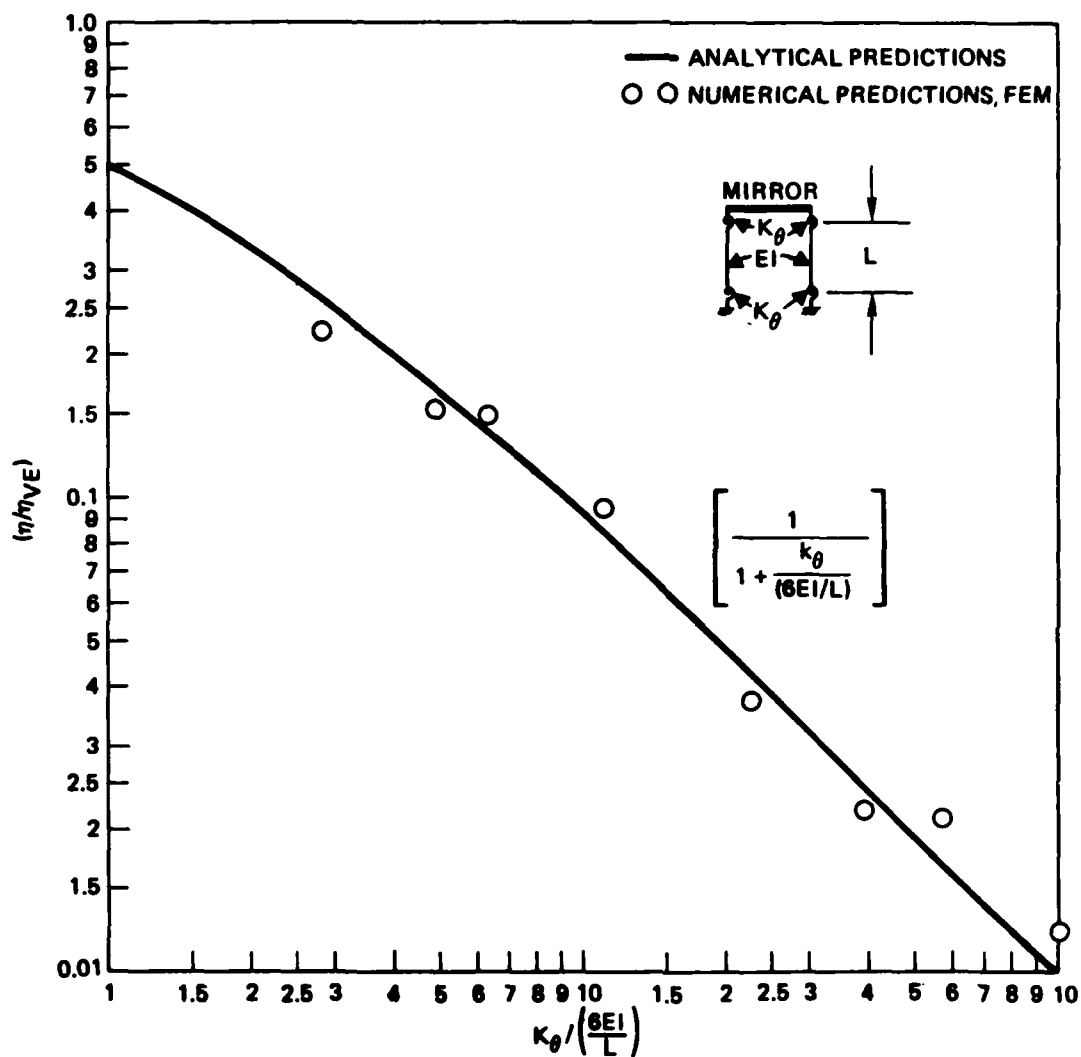


Figure 4-18. Comparison of Analytical and Numerical Predictions Damping for the First Three Modes

Finally, it is worth mentioning that, in addition to the damping results stated above, the finite element analysis also revealed significant damping of local column bending modes. These were excluded from Table 2, however, due to the very weak coupling exhibited by these modes with the simulated mirror modes -- the primary concern of the TRW LSS experiment.

5. CLOSURE

Presented herein is a methodology for the passive damping augmentation of LSS, leading to a capability for the optimal blending of active and passive control of these space systems. The methodology incorporates several innovative concepts which significantly contribute to the practicality of the proposed procedure. These include:

- a) A simple conceptual design of passive dampers
- b) A cost effective design, including standardized, modular, and discrete VE dampers, which is easy to manufacture and which lends itself well to high quality control standards
- c) An efficient design procedure which is relatively inexpensive to analyze, using existing finite element analysis tools.
- d) A damper configuration with a minimum weight penalty.

The study results obtained to date stem from finite element modeling techniques which were subsequently verified by closed form analytical approximations. These results show a capability of the proposed damper design to substantially augment the structural damping of LSS over a wide frequency band. Furthermore, and unlike active control systems, the evolved damper design was shown to be insensitive to the frequency parameter, providing vibration control at both low and high frequencies without incurring a cost penalty.

REFERENCES

1. Holman, R. E., et al., "Damping of Precision Pointing Systems and the Use of Finite Element Computational Program for Performance Prediction," a paper presented at the AIAA/ASME 23rd Structures, Structural Dynamics, and Materials Conference, April 1982.
2. Balas, M. J., "Modal Control of Certain Flexible Dynamic Systems," SIAM J. Control and Optimization, No. 16, 1978.
3. Major, C. S., et al., "An Experiment to Demonstrate Active and Passive Control of a Flexible Structure," to be presented at the American Control Conference San Diego, California, June 6-8, 1984.
4. Benhabib, R. J., et al., "Final Technical Report, Active Control of Space Structures (ACOSS-14)," November 1982.
5. MacFarlane, A. G. J., and Kouvaritakis, B., "A Design Technique for Linear Multivariable Feedback Systems," December 1976.
6. Drake, M. L., ed., "Vibration Damping Short Course Notes," University of Dayton Research Institute, 1982.
7. Johnson, C. D., et al., "Finite Element Prediction of Damping in Beams with Constrained Viscoelastic Layers," The Shock and Vibration Bulletin, No. 51, published by NRL, Washington, D. C., May 1981.
8. TRW Report F33615-81-C-3235, "VCOSS, Final Report," May 1983.
9. Simonian, S. S., "LSS Truss Experiment Dynamic Model," TRW IUC L013.2.83-140, September 1983.
10. TRW Space and Technology Group, "A Proposal for Large Spacecraft Point and Shape Control", TRW No. 43016.000, prepared for USAF WAL, May 1983.
11. Neiswander, R. S., "Conceptual Design of a Surface Measurement System for Large Deployable Space Antennas," Large Space Systems Technology - 1981, NASA Conference Publication 2251, Part 1, 1982.

ACKNOWLEDGEMENT

The authors wish to express their appreciation to Larry N. Gilman of TRW SED Engineering Design Laboratory for his detailed design of the TRW LSS experiment, and to Wallace T. Lee of TRW Dynamics Department for his assistance in the NASTRAN DMAP coding used in the MSE analysis procedure.

SIZING OF DISCRETE VISCOUS DAMPERS
ON A FLEXIBLE BODY IN THE PRESENCE OF
A FIXED CONTROLLER

George R. Rapacki and Dr. Robert B. Rice
Guidance and Control Section
Martin Marietta Aerospace
Denver, Colorado 80201

SIZING OF DISCRETE VISCOUS
DAMPERS ON A FLEXIBLE BODY IN THE PRESENCE
OF A FIXED CONTROLLER

George R. Rapacki

Dr. Robert B. Rice

Guidance and Control Section

Martin Marietta Aerospace

Denver, Colorado 80201

Abstract

The authors investigated the effects of discrete viscous dampers on a spacecraft's rigid body control loop. The damper's affect on the open loop gain and phase margins, the shape of the open loop gain-phase plot and the flexible body dynamics were determined as a function of the viscous damper's strength and the mass connected to the damper. The damper was sized for those configurations where the added damper improved the system robustness.

1.0 Introduction

Sympathetic dampers have been used on dual spin satellites to stabilize a spacecraft in what would normally be an unstable orientation (Ref. 1). In addition, previous studies at Martin Marietta Aerospace (Ref. 2) demonstrated that strategically placed dampers can stabilize an otherwise unstable control system. This study was motivated by the promise of improvements achievable using sympathetic and strategically located passive dampers. The following three approaches were investigated: (1) sympathetic dampers connected to the rigid body of a spacecraft that had a significant flexible appendage, (2) a viscous damper connected between the rigid body and the tip of the flexible appendage of the same spacecraft, and (3) a spacecraft without flexible appendages but with part of the rigid body inertia intentionally mounted on springs and dampers. For the first configuration the changes in control loop stability margins and modal damping ratios were determined as a function of the sympathetic damper's damping ratio. The second configuration was analyzed to determine the same information but calculated as a function of the rigid body-to-tip damper strength. The third configuration, in which components (mass) were isolated from the main body with springs and dampers, was analyzed to determine the control loop stability margins as a function of the suspended mass, damper, and spring's own damping ratio. In addition, each configuration was analyzed for the peak displacement and rate seen by the added damper in response to an input step command. The equations of motion were derived and a reasonable rigid body controller designed for each configuration. Where appropriate, actuator dynamics were added to complete the model. Open loop transfer functions were determined and analyzed with LADCAP, Martin Marietta's Linear Systems Analysis Program.

2.0 Summary and Results

The most effective technique found in this study for stabilizing an unstable rigid body control loop, caused by a flexible appendage, is to connect a damper between the rigid body and the tip of the appendage. A less effective approach was to mount sympathetic dampers on the rigid body. These may be easier to apply, can also improve the stability margins and advantageously alter the open loop gain-phase plot. Unfortunately they do not produce the dramatic results of a damper connected between the rigid body and the tip of a flexible appendage.

For all configurations analyzed, a damping ratio between 0.1 and 0.2 for the Inertia-Damper-Spring mechanisms with a natural frequency equal to the offending mode frequency or to the control bandwidth was most effective. The damper connected between the rigid body and the tip of the flexible appendage changed the damping ratio of the first mode (the destabilizing mode) from 0.00576 to 0.489. The same damper changed the second and third mode's damping ratio from 0.0110 and 0.0159 to 0.0319 and 0.192 respectively. The resulting modal gain margin went from -6.43 dB (unstable) to 13.1 dB. The phase margin of the first mode was changed from -9.32 deg. (unstable) to completely phase stabilized. The damper's stronger influence on the first and third modes is explainable by the greater tip displacement for the first and third modes relative to the rigid body than for the second mode.

A sympathetic damper coupled to the rigid body of a spacecraft that includes a flexible appendage, (the same configuration as above without the damper between the rigid body and the appendage tip) completely stabilized the first mode. The inertia of the sympathetic damper used 10 percent of the rigid body inertia, the damping ratio was 0.1 and the natural frequency of the Inertia-Damper-Spring combination was the same as the first mode frequency, 11.52 rad/sec. A significant decrease in the first mode's phase margin resulted if the Inertia-Damper-Spring's natural frequency differed from the first modal frequency. However, with a sympathetic damper's natural frequency 20 percent higher than the first mode's natural frequency and a damping ratio of 0.2, the first mode was phase stabilized by 16.07 deg. and gain stabilized by 7.54 dB.

A spring-mass-damper combination mounted to a rigid spacecraft with control loop changed the open loop rigid body phase margin from 45 deg. to 53 deg. This was achieved with 10 percent of the rigid body's inertia suspended on a spring-damper tuned at a natural frequency equal to the control loop bandwidth of 1.0 rad/sec and a damping ratio of 0.2. This damper arrangement also has an important effect on the shape of the open-loop gain-phase plot. The damper causes the open loop gain phase plot to do a three quarter turn, resulting in a phase margin insensitive to gain changes. Such an alteration in shape would be difficult to achieve with conventional compensation. Additional dampers did not improve the phase margin sufficiently to warrant their increased complexity. In some cases studied, no improvement resulted from additional sympathetic dampers. A small improvement, 3.3 deg. rigid body phase margin, was achieved by suspending 20 percent of the rigid body's inertia but this seems an unreasonable proportion of the spacecraft's inertia to suspend.

3.0 Sympathetic Dampers to Control Flexible Body Modes

Approach

A flexible body spacecraft augmented with either one, or two sympathetic dampers coupled directly to the rigid body served as the hypothetical model for this study. The joint damping of the lumped mass appendage model was 0.1 percent of each joint's rotational spring constant, 221.83 ft-lb/rad. Joint damping here refers to the strength of a damper at each joint of the ten segment model for the flexible appendage. This joint damping is included to account for the natural damping inherent in the structure. Ten percent of the rigid body inertia was assumed available to allocate to the sympathetic dampers as suspended mass.

A controller with actuator dynamics completed the model. The natural frequency of the sympathetic damper was set nominally at the first mode frequency and perturbed by ± 20 percent. Prior experience indicated that a damping ratio between 0.1 and 0.2 would have the greatest affect on the modes, hence these were examined. The open loop gain and phase margins, modal damping, relative displacements, and rates were determined using LADCAP.

Model and Equations of Motion

Figure 1 shows a schematic of the rigid body, flexible appendage and sympathetic damper. The corresponding equations of motion are in Table 1. Figure 2 shows the spacecraft and controller in block diagram form. The controller was designed to provide a closed loop natural frequency of 1.0 rad/sec and a damping ratio of 0.7. The inertia of the rigid body includes the hub and boom. The sympathetic dampers work with an inertia of 10 percent of the hub. This proportion was maintained for both the one and two damper cases. The sympathetic damper's spring and damper strength were sized to give a natural frequency equal to the first mode frequency (11.52 rad/sec), ± 20 percent and damping ratio of 0.1 or 0.2 for the sympathetic damper inertia-damper-spring assembly.

Analysis Results

Table 2 summarizes the analysis results for a single sympathetic damper showing the modal dampings, modal gain margins, and phase margins. Negative gain or phase margins indicate an unstable system. Table 3 presents the same information for the two sympathetic damper case. The second sympathetic damper's natural frequency and damping ratio were chosen to control the second mode (21.98 r/s). These two tables indicate clearly that the sympathetic dampers should be sized as near to the modal frequencies as possible. The single damper analysis shows that if the modal frequency is uncertain then it is better to use the higher estimate of the modal frequency to size the sympathetic damper. The two damper case analysis shows that the dampers should be sized between the two estimates of the modal frequencies. This is true even though this combination did not produce the greatest increase in modal damping. The reason the second damper is sized to the lower estimate of the second mode's frequency is that only the first mode is unstable; hence the

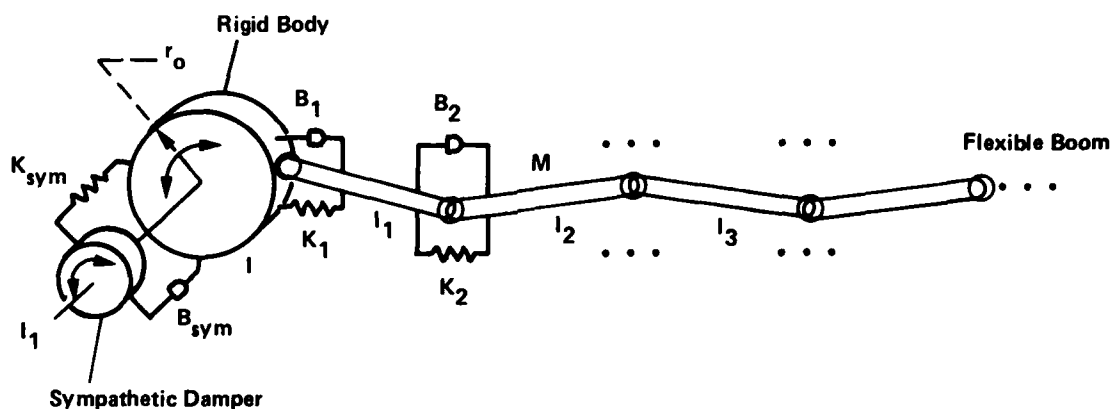
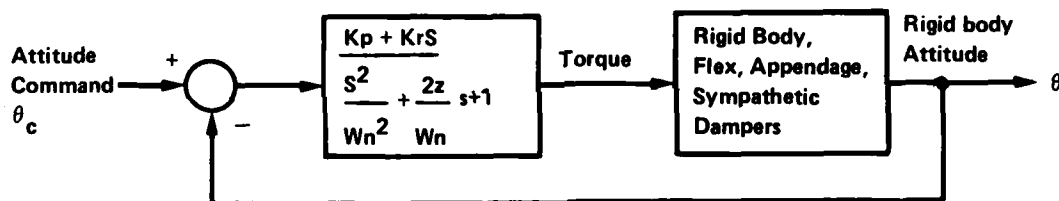


Figure 1
Rigid Body, Ten Segment Flexible Boom and Sympathetic Damper Schematic



Controller Sized to Rigid Body Only, Neglect Actuator Dynamics.
Closed Loop Transfer Function:

$$\frac{\theta}{\theta_c} = \frac{K_p + K_r s}{(I_o + M N r_o^2 + I_i) s^2 + K_r s + K_p}$$

For a Bandwidth of 1.0 Rad/sec, Damping Ratio of 0.7,

$$K_p = W^2 (I_o + M N r_o^2 + I_i) = 1.986 \text{ ft-lbs/rad}$$

$$K_R = 2 Z W (I_o + M N r_o^2 + I_i) = (1.4)(1.986) \frac{\text{ft-lbs}}{\text{rad/sec}}$$

Actuator: $W_n = 10.0 \text{ rad/sec}$

$Z = 0.8$

Figure 2
Controller, Actuator, Spacecraft Dynamics, and Sympathetic Dampers Block Diagram

Table 1
Equations of Motion for Rigid Body, Flexible Boom and Two Symathetic Dampers

$$\begin{bmatrix} I_0 \\ I_1 \\ I_2 \\ \vdots \\ I_N \\ 0 \\ I_1^* \\ I_2^* \end{bmatrix} \ddot{\theta} + \begin{bmatrix} B_1+B_1^*+B_2^* & -B_1 & 0 & & 0 & -B_1^* & -B_2^* \\ -B_1 & B_1+B_2 & -B_2 & 0 & & 0 & 0 \\ 0 & -B_2 & B_2+B_3 & -B_3 & & & \\ & & & & & & \\ & & & & & & \\ & & & & & & \\ & & & & & & \\ & & & & & & \\ & & & & & & \\ & & & & & & \\ & & & & & & \\ 0 & -B_1^* & 0 & & 0 & 0 & B_1^* \\ -B_2^* & 0 & & 0 & 0 & 0 & B_2^* \end{bmatrix} \dot{\theta}$$

$$+ \begin{bmatrix} K_1+K_1^*+K_2^* & -K_1 & 0 & & -K_1^* & -K_2^* \\ -K_1 & K_1+K_2 & -K_2 & 0 & 0 & 0 \\ 0 & -K_2 & +K_3 & -K_3 & & \\ & & & & & \\ & & & & & \\ & & & & & \\ & & & & & \\ & & & & & \\ & & & & & \\ & & & & & \\ & & & & & \\ 0 & -K_1^* & & & 0 & 0 \\ -K_2 & & & & 0 & K_2^* \end{bmatrix} \theta = \begin{bmatrix} 1 \\ 0 \\ 0 \end{bmatrix} \tau$$

$$I^1 = I_0 - I_1^* - I_2^* + MNr_0^2$$

$$I_i = I + Mr^2 (N-i) + r^2 M/4 \quad i = 1, 2, 3 \dots N$$

$$I_1^* = I_2^* = (0.05) (I_0 + MNr_0^2)$$

T	Actuator torque
θ_0	Hub inertial angle
θ_1	Segment 1 inertial angle
θ_2	Segment 2 inertial angle
\vdots	\vdots
\vdots	\vdots
\vdots	\vdots
θ_n	Segment N inertial angle
θ_1^*	Sympathetic damper 1 inertial angle
θ_2^*	Sympathetic damper 2 inertial angle

Table 2

RESULTS FOR ONE SYMPATHETIC DAMPER

SYMPATHETIC DAMPER		MODAL DAMPING RATIO			MODAL STABILITY MARGINS		
Z	ω_n	1st	2nd	3rd	MODE 1	MODE 2	MODE 1
	R/S	Z_1	Z_2	Z_3	GM_1	GM_2	QM
					db	db	deg
0.0	0.0	0.0057	0.0109	0.0158	-6.4	5.3	-9.3
0.1	11.52	0.0417	0.0638	0.0133	8.7	6.9	-----
0.1	9.217	0.0185	0.0124	0.0165	1.7	6.3	5.2
0.1	13.826	0.0133	0.0149	0.0171	7.5	7.8	11.4
0.2	11.52	0.0569	0.0155	0.0176	8.9	8.2	51.9
0.2	9.217	0.0258	0.0139	0.0171	4.0	7.3	14.6
0.2	13.826	0.0177	0.0183	0.0183	7.5	9.6	16.0

Table 3

RESULTS FOR TWO SYMPATHETIC DAMPERS

SYMPATHETIC DAMPER				MODAL DAMPING RATIO			MODAL STABILITY MARGINS		
1		2		1st	2nd	3rd	MODE 1	MODE 2	MODE 1
Z	W	Z	W	Z_1	Z_2	Z_3	Gm_1	Gm_2	ϕ_m
	r/s		r/s				db	db	deg
0.1	11.52	0.1	21.98	0.037	0.042	0.018	6.7	17.1	52.3
	9.216		26.38	.0129	0.015	0.022	- .4	9.7	-0.9
	13.82		17.58	.0107	0.018	0.017	2.6	9.7	4.3
	9.216		17.58	.0137	0.017	0.017	0.5	9.2	1.1
	13.82		26.38	.0102	0.016	0.022	1.9	10.4	3.1
0.2	11.52	0.2	21.98	.0251	0.030	0.020	5.6	14.0	18.5
	9.216		26.38	.0162	0.017	0.024	1.3	10.6	3.4
	13.82		17.58	.0135	0.023	0.019	3.7	11.6	7.2
	9.216		17.58	.0177	0.021	0.018	2.5	10.7	6.7
	13.82		26.38	.0124	0.020	0.025	2.5	11.5	4.8

dampers will have the greatest effect on the stability margins if they are sized to the first modal frequency. Figure 3 shows the open loop gain-phase plot without the sympathetic dampers. The first mode, which peaks at 18.2 dB, is clearly the only unstable mode. The second mode has a gain margin of only 5.3 dB. Any candidate compensation scheme should also improve the second mode's gain margin. Figure 4 shows the open loop gain-phase plot for one damper sized exactly for the first mode, $W_n = 11.52$ rad/sec with a damping ratio of 0.1. The first mode is completely stabilized and the second mode's gain margin is now 6.9 dB. If the single sympathetic damper's natural frequency is set 20 percent higher than the first mode's natural frequency, the open loop gain-phase plot in Figure 5 results. The first mode is still stable although not as effectively. Increasing the damping ratio to 0.2 produces a slightly more stabilized first mode and a second mode with even more gain margin. These results are seen in the open loop gain-phase plot shown in Figure 6. The sympathetic damper's natural frequency is still 20 percent higher than the first mode's natural frequency, as in Figure 5, but the damping ratio is 0.2. The first mode has a gain margin of 7.5 dB and a phase margin of 16 deg while the second mode's gain margin is an adequate 9.6 dB.

Comparing the stability margins in Tables 2 and 3, the design shown in Figure 6 has the best stability margins in the presence of uncertainty in the modal frequency. This design having a single sympathetic damper mass, damping ratio of 0.2, and a natural frequency of 13.83 rad/sec had a maximum damper deflection angle relative to the rigid body of .735 deg and a maximum relative rate of 9.60 deg/sec when the angle command was a step of five degrees. The damper strength was 0.222 ft-lb/rad/sec and the spring constant was 7.68 ft-lb/rad. The resulting torques on the rigid body from the sympathetic damper are 0.098 ft-lb from the spring and 0.037 ft-lb from the damper.

Conclusions

A single sympathetic damper, sized with a natural frequency equal to the modal frequency, is needed for each troublesome mode of the system. The damping ratios should be about 0.2. If the modal frequency is uncertain, then the sympathetic damper's natural frequency is sized to the higher estimate of the modal frequency.

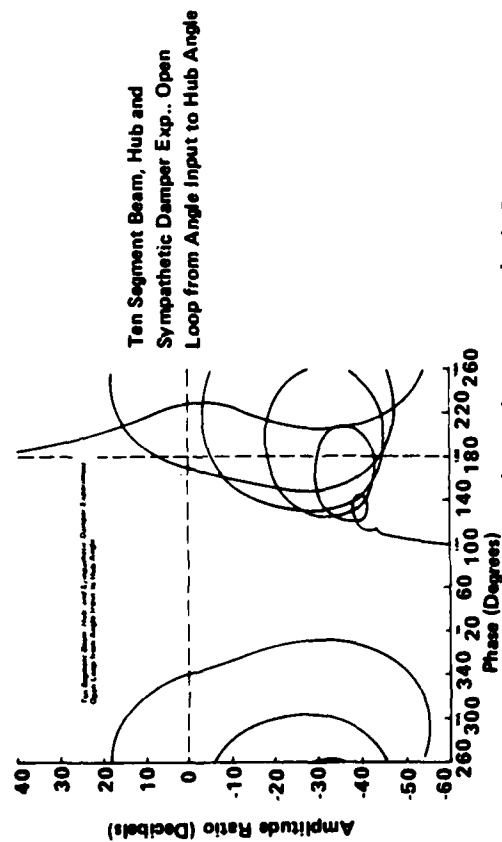


Figure 3 Open Loop Gain - Phase Plot Without Sympathetic Dampers

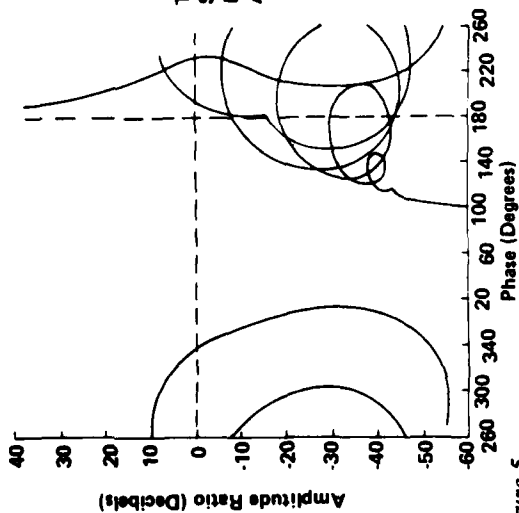


Figure 5 Open Loop Gain - Phase Plot with a Single Sympathetic Damper, W_n (Dampers) = 120% of W_n (Mode 1) $z = 0.1$, $W_n = 13.83$ rad/sec

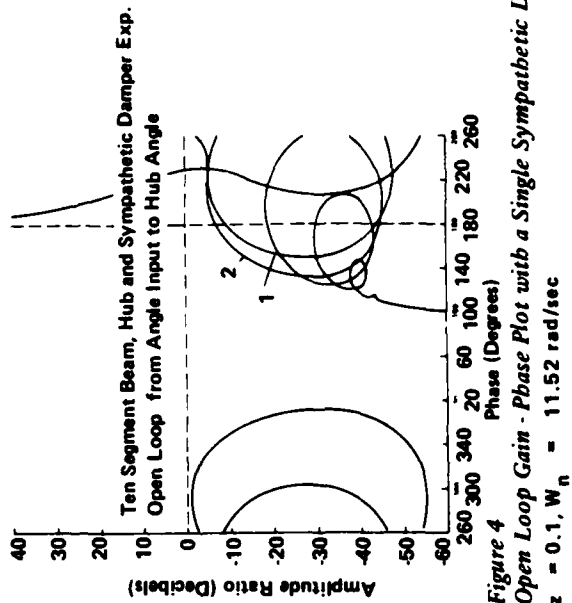


Figure 4 Open Loop Gain - Phase Plot with a Single Sympathetic Damper $z = 0.1$, $W_n = 11.52$ rad/sec

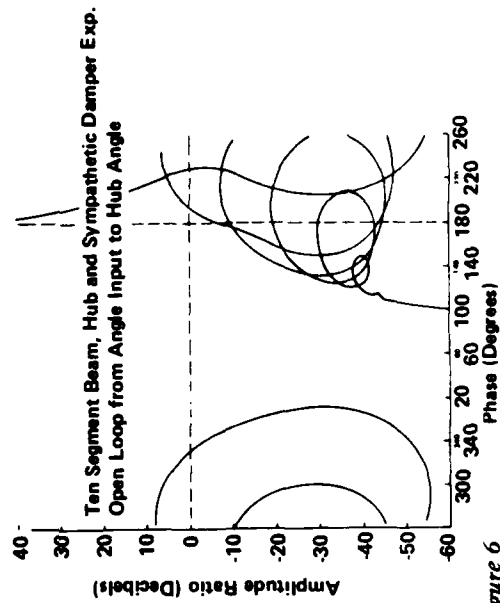


Figure 6 Open Loop Gain - Phase Plot with a Single Sympathetic Damper W_n (Dampers) = 120% of W_n (Mode 1) $z = 0.2$, $W_n = 13.83$ rad/sec

4.0 Single Damper Control of Flexible Body Modes

Approach

The model described in the previous section was modified by deleting the sympathetic dampers and adding a damper between the rigid body and the tip of the flexible appendage. The controller and actuator dynamics remained the same. The strength of the damper between the rigid body and the appendage tip was varied from $0.001K$ to $0.05K$ where K is the stiffness of the flexible appendage modelled as a spring at each of the ten joints, (221.83 ft-lbs/rad). The equations of motion were derived then analyzed with LADCAP to yield the modal damping, gain margin and phase margin of the open loop transfer function from the position command to the rigid body angle.

Model and Equations of Motion

Figure 7 shows a schematic of the rigid body, the flexible appendage and the damper connected between the rigid body and the tip of the appendage. Table 4 presents the equations of motion in matrix form and the values of the elements of the model. The design of the controller and the included actuator dynamics shown in the block diagram of Figure 8, gave a closed loop natural frequency of 1.0 rad/sec with a damping ratio of 0.7. The inertia of the rigid body includes the hub and boom. Hence its inertia is $I_0 + MNR_i^2 + I_i$ where I_0 is the hub inertia, M is the mass of a segment of the boom, N is the number of boom segments at the i th joint.

Analysis Results

Table 5 summarizes the results of this analysis. The open loop modal damping is listed as a function of damper strength. The damping ratio in the third column is the damping ratio of the hub, damper and first joint spring combination. The modal damping ratios are plotted versus the damper strength, expressed as a fraction of the boom's stiffness, in Figure 9. Clearly, each mode is most effectively damped by a particular damper strength.

The most effective strength for each mode is different; however, for the first and third modes, the most effective damper strengths are approximately equal; specifically, $B^* = 0.011 \times K$ or 2.44013 ft-lb/rad/sec. The open loop gain-phase plot for the transfer function from the command to the rigid body angle is shown in Figure 10. Comparing this with Figure 3, the uncompensated open loop gain-phase plot, illustrates the dramatic improvement in modal damping achievable with a single damper. The modes of this system are completely stabilized giving a rigid body phase margin of 50.9 deg and a gain margin of 13.1 dB. The damper strength of $0.011 \times K$ produces a damping ratio for the rigid body-damper-first joint spring assembly of 0.141 which is consistent with the other stabilization techniques analyzed in this report and in previous year's studies under this IRAD task.

The single damper connected between the rigid body and the tip was most effective on the first and third modes, improving the damping ratio by a factor of 85 for the first mode and a factor of 12 for the third mode, while

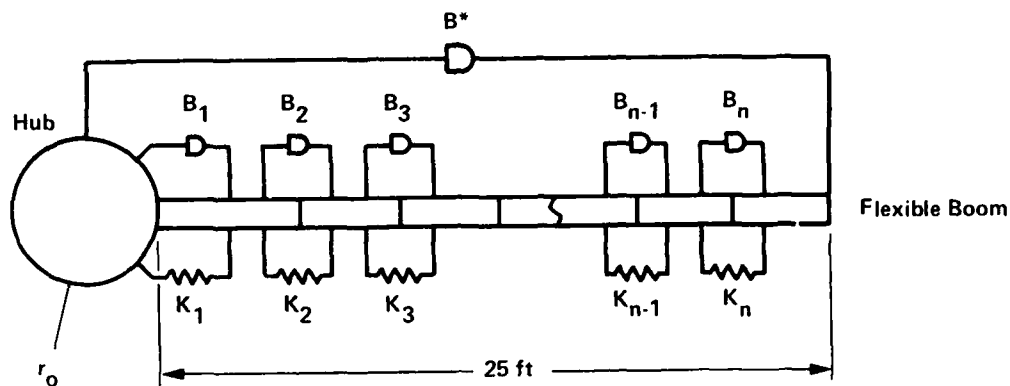
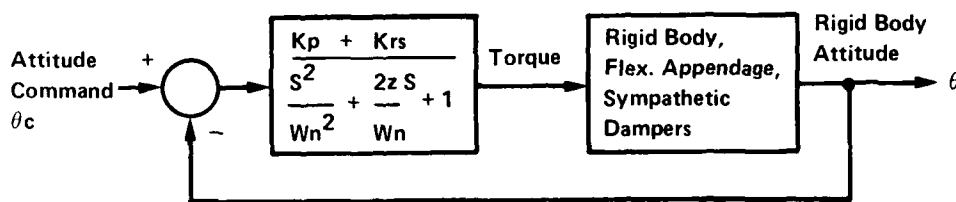


Figure 7
Rigid Body (Hub), Ten Segment Flexible Boom and Stabilizing Damper (B*) Schematic



Controller Sized to Rigid Body Only, Neglect Actuator Dynamics
Closed Loop Transfer Function:

$$\frac{\theta}{\theta_c} = \frac{K_p + K_r s}{(I_o + M N r_o^2 + I_i) s^2 + K_r s + K_p}$$

For a Bandwidth of 1.0 Rad/sec, Damping Ratio of 0.7,

$$K_p = W^2 (I_o + M N r_o^2 + I_i) = 1.986 \text{ ft-lbs/rad}$$

$$K_r = 2zW (I_o + M N r_o^2 + I_i) = (1.4) (1.986) \text{ ft-lbs/rad/sec}$$

$$\text{Actuator: } W_n = 10.0 \text{ rad/sec}$$

$$z = 0.8$$

Figure 8
Controller, Actuator, Spacecraft Dynamics and Hub to Tip Block Diagram

Table 4
Equations of Motion for Rigid Body, Flexible Boom and Hub to Tip Damper

$$\begin{bmatrix} I' \\ I_1 \\ I_2 \\ \vdots \\ I_N \end{bmatrix} \ddot{\theta} + \begin{bmatrix} B_1+B^* & -B_1 & 0 & 0 & 0-B^* \\ -B_1 & B_1+B_2 & -B_2 & 0 & 0 \\ 0 & -B_2 & B_2+B_3 & -B_3 & 0 \\ \vdots & \vdots & \vdots & \vdots & \vdots \\ 0 & 0 & 0 & -B_N & B_N+B^* \\ -B^* & 0 & 0 & 0 & 0 \end{bmatrix} \dot{\theta} + \begin{bmatrix} K_1 & -K_1 & 0 & 0 & 0 \\ -K_1 & K_1+K_2 & -K_2 & 0 & 0 \\ 0 & -K_2 & K_2+K_3 & -K_3 & 0 \\ \vdots & \vdots & \vdots & \vdots & \vdots \\ 0 & 0 & 0 & -K_N & K_N \end{bmatrix} \theta = \begin{bmatrix} 1 \\ 0 \\ 0 \\ \vdots \\ 0 \end{bmatrix} T$$

$$I^1 = I_o + MNr_o^2$$

$$I_i = I + Mr^2 (N-i) + r^2 M/4 \quad i = 1, 2, 3 \dots N$$

T = Actuator Torque
 θ_o = Hub inertial angle
 θ_1 = Segment 1 inertial angle
 $\theta = \theta_2$.
 .
 .
 .
 θ_n = Segment N inertial angle

M = 5.2449 E-3 slugs, segment mass
 N = 10 number of segments
 r_o = 0.5 ft hub radius
 r = 2.5 ft segment length
 I_o = 0.3885 slug-ft² hub inertia
 I = 2.7317 E-3 slug-ft² segment inertia
 B_i = 0.22183 ft-lbs/rad/sec joint damping
 K_i = 221.83 ft-lbs/rad joint spring constant
 B^* = Hub to tip damper strength

Table 4 (concl)

M	=	5.2449 E-3 slugs, segment mass
N	=	10 number of segments
r_o	=	0.5 ft. hub radius
r	=	2.5 ft. segment length
I_o	=	0.3885 slug-ft ² hub inertia
I	=	2.7317 E-3 slug-ft ² segment inertia
B_i	=	0.22183 ft-lbs/rad/sec joint damping
K_i	=	221.83 ft-lbs/rad joint spring constant
I_1^*, I_2^*	=	sympathetic damper inertia
Z_1^*, Z_2^*	=	sympathetic damper damping ratio
W_1^*, W_2^*	=	sympathetic damper natural frequency
$B^* = 2 I^* Z^* W_n^*$	=	sympathetic damper strength
$K^* = I^* W_n^{*2}$	=	sympathetic damper's spring constant

Table 5

MODAL DAMPING VS. HUB TO TIP DAMPER STRENGTH

X sec	$B^* =$ $X \cdot K$ ft-lb/r/s	Z = $B/2 \sqrt{I_{RB} K}$	MODAL DAMPING		
			1st Z_1	2nd Z_2	3rd Z_3
0.0	0	0.0117	0.0057	0.010	0.015
0.001	0.221	0.023	0.047	0.012	0.030
0.005	1.10	0.070	0.218	0.020	0.091
0.006	1.33	0.082	0.262	0.021	0.108
0.007	1.55	0.094	0.307	0.024	0.126
0.008	1.77	0.105	0.354	0.025	0.146
0.009	1.99	0.117	0.401	0.027	0.167
0.010	2.21	0.129	0.448	0.029	0.186
0.011	2.44	0.141	0.489	0.031	0.192
0.012	2.66	0.152	0.494	0.033	0.174
0.015	3.32	0.188	0.318	0.040	0.108
0.020	4.43	0.246	0.190	0.048	0.072
0.022	4.88	0.270	0.163	0.050	0.065
0.025	5.54	0.305	0.135	0.051	0.058
0.030	6.65	0.364	0.107	0.048	0.050
0.050	11.0	0.599	0.063	0.035	0.037

$$K = 221.83 \text{ ft-lb/rad}$$

$$I_{RB} = I_0 + M N r_0^2 = 0.401612 \text{ slug-ft}^2$$

$$B = B^* + 0.001 \cdot K \text{ ft-lb/rad/sec}$$

$$B^* = \text{Rigid body to tip damper strength, ft-lb/rad/sec}$$

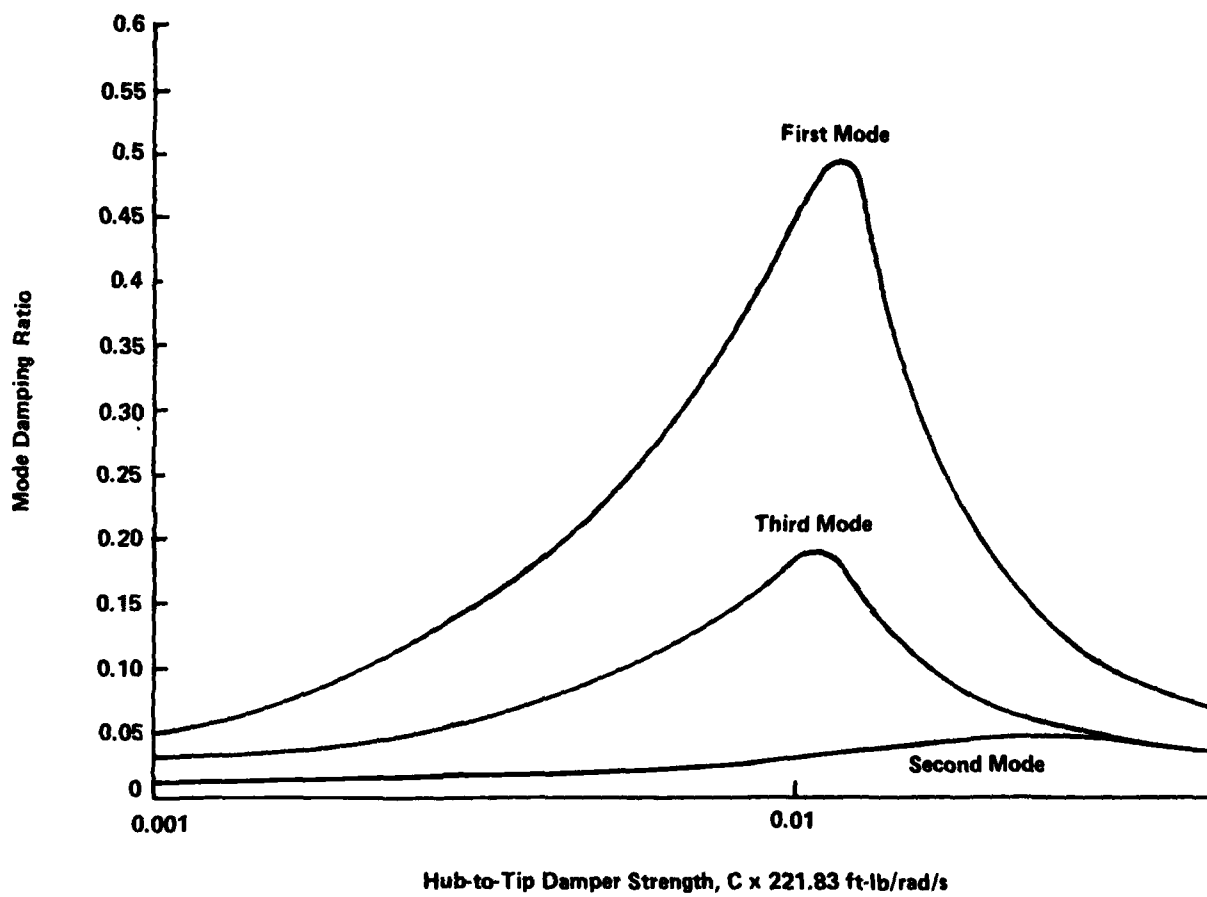


Figure 9 Modal Damping Ratio vs Hub-to-Tip Damper Strength

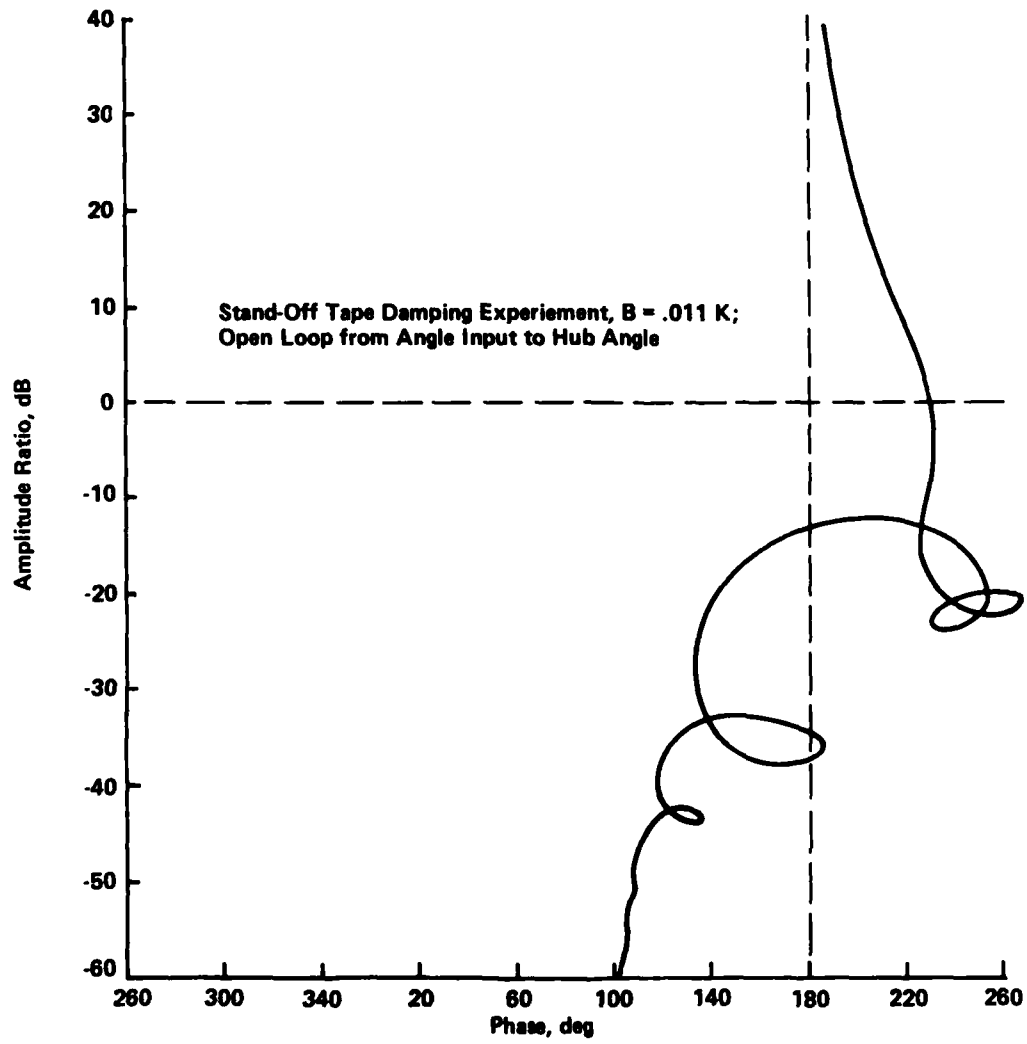


Figure 10 Open-Loop, Hub-to-Tip Damper

the second mode's damping ratio was improved by only a factor of 3. The reason for this is illustrated in Figure 11. The rigid body angle and the tip angle are out of phase for the first and third modes while the rigid body angle and tip angle are in phase for the second mode; hence the damper connected between the rigid body and the tip sees more relative motion for the first and third modes. If the second mode were unstable, a separate damper between the rigid body and approximately the midpoint of the boom would be needed to channel the second mode's energy into a damper.

The damper is connected to the tip by a 4-inch long standoff and to the outer radius of the hub (6 inches). Although in the equations of motion these standoffs drop out, the damper strength should be expressed in lbs per inch per second and the displacement and velocity in inches and inches per second. For a damper strength of $0.011 \times K$, the maximum displacement seen by the damper is 0.054 inches, the maximum velocity seen by the damper is 0.419 inches per second, and the maximum damper force is 0.760 lbs. The damper strength is then 0.160 lbs/inch/sec. The maximum displacement, velocity and force are for a step command to the rigid body of five degrees.

Conclusions

A damper connected between the rigid body and a point on a flexible appendage will have a dramatic affect on the modal damping, increasing the modal damping by a factor of 85 for some cases depending on the mode and connection point to the flexible appendage.

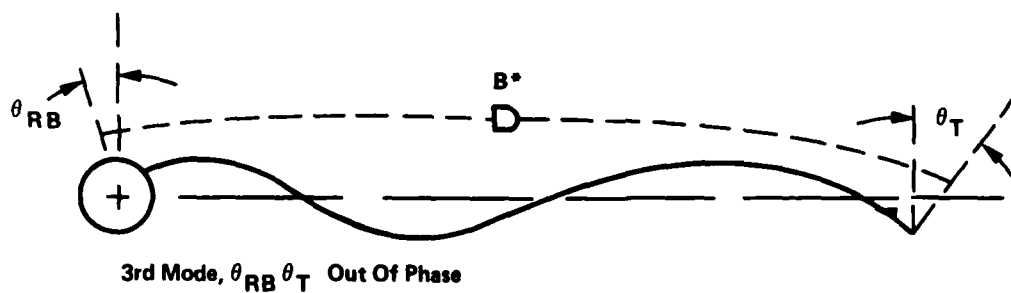
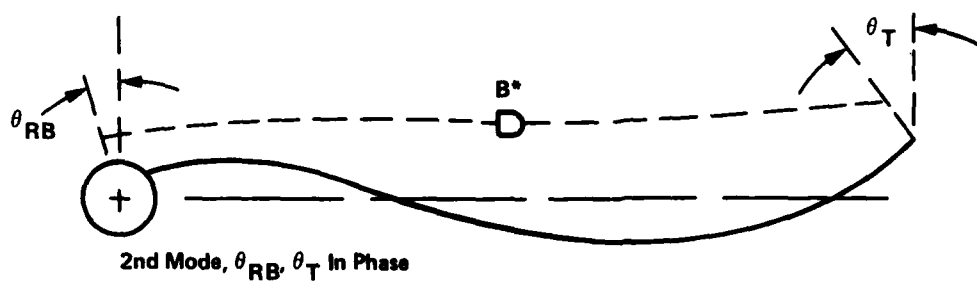
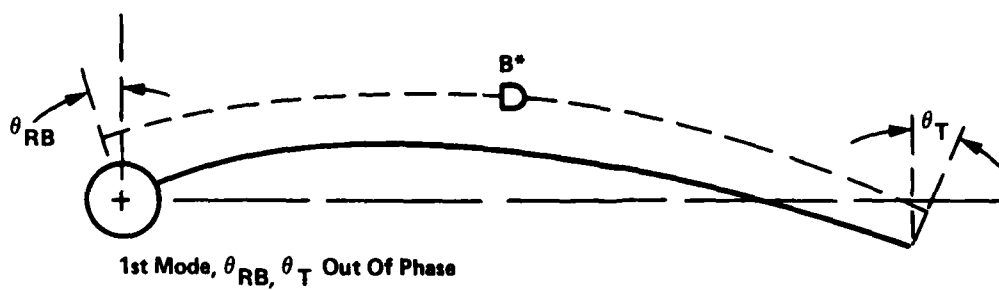


Figure 11
Mode Shapes, In Phase and Out Of Phase Tip Angle Relative to the Rigid Body Hub Angle

5.0 Suspended Components to Augment Rigid Body Control

Approach

The objective of this analysis was to study the effect of intentionally mounting a percentage of a spacecraft's components on spring/dampers and observing the effect on the spacecraft's stability margins. A rigid spacecraft was modelled with one degree-of-freedom rotation plus a portion of the inertia suspended on springs and dampers. The model was analyzed with LADCAP to determine the stability margins, forces, displacements and velocities experienced by the components due to a step change in attitude. The strengths of the springs and dampers were varied along with the suspended mass and number of suspended masses. However, the total spacecraft inertia and mass were held constant.

Model and Equations of Motion

Figure 12 shows a schematic of the spacecraft and two suspended components. A controller was designed to provide a closed loop natural frequency of 1.0 rad/sec and a damping ratio of 0.5. A reaction wheel model with a bandwidth of 10 rad/sec was added to complete the model. The block diagram of the control system is shown in Figure 13. Table 6 provides the equations of motion for the spacecraft and the two suspended components. The equations of motion for one and three suspended components are similar.

Analysis Results.

Table 7 summarizes the results of this analysis. Shown is the rigid body phase margin when a total of ten slugs are suspended, distributed between one, two or three masses, as a function of the damping ratio and natural frequency of the suspended mass, spring and damper combination. Where more than one component was suspended, the lowest natural frequency of the mass-spring-damper combination was listed. Table 7 also presents the rigid body phase margin when 20 slugs are suspended, distributed between one, two and three masses.

Table 7 shows that the most effective damping ratio is approximately 0.2 and that as the natural frequency of the suspended component-damper-spring combination increases, the improvement in rigid body phase margin decreases. Furthermore, little is gained by distributing the suspended mass among several components. The phase margin improvement is less than or equal to 1.1 degrees. Although suspending 20 slugs improved the phase margin, the improvement was only 4.5 degrees, maximum. From Table 7 it is clear that a damping ratio of 0.2 with a natural frequency for the suspended component-damper-spring combination less than or equal to the rigid body bandwidth is near the optimum combination.

Comparing Figures 14a and 14b through 14e, suspending components affects the shape of the open loop gain-phase plot in a way that would be difficult to achieve with compensation filters. Figure 14a shows the open loop gain - phase plot for a spacecraft with no suspended components.

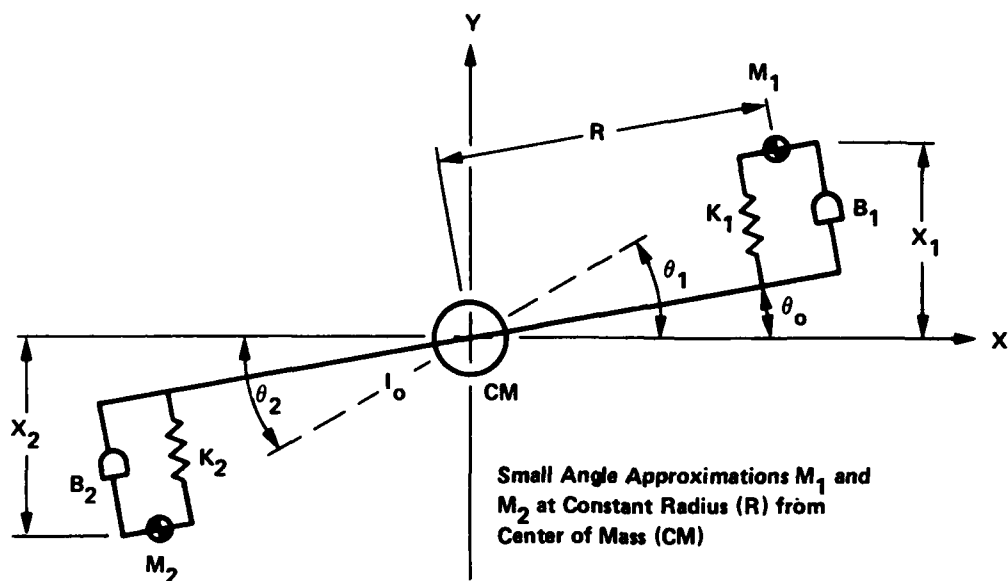


Figure 12 Spacecraft and Two Suspended Components

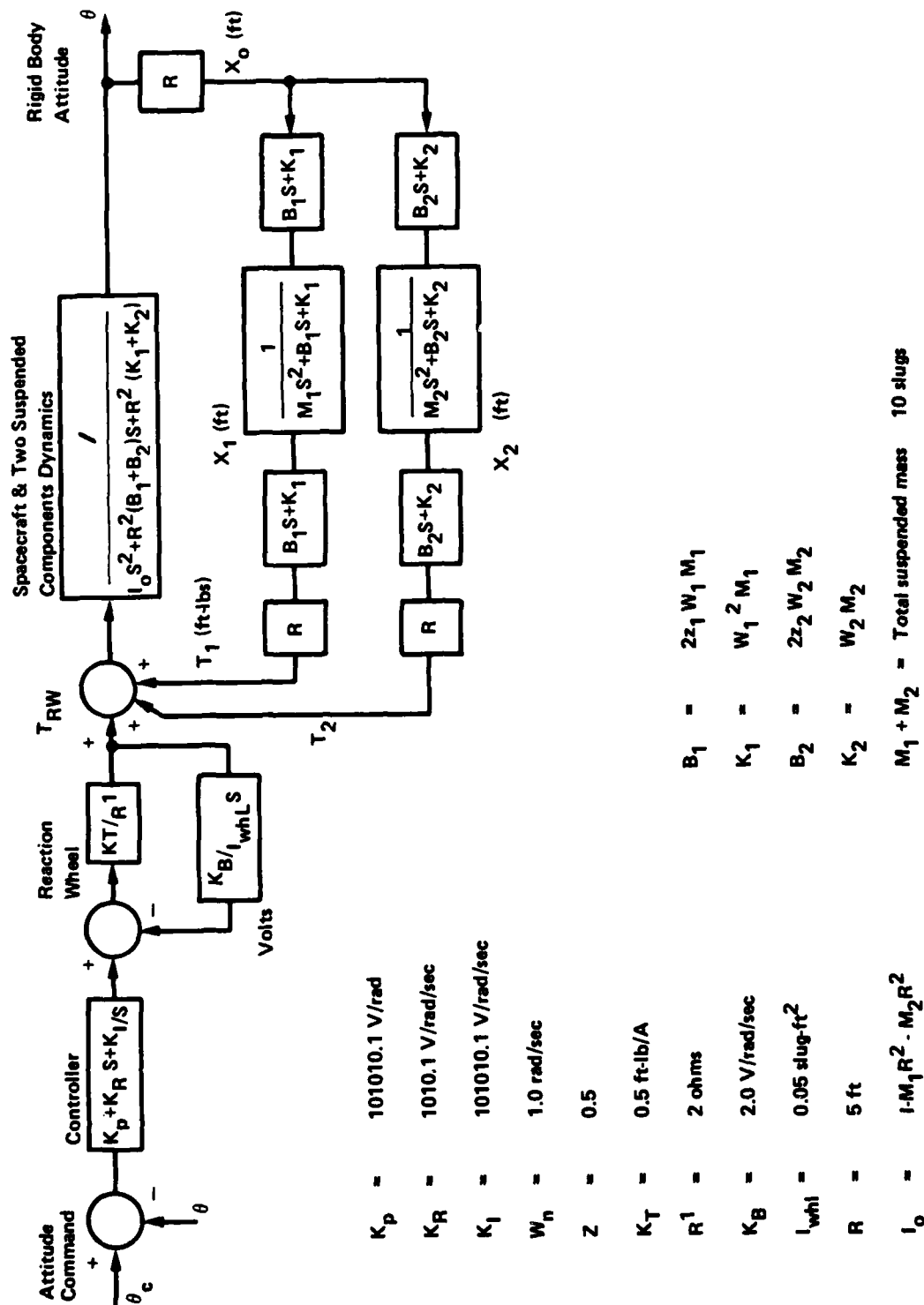


Figure 13
Controller, Reaction Wheel, Spacecraft and Two Suspended Components Block Diagram

Table 6
Equations of Motion for a Rigid Body and Two Suspended Components

$$\begin{bmatrix} I_0 s^2 + R^2 (B_1 + B_2) s & -R(B_1 s + K_1) & -R(B_2 s + K_2) \\ +R^2 (K_1 + K_2) & R [M_1 s^2 + B_1 s + K_1] & 0 \\ -R^2 (B_1 s + K_1) & 0 & R [M_2 s^2 + B_2 s + K_2] \end{bmatrix} \begin{bmatrix} \theta \\ x_1 \\ x_2 \end{bmatrix} = \begin{bmatrix} T_{RW} \\ 0 \\ 0 \end{bmatrix}$$

I = Total S/C inertia, 2500 fps²

R = Location of suspended components 5 ft

$M_{1,2}$ = Mass of suspended components, 4, 6 slugs

$B_{1,2}$ = Suspension damper, lbs/ft/sec

$K_{1,2}$ = Suspension spring lbs/ft

I_0 = $I - R^2 M_1 - R^2 M_2$ Inertia seen by the reaction wheel

T_{RW} = Reaction wheel torque ft-lbs

θ = Rigid body angle radians

$x_{1,2}$ = Displacement of suspended components, ft

s = Laplace transform variable

I_0 = $I - M_1 R^2 - M_2 R^2$

K_2 = 4.86 lbs/ft

R = 5 ft

RK_2 = 24.30

I_0 = 2250 fps²

$R^2 K_2$ = 121.50

W_1 = 1.1 R/S

$2z W M$ = B lbs/ft/sec

W_2 = 0.9

I = 2500 fps²

K_1 = $W_1^2 M_1$

$R^2 (M_1 + M_2) = 10\% (I) = 250$

= 4.84

$M_1 + M_2$ = 10 slugs

RK_1 = 24.20

M_1 = 4.0 slugs

$R^2 K_1$ = 121.00

RM_1 = 20.0

$R^2 (K_1 + K_2) = 242.50$

M_2 = 6.0 slugs

K_2 = $W_2^2 M_2$

RM_2 = 30.0

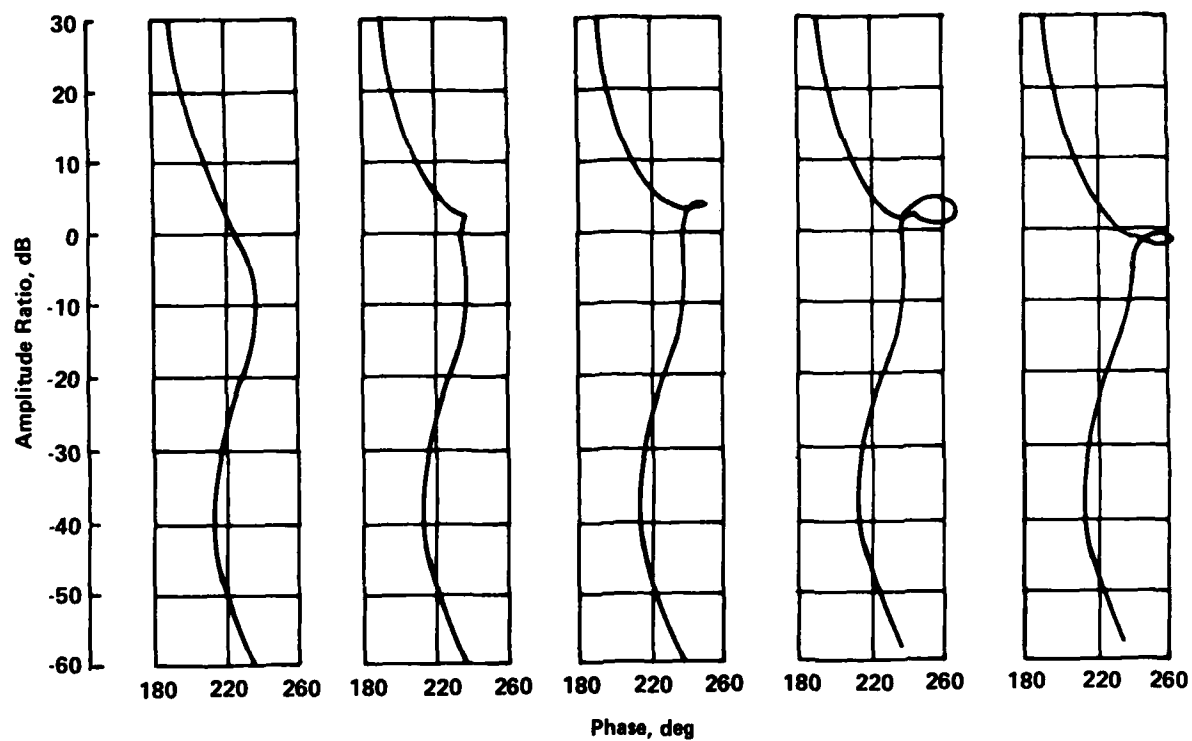
Rigid Body Phase Margin (deg) For 10 Slugs Suspended

			Z_m					
	Wm	0	0.1	0.2	0.4	0.5	0.6	0.8 0.9
	0.0	45.0						
Two Masses	0.9		51.1	53.0	52.6		50.8	49.6 49.1
One Mass	1.0			53.0		51.8		49.6
Two Masses	1.072				50.1			
3 Masses	1.072				50.8			
Two Masses	1.136			51.6				
3 Masses	1.136			52.0				
Two Masses	1.160		52.6					
3 Masses	1.16		53.7					
One Mass	1.32		47.7	52.2				
One Mass	1.35		47.2					
One Mass	1.42		46.3	49.1				
One Mass	1.45		46.0					
One Mass	1.52		45.5	47.5				
One Mass	1.55		45.4					

FOR 20 Slugs Suspended

One Mass	0.9		56.3
Two Masses	0.9	55.6	
3 Masses	1.16	50.5	

Table 7



Dampers	None	One	One	Two	Three
Mass	—	10 slugs	20 slugs	8 & 12 slugs	6, 8, 6 slugs
ω_n	—	1 R/S	0.9 R/S	0.9, 1.1 R/S	1.16, 1.45, 1.74 R/S
ζ	—	0.2	0.2	0.1, 0.1	0.1, 0.1, 0.1

Figure 14 A, B, C, D, E Open-Loop Margins vs Added Dampers

Comparing figure 14a with the open loop gain-phase plot of figure 14b, one suspended component-damper-spring natural frequency of 1.0 rad/sec and a damping ratio of 0.2 shows that the latter gain-phase plot does a three-quarter loop at 1.0 rad/sec. Not only does this twist improve the phase margin but the sensitivity of the phase margin to gain changes is nearly zero. The three-quarter twist is even more pronounced when 20 slugs are suspended, as shown in figure 14c. Each suspended component will produce a loop in the open loop gain-phase plot. However, only the highest frequency loop will be a three-quarter turn, all others will be full turns. Figure 14d and 14e provide the evidence for the preceding statement. Both figures are for 20 slugs suspended (shown because the loops are larger than those for 10 slugs suspended) all component-damper-spring assemblies have a damping ratio of 0.1. Figure 14d shows the open loop gain-phase plot for a spacecraft with two suspended components while figure 14e is for three suspended components. Figures 14c through 14e also show that since the improvement in the rigid body phase margin results from the three-quarter twist in the open loop gain-phase plot and there is only one three-quarter twist in all these plots, little improvement in rigid body phase margin will be achieved by suspending more components. The analyst should note, however, that if more than one component needs to be suspended to achieve a given quantity of suspended mass then the damping ratios and natural frequencies of the component-damper-spring assemblies should all be equal. This is equivalent to suspending one mass of the desired quantity with the same natural frequency and damping ratio. An important consideration when applying this compensation technique is the required displacements and velocities of the suspended components. For the system described by figure 14b, a single component of 10 slugs, component-damper-spring natural frequency of 1.0 rad/sec and damping ratio of 0.2, the maximum displacement of the component, relative to the spacecraft, for a 5.0 degree step input command is 3.88 in. The maximum velocity of the component relative to the spacecraft is 5.03 in/sec. Suspending two or three components did not result in smaller displacements or velocities. Table 8 summarizes the maximum relative displacements and velocities for 10 slugs suspended distributed between one, two and three components and a five degree step input.

Conclusions

Suspending a portion of a spacecraft's mass on springs and dampers can improve the rigid body phase margin. The resulting insensitivity of the phase margin to gain changes is another benefit of suspended components. However, suspending more components at different component-damper-spring natural frequencies does not provide a commensurate improvement in rigid body phase margin.

References

- 1) Lecture by Dr. Athur Bryson, 1983 Rocky Mountain Guidance and Control Conference, Feb 83, Keystone, Colorado.
- 2) Control of Large Flexible Structures IRAD-D-39R, Dec '80, R80-48639-001, Martin Marietta Aerospace, Denver.

Component-Damper-Spring			Maximum Displacement,	Relative Velocity
	Lowest Wn, r/s	Damping Ratio	in	in/Sec
One Mass	1.0	0.2	3.88	5.07
Two Masses	0.9	0.2	4.03	5.14
Three Masses	1.16	0.1	4.43	5.51

Table 8 Maximum Relative Displacement and Velocity For 10 Slugs Suspended

CRITICAL DAMPING IN COMPLEX STRUCTURES AND CONTROL SYSTEMS

D. J. Inman
Department of Mechanical and Aerospace Engineering
University at Buffalo
State University of New York
Buffalo, New York 14260

Critical Damping In Complex Structures and Control Systems*

D.J. Inman
Department of Mechanical and Aerospace Engineering
University at Buffalo
State University of New York
Buffalo, New York 14260
(716) 636-2733

Abstract: This work examines the concept of critical damping normally defined for single degree of freedom systems as applied to more complex models of structures and their control systems. Here, complex models refers to lumped mass models, such as finite element models (FEM), full distributed parameter (DPS) models (described by sets of partial differential equations), hybrid systems (systems with lumped and distributed parameter elements, such as passive control systems) and active control systems consisting of the above mentioned models subject to position and velocity feedback. Recent work on critical damping of FEM and DPS models is reviewed and applied to more general linear models.

Introduction: Recently several authors have defined the concept of critical damping for linear lumped parameter systems with n degrees of freedom [1-4] and for damped distributed parameter systems [5-6]. These definitions are reviewed here and extended to include systems which are distributed in nature and have point (lumped) appendages acting as either active or passive controls.

The concept of critical damping for the usual single degree of freedom system is extended to the above mentioned structures on a per mode basis. Once this extension is made conditions, both analytical [3-5] and numerical [7], are presented that specify the critical damping condition for a given structure or structure and control system in terms of the systems physical parameters and feedback gains. Several examples, from each classification, are presented and discussed.

The systems considered here are those that can be successfully modeled by a linear partial differential equation of the form

$$u_{tt}(x,t) + L_1 u_t(x,t) + L_2 u(x,t) = f(x,t) \quad (1)$$

* Research sponsored by AFOSR, Air Force Systems, Command, USAF, under grant No. AFOSR 820242. The U.S. government is authorized to reproduce and distribute reprints for Government purposes not withstanding any copyright notation hereon.

where $(\)_t$ denotes time differentiation, u is a vector of deflections from equilibrium, x is a vector of displacements, $f(x,t)$ represents a disturbance and/or a feedback control and the operators L_1 and L_2 are linear partial differential operators of the spatial variables and contain the physical properties of the material (mass density, stiffness and damping). The appropriate mathematical assumptions on the operators L_1 and L_2 are presented in Appendix 1. In the case of a finite element model (FEM) modal truncation or other discretized version of equation (1) the system reduces to the familiar matrix equation

$$M\ddot{x} + C\dot{x} + Kx = f(t) \quad (2)$$

The coefficient matrices M , C and K are the mass damping and stiffness matrices respectively and in many cases are real symmetric and positive definite. However, an asymmetric version of (2) will also be discussed.

In the case of active discrete control, $f(x,t)$ in equation (1) may take on the form

$$f(x,t) = - \sum_{i=1}^n \left[\delta(x-x_i) c_i \dot{u}_t(x,t) + \delta(x-x_i) k_i u(x,t) \right] \quad (3)$$

where δ denotes the delta function, c_i and k_i represent various feedback gains and n is the number of point actuators. Likewise the vector $f(t)$ in (2) would have the form

$$f(t) = -G_1 \dot{x} - G_2 x \quad (4)$$

where G_1 and G_2 are real valued gain matrices. In addition, distributed control laws will be considered which have the form

$$f(x,t) = -L_3 \dot{u}_t(x,t) - L_4 u(x,t) \quad (5)$$

where L_3 and L_4 are partial differential operators of the spatial variable. A discretized version of (5) would also yield equation (4).

Definitions of Critical Damping: The basic concept of critical damping as commonly used in vibration analysis resulted from considering the linear vibrations of a single degree of freedom model of a structure consisting of a mass, m , connected to ground by a spring of stiffness k in parallel with a dashpot of viscous damping rate c . The equation of motion for the linear displacement, $x(t)$, of the mass from its equilibrium position subject to some arbitrary initial conditions is given by

$$m\ddot{x}(t) + c\dot{x}(t) + kx(t) = 0 \quad (6)$$

Two distinct approaches can be used to define critical damping for such a system. Both approaches lead to the same definition for equation (6) but to different meanings for equation (1) and (2)

The first approach is to view critical damping as that value of the

damping rate c for which the characteristic equation for (6), i.e.

$$m\lambda^2 + c\lambda + k = 0 \quad (7)$$

has equal negative real roots. In this case the solution of (6) is of the form

$$x(t) = (a_1 + a_2 t)e^{-c_{cr}/2m} \quad (8)$$

where a_1 and a_2 are constants determined by the initial conditions. The response given in (8) is of course nonoscillatory. This value of c is referred to as the critical damping rate and is denoted c_{cr} . Solving the characteristic equation and adjusting the parameters so the roots are equal yields the value of c_{cr} .

$$c_{cr} = 2(km)^{1/2} \quad (9)$$

This definition follows from very simple algebraic manipulations.

A second approach to defining the critical damping condition is to view critical damping as the smallest value of the damping rate c such that the solution of (6) is nonoscillatory. This is realized by forcing λ to be a negative real number in the characteristic equation and minimizing with respect to the damping rate, i.e.

$$\frac{d}{db} (mb^2 - cb + k) = 0 \quad (10)$$

The value of c_{cr} obtained this way again yields (9). However, the interpretation is a little different. Namely, the value of c_{cr} obtained from (10) represents the transition between oscillation and nonoscillation.

While these two approaches are essentially the same for simple single degree of freedom systems, they lead to very different definitions for more complicated structures given by equations (1) and (2). Hence, for these structures two distinct definitions of critical damping have been developed.

The first definition of critical damping for lumped parameter systems, equation (2), was presented by Beskos and Boley [1]. Their work extends the minimum damping concept and defines critical damping to be that value of the damping matrix C such that

$$\frac{d}{db} [\det(b^2 M - bC + K)] = 0 \quad (11)$$

where M, C and K are the coefficient matrices of equation (2). This definition requires repeated numerical solutions of polynomials and is somewhat forbidding for more than two degree of freedom systems. For a two degree of freedom system it yields modes which are not oscillatory but are not necessarily critically damped. Rather, the condition yields the transition between oscillation and nonoscillation. As will be pointed out later, the definition provided by (11) is theoretically more general than following the algebraic approach.

The algebraic approach suggested by equation (9) is extended to the multidegree of freedom system of equation (2) in [3] and is the method that is followed in this work. Basically a critical damping matrix, denoted C_{cr} is defined by mimicking equation (9). Since, the matrix M is symmetric and positive definite, it has a symmetric positive definite square root, the inverse of which is denoted by $M^{-1/2}$ (see appendix II for details). By defining the symmetric matrices \tilde{C} and \tilde{K} by

$$\tilde{C} = M^{-1/2} C M^{-1/2} \quad (12)$$

$$\tilde{K} = M^{-1/2} K M^{-1/2} \quad (13)$$

the critical damping matrix is defined to be

$$C_{cr} = 2\tilde{K}^{1/2} \quad (14)$$

Multiple degree of freedom systems are then defined to be critically damped if $\tilde{C} = C_{cr}$. It is shown in [3] that critically damped systems are critically damped in each mode. That is, that all the eigenvalues associated with (2) appear as negative real pairs of numbers and each modal coordinate describes a critically damped motion.

In a similar manner the definition in both (11) and (14) have been extended to distributed parameter systems modeled by equation (1). In [6], solutions of (1) are assumed to be of the form $u(x,t) = U(x)e^{\lambda t}$ which yields a characteristic equation, which is differentiated, similar to the approach taken in (11). The result is the generation of an infinite set of surfaces representing loci of combinations of damping leading to critically damped motion separation regions of partial or complete underdamping from those of overdamping. References [2] and [6] should be consulted for details.

The extension of the critical damping condition of (14) to the distributed parameter case (1) is outlined in reference [5] and requires the comparison of two differential operators, L_1 and L_2 , on a set of functions satisfying the appropriate boundary conditions and differentiability. Basically (1) is defined to be critically damped if the damping and stiffness operators satisfy the equality

$$L_1^2 = 4L_2 \quad (15)$$

with respect to the boundary conditions. Along with some additional assumptions, described in Appendix 1, if (15) holds then each of the functions $a_n(t)$ in the solution

$$u(x,t) = \sum_n a_n(t) \phi_n(x) \quad (16)$$

is of the form given in (8), i.e. a critically damped function of time. Here, the functions $\phi_n(x)$ are the normalized eigenfunctions of the stiffness operator L_2 .

In what follows, the definitions of critical damping given by equations (14) and (15) will be combined and applied to include systems with asymmetries, control systems and hybrid systems with both lumped and distributed elements. Computational aspects of calculating C_{cr} will also be discussed.

Computational Methods for Lumped Systems: Direct application of the definition of C_{cr} as given by (14) requires the calculation of several matrix square roots. As seen in Appendix 2, calculation of these square roots requires eigenvalue and eigenvector information about both of the matrices M and K . Hence, some alternative procedures for calculating the critical damping matrix have appeared in the literature. Gray and Andry [4] showed that the critical damping matrix for equation (2) could be written without the use of the transformation $M^{-1/2}$ and found that

$$C_{cr} = 2M\Phi\Lambda^{1/2}\Phi^T M, \quad (17)$$

Here, Φ is the modal matrix for K and $\Lambda^{1/2}$ is the diagonal matrix of the square roots of the eigenvalues of K (i.e., the undamped natural frequencies). While equation (17) requires less computation than (14) it still requires the computation of the undamped eigenvectors.

Inman and Orabi [7] found a way to avoid calculating eigenvectors and showed that the critical damping matrix could be calculated from,

$$C_{cr} = \sum_{j=0}^{n-1} \beta_j \tilde{K}^j \quad (18)$$

where β_j then are calculated from,

$$\beta_j = 2 \begin{bmatrix} 1 & \omega_1 & \cdot & \cdot & \cdot & \omega_1^{n-1} \\ 1 & \omega_2 & \cdot & \cdot & \cdot & \omega_2^{n-1} \\ \cdot & & & & & \cdot \\ \cdot & & & & & \cdot \\ \cdot & & & & & \cdot \\ 1 & \omega_n & \cdot & \cdot & \cdot & \omega_n^{n-1} \end{bmatrix}^{-1} \begin{bmatrix} \omega_1^{1/2} \\ \omega_2^{1/2} \\ \cdot \\ \cdot \\ \cdot \\ \omega_n^{1/2} \end{bmatrix} \quad (19)$$

and where ω_n are the natural frequencies of the undamped system.

Ly [8] responded to [7] and noted that the β_j in (18) could also be calculated by comparing the coefficients of Λ^j in the two expansions given by

$$\sum_{j=0}^{n-1} \beta_j \Lambda^j = \sum_{k=1}^n 2\omega_k^{1/2} \frac{\prod_{i=k}^n (\Lambda - \omega_i I)}{\prod_{i=k}^n (\omega_k - \omega_i)} \quad (20)$$

where Λ is the diagonal matrix of undamped natural frequencies. Both (19) and (20) are independent of eigenvector information, but do depend on the spacing of the undamped natural frequencies. In addition, if n is very large so that ω_n^{n-1} is large the inverse in (19) could potentially be very difficult to calculate. Hence, it is desired to find a method which does not depend on powers of the natural frequencies or inverses of potentially ill conditioned matrices.

Such a method is provided by considering an earlier work of Wilson and Penzien [9]. Their work addressed and compared two methods for the numerical evaluation of orthogonal damping matrices which would produce specified modal damping ratios. A direct application of their method to the critical damping definition given in (14) yields

$$C_{cr} = \phi \left(\sum_{i=1}^n 2\omega_i \phi_i \phi_i^T \right) \phi^T \quad (21)$$

Here, ϕ_i is the i th eigenvector of the K matrix corresponding to the i th natural frequency ω_i , and ϕ is the orthogonal matrix of eigenvectors of K . Although this method requires eigenvectors it does not require the calculation of a matrix universe or powers of ω_i . It also does not have difficulty with closely spaced eigenvalues of the stiffness operator.

Example: As an example of calculating the critical damping condition for a lumped parameter system, consider the three degree of freedom system of figure 1. The method of equation (21) will be applied to the mass and stiffness matrices given by

$$M = \begin{bmatrix} 2 & 0 & 0 \\ 0 & 1.5 & 0 \\ 0 & 0 & 1.0 \end{bmatrix} \text{ lb-sec}^2/\text{ft} \quad (22)$$

and

$$K = \begin{bmatrix} 3000 & -1200 & 0 \\ -1200 & 1800 & -600 \\ 0 & -600 & 600 \end{bmatrix} \text{ lb/ft} \quad (23)$$

Applying equation (21) then yields

$$C_{cr} = \begin{bmatrix} 149.27 & -35.49 & -4.51 \\ -35.49 & 95.26 & -22.81 \\ -4.51 & -22.81 & 45.2 \end{bmatrix} \text{ lb-sec/ft} \quad (24)$$

Now comes an interesting point. In order to physically realize this damping matrix all the dashpots indicated in the figure have to be added to the model. If this is not done, then the system cannot be made to vibrate with a critically damped motion in each mode. Matching the damping matrix resulting from the figure with the critical damping matrix of equation (24) yields

$$\begin{aligned} C_1 &= 109.27 \text{ lb-sec/ft} \\ C_2 &= 35.49 \text{ lb-sec/ft} \\ C_3 &= 4.51 \text{ lb-sec/ft} \end{aligned}$$

$$\begin{aligned} C_4 &= 22.81 \text{ lb-sec/ft} \\ C_5 &= 17.88 \text{ lb-sec/ft} \\ C_6 &= 36.96 \text{ lb-sec/ft} \end{aligned}$$

Control Systems for MDOF: If velocity and position feedback control is used on a structure such as (2) then the response is governed by

$$M\ddot{x} + C\dot{x} + Kx = -K_1\dot{x} - K_2x \quad (25)$$

where K_1 and K_2 are feedback gain matrices. Generally K_1 and K_2 are chosen by pole placement [10] or optimal control techniques [11]. However, the transient response of this system can be forced to be critically damped if all the terms of (25) are placed on the lefthand side of (25) and the condition given by (14) applied. This yields

$$(\tilde{C} + K_1)^2 = 4(\tilde{K} + K_2) \quad (26)$$

This yields a set of nonlinear equalities in the mass, damping, stiffness and control parameters. These equalities can be used to perform a simultaneous design and control procedure to cause the response of (25) to be critically damped in each mode. Additionally, since the equations are nonlinear in the parameters, and thus have many solutions (or possibly none), they can be viewed as constraints to be used in solving a conventional control problem.

For example it might be desirable to choose the design and control parameters in such a way as to minimize the damping effort and control effort while causing the system to be critically damped.

Asymmetric Systems: All of the above analysis assumes that the coefficient matrices are symmetric and in the presence of control, that the gain matrices are symmetric. If the system includes gyroscopic forces or follower forces then the equations of motion may take the form

$$A_1\ddot{x} + A_2\dot{x} + A_3x = 0 \quad (27)$$

where A_1, A_2 and A_3 are asymmetric square arrays of real numbers. The asymmetries in A_2 and A_3 can also arise if the gain matrices K_1 and K_2 in equation (25) are asymmetric. If the matrix A_1 is nonsingular and if the products $A_1^{-1}A_2$ and $A_1^{-1}A_3$ have distinct real eigenvalues then the critical damping condition for (27) becomes [12]

$$A_2A_1^{-1}A_2 = 4A_3 \quad (28)$$

Again, this relation yields nonlinear equalities in the various physical parameters and control gains.

Distributed Parameter Control Systems: The control of distributed parameter systems poses some interesting questions regarding truncation and regarding the use of point actuators with distributed mass structures. There are two classifications of DPS controls. The first consists of distributed control actuators (an example of which is given in this volume [13]) such that the velocity and position feedback can be represented by equation (5). The second classification consists of those controls which result from the use of point actuators and yield velocity and position

feedback described by equation (3).

In the case of distributed feedback, it has been shown [14] that the closed loop system decouples if and only if the operators L_1, L_2, L_3 and L_4 satisfy the assumptions in Appendix 1 and they all commute with each other. If this condition is satisfied then the closed loop system defined by (1) and (5) is critically damped if and only if

$$(L_1 + L_3)^2 = 4(L_2 + L_4) \quad (29)$$

with respect to the boundary conditions.

For point actuator control the situation becomes more difficult to prove mathematically. However in most control applications, point actuators are used to provide the control action. Proceeding formally, the critical damping condition for (1) and (3) become

$$\left[L_1 + \sum_{i=1}^R \delta(x-x_i) c_i \right]^2 = 4 \left[L_2 + \sum_{i=1}^R \delta(x-x_i) k_i \right] \quad (30)$$

Both equations (29) and (30) can be used to design systems with critically damped modes.

Example: As an example of applying the critical damping condition to distributed parameter systems consider the longitudinal vibrations of a clamped beam with both internal and external damping. In this case (a, b , and γ positive constants):

$$L_1 + L_3 = 2\left(\gamma - b \frac{\partial^2}{\partial x^2}\right) \quad (31)$$

$$L_2 = -a \frac{\partial^2}{\partial x^2} \quad (32)$$

with $w(0,t)=w(l,t)=0$. Here, the control is provided by external viscous damping (resulting from, say, a surrounding fluid). The eigenvalues of the operation $(L_1+L_3)^2 - 4(L_2+L_4)$ are all zero if and only if (29) is satisfied. The eigenvalues are

$$4\left[\left(\gamma + \frac{b}{a} \lambda_n\right)^2 - \lambda_n\right] \quad (33)$$

where $\lambda_n = a n^2 \pi^2$. It is clear from (33) that the physical parameters and the control constant cannot be chosen such that (33) is zero for all values of n . Thus, this system can be critically damped in at most one mode.

Summary and Conclusions: The concept of critical damping for a single degree of freedom system can be extended to more complex systems in two ways. One method involves matrix manipulation the other involves derivatives. Following the matrix definition, several numerical schemes for

computing C_{cr} were listed and compared. Each of these conditions result in a system which is critically damped in each mode. The matrix definition of critical damping was then extended to include asymmetric systems, control systems and distributed parameter systems.

It is worth noting that while it is difficult to attach dashpots together in such a way as to make a lumped parameter system critically damped it is theoretically possible to do so. However, in a distributed parameter system it seems quite clear that at most one mode can be critically damped in most systems. This poses somewhat of a dilemma in the sense that one could conceivably design a critically damped FEM model of a distributed system. In which case the FEM model would have a drastically different physical response than the actual physical system it is supposed to model.

The greatest potential use of the concept of critical damping for complex structures is not in designing critically damped systems but rather in providing a point of comparison. Just as in the single degree of freedom case, C_{cr} may be most useful in providing a measure of the amount of damping in a system.

References

- [1] Beskos, D.E., and Boley, B.A., "Critical Damping in Linear Discrete Dynamics Systems," ASME Journal of Applied Mechanics, Vol. 47, 1980, pp. 627-630.
- [2] Beskos, D.E., and Boley, B.A., "Critical Damping in Linear Discrete Dynamic Systems," Office of Naval Research Report No. 1979-2, Nov. 1979.
- [3] Inman, D.J., and Andry, A.N., Jr., "Some Results on the Nature of Eigenvalues of Discrete Damped Linear Systems," ASME Journal of Applied Mechanics, Vol. 47, 1980, pp. 927-930.
- [4] Gray, J., and Andry, A.N., Jr., "Simple Calculations for the Critical Damping Matrix of a Linear Multidegree of Freedom System," Mechanics Research Communications, Vol. 9, No. 6, 1982, pp. 379-380.
- [5] Inman, D.J. and Andry, A.N., "The Nature of the Temporal Solutions of Damped Distributed Systems with Classical Normal Modes," ASME Journal of Applied Mechanics, Vol. 49, 1982, pp. 867-870.
- [6] Beskos, D.E., and Boley, B.A., "Critical Damping in Certain Linear Continuous Dynamic Systems," International Journal of Solids and Structures, Vol. 17, 1981, pp. 575-588.
- [7] Inman, D.J. and Orabi I., "An Efficient Method for Computing the Critical Damping Condition," ASME Journal of Applied Mechanics, Vol. 50, 1983, pp. 679-682.

- [8] Ly, B.L, discussion on [7] above, to appear Journal of Applied Mechanics.
- [9] Wilson, E.L. and Penzien, J., "Evaluation of Orthogonal Damping Matrices," International Journal for Numerical Methods in Engineering, Vol. 4, 1972, pp. 5-10.
- [10] Andry, A.N., Jr., Shapiro, E.Y. and Chang, J.C., "Eigenstructure Assignment for Linear Systems," IEEE Transactions on Aerospace and Electronic Systems, Vol. 19, No. 5, September 1983, pp. 711-729.
- [11] Kirk, Optimal Control Theory -- An Introduction, Prentice Hall, 1970.
- [12] Ahmadian, M. and Inman, D.J., "On the Nature of Eigenvalues of General Non-Conservative Systems," ASME Journal of Applied Mechanics, Vol. 15, No. 1, 1984, pp. 193-194.
- [13] Bailey, T. and Hubbard, J.E., Jr., "Distributed Piezoelectric Polymer Active Vibration Control of a Cantilever Beam," This volume, paper No. 42.
- [14] Inman, D.J., "Decoupling Conditions for Distributed Control of Flexible Structures," to appear AIAA Journal of Guidance, Control and Dynamics, May-June 1984.

Appendix 1 Operator Assumptions

Some substantial mathematical tools are needed in order to define the idea of critical damping for a system described by partial differential equations. Namely, not every unbounded operator L_1 admits eigenvalues (natural frequencies) and eigenfunctions (mode shapes). This appendix lists a set of assumptions which guarantees the existence of eigenfunctions and that the critical damping computation can be made. It is assumed in the above that L_1 and L_2 satisfy the following

$$u_{tt}(x,t) + L_1[u_1(x,t)] + L_2[u(x,t)] = 0 \quad \text{in } \Omega \quad (\text{A.1})$$

$$B[u(x,t)] = 0 \quad \text{on } \partial\Omega \quad (\text{A.2})$$

where

- a. $(\cdot)_1$ indicates partial differentiation of (\cdot) with respect to t ;
- b. Ω is a bounded, open region in R^n , $n=1,2$, or 3 with boundary $\partial\Omega$;
- c. L_1, L_2 are linear spatial differential operators of order n_1, n_2 , respectively, and are self-adjoint on the domain $D(L) = \{u(\cdot, t) \in L^2(\Omega) \text{ such that all partial derivatives with respect to } x \text{ of order up to and including } k \text{ are in } L^2(\Omega) \text{ where } k = \max(2n_1, 2n_2) \text{ and } B[u(x,t)] = 0 \text{ for } x \in \partial\Omega, \text{ for all } t \geq 0\}$;

- d. L_1 and L_2 commute on $D(L)$, L_1, L_2 are positive definite operators on $D(L)$ and each has a compact resolvent,
- e. B is a linear operator (and may be a differential operator of order up to $\max(n_1, n_2) - 1$) which reflects boundary conditions.

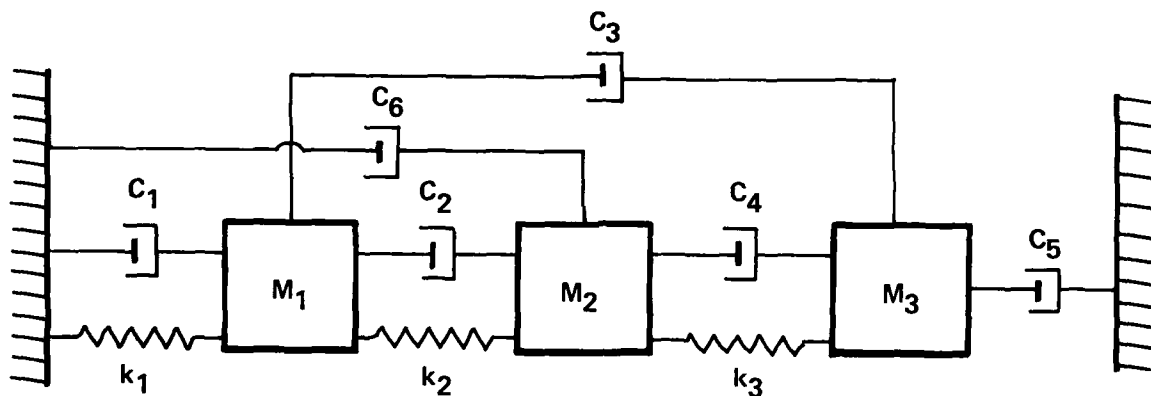
Appendix 2 Matrix Square Roots

If A is a symmetric positive definite matrix then it has a unique positive definite square root denoted $A^{1/2}$ given by

$$A^{1/2} = S^T \Lambda^{1/2} S$$

where S is the matrix of normalized eigenvector of the matrix A and $\Lambda^{1/2}$ is a diagonal matrix with diagonal elements consisting of the positive square roots of the eigenvalues of the matrix A .

Figure 1



AN APPROACH TO THE SIZING OF DISCRETE VISCOUS
STRUCTURAL DAMPERS USING AN EXTENSION OF THE
FINITE ELEMENT APPROACH AND MODAL STRAIN ENERGY

Dr. Robert B. Rice
Martin Marietta Corporation
Denver, Colorado

and

Eric C. Dalton
Teledyne Brown Engineering
Huntsville, Alabama

AD-A152 547

VIBRATION DAMPING WORKSHOP PROCEEDINGS HELD AT LONG
BEACH CALIFORNIA ON 2. (U) AIR FORCE WRIGHT
AERONAUTICAL LABS WRIGHT-PATTERSON AFB OH L ROGERS

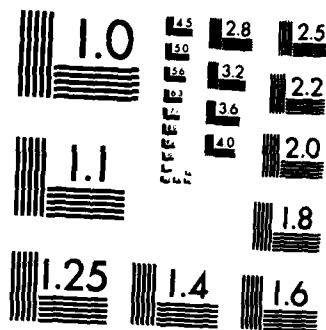
10/11

UNCLASSIFIED

11 NOV 84 AFWAL-TR-84-3064

L ROGERS
F/G 20/11

NL



MICROCOPY RESOLUTION TEST CHART
NATIONAL BUREAU OF STANDARDS-1963-A

An Approach to the Sizing of Discrete Viscous
Structural Dampers Using an Extension of the
Finite Element Approach and Modal Strain Energy

By

Dr. Robert B. Rice
Martin Marietta Corporation

and

Eric C. Dalton
Teledyne Brown Engineering

ABSTRACT

A method for determining viscous damper values and damper locations for a structure which has particular damping requirements is presented in this paper. The method is intended as a starting point in a design process. The finite element approach and concept of modal strain energy are heavily relied upon.

To illustrate the solution sequences, a sample problem is included in the report. The method was applied to a large space-based telescope in which damping of optical support structures is critical for tracking and pointing accuracy. The results of the sample problem indicated that the method will yield the desired amount of damping in a structure provided that the complex mode shapes do not significantly deviate from the classical mode shapes.

Since the characterization of non-viscous dampers is considerably more complicated than viscous dampers, the author suggests that the method presented in this paper be used in the early phases of design. If viscous damping values are known, the range of other candidate dampers may be narrowed.

INTRODUCTION

A structure often has a requirement that its response must be as highly damped as possible. The required levels of damping are usually not attained with common engineering materials such as steel or aluminum because of a low level of inherent material damping. The cost as well as the weight penalty of adding dampers to the structure can be moderate, and furthermore, haphazard application may even be detrimental. The designer is faced with the problem of where to locate the dampers and also the type of damper which should be used.

Selection of the damper design is a difficult task because there are such a wide variety (eg, hysteretic, velocity squared etc) that have different mathematical characterizations. Some of the mathematical characterizations of damping have not yet matured to a level in which efficient numerical solutions such as finite elements exist. The viscous damper, however, can be easily characterized by finite elements. In this paper, a method to efficiently determine viscous damper locations and damping values will be discussed.

The sizing of viscous dampers which is obtained by the method presented in this report will be useful in selecting other types of dampers as well. For example, from the stress strain curve of a viscoelastic damper at a given frequency, a value of equivalent viscous damping may be obtained [1]. If the equivalent viscous damping values do not significantly change with frequency, the viscous damping values obtained analytically will be useful in selection of the viscoelastic damper. Conversely, if the equivalent viscous damping values change significantly with frequency, the analytic viscous damping values may still be useful if the frequency range may be narrowed by attempting only to damp a predominant vibration mode. The latter assumes that other vibration modes will not be adversely affected.

METHOD

Efficient placement of dampers in a structure requires that the vibration modes which significantly effect performance be identified. In the method presented herein, the classical vibration modes which dominate the frequency response of key parameters to system performance are those which must be identified. The term classical vibration modes refers to the mode shapes which are derived from the undamped system. Examples of key parameters are sensor motions or linear combinations of optical component motions such as the line of sight of a laser tracker. Viscous damper placement and value will be found using modal strain energy concepts for the selected classical modes. Subsequently, the complex mode shapes will be derived and the resulting level of damping compared to the original desired value. The complex mode shapes are those which are derived from a damped system.

There have been several methods proposed for modal selection. A traditional approach, in which the dominant modes of a particular parameter of interest are selected from its frequency response, was adopted as part of the overall solution sequence. The latter approach was chosen because it was simple but it could be replaced by other modal selection processes.

The frequency response for a parameter of interest is obtained from the steady state value of the corresponding transfer function. To obtain the transfer function, a finite element model of the structure is constructed and the equations of equilibrium:

$$[M] \{\ddot{q}\} + [B] \{\dot{q}\} + [K] \{q\} = \{F\} \quad (1)$$

where $[M]$ is the discrete mass
 $[B]$ is the discrete damping
 $[K]$ is the discrete stiffness
 $\{F\}$ is the discrete force vector
 $\{q\}$ are the discrete coordinates

are set up. The classical vibration modes $[\phi]$ are the eigenvectors of the undamped homogeneous form of Eq (1). Due to the orthogonality of $[\phi]$, a coordinate transformation which decouples the equations of motion is possible (for a lightly damped system), [2]. The resulting equations of motion are:

$$[I] \{\ddot{z}\} + 2\xi\omega \{\dot{z}\} + \omega^2 \{z\} = [\phi]^T \{F\} \quad (2)$$

where $[I]$ is the identity matrix
 ξ is the percent of critical damping
 ω is the circular frequency
 z are modal coordinates

By application of the Laplace transform and transformation back to discrete coordinates, the general form of the transfer function for the parameter θ due to the i th force is:

$$\frac{\theta(s)}{F_i(s)} = \sum_{K=1}^N \frac{\theta_k \theta_{ik}}{s^2 + 2\xi_k \omega_k s + \omega_k^2} \quad (3)$$

where θ_k is the parameters' motion in the kth mode (this could be a linear combination of structural motions)

θ_{ik} is the structural motion at the ith point in the kth mode

ζ_k percent of modal damping for the kth mode

ω_k circular frequency of the kth mode

N total number of modes

The modal coefficient of Eq (3) for the kth mode is

$$P_k = \frac{\theta_k \theta_{ik}}{\omega_k^2} \quad (4)$$

Other forms of Eq (3) may be found (parameter velocities or accelerations) by applying the Laplace transform rules.

The number of modes which must be considered for selection may be found by including only the modes with the larger modal coefficients (modal participation factors) in the summation of Eq (3) until the Bode plot of the selected mode set is a good match to that of the complete mode set.

To find the damper locations, the modal strain energy of each selected mode is calculated. Dampers are placed in regions of the structure which have the highest modal strain energy in each of the selected modes. To further discuss the method of using modal strain energy to locate dampers, a brief discussion of the finite element method of discretized stiffness generation is necessary.

In the finite element method, a local stiffness matrix or stiffness kernel is developed for each element of the system. The global stiffness matrix which is used for the equations of equilibrium is assembled by adding all of the stiffness kernels, i.e.,

$$[K] = \sum_{j=1}^n [k]_j \quad (5)$$

where $[k]_j$ is the stiffness kernel for the jth element, and

n is the total number of elements

In addition, the stiffness kernal is composed of several sub-kernels. In a beam element (Fig. 1), for example, there is a sub-kernal for axial, torsion, and two bending degrees of freedom (DOF). This may be shown as

$$[k] = [k]_{\text{Bending } Y} + [k]_{\text{Bending } Z} + [k]_{\text{Torsion}} + [k]_{\text{Axial}} \quad (6)$$

The modal strain energy for an element is calculated by

$$S.E._j = [\phi]_K^T [k]_j [\phi]_K \quad (7)$$

and the total strain energy for that mode is

$$S.E._{\text{TOTAL}} = \sum_{j=1}^n S.E._j = \omega_K^2 \quad (8)$$

A map of the modal strain energy may be constructed by dividing each element's modal strain energy by the total for that mode. For purposes of applying dampers, it is also necessary to calculate the modal strain energy for each sub-kernal by

$$S.E._{ij} = [\phi]_K^T [k]_{ij} [\phi]_K \quad (9)$$

where $[k]_{ij}$ is the i th sub-kernal of the j th stiffness kernal. If most of the strain energy is due to bending, for example, a damper which damps the rotational movement of the ends of the beam should be employed. A schematic of a simplified damper design which exhibits the rotational damping is shown in Fig 2.

With damper locations identified, the modal strain energy concept will be used to determine viscous damping values which will satisfy a particular level of damping. The problem is simplified if it is assumed that the viscous damping values are proportional to the stiffness at each element by a factor α . This porportionality factor may be determined as follows: Let $[\bar{K}]$ be equal to the global stiffness matrix for the elements with high modal strain energy for the mode of interest. The stiffness



FIGURE 1a. FINITE ELEMENT BEAM FOR EXTENSION (FORMS AN AXIAL STIFFNESS KERNEL $[K]_{\text{AXIAL}}$).



FIGURE 1b. FINITE ELEMENT BEAM FOR TWIST (FORMS A TORSIONAL STIFFNESS KERNEL $[K]_{\text{TORSION}}$).



FIGURE 1c. FINITE ELEMENT BEAM FOR BENDING (FORMS A BENDING STIFFNESS KERNEL $[K]_{\text{BENDING}}$).

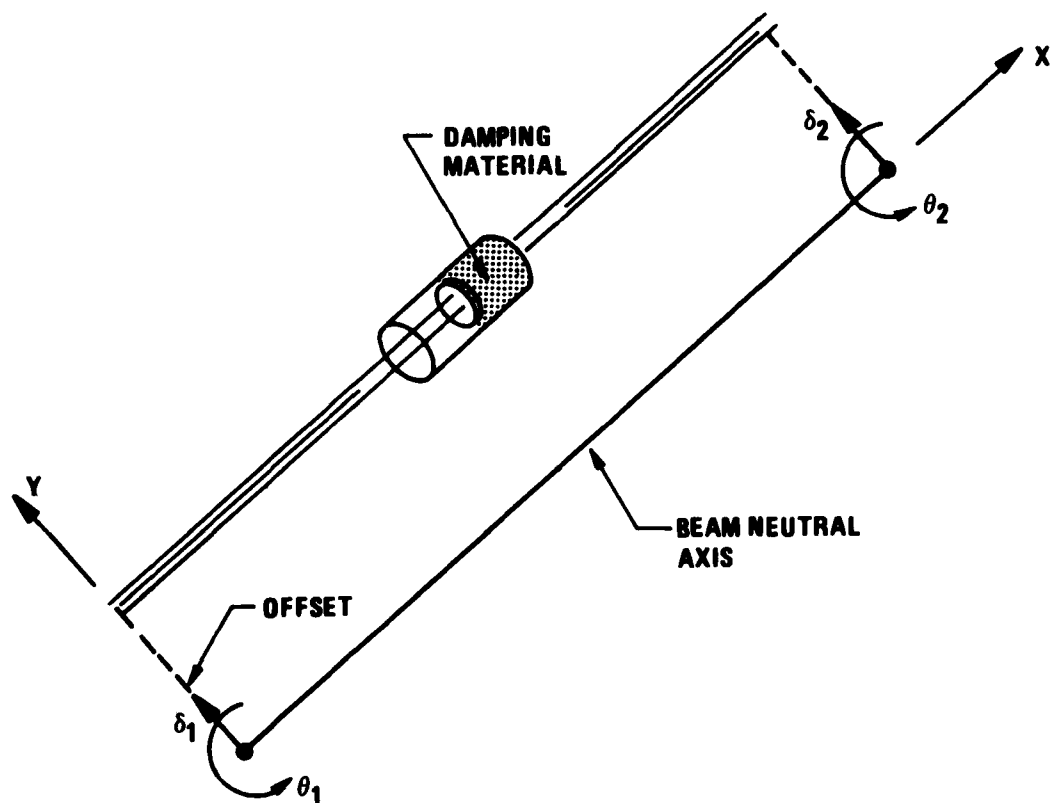


FIGURE 2. IDEAL ROTATIONAL DAMPER FOR A BEAM.

associated with elements of low modal strain energy is made zero. Then

$$\bar{\omega}_K^2 = \{\phi\}_K^T [\tilde{K}] [\phi]_K \quad (10)$$

where $\bar{\omega}^2$ = an adjusted total modal strain energy

By definition of classical modes

$$\{\phi\}_K^T [B] \{\phi\}_K = 2\zeta_K \omega_K \quad (11)$$

Therefore, it may be assured that

$$\alpha \{\phi\}_K^T [\tilde{K}] \{\phi\}_K = 2\zeta_K \omega_K \quad (12)$$

and

$$\alpha \bar{\omega}_K^2 = 2\zeta_K \omega_K \quad (13)$$

and then

$$\alpha = \frac{2\zeta_K \omega_K}{\bar{\omega}_K^2} \quad (14)$$

As a means of mathematically testing the derived damper treatment configuration, an equivalent percent modal damping is calculated for the complex mode shapes. The equivalent percent modal damping is a means of relating the damping of a complex mode with the desired value which was originally selected based on a classical mode. If the complex mode shapes are very similar to the classical mode shape, the equivalent modal damping will be an excellent test.

If the complex mode shapes do not resemble the classical modes, the equivalent percent modal damping becomes meaningless. In fact, the method of determining damping values will break down if the complex modes do not resemble the classical modes. Methods of determining the degree of which the mode shapes are complex (and hence the effectiveness of this method) will be discussed.

Complex mode shapes may be extracted by expressing the state equation in terms of the original classical mode shapes [3, 4]:

$$\lambda \begin{Bmatrix} \dot{\psi}_i \\ \psi_i \end{Bmatrix} = \begin{bmatrix} -[\phi]^T[B][\phi] & -\omega_i^2 \\ \frac{1}{r_i} & 0 \end{bmatrix} \begin{Bmatrix} \dot{\psi}_i \\ \psi_i \end{Bmatrix} \quad (15)$$

where λ are the complex eigenvalues, and $[\psi]$ are the complex eigenvectors (modes)

After extraction of complex modes and frequencies from Eq (15), the modes may be transformed into discrete coordinates by

$$[\Phi] = [\phi] [\psi] \quad (16)$$

The relation between eigenvalue real and imaginary parts is

$$\omega_{N_K}^2 = (\lambda_r^2 + \lambda_i^2)_K \quad (17)$$

and the equivalent percent damping is

$$\zeta_K = -\frac{\lambda_{rK}}{\omega_{N_K}} \quad (18)$$

where

- λ_r = real part of the kth complex frequency (eigenvalue)
- λ_i = imaginary part of the kth complex frequency
- ω_{N_K} = natural frequency of the kth complex mode
- ζ = equivalent percent damping for the kth complex mode

The equivalent percent damping values which result from Eq (18) may then be compared to the originally desired values as a test of the effectiveness of this method.

At the levels of system damping which physical damper design will allow, the complex mode shapes may resemble the classical mode shapes and consequently the method described herein will be effective. By expressing Eq (9) in summation notation

$$\phi_{ik}' = \sum_{K=1}^N \phi_{iK} \psi_{KK}' \quad (19)$$

where ϕ_{ik}' = K'th complex mode shape for the ith DOF (discrete coordinates)
 ϕ_{ik} = Kth classical mode shape for the ith DOF
 ψ_{KK}' = K'th complex mode shape for the Kth DOF (classical modal coordinates)

it can be seen that if one term of each summation is larger than the other terms, the complex modes will resemble the classical modes.

In summary, a road map of this method is shown in Fig 3. The example problem which follows in the next section is intended to clear up portions of the method which may seem rather vague at this point.

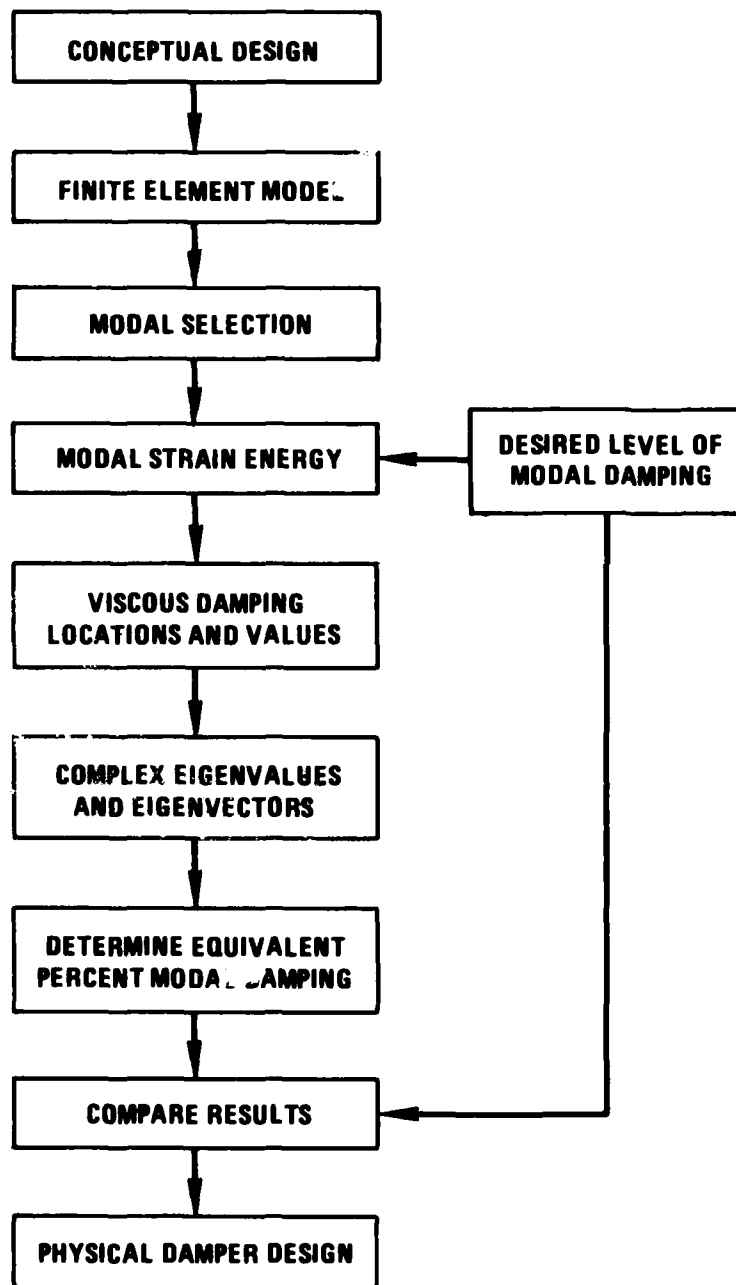


FIGURE 3. ROADMAP OF METHOD FOR DETERMINING VISCOUS DAMPER LOCATIONS AND VALUES

EXAMPLE PROBLEM

The method of analysis described in the latter section was applied to a conceptual space based telescope (SBT). The SBT is ideally suited as a sample structure because there is a critical performance parameter or index which is directly associated with vibration. The parameter is the telescope line-of-sight (LOS), which is perturbed when structural components of the optical train vibrate with respect to each other. During operation, the SBT has a two-axis gimbal which maneuvers the optical train into position. Overshoot and settle time of the LOS are critical to mission effectiveness and hence the addition of dampers to the structure will improve the effectiveness.

The SBT has three main subsystems: pointing body, gimbal, and reaction body. A finite element model (Figure 4) was constructed for the SBT which had enough fidelity to describe the structure supporting the optical train. Application of the method to this model will follow the roadmap of Figure 3.

The form of Eq (3) for the LOS with a single symmetric torque about one axis is:

$$\frac{\theta_{LOS}(s)}{T_{GIMBAL}(s)} = \sum_{K=1}^N \frac{\phi_{LOS} \phi_{GIMBAL}}{s^2 + 2\zeta_K \omega_K s + \omega_K^2} \quad (20)$$

where ϕ_{LOS} modal LOS deflection
 ϕ_{GIMBAL} modal slope at the gimbal
 ζ_K percent of modal damping for the kth mode
 ω_K circular frequency of the kth mode
 N total number of modes

The parameter ϕ_{LOS} is obtained from the LOS equation which is a linear combination of structure motions;

$$\phi_{LOS} = \Delta\theta_I \left(\frac{F_S}{F_P} \right) + (\Delta X_S - \Delta X_P) \left(\frac{1}{F_P} \right) - \Delta\theta_S \left(\frac{2F_S}{F_P} \right) + 2\Delta\theta_P \quad (21)$$

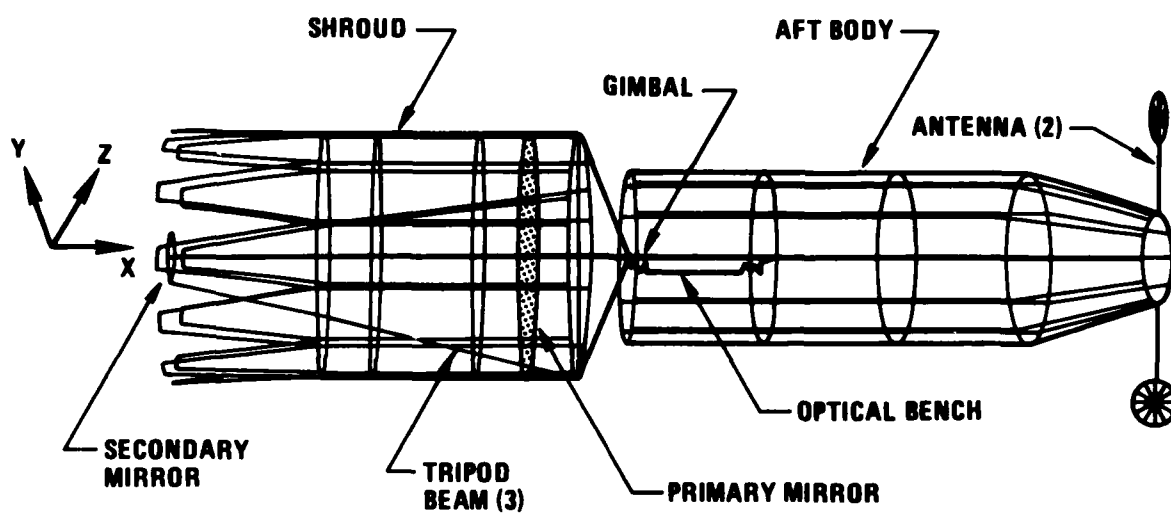


FIGURE 4. ENGINEERING MODEL OF SBT

where $\Delta\theta_I$ = input beam modal rotation,

ΔX_s = secondary mirror modal translation,

ΔX_p = primary mirror modal translation,

$\Delta\theta_s$ = secondary mirror modal rotation,

$\Delta\theta_p$ = primary mirror modal rotation,

F_s = secondary mirror focal length, and

F_p = primary mirror focal length.

A complete set of vibration modes and frequencies were determined from the model and Eq (20) was used for modal selection (truncation). Bode plots were made for the various truncated mode sets by retaining the modes having a large modal coefficient or modal participation factor. The results indicated that at least five modes were necessary to match a truncated mode set to a complete set for the LOS transfer function. The Bode plot comparing the final truncated mode set with the complete set is shown in Figure 5.

Of the five modes which were retained in the truncated mode set, the first two modes were fundamental modes of the tripod (the tripod is symmetrical so there will be a pair of modes at the lowest frequency). The third mode was the fundamental mode of the primary mirror, which was virtually decoupled from the rest of the structure. The remaining modes were a coupling of all the components in the optical train. Since the third mode and first two modes were both uncoupled, low frequency, and created the largest peaks in the frequency response, it was decided to apply the method to those modes only. The higher frequency modes would obtain some damping through association with the low frequency modes. For this particular example, it would not be economical to apply the method to the higher frequency modes because the damper treatment would have to be placed over almost the whole structure, resulting in a large mass addition. Furthermore, in the transient response of the structure, the motion associated with the higher frequency modes will die out quicker because of the larger number of cycles of oscillation experienced.

The damper locations for the tripod were found by applying Eq (9) for the first few modes of the tripod. Results were obtained in the form of matrices for axial, torsion, and two bending axes for the beam elements (Table 1). Rows of the matrices correspond to each element and the columns correspond to each mode. For all the modes, the strain energy values for axial and torsion were much lower than the strain energy values for the bending axes. For the fundamental mode, the distributions of strain energy

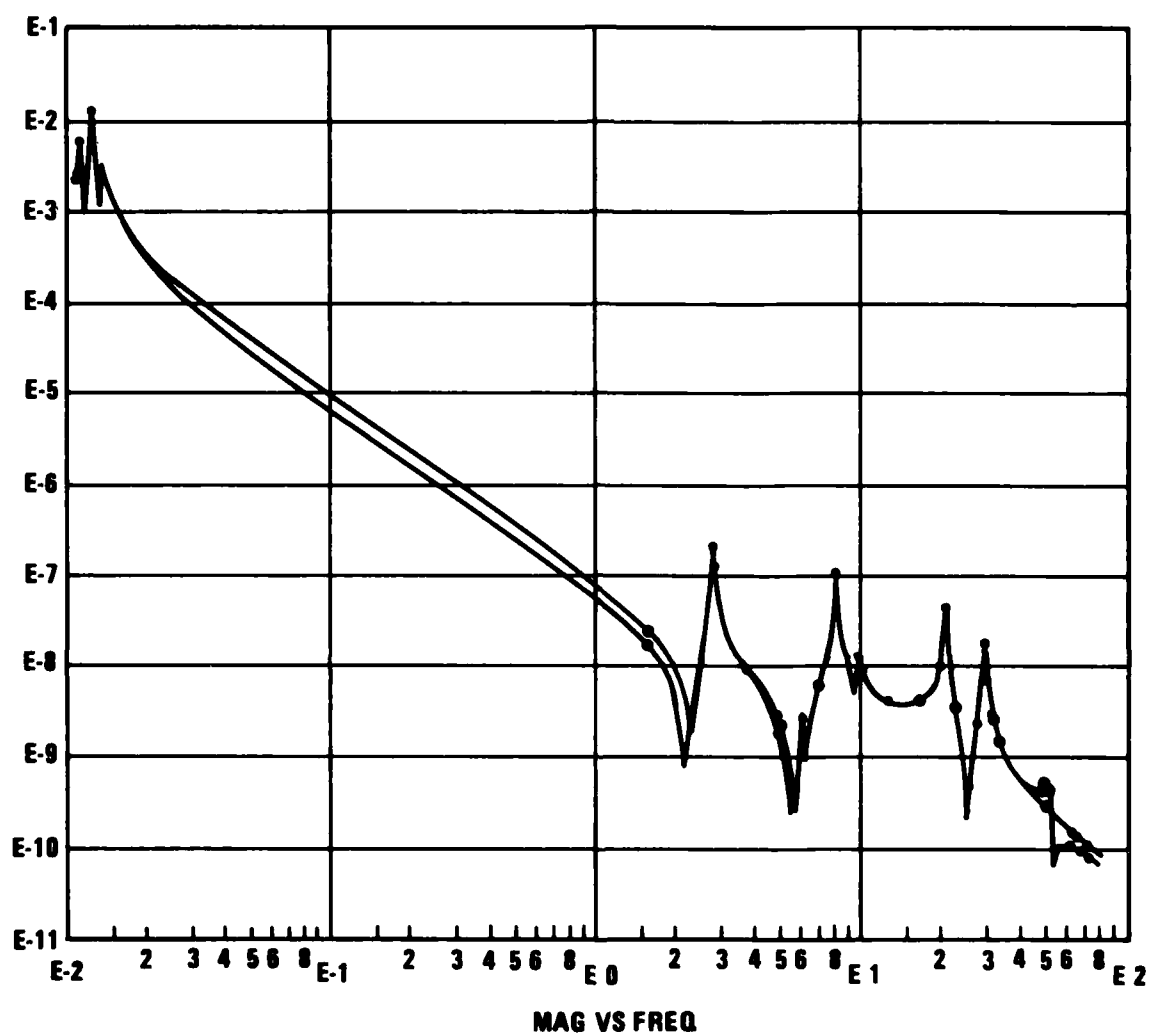


FIGURE 5. COMPARISON OF COMPLETE AND TRUNCATED LOS FREQUENCY RESPONSE - MAGNITUDE VS. FREQUENCY.

value in the first column of the bending matrices indicated bending of the tripod about one global axis. The second mode was symmetrical to the first; bending about the other global axis. The bending behavior of the tripod in the lower modes was also observed in the plots of the mode shapes (Figure 6). The configuration of dampers found by applying the method to the fundamental tripod mode is shown schematically in Figure 7. It should be noted that damping for the axial and torsional motions for the beam elements will have only a slight effect upon the modal damping, thus the configuration shown in Figure 7 employs the ideal rotational damper discussed in the previous section. The damping locations for the third mode were found in a similar manner.

After the damping configuration was identified, the $[K]$ matrix was assembled and the stiffness proportionality factor α for calculating the damping matrix $[B]$ was calculated from Eq (14). In this case, the desired level of damping for the three modes was 10% critical. The complex modes were calculated from Eq (15) and the percent equivalent damping from Eq (18). The results for the selected five modes are shown in Table 2. It can be seen that the desired level of damping was achieved (with small error) for the first three modes to which the method was applied. The other two modes obtained damping by association with the first three, but the damping diminished as the frequency increased. Since the desired level of damping was very nearly achieved for the first three modes, the complex modes must closely resemble the classical modes.

The configuration for damping the tripod (Figure 7) is actually quite realistic in terms of an actual physical device. The two beam elements adjacent to the secondary mirror on each tripod leg have two axial dampers located at a distance of 18 cm. The length of each beam is 3.72m. One damper is oriented such that the damper lies in the plane formed by the beam element and the center of mass of the secondary mirror. The other damper is identical but is placed 90° from the plane described. The damping value for each damper is $3.27E+04$ N·s/m. This value of viscous damping is in the neighborhood of equivalent viscous damping values obtained from stress-strain hysteresis curves for visco-elastic dampers in the PACOSS program [5].

CONCLUSION

The method for determining the damper locations and viscous damping constants was shown to be very effective at a desired 10% critical damping for the sample structure. Continuing analyses with the SBT should investigate the point at which the method becomes unreliable, ie., when there is a significant deviation between the classical and complex vibration modes. Additionally, the investigator must determine if the viscous damping values are realistic in terms of a physical device.



FIGURE 6. FUNDAMENTAL VIBRATION MODE OF THE SBT TRIPOD

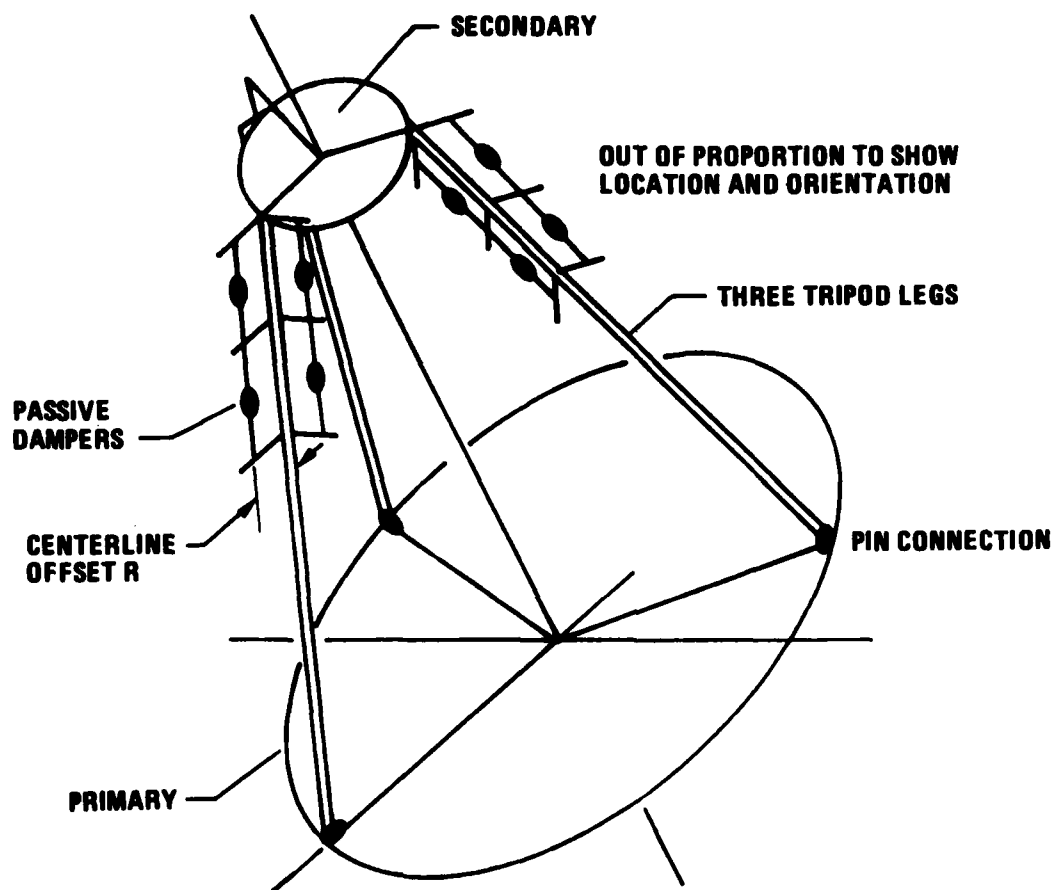


FIGURE 7. TRIPOD DAMPER LOCATIONS OF EXAMPLE CASE

AXIAL	1.294E-20	7.113E-01	1.224E-22	8.461E-02	4.669E-20
	1.302E-20	7.094E-01	1.224E-22	8.461E-02	4.669E-20
	8.682E-21	7.102E-01	9.234E-22	8.397E-02	7.360E-20
	8.162E-21	7.096E-01	1.264E-22	8.191E-02	1.247E-20
	8.158E-01	1.778E-01	3.276E-06	2.364E-03	1.782E-02
	8.158E-01	1.773E-01	3.072E-06	2.366E-03	1.782E-02
	8.167E-01	1.774E-01	3.242E-06	2.332E-03	1.777E-02
	8.162E-01	1.773E-01	3.486E-06	2.227E-03	1.736E-02
	8.168E-01	1.775E-01	3.276E-06	2.364E-03	1.782E-02
	8.168E-01	1.772E-01	3.072E-06	2.366E-03	1.782E-02
TORSION	8.167E-01	1.774E-01	3.242E-06	2.332E-03	1.777E-02
	8.162E-01	1.773E-01	3.486E-06	2.227E-03	1.736E-02
	8.168E-01	1.775E-01	3.276E-06	2.364E-03	1.782E-02
	8.168E-01	1.772E-01	3.072E-06	2.366E-03	1.782E-02
	8.167E-01	1.774E-01	3.242E-06	2.332E-03	1.777E-02
	8.162E-01	1.773E-01	3.486E-06	2.227E-03	1.736E-02
	8.168E-01	1.775E-01	3.276E-06	2.364E-03	1.782E-02
	8.168E-01	1.772E-01	3.072E-06	2.366E-03	1.782E-02
	8.167E-01	1.774E-01	3.242E-06	2.332E-03	1.777E-02
	8.162E-01	1.773E-01	3.486E-06	2.227E-03	1.736E-02
Z BENDING	6.465E-02	1.739E-21	1.261E+01	2.924E-22	9.896E-03
	4.314E-02	1.316E-21	1.231E+01	1.485E-21	1.487E-02
	6.072E-02	1.681E-21	1.284E+01	1.063E-22	7.532E-05
	4.125E-02	1.240E-21	1.308E+01	8.031E-23	1.247E-06
	9.296E-03	3.239E-02	1.307E+01	8.573E-04	2.899E-03
	5.238E-03	3.359E-02	1.317E+01	2.172E-04	2.899E-06
	8.961E-02	4.107E-02	1.283E+01	3.136E-04	6.689E-04
	4.938E-03	3.266E-02	1.295E+01	4.276E-04	7.739E-04
	9.396E-03	3.339E-02	1.307E+01	8.573E-04	2.899E-03
	5.238E-03	3.359E-02	1.317E+01	2.172E-04	2.899E-06
Y BENDING	8.961E-02	4.107E-02	1.283E+01	3.136E-04	6.689E-04
	4.938E-03	3.266E-02	1.295E+01	4.276E-04	7.739E-04
	9.396E-03	3.339E-02	1.307E+01	8.573E-04	2.899E-03
	5.238E-03	3.359E-02	1.317E+01	2.172E-04	2.899E-06
	8.961E-02	4.107E-02	1.283E+01	3.136E-04	6.689E-04
	4.938E-03	3.266E-02	1.295E+01	4.276E-04	7.739E-04
	9.396E-03	3.339E-02	1.307E+01	8.573E-04	2.899E-03
	5.238E-03	3.359E-02	1.317E+01	2.172E-04	2.899E-06
	8.961E-02	4.107E-02	1.283E+01	3.136E-04	6.689E-04
	4.938E-03	3.266E-02	1.295E+01	4.276E-04	7.739E-04

TABLE 1 - MODAL STRAIN ENERGY FOR THE TRIPOD: ROWS CORRESPOND TO THE BEAM ELEMENTS AND THE COLUMNS CORRESPOND TO THE FIRST FIVE MODES

MODE	EQUIVALENT PERCENT DAMPING	UNDAMPED NATURAL FREQUENCY (Hz)	RSS OF COMPLEX FREQUENCY (Hz)
1	9.296	2.747	2.752
2	9.712	2.791	2.795
3	11.03	7.951	7.993
4	3.918	20.84	22.66
5	0.535	29.0	29.81

TABLE 2 - RESULTS OF THE SAMPLE PROBLEM FOR THE FIVE SELECTED MODES

REFERENCES

1. Scott R. Dahl and Robert B. Rice, "A Derivation of Equivalent Linear Viscous and Elastic Constants for Viscoelastic Materials", Vibration Damping Workshop, USAF, Long Beach, California, 1984.
2. Hurty, W. C., and M. F. Rubinstien, Dynamics of Structures, Prentice Hall, Inc., Englewood Cliffs, New Jersey, 1964.
3. Martin Marietta Company; IR&D D39-R. 1983, Document No. R83-48639-001, "Control of Large Space Systems", Chapter 2.
4. Henderson, Timothy C.; and Canavin, Joseph R.: Damping Augmentation for Large Space Structures. American Institute of Aeronautics and Astronautics, 1978.
5. White, C. W.; and Morosow, G.: Passive and Active Control of Space Structures (PACOSS), Vibration Damping Workshop, USAF, Long Beach, California, 1984.

FLEXIBLE STRUCTURE CONTROL IN THE FREQUENCY DOMAIN

R. Harding and Dr. A. Das
General Electric Space Division
Spacecraft Operations
Control Systems Design
Philadelphia, Pennsylvania

Flexible Structure Control in the Frequency Domain

R. Harding

Dr. A. Das

General Electric Space Division
Spacecraft Operations
Control Systems Design

Abstract

New techniques to analyze structure and controller interaction in the frequency domain are defined and used to determine the modal damping requirements of the spacecraft structure to assure control system stability and performance. Gain and phase versus frequency (Bode and Nyquist) techniques are described which predict system stability in the presence of uncontrolled structural modes and errors in a priori natural frequencies and quantify control system margin for these modes. The techniques are applied to an optimally controlled single axis satellite with very large solar arrays. Control system actuator and sensor configurations are based upon system controllability and observability of four dominant structural modes. Verification of the techniques is by simulation.

INTRODUCTION

Preliminary analyses of Large Space Structures (LSS) have brought to light difficult problems of designing a control system that has to meet very accurate pointing requirements in the presence of low frequency structural modes. To satisfy pointing accuracy requirements, the bandwidths of the attitude control system (ACS) have to be at least one or two orders of magnitude higher than classical development techniques can provide. Nearly all past and present spacecraft have an ACS with frequency bandwidths which are about 2% of the frequency of the fundamental structural mode. This frequency ratio allows the response of the ACS to be attenuated sharply at frequencies above the bandwidth of the controller through the use of low pass filters.

Higher bandwidths can be achieved for spacecraft with linearizable dynamic systems by optimizing quadratic cost functionals in the presence of gaussian noise. These optimal linearizable quadratic Gaussian (LQG) designs seem to be a good choice, although, they have several drawbacks. The LQG controllers require much greater resources in the onboard computers and can be unstable if the spacecraft have dominant high frequency structural modes not accounted for in the design. Good estimates of the modeshapes, the modal critical damping ratios and the natural frequencies of the spacecraft structure are required for the LQG controllers to be effective. Errors in any of these parameters may result in unstable conditions and necessitate structure redesign, controller redesign, or inclusion of some kind of parameter estimation/correction technique. The LSS trend causes the control and structure frequency spectrums to overlap. Interaction of these disciplines becomes of paramount importance to insure stability as well as to meet structure size, weight, stress and other constraints. Preliminary design will be an extremely dynamic process that must include trades with controller complexity and structure damping design. Active versus passive structure damping is such a trade that is addressed in this paper.

Frequency domain design and analysis for multivariable control problems has been a subject of intense investigation in recent years. Unconditional system stability methods for multivariable control is approached in a variety of ways that include eigenvalue analysis, singular value determination [7], positivity concepts [2], and generalized Nyquist trajectories [6,9]. The approach presented here is pragmatic in that LQG methods are applied to a flexible spacecraft, but, it is also innovative with frequency response analysis techniques that give insight into particular state element sensitivities and stability margins.

SUMMARY

Attitude and flexible mode control of a spacecraft with very large solar arrays is simulated and analyzed for stability in the frequency domain. The LQG controller developed for this investigation uses three torque producing actuators, a rate sensor, an absolute position sensor, and four relative position sensors. The LQG controller actively damps structural modes while causing the attitude transient response settling time to be an order of magnitude faster than the response of a classical controller. Frequency response analyses show the second dominant mode to be notched from the LQG controller response due to that mode's small observability and controllability.

This conclusion is verified by simulation. Adding passive damping to the second dominant mode significantly enhances plant stability margin and decreases solar array transient response settling time. Control spillover analysis is accomplished by adding two uncompensated modes to the true plant system dynamics. Frequency response analysis with simulations show the system to be stable with uncompensated modes even with large errors in a priori structure critical parameters. The frequency response techniques provide a graphic means of measuring stability margins of state elements and prediction of critical parameter errors that can cause instability. Examples of a priori natural frequency error and modal admittance error tolerances are given with results from simulations to validate these assertions.

OPTIMAL CONTROL SYNTHESIS

Most previous satellite controller designs have been able to meet the performance specification while avoiding active control of any structural mode. The standard design procedure rolls off the controller response at higher frequencies so that the system response is highly attenuated at the modal natural frequencies. Avoiding these modes while increasing the bandwidth of the controller requires additional compensation for notching the controller at the structure natural frequencies. A quadratic performance index optimization method that allows the designer to choose the states to be controlled has gained widespread appreciation as an alternative to the classical approach. This LQG design approach leads to optimal state estimation and the control gains based upon a weighting of the state elements and control effort. In this manner, identifiable structural modes can be included in the controller instead of avoided as in the case of a classical control design. This type control will actively damp controllable and observable modes and enhance attitude control performance. Development of an LQG controller is outlined in the following paragraphs.

A linear time-invariant system can be represented in the form

$$\dot{x} = Ax + Bu + w$$

$$y = Cx + v$$

where,

A = nxn system matrix

B = nxr control matrix

C = mxn measurement matrix

x = nx1 state vector

y = mx1 sensor output vector

u = rx1 control vector

w = nx1 noise vector

v = $m \times 1$ measurement noise vector

n = number of states

r = number of actuators

m = number of sensors

The controller is designed based on estimates of A, B, C , and x so the equations for the LQG design become

$$\dot{\hat{x}} = \hat{A}\hat{x} + \hat{B}u + w$$

$$y = \hat{C}\hat{x} + v$$

where, $\hat{}$, signifies an estimated entity and w and v are uncorrelated white noise vectors with zero mean. Detailed information for minimizing a scalar performance index as a function of the weighted norm of the state and control effort can be found in several optimization texts [3,8,10]. Minimizing the performance index leads to an optimal control law

$$u(t) = K_1(t)\hat{x}(t) \quad (1)$$

where K_1 is $r \times n$ optimal gain matrix which is found via the following relation.

$$K_1(t) = -R^{-1}(t)\hat{B}^T(t)P_1(t) \quad (2)$$

The $P_1(t)$ matrix is obtained by solving the backward matrix Riccati Equation given by

$$\dot{P}_1(t) = -P_1(t)\hat{A}(t) - \hat{A}^T(t)P_1(t) + P_1(t)\hat{B}(t)R^{-1}(t)\hat{B}^T(t)P_1(t) - Q_1(t) \quad (3)$$

where,

R_1 = constant $m \times m$ control weighting matrix

Q_1 = constant $\hat{n} \times \hat{n}$ control error weighting matrix

\hat{n} = number of estimated states

In a similar fashion, the optimal state estimate, \hat{x} , is found by solving the following equation.

$$\dot{\hat{x}} = \hat{A}\hat{x} + \hat{B}u + K_2(y - \hat{C}\hat{x}) \quad (4)$$

The optimal estimation gains, K_2 , are found via

$$K_2(t) = P_2(t)\hat{C}^T(t)R_2^{-1}(t) \quad (5)$$

and P_2 is found by solving the forward matrix Riccati equation

$$\dot{P}_2(t) = \hat{A}(t)P_2(t) + P_2(t)\hat{A}^T(t) - P_2(t)\hat{C}^T(t)R_2^{-1}(t)\hat{C}(t)P_2(t) + Q_2(t) \quad (6)$$

where,

R_2 = constant $m \times m$ measurement noise covariance matrix

Q_2 = constant $\hat{n} \times \hat{n}$ state noise covariance matrix

The matrix Riccati equations, (3) and (6), are integrated until P_1 and P_2 reach steady state values. Due to nonlinearities of these equations, it is useful to transform (3) and (6) to a set of linear equations to expedite their solutions [8].

REDUCED ORDER MODEL

Truncation of the structural modes to only those modes that must be controlled is very important in order to minimize onboard processing. However, a robust controller must include all dominant modes in its state space, otherwise instabilities may result. Truncation of an infinite set of structural modes to a reduced order model (ROM) is based upon the determination of the dominant modes which will yield maximum deflections for a given input. The following equation facilitates dominant mode identification.

$$\frac{\theta_{m,i}}{f_m} = \frac{\phi_i^2}{2\zeta_i W_{n,i}} \quad (7)$$

where,

$\theta_{m,i}$ = maximum deflection at the actuator due to the i th mode

f_m = max torque of the actuator

ϕ_i = modal admittance at the actuator of the i th mode

ζ_i = critical damping ratio for i th mode

$W_{n,i}$ = natural frequency for i th mode

Equation (7) relates maximum modal deflection for a maximum input torque. The greatest structural deflections are due to the modes with the largest modeshapes at the lowest frequencies. The first thirty modes for the structure considered are generated from a finite element computer program. The rigid body states and four out of the thirty computed modeshapes comprise the ROM. The four dominant modes and natural frequencies are

First Symmetric Bending (.0407 Hz)

First Asymmetric Bending (.0904 Hz)

Second Asymmetric Bending (.1500 Hz)

Third Asymmetric Bending (.2212 Hz)

Two additional modes are used in the truth model for spillover investigation. Their maximum deflections are at least one order of magnitude less than the four dominant modes and, therefore, not included in the ROM controller. These two uncontrolled or residual modes are

Second Symmetric Bending (.0957 Hz)

Third Symmetric Bending (.1641 Hz)

The capability of the controller to maintain attitude and modal control without knowledge of residual modes is one aspect of the robustness of the system in the presence of destabilizing factors. All structural modes respond in varying degrees to an actuating input, but, a robust controller does not excite residual modes to the point of instability. Instead, it ignores these modes allowing the structure to damp their response. To date, as many as four residual modes have been included in the true plant and results from simulations show only slight performance degradation.

CONTROLLABILITY AND OBSERVABILITY

Actuator and sensor configurations also have a large impact on the controller performance and stability. System observability and controllability must be investigated when designing any control system to insure that the controlled and estimated states adequately span the true state space. Several methods to check for system observability and controllability give go/no-go type information but do not necessarily indicate one configuration as better or worse than another. This investigation applies two different approaches to define the sensor and actuator configurations. One approach maximizes the determinant of the observability and controllability Gramian matrices as a quantitative configuration selection criteria. The other approach maximizes the real part of the eigenvalues for the closed loop estimator and controller. Both methods evaluate various number and locations of torque producing actuators and various number, location, and type of sensors.

Briefly, observability and controllability Gramian matrices are defined by the following equations [10].

$$M_o(t_o, t_f) = \int_{t_o}^{t_f} \hat{F}^T(t, t_o) \hat{C}^T(t) \hat{C}(t) \hat{F}(t, t_o) dt$$

$$M_c(t_o, t_f) = \int_{t_o}^{t_f} \hat{F}(t_f, t) \hat{B}(t) \hat{B}^T(t) \hat{F}^T(t_f, t) dt$$

Where \hat{F} is the system state transition matrix and \hat{B} and \hat{C} are time-invariant matrices defined earlier. A zero determinant is indicative of an unobservable or uncontrollable system.

Evaluation of the closed loop controller and observer eigenvalues is an alternative to the gramian matrix approach. The closed loop dynamics of each can be represented in state variable form as

$$\dot{\hat{x}} = [\hat{A} - K_2\hat{C}]\hat{x}$$

$$\dot{x} = [\hat{A} + BK_1]x$$

Maximizing the negative real parts of the eigenvalues is the configuration selection criteria which provides the most stable system possible. The eigenvalues are a direct indication of system controllability and observability. An eigenvalue with a zero or positive real part is indicative of an unstable system.

Results of the two methods correlate well which provides an easy and straight forward method for selection of actuator and sensor configurations. At this point in the design phase, the final configurations comprise the minimum amount of hardware for simplicity while assuring adequate system controllability and observability. Baseline actuator and sensor locations are shown in figure 1. The sensor and actuator complements that are used throughout the analysis portion of this study are listed in table 1.

LQG AND CLASSICAL CONTROL COMPARISON

The frequency and time responses from LQG and classical controllers will now be compared. The functional block diagram of the classical controller is shown in figure 2. This block diagram is in the form of a single input single output (SISO) system to control the center body rate and attitude. The open loop frequency responses of the classical controller are shown in figures 3 and 4. The gain plot in figure 3 clearly exhibits the low bandwidth in order avoid the first mode.

The multiple input multiple output (MIMO) frequency response of the rigid body rate and position states can be evaluated to provide a comparison of the capabilities of the two different controllers. The open and closed loop response of the LQG controller is shown in figures 5 and 6. The gain plot in figure 5 indicates a bandwidth which is almost an order of magnitude higher than that for a classical controller because of multiple leads near cross over. At structural frequencies, it is apparent that three modes are actively controlled and one mode, the second dominant mode, is notched from the controller due to that modes poor controllability and observability. One expects effects of this mode to be the most evident. Transient response, figures 7 and 8, of the center body and solar array angular position show that the LQG controller has a much faster response with a settling time less than 300 seconds while the classical controller requires more than 3000 seconds to settle. The extremely long settling time for the classical controller is indicative of it's inability to maintain precise attitude control when the spacecraft is influenced by outside disturbances such as payload or environmental torques. The quick transient response of the center body is performed at some expense of exciting the flexible modes while the classical controller accomplishes its objective since it does not excite any flexible modes. In fact, the difficult second dominant mode is the cause of the LQG controller oscillations beyond 200 seconds. Controllability and observability

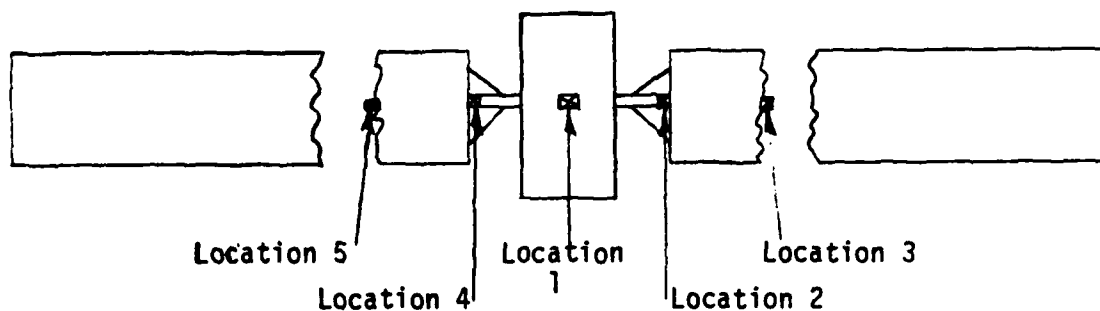


FIGURE 1. ACTUATOR AND SENSOR LOCATIONS

ELEMENT	LOCATION	TYPE
Actuator	1	Torque producing
Actuator	2	Torque producing
Actuator	4	Torque producing
Sensor	1	Angular rate
Sensor	1	Angular position
Sensor	2	Relative angular position (1)
Sensor	3	Relative angular position
Sensor	4	Relative angular position
Sensor	5	Relative angular position

Table 1. ACTUATOR AND SENSOR COMPLEMENT

Note 1. A relative position sensor measures local angular deflections relative to the center body.

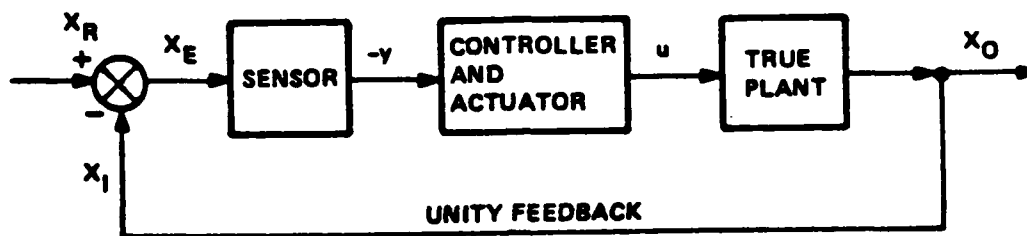


FIGURE 2. CLOSED LOOP SISO SYSTEM

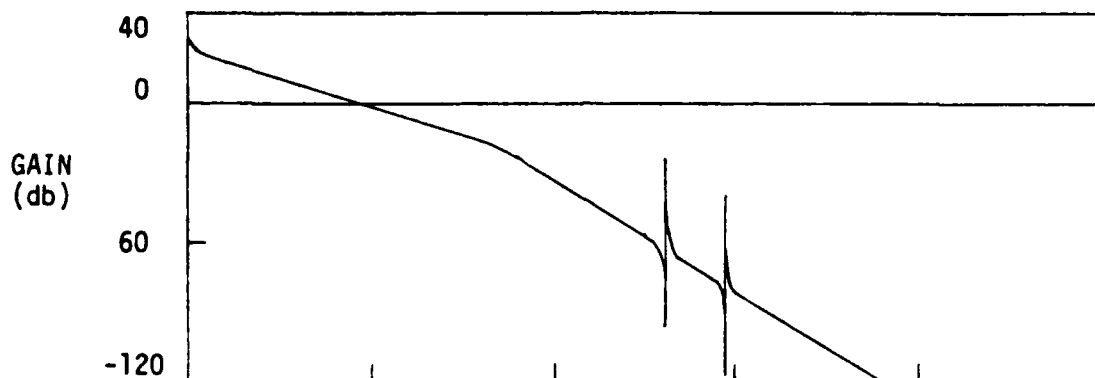


FIGURE 3. CLASSICAL CONTROLLER (OPEN LOOP GAIN)

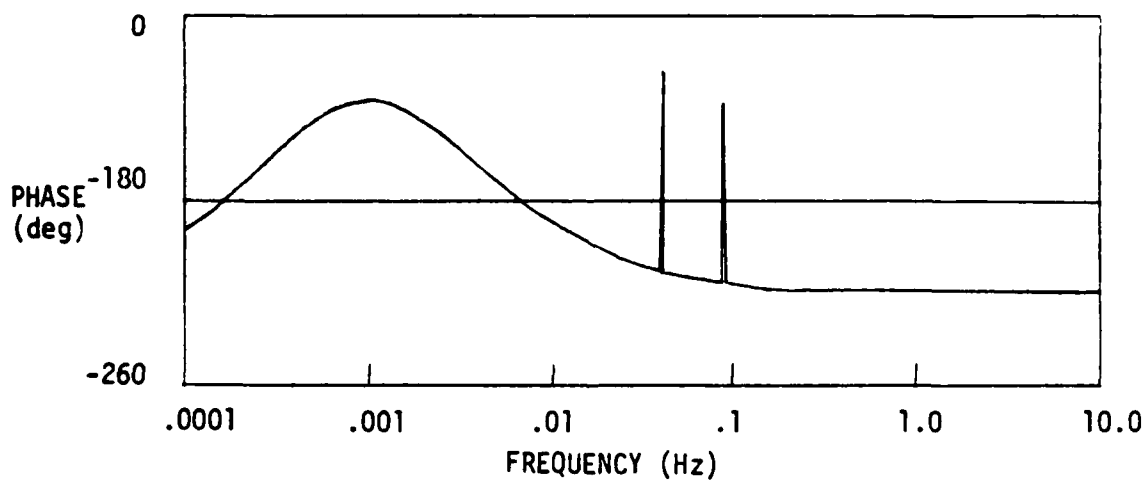


FIGURE 4. CLASSICAL CONTROLLER (OPEN LOOP PHASE)

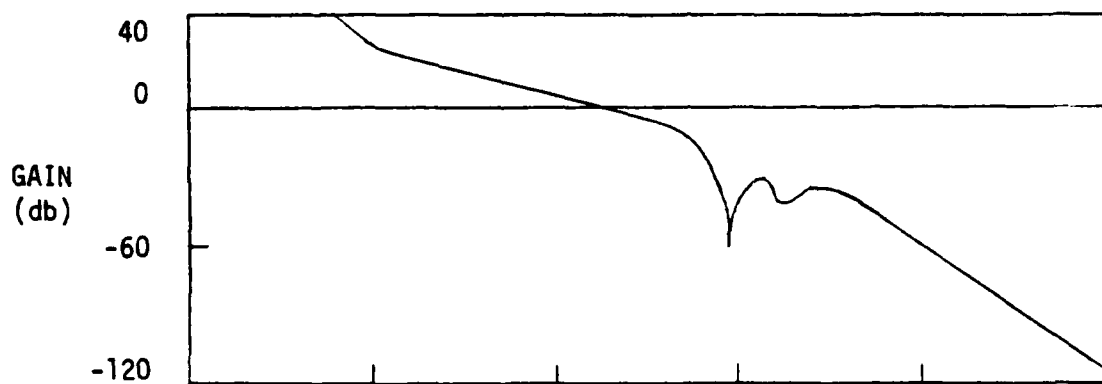


FIGURE 5. LQG CONTROLLER (OPEN LOOP GAIN)

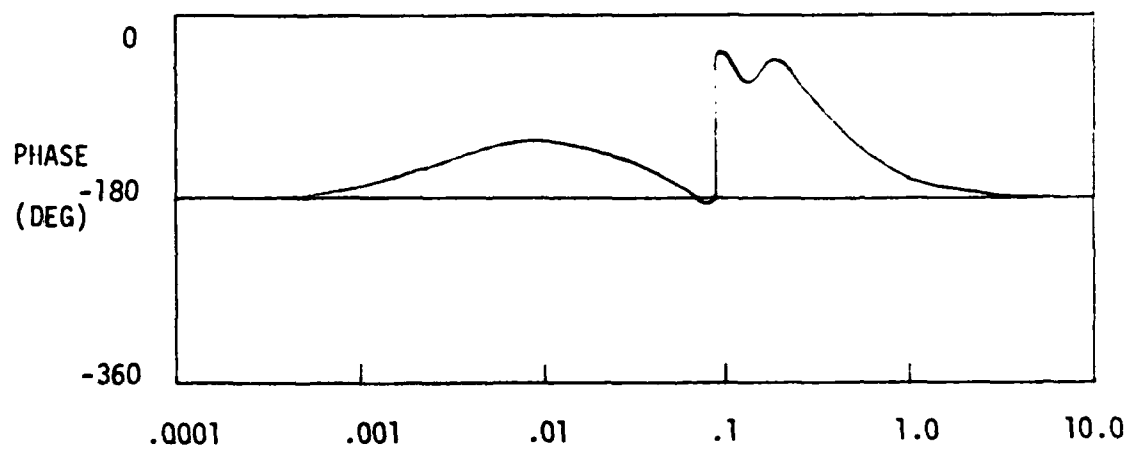


FIGURE 6. LQG CONTROLLER (OPEN LOOP PHASE)

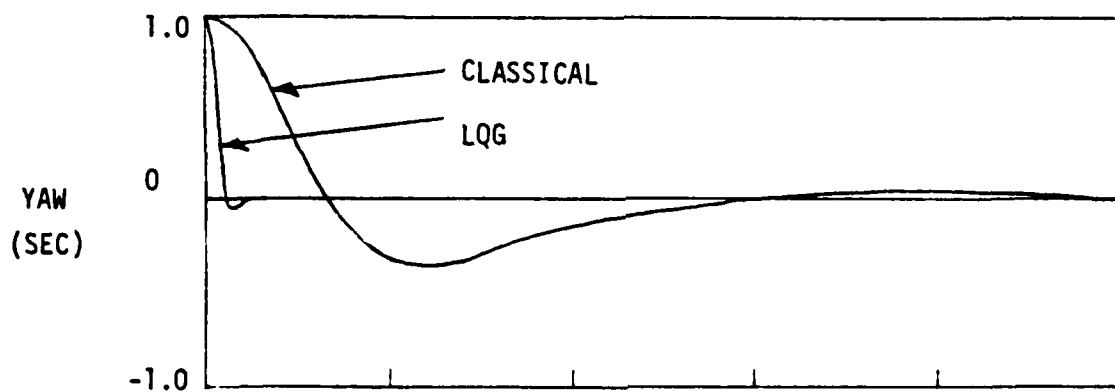


FIGURE 7. CENTER BODY TRANSIENT RESPONSE

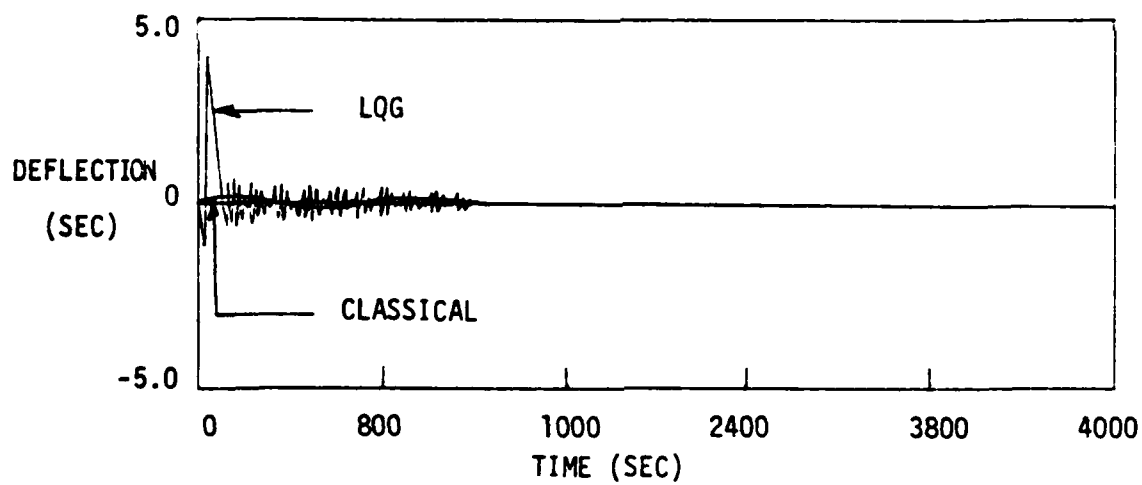


FIGURE 8. SOLAR ARRAY TRANSIENT RESPONSES

of this mode can be increased by adding, or to some degree relocating, sensors and actuators. Instead of increasing the complexity of the control system, we first investigate the advantages of adding passive damping in order to damp the second dominant mode.

EFFECTS OF PASSIVE DAMPING

The LQG controller gains are based on a very small damping ratio, 0.0005, for all flexible modes. This overly conservative and simplistic approach is taken to observe the capabilities of an LQG controller when, essentially, all damping had to be provided by the control system. Realistically, damping ratios will vary and are expected to be an order of magnitude greater which should make the controller design somewhat more stable than shown in these analyses. Indeed, this assertion is graphically depicted by figure 9. Stability of the controller increases with larger values for the damping ratio. The real part of the eigenvalue associated with the second dominant mode is a direct measure of stability and can be thought of as the effective system damping for that mode due to combined structure and controller damping. Transient response simulations, figure 10, also indicate a more stable system as the damping ratio is increased. However, increased damping reaches a point of diminishing return. Increased active modal control derived from damping ratios greater than .05 will require controller gain recalculation. So, it appears that active and passive damping trades can be made with performance and stability margins. This type of trade-off is certainly not new to system designers and it is encouraging to be able to quantify such trades in modern control theory applications.

FREQUENCY DOMAIN ANALYSES

Assuming the synthesis of an LQG controller leads to an acceptable system, a designer must then acquire control system margin and sensitivity information. Many studies during the last several years have shown that ROM controllers are sensitive to certain critical parameters [1]. Modelling errors of parameters such as damping ratios, modal natural frequencies, and modal admittances can invalidate whatever stability margins the designer thought existed in the approximated plant. Appropriate truncation of the distributed parameter system is also crucial to controller robustness for residual mode rejection. Further, inclusion of a particular mode in the ROM state space does not assure adequate modal control. Identifying problem modes early in the design phase is extremely useful for structure or passive damping design. All these concerns motivate development of analysis tools to show strengths and weakness of a control system design.

Most SISO controller designs rely heavily on frequency domain analysis (as well as frequency domain synthesis such as root locus [5]), but, these well known methods are currently in use only when system dynamics can be modelled in terms of scalar quantities and ordinary differential equations. A distributed parameter system with infinite modes is reduced (at some risk) to the major modes in order to simplify system dynamic models from partial to ordinary differential equations. This reduction allows the plant to be expressed as a finite MIMO system. Recent MIMO frequency response techniques draw parallels with SISO stability criteria in order to assure global stability over some

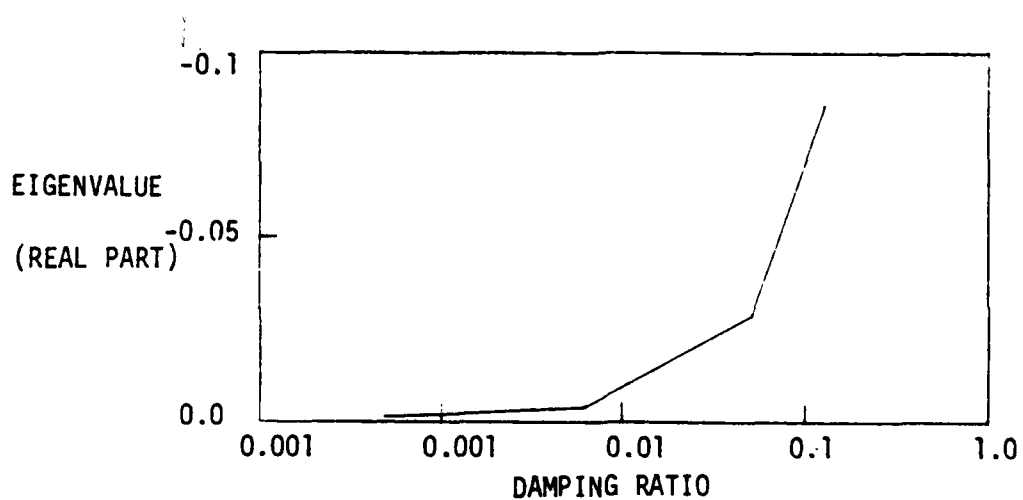


FIGURE 9. SECOND DOMINANT MODE STABILITY

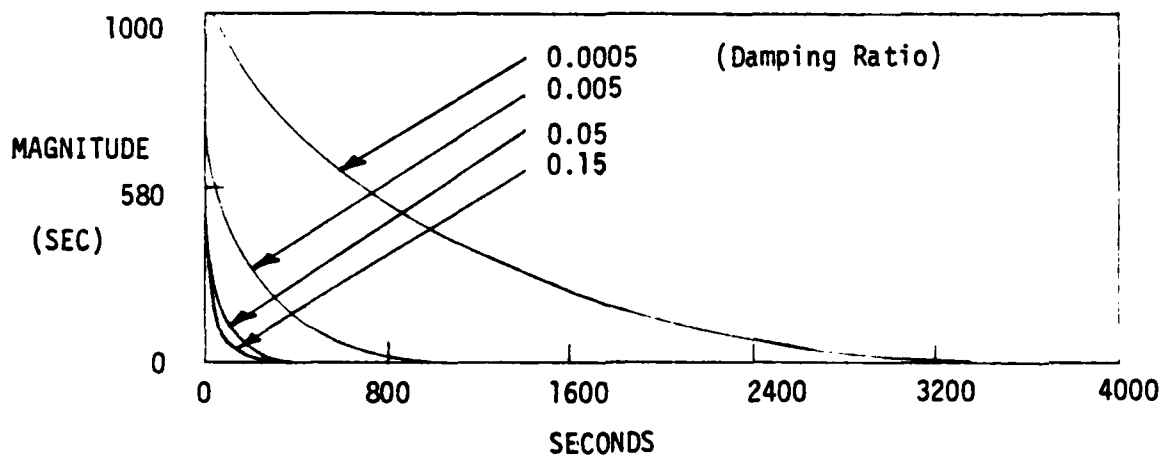


FIGURE 10. SECOND DOMINANT MODE TRANSIENT RESPONSE ENVELOPE

range of plant perturbations. Yet, these other MIMO techniques seem to give a stable/unstable indication at the system level with little insight into the stability or sensitivity of the state elements.

This paper presents results of frequency analysis methods that answer many of the stated concerns as well as provide insight into the state elements of a ROM controller. The examples highlight these capabilities and include simulation results to support frequency response predictions. One concludes that the frequency response analysis technique shown here is indeed useful and the wealth of information derived for SISO systems is applicable to MIMO systems as well.

FREQUENCY DOMAIN APPROACH

All frequency response analyses rely on development of the system transfer function. The concept of relating a systems output to the input, figure 11, is fundamental to system dynamics and feedback control. The MIMO open loop transfer function, G , is defined by

$$G = - (x_0/x_I)$$

where,

$$G = G(\hat{A}, \hat{A}, \hat{B}, \hat{B}, \hat{C}, \hat{C}, K1, K2, jw)$$

Derivation of the system open loop transfer function is a straight forward time to frequency domain transformation with appropriate substitutions using equations (1) through (4). Open loop response requires loop closure of all states except the state of interest which results in a scalar transfer function. This transfer function is used to generate familiar Bode, Nyquist, and Nichols plots or other frequency domain type graphs which have been widely used for SISO analyses. Once the open loop response is obtained, the closed loop frequency response is easily calculated from the relation

$$g_{CL} = g_{OL} / (1 + g_{OL})$$

The following examples are intended to show the validity of this approach as well as some interesting applications.

EXAMPLE: NATURAL FREQUENCY ERROR TOLERANCE

LQG derived control and estimation gains are based on critical, a priori structure parameters such as modal natural frequencies. Errors in the assumed dynamics will result in non-optimal gain calculations such that system instability will eventually result as errors become too large. Tolerances to this type of error is essential because the true plant parameters are unknown to the control systems designer. Open loop gain and phase (Bode) plots for the second dominant mode are shown in figures 12 and 13. A characteristic 180 degree phase shift coincides with the peak in gain at the modal natural frequency. It is apparent from figure 13 that the phase margin of the system may be negative at .014 Hz (i.e. an 84% error). Therefore, one expects the system to be unstable if the natural frequency of this mode was overestimated

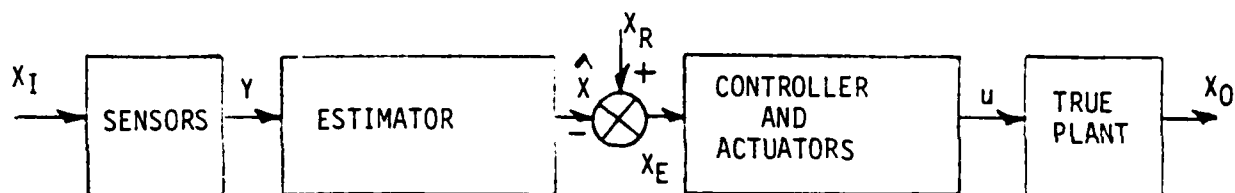


FIGURE 11. OPEN LOOP MIMO SYSTEM

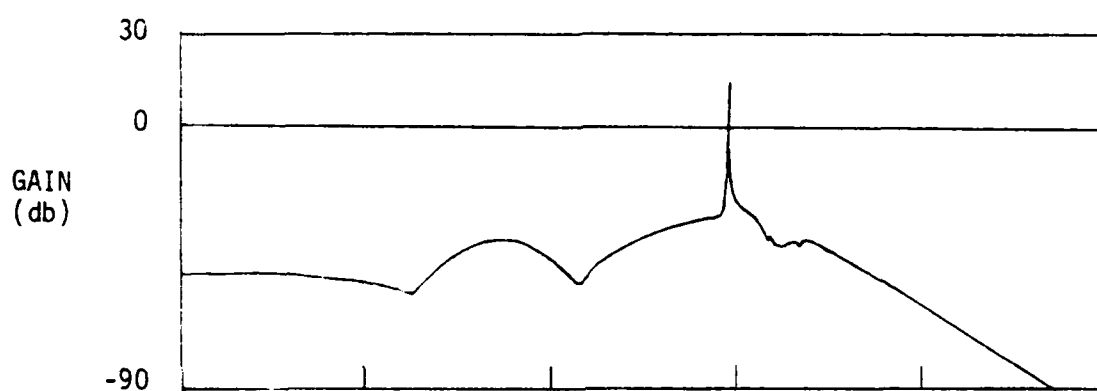


FIGURE 12. SECOND DOMINANT MODE OPEN LOOP GAIN

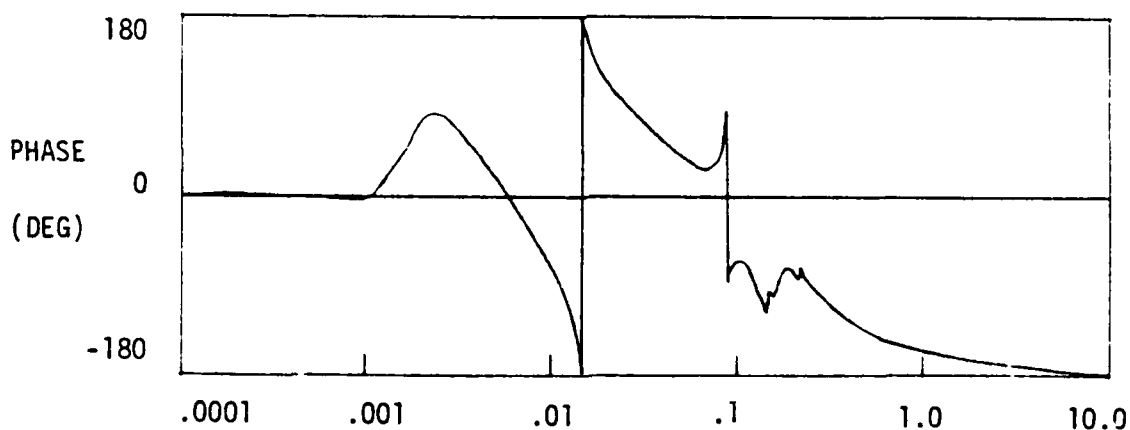


FIGURE 13. SECOND DOMINANT MODE OPEN LOOP PHASE

by some amount greater than 84%. Nyquist plots are very useful for modal analysis because of a modes characteristic circular contour when mapped onto the G plane. Nyquist stability criterion relates number of encirclements of the $-1 + j0$ point to system poles and zeroes in the right half plane. The Nyquist plot, figure 14 exhibits an encirclement of $-1 + j0$ with an 84% natural frequency error as expected from the Bode plots. Transient response simulations, figure 15, correlate very well with the Bode and Nyquist stability predictions that successful control is possible until the a priori second dominant modal frequency is overestimated approximately 84%. One should note from the Bode plots that underestimating this natural frequency will always result in a stable system due to some small amount of phase margin at higher frequencies.

EXAMPLE: MODAL ADMITTANCE ERROR TOLERANCE

Any ROM controller is susceptible to controller spillover. Two residual modes are included in the true plant for closer examination of this phenomenon. Figures 16 and 17 depict the Bode plots for the larger of these two residual modes. Closer inspection at the modal natural frequency shows a 27 DB of gain margin which at first glance appeared to be marginally stable. This is actually an indication of modal admittance error margin because the mode shape magnitude defines the height of this curve. In short,

$$\text{gain margin (DB)} = 20 \log(f(\phi^2))$$

where ϕ is the modal admittance. Working backward, one finds that 27 DB of gain margin equates to a factor of 4.73 error margin in the modal admittance values. Multiplying the admittances by 4.73 raises the gain curve so that the system is marginally stable due to zero gain and phase margins. Multiplying by a factor greater than 4.73 results in negative gain margin thus predicting system instability. Transient response simulations, figure 18, support the frequency response predictions.

CONCLUSIONS

The control synthesis and analysis techniques presented here will supplement other MIMO control system approaches to provide important capabilities for LSS control design. The performance advantages of LQG controllers for LSS are readily apparent. Precision pointing and quick transient response are very desirable attributes that an LQG controller can provide even with negligible structural damping.

However, to say the LQG controller can "do it all" oversimplifies the LQG controller synthesis problem. Constraints on number, location, and, accuracy of the actuators and sensors as well as onboard computational resource limitations will have to be considered early in the design. The designer may not have the desired flexibility in order to actively control all dominant modes. The inability to control the second dominant mode is a case in point. Simulations show that the center body can maintain precise pointing in spite of continued oscillation of the second dominant mode. This condition may be acceptable from a control system point of view, however, concerns with component or structure fatigue could render this design unacceptable thus

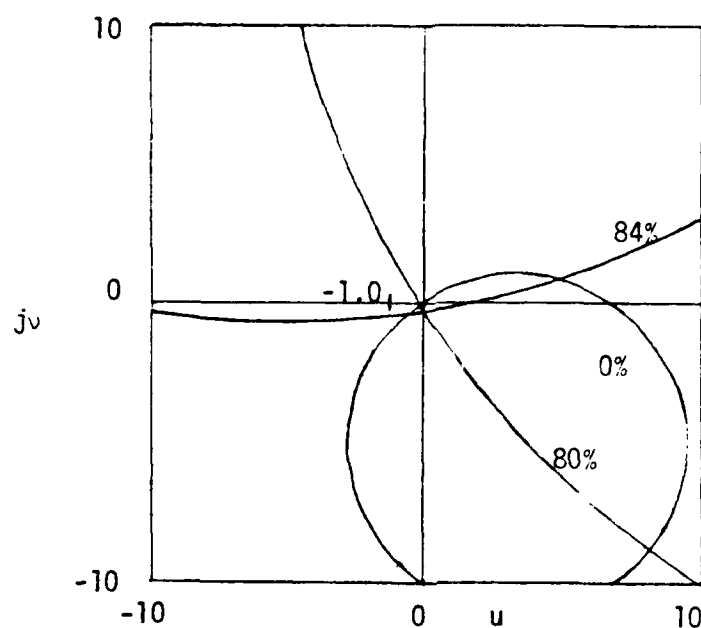


FIGURE 14. NYQUIST

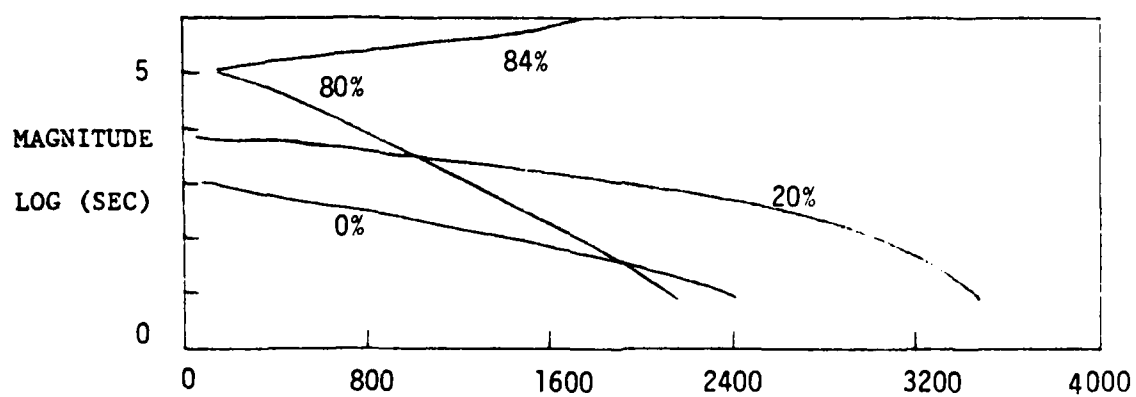


FIGURE 15. SECOND DOMINANT MODE TRANSIENT RESPONSE ENVELOPES

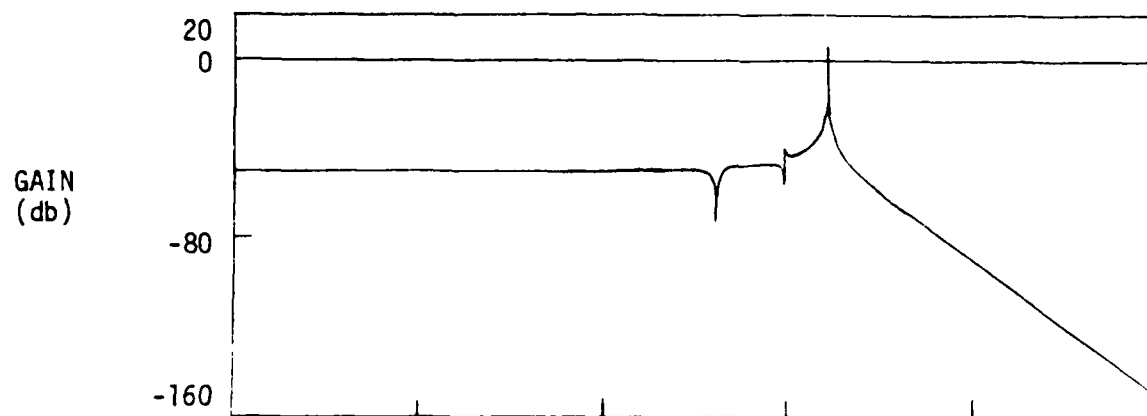


FIGURE 16. RESIDUAL MODE (OPEN LOOP GAIN)

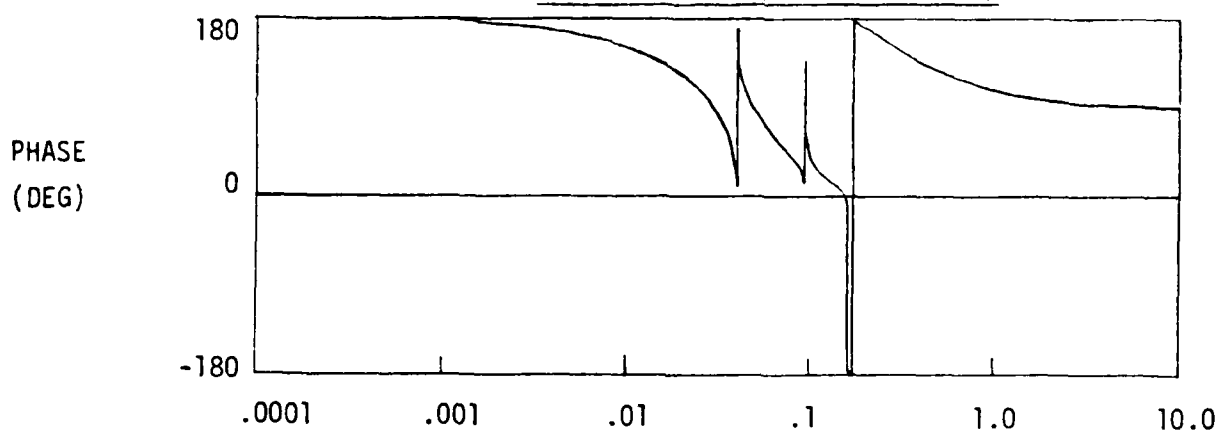


FIGURE 17. RESIDUAL MODE (OPEN LOOP PHASE)

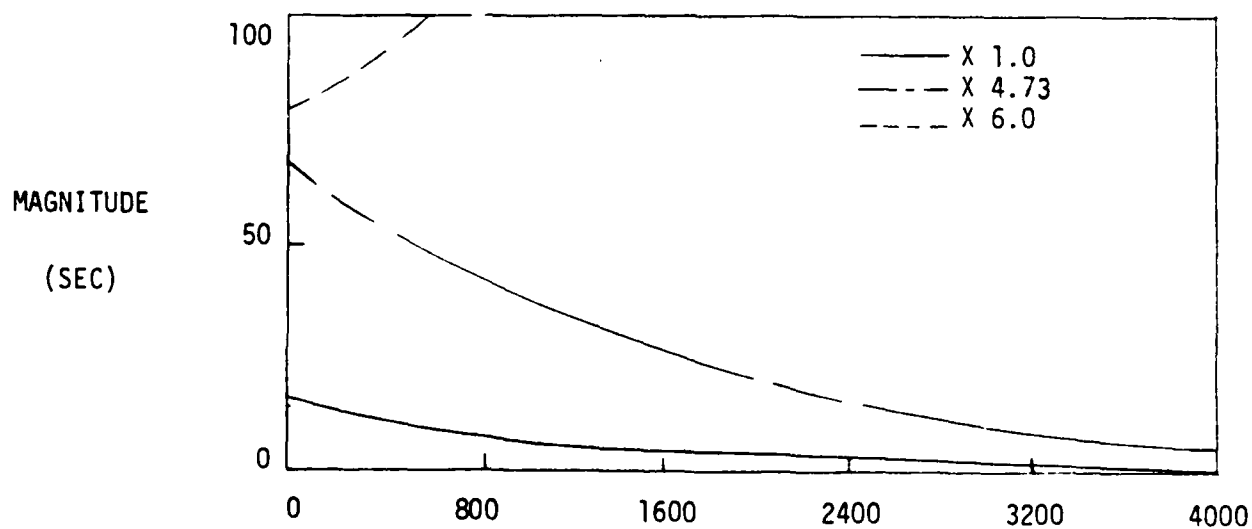


FIGURE 18. RESIDUAL MODE TRANSIENT RESPONSE ENVELOPE

establishing a requirement for passive damping in lieu of additional actuators and sensors for greater active control. Passive damping can also increase stability margins so that performance enhancements are possible.

System design trades to optimize cost, performance, and reliability as a combination of active and passive damping will require more detailed investigation as spacecraft requirements become identified. Development and further refinement of frequency response analyses such as the technique presented in this paper will become the tools to perform system trades necessary for successful LSS control system design.

References

1. Balas, M.J., "Trends in Large Space Structure Control Theory: Fondest Hopes, Wildest Dreams", IEEE Transactions on Automatic Control, Vol. AC-27, No. 3, June 1982.
2. Benhabib, R., et al, "Stability of Large Space Structure Control Systems Using Positivity Concepts", J. Guidance and Control, Vol. 4, No. 5, Sep.-Oct. 1981.
3. Bryson and Ho, "Applied Optimal Control", Blaisdell Publishing Co., 1969.
4. Chan, S. and Athans, M., "Applications of Robustness Theory to Power System Models", IEEE Transactions on Automatic Control, Vol. 29, No. 1, Jan. 1984.
5. Dazzo and Houpsis, "Linear Control Systems Analysis and Design", McGraw Hill Inc., 1975.
6. DeCarlo, R., et al, "Multivariable Nyquist Theory", Int. Journal of Control, Vol. 25, No. 5, 1977.
7. Frame, J. and Garrett, S., "Robust Control: An Overview", IEEE Conference, CH1749-1/82.
8. Gelb, A. (Editor), "Applied Optimal Estimation", M.I.T. Press, 1974.
9. Postlewaite, I., et al, "Principal Gains and Principal Phases in the Analysis of Linear Multivariable Feedback Systems", IEEE Transactions Automatic Control, Vol. 26, No. 1, Feb. 1981.
10. Sage, A.P. and White, C.C., "Optimum Systems Control", 2nd Edition, Prentice-Hall Inc., 1977.

PASSIVELY DAMPED JOINTS FOR ADVANCED SPACE STRUCTURES

Richard W. Trudell
Principal Engineer/Scientist
McDonnell Douglas Astronautics Company
Huntington Beach, California

Lawrence Rehfield
Professor of Aerospace Engineering
Georgia Institute of Technology
Atlanta, Georgia

Ambur Reddy
Senior Research Engineer
Georgia Institute of Technology
Atlanta, Georgia

Jacky Prucz
Graduate Research Assistant
Georgia Institute of Technology
Atlanta, Georgia

and

James Peebles
Engineer/Scientist Specialist
McDonnell Douglas Astronautics Company
Huntington Beach, California

PASSIVELY DAMPED JOINTS FOR ADVANCED SPACE STRUCTURES

Richard W. Trudell (1)

Lawrence Rehfield (2)

Ambur Reddy (3)

Jacky Prucz (4)

James Peebles (5)

ABSTRACT

In the past, damping treatments have been added to structures rather than designed in. This work-in-progress paper describes the benefits to be gained by designing damping into the joints of large space structures. Also, an analysis of a typical joint is developed and two new non-resonant test techniques are outlined.

The joints, as envisioned, are double-lap shear joints that dissipate energy when worked in an axial direction. To better understand the relationship between structural stiffness and structural damping as a function of important physical parameters, a one-dimensional analysis of a typical joint was developed.

Two new non-resonant forced vibration test methods (steady state and transient) have been developed that are particularly well suited for obtaining the damping characteristics of joints in large space structures. The advantage of the steady state method is that it does not require measurement of relative displacements. The transient sine-pulse approach frees the specimen from fixture/joint interaction effects. Preliminary damping and stiffness results obtained from the sine-pulse technique are provided for several aluminum test specimens.

- 1) Principal Engineer/Scientist, McDonnell Douglas Astronautics Co.
- 2) Professor of Aerospace Engineering, Georgia Institute of Technology
- 3) Senior Research Engineer, Georgia Institute of Technology
- 4) Graduate Research Assistant, Georgia Institute of Technology
- 5) Engineer/Scientist Specialist, McDonnell Douglas Astronautics Co.

INTRODUCTION

Mission requirements for future space structures dictate that many will be extremely large by today's standards. The missions for these large structures raise fundamental questions about controllability and general vibration control. Many missions require that extremely tight orientation tolerances and low vibration levels be maintained. A key element of any vibration control approach is passive damping. The enhancement of structural damping causes several favorable synergisms such as improved vibration isolator performance and more robust control systems with fewer modes to control [1]. Past practice in the damping field has been limited to add-on approaches. Numerous examples of this approach are contained in the literature in the form of case histories of constrained-layer viscoelastic damping treatments applied over large areas and viscous dampers applied to problem components. While generally successful, some penalties are usually attendant because of the add-on nature of the approach. This research is directed at methods to make the joints, which must inevitably exist in large structures, damping elements that form an integral part of the structural design. This designed-in approach provides the opportunity to minimize the penalties while maximizing the damping benefit. An example of such an approach for a space experiment platform is shown pictorially in Figure 1. In this case, a simple extensional damper in each strut of the platform truss structure constitutes a well integrated approach to damping enhancement [2].

The basis for utilization of the joints for damping is the hypothesis that a favorable tradeoff results when structural stiffness is exchanged for increased structural damping. The need to accept reduced structural stiffness arises from the requirement to make the joints somewhat flexible so that a reasonable portion of the total strain energy in the structure is resident in the joints. This strain energy is then available for dissipation in the joint materials selected expressly for this purpose. This approach seems particularly useful for increasing the damping of low loss factor structures (on the order of 0.05 or less) to the order of 0.1 as is illustrated in Figure 2. The reduction in stiffness is only on the order of 10%, which reduces the platform frequencies by only 5%.

The benefits of such a change are illustrated in Figures 3 and 4, which show the effects of a uniformly distributed damping change on transfer function magnitude and phase. The magnitude effect is the most well known because damping has been consistently applied to reduce resonant stresses and loads. The phase effect, though academically well known, has not been so widely applied.

The reduction of the rate of change of the phase versus frequency is a key element to increasing control system robustness by reducing sensitivity to plant estimation errors. Even if active control of the vibration response of large structures is not an objective, because of slew rate requirements, the control systems for large structures will inevitably have many resonant modes in the control bandwidth. The sheer size and weight of some experiment platforms, such as the example of Figures 3 and 4, generate resonances

within the control bandwidth of the experiments mounted on them. The smoother phase response of the damped structure reduces the sensitivity of both the experiment control systems and the platform control systems to plant estimation errors whether made a priori or adaptively.

In the platform case illustrated, the damping approach involved only the platform truss structure and not the payloads or solar panels. This fact violates the presumption of uniform damping in the data shown in Figures 3 and 4. The results of a non-proportional damping analysis, which accounts for the uneven distribution of dampers, are summarized in Figures 5, 6 and 7. Figure 5 shows that many modes have the low damping associated with the untreated portions of the structure, and the magnitude of the frequency response shown in Figure 6 shows some peaks that are not effectively reduced. The phase response shown in Figure 7, however, shows that the smoothing trend is well maintained with only small perturbations introduced at localized frequencies. These examples serve to show that locally placed damping in the struts of the platform truss will achieve practical and useful results.

The thrust of this research is the characterization and modeling of generic joints for the damping of structures. An example of one type of joint being studied is shown in Figure 8. This joint is a symmetric lap joint that also contains a return-to-zero feature. The damping is achieved by the shearing of the viscoelastic material that results when an axial force is applied to the joint. The unidirectional glass shown limits the maximum flexibility of the joint at elevated temperatures and also provides the return-to-zero function. Test specimens are being fabricated for evaluation of both the concept and suitable materials.

LAP JOINT ANALYSIS

An analytic model of the joint shown in Figure 8 was developed to determine the effects of important design parameters on the performance of the joint. For this analysis the important design parameters are considered to be G , n , t_0 , t_1 , l_g , l , and K as defined in Figure 9, and the performance of the joint will be evaluated in terms of its overall stiffness and damping characteristics.

The physical and analysis half models of the joint are shown in Figure 9. The joint consists of two outer adherend layers bonded to a single inner adherend via a viscoelastic adhesive. Also included are two thin layers of material bonded to the inner adherend. These two layers are very stiff in tension and are intended to alleviate creep effects by returning the inner adherend to its initial position of zero deflection.

To study the effects of particular design parameters on joint damping and stiffness, a one-dimensional analysis of a double-lap shear joint was modified to include the effect of a restoring spring acting on the inner adherend. The original analysis of the double lap joint performed by Hart-Smith [3] is a fully elastic, one-dimensional problem. The differential equation governing the shear stress distribution is shown as equation 1 in Figure 10. This equation relates the shear stress in the adherends to the shear stress in the adhesive and is obtained by combining equilibrium relationships with derivatives of the stress/strain equations 2, 3 and 4.

The basic assumption that makes this form of the equation possible is described by equation 2 and its accompanying illustration showing the elongation at the surfaces of the adhesive layer. Equation 2 states that the shear stress in the adhesive layer is linearly proportional to the strain and only varies with x . This relationship is valid when the adhesive layers are thin.

The general solution of equation 1 is prescribed as equation 5, which assumes the spatial distribution for the shear stress in terms of the unknown constants A and B. The constants A and B can be determined by evaluating the appropriate boundary conditions shown in Figure 11. Evaluating equation 6 (Figure 10) at $x = l/2$ and $x = -l/2$ yields equations 7 and 8, respectively. These two equations used in conjunction with the additional boundary condition equations 9 through 12 can be solved simultaneously to yield the six unknowns listed in Figure 12. Having now obtained explicit values for the constants A and B, a closed form expression for the shear stress distribution $\tau(x)$ is available.

The closed form expression for $\tau(x)$ can be integrated as shown in Figure 12 to yield closed form expressions for strain energy in the adhesive layer and deflection of the inner adherend. Strain energy in the adhesive serves as a measure of damping potential and deflection of the inner adherend provides a relative measure of the stiffness in the joint. A parameter study can now be conducted to determine the sensitivity of strain energy and deflection to changes in the design parameters discussed previously.

EXPERIMENTAL TECHNIQUES

The major problem related with the experimental evaluation of dynamic properties is the limited accuracy of the generated damping data. Since reasonably accurate damping information is needed for proper design of a system for vibratory loadings, many measurement techniques have been developed. The basic approaches are reviewed in References 4-8, along with discussions about the different effects that may degrade the accuracy of the damping data. The main deteriorating effect seems to be the vibratory energy loss in the testing apparatus through the boundaries of the specimen.

The most popular methods for extracting the damping properties from test data rely upon modal analysis techniques [9]. All the collected data is associated with specific modes of vibration and it may be analyzed either in the time domain (transient methods) or the frequency domain (steady state methods). The modal techniques are suitable mainly for system damping characterization where the structural configuration and the real boundary conditions may be known in advance [8]. They provide both stiffness and damping properties, but are confined to linear systems and natural frequencies of vibration.

Non-resonant forced vibration techniques [4-6] seem to be more suitable than the modal methods for the experimental investigation of passively damped joints, since their results can cover a continuous frequency spectrum. The test specimen is subjected to cyclic loading at the desired frequency and the damping is measured by the amount of energy dissipated per cycle. This

can be evaluated by different ways, like direct measurement of storage and dissipation moduli, phase angle measurement between excitation and response, or measurement of the area enclosed inside the corresponding hysteresis loop. The last approach is the most common one, but it is restricted to low frequencies [10, 11]. The hysteresis loop approach also has been used for energy dissipation measurements in structural joints [12], since it can be applied to non-linear and non-homogeneous systems. The non-resonant forced vibration methods are more appropriate than the modal techniques to material damping characterization. However, since they are actually based on a load deformation measurement in a physical testing machine, the specimen-fixture interaction effects must be included properly in the analysis in order to obtain generic test data.

One of the most promising new approaches for realistic dynamic characterization of structural materials and elements is the pulse propagation technique [6]. Its main advantage lies in the possibility of eliminating the specimen-fixture interaction effects from the test data, which will improve the accuracy of damping measurements. Furthermore, general dynamic properties can be measured that characterize the test specimen alone and do not depend on the particular boundary conditions at its ends. The pulse propagation approach is particularly well suited to structural joints in large space structures, whose dynamic behavior might be better described by a traveling wave approach rather than a vibration approach.

A stress pulse is both attenuated and dispersed during its propagation through a viscoelastic medium. The dynamic properties of the medium can be deduced from the development of the propagating pulse [13, 14]. So far, this approach has been experimentally applied mostly in connection with axial excitation of long and slender rods [13-15]. In this case, it permits a complete dynamic-stiffness characterization of the test specimen, since its axial stiffness is determined by the phase velocity, whereas its damping capability is measured by the pulse attenuation.

The major drawback of the available techniques is that the stress pulse is always generated by an axial impact on one end of the specimen. These tests are confined, therefore, to extremely high loading rates and do not permit any control on the pulse frequency. Furthermore, the use of the pulse propagation approach in connection with the conventional measures of damping [5, 17] requires the modeling of the joint as a homogeneous equivalent material.

The major categories of conventional testing methods have been reviewed above in the light of their suitability to the particular requirements for passively damped joints. A conclusive comparison between these techniques is presented in Table 1, along with the new approach proposed in this paper. The comparing criteria are the basic features required from the experimental data for the development of the new joining concepts.

SIMPLIFIED STEADY STATE TECHNIQUE

A simplified steady state test technique has been developed to determine the complex modulus of viscoelastic materials at arbitrary frequencies and

displacement. As discussed previously, the complex modulus of viscoelastic materials is presently determined by existing resonant test techniques or by measurement of the hysteresis loop in a physical test machine providing force and displacement data. However, these conventional resonant and non-resonant forced vibration test methods have some significant limitations which can be overcome by this new measurement approach.

Resonant techniques provide data only at specific frequencies and, therefore, require a new test setup for each new set of frequencies desired. Conventional physical test machines provide data at arbitrary frequencies and amplitudes, but operate well only at very low frequencies. Accurate, independent measurements of both the relative displacement of the specimen ends and the applied force are required in addition to the control functions of the test machine. The test apparatus shown in Figure 13 will determine the complex modulus of the test specimen without an independent relative displacement measurement. Vectors of the applied voltage and the measured force are the only data required, thereby greatly simplifying test setup and conduct. Because the viscoelastic joints being considered for large space structures have high stiffness and, therefore, very low displacement, the lack of a requirement for measuring relative displacement is a very attractive feature of this test method.

The physical arrangement and structural schematic identifying the relevant stiffness characteristics of the test setup are shown in Figure 13. A harmonic voltage applied to the piezoelectric exciter L_1 generates a small harmonic motion at X_1 . This motion is transmitted through the test specimen resulting in measured forces at the piezoelectric load cell L_2 . As shown in Figure 14, the complex stiffness of the specimen can be calculated from the harmonic transducer inputs and outputs just described. When the specimen is much more flexible than the test apparatus, the approximate relationships on the left-hand side of Figure 14 apply. When the specimen stiffness approaches that of any other element, the exact relationships on the right-hand side must be used.

The non-resonant steady state technique, which does not require relative displacement measurements, seems to be well suited to the task of characterizing damped joints for large space structures. In the near future this approach will be applied to some representative joint specimens.

NEW SINE-PULSE TECHNIQUE

Since none of the conventional testing techniques provide a satisfactory means of acquiring the joint characteristics free of specimen-test fixture interaction effects, a new approach for measuring damping in structural joints is being developed. A sine-pulse of the desired frequency is applied at one end of the specimen and the corresponding longitudinal response is measured at two fixed locations, before and after the joint section. The damping information is extracted from the changes that occur in certain characteristics of this stress wave as a result of its passage through the joint.

The energy balance between the input and the output signals is, probably, the most suitable measure of damping in the joint. A "composite loss factor" of the joint can be defined as the ratio between the energy dissipated inside the joint over a certain period of time. This damping parameter is more general and more realistic than the conventional measures of damping, that are usually confined to one or more restrictions like specific modes of vibration, linear, single-degree-of-freedom systems, homogeneous, complex modulus materials and harmonic loading [5, 17].

Therefore, the new technique preserves the advantages of the pulse propagation approach, but it overcomes its two major restrictions, namely the very high rates of loading and the assumption of homogeneous, linear viscoelastic materials (see Table 1). The use of a sine-pulse rather than an end impact enables full control on the frequency of excitation, so that the frequency dependence of dynamic properties can be experimentally investigated. Furthermore, the longer wavelengths associated with lower frequency pulses allow the use of shorter and "less slender" specimens without introducing geometric dispersion effects. The measurement of damping directly in terms of energy balance permits a more realistic treatment of the joints as non-linear discontinuities in the way of disturbances propagation along a structure. Although the energy balance can be measured for any shape of the excitation signal and over arbitrary time intervals, its application in this program is focused on sinusoidal loading and full number of cycles.

The feasibility of the new technique has been checked through a series of preliminary tests on five different aluminum specimens:

1. Specimen A - a reference continuous beam.
2. Specimen B - a first riveted joint.
3. Specimen C - a second riveted joint, similar to the first.
4. Specimen D - Specimen B filled up with silicone rubber with a constraining steel shim.
5. Specimen E - Specimen C filled up with silicone rubber with a constraining steel shim.

A block diagram of the experimental setup is shown in Figure 15. The geometrical configuration of the specimens is given in Figure 16.

The desired excitation signal is provided by a Gated Pulse Generator, applied on the specimen by an electromagnetic shaker. The response of the specimen to each excitation pulse is picked up by two accelerometers - one just before the test joint, and the other just after it. After suitable amplification, the response signals are displayed on a digital oscilloscope that can store them on a magnetic disk or transfer them to a computer for processing and analysis. The analog oscilloscope is mainly used for real time monitoring of all the input and output signals.

For high frequency tests, the far end of the specimen may be sufficiently distanced from the second transducer to enable the recording of the entire pulse length without any interference from end reflections. At low frequencies, however, a similar approach cannot be taken considering the practical limitations and the size of the specimen, especially when the setup has to fit in an environmental chamber. A special signal analysis algorithm is being developed in order to eliminate most of the effects due to end reflections in the low-frequency tests. The algorithm is based on the assumption that, at any instant of time, the response measured by a transducer is a resultant superposition of different effects at its location.

The damping information was extracted from sine-pulse excitations after "preparatory" processing of the corresponding response signals, for removal of the end reflection effects. The damping capability of the tested joints was evaluated in terms of the energy dissipated over a time interval corresponding to the pulse length, i.e., over a full excitation cycle. The results are given in Table 2. Their trend and order of magnitude are as expected, but they seem to be more accurate at 100 Hz than at 500 Hz, especially for the second joint. The joints were manually riveted and their built-in nonuniformities and clearances caused slip and backlash effects that may have altered the results, especially for the second joint and at the higher frequency. The damping enhancement associated with the use of silicone rubber is slightly higher for the first joint (6.5 times as compared with 4.9 times for the second joint). This is probably because its initial loss factor (without VEM) is lower so that it is more sensitive to the visco-elastic treatment.

The axial stiffness of specimens A, B and C has been measured both dynamically, based on the propagation velocity of the stress pulse, and statically, by performing tension tests and linearly fitting the corresponding load versus strain data. Both the static and the dynamic methods predict similar ratios between the extensional moduli of specimens A and B, but their results are inconclusive for specimen C, perhaps because of the higher level of mechanical clearance existent in that specimen.

The sine-pulse approach proposed in this paper fulfills all the basic requirements for a reliable and realistic dynamic characterization of the new passively damped structural joints. Its application can be extended beyond the areas of space structures and structural joints, to the dynamic characterization of most kinds of structural materials and components. A preliminary application of the new technique to aluminum made joint specimens has provided promising results.

SUMMARY

A "designed-in" approach for incorporating passive damping into the joints of large space structures has been shown to be of great benefit for reducing vibratory response and making active control systems more robust. Successful application of damping material into the joints of an actual structure will depend on attaining a clear understanding of the structural characteristics of the joint and the mechanism of dissipation. Toward this end, a one-dimensional, fully elastic analysis of a double-lap shear joint has been

developed along with two new non-resonant test techniques. These two test techniques, a steady state and a transient sine-pulse approach, are particularly well suited for obtaining damping and stiffness characteristics of joints suitable for large space structure applications. Preliminary results using the sine-pulse technique on some aluminum/silicone rubber test specimens are very promising.

ACKNOWLEDGEMENTS

This research was sponsored by the AFOSR under contract F49620-83-C-0017, with Dr. Anthony Amos serving as technical monitor.

REFERENCES

1. Trudell, Curley and Rogers. Passive Damping in Large Precision Space Structures. AIAA paper 80-0677-CP, May 1980.
2. McDonnell Douglas funded work in support of NASA Science Applications Space Platform studies.
3. L. J. Hart-Smith. Adhesive-Bonded Single-Lap Joints. NASA CR-112236, January 1973.
4. Read, B. E. and G. D. Dean. The Determination of Dynamic Properties of Polymers and Composites. John Wiley and Sons, New York, 1978.
5. Plunkett, R. Measurement of Damping. Section 5, Structural Damping, J. E. Rizicka, ed. ASME Annual Meeting in Atlantic City, NJ, 1959.
6. Bert, C. W. and R. R. Clary. Evaluation of Experimental Methods for Determining Dynamic Stiffness and Damping of Composite Materials. Composite Materials: Testing and Design (3rd Conference), ASTM STP 546, 1974, pp 250-265.
7. Gibson, R. F. and R. Plunkett. Dynamic Stiffness and Damping of Fiber-Reinforced Composite Materials. The Shock and Vibration Digest, Vol. 9, No. 2, February 1977.
8. Chu, F. H. and B. P. Wang. Experimental Determination of Damping in Materials and Structures. Damping Applications for Vibration Control, P. J. Torvik, ed. ASME Winter Annual Meeting, Chicago, 1980.
9. Ramsey, K. A. Effective Measurements for Structural Dynamics Testing, Part I. Sound and Vibration, November 1975, pp 24-35.
10. Mentel, T. J. and S. H. Chi. Experimental Study of Dilatational- versus Distortional-Straining Action in Material-Damping Production. The Journal of the Acoustical Society of America, Vol. 36, No. 2, February 1964.
11. Smith, S. and R. C. Yee. A New Technique for the Characterization of Structural Materials under Dynamic Loading. AIAA Paper No. 78-510.

12. Richardson, R. S. H. and H. Nolle. Energy Dissipation in Rotary Structural Joints. *Journal of Sound and Vibration*, Vol. 54, No. 4, 1977, pp 577-588.
13. Kolsky, H. The Propagation of Stress Pulses in Viscoelastic Solids. *Philosophical Magazine*, Vol. 1, Series 8, No. 8, 1956, pp 693-710.
14. Blanc, R. H. and F. P. Champomier. A Wave-Front Method for Determining the Dynamic Properties of High Damping Materials. *Journal of Sound and Vibration*, Vol. 49, No. 1, 1976, pp 37-44.
15. Tauchert, T. R. and F. C. Moon. Propagation of Stress Waves in Fiber-Reinforced Composite Rods. *AIAA Journal*, Vol. 9, No. 8, 1971, pp 1492-1498.
16. Lifshitz, J. M. Specimen Preparation and Preliminary Results in the Study of Mechanical Properties of Fiber Reinforced Materials. AFML-TR-69-89, Part I, Air Force Materials Laboratory, Wright-Patterson Air Force Base, Ohio, 1969.
17. Bert, C. W. Material Damping: An Introductory Review of Mathematical Models, Measures and Experimental Techniques. *Journal of Sound and Vibration*, Vol. 29, No. 2, 1973, pp 129-153.

Table I. Comparative Evaluation

Testing Method	Generic Results	Interaction Effects	Non-Homogeneous Specimen	Non-linear Behavior	Continuous Frequency Range
Modal Techniques	-	-	+	-	-
Non-resonant Forced Vibration	-	-	+	+	+
Wave Propagation	+	+	-	+	-
New Sine-Pulse Approach	+	+	+	+	+

- + The method meets the corresponding requirement.
- The method does not meet the corresponding requirement.

Table 2. "Modified" Loss Factor From Preliminary Tests

Tested Specimen	First Joint		Second Joint	
	Without VEM*	With VEM*	Without VEM*	With VEM*
Frequency (Hz)	(Specimen B)	(Specimen D)	(Specimen C)	(Specimen E)
100	0.0161	0.1052	0.0275	0.1359
500	0.0276	0.5359	0.1479	0.5017

*VEM - Viscoelastic Material

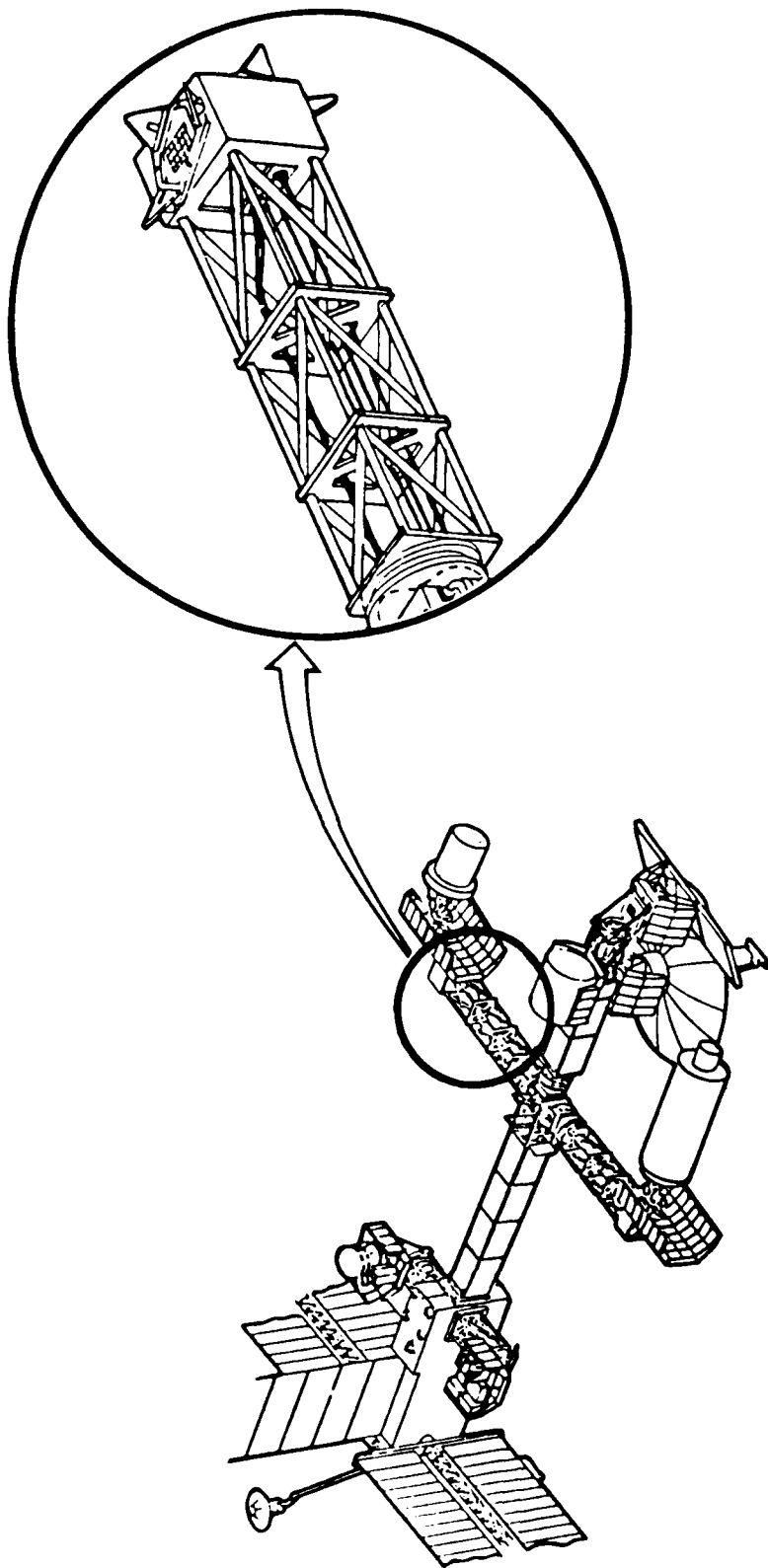


Figure 1. Viscoelastic Damper Built Into Each Strut

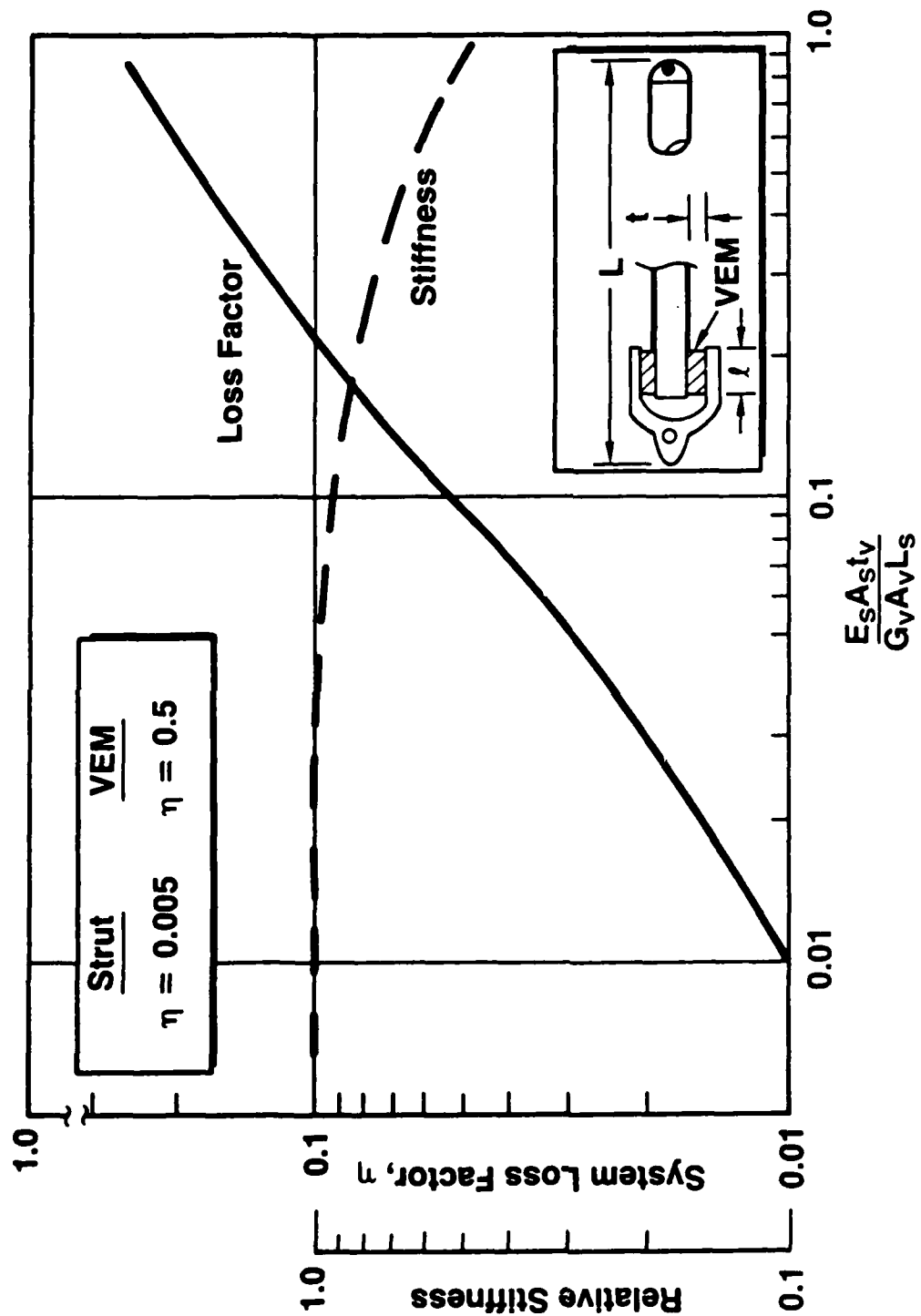


Figure 2. Viscoelastic Materials Effectiveness of Damping Treatment on Strut Extensional Damping

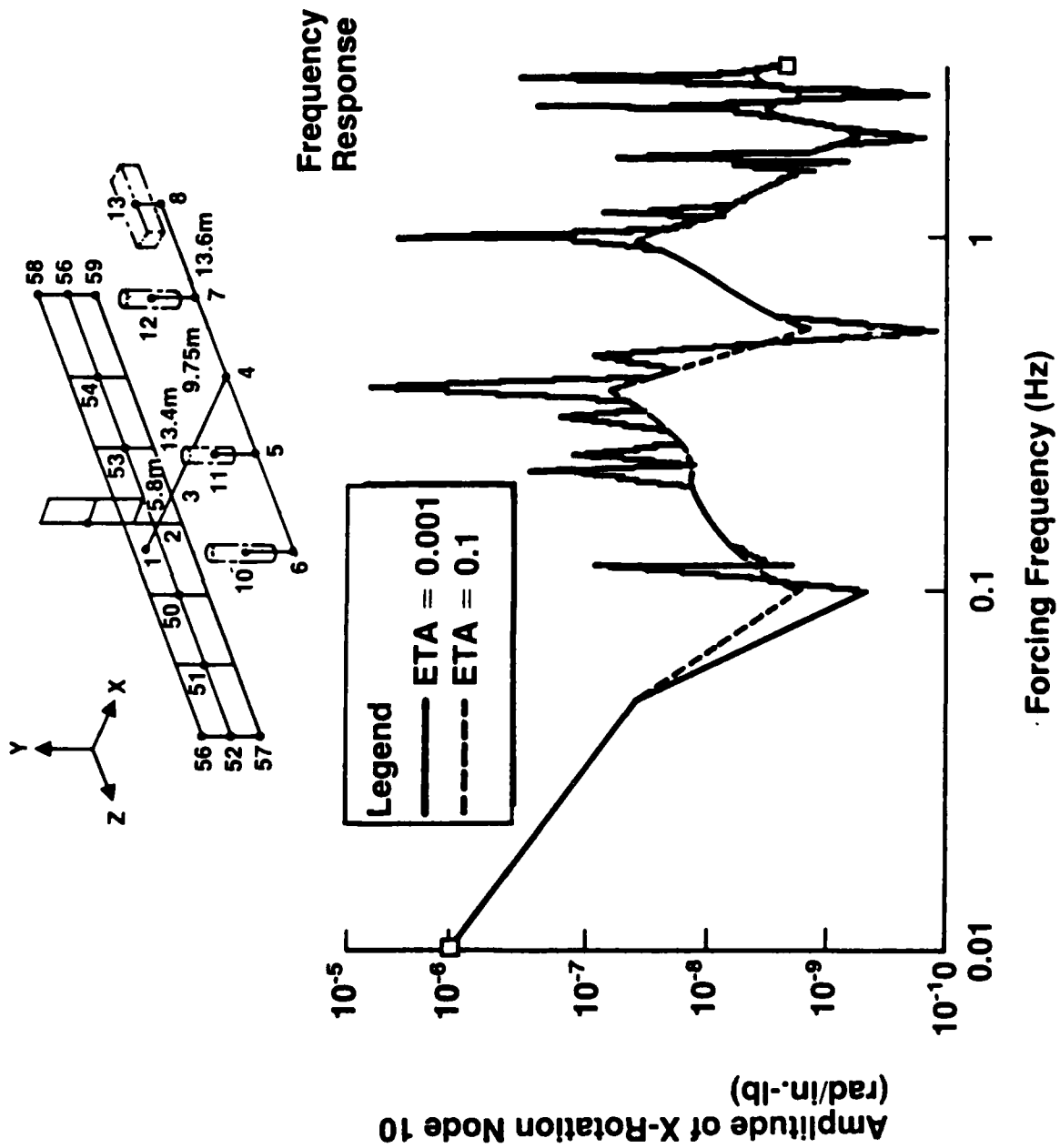


Figure 3. Long T-Bar Configuration Amplitude Response of Node 10 From a Unit Torque

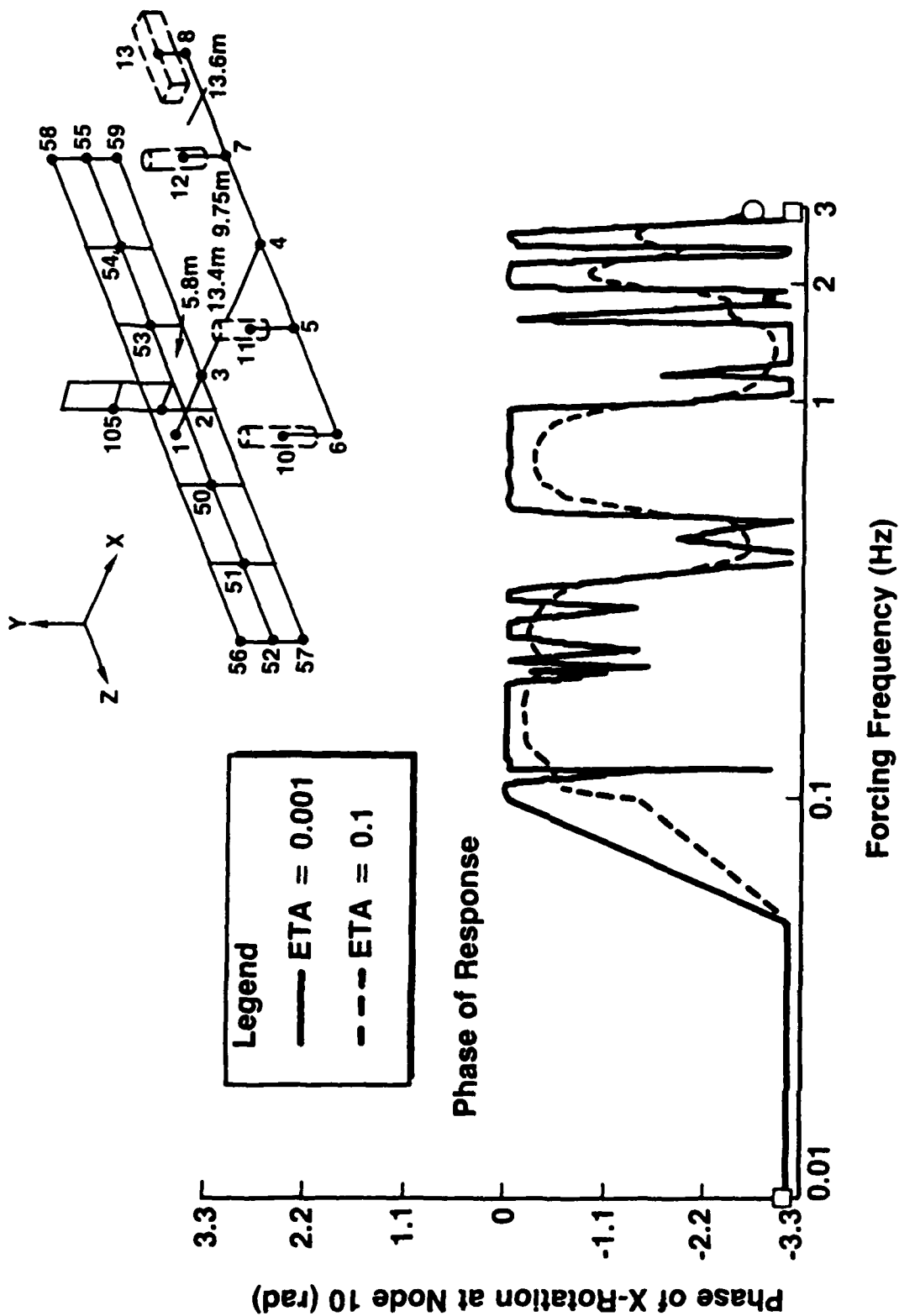


Figure 4. Long T-Bar Configuration Phase Response of Node 10 From a Unit Torque

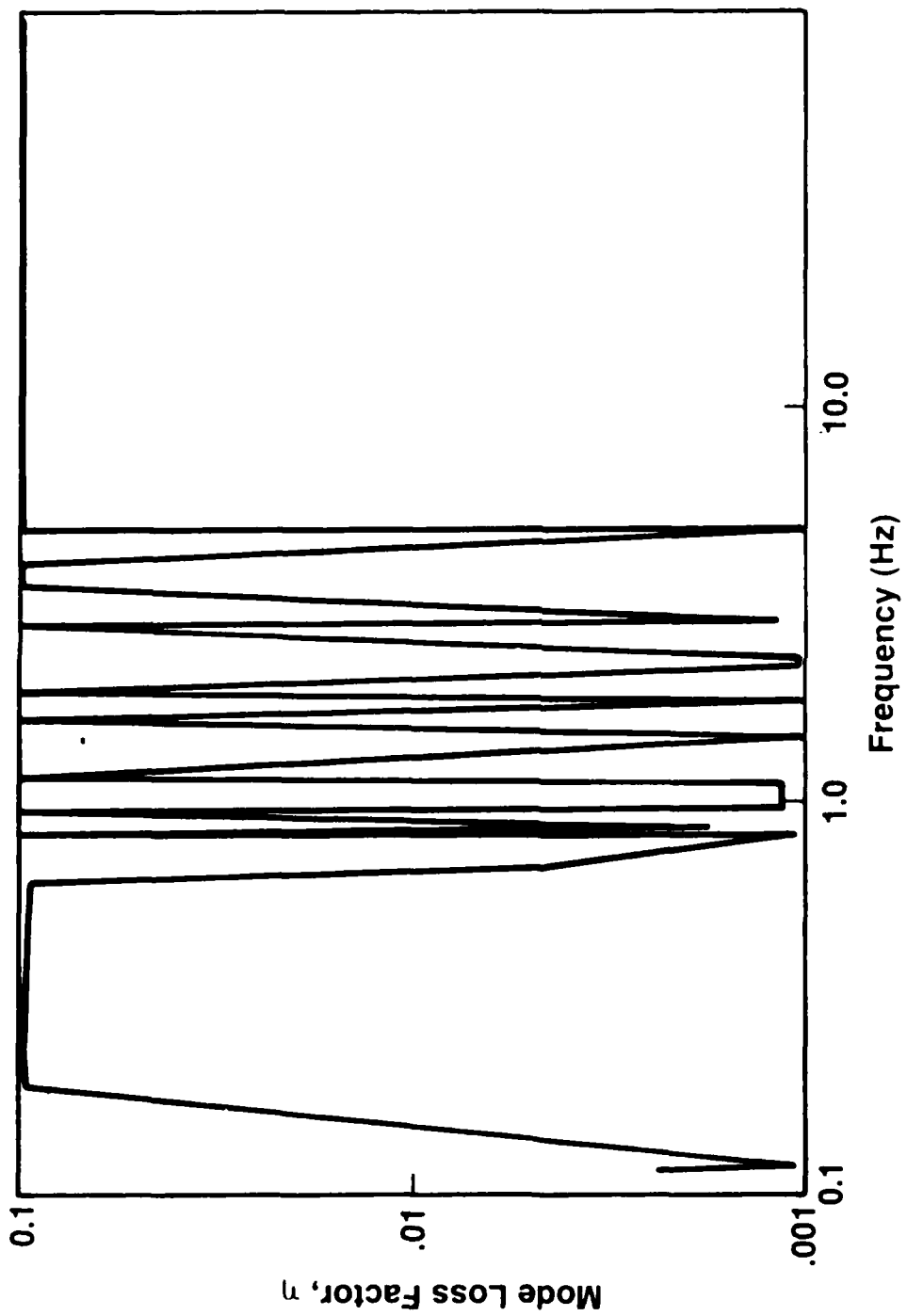


Figure 5. Effect of Truss Member Dampers on System Damping - Short T-Bar

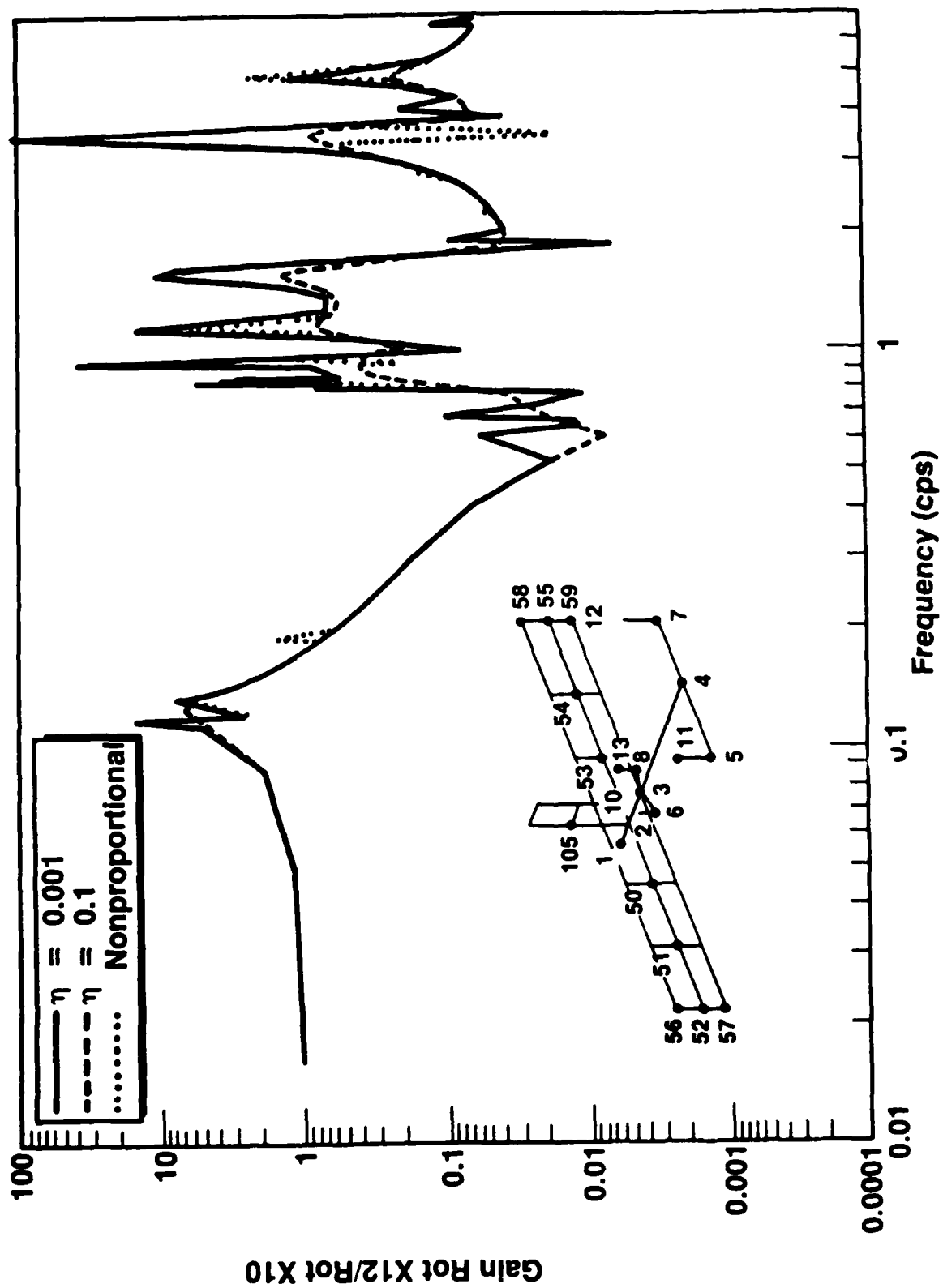


Figure 6. Short T-Bar Configuration Transfer Function ROT X12/ROT X10

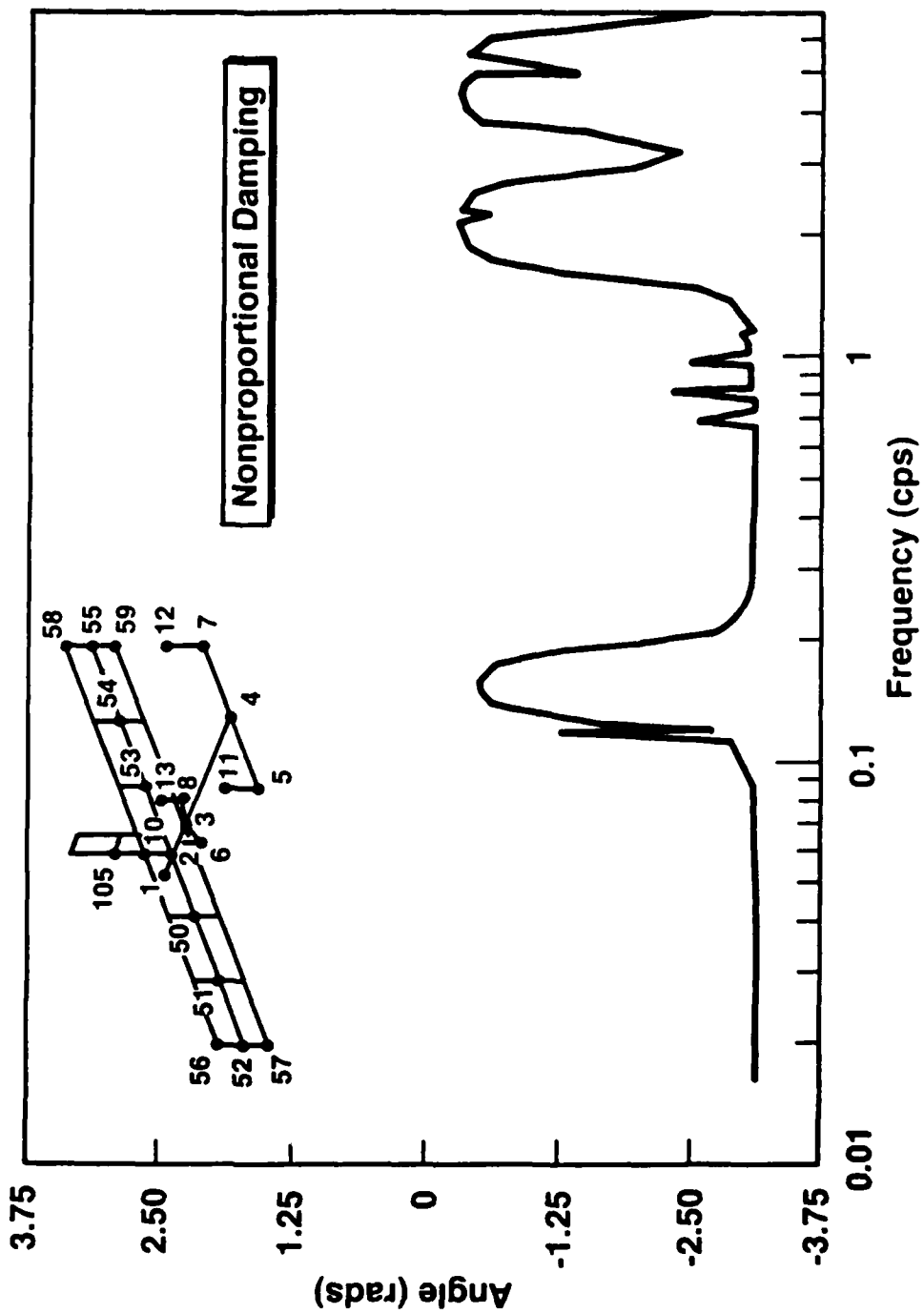
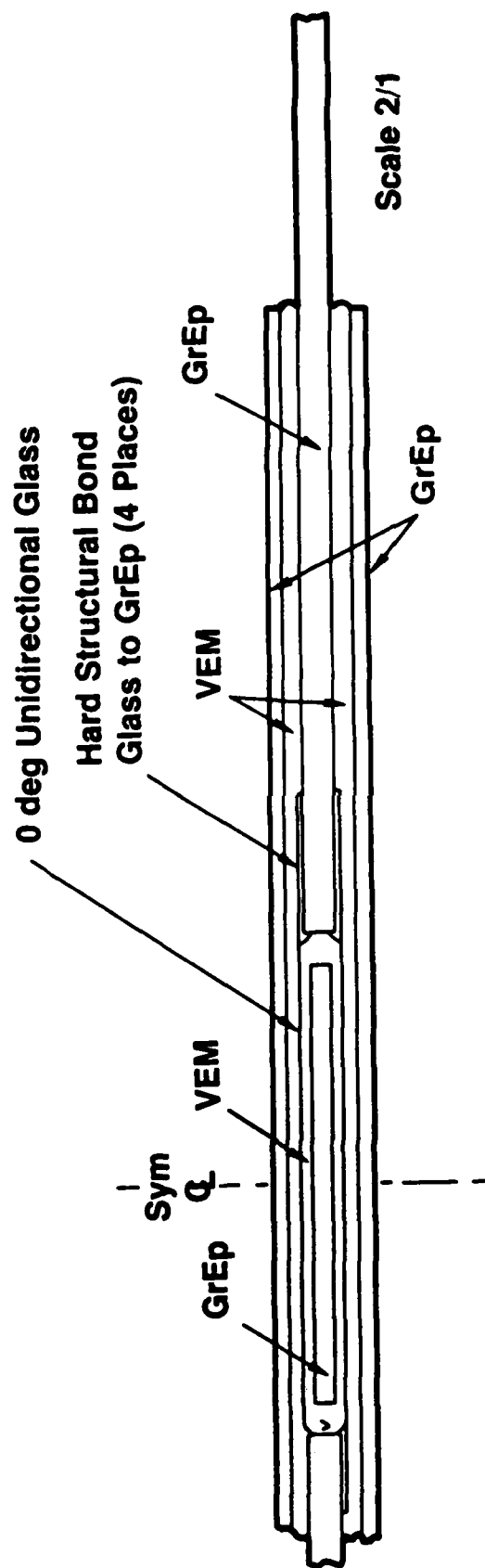


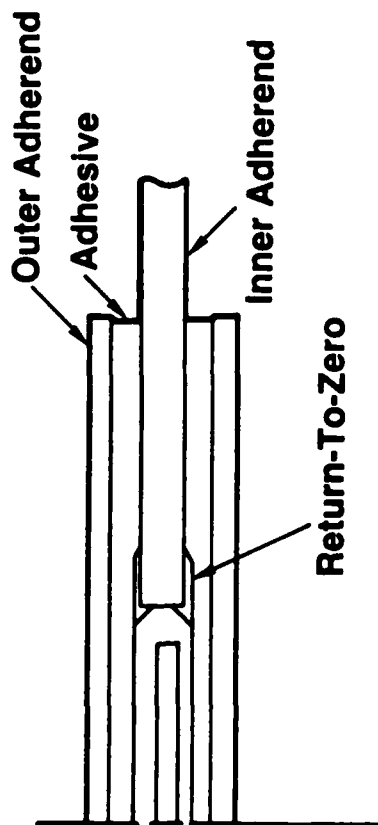
Figure 7. Short T-Bar Configuration Phase - ROT X10



DDD-21

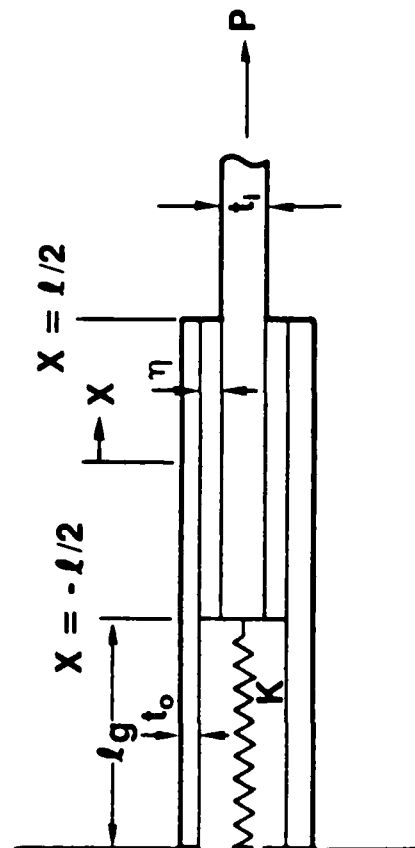
Figure 8. Structural Damping Joint Configuration

Physical Model



Sym
 ζ

Analysis Model



Structural Parameters

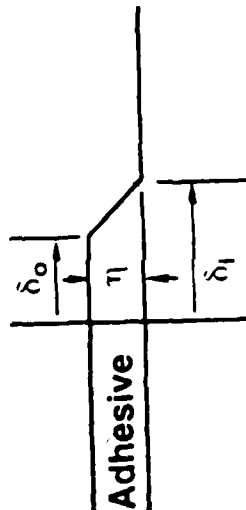
G	=	Adhesive Shear Modulus
η	=	Adhesive Layer Thickness
E_o	=	Outer Adherend Young's Modulus
E_i	=	Inner Adherend Young's Modulus
t_o	=	Outer Adherend Thickness
t_i	=	Inner Adherend Thickness
T_o	=	Force in Outer Adherend
T_i	=	Force in Inner Adherend
l_g	=	Gap Length
l	=	Overlap Length
K	=	EA_{Spring}/l_g
P	=	Applied Load

Figure 9. Lap Joint Analysis (Based on Hart-Smith Model)

Differential : $\frac{d^2 \tau}{dx^2} - \lambda^2 \tau = 0$ (1)

Where $\lambda^2 = \frac{G}{\eta} \left(\frac{1}{E_o t_o} + \frac{2}{E_i t_i} \right)$

Adhesive Stress/Strain : $\tau(x) = \frac{G}{\eta} (\delta_i(x) - \delta_o(x))$ (2)



Adherend Stress/Strain : $\frac{d\delta_o}{dx} = \frac{T_o(x)}{E_o t_o}$ $\frac{d\delta_i}{dx} = \frac{T_i(x)}{E_i t_i}$ (3),(4)

General Solution : $\tau(x) = A \sinh(\lambda x) + B \cosh(\lambda x)$ (5)

Differentiating (2) and (5) and Substituting (3), (4) Yields

$\frac{d\tau(x)}{dx} = A\lambda \cosh(\lambda x) + B\lambda \sinh(\lambda x) - \frac{G}{\eta} \left(\frac{T_i(x)}{E_i t_i} - \frac{T_o(x)}{E_o t_o} \right)$ (6)

Figure 10. Double-Lap Joint Equations

Evaluate (6) At $X = \ell/2$ and $x = -\ell/2$

$$A\lambda \cosh(\lambda \ell/2) + B\lambda \sinh(\lambda \ell/2) = \frac{G T_i(\ell/2)}{\eta E_i t_i} \quad (7)$$

$$A\lambda \cosh(-\lambda \ell/2) + B\lambda \sinh(-\lambda \ell/2) = \frac{G}{\eta} \left(\frac{T_i(-\ell/2)}{E_i t_i} - \frac{T_o(-\ell/2)}{E_o t_o} \right) \quad (8)$$

Evaluate (5) At $X = -\ell/2$

$$\tau(-\ell/2) = A \sinh(-\lambda \ell/2) + B \cosh(-\lambda \ell/2) \quad (9)$$

Integrate (3), Substitute Into (2), and Evaluate At $X = -\ell/2$

$$\delta_i(-\ell/2) = \left(\frac{T_o(-\ell/2) \ell g}{E_o t_o} \right) + \left(\frac{\tau(-\ell/2) \eta}{G} \right) \quad (10)$$

Equilibrium Evaluated At $X = -\ell/2$

$$\delta_i(-\ell/2) = \frac{1}{K} (P - 2 T_o(-\ell/2)) \quad \text{Where } P = T_i(\ell/2) = 1 \text{ lb} \quad (11)$$

Spring Equation Evaluated At $X = -\ell/2$

$$T_i(-\ell/2) = K \delta_i(-\ell/2) \quad (12)$$

Figure 11. Boundary Conditions

Solving (7) \Rightarrow (12) Yields A, B, T_1 (- $\ell/2$), T_o (- $\ell/2$), τ (- $\ell/2$), δ_1 (- $\ell/2$)

Substituting A and B into (5) Yields the General Solution From Which Strain Energy and Deflection Can Be Calculated

Strain Energy In An Adhesive Layer Is

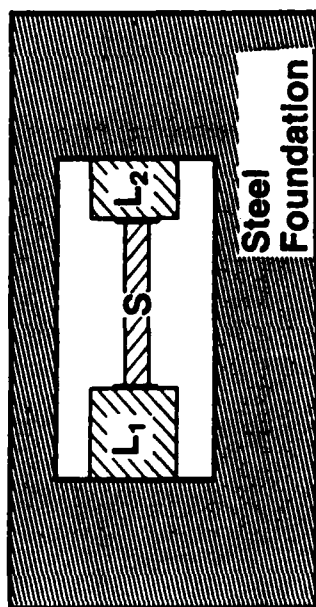
$$U = \frac{1}{2G} \int_V \tau^2 dV$$

Deflection In Inner Adherend At $X = \ell/2$ Is

$$\delta_1(\ell/2) = \delta_1(-\ell/2) + \frac{2}{E_1 t_1} \int_{-\ell/2}^{\ell/2} \tau(\vartheta) d\vartheta dx$$

Figure 12. Strain Energy and Deflection

Physical Arrangement



Structural Parameters

L_1 = Piezoelectric Exciter
 K_1 = Exciter Stiffness
 K_2 = Cell Case Stiffness
 L_2 = Piezoelectric Load Cell
 K_3 = Load Cell Stiffness
 S = Test Specimen
 K_s = Specimen Stiffness

Steel Foundation

K_4 = Foundation Stiffness
 \hat{X}_1 = Unloaded Motion Applied
 F_3 = Load Measured

Structural Schematic

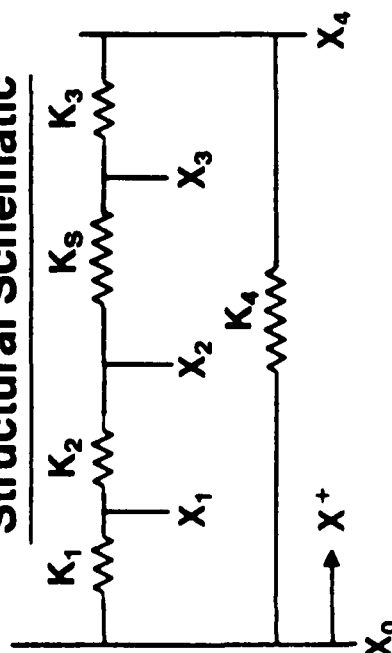


Figure 13. Steady-State Test Apparatus

The Method to Determine the Complex Stiffness from Transducer Inputs and Outputs is:

$$\hat{X}_1 = A \cos \omega t \text{ Where } A = (\mu\text{in./V}) \text{ (Volts Applied)}$$

$$F_3 = B \cos (\omega t + \theta) \text{ Where } B = (l \text{ b/V}) \text{ (Volts Output)}$$

If $k_s \ll \text{Any } k_i$, Then

$$k_s \approx F_3 / \hat{X}_1$$

If $k_s \Rightarrow \text{Any } k_i$ Then the Exact Relations Must Be Used

$$k_s \equiv \left[\frac{\hat{X}_1}{F_3} - \Delta \right]^{-1} \text{ Where } \Delta = \sum_{i=1}^4 \frac{1}{k_i}$$

$$\text{re}(k_s) \equiv \frac{\frac{B}{A} \cos \theta - \frac{B^2}{A^2} \Delta}{1 - 2\Delta \frac{B}{A} \cos \theta + \frac{B^2 \Delta^2}{A^2}}$$

$$\text{re}(k_s) \approx \frac{B}{A} \cos \theta$$

$$\text{imag}(k_s) \equiv \frac{i \frac{B}{A} \sin \theta}{1 - 2\Delta \frac{B}{A} \cos \theta + \frac{B^2 \Delta^2}{A^2}}$$

$$\text{imag}(k_s) \approx \frac{B}{A} \sin \theta$$

$$\eta k_s \equiv \frac{\text{imag}(k_s)}{\text{re}(k_s)}$$

$$\eta k_s \approx \tan \theta$$

Figure 14. Steady-State Equations

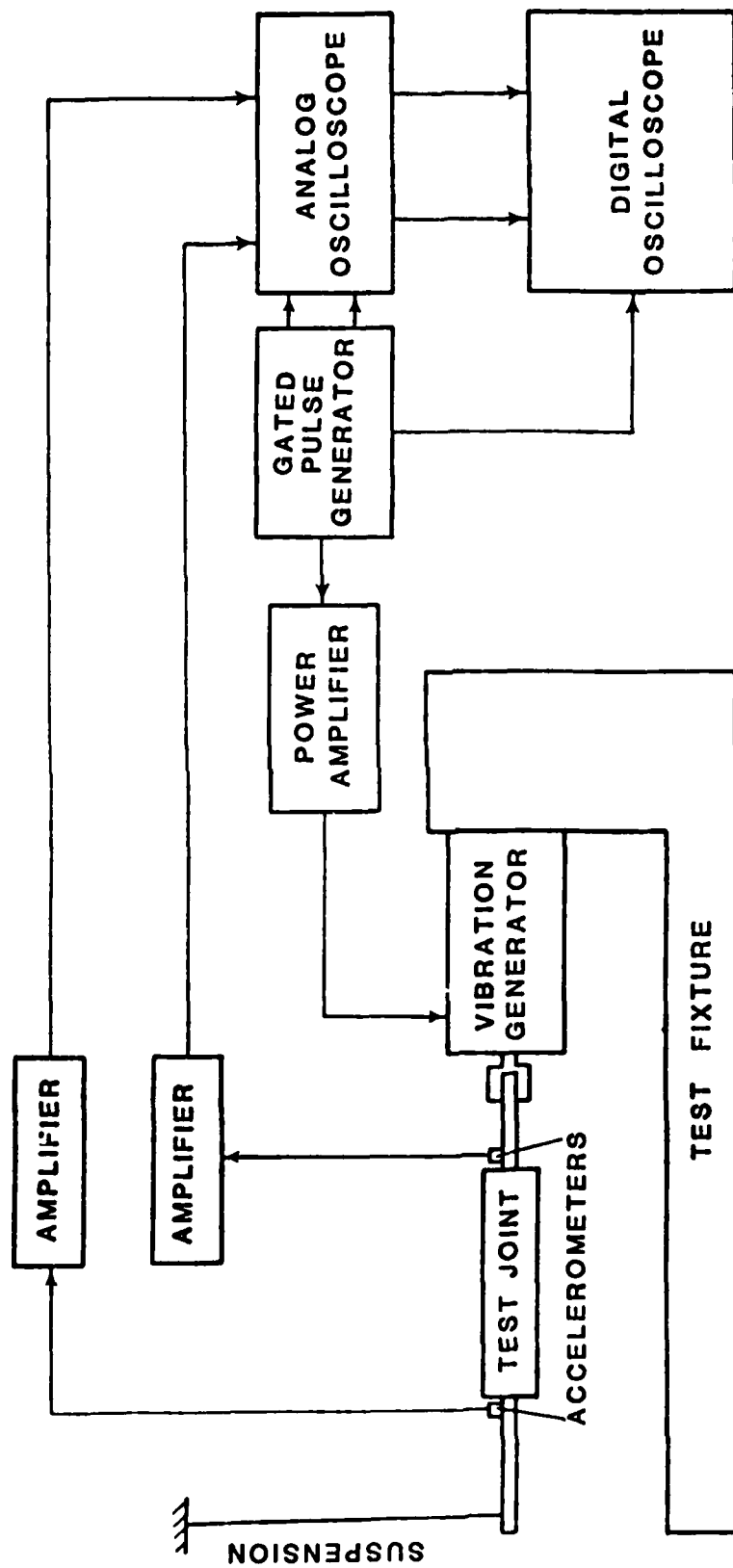
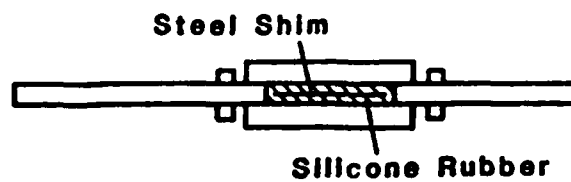
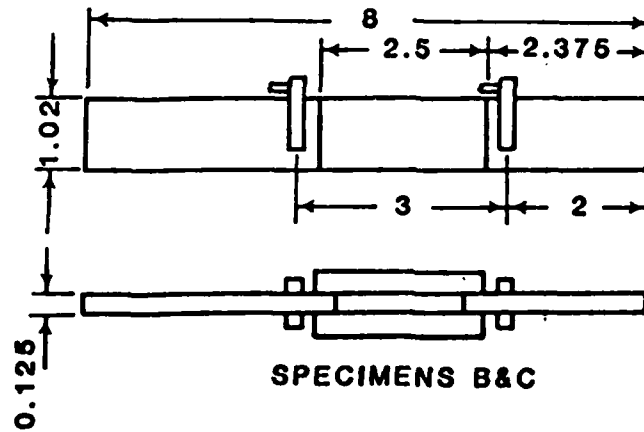
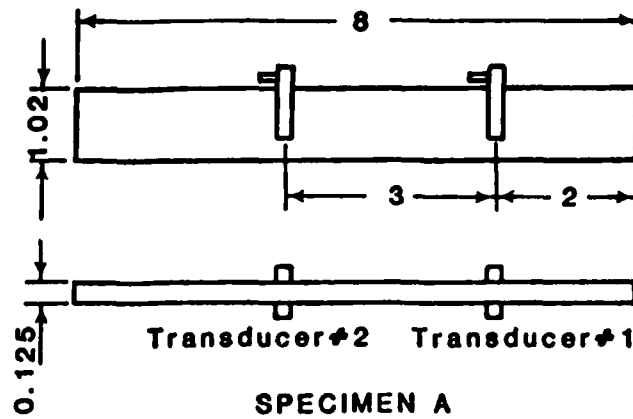


Figure 15. Experimental Setup



(Dimensions in inches)

Figure 16. Specimens with Mounted Transducers for Preliminary Tests

PASSIVE AND ACTIVE CONTROL OF SPACE STRUCTURES (PACOSS)

Charles W. White
Martin Marietta Denver Aerospace
Denver, Colorado

PASSIVE AND ACTIVE CONTROL OF SPACE STRUCTURES (PACOSS)

Charles W. White
Martin Marietta Denver Aerospace

An early objective of the PACOSS program was to experimentally verify that substantial passive damping was practical in test articles generically representative of large space structure in arrangement, dimensional size, and frequency range. Two 60-foot, truss-type test articles were designed, fabricated, and tested (see Figure). For one Large Generic Test Article (LGTA) in one plane, the diagonal members are Lexan; in the other plane, the five lower bays have included discrete link dampers in the diagonals. The other LGTA has only Plexiglas diagonals in one plane, and also includes the five bays of link dampers in the other plane.

The experimental results are tabulated.

	<u>Damping</u>	<u>Frequency (Hz)</u>
LEXAN		
Baseline	0.006	1.59
Discrete Dampers	0.080	1.60
PLEXIGLAS		
Baseline	0.031	1.73
Discrete Dampers	0.081	1.67

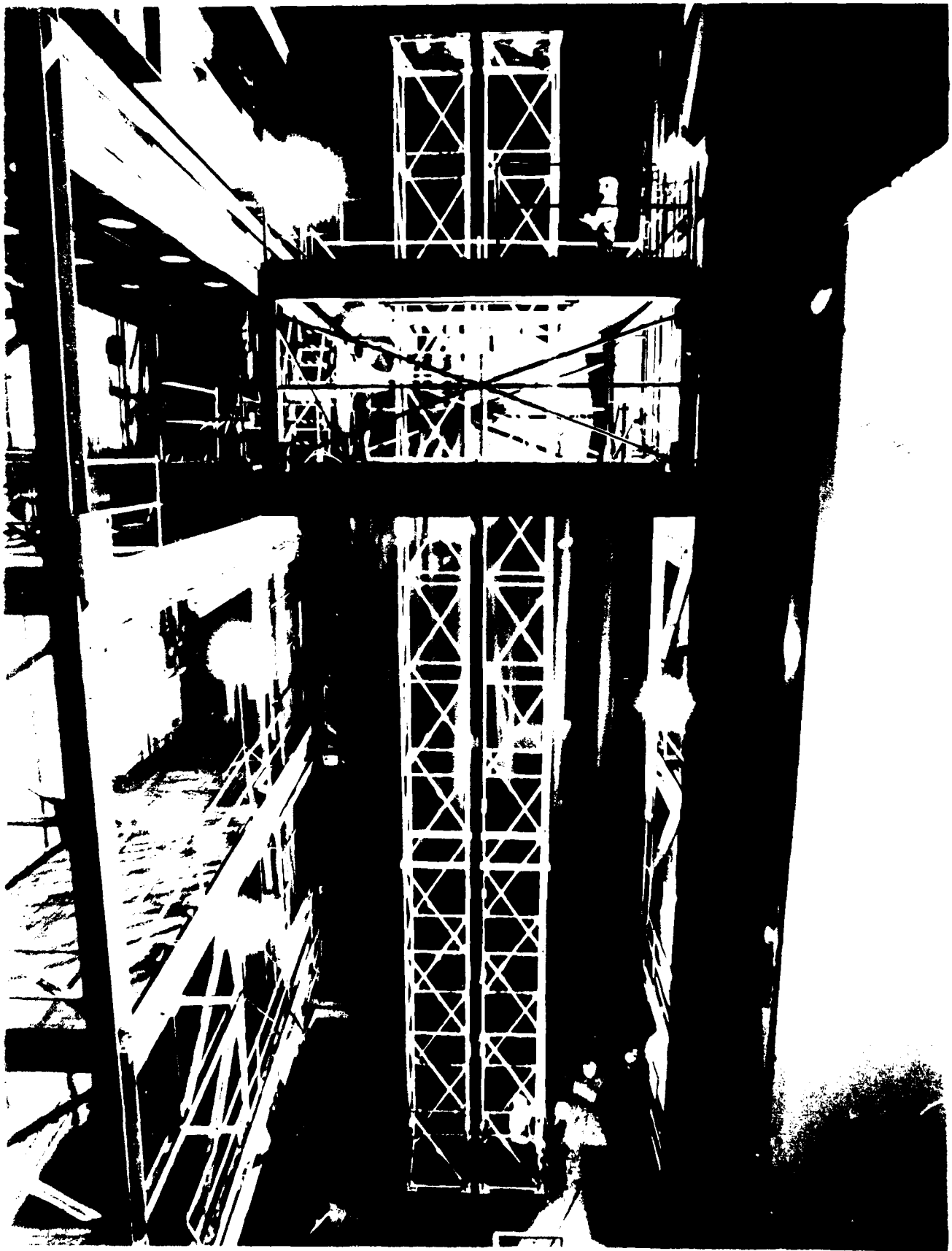


Figure 1. Large Generic Test Articles.

EFFECTS OF DISSIPATION OF ENERGY (DAMPING)
IN PARAMETRIC RESONANCE RESPONSES

R. M. Evan-Iwanowski
Syracuse University
Syracuse, New York

Paper was not presented; not available for publication.

APPENDIX 1

FINAL PROGRAM AGENDA
VIBRATION DAMPING WORKSHOP

27-29 February 1984
Hotel Queen Mary
Long Beach, California

Sponsored by
Flight Dynamics Laboratory
of the Air Force
Wright Aeronautical Laboratories

SUNDAY AFTERNOON, 26 FEBRUARY 1984

3:00 pm REGISTRATION

MONDAY MORNING, 27 FEBRUARY 1984

7:30 am REGISTRATION

9:00 am WELCOME

9:05 am OPENING REMARKS

Dr. Lynn Rogers
Flight Dynamics Laboratory of the
Air Force Wright Aeronautical
Laboratories
and
Harry Harcrow
Martin Marietta Denver Aerospace

9:15 am KEYNOTE ADDRESS

DAMPING--AN UNAPPRECIATED FACTOR FOR
DESIGN

Professor James W. Mar
Massachusetts Institute of Technology
Former Chief Scientist of the Air Force

SESSION I MATERIAL PROPERTIES

Chairman Dr. J. P. Henderson
Materials Laboratory of the
Air Force Wright Aeronautical Laboratories

Co-Chairman Dr. Y. P. Lu
David Taylor Naval Ship R&D Center

- 9:45 am Paper 1 - FRACTIONAL CALCULUS TO REPRESENT
COMPLEX MODULUS
 Dr. Lynn Rogers
 Flight Dynamics Laboratory of the
 Air Force Wright Aeronautical
 Laboratories
- 10:10 am COFFEE BREAK
- 10:35 am Paper 2 - COMPARISON OF DAMPING MATERIAL
PROPERTIES MEASURED BY A NUMBER OF
ORGANIZATIONS
 M. L. Parin
 Anatrol Corporation
- 11:00 am Paper 3 - INFLUENCE OF THE GEOMETRIC
STIFFNESS ON THE DETERMINATION OF THE
DYNAMIC CHARACTERISTICS OF VISCOELASTIC
MATERIAL PROPERTIES
 M. Lalanne, P. Berthier,
 J. Der Hagopian,
 and
 I. A. R. El Halawani
 Institut National Des Sciences
 Appliquees
 Lyon, France
 and
 B. Duperray
 Metravib
 Ecully, France

 Presented by Dean F. C. Nelson
 Tufts University
- 11:25 am Paper 4 - COMPLEX MODULUS BEHAVIOR OF A
VISCOELASTIC ADHESIVE MEASURED AT HARMONIC
STRAINS AS LOW AS $1E-10$
 T. J. Lagnese
 Universal Energy Systems
 and
 Dr. D. I. G. Jones
 Materials Laboratory of the
 Air Force Wright Aeronautical
 Laboratories

11:50 am Paper 5 - EXPERIMENTAL MEASUREMENT OF
MATERIAL DAMPING IN SIMULATED ZERO-G
 Captain R. L. Sheen
 Air Force Systems Command
 Ballistic Missile Office
 and
 Professor E. F. Crawley
 Massachusetts Institute of Technology

12:15 pm LUNCHEON BREAK

MONDAY AFTERNOON, 27 FEBRUARY 1984

SESSION II COULOMB FRICTION

Chairman Dr. D. I. G. Jones
 Materials Laboratory of the
 Air Force Wright Aeronautical Laboratories

1:30 pm OPENING OF SESSION

1:35 pm Paper 6 - COULOMB FRICTION APPLICATIONS
 Professor H. A. Scarton
 Rensselaer Polytechnic Institute

2:00 pm Paper 7- DAMPING APPLICATIONS IN GAS
TURBINE ENGINES
 R. L. Jay and D. W. Burns
 Allison Gas Turbine Operations
 General Motors Corporation

2:25 pm Paper 8 - CHARACTERISTICS OF DRY FRICTION
DAMPING
 Dr. A. V. Srinivasan,
 Dr. B. N. Cassenti, and D. G. Cutts
 United Technologies Research Center

2:50 pm Paper 9 - PRACTICAL ASPECTS OF DRY
FRICTION DAMPING IN TURBINES
 T. J. Oldakowski
 General Electric Company

3:15 pm COFFEE BREAK

- 3:40 pm Paper 10 - THE RELATIVE SIGNIFICANCE OF
DAMPING CONTRIBUTIONS IN TURBINE BLADES
Dr. N. F. Rieger
Stress Technology Incorporated
- 4:05 pm Paper 11 - CONCEPTS AND EFFECTS OF DAMPING
IN ISOLATORS
J. J. Kerley
NASA-Goddard
- 4:30 pm Paper 12 - FRICTION DAMPING IN JET ENGINES
AT CARNEGIE-MELLON
Dr. J. H. Griffin
Carnegie-Mellon University
- 4:55 pm Paper 13 - FRICTION STUDIES AT IMPERIAL
COLLEGE
Professor C. F. Beards
Imperial College
London, England
- 5:20 pm ADJOURNMENT OF SESSION
- 5:30 pm COCKTAIL RECEPTION

TUESDAY MORNING, 28 FEBRUARY 1984

SESSION III COMPOSITES AND MATERIAL CHARACTERIZATION

- Chairman Professor P. J. Torvik
Air Force Institute of Technology
- Co-Chairman Dr. P. M. Niskode
General Electric Company
- 8:00 am OPENING OF SESSION
- 8:05 am Paper 14 - DERIVATION OF EQUIVALENT
VISCOUS AND ELASTIC CONSTANTS FOR
VISCOELASTIC MATERIALS
S. R. Dahl and Dr. R. B. Rice
Martin Marietta Denver Aerospace

- 8:30 am Paper 15 - IMPULSE MEASUREMENT OF
COMPOSITE MATERIAL DAMPING
C. T. Sun and B. T. Lee
University of Florida
and
S. K. Chaturvedi
University of Missouri
- 8:55 am Paper 16 - IMPROVED EXTENSIONAL MODULUS
MEASUREMENTS FOR POLYMERS AND METAL MATRIX
COMPOSITES
Dr. W. M. Madigosky
Naval Surface Weapons Center
- 9:20 am Paper 17 - MATERIAL DAMPING OF
CARBON/EPOXY AND GRAPHITE/EPOXY COMPOSITES
BY MEANS OF FREE-FREE BEAM RESONANCE TESTS
Dr. D. W. Haines
Manhattan College
and
Dr. H. S. Kliger
Celanese Corporation
- 9:45 am Paper 18 - OPTIMIZATION OF DAMPING IN
FIBER REINFORCED POLYMER COMPOSITES
Professor R. F. Gibson
University of Idaho
- 10:10 am COFFEE BREAK
- 10:35 am Paper 19 - DYNAMIC MECHANICAL PROPERTIES
OF GRAPHITE/ALUMINUM WIRES AT AUDIO-
FREQUENCIES
G. F. Lee and C. W. Anderson
Naval Surface Weapons Center
- 11:00 am Paper 20 - DAMPING CHARACTERISTICS OF
FIBER REINFORCED METAL MATRIX COMPOSITES
Dr. M. S. Misra
Martin Marietta Denver Aerospace
- 11:25 am Paper 21 - DAMPING IN METAL MATRIX
COMPOSITES
Dr. G. L. Steckel
The Aerospace Corporation

11:50 am Paper 22 - DAMPING IN METAL MATRIX
COMPOSITES: MEASUREMENT AND MODELING
Dr. H. M. Ledbetter
National Bureau of Standards

12:15 pm LUNCHEON BREAK

TUESDAY AFTERNOON, 28 FEBRUARY 1984

SESSION IV ANALYSIS AND DESIGN

Chairman Dean F. C. Nelson
Tufts University

1:30 pm OPENING OF SESSION

1:35 pm Paper 23 - DAMPING MEASUREMENT BY DYNAMIC
STIFFNESS
Dr. D. I. G. Jones
Materials Laboratory of the
Air Force Wright Aeronautical
Laboratories
and
Dr. A. Muszynska
Bently Rotor Dynamics Research
Corporation

2:00 pm Paper 24 - COMPARISON OF THE MODAL DAMPING
VALUES DETERMINED BY VARIOUS MODAL TEST
TECHNIQUES ON THE GALILEO SPACECRAFT
Drs. B. K. Wada and J. C. Chen
Jet Propulsion Laboratory

2:25 pm Paper 25 - MODAL LOSS FACTORS IN
STATISTICAL ENERGY ANALYSIS
K. T. Brown
Institute of Sound and Vibration
Research
Southampton University
and
Professor B. L. Clarkson, The Principal
University College of Swansea
University of Wales

- 2:50 pm Paper 26 - STRUCTURAL DAMPING POTENTIAL OF
WAVEGUIDE ABSORBERS
Dr. E. E. Ungar and L. G. Kurzweil
Bolt Beranek and Newman
- 3:15 pm COFFEE BREAK
- 3:40 pm Paper 27 - EXTENSIONS OF THE RITZ-GALERKIN
METHOD FOR THE FORCED DAMPED VIBRATIONS OF
STRUCTURAL ELEMENTS
Professor A. W. Leissa and T. H. Young
The Ohio State University
- 4:05 pm Paper 28 - FINITE ELEMENT DESIGN OF
VISCOELASTICALLY DAMPED STRUCTURES--
METHODS
Drs. C. D. Johnson and D. A. Kienholz
CSA Engineering Incorporated
- 4:30 pm Paper 29 - FINITE ELEMENT DESIGN OF
VISCOELASTICALLY DAMPED STRUCTURES--
APPLICATIONS
Dr. D. A. Kienholz, Dr. C. D. Johnson,
E. M. Austin, and M. E. Schneider
CSA Engineering Incorporated
- 4:55 pm Paper 30 - RESULTS OF FINITE ELEMENT
ANALYSIS OF DAMPED STRUCTURE
M. F. Kluesener
University of Dayton Research Institute
- 5:20 pm ADJOURNMENT OF SESSION
- 6:00 pm HARBOR CRUISE

WEDNESDAY MORNING, 29 FEBRUARY 1984

SESSION V APPLICATIONS

Chairman Dr. J. L. Gubser
McDonnell Douglas Astronautics Company

Co-Chairman Dr. G. SenGupta
Boeing Commercial Airplane Company

8:00 am OPENING OF SESSION

8:05 am Paper 31 - SEGMENTED VISCOELASTIC
LAMINATES (CONSTRAINED LAYER TREATMENTS)
FOR DAMPING EXTENSIONAL WAVES IN PLATES
AND SHELLS
E. M. Kerwin and P. W. Smith
Bolt Beranek and Newman

8:30 am Paper 32 - DESIGN, EVALUATION, AND FIELD
QUALIFICATION OF A DAMPING SYSTEM FOR AN
AUXILIARY POWER UNIT
M. L. Drake
University of Dayton Research Institute

8:55 am Paper 33 - DAMPING APPLICATIONS IN MASS
PRODUCTION
A. D. Nashif
Anatrol Corporation

9:20 am Paper 34 - LAMINATED DAMPED FUSELAGE
STRUCTURES
R. A. Ely
LTV Vought Corporation

9:45 am Paper 35 - BEAM DAMPERS FOR SKIN VIBRATION
AND NOISE REDUCTION IN THE 747
R. N. Miles
Boeing Commercial Airplane Company

10:10 am COFFEE BREAK

10:30 am Paper 36 - INTEGRATED DAMPED FUSELAGE
STRUCTURE
Dr. L. M. Butzel
Boeing Commercial Airplane Company

10:55 am Paper 37 - DAMPING APPLICATIONS TO
SPACECRAFT
Dr. T. S. Nishimoto
Rockwell International

- 11:20 am Paper 38 - APPLICATION OF DAMPING TO
IMPROVE RELIABILITY OF IUS TYPE SATELLITE
EQUIPMENT--RELSAT PROGRAM
Dr. R. Ikegami, W. J. Walker, and
C. J. Beck
Boeing Aerospace
- 11:45 am Paper 39 - DAMPING IN SUPPORT STRUCTURES
FOR SATELLITE EQUIPMENT RELIABILITY
J. A. Staley and C. V. Stahle
General Electric Company
- 12:10 pm Paper 40 - A DESIGN GUIDE FOR DAMPING OF
AEROSPACE STRUCTURES
M. L. Drake
University of Dayton Research
Institute,
J. Soovere
Lockheed California Company,
and
V. R. Miller
Flight Dynamics Laboratory of the
Air Force Wright Aeronautical
Laboratories
- 12:35 pm LUNCHEON BREAK

WEDNESDAY AFTERNOON, 29 FEBRUARY 1984

SESSION VI VIBRATION-CONTROLS INTERACTION

- Chairman Dr. K. Soosar
The Charles Stark Draper Laboratory
- Co-Chairman Dr. S. Rubin
The Aerospace Corporation
- 1:30 pm OPENING OF SESSION
- 1:35 pm Paper 41 - DAMPED OPTICS FOR PULSED LASER
APPLICATIONS
R. G. Jaeger and M. J. Laughlin
United Technologies Research Center

- 2:00 pm Paper 42 - DISTRIBUTED PIEZOELECTRIC
POLYMER ACTIVE VIBRATION CONTROL OF A
CANTILEVER BEAM
T. Bailey and Dr. J. E. Hubbard, Jr.
Massachusetts Institute of Technology
- 2:25 pm Paper 43 - AN EXPERIMENTAL STUDY OF
PASSIVE DAMPING AND ACTIVE CONTROL OF
LARGE SPACE STRUCTURES
S. S. Simonian, C. S. Major, and
Dr. R. Gluck
TRW, Space and Technology Group
- 2:50 pm Paper 44 - SIZING OF DISCRETE VISCOUS
DAMPERS ON A FLEXIBLE BODY IN THE PRESENCE
OF A FIXED CONTROL
G. R. Rapacki and Dr. R. B. Rice
Martin Marietta Denver Aerospace
- 3:15 pm COFFEE BREAK
- 3:35 pm Paper 45 - CRITICAL DAMPING IN COMPLEX
STRUCTURES AND CONTROL SYSTEMS
Professor D. J. Inman
State University of New York at Buffalo
- 4:00 pm Paper 46 - AN APPROACH TO SIZING DISCRETE
VISCOUS STRUCTURAL DAMPERS USING AN
EXTENSION OF THE FINITE ELEMENT APPROACH
AND MODAL STRAIN ENERGY
E. C. Dalton
Teledyne-Brown
and
Dr. R. B. Rice and C. W. White
Martin Marietta Denver Aerospace
- 4:25 pm Paper 47 - FLEXIBLE STRUCTURE CONTROL
DESIGN IN THE FREQUENCY DOMAIN
R. J. Harding and Dr. A. Das
General Electric Company
- 4:50 pm Paper 48 - PASSIVELY DAMPED JOINT CONCEPTS
FOR SPACE STRUCTURES
R. W. Trudell
McDonnell Douglas Astronautics
and
Professor L. Rehfield
Georgia Institute of Technology

5:15 pm Paper 49 - PASSIVE AND ACTIVE CONTROL OF
SPACE STRUCTURE (PACOSS)
C. W. White and Dr. G. Morosow
Martin Marietta Denver Aerospace

5:40 pm CLOSING REMARKS

5:55 pm ADJOURNMENT OF MEETING

ALTERNATE PRESENTATIONS

Paper 50 - STRUCTURAL DAMPING OF SPACE
SHUTTLE ORBITER AND ASCENT VEHICLES
D. L. Jensen
Rockwell International

Paper 51 - EFFECTS OF DISSIPATION OF
ENERGY (DAMPING) IN PARAMETRIC RESONANCE
RESPONSES
R. M. Evan-Iwanowski
Syracuse University

Paper 52 - VIBRATION ISOLATION OF AN
ELEVATOR SYSTEM
Dr. H. S. Tzou
North Carolina A&T State University
and
A. J. Schiff
Purdue University

PAPER 53 - THE USE OF SKIN DAMPING
TREATMENTS TO CONTROL AIRFRAME DYNAMIC
RESPONSE
C. I. Holmer
EAR Division
Cabot Corporation

PAPER 54 - NEW PROPOSED DYNAMIC VIBRATION
ABSORBERS FOR EXCITED STRUCTURES
Prof. Dr. H. F. Bauer
Professor, Institute of Spacetechnology
University of German Armed Forces

PAPER 55 - MEASURED DAMPING OF SHUTTLE ACOUSTIC
TEST STRUCTURES

Dr. C. E. Wallace and Mark Mielke
Arizona State University
and
Jack Joanides
Rockwell International

SUPPLEMENTARY PAPER

ON VIBRATION DAMPING ANALYSIS USING THE FINITE
ELEMENT METHOD

R. A. Brockman

APPENDIX 2

LIST OF PAID REGISTRANTS

VIBRATION DAMPING WORKSHOP

27-29 February 1984
Hotel Queen Mary
Long Beach, California

Ray Adsit
H. R. Textron
2485 McCabe Way
Irvine, CA 92714

Greg C. Anderson
NASA Langley
Space Systems Division
Hampton, VA 23665

Jimmie D. Anderson
General Dynamics
Fort Worth Division
Box 741, M-2851
Fort Worth, TX 76101

Daniel R. Andre
The MacNeal-Schwendler Corp.
Marketing
815 Colorado Boulevard
Los Angeles, CA 90041

Mohan Aswani
Aerospace Corporation
Structures Department
2350 East El Segundo
El Segundo, CA 90245

Thomas Bailey
Massachusetts Institute of Technology
Mechanical Engineering (Sys. & Controls)
77 Massachusetts Avenue, Room 3-443
Cambridge, MA 02139

Mary Baker
Structural Dynamics Research Corp.
Western Operations
11055 Roselle Street
San Diego, CA 92014

Gary Balas
University of California, Irvine
Civil Engineering
Irvine, CA 92714

Wayne R. Bassett
Air Force Wright Aeronautical Labs.
Flight Dynamics Laboratory
AFWAL/FIBAA
Wright-Patterson AFB, OH 45433

Glenn D. Bates
Bolt Beranek & Newman, Inc.
1300 N. 17th Street
Arlington, VA 22209

H. P. Bausch
Wyle Laboratories
Applied Mechanics
1840 Hillside
Norco, CA 91760

Clark J. Beck
Boeing Aerospace Company
Structural Development
MS 8K-89, P.O. Box 3999
Seattle, WA 98124

Douglas E. Bernard
Stanford University
Aeronautics and Astronautics
Stanford, CA 94305

Jacobo Bielak
Carnegie-Mellon University
Civil Engineering Department
Proper Hall 123K
Pittsburgh, PA 15213

Ken D. Blakely
The MacNeal-Schwendler Corp.
815 Colorado Boulevard
Los Angeles, CA 90041

Donald A. Blessen
Newport Corporation
Structural Dynamics
18235 Mt. Baldy Circle
Fountain Valley, CA 92708

Creed E. Blevins
McDonnell-Douglas Astronautics
Nonmetallics
5301 Bolsa Avenue
Huntington Beach, CA 92647

David Brown
Wyle Laboratories
128 Maryland Street
El Segundo, CA 90245

Gerald V. Brown
NASA Lewis Research Center
Structures & Mech. Technologies Div.
21000 Brookpark Road
Cleveland, OH 44135

Kenneth T. Brown
Southampton University
Institute of Sound & Vibration Research
Highfield
Southampton, SO9 5NH, ENGLAND

Dr. Courtney B. Burroughs
Pennsylvania State University
Applied Research Laboratory
P.O. Box 30 North Atherton Street
State College, PA 16804

Dr. Leo M. Butzel
Boeing Commercial Airplane Co.
MS 73-16
P.O. Box 3707
Seattle, WA 98124

Paul E. Campos
Aerospace Corporation
Advanced Orbital Systems Div.
P. O. Box 92957, MS M6/206
Los Angeles, CA 90009

Samuel J. Caprette, Jr.
B. F. Goodrich
Aerospace and Defense Div.
500 S. Main St., D/1874, Plant 6
Akron, OH 44318

Chris Caseiro
General Dynamics Corp.
Electric Boat Div., Dept. 443
Eastern Point Road
Groton, CT 06340

A. Dorian Challoner
Hughes Aircraft Company
Space & Comm. Group, Technology Div.
P.O. Box 92919, Airport Station
Los Angeles, CA 90009

William V. Chambers
United Technologies Research Center
Research Marketing Manager
Silver Lane
East Hartford, CT 06108

James A. Chapman
Air Force Rocket Propulsion Laboratory
Interdisciplinary Space Technology
AFRPL/DYS, Stop 24
Edwards Air Force Base, CA 93523

Robert G. Cheatham
Sikorsky Aircraft
Engineering Research & Development
Stratford, CT 06611

Darryl G. Chong
IBM
General Products Division
5600 Cottle Road, H27-030
San Jose, CA 95193

John J. Cleary
Itek Corp.
1-510
10 Maguire Road
Lexington, MA 02173

William K. Connor
Tracor Applied Sciences
Analysis and Applied Research Div.
9150 Chesapeake Drive
San Diego, CA 92123

Leonard P. Cuzzupe
U. S. Army
Army Materials & Mechanics Res. Center
Arsenal Street
Watertown, MA 02172

Phil Dahl
The Aerospace Corporation
Guidance & Control Division
P. O. Box 92957
El Segundo, CA 90009

Scott R. Dahl
Martin Marietta Corp.
Denver Aerospace
P. O. Box 179, MS-T0510
Denver, CO 80201

Dr. Peter K. Dai
TRW
Development Program
P. O. Box 1310, M/S 953/2130
San Bernardino, CA 92402

Eric C. Dalton
Teledyne Brown Engr.
Systems
Cummings Research Park
Huntsville, AL 35807

Gary A. Davis
Rockwell International
545-128, AC15
6633 Canoga Avenue
Canoga Park, CA 91304

Hugh W. Davis
Ball Corporation
Ball Aerospace Systems Div.
P.O. Box 1062
Boulder, CO 80306

Paul H. Denke
Douglas Aircraft
Engineering Department
3855 Lakewood Boulevard
Long Beach, CA 90846

Scott T. Dennis
Structural Analysis Group
AFWL/ARTC
Kirtland Air Force Base, NM 87117

Tommy L. Dobson
6585 Test Group (AFSC)
Guidance Test Division/GDL
Holloman Air Force Base, NM 88330

Robert E. Donham
Lockheed California Company
Dynamics & Vibration
Mail Stop 76-12
Burbank, CA 91520

Bennie F. Dotson
The Boeing Military Airplane Company
Structures
P.O. Box 3707, MS 41-10
Seattle, WA 98039

Michael L. Drake
University of Dayton
Research Institute
300 College Park
Dayton, OH 45469

Robert R. Dunning
TRW
Applied Technology Division
01/2044, One Space Park
Redondo Beach, CA 90278

Don Edberg
Stanford University
Dept. of Aeronautics & Astronautics
250 Durand Building
Stanford, CA 94305

Arthur Edelstein
NTS
Engineering Div.
26525 Golden Valley Road
Saugus, CA 91350

James A. Eichenlaub
U.S. Air Force
AFWAL/FIBAA
Wright-Patterson AFB, OH 45433

Lee E. Elliott
TRW
Dynamics
One Space Park, 03-2237
Redondo Beach, CA 90278

Richard A. Ely
LTV Vought
Structural Technologies
Box 225907, MS 194-51
Dallas, TX 75265

Remi C. Engels
University of Tennessee Space Institute
ES&M
Tullahoma, TN 37388

Dr. Rena S. Fersht
Litton Industries
Guidance & Control Systems Div.
5500 Canoga Ave., MS 87, Bldg. 31
Woodland Hills, CA 91365

Lawrence E. Flood
The Boeing Company
B-1B Avionics
P.O. Box 3707
Seattle, WA 98124

Norman K. Frater
IBM Corporation
Dept. E34, Bldg. 026
5600 Cottle Road
San Jose, CA 95193

Dr. Joseph A. Fromme
Martin Marietta Denver Aerospace
Analytical Mechanics Department
P.O. Box 179
Denver, CO 80201

William T. Gaddis
Pratt & Whitney
Government Products Div. ME&T
P.O. Box 2691
West Palm Beach, FL 33402

Tony G. Gardner
Gulfstream Aerospace
Commander Division
Box 22500
Oklahoma City, OK 73123

Joseph J. Garibotti
H. R. Textron
2485 McCabe Way
Irvine, CA 92714

Gary A. Gesellchen
IBM
G02/142
5600 Cottle Road
San Jose, CA 95193

Gordon L. Getline
Consultant
4340 Piedmont Drive
San Diego, CA 92107

Ronald F. Gibson
University of Idaho
Mechanical Engineering Department
Gauss Engineering Laboratory
Moscow, ID 83843

Rafael Gluck
TRW STG
Spacecraft Engineering Division
Building R5/2271, One Space Park
Redondo Beach, CA 90278

Gerald E. Goodblood
Federal Aviation Administration
Aircraft Certification Division
601 E. 12th Street
Kansas City, MO 64106

Robert G. Gordon
125 Pacific Street
Santa Monica, CA 90405

Robert W. Gordon
Air Force Wright Aeronautical Labs.
Flight Dynamics Laboratory
AFWAL/FIBAA
Wright-Patterson AFB, OH 45433

Frank Gossett
E-Systems, ECI Division
Mechanical Engineering
P.O. Box 12248
St. Petersburg, FL 33733

Gerald L. Graf
Caterpillar Tractor Co.
Research Department
100 N.E. Adams
Peoria, IL 61629

Inge I.G. Green
Saab-Scania AB
Aircraft Division, Technology Sector
S-58188 Linkoping
SWEDEN

Peter L. Green
Army Missile Command
Army Missile Laboratory, DRSMI-RLA
Redstone Arsenal, AL 35898

Dr. Jerry H. Griffin
Carnegie-Mellon University
Dept. of Mechanical Engineering
Pittsburgh, PA 15213

William S. Griffin
Hughes Aircraft Company
Electrooptical and Data Systems
Bldg. E1, MS D149, P.O. Box 902
El Segundo, CA 90245

John L. Gubser
McDonnell Douglas Astronautics Company
E237-Structural Dynamics and Loads
P. O. Box 516, Room 478
St. Louis, MO 63166

Dr. Walter E. Haisler
Texas A&M University
Aerospace Engineering
College Station, TX 77843

Arthur L. Hale
University of Illinois
Aeronautical & Astronautical Engr.
104 S. Mathews Avenue
Urbana, IL 61801

James H. Hamilton
Lawrence Livermore National Laboratory
Metrology
P.O. Box 808, L-332
Livermore, CA 94550

Brantley R. Hanks
NASA Langley Research Center
Structures & Dynamics Division, SDB
MS-230
Hampton, VA 23665

Harry Harcrow
Martin Marietta Aerospace Corporation
Denver Aerospace
P.O. Box 179, Mail No. M0486
Denver, CO 80201

Roger J. Harding
General Electric Company
Spacecraft Operations
P.O. Box 8555, Bldg. 100, Rm. U7025
Philadelphia, PA 19101

Owen T. Hata
University of Southern California
Civil Engineering
Los Angeles, CA 90007

Richard A. Heller
Ford Aerospace & Communications Corp.
Aeronutronic Division
Ford Road
Newport Beach, CA 92660

Dr. John P. Henderson
Air Force Wright Aeronautical Laboratory
Materials Laboratory
AFWAL/MLLN
Wright-Patterson AFB, OH 45433

Manuel A. Hernandez
IBM
G02/142
5600 Cottle Road
San Jose, CA 95193

Ralph A. Hester
Space Vector Corp.
Mechanical Engineering
19631 Prairie Avenue
Northridge, CA 91324

Robert E. Holman
Hughes Aircraft Company
Electrooptical and Data Systems
Bldg. E1, MS A145, P.O. Box 902
El Segundo, CA 90245

Curtis I. Holmer
E.A.R. Division of Cabot Corp.
Noise Control Application Engineering
7911 Zionsville Road
Indianapolis, IN 46268

Harold F. Honath
Pittsburgh-Des Moines Corp.
Tech. Products Engineering
Neville Island
Pittsburgh, PA 15225

Tateo Hosomura
Nissan Motor Co., LTD.
Aero. & Space Div., Adv. Proj. Promotion
5-1, 3-chome, Momoi, Suginami-ku,
Tokyo 167, JAPAN

Whittak H. Huang
Martin Marietta Aerospace
Denver Division
P.O. Box 179, S0423
Denver, CO 80201

Prof. James Edward Hubbard, Jr.
Massachusetts Institute of Technology
Mechanical Engineering (Sys. & Control)
77 Massachusetts Ave., Room 3-443A
Cambridge, MA 02139

Alexis Hubert
Martin Marietta Aerospace
Denver Division
P.O. Box 179, M/S T0510
Denver, CO 80201

Ronald G. Hund
Beech Aircraft Co.
Engineering, Dept. 90
9709 E. Central
Wichita, KS 67206

James M. Hurdle
General Dynamics Corp.
Fort Worth Division
P.O. Box 748, Mail Zone 2830
Fort Worth, TX 76101

Carl F. Husen
Ford Aerospace & Communications Corp.
Mechanical Engineering Department
Ford Road, Mail Station 5K
Newport Beach, CA 92660

Roy Ikegami
Boeing Aerospace Company
Structural Development
Mail Stop 8C-43, P.O. Box 3999
Seattle, WA 98124

Norman L. Ingold
U.S. Air Force
6585th Test Group/GDA
Holloman Air Force Base, NM 88330

Daniel J. Inman
University at Buffalo
Dept. of Mechanical & Aerospace Eng.
State University of New York
Buffalo, NY 14260

Chingu Ip
TRW, Inc.
Ballistic Missile Division
P.O. Box 1310
San Bernadino, CA 92402

Robert L. Jay
Allison Gas Turbine Operations
Dynamics Department
P.O. Box 420, Mail Code U29A
Indianapolis, IN 46206

Dale L. Jensen
Rockwell International
Dept. 385, Mail Stop AA96
12214 Lakewood Blvd.
Downey, CA 90241

James W. Jeter
Hughes Aircraft Company
Albuquerque Engineering Center
P.O. Box 9301
Albuquerque, NM 87119

Conor D. Johnson
CSA Engineering, Inc.
560 San Antonio Road
Palo Alto, CA 94306

David I.G. Jones
U.S. Air Force
AFWAL/MLLN
Wright-Patterson AFB, OH 45433

Allen Kandelman
Northrop Corporation
Flight Controls
One Northrop Avenue, Dept. 3320/AL
Hawthorne, CA 90250

Abner Kaplan
TRW, Inc.
Structures Department
One Space Park - R5B310
Redondo Beach, CA 90278

Donald J. Karbo
Gould, Inc.
Advanced Technology Center
540 East 105 Street
Cleveland, OH 44120

Keith T. Kedward
Global Analytics Inc.
Structures & Design
10065 Old Grove Road
San Diego, CA 92131

James J. Kerley
Goddard Space Flight Ctr., NASA
Code 7541
Greenbelt Road
Greenbelt, MD 20771

Edward Kerwin
Bolt Beranek and Newman, Inc.
Underwater Technologies, Science Dev. Div.
10 Moulton Street
Cambridge, MA 02238

Gilbert E. Key
Boeing Military Airplane Co.
B-1B
P.O. Box 3707, MS 9H-SS
Seattle, WA 98124

David A. Kienholz
CSA Engineering, Inc.
Dynamic Testing
560 San Antonio Road
Palo Alto, CA 94306

Vikram K. Kinra
Texas A&M University
Aerospace Engineering
College Station, TX 77843

Frank G. Kirschner
Soundcoat Company
1 Burt Drive
Deer Park, LI, NY 11729

Matthew F. Kluesener
University of Dayton
Research Institute
300 College Park, JPC 36
Dayton, OH 45469

James E. Koeqler
Naval Sea Systems Command
Code 05M3
Washington, DC 20362

Frank X. Konsevich
Boeing Military Airplane Company
B-1B
P.O. Box 3707, MS 9H-55
Seattle, WA 98124

Edward F. Korn
Lockheed Missiles and Space
Department 7740
P.O. Box 1506
Vandenburg Air Force Base, CA 93437

Thomas J. Lagnese
Universal Energy Systems, Inc.
4401 Dayton-Xenia Road
Dayton, OH 45432

Chung Lam
IBM
G02/142
5600 Cottle Road
San Jose, CA 95193

Hassel Ledbetter
National Bureau of Standards
Fracture and Deform.
325 S. Broadway
Boulder, CO 80303

Eric S. Lee
Soundcoat Company
3002 Croddy Way
Santa Ana, CA 92704

Gilbert F. Lee
Naval Surface Weapons Center
Nonmetallic Materials, Code R31
White Oak Laboratory
Silver Spring, MD 20910

Howard Lee
IBM Corporation
GPD
5600 Cottle Road, E34/026
San Jose, CA 95193

Usik Lee
Stanford University
Mechanical Engineering
Applied Mechanics Division
Stanford, CA 94305

Arthur W. Leissa
The Ohio State University
Department of Engineering Mechanics
155 W. Woodruff
Columbus, OH 43210

Peter W. Lenkey
Douglas Aircraft Company
Dynamics
3855 Lakewood Boulevard
Long Beach, CA 90802

Walt Leodolter
Douglas Aircraft Company
Structural Design, Dept. Cl-E24
3855 Lakewood Boulevard
Long Beach, CA 90846

George Lesieutre
H. R. Textron
2485 McCabe Way
Irvine, CA 92714

Karl Liehr
Lockheed California Company
Dynamics
P.O. Box 551
Burbank, CA 91520

Yu-Jyi Lin
Hughes Aircraft Company
Space and Strategic Eng.
2000 El Segundo Blvd.
El Segundo, CA 90245

Kenneth G. Lindh
Northrop Corporation
Aircraft Group
One Northrop Avenue, 3858/82
Hawthorne, CA 90250

Chang P. Liu
Hughes Aircraft Company
Mechanical Devices Department
2000 E. El Segundo Boulevard
El Segundo, CA 90245

Malcolm H. Lock
R&D Associates
Engineering Sciences
International Airport ATO-9377
Albuquerque, NM 87119

Irvin J. Loeffler
NASA Lewis Research Center
Propulsion Systems Division
21000 Brookpark Road
Cleveland, OH 44135

Daniel R. Lorch
Douglas Aircraft Company
Acoustics Engineering
3855 Lakewood Boulevard
Long Beach, CA 90846

Leo K. Lu
Westinghouse
Marine Division
Sunnyvale, CA 94088

Y. P. Lu
David Taylor Naval Ship R&D Center
Machinery Silencing Div., Code 2742
Annapolis, MD 21402

Sash Lulla
RCA
Astro-Electronics, Suite 210
2627 Manhattan Beach Blvd., Bldg. C
Redondo Beach, CA 90278

Michael P. MacDonald
The Babcock and Wilcox Company
Research and Development Division
1562 Beeson Street
Alliance, OH 44601

Walter M. Madigosky
Naval Surface Weapons Center
Materials Division, Code R31
White Oak Laboratory
Silver Spring, MD 20910

Carolyn S. Major
TRW
Control Systems Engineering Dept.
1 Space Park, M.S. 82/2033
Redondo Beach, CA 90278

James A. Malthan
Agbabian Associates
250 North Nash Street
El Segundo, CA 90245

James W. Mar
Massachusetts Institute of Technology
Dept. of Aeronautics and Astronautics
33-309 - 77 Massachusetts Ave.
Cambridge, MA 02139

Larry D. Mardis
General Dynamics
Pomona Division
P.O. Box 2507, MZ4-40
Pomona, CA 91769

WD-A152 547

VIBRATION DAMPING WORKSHOP PROCEEDINGS HELD AT LONG
BEACH CALIFORNIA ON 2..(U) AIR FORCE WRIGHT
AERONAUTICAL LABS WRIGHT-PATTERSON AFB OH L ROGERS

11/11

UNCLASSIFIED

11 NOV 84 AFMAL-TR-84-3064

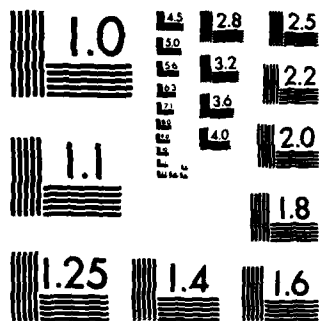
F/G 20/11

NL

END

FILMED

DTL



MICROCOPY RESOLUTION TEST CHART
NATIONAL BUREAU OF STANDARDS-1963-A

Sami F. Masri
University of Southern California
Civil Engineering
VHE 406
Los Angeles, CA 90089

Gary G. Matthews
Eastman Kodak
Research and Engineering
901 Elmgrove Road
Rochester, NY 14650

Ron A. Mayo
TRW, Inc.
Control Systems Engineering Dept.
One Space Park, 03/2687
Redondo Beach, CA 90278

James J. McEnnan
Hughes Aircraft Company
Space & Communications, Bldg. S41
M/S B323, P.O. Box 92917, Airport Station
Los Angeles, CA 90009

Ronald L. McLean
Houdaille Industries
Hydraulics Division
537 East Delavan Avenue
Buffalo, NY 14211

F. Ward Melching
Aerospace Corporation
Structural Dynamics, M4-911
2350 E. El Segundo Blvd.
El Segundo, CA 90245

Stanley C. Mellin
Rockwell International
North American Aviation Operations
Box 92008
Los Angeles, CA 90009

William W. Metzger
RCA
Astroelectronics Division
P.O. Box 800
Princeton, NJ 08540

Ronald N. Miles
The Boeing Company
Noise Research Unit
P.O. Box 3707, M/S 9W-65
Seattle, WA 98124

Timothy M. Minahen
Rockwell International
Rocketdyne
6633 Canoga Avenue
Canoga Park, CA 91304

Mohan S. Misra
Martin Marietta Aerospace
Materials Engineering
P.O. Box 179, MS 80487
Denver, CO 80201

Dr. Mehran Mobrem
Astro Research Corporation
6390 Cindy Lane
Carpinteria, CA 93013

Zafar A. Momin
General Motors Research Labs.
Engineering Mechanics
GM Technical Center
Warren, MI 48090

Dr. George Morosow
Martin Marietta Corporation
Analytical Mechanics, Mail #M0486
P.O. Box 179
Denver, CO 80201

Bruce Morton
General Electric Company
Space Systems Division
P.O. Box 8555
Philadelphia, PA 19101

Ahid D. Nashif
Anatrol Corporation
10895 Indeco Drive
Cincinnati, OH 45241

Hank E. Nauert
Federal Aviation Administration
Aircraft Certification Division
601 East 12th Street, Mail Code ACE-112
Kansas City, MO 64106

Frederick C. Nelson
Tufts University
College of Engineering
Medford, MA 02155

John H. Nester
General Electric Company
Engine Product Integrity
Jimson Road, Mail Drop J40
Cincinnati, OH 45215

Ted S. Nishimoto
Rockwell International
Satellite Sys., D/794-500, M/C SL26
12214 Lakewood Boulevard
Downey, CA 90241

Dr. Patrick M. Niskode
General Electric Company
Aircraft Engines Division
Mail Stop G-62
Cincinnati, OH 45215

Robert P. O'Donnell
MRJ, Inc.
10400 Eaton Pl.
Fairfax, VA 22030

George S. Pal
IBM
GPD E34-026
5600 Cottle Road
San Jose, CA 95193

Michael L. Parin
Anatrol Corporation
10895 Indeco Drive
Cincinnati, OH 45241

K. C. Park
Lockheed Palo Alto Research Lab.
Applied Mechanics Laboratory
Palo Alto, CA 94304

James H. Peebles
McDonnell Douglas Astronautics Co.
Engineering
5301 Bolsa Avenue, M.S. 13-3
Huntington Beach, CA 92647

Robert C. Peller
General Dynamics
Convair San Diego Division
P.O. Box 85357, M/Z 84-6970
San Diego, CA 92138

Al R. Pena
Aerospace Corporation
NAVSTAR Program Office
2350 East El Segundo Blvd., MS M5686
El Segundo, CA 90245

Thomas E. Pollak
RCA Astro Electronics
Government Systems Division
P.O. Box 800
Princeton, NJ 08540

Robert W. Postma
The Aerospace Corporation
Vehicle Engineering
P.O. Box 92957, M4/923
Los Angeles, CA 90009

Richard C. Quartaro
H. R. Textron
2485 McCabe Way
Irvine, CA 92714

Kenneth W. Ranger
Aerojet Electro Systems
Applied Mechanics, 4325
P.O. Box 296
Azusa, CA 91702

Dantam K. Rao
Air Force Wright Aeronautical Labs.
Materials Laboratory, AFWAL/MLLN
Metals and Ceramics Division
Wright-Patterson AFB, OH 45433

George R. Rapacki
Martin Marietta Aerospace
Guidance Navigation & Control
P.O. Box 179, MS T-0510
Denver, CO 80201

Lawrence W. Rehfield
Georgia Institute of Technology
Aerospace Engineering
Atlanta, GA 30332

Robert B. Rice
Martin Marietta Aerospace, Denver
Guidance & Control
P.O. Box 179, MS T0510
Denver, CO 80201

John M. Richardson
Air Force Weapons Laboratory
AFWL/ARAA
Kirtland Air Force Base, NM 87117

Richard A. Russell
NASA
RTH-6
Washington, DC 20546

E. C. Ricker
Hughes Aircraft Company
Mechanical Development Dept.
P.O. Box 3310, Bldg. 604 M/S D230
Fullerton, CA 92634

Celeste M. Satter
The Charles Stark Draper Lab.
Advanced Systems Department
555 Technology Square
Cambridge, MA 02139

Neville F. Rieger
Stress Technology Incorporated
Technical Manager
1800 Brighton-Henrietta Townline Rd.
Rochester, NY 14623

Dwaine E. Schilling
Martin Marietta Corporation
Denver Aerospace Division
P.O. Box 179
Denver, CO 80201

John A. Roberts
Atlantic Richfield Co.
Corporate Technology
20717 Prairie Street
Chatsworth, CA 91311

Daniel J. Scott
U. S. Air Force
6585 TG-GDOI
Holloman AFB, NM 88330

Philip Robertson
Aerospace Corporation
AOSD, M6/213
2350 E. El Segundo Blvd.
El Segundo, CA 90245

William D. Sell
3M Company
Structural Products
3M Center, Bldg. 230-1S
St. Paul, MN 55144

Dr. Lynn C. Rogers
Air Force Wright Aeronautical Labs.
Flight Dynamics Laboratory
AFWL/FIBA
Wright-Patterson AFB, OH 45433

Gautam SenGupta
Boeing Comm. Airplane Company
Noise Research
P.O. Box 3707, M/S 9W-65
Seattle, WA 98124

Joseph S. Rosenthal
Rockwell International
North American Aircraft Operation
P.O. Box 92098
Los Angeles, CA 90009

John R. Sesak
General Dynamics Convair
Advanced Space Systems
5001 Kearny Villa Road
San Diego, CA 92138

Dr. Sheldon Rubin
The Aerospace Corporation
M/S 4/899
P.O. Box 92957
Los Angeles, CA 90009

Capt. Raymond L. Sheen
Air Force Systems Command
Ballistics Missile Office
BMO/ENMR
Norton Air Force Base, CA 92409

Carl L. Rupert
Air Force Wright Aeronautical Labs.
Flight Dynamics Laboratory
AFWL/FIBED
Wright-Patterson AFB, OH 45433

Frederick A. Shen
Rockwell International
Rocketdyne Div., Structural Dynamics
6633 Canoga Avenue
Canoga Park, CA 91304

George D. Shipway
Wyle Laboratories
P.O. Box 160
Norco, CA 91760

Dr. Keto Soosaar
The Charles Stark Draper Laboratory
Structures & Dynamics Division
555 Technology Square
Cambridge, MA 02139

Edward F. Shroyer
Rockwell International - NAAO
Structures and Design
P.O. Box 92098, M.S. GD04
Los Angeles, CA 90009

Jaak Soovere
Lockheed-California Company
D 76-12, B63G, Plt. A1
P.O. Box 551
Burbank, CA 91520

Dr. Emile M. Shtarkman
Imperial Clevite, Inc.
Technology Center
540 E. 105th Street
Cleveland, OH 44108

A. V. Srinivasan
United Technologies Research Center
Applied Mechanics Research
Silver Lane, Mail Stop 18
East Hartford, CT 06108

Joel Signorelli
Air Force Rocket Propulsion Laboratory
Interdisciplinary Space Technology
AFRPL/DYS, Stop 24
Edwards Air Force Base, CA 93523

Clyde V. Stahle
General Electric Company
Space Systems Div., VFSC 100/M4018
P.O. Box 8555
Philadelphia, PA 19101

1st Lt. Kevin J. Silva
U.S. Air Force
Space Division, YNAV
Los Angeles Air Force Station, CA 90009

James A. Staley
General Electric
Space Systems Div., VFSC 100/M4018
P.O. Box 8555
Philadelphia, PA 19101

Wayne E. Simon
Martin Marietta
Denver Aerospace
P.O. Box 179
Denver, CO 80201

Dave S. Steinberg
Litton GCS
Mechanical Engineering, M.S. 86/31
5500 Canoga Avenue
Woodland Hills, CA 91365

S. S. Simonian
TRW, Inc.
Space and Technology Group
One Space Park, R4-1082
Redondo Beach, CA 90278

Jay W. Stuart
Spacecom
Spacecraft Engineering
5155 West Rosecrans Avenue
Hawthorne, CA 90250

Scott S. Simpson
Rogers Corporation
One Technology Drive
Rogers, CT 06263

C. T. Sun
University of Florida
Department of Engineering Sciences
231 Aerospace Engineering Bldg.
Gainesville, FL 32611

S. R. Skale
AiResearch Mfg. Co.
2525 West 190th Street
Torrance, CA 90509

Mark W. Sutterlin
Bolt Beranek & Newman, Inc.
1300 N. 17th Street
Arlington, VA 22209

Charles Sve
Aerospace Corporation
Mechanics Research Department
P.O. Box 92957, M5-753
Los Angeles, CA 90009

Keithie D. Tabor
Air Force Rocket Propulsion Laboratory
Interdisciplinary Space Technology
AFRPL/DYSS, Stop 24
Edwards Air Force Base, CA 93523

Capt. David V. Thyfault
Air Force Space Division
Los Angeles AF Station/YNS
P.O. Box 92960, World Way Postal Center
Los Angeles, CA 90009

Al G. Tipton
Rockwell
NAAO
P.O. Box 92098
Los Angeles, CA 90009

Peter John Torvik
Air Force Institute of Technology
Department of Aero. & Astro./ENY
Wright-Patterson AFB, OH 45433

Joseph M. Toth, Jr.
Martin Marietta Denver Aerospace
Denver Aerospace
P.O. Box 179
Denver, CO 80201

Richard W. Trudell
McDonnell Douglas Astronautics Co.
Engineering
5301 Bolsa Avenue, M.S. 13-3
Huntington Beach, CA 92647

G. T. Tseng
The Aerospace Corporation
Guidance & Control
P.O. Box 92957, MS M4/971
Los Angeles, CA 90009

Dr. Horn-Sen Tzou
North Carolina A&T State University
Dept. of Mechanical Engineering
Greensboro, NC 27411

Eric E. Ungar
Bolt Beranek and Newman, Inc.
BBN Laboratories
10 Moulton Street
Cambridge, MA 02238

James F. Unruh
Southwest Research Institute
Department of Engineering Mechanics
6220 Culebra Road
San Antonio, TX 78284

Robert H. VanVooren
TRW Space and Technology Group
Engineering Division
One Space Park, R4 1198
Redondo Beach, CA 90278

Charles A. Vickery
TRW
Defense Systems Group
P.O. Box 1310, Mail Stop 526/626
San Bernadino, CA 92402

Sasto J. Voce
TRW, Inc.
Structures Department
One Space Park - R5B310
Redondo Beach, CA 90278

Ben K. Wada
Jet Propulsion Laboratory
Applied Mechanics Technology Section
4800 Oak Grove Drive, M/S 157/507
Pasadena, CA 91109

William J. Walker
Boeing Aerospace Company
Structural Development
Mail Stop 8C-43, P.O. Box 3999
Seattle, WA 98124

Dr. C. E. Wallace
Arizona State University
Dept. of Mechanical and Aerospace Eng.
Tempe, AZ 85287

Joe S. Warrick
Oklahoma City Air Logistics Center
OC-ALC/MMBRE
Tinker Air Force Base, OK 73145

Charles E. Wedell
AFFDL Representative
West Coast Office
Box 92960 Worldway Postal Center
Los Angeles, CA 90009

Charles W. White
Martin Marietta Corporation
Analytical Mechanics - Mail #M0486
P.O. Box 179
Denver, CO 80201

James S. Whittier
Aerospace Corporation
Mechanics Research Department
P.O. Box 92957, M5-753
Los Angeles, CA 90009

James F. Wilson
Sperry Corporation
Flight Systems/Mechanical Engr. Dept.
P. O. Box 29222
Phoenix, AZ 85038

Sherry A. Winkleblack
Boeing Aerospace Company
Flight Technology
P.O. Box 3999, MS 8C-39
Seattle, WA 98124

N. X. Xinh
University of Colorado
Dept. of Aerospace Engineering Sciences
Campus Box 429
Boulder, CO 80309

END

FILMED

5-85

DTIC